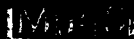
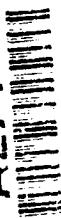


Jonker
Chambers
Farrow
Chappert
Clarke
de Jonge
Egami
Grünberg
Krishnan
Marinero
Rau
Tsunashima
EDITORS



VOLUME 313

AD-A271 402



VOLUME 313

Magnetic Ultrathin Films

*Multilayers and Surfaces,
Interfaces and Characterization*

EDITORS

B.T. Jonker
Scott A. Chambers
R.F.C. Farrow
C. Chappert
R. Clarke
W.J.M. de Jonge
Takeshi Egami
P. Grünberg
Kannan M. Krishnan
Ernesto E. Marinero
Carl Rau
Shigeru Tsunashima

Magnetic Ultrathin Films
Multilayers and Surfaces, Interfaces and Characterization

for public release and sale in
unlimited quantities

93-25506



Magnetic Ultrathin Films
Multilayers and Surfaces
Interfaces and Characterization

DTIC QUALITY INSPECTED 2

Accession For		
NTIS	CRA&I	<input checked="" type="checkbox"/>
DTIC	TAB	<input type="checkbox"/>
Unannounced		<input type="checkbox"/>
Justification		
By		
Distribution /		
Availability Codes		
Dist	Avail and/or Special	
A-1		

93 10 21 189

Magnetic Ultrathin Films
Multilayers and Surfaces
Interfaces and Characterization

Symposium held April 12-16, 1993, San Francisco, California, U.S.A.

EDITORS:

B.T. Jonker

Naval Research Laboratory
Washington, D.C., U.S.A.

Scott A. Chambers

Pacific Northwest Laboratory
Richland, Washington, U.S.A.

R.F.C. Farrow

IBM Almaden Research Center
San Jose, California, U.S.A.

C. Chappert

CNRS-Université Paris Sud
Orsay, France

R. Clarke

University of Michigan
Ann Arbor, Michigan, U.S.A.

W.J.M. de Jonge

Eindhoven University
of Technology
Eindhoven, The Netherlands

Takeshi Egami

University of Pennsylvania
Philadelphia, Pennsylvania, U.S.A.

P. Grünberg

Forschungszentrum Jülich
Jülich, Germany

Kannan M. Krishnan

Lawrence Berkeley Laboratory
Berkeley, California, U.S.A.

Ernesto E. Marinero

IBM Almaden Research Center
San Jose, California, U.S.A.

Carl Rau

Rice University
Houston, Texas, U.S.A.

Shigeru Tsunashima

Nagoya University
Nagoya, Japan



MATERIALS RESEARCH SOCIETY
Pittsburgh, Pennsylvania

This work relates to Department of Navy Grant N00014-93-1-0472 issued by the Office of Naval Research. The United States Government has a royalty-free license throughout the world in all copyrightable material contained herein.

This work relates to Department of Navy Grant N00014-93-1-0365 issued by the Office of Naval Research. The United States Government has a royalty-free license throughout the world in all copyrightable material contained herein.

Single article reprints from this publication are available through
University Microfilms Inc., 300 North Zeeb Road, Ann Arbor, Michigan 48106

CODEN: MRSPDH

Copyright 1993 by Materials Research Society.
All rights reserved.

This book has been registered with Copyright Clearance Center, Inc. For further information, please contact the Copyright Clearance Center, Salem, Massachusetts.

Published by:

Materials Research Society
9330 McKnight Road
Pittsburgh, Pennsylvania 15237
Telephone (412) 367-3003
Fax (412) 367-4373

Library of Congress Cataloging in Publication Data

Magnetic ultrathin films / editors, B.T. Jonker, Scott A. Chambers, R.F.C. Farrow, C. Chappert, R. Clarke, W.J.M. de Jonge, Takeshi Egami, P. Grünberg, Kannan M. Krishnan, Ernesto E. Marinero, Carl Rau, Shigeru Tsunashima
p. cm.—(Materials Research Society symposium proceedings ; v. 313)
Includes bibliographical references and index.

Contents: Session A. Multilayers and surfaces — Session B. Interfaces and characterization.

ISBN 1-55899-211-1

1. Thin films, Multilayered—Magnetic properties—Congresses. 2. Thin films—Surfaces—Magnetic properties—Congresses. 3. Magnetic films—Congresses. 4. Magnetoresistance—Congresses. I. Jonker, B.T. II. Chambers, Scott A. III. Farrow, R.F.C. IV. Chappert, C. V. Clarke, R. VI. de Jonge, W.J.M. VII. Egami, Takeshi VIII. Grünberg, P. IX. Krishnan, Kannan M. X. Marinero, Ernesto E. XI. Rau, Carl XII. Tsunashima, Shigeru XIII. Materials Research Society XIV. Series: Materials Research Society symposium proceedings ; v. 313.

QC176.9.M84M38 1993
530.4'275—dc20

93-30191
CIP

Manufactured in the United States of America

Contents

PREFACE	xv
ACKNOWLEDGMENTS	xvii
MATERIALS RESEARCH SOCIETY SYMPOSIUM PROCEEDINGS	xviii

Section A *Multilayers and Surfaces*

PART I: GIANT MAGNETORESISTANCE IN MULTILAYERS: ROLE OF INTERFACE STRUCTURE

*OSCILLATIONS IN EXCHANGE COUPLING IN Co/Cu MULTILAYERS GROWN BY MBE D. Greig, M.J. Hall, M.A. Howson, B.J. Hickey, M.J. Walker, and J. Xu	3
*PERPENDICULAR MAGNETORESISTANCE OF MICROSTRUCTURED PILLARS IN Fe/Cr MAGNETIC MULTILAYERS M.A.M. Gijs, S.K.J. Lenczowski, and J.B. Giesbers	11
*THEORY OF THE NEGATIVE MAGNETORESISTANCE IN MAGNETIC METALLIC MULTILAYERS Randolph Q. Hood and L.M. Falicov	23
HIGH-FIELD GIANT MAGNETORESISTANCE IN Co-Cu SUPERLATTICES Darryl Barlett, Frank Tsui, Lincoln Lauhon, Tushar Mandrekar, Citrad Uher, and Roy Clarke	35
GROWTH TEMPERATURE DEPENDENCE OF MAGNETORESISTANCE IN Co/Cu(111) WEDGED SUPERLATTICES G.R. Harp, S.S.P. Parkin, R.F.C. Farrow, R.F. Marks, M.F. Toney, Q.H. Lam, T.A. Rabedeau, A. Cebollada, and R.J. Savoy	41
PERPENDICULAR MAGNETORESISTANCE IN Cu/Co AND Cu/(NiFe) MULTILAYERS P.A. Schroeder, J. Bass, P. Holody, S.-F. Lee, R. Loloee, W.P. Pratt, Jr., and Q. Yang	47
INFLUENCE OF SUPERLATTICE POTENTIALS ON TRANSPORT IN MAGNETIC MULTILAYERS Shufeng Zhang and Peter M. Levy	53
GIANT MAGNETORESISTANCE CALCULATED FROM FIRST PRINCIPLES W.H. Butler, James M. MacLaren, and X.-G. Zhang	59
CALCULATIONS OF BULK AND SURFACE MAGNETIC POLARITONS IN MODULATED ANTIFERROMAGNETIC/NON-MAGNETIC SUPERLATTICES Fred Lacy, Ernest L. Carter, Jr., and Steven L. Richardson	65

*Invited Paper

**PART II: GIANT MAGNETORESISTANCE IN ALLOYS:
A SIMPLE ROUTE TO MAGNETIC DEVICES?**

MODELING GIANT MAGNETORESISTANCE AND RELATIVE PERMEABILITY IN GRANULAR FILMS M.R. Parker, J.A. Barnard, S. Hossain, D. Seale, M. Tan, and A. Wakis	73
GIANT MAGNETORESISTANCE IN SPUTTER-DEPOSITED GRANULAR Ag-Co THIN FILMS W.Y. Lee, V.R. Deline, G. Gorman, A. Kellock, D. Miller, D. Neiman, R. Savoy, J. Vazquez, and R. Beyers	79
THE MICROSTRUCTURE AND GIANT MAGNETORESISTANCE OF NiFeAg THIN FILMS Michael A. Parker, K.R. Coffey, T.L. Hylton, and J.K. Howard	85

PART III: INTERLAYER COUPLING I

*ORIENTATIONAL DEPENDENCE OF OSCILLATORY EXCHANGE COUPLING M.T. Johnson, P.J.H. Bloemen, R. Coehoorn, J.J. de Vries, N.W.E. McGee, R. Jungblut, A. Reinders, and J. aan de Stegge	93
*OSCILLATORY INDIRECT COUPLING BETWEEN PERPENDICULARLY MAGNETIZED Co MONOLAYERS THROUGH Cu(111) Ulrich Gradmann, Hans-Joachim Elmers, and Juergen Kohlhepp	107
STUDIES OF EXCHANGE COUPLING IN Fe(001) WHISKER/Cr/Fe STRUCTURES USING BLS AND RHEED TECHNIQUES B. Heinrich, M. From, J.F. Cochran, L.X. Liao, Z. Celinski, C.M. Schneider, and K. Myrtle	119
MAGNETIC AND TRANSPORT BEHAVIOR OF AF-COUPLED LAYERS WITH A LIMITED NUMBER OF REPETITIONS M.M.H. Willekens, H.J.M. Swagten, A.M. Duif, P.J.H. Bloemen, R.J.T. Van Kempen, S.K.J. Lenczowski, and W.J.M. de Jonge	129
DIRECT EVIDENCE OF BIQUADRATIC COUPLING IN MULTILAYERS BY NEUTRON SCATTERING EXPERIMENTS Stéphane Andrieu, Martine Hennion, and Michel Picuch	135

PART IV: INTERLAYER COUPLING II

*ELECTRONIC STATES IN MAGNETIC QUANTUM WELLS J.E. Ortega, F.J. Himpsel, G.J. Mankey, and R.F. Willis	143
*QUANTUM WELL STATES IN Fe(100) ULTRATHIN FILMS OBSERVED BY MAGNETO-OPTICAL EFFECT Yoshishige Suzuki and Toshikazu Katayama	153
QUANTUM-WELL CONTRIBUTIONS TO THE RKKY COUPLING IN MAGNETIC MULTILAYERS B.A. Jones and C.B. Hanna	165
EFFECT OF HYBRIDIZATION ON EXCHANGE COUPLING IN MAGNETIC MULTILAYERS J. Mathon, M.A. Villeret, J.M. Mander, D.M. Edwards, and R.B. Muniz	171

*Invited paper

PART V: GIANT MAGNETORESISTANCE IN MULTILAYERS I

INCREASE IN PERIOD OF OSCILLATORY COUPLING IN Cu BY DOPING WITH Ni S.S.P. Parkin, C. Chappert, and F. Herman	179
GIANT MAGNETORESISTANCE IN SPUTTERED NiFe/Ag MULTILAYERS B. Rodmacq, A. Mallon, and Ph. Gerard	185
GIANT MAGNETORESISTANCE IN Co/Ag MULTILAYERS M. Tan, J.A. Barnard, M.R. Parker, and D. Seale	191
GIANT MAGNETORESISTANCE IN ANNEALED Fe/Cr MULTILAYERS Noa More Rensing and Bruce M. Clemens	197

PART VI: STRUCTURE AND MAGNETISM I

GRAIN BOUNDARY DIFFUSION IN Co/Cu AND Co/Cr MAGNETIC THIN FILMS John G. Holl-Pellerin, S.G.H. Anderson, P.S. Ho, K.R. Coffey, J.K. Howard, and K. Barmak	205
QUANTITATIVE ANALYSIS OF POLARIZED NEUTRON SPECULAR REFLECTIVITY FROM A Co/Cu(111) SUPERLATTICE AT THE SECOND ANTIFERROMAGNETIC MAXIMUM J.F. Ankner, A. Schreyer, C.F. Majkrzak, K. Bröhl, Th. Zeidler, P. Bödeker, and H. Zabel	213
SPIN POLARIZED LOW ENERGY ELECTRON MICROSCOPY (SPLEEM) OF SINGLE AND COMBINED LAYERS OF Co, Cu, AND Pd ON W(110) Helmut Poppa, Heiko Pinkvos, Karsten Wurm, and Ernst Bauer	219
OBSERVATION OF X-RAY ABSORPTION MAGNETIC CIRCULAR DICHROISM IN WELL-CHARACTERIZED IRON-COBALT-PLATINUM MULTILAYERS A.F. Jankowski, G.D. Waddill, and J.G. Tobin	227

PART VII: STRUCTURE AND MAGNETISM II

MAGNETIC PROPERTIES OF EPITAXIAL 6 ML fcc-Fe/Cu(100) FILMS L.J. Swartzendruber, L.H. Bennett, M.T. Kief, and W.F. Egelhoff, Jr.	237
CRYSTALLOGRAPHIC STRUCTURE OF COBALT FILMS ON Cu (100) O. Heckmann, H. Magnan, P. Le Fevre, and D. Chandesris	245
IN SITU RHEED AND MAGNETO-OPTIC STUDY OF ULTRATHIN COBALT FILMS ON (111) GOLD SUBSTRATE: EFFECT OF A METALLIC OVERLAYER S. Ould-Mahfoud, R. Megy, N. Bardou, B. Bartenlian, P. Beauvillain, C. Chappert, J. Corno, B. Lecuyer, G. Sczigel, P. Veillet, and D. Weller	251
*THEORETICAL STUDIES ON THE MAGNETIC MOMENTS OF IRON NITRIDES INCLUDING Fe ₁₆ N ₂ Akimasa Sakuma and Yutaka Sugita	257

*Invited Paper

**PART VIII: GIANT MAGNETORESISTANCE IN LOW FIELDS:
MULTILAYERS AND SPIN VALVES**

*GIANT MAGNETORESISTANCE AND SOFT MAGNETIC PROPERTIES OF NiFeCo/Cu MULTILAYERS S. Tsunashima, M. Jimbo, T. Kanda, S. Goto, and S. Uchiyama	271
COMBINED SPIN VALVE AND ANISOTROPIC MAGNETORESISTANCE IN NiFe/Cu/NiFe LAYERED THIN FILMS Th. G.S.M. Rijks, R. Coehoorn, and W.J.M. de Jonge	283
ANNEALED Cu/Co/Cu/NiFe/FeMn SPIN VALVES: NANOSTRUCTURE AND MAGNETISM C. Meny, J.P. Jay, P. Panissod, P. Humbert, V.S. Speriosu, H. Lefakis, J.P. Nozieres, and B.A. Gurney	289

**PART IX: MAGNETISM AND STRUCTURE IN
ULTRATHIN FILMS**

A TIGHT-BINDING STUDY OF VERY THIN TRANSITION METAL FILM MAGNETIC ANISOTROPY Š. Pick and H. Dreysse	297
SPIN WAVE PROPAGATION AND BRILLOUIN LIGHT SCATTERING ON ANTIFERROMAGNETICALLY COUPLED BILAYERS R.L. Stamps and R.E. Camley	303
MAGNETIC ANISOTROPY IN EPITAXIAL Ni/Cu (100) THIN FILMS C. Bochi, C.A. Ballentine, H.E. Inglefield, S.S. Bogomolov, C.V. Thompson, and R.C. O'Handley	309
MAGNETIZATION REVERSAL IN CoPt MAGNETOOPTIC RECORDING ALLOYS T. Kleinfeld, W.S. Kim, J. Valentin, and D. Weller	315
VANADIUM AS OVERLAYER ON Ag(001) H. Nait-Laziz, C. Demangeat, and A. Mokrani	321
STRONG INFLUENCE OF Tb CONCENTRATION ON DOMAIN STRUCTURE AND KERR EFFECT OF Tb _{1-x} Fe _x THIN FILMS V. Florescu, C. Rau, and N.J. Zheng	327
NEUTRON AND X-RAY SCATTERING STUDIES OF (FeF ₂) _m (CoF ₂) _n MULTILAYERS D. Lederman, D.P. Belanger, J. Wang, S-J. Han, C. Paduani, C.A. Ramos, and R.M. Nicklow	333
MAGNETIC PROPERTIES AND CRYSTAL STRUCTURE OF HIGH MOMENT FeTaN THIN FILMS G. Qiu, E. Haftek, J.C. Cates, C. Alexander, Jr., and J.A. Barnard	339
MAGNETOSTRICTION AND STRESS IN HIGH MOMENT FeTaN FILMS J.C. Cates, G. Qiu, E. Haftek, C. Alexander, Jr., and J.A. Barnard	345
FERRIMAGNETIC COBALT FERRITE FILMS PREPARED BY THE SOL-GEL PROCESS Eva M. Wong, Haixing Zheng, John D. Mackenzie, and T. Tsuchiya	351
DEVELOPMENT OF CRYSTALLOGRAPHIC TEXTURE IN RF SPUTTER DEPOSITED CoCrTa/Cr THIN FILMS Y.C. Feng, D.E. Laughlin, and D.N. Lambeth	357

*Invited Paper

IN SITU ANALYSIS OF MAGNETIC AND STRUCTURAL PROPERTIES OF EPITAXIAL AND POLYCRYSTALLINE $\text{Ni}_{80}\text{Fe}_{20}$ THIN FILMS I. Hashim and H.A. Atwater	363
EPITAXIAL GROWTH OF fcc Fe AND Cu FILMS ON DIAMOND D.P. Pappas, J.W. Glesener, V.G. Harris, J.J. Krebs, Y.U. Idzerda, A.A. Morrish, and G.A. Prinz	369
THE INFLUENCE OF QUANTIZING MAGNETIC FIELD ON THE MAGNETIC SUSCEPTIBILITIES IN ULTRA THIN FILMS OF DILUTE MAGNETIC MATERIALS Kamakhya P. Ghatak and S.N. Biswas	375
MAGNETIC ORDERING OF Mn OVERLAYERS ON Fe(100) T.G. Walker and H. Hopster	381
STRUCTURAL AND MAGNETIC PROPERTIES OF e^- -BEAM PREPARED $\text{Co}_x\text{Pt}_{1-x}$ ALLOY FILMS J.V. Harzer, B. Hillebrands, I.S. Pogosova, M. Herrmann, G. Güntherodt, and D. Weller	387
MAGNETORESISTANCE AND STRUCTURE OF GRANULAR Co/Ag THIN FILMS Mary Beth Stearns and Yuanda Cheng	393
GIANT MR IN GRANULAR SYSTEMS PREPARED BY MELT-SPINNING AND SPUTTERING B. Dieny, S.R. Teixeira, B. Rodmacq, A. Chamberod, J.B. Genin, S. Auffret, P. Gerard, O. Redon, J. Pierre, R. Ferrer, and B. Barbara	399
GIANT MAGNETORESISTANCE IN GRANULAR $\text{Ni}_{81}\text{Fe}_{19}$ /Ag FORMED FROM ANNEALED MULTILAYERS X. Bian, A. Zaluska, Z. Altounian, J.O. Ström-Olsen, Y. Huai, and R.W. Cochrane	405
GIANT MAGNETORESISTANCE AND STRUCTURE OF PHASE- SEGREGATED EPITAXIAL METALS R.F. Marks, R.F.C. Farrow, G.R. Harp, S.S.P. Parkin, T.A. Rabedeau, M.F. Toney, A. Cebollada, N. Thangaraj, and Kannan M. Krishnan	411
GIANT MAGNETORESISTANCE IN SINGLE LAYER AND MULTILAYER PHASE SEPARATING ALLOY FILMS S. Hossain, A. Wakis, D. Seale, M. Tan, M.R. Parker, and J.A. Barnard	419
A MICROSTRUCTURAL STUDY OF IRON CARBIDES FORMED BY PLASMA-ENHANCED CHEMICAL VAPOR DEPOSITION (50-800 nm THICK) H. Siriwardane, W.J. James, O.A. Pringle, and J.W. Newkirk	425
DYNAMICAL SCATTERING OF POLARIZED NEUTRONS BY THIN MAGNETIC FILMS V. Nunez, C.F. Majkrzak, and N.F. Berk	431
STRUCTURAL CHARACTERIZATION OF THIN Co/Cu SUPERLATTICES David J. Smith, A.R. Modak, and S.S.P. Parkin	437
PART X: SURFACE MAGNETISM	
THEORY FOR THE NONLINEAR MAGNETO-OPTICAL KERR-EFFECT AT FERROMAGNETIC TRANSITION METAL SURFACES U. Pustogowa, W. Hübner, and K.H. Bennemann	445

CANTED MAGNETIC MOMENTS AT THE Gd(0001) SURFACE Dongqi Li, Jiandi Zhang, P.A. Dowben, K. Garrison, P.D. Johnson, H. Tang, T.G. Walker, H. Hopster, J.C. Scott, D. Weller, and D.P. Pappas	451
IN-SITU MAGNETO-OPTICAL KERR EFFECT OF EPITAXIAL Gd(0001) C. Chappert, D. Weller, H. Tang, J.C. Scott, H. Hopster, and D.P. Pappas	457
PART XI: MAGNETIC BILAYERS, TRILAYERS AND MULTILAYERS	
MODIFICATION OF MAGNETIC COUPLING IN ANTIFERROMAGNETICALLY COUPLED BILAYERS DUE TO THE EXISTENCE OF FERROMAGNETIC PIN HOLES J.F. Bobo, H. Fischer, and M. Piecuch	467
NEW BCT IRON PHASE IN (100) FeIr SUPERLATTICES S. Andrieu, J. Hubsch, M. Piecuch, L. Hennen, and H. Fischer	473
SPIN CONFIGURATIONS AND THE DYNAMIC RESPONSE OF ANTIFERROMAGNETICALLY COUPLED SYSTEMS F.C. Nörtemann, R.L. Stamps, and R.E. Camley	479
MAGNETIZATION LOOPS IN Fe/Ag/Fe/Ni(001) STRUCTURES B. Heinrich, Z. Celinski, H. Konno, A.S. Arrott, M. Rührig, and A. Hubert	485
PART XII: MAGNETIC ANISOTROPY, MAGNETO-OPTICS	
MAGNETO OPTICAL KERR SPECTROSCOPY AS A PROBE OF CHEMICAL ORDERING IN CoPt G.R. Harp, D. Weller, T.A. Rabedeau, R.F.C. Farrow, and R.F. Marks	493
MAGNETO-OPTICAL SPECTRA OF CoPt ₃ : EXPERIMENTS AND FIRST PRINCIPLES CALCULATIONS D. Weller, J. Sticht, G.R. Harp, R.F.C. Farrow, R.F. Marks, and H. Brändle	501
EPITAXIAL FERROMAGNETIC MnGa AND (MnNi)Ga THIN FILMS WITH PERPENDICULAR MAGNETIZATION ON GaAs M. Tanaka, J.P. Harbison, T.D. Sands, B.A. Philips, J. De Boeck, T.L. Cheeks, L.T. Florez, and V.G. Keramidas	507
STUDIES OF MAGNETO-OPTICAL RECORDING IN MULTI-MAGNETIC- LAYER DISK BY ANALYTIC AND SIMULATING APPROACHES Yoshiyuki Kawazoe, Xiao Hu, and Shigeru Honma	513
GROWTH, STRUCTURE AND MAGNETISM OF COBALT-PLATINUM ULTRATHIN FILMS AND SANDWICHES J.P. Deville, A. Barbier, C. Boeglin, and B. Carriere	519
ROUGHNESS AND MAGNETIC PROPERTIES OF Pt/Co MULTILAYERED FILMS S. Sumi, Y. Kusumoto, Y. Teragaki, K. Torazawa, S. Tsunashima, and S. Uchiyama	525
ANOMALOUS PERPENDICULAR ANISOTROPY IN ULTRA-THIN Co FILMS Michael H. Wiedmann, Brad N. Engel, Robert A. Van Leeuwen, Ko Mibu, Teruya Shinjo, and Charles M. Falco	531

Section B

Interfaces and Characterization

PART I: THEORIES AND SPIN POLARIZED SPECTROSCOPIES

*MAGNETISM AND MAGNETIC INTERACTIONS AT TRANSITION METAL SURFACES AND INTERFACES Ruqian Wu, Dingsheng Wang, and A.J. Freeman	541
*MECHANISM FOR THE MAGNETORESISTANCE OF PURE BULK FERROMAGNETS AND COMPOSITE THIN FILM STRUCTURES Mary Beth Stearns	553
SPIN POLARIZED ELECTRON SPECTROSCOPIES OF 3d AND 4f SYSTEMS H. Hopster	565
*PROBING THE SURFACE-VACUUM INTERFACE WITH SPIN-SENSITIVE METASTABLE ATOM DEEXCITATION, ELECTRON CAPTURE AND ELECTRON EMISSION SPECTROSCOPIES G.K. Walters and C. Rau	577
SPIN-RESOLVED PHOTOEMISSION STUDY OF $n=2$ CORE LEVELS OF IRON L.E. Klebanoff, D.G. Van Campen, and R.J. Pouliot	589
SPIN POLARIZATION IN ULTRATHIN Rh LAYERS ON Fe(001) A. Chouairi, H. Dreyse, H. Nait-Laziz, and C. Demangeat	595
MAGNETIC ORDER OF Fe AND Co ON Cu(001) A. Haroun, A. Chouairi, S. Ouannasser, P.J. Jensen, K.H. Bennemann, and H. Dreyse	601

PART II: APPLICATIONS OF SYNCHROTRON RADIATION TECHNIQUES TO MAGNETIC MATERIALS

*SPIN POLARIZED PHOTOEMISSION STUDIES OF QUANTUM WELL STATES IN THIN FILMS P.D. Johnson, N.B. Brookes, Y. Chang, and K. Garrison	609
*MAGNETIC CIRCULAR DICHROISM IN X-RAY ABSORPTION AND CORE-LEVEL PHOTOEMISSION J.G. Tobin, G.D. Waddill, T.H. Gouder, C.A. Colmenares, and D.P. Pappas	619
EVIDENCE FOR SPIN POLARIZATION OF METALLIC COPPER IN Co/Cu AND Fe/Cu MULTILAYERS S. Pizzini, C. Giorgetti, A. Fontaine, E. Dartyge, G. Krill, J.F. Bobo, and M. Piecuch	625
MAGNETIC SPECTRO-MICROSCOPY USING MAGNETO-DICHOIC EFFECTS IN PHOTON-INDUCED AUGER ELECTRON EMISSION C.M. Schneider, K. Meinel, B. Holldack, H.P. Oepen, M. Grunze, and J. Kirschner	631
MCD OBSERVED BY PHOTOEMISSION ON THE 2p LINES OF IRON FILMS UNDER AN EXTERNAL APPLIED FIELD C. Boeglin, E. Beaurepaire, B. Carrière, K. Hricovini, and G. Krill	637

*Invited Paper

STRONG MAGNETIC CIRCULAR DICHROISM IN 4f PHOTOEMISSION Kai Starke, E. Navas, L. Baumgarten, and G. Kaindl	643
--	-----

PART III: STRUCTURAL AND INTERFACIAL CHARACTERIZATION

*MAGNETIC AND STRUCTURAL ANALYSIS OF ULTRA-THIN MAGNETIC FILMS, MULTILAYERS, AND SUPERLATTICES BY MOSSBAUER SPECTROSCOPY J. Freeland, D. Keavney, D. Storm, and J. Calvin Walker	651
*AUGER ELECTRON AND PHOTOELECTRON DIFFRACTION IN MAGNETIC THIN FILMS Y.U. Idzerda and D.E. Ramaker	659
PERPENDICULAR MAGNETIC ANISOTROPY IN ULTRATHIN Fe(110) FILMS ON Cr(110) Helmut Fritzsche and Ulrich Gradmann	671
MICROSTRUCTURAL DEPENDENCE OF THE PERPENDICULAR MAGNETIC ANISOTROPY IN Co-Pt ALLOYS E.E. Marinero, R.F.C. Farrow, G.R. Harp, R.H. Geiss, J.A. Bain, and B. Clemens	677
HYPERFINE FIELDS IN ULTRATHIN Fe AND FeAu ALLOY FILMS ON Au(111) M. Brockmann, L. Pfau, G. Lugert, and G. Bayreuther	685
THE MICROSTRUCTURE OF Fe-C ₃ FORMED AT 300°C BY PLASMA ENHANCED CHEMICAL VAPOR DEPOSITION (PECVD) H. Siriwardane, P. Fraundorf, J.W. Newkirk, O.A. Pringle, and W.J. James	691
UHV PREPARATION AND IN-SITU SURFACE ANALYSIS OF MnFe/NiFe EXCHANGE STRUCTURES: INTERFACIAL IMPURITY INCORPORATION Susan L. Cohen, John M. Baker, Michael A. Russak, Gerald J. Scilla, Cherngye Hwang, and Stephen M. Rossnagel	697

PART IV: NANOSTRUCTURAL CHARACTERIZATION

*APPLICATION OF HIGH-RESOLUTION ELECTRON MICROSCOPY TO THE STUDY OF MAGNETIC THIN FILMS AND MULTILAYERS R. Sinclair, T.P. Nolan, G.A. Bertero, and M.R. Visokay	705
INITIAL GROWTH AND MORPHOLOGY OF ULTRATHIN MAGNETIC FILMS STUDIED USING SCANNING TUNNELING MICROSCOPY David D. Chambliss, K.E. Johnson, K. Kalki, S. Chiang, and R.J. Wilson	713
SCANNING-ION MICROSCOPY WITH POLARIZATION ANALYSIS (SIMPA) N.J. Zheng and C. Rau	723

PART V: MAGNETISM IN MULTILAYERS: STRUCTURE AND PROPERTIES

STRUCTURE AND MAGNETIC PROPERTIES OF Fe/Zr MULTILAYER FILMS Toyohiko J. Konno, Takenori Nakayama, Bruce M. Clemens, and Robert Sinclair	731
---	-----

*Invited Paper

STRUCTURAL AND MAGNETORESISTANCE PROPERTIES OF Co/Cu MULTILAYERS DOPED WITH Fe	737
J.M. George, A. Barthelemy, O. Durand, J.L. Duvail, A. Fert, P. Galtier, O. Heckmann, L.G. Pereira, F. Petroff, and T. Valet	
RESISTANCE AND MAGNETORESISTANCE OF GADOLINIUM/TUNGSTEN MULTILAYERS	743
A. Heys, P.E. Donovan, E.G. Astrakharchik, and B. George	
TRANSMISSION ELECTRON MICROSCOPY STUDIES OF NiFe/Cu/Co/Cu ON Si	749
P. Galtier, T. Valet, O. Durand, J.C. Jacquet, and J.P. Chevalier	
NEUTRON SCATTERING MEASUREMENTS OF THE STAGGERED MAGNETIZATION OF AN ANTIFERROMAGNETIC EPITAXIAL THIN FILM FeF ₂	755
D.P. Belanger, M. Lui, and R.W. Erwin	
POLARIZED NEUTRON REFLECTIVITY MEASUREMENTS OF COLLINEAR AND NON-COLLINEAR MAGNETIC STRUCTURES IN Fe/Cr(100) SUPERLATTICES	761
J.F. Ankner, A. Schreyer, Th. Zeidler, C.F. Majkrzak, H. Zabel, J.A. Wolf, and P. Grünberg	
NEUTRON SCATTERING STUDY OF ANTIFERROMAGNETIC AND FERROMAGNETIC COUPLING IN Ni/Ag MULTILAYERS	767
B. Rodmacq, P. Burlet, Ph. Mangin, and M. Hennion	
A COMPARATIVE STUDY OF STRUCTURAL, MAGNETIC, AND TRANSPORT PROPERTIES OF Co-Re SUPERLATTICES SPUTTERED ON GLASS AND Si SUBSTRATES	773
J.L. Leal, N.P. Barradas, J.C. Soares, M.F. da Silva, M. Rots, and P.P. Freitas	
INTERFACIAL EXCHANGE COUPLING AND THE MAGNETIZATION OF IRON OXIDE/NICKEL OXIDE SUPERLATTICES	779
S.D. Berry, D.M. Lind, E. Lochner, K.A. Shaw, D. Hilton, R.W. Erwin, and J.A. Borchers	
MAGNETIC AND MAGNETO-OPTIC PROPERTIES OF dc MAGNETRON SPUTTERED Co-Cr/Al MULTILAYERS	785
G.W. Auner, R. Naik, U.M. Rao, Y. Zhao, and B. Wang	
INTERFACE AND VOLUME ANISOTROPY OF MBE-GROWN Co/Pt (111), (110) AND (001) AND SPUTTERED Co/Pt MULTILAYERS	791
D. Weller, R.F.C. Farrow, R.F. Marks, G.R. Harp, H. Notarys, and G. Gorman	
STRUCTURAL CHARACTERIZATION OF Pt/Co MULTILAYERS FOR MAGNETOOPTIC RECORDING USING X-RAY DIFFRACTION	799
James A. Bain, Bruce M. Clemens, and Sean Brennan	
MAGNETIC AND MAGNETO-OPTIC PROPERTIES OF PtFe(001) AND PtCo(001) THIN FILMS	805
Bruce M. Lairson, Mark R. Visokay, Robert Sinclair, and Bruce M. Clemens	
VALENCE INSTABILITY AND MAGNETIC POLARIZATION OF Ce ATOMS NEAR THE INTERFACE OF Ce/Fe MULTILAYERS STUDIED BY MAGNETIC CIRCULAR X-RAY DICHROISM	811
F. Klose, S. Pizzini, C. Giorgetti, O. Schulte, F. Baudalet, E. Dartyge, G. Krill, W. Felsch, and A. Fontaine	

MAGNETIC PROPERTIES AND CRYSTALLOGRAPHY OF SELECTED Co/Pt MULTILAYERS WITH RARE-EARTH ADDITIONS G.A. Bertero, R.L. White, and R. Sinclair	817
AUTHOR INDEX	823
SUBJECT INDEX	827

Preface

The field of magnetic ultrathin films continues to be an exciting and rapidly expanding one, as demonstrated by recent advances in novel materials, multilayer structures and the observation of new phenomena. This expanding activity is reflected in the organization of two symposia for the 1993 MRS Spring Meeting which emphasized different aspects of magnetic behavior in thin film systems. Symposium Q1 focused on magneto-transport, surface magnetism and optical phenomena, with giant magnetoresistance (GMR) and enhanced Kerr effects among the central themes of several sessions. The symposium included joint sessions with related symposia, topical sessions, a special evening session on GMR in heterogeneous alloys, and two large and very interactive poster sessions. Symposium Q2 emphasized new characterization techniques and film structure, with invited and contributed talks on spin-resolved spectroscopies and the application of synchrotron radiation techniques such as magnetic circular dichroism to magnetic materials. These symposia brought together representatives of leading groups from Europe, Japan and the U.S.A. The list of sponsors reflects this international flavor, as well as the industrial interest in this rapidly developing arena in which materials research plays such a key role.

Although the two symposia were organized independently, the co-chairs elected to publish a joint proceedings to present a more cohesive and comprehensive summary of this broad and active field of research. The co-chairs of the two symposia were:

Symposium Q1: C. Chappert, R. Clarke, W.J.M. de Jonge, R.F.C. Farrow, P. Grünberg, B.T. Jonker, K.M. Krishnan, and S. Tsunashima.

Symposium Q2: S.A. Chambers, T. Egami, E.E. Marinero, and C. Rau.

All of the manuscripts were subject to the usual peer review process. The organization of this volume generally reflects the individual sessions of the symposia. Section A contains most of the papers presented in Symposium Q1, while Section B contains the papers presented in Symposium Q2 together with the papers from session Q1-11, which emphasized the close relationships between film structure and magnetic properties.

B.T. Jonker
S.A. Chambers
R.F.C. Farrow
C. Chappert
R. Clarke
W.J.M. de Jonge
T. Egami
P. Grünberg
K.M. Krishnan
E.E. Marinero
C. Rau
S. Tsunashima

June 1993

Acknowledgments

We would like to thank the invited speakers for providing a stimulating framework for the topics covered, and the presenters of the contributed oral and poster papers for their participation. We also thank the session chairpersons for their help in running the sessions, and all of the individuals who served as referees for the published proceedings. One of us (BTJ) wishes to acknowledge the assistance of Dr. Hisham Abad in assembling the indices and table of contents for Section A. One of us (SAC) wishes to acknowledge the assistance of Dr. T.T. Tran in assembling the indices and table of contents for Section B. We further acknowledge the invaluable assistance of the MRS staff in all phases of organizing the symposia and publishing the proceedings.

Finally, we gratefully acknowledge the symposia sponsors listed below, whose generous financial support made these two symposia possible.

Symposium Q1

Office of Naval Research
Mitsubishi Electric Corp.
Tosoh Corp.
Philips Corp.
Hitachi Research Laboratories
Fisons Instruments/VG Semicon
IBM Almaden Research Center
Sanyo Electric Co., Ltd.
NEC Corp.

Symposium Q2

Office of Naval Research
Matsushita Co.
Tosoh Corp.
IBM Almaden Research Center

MATERIALS RESEARCH SOCIETY SYMPOSIUM PROCEEDINGS

- Volume 279—Beam-Solid Interactions—Fundamentals and Applications, M.A. Nastasi, N. Herbots, L.R. Harriott, R.S. Averbach, 1993, ISBN: 1-55899-174-3
- Volume 280—Evolution of Surface and Thin Film Microstructure, H.A. Atwater, E. Chason, M. Grabow, M. Lagally, 1993, ISBN: 1-55899-175-1
- Volume 281—Semiconductor Heterostructures for Photonic and Electronic Applications, D.C. Houghton, C.W. Tu, R.T. Tung, 1993, ISBN: 1-55899-176-X
- Volume 282—Chemical Perspectives of Microelectronic Materials III, C.R. Abernathy, C.W. Bates, D.A. Bohling, W.S. Hobson, 1993, ISBN: 1-55899-177-8
- Volume 283—Microcrystalline Semiconductors—Materials Science & Devices, Y. Aoyagi, L.T. Canham, P.M. Fauchet, I. Shimizu, C.C. Tsai, 1993, ISBN: 1-55899-178-6
- Volume 284—Amorphous Insulating Thin Films, J. Kanicki, R.A.B. Devine, W.L. Warren, M. Matsumura, 1993, ISBN: 1-55899-179-4
- Volume 285—Laser Ablation in Materials Processing—Fundamentals and Applications, B. Braren, J. Dubowski, D. Norton, 1993, ISBN: 1-55899-180-8
- Volume 286—Nanophase and Nanocomposite Materials, S. Komarneni, J.C. Parker, G.J. Thomas, 1993, ISBN: 1-55899-181-6
- Volume 287—Silicon Nitride Ceramics—Scientific and Technological Advances, I-W. Chen, P.F. Becher, M. Mitomo, G. Petzow, T-S. Yen, 1993, ISBN: 1-55899-182-4
- Volume 288—High-Temperature Ordered Intermetallic Alloys V, I. Baker, J.D. Whittenberger, R. Darolia, M.H. Yoo, 1993, ISBN: 1-55899-183-2
- Volume 289—Flow and Microstructure of Dense Suspensions, L.J. Struble, C.F. Zukoski, G. Maitland, 1993, ISBN: 1-55899-184-0
- Volume 290—Dynamics in Small Confining Systems, J.M. Drake, D.D. Awschalom, J. Klafter, R. Kopelman, 1993, ISBN: 1-55899-185-9
- Volume 291—Materials Theory and Modelling, P.D. Bristowe, J. Broughton, J.M. Newsam, 1993, ISBN: 1-55899-186-7
- Volume 292—Biomolecular Materials, S.T. Case, J.H. Waite, C. Viney, 1993, ISBN: 1-55899-187-5
- Volume 293—Solid State Ionics III, G-A. Nazri, J-M. Tarascon, M. Armand, 1993, ISBN: 1-55899-188-3
- Volume 294—Scientific Basis for Nuclear Waste Management XVI, C.G. Interrante, R.T. Pabalan, 1993, ISBN: 1-55899-189-1
- Volume 295—Atomic-Scale Imaging of Surfaces and Interfaces, D.K. Biegelson, D.S.Y. Tong, D.J. Smith, 1993, ISBN: 1-55899-190-5
- Volume 296—Structure and Properties of Energetic Materials, R.W. Armstrong, J.J. Gilman, 1993, ISBN: 1-55899-191-3

MATERIALS RESEARCH SOCIETY SYMPOSIUM PROCEEDINGS

- Volume 297—Amorphous Silicon Technology—1993, E.A. Schiff, M.J. Thompson, P.G. LeComber, A. Madan, K. Tanaka, 1993, ISBN: 1-55899-193-X
- Volume 298—Silicon-Based Optoelectronic Materials, R.T. Collins, M.A. Tischler, G. Abstreiter, M.L. Thewalt, 1993, ISBN: 1-55899-194-8
- Volume 299—Infrared Detectors—Materials, Processing, and Devices, A. Appelbaum, L.R. Dawson, 1993, ISBN: 1-55899-195-6
- Volume 300—III-V Electronic and Photonic Device Fabrication and Performance, K.S. Jones, S.J. Pearton, H. Kanber, 1993, ISBN: 1-55899-196-4
- Volume 301—Rare-Earth Doped Semiconductors, G.S. Pomrenke, P.B. Klein, D.W. Langer, 1993, ISBN: 1-55899-197-2
- Volume 302—Semiconductors for Room-Temperature Radiation Detector Applications, R.B. James, P. Siffert, T.E. Schlesinger, L. Franks, 1993, ISBN: 1-55899-198-0
- Volume 303—Rapid Thermal and Integrated Processing II, J.C. Gelpey, J.K. Elliott, J.J. Wortman, A. Ajmera, 1993, ISBN: 1-55899-199-9
- Volume 304—Polymer/Inorganic Interfaces, R.L. Opila, A.W. Czanderna, F.J. Boerio, 1993, ISBN: 1-55899-200-6
- Volume 305—High-Performance Polymers and Polymer Matrix Composites, R.K. Eby, R.C. Evers, D. Wilson, M.A. Meador, 1993, ISBN: 1-55899-201-4
- Volume 306—Materials Aspects of X-Ray Lithography, G.K. Celler, J.R. Maldonado, 1993, ISBN: 1-55899-202-2
- Volume 307—Applications of Synchrotron Radiation Techniques to Materials Science, D.L. Perry, R. Stockbauer, N. Shinn, K. D'Amico, L. Terminello, 1993, ISBN: 1-55899-203-0
- Volume 308—Thin Films—Stresses and Mechanical Properties IV, P.H. Townsend, J. Sanchez, C-Y. Li, T.P. Weihs, 1993, ISBN: 1-55899-204-9
- Volume 309—Materials Reliability in Microelectronics III, K. Rodbell, B. Filter, P. Ho, H. Frost, 1993, ISBN: 1-55899-205-7
- Volume 310—Ferroelectric Thin Films III, E.R. Myers, B.A. Tuttle, S.B. Desu, P.K. Larsen, 1993, ISBN: 1-55899-206-5
- Volume 311—Phase Transformations in Thin Films—Thermodynamics and Kinetics, M. Atzmon, J.M.E. Harper, A.L. Greer, M.R. Libera, 1993, ISBN: 1-55899-207-3
- Volume 312—Common Themes and Mechanisms of Epitaxial Growth, P. Fuoss, J. Tsao, D.W. Kisker, A. Zangwill, T.F. Kuech, 1993, ISBN: 1-55899-208-1
- Volume 313—Magnetic Ultrathin Films, Multilayers and Surfaces/Magnetic Interfaces—Physics and Characterization (2 Volume Set), C. Chappert, R.F.C. Farrow, B.T. Jonker, R. Clarke, P. Grünberg, K.M. Krishnan, S. Tsunashima/E.E. Marinero, T. Egami, C. Rau, S.A. Chambers, 1993, ISBN: 1-55899-211-1
- Volume 314—Joining and Adhesion of Advanced Inorganic Materials, A.H. Carim, D.S. Schwartz, R.S. Silberglitt, R.E. Loehman, 1993, ISBN: 1-55899-212-X
- Volume 315—Surface Chemical Cleaning and Passivation for Semiconductor Processing, G.S. Higashi, E.A. Irene, T. Ohmi, 1993, ISBN: 1-55899-213-8

Section A—Multilayers and Surfaces

PART I

**Giant Magnetoresistance in Multilayers:
Role of Interface Structure**

OSCILLATIONS IN EXCHANGE COUPLING IN Co/Cu MULTILAYERS GROWN BY MBE

D. GREIG, M.J. HALL, M.A. HOWSON, B.J. HICKEY, M.J. WALKER AND J. XU
Department of Physics, University of Leeds, Leeds LS2 9JT, U.K.

ABSTRACT

We have observed oscillations with non-magnetic spacer layer thickness in the saturation fields and characteristic exchange fields of Co/Cu multilayers grown by MBE. The specimens consisted of a set of samples in which the thickness of copper layers took a series of values between 5Å and 20Å, while the cobalt layer thickness was set at 15Å throughout. The multilayers were grown epitaxially on GaAs (110) with Ge, Co (110) and Au in the buffer region, resulting in Co/Cu bilayers in the (111) orientation. Although oscillations were observed in these magnetic measurements, no oscillations were observed in the magnetoresistance itself. These observations are somewhat at odds with similar measurements made on samples prepared by sputtering. We conclude with a discussion involving exchange coupling, in-plane anisotropy and defects in the magnetic structure in an attempt to account for these conflicting results.

INTRODUCTION

Two years ago the equivalent Spring Meeting was one of the first conferences to devote entire sessions to discussions of the Giant Magnetoresistance (GMR) and at this meeting we review the situation two years and several conferences on. It is now generally accepted that some of the largest fractional changes of resistance with magnetic field are seen in Co/Cu multilayers and that this magnitude oscillates with spacer layer thickness. Nevertheless one curious feature remains. That is that the greatest values of the GMR are found in specimens produced by sputtering.

For samples produced by the more controlled technique of MBE the values of GMR are always smaller; indeed two years ago the values were extremely small at the 1% level but the situation has changed significantly since then and that is the basis of this presentation. By making a small change in the growth technique we were able to obtain an order of magnitude increase in the value of the GMR. In this paper we present some detailed information about the 'quality' of specimens produced in this way and a survey of possible factors that influence the value of the GMR and the evidence for oscillatory coupling.

SPECIMEN PREPARATION

Co/Cu multilayers have been grown in many laboratories on a wide variety of substrates including single crystal Cu(100) and (111), MgO(110), Al₂O₃(1120) and (0001), Si(100), GaAs(100) and (110) and, of course, glass. At Leeds we have followed the route developed by the University of Michigan [1] growing on GaAs(110). The process is started by heating the substrates to about 600°C until a RHEED pattern indicates a surface reconstruction characteristic of GaAs(110). The quality of the RHEED pattern is greatly improved by depositing a 500Å layer of Ge at 500°C, and this is followed by a single layer of bcc (110) Co which has been found essential to seed epitaxy. This is grown on the Ge at a much lower temperature of about 150°C. From that point onwards a Co/Cu superlattice can be grown in the (111) orientation, but the special 'trick' that we developed was to use 10Å of gold as the final layer in the buffer region. Cobalt and gold do not mix and it was

known from the work described in reference [1] that once the correct buffer region had been developed it was relatively easy to grow Co/Au superlattices with extremely sharp interfaces. As described in our first publications [2,3] the addition of this gold layer produced RHEED and XRD patterns characteristic of flat surfaces, and, at the same time, resulted in an order of magnitude increase in the magnitude of the GMR.

In figure 1 we show a recent low-angle X-ray scan of a Co(15Å)/Cu(24Å) superlattice grown at 100°C with the substrate rotating at 60 revolutions per minute. The high frequency oscillations are interference fringes arising from scattering between the gold layer on top of the buffer region and a gold capping layer added to prevent contamination of the specimen. The clarity of these fringes together with the existence of more than one Bragg peak is an indication that the layers are reasonably flat. It is generally difficult to see more than one Bragg peak in Co/Cu multilayers as the form factors of Co and Cu are very similar leading to a lack of X-ray contrast.

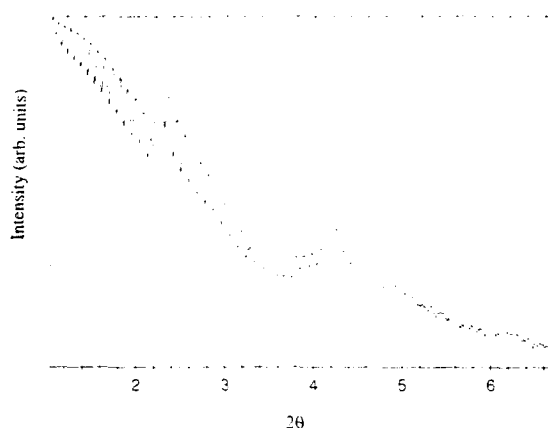


Fig. 1: Low angle diffraction profile of a [Co(15)/Cu(24)] multilayer grown on GaAs(110)/Ge/Au.

The evidence for (111) growth is set out in detail in our earlier publications [2,4].

There are two points:

- (a) There are X-ray 'texture' scans in which the X-ray source and detector are set at fixed angles and the specimen rotated about two perpendicular axes. The results show clearly the existence of (111) reflections at all the correct angles and a complete absence of growth in the (100) orientation.
- (b) Likewise the RHEED patterns observed during growth show clearly the streaky appearance that is the signature of a flat surface and show the 6-fold rotational symmetry that is a characteristic of the close-packed atomic arrangement in (111) growth. The surface of a (111) plane can be represented by a 2-dimensional hexagonal net where a , the lattice constant of the net is related to the separation, d_{hk} , of the rows (hk) by,

$$d_{hk}^2 = (3/4)a^2/(h^2 + k^2 + hk).$$

As in any diffraction experiment the separation of the lines or spots in the pattern is inversely proportional to the separation of the diffracting elements, and here again we find

excellent agreement between the separations of the RHEED streaks in two different orientations and the expected ratios of the d_{hk} given by the above expression.

All these diffraction experiments lead us to conclude that the superlattices grown in this way are of high quality. However on examining an area of the gold film in the buffer region by STM, the picture looks much less satisfactory. Although there are large flat areas present -- and hence the high quality diffraction effects -- there are also pronounced wells penetrating the completed thickness of the thin gold layer. As these wells will certainly extend into any superlattice grown on top of the gold it is clear that these could have a serious effect on the magnetic and transport properties of the multilayers, and could be another form of the 'pinholes' that had been cited earlier as the reason for the very low values of GMR in samples produced by MBE. We shall see in what follows that well defined multilayers are essential to obtain the magnetic structure required to obtain a GMR.

THE GIANT MAGNETORESISTANCE

Co/Cu multilayers form one of the archetypal systems that exhibit a GMR. Compared to the magnetoresistance effects seen at very low temperatures in crystals of pure metals the effect is actually relatively small, but the word 'giant' refers to the unusually large decrease in resistance observed at room temperature. As mentioned above the largest change to date is a fractional change of about 65% at 290K rising to over 100% at 4.2K [5]. In a recent paper on the effect of magnetic defects on the GMR Highmore et al. [6] have argued that 65% at room temperature is likely to be about the maximum value of the GMR in Co/Cu multilayers, but that is not a universal figure for all systems. As regards specimens prepared by MBE the maximum values that we have obtained in samples prepared as outlined above has been about 30% measured at 4.2K. A further significant increase in magnitude for MBE grown samples has recently been reported by Kobayashi et al. [7] who have observed values again of order 80% at 4.2K for Co/Cu multilayers grown on sapphire (0001). It is now universally agreed that the GMR is a consequence of the ordering of misaligned spins, which, in the case of well-formed multilayers, implies a change from antiferromagnetic (AFM) to ferromagnetic (FM) coupling between adjacent magnetic layers on application of a magnetic field. However, within this model there are two important issues that require comment.

Oscillations

Although oscillations in the magnitude of the GMR as a function of spacer layer thickness are seen quite clearly in specimens prepared by sputtering [5,8,9], there has been a complete lack of similar evidence in Co/Cu multilayers prepared by MBE. However, very recently one of the Orsay groups [10] have finally seen oscillations with a period of between 8Å and 10Å in Co/Cu/Co trilayers grown by evaporation in UHV -- oscillations that are in accordance with the predictions of RKKY theory for interlayer coupling across Cu(111). We shall return to the question of the illusive nature of these oscillations after discussing magnetisation.

Bulk versus Interface Scattering

Magnetoresistance is a transport property so that in addition to the strength of the magnetic coupling we must also consider the role of electron scattering and the relative importance of effects within the layers and at the interfaces. It is certainly easy to show that the magnitude of the GMR accompanying the change from AFM to FM coupling

depends on the scattering probability of spin-up and spin-down electrons, but whether this takes place primarily in the layers or at the interfaces is altogether more subtle. In two recent papers [3,4] we have described the effect of annealing on the magnitude of the GMR and have analysed the results in terms of two parameters, p_b and p_i , the proportion of electron scattering that takes place in the bulk and at the interfaces respectively. (Note that $p_b + p_i = 1$). If we further assume that diffuse scattering at the interfaces is "catastrophic" and so independent of spin, then in terms of this simple model it is easy to show that for Co/Cu multilayers the decrease of the GMR on annealing can be accounted for by increasing the ratio p_i/p_b .

Of course the magnitude of the GMR can equally be accounted for by a different set of assumptions, and several authors have interpreted their results on the basis of spin-dependent interfacial scattering [11], and the interpretation of GMR measurements in which the current is perpendicular to the layers gives some support to that model [12]. Nevertheless we repeat that results of experiments on annealed Co/Cu multilayers in which annealing increases the interface scattering but decreases the GMR greatly favour the former interpretation.

MAGNETISATION

More direct evidence for the existence of AFM or FM coupling must come from measurements of the magnetisation itself, and in figures 2 and 3 we show the field dependence of magnetisation at both low and high fields in four of our samples. Each specimen consisted of 20 bilayers of 15Å of fcc cobalt interspersed with fcc copper layers of various thicknesses as indicated on the diagrams. From the low field data there is clear evidence of a variation between AFM and FM coupling, although the marked hysteresis shows that the latter is present in all samples. We have indicated on the high field curves likely values of the fields, H_s , at which the magnetisation appears to have saturated, and in figure 4 we show their variation with copper layer thickness. The marked oscillation is an indication of a switch between AFM and FM coupling. Interestingly this oscillation is not observed in the samples referred to in reference [7] that show the very high values of the GMR.

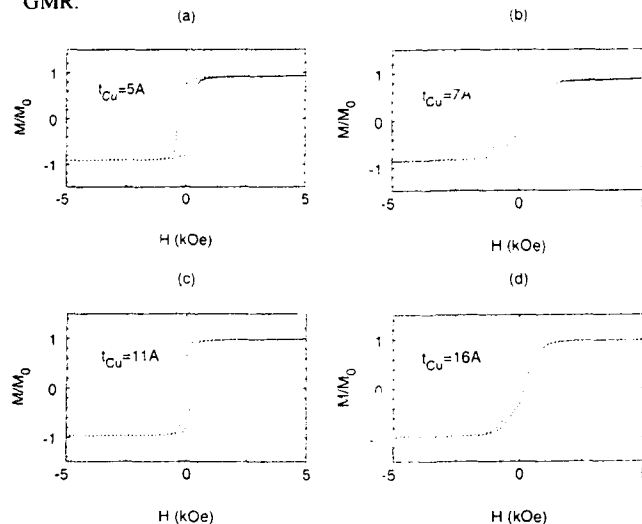


Fig. 2: Ratios of magnetisation to saturation magnetisation (M/M_0) at low fields.

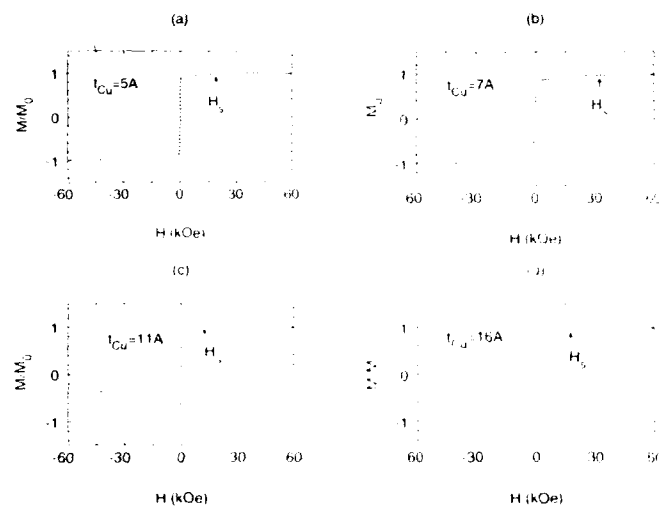


Fig. 3: Measurements in figure 2 extended to higher fields.

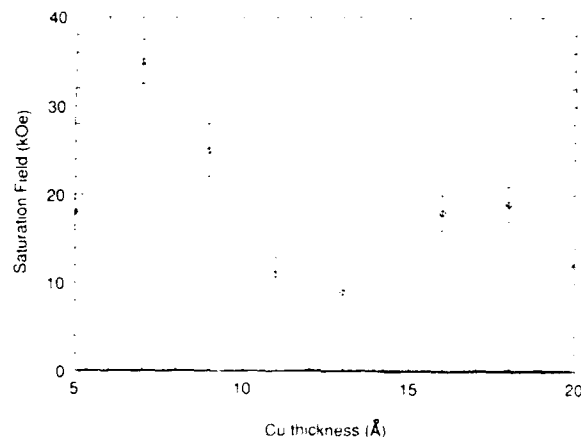


Fig. 4: Variation of saturation fields with thickness of copper layers.

Examining the high field data more carefully we find further evidence of AFM coupling. In the range close to saturation there is a linear rise of magnetisation with applied field that is a characteristic of AFM coupling. A detailed example of this evidence is shown in figure 5 where the greater noise is a consequence of the small volume of that particular sample. The extrapolated exchange field, H_{AFM} , characteristic of the strength of the exchange coupling, J , between adjacent magnetic layers is given by $H_{AFM} = 2J/M_0$, where M_0 is the saturation magnetisation. The slow approach to saturation in the presence of anisotropy follows the expression $M = M_0 \{1 - a/(H - H_{AFM})^2\}$, where the coefficient depends on the

anisotropy constant and the angle between the field and some easy axis. The variation of H_{AFM} with copper layer thickness is shown in figure 6 where we see further evidence of the oscillations that are even more marked than in figure 4. The reason is that H_{AFM} is a true measure of the exchange coupling while H_s in figure 4 is a somewhat arbitrary effective saturation field which depends on both anisotropy and exchange coupling in addition to the rather delicate judgment required to obtain its value from the data in figure 3.

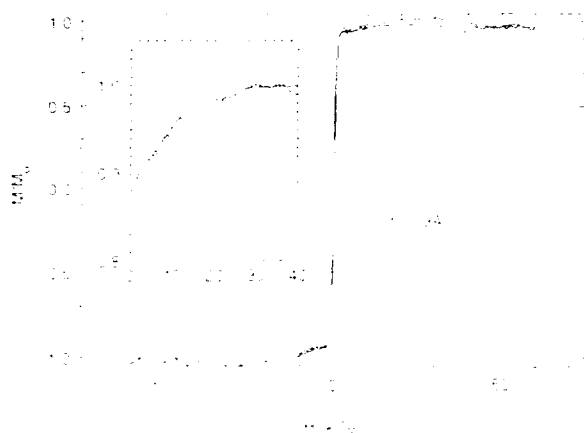


Fig. 5: Detailed variation of magnetisation with applied field on the approach to saturation. The linear region and the dashed curve are discussed in the text.

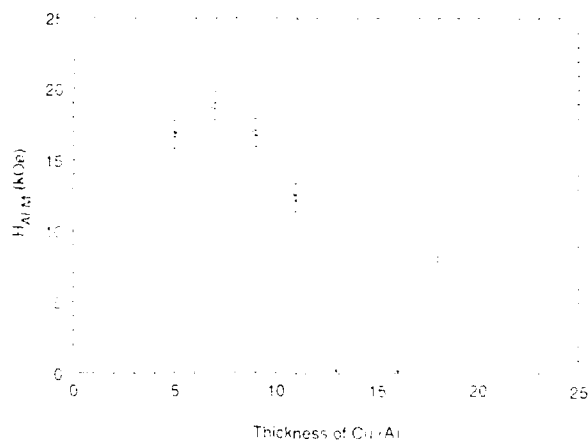


Fig. 6: Variation of the apparent exchange field for AFM coupling, H_{AFM} , with thickness of copper layers.

SUMMARY AND FURTHER COMMENTS

The evidence from magnetisation data seems clear; the multilayers are predominantly ferromagnetic but with a sufficient volume of AFM coupling at certain layer thicknesses to generate a GMR. The AFM regions probably grow over the "flat" areas identified in the STM scans, while the remaining rough regions are simply ferromagnetic. In figure 7 we show the marked difference in the approach to saturation of the magnetisation on the one hand and the GMR on the other. It is clear that the major difference is the very rapid rise in magnetisation at low fields -- a signature of ferromagnetism. The much more gradual decrease in resistance takes place over the range of fields in which the magnetisation increases from about 80% to 100% of its saturation value -- that is over precisely that part of the magnetisation curve that we attribute to the fraction of the sample that is AFM coupled.

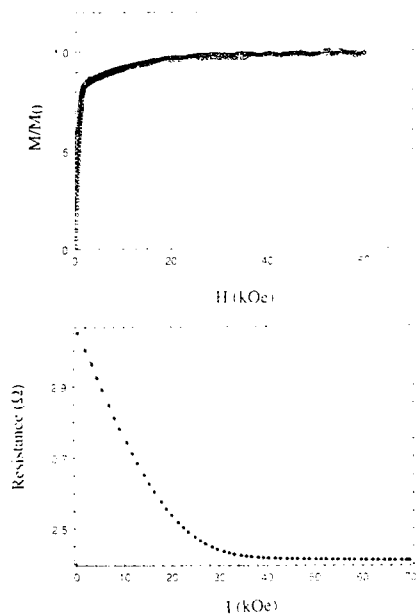


Fig. 7: Marked difference in magnetisation and resistance in the approach to saturation.

Several questions remain. It is still not absolutely clear why the volume of material that is AFM coupled -- and hence the maximum GMR -- is generally greater in sputtered specimens although over the last year the difference has become less. The change has been brought about by improving the quality of the specimens grown by MBE. It is also not clear why, apart from the recent paper on trilayers [10], there is no evidence of oscillations with spacer layer thickness in the GMR. We may speculate that this is because the presence of defects in the magnetic structures including roughness at the interfaces reduces the magnitude of the maximum GMR but retains an AFM coupled component when the expected GMR is a minimum. In their recent publications Highmore et al. [6] have demonstrated the importance of what they term "antiphase domain boundaries", that are

introduced between growth fronts during deposition, resulting in more complex coupling than would be found in ideal parallel layers.

ACKNOWLEDGEMENTS

We are greatly indebted to the Magnetism and Magnetic Materials Initiative of the SERC and to the University of Leeds for their strong support of this project. We are also grateful to Dr Peter de Groot for his assistance in the use of the VSM at the University of Southampton.

REFERENCES

1. C.H. Lee, H. He, F. Lamelas, W. Vavra, C. Uher and R. Clarke, *Phys. Rev. Lett.* **62**, 653 (1989).
2. D. Greig, M.J. Hall, C. Hammond, B.J. Hickey, H.P. Ho, M.A. Howson, M.J. Walker, N. Wiser and D.G. Wright, *J. Magn. Magn. Mater.* **110**, L239 (1992).
3. M.J. Hall, B.J. Hickey, M.A. Howson, C. Hammond, M.J. Walker, D.G. Wright, D. Greig and N. Wiser, *J. Phys.: Condens. Matter* **4**, L495 (1992).
4. M.J. Hall, B.J. Hickey, M.A. Howson, M.J. Walker, J. Xu, D. Greig and N. Wiser, *Phys. Rev. B*, (in press).
5. S.S.P. Parkin, R. Bhadra and K.P. Roche, *Phys. Rev. Letts.* **66**, 2152 (1991); S.S.P. Parkin, Z.G. Li and D.J. Smith, *Applied Phys. Letts.* **58**, 2710 (1991).
6. R.J. Highmore, J.E. Evetts and R.E. Somekh, *J. Magn. Magn. Mater.* (in press); R.J. Highmore, R.E. Somekh, W.C. Shih, I.M. McLoughlin and J.E. Evetts, *Applied Surface Science* **65**, 124 (1993).
7. Y. Kobayashi, Y. Aoki, H. Sato, A. Kamijo and M. Abe (preprint).
8. D.H. Mosca, F. Petroff, A. Fert, P.A. Schroeder, W.P. Pratt Jr. and R. Laloe, *J. Magn. Magn. Mater.* **94**, L1 (1991).
9. M.E. Tomlinson, R.J. Pollard, D.G. Lord and P.J. Grundy, *J. Magn. Magn. Mater.* **111**, 79 (1992).
10. C. Dupas, E. Kolb, K. Le Dang, J.P. Renard, P. Veillet, E. Velu and D. Renard, *J. Magn. Magn. Mater.* (in press).
11. S.S.P. Parkin, presented at Nagoya International Workshop, 1993 (unpublished).
12. S.F. Lee, W.P. Pratt Jr., R. Laloe, P.A. Schroeder and J. Bass, *Phys. Rev. B* **46**, 548 (1992).

PERPENDICULAR MAGNETORESISTANCE OF MICROSTRUCTURED PILLARS IN Fe/Cr MAGNETIC MULTILAYERS

M.A.M. GIJS ^{*}, S.K.J. LENCZOWSKI ^{**} AND J.B. GIESBERS ^{*}

^{*} Philips Research Laboratories, 5600 JA Eindhoven, The Netherlands

^{**} Eindhoven University of Technology, Department of Physics, 5600 MB Eindhoven,
The Netherlands

ABSTRACT

We have fabricated pillar-like microstructures of high vacuum sputtered Fe/Cr magnetic multilayers and measured the giant magnetoresistance effect in the configuration where the measuring current is perpendicular to the film plane from 4.2 K to 300 K. At 4.2 K we find a magnetoresistance of 108 % for multilayers with a Fe thickness of 3 nm and a Cr thickness of 1 nm. The pronounced temperature dependence of the perpendicular magnetoresistance is studied for samples with different Cr thicknesses and tentatively explained by electron-magnon scattering. The low-temperature data are compared with existing low-temperature models.

INTRODUCTION

Since the discovery of the giant magnetoresistance (MR) effect in magnetic multilayers [1], numerous studies on a variety of multilayer systems have been reported (e.g. [2, 3]). In practically all these experiments, the measuring current is in the plane of the multilayer, the so-called current-in-plane (CIP) geometry. Nevertheless, the great importance of experiments with the measuring current perpendicular to the multilayer plane (the so-called CPP-geometry) has been emphasized in several theoretical papers [4, 5, 6, 7, 8, 9]. All these theories are valid only at low temperatures and predict a considerably larger MR effect for the CPP geometry than for the CIP geometry. The first experiments on the CPP-MR were done for Co/Ag and Co/Cu multilayers [10]. In these experiments no microfabrication techniques were used; the multilayer was sandwiched between a superconducting Nb top and bottom contact electrode and the very small multilayer resistance (typically 0.01-0.1 $\mu\Omega$) was measured at 4.2 K using an ultra-sensitive SQUID-based system. This implies that measurements are only possible at liquid helium temperatures. Initially relatively weak magnetic fields ($H \leq 40$ kA/m) were applied; in an improved experimental setup it is now possible to use this experimental method in external fields up to several 1000 kA/m [11]. The CPP-MR of the strongly antiferromagnetically (AF) coupled Fe/Cr system (switching fields of typically 400 kA/m [12]), which is optimally suited for comparison with existing low-temperature models, was only measured quite recently by us using microstructured samples [13]. At the same time, these experiments provided the first data on the *temperature dependence* of the CPP-MR effect, which still represents a theoretical challenge. In particular the role of spin-flip scattering on the giant MR remains to be elucidated.

Here, we will discuss our experiments on the low-temperature CPP-MR and on the temperature dependence of the CPP-MR of microstructured Fe/Cr multilayers. Pillar structures a few microns in size were fabricated using optical lithography and reactive ion etching techniques. The perpendicular giant MR effect was measured for $100 \times (3 \text{ nm Fe} + t_{\text{Cr}} \text{ Cr})$ multilayers with Cr thicknesses $t_{\text{Cr}} = 1 \text{ nm}$, 2.8 nm and 4 nm. The first two thicknesses are in the first two AF regions of the oscillatory coupling between neighbouring Fe layers [12, 14], while the last one corresponds to a weaker coupled configuration. The CPP-MR [15] is larger than the corresponding CIP-MR, e.g. if $t_{\text{Cr}} = 1 \text{ nm}$, we find a

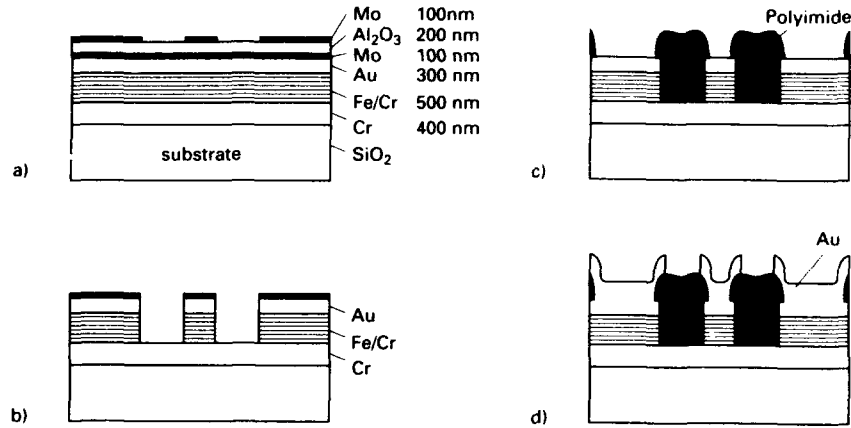


Figure 1: Schematic diagram of different processing steps in the pillar structuring and contact fabrication.

CPP-MR of 108 % at 4 K, more than four times larger than the CIP-MR in similarly prepared multilayers [12]. We demonstrate that our low-temperature data are consistent with the models of Valet and Fert [9] and Bauer [6]. The CPP-MR decreases strongly on increasing the temperature. This probably can be understood in terms of a spin-mixing process by electron-magnon scattering in an anisotropic AF superlattice [16, 17].

SAMPLE FABRICATION

The processing of the pillar structure is schematically shown in figure 1(a,b,c,d). First a 0.4 μm thick Cr base layer is rf sputtered onto a SiO_2 substrate held at room temperature. Then a 0.4-0.7 μm thick Fe/Cr multilayer is deposited, using dc sputtering for the Fe and rf sputtering for the Cr, followed by a dc sputter deposition of a 0.3 μm thick Au layer. All these depositions were done during one vacuum run. The system pressure prior to deposition was 4×10^{-7} mbar and the Ar-pressure during sputtering was 4×10^{-3} mbar. X-ray diffraction shows a predominantly (110) growth of the multilayer. For lithography the sample is covered by a 0.1 μm thick Mo layer, then by a 0.2 μm thick Al_2O_3 layer, followed by the deposition of another 0.1 μm thick Mo layer. The latter is structured using conventional lithography and using wet etching (figure 1(a)) and serves as a mask for the structuring of the Al_2O_3 layer, which is done in an CHF_3/Ar plasma (10 sccm CHF_3 /40 sccm Ar, 25 μbar , 0.52 W/cm^2). The structured Al_2O_3 layer in turn is used as a mask for the etching of the Au and the Fe/Cr multilayer; this is done in an HCl plasma (40 μbar , 2.1 W/cm^2) (figure 1(b)). After removal of the remaining Al_2O_3 , the sample is covered with an insulating polyimide layer. Contact holes in the polyimide are made using reactive ion etching, after which the remaining Mo in the hole is removed by wet etching (figure 1(c)). Subsequently, the structure is covered by a 1.9 μm thick Au film, in which the contact electrode pattern is made (figure 1(d)). The pillar in the middle is the actual sample; finally two Au contact leads will be attached on top of it for the resistance measurement; also the side parts of the structure will be contacted and they will serve as

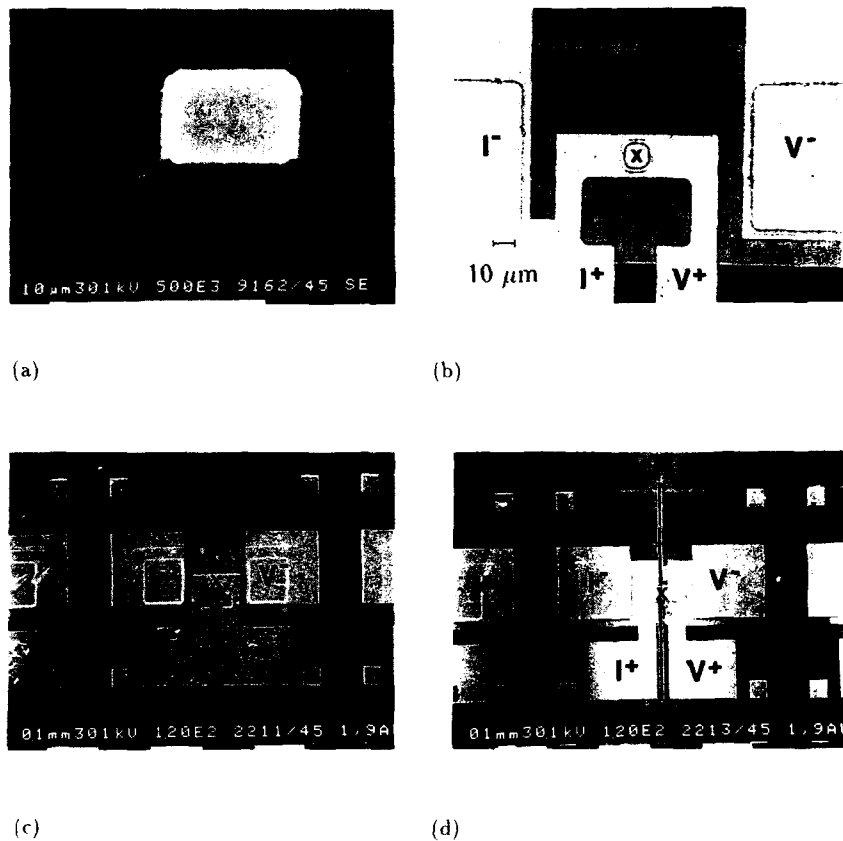


Figure 2: (a) Micrograph of a pillar structure after the etching in the HCl plasma; (b) Micrograph showing the upper Au contact electrode on top of the hole in the polyimide; (c) Graph of a complete pillar device; (d) Graph of the pillar device with additional laser trench. Current (I^+ , I^-) and voltage (V^+ , V^-) contacts are indicated, the pillar is marked by a cross (\times).

the lower contact leads for the pillar in the middle.

In figure 2(a,b,c,d), microscopic images of the structure are shown. Figure 2(a) corresponds to the schematic diagram of figure 1(b) and shows the pillar after the structuring in the HCl-plasma. Figure 2(b) is a top view of the final structure, showing the upper Au contact structured on top of the hole in the polyimide layer. Figure 2(c) is an over-all view of the structure, as described so far, showing clearly the relative magnitude of the pillar with respect to the contact electrodes. Figure 2(d) is an improved measuring structure, which differs from figure 2(c) only by the presence of two trenches, etched down to the substrate using a Nd-YAG laser (532 nm). For the largest pillars fabricated on the substrate (width 10-12 μm), the trench ends at the edges of the pillar, so that the only connection between the two parts of the structure is established through the pillar. This

trench plays a crucial role in the measurement, because it strongly reduces the spurious spreading resistance effect of the contact leads, which is necessary for a proper measurement of the very small perpendicular resistance (typically 1 m Ω). The structure without the trench (figure 2(c)) gives rise to a total resistance measurement, which is dominated by resistance contributions from the electrodes. The measuring current coming from the pillar, spreads radially in the electrode contact region and thereby induces a pronounced voltage drop in the voltage leads of the structure. The magnitude of this voltage can be two orders of magnitude larger than the actual voltage signal coming from the pillar itself, as we have verified both experimentally and by numerical calculations. In the measurement geometry given in figure 2(d), a radial current spread in the electrodes no longer is possible. A more extended discussion of this geometry can be found elsewhere [18]. The resistance of the multilayer is of the same order of magnitude as the residual contact resistance, as is determined experimentally by comparing different multilayer thicknesses. Also the pillar height is relatively small compared to its width w , which gives rise to a non-uniform current distribution in the pillar. Ohms law gives for our geometry that $(V^+ - V^-)w^2 \propto (w/L)/\sinh(w/L)$ with V^+ and V^- the measured voltage on top and below the pillar and L a parameter of typically 2-3 μm , representing the distance of radial current spread in the electrodes. This dependence was checked independently by simulations based on the finite element method. In the following, quoted MR values are extrapolations for $w \rightarrow 0$ and typically are a factor 1.1-1.2 higher than the actual measured value for the smallest pillar dimension on the substrate.

Typically, a few hundred pillars with a cross section S ranging between 6 μm^2 and 130 μm^2 are fabricated on one substrate. 15-20 different pillar structures with variable cross-section were measured for each Cr thickness to check reproducibility. After wire bonding, the samples are mounted in a ^4He flow cryostat. Pillar resistances are measured using an ac bridge technique in the 4-300 K temperature range and in fields up to 1600 kA/m (2 Tesla).

EXPERIMENTAL RESULTS AND DISCUSSION

Figure 3 shows CPP-MR curves at different temperatures for a pillar with a cross-section $S = 90 \mu\text{m}^2$ structured in a $100 \times (3 \text{ nm Fe} + 1 \text{ nm Cr})$ multilayer; for clarity the curves are displaced vertically. At 9.3 K we observe a MR effect of 108 %, more than four times higher than the corresponding CIP-MR effect in unstructured films [12]. The MR effect is weakly temperature dependent below about $T=60$ K; above that temperature the decrease is much stronger. At room temperature a 14 % CPP-MR remains, two times larger than the corresponding CIP-MR. The saturation field $B_s (\equiv \mu_0 H_s)$ is defined by the crossing point of the low field resistance decrease with the horizontal line of constant resistance at higher fields. We find that $B_s = 0.54$ T, nearly independent of temperature. This is comparable to the $B_s = 0.51$ T value found for the corresponding CIP-sample [12]; the small difference can be explained by a slightly different demagnetization factor. This B_s -value corresponds with an interlayer exchange coupling energy per unit surface of 1.3 mJ/m 2 (see ref. [12]). Hence, the interlayer coupling energy is orders of magnitude larger than the thermal energy for our microstructures. This implies that the strong temperature dependence of the CPP-MR cannot be attributed to incomplete AF-coupling at higher temperatures. Another remarkable observation is the absence of hysteresis in the magnetoresistance. For the corresponding CIP-sample, we found a small, but clear hysteretic effect [12]. We notice that in the (very weakly) AF coupled Ag/Co and Cu/Co CPP-samples of ref. [10] magnetoresistive hysteresis is very important. We therefore believe that both strong AF coupling and microstructuring, which leads to a

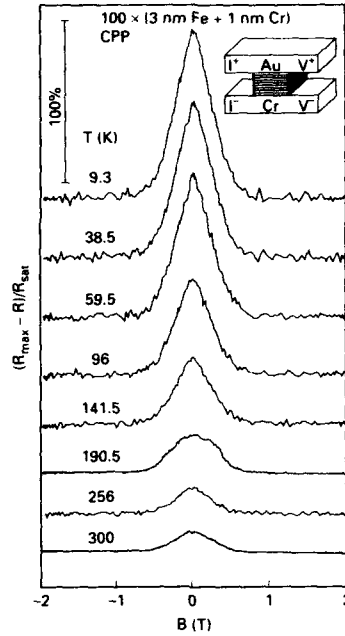


Figure 3: Giant magnetoresistance effect of a microstructured pillar in a $100 \times (3 \text{ nm Fe} + 1 \text{ nm Cr})$ multilayer with the current perpendicular to the multilayer plane (CPP) and as a function of temperature.

reduction in the number of magnetic domains, are important for obtaining non-hysteretic MR characteristics.

We did find a hysteretic magnetoresistance for the $100 \times (3 \text{ nm Fe} + 4 \text{ nm Cr})$ sample, as is clear from figure 4. This seems very reasonable as, for this Cr-thickness, we do not expect perfect AF coupling anymore. Rather, one is in a weakly AF coupled/uncoupled situation, which also is confirmed by magnetization data for this sample.

In figure 5(a,b,c) the temperature dependence of the CPP-MR is shown for multilayers with different t_{Cr} ; comparison is made with the corresponding CIP data [12]. Figure 5(a) is for $t_{\text{Cr}} = 1 \text{ nm}$ and corresponds with the measurements presented in figure 3. The enlarged CPP-MR effect and its strong decrease with temperature is immediately clear. This decrease is also pronounced for the sample of figure 5(b) ($t_{\text{Cr}} = 2.8 \text{ nm}$, $S = 20 \mu\text{m}^2$). Above about 100 K, the CPP-MR even becomes smaller than the CIP-MR. In figure 5(c), the sample with $t_{\text{Cr}} = 4 \text{ nm}$ and $S = 6 \mu\text{m}^2$ is shown. Again, we observe that the CPP-MR is enhanced with respect to the CIP-MR and that the temperature dependence is markedly stronger.

The origin for the strong decrease with temperature of the CPP-MR can be clarified by investigating the quantity $\Delta R(T) = R_{\text{max}}(T) - R_{\text{sat}}(T)$. In figure 6 we plot $\Delta R(4\text{K}) - \Delta R(T)$ against temperature on a double logarithmic scale for the samples of figure 5. Within experimental accuracy, the increase with temperature of $\Delta R(4\text{K}) - \Delta R(T)$

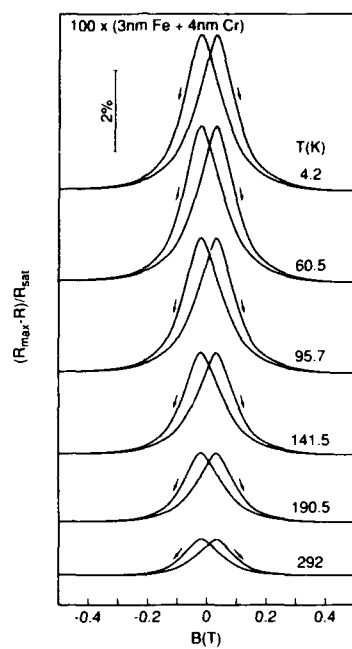


Figure 4: Giant magnetoresistance effect of a microstructured pillar in a $100 \times (3 \text{ nm Fe} + 4 \text{ nm Cr})$ multilayer with the current perpendicular to the multilayer plane (CPP) and as a function of temperature.

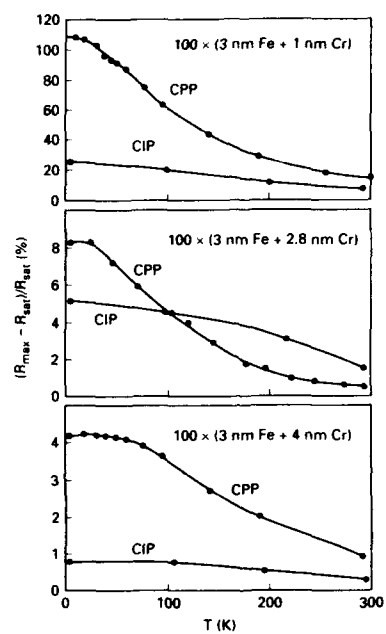


Figure 5: Temperature dependence of the CPP-magnetoresistance of pillar structures made in $100 \times (3 \text{ nm Fe} + t_{\text{Cr}} \text{ Cr})$ multilayers with (a) $t_{\text{Cr}} = 1 \text{ nm}$, (b) $t_{\text{Cr}} = 2.8 \text{ nm}$ and (c) $t_{\text{Cr}} = 4 \text{ nm}$. Corresponding CIP-MR data are given for comparison. The full curves are a guide to the eye.

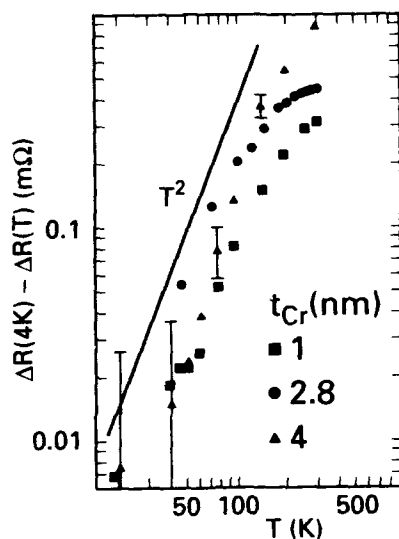


Figure 6: Temperature dependence of $\Delta R(4K) - \Delta R(T)$ on a double logarithmic scale. Typical error bars are indicated for a few points. The solid line indicates a T^2 behaviour, characteristic for electron-magnon scattering in an anisotropic AF system.

below about 150 K can be described by a T^2 behavior for all samples. We believe that this temperature dependence is indicative for electron-magnon scattering as the MR-decreasing mechanism. Previously, the temperature dependence of the low-temperature resistivity of dilute magnetic alloys was explained by incoherent (i.e. spin wave-vector-nonconserving) electron-magnon scattering, mixing the two spin channels [16]. In the case of a multilayer consisting of quasi-two-dimensional AF coupled magnetic layers, this mechanism leads to a T^2 dependence of the CIP resistance variation at low temperature [17], as also observed for our AF coupled CIP-samples. At higher temperatures, additionally, coherent (i.e. spin wave-vector-conserving) electron-magnon scattering processes contribute, giving rise to a more complicated behavior. Physically, spin-flip scattering due to thermally excited magnons results in equalizing the two spin currents (the classical spin-mixing effect) and also reduces the spin-flip diffusion length l_{sf} . At the moment, a detailed microscopic calculation on the temperature dependence of the CPP-MR does not exist, so that the above interpretation remains to be proven.

Here, we compare our low-temperature results firstly with the low-temperature model of Valet and Fert [9], which is similar in approach to the model of Lee *et al.* [7], and secondly with the model of Bauer [6]. The Valet-Fert model is a theory on a microscopic basis and takes into account interface spin accumulation effects coming from a difference in chemical potential for spin-up and spin-down electrons. It is argued that the most

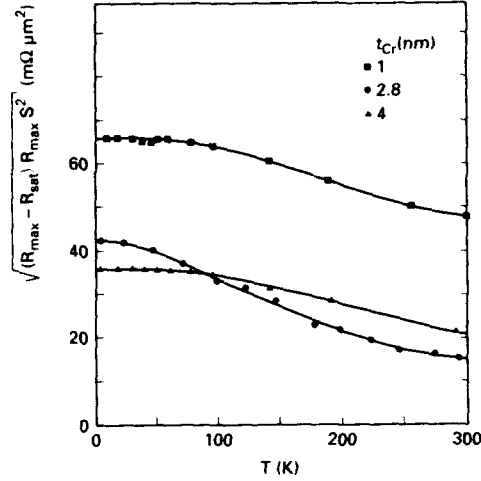


Figure 7: Plot of the temperature dependence of the experimental quantity $\sqrt{(R_{max} - R_{sat}) R_{max} S^2}$ given by the Valet-Fert CPP-theory for samples with different t_{Cr} . Data are derived from experiment using the extrapolation scheme described in the text. Full curves are a guide to the eye.

appropriate experimental quantity to compare with theory is

$$\sqrt{(R_{max} - R_{sat}) R_{max} S^2} = \left[\frac{\beta}{1 - \beta^2} t_{Fe} \rho_{Fe} + \frac{2\gamma}{1 - \gamma^2} r_b \right] \times N \quad (1)$$

where β and γ are spin asymmetry coefficients for bulk and interface scattering, respectively ($0 \leq \beta, \gamma \leq 1$). t_{Fe} and ρ_{Fe} are the Fe thickness and Fe resistivity; r_b is the spin-averaged Fe/Cr boundary resistance per unit surface in the ferromagnetic state and N is the number of Fe/Cr bilayers in the structure. Eq. (1) is valid when the spin-flip diffusion length l_{sf} is much larger than the individual layer thicknesses in the structure, a condition which is generally well fulfilled at low temperatures [9]. A plot of the left hand side of eq.(1) is shown in figure 7 for all temperatures studied. At 4 K, we observe that $\sqrt{(R_{max} - R_{sat}) R_{max} S^2} \simeq 65 \text{ m}\Omega\mu\text{m}^2$ for the sample with $t_{Cr} = 1 \text{ nm}$, while for the other two samples this value is reduced to a number around $40 \text{ m}\Omega\mu\text{m}^2$. One should note that, according to the model, these values would be the same, in the case of perfect AF coupling. To estimate the magnitude of r_b , we take $\beta = 0.33$ and $\gamma = 0.78$; these values correspond to a ratio of spin-down to spin-up scattering length $l_1/l_1 = \frac{1+\beta}{1-\beta} \simeq 2$ for Fe bulk scattering and $l_1/l_1 = \frac{1+\gamma}{1-\gamma} \simeq 8$ for interface scattering, as obtained from a theoretical analysis of the corresponding CIP-MR data [12, 19]. With $N = 100$, $t_{Fe} = 3 \text{ nm}$ and $\rho_{Fe} = 5 - 10 \mu\Omega\text{cm}$ we find that $r_b = 1 - 1.5 \times 10^{-16} \Omega\text{m}^2$ for $t_{Cr} = 1 \text{ nm}$. For the other Cr thicknesses r_b is somewhat reduced. These values are close to the value for r_b found from a similar analysis for the Co/Cu and Co/Ag multilayer system [10]. Hence, the model seems to describe various multilayer systems consistently. Although comparison with theory is most convenient at low temperature, where spin-flip scattering

is minimum and the two-current model is well applicable, the temperature dependence of the effect is particularly interesting because it provides important new information on the critical length scale of the CPP-MR effect, which we can identify as l_{sf} . Due to the increasing importance of electron-magnon scattering, the currents are equalized (as in the CIP-geometry) and, moreover, the reduction of l_{sf} could limit the number of layers and interfaces contributing to the CPP-MR effect.

We also compare our low-temperature experiments with the theory of Bauer [6, 19], which is based on the Landauer-Büttiker scattering formalism of electron transport [20]. In this approach charge and spin accumulation effects in the multilayer are implicitly integrated out. Again absence of spin-flip scattering is assumed, which favors application of the model to low-temperature MR measurements. For the Fe/Cr system, where barrier potentials play a minor role in the giant MR effect, the normalized conductance for the channel with spin σ ($\sigma: \uparrow, \downarrow$) is given by

$$G_{\sigma} = 1 - \frac{2N}{\bar{N}_{\sigma}} + 2\left(\frac{N}{\bar{N}_{\sigma}}\right)^2 \ln\left(1 + \frac{\bar{N}_{\sigma}}{N}\right). \quad (2)$$

Here N is the number of repetitions and \bar{N}_{σ} the mean number of traversed interfaces for spin σ ($\bar{N}_{\sigma} = 1$ corresponds to a mean free path of length $(t_{Cr} + t_{Fe})$). We define the normalized conductance in the ferromagnetic alignment case as $G_F = \frac{1}{2}(G_{\uparrow} + G_{\downarrow})$ and for the AF alignment case we define G_{AF} by eq.(2) with $\frac{1}{\bar{N}_{AF}} = \frac{1}{2}\left(\frac{1}{\bar{N}_{\uparrow}} + \frac{1}{\bar{N}_{\downarrow}}\right)$. Then $MR = (G_F - G_{AF})/G_{AF}$ with $\frac{\bar{N}_{\downarrow}}{\bar{N}_{\uparrow}}$ as a fitting parameter representing the integrated contributions of both magnetic bulk and interface scattering. For the sample with $t_{Cr}=1$ nm and a low temperature MR of 108 %, we find that $\frac{\bar{N}_{\downarrow}}{\bar{N}_{\uparrow}} = 6.4$, while for the sample with $t_{Cr}=2.8$ nm and a MR of 8 % we find that $\frac{\bar{N}_{\downarrow}}{\bar{N}_{\uparrow}} = 1.8$. These numbers reflect an 'effective' spin-dependent mean free path, which is consistent with the ratios of spin-down over spin-up mean free paths quoted in the discussion of the Valet-Fert model. Hence, both models, although of different origin, give similar results for the relevant scattering lengths.

CONCLUSION

We have fabricated pillar-shaped microstructures in Fe/Cr magnetic multilayers and determined the CPP-MR effect for this strongly AF coupled system. Moreover we present the first experiments on the temperature dependence of the CPP-MR effect and make a comparison with the CIP-MR of similarly prepared samples. The decrease of the CPP-MR with temperature has been interpreted tentatively in terms of scattering by thermally excited magnons. Finally we performed a quantitative analysis of our low-temperature data with the Valet-Fert and Bauer models, yielding consistent values for the magnetic scattering parameters.

ACKNOWLEDGEMENTS

We would like to thank H.T. Munsters, H.C. Donkersloot, J.F.M. Janssen, M.M. den Dekker, H.M.M. Bakermans and O.J.A. Buyk for their contributions to the sample preparation, H.H.J.M. Janssen for the finite element simulations and G.E.W. Bauer, R. Coehoorn, A. Fert, H. van Houten, M.T. Johnson, and W.J.M. de Jonge for valuable discussions.

REFERENCES

- [1] M.N. Baibich, J.M. Broto, A. Fert, F. Nguyen van Dan, F. Petroff, P. Etienne, G. Creuzet, A. Friederich, and J. Chazelas, Phys. Rev. Lett. **61**, 2427 (1988).
- [2] G. Binasch, P. Grünberg, F. Saurenbach, and W. Zinn Phys. Rev. B **39**, 4821 (1989).
- [3] S.S.P. Parkin, R. Bhadra, and K.P. Roche, Phys. Rev. Lett. **66**, 2152 (1991).
- [4] S. Zhang, and P.M. Levy, J. Appl. Phys. **69**, 4786 (1991).
- [5] M. Johnson, Phys. Rev. Lett. **67**, 3594 (1991).
- [6] G.E.W. Bauer, Phys. Rev. Lett. **69**, 1676 (1992).
- [7] S.-F. Lee, W.P. Pratt Jr., Q. Yang, P. Holody, R. Loloee, P.A. Schroeder, and J. Bass, J. Magn. Magn. Mat. **118**, L1 (1993).
- [8] H.E. Camblong, S. Zhang, and P.M. Levy, Phys. Rev. B **47**, 4735 (1993).
- [9] T. Valet, and A. Fert, submitted to Phys. Rev. B.
- [10] W.P. Pratt, Jr., S.-F. Lee, J.M. Slaughter, R. Loloee, P.A. Schroeder, and J. Bass, Phys. Rev. Lett. **66**, 3060 (1991); S.-F. Lee, W.P. Pratt, Jr., R. Loloee, P.A. Schroeder, and J. Bass, Phys. Rev. B **46**, 548 (1992); P.A. Schroeder, J. Bass, P. Holody, S.-F. Lee, R. Loloee W.P. Pratt, Jr., and Q. Yang, to be published.
- [11] P. Schroeder, private communication.
- [12] M.A.M. Gijs, and M. Okada, Phys. Rev. B **46**, 2908 (1992); M.A.M. Gijs, and M. Okada, J. Magn. Magn. Mat. **113**, 105 (1992).
- [13] M.A.M. Gijs, S.K.J. Lenczowski, and J.B. Giesbers, Phys. Rev. Lett., to be published.
- [14] S.S.P. Parkin, N. More, and K.P. Roche, Phys. Rev. Lett. **64**, 2304 (1990).
- [15] We define the MR as $(R_{max} - R_{sat})/R_{sat}$, where R_{max} is the maximum resistance at zero field and R_{sat} the resistance value at saturation of the giant MR effect.
- [16] D.L. Mills, A. Fert, and I.A. Campbell, Phys. Rev. B **4**, 196 (1971).
- [17] J.E. Mattson, M.E. Brubaker, C.H. Sowers, M. Conover, Z. Qiu, and S.D. Bader, Phys. Rev. B **44**, 9378 (1991).
- [18] M.A.M. Gijs, J. B. Giesbers, S.K.J. Lenczowski, and H.H.J.M. Janssen, Appl. Phys. Lett., to be published.
- [19] G.E.W. Bauer, M.A.M. Gijs, S.K.J. Lenczowski, and J.B. Giesbers, J. Magn. Magn. Mat., to be published.
- [20] M. Büttiker, IBM J. Res. Dev. **32**, 317 (1988).

THEORY OF THE NEGATIVE MAGNETORESISTANCE IN MAGNETIC METALLIC MULTILAYERS

RANDOLPH Q. HOOD AND L. M. FALICOV

Department of Physics, University of California at Berkeley, and
Materials Sciences Division, Lawrence Berkeley Laboratory, University of California,
Berkeley, California, 94720, USA

ABSTRACT

The Boltzmann equation is solved for a system consisting of alternating ferromagnetic-normal metallic layers. The in-plane conductance of the film is calculated for two configurations: successive ferromagnetic layers aligned (i) parallel and (ii) antiparallel to each other. The results explain the giant negative magnetoresistance encountered in these systems when an initial antiparallel arrangement is changed into a parallel configuration by application of an external magnetic field. The calculation depends on (A) geometric parameters (the thicknesses of the layers); (B) intrinsic metal parameters (number of conduction electrons, magnetization and effective masses in the layers); (C) bulk sample properties (conductivity relaxation times); and (D) interface scattering properties (diffuse scattering versus potential scattering at the interfaces). It is found that a large negative magnetoresistance requires, in general, considerable asymmetry in the interface scattering for the two spin orientations. All qualitative features of the experiments are reproduced. Quantitative agreement can be achieved with sensible values of the parameters. The effect can be conceptually explained based on considerations of phase-space availability for an electron of a given spin orientation as it travels through the multilayer sample in the various configurations and traverses the interfaces.

1. INTRODUCTION

Ferromagnetic-normal metallic superlattices and sandwiches [1,2] display a number of interesting properties, such as a varying interlayer magnetic coupling [3] and a negative, sometimes very large magnetoresistance (MR) effect [4-15]. Examples are (NiFe/Cu/NiFe), (NiFe/Ag/NiFe), (Fe/Cr)_n, (Co/Cu)_n, (Fe/Cu)_n, and (Co/Ru)_n, to name just a few. It has been found that the magnetic moment of each ferromagnetic layer is arranged with respect to that of the neighboring ferromagnetic layers either in a parallel fashion, or in an antiparallel one, depending on the thickness of the metal spacers and on the quality of the interfaces.

When the conditions are such that the consecutive moments are arranged antiparallel to each other, the application of an external magnetic field to the sample results in two effects: (1) the moments rearrange themselves into a completely parallel arrangement in fields of the order of 1 T; and (2) the sample decreases its resistance -- negative MR -- in all directions (in-plane in particular) by varying amounts which can be as small as a few percent, and as large as 55% (for Co/Cu at liquid Helium temperatures) [13]. A decrease by more than 20% is generally known as the *giant magnetoresistance effect* (GMR).

Even though the current knowledge of the MR effect is incomplete, one fact that has emerged is that spin-dependent interfacial scattering plays an important role. Experiments by Fullerton *et al.* [16] indicate that increased interfacial roughness enhances the GMR. Baumgart *et al.* [17] have found that ultrathin layers of elements (V, Mn, Ge, Ir, or Al) deposited at the Fe/Cr interface lead to changes in the MR which correlate with the ratio of spin-up and spin-down resistivities arising from spin-dependent impurity scattering of these elements when alloyed with Fe. This result is in agreement with the suggestion of Baibich *et al.* [4] that the spin-dependence of impurity scattering at the interfaces is related to that observed [18] in alloyed ferromagnetic metals such as Fe, Co, and Ni.

Further confirmation of the importance of the interface in the MR effect was provided by Barthélémy *et al.* [19] who point out that the experimental data they obtained for epitaxially

grown Fe(001)/Cr(001) multilayers seem to be in agreement with a variation of the MR of the form

$$\exp(-t_{Cr}/\lambda^*)$$

where t_{Cr} is the thickness of Cr layer and λ^* is a length of the order of the mean free path. Such a variation of the MR with layer thickness is expected from spin-dependent interface scattering.

It should be emphasized that it is important to distinguish between the concepts of spin-flip scattering and spin-dependent scattering. The first refers to an event in which, during scattering, an electron reverses its spin orientation; such a phenomenon is normally caused by spin-orbit effects and/or by scattering from impurities with a localized magnetic moment. Spin-flip scattering is neglected in this contribution. The second one refers to the fact that electrons with different spin orientations experience different potentials and have different phase-space distributions. Consequently they have very different scattering cross sections both in the bulk and at the interfaces. The latter is extremely relevant for the purposes of this study.

It is the aim of this contribution to present a model that incorporates spin-dependent interfacial scattering in a more realistic way. While the model presented here is similar in many respects to that of Camley and Barnaś [20,21] it does not suffer from the shortcomings in the description of interfacial scattering encountered there. Utilization of a more accurate description of the interface permits a study and separation of the various scattering mechanisms and their relevance in the MR effect.

The present model, an extension of the Fuchs-Sondheimer theory [22,23], uses a Stoner description [24] of the itinerant ferromagnetic layers: it introduces different potentials for majority and minority spins. Band-structure and electron-density effects are included only by means of a constant, metal- and spin-dependent potential, and an isotropic effective mass for each spin in each layer. The different potentials in neighboring layers results in coherent potential scattering (i.e., refraction) of electrons as they traverse the interface. It has been suggested [17] that this effect alone could account for the observed spin-dependent transport properties and the oscillatory effects with layer thickness [3]. Spin-dependent potentials are also responsible for different densities of states at the Fermi level, i.e., different available phase space for the two different spin orientations. The angular-dependent effects are treated by a quantum-mechanical matching of the electron wave functions at the interfaces. Impurity scattering at the interface and interfacial roughness are also a source of spin-dependent scattering, and they contribute to the present model through a spin-dependent function, in a way similar to that used by Camley and Barnaś.

The model predicts the dependence of the MR on the thickness of the layers, on the quality of the samples (mean free path) and on the quality (roughness) of the interfaces.

2. THE MODEL

The in-plane conductivity has been calculated for a multilayer structure consisting of alternating layers of a ferromagnet (F) of thickness d_F , and a spacer layer of thickness d_s . The coordinate system is chosen with the z axis perpendicular to the layers, and with complete isotropy in the (x,y) plane.

For a given structure the conductivity was calculated for both antiparallel alignment, denoted $\sigma_{\uparrow\downarrow}$, and for parallel alignment, denoted $\sigma_{\uparrow\uparrow}$, of the moments of successive F layers. In the antiparallel arrangement the structure repeats itself after four layers (.../F \uparrow /s/F \downarrow /s/...); in the parallel arrangement the period consists of two layers (.../F \uparrow /s/...). Application of a sufficiently large magnetic field to a sample in the antiparallel arrangement causes the magnetic moments to align parallel to one another. The magnetoresistance ($\Delta\rho/\rho$), is defined by

$$\frac{\Delta\rho}{\rho} = \frac{\rho_{\uparrow\downarrow} - \rho_{\uparrow\uparrow}}{\rho_{\uparrow\downarrow}} = \frac{\sigma_{\uparrow\uparrow} - \sigma_{\uparrow\downarrow}}{\sigma_{\uparrow\uparrow}} \quad (1)$$

where $\rho_{\mu\nu} = (\sigma_{\mu\nu})^{-1}$. Note that this quantity varies between zero and one (or 0 and 100%)

whenever the resistance decreases upon the application of an external magnetic field.

The conductivity for both alignments is obtained by adding the contributions of the spin-up and the spin-down electrons, calculated separately. This is the two-current model [18], which provides a good description of electron transport in magnetic 3d metals. As mentioned above spin-flip processes, which mix the two currents, are neglected. It is known that their effect is small at low temperatures.

The electrons involved in transport are regarded as free electron-like with spherical Fermi surfaces. Within each layer the electrons move in a constant potential $V_{i\sigma}$ which depends on the particular layer i and the spin σ of the electron.

The electron distribution function within each layer i and for each spin σ is written in the form

$$f_{i\sigma}(v, z) = f_{i\sigma}^0(v) + g_{i\sigma}(v, z) \quad (2)$$

which is independent of x and y by symmetry. In (2), the first term $f_{i\sigma}^0(v)$ is the equilibrium distribution in the absence of an electric field and $g_{i\sigma}(v, z)$ is the deviation from that equilibrium in the presence of the electric field. For an electric field of magnitude E in the \hat{x} direction, the Boltzmann equation in the relaxation time approximation reduces to

$$\frac{\partial g_{i\sigma}}{\partial z} + \frac{g_{i\sigma}}{\tau_{i\sigma} v_z} = \frac{|e| E}{m_{i\sigma} v_z} \frac{\partial f_{i\sigma}^0}{\partial v_z} \quad (3)$$

where $\tau_{i\sigma}$ is the relaxation time in layer i for spin σ , and e is the charge of the electron. The second-order term, proportional to the product $(E \cdot g_{i\sigma})$, has been discarded since non-linear effects (deviations from Ohm's law) are neglected. The Lorentz-force term, proportional to $(v \times H/c)$, has also been dropped from the Boltzmann equation since it gives an effect which is orders of magnitude smaller than those considered here [20].

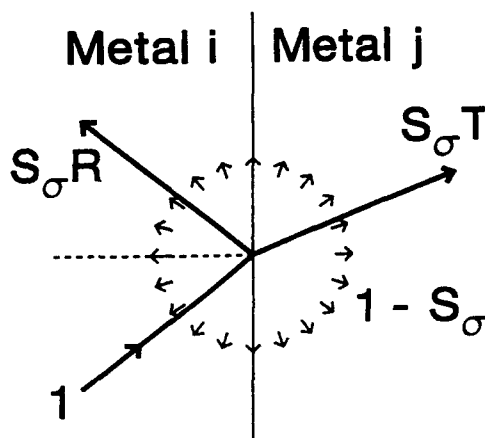


Figure 1. Schematic diagram of the scattering process at the metal-metal interface. The parameter S_σ defines the fraction controlled by the potentials; $S_\sigma R$ is the probability of specular scattering; $S_\sigma T$ is the probability of transmission (refraction) into the other metal.

Because of the boundary conditions it is useful to divide $g_{i\sigma}$ into two parts: $g_{i\sigma}^+(v, z)$ if $v_z \geq 0$ and $g_{i\sigma}^-(v, z)$ if $v_z < 0$. The boundary conditions for the potential (non-diffusive)

scattering at the (i, j) interface then take the form

$$\begin{aligned} g_{i\sigma}^- &= S_{ij,i;\sigma} R_{ij;\sigma} g_{i\sigma}^+ + S_{\mu i,i;\sigma} T_{\mu;\sigma} g_{j\sigma}^- \\ g_{j\sigma}^+ &= S_{\mu j,j;\sigma} R_{\mu;\sigma} g_{j\sigma}^- + S_{ij,j;\sigma} T_{ij;\sigma} g_{i\sigma}^+ \end{aligned} \quad (4)$$

Here $S_{ij,k;\sigma}$, which varies between zero and one, is a factor that indicates the degree of potential scattering at the interface (i, j) for an electron of spin σ arriving at the interface from the layer i and being scattered into the layer k . The scattering follows the reflection-refraction laws when all $S = 1$ and is completely diffusive when $S = 0$. The notation used for the transmission T and the reflection R coefficients is the following: $T_{ij;\sigma}$ = probability for an electron of spin σ in layer i to be transmitted (refracted) into layer j ; $R_{ij;\sigma}$ = probability for an electron of spin σ in layer i with a velocity directed towards layer j to be reflected back into layer i . The equations and boundary conditions, as written, satisfy all necessary conservation laws.

The functional dependence of the coefficients was determined [25] by matching the free electron-like (plane-wave) functions and their derivatives at each interface. The solution to this problem, which is identical to that encountered in optics for an interface between two media with different index of refraction, is shown schematically in figure 1.

The current density along the electric field in each layer i for electrons with spin σ is given by

$$J_{i\sigma}(z) = -|e| \left(\frac{m_{i\sigma}}{h} \right)^3 \int v_x g_{i\sigma}(v, z) d^3v \quad (5)$$

where h is Planck's constant. The conductivity of the multilayer is obtained by averaging over the whole film

$$\sigma = \frac{1}{E} \sum_i \sum_{\sigma=\uparrow, \downarrow} \int J_{i\sigma}(z) dz$$

The MR, $(\Delta\rho/\rho)$, is found by calculating independently the conductivities σ_{\uparrow} and σ_{\downarrow} . The number of parameters necessary to characterize a structure is large. Associated with the electrons in the F layers are the minority (denoted using a small subscript m) and the majority (denoted using a capital subscript M) spins with effective masses m_m and m_M , relaxation times τ_m and τ_M , and potentials V_m and V_M . The spin-up and spin-down electrons in the spacer layer s move in a potential V_s with an effective mass m_s and relaxation time τ_s . At the interfaces, the functions $S_{ij,k;\sigma}$, which vary with angle of incidence, describe the interfacial scattering of the majority and the minority spins.

The values of the potentials are determined by treating all of the valence s and d electrons as being in a single free electron-like band with an isotropic effective mass. The effective mass is, in general, taken to be larger than the electron mass, since the d electrons, which contribute to the density of electrons, are in narrower bands than the free-electron-like s electrons. Within the F layers the bands for the minority and the majority spins are shifted by a k -independent exchange potential, yielding two different spin-dependent, constant potentials, V_m and V_M . The value of the exchange splitting is chosen so that the difference in the density of the majority and the minority electrons yields the net magnetic moment of the bulk ferromagnetic material.

3. RESULTS

The theory, as developed thus far, includes eleven parameters and eight angular functions:

three effective masses m_M , m_m , and m_s ;

three constant potentials V_M , V_m , and V_s ;

three relaxation times τ_M , τ_m , and τ_s ;

two thicknesses d_F , and d_s ;

and eight interface scattering functions

$S_{F,F;M}$, $S_{F,F;m}$, $S_{F,s;M}$, $S_{F,s;m}$, $S_{s,F;M}$, $S_{s,F;m}$, $S_{s,F;F;M}$, and $S_{s,F;F;m}$.

The results presented here include only the cases for which the *relaxation times* are identical $\tau = \tau_m = \tau_M = \tau_s$. (The *mean free paths* of the minority and the majority spins within the F layers and for the spacer metal are still different, however, since the Fermi velocities are different.) The interfaces are treated in two different ways. In the first approach the angular dependence of the functions $S_{ij;k;\sigma}$ is neglected and the eight functions are replaced by two constants

$$\begin{aligned} S_{F,s;F;M} = S_{F,s;s;M} = S_{s,F;s;M} = S_{s,F;F;M} &= S_M \\ S_{F,s;F;m} = S_{F,s;s;m} = S_{s,F;s;m} = S_{s,F;F;m} &= S_m \end{aligned}$$

Now the system is defined by eleven constants.

In the second approach the different angular dependences in various $S_{ij;k;\sigma}$ are explicitly included.

Results are given for two different multilayer systems, $(\text{Fe/Cr})_n$ and $(\text{Fe/Cu})_n$. In these three metals the isotropic effective mass is assumed to be independent of the material and spin orientation with a value $m_M = m_m = m_s = 4.0 \times$ free-electron mass. With this effective mass the potentials, with respect to the Fermi energy E_F chosen to be at $E_F = 0$, are

$$V_M = -8.23 \text{ eV}, V_m = -5.73 \text{ eV for Fe};$$

$$V_s = -5.77 \text{ eV for Cr};$$

$$V_s = -8.54 \text{ eV for Cu}.$$

The parameters that remain to be specified for each case -- $(\text{Fe/Cr})_n$ and $(\text{Fe/Cu})_n$ -- in the constant- S approximation are altogether five: (A) two geometric parameters d_F and d_s ; (B) one relaxation time τ , which depends on bulk sample properties; and (C) two interface scattering parameters S_M , S_m (diffuse scattering versus potential scattering at the interfaces for the majority and the minority spins respectively).

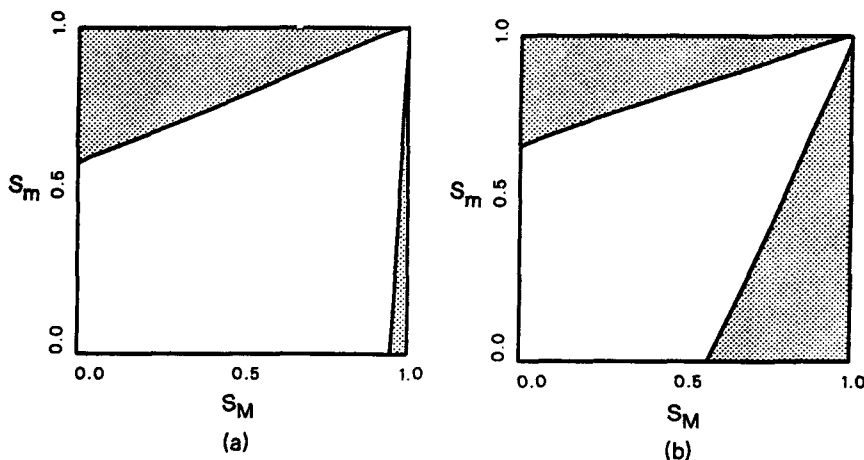


Figure 2. The region in the two-dimensional parameter space (S_M, S_m) where $(\Delta\rho/\rho) > 0.2$ for $d_F = 20 \text{ \AA}$, $d_s = 10 \text{ \AA}$, and $\tau = 5.0 \times 10^{-13} \text{ s}$. (a) Potential parameters corresponding to $(\text{Fe/Cr})_n$. (b) Potential parameters corresponding to $(\text{Fe/Cu})_n$.

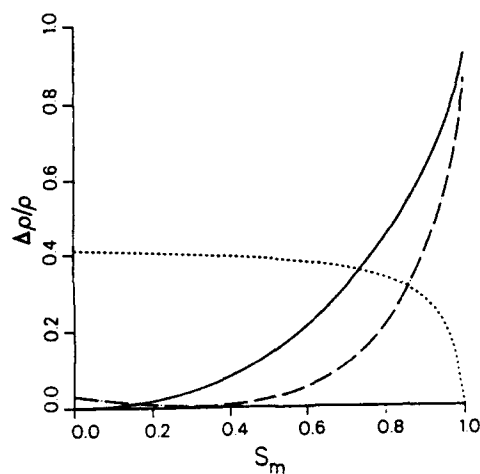


Figure 3. Variation of $(\Delta\rho/\rho)$ as a function of S_m for the parameters of $(\text{Fe/Cr})_n$, $\tau = 5.0 \times 10^{-13} \text{ s}$, $d_F = d_r = 10 \text{ \AA}$ and three values of S_M : (1) dashed curve $S_M = 1$; (2) chain dotted curve $S_M = 0.5$; and (3) solid curve $S_M = 0$.

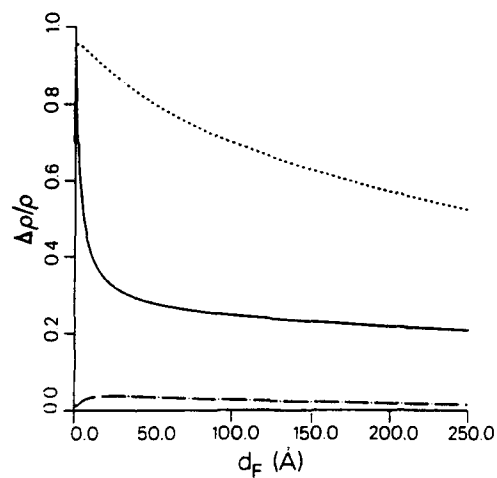


Figure 4. Variation of $(\Delta\rho/\rho)$ as a function of d_F for the parameters of $(\text{Fe/Cr})_n$, $d_r = 10 \text{ \AA}$, $\tau = 5.0 \times 10^{-13} \text{ s}$ and three different values of S_M and S_m : (1) chain dotted curve $S_M = S_m = 0.8$; (2) dashed curve $S_M = 0$, $S_m = 1$; and (3) solid curve $S_M = 1$, $S_m = 0$.

Even with these simplifications, the phenomena under consideration are complicated functions of the 5 variables, and the task of describing these dependencies is not simple. In general terms, and with exceptions, it is found that $(\Delta\rho/\rho)$ is a strong function of the interface parameters S_M and S_m , and a relatively weak function of the thicknesses and the mean free path. For example, as S_M and S_m independently vary between 0 and 1, the calculated $(\Delta\rho/\rho)$ varies between 0 and 92.7% for $(\text{Fe/Cr})_n$ and 0 and 94.4% for $(\text{Fe/Cu})_n$, when values of $d_F = 20.0 \text{ \AA}$; $d_s = 10.0 \text{ \AA}$ and $\tau = 5.0 \times 10^{-13} \text{ s}$ are chosen. Figure 2 shows the regions in the two-dimensional $(S_M - S_m)$ parameter space where $(\Delta\rho/\rho)$ is greater than 20% for these values of d_F , d_s , and τ . With this choice of τ , the mean free paths are: (i) 4,250 \AA for the majority-spin and 3,540 \AA for the minority-spin electrons in Fe; (ii) 3,560 \AA for electrons in Cr; and (iii) 4,330 \AA for electrons in Cu. These values correspond to all mean free paths which are orders of magnitude larger than the film thicknesses, i.e., the clean-film limit, where interface effects are supposed to be paramount.

Some of the interesting results of the calculations are illustrated in figures 2-6. It was found in general that:

(A) $(\Delta\rho/\rho)$ is in general small (only a few percent) when $S_M = S_m$, except [26] when both parameters are very close to 1 (see figures 2 and 3).

(B) $(\Delta\rho/\rho)$, as a function of d_F , exhibits a variety of behaviors which include (i) a monotonic decrease with increasing d_F ; and (ii) an initial increase followed by a decrease (a single maximum); in all cases the asymptotic value as $d_F \rightarrow \infty$ is zero (see figure 4).

(C) $(\Delta\rho/\rho)$, as a function of increasing d_s , exhibits either (i) a continuous monotonic decrease, or, most commonly, (ii) a single maximum at a value of d_s of the order of d_F ; the asymptotic value as $d_s \rightarrow \infty$ is also zero (see figure 5).

(D) $(\Delta\rho/\rho)$, as a function of the relaxation time τ , either (i) increases monotonically and saturates at a maximum value, or, most commonly, (ii) increases to a maximum, and then very gradually decreases (see figure 6).

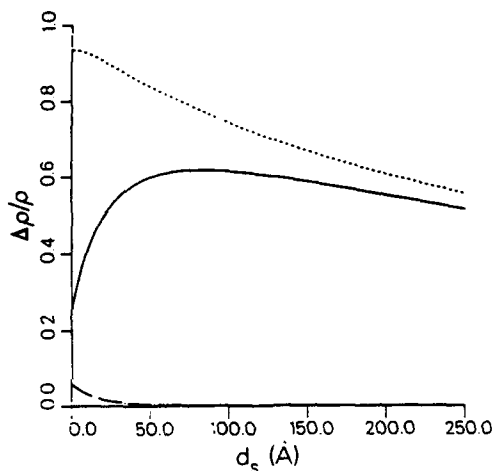


Figure 5. Variation of $(\Delta\rho/\rho)$ as a function of d_s for the parameters of $(\text{Fe/Cr})_n$, $d_F = 20 \text{ \AA}$, $\tau = 5.0 \times 10^{-13} \text{ s}$ and different values of S_M and S_m : (1) solid curve $S_M = 1$, $S_m = 0$; (2) dashed curve $S_M = 0$, $S_m = 1$; and (3) chain-dotted curve $S_M = S_m = 0.9$.

Figure 2 contains information on how, for specific values of d_F , d_I , and τ , the quality of the interfaces influences the MR. It is evident from the figure that the region of large MR is close either to the line $S_M = 1$, or to the line $S_m = 1$, and away from the line $S_M = S_m$. There is a very large asymmetry between S_M and S_m in $(\text{Fe/Cr})_n$, but considerably less so in $(\text{Fe/Cu})_n$.

A more realistic approach to the diffuse-versus-potential scattering at the interface requires a full angular dependence of the eight functions $S_{ij,k,\sigma}$. In general [27-30] the diffuse scattering is considerably larger for electrons impinging upon the interface in directions close to the normal. Grazing-angle electrons are less effectively scattered, and they tend to be almost completely internally reflected. A common (first-order) approximation to these functions [27-30] is

$$S_{ij,i,\sigma} = S_\sigma \exp \left[-4\eta^2 (k_{i\sigma} \cos \Theta_i)^2 \right] ; \quad (6)$$

$$S_{ij,j,\sigma} = S_\sigma \exp \left[-\eta^2 (k_{i\sigma} \cos \Theta_i - k_{j\sigma} \cos \Theta_j)^2 \right] . \quad (7)$$

Here η is a parameter which depends on the roughness of the interface as well as the strength and physical distribution of the scattering centers at the interface, $k_{i\sigma}$ is the magnitude of the k-vector at the Fermi sphere of the spin- σ electrons in layer i , and Θ_i is the angle between the electron velocity and the normal to the interface; S_σ is the overall diffuse scattering strength at grazing angle $\Theta = \pi/2$. It should be noted that the limit $\eta = 0$ reduces the approximation to the one previously discussed.

Figure 7 shows the influence of this angular dependence on the MR. As η increases, the MR in general decreases, except for the case in which S_M and S_m are very close in value; in the latter, the difference in k-vector between the two spins, and the non-vanishing η produce an asymmetry in the diffuse interface scattering between the spins, and thus increases the MR.

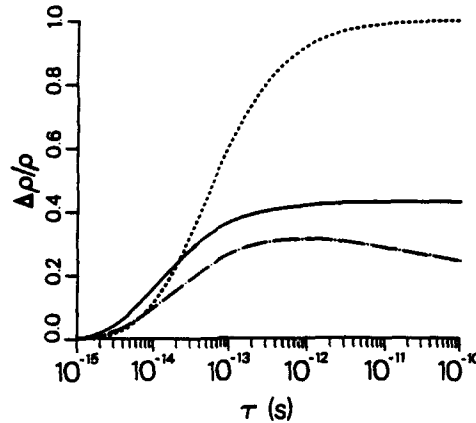


Figure 6. Variation of $(\Delta\rho/\rho)$ as a function of τ for the parameters of $(\text{Fe/Cr})_n$, $d_F = 10\text{\AA}$, $d_I = 20\text{\AA}$, and three different values of S_M and S_m : (1) chain dotted curve $S_M = 0$ and $S_m = 0.7$; (2) dashed curve $S_M = 0.5$ and $S_m = 1$; and (3) solid curve $S_M = 1$ and $S_m = 0$.

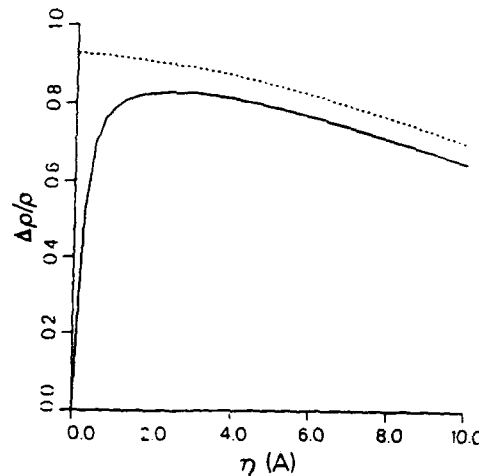


Figure 7. Variation of $(\Delta\rho/\rho)$ as a function of η for the parameters of $(\text{Fe/Cr})_n$, $d_F = 10 \text{ \AA}$, $d_P = 20 \text{ \AA}$ and two different values of S_σ in equations (6) and (7): (1) solid curve $S_M = S_m = 1$; and (2) dashed curve $S_M = 0$, $S_m = 1$.

4. DISCUSSION AND CONCLUSIONS

Figure 2(a) shows a marked asymmetry in the dependence of $(\Delta\rho/\rho)$ for $(\text{Fe/Cr})_n$ on S_M and S_m , i.e., the majority- and minority-spin interface scattering have a very different effect on the MR. For this system

$$|V_M| < |V_s| \approx |V_m|$$

By contrast, a large asymmetry is not present in $(\text{Fe/Cu})_n$, figure 2(b). Here

$$|V_s| \approx |V_M| < |V_m|$$

The difference in V_s has a large effect on the MR, as can be seen in plots of the in-plane current distribution across the layers [25]. In many cases when $(\Delta\rho/\rho)$ is very large, the current distribution responsible for the large value of σ_{\parallel} is such that it is highly concentrated in one type of layer, either in the ferromagnet or in the spacer. This effect, which can be called *channeling*, appears frequently when there is a GMR. When the channeling is in the spacer layer it occurs *only when there is parallel alignment*. Channeling in the FM layers, on the other hand, occurs (in one type of F layer for each electron spin orientation) for both the parallel and the antiparallel configurations. From these considerations it is obvious that channeling in the spacer layer should be more intimately connected with a GMR. It should be emphasized that channeling is present when the potentials are different; GMR requires, in addition, asymmetric values of S_σ . Channeling and GMR are strongly correlated [31].

The experimentally observed values of MR in $(\text{Fe/Cr})_n$ and $(\text{Fe/Cu})_n$ multilayers can be matched by the calculation with a proper choice of the parameters. However, the model in its present form, which considers all of the valence s and d electrons as comprising a single band with a single isotropic effective mass, yields effective resistivities ρ_{\parallel} and ρ_{\perp} which are about an order of magnitude smaller than those measured in multilayer structures. The effective resistivities are too small because the model has too many free-electron-like conduction electrons: eight in Fe, six in Cr, and eleven in Cu. Proper consideration must be taken of the fact that, in

these metals, s and d electrons contribute very differently to the transport properties. The narrow character of the d -bands has been accounted for in the single-band approach by a single, large, isotropic effective mass, four times larger than the free-electron mass. A better approach to the problem would be to include a realistic band structure with its 12 bands, wide and narrow, as well as the hybridization and spin polarization. Such a treatment would make the calculations much more involved.

Within the confines of a single-band model a simple, natural way to decrease the number of conduction electrons is by reducing the density of the electrons in each layer by a constant scaling factor, γ , independent of the material and the spin of the electron. It should be stressed that the introduction of such a scaling factor does not change the form of the results found above. The number of electrons and the magnetization decreases by a factor of γ . The resistivi-

ties $\rho_{\uparrow\uparrow}$ and $\rho_{\uparrow\downarrow}$ increase by a factor of about γ , and $(\Delta\rho/\rho)$ decreases by a factor of about $\gamma^{1/3}$. A value of $\gamma = 8$ was chosen for making comparisons with experimental data. With this value the number of effective free-electron-like conduction electrons are: 1.00 in Fe, 0.75 in Cr, and 1.38 in Cu. Calculations were able to yield values of the MR and the resistivities, $\rho_{\uparrow\uparrow}$ and $\rho_{\uparrow\downarrow}$, similar to those measured experimentally.

Baibich *et al.* [4] found that a multilayer of $(\text{Fe } 30 \text{ \AA} / \text{Cr } 9 \text{ \AA})_{60}$, prepared by molecular beam epitaxy, had $(\Delta\rho/\rho) = 0.46$ and a absolute resistivity change of about $23 \mu\Omega \text{ cm}$. With $S_M = 0.23$, $S_m = 0.98$, $d_F = 30 \text{ \AA}$, $d_s = 9 \text{ \AA}$ and $\tau = 1 \times 10^{-13} \text{ s}$ values of $\rho_{\uparrow\uparrow} = 30.6 \mu\Omega \text{ cm}$ and $\rho_{\uparrow\downarrow} = 56.6 \mu\Omega \text{ cm}$ were calculated, which corresponds to $(\Delta\rho/\rho) = 0.46$ for the MR. Experimental values of ρ are between 20 and $80 \mu\Omega \text{ cm}$. With this choice of γ , τ , and effective mass (i.e., an effective mass of four times the electron mass), the bulk mean free paths are: 425 \AA for the majority-spin and 354 \AA for the minority-spin electrons in Fe; and 356 \AA for the electrons in Cr.

Pédroff *et al.* [14] report that a multilayer $(\text{Fe } 15 \text{ \AA} / \text{Cu } 15 \text{ \AA})_{60}$ made by sputtering, had the following characteristics: $\rho_{\uparrow\uparrow} = 24.8 \mu\Omega \text{ cm}$, $\rho_{\uparrow\downarrow} = 27.8 \mu\Omega \text{ cm}$, and $(\Delta\rho/\rho) = 0.108$. With $S_M = 0.71$, $S_m = 0.92$, $d_F = d_s = 15 \text{ \AA}$ and $\tau = 1 \times 10^{-13} \text{ s}$ values of $\rho_{\uparrow\uparrow} = 25.2 \mu\Omega \text{ cm}$ and $\rho_{\uparrow\downarrow} = 28.3 \mu\Omega \text{ cm}$ were calculated, which correspond to $(\Delta\rho/\rho) = 0.11$. Here the bulk mean free paths are: 425 \AA for the majority-spin and 354 \AA for the minority-spin electrons in Fe; and 433 \AA for the electrons in Cu.

As clearly seen above, a large MR requires, in general, a large difference in interface scattering for the different spins. When $S_M = S_m$ the MR is found to be not more than a few percent. Therefore a large MR cannot be explained as being caused solely by different densities of electrons with different spins, which vary from layer to layer. What is required is a spin imbalance and a spin-dependent scattering mechanism at the interface, i.e., $S_M \neq S_m$. When such a spin-dependent scattering mechanism exists, for example when magnetic impurities are present at the interfaces, the MR is profoundly influenced by spatial variations in the density of electron spins. This is the main cause of the GMR effect in ferromagnetic multilayers.

ACKNOWLEDGMENTS

We acknowledge helpful discussions with A. da Silva, P. Levy and D. R. Penn. RQH acknowledges the support of the Department of Education. This research was supported, at the Lawrence Berkeley Laboratory, by the Director, Office of Energy Research, Office of Basic Energy Sciences, Materials Science Division, U.S. Department of Energy, under contract No. DE-AC03-76SF00098.

REFERENCES

- [1] Thin Film Growth Techniques for Low-Dimensional Structures, edited by R. F. C. Farrow, S. S. P. Parkin, P. J. Dobson, J. H. Neave, and A. S. Arrott (Plenum, New York, 1987).
- [2] Synthetic Modulated Structures, edited by L. L. Chang and B. C. Giessen (Academic, New York, 1985); Metallic Superlattices: Artificially Structured Materials, edited by T. Shinjo

- and T. Takada, *Studies in Physical and Theoretical Chemistry* Vol. 49 (Elsevier, Amsterdam, 1987); B. Y. Jin and J. B. Keuerson, *Adv. Phys.* **38**, 189 (1989).
- [3] S. S. P. Parkin, *Phys. Rev. Lett.* **67**, 3598 (1991).
 - [4] M. N. Baibich, J. M. Broto, A. Fert, F. Nguyen Van Dau, F. Pétroff, P. Etienne, G. Creuzet, A. Friederich, and J. Chazelas, *Phys. Rev. Lett.* **61**, 2472 (1988).
 - [5] S. S. P. Parkin, N. More, and K. P. Roche, *Phys. Rev. Lett.* **64**, 2304 (1990).
 - [6] G. Binasch, P. Grünberg, F. Saurenbach, and W. Zinn, *Phys. Rev. B* **39**, 4828 (1989).
 - [7] B. Dieny, V. S. Speriosu, S. S. P. Parkin, B. A. Gurney, D. R. Wilhoit, and D. Mauri, *Phys. Rev. B* **43**, 1297 (1991).
 - [8] A. Chaiken, P. Lubitz, J. J. Krebs, G. A. Prinz, and M. A. Harford, *J. Appl. Phys.* **70**, 5864 (1991).
 - [9] B. Dieny, V. S. Speriosu, S. Metin, S. S. P. Parkin, B. A. Gurney, P. Baumgart, and D. R. Wilhoit, *J. Appl. Phys.* **69**, 4774 (1991).
 - [10] A. Chaiken, T. M. Tritt, D. J. Gillespie, J. J. Krebs, P. Lubitz, M. Z. Harford, and G. A. Prinz, *J. Appl. Phys.* **69**, 4798 (1991).
 - [11] A. Chaiken, G. A. Prinz, and J. J. Krebs, *J. Appl. Phys.* **67**, 4892 (1990).
 - [12] T. Miyazaki, T. Yaoi, and S. Ishio, *J. Magn. and Magn. Mat.* **98**, L7 (1991).
 - [13] S. S. P. Parkin, Z. G. Li, and D. J. Smith, *Appl. Phys. Lett.* **58**, 2710 (1991).
 - [14] F. Pétroff, A. Barthélémy, D. H. Mosca, D. K. Lottis, A. Fert, P. A. Schroeder, W. P. Pratt Jr., and R. Loloee, *Phys. Rev. B* **44**, 5355 (1991).
 - [15] W. P. Pratt, Jr., S. F. Lee, J. M. Slaughter, R. Loloee, P. A. Schroeder, and J. Bass, *Phys. Rev. Lett.* **66**, 3060 (1991).
 - [16] E. E. Fullerton, D. M. Kelly, J. Guimpel, I. K. Schuller, and Y. Bruynseraede, *Phys. Rev. Lett.* **68**, 859 (1992).
 - [17] P. Baumgart, B. A. Gurney, D. R. Wilhoit, T. Nguyen, B. Dieny, and V. Speriosu, *J. Appl. Phys.* **69**, 4792 (1991).
 - [18] A. Fert and I. A. Campbell, *J. Phys. F: Metal Phys.* **6**, 849 (1976); I. A. Campbell and A. Fert, in *Ferromagnetic Materials*, edited by E. P. Wohlfarth (North-Holland, Amsterdam, 1982), Vol. 3, p. 769.
 - [19] A. Barthélémy, A. Fert, M. N. Baibich, S. Hadjoudj, F. Pétroff, P. Etienne, R. Cabanel, S. Lequien, F. Nguyen Van Dau, and G. Creuzet, *J. Appl. Phys.* **67**, 5908 (1990).
 - [20] J. Barnaś, A. Fuss, R. E. Camley, P. Grünberg, and W. Zinn, *Phys. Rev. B* **42**, 8110 (1990).
 - [21] R. E. Camley and J. Barnaś, *Phys. Rev. Lett.* **63**, 664 (1989).
 - [22] K. Fuchs, *Proc. Cambridge Philos. Soc.* **34**, 100 (1938).
 - [23] E. H. Sondheimer, *Adv. Phys.* **1**, 1 (1952).
 - [24] E. C. Stoner, *Proc. R. Soc. London A* **165**, 372 (1938).
 - [25] R. Q. Hood and L. M. Falicov, *Phys. Rev. B* **46**, 8287 (1992).
 - [26] The particular result $(\Delta\rho/\rho) = 0$ is valid for $S_M = S_m = 1$ and for any combination of geometric and intrinsic metal parameters as long as $\tau_{i\sigma} = \tau_{\sigma}$, i.e., the relaxation times for each spin is the same in all layers of the system.
 - [27] S. B. Soffer, *J. Appl. Phys.* **38**, 1710 (1967).
 - [28] V. Bezák and J. Krempaský, *Czech. J. Phys. B* **18**, 1264 (1968).
 - [29] V. Bezák, M. Kedro, and A. Pevala, *Thin Solid Films* **23**, 305, (1974).
 - [30] D. R. Penn, R. Q. Hood, and L. M. Falicov (private communication).

- [31] It should be noted that the channeling effect, *per se*, does not necessarily lead to a GMR, as can be seen from the case shown in figure 3 [$(\Delta\rho/\rho) = 0$ for $S_M = S_m = 1$; the current distribution is nevertheless concentrated in the ferromagnetic layers]. The GMR appears when, in the parallel arrangement, there is channeling for *only one spin* and diffuse interface scattering for the other one. In that case, in the antiparallel arrangement, both spins partake in the diffuse scattering, and the long electron trajectories (and the channeling) are lost.

HIGH-FIELD GIANT MAGNETORESISTANCE IN Co-Cu SUPERLATTICES

DARRYL BARLETT, FRANK TSUI, LINCOLN LAUHON, TUSHAR MANDREKAR,
CTIRAD UJER AND ROY CLARKE
University of Michigan, Harrison Randall Laboratory of Physics, Ann Arbor, MI 48109.

ABSTRACT

We present evidence for a new type of giant magnetoresistance in (111) cobalt-copper superlattices with atomically smooth interfaces. We propose that the lowered dimensionality of the structure leads to an enhancement of the scattering of conduction electrons from paramagnetic interfaces obeying a Langevin-like saturation at very high fields, well beyond the switching field of the Co layers. The findings help to explain similarities in magnetotransport behavior with recently reported granular systems as well as differences with antiferromagnetically coupled multilayers.

INTRODUCTION

Several groups¹⁻³ have reported magnetoresistance (MR) values in MBE-grown Co-Cu (111) superlattices approaching the 'giant' effects associated with antiferromagnetic (AFM) coupling in Fe-Cr samples⁴. Whether the MR behavior observed in Co-Cu (111) samples also originates from AFM coupling is somewhat unclear at this point: their magnetization seems to be predominantly ferromagnetic in character with only a small fraction of the sample showing indications of AFM coupling.⁵ In another recent experiment⁶, on Co-Cu (111) multilayers grown on Cu single crystal substrates, there was no consistent evidence of AFM coupling.

Sample defects have been invoked as a possible explanation of why AFM may be masked in the Co-Cu (111) system. For example, it has been suggested that stacking faults⁷ and pinholes⁸ may lead to ferromagnetic bridging across neighboring layers. Well-controlled sample growth and detailed atomic-scale characterization are therefore crucial to understanding the magnetic behavior of these materials.

Here we present MR and magnetization results on a series of (111) single crystal Co-Cu superlattices, prepared by molecular beam epitaxy techniques with atomically smooth interfaces. We observe the appearance of a new type of giant magnetoresistance, one which is not dependent on AFM coupling and is operative up to high magnetic fields. By careful control of the interfacial quality, and consequently the uniformity of the layering, we are able to probe in some detail the role of the interfaces. In the limit of atomically smooth interfaces, our results suggest that the lowered dimensionality of the interfaces dominates the behavior rather than sample defects.

SAMPLE GROWTH AND CHARACTERIZATION

The series of samples were grown by molecular beam epitaxy on Ge-buffered (110) GaAs substrates. Buffer layers of 15Å (110) bcc Co, followed by 20Å (111) Au, were deposited on the Ge to initiate layer-by-layer superlattice growth in the (111) orientation. The subsequent superlattice layers were of the form $[\text{Co}(7.5\text{ML})/\text{Cu}(x\text{ML})]_n$ with $x = 2$ to 17 ML; n , the number of bilayers, was typically 30. The pressure during superlattice growth was $<4 \times 10^{-10}$ mbar, and the substrate temperature was held at 150°C. Co was deposited from an electron beam hearth at rates between 0.15 and 0.30Å⁻¹ sec, and Cu from a Knudsen cell at a rate of 0.325Å/sec. The thickness variations of individual layers of Co and Cu were controlled to about 0.1 ML. Details of the growth are described in a previous publication⁹. The growth was monitored *in-situ* by reflection high energy electron diffraction (RHEED) using a CCD imaging and analysis system¹⁰. X-ray scattering performed after growth confirmed that the layer stacking was fcc in the (111) orientation⁹.

A critical aspect of the interface characterization involved spin-echo NMR measurements of the local cobalt environment. These results are described in a separate publication¹¹; suffice it to point out here that the Co NMR spectra provide definitive evidence for atomically abrupt interfaces in these samples. The high quality of our MBE samples is illustrated by cross-sectional HRTEM (Fig. 1). Note that the atomic layers are coherent over hundreds of Å. Our TEM studies do not support the existence of gross defects^{7,8} of the kind that may give rise to ferromagnetic bridging.

The MR measurements were made using the standard DC 4-point probe technique, with the field applied parallel to the current (longitudinal MR). The magnetization was measured in a commercial SQUID magnetometer and the measured saturation moments are within 5% of the bulk value of Co. Both the magnetization and MR measurements were made for the fields applied in the growth plane along the [110] and [112] directions of the superlattice¹².

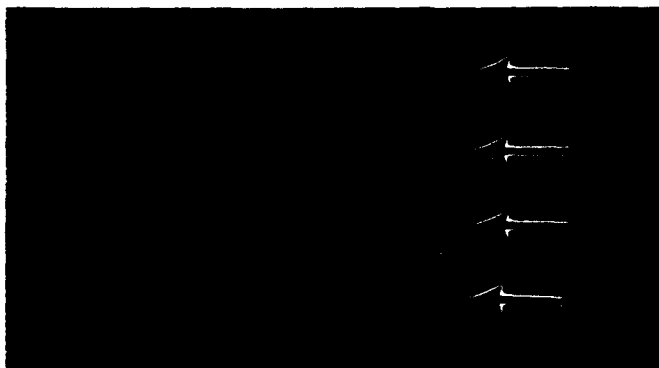


Fig. 1: High resolution transmission electron micrograph of cross-section of $x = 5.5$ ML sample. The bilayer-periodicity (27Å) is indicated by the arrows.

COMPARISON OF MAGNETIZATION BEHAVIOR AND MAGNETORESISTANCE

Fig. 2 compares the MR of an $x = 5.5$ ML sample with its magnetization for fields applied along the [112] direction. Immediately it is apparent that the magnetization saturation field is more than 100 times smaller than that of the MR. In fact the MR is still changing significantly at the highest field we can achieve in our cryostat (5T). Some authors have ascribed this high-field behavior of the MR to very strong AFM coupling^{1,2,3,8}. Here we provide an alternative explanation which resolves the discrepancy between the different saturation behaviors of the MR and the magnetization.

Fig. 3 again compares the MR with the magnetization, except this time focusing on the low-field regime. The data shown are for a sample with 4 ML Cu spacer-layer thickness, which is slightly thinner than that for the data shown in Fig. 2. Note that the MR is about 3 times smaller in the 4 ML sample than in the 5.5 ML sample. The data in Fig. 3 exhibit small and hysteretic dips ($\sim 0.4\%$) at low fields which correlate with the switching fields of the magnetization. Thick Co films grown by the same techniques also exhibit such low field features which evidently arise from anisotropy induced spin-dependent scattering in Co. There is no such dip in the giant MR signal of the 5.5 ML sample [see inset of Fig. 2(a)]. On all our samples we observe that the giant values of MR and the presence of the hysteretic magnetization-dependent MR are mutually exclusive. As discussed below, this turns out to be an important clue as to the origin of the giant MR in these samples.

Fig. 4:

a) $T = 300\text{K}$ magnetoresistance vs. field (Tesla) for a $[\text{Co } 7.5 \text{ ML}/\text{Cu } 5.5 \text{ ML}]_{28}$ superlattice. The dashed line is a theoretical fit to the Langevin function described in the text, where $N = 480$ and $B = 0.194$. Inset: low-field MR vs field dependence.

b) Magnetization curve for same sample. $M_{\text{sat}} = 1400 \text{ emu/cm}^3$. Inset: low-field magnetization curve. $T = 300\text{K}$.

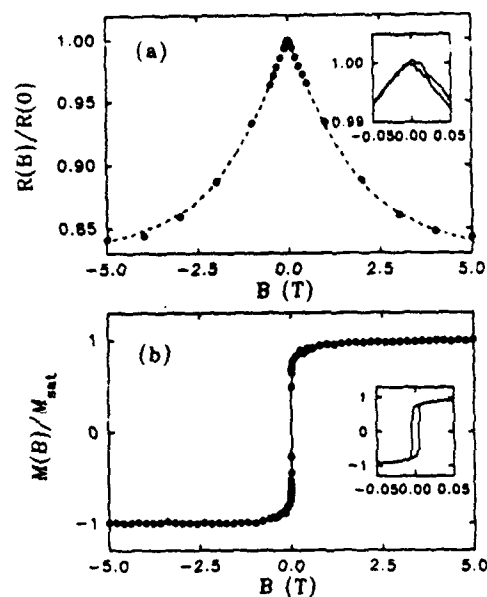
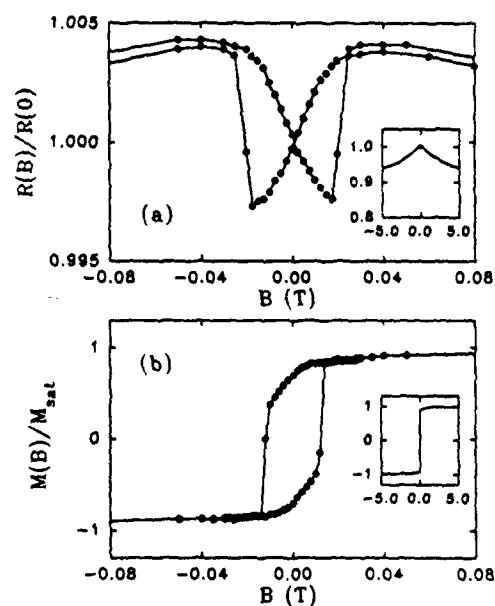


Fig. 3:

a) $T = 300\text{K}$ low-field MR vs. field (Tesla) for a $[\text{Co } 7.5 \text{ ML}/\text{Cu } 4 \text{ ML}]_{40}$ superlattice. Inset: High field MR vs field dependence.

b) Magnetization curve for same sample. $M_{\text{sat}} = 1400 \text{ emu/cm}^3$. Inset: High field magnetization curve. $T = 300\text{K}$.



The field dependence of the MR shown in Fig. 2(a) can be described accurately by a Langevin-like saturation function, $1 - B[\coth\alpha - 1/\alpha]$, where $\alpha = N\mu_0 B/k_B T$, B is a scale factor and μ_0 is the Bohr magneton. This specific field dependence suggests that scattering from an assemblage of paramagnetic spins, most likely at the interfaces between Co and Cu layers, is responsible for the giant MR in our samples. Such "loose" spins have been postulated¹³ to account for the observation of biquadratic coupling in ideal multilayers. We also note the possibility that the Cu conduction electron band could itself become partially polarized in proximity to the Co layers¹⁴.

It is interesting to point out here that the character of the paramagnetism is not that of isolated spins; rather, we find that there are substantial correlations, akin to a superparamagnetic layer. We envision the paramagnetic spin arrangement as forming small patches of correlated spins of size \sqrt{N} . The values of N returned by the Langevin fit at ambient temperature are roughly 500, falling approximately linearly towards unity at $T=0$ (Fig. 4), presumably as more and more of the interface spins lock into the (saturated) bulk Co magnetization. The value of B , corrected for electron-phonon scattering, is practically temperature independent showing that the temperature dependence is controlled by coupling to the bulk ferromagnetic magnetic moment. We note in passing that these findings make contact with recent observations of giant MR in annealed granular Co-Cu films.¹⁵ In these systems the field dependence is also Langevin-like, very similar to that described here, indicating the importance of specular scattering at the surfaces of the precipitates in the granular systems.

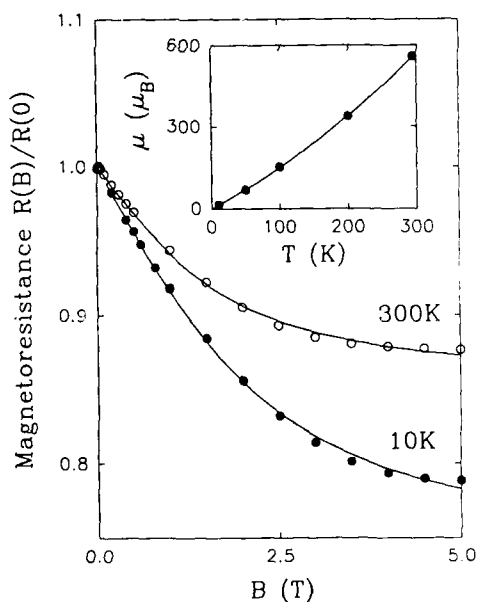


Fig. 4: Field dependence of MR at two different temperatures. The solid lines are fits to the Langevin function described in the text. Inset: number of correlated spins as a function of temperature.

The field dependent MR results discussed here point to a new mechanism for GMR that depends on the high electron reflectivity of the interfaces, not the ferromagnetic spins in the Co layers, since the Co layers are already fully saturated at low fields. The traditional spin dependent scattering mechanism, as it has been discussed previously⁴ in the context of AFM coupling is not present in the results discussed here, since it requires one-to-one correlation between MR and magnetization. However, in the sputtered samples, which typically have somewhat diffuse interfaces, it describes the MR rather well.¹⁶

Lastly, we mention briefly the Cu thickness dependence of the MR. We have observed very abrupt increases in the MR at $t_{\text{Cu}} \sim 5.5$ ML. This is not indicative of an oscillatory interlayer coupling; rather, the discrete nature of the thickness dependence suggests quantum confinement of the conduction electrons in the Cu layers. A number of previous publications have reported evidence for quantum well states¹⁷ in metal overlayers. It is not clear why the peaks in the MR occur at the specific Cu layer thicknesses we observe (multiples of ~ 5 ML). One possible explanation invokes the intersection of quantized mini-zone boundaries with specific regions of the Cu Fermi surface, leading to a significant reduction in conductivity as a result of the alteration of the bulk-like density of states. The bulk Cu Fermi surface is nearly spherical with "necks" along the $[111]$ directions near the L-point of the Brillouin zone. The wavevectors that span the Fermi surface are the "belly" vector, $k_B = 1.35 \text{ \AA}^{-1}$, and the "neck" vector, $k_N = 0.26 \text{ \AA}^{-1}$. Such an intersection at the necks for the (111) growth direction occurs at an estimated wavevector $\sim 0.28 \text{ \AA}^{-1}$.¹⁸ At multiples of this wavevector one might expect the largest effects in the MR. In real space these vectors correspond to Cu thicknesses in multiples of $\pi/0.28 \text{ \AA}^{-1} \sim 11.3 \text{ \AA}$ (5.5 ML).

CONCLUSIONS

In light of the above interpretation, what are the consequences for interlayer coupling? Due to enhanced scattering by the interfacial paramagnetic layers, we suggest that the exchange interactions between the neighboring magnetic Co layers are significantly weakened. We find that for the superlattices with the smoothest interfaces, the low-field magnetization dependant MR is completely absent. In this case we perhaps obtain complete confinement in the Cu layers, so that the conduction electrons are 'rattling' between neighboring Co layers. We emphasize that the amount of confinement would be very sensitive to the quality of the interfaces and it can vary through the sample and from sample to sample. Magnetic neutron scattering on our 5.5 ML and 11 ML samples has so far revealed no evidence for coupling, consistent with the picture described above. We believe the presence of AFM coupling and the absence of high-field MR in sputtered films are the result of atomically rough interfaces. In this case there would be no confinement. The observed giant MR in such samples arises from the spin-dependent AFM scattering mechanism.

In summary we have demonstrated what we believe is a new type of high field MR mechanism which results from scattering of conduction electrons from paramagnetic Co-Cu interfaces. We hope that our results will stimulate additional theoretical work in this area.

ACKNOWLEDGMENTS

We acknowledge the help of B. Demczyk and J. Mansfield of the University of Michigan Electron Microbeam Analysis Laboratory in obtaining HRTEM data. Funding for this work was provided by ONR Grant No. N00014-92-J-1335.

REFERENCES

1. D. Greig, M.J. Hall, C. Hammon, B.J. Hickey, H.P. Ho, M.A. Howson, M.J. Walker, N. Wiser, and D.G. Wright, *J. Magn. Magn. Mater.* **110**, L239 (1992); see also this Proceedings.
2. J.P. Renard, P. Beauvillain, C. Dupas, K. Le Dang, P. Veillet, E. Vélú, C. Marlière, and D. Renard, *J. Magn. Magn. Mater.* **115**, L147 (1992).
3. J. Kohlhepp, S. Cordes, H. J. Elmers, and U. Gradmann, *J. Magn. Magn. Mater.* **111**, L231 (1992).
4. M.N. Baibich, J.M. Broto, A. Fert, F. Nguyen Van Dau, F. Petroff, P. Eitenne, G. Creuzet, A. Friederich, and J. Chazelas, *Phys. Rev. Lett.* **61**, 2472 (1988).
5. J.F. Ankner, A. Schreyer, C.F. Majkrzak, K. Bröhl, Th. Zeidler, P. Bödeker and H. Zabel, in this Proceedings.
6. W.F. Egelhoff, Jr. and M.T. Kief, *Phys Rev B* **45**, 7795 (1992).
7. U. Gradmann, in this Proceedings.
8. S.S.P. Parkin, R.F. Marks, R.F.C. Farrow, G.R. Harp, Q.H. Lam and R.J. Savoy, *Phys. Rev. B* **46**, 9262 (1992).
9. F.J. Lamelas, C.H. Lee, H. He, W. Vavra, and R. Clarke, *Phys. Rev. B* **40**, 5837 (1989).
10. Model KSA 300, manufactured by k-Space Associates, Inc.
11. K. Le Dang, P. Veillet, H. Hui, F.J. Lamelas, C.H. Lee, and R. Clarke, *Phys. Rev. B* **41** 12902 (1990).
12. The observed MR is nearly isotropic while the in-plane magnetization anisotropy is significant. This perhaps is due to the symmetry of the substrate. This result is not central to the work presented here and will be reported in a subsequent publication.
13. J. C. Slonczewski, *J. Appl. Phys.* **73**, 5957 (1993).
14. S. Pizzini, A. Giorgetti, F. Baudalet, E. Dartyge, A. Fontaine, J. F. Bobo, M. Piccuch, S. Stabler, G. Schutz, S.S.P. Parkin, J. Stöhr and C. Marlière, see this Proceedings.
15. A.E. Berkowitz, J. R. Mitchell, M.J. Carey, A.P. Young, S. Zhang, F.E. Sapda, F.T. Parker, A. Hutten and G. Thomas, *Phys. Rev. Lett.* **68**, 3745 (1992); J.Q. Xiao, J.S. Jainag and C.L. Chien, *ibid.* **68** 3749 (1992).
16. S.S.P. Parkin, R. Bhadra and K.P. Roche, *Phys Rev. Lett.* **66**, 2152 (1991); V.S. Speriosu, B. Dieny, P. Humbert, B.A. Gurney, and H. Lefakis, *Phys. Rev. B* **44**, 5358 (1991).
17. J.E. Ortega and F.J. Himpsel, *Phys. Rev. Lett* **69**, 844 (1992); see also this Proceedings.
18. R. Coehoorn, M.T. Johnson, W. Folkerts, S.T. Purcell, N.W.E. McGee, A. De Veirman, and P.J.H. Bloemen, in Magnetism and Structure in Systems of Reduced Dimension, (Plenum, New York, 1993); also see this Proceedings.

Growth Temperature Dependence of Magnetoresistance in Co/Cu(111) Wedged Superlattices

G. R. Harp, S. S. P. Parkin, R. F. C. Farrow, R. F. Marks, M. F. Toney, Q. H. Lam, T. A. Rabedeau, A. Cebollada, and R. J. Savoy
IBM Almaden Research Center, 650 Harry Rd., San Jose, CA 95120-6099

Abstract

The magnetoresistance of MBE deposited Co/Cu(111) superlattices as a function of Cu layer thickness is studied at various growth temperatures. Wedged superlattices are fabricated with uniform Co layers but with Cu layers whose thickness varies with position along the length of the substrate. Cu thickness is varied over the range 7-75 Å. Only one maximum in magnetoresistance (MR) is observed for a Cu layer thickness ≈ 10 Å for all growth temperatures studied (0°, 150°, 200°C). The optimal magnetoresistance values are achieved with 150°C growth temperature.

1 Introduction

The Co/Cu multilayer system has received much attention because record values of magnetoresistance (65% at room temperature) are observed in polycrystalline-sputtered Co/Cu multilayers[1]. This giant magnetoresistance (GMR) is associated with antiferromagnetic exchange coupling between alternating Co layers, and the exchange coupling is itself oscillatory with Cu layer thickness, oscillating between antiferromagnetic (AFM) and ferromagnetic (FM) coupling with increasing Cu layer thickness[2, 3]. Such sputtered multilayers are weakly textured in the (111) orientation. However, GMR and oscillatory exchange coupling have proven elusive in single-orientation (111) multilayers of Co/Cu grown by MBE.

Prior to 1992, a number of groups published results showing neither GMR nor oscillatory exchange coupling in (111) Co/Cu multilayers[4, 5, 6]. Then in 1992, GMR was observed by several groups[7, 8, 9, 10, 11], but only at one Cu layer thickness (≈ 10 Å), so there was no evidence for oscillatory exchange coupling. It was found that subtle defects appear to quench the AFM coupling (and hence GMR) so that even samples deposited under nominally identical conditions on similar substrates could show large variations in GMR[11].

The search for oscillatory exchange coupling in Co/Cu(111) continues in 1993 with several groups having made more in-depth studies of the magnetic and transport properties of such multilayers[12, 13, 14, 15, 16, 17]. The results from these studies are not at all in agreement, and naturally highlight different growth and/or measurement techniques. Our particular approach focuses on improving reproducibility in sample preparation, and on structural characterization of our samples to try to identify defects which might inhibit AFM coupling.

2 Experiment

The substrates for film growth are basal-plane sapphire strips (Insaco Inc.). Single samples were deposited on 25mm diameter substrates, and wedged samples onto rectangular substrates about 50mm long by 11mm wide. The back sides of the wedge substrates are scribed to a depth of 0.25mm (one half their thickness) at 2mm intervals across the along the length



of the strip. After growth of the superlattice, these strips can be broken into many pieces for measurement of magnetoresistance.

The final structure of the superlattice wedges is depicted in figure 1. The thickness variation of the Cu spacer layers is obtained by orienting the effusion cell at about 30° to the sample surface normal direction, with a sample to source distance of about 30cm. This gives rise to a copper deposition rate which varies by more than a factor of 2 over a two-inch sample. All of the SL's and structures discussed here show good crystalline ordering, as determined by RHEED and LEED. The Co/Cu [111] texture axis for these samples had a dispersion of 0.5° FWHM[11].

Figure 2 (a) shows the room temperature magnetoresistance (MR) measurements made on a number of samples grown one at a time onto 1" sapphire substrates. Note there is evidence for a single peak in MR for Cu layer thickness, $t_{\text{Cu}} = 9 \text{ \AA}$. However, there is significant scatter in the data due to uncontrolled variations in sample preparation. Such uninterpretable variations are observed by other groups for various substrates and deposition techniques (see e.g. [7, 6]). This indicates one of the major challenges in the study of Co/Cu(111) superlattices, and our response to this problem has been the development of the wedged superlattices technique. Here we deposit superlattices with uniform Co layers but with Cu layers which vary in thickness along the substrate. Thus a large number of superlattices may be deposited simultaneously under identical conditions, controlling the otherwise uncontrollable variations seen in figure 2.

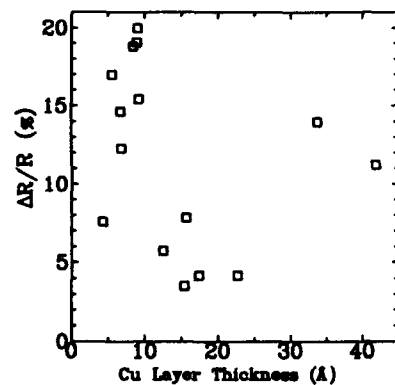


Figure 2: Room temperature magnetoresistance versus Cu layer thickness for Co/Cu(111) superlattices grown one at a time.

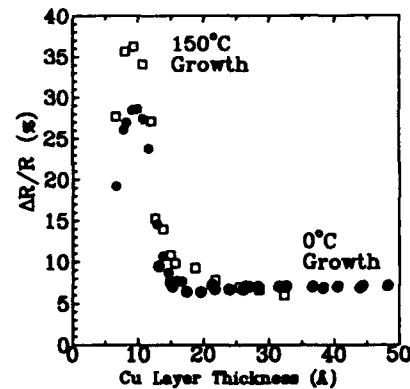


Figure 3: Room temperature magnetoresistance versus Cu layer thickness for superlattice wedges deposited at 0°C and 150°C.

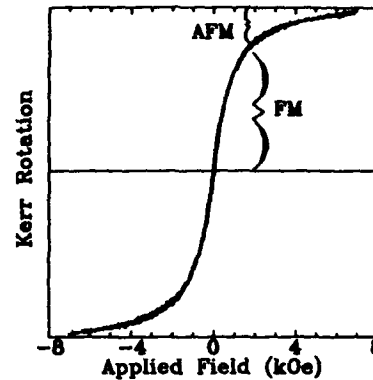
The MR results from the superlattice wedge samples are displayed in figure 3 for two different deposition temperatures. Considering only the 0°C deposited samples for the moment, we see that this technique has two great advantages over single-sample deposition. Firstly, MR is sampled with a uniform and high point density as a function of Cu layer thickness, and secondly, the scatter (noise) in the data is reduced to a very low level. It becomes possible to reliably measure even small variations in MR with t_{Cu} , if such variations exist.

One perhaps surprising result is that in figures 2 and 3, no evidence of oscillatory MR (indicating oscillatory exchange coupling) is observed. One peak in MR is seen at $\approx 9\text{\AA}$, but no subsequent peaks at higher t_{Cu} are observed. Instead, there is only a monotonic decay of MR with increasing t_{Cu} . In an attempt to optimize the growth properties of these structures, samples were deposited at elevated temperatures (150°C, 200°C). It was found that 150°C deposition gave improved MR in the first peak at 9Å, and these data are also plotted in figure 3. But no subsequent oscillations in MR were observed beyond the 9Å peak for samples grown at any temperature.

The magneto-optic Kerr effect (MOKE) is used to generate the in-plane magnetization loop depicted in figure 4 from a sample deposited at 0°C with Cu layer thickness of 11Å. We deduce that all samples, even those with t_{Cu} corresponding to the first MR peak, are primarily ferromagnetic in behavior, but that all show a small antiferromagnetic remnant. That is, the magnetization loops consist of two distinct parts. There is a ferromagnetic-like region where the magnetization increases rapidly with applied field to 70-95% its saturation value in a field of $\approx 1.5\text{ kOe}$ (the small remanence observed here is due to a weak perpendicular anisotropy in the ferromagnetic component[11]). This is followed by an antiferromagnetic-like region which saturates much more slowly, and is in fact never saturated in the available applied field here of $\approx 7\text{ kOe}$. We find that this antiferromagnetic-like component of the sample is the component giving rise to the GMR, and that this component can require very large fields ($>6\text{T}$) for saturation[11, 12].

Interestingly, the AFM coupled region of the magnetization loops do not follow straight lines as a function of applied field. This might lead one to suspect that biquadratic coupling

Figure 4: MOKE loop for Co/Cu superlattice with $t_{Cu} = 11\text{\AA}$.



is present in these samples, in addition to the usual bilinear coupling. However, recent calculations of the effects of pinholes on a one-dimensional model of AFM coupled layers by Piecuch et. al.[18] suggest that ferromagnetic pin-holes coupling adjacent Co layers would show magnetization loops similar to the ones observed here. That is, for some AFM coupling strength and pinhole strength/density, the magnetization loops show a region which magnetizes in a very small applied field, followed by a region which magnetizes more slowly, with a nonlinear response to applied field. Thus, biquadratic exchange coupling need not be invoked to explain the observed magnetization loops here.

4 Discussion

Clearly, these samples are far from ideal. In sputtered multilayers, samples can be prepared showing 100% AFM coupling and zero remanent magnetization. The samples in the present study instead are no more than 30% AFM coupled, indicating that significant defects exist causing FM coupled regions which dominate the magnetization loops. However, it is interesting to speculate that even if only minority regions of the samples are AFM coupled, oscillations in MR should still be present but with a reduced magnitude, if such oscillations exist. If this were true, then our results would indicate that in fact oscillatory exchange coupling does not exist for single-orientation Co/Cu(111) superlattices. This would be in agreement with recent total energy calculations of exchange coupling in Co/Cu(111) superlattices made by van Schilfgaarde and Herman[19], where only a single peak in AFM coupling with increasing t_{Cu} is observed.

On the other hand, it is also possible that the ferromagnetic bridges do not affect all samples equally, and that AFM coupling is preferentially suppressed in samples where the AFM coupling is weak - i.e. samples with greater t_{Cu} . In this case the AFM coupling might survive only in the first peak where it is strongest, and thus we would be incapable of measuring the other oscillations of the AFM coupling. Unfortunately, we have no means at present to distinguish these two possibilities, except for attempting to further improve the

structure of the superlattices to eliminate the ferromagnetic defects.

Concerning the origin of ferromagnetic defects in these structure, we note that the present samples grow with their (111) axes very well aligned with the surface normal, but in two in-plane azimuthal orientations which are 180° apart. It is plausible that the boundaries between these two types of domains offer a region through which separate Co layers might communicate, giving rise to the observed ferromagnetic bridging in the magnetization loops. Such defects are intrinsic to the methods used for seeding (111) growth on other insulating and semiconducting substrates as well (e.g. glass, GaAs, sapphire(11 $\bar{2}$ 0)). Moreover, it is well known that stacking faults are common in the growth of Co/Cu(111), even for Co layers only 3ML thick[20]. Such stacking faults lead to the same kind of domains boundaries mentioned above even for growth on single crystal metal substrates. Therefore, the above mentioned domain boundaries are a defect common to *all* techniques for the growth of highly oriented Co/Cu(111) structures, and might be the reason why all groups experience difficulty observing AFM coupling in vapor deposited Co/Cu(111). Furthermore, because this type of defect is inescapable with the present deposition techniques, there is faint hope of eliminating it in the near future.

There is still an open question about why sputtered multilayers, which would appear to have a much higher defect density in fact do show strong oscillations in AFM coupling. Part of the answer might be found in recent transmission electron microscopy experiments which indicate that although sputtered multilayers are polycrystalline, they can also exhibit excellent quality flat layering with well defined interfaces[21].

We have made a detailed study of the growth mode of Co/Cu(111) for the two deposition temperatures of 0°C and 150°C , published elsewhere[12]. We review only a few of the main results of that work here. We find that Co does not grow layer by layer on Cu(111) at any temperature. At low temperatures, the Co and Cu do not appreciably interdiffuse, but the Co grows with a rough surface. This surface roughness is compounded as the structure grows, until the outer surface of the superlattice is very rough (20Å rms by X-ray diffraction). Such roughness could lead to the ferromagnetic bridging seen in the magnetization loops. At elevated temperatures, the Co layers grow more smoothly, but interdiffusion between the Co and Cu begins to occur, probably along the above mentioned domain boundaries. It is easy to see how grain boundary diffusion could lead to ferromagnetic bridges. At 150°C growth temperature, we seem to strike a balance between these competing defect factors, and this gives rise to the samples of optimal quality.

5 Conclusions

We have developed a technique for the preparation of Co/Cu(111) wedged superlattices. This technique eliminates the effects of uncontrolled variations in sample preparation since a large number of samples with different Cu layer thickness are produced simultaneously under identical conditions. This is especially important in the Co/Cu(111) system where subtle defects can very strongly affect the extent of AFM coupling observed.

We find only one peak in MR as a function of Cu layer thickness near 9Å, for samples deposited at various temperatures. The optimal growth temperature for this system would appear to be 150°C . Even samples with Cu layer thickness corresponding to the peak in MR show a majority ferromagnetic component and minority antiferromagnetically coupled component in the magnetization loops. This indicates that structural defects cause ferromagnetic bridging of adjacent Co layers. A likely candidate for these defects are the domain

boundaries between adjacent grains in the film. Such domain boundaries are inescapable in Co films deposited on Cu(111) using vapor deposition techniques, and thus the problem of ferromagnetic bridging in such films is unlikely to be overcome in the near future.

References

- [1] S. S. P. Parkin, Z. G. Li, and D. J. Smith, *Appl. Phys. Lett.* **58**, 2710 (1991).
- [2] S. S. P. Parkin, N. More, K. P. Roche, *Phys. Rev. Lett.* **64**, 2304 (1990).
- [3] S. S. P. Parkin, R. Bhadra and K. P. Roche, *Phys. Rev. Lett.* **66**, 2152 (1991).
- [4] R. F. Marks, R. F. C. Farrow, S. S. P. Parkin, C. Lee, B. D. Hermismeyer, C. J. Chien, and S. B. Hagstrom, *Mat. Res. Soc. Symp. Proc.* **21**, 15 (1991).
- [5] W. F. Egelhoff and M. T. Kief, *Phys. Rev. B* **45**, 7795 (1992).
- [6] A. Schreyer, N. Metoki, Th. Zeidler, P. Bödecker, A. Abromeit, Ch. Morawe, U. Romahn, P. Sonntag, K. Bröhl, H. Zabel, *J. Magn. Magn. Mater.*, in press.
- [7] J. P. Renard, P. Beauvillian, C. Dupas, K. Le Dang, P. Veillet, E. Vélú, C. Marlière, and D. Renard, *J. Magn. Magn. Mater.* **115**, L147 (1992).
- [8] M. T. Johnson, R. Coehoorn, J. J. de Vries, N. W. E. McGee, J. ann de Stegge, P. J. H. Bloemen, *Phys. Rev. Lett.* **68**, 2688 (1992).
- [9] J. Kohlhepp, S. Cordes, H. J. Elmers, and U. Gradmann, *J. Magn. Magn. Mater.*, in press.
- [10] D. Greig, M. J. Hall, C. Hammond, B. J. Hickey, H. P. Ho, M. A. Howson, M. J. Walker, N. Weiser, and D. G. Wright, *J. Magn. Magn. Mater.* **110**, L239 (1992).
- [11] S. S. P. Parkin, R. F. Marks, R. F. C. Farrow, Q. H. Lam, G. R. Harp, R. J. Savoy, *Phys. Rev. B* **46**, 9262 (1992).
- [12] G. R. Harp, S. S. P. Parkin, R. F. C. Farrow, R. F. Marks, M. F. Toney, Q. H. Lam, T. A. Rabedeau, and R. J. Savoy, *Phys. Rev. B*, to be published 1-April-1993.
- [13] M. T. Johnson, P. J. H. Bloemen, R. Coehoorn, J. J. de Vries, N. W. E. McGee, R. Jungblut, A. Reinders, and J. ann de Stegge, this publication.
- [14] A. Schreyer, K. Bröhl, J. F. Ankner, Th. Zeidler, P. Bödeker, N. Metoki, C. F. Majkrzak, and H. Zabel, *Phys. Rev. B*, in press.
- [15] J. P. Renard, et. al., unpublished.
- [16] D. Greig, M. A. Howson, B. J. Hickey, M. J. Walker and J. Xu, this publication.
- [17] R. Clarke, D. Barlett, L. Lauhon, D. Glick, F. Tsui, and C. Uher, this publication.
- [18] Jean Francois Bobo, Hélène Fischer, and Michel Picuch, this publication.
- [19] M. van Schilfgaarde, and F. Herman, unpublished.
- [20] B. P. Tonner, Z.-L. Han, and J. Zhang, *Phys. Rev. B*, in press.
- [21] A. R. Modak, D. J. Smith, and S. S. P. Parkin, this publication.

PERPENDICULAR MAGNETORESISTANCE IN Cu/Co AND Cu/(NiFe) MULTILAYERS

P. A. SCHROEDER, J. BASS, P. HOLODY, S.-F. LEE, R. LOLOEE, W. P. PRATT, JR. AND Q. YANG

Department of Physics and Astronomy, and Center for Fundamental Materials Research, Michigan State University, East Lansing, Michigan 48824-1116

ABSTRACT

The Magnetoresistance measured perpendicular to the plane of the multilayer, (CPP-MR) has been measured for the Cu/Co and Cu/(NiFe) systems. The predictions of a two spin-channel model are summarized, and the Cu/Co data are analysed in terms of this theory. The Cu/(NiFe) data show a more complex behaviour.

INTRODUCTION

Theories of magnetoresistance (MR) in ferromagnetic/normal metal multilayers generally depend on the existence of spin dependent scattering in the ferromagnetic metal (F) and at the ferromagnetic/normal (F/N) interfaces. One of the important questions to be resolved is, what is the relative importance of F and F/N interfaces in providing this spin dependent scattering. Recent work [1] on magnetic multilayers has indicated that the magnetoresistance measured perpendicular to the plane of the layers (CPP-MR) is both considerably larger, and easier to interpret than that measured in the plane of the layers (CIP-MR), and furthermore gives a quantitative answer to the above question. In this paper we give results for the Cu/Co and the Cu/permalloy (hereafter abbreviated Cu/(NiFe)) systems. We note that preliminary results for the Cu/Co system [2] have been published elsewhere and that Parkin [3] has measured the CIP-MR of the Cu/(NiFe) system.

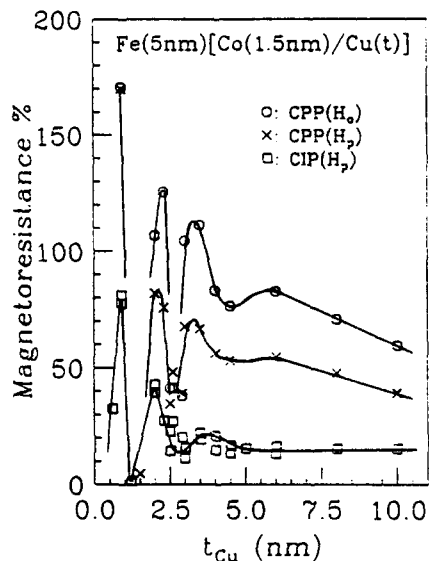


Fig. 1. Magnetoresistance of the series $Fe(5nm)[Cu(t_{Cu})/Co(1.5nm)]_N$ plotted as a function of copper thickness t_{Cu} .

Our measurements are on sputtered samples. Sample preparation and measuring techniques are described elsewhere [4]. A sample is composed of crossed Nb superconducting (S) current and potential strips above and below the multilayer of interest. We first look at some data which serves as an introduction to the analysis using a 2-spin channel model. We then give the predictions of this model and apply it to our Cu/Co and Cu/(NiFe) samples.

In Fig. 1 we show the magnetoresistance of a series of multilayers with a 5nm Fe buffer layer [5] and fixed $t_{Co} = 1.5\text{nm}$, as a function of t_{Cu} . This data differs from data already published [2] in two ways. First, we now have a 3T superconducting solenoid installed in our system, which permits us to saturate the magnetoresistance at the first peak, and hence to produce the new point for $t_{Cu} = 0.9\text{nm}$, with an MR of 170%. We intend to extend the range of magnetic field even further by using NbTi in place of the Nb leads. We have already performed preliminary experiments with fields up to 2.1T. Second, as H approaches the saturation field for this sample, it also approaches the critical field of the Nb, and $R_{Co/Nb}$ changes appreciably with field. This phenomenon was studied in an auxiliary experiment and the necessary corrections were made to all points in Fig. 1.

In the region where $t_{Cu} < 6\text{nm}$, the oscillations indicate that the exchange coupling is strong. We designate this region the coupled region, and the region for $t_{Cu} > 6\text{nm}$ the uncoupled region. We are primarily interested here in the uncoupled region, where there are no complications due to oscillating exchange interactions. We assume that the virgin sample in zero field either is antiferromagnetically aligned or, more probably, that the magnetizations M_i in each layer are distributed randomly, so that $\sum M_i = 0$. According to Zhang and Levy [6] both these distributions should give the same results.

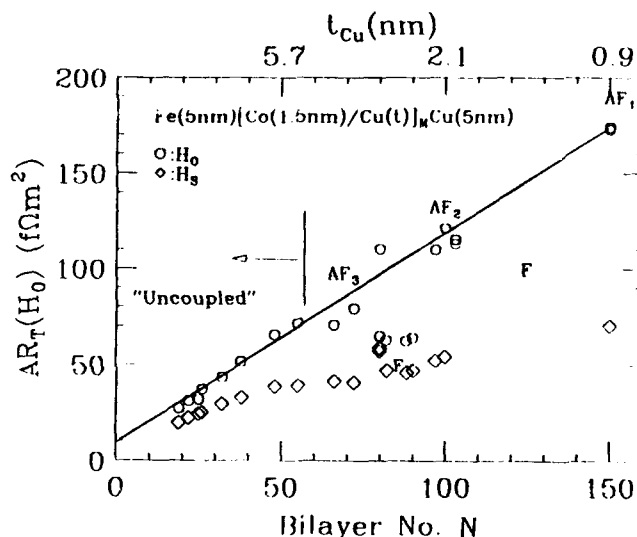


Fig. 2. AR_T vs the number of bilayers N for the $\text{Fe}(5\text{nm})[\text{Cu}(t_{Cu})/\text{Co}(1.5\text{nm})]_N$ system.

We see strong experimental evidence for this equivalence in Fig. 2 which displays results for a series of Cu/Co multilayers with a buffer layer of Fe [5]. Each sample has area A , the same total thickness t , and Co layer thickness t_{Co} , but differing values of the copper thickness t_{Cu} and the number of bilayers N . The theory below indicates that, for the $H = 0$ data, the total

resistance R_T should vary linearly with N . The straight line is drawn through the best point ($t_{Cu} = 0.9\text{nm.}$) and the theoretical intercept. The important point is that the line not only fits the points in the uncoupled region well, but also passes through the points in the coupled region where the antiferromagnetic exchange forces are large. This behaviour strongly suggests that in the uncoupled region the magnetizations behave as if they were antiferromagnetically aligned.

TWO SPIN CHANNEL THEORY

In this section we briefly review the two spin channel theory presaged by Zhang and Levy [7], first applied by Pratt et al. [8], and further developed by Valet and Fert [9]. For this paper we make the basic assumption that the scattering length for spin flip scattering is much greater than $t_F + t_N$, where t_F and t_N are the thicknesses of the ferromagnetic and normal metal layers respectively. The current then consists of two independent parts corresponding to spin up (+) and spin down (-) electrons.

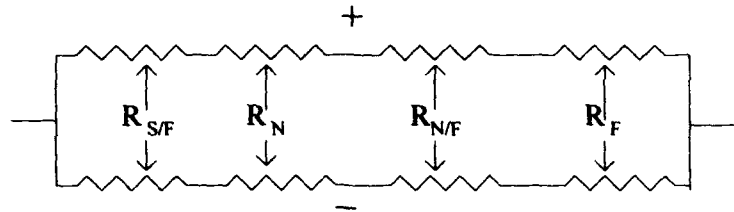


Fig. 3. Equivalent circuit for the two spin band model.

The equivalent circuit corresponding with this situation is shown in Fig. 3. The resistances in each arm are added in series to give R^+ and R^- , which are then combined in parallel. We define $\rho_F^\uparrow = 2\rho_F/(1+\beta)$ to be the resistivity of an F layer when the electron spin and the local magnetization are parallel to each other, and $\rho_F^\downarrow = 2\rho_F/(1-\beta)$ to be the resistivity when they are antiparallel. Here ρ_F is the F resistivity measured on an independent thin F film. Similarly, we take $R_{F/N}^\uparrow = (2R_{F/N})/(1+\gamma)$ and $R_{F/N}^\downarrow = (2R_{F/N})/(1-\gamma)$. We further define

$$\alpha_F = \rho_F^\downarrow / \rho_F^\uparrow = (1+\beta)/(1-\beta)$$

and

$$\alpha_{F/N} = R_{F/N}^\downarrow / R_{F/N}^\uparrow = (1+\gamma)/(1-\gamma)$$

and finally

$$\rho_F^* = \rho_F/(1-\beta^2) \quad \text{and} \quad R_{F/N}^* = R_{F/N}/(1-\gamma^2)$$

For simplicity we neglect the difference between N , $N+1$, and $N-1$ where N is the total number of bilayers, and consider the experimental situation in which all our samples have a constant thickness t .

Antiferromagnetic Alignment

We assume that for the virgin sample with $H = 0$, consecutive layers are antiferromagnetically aligned. Then $R^+ = R^-$, and for a sample of area A detailed analysis gives for the total resistance $AR_T(H_0)$:

$$AR_T(H_0) = 2AR_{S/F} + N[\rho_F^* t_F + \rho_N t_N + 2AR_{F/N}^*] = P + QN \quad (1)$$

where P and Q are constants. $R_{S/F}$ is the interface resistance between superconductor (Niobium) and ferro-magnetic metal. For samples with constant t_F :

$$P = 2AR_{S/F} + \rho_N t \quad \text{and} \quad Q = [\rho_F^*(H) - \rho_N] t_F + 2AR_{F/N}(H) \quad (2)$$

For samples with $t_F = t_N$:

$$P = 2AR_{S/F} + [\rho_N + \rho_F^*(H)] t / 2 \quad \text{and} \quad Q = 2AR_{F/N}^*(H) \quad (3)$$

Hence for antiferromagnetic alignment we expect linear relations between AR_T and the number of bilayers. With $R_{S/F}$ measured in an auxiliary experiment on S/F/S sandwiches, $\rho_F^*(H=0)$, and $R_{F/N}^*$ can be obtained from the intercepts and slopes.

Ferromagnetic Alignment

For saturation field H_S , $R^+ \neq R^-$. Detailed analysis then yields

$$AR_T(H_S) = AR_T(H_0) - N^2(\beta \rho_F^* t_F + 2\gamma AR_{F/N}^*)^2 / [AR_T(H_0)] \quad (4)$$

The linear relationship between R_T and N breaks down. However, for large N and small ρ_N the second term again becomes linear in N, and the results remain linear in N down to quite small N.

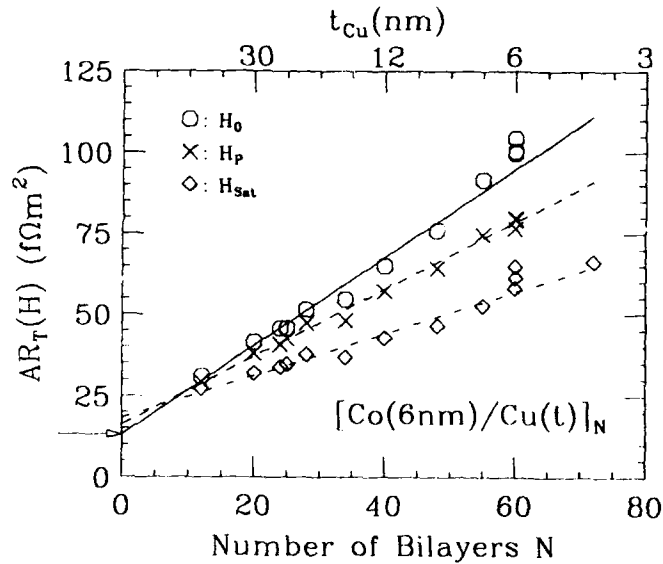


Fig. 4. AR_T vs N for the $Cu(t_{Cu})/Co(6nm)$, $t = 360nm$ series. H_p is the field corresponding to the peak MR.

RESULTS

(a) Cu/Co. In Fig. 4 we illustrate the linear relation between AR_T and N for the series with $t_{Co} = 6\text{nm}$. We analyse our data as follows. For each of the three series, $t_{Co} = 1.5$ and 6nm , and $t_{Co} = t_{Cu}$, we make weighted least square fits of AR_T vs. N , and compute χ^2 . We then minimize $\Sigma\chi^2$ using ρ_F^* , ρ_N , and $R_{F/N}^*$ as variable parameters. Taking the values for the best fit of these parameters, we calculate $AR_T(H_0) - AR_T(H_S)$ using Eq. 4. We repeat these calculations for many combinations of β and γ , obtaining χ^2 for each combination. The combination which gives a minimum χ^2 gives the best values for β and γ . For the Cu/Co system these values are:

$$\begin{aligned}\rho_{Co}^* &= (7.5 \pm 0.4) \times 10^{-8} \Omega\text{m} & \beta &= 0.47 \pm 0.14 & \gamma &= 0.72 \pm 0.06 \\ AR_{Co/Cu}^* &= (0.5 \pm 0.03) \Omega\text{m}^2 & \alpha_{Co} &= 2.8 \pm 0.8 & \alpha_{Co/Cu} &= 6.1 \pm 1.5 \\ \rho_{Cu} &= (0.78 \pm 0.2) \times 10^{-8} \Omega\text{m}\end{aligned}$$

(Note that these results are a little different from those previously reported [2], due to the inclusion of additional data). For comparison, α_{Co} measured for the Ag/Co system [10] is $2.9(+0.5, -0.3)$ and $\alpha_{Co/Ag} = 12(+5, -2)$.

(b) Cu/(NiFe). In Parkin's paper [3] the oscillations in CIP-MR for Cu/(NiFe) die out at $t_{Cu} \sim 3.5\text{nm}$. We therefore set out to study the Cu/(NiFe) system in the region $t_{Cu} > 3.5\text{nm}$ which we expected to be uncoupled. The samples were sputtered on Si (100) with a 5nm NiFe buffer. Very recently we have discovered, from x-ray fluorescence studies, that, although the Fe concentration in our sputtering targets is the $\sim 20\%$ for permalloy, the concentration of Fe in our sputtered samples is $\sim 16\%$. We therefore cannot claim to have measured the Cu/permalloy system. However the concentration does not change appreciably from sample to sample so that the data should be good for the Cu/(Ni₈₄Fe₁₆) system. Results for the series with $t_{NiFe} = 6\text{nm}$ are shown in Fig. 5.

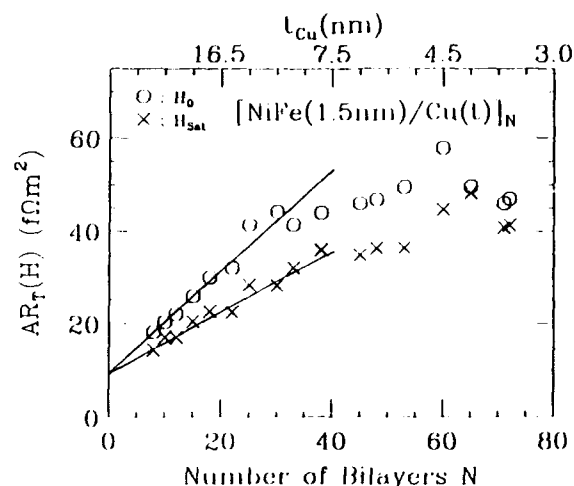


Fig. 5. AR_T as a function of N for the $[Cu(t_{Cu})/NiFe(1.5\text{nm})]_N$ system.

The data show more scatter than those in the Cu/Co system, but it is clear that the expected linear dependences over the whole range of measurement are not present. The lines in Fig. 5 indicate least square fits to the initial data for which there is a good linear dependence. The overall data are significantly different in character from that for the Cu/Co system in Fig. 4. The lines in Fig. 4 continue to diverge over the range of N considered. The NiFe data in contrast show both a bend in the curves and a tendency for the two data sets to converge at the higher values of N . Data for the series with $t_{\text{NiFe}} = 6\text{nm}$ show similar overall characteristics, and the convergence is more obvious. A convergence on these plots corresponds with a decrease in MR. We may be seeing further oscillations in MR as a function of t_{Cu} beyond those seen by Parkin in the CIP-MR. That is, for the higher N values we are probably not in the uncoupled region. A more complete study of CPP-MR as a function of t_{Cu} should confirm this. While this picture accounts for the divergence from linearity for the $H = 0$ data it is difficult to understand why the saturation field data should not be linear. More high- N points are required to confirm that the H_S data are in fact nonlinear.

We have done non global fits to the low N data for the $t_{\text{NiFe}} = 1.5\text{nm}$ and 6nm systems using Eqs. 1-4 and obtained the tentative values $\alpha_{\text{NiFe}} = 3.2$ and $\alpha_{\text{NiFe/Cu}} = 5.5$. More measurements are planned to clarify the source of the behavior of Cu/(NiFe).

Acknowledgements

This research was supported in part by the US National Science Foundation under Grant DMR-91-22614, the Michigan State University Center for Fundamental Materials Research, and the Ford Scientific Laboratory.

References

- [1] W.P. Pratt, Jr., S.-F. Lee, J.M. Slaughter, R. Loloee, P.A. Schroeder, and J. Bass, Phys. Rev. Lett. **66**, 3060 (1991); and S.-F. Lee, W. P. Pratt, Jr., Q. Yang, P. Holody, R. Loloee, P. A. Schroeder, and J. Bass. J. Mag. Mag. Mat. **118**, L1, (1993).
- [2] P. A. Schroeder, J. Bass, P. Holody, S. -F. Lee, R. Loloee, W. P. Pratt, Jr., and Q. Yang, Nato Advanced Research Workshop, Cargese, Corsica France June 15-19 1992. To be published in NATO ASI Series.
- [3] S. S. P. Parkin, Appl. Phys. Lett. **60**, 512 (1992).
- [4] J. M. Slaughter, W. P. Pratt, Jr., and P. A. Schroeder, Rev. Sci. Instrum. **60**, 127, (1989).
- [5] S.S.P. Parkin, Z.G. Li, and D.J. Smith, Appl. Phys. Lett. **56**, 2710 (1991).
- [6] S. Zhang and P. M. Levy, Phys. Rev. **B47**, 6776 (1993)
- [7] S. Zhang and P.M. Levy, J. Appl. Phys. **69**, 4735 (1991).
- [8] S.F. Lee, W.P. Pratt, Jr., Q. Yang, P. Holody, R. Loloee, P.A. Schroeder, and J. Bass, J. Mag. Mag. Mat. **118**, L1 (1993).
- [9] T. Valet and A. Fert. Submitted for publication.
- [10] W.P. Pratt, Jr., S.-F. Lee, Q. Yang, P. Holody, R. Loloee, P. A. Schroeder, and J. Bass, to be published J. Appl. Phys. **73** (10) 15 May 1993.

INFLUENCE OF SUPERLATTICE POTENTIALS ON TRANSPORT IN MAGNETIC MULTILAYERS

Shufeng Zhang, and Peter M. Levy, Department of Physics, New York University, 4 Washington Place, New York, NY 10003

ABSTRACT

We discuss the effect of the superlattice potential on the magnetotransport properties of magnetic multilayers for current parallel and perpendicular to the plane of the layers. While quantum well states affect the magnetotransport, they are *not* the primary origin of the *giant* magnetoresistance observed in these materials for currents in the plane of the layers. In general, it is necessary to include *both* spin-dependent scattering and the effects of superlattice potentials in order to explain the magnetoresistance of multilayered structures.

Giant magnetoresistance in magnetic multilayers is usually understood in terms of spin-dependent scattering [1], i.e., the scattering of a conduction electron by a local magnetic impurity depends on its spin direction relative to that of the local moment. With this picture, one uses unpolarized plane waves to represent conduction electrons in the structures and calculates the conductivity for different magnetic configurations, e.g., ferro and antiferro aligned magnetic layers [2]. Recently, there is an emerging realization that quantum well states may be formed in these multilayers [3], at least for some directions in momentum space. The existence of these states implies that the conduction electrons are *not* plane waves for some momenta, and that layering changes the electronic states of the conduction electrons. To model these states, Hood and Falicov [4] introduced spin-dependent potentials in different magnetic layers and considered the effects of these potentials on the conduction electrons by using reflection and transmission probabilities at the interfaces (potential steps). However, as the quantum coherence length (inelastic mean free path) at low temperatures is much larger than the thicknesses of the layers, it is necessary to include effects from the interference of conduction electrons reflected at different interfaces [5]. Therefore, one should *first* determine the proper wavefunctions and energy spectrum of conduction electrons quantum mechanically, and *then* evaluate their scattering rates due to impurities in the layers and at the interfaces.

Kalmeyer [6] considered the influence of spin-dependent wave functions on the magnetoresistance; by focusing on the scattering at interfaces, he was able to conclude that the spin-dependent potential alone can give rise to large magnetoresistance. To examine this conclusion, we select superlattices as our prototypical structures in order to eliminate the confinement effect of outer boundaries. To obtain complete information on the effect of spin-dependent potentials, one also needs to *simultaneously* work out the magnetoresistance for the CIP (current in the plane of the layers) and CPP (current perpendicular to the plane of the layers). Although most of the experimental data studied to date are for the CIP geometry, the CPP-MR measurements are now available at least for three systems: Co/Cu, Co/Ag [7] and Fe/Cr [8]. By choosing parameters that fit data on CIP-MR alone, one might predict values for CPP-MR that are wrong.

In our study, we use Kronig-Penney type potentials to study the interplay between the effects of spin-dependent potentials and spin-dependent scattering. We first solve for the wavefunctions and energy spectrum in the entire superlattice, then use transport theory to calculate the conductivity and magnetoresistance for both CIP and CPP in the

presence of impurities. The main result we find is that a spin-dependent potential has more influence on CPP-MR than on CIP, and that a spin-dependent potential without spin-dependent scattering can *not* account for the CIP experiments. However, in the presence of spin-dependent scattering, both CIP-MR and CPP-MR are significantly modified by spin-dependent potentials.

Conduction band wavefunctions appropriate to transition metal magnetic superlattices are not reliably known. Therefore we resort to the Stoner description which postulates that conduction electrons in ferromagnetic layers have different potentials for majority and minority spins. To ascertain the role of spin-dependent potentials on the magnetoresistance of multilayers, we use a Kronig-Penney potential in the growth direction z and a constant potential in the plane of the layers.

The Hamiltonian that describes conduction electrons in metallic multilayers is

$$H_M = \frac{p^2}{2m} + V_{pot,M}(z, \sigma) + \sum_i V_{scatt,M}(z - z_i, \sigma), \quad (1)$$

where V_{pot} represents the spin-dependent potentials of the electrons in the different layers. V_{scatt} is the scattering at impurity sites within the layers and at the interfaces, and M denotes the magnetic configurations of the layers, e.g., ferro or antiferromagnetic. Since the origins for the V_{pot} and V_{scatt} are different, we treat them as *independent* parameters. This is in contrast to some treatments which assume that the diffusive scattering at interfaces depends on the potential difference between the two metals in contact [9].

In past treatments the scattering has been evaluated by using plane wave states [2]. However, one should use states appropriate to multilayered structures, i.e., to use *eigenstates* of

$$H_M^0 = \frac{p^2}{2m} + V_{pot,M}(z, \sigma). \quad (2)$$

This leads to energy eigenvalues of the form

$$\epsilon_M(\mathbf{k}, \sigma) = \epsilon_{||}(k_{||}) + \epsilon_M(\nu, \sigma), \quad (3)$$

where $\epsilon_{||}(k_{||}) = \hbar^2(k_x^2 + k_y^2)/2m$, $\nu = k_z$, and to eigenstates

$$\phi_M(\mathbf{k}, \sigma; \mathbf{r}) = e^{i(k_x x + k_y y)} \phi_M(\nu, \sigma; z). \quad (4)$$

These wavefunctions exist over a length scale known as the inelastic mean free path; they are the appropriate ones to use as long as the coherence of the electron wavefunctions can be maintained over several repeat distances of a *periodic superlattice*.

The potentials we consider consist of a *periodic* array of barriers of thickness a with height U and wells of thickness b ; the Fermi level is at energy E_F from the bottom of the wells. For the ferromagnetic configuration of the layers, the potential for the majority (spin up) electrons has $a = t_{nm}$ and $b = t_m$, where t_{nm} is the thickness of non-magnetic layers and t_m of magnetic layers; for the minority electrons $b = 0$, i.e., there are no wells, and the Fermi level is at $E_F - U$ [10]. For antiferromagnetic configurations the potentials for spin up and spin down electrons are the same but shifted in space relative to one another; $a = 2t_{nm} + t_m$ and $b = t_m$. This description of the superlattice potentials is believed to be reasonable at least for Fe/Cr superlattices [11]. The wavefunctions for the periodic potential can be written in Bloch form

$$\phi_M(\nu, \sigma; z) = e^{i\nu z} u_M^\sigma(\nu; z), \quad (5)$$

where

$$u_M^\sigma(\nu; z + a + b) = u_M^\sigma(\nu; z). \quad (6)$$

We have calculated the energy spectrum $\epsilon_M(\nu, \sigma)$ and Bloch functions $u_M^\sigma(\nu, z)$ for the spin-dependent periodic potentials described above.

To determine the magnetoresistance, we evaluate the conductivity given in Ref. 2 for the simple cases in which the layers are ferro and antiferromagnetically aligned. Since the purpose of the present letter is to illustrate the influence of the superlattice potential on the MR, we only consider the case that the mean free path is larger than the layer thickness. In this limit, we can neglect the off-diagonal t-matrix entering the expression for the global conductivity [2] and we find the conductivity is given as

$$\sigma_M = \frac{e^2}{2m} \sum_{k_{\parallel}\nu\sigma} \frac{\xi(k_{\parallel}, \nu) \delta(\epsilon_F - \epsilon_{k_{\parallel}\nu}^\sigma)}{\Delta_M^\sigma(\nu)} \quad (7)$$

where $\xi(k_{\parallel}, \nu) = k_{\parallel}^2/2$ for CIP while for CPP $\xi(k_{\parallel}, \nu) = (m/\hbar^2 \partial \epsilon_\nu^\sigma / \partial \nu)^2$, and $\Delta_M^\sigma(\nu)$ is the imaginary part of the scattering. For a short-range impurity scattering potential $V_M^\sigma = \sum_i V_M^\sigma(i) \delta(z - z_i)$, where $V_M^\sigma(i) = v_i + j_i \hat{M}_i \cdot \hat{\sigma}$, the imaginary part of the self-energy in the second order Born approximation is

$$\Delta_M^\sigma(\nu) = \pi \sum_i |V_M^\sigma(i) u_M^\sigma(\nu, z_i)|^2 \rho_M^\sigma(\epsilon_F, z_i), \quad (8)$$

where

$$\rho_M^\sigma(\epsilon_F, z_i) = \sum_{k, \nu_1} |u_M^\sigma(\nu_1, z_i)|^2 \delta(\epsilon_F - \epsilon_{k\nu_1}). \quad (9)$$

The differences between these results and previous expressions [2] are 1) Δ depends on the momenta ν , and 2) the dependence on the magnetic configuration M and spin σ enters in two places: in the scattering V_M^σ and in the wave functions u_M^σ .

Here we present results and conclusions based on Eqs. (7) and (8). We emphasize that they are applicable to CPP with no restrictions (assuming there are no spin flips) and to CIP for $\lambda > t_m + t_{nm}$. In the limit $\lambda \ll t_m + t_{nm}$, the CIP-MR is zero. Also, we define the magnetoresistance as the ratio of the difference of the conductivities for ferromagnetic and antiferromagnetic alignments of the layers divided by the conductivity for the antiferromagnetic alignment.

There are at least 8 parameters involved in the conductivity expression. They are, scattering rates in nonmagnetic layers, in magnetic layers for spin up and down electrons if they are spin-dependent, and at interfaces for spin up and down electrons if they are spin-dependent, the potential barrier height relative to Fermi energy, and layer thicknesses for nonmagnetic and magnetic layers. The magnetoresistance is a complicated function of these parameters. Here we mention some of the salient results.

First of all, the wave functions Eqs. (4) and (5) appropriate to the superlattice potential affect the CPP-MR much more than they do the CIP-MR in the absence of spin-dependent scattering. When we neglect the spin-dependence of the scattering V_M^σ , take for the potential $U/E_F = 1/3$, and use $k_F t_{nm} = k_F t_m = 60$, we find 0.4% for the CIP-MR and 12% for CPP-MR. For $U/E_F = 2/3$ and the same $k_F t$, the CIP-MR is 2% and CPP-MR is 34%. If we neglect the ν and σ dependence of the scattering $\Delta_M^\sigma = \Delta$, we find approximately the same CPP-MR, while the CIP-MR is zero. As we have shown elsewhere [12], the CIP conductivity is proportional to the total number of conduction electrons when $\Delta_M^\sigma = \Delta$; as this number does not depend on the magnetic configuration

the CIP-MR is zero under these considerations. However, the same argument does not hold for CPP, because the CPP conductivity is *not* related to the total number of electrons. As the experimental MR ratios that are observed in magnetic superlattices are in the range of 20% to 170%, we conclude that the spin and configuration dependence of the superlattice wavefunctions do not *by themselves* contribute much to the CIP-MR, while they *do* play an important role in the CPP-MR.

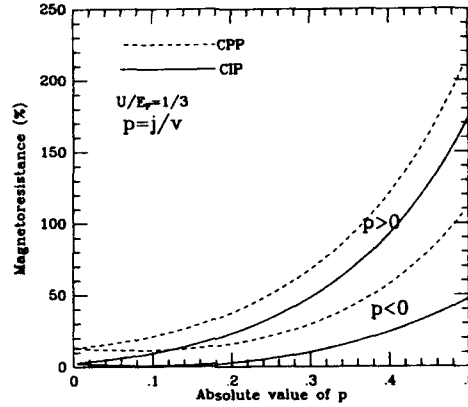


Fig.1 The CIP and CPP magnetoresistance as function of $p = p_s = p_b$ for a fixed barrier height $U/E_F = 1/3$. We choose $k_{F1nm} = k_{F2nm} = 60$ and the total scattering at the interfaces is the same as that in the bulk.

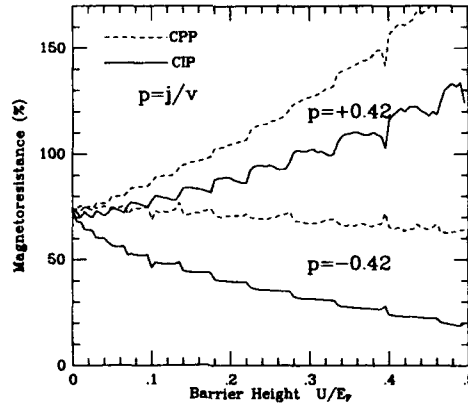


Fig.2 The CIP and CPP magnetoresistance as function of barrier height with fixed $p = p_s = p_b = \pm 0.42$. The remaining parameters are the same as Fig.1.

Second, the contributions of the spin-dependent potential and spin-dependent scattering to the magnetoresistance are intertwined. For example, MR depends on the sign of p , where $p = j/v$ is the ratio of spin-dependent to spin-independent scattering [2], see Figs.1 and 2. This asymmetric behavior for the MR with respect to the sign of p reflects the different band structures for spin up and spin down electrons. In bulk ferro-

magnetic metals [13] or multilayers *without* spin-dependent potentials [2], the resistivity is *symmetric* respect to the sign of p . Since a large number of parameters are involved in estimating the magnetoresistance, one should be cautious when one tries to quote the parameters that best fit the experimental data. A comprehensive comparison between theory and experiment should include both conductivities and magnetoresistance in the CIP and CPP geometries.

Third, the oscillatory behavior of charge density leads to rapid oscillations in magnetoresistance with respect to barrier height, see Fig.2, and layer thickness. These oscillations reflect gaps in the eigenvalue spectrum ϵ_p^0 that are caused superlattice potentials or Bloch states. However, this behavior has *not* been observed experimentally; we are now currently investigating the origin for this conundrum.

Fourth, the dependence of the MR on the thickness of the layers is controlled by the scattering [2], *not* by the potentials. If one assumes the MR is due solely to superlattice potentials with no spin-dependent scattering $p = 0$ both the CIP-MR and CPP-MR are weakly dependent on the thicknesses of the layers; this is contrast to the experimental results [14]. Therefore we conclude that the spin-dependent scattering is necessary to explain the observed dependence of the MR on layer thicknesses.

For multilayered structures with transition metal magnetic and non-magnetic layers, e.g., iron and chromium, the potential wells exist in the magnetic layers; the non-magnetic layers act as barriers. However, if a noble metal, e.g., copper, is the non-magnetic layer, the *roles are reversed*; the copper layer now contains the well states [3], and the magnetic layers are the barriers. If the barrier height for *one* spin direction is above the Fermi level there is no conduction for CPP in the antiferromagnetic configuration while in the ferromagnetic state one of the spin channels still conducts. In this case the CPP-MR is limited only by the size of the spin diffusion length relative to the mean free path; at low temperatures this is a very large number [15], e.g., the spin diffusion length is an order of magnitude larger than the mean free path. As this behavior has not been observed in the CPP experiments done to date on *Co/Cu*, *Co/Ag* [7] and *Fe/Cr* [8], we conclude that *both* quantum well and continuum states are needed to describe their transport properties, i.e., $U/E_F < 1$.

Our analysis indicates that the MR is sensitive to the position of scatterers relative to the superlattice potential. This is reminiscent of recent experimental data [16] in which the CIP-MR is more sensitive to the presence of a cobalt monolayer at an interface between layers than when the cobalt is embedded within a magnetic layer. Due to existence of quantum well states in the *Cu* layers, the wavefunctions of these states fall off exponentially in the magnetic layers with a length scale of $(2mU/\hbar^2 - k_F^2 + k_{||}^2)^{-1/2}$. For example, electrons in states which carry the current in CIP with $k_{||}$ close to k_F are not scattered if the Co layer is more than 2\AA inside a barrier whose height is $U = 1\text{eV}$. Undoubtedly adding a monolayer of cobalt at the interfaces or inside of the magnetic layers is more complex than merely moving a scattering plane from one region to another. Nonetheless, our analysis does show that scattering at interfaces is magnified relative to that inside magnetic layers which act as barriers.

In conclusion, we have studied the magnetoresistance in magnetic superlattices in the presence of spin-dependent potentials and spin-dependent scattering. Although we show that the spin-dependent potential alone can not account for the large magnetoresistance, it does strongly affect the magnetoresistance in the presence of spin-dependent scattering. A quantitative comparison between theory and experimental data should include *both* mechanisms. Also, precise superlattice band structures are needed to better understand the interplay between spin-dependent scattering and spin-dependent potentials.

We would like to thank H. E. Camblong and A. Fert for helpful discussions. This work is partially supported by the Office of Naval Research Grant N00014-91-J-1695 and by a grant from NATO: 5-2-05/RG No. 890599.

1. R. E. Camley and J. Barnas, Phys. Rev. Lett. **63**, 664 (1989); P. M. Levy, S. Zhang and A. Fert, Phys. Rev. Lett. **65**, 1643 (1990); A. Barthelemy and A. Fert, Phys. Rev. B **43**, 13124 (1992); B. L. Johnson and R. E. Camley, Phys. Rev. B **44**, 9997 (1991); A. Vedyayev, B. Dieny and N. Ryzhanova, Europhys. Lett. **19**, 329 (1992); H. E. Camblong and P. M. Levy, Phys. Rev. Lett. **69**, 2835 (1992).
2. S. Zhang, P. M. Levy and A. Fert, Phys. Rev. B **45**, 8689 (1992).
3. J. E. Ortega and F. J. Himpsel, Phys. Rev. Lett. **69**, 844 (1992).
4. R. Q. Hood and L. M. Falicov, Phys. Rev. B **46**, 8287 (1992).
5. P. B. Visscher, preprint; P. B. Visscher and H. Zhang, preprint. These authors carried out calculations similar to ours.
6. V. Kalmeyer, private communication.
7. W. P. Pratt, Jr., S.-F. Lee, J. M. Slaughter, R. Loloee, P. A. Schroeder and J. Bass, Phys. Rev. Lett. **66**, 3060 (1991); S.-F. Lee, W. P. Pratt, Jr., R. Loloee, P. A. Schroeder and J. Bass, Phys. Rev. B **46**, 548 (1992).
8. M. A. M. Gijs, S. K. J. Lenczowski and J. B. Giesbers, Phys. Rev. Lett. **70**, 3343 (1993).
9. M. B. Stearns, J. Magn. Magn. Mater. **104-107**, 1745 (1992); A. C. Ehrlich, Bull. Am. Phys. Soc. **37**, 198 (1992); Y. Asano, A. Oguri and S. Maekawa, to be published.
10. By taking into account putative differences in the potentials for minority electrons in the layers we engender additional parameters.
11. K. B. Hathaway and J. R. Cullen, J. Magn. Magn. Mater. **104-107**, 1840 (1992); J. Inoue, A. Oguri and S. Maekawa, J. Phys. Soc. Japan **60**, 376 (1991).
12. P. M. Levy, Z.-P. Shi, S. Zhang, H. E. Camblong and J. L. Fry, J. Magn. Magn. Mater. **121**, 357 (1993).
13. A. Fert and I. A. Campbell, J. Phys. F **6**, 849 (1976).
14. See, for example, M. N. Baibich, *et al.*, Phys. Rev. Lett. **61**, 2472 (1988); S. S. P. Parkin, N. More and K. P. Roche, Phys. Rev. Lett. **64**, 2304 (1990);
15. T. Valet and A. Fert, J. Magn. Magn. Mater. **121**, 378 (1993).
16. S. S. P. Parkin, private communication; B. Dieny, V. S. Speriosu, *et al.*, to be published in **Magnetism and Structure in Systems of Reduced dimension**, NATO ASI Series, edited by R. F. C. Farrow *et al.* (Plenum, New York); A. Fert, private communication.

Giant Magnetoresistance Calculated From First Principles

W. H. Butler*, James M. MacLaren** and X.-G. Zhang†

*Metals and Ceramics Division, Oak Ridge National Laboratory, Oak Ridge, TN 37831-6114

**Department of Physics, Tulane University, New Orleans, Louisiana 70118

†Center for Computational Sciences, University of Kentucky, Lexington, Kentucky 40506-0045

ABSTRACT

The Layer Korringa Kohn Rostoker-Coherent Potential Approximation technique was used to calculate the low temperature Giant Magnetoresistance from first principles for Co/Cu and permalloy/Cu superlattices. Our calculations predict large giant magnetoresistance ratios for Co/Cu and extremely large ratios for permalloy/Cu for current perpendicular to the layers. Mechanisms such as spin-orbit coupling which mix spin channels are expected to greatly reduce the GMR effect for permalloy/Cu.

Introduction

An unexpectedly large effect of an applied magnetic field on the electrical resistance has been observed in a number of multilayer systems involving transition metals. The effect consists of a dramatic decrease in the electrical resistance in the presence of an applied magnetic field and has been observed in Fe-Cr multi-layers[1, 2, 3, 4, 5, 6], in Co-Cu multilayers[3, 4, 7], in Co-Ru multilayers[3], and in bi-layers of Ni₈Fe₂ separated by a thin layer of Cu[7, 8]. The effect is seen in systems in which alternate layers of magnetic atoms are aligned anti-parallel with one another in the absence of the applied field. Application of the magnetic field brings the layers into alignment and causes a decrease in the electrical resistivity both parallel to the layers and perpendicular to them.

The resistances of bcc (100)Fe/(100)Cr[1] and fcc (111)Co/(111)Cu[4] have been observed to decrease by almost a factor of two when an applied magnetic field brings the magnetic moments on the layers into alignment. In this paper we present calculations of this giant magnetoresistance effect directly from first principles.

Previous Theory

Baibich *et. al.*[1] who first reported the effect based on their observations on Fe-Cr multi-layer systems observed that dilute Cr impurities in bulk Fe scatter majority spin electrons much more strongly than minority spin electrons. They proposed that the Cr atoms in the spacer layers might act the same way leading to a low resistance for the down spin electrons when the layers are aligned in parallel. The anti-parallel alignment would, in this picture, lead to a higher resistance by mixing the spin channels. Binasch *et. al.*[2] described the effect in terms of the necessity for electrons to undergo spin-flip scattering when traveling from one Fe layer into an adjacent one when the layers were aligned anti-parallel.

Camely and Barnas and Barnas *et. al.*[9, 10] generalized the semi-classical Boltzmann theory approach of Fuchs[11] and Sondheimer[12] to treat layered systems with different scattering properties in the two spin channels. Levy *et. al.*[13] and Zhang and Levy[14] developed a quantum mechanical treatment for spin dependent scattering in multilayer

systems including both interfacial and bulk scattering. Both of these treatments utilize numerous adjustable parameters to account for the microscopic properties of these systems.

Calculation Technique

We have calculated the electronic structure of superlattices of copper and cobalt and of permalloy ($\text{Ni}_{80}\text{Fe}_{20}$) and Cu using the layer Korringa-Kohn-Rostoker technique[15] (LKKR) to solve the equations of density functional theory in the local spin density approximation[16, 17]. The LKKR technique is particularly well adapted for calculating the properties of layered materials. It has the advantage over most other electronic structure techniques that the time required for a calculation scales linearly with the number of layers rather than as the third power of the number of layers. The LKKR also does not require that one treat all structures as three dimensional superlattices. The properties of isolated interfaces, for example, can be calculated directly. In the work described here, however, we have modeled the systems as superlattices because this simplified the application of transport theory.

The systems which we have chosen to model in these initial calculations consist of (111) superlattices of copper and of either cobalt or permalloy. For the Co/Cu superlattices, scattering arises from the interfacial layers which we have assumed to be 1% interdiffused; i.e. the interfacial Cu layers are assumed to have 1% of the copper atoms replaced by cobalt atoms which are randomly distributed within the layer. Similarly the interfacial cobalt layers are assumed to have 1% of their atoms randomly replaced by copper atoms. For the permalloy/Cu superlattices, scattering arises from the permalloy layers which are assumed to be random solid solution alloys.

The disorder is treated in the coherent potential approximation[18, 19] which provides a means of constructing an average Green function for a disordered solid solution alloy and which has been successfully applied to the calculation of many properties of alloys[20]. A novel feature of the LKKR is the ability it provides for allowing the concentration of each species to vary from layer to layer.

The calculation of the electrical resistivity is based on the use of a CPA-like approximation to evaluate the product of two Green functions which appears in the Kubo-Greenwood expression for the conductivity[21]. For these initial calculations of the GMR it is convenient to make two approximations in addition to those implicit in the KKR-CPA theory of resistivity described in reference[21]. Firstly, we assume that the energy bands are reasonably well defined, i.e. that the mean free path is significantly greater than a typical interatomic spacing. This assumption allows the KKR-CPA theory of transport to be reduced to a Boltzmann equation in which the scattering probabilities are determined from first principles. The validity of this approximation can be checked since we calculate the mean free path for each point on the Fermi surface.

The second additional approximation that we have made in these calculations is the neglect of vertex corrections to the two particle propagator. This is equivalent to the neglect of the "scattering-in" terms in solving the Boltzmann equation. The regime of validity of this approximation is not quite so evident. It can be shown[22] that vertex corrections vanish if the individual scattering events are isotropic, or more generally, if they only connect states of the same parity, e.g. $s \rightarrow s$, $s \rightarrow d$, or $p \rightarrow p$. If the scattering is primarily in the forward direction, e.g. from a weak relatively long ranged potential (compared with the electron wavelength) the vertex corrections can be significant[23].

With these approximations the conductivity for spin i in the z -direction in response to an electric field in the z -direction can be calculated as a sum over the states, k , of the

superlattice,

$$\sigma_{xx}^i = \frac{e^2}{V} \sum_k v_z^i(k) v_z^i(k) \tau^i(k) \left(-\frac{\partial f_\mu(E)}{\partial E} \right). \quad (1)$$

Here V is the volume of the superlattice cell, $v_z^i = \hbar^{-1} \nabla_k E^i(k)$ is the electron group velocity, $\tau^i(k)$ is the Boltzmann lifetime defined below, and $f_\mu(E)$ is the Fermi function. At reasonable temperatures $(-\frac{\partial f_\mu(E)}{\partial E})$ is effectively a delta function at the Fermi energy and the conductivity can be written as

$$\sigma_{xx}^i = \frac{e^2}{\hbar(2\pi)^3} \int_{\mu} \frac{dS_k}{|v_z^i(k)|} v_z^i(k) v_z^i(k) \tau^i(k). \quad (2)$$

Using the fact that

$$\frac{dS_k}{|v_z^i(k)|} v_z^i(k) = dk_x dk_y, \quad (3)$$

and recognizing that $v_z^i(k) \tau^i(k)$ is simply the mean free path in the z -direction, l_z^i , we have,

$$\sigma_{xx}^i = \frac{e^2}{\hbar(2\pi)^3} \int dk_x dk_y l_z^i \quad (4)$$

where the z -component of the mean free path, $l_z^i(k_x, k_y)$ is determined by the imaginary part of the solution of the secular equation. Thus $l^i(k_x, k_y) = 1/(2\text{Im}k_z)$ where k_z is the (generally complex) solution to

$$E(k_x, k_y, k_z) = \mu \quad (5)$$

for given k_x and k_y . The detailed justification for this identification of the mean free path or the lifetime with the complex dispersion relation within KKR-CPA theory is given in reference[21] and was used to successfully calculate the electrical resistivity of Ag-Pd and other alloys[22].

Finally, in the calculations presented here, we neglect mechanisms that would mix the majority and minority scattering channels. Examples of such mechanisms which would be effective at zero temperature are spin-orbit coupling and any misalignment in the orientation of the moments of the impurities. At higher temperature, spin waves would be effective in mixing the scattering channels.

Results for Cu|Co

Table I gives the calculated conductivities, lifetimes, and resistivities for multilayers with equal thicknesses of Cu and Co. The quoted conductivities and resistivities are for a single spin channel. The \uparrow symbol indicates the majority spin channel, \downarrow denotes the minority spin channel, and A indicates either of the spin channels for the case in which the ferromagnetic layers alternate in moment direction (anti-ferromagnetic alignment). The calculated mean free path $\langle l_z^i \rangle$ is the average of the component of the mean free path in the z -direction defined as

$$\langle l_z^i \rangle = \frac{\int dk_x dk_y \sum_n l_z^{in}}{\int dk_x dk_y} \quad (6)$$

where the sum over n indicates that more than one sheet of the Fermi surface may have a projection on a given point in the two dimensional zone. This definition of an average mean free path may differ from other definitions and the appropriate definition for use in comparison to experiments on realistic systems may depend on the experiment and on the details of the Fermi surface.

Table I: Calculated mean free paths, single channel resistivities, parallel and anti-parallel resistivities and GMR ratios for Cu|Co superlattices. Currents are assumed to be perpendicular to the layers. Cu6Co6, for example, is a superlattice with 6 layers of Cu alternating with 6 layers of Co.

system	$\langle l_z^I \rangle$	$\langle l_z^I \rangle$	$\langle l_z^{AP} \rangle$	ρ^I	ρ^I	ρ^{AP}	ρ^P	ρ^{AP}/ρ^P
units	nm	nm	nm	$\mu\Omega\text{cm}$	$\mu\Omega\text{cm}$	$\mu\Omega\text{cm}$	$\mu\Omega\text{cm}$	
Cu1Co1	495	14.8	17.7	0.588	19.66	8.24	0.639	12.90
Cu2Co2	335	10.5	16.4	0.867	27.59	8.86	0.903	9.80
Cu3Co3	755	11.7	19.9	0.385	24.87	7.30	0.425	17.17
Cu4Co4	860	12.1	18.0	0.338	24.12	8.06	0.379	21.23
Cu5Co5	794	18.8	25.3	0.366	15.45	5.72	0.431	13.28
Cu6Co6	1733	24.8	33.5	0.168	11.73	4.34	0.253	17.14

The column labeled ρ^{AP} is the calculated resistivity for anti-parallel arrangement of the magnetic moments in neighboring Co layers for both spin channels. The resistivity for the two spin channels is identical in this case so the total resistance for both spin channels will be half of the single channel value. The column labeled ρ^P is the net resistance (both channels) when the Co moments on all layers are parallel.

The magnitudes of the resistances depend on the amount of assumed interfacial interdiffusion, but we expect that the GMR ratio would not be affected if the amount of interdiffusion were increased under the assumption used here that all of the moments are aligned. The magnitude of the GMR effect would be reduced by scattering mechanisms such as phonons, vacancies, or grain boundaries that scatter the majority and minority spins more democratically and it would be greatly reduced by scattering mechanisms such as misaligned moments, e.g. in the interfacial regions, that cause a mixing of the spin channels and by spin waves at higher temperatures.

For reference, the calculated single channel resistivities (in $\mu\Omega\text{cm}$) of the dilute bulk alloys were Cu(1%Co): $\rho^I = 1.6$, $\rho^I = 19.2$ and Co(1%Cu): $\rho^I = 0.42$, $\rho^I = 4.92$. These are in reasonable agreement with the experimental values of the total resistance of 5.8 for Cu(Co)[24] and 0.89 for Co(Cu)[25] if it is remembered that the interpretation of the resistance of dilute Co in Cu is complicated by spin orientation and Kondo effects.

Results for Permalloy|Cu

Table II gives the calculated results for permalloy|Cu superlattices for equal thicknesses of the Ni₈Fe₂ layers and the copper layers. The calculations are for currents perpendicular to the layers. The remarkable feature of the results is that the calculated mean free paths are extremely long for the majority channel and extremely short for the minority channel. This leads to extremely large values of the predicted GMR ratio. Values of the resistivity in excess of $200\mu\Omega\text{cm}$ in the minority channel are unrealistic and result from a breakdown in the assumption that the bands are well defined. However, very strong scattering and high resistivities (on the order of $100\mu\Omega\text{cm}$) in the down spin channel should be expected since the potentials of Cu, Ni, and Fe are very different for minority electrons.

The long mean free paths and low resistivities calculated for the majority electrons result from the fact that the calculated majority Ni and Fe potentials have almost identical scattering properties at the Fermi energy. The scattering properties of the Cu atoms are almost as close but do not match quite as well. This should not be surprising since Cu has 11, valence electrons per atom, Ni has 10 and Fe has 9. Since Fe forms a moment of about $2.6\mu_B$ and Ni a moment of about $0.6\mu_B$, the number of electrons per atom for the

Table II: Calculated mean free paths, single channel resistivities, parallel and anti-parallel resistivities and GMR ratios for permalloy(P)/Cu superlattices. Currents are assumed to be perpendicular to the layers.

system	$\langle l_z^I \rangle$	$\langle l_z^P \rangle$	$\langle l_z^{AP} \rangle$	ρ^I	ρ^P	ρ^{AP}	ρ^P	ρ^{AP}/ρ^P
units	nm	nm	nm	$\mu\Omega\text{cm}$	$\mu\Omega\text{cm}$	$\mu\Omega\text{cm}$	$\mu\Omega\text{cm}$	
P1Cu1	707	0.782	1.291	0.202	183	55.5	0.202	274
P2Cu2	681	1.118	1.668	0.210	128	43.0	0.210	204
P3Cu3	662	0.557	1.062	0.216	256	67.5	0.216	312
P4Cu4	528	0.286	0.540	0.271	500	132.5	0.271	489
P5Cu5	623	0.191	0.468	0.230	750	152.5	0.230	664
P6Cu6	794	0.119	0.243	0.180	1206	294.1	0.180	1633

majority spins is 5.5 for Cu, 5.3 for Ni, and 5.3 for Fe. According to our calculations the difference in the number of electrons per atom in the self-consistent majority potentials for Ni and Fe is approximately 0.03. In contrast, the numbers of minority electrons per atom on the Cu, Ni, and Fe atoms is approximately, 5.5, 4.7, and 3.2. It should be remembered that the scattering rates scale as the square of the potential difference.

It is clear, however, that the calculation omits a scattering mechanism that significantly affects the majority electrons. The calculated resistivity of bulk permalloy is $0.038 \mu\Omega\text{cm}$, approximately 100 times smaller than the experimental value[26]. It is interesting to note that Mertig *et al.* [27] obtained a calculated resistivity that is also two orders of magnitude too small in a very thorough study of the single impurity limit for Fe in Ni. The resistance of very dilute alloys of Fe in Ni is reported to be[28] $0.39 \mu\Omega\text{cm/at.}\%$. If these calculations are correct, the implication is that most of the resistance in Ni(Fe) alloys is due to mechanisms outside the standard model. One obvious omission is the neglect of spin-orbit coupling.

ACKNOWLEDGEMENTS

It is a pleasure to acknowledge helpful discussions with V. S. Speriosu, B. A. Gurney, S. S. P. Parkin, R. K. Nesbet, B. A. Jones, P. A. Schroeder, D. M. Nicholson, and G. M. Stocks. Work at Oak Ridge was supported by the ORNL Exploratory Studies Program; work at Kentucky was supported by the High Performance Computing and Communication Program, U. S. Department of Energy under Contract No. DE-AC05-84OR21400 with Martin Marietta Energy Systems, Inc.

REFERENCES

1. M. N. Baibich, J. M. Broto, A. Fert, F. N. Van Dau, and F. Petroff, *Phys. Rev. Lett.* **61**, 2472 (1988).
2. G. Binasch, P. Grünberg, F. Saurenbach, and W. Zinn, *Phys. Rev.* **39**, 4828 (1989).
3. S. S. P. Parkin, N. More, K. P. Roche, *Phys. Rev. Lett.* **64**, 2304 (1990).
4. S. S. P. Parkin, R. Bhadra, and K. P. Roche, *Phys. Rev. Lett.* **66**, 2152 (1991).
5. A. Chaiken, T. M. Tritt, D. J. Gillespie, J. J. Krebs, P. Lubitz, *J. Appl. Phys.* **69**, 4798 (1991).

6. P. Grünberg, S. Demokritov, A. Fuss, M. Vohl, and J. A. Wolf, *J. Appl. Phys.* **69**, 4789 (1991).
7. B. Dieny, V. S. Speriosu, S. Metin, S. S. P. Parkin, B. A. Gurney, P. Baumgart, and D. R. Wilhoit, *J. Appl. Phys.* **69**, 4774 (1991).
8. B. Dieny, V. S. Speriosu, S. S. P. Parkin, B. A. Gurney, D. R. Wilhoit, and D. Mauri, *Phys. Rev. B* **43**, 1297 (1991).
9. R. E. Camely, and J. Barnaś, *Phys. Rev. Lett.* **63**, 664 (1989).
10. J. Barnaś, A. Fuss, R. E. Camley, P. Grünberg, and W. Zinn, *Phys. Rev. B* **42**, 8119 (1990).
11. K. Fuchs, *Proc. Cambridge Philos. Soc.* **34**, 100 (1938).
12. E. H. Sondheimer, *Adv. Phys.* **1**, 1 (1952).
13. P. M. Levy, S. Zhang, and A. Fert, *Phys. Rev. Lett.* **65**, 1613 (1990).
14. S. Zhang, P. M. Levy, *J. Appl. Phys.* **69**, 4786 (1991).
15. J. M. MacLaren, S. Crampin, D. D. Vvedensky and J. B. Pendry, *Phys. Rev. B* **40**, 12164 (1989).
16. P. Hohenberg and W. Kohn, *Phys. Rev.* **136 B**, 864 (1964).
17. W. Kohn and L. J. Sham, *Phys. Rev. B* **140**, A1133 (1965).
18. P. Soven, *Phys. Rev.* **156**, 809 (1967).
19. D. W. Taylor, *Phys. Rev.* **156** 1017 (1967).
20. J. S. Faulkner, *Prog. Mat. Sci.* **27**, 1 (1982).
21. W. H. Butler, *Phys. Rev. B*, **31**, 3260 (1985).
22. W. H. Butler and G. M. Stocks, *Phys. Rev. B*, **29**, 4217 (1984).
23. J. C. Swihart, W. H. Butler, G. M. Stocks, D. M. Nicholson, and R. C. Ward, *Phys. Rev. Lett.* **57**, 1181 (1986).
24. G. J. van den Berg, J. van Hook, B. Knook, *Proc. L.T.* **10 4**, 272 (1966).
25. J. Hugel, *J. Phys. F* **3**, 1723 (1973).
26. J. Smit, *Physica*, **21**, 877 (1955).
27. I. Mertig, R. Zeller, and P. H. Dederichs, in *Application of Multiple Scattering Theory to Materials Science*, edited by W. H. Butler, A. Gonis, P. H. Dederichs, and R. Weaver, MRS Symposia Proceedings No. 253 (Materials Research Society, Pittsburg, 1992)
28. T. Farrell and D. Greig, *J. Phys. C: Solid St. Phys.* **1**, 1359 (1968).

CALCULATIONS OF BULK AND SURFACE MAGNETIC POLARITONS IN MODULATED ANTIFERROMAGNETIC / NON-MAGNETIC SUPERLATTICES

Fred Lacy, Ernest L. Carter, Jr., and Steven L. Richardson
 Department of Electrical Engineering and Materials Science Research Center,
 School of Engineering, Howard University, 2300 Sixth Street NW, Washington, DC 20059

ABSTRACT

Recent advances in molecular beam epitaxy have renewed research on the physics of artificially structured magnetic superlattices.¹ In particular, there has been much theoretical research on the propagation of magnetic spin waves or magnetic polaritons in magnetic superlattices.^{2,3} In this work, we have studied the effect of modulating both the period of an antiferromagnetic/non-magnetic semi-infinite superlattice and the relative thickness of its individual layers to see how the dispersion relationships $\omega(k)$ for bulk and surface magnetic polaritons are effected. We have also calculated the effect of an external magnetic field on $\omega(k)$ and our calculation goes beyond the magnetostatic approximation by taking retardation effects into account.

METHODOLOGY

The geometry of the magnetic unit cell or bilayer for our superlattice calculation is shown below in Figure 1, where d_1 is the width of the antiferromagnetic layer, d_2 is the width of the non-magnetic layer, and r is the ratio of these two widths (i.e. $r = d_1/d_2$).

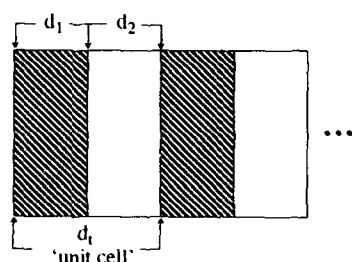


Figure 1. The geometry for the antiferromagnetic/non-magnetic superlattice. The dark regions represent the magnetic layers of width d_1 , and the light regions represent the non-magnetic layers of width d_2 . The unit cell has a total width of $d_t = d_1 + d_2$.

Our system is semi-infinite for $z > 0$ and extends to infinity in both the x and y directions. We assume that the magnetic superlattice is placed in the Voigt configuration, where the propagation of the magnetic polariton is parallel to the surface and perpendicular to the static magnetization M_S , the exchange field, H_{ex} , anisotropy field H_A , and the external magnetic field H_0 . For this calculation, MnF_2 is the antiferromagnetic material, where $M_S = 0.6$ kG, $H_{ex} = 550$ kG, $H_A = 3.8$ kG, and $\omega_0 = 1168$ Grad/s. We solve Maxwell's equations by using an anisotropic magnetic permeability tensor for the antiferromagnetic layers and employ Bloch's theorem and the transfer matrix technique⁴ to compute dispersion relationships for the bulk and magnetic surface magnetic polaritons, both in the absence and presence of H_0 , for various values of d_1 and r .

RESULTS

Illustrated in the figures below are the results of our calculations of $\omega(k)$ for bulk and surface magnetic polaritons as a function of geometry and applied magnetic field:

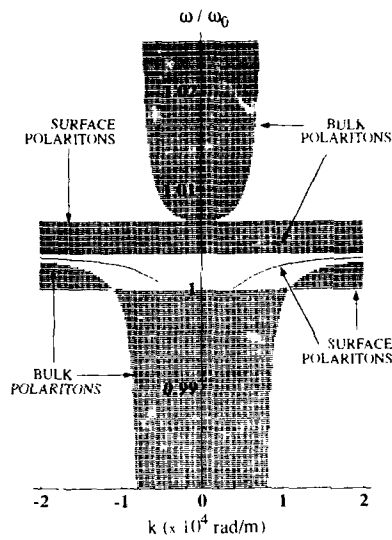
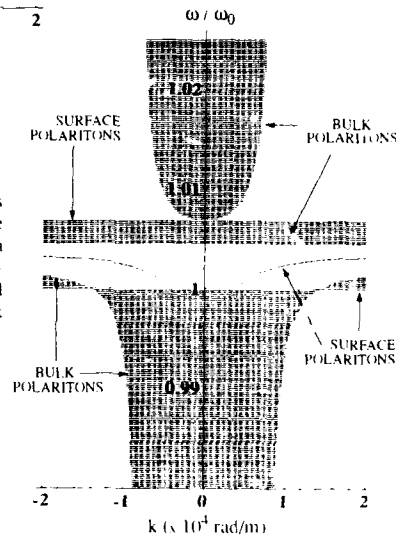


Figure 2. The dispersion relationships for bulk (hatched region) and surface (dotted line) magnetic polaritons for an antiferromagnetic/non magnetic superlattice where $H_0 = 0$, $d_t = 2 \times 10^{-6}$ m and $r = 1$.

Figure 3. The dispersion relationships for bulk (hatched region) and surface (dotted line) magnetic polaritons for an antiferromagnetic/non-magnetic superlattice where $H_0 = 0$, $d_t = 2 \times 10^{-6}$ m and $r = 2$. Note that the gap between the bulk modes increases as r is increased.



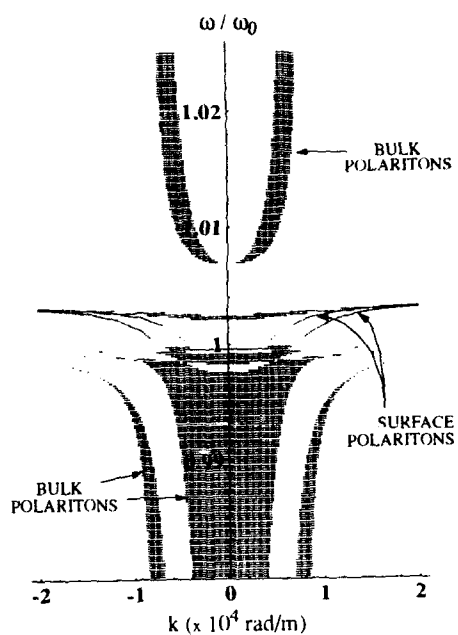
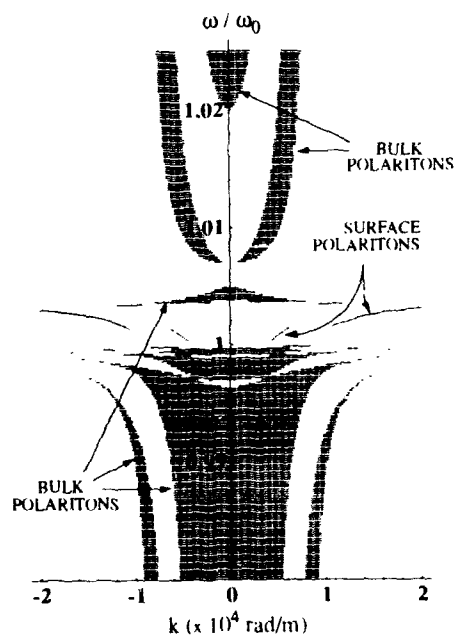


Figure 4. The dispersion relationships for bulk (hatched region) and surface (dotted line) magnetic polaritons for an antiferromagnetic/non-magnetic superlattice where $H_0 = 0$, $d_l = 0.5 \times 10^{-3} \text{ m}$ and $r = 1$. Note that as the period of the superlattice d_l is increased, the bulk modes are split into mini-bands due to the periodicity of the system.

Figure 5. The dispersion relationships for bulk (hatched region) and surface (dotted line) magnetic polaritons for an antiferromagnetic/non-magnetic superlattice where $H_0 = 0$, $d_l = 0.5 \times 10^{-3} \text{ m}$ and $r = 2$. Note that as r increases, some of the gaps between bulk modes increase.



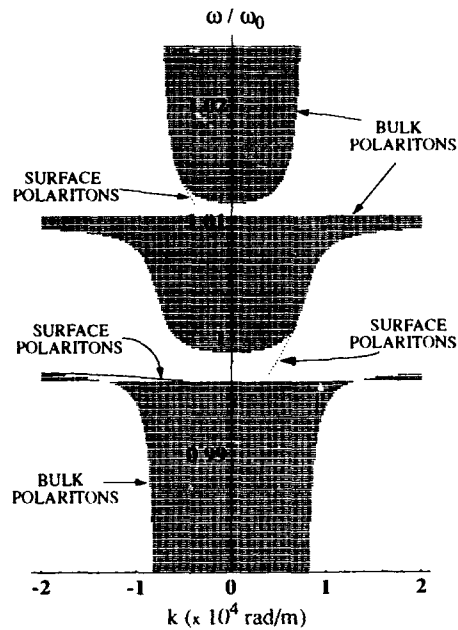
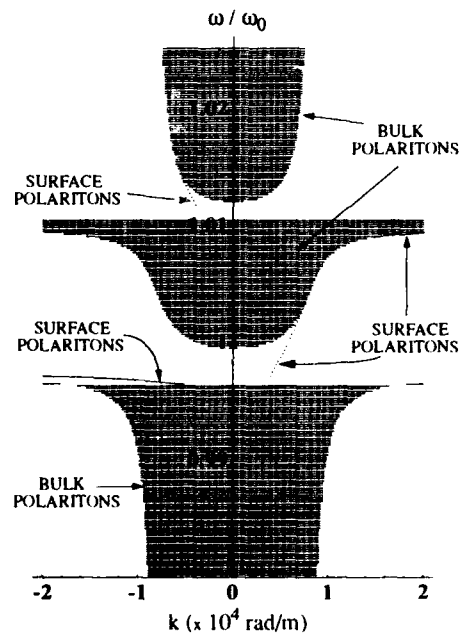


Figure 6. The dispersion relationships for bulk (hatched region) and surface (dotted line) magnetic polaritons for an antiferromagnetic/non-magnetic superlattice where $H_0 = 400\text{G}$, $d_l = 2 \times 10^{-6}\text{m}$ and $r = 1$. The application of the external magnetic field introduces a non-reciprocal nature for the surface magnetic modes of the superlattice.

Figure 7. The dispersion relationships for bulk (hatched region) and surface (dotted line) magnetic polaritons for an antiferromagnetic/non-magnetic superlattice where $H_0 = 400\text{G}$, $d_l = 2 \times 10^{-6}\text{m}$ and $r = 2$. Note that by increasing r , the width of the antiferromagnetic layer increases and the gaps between bulk modes are slightly increased, giving more allowed surface modes.



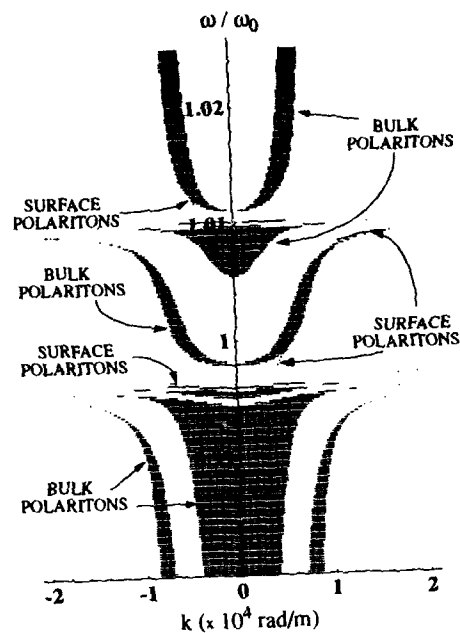
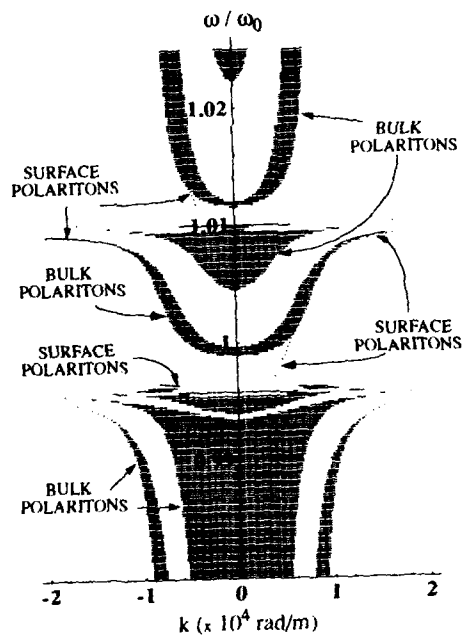


Figure 8. The dispersion relationships for bulk (hatched region) and surface (dotted line) magnetic polaritons for an antiferromagnetic/non-magnetic superlattice where $H_0 = 400\text{G}$, $d_l = 0.5 \times 10^{-3}\text{m}$ and $r = 1$. Again, an increase in the period of the superlattice causes the appearance of mini-bands in the bulk magnetic polariton spectrum.

Figure 9. The dispersion relationships for bulk (hatched region) and surface (dotted line) magnetic polaritons for an antiferromagnetic/non-magnetic superlattice where $H_0 = 400\text{G}$, $d_l = 0.5 \times 10^{-3}\text{m}$ and $r = 2$. An increase in d_l causes a slight increase in the width of some of the gaps between bulk modes in the excitation spectrum.



CONCLUSIONS

Our calculations for the bulk and surface magnetic polaritons for a semi-infinite antiferromagnetic/non-magnetic superlattice have shown a strong dependence on the modulation of the period of the superlattice and relative thicknesses of the two components of the bilayer, both with and without an external magnetic field. We have discovered that the bulk magnetic polariton dispersion spectrum is invariant to the relative ordering of the components in the bilayers; however, the dispersion relationships for surface magnetic polaritons are very similar, but not identical (note that this result is not explicitly shown in our figures, but nevertheless is correct)^{5,6}. Furthermore, the bulk magnetic polaritons have a dispersion relationship which is reciprocal both in the presence and absence of an external magnetic field, but for surface magnetic polaritons, the reciprocity is broken in the presence of an applied magnetic field. The effect of periodicity on the excitation spectrum becomes evident with minibands appearing in the bulk spectrum as d_i increases. The range of allowed frequencies for our calculated magnetic surface polaritons is restricted as r reaches some critical value $r_c = r_c(d_i)$. Finally, we suggest the use of ATR and Brillouin light scattering experiments to verify the effect of modulation on the surface magnetic polaritons for these systems.

ACKNOWLEDGEMENTS

We wish to thank the National Science Foundation, the U. S. Army Research Office, the Howard University Faculty Research Support Grant Program, the Digital Equipment Corporation, and the NASA DC Space Science Consortium for their financial support of this research. We also wish to thank Prof. Shirley A. Jackson for bringing the relevance of the transfer matrix technique to our attention.

REFERENCES

- ¹M. G. Cottam and D. R. Tilley, Introduction to Surface and Superlattice Excitations, (Cambridge University Press, Cambridge, 1989); R. E. Camley and D. L. Mills, *Phys. Rev. B* **26**, 1280 (1982).
- ²J. Barnas, *J. Phys. C: Solid State Phys.* **21**, 1021 (1988); J. Barnas, *ibid.*, **21**, 4097 (1988); J. Barnas, *J. Phys.: Condens. Matter* **2**, 7173 (1990).
- ³F. A. Oliveira, *Solid State Commun.* **78**, 759 (1991).
- ⁴J. Barnas, *Solid State Commun.* **61**, 405 (1987).
- ⁵M. C. Oliveros, N. S. Almeida, D. R. Tilley, J. Thomas, and R. E. Camley, *J. Phys.: Condens. Matter* **4**, 8497, (1992).
- ⁶F. Lacy, E. L. Carter, Jr., and S. L. Richardson (to be published).

Section A—Multilayers and Surfaces

PART II

**Giant Magnetoresistance in Alloys:
A Simple Route to Magnetic Devices?**

MODELING GIANT MAGNETORESISTANCE AND RELATIVE PERMEABILITY IN GRANULAR FILMS

M.R. PARKER*, J.A. BARNARD**, S. HOSSAIN*, D. SEALE*, M. TAN**, and A. WAKNIS**

The University of Alabama, *Department of Electrical Engineering and
**Department of Metallurgical and Materials Engineering
Tuscaloosa, AL 35487-0202

ABSTRACT

A model for the field dependence of giant magnetoresistance (GMR) in 'granular' co-sputtered alloy thin films (based on a relatively simple spin-dependent scattering concept appropriate to superparamagnetic and weakly ferromagnetic films) is applied to new experimental data from the $\text{Co}_{90}\text{Fe}_{10}\text{-Ag}$ system. The model and the experimental data can be shown to compare very well with the help of a single adjustable parameter related to spin correlation of adjacent Co-Fe clusters. A careful fit of field-dependent MR data and theory leads to a fairly reliable determination of spin-cluster radius. An analysis of the relative permeability of granular GMR films derived from the generalized form of the Clausius-Mossotti relationship is also presented. For a non-magnetic matrix the effective relative permeability is shown to be materials independent. The permeability model is applied to Co-Au granular films.

1. INTRODUCTION

In the last year, remarkably large GMR ratios have been observed[eg.,1-6] in *single layer films* variously described as 'granular', 'metastable alloys', and 'heterogeneous', but which are generally prepared by co-sputtering a ferromagnet and a nonmagnet which phase separate (cluster) under equilibrium conditions (eg., Co-Cu, Co-Ag). The occurrence of GMR is associated with a microstructure which can be described as consisting of very small ferromagnetic clusters in a 'nonmagnetic' matrix.

The field dependence of GMR in granular films has been successfully accounted for[7] by extending a simple model of magnetoresistive scattering in granular films due to Gittleman et al[8]. The size of an average spin cluster in the Co-Ag system has been tracked as a function of annealing using this model[7]. The model is outlined below and further refined to allow for assessment of the range of spin cluster sizes present in real films.

The relative permeability of granular GMR materials (despite its obvious technological relevance) has not received attention to date. In the second part of this paper a model for the effective relative permeability based on the generalized form of the Clausius-Mossotti relationship is developed. This analysis demonstrates that the effective relative permeability is materials independent and will be determined by geometrical factors alone.

2. FIELD DEPENDENCE OF GMR IN GRANULAR MAGNETIC FILMS[7]

A simple model of electron scattering due to Gittleman et al[8] is adopted here and reformulated in terms of explicit field dependence. The scattering probability is assumed to be linearly dependent on the degree of correlation of the moments of adjacent pairs of spin clusters averaged over all possible configurations within the film. This is expressed as $\langle m_i(H) \cdot m_j(H) \rangle / m^2$, where m_i is

the magnetic moment of the i^{th} spin cluster and where $|m_i| = m$. The units of m are $\text{A}\cdot\text{m}^2$. If scattering within the clusters is ignored, then the resistivity of the film in the magnetized state may be expressed as [8]

$$\rho(H) = \rho_0 - \kappa \langle m_i(H) \cdot m_i(H) \rangle / m^2 \quad (1)$$

where ρ_0 is the resistivity in zero field and κ is a scattering parameter which may be regarded as a temperature-dependent materials constant. In accordance with [8], molecular field theory is used to determine $\langle m_i \cdot m_j \rangle$. Since the clusters are assumed to be relatively large compared with atomic dimensions, classical magnetism allows the above average to be expressed as $m^2 [L(\alpha)]^2$, where $L(\alpha)$ is the Langevin function and α is the dimensionless parameter $\alpha = \mu_0 m (H + \lambda M) / kT$. In relatively 'dilute' granular films, in which the largest GMR effects have been observed (typically less than 40 atomic percent ferromagnetic component), λ may be ignored and α expressed as H/H_0 , where H_0 (A/m) is a characteristic field given by $H_0 = kT/\mu_0 m$. Eq. (1) may therefore be expressed as

$$\rho(H/H_0) = \rho_0 [1 - A \{L(H/H_0)\}^2] \quad (2)$$

where A is a normalized scattering parameter. Eq. (2) can achieve a relatively good fit to the experimental data by a suitable independent adjustment of the two parameters A and α . The first of these is solely responsible for the amplitude of the field profile. Independently, α controls the 'width' of the profile. By a careful fit of field-dependent magnetoresistance data and the model described in Eq. (2), the characteristic field, H_0 , may be determined with reasonable accuracy. As a result, the average volume of a spin cluster, V_{sc} (in m^3), may be expressed as

$$V_{sc} = kT/\mu_0 M_s H_0 \quad (3)$$

where M_s is the saturation magnetization of the magnetic component. An example of the fit that can be obtained is shown in Fig. 1 where the model is matched to experimental data for a $\text{Co}_{90}\text{Fe}_{10}\text{-Ag}$ granular alloy film. The value of H_0 here, (1.0×10^5 A/m) is related to a spin cluster volume of $2.22 \times 10^{-26} \text{ m}^3$ which is equivalent to a sphere of radius 1.7 nm. A closer fit of the model to the data at the low field end of Fig. 1 results in a reduced value for H_0 of 0.67×10^5 A/m (equivalent to a cluster radius of 2.5 nm). Conversely, a good fit of the model at the high field end results in an H_0 of 1.43×10^5 A/m (equivalent to a cluster radius of 1.2 nm). This result is not surprising in the sense that, in low fields, the larger clusters will dominate contributions to the magnetic susceptibility, while, close to saturation, magnetic behavior will be dictated by the smallest clusters with the largest interfacial anisotropy contributions. The above result suggests a standard deviation on the mean spin cluster volume of ~40% for the sample of Fig. 1.

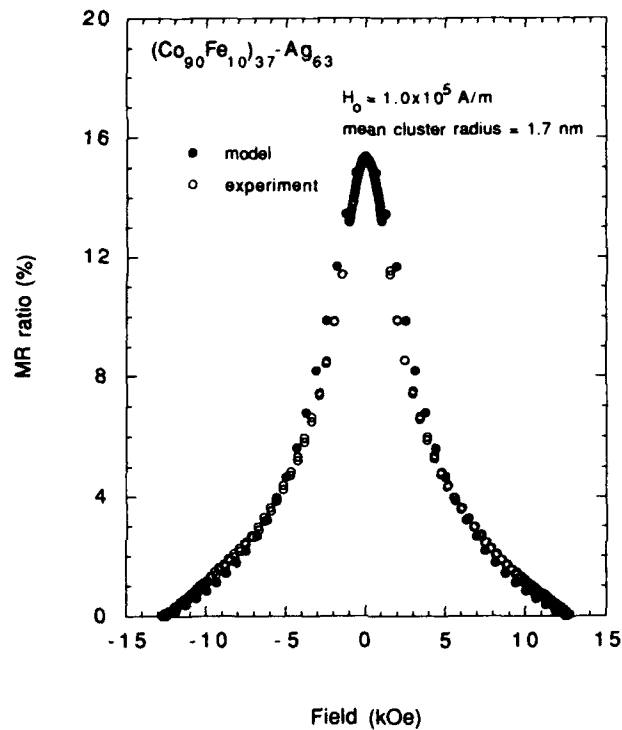


Figure 1. Comparison of experimental and calculated (using Eq. 2) MR ratio versus magnetic field for a $\text{Co}_{90}\text{Fe}_{10}\text{-Ag}$ granular alloy film.

3. PERMEABILITY OF GRANULAR FILMS

For superparamagnetic or quasi-superparamagnetic films of the sort described above, the relative permeability can be determined fairly easily from related magnetic measurements using the Langevin function[7]. As we have already shown[7], the reduced magnetization of the film in small fields can be expressed as

$$M/M_S = \alpha/3 = \mu_0 m H / 3kT \quad (4)$$

Thus

$$\mu'_{eff} = 1 + \chi = 1 + \mu_0 m M_s / 3kT \quad (5)$$

where μ'_{eff} is the relative effective permeability and $\chi = M/H$. If we consider, for example, (say) a Co-Ag alloy film containing 30% Co, H_0 is of the order 4×10^5 A/m, $\mu_0 M_s$ is around 0.51T, resulting in a relative susceptibility of ~4 and a relative permeability of ~5.

3.1 Effective Medium Theory and Magnetic Permeability

By applying the generalized form of the Clausius-Mossotti relationship to the case of magnetic fields in granular media it has been shown[9] that it is possible to arrive at two alternative formulations for the relative permeability (μ'_{eff}) of a granular alloy or cermet. These are based upon well-known effective field formulations for effective permittivity introduced separately by Bruggeman and by Maxwell Garnett[10]. The Bruggeman formulation is probably marginally better-suited to alloy systems, but, in the interests of algebraic simplicity the Maxwell Garnett approach is the one summarized here.

The effective magnetic permeability, μ_{eff} , with this approach, becomes[9]

$$\mu_{eff} = \frac{\mu_c [\mu_m + x(L-1)(\mu_m - \mu_c)]}{\mu_c + Lx (\mu_m - \mu_c)} \quad (6)$$

where μ_m is the permeability of the magnetic clusters, $\mu_c (= \mu_0)$, is the permeability of the conducting matrix, x is the volume fraction of the matrix, and L is the shape depolarization factor of the granules. This model breaks down at values of x close to the percolation limit ($x \approx 0.6$). At greater magnetic volume content, there is increasing 'networking' of the clusters with consequent rapid increase in magnetic permeability. Typically, the disparity in μ between cluster and matrix is such that Eq. (6) can be approximated to a simple generic formula[9], valid for all granular media below the percolation limit, of the form

$$\mu'_{eff} = [1 + x(L - 1)]/Lx \quad (7)$$

Clearly, for spherical granules, Eq. (7) reduces to

$$\mu'_{eff} = (3 - 2x)/x \quad (8)$$

Some preliminary permeability data are shown in Fig. 2 for as-deposited granular Co-Au films. As predicted, the experimental data indicate a rapid escalation of μ'_{eff} above the percolation limit. In the Au-rich regime, Eq. (7), with L of ~ 0.1, seems to give the best fit to the (limited) data. If this is correct, it suggests rather oblate spin clusters whose major axes lie in the (111) lattice planes of these (111) textured samples. This is too drastic a conclusion to be drawn from such

limited data but it does indicate a useful future direction for magnetic studies on these systems.

One final comment must be made here concerning *inverted* granular films[9]: i.e., films in which the ferromagnetic component forms the matrix and encapsulates granules of Ag, Cu, Au, etc. Under these circumstances, effective medium theory gives

$$\mu_{\text{eff}} = \mu_m x(1 - L)/(1 - Lx) \quad (9)$$

which, obviously, can reach high numerical values for small x . None of these systems has yet shown large amplitude GMR but some do appear to have unusual AMR characteristics.

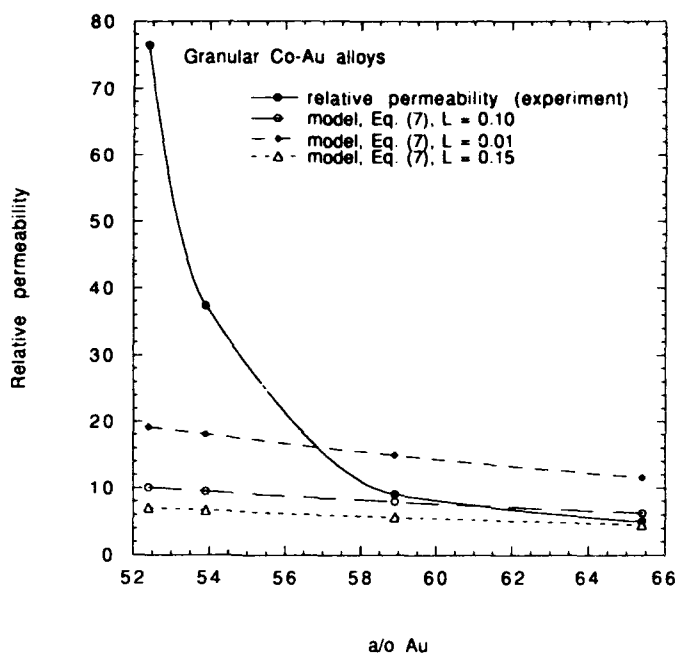


Figure 2. Comparison of experimental and calculated (using Eq. 7) relative permeability versus magnetic field for Co-Au granular alloy films.

ACKNOWLEDGEMENTS

Acknowledgement is made to the National Storage Industry Consortium Advanced Technology Program, the National Science Foundation (grants DMR-8918403 and DMR-9157402), and the MINT Center at The University of Alabama for support of this research.

References

- [1] J.A. Barnard, A. Waknis, M. Tan, E. Hafeek, M.R. Parker, and M.L. Watson, *J. Mag. Mag. Mat.* **114**, 203 (1992).
- [2] J.A. Barnard, S. Hossain, M.R. Parker, A. Waknis, and M.L. Watson, *J. Appl. Phys.*, in press.
- [3] M.L. Watson, J.A. Barnard, S. Hossain, and M.R. Parker, *J. Appl. Phys.*, in press.
- [4] A.E. Berkowitz, J.R. Mitchell, M.J. Carey, A.P. Young, S. Zhang, F.E. Spada, F.T. Parker, A. Hutten, and G. Thomas, *Phys. Rev. Lett.* **68**, 3745 (1992).
- [5] J.Q. Xiao, J.S. Jiang, and C.L. Chien, *Phys. Rev. Lett.* **68**, 3749 (1992).
- [6] J.S. Jiang, J.Q. Xiao, and C.L. Chien, *Appl. Phys. Lett.* **61**, 2362 (1992).
- [7] M.R. Parker, J.A. Barnard, D. Seale, and A. Waknis, *J. Appl. Phys.*, in press.
- [8] J.L. Gittleman, Y. Goldstein, and S. Bozowski, *Phys. Rev.* **B5**, 3609 (1972).
- [9] M.R. Parker, National Storage Industry Consortium Report: Advanced Technology Program, 1993.
- [10] M.R. Parker, *Proc. 13th Intl. Colloquium on Magnetic Films and Surfaces*, Glasgow, p. 119, (Aug. 1991).

GIANT MAGNETORESISTANCE IN SPUTTER-DEPOSITED GRANULAR Ag-Co THIN FILMS

W. Y. LEE, V. R. DELINE, G. GORMAN, A. KELLOCK, D. MILLER, D. NEIMAN,
R. SAVOY, J. VAZQUEZ and R. BEYERS
IBM Almaden Research Center, San Jose, CA 95120

ABSTRACT

Giant magnetoresistance (GMR) is reported in as-deposited $\text{Ag}_{1-x}\text{Co}_x$ ($x = 0.26-0.53$) films co-sputtered on Si from separate Ag and Co targets. GMR ratios (10 KOe maximum field) exceeding 0.50 and 0.19 at 5 and 295 K, respectively, are observed for the $\text{Ag}_{0.67}\text{Co}_{0.33}$ films deposited at ≈ 28 to 175°C . The maximum ratios of 0.55 and 0.24 occur at a substrate temperature of $\approx 125^\circ\text{C}$ for these films. The ratios decrease rapidly for the films deposited at temperatures $> 175^\circ\text{C}$ and reduce to ≈ 0.15 and 0.04 at deposition temperatures $\geq 300^\circ\text{C}$. This deposition temperature dependence of GMR ratios is interpreted in terms of the change in the spin-dependent interfacial electron scatterings due to the change in the size and number of ferromagnetic Co particles within the electron mean free path. The initial increase and the subsequent decrease in GMR ratios with increasing deposition temperature are attributed to the increase in the mean free path, and the Co and Ag particle size, respectively. Changes in mean free path are obtained from the resistivities of these films while changes in Ag and Co particles are deduced mainly from the X-ray diffraction patterns, transmission electron micrographs, and the coercivities of these films.

INTRODUCTION

The recent reports¹⁻³ of giant magnetoresistance (GMR) effect in granular thin film composites of ferromagnetic particles imbedded in a non-magnetic metallic matrix have stimulated a great deal of research activities because of its potential technological importance and fundamental scientific interest. These films are prepared by co-deposition of immiscible magnetic and non-magnetic components at ambient or lower temperatures followed by annealing to precipitate magnetic particles from the non-magnetic matrix. As in the magnetic/nonmagnetic multilayer systems, interpretations of this GMR effect generally are based on spin-dependent electron scattering at the interfaces between the ferromagnetic particles and matrix⁴. So far, the GMR results reported in granular Co-Ag films^{3, 5-8} were obtained from films deposited at either ambient temperature or lower followed by a high temperature post annealing. To our knowledge, no systematic studies on the effect of film deposition temperature has been made. In this paper, GMR of as-deposited $\text{Ag}_{1-x}\text{Co}_x$ ($x = 0.26-0.53$) thin films prepared by sputtering separate Ag and Co targets at substrate temperatures ranging from 28 to 354°C is reported. A GMR ratio as high as 0.24 at room temperature is achieved for the films with $x = 0.33$ and deposited at 125°C . The GMR ratio was found to degrade substantially for the films deposited at $> 175^\circ\text{C}$. This degradation is attributed to the decrease in spin-dependent interfacial scattering due to excessive growth of Ag and Co particles in the films deposited at higher temperatures.

EXPERIMENTAL

Thin ($\approx 1500 \text{ \AA}$ thick) films of $\text{Ag}_{1-x}\text{Co}_x$ ($x = 0.26$ to 0.53) were deposited on (100) Si at $28-354^\circ\text{C}$ from separate Ag (99.99%) and Co (99.9%) targets in $\approx 13 \text{ mTorr}$ Ar (99.99%), using a RF magnetron sputtering technique. The background pressure in the sputtering chamber is typically $\approx 5-8 \times 10^{-8} \text{ Torr}$. The deposition rate is $\approx 50 \text{ \AA/min}$ with a typical RF power input to the target of 50 and 50-150 W for the Ag and Co target, respectively. During deposition, the substrate holder rotates at a rate of 30 rpm between the two targets to ensure the compositional uniformity of the films. The temperature of the substrate (T_s) was

measured with a chromel-alumel thermocouple located at ≈ 1 mm away from the edge of the substrate holder. The substrate holder and thermocouple are enclosed in a quartz-lamp heater housing shielded with glazed Au-reflectors to minimize the heat loss and temperature gradient.

The resistivity of the film was obtained from an 1-inch diameter sample, using a commercial four point probe. The thickness of the film was determined with a commercial profilometer across a chemically etched step. The dependence of resistance of these films on DC magnetic fields (10 KOe maximum) was obtained using a low frequency (85 Hz) four point probe with the DC field applied parallel or perpendicular to the film, and with the current (0.5 mA) flowing in the direction parallel or transverse to the in-plane magnetic field. Magnetic properties were investigated at room temperature using a Princeton Measurements Corporation alternating gradient magnetometer. The composition of the films were determined by Rutherford back scattering (RBS), electron microprobe (EMP), and X-ray fluorescence (XRF) techniques. Scanning electron microscopy (SEM), transmission electron microscopy (TEM), and X-ray diffraction (XRD) were used to study the film morphology and crystal structure. Depth profiles of some of these films were obtained using secondary ion mass spectrometry (SIMS), Auger electron spectroscopy (AES), and X-ray photoelectron spectroscopy (XPS) to study the possible impurity contamination in the films.

RESULTS AND DISCUSSION

The SIMS and AES depth profiles obtained at different regions of the films show a constant Ag to Co ratio throughout the bulk of the film. No significant C, O, or Si contamination in the films were detected, except on the film surfaces and at the film-substrate interfaces. From the results of XPS analysis, Ag is found to remain in its metallic state (Ag 3d at 367.9 eV) while Co oxide or hydroxide (Co 2p at 780.0 eV) are detected on the air-exposed surfaces of these films. These Co compounds are limited only to the surfaces of these films since they disappear rapidly after brief sputter cleaning. The binding energy of Co and Ag obtained from the regions underlying the surfaces of these films corresponds to that of elemental Co (Co 2p at 777.9 eV) and Ag (Ag 3d at 367.9 eV). These results indicate that no intermetallic compound is forming between Co and Ag, as expected from the Ag-Co phase diagram. This is true for all the Ag-Co films studied, regardless of deposition temperatures. However, Ag and Co atoms are quenched into a metastable solid solution during sputter deposition at low temperatures, as discussed later.

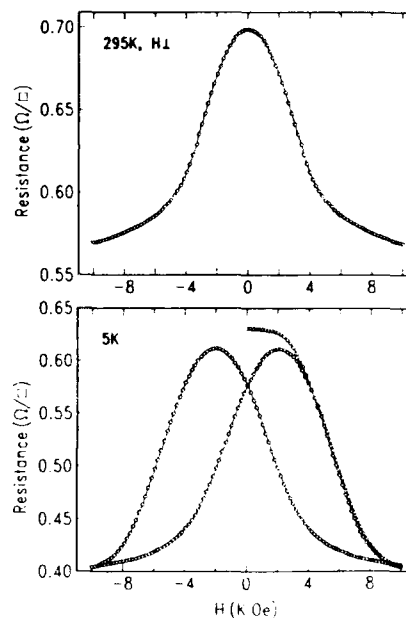


Figure 1. Sheet resistance measured at 5 and 295 K vs magnetic field for a $\text{Ag}_{0.67}\text{Co}_{0.33}$ film deposited at 125 K.

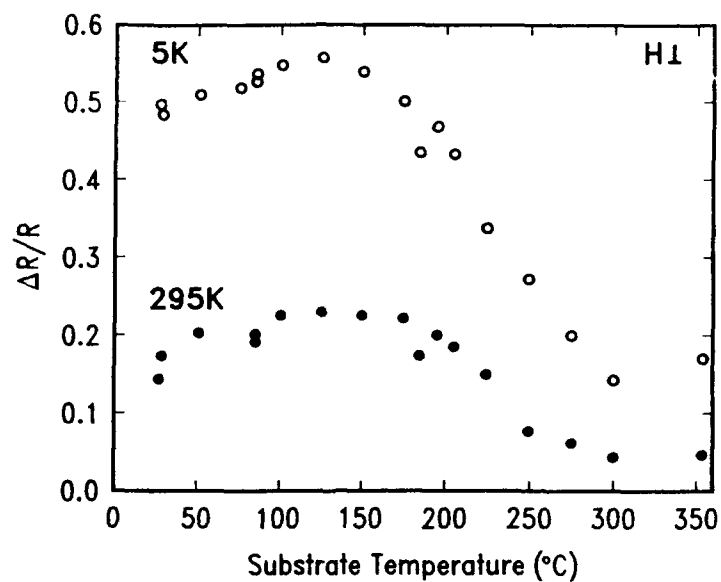


Figure 2. Magnetoresistance ratio ($\Delta R/R$) of $\text{Ag}_{0.67}\text{Co}_{0.33}$ films vs film deposition temperature. $\Delta R/R$ were measured at 5 and 295 K.

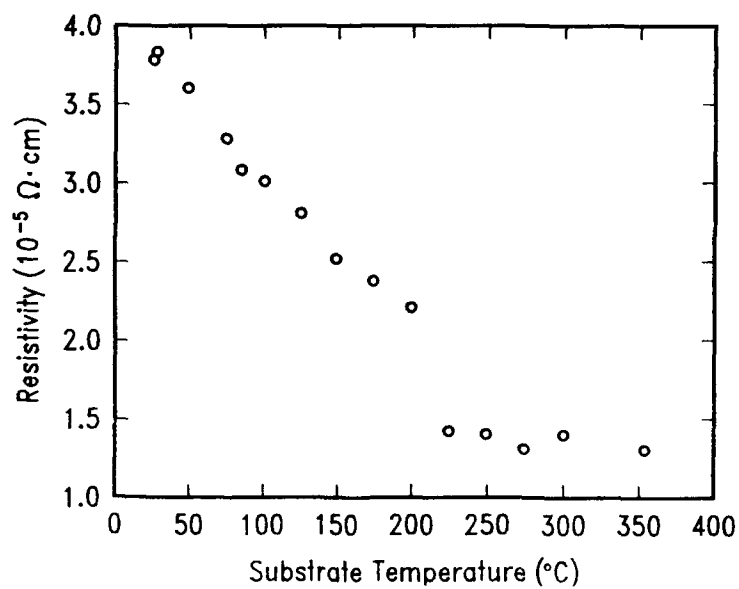


Figure 3. Room temperature resistivity of $\text{Ag}_{0.67}\text{Co}_{0.33}$ films vs film deposition temperature.

The sheet resistance at 295 and 5 K vs DC field applied perpendicular to the film is shown in Fig. 1 for the $\text{Ag}_{0.67}\text{Co}_{0.33}$ film deposited at 125 °C. It can be seen that the resistance is not fully saturated even at the highest field available (10 KOe). This is typical for all the granular Ag-Co films studied so far. The magnetoresistance ratio ($\Delta R/R$), calculated from the ratio of the maximum change in resistance over the field range (0-10 KOe) to the resistance at the highest field, is ≈ 0.24 and 0.55 at 295 and 5 K, respectively, for this film. For the films deposited at 125 °C, the Co concentration that shows the highest $\Delta R/R$ was found to be ≈ 0.33 . The values of $\Delta R/R$ measured at 5 and 295 K are given in Fig. 2 as a function of T_s (28-354 °C) for the films with this Co concentration. The Co concentration in these films is kept at a constant value of 0.33 ± 0.01 , as shown by RBS, EMP and XRF analysis. The $\Delta R/R$ value measured at 295 K increases only slightly from ≈ 0.18 to ≈ 0.24 when T_s changes from 28 to 125 °C. It starts to decrease at higher T_s , more rapidly at $T_s > 200$ °C and reaching a value of ≈ 0.04 for the films deposited at ≥ 300 °C. Similar T_s dependence was observed for the data measured at 5 K, with $\Delta R/R$ increasing from ≈ 0.50 to 0.55 when T_s changes from 28 to 125 °C and decreasing to ≈ 0.15 at $T_s \geq 300$ °C.

To understand the effect of T_s on $\Delta R/R$, especially the degradation of $\Delta R/R$ at higher T_s , a variety of techniques were used to characterize these films. Electron diffraction patterns indicate that the films deposited at lower temperatures consist of a metastable fcc Ag-Co solid solution. X-ray diffraction patterns of these films exhibit essentially single phase fcc peaks attributable to the (111), (220), and (311) planes of the metastable Ag-Co solid solution. No evidence of fcc or hcp Co was detected in these films by XRD and TEM. On the other hand, fcc Co (on the order of 100 Å in size) was unambiguously identified in the film deposited at 350 °C by the diffraction patterns of the fcc Co (200) planes. The films deposited at higher temperatures thus consist of separate fcc Ag and fcc Co particles. The d-spacings of (111) planes in these films systematically increase with increasing T_s , e.g., from 2.328 Å for the film deposited at 28 °C to 2.358 Å for the film deposited at 354 °C. The latter value is very close to that of pure Ag (2.359 Å), due to enhanced phase separation between Ag and Co in the films deposited at higher T_s . The crystallite size of Ag also appears to increase with increasing T_s , since the line width of the Ag (111) reflection peaks decreases with increasing T_s . This result is consistent with the formation of a network of Ag-rich nodules ≈ 0.5 μm in size as revealed by SEM (under both secondary and back-scattered electron modes) for the films with $T_s \geq 250$ °C. High spatial resolution AES depth profiles show that the Ag concentration in the nodules is $\approx 80\%$, compared to the average Ag concentration of 67% observed for the films without nodules. These Ag-rich nodules are thought to form by aggregation of Ag as Ag atoms are more mobile during high temperature deposition due to the lower melting temperature of Ag (960.8 °C) than Co (1495 °C). The presence of a network of Ag-rich nodules is also consistent with the fact that the resistivity (ρ) of the films deposited at 225-354 °C reaches a value $\approx 3\times$ of that observed for pure Ag films (3.7×10^{-6} Ω.cm) as can be seen from the ρ vs T_s data given in Fig. 3. This figure also shows that the ρ of these films decreases approximately linearly with increasing T_s to 200 °C, before leveling off to the value mentioned above at higher T_s . The decrease in ρ with increasing T_s can be attributed to the increasing lattice ordering and particle size. The growth and aggregation of Ag particles were evident from the XRD and SEM data shown earlier. The growth of Co particles with increasing T_s can also be inferred from the magnetic coercivity (H_c) measured at room temperature vs the T_s of these films, shown in Fig. 4 for the magnetic field applied both perpendicular and parallel to the film surface. The H_c 's of these films are obtained from their magnetic hysteresis loops. The presence of hysteresis loops in the magnetization measurements indicates that the Co particles in the films are ferromagnetic, not superparamagnetic. The H_c 's are small (20-50 Oe) and increase only slightly with increasing T_s for the films deposited at $T_s < 200$ °C. They increase more rapidly with increasing T_s for $T_s \geq 200$ °C. This increase in H_c with T_s is consistent with an increasing Co particle size in these films with increasing T_s . The Co particles in the films deposited at

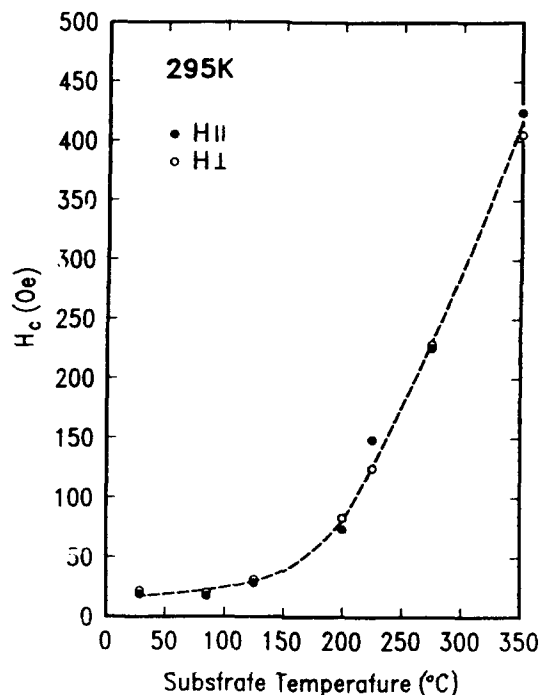


Figure 4. Room temperature coercivity of $\text{Ag}_{0.67}\text{Co}_{0.33}$ films vs film deposition temperature.

$T_s < 200$ $^{\circ}\text{C}$ are nearly superparamagnetic and grow more rapidly at higher T_s s. However, the Co particles in these films remain as single-domain particles with their H_s s decreasing with decreasing particle size due to thermal effects⁹. It should also be pointed out that no significant anisotropy was observed for H_c , since the values shown in Fig. 4 are about the same in both field orientations. Similar T_s and field-orientation dependence of H_c was reported previously for a series of Co-Ag composite films with 19% Co¹⁰.

The T_s dependence of $\Delta R/R$ can be interpreted in terms of the change in size and number of ferromagnetic particles within the electron mean free path discussed previously^{1,2,4,5,11}. From the decrease in ρ with T_s for the films deposited at $T_s < 200$ $^{\circ}\text{C}$ (Fig. 3), the electron mean free path should increase with T_s . The slight increase in $\Delta R/R$ with T_s for these films is probably a consequence of increasing spin-dependent interfacial scattering due to increasing mean free path. For the films deposited at $T_s \geq 200$ $^{\circ}\text{C}$, the decrease in $\Delta R/R$ with T_s can be attributed to the growth of Co particles and the aggregation of Ag. The growth of Co particles and the larger spacings between Co particles due to the aggregation of Ag both have the effect of reducing the surface to volume ratio and thus the number of Co particles within the mean free path. This again leads to a reduction in the spin-dependent interfacial electron scattering responsible for GMR. The magnetic couplings between Co particles are also weakened due to the larger Ag spacings. This could also result in a reduced $\Delta R/R$, analogous to the long range behavior of $\Delta R/R$ observed in magnetic/nonmagnetic multilayer systems.

SUMMARY

Giant magnetoresistance in as-deposited granular $\text{Ag}_{1-x}\text{Co}_x$ films is reported. For the $\text{Ag}_{0.67}\text{Co}_{0.33}$ films, the value of $\Delta R/R$ increases slightly when the film deposition temperature increases from 28 to 125 °C, and decreases substantially at deposition temperatures higher than 200 °C. The deposition temperature dependence of $\Delta R/R$ is interpreted in term of the change in the spin-dependent interfacial electron scattering of these films. The initial increase and the subsequent decrease in $\Delta R/R$ can be attributed to the increase in the electron mean free path and the increase in Ag and Co particle size, respectively. The change in electron mean free path is obtained from the resistivities of these films, while the growth of Co and Ag particles is deduced from the X-ray diffraction patterns and the magnetic coercivities of these films. The larger mean free path increases the number of ferromagnetic Co particles and thus increases the interfacial electron scattering. On the other hand, the larger Co and Ag particles reduce the surface to volume ratios and increase the spacings between ferromagnetic Co particles, and thus reduce the spin-dependent interfacial electron scattering.

ACKNOWLEDGMENT

The authors are indebted to Princeton Measurement Corporation for measuring the magnetization of Ag-Co films reported in this paper.

REFERENCES

1. A. E. Berkowitz, J. R. Mitchell, M. J. Carey, A. P. Young, S. Zhang, F. E. Spada, F. T. Parker, A. Hutten, and G. Thomas, *Phys. Rev. Lett.* 22, 3745 (1992).
2. J. Q. Xiao, J. S. Jiang, and C. L. Chien, *Phys. Rev. Lett.* 22, 3749 (1992).
3. J. A. Barnard, A. Wakis, M. Tan, E. Haftek, M. R. Parker, and M. L. Watson, *J. Magn. Mater.* 114, 1230 (1992).
4. S. Zhang, *Appl. Phys. Lett.* 61, 1855 (1992).
5. J. Q. Xiao, J. S. Jiang, and C. L. Chien, *Phys. Rev. B* 46, 9266 (1992).
6. M. J. Carey, A. P. Young, A. Starr, D. Rao, and A. E. Berkowitz, *Appl. Phys. Lett.* 61, 2935 (1992).
7. A. Tsoukatos, H. Wan, G. C. Hadjipanayis, and Z. G. Li, *Appl. Phys. Lett.* 61, 3059 (1992).
8. S. S. P. Parkin, R. F. C. Farrow, T. A. Rabedeau, R. F. Marks, G. R. Harp, Q. Lam, C. Chappert, M. F. Toney, R. Savoy, and R. Geiss, to be published in *Europhys.*
9. F. E. Luborsky, *J. Appl. Phys.* 32, 1715 (1961).
10. S. H. Liou, S. Malhotra, Z. S. Shan, D. J. Sellmyer, S. Nafis, J. A. Woollam, C. P. Reed, R. J. DeAngelis, G. M. Chow, *J. Appl. Phys.* 70, 5882 (1991).
11. P. Xiong, G. Xiao, J. Q. Wang, J. Q. Xiao, J. S. Jiang, and C. L. Chien, *Phys. Rev. Lett.* 69, 3220 (1992).

THE MICROSTRUCTURE AND GIANT MAGNETORESISTANCE OF NiFeAg THIN FILMS

MICHAEL A. PARKER, K. R. COFFEY, T. L. HYLTON AND J. K. HOWARD
IBM, Advanced Storage and Retrieval, IBM Fellow Program, 5600 Cottle Road,
San Jose, CA 95193

ABSTRACT

Although much has been published on giant magnetoresistance (GMR) in co-deposited thin films [1-4], only little [5] has been published on the structure-property relationships limiting the effect. Here, we report the results of microstructural characterization of NiFeAg thin films that exhibit a GMR effect. The as-deposited films show a sizeable GMR effect. The maximum GMR effect observed was 6.4% with 4kOe FWHM of the $\delta\rho/\rho$ peak. Upon annealing these films, the GMR at first increases, and then decreases. We present microstructural evidence from TEM and XRD, amongst other techniques, which shows that this is a consequence of the initial NiFeAg thin film agglomerating into NiFe grains in a predominantly Ag segregant matrix. Upon extended annealing, excessive grain growth leads to a decrease in the GMR as predicted by the model of Berkowitz, et al. [1].

INTRODUCTION

The phenomenon of giant magnetoresistance (GMR) is well established in multilayers containing antiferromagnetically coupled ferromagnetic materials separated by non-magnetic interlayers [6-8]. The phenomenon of giant magnetoresistance in granular ferromagnetic materials isolated in a non-magnetic matrix, or granular giant magnetoresistance (GGMR, G^2MR), has only recently been discovered [1-4]. The structure-property relationships in these materials is just beginning to be understood [5]. To gain insight into the mechanisms underlying this effect, we compared the unannealed microstructure of a NiFeAg thin film and that of samples annealed at 300°C, 350°C, and 400°C for 10 min each with the accompanying changes in the G^2MR .

EXPERIMENTAL DETAILS

The samples were produced in a Sputtered Films Incorporated (SFI) S-gun magnetron sputtering system by codeposition from a pure Ag and a $Ni_{81}Fe_{19}$ target so that the films were 75% by volume Ag, the remainder $Ni_{81}Fe_{19}$. The films were nominally 300Å thick. They were annealed by rapid thermal processing in an AG Heatpulse model 610 system for 10 min at 300°C, 350°C, and 400°C, respectively. The magnetoresistance was measured in a Digital Measurement Systems VSM equipped with a four point probe for measuring resistance changes. GMR measurements were performed at room temperature.

The microstructural changes in the samples were characterized by x-ray diffraction (XRD) analysis on the Rigaku DMAX-1000 system using the conventional Bragg-Brentano reflection geometry, and at a grazing incidence angle of 5° whilst scanning 2θ. Through foil (TF) transmission electron microscopy (TEM) was performed on the samples using the JEOL 4000FX analytical TEM. The samples were prepared for microscopy by lapping them

until they became transparent to the transmission of light, which is somewhat less than $5\ \mu$ in thickness. Final thinning was accomplished by ion milling using a liquid nitrogen cooled stage in a Gatan dual ion mill. Both bright field (BF) and dark field (DF) images using the 220 reflection were obtained of the samples. Selected area electron diffraction (SAD) patterns were obtained of these TF samples both at normal incidence to the sample surface and at tilt angles of $\sim 30^\circ$. Scanning electron microscopy (SEM) using a Hitachi S-800 high resolution field emission SEM was performed to corroborate the XRD data on phase separation. Similarly, atomic force microscopy was used to confirm the TEM observations using the Nanoscope model II.

RESULTS AND DISCUSSION

Figure 1 shows the results of the magnetoresistance measurements of the as-deposited and the three annealed samples as a function of the applied field. Table I summarizes the key features of these $\Delta\rho/\rho$ plots. The maximum $\Delta\rho/\rho$ of the as-deposited sample is $\sim 3\%$, but the curve is extremely broad with a fairly large FWHM, i. e. $H(50\%)$, of ~ 12 kOe. Upon annealing, the maximum $\Delta\rho/\rho$ more than doubles and the FWHM falls by about a factor of two. Upon further annealing at 350°C , this trend continues but at a substantially slower pace. However, upon annealing at 400°C , the maximum $\Delta\rho/\rho$ begins to drop even though the FWHM improves, which is evident from the narrowing of the $\Delta\rho/\rho$ plot.

Figure 2 shows the XRD data, and Table I, the peak broadening and grain sizes giving rise to this broadening obtained for the respective samples. It is apparent that the as-deposited film has a small grain size, as well as minimal intensity at the location of the $\text{Ni}_{31}\text{Fe}_{19}$ 111 reflection, which suggests that the film is primarily a metastable FCC alloy of NiFeAg. In addition, the strong Ag 111 reflection indicates that these films have a significant Ag 111 fiber texture. As annealing progresses, finite intensity grows at the position of the 111 reflection of $\text{Ni}_{31}\text{Fe}_{19}$, and the intensity of the 111 Ag reflection increases. There is also a steady progressive narrowing of both 111 reflections for Ag and $\text{Ni}_{31}\text{Fe}_{19}$, which is indicative of grain growth in both the Ag matrix and the $\text{Ni}_{31}\text{Fe}_{19}$ grains entrained within it. The respective grain sizes can be calculated from the width of these peaks using the well-known Scherrer formula [9] for x-ray peak broadening as a function of the coherent scattering domain size, presumably the grain size of the respective phases within the material.

Table I. Results of Magnetoresistance Measurements and X-ray Diffraction Grain Size Analysis

Sample	$\Delta\rho/\rho$ [%]	$H(50\%)$ [Oe]	Broadening		Grain Size	
			Ag	NiFe	Ag	NiFe
As-Deposited	2.93	11947	1.80°	3.80°	47Å	23Å
300°C/10min	6.32	5576	1.20°	3.40°	73Å	25Å
350°C/10min	6.43	4088	0.90°	2.60°	100Å	33Å
400°C/10min	4.31	2251	0.60°	1.40°	167Å	63Å

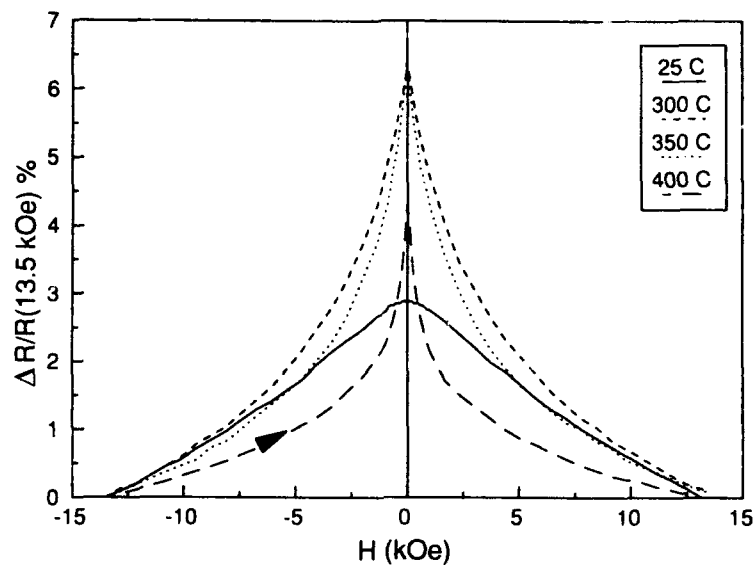


Fig. 1. Results of magnetoresistance measurements on NiFeAg thin films measured at room temperature comparing the as-deposited state with that after anneals at 300°C, 350°C, and 400°C for 10 mins.

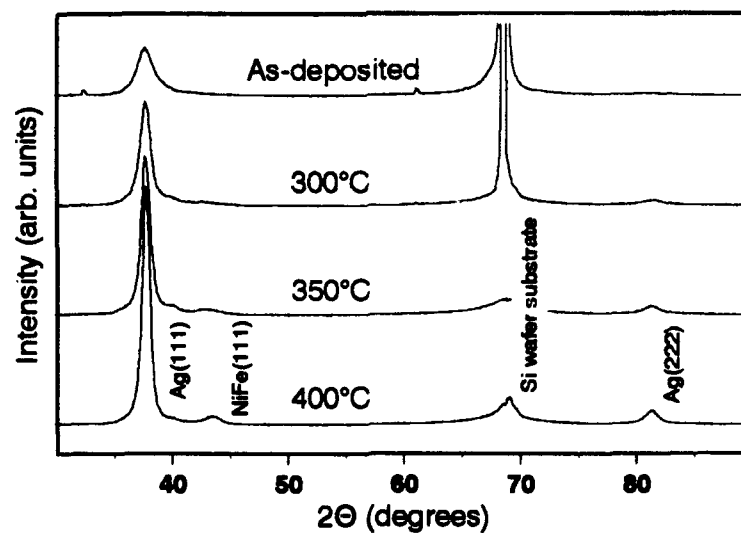


Fig. 2. $\theta/2\theta$ (Bragg-Brentano) XRD scans of NiFeAg thin films comparing the as-deposited state with that after anneals at 300°C, 350°C, and 400°C for 10 mins.

What is evident from inspection of Table I and Figures 1 and 2 is that $\delta\sigma/\sigma$ increases with the precipitation of the equilibrium $\text{Ni}_{81}\text{Fe}_{19}$ phase, but subsequently decreases. Qualitatively, this behavior can be explained as follows. Since the as-deposited film is primarily metastable FCC Ag with NiFe impurities, it is expected to have relatively poor ferromagnetism; the ferromagnetism which is present is presumably due to impure $\text{Ni}_{81}\text{Fe}_{19}$ grains which give rise to the broad weak peak appearing as a shoulder on the primary 111 Ag peak at the location of the 111 $\text{Ni}_{81}\text{Fe}_{19}$ reflection. Annealing results in the demixing of the NiFe and Ag in the initial metastable alloy to produce both purer Ag and, what's more important, purer ferromagnetic $\text{Ni}_{81}\text{Fe}_{19}$. Thus, the effect of scattering from decoupled ferromagnetic $\text{Ni}_{81}\text{Fe}_{19}$ grains of random polarization increases, which gives the observed GMR [1-5]. This effect continues until the grain size of these ferromagnetic grains becomes so large that electrons undergo fewer scattering encounters with grains of differing polarization, whence the GMR begins to decrease in accord with the predictions of Berkowitz et al. model [1].

To shed further light on these observations, the samples were examined in the SEM. Secondary electron images showed the presence of asperities on the surface of these samples which was most pronounced in the most severely annealed samples. In addition, backscattered images showed the separation of material into regions of increased and diminished scattering power consistent with the demixing hypothesis. Subsequent AFM imaging indeed confirmed the presence of hillocks on the surface of the samples which were largest in the case of the highest temperature anneal.

TF TEM samples were also prepared. Figures 3a-d show BF images of the microstructure of this material in the as-deposited and post-annealed conditions. The as-deposited sample shows a fine grain size $< 50\text{\AA}$, and the presence of small Ag-rich hillocks with faceting indicative of a 111 growth habit perpendicular to the substrate. The identification of these features as hillocks residing on the surface of the film was done by comparing their shape with similar features identified as asperities in the AFM images. Their high Ag content was confirmed by energy dispersive (EDS) x-ray analysis using a small electron probe confined to the particle during the TEM analysis. The grain size increases upon annealing to $\sim 100\text{\AA}$. However, the size of the hillocks increases dramatically $> 1500\text{\AA}$. SAD patterns taken from these samples (see Figs. 4a-d) confirm the presence of a strong 111 fiber axis texture in these films from the enhanced intensity of the 220 reflection ring. When the samples were tilted, the diffraction rings broke up into arcs which is consistent with a fiber axis texture and confirms the earlier XRD observations. The increasing grain size is also confirmed by the progressively increasing "spottiness" of the diffraction patterns. Using the 220 reflection, DF images (see Figs. 3e-h) were obtained of these samples which is consistent with a 111 growth habit for the Ag-rich hillocks that appear in strong contrast. The grain size of the films exclusive of the Ag-rich hillocks was also made more apparent in DF. The observation of Ag-rich hillocks suggests that not only Ag is the more mobile species during the anneal, but also the action of an Ostwald ripening mechanism [10] in their formation and growth.

CONCLUSIONS

Three mechanisms have been identified for the observed changes in $G^2\text{MR}$ in NiFeAg thin films: 1) demixing of the metastable FCC phase, 2) Ostwald ripening of precipitates, 3) Ag hillock formation. Demixing and $\text{Ni}_{81}\text{Fe}_{19}$ grain growth at first give rise to increasing $G^2\text{MR}$, but beyond a critical grain size $G^2\text{MR}$ decreases consistent with the model of Berkowitz et al. [1].

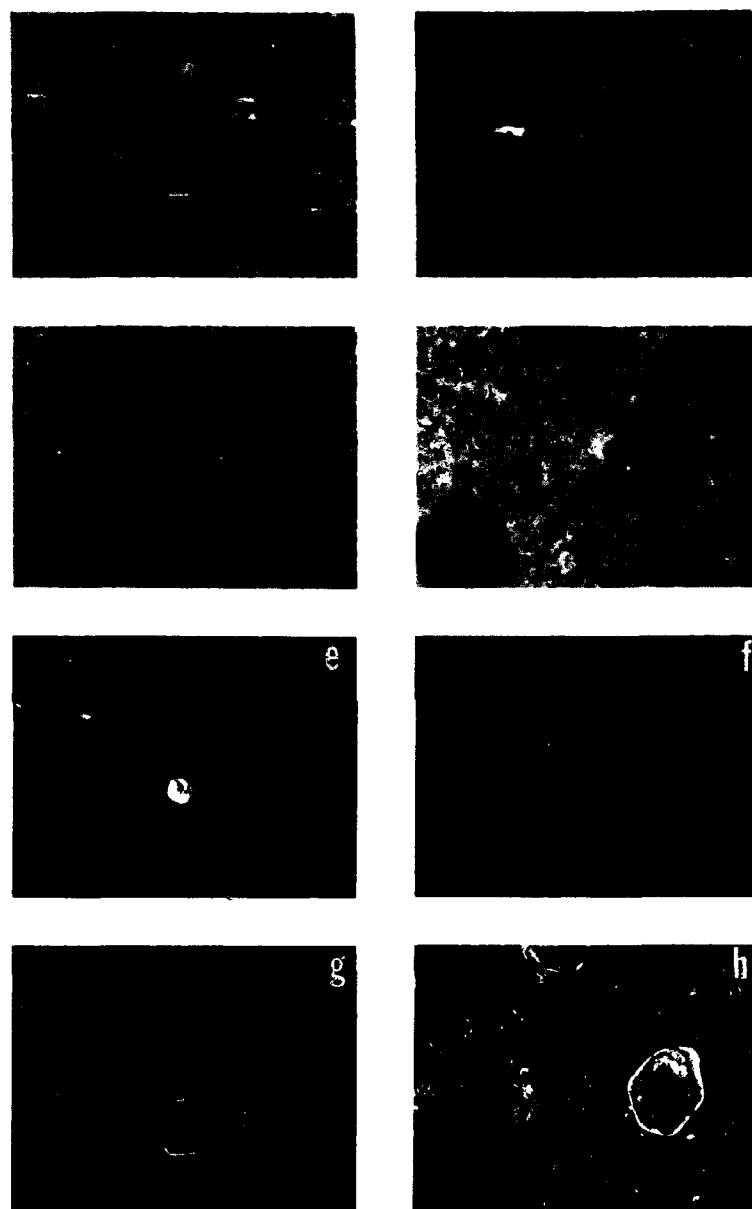


Fig. 3. Through-foil TEM micrographs of the microstructure taken in bright field of NiFeAg thin films comparing a) the as-deposited state with that after anneals at b) 300°C, c) 350°C, and d) 400°C for 10 mins; and taken in dark field, comparing e) the as-deposited state with that after anneals at f) 300°C, g) 350°C, and h) 400°C for 10 mins. Bar = 50nm.

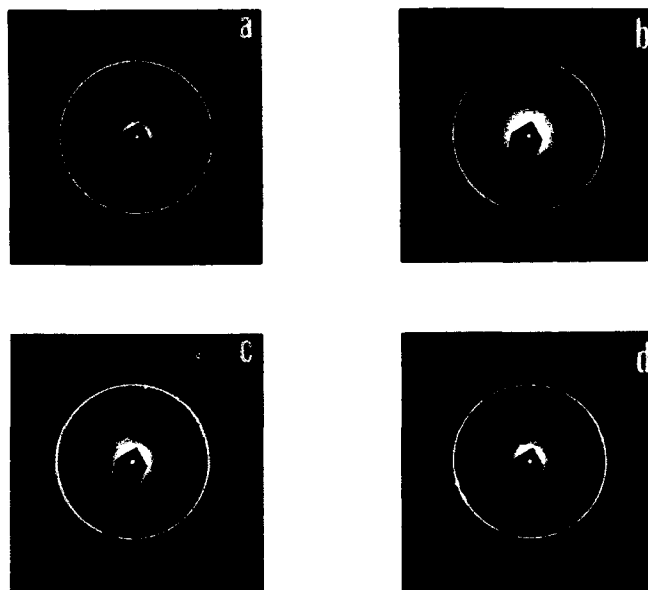


Fig. 4. Selected area electron diffraction (SAD) patterns of NiFeAg thin films in through-foil geometry comparing a) the as-deposited state with that after anneals at b) 300°C, c) 350°C, and d) 400°C for 10 mins. Ring Indices: 1st (inner most) - 111, 2nd - 200, 3rd (most intense) - 220, 4th - 311, etc.

REFERENCES

1. A. E. Berkowitz, J. R. Mitchell, M. J. Carey, A. P. Young, S. Zhang, F. E. Spada, F. T. Parker, A. Hutten, and G. Thomas, *Phys. Rev. Lett.*, **68**, 3745 (1992).
2. J. Q. Xiao, J. S. Jiang, and C. L. Chien, *Phys. Rev. Lett.*, **68**, 3749 (1992).
3. J. A. Barnard, A. Wakis, M. Tan, E. Haftek, M. R. Parker, and M. L. Watson, *J. Magn. Magn. Mat.*, **114**, L230 (1992).
4. J. S. Jiang, J. Q. Xiao, and C. L. Chien, *Appl. Phys. Lett.*, **61**, 2362 (1992).
5. T. L. Hylton, accepted by *Appl. Phys. Lett.*, (1993).
6. M. N. Baibich, J. M. Bronto, A. Fert, F. Nguyen van Dau, F. Petroff, P. Etienne, G. Creuzet, A. Friedrich, and J. Chazelas, *Phys. Rev. Lett.*, **61**, 2472 (1988).
7. S. S. P. Parkin, N. More, and K. P. Roche, *Phys. Rev. Lett.*, **64**, 2304 (1990).
8. W. P. Pratt, S. F. Lee, J. M. Slaughter, R. Loloee, P. A. Schroeder, and J. Bass, *Phys. Rev. Lett.*, **66**, 3060 (1991).
9. C. S. Barrett and T. B. Massalski, *Structure of Metals: Crystallographic Methods, Principles, Data*, 3rd ed. (Pergamon, Oxford, 1980), p. 156.
10. H. Schmalzried, *Solid State Reactions*, 2nd ed. (Verlag Chemie, Weinheim, 1981), p. 161.

Section A—Multilayers and Surfaces

PART III

Interlayer Coupling I

ORIENTATIONAL DEPENDENCE OF OSCILLATORY EXCHANGE COUPLING

M.T. JOHNSON ⁽¹⁾, P.J.H. BLOEMEN ⁽²⁾, R. COELHOORN ⁽¹⁾, J.J. de VRIES ⁽²⁾,
N.W.E. MCGEE ⁽¹⁾, R. JUNGBLUT ⁽¹⁾, A. REINDERS ⁽¹⁾ AND J. aan de STEGGE ⁽¹⁾

⁽¹⁾ Philips Research, P.O. Box 80000, 5600 JA Eindhoven, The Netherlands.

⁽²⁾ Physics Department, Eindhoven University of Technology, 5600 MB Eindhoven, The Netherlands.

ABSTRACT

The role of the interlayer Fermi surface in driving oscillatory exchange coupling of ferromagnetic layers has been critically tested in a series of MBE-grown coherent epitaxial sandwiches prepared on single-crystal substrates. The wedge-shaped Cu (or Cu-based) interlayers have been modified in a number of different ways, achieving orientational, compositional and structural alteration of the Cu Fermi surface. Observed phenomena include multiperiodic coupling oscillations in both the ferromagnetically and antiferromagnetically coupled regions of (100)-oriented Co/Cu/Co samples, extended oscillatory periods across CuNi alloy interlayers, and extremely short-period oscillations in a bcc (100) Fe/Cu/Fe system. These phenomena are straightforwardly explained in terms of calculated Fermi surface variations.

INTRODUCTION

The discovery that the exchange coupling across non-magnetic interlayers in a wide variety of magnetic multilayers can oscillate between antiferromagnetic (AF) and ferromagnetic (F) as a function of the interlayer thickness [1-4] has presented a considerable challenge to solid state physicists. The long period Λ (8-22 Å) of these oscillations was quickly ascribed to the *aliasing effect*, whereby rapid RKKY oscillations with period k_F are only sampled at discrete thicknesses of the interlayer (spacing d) resulting in $\Lambda = 2\pi/|2k_F - n\frac{2\pi}{d}|$ [5]. This argument subsequently led to a prediction of orientation-dependent oscillation-periods in the coupling, even in the case of a nearly-free-electron metallic interlayer [6]. Further refinement by Bruno and Chappert [7] emphasized the role of the Fermi surface extremal points of which, connected by vectors \mathbf{q} parallel to the growth-direction, generate oscillation-periods equal to $2\pi/|\mathbf{q}|$. In this light, a multiplicity of oscillation-periods may be encountered, the number and values of which are predicted to depend upon the growth-direction of the samples.

Oscillatory exchange coupling across Cu interlayers has attracted much attention from both the fundamental and application viewpoint. On the one hand, the relatively simple nature of the Cu Fermi surface makes this a suitable candidate for the verification of exchange coupling theories; on the other hand, the discovery of sizeable antiferromagnetic (AF) coupling and giant magnetoresistance (MR) effects in sputtered (111)-textured Co/Cu [1,2] and Fe/Cu [8] multilayers is of great interest to theorists and application engineers alike.

In this paper, we test the validity of the Fermi surface approach. Through the observation of oscillatory coupling in a series of samples, we have probed several aspects of the Fermi surface of Cu (or Cu-based) interlayers — akin to carrying out de Haas-van Alphen experiments in applied fields of 1000 T [9]. Specifically, probed extremal Fermi surface vectors have been modified by altering either the orientation, composition or structure of the intermediate layers, with attendant comparison of measured coupling periods and theoretically predicted values.

label	ref.	substrate	magnetic underlayer	interlayer wedge	magnetic overlayer	cap layers
<i>A</i>	[10]	Cu(100)	Co (60 Å)	Cu (0-40 Å)	Co (60 Å)	Cu (7 Å), Au (20 Å)
<i>B</i>	[11]	Cu(100)	Co (80 Å)	A: Cu (5-18 Å), Co (30 Å), B: Cu (0-40 Å)	Co (30 Å)	Cu (7 Å), Au (30 Å)
<i>C</i>	[12]	Cu(110)	Co (40 Å)	Cu (0-44 Å)	Co (40 Å)	Cu (7 Å), Au (20 Å)
<i>D</i>		Cu(110)	Co (40 Å)	Cu ₉₀ Ni ₁₀ (0-40 Å)	Co (40 Å)	Cu (10 Å), Au (20 Å)
<i>E</i>	[12]	Cu(111)	Co (40 Å)	Cu (0-35 Å)	Co (40 Å)	Cu (7 Å), Au (20 Å)
<i>F</i>	[13]	Cu(111)	M ₁	Cu (0-40 Å)	M ₂	Au (30 Å)
<i>G</i>		Cu(111)	Co (5 Å)	Cu (0-37 Å)	Co (5 Å)	Cu (7 Å), Au (30 Å)
<i>H</i>	[10]	Fe(100)	-	Cu (0-40 Å)	Fe (80 Å)	Au (20 Å)

Table 1: Overview of the samples used for coupling studies. In sample *F*, the magnetic under- and overlayers are actually Co/Ni multilayers (see text for composition).

EXPERIMENTAL

The overlayers were deposited on single-crystal Cu substrates in a multichamber molecular beam epitaxy system (VG Semicon V80M). In addition, a single sample was deposited on an Fe(100) single-crystal 'whisker'. The composition of the completed samples is given in Table 1. Wedge shapes were formed by slowly withdrawing an eclipsing shutter located between each single crystal and the Cu source. The substrate temperature was 50 °C during the Cu wedge depositions, except for sample *F*, for which it was 20 °C; for all other depositions, the temperature was kept at a value of 20 °C. In the Fe/Cu system, the Cu thickness was derived directly from observed intensity-oscillations in reflection high-energy electron diffraction (RHEED) during monolayer-by-monolayer growth on the Fe whisker. For the other samples, Cu thicknesses were determined using a quartz crystal monitor calibrated both from comparison with chemically analysed reference samples and from RHEED intensity oscillations occurring during deposition of Cu on Cu(100). Thicknesses thus determined were subsequently confirmed after deposition using combined *in situ* Auger electron spectroscopy (AES) and scanning electron microscopy (SEM). The other film-thicknesses were also determined using AES. More precise details concerning the substrate-preparation and growth-technique can be found in [10].

The perpendicular and parallel lattice spacings were determined by measuring the energies of the primary Bragg low-energy electron diffraction (LEED) reflections along the [00] rod, and by analysis of LEED patterns at constant electron energy, respectively. The Co layers in samples *A* – *E* and *G* displayed near identical fcc surface nets to those of the Cu substrates, and all Cu wedges were observed to have identical lattice constants to those of the underlying material. Representative LEED patterns are shown in Figure 1.

The AF coupling strengths J were determined from analysis of hysteresis loops measured at room temperature along the wedges (i.e. as a function of Cu thickness) via the magneto-optical Kerr effect (MOKE). Quoted values were derived from characteristic fields in these loops (H_{flip} , H_1 , H_2 , H_{sat}) which to a good approximation are known to be proportional to the AF coupling strength, and are defined in references [10,12].

RESULTS

The relevant \mathbf{q} vectors, which, within the theory of Bruno and Chappert, determine the period of the oscillatory exchange interaction across Cu, have been indicated for the

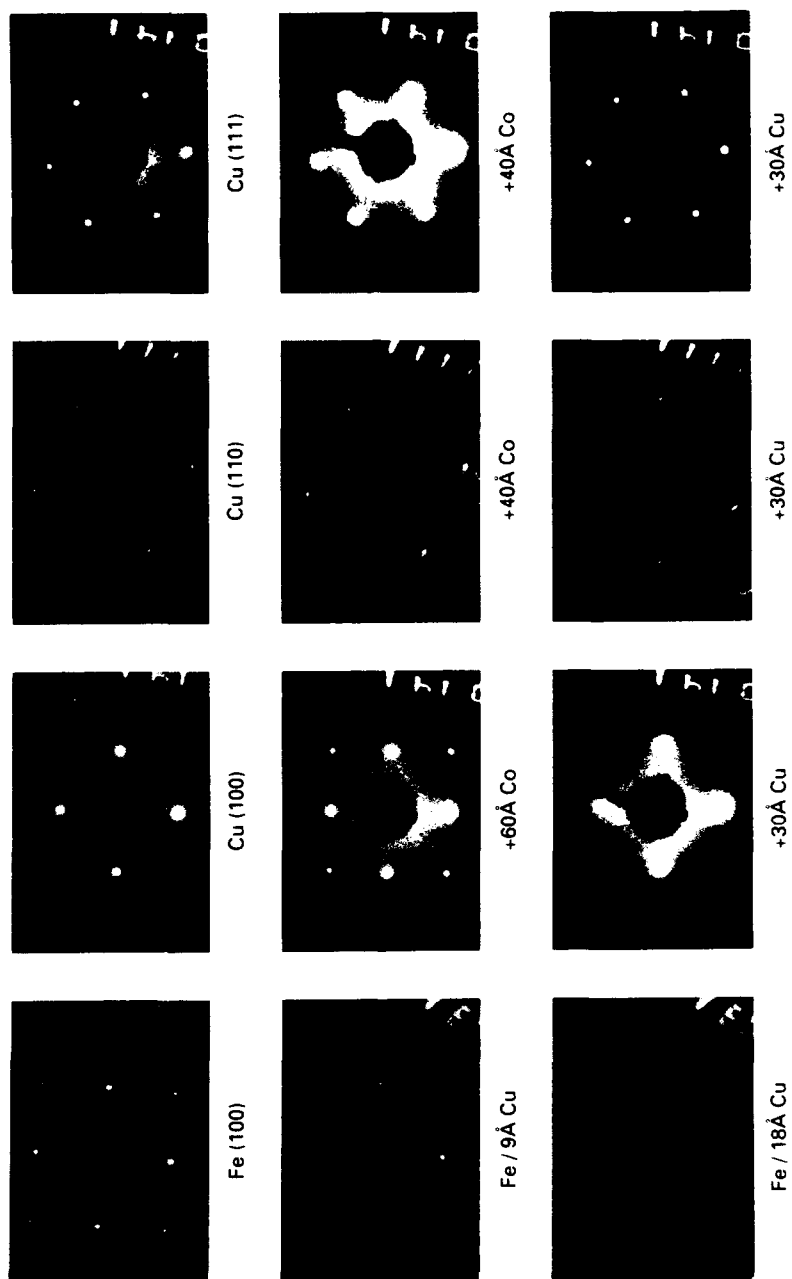


Figure 1: LEED patterns for a representative selection of samples.

fcc (100), (110) and (111) growth directions in Figures 2(a) - 2(c), where, for the (110) direction, only two of the four vectors are depicted. The figures show cross-sections of the Fermi surface obtained from augmented spherical wave (ASW) band structure calculations. Almost identical cross-sections, derived from de Haas-van Alphen measurements, are given by Bruno and Chappert in reference [7]. The resulting periods are listed in Table 2.

(100) System

Figure 2(d) (discs) depicts the thickness dependence of the oscillatory AF coupling in sample A, with 5 AF peaks clearly visible. We have attempted to fit the experimental coupling data for this sample in terms of a superposition of a short-period (Λ_1) and a long-period (Λ_2) oscillation [7]. The decay in J was assumed to be quadratic with increasing Cu thickness, and the phases, periods and relative strengths of both oscillations were regarded as free parameters. The corresponding extremal vectors \mathbf{q} are depicted in Figure 2(a). Our results are rendered in Figure 2(d) (inset). The form of the fit is in good agreement with the experimental results: a strong AF peak at 12 Å is followed by a predominantly ferromagnetic region and subsequently by a series of 4 alternately sharp and rounded AF peaks of decaying intensity. It was not necessary to add a roughness parameter to the theory to obtain this fit, perhaps highlighting the extremely high growth-quality of our sample. However, a certain amount of roughness is of course present, even in the best samples. This roughness may slightly smear out certain predicted features, such as the AF peaks at ~ 15 Å (weak) and ~ 6 Å (strong).

The experimental periods are $\Lambda_1 = 4.6$ Å and $\Lambda_2 = 14$ Å. From de Haas-van Alphen data on the Fermi surface of Cu, Bruno and Chappert have predicted periods of 4.6 Å and 10.6 Å, whereas we have found that their theoretical approach, when applied to the extremal \mathbf{q} vectors which follow from first principles self-consistent ASW band structure calculations, leads to periods of 4.6 and 11.6 Å, respectively. The predicted short-period oscillations are in excellent agreement with experiment. However, there is a discrepancy with respect to the long period. We note that the observed long period is essentially the same as in epitaxial fcc(100) Fe/Cu structures, for which a value of ~ 13.6 Å has been found [4].

Because the data for sample A were derived from hysteresis loops measured on a sandwich containing two identical magnetic layers, the coupling behavior in the F regime could not be investigated. As shown previously [14,15,16], the use of structures consisting of three magnetic layers, one pair of which is strongly AF coupled, enables one to investigate the F (and AF) coupling across a given spacer material (in this case, the layer separating the other pair of magnetic layers). We decided to apply this technique in an attempt to investigate the F regime immediately following the first AF maximum of sample A.

The employed sample (B) consisted of three Co layers with thicknesses of 80, 30 and 30 Å, separated by Cu wedges oriented *perpendicular* to each other and grown along the two equivalent in-plane [110] (easy) directions. The detailed composition of the sample is given in Table 1. The slope of wedge A was chosen so as to position the coupling between the 80 Å and 30 Å Co layers on the first (relatively narrow) AF maximum. Wedge B was applied for the purpose of investigating the oscillatory coupling itself.

Several positional scans were performed along the Cu wedges. To start with, a scan along wedge A was conducted with the aim of determining the position of maximum AF coupling. In this scan, the Cu thickness in wedge B remained fixed (thanks to the perpendicular orientation of the wedges) at a position which was chosen to correspond to strong F coupling (small Cu thickness). Three scans were subsequently performed along wedge B (at constant thickness on wedge A), corresponding, respectively, to F coupling, maximum AF coupling, and AF coupling slightly off the maximum.

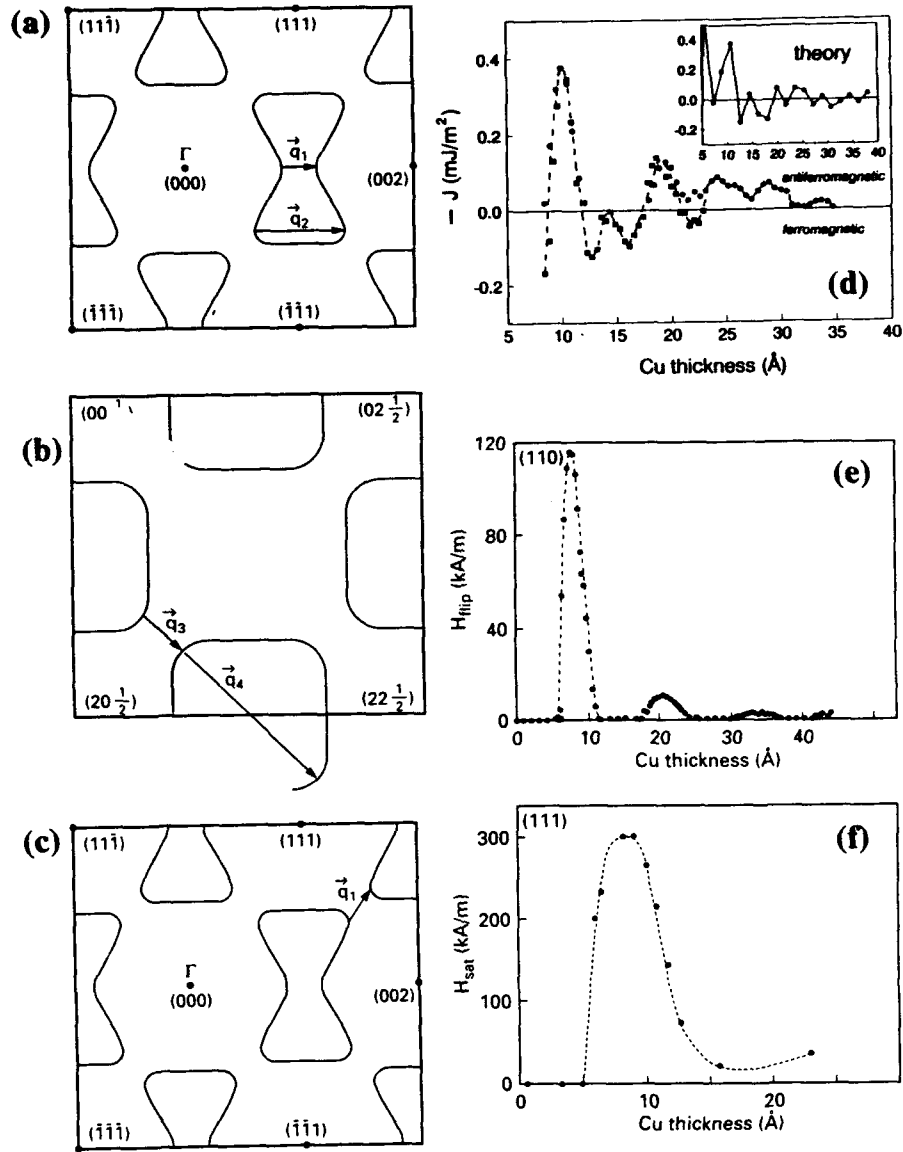


Figure 2: Calculated Fermi surface topology and measured oscillatory coupling behavior in the Co/Cu/Co system. The respective crystallographic orientations are: (100), (110) and (111).

The resulting coupling behavior is incorporated in Figure 2(d) (squares). As the figure shows, an oscillation with a period of approximately 5 Å extends clearly through both the AF and F regimes. This shows that, although the (100) Cu single crystal was first covered with an 80 Å Co layer and a Cu wedge, both 30 Å Co layers and the Cu wedge separating them were still of high structural quality. The two F peaks (with interposed F minimum) observed in the present experiment agree very well with the *ferromagnetic* behavior predicted by the two-oscillation fit of the *antiferromagnetic* data. The strength of the AF coupling in the first peak (-0.39 mJ/m^2) agrees remarkably well with the value obtained for sample A (-0.4 mJ/m^2). However, in the raw data, the position of the first peak — in fact, the whole 'coupling picture' — was shifted towards lower Cu thicknesses by about 2 Å, probably due to small combined errors in determining the slopes or starting points of the relatively steep Cu wedges. For clarity of presentation, this shift has been removed from Figure 2(d), so that the first AF peaks of the two curves accurately overlap.

(110) System; Compositional Dependence of the Coupling

The (110)-oriented Co/Cu sandwich (sample C) displayed only one oscillatory period (Figure 2(e)), whose value of 12.5 Å agrees well with the theoretical period following from the neck diameter of the Cu Fermi surface (vector \mathbf{q}_3 in Figure 2(b)). Additional shorter periods of 2.7, 3.2 and 4.2 Å are predicted to appear [7], but these were not found in the first sample to be investigated. A second sandwich, with a shallower Cu wedge, was therefore prepared and carefully scanned, but this too failed to reveal any evidence of additional shorter-period oscillations. Extremely high interface-quality would be required to detect such periods.

Because only one of its predicted periods is easily observable, the (110) system lends itself ideally to experimental examination of the period-variation predicted to arise from compositional modification of the Cu interlayer. The results discussed above demonstrate how the exact nature of the oscillatory coupling is determined by details of the interlayer's Fermi surface. Recent observations in Fe/Au [17] and Fe/Ag [18] support the validity of this Fermi surface approach, but confidence can be further tested by investigating the effect of modifying the composition of the noble metal spacer layer (and thus its electronic structure). A particularly suitable test spacer layer is CuNi, whose alloys readily form solid solutions displaying fcc structures and lattice constants which, for limited Ni concentrations, are extremely similar to those of Cu. When Ni is alloyed with Cu, the Fermi energy decreases and the Fermi surface contracts. Consequently, the oscillatory periods will be defined by new vectors linking extremal points of the alloy's Fermi surface, so that modified oscillatory behavior should be observed.

To verify such behavior, we prepared a (110) sample in which the Co layers were separated by a $\text{Cu}_{90}\text{Ni}_{10}$ alloy spacer (sample D). The (110) system's single long-period oscillation, which is associated with the neck of the Fermi surface (Figure 2(b)), would be expected to expand as the critical vector \mathbf{q}_3 is shortened by neck contraction. Assuming a rigid band approximation, the reduction of the Fermi energy in a $\text{Cu}_{90}\text{Ni}_{10}$ alloy (around 0.4 eV) would correspond to a decrease in \mathbf{q}_3 of around 15 %, and a corresponding increase in the oscillatory period.

The observed coupling behavior is rendered in Figure 3. Again, we find oscillatory coupling, but the oscillatory period of about 15 Å exceeds the 12.5 Å value found for sample C, in good quantitative agreement with the predictions made above. Similar behavior has been observed by Okuno *et al.* [19], who report an increase of the period of oscillatory magnetoresistance in sputtered (110)-oriented Co/ $\text{Cu}_{88}\text{Ni}_{14}$ /Co multilayers — the observed period slightly exceeding 15 Å. This once again illustrates the equivalence of oscillatory coupling behavior in sputtered and MBE-grown samples.

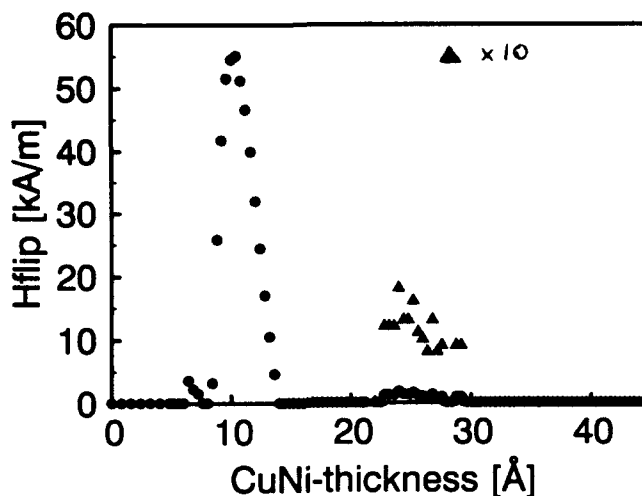


Figure 3: Coupling behavior in (110) Co/CuNi/Co (sample D).

(111) System

Following initial reports of the absence of AF coupling in MBE-prepared (111) Co/Cu multilayers, it was proposed [20] that the oscillatory coupling observed in sputtered (111)-textured Co/Cu multilayers might be attributable to the presence of minority components of different crystallographic orientation. In this light, several attempts were made to detect *intrinsic* coupling in MBE-grown (111) samples, finally culminating in the unambiguous establishment of strong intrinsic AF coupling in a Co/Cu(wedge)/Co sandwich (sample E).

The observed coupling behavior for this sample is shown in Figure 2(f). A strong AF peak occurs at 8.5 Å, with a faint indication of a second (much weaker) peak at about 20 Å, suggesting a similar oscillatory period to that in the (110) system (11–12 Å). The saturation field in the primary peak corresponds to an AF coupling strength $J_{111} \approx -1.1$ mJ/m², which is even higher than the (110)-value (~ -0.7 mJ/m²). It is remarkable that, even in this strong primary AF peak, there is a ~ 30 % occurrence of intermixed F regions, as evidenced by the non-zero remanence. In the second AF peak, this F character has increased to ~ 85 %, making it extremely difficult to confidently determine the saturation fields. However, confirmation that this second region was indeed AF-coupled has been provided by Schreyer *et al.* [21] for MBE-grown (111) Co/Cu multilayers. Here, despite the minority AF content of the layers (1–20 %), a combined Kerr and spin-polarized neutron reflectivity approach also indicated the presence of weak second and third AF regions, with an associated oscillatory period (~ 9 Å) close to that predicted from the Fermi surface approach.

Several explanations have been forwarded to account for the intermixing of F and AF regions in these MBE samples [12,21,22], invoking phenomena such as sample roughness,

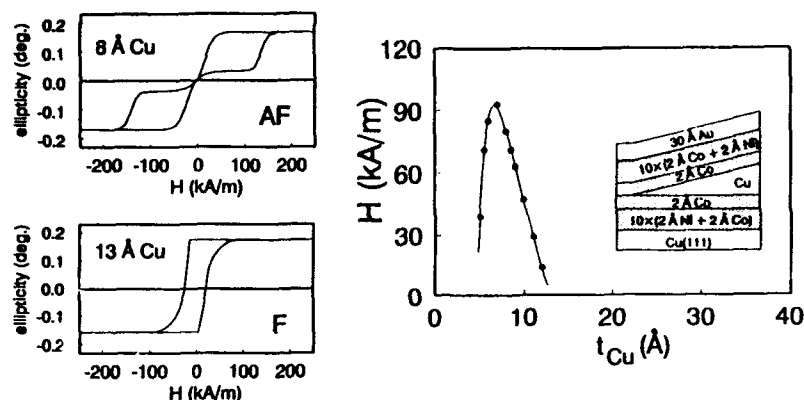


Figure 4: Representative MOKE hysteresis loops and coupling behavior for the (111) (Co/Ni)/Cu/(Co/Ni) system (sample F).

pinholes caused by possible migration of Cu onto Co, or the increased sensitivity of the (111) coupling to lateral coherence in the Cu layers — sensitivity which is due to the large angle between the extremal points of the Fermi surface and the Fermi velocity vectors of the corresponding electrons. Although the matter is certainly open to debate, one might still ascribe the absence of *complete* AF coupling in (111) systems to the mediation of the coupling at defects.

To obtain stronger evidence for AF coupling across MBE-grown Cu(111) interlayers, an entirely different sample was grown on a Cu(111) single crystal, with the form: $M_1/\text{Cu}(\text{wedge})/M_2$ (sample F) [13]. The magnetic stacks M_1 and M_2 were tailored to exhibit an easy direction perpendicular to the film-plane [23], and were composed as follows:

$$M_1 = 10 \times (2 \text{ \AA Ni} / 2 \text{ \AA Co}) + 2 \text{ \AA Co}; \quad M_2 = 2 \text{ \AA Co} + 10 \times (2 \text{ \AA Co} / 2 \text{ \AA Ni}).$$

The number of repetitions was tuned to obtain a 100 % perpendicular remanence for each stack, combined with the lowest possible ratio of the coercive field to the expected maximum coupling field (the latter demonstrating an approximate inverse dependence on magnetic layer thickness and, thus, on the number of repetitions). The mirrored sequencing of the Co and Ni layers in each magnetic stack, and the additional monolayer of Co incorporated at each interface of the stacks with the Cu spacer layer, guaranteed complete stack symmetry with respect to the interlayer, and two identical Co/Cu interfaces. Intuitively, the type of element at the interface is expected to predominantly determine the phase and the amplitude of the oscillatory coupling.

The applied field in the polar MOKE measurements was oriented perpendicular to the film-plane. Square loops (with 100 % remanence) were observed for Cu thicknesses of 2 Å and 13 Å (Figure 4), confirming the perpendicular easy axis of the Co/Ni multilayers, and indicating F (or weakly AF) coupled layers. On the other hand, the intricate shape of the loops observed for Cu thicknesses in the range 6 – 12 Å is clearly indicative of strong AF coupling. It should be noted that the spin-flip transitions in these loops are accompanied by considerable hysteresis, which we attribute to the presence of uniaxial anisotropy. Obviously, the reversing stack magnetizations do not follow a path of global minimum energy, but are hindered by anisotropy energy barriers.

The Cu thickness-dependence of the average experimental flip-field for the up and down transitions is also rendered in Figure 4. The strong AF peak at about 7 Å confirms the

presence of oscillatory exchange coupling. However, no trace was seen of the faint second peak observed in sample *E* at ~ 20 Å (Figure 2(f)). At thicknesses above 12 Å, all loops were of the F coupling type. The coupling possibly decays so quickly that its strength in the second and subsequent peaks is too low compared to the coercive field ($H_c \approx 25$ kA/m) to be detectable. In fact, if we assume that the ratio of the coupling strengths in the first and second peak of sample *E* is also applicable in the present case (value ~ 8), we then deduce an average second-peak flip-field in sample *F* of about 11 kA/m, which is indeed lower than the coercive field.

The position of the first peak is shifted by 1.5 Å with respect to the position observed in sample *E*. This shift, however, is comparable to the sum of the errors made in both experiments in locating the start of the wedge, determining the wedge slope, and positioning the MOKE laser beam with respect to the wedge. It is also interesting to note that the loops at 7–11 Å Cu do not reveal contributions from F coupling, in contrast to the loops observed in sample *E*. This absence is possibly due to the relatively large uniaxial anisotropy in the present sample [13]. The calculated maximum AF coupling strength, which is estimated from the average flip-field, is -0.34 mJ/m². This is roughly a factor of 3 lower than the value obtained in sample *E*. The presence of Ni at the interface with Cu cannot be excluded, and may account for this difference. However, we should also note that, at present, it is not known to what extent deeper layers may contribute to the exchange coupling.

To avoid the difficulties of potentially low coupling fields, and yet maintain the benefits of 100 % AF coupling afforded by uniaxial (perpendicular) anisotropy, a further sample was prepared, with magnetic layers consisting of 5 Å Co films (sample *G*). Separate anisotropy measurements [24] revealed that the presence of interface anisotropy in Co/Cu(111) is sufficient to cause perpendicular alignment of the magnetization vectors of such thin Co layers. Consequently, the coupling fields, which scale inversely with the magnetic layer thickness, will be enhanced by about an order of magnitude compared to the other samples. This facilitates identification of weak coupling features, while still exploiting the intrinsically higher signal intensities offered by the polar Kerr geometry relative to the longitudinal Kerr geometry (around an order of magnitude).

A series of polar Kerr hysteresis loops for this sample is presented in Figure 5. Before the start of the Cu wedge (-2 Å Cu), there exists a single Co layer of thickness 10 Å. For this layer, it is clear that the interface anisotropy is insufficient to fully balance the demagnetization energy, and a field is needed to obtain perpendicular saturation. However, introducing a small Cu separation layer directly creates the desired 100 % perpendicular remanence. At Cu thicknesses above 6 Å, a clear transition to AF coupling occurs, with a coupling maximum appearing at 9 Å (where the available applied magnetic fields were insufficient to saturate the sample). Note once again the complete absence of an F component in the first AF peak. Increasing the Cu thickness above 13 Å again resulted in F loops and, despite careful study, further AF regions remained undetected at greater Cu thicknesses. This quashes the theory that low coupling strength prevented detection of a second AF peak in sample *F*.

Although the presence of intrinsic coupling in the (111) Cu/Co system is thus established beyond doubt, it is also apparent that a definitive experiment to establish the oscillatory phase and period is still required.

STRUCTURAL DEPENDENCE OF THE COUPLING

Up to now, the Fermi surface picture of oscillatory interlayer exchange coupling has been tested and supported by exploiting the dependence of the form of the interlayer's Fermi surface on both crystallographic orientation and compositional modification. To further test the picture, the effect of differing crystallographic structure on the coupling

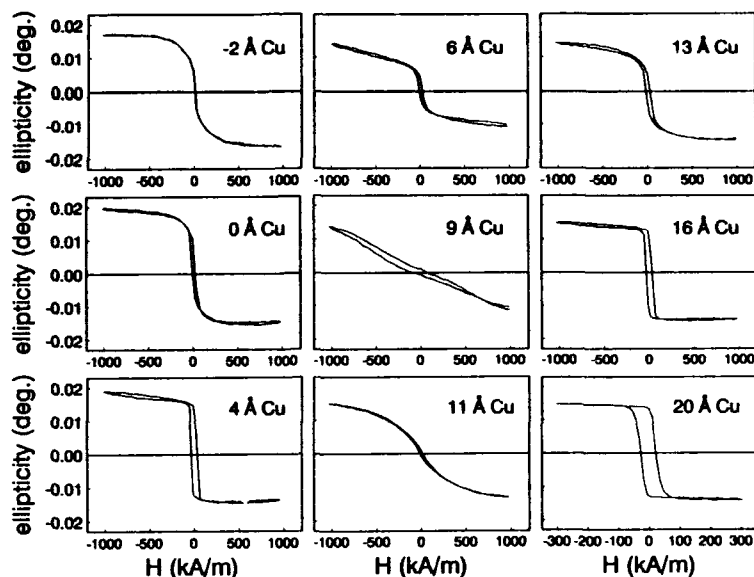


Figure 5: MOKE hysteresis loops for the (111) Co(5 Å)/Cu/Co(5 Å) system (sample G).

(via changes in the Fermi surface) was investigated by examining the exchange interaction across a bcc Cu wedge sandwiched between a bcc (100) Fe whisker substrate and a capping Fe layer (sample H).

Our observations both during and after the growth of the Cu wedge on the Fe substrate were in agreement with the RHEED measurements of Heinrich *et al.* [25], which suggest that the Cu initially grows in a bcc structure with an in-plane lattice very similar to that of the Fe substrate. LEED analysis of both the in-plane and perpendicular lattice confirmed the RHEED observation of an almost unaltered surface net and, furthermore, revealed that the perpendicular lattice constant remains identical to that of the bcc Fe(100) substrate [10].

Figure 6 depicts the switching fields in Fe/Cu/Fe as a function of Cu thickness [10]. In this sandwich, all measurements below a Cu thickness of 10 ML (14.3 Å) showed F (or weak AF) coupling of the Fe overlayer to the Fe(100) substrate, in close agreement with the observations in [25]; above 10 ML, the coupling became strongly AF. The switching fields oscillate as a function of the bcc Cu thickness, showing 4 strong oscillations in magnitude with a period of 2 ML Cu. The maximum critical fields (at ~ 12 ML Cu) correspond to $J = -0.1$ mJ/m², which is somewhat weaker than expected from the Co/Cu/Co sample at an equivalent Cu thickness.

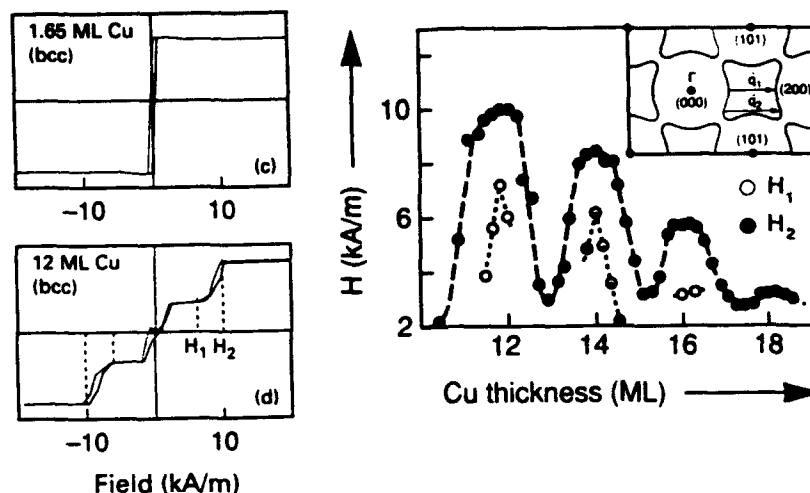


Figure 6: Representative MOKE hysteresis loops and coupling behavior for the bcc (100) Fe/Cu/Fe system (sample H).

Comparison of Figures 2(d) and 6 shows that the variation of the exchange coupling with the interlayer thickness is entirely different for these two (100)-oriented samples. The most apparent explanation of this difference is the different structure of the Cu interlayers. No theoretical indications have been given that the different nature of the magnetic atoms (Fe or Co) by itself would result in different periods (although the amplitude and phase of the oscillations are likely to be affected by this difference [22]).

To extend the analysis of the previous section to the Fe/Cu/Fe system, we have calculated the Fermi surface of hypothetical bcc Cu using the ASW method. The relevant cross-section of the Fermi surface is shown in Figure 6 (inset). The most obvious difference from the fcc case (Figure 2(a)) is that the hole orbits around the N point (bcc) have a considerably squarer character than the 'dog bone' orbits around the X point (fcc). The extremal q vectors for the (100) direction, q_1 and q_2 , correspond to periods of 2.56 ML and 2.22 ML, respectively. The consequence of a period of 2.22 ML would be that 4 oscillations of precisely 2 ML would be found, followed by a phase-shift. Such a series of oscillations is indeed seen in Figure 6. The thickness-interval in which the oscillatory exchange coupling was observed was too small to analyse the experimental results more quantitatively, as for the Co/Cu/Co case. In particular, no assessment of the possible contribution of longer-period oscillations, such as the predicted one with a period of 2.56 ML, can be given. It remains unclear why the Fe/Cu/Fe system is F (or weak AF) up to 10 ML: no long period can be anticipated from the Fermi surface. Furthermore, the first principles band structure calculations of the coupling by Herman *et al.* [26], which also predict 2 ML oscillations, indicate that the system should become AF for Cu thicknesses above 5 ML. The anomaly suggests the possible presence of pinholes in the Cu interlayer.

Sample	t_1 (Å)	$-J$ (mJ/m ²)	$\Lambda_1(\Lambda_2)$ (Å)		
			measured	predicted (dHvA) ^a	predicted (ASW) ^b
A (100)	12	0.4	14 (4.6)	10.6 (4.6)	11.6 (4.6)
B (100)	10	0.39	14 (4.6)	10.6 (4.6)	11.6 (4.6)
C (110)	8.5	0.7	12.5	12.2 (3x)	11.2 (3x)
D (110) CuNi	10		15		13
E (111)	8.5	1.1	11 - 12	9.4	9.0
H (100) bcc	17 (12 ML)	0.1	2.86 (2 ML)		3.7, 3.2

Table 2: Measured coupling data for the Co/Cu/Co system, comprising the position of the first AF peak (t_1), the maximum AF coupling strength ($-J$), and the long (λ_1) and short (λ_2) oscillatory periods. Also included are predicted periods derived (a) from reference [7], where de Haas-van Alphen data (dHvA) are employed, and (b) from the same theoretical approach applied to ASW calculations. For the (110) system, 3 short periods are predicted (see text).

SUMMARY

Table 2 clearly reveals the orientational, compositional and structural dependence of the (longest) oscillatory period (Λ_1) and position (t_1) of the primary AF peak, and the maximum AF coupling strength ($-J$). The table also gives the theoretical periods, both as predicted in [7] from de Haas-van Alphen measurements of the Fermi surface and as rendered by the same theory applied to self-consistent *ab initio* ASW calculations of the Fermi surface. The measured periods for the (100) and (111) directions are somewhat greater than those predicted in [7], and this is also the case for the (110) direction if comparison is made with the ASW results. This finding may stimulate further investigations, in particular regarding the question of whether bulk properties (i.e. period and phase independent of the interlayer thickness) have already been effectively reached for Cu thicknesses near the first AF peak.

ACKNOWLEDGEMENT

This work was partially supported by the SCIENCE program of the European Community (contract SC1-0387-C of the GP2M3).

References

- [1] S. S. P. Parkin, R. Bhadra, and K. P. Roche, Phys. Rev. Lett. **66**, 2152 (1991).
- [2] D. H. Mosca, F. Petroff, A. Fert, P. A. Schroeder, W. P. Pratt, Jr., and R. Loloee, J. Magn. Magn. Mater. **94**, L1 (1991).
- [3] S. S. P. Parkin, Phys. Rev. Lett. **67**, 3598 (1991).
- [4] W. R. Bennett, W. Schwarzacher, and W. F. Egelhoff, Jr., Phys. Rev. Lett. **65**, 3169 (1990).

- [5] R. Coehoorn, Phys. Rev. B **44**, 9331 (1991); C. Chappert and J. P. Renard, Europhys. Lett. **15**, 553 (1991); D. M. Deaven, D. S. Rokhsar, and M. Johnson, Phys. Rev. B **44**, 5977 (1991).
- [6] An orientational and structural dependence of the exchange coupling was also predicted from *ab initio* band structure calculations for a variety of systems containing Cu interlayers: see F. Herman, J. Sticht, and M. van Schilfgaarde, Mat. Res. Soc. Symp. Proc. **231**, 195 (1992).
- [7] P. Bruno and C. Chappert, Phys. Rev. Lett. **67**, 1602 (1991).
- [8] F. Petroff, A. Barthélemy, D. H. Mosca, D. K. Lottis, A. Fert, P. A. Schroeder, W. P. Pratt, Jr., R. Loloee, and S. Lequien, Phys. Rev. B **44**, 5355 (1991).
- [9] D. M. Edwards, J. Mathon, R.B. Muniz, and M.S. Phan, Phys. Rev. Lett. **67**, 493, (1991).
- [10] M. T. Johnson, S. T. Purcell, N. W. E. McGee, R. Coehoorn, J. aan de Stegge, and W. Hoving, Phys. Rev. Lett. **68**, 2688 (1992).
- [11] P. J. H. Bloemen, R. van Dalen, W. J. M. de Jonge, M. T. Johnson, and J. aan de Stegge, *Short period oscillation of the interlayer exchange coupling in the ferromagnetic regime in Co/Cu/Co(100)*, Proceedings of the MMM conference, Houston, 1992 (to be published in J. Appl. Phys.).
- [12] M. T. Johnson, R. Coehoorn, J. J. de Vries, N. W. E. McGee J. aan de Stegge, and P. J. H. Bloemen, Phys. Rev. Lett. **69**, 969 (1992).
- [13] P. J. H. Bloemen, M. T. Johnson, J. aan de Stegge, and W. J. M. de Jonge, J. Magn. Magn. Mater. **116**, L315 (1992).
- [14] S. S. P. Parkin and D. Mauri, Phys. Rev. B **44**, 7131 (1991).
- [15] A. Fert, A. Bartélémy, P. Etienne, S. Lequin, R. Laloee, D. K. Lottis, D. H. Mosca, F. Petroff, W. P. Pratt, and P. A. Schroeder, J. Magn. Magn. Mater. **104-107**, 1712 (1992).
- [16] P. J. H. Bloemen, W. J. M. de Jonge, and H. C. Donkersloot, *Determination of the ferromagnetic coupling across Pd by magneto-atomic engineering*, J. Appl. Phys. (accepted).
- [17] A. Fuß, S. Demokritov, P. Grünberg, and W. Zinn, J. Magn. Magn. Mater. **103**, L221 (1992).
- [18] J. Unguris, R. J. Celotta, and D. T. Pierce, *Oscillatory magnetic coupling in Fe/Ag/Fe(100) sandwich structures*, (submitted).
- [19] S. N. Okuno, K. Inomata, and Y. Saito, 16th Annual Conference on Magnetism in Japan, digest 7pC-7, p 52 (1992).
- [20] W. F. Egelhoff, Jr. and M. T. Kief, Phys. Rev. B **45**, 7795 (1992).
- [21] A. Schreyer, K. Brohl, J. F. Ankner, Th. Zeidler, P. Bodeker, N. Metoki, C. F. Majkrzak, and H. Zabel, *Oscillatory exchange coupling in Co/Cu(111) superlattices*, (submitted).

- [22] P. Bruno and C. Chappert, Phys. Rev. B **46**, 261 (1992), P. Bruno, J. Magn. Magn. Mater. **116**, 213 (1992).
- [23] F.J.A. den Broeder, E. Janssen, W. Hoving, and W.B. Zeper, IEEE Trans. Mag. **28**, 2760 (1992).
- [24] R. Jungblut *et al.* (unpublished)
- [25] B. Heinrich, Z. Celinski, J. F. Cochran, W. B. Muir, J. Rudd, Q. M. Zhong, A. S. Arrott, K. Myrtle, and J. Kirschner, Phys. Rev. Lett. **64**, 673 (1990).
- [26] F. Herman, J. Sticht, and M. van Schilfgaarde, J. Appl. Phys. **69**, 4783 (1991).

OSCILLATORY INDIRECT COUPLING BETWEEN PERPENDICULARLY MAGNETIZED Co MONOLAYERS THROUGH Cu(111)

ULRICH GRADMANN, HANS-JOACHIM ELMERS AND JUERGEN KOHLHEPP

Physikalisches Institut, Technische Universität Clausthal,
D 3392 Clausthal-Zellerfeld, Germany

ABSTRACT

Co-monolayers, prepared by MBE on Cu(111)-surfaces at room temperature and covered by Cu, are ferromagnetic with a Curie-temperature of about 430 K. They are magnetized perpendicularly because of a strong perpendicular magnetic surface anisotropy of the Cu/Co(111)-interface. They provide a remarkably good representation of the 2-dimensional Ising model. The indirect coupling between these perpendicularly magnetized ferromagnetic monolayers was investigated using samples of type Cu(111)/1Co/D_{Cu}Cu/1Co/Cu, containing Co/Cu/Co-trilayers composed of Co-monolayers and a spacer consisting of D_{Cu} atomic layers of Cu(111). Torsion oscillation magnetometry of these samples showed clearly a coupling between the monolayers with an oscillatory dependence on D_{Cu}. The amplitude of the oscillation is strongly reduced if the coupled Co-films consist of 5 ML instead of 1 ML. The present controversy on the presence or absence of antiferromagnetic and oscillatory indirect coupling in the Co/Cu(111)-system is discussed in the light of these experiments. The discussion shows that the oscillatory coupling is an intrinsic property of ideal (111)-structures, and can be understood by the RKKY-type theory of indirect coupling between ferromagnetic monolayers. The usual application of this theory to the coupling between thicker films is justified. However, in the fcc(111)-system there is apparently a specific barrier against complete coalescence, resulting in a tendency to retain holes and channels in the Cu-spacer. This tendency is stronger in flat single-crystal samples than in sputtered films with high densities of atomic steps. Apparently, this results in competing ferromagnetic hole coupling which may more or less completely obscure the intrinsic oscillatory coupling, preferentially in samples grown on extremely flat single crystal surfaces.

INTRODUCTION

The oscillatory character of indirect magnetic coupling by the spin-polarized electron gas of a nonmagnetic metallic medium has been first predicted for the case of coupling between localized atomic magnetic moments, by the famous Ruderman-Kittel-Kasuya-Yoshida (RKKY) model [1]. After the experimental confirmation of this oscillatory coupling for the case of Fe in Cu [2] and Mn in Cu [3], it was quite natural to expect that a similar oscillatory coupling should occur between ferromagnetic monolayers through a nonmagnetic spacer layer. Nevertheless it was a surprise when Parkin et al. [4] detected an oscillatory coupling of this type in sputtered Co/Ru, Co/Cr and Fe/Cr superlattices with (111) texture. The refined analysis of this coupling in single-crystalline samples was extremely successful for the case of coupling between Fe(100)-layers through Cr(100) [5], Al(100) and Au(100) [6], where a superposition of long-period and short-period oscillations could be detected. Apparently, this success was to a large extent based on the fortunate epitaxial growth conditions in those systems, in particular on the extremely small misfits $f_{\text{FeCr}} = -0.7\%$, $f_{\text{FeAl}}^* = 0.1\%$ (effective misfit of the coinciding square nets of fcc(100) and bcc(100), rotated by 45°) and $f_{\text{FeAu}}^* = -0.6\%$, respectively. The periods found in Au are in good agreement with a RKKY-type theory of coupling between monolayers [7], although the experiments were done with Fe-films consisting of at least 10 ML (monolayers), or even with bulk whisker substrates.

Similar promising structural preconditions are given in the system Cu/Co, because of the common crystal structure and small misfit of $f_{\text{CoCu}} = -1.8\%$. The simple band-structure of Cu made it previously an outstanding model system for the investigation of the original RKKY-coupling between atomic moments in bulk samples [2,3]; in addition, a rather extended RKKY-calculation for the coupling between ferromagnetic monolayers through Cu is now available [7]. Further interesting evidence for indirect coupling in the Co/Cu system resulted recently for the case of granular Co-Cu-samples and the giant magnetoresistance observed in them [8]. Accordingly, oscillatory indirect coupling has been detected by several groups [9,10] in sputtered Co/Cu-multilayers with (111)-texture. As for epitaxial samples, indirect coupling in Co/Cu(100)-samples has been detected first by neutron diffraction [11] and spin-polarized electron scattering [12]. Its oscillatory character could be confirmed unambiguously for this (100)-orientation by Kerr-magnetometry, and the observations could again be interpreted in terms of a superposition of long- and short-period oscillations [13]. The indirect and oscillating coupling through Cu(100) had been observed before for the case of fcc Fe(100)-films in Fe/Cu/Fe-sandwiches [14].

However, a quite surprising controversy evolved from more extended investigations of the coupling in Co/Cu/Co(111) using single-crystal samples. In a careful Kerr-magnetometric study of Co/Cu/Co-multilayers on Cu(111) single crystal substrates, prepared at substrate temperatures of 80, 300 and 500 K, Egelhoff and Kief [15] could not detect any indication of indirect coupling at all, in sharp contrast to Johnson et al. [16], who found strong antiferromagnetic coupling in Co/Cu/Co(111)-samples, prepared on Cu(111)-single crystal surfaces at 20 to 50°C , with a maximum of the antiferromagnetic coupling strength at $t_{\text{Cu}} = 0.85\text{ nm}$, in good agreement with the results from sputtered multilayers [9,10]. The structural origin for these contradicting results remains to be clarified.

We performed some experiments on oscillatory coupling between perpendicularly magnetized Co(111)-monolayers through a Cu(111)-spacer [17], in which we could confirm the oscillations with an antiferromagnetic maximum at 0.8 nm. To our knowledge, this is

the first experiment in which the indirect coupling phenomenon was really followed between ferromagnetic monolayers. This is of interest because the theoretical RKKY-models [7] treat just this coupling between monolayers, whereas all experiments available before had been performed with ferromagnetic films consisting of 10 ML or more. The present paper intends to be a report on this indirect coupling between perpendicularly magnetized Co(111)-monolayers through a Cu(111) spacer, and a general discussion of the controversy on indirect coupling by Cu(111).

The perpendicularly magnetized Co-monolayer, which is a building block of our structures, is an interesting subject in itself; it turns out that it is a surprisingly good and informative realization of the 2-dimensional Ising-model (2DIM) [18]. Because some understanding of this monolayer is needed for a proper understanding of the coupling samples, we present in the following first a discussion of the Co-monolayer on Cu, followed then by a presentation of the coupling experiments. In the final discussion, we will compare our results with the controversial data of other authors, and provide some ideas on possible structural origin for the controversial magnetic results.

THE PERPENDICULARLY MAGNETIZED MONOLAYER Co ON Cu(111)

The perpendicularly magnetized ferromagnetic monolayer Co on Cu(111) has been observed many years ago [19,20]. The Co-films of this early work were prepared on epitaxial Cu(111)-films on mica, at temperatures between 110 and 150°C, and covered by Cu. They showed a reduced Curie-temperature $T_C(1) = 400 \text{ K} \approx 0.3 T_C(\text{bulk})$, in remarkable agreement with early theories of this size-effect. Perpendicular magnetization was restricted to the very monolayer, whereas films from 2 ML upwards were magnetized in the plane. However, a plot of the film anisotropies versus $1/D$ (number of ML D) did not result in the linear dependence which had been observed before for similar NiFe-films on Cu(111) and enabled there the first experimental detection and quantitative determination of magnetic surface anisotropy (MSA) [21] (for reviews of this early work see [22,23]).

Recently, we reexamined this perpendicular monolayer-magnetism of Co on Cu(111), using improved epitaxial techniques [17]. The Cu(111)-substrates were epitaxial films of 250 nm thickness, prepared on sapphire (11-20) substrates by evaporation in UHV at 800 K. The LEED pattern of these Cu(111)-substrates indicated a perfect (111) texture with preference of spots in one special epitaxial orientation. SEM pictures showed Cu grains with lateral dimensions of some μm , separated by channels which extended to some 10% of the film area. Whereas the substrates as a whole are therefore not perfect, the surface of the grains can be considered to be atomically flat and of good single crystalline quality. Co-films were prepared on these Cu(111)-surfaces at room temperature. In the monolayer regime, they showed the same LEED pattern as the Cu(111)-substrate, thus confirming the pseudomorphism which is expected as a result of the small misfit $f_{\text{CoCu}} = -1.8\%$ and has been confirmed before [23] to persist up to a thickness of $t_{\text{Co}} = 1.3 \text{ nm}$. Testing of the films by AES showed the usual break of the Co-amplitude, situated at 2ML. Therefore, it could be assumed that rather good Co-film elements were formed on top of the Cu-grains, superimposed in the whole sample by a contribution of about 10 % of some other film elements of ill-defined structure, situated in the channels between. All Co-films were finally covered by Cu.

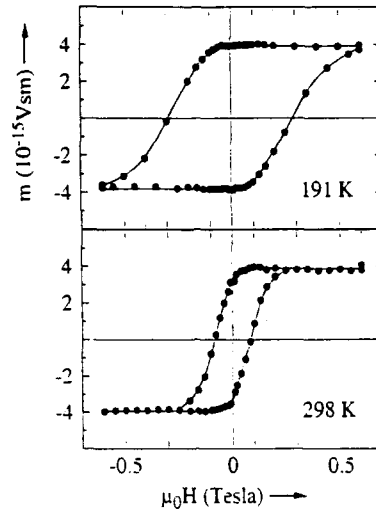


Figure 1: Perpendicular hysteresis loops for the perpendicularly magnetized pseudomorphic monolayer Co on Cu(111), measured by TOM at 191 K and 298 K, respectively. The film was prepared at 300 K and coated by Cu. (From [18]).

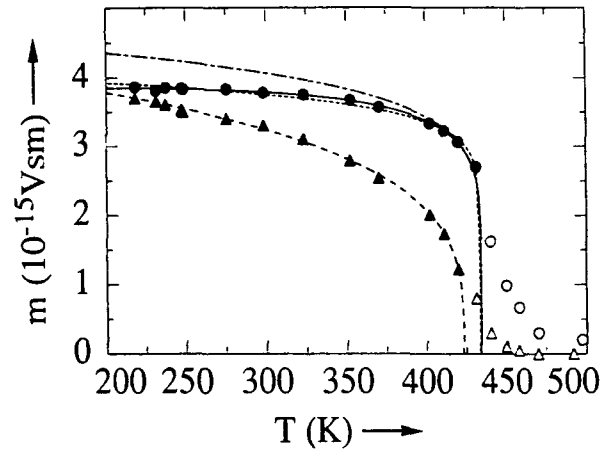


Figure 2: Temperature dependence of magnetic order in a perpendicularly magnetized pseudomorphic monolayer of Co on Cu(111). The saturation moment m_s (●, ○) is fitted by the exact solution of the 2DIM (—) with $T_c = 434$ K, and alternatively by a phenomenological power law (---) with a power-law exponent $\beta_s^* = 0.081$ and $T_{c,s}^* = 433$ K. The asymptotic power law of the 2DIM, $m_s \sim (T_c - T)^{1/8}$ is given for comparison (- · - · -); it is inappropriate for a description of the experiments. Data for the remanent moment are included (▲, △). Solid symbols only are used for the fits. Open symbols from the tails, which are expected to result from defects, are omitted. (From [18]).

The films were analyzed magnetically using Torsion Oscillation Magnetometry (TOM) at atmospheric pressures [24]. The advantage of this method is to provide combined quantitative data on magnetic moments and magnetic anisotropies of the films. It turned out that the film anisotropies followed clearly the $1/D$ -dependence which enables the determination of MSA [25]. This confirms the good overall structural quality of the films, down to the monolayer.

For such a ferromagnetic monolayer, hysteresis loops have been obtained as shown in Figure 1 for temperatures of 191K and 298K, respectively. Note that they were taken with the field along the film normal. The films, suspended in TOM on a thin torsion filament, oriented themselves spontaneously with the film normal parallel to the field, thus clearly demonstrating the perpendicular magnetization, in contrast for the films above 3 monolayers, which oriented themselves parallel to the field, that means that they were magnetized in the plane, of course. The hysteresis loops of Figure 1 can be characterized by the saturation value m_s of the magnetic moment and by its remanent value m_r ; both are shown in Figure 2 versus temperature. The most important point is that m_s follows, in a wide regime of temperatures, the exact solution of the 2-dimensional Ising-model, much better than the asymptotic power law $m \propto (T_c - T)^{1/8}$ which is frequently used in the literature for the discussion of temperature-dependent magnetic order in perpendicularly magnetized films in the monolayer regime. The low-temperature moment of $4 \cdot 10^{-15}$ Vsm should be compared with the moment of a bulk monolayer, $m_{ML} = 7 \cdot 10^{-15}$ Vsm. Apparently, the monolayer component observed in Figure 2 represents only roughly 60% of the sample, other components being situated probably in the channels of the film structure. The Curie-temperature is again strongly reduced, as expected for ferromagnetic monolayers. For the following discussion of coupling samples, composed of those monolayers and a Cu(111)-spacer, the data presented in Figure 2 may be taken as a further indication of the very good quality of these ferromagnetic monolayers.

INDIRECT COUPLING BETWEEN Co-MONOLAYERS THROUGH Cu(111)

For the investigation of indirect coupling, we prepared samples of type Cu(111)/1Co/ D_{Cu} Cu/1Co/Cu, composed of 2 monolayers of Co, separated by a Cu-film consisting of D_{Cu} ML of Cu; the whole sample was finally covered by a thick Cu-layer. The Co/Cu/Co trilayer was prepared at room temperature. Hysteresis loops for a series of samples with variable D_{Cu} , as measured by TOM, are shown in Figure 3. In order to explain these loops, we recall what is measured primarily in TOM. What is measured by this method is the period of small amplitude torsion oscillations of the sample, near its equilibrium position with the spontaneous magnetization parallel to an external field. For our present perpendicularly magnetized samples, this is a orientation with the film plane at right angles to the field. The change of the period with the magnetic field can be easily expressed by a magnetic torque constant R , which is conveniently normalized by the external field H . The ratio R/H , which is shown in Figure 3 versus magnetic field H , equals the remanent moment in the limit $H \approx 0$. For samples with homogeneous magnetization, R/H is connected in general with the magnetic moment component along the field, m , by

$$R/H = m/(1 + H/H_L) \quad (1),$$

where H_L is an anisotropy field describing the coupling of the magnetization to its easy

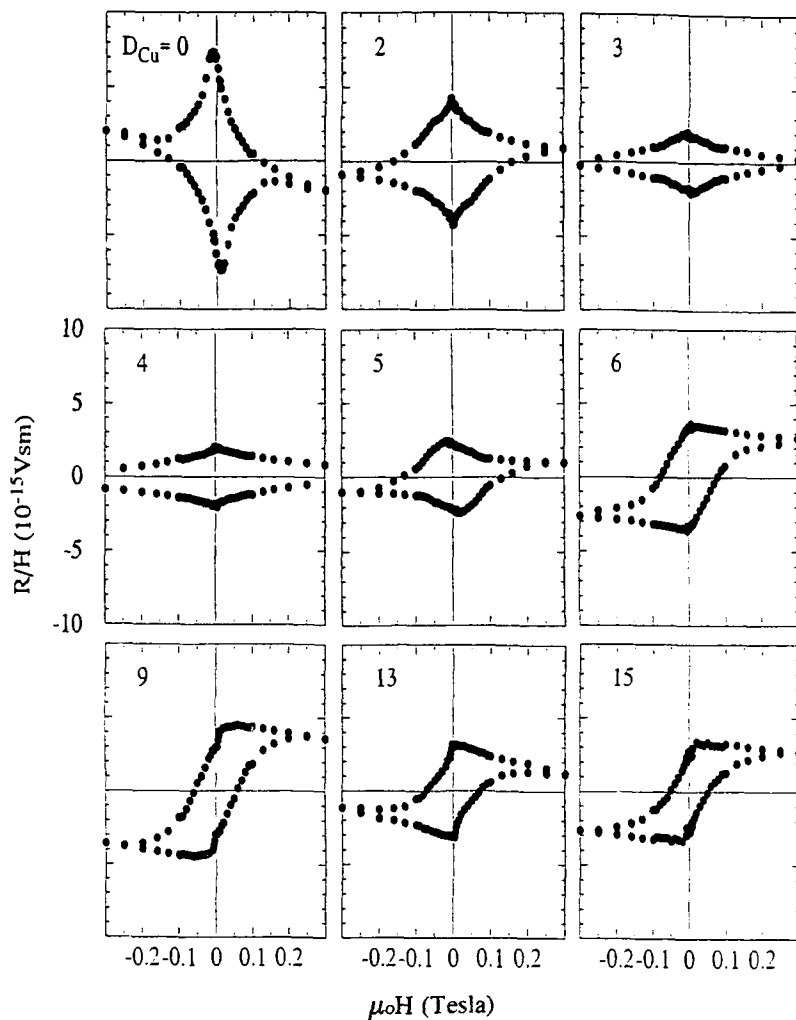


Figure 3: Hysteresis loops of R/H versus H for samples $\text{Cu}(111)/1\text{Co}/D_{\text{Cu}}\text{Cu}/1\text{Co}/\text{Cu}$, composed of two perpendicularly magnetized monolayers Co , separated by a Cu -spacer consisting of a varying number D_{Cu} of atomic Cu -layers. Magnetometry was done at room temperature, with the samples oriented spontaneously at right angles to the field, so they represent a perpendicular magnetization. (From [18]).

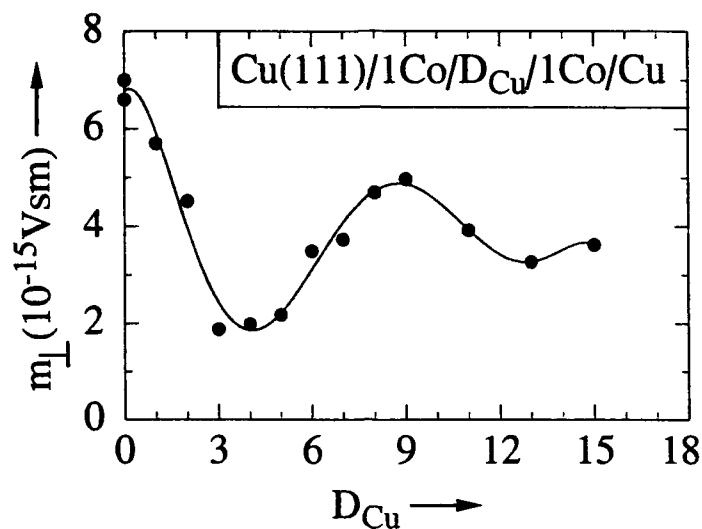


Figure 4: Remanent perpendicular moment m_{\perp} , taken from loops as shown in Figure 3, versus D_{Cu} , for samples Cu(111)/1Co/ D_{Cu} /1Co/Cu. (From [18]).

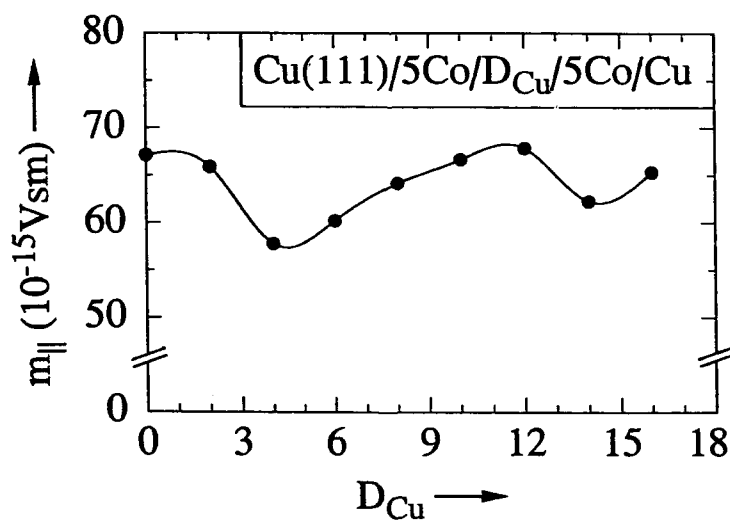


Figure 5: Remanent in-plane moment m_{\parallel} versus D_{Cu} , for samples Cu(111)/5Co/ D_{Cu} /5Co/Cu. (From [18]).

direction in the sample. An example of this behaviour is given by the sample with $D_{Cu} = 9$. This is a sample with ferromagnetic coupling between the two monolayers contained in it, where for decreasing field both these monolayers are magnetized homogeneously and parallel and R/H therefore follows Equation 1, with an anisotropy field $\mu_0 H_L = 0.83$ Tesla; the same anisotropy field was measured for the single monolayer. Ferromagnetic coupling of the two monolayers of course is given too in the limiting case $D_{Cu} = 0$, see the first loop in Figure 3. The difference to the case $D_{Cu} = 9$ is the loss of two internal Cu/Co-interfaces, which are the origin of the perpendicular magnetization by virtue of their perpendicular MSA. Accordingly, the sample $D_{Cu} = 0$ is very near the reorientation transition to in-plane magnetization. Apparently, some part of the film is again magnetized in the plane, that means at right angles to the magnetic field. It has been shown elsewhere [26] in detail that such anomalously oriented film elements produce strong negative values of R/H , for $H > 0$. The first loop in Figure 3 therefore quantitatively speaking presents only the remanent moment of $7 \cdot 10^{-15}$ Vsm, which is twice the moment of the monolayer sample of Figure 2. The rapid decrease of R/H with increasing H is connected with the weak anisotropy and with inhomogeneities in the sample, in a mode which cannot be interpreted quantitatively at present. Similar difficulties for the interpretation of the data, for $H = 0$, are observed for the other samples, superimposed now even by the antiferromagnetic coupling, which of course makes the magnetization intrinsically inhomogeneous. Obviously a further important complication is given in those perpendicularly magnetized double layers by a strong magnetostatic coupling, which in turn can be neglected widely for the common case of in-plane magnetization.

What definitely remains despite of all these complications is that the value of R/H at $H = 0$ represents the remanent moment of the samples and that, because all data of Figure 3 were measured with the film at right angles to the field, this is a remanent perpendicular moment. This remanent perpendicular moment m_{\perp} is shown in Figure 4 as a function of D_{Cu} . It shows a clear oscillation. The deep minimum at $D_{Cu} = 4$ indicates a far-reaching compensation of both monolayer moments, that means a maximum antiferromagnetic coupling. A further minimum of m_{\perp} indicating maximum antiferromagnetic coupling is observed at $D_{Cu} = 13$, a maximum indicating ferromagnetic coupling near $D_{Cu} = 9$. The amplitude of the oscillation decreases with increasing D_{Cu} , and m_{\perp} fades out at the moment of one monolayer only, not of two. This indicates that the indirect coupling persists up to $D_{Cu} = 15$ and the samples must be interpreted in terms of intermixed coupling as a result of inhomogeneous Cu-thickness, rather than consisting of two decoupled monolayers, which should show a remanent moment of two monolayer moments, twice of what is observed.

A second series, $Cu(111)/5Co/D_{Cu}Cu/5Co/Cu$, was prepared and investigated, containing Co-films consisting of 5 ML. This Co thickness is well above the reorientation transition, and the samples were therefore all magnetized in the plane. Accordingly, they were measured in TOM with the film plane parallel to the field. As a result of these measurements, we show in Figure 5 the remanent in-plane moment m_{\parallel} versus D_{Cu} . It again shows an oscillation, but with a strongly reduced amplitude, around a mean value which very nearly equals the magnetic moment of 10 bulk monolayers, $70 \cdot 10^{-15}$ Vsm. This means that the magnetic moment per atom, in these thicker samples, has nearly its bulk value, which is reasonable. The oscillation again clearly indicates antiferromagnetic minima at 4 and 14 ML Cu, and a ferromagnetic maximum between. The strong reduction of the oscillation amplitude with increasing Co-thickness can easily be explained by assuming that

the Cu-interlayer is not completely closed, but contains some holes or channels. Apparently, the material of the 5 ML Co in the second series of samples is enough to widely fill these holes and channels by Co, forming ferromagnetic bridges which dominate the coupling. The residual antiferromagnetic coupling across the Cu-islands, which may well cover the overwhelming part of the film area, can be detected only by the high sensitivity of TOM. The oscillations of Figure 5 could hardly be detected by MOKE. On the other hand, the material of the monolayers Co in Figure 4 is not sufficient for filling the holes and channels and the competing ferromagnetic hole-coupling is weak, resulting in the well expressed oscillations of Figure 4.

DISCUSSION

As a main result of our experiments, we observe that indirect coupling between monolayers through Cu(111) could clearly be confirmed. What could be confirmed too is a pronounced tendency of this indirect and potentially antiferromagnetic coupling to be obscured by a competing ferromagnetic coupling, caused by defects in the Cu-spacer, which are filled with ferromagnetic material. With this interpretation, our results are in agreement with the work of Egelhoff and Kief [15]: With their Co-thicknesses near 5 ML, we observed a tiny oscillation amplitude only which might well have been disappeared for tiny changes of the preparation conditions. In comparison with the very clearly detected oscillations of coupling in samples with cubic spacers in (100)-orientation, we then find phenomenologically an enhanced tendency for retaining holes or channels in (111)-spacers, and in comparison with the well expressed oscillations in sputtered samples [9,10], we find that the tendency to retain these defects is stronger in single-crystalline samples than in the sputtered ones. In this situation, we recall that it has been observed many years ago that for the epitaxial growth of fcc metals in (111)-orientation on nonmetallic substrates like molybdenite, that there is in the coalescence phase a conspicuous tendency to retain narrow metal-free channels between neighboring metal crystallites [27]. This can be explained by the natural double-twinning by two types of crystallites with different stacking, and the resulting stacking faults which must be formed during their coalescence [28]. This creates a special barrier against coalescence, specific for fcc(111) systems. Recent STM-work on the related growth of fcc Fe(111) on Cu(111) [29] indicates that the same hindrance of coalescence takes place in metallic fcc(111) systems too, in a nm-scale of crystallites. It is restricted to the case where the film growth starts by nucleation on extended single crystal surfaces. For the case of step flow from a high density of atomic steps in the substrate, the stacking is transferred from the substrate to the film and this barrier disappears (Co is mainly fcc in the Cu/Co-multilayer and sandwich systems). We therefore suggest that a high density of steps in the sputtered samples facilitates the unhampered coalescence and therefore the well-expressed coupling oscillations. In general, the step structure of the first Co-layer and the defect structure of the Cu-spacer can sensitively depend on details of the preparation condition, which can hardly be defined. It is therefore not surprising that Johnson et al.[16] could detect antiferromagnetic coupling in Co/Cu/Co(111)-sandwiches on single crystal substrates. Accordingly, antiferromagnetic coupling has been detected by magnetoresistance in Co/Cu(111) superlattices [30,31,32]; the amplitude of the effect depended sensitively on the choice of the substrates [30], in agreement of our picture. Our interpretation that the antiferromagnetic coupling tends to be obscured preferentially in good epitaxial samples is supported by recent work of Schreyer et al.[33], who analyzed MBE-grown Co/Cu-lattices by neutron reflection and by MOKE, with the result that antiferromagnetic coupling occurs, but only in a small fraction of the volume. Our interpretation is further in agreement of recent work of Pinkvos et al.[34], who followed

Co/Cu/Co(111) trilayers using spin polarized low energy electron microscopy (SP-LEEM, [35]). Using a lateral resolution of about 100 nm, they found in the antiferromagnetic regime of $D_{Cu} = 4$ a fine-grained intermixing of ferro- and antiferromagnetic coupling, which fits well in our picture. As a whole, the indirect coupling between Co-layers through a Cu(111)-spacer can now be taken as a well established intrinsic property of the ideal structure. However, the tendency to be obscured by defects in the spacer is a property of the system too.

We would like to compare finally the experimental results from different groups relating the positions of the maxima of the antiferromagnetic coupling. They are collected in Table 1. There is complete agreement in the position of the first antiferromagnetic maximum at $t_{Cu} = (0.85 \pm 0.15)$ nm. Most experiments detect further maxima at roughly 2.0 and 3.0 nm. This is in fair agreement with the theoretical prediction [7] of a period of 0.94 nm. The antiferromagnetic maximum at 2 nm is missing in our experiments. One might speculate whether the first maximum is strong enough to survive the competing hole-coupling, and for the third one the holes are closed again, whereas in the second one the antiferromagnetic coupling is weak enough to be obscured by the yet considerable hole-coupling. STM-experiments are clearly required to further clarify the structural details.

Table 1: Experimental values for the Cu-thickness t_{Cu} for which maxima of the antiferromagnetic indirect coupling are observed in Co/Cu/Co(111) trilayers or sandwiches.

Reference	Type of samples	$t_{Cu}(\text{nm})$
Parkin et al. [9]	sputtered multilayers	0.85 1.95 3.0
Mosca et al. [10]	sputtered multilayers	0.75 2.0 3.5
Schreyer et al. [33]	MBE-multilayers	1.0 2.0 2.8
Dupas et al. [32]	epitaxial multilayers	0.86 1.65
This work	epitaxial trilayers, containing Co-monolayers	0.83 2.9

CONCLUSIONS

In conclusion, we have shown that oscillatory indirect coupling between Co-monolayers through a Cu(111)-spacer is an intrinsic phenomenon of the system. It can easily be obscured by competing ferromagnetic hole-coupling, the tendency for which is stronger in single-crystal samples than in sputtered multilayers. The coupling between the monolayers depends on the Cu-thickness in the same manner as the coupling between thicker Co-films; this justifies the usual comparison of the theory, which treats the coupling between monolayers, with experiments on coupling of thicker ferromagnetic films.

ACKNOWLEDGEMENTS

This work was supported by the Deutsche Forschungsgemeinschaft.

REFERENCES

- [1] C. Kittel in Solid State Physics, ed. F. Seitz, D. Turnbull and H. Ehrenreich, New York 1968, Vol 22, p.1
- [2] J.B. Boyce and C.P. Slichter, Phys. Rev. B 13, 379 (1976)
- [3] L.R. Walker and R.E. Wernstedt, Phys. Rev. B 22, 3816 (1980)
- [4] S.S.P. Parkin, N. More and K.P. Roche, Phys. Rev. Lett. 64, 2304 (1990)
- [5] J. Unguris, R.J. Celotta and D.T. Pierce, Phys. Rev. Lett. 67, 140 (1991)
- [6] A. Fuß, S. Demokritov, P. Grünberg and W. Zinn, J. Magn. Magn. Mat. 103, L 221 (1992)
- [7] P. Bruno and C. Chappert, Phys. Rev. Lett. 67, 1602 (1991)
- [8] J.Q. Xiao, J.S. Jiang and C.L. Chien, Phys. Rev. Lett. 68, 3749 (1992)
- [9] S.S.P. Parkin, R. Bhadra and K.P. Roche, Phys. Rev. Lett. 66, 2152 (1991)
- [10] D.H. Mosca, F. Petroff, A. Fert, P.A. Schroeder, W.P. Pratt Jr. and R. Laloe, J. Magn. Magn. Mat. 94, L1 (1991)
- [11] A. Cebollada, J.L. Martinez, J.M. Gallego, J.J. de Miguel, R. Miranda, S. Ferrer, G. Fillion and J.P. Rebouillat, Phys. Rev. B 39, 9726 (1989)
- [12] D. Pescia, D. Kerkmann, F. Schumann and W. Gudat, Z. Phys. B 78, 475 (1990)
- [13] M.T. Johnson, S.T. Purcell, N.W.E. McGee, R. Coehoorn, J. aan de Stegge and W. Hoving, Phys. Rev. Lett. 68, 2688 (1992)
- [14] W.R. Bennett, W. Schwarzacher and W.F. Egelhoff, Jr., Phys. Rev. Lett. 65, 3169 (1990)
- [15] W.F. Egelhoff Jr. and M.T. Kief, Phys. Rev. B 45, 7795 (1992)
- [16] M.T. Johnson, R. Coehoorn, J.J. de Vries, N.W.E. McGee, J. aan de Stegge and P.J.H. Bloemen, Phys. Rev. Lett. 69, 969 (1992)
- [17] J. Kohlhepp, S. Cordes, H.J. Elmers and U. Gradmann, J. Magn. Magn. Mat. 111, L 231 (1992)
- [18] J. Kohlhepp, H.J. Elmers, S. Cordes and U. Gradmann, Phys. Rev. B 45, 12287 (1992)
- [19] U. Gradmann and J. Müller, Z. angew. Physik 30, 87 (1970)
- [20] U. Gradmann and J. Müller, Czech. J. Physics B 21, 553 (1971)
- [21] U. Gradmann and J. Müller, phys. stat. sol. 27, 313 (1968)
- [22] U. Gradmann, J. appl. Phys. 40, 1182 (1969)
- [23] U. Gradmann, Appl. Phys. 3, 161 (1974)
- [24] U. Gradmann, W. Kümmerle and R. Tham, Appl Phys. 10, 219 (1976)
- [25] J. Kohlhepp, H.J. Elmers and U. Gradmann, J. Magn. Magn. Mat., in the press
- [26] U. Gradmann, Ann. Phys. (Leipzig) 17, 91 (1966)
- [27] D.W. Pashley, Advan. Phys. 14, 327 (1965)
- [28] J.W. Matthews, in Physics of Thin Films, ed. G. Hass and R. Thun, Vol 4, p 137 (1967)
- [29] A. Brodde and H. Neddermeyer, Ultramicroscopy 42-44, 556 (1992)
- [30] D. Greig, M.J. Hall, C. Hammond, B.J. Hickey, H.P. Ho, M.A. Howson, M.J. Walker, N. Wiser and D.G. Wright, J. Magn. Magn. Mat. 110, L 239 (1992)
- [31] J.P. Renard, P. Beauvillain, C. Dupas, K. Le Dang, E. Vélú, C. Marlière and D. Renard, J. Magn. Magn. Mat. 115, L 147 (1992)
- [32] C. Dupas, E. Kolb, K. Le Dang, J.P. Renard, P. Veillet and E. Vélú, preprint 1993
- [33] A. Schreyer, K. Bröhl, J.F. Ankner, Th. Zeidler, P. Bödeker, N. Metoki, C.F. Majkrzak and H. Zabel, preprint 1993
- [34] H. Pinkvos, private communication
- [35] H. Pinkvos, H. Poppa, E. Bauer and J. Hurst, Ultramicroscopy 47, 339 (1992)

STUDIES OF EXCHANGE COUPLING IN Fe(001) WHISKER/Cr/Fe STRUCTURES USING BLS AND RHEED TECHNIQUES.

B. Heinrich, M. From, J.F. Cochran, L. X. Liao, Z. Celinski, C.M. Schneider* and K. Myrkle, Physics Department, Simon Fraser University, BURNABY, Canada, V5A1S6.

ABSTRACT

The conditions for an almost perfect growth of smooth Cr(001) films on an iron whisker substrate have been investigated by means of reflection high energy electron diffraction (RHEED). The exchange interaction between 20 monolayer thick Fe(001) films separated from a bulk whisker Fe(001) substrate by a variable number of Cr(001) monolayers (ML) has been investigated by means of Brillouin light scattering experiments (BLS). These experiments show unambiguously that the exchange coupling strength between the iron film and the iron whisker can be described by a short wavelength oscillatory term superposed on a slowly varying antiferromagnetic background. The BLS data enabled one to separate the bilinear and the biquadratic contributions to the antiferromagnetic exchange coupling terms. Both the bilinear and the biquadratic coupling strengths exhibited a short period oscillatory dependence on the Cr interlayer thickness (~2 monolayers). Maxima in the bilinear antiferromagnetic coupling strength occur for an odd number of Cr monolayers. This observation is not in agreement with first principles calculations. The first phase inversion has been found to occur between 4 and 5 ML of Cr.

INTRODUCTION

Fe/Cr/Fe(001) structures have played an immense role in the study of the exchange coupling between ferromagnetic films separated by a non-ferromagnetic interlayer. A new era in the study of the exchange coupling was begun with the discovery of short wavelength oscillations ($\lambda=2.11$ ML) in Fe/Cr/Fe(001) systems [1,2]. Smooth interfaces are a necessary prerequisite for the observation of short wavelength oscillations, and Fe[001] whiskers have provided substrates which allow one to grow very smooth interfaces. By choosing the right growth conditions one can observe short wavelength oscillations up to thicknesses as large as 80 ML of Cr [3]. This result is certainly not universal even for samples grown on Fe[001] whisker templates. In their quantitative measurements Purcell et al [2], and Grünberg et al [4], observed only a few oscillations. The measurements by Purcell et al [2] and Grünberg et al [4] indicated that the maxima of the antiferromagnetic coupling (AFM) occurred at an even number of Cr atomic layers (ML). However, in the thickness range studied by Purcell et al, and by Grünberg et al, [2,4], the NIST group showed [3], and our BLS studies [5] on Fe/whisker/Cr/Fe samples showed, that the maxima of the AFM coupling appear at an odd number of ML. Recent results by Grünberg et al [6] on improved interfaces produced a larger number of oscillations (up to 26 ML) than their earlier studies on Fe whiskers [4]. The maxima of the AFM coupling reported in this latest work were observed to occur somewhere between an even and an odd number of Cr ML. The phase of the exchange coupling oscillations through Cr(001) is important because it can be theoretically predicted from the sign of the exchange coupling between Fe and Cr and from the antiferromagnetic spin density wave in Cr(001). A strong antiferromagnetic interaction between the adjacent Fe and Cr atomic layers and the short wavelength (2.11 ML) antiferromagnetic configuration of the Cr magnetic moments leads to AFM coupling in Fe/Cr/Fe(001) for an even number of Cr ML and ferromagnetic (FM) coupling for an odd number of Cr ML (for the first 23 ML of Cr). All available first principle calculations predict this behavior. This is exactly opposite to the behaviour found in the NIST measurements and in our experiments. The NIST group suggested that within the first 5 ML of Cr the phase of the oscillations undergoes the first phase slip. One should point out that the NIST studies do not determine the strength of the exchange coupling. In fact no quantitative data are so far available for FM coupling. Quantitative studies [2,4,6] have shown that the exchange coupling for thicknesses between 4 and 10 ML of Cr

[2,4,6] have shown that the exchange coupling for thicknesses between 4 and 10 ML of Cr always remains AFM. Recent calculations by Zhu-Pei Shi et al [7] have tried to explain this behavior as due to the presence of superexchange. The calculated strength of the exchange coupling is far bigger, by a factor 20-50 times, than that observed experimentally. This discrepancy is usually explained by the presence of interface roughness.

Clearly more measurements have to be carried out in order to find adequate answers for the above discrepancies. The purpose of this paper is to investigate the exchange coupling through Cr(001) in Fe whisker/Cr/Fe(001) samples which possess nearly perfect interfaces so that interface roughness plays only a minor role. We intentionally did not use wedged samples because we were interested in making measurements on samples in which the interface thickness was well defined; in wedged samples one does not know the precise thicknesses of those parts of the sample which exhibit the best interfaces. Our measurements were restricted to the first 14 ML of Cr which is the thickness region concerned with most of the discrepancies between various reports.

Quantitative studies were carried out by means of the Brillouin Light Scattering technique (BLS) [8]. The growth of Cr and Fe layers was monitored by means of Reflection High Energy Electron Diffraction (RHEED) equipped with a charge coupled imaging sensor [9] which allowed us to carry out a lineshape analysis of the specular beam intensity. We found that the quality of the growth very strongly affects the behavior of the exchange coupling: this statement is true even for growths that exhibit strong stationary RHEED intensity oscillations. The lineshape analysis of the specular beam turned out to be essential for the identification of the optimum growth conditions. Only samples which were grown under optimal growth conditions exhibited a reproducible exchange coupling.

THE GROWTH OF Cr(001) on Fe(001) WHISKERS

Well prepared Fe(001) whiskers represent the best available metallic templates and are characterized by atomic terraces whose dimensions are in excess of 1 μm . The cross-section of a typical Fe(001) whisker is rectangular, approximately 0.15 to 0.20 μm square, and a typical whisker length lies between 7-15 mm. The whisker surfaces are bounded by {100} planes.

The Fe whiskers were fabricated by means of chemical vapor deposition. An Fe whisker surface was cleaned in UHV by using the following procedure: The whisker was first sputtered at room temperature in order to remove any residual surface contamination which was created during the whisker growth. The whisker was then brought to a temperature of 550 C and sputter cleaned for 90-120 minutes using a 2keV Ar ion beam. Sputtering at elevated temperatures is necessary to remove subsurface carbon contamination. The temperature of the whisker was then briefly raised to 700 C (for approximately 10 min.) and then quickly cooled to room temperature. Fe whiskers prepared in this way exhibited nearly perfect RHEED patterns. Only the intersects with Ewald's sphere were observed. The diffraction spots were very sharp showing that the reciprocal lattice rods were very narrow. Typical RHEED streaks were not observed, only very sharp and very short streaks accompanied the main diffraction spots. Kikuchi bands were very sharp but showed very low intensity. All of these diffraction features indicated that the Fe whiskers possessed atomically smooth surfaces with atomic terraces whose dimensions far exceeded the instrumental resolution of our RHEED system. The RHEED intensity oscillations were studied by directing the RHEED electron beam at an angle which satisfied the second anti-Bragg condition (zero intensity for a half filled atomic layer).

The Cr was grown at elevated substrate temperatures. The choice of substrate temperature is very crucial. We found that the growth of Cr proceeds properly only if the substrate temperature lies within a very narrow range. For sufficiently high substrate temperatures the first RHEED intensity oscillation always shows a very cuspy dependence on time, see Figs. 1a, 1c and 2. For low temperatures the RHEED oscillations exhibit a clearly deteriorating behavior. The amplitude of the RHEED oscillations decreases with an increasing number of deposited ML, and the character of the oscillations changes from a cuspy to a clearly sinusoidal behavior. If the substrate temperature is too high the second minimum (1.5 ML) of the RHEED oscillations is appreciably higher than the first minimum (0.5 ML), see Fig. 1a. The RHEED oscillations then very quickly develop a sinusoidal character, see Fig. 1a, but otherwise the oscillation amplitude is very stationary and the oscillations can be followed for an indefinite time. It is also typical that the RHEED oscillations are superimposed on a background intensity which slowly increases with time, see Fig. 1a. Low and high substrate

temperatures produce inadequate Cr(001) layers. Line scans of the specular spot clearly reveal that the quality of the growth deteriorates with an increasing number of atomic layers even for growths at high substrate temperatures: Fig. 1b shows that the width of the specular spot line scan increases to values which are much larger than those corresponding to a free Fe surface. A deterioration of the quality of Cr films for growths carried out at low substrate temperatures is not surprising, but a deterioration in quality for high substrate temperatures is definitely unexpected. One would expect the quality of the growth to improve with increasing substrate temperature, but fig. 1b shows that the contrary is true. The deterioration of the growth quality is not due to Fe,Cr atomic intermixing. The same behavior is observed for the growth of Fe on Fe.

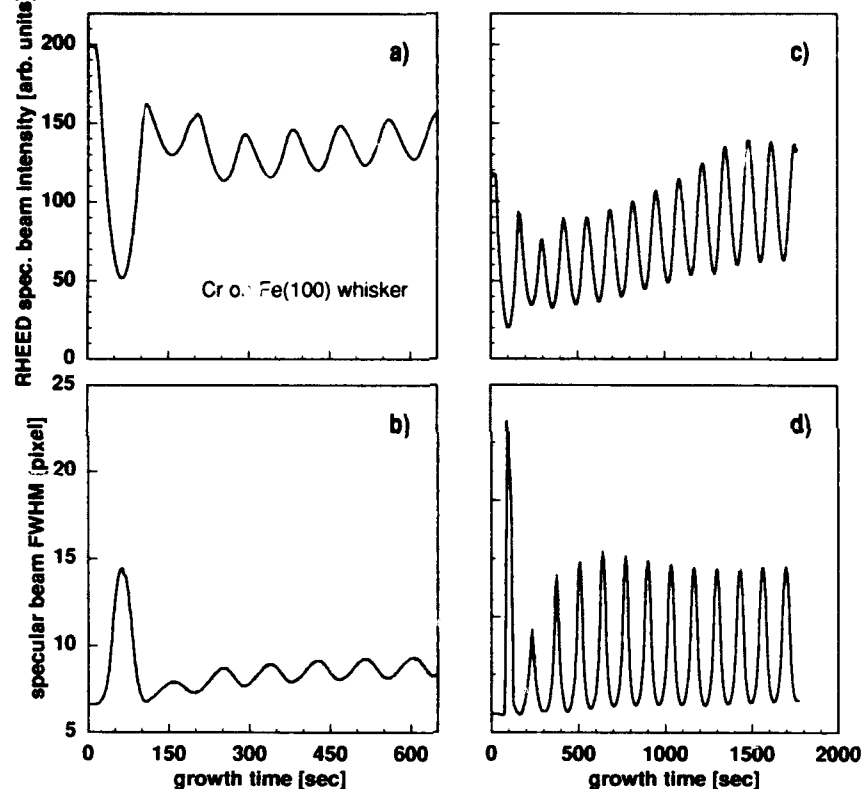


Fig. 1. (1a) The RHEED intensity oscillations measured at the specular spot of a sample which was grown at too high a substrate temperature. The electron beam angle is close to the second anti-Bragg condition. (1b) The half width at half maximum (HWHM) of the specular beam intensity along the (0,0) reciprocal rod. The HWHM analyses were obtained from line scans which were monitored during the RHEED intensity oscillation measurements. Fig. 1c and 1d show similar data for a sample which was grown close to the optimal substrate temperature. The HWHM of the specular spot in Fig. 1d slightly increases with an increasing Cr coverage. Note also that the minima of the RHEED intensity oscillations increase with increasing Cr coverage. This implies that the growth was carried out at a somewhat higher than optimal temperature.

The best growth was achieved when the RHEED oscillations maintained their intensity minima close to that of the first minimum (0.5ML) and the RHEED intensity maxima were comparable to, or larger than, the specular spot intensity for the bare Fe substrate, see Fig. 2.

The oscillations in that case were clearly cuspy, and that cuspy behavior does not deteriorate with the number of deposited atomic layers, see Fig. 2. The presence of well defined cusps is the strongest indication that the growth proceeded in a nearly perfect layer by layer mode [10]. It is also interesting to note that in that case the formation of atomic layers proceeded very repeatably. The specular spot line scans at the RHEED intensity maxima showed narrow lines whose linewidths were very nearly the same as those for the Fe substrate, see Fig. 1d and therefore the Cr layers at that point were nearly as smooth as the uncovered Fe whisker substrate. When a new atomic layer started to nucleate the intensity decreased and the line scans started to exhibit a noticeable broadening away from the specular spot along the direction of the (0,0) reciprocal rod. The broadening reached a maximum for a half filled atomic layer. This behavior is shown in Fig. 1d. In fact the line scan for a half filled atomic layer showed a clear splitting (two separated maxima) and this indicated that the mean separation between deposited atomic islands was well defined. The mean separation between atomic islands was $\sim 700\text{-}800\text{\AA}$ (at half ML coverages). Note that at these temperatures the size of an atomic island was large even for a half covered surface.

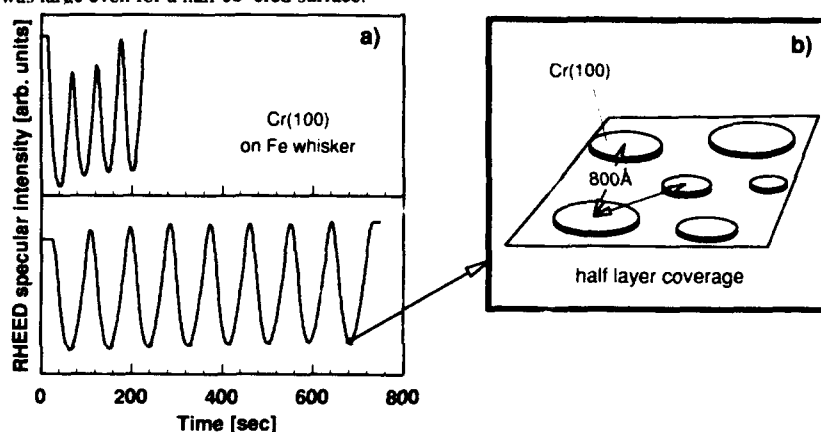


Fig.2. (2a) The RHEED intensity oscillations measured at the specular spot. Note that the amplitude of RHEED intensity oscillations is stationary and that the oscillations exhibit well defined cusps at the RHEED intensity maxima. These features represent optimal growth conditions. (2b) The line scan for a half filled atomic layer showed a clear splitting and this indicates that the mean separation between atomic islands is well defined. The splitting along the (0,0) rod suggests that the mean separation between islands was $\sim 700\text{-}800\text{\AA}$.

Proper growth is possible only in a very narrow range of substrate temperatures, over an interval of 20-30 C. It is difficult to determine this temperature range accurately since the thermal contact between the whisker and the substrate is different from that between the thermocouple and the substrate. We estimate that the required temperature lies in the neighborhood of 280-300 C. the proper substrate temperature has to be adjusted during the growth. It is important to start at a somewhat lower substrate temperature and then to increase the temperature until the desirable growth pattern develops. The growth can not be improved by decreasing the substrate temperature once a growth has been initiated at a higher temperature than that corresponding to optimal conditions. Large in-plane diffusion of Cr surface atoms creates a new set of unfavourable atomic steps which can not be removed simply by decreasing the temperature, and hence by decreasing the radius of diffusion.

Specimens for the magnetic studies were prepared by depositing the desired number of Cr(001) monolayers on the clean iron whisker following the above prescription. 20 ML of iron were deposited at room temperature, followed by 20 ML of gold also deposited at room temperature. The gold film provided a protective overlayer which prevented the iron from oxidizing when the specimens were removed from the vacuum chamber in order to carry out the BLS measurements.

RESULTS OF MAGNETIC STUDIES

The BLS spectra exhibited the two distinct forms of behaviour illustrated in Fig.3a,3b. In Fig.3a the scattered light spectrum exhibits features which can be clearly identified with the bulk whisker substrate plus two peaks, labeled TF in Fig.3a, which can be identified with the 20ML thick Fe film. The bulk spectrum has major features which are labeled SM (for surface mode) and E (for bulk manifold edges): these features are exactly the same, within experimental error, as are observed for an iron whisker covered with gold. The prominent surface mode feature is extremely useful because its intensity and frequency are nearly independent of the Cr and Fe thin film overlayers and it therefore provides a built-in intensity calibration and frequency check. By contrast, the position in frequency of the thin film peaks, TF in Fig 3a, are dependent upon the number of layers of Cr which intervene between the bulk substrate and the 20ML thick iron film overlayer. We interpret a spectrum of the type shown in Fig. 3(a) to be indicative of the presence of an AFM exchange coupling interaction between the bulk Fe substrate and the thin Fe film. The second type of spectrum is illustrated in Fig. 3b. In this case one can clearly identify the bulk surface mode frequency, indicated by SM in Fig.3b, whose intensity and frequency are the same, within experimental error, as the surface mode intensity and frequency measured for a given applied field on a bulk whisker substrate which carries no magnetic thin film overlayer. However, the thin film peak, TF, has merged with the bulk substrate edge frequencies. We interpret a spectrum of the type shown in Fig.3b to indicate that the magnetization in the 20ML Fe film is either ferromagnetically exchange coupled, or is uncoupled, from the magnetization in the bulk Fe substrate.

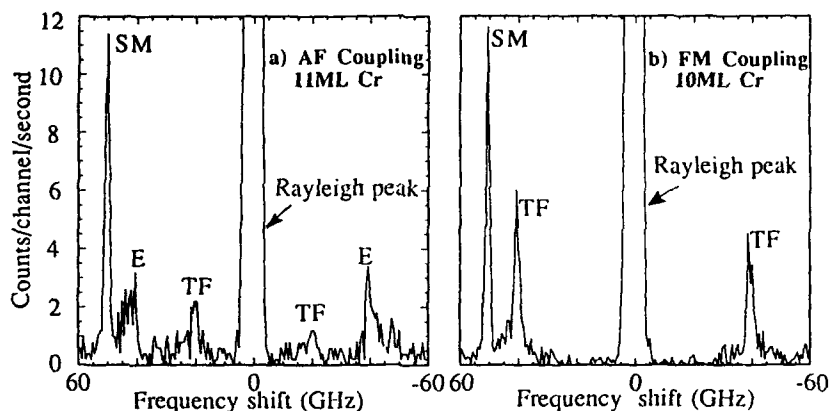


Fig. 3. Typical BLS intensity vs. frequency shift data for anti-ferromagnetically (a) and ferromagnetically (b) coupled specimens. The data shown are for the two specimens (a) Fe whisker/11 Cr/20 Fe/20 Au and (b) Fe whisker/10 Cr/20 Fe/20 Au. These two specimens were grown side by side on a single whisker. The applied magnetic field in both cases is 6 kOe. The data were obtained using 0.5145 μ m laser light incident at 45°, and using an f2 collection lens in the back scattering configuration. The data have been normalized to an incident power of 100mW and a collection time of 1 second per channel. SM is the bulk surface mode; TF the thin film modes; E the bulk manifold edges.

The magnetic field dependence of the frequencies of the features labeled SM, E, and TF have been measured for each specimen over the range 0-10 kOe. A typical result of such measurements is shown in Fig.4a for an AFM coupled thin film specimen whose BLS spectrum is of the type shown Fig.3a. It is obvious from Fig.4a that both the surface mode frequency and the thin film frequency exhibit a non-monotonic variation with increasing applied magnetic field. Part of the data for the magnetic field interval 0-2 kOe have been redrawn in the insert of Fig.4a for clarity: the frequencies corresponding to the thin film peak on the left hand side of the central Rayleigh peak have been plotted in the insert. The magnetic field variation of the thin film frequency is characterized by the presence of two cusps which occur at fields labeled H₁ and H₂ in Fig.4a. It is to be noted that for an applied field near that

corresponding to H_1 the surface mode frequency also exhibits an abrupt change in its magnetic field dependence. Neither the field dependence of the surface mode frequencies, nor the field dependence of the thin film frequencies exhibit any detectable magnetic hysteresis as the applied field is cycled up and down. The intensities of the thin film peaks, as well as the ratio of the intensities of the peaks on the left and on the right hand side of the central Rayleigh peak, vary considerably according to whether the value of the applied field is less than H_1 , lies between H_1 and H_2 , or is greater than H_2 . The magnetic field dependence of these intensities is very complex and is not completely understood, however it is clear that the orientation of the thin film magnetization is undergoing a considerable re-orientation as the field is increased from zero through H_1 and H_2 . For fields greater than the critical value H_2 , (Fig.4a), the magnetic field dependence of the surface mode and bulk edge frequencies are the same, within experimental uncertainty, as those observed for an Fe whisker covered only by a 20 ML Au(001) film.

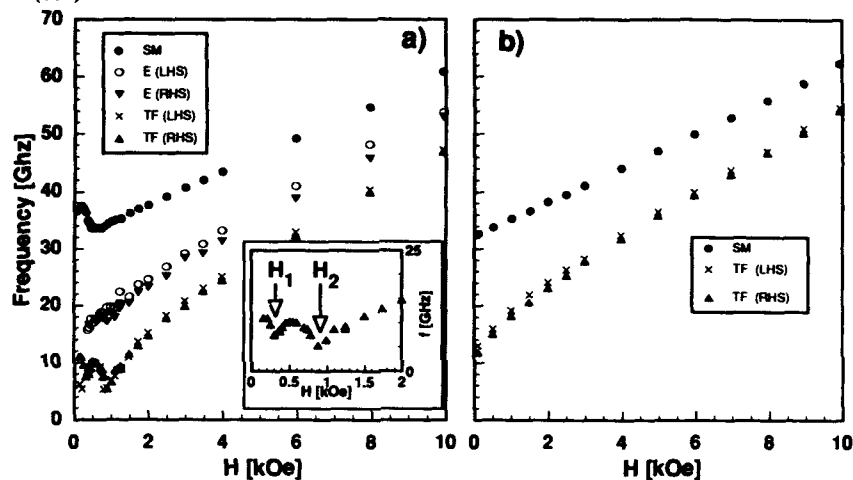


Fig. 4. BLS peak frequencies vs. applied magnetic field. The peak frequencies were obtained by fitting Lorentzians to the features labeled SM and TF in Figure 3.

(a) Fe Whisker/8 Cr/20 Fe/20 Au. The inset shows details of the low field region. The presence of the cusps at the fields H_1 and H_2 is a signature of anti-ferromagnetic coupling between the Fe thin film and the bulk whisker.

(b) Fe Whisker/10 Cr/20 Fe/20 Au. The monotonic increase of the BLS frequencies indicates ferromagnetic coupling.

A typical magnetic field dependence of the surface mode and thin film frequencies observed for a ferromagnetically coupled thin film of the spectral type shown in Fig.3b is illustrated in Fig.4b. Neither the surface mode frequency magnetic field dependence nor the thin film frequency dependence exhibits the non-monotonic behaviour shown in Fig.4a for an AFM coupled thin film. The magnetic field dependence of the surface mode frequency is the same, within experimental uncertainty, as that observed for a whisker which carries no Fe overlayer. The frequencies associated with the thin film exhibit a monotonic behaviour with increasing field, but these frequencies are observed to shift up or down from specimen to specimen as the thickness of the Cr interlayer is varied. The intensities of these thin film peaks, as well as the ratio of intensities of the left- and right-hand peaks, varies slowly and smoothly with an increase in applied field.

ANALYSIS

The magnetic field dependence of the thin film frequencies of the type shown in Fig.4a, and which correspond to BLS spectra of the type shown in Fig.3a, can be understood on the

basis of a model in which the magnetization in the thin film is coupled to the magnetization in the bulk substrate through a surface contact interaction of the form [11]

$$E_{AB} = -J_1 \cos(\Delta\phi) + J_2 \cos^2(\Delta\phi) \quad (1)$$

where E_{AB} , J_1 , and J_2 are measured in ergs/cm² and $\Delta\phi$ is the angle between the film magnetization and the bulk magnetization at their facing surfaces. The term proportional to $\cos(\Delta\phi)$ is called the bilinear exchange coupling, and the term proportional to the square of the cosine term is called the biquadratic exchange coupling. If J_1 is negative, corresponding to AFM coupling, one expects the thin film magnetization and the bulk magnetization to lie antiparallel along one of the easy Fe cube axes for small magnetic fields. Since in our experiments the applied field is directed along a cubic axis, for fields smaller than the first critical field, H_1 of Fig. 4a, one expects the bulk magnetization to be oriented along the applied field and the thin film magnetization to be oriented anti-parallel to the applied field. However, at the field H_1 the free energy of the system can be reduced if the thin film magnetization begins to rotate away from the antiparallel configuration. Once the thin film magnetization at the film surface has rotated away from the antiparallel configuration one can no longer expect the static magnetization distribution in the thin film, or in the bulk substrate, to be uniform. Both magnetizations will exhibit a spatial variation along the direction of the surface normal, the z-direction, in which the magnetization rotates in the x-y plane. Eventually the torque due to the applied field brings the thin film magnetization into alignment with the applied field direction, and for fields greater than that corresponding to the high field cusp, H_2 of Fig. 4a, the thin film magnetization becomes uniform and parallel with the applied field direction, and the bulk magnetization becomes also uniform and parallel with the applied field direction. According to this model the critical fields H_1 and H_2 can be used to deduce values for the bilinear and biquadratic exchange coupling term J_1 , and J_2 of eqn.(1). If it is assumed that (1) the magnetization of the bulk Fe remains uniform and parallel with the applied field, (2) that the thin film magnetization rotates uniformly, and (3) that the thin film has the same magnetization as the bulk, it is easy to show from a small angle expansion of the free energy that

$$J_1 - 2J_2 = -dM_s \left(H_2 + \frac{2K_1}{M_s} \right) \quad (2)$$

and that

$$J_1 + 2J_2 = -dM_s \left(H_1 - \frac{2K_1}{M_s} \right), \quad (3)$$

where d is the film thickness, M_s is the saturation magnetization, and K_1 is the cubic anisotropy constant for rotation of the magnetization in the plane of the thin film. Equations (2) and (3) correspond to the infinite exchange stiffness limit. The problem becomes much more complicated if the thin film and bulk static magnetizations are permitted to rotate in the plane perpendicular to the film normal. However, a small angle expansion around the fields corresponding to H_1 and H_2 can be used in conjunction with the theories described by Mills [12] and by O'Handley and Woods [13] to deduce that

$$J_1 - 2J_2 = aA [\exp(-2ad) - 1], \quad (4)$$

where A is the exchange stiffness parameter in ergs/cm and

$$a^2 = \frac{\left(H_2 + \frac{2K_1}{M_s} \right)}{2A/M_s}. \quad (5)$$

In deriving equations (4) and (5) it has been assumed that the magnetic parameters of the thin film material are the same as the bulk magnetic parameters. This assumption is very well satisfied for 20 ML thick iron films and a bulk iron substrate. Similarly, one can deduce for fields near the cusp field H_1

$$J_1 + 2J_2 = - \frac{2Adb^2}{(1 - b^2d/a)}, \quad (6)$$

where
and

$$b^2 = \frac{(H_1 - \frac{2K_1}{M_s})}{2A/M_s} \quad (7)$$

$$a^2 = \frac{(H_1 + \frac{2K_1}{M_s})}{2A/M_s} \quad (8)$$

In the limit of large exchange stiffness equations (4) and (6) go over into equations (2) and (3). Equations (2), (3), (4) and (5) have been used along with the room temperature properties of Fe ($M_s=1.706$ kG, $A=2 \times 10^{-6}$ ergs/cm, and $2K_1/M_s=0.51$ kOe) to calculate values of J_1 and J_2 for our specimens that exhibited AFM coupling. The results are listed in Table I. It is worth noting that a rather large biquadratic exchange term, J_2 , is required to fit the observed critical fields H_1 and H_2 . In most cases J_2 is nearly 50% of the bilinear term J_1 .

Table I. Observed exchange coupling constants at room temperature for the 12 specimens studied. The composition of the specimens was: Fe Whisker/N Cr/20 Fe/20 Au/. The thickness of the Cr film in ML, N, is given in the first column of the table. The upper and lower cusp fields, H_1 and H_2 correspond to the fields identified in the inset of fig. 4(a). J_1 and J_2 are the bilinear and biquadratic exchange coupling constants deduced from the measured values of H_1 and H_2 (see eqn.(1) in the text).

N ML of Cr	Lower Cusp Field, H_1 (kOe)	Upper Cusp Field, H_2 (kOe)	$ J_1 + 2J_2$ from upper Cusp Field		$ J_1 $ (ergs/cm ²)	J_2 (ergs/cm ²)
			Rigid Magnetization	Twist in Magnetization		
4	—	1.0 ± 0.5	0.74	0.59	—	—
5	0.25 ± 0.25	$4.5 \pm .25$	2.44	1.65	0.89	0.38
6	0.7 ± 0.2	$2.0 \pm .25$	1.22	0.93	0.51	0.28
7	0.75 ± 0.1	2.7 ± 0.1	1.57	1.14	0.85	0.36
8	0.5 ± 0.1	1.0 ± 0.1	0.74	0.59	0.30	0.15
8	0.3 ± 0.1	0.9 ± 0.1	0.69	0.56	0.33	0.12
9	0.75 ± 0.2	2.75 ± 0.2	1.59	1.16	0.64	0.26
9	0.75 ± 0.2	> 5.0	—	—	—	—
10	FM coupled	FM coupled	—	—	—	—
11	1.2 ± 0.2	4.0 ± 0.2	2.20	1.52	0.96	0.28
12	FM coupled	FM coupled	—	—	—	—
13	< 0.5	1.8 ± 0.2	1.13	0.86	$\approx 0.43^*$	$\approx 0.21^*$

* Using $J_1 = 2J_2$

DISCUSSION

Our results clearly demonstrate that in the thickness range of 4-13 ML the AFM coupling exhibits short wavelength oscillations with a period close to 2ML. Maxima of the AFM coupling are observed for an odd number of Cr monolayers. For thicknesses less than 10ML the short-wavelength oscillations are superposed on a background of a slowly varying AFM coupling. The amplitude of the short-wavelength oscillations is significantly enhanced for thicknesses greater than 9ML of Cr. FM coupling is observed for Cr interlayers 10 and 12 ML thick. The BLS data enables one to separate the bilinear and the biquadratic contributions to the antiferromagnetic exchange coupling terms. Both the bilinear and the biquadratic coupling strengths exhibit a short period oscillatory dependence on the Cr interlayer thickness (~2 monolayers), see fig.5. One can ask "is the biquadratic coupling term caused by an intrinsic mechanism, or does it have its origin in an interface roughness through the mechanism proposed by Slonczewski?". The Slonczewski model [14] predicts a biquadratic coupling strength that varies quadratically with the change in exchange coupling for a change in thickness of one atomic layer, ΔJ (due to residual interface roughness). Note that the biquadratic term has approximately the same strength for 7 ML as it has for 11 ML (see fig.5b) even though ΔJ increases by at least a factor of two between 7 and 11 ML. This observation, coupled with the very smooth Fe substrate and almost equally smooth Cr(001) films, argues

against the Slonczewski mechanism. Note that the maxima in the biquadratic exchange coupling strength appear to be in phase with the maxima in the strength of the antiferromagnetic bilinear coupling. One would like to know if this feature would be reproduced by a realistic model for the exchange coupling through Cr(001).

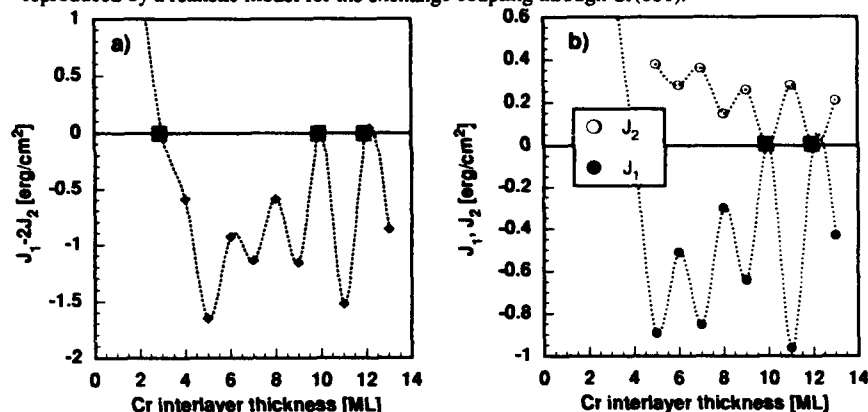


Fig. 5. (a) The total exchange coupling ($J_1 - 2J_2$ from eqn.(4) in the text) plotted as a function of Cr(001) interlayer thickness. The coupling ($J_1 - 2J_2$) corresponds to applied fields such that the magnetizations in the two ferromagnetic regions are parallel.

(b) The thickness dependence of the bilinear exchange coupling term, J_1 , and the biquadratic exchange coupling term, J_2 .

All measurements were carried out at room temperature. In both (a) and (b) the black squares indicate weak ferromagnetic coupling. We are unable at present to provide a quantitative evaluation of this ferromagnetic coupling strength so we have put these values equal to zero. We were also unable to determine the strength of the biquadratic exchange coupling for ferromagnetically coupled specimens; those values are likely to be small so we have arbitrarily set $J_2 = 0$. The dashed lines are a cubic spline fit to the points as an aid to the eye.

According to first principles calculations [15] the phase of the coupling between two iron layers separated by a Cr(001) interlayer is determined by two principles: (1) the Cr spins are antiferromagnetically coupled to the iron surface spins, and (2) the Cr contains an antiferromagnetic spin density wave with a period close to 2 monolayers (ML). For Cr interlayer thicknesses in the range of our measurements the first principles calculations predict maxima in the antiferromagnetic coupling strength for an even number of Cr(001) ML. Our results for 3 and 4 ML of Cr(001) are in agreement with this prediction. However, for interlayers having a thickness equal to or greater than 5 ML we find that the maxima in antiferromagnetic coupling strength occurs for an odd number of Cr ML. This phase is opposite to that predicted by the first principles calculations, and therefore the first phase slip occurs for a thickness between 4 and 5 ML.

Zhu-Pei Shi et al [7], using a coupling scheme based on the interface hybridization of magnetic and interlayer electron states, predicted an AFM coupling for Fe(001) layers separated by Cr(001) thicknesses between 4 and 12 ML. The phase of their short wavelength oscillations agrees with the phase of our measurements for Cr interlayers thinner than 10 ML. However, the calculations predict a maximum AFM coupling for 7 ML of Cr, whereas we observe a maximum AFM coupling for 11 ML of Cr. The calculations of Zhu-Pei Shi et al [7] predict a strong FM coupling for Cr interlayers thinner than 4 ML. Our results show that the measured crossover to FM coupling is more gradual than that predicted by their calculations and therefore our results are very likely unaffected by structural imperfections even in a Cr layer only a few monolayers thick.

There is a similarity between our total exchange coupling ($J_1 - 2J_2$) measured at room temperature and the total exchange coupling measured by Grünberg et al [6] measured at raised temperatures, $T = 443$ K. However, the phase of the short-period oscillations on wedged samples [6] exhibited extrema in the exchange coupling at a non-integral number of ML. The

maximum amplitude of the short-period oscillations in the measurements of Grünberg et al [6] was observed for a Cr thickness of approximately 5-6 ML, whereas in our measurements a maximum amplitude was observed at 9-13 ML. The strength of the exchange coupling was found to be comparable in both studies, $J_{\text{max}} \sim 1$ ergs/cm². The measured values of the exchange coupling were significantly weaker than those predicted by first principles calculations, $J \sim 40$ ergs/cm² [15]. It is unlikely that in our high quality samples this difference was caused by surface roughness.

The interface roughness affects very strongly the measured values of the exchange coupling. We found that in samples with a partially filled last atomic layer (away from a RHEED intensity maximum), but with an otherwise properly grown Cr layer, the measured exchange coupling was changed by a noticeable AFM contribution [5]. It is also interesting to note that in samples with the Cr layer grown at too high a substrate temperature (see Fig. 1a,1b) the exchange coupling can even change its sign. E.g. samples with 13 ML of Cr which were grown at too high a substrate temperature showed FM coupling. In wedged samples a wide range of interfaces is present; it is difficult to identify the regions which correspond to the best available interfaces. It is therefore difficult to determine the intrinsic exchange coupling for an integral number of ML using a wedged sample.

Unfortunately no simple analysis can be used to deduce the strength of the exchange coupling in the case in which the coupling is very weak or is ferromagnetic. We hope that an analysis of the BLS scattering intensity along the lines of the calculation reported by Camley and Mills [16] can be used to estimate the FM coupling strength.

The Authors would like to thank the National Science and Engineering Research Council of Canada for grants that supported this work.

+ Permanent address: MPI f. Mikrostrukturphysik, Weinberg 2, O4050 Halle/Salle.

REFERENCES

1. J. Unguris, R.J. Celotta, D.T. Pierce, Phys.Rev.Lett. **67**, 140 (1991).
2. S.T. Purcell, W. Folkerts, M.T. Johnson, N.W. W. McGee, K. Jager, J. aan de Stegge, W.B. Zeper, W. Hoving and P. Grünberg, Phys.Rev.Lett. **67**, 903 (1991).
3. J. Unguris, R.J. Celotta and D.T. Pierce, Workshop on "Magnetism and Structure in Systems of Reduced Dimension", Cargese, Corsica, France, June 1992, to be published in NATO ASI series.
4. P. Grünberg, S. Democritov, A. Fuss, R. Schreiber, J.A. Wolf, and S.T. Purcell, JMMM **104-107**, 1734 (1992).
5. B. Heinrich, Z. Celinski, J.F. Cochran, and M. From, Workshop on "Magnetism and Structure in Systems of Reduced Dimension", Cargese, Corsica, France, June 1992, to be published in the NATO ASI series.
6. P.A. Grünberg, A. Fuss, Q. Leng, R. Schreiber, J.A. Wolf, Workshop on "Magnetism and Structure in Systems of Reduced Dimension", Cargese, Corsica, France, June 1992, to be published in the NATO ASI series.
7. Zhu-Pei Shi, P. M. Levy and J.L. Fry, Phys.Rev.Lett., **69**, 3678 (1992).
8. P. Grünberg, Progress in Surface Science, **18**, 1 (1985).
9. k-Space Associates, 2379 Leslie Circle, Ann Arbor, Michigan 48105.
10. A.S. Arrott, B. Heinrich and S.T. Purcell, Kinetics of Ordering and Growth at Surfaces, edited by M.G. Legally, Plenum Press, New York, 321 (1990).
11. B. Heinrich, J.F. Cochran, M. Kowalewski, J. Kirschner, Z. Celinski, A.S. Arrott, and K. Myrtle, Phys.Rev.B, **44**, 9348 (1991).
12. D.L. Mills, Phys.Rev.B, **39**, 12306 (1989).
13. R.C. O'Handley and J.P. Woods, Phys.Rev.B, **42**, 6568 (1990).
14. J.C. Slonczewski, Phys.Rev.Lett. **67**, 3172 (1991).
15. (a) H. Hasegawa, Phys.Rev.B **42**, 2368 (1990)
(b) F. Herman, J. Sticht, and M. van Schilfgaarde, J.Appl.Phys. **69**, 4783 (1991).
(c) D. Stoeffler and F. Gautier, Phys.Rev.B **44**, 10389 (1991); J.Magn.Magn.Mater. **104-107**, 1819 (1992).
16. R.E. Camley and D.L. Mills, Phys.Rev.B, **18**, 4821 (1978).

MAGNETIC AND TRANSPORT BEHAVIOR OF AF-COUPLED LAYERS WITH A LIMITED NUMBER OF REPETITIONS

M.M.H. WILLEKENS*, H.J.M. SWAGTEN*, A.M. DUIF*, P.J.H. BLOEMEN**, R.J.T. VAN KEMPEN*, S.K.J. LENCZOWSKI** AND W.J.M. DE JONGE*

*Department of Physics; Eindhoven University of Technology; P.O.Box 513, 5600 MB Eindhoven, The Netherlands.

**Also at Philips Research Laboratories, Eindhoven, The Netherlands.

ABSTRACT

We investigated the magnetization behavior of $[(\text{Co/Pd})_x\text{-Ru}]_x$ samples with perpendicular anisotropy and a limited number of repetitions ($x = 1, \dots, 22$). In these systems the Co/Pd multilayers behave as single magnetic entities. A detailed analysis and comparison of the magnetization curves observed by MOKE and VSM permits us to observe the magnetization reversal and hysteresis of the individual layers and to determine the antiferromagnetic coupling J between each pair of layers. A gradual increase in J is observed in all samples when going from the bottom layer to the top layer. Magnetoresistance curves show the same sharp transitions as the magnetization curves. A clear distinction can be made between an outer layer and an inner layer. These results will be compared with model calculations.

INTRODUCTION

The last few years magnetic multilayers have been the subject of intensive investigation. Especially a large (perpendicular) anisotropy, an oscillating exchange coupling and a giant magnetoresistance have attracted much attention [1,2,3]. Values for anisotropy (K) and exchange coupling (J) are often determined from transition and/or saturation fields of magnetization curves. However this determination is not a trivial calculation.

Calculations of the magnetization [4,5] and magnetoresistance [5] for a sandwich containing two AF-coupled magnetic layers with uniaxial anisotropy have been performed in two limiting cases. In one case the system is always in a state of absolute minimum energy. In the other case the system finds itself in a local energy minimum due to anisotropy induced energy barriers.

Measurements on these systems however show a wide variety of magnetization curves lying between the two limiting curves [6,7]. It is believed that the exact shape of the magnetization curve is determined by microscopic phenomena such as local anisotropy fluctuations and pinholes. Therefore, the derived equations for the limiting cases are not applicable. In the case of a multilayer also the number of repetitions can play a crucial role.

To gain more insight in the magnetic behavior of these systems we have grown a series of multilayers with perpendicular anisotropy and AF-coupling. The number of layers was varied between 1 and 22. Magnetization loops have been measured with the Magneto Optical Kerr Effect (MOKE) as well as Vibrating Sample Magnetometer (VSM). Magnetoresistance measurements have been performed at room temperature and at low temperature. A detailed investigation of the magnetization and magnetoresistance effect leads to an analysis in which it is possible to distinguish between the magnetization reversal and hysteresis of the individual layers. The measurements will be compared with theory.

EXPERIMENTAL

The multilayers were composed of $200\text{\AA Ru} + N \cdot (M + 8\text{\AA Ru}) + 22\text{\AA Ru}$. Here M is a magnetic layer composed of $M = 2\text{\AA Co} + 4 \cdot (3\text{\AA Co} + 6\text{\AA Pd}) + 5\text{\AA Co}$. The number of repetitions, N , varied from 1 to 22. All samples were prepared at Philips Research Laboratories. The multilayers were deposited at room temperature on oxidized silicon substrates by three source HV-magnetron sputtering. Prior to the baselayer growth the substrates were given 30 min. glow-discharge treatment. The sputtering occurred at a background pressure of $7 \cdot 10^{-3}$ Torr.

Before sputtering the sputtering chamber was evacuated to $4 \cdot 10^{-7}$ Torr. The sputtering rates for Ru, Co and Pd were 1, 2, and 3 \AA/s respectively.

The magnetic layers M act as ferromagnetic layers with a large perpendicular anisotropy. To achieve this we composed each magnetic layer of strongly ferromagnetically coupled Co-layers using $(3\text{ \AA Co} + 6\text{ \AA Pd})$ as magnetic building blocks. The use of such a multilayer instead of a single Co-layer provides a larger magnetic moment with conservation of a (large) perpendicular anisotropy. Such a system has been used successfully by Bloemen et al. [6].

To assure large AF-coupling we chose a spacer layer of 8 \AA Ru . For this Ru-thickness the coupling between two Co-layers displays a maximum [8].

RESULTS

Fig. 1 shows magnetoresistance measurements as well as magnetization loops obtained with VSM and MOKE as a function of applied field for $N=2, 4$ and 7 . In all the measurements the field was applied normal to the film plane, along the easy axis. Each transition shown in Fig. 1 corresponds to the magnetization reversal of an individual layer. For a given N all the measurements show the same transitions.

The bilayer ($N=2$) clearly shows a spin-flip transition. This behavior indicates that there is indeed antiferromagnetic (AF) coupling between the magnetic layers. It indicates also that the magnetic anisotropy is larger than the exchange coupling $-J$ (AF-coupling corresponds to $J < 0$). If this were not the case one would rather expect a spin-flop transition than a spin-flip [4].

Note that the Kerr-rotation is more sensitive to layers closer to the surface due to the finite penetration depth of the light. As a result the Kerr-signal at low fields (state with AF-alignment) is non zero. This enables us in some cases to determine the magnetization direction of a layer. For instance, if we consider the bilayer we can see that the magnetization direction of the lower layer always reverses first as the Kerr-rotation does not change in sign when going from saturation to AF-alignment. This is indicated by the arrows in Fig. 1.

In the case of 4 magnetic layers the magnetization loops display 4 transitions between negative and positive saturation. For the Kerr-loop the change in Kerr-rotation is different for each transition. This difference enables us again to determine which magnetic layer reverses the direction of its magnetization at that transition. If we number the layers in the sequence as they are grown (first grown layer = layer 1), the first transition when the field is decreased from saturation is a magnetization reversal of layer 3 (from $\uparrow\uparrow\uparrow\uparrow$ to $\uparrow\downarrow\uparrow\uparrow$). Equivalently the second transition corresponds to a reversal of layer 1 ($\uparrow\downarrow\uparrow\uparrow$ to $\uparrow\downarrow\downarrow\uparrow$), the third transition, which presents the largest step, corresponds with layer four ($\uparrow\downarrow\downarrow\uparrow$ to $\downarrow\downarrow\downarrow\downarrow$) and the fourth transition with layer 2 ($\downarrow\downarrow\downarrow\downarrow$ to $\downarrow\downarrow\uparrow\downarrow$).

When the number of layers increases, the MOKE-loops, which are insensitive to the lower layers, display less transitions than the VSM and magnetoresistance measurements. Therefore it is no longer possible to establish the exact order in which the layers reverse their magnetization direction. However, from VSM and MR measurements it is clear that the layers still reverse one by one. As far as we can see from the MOKE-loops the sequence in which the layers reverse their magnetization direction is always the same. Using the same numbering as above, the sequence in which the layers reverse their magnetization direction is: $N-1, N-3, \dots, 3, 1, N, 2, 4, \dots, N-2$ for N is even and $N-1, N-3, \dots, 2, 1, N, 3, 5, \dots, N-2$ for N is odd. This is consistent with the MR-curves since the smallest changes in MR (around the origin) then correspond to the reversal of the outer layers. We will return to this in the discussion.

DISCUSSION

From the fact that within one sample each individual layer reverses its magnetization direction at a different field we can deduce that the layers are not all identical. For all the samples the sequence in which the layers reverse their magnetization direction is always the same. Starting from saturation and decreasing the field, the first layer to reverse its magnetization direction will be the layer which is AF-coupled most strongly to its neighbors. For $N \geq 3$ this will always be an inner layer for such a layer is coupled with two neighbors whereas an outer layer only has one magnetic neighbor.

Since the layers always start to reverse from the top apparently the top layers are coupled more strongly than the bottom layers. The fact that the bottom layers are coupled differently from the top layers has also been measured for Fe/Si multilayers [9]. This could be due to an

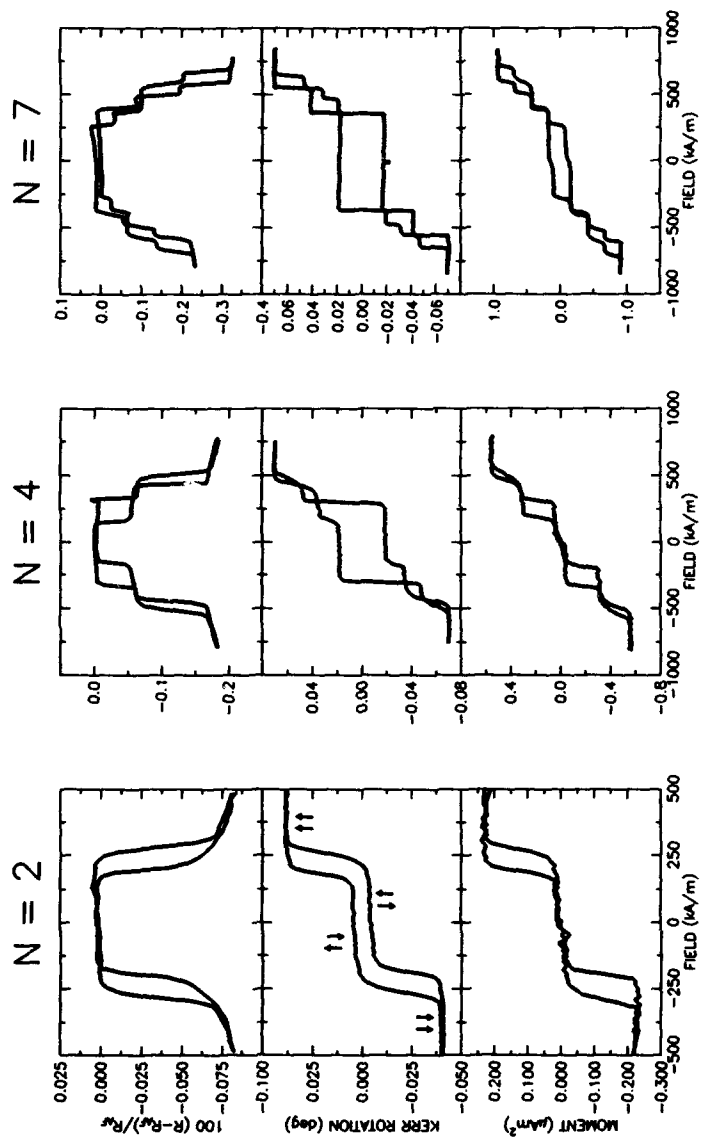


Fig. 1: From top to bottom the room-temperature magnetoresistance, Kerr-rotation and magnetization as a function of applied field for $\text{SiO}_2 + 200\text{ÅRu} + N(M + 8\text{ÅRu}) + 22\text{ÅRu}$ with $M = 2\text{ÅCo} + 4(3\text{ÅCo} + 6\text{ÅPd}) + 5\text{ÅCo}$. The field was applied perpendicular to the film plane in all the measurements.

improvement of texture as is reported for Co/Pt multilayers [10]. Another possible explanation would be that the interfaces grow flatter when the number of layers increases. Because of thickness variations of the spacer layer the coupling between the layers closest to the substrate would not reach the maximum value. This reduction of the roughness when the number of layers increases is also indicated by the increase of anisotropy of the Co/Pd layers measured in these samples with a capacitive torque magnetometer. This increase with roughly a factor of 3 can be understood, according to Bruno [11], by assuming an increase of $2\sigma/L$ (where 2σ is the height and L the width of the terraces) with a factor of 2.

Determination of a value for the exchange coupling is not trivial. As mentioned above we are not in one of the two limiting cases of absolute minimum energy or local energy minimum due to anisotropy induced energy barriers. Thus the formulas for these cases derived by Dieny et al. and Folkerts [4,5] are not valid in this case. Therefore we write the energy of the multilayers as:

$$E = -\mu_0 H M_s \sum_{i=1}^N t_i \cos \theta_i - \sum_{i=1}^{N-1} J_i \cos (\theta_i - \theta_{i+1}) \quad (1)$$

Here t_i is the thickness of layer i and θ_i is the angle between the magnetization direction of layer i and the easy axis (normal to the film plane). We now assume that a layer will reverse its magnetization direction whenever the energy difference between initial and final state is large enough to surmount a coercive force H_C : $E_i - E_F = 2\mu_0 M_s t_i H_{C,i}$. According to this model the transition field H_F for an inner layer i , when the field is decreased from saturation, is given by

$$H_F = \frac{-J_{i-1} - J_i}{\mu_0 M_s t_i} - H_{C,i} \quad (2)$$

where J_i is the exchange coupling between layer i and layer $i+1$. For an outer layer this field is

$$H_F = \frac{-J}{\mu_0 M_s t} - H_C \quad (3)$$

Starting from the antiferromagnetic situation the coercive field should be added instead of subtracted.

Values for the exchange coupling can now be found by averaging two magnetization reversal transition fields of the same magnetic layer. This can be accomplished by reversing the field course after a magnetization reversal until the magnetic layer reverses again. This procedure is shown in Fig. 2. The sequence of the successive transitions is indicated by numbers in the figure. For this particular sample ($N=4$) the increase of J following from the averaging amounts 24%.

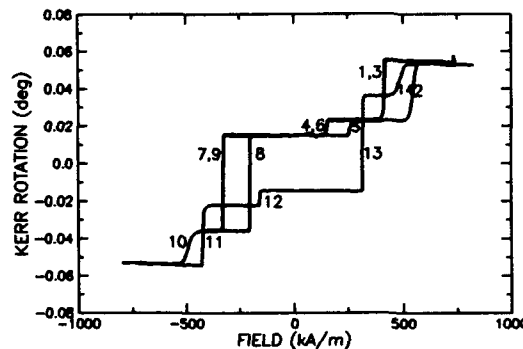


Fig. 2: Kerr rotation as a function of applied field for the sample with 4 magnetic layers. The field course was reversed after each transition. The sequence of the successive transitions is indicated by numbers.

The magnetoresistance displays a similar sequence of transitions as observed by VSM and MOKE. It appears that all transitions give rise to an equal change in MR, except for the change of MR due to the reversal of an outer layer which is systematically smaller (roughly a factor 2) than all the others. As we are dealing with transitions between well defined configurations as pointed out before, we are tempted to explain this interesting phenomenon first by a very simple resistor network.

With such a network, introduced by Edwards et al. [12], it was possible to predict the giant MR as well as the damping of the effect with increasing spacer thickness. However, the model was designed essentially for a mean free path much longer than the layer thicknesses which justifies an averaging of resistivities in the up- and down electron channels. This means implicitly that one can never discern between the magnetization reversal of an inner layer or one of the outer layers.

For this reason we have developed an alternative resistor model, in which the multilayer is represented by $N-1$ resistors in parallel, each resistor representing a bilayer of two half magnetic layers. The parallel and antiparallel configuration of the bilayer's magnetization relates to a difference in resistance due to the spin-dependent scattering mechanism. A similar procedure has been used by Dieny et al. to account for the shunting of the 'nonactive' part of a magnetic layer in a magnetically soft sandwich [13]. It should be emphasized that in our model an outer layer is a part of only one sandwich resistor, whereas an inner layer is incorporated into two resistors. In other words, due to a reversal of an outer-layer magnetization a mobile electron experiences only once a change in M , whereas a double change is seen when an inner layer changes its magnetization. In Fig. 3 the data for $N=6$ are shown together with results of the parallel-resistor model. The relative changes in MR, and in particular the exclusive role of the outer layer, is very well recovered with a set of parameters applicable for all N , which is shown in the fit of the total MR in fig 3c.

To substantiate the parallel-resistor model introduced above we have solved the Boltzmann transport equation (see Camley et al. [14]) numerically for a limited number of magnetic layers. The basic features of the calculations are as follows (details will be published separately [15]): (i) The raise of the total MR with increasing N can, in principle, be explained, which is not unique for the present systems. A similar calculation was applied to e.g. Fe/Cr multilayers with limited N [16]. (ii) The magnetization reversal of inner layers exhibits minor differences due to the asymmetry introduced by the presence of the base layer; however, when an outer layer reverses its sign the change in MR is substantially smaller and a similar fit to the data obtained by the resistor model can be obtained.

It should be emphasized that, to our knowledge, the decisive role of the position of a magnetic layer within the multilayered structure for the size of the relative MR has never been recognized so far and might be a general phenomenon in layered systems. However, we should realize that the applied Boltzmann transport equation assumes no spin-flip processes, which is a $T = 0$ approximation. In this respect, we have performed MR measurements at temperatures

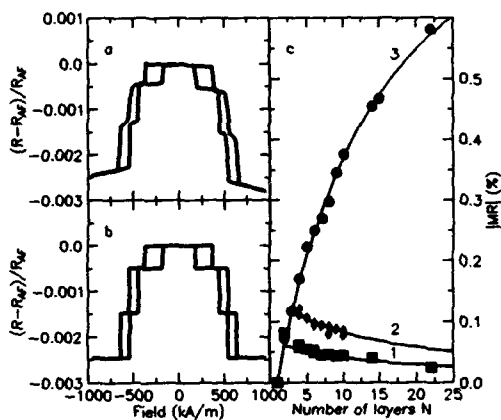


Fig. 3: a) and b) data and model calculations resp. of the relative change in MR obtained for perpendicular fields at $T=300K$ for the sample with 6 magnetic layers; c) (\bullet , line 3) total magnetoresistance; (\blacksquare , line 1) relative change in MR due to the reversal of an outer magnetic layer; (\blacklozenge , line 2) relative change in MR due to the reversal of an inner magnetic layer. Lines are fits obtained with the parallel resistor model.

down to $T = 4$ K. Except for the increasing magnitude of the MR at lower temperatures, there is no visible effect on the relative MR changes for inner and outer layers. Apparently, even at room-temperature the spin-flip scattering length is still large enough to justify the present description of the observed transport effects.

CONCLUSIONS

We have measured the magnetization and magnetoresistance of $[(\text{Co/Pd})_4\text{-Ru}]_n$ multilayers. All the measurements show sharp transitions corresponding to the magnetization reversal of the individual layers. This enables us to determine the exchange coupling J between each pair of layers. J increases when the number of layers increases. In the MR-curves, in combination with the MOKE-loops, we can clearly distinguish between the reversal of an outer layer or an inner layer. This fact as well as the N -dependence of the MR can be described with a simple resistor model.

ACKNOWLEDGEMENT

This research was supported in part by the European Community Science Project: ESPRIT3 Basic Research, 'Study of Magnetic Multilayers for Magnetoresistive Sensors' (SmMmS).

REFERENCES

1. P. Grünberg, R. Schreiber and Y. Pang, Phys. Rev. Lett. **57**, 2442 (1986).
2. M.N. Baibich, J.M. Broto, A. Fert, F. Nguyen Van Dau and F. Petroff, Phys. Rev. Lett. **61**, 2472 (1988).
3. S.S.P. Parkin, N. More and K.P. Roche, Phys. Rev. Lett. **64**, 2304 (1990).
4. B. Dieny, J.P. Gavigan, J.P. Rebouillat, J. Phys. Condens. Matter **2**, 159 (1990); B. Dieny, J.P. Gavigan, J. Phys. Condens. Matter **2**, 187 (1990).
5. W. Folkerts, J. Magn. Magn. Mater. **94**, 302 (1991).
6. P.J.H. Bloemen, M.T. Johnson, J. aan de Stegge and W.J.M. de Jonge, J. Mag. Magn. Mater. **116**, L315 (1992);
7. W.R. Bennet, W. Schwarzacher and W.F. Egelhoff, Jr, Phys. Rev. Lett. **65**, 3169 (1990).
8. P.J.H. Bloemen, H.W. van Kesteren, H.J.M. Swagten and W.J.M. de Jonge (To be published).
9. Eric E. Fullerton, J.E. Mattson, S.R. Lee, C.H. Sowers, Y.Y. Huang, G. Felcher, S.D. Bader and F.T. Parker, J. Magn. Magn. Mater. **117**, L301 (1992).
10. C.J. Lin, G.L. Gorman, C.H. Lee, R.F.C. Farrow, E.E. Marinero, H.V. Do, H. Notarys and C.J. Chien, J. Magn. Magn. Mater. **93**, 194 (1991).
11. P. Bruno, J. Phys. F: Met. Phys. **18**, 1291 (1988).
12. David M. Edwards, Jiri Mathon and R. Bechara Muniz, IEEE Transactions on magnetics, **27**, 3548 (1991).
13. B. Dieny, P. Humbert, V.S. Speriosu, S. Metin, B.A. Gurney, P. Baumgart and H. Lefakis, Phys. Rev. B, **45**, 806 (1992).
14. R.E. Camley and J. Barnás, Phys. Rev. Lett. **63**, 664 (1989).
15. M.M.H. Willekens et al. (To be published).
16. J. Barnas, A. Fuss, R.E. Camley, P. Grünberg and W. Zinn, Phys. Rev. B, **42**, 8110 (1990).

DIRECT EVIDENCE OF BIQUADRATIC COUPLING IN MULTILAYERS BY NEUTRON SCATTERING EXPERIMENTS.

Stéphane ANDRIEU*, Martine HENNION**, Michel PIECUCH*.

*Laboratoire mixte CNRS Saint Gobain BP 109 54704 Pont à Mousson CEDEX France.

**Laboratoire Léon Brillouin Saclay France.

ABSTRACT

We present small angle neutron scattering experiments on (001) Fe/Ir superlattices. A short period oscillated coupling is observed. However, antiferro and ferromagnetic peaks are simultaneously measured on neutron diagram, which cannot be simply explained. A biquadratic coupling model is proposed to account for this behaviour.

INTRODUCTION:

One of the most interesting problem in the field of magnetic multilayers is the existence of the interlayer coupling through the nonmagnetic spacer. The coupling is antiferromagnetic in certain cases^{1,2,3} and is responsible of the so called giant magnetoresistance effect^{2,4}. Recently, P. Grünberg and his group⁵ have proposed a second type of coupling, the biquadratic coupling, which leads to a perpendicular orientation of the magnetic moment. J. Sloniewski⁶ gives a possible explanation of this coupling based on interface defects like steps. Another type of defect can also lead to this kind of frustration and to biquadratic coupling: the existence of pin holes which couples ferromagnetically the layers at some localized sites⁷. However, more general mechanisms may lead to such a biquadratic coupling but it has to be detected in new systems. Neutron scattering is the most general tool to test the magnetic structure and to determine the nature of the coupling. In that way, the Fe/Ir system is a very good candidate since the products of the neutron scattering length b , by the atomic density n is similar in these two metals: $bn=7.5 \cdot 10^{10} \text{ cm}^{-2}$ for Ir and $bn=8.1 \cdot 10^{10} \text{ cm}^{-2}$ for normal BCC iron (in our case iron is slightly expanded and these two parameters become even closer). The nuclear contrast is therefore very weak and only the magnetic scattering is measured. The paper is divided in two parts: the first one describes the experimental results and the second one discusses the results in the framework of a simple kinematical approximation.

EXPERIMENTAL RESULTS:

The neutron experiments are performed on a series of Ir/Fe monocrystalline superlattices prepared by Molecular Beam Epitaxy (MBE) on (100) MgO^8 substrates. The structure and growth of these superlattices are described elsewhere⁸ but we can shortly summarize them. The Fe growth on (100) FCC Ir is pseudomorphic in the plane of the growth up to 4 atomic layers. The bulk structure of Fe in these superlattices is BCT (body centered tetragonal) and Fe is thus not magnetic at room temperature⁹. However for iron thicknesses greater than 5 monolayers we can get non matched epitaxy between (100) BCC Fe and FCC (100) Ir. The crystalline quality of these superlattices is not as good as in the pseudomorphic case but the magnetic moments of Fe layers are thus large at room temperature (close to the bcc Fe one)⁸. The magnetization is in the plane of the Fe layers⁸. Naturally, the neutron scattering experiments are carried on this kind of superlattices in this study. The iridium thickness was varied between 1.5 and 24 Å. The number of bilayers is typically 20 with a total sample thickness between 300 Å and 1000 Å.

The neutron diffraction experiments are performed at the Léon Brillouin laboratory in Saclay using the triple axis G 4 3 spectrometer. The small angle experiments are carried out with an incident wave vector of 1.4 Å^{-1} selected by a PG monochromator. The PG analyzer is set at zero energy transfer to reduce the inelastic background. The experiments are carried out at room temperature with unpolarized neutrons at small angles.

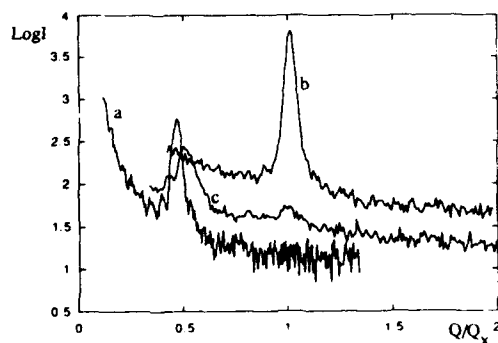


Figure 1: Neutron spectra for three typical samples.

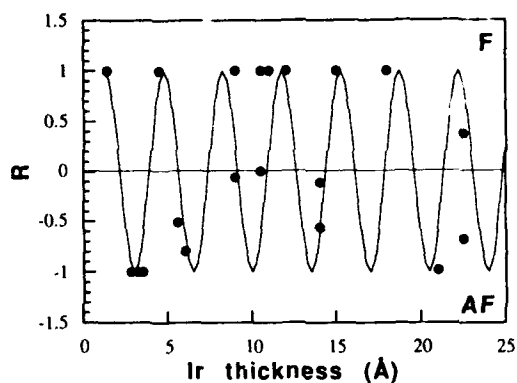


Figure 2: $R = \frac{I_F - I_{AF}}{I_F + I_{AF}}$ plot versus the iridium thickness.

The full curve is a cosine function with a period of 3.5\AA .

Some typical spectra are presented in figure 1. One can see, for the sample a, that only a single peak is present at the antiferromagnetic position: $q\Lambda = \pi$. The sample b exhibits a single peak at the ferromagnetic position $q\Lambda = 2\pi$. By contrast, we observe peaks on both positions on the sample c. We thus record long time spectra around the antiferromagnetic (AF) and ferromagnetic (F) peaks for all the samples in order to have a good signal to noise ratio. The figure 2 gives the F and AF peaks intensity ratio R defined as:

$$R = \frac{I_F - I_{AF}}{I_F + I_{AF}} \quad (1)$$

This figure clearly shows that the period of the AF coupling is very short : for Ir thicknesses varying from 1.5 to 7Å, an AF, F, AF, F coupling sequence is actually observed. Therefore, in order to describe a well define R curve, a precise control of the Ir thickness (less than 0.5Å) from one superlattice to another is needed. Moreover, a large number of samples is necessary to describe all the AF and F oscillations (which represents a lot of work to prepare them by MBE and characterize them by neutrons!). Indeed, the 3rd and 5th oscillations of the AF coupling are not described. However, even if it is not possible to reach an accuracy on the Ir thickness (evaporated by an e-gun) better than $\pm 5\%$, it is possible to estimate a period of the oscillating coupling around 3.5Å. This period is estimated at low Ir thicknesses where the accuracy is the smallest one. Above 10Å, nothing can be said since the uncertainty on Ir thicknesses is too large, even if the cosine law of figure 2 correctly describes the experimental result. This short period is close to two Ir planes thickness, which suggest an exact AF coupling in Ir.

However, it should be noted that both AF and F peaks appear on neutron diagram for 7 samples. This result may be explained by the coexistence of AF and F coupling in the same superlattice, due to a thickness variation for example. In that case, the determination of the coupling period becomes unaccurate. However, we demonstrate in the following discussion that thicknesses variations cannot explain this result. A biquadratic coupling assisted by a second layer interaction has thus to be taken into account.

DISCUSSION:

The elastic magnetic differential cross section of neutron scattering in the kinematical approximation can be written as¹⁰:

$$\frac{d\sigma}{d\Omega} = (\gamma_0)^2 \frac{k'}{k} \sum_{\alpha\beta} (\delta_{\alpha\beta} - n_{\alpha}n_{\beta}) \langle Q_{\alpha}^{+} Q_{\beta} \rangle \quad (2)$$

Where $Q = \int M(r) \exp iqr \, dr$ is the Fourier transform of the magnetization $M(r)$, n is a unit vector parallel to the diffusion vector $q = k - k'$. In the Bragg geometry, $q = qu_z$ where u_z is the unit vector perpendicular to the layer plane. Moreover, the geometrical factor is unity in this case, since the magnetization is in the layer plane, i.e. perpendicular to the diffusion vector q .

The total magnetization $M(r)$ is the sum of the magnetization of individual magnetic layers $M_n(r)$. Let now define an arbitrary (v,w) reference in the plane of the layers, and ϕ_n the angle of the magnetic moment $M_n(r)$ with v. We can write :

$$M_n(r) = M_n(r)(v \cos \phi_n + w \sin \phi_n) \quad (3)$$

Where $M_n(r)$ is a scalar function of r. The next assumption is that $M_n(r)$ is independent of n, supported by the fact that the error on Fe thickness is much smaller than Ir one, since Fe is evaporated using a Knudsen cell. This means that the coupling through the non magnetic spacer do not modify the band structure of the different sites of the ferromagnetic layer and the absolute value of the magnetization. The neutron intensity can thus be written as :

$$I \propto M_0^2 |f_{Mag}(q)|^2 (N+2) \sum_{n=1}^{N-1} (N-n) \langle \cos(\alpha_n) \rangle \cos(nq\Lambda) \quad (4)$$

Where $f_{Mag}(q)$ is a scalar magnetic form factor for an individual layer and $\alpha_n = \phi_{n+m} - \phi_m$ is the angle between the magnetization in two layers separated by $n\Lambda$. The mean value concerns the distribution of ϕ_m . N is the number of magnetic layers. Let now write the general magnetization energy of the superlattice without magnetic field E, taking into account the direct coupling (J), a second layer interaction (J'), and a biquadratic coupling (B) :

$$E = 2 \sum_{i=1}^{N-1} (-J_i \cos \beta_i - J_i' \cos(\beta_i + \beta_{i+1}) + B \cos^2 \beta_i) \quad (5)$$

where β_i is the angle between the magnetizations of the i and $i+1$ layers. Note that $\beta_1 = \alpha_1$ and $\beta_i + \beta_{i+1} = \alpha_2$ which actually describe the interaction with the adjacent and second layer respectively. The minimization of the energy thus gives :

$$\sin \beta_i (J_i - 2B \cos \beta_i) + J_i' \sin(\beta_i + \beta_{i+1}) = 0 \quad (6)$$

Equations (2) to (6) thus leads to several cases as :

1st case : direct F coupling : $J_i > 0$, $B = J_i' = 0$, $\beta_i = \phi_n = \alpha_n = 0$. We thus get standard neutron diagram with peaks at $q\Lambda = 2n\pi$.

2nd case : direct AF coupling : $J_i < 0$, $B = J_i' = 0$, $\cos \beta_i = -1$, $\cos \phi_n = (-1)^n$, $\langle \cos \alpha_n \rangle = (-1)^n$. The diffracted peaks are thus situated at $q\Lambda = (2n+1)\pi$.

3rd case : randomly coupled superlattice : $J_i > 0$ or < 0 , $B = J_i' = 0$, $\beta_i = 0$ or π depending on the sign of J_i . A random β_i distribution can be expressed as :

$$P(\beta_i) = p \delta(\beta_i) + (1-p) \delta(\beta_i - \pi) \quad (7)$$

Where p is the probability of $J_i > 0$. One can calculate the distribution of α_n as¹¹:

$$P_n(\alpha_n) = P_{n-1}(\alpha_{n-1}) * P(\alpha_1) \quad (8)$$

Where $*$ means convolution product. The calculation gives:

$$\langle \cos(\alpha_n) \rangle = (2p-1)^n \quad (9)$$

One can easily see that this gives only ferromagnetic peaks if $p > 1/2$ and antiferromagnetic peaks if $p < 1/2$ (the intensities and the positions of the peaks are entirely determined by the mean value of J_i , with however a large background due to the disorder).

4th case : biquadratic coupling: $J_i' = 0$ but $B \neq 0$

- a) $|J| > 2B$. The only solution is then: $\sin \beta_i = 0$. The lowest energy is obtained for $\beta_i = 0$ if $J > 0$ (ferromagnetic solution) or for $\beta_i = \pi$ if $J < 0$ (antiferromagnetic solution).
b) $|J| < 2B$. Another solution is possible:

$$\cos \beta_i = \frac{J}{2B} = \cos \beta_0 \quad (10)$$

This solution is the most stable one (if B positive). This kind of solution can lead to new type of neutrons spectra or magnetization curves. However, we have a problem with equation (10): the sign of β_i is not fixed and then the ground state is degenerated (multiple equivalent solutions). The first natural idea is to suppose that the sign of β_i is also randomly distributed with equal probability to be equal to $+\beta_0$ or $-\beta_0$. The angle distribution is then:

$$P(\beta_i) = \frac{1}{2} (\delta(\beta_i - \beta_0) + \delta(\beta_i + \beta_0)) \quad (11)$$

And, using the same trick as equation (8) we get:

$$\langle \cos(\alpha_n) \rangle = \cos^n(\beta_0) \quad (12)$$

Qualitatively this equation behaves as equation (9) and leads to the same type of spectra: ferromagnetic peaks if $\cos(\beta_0)$ is positive ($J>0$) and antiferromagnetic peaks if $\cos(\beta_0)$ is negative ($J<0$).

5th case : biquadratic coupling + second layer interaction : there is then two simple solutions: an helicoidal one ($\beta_i = \beta_{i+1}$ or $\phi_{i+2} = \phi_i + 2\beta_0$) and a ferromagnetic one ($\beta_i = -\beta_{i+1}$ or $\phi_{i+2} = \phi_i$). The helicoidal solution is stable if J' is negative (antiferromagnetic second neighbor interaction) while the ferromagnetic one is stable if J' is positive (in the case of predominant biquadratic coupling, i.e; if β_0 exists). The helicoidal solution allows peaks for $q\Lambda = n\beta_0$ ($\langle \cos(\alpha_n) \rangle = \cos(n\beta_0)$) and cannot describes the experiments. The ferromagnetic solution gives $\langle \cos(\alpha_n) \rangle = \cos(\beta_0)$ if n is odd or $\langle \cos(\alpha_n) \rangle = 1$ if n is even.

One calculated spectrum is shown in figure 3 and exhibits ferromagnetic and antiferromagnetic peaks. This solution is the only one tested which can explain our experiments. The intensities of the peaks at $q\Lambda=2\pi$ and $q\Lambda=\pi$ are respectively:

$$I \propto |f_{\text{Mag}}(\frac{2\pi}{\Lambda})|^2 \frac{N^2-1}{2} (1+\cos(\beta_0)) \quad (13a)$$

$$I \propto |f_{\text{Mag}}(\frac{\pi}{\Lambda})|^2 \frac{N^2-1}{2} (1-\cos(\beta_0)) \quad (13b)$$

Then, neutron experiments can give values of $\cos(\beta_0)$ and J/B .

In summary, this analysis clearly demonstrates that the coexistence of both AF and F diffraction peaks on neutron diagram cannot be explained by thickness errors during the synthesis of the superlattice. A more complicated magnetic energy has to be taken into account : a biquadratic coupling assisted by a second layer interaction is thus necessary to describe the neutron diagram.

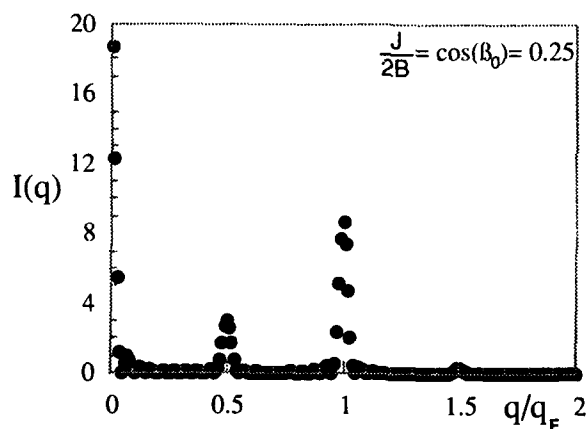


Figure 3 : Calculated spectrum in the case of a ferromagnetic second neighbors interaction.

CONCLUSION:

The small angles neutron scattering experiments clearly show the alternative existence of ferromagnetic and antiferromagnetic coupling in (100) Fe/Ir superlattices. On the one hand, a short oscillating period of around 2 Ir atomic planes is established for small Ir thicknesses. For large Ir thicknesses, the oscillating behaviour is not so clear, which can be attributed to the uncertainty on the determination of Ir thicknesses. On the other hand, the existence of both AF and F peaks on neutron diagram cannot be explained by a simple alternative coupling due to thicknesses errors. A biquadratic coupling completed by some second layer interaction must be taken into account to explain this result. The neutron diagram thus allows the determination of the coupling parameters (J/B). Using equation (6), the fit of the hysteresis loops on these samples also allows a determination of this parameter which can be compared to neutron one. This work is in progress.

references:

1. A. Cebollada, J.L. Martinez, J.M. Gallego, R. Miranda, S. Ferrer, F. Batallan, G. Fillion, J.P. Rebouillat, Phys. Rev. B., **39**, 9726 (1989)
2. S.S.P. Parkin N. More and K.P. Roche, Phys. Rev. Let., **61**, 2472 (1990)
3. F. Nguyen Van Dau Thesis, University Paris Sud, Orsay (1988)
4. M.N. Baibich, J.M. Broto, A. Fert, F. Nguyen Van Dau, F. Petroff, P. Etienne, G. Creuset, A. Friederich, G. Chazelas, Phys. Rev. Let. , **61**, 2472 (1988)
5. P. Grünberg, S. Demokritov, A. Fuss, R. Shreiber, J.A. Wolf and S.T. Purcell, J. Mag. Mat., **104-107**, 1734 (1992).
6. J.C. Slonczewski, Phys. Rev. Lett , **67** , 3172 (1991)
7. J.F. Bobo et al., these proceedings
8. S. Andrieu, M. Piecuch, H. Fischer, J.F. Bobo, F. Bertran, Ph. Bauer, M. Hennion, J. Mag. Mat., **121**, (1993), 30
9. S. Andrieu et al., these proceedings
10. S. Lovesey, Theory of neutron scattering from condensed matter Clarendon press- Oxford (1984)
11. M. Piecuch and L. Nevot, in Metallic Multilayers, edited by A. Chamberod and J. Hillairet (Material science Forum) **59-60**, 93 (1990))

Section A—Multilayers and Surfaces

PART IV

Interlayer Coupling II

Electronic States in Magnetic Quantum Wells

J. E. ORTEGA*, F. J. HIMPSEL*, G. J. MANKEY**, and R. F. WILLIS**

*IBM T. J. Watson Research Center, P.O. Box 218 Route 134, Yorktown Heights, NY 10598, USA

**Physics Department, Penn State University, University Park, PA 16802

ABSTRACT

We have searched for the electronic states that mediate oscillatory magnetic coupling in superlattices, and have found strong evidence that these are quantum well states, which are created by quantizing the momentum of s,p-band states perpendicular to the interfaces. The quantum well picture also explains how quantum well states in noble metals become spin-polarized, due to a spin-dependent electron reflectivity at the interface with the ferromagnet. The resulting implications for magnetoresistance are discussed.

MAGNETIC COUPLING VIA QUANTUM WELL STATES

Magnetic multilayers have become very popular recently since they exhibit a "giant" magnetoresistance, which has an impact on the development of magnetoresistive reading heads in magnetic storage.¹⁻⁶ Here we explore the nature of the electronic states that mediate magnetic coupling across a non-magnetic spacer layer. In this first section we will provide evidence that these are quantum well states, confined to the spacer layer by Bragg reflection at the interfaces. In the second section the implications of the quantum well model onto magnetoresistance will be discussed, in particular the spin dependent interface reflectivity that is a natural consequence of the model.

One of the strong clues of a connection between magnetic coupling and quantum well states is shown in Fig. 1. It compares magnetic oscillations^{7,8} with oscillations in the density of states at the Fermi level, found by inverse photoemission.^{9,10} Both exhibit the same periodicity of about 6 layers. The oscillations in the density of states are due to thickness-dependent quantum well states crossing the Fermi level, as shown in Fig. 2.^{9,10} Here we have plotted a series of inverse photoemission spectra, taken for Cu films on fcc Fe(100) at thickness intervals of about two monolayers (the exact thickness can be read from Fig. 1, top curve). These spectra represent the density of unoccupied electronic states at a momentum parallel to the surface $k^{\parallel} = 0$. Compared to the bulk spectrum of Cu(100) top we find that the s,p-band continuum has been discretized into several quantum well states in the thin films. This is exactly what one expects theoretically, as shown in Fig. 3. Looking at the band structure of Cu(100) at $k^{\parallel} = 0$ we find a continuum up to the band edge at X'_4 , given by the $E(k^{\perp})$ dispersion of the s,p-band (line in Fig. 3, bottom). For a thin film this continuum is expected to split up into a number of discrete states (numbered dots in Fig. 3, bottom). This effect may be viewed as a quantization of the momentum perpendicular to the film, k^{\perp} , due to the matching conditions for the wavefunction at the confining interfaces (Fig. 3, top). Roughly-speaking, a discrete number of half-periods of the so-called envelope function¹¹ has to fit between the interfaces. From this picture it is straightforward to qualitatively predict the movement of these dis-

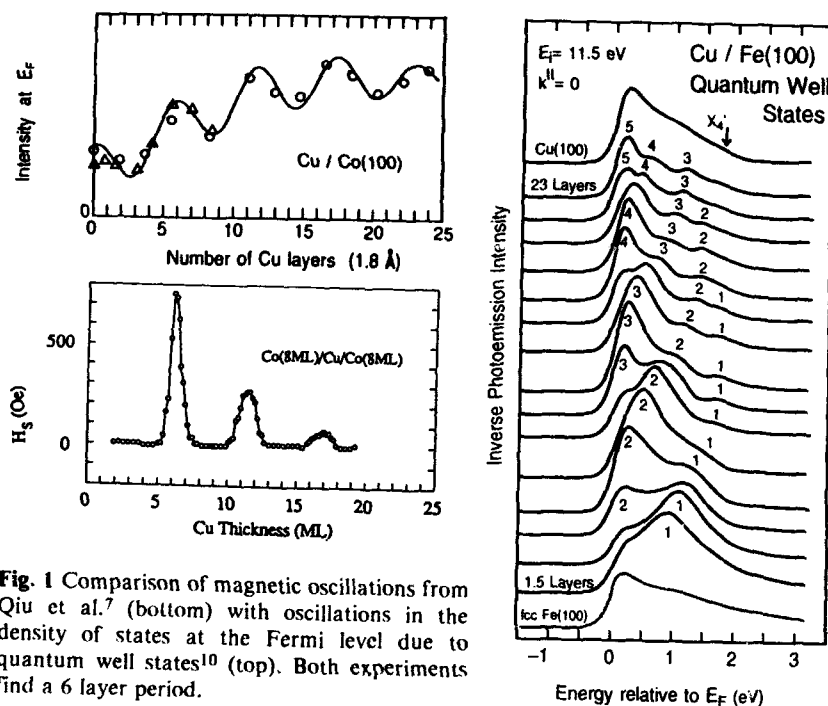


Fig. 1 Comparison of magnetic oscillations from Qiu et al.⁷ (bottom) with oscillations in the density of states at the Fermi level due to quantum well states¹⁰ (top). Both experiments find a 6 layer period.

Fig. 2 Inverse photoemission spectra for Cu/fcc Fe(100) versus thickness, showing discrete quantum well states (numbered, Ref. 10). The thickness increments are about 2 layers (see circles in the curve of Fig. 1).

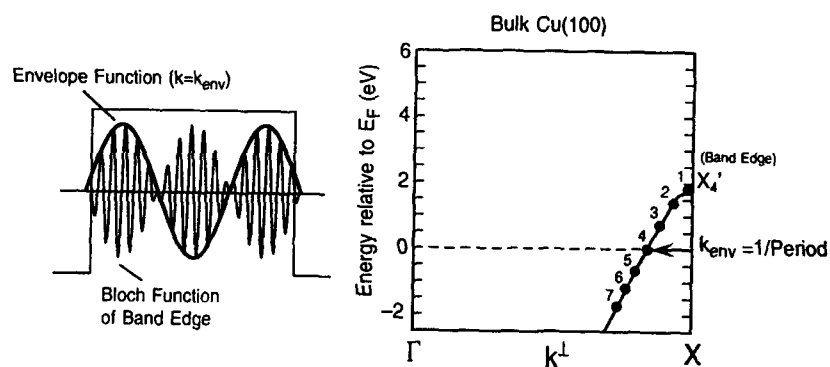


Fig. 3 Wavefunction of quantum well states, consisting of a fast-oscillating Bloch function from the nearest band edge and an envelope function. The latter determines the period in the density-of-states oscillations in Fig. 1. Its wavevector is given by the distance of the Fermi wavevector from that of the band edge.

crete quantum well states with film thickness. If we number the states from the top down, as done in Figs. 2 and 3, we find that all the states appear to move towards the band edge at X'_4 . The reason is that the number of discrete quantum well states per band goes up as the number of layers in the film, therefore reducing their spacing. With the adopted numbering scheme all states will have a tendency of moving towards the upper band edge, with new states appearing at the bottom of the band. As these states cross the Fermi level with increasing film thickness they cause the periodic maxima in the density of states that are shown in Fig. 1. The periodicity of these maxima is directly related to the Fermi wave vector, as indicated in Fig. 3, bottom (for a collection of the rather simple formulas relating Fermi surface parameters to quantum well state energies and periodicities see Ref. 10). The units work out such that a period of 6 layers (as in Cu(100)) corresponds to a wavevector k_{env} of $1/6$ of the Brillouin zone boundary. Thus, the unexpected, long period is explained by the fact that the Fermi level crossing of the s,p-band is close to the band edge at X , which is the origin for k_{env} in the quantum well picture.^{10,11} This conclusion is identical with the results of RKKY theory, which predicts that the oscillation period is given by extremal Fermi surface spanning vectors perpendicular to the interface.¹² These spanning vectors are exactly twice the wavevector of the envelope function, k_{env} , and the factor of two reflects the fact that we get a quantum well state for ever half-period of the envelope function. A path for connecting the quantum well picture with RKKY and similar theories has been pointed out in Ref. 13. Essentially, one has to integrate over all occupied quantum well states and minimize the total energy. Quantum well states that cross the Fermi level with changing thickness become decisive in the energy balance.

This simple quantum well model is consistent with the magnetic periodicities and with RKKY predictions for all systems where data on quantum well states and magnetic oscillations exist. We have seen quantum well states at the Fermi level of Cu/fcc Co(100) and Cu/fcc Fe(100) with a period of 5.9 layers, and for Ag/bcc Fe(100) with a period of 5 layers. The magnetic oscillations periods reported^{7,8} for Cu/Co(100) and Cu/Fe(100) in the fcc phase are also about 6 layers. An additional, shorter period of 2.6 layers has been reported on one occasion.⁸ Both periods are expected from RKKY theory,¹² the long one from states at $k^{\parallel} = 0$, the short one from states at large k^{\parallel} . In our quantum well state picture we have the same physics, with quantum well states at $k^{\parallel} = 0$ giving the long period, and quantum well states at large k^{\parallel} the short period.¹⁰ The latter are not detected in our measurement geometry, which is restricted to $k^{\parallel} = 0$. Recent magnetic measurements on the Ag/Fe(100) system¹⁴ indicate equally as good an agreement with the quantum well state oscillations as for Cu/Co(100) and Cu/Fe(100). Again, there is a long period (5.7 layers) and a short period (~4 layers) with the long period corresponding to the quantum well state oscillations at $k^{\parallel} = 0$. The situation is the same as for Cu(100) spacers, since the Fermi surfaces of Cu and Ag are similar near the [100] direction. This can be seen from the de Haas van Alphen Fermi wave vectors of $0.827k_{\text{ZB}}$ for Cu and $0.819k_{\text{ZB}}$ for Ag (k_{ZB} is the wavevector of the Brillouin zone boundary along the [100] direction), which give rise to periods of $1/(1-0.827) = 5.8$ layers for Cu(100) and $1/(1-0.819) = 5.5$ layers for Ag(100).

An important property of quantum well states in magnetic multilayers is their spin-polarization. As explained in more detail elsewhere,^{9,10} quantum well states become spin-polarized by a spin-dependent electron reflectivity at the interface to the ferromagnet. A particularly clear case is Ag/bcc Fe(100), where the minority spin quantum well states in the Ag film are totally reflected at the interface since there are

no states of the same symmetry and spin available in the Fe(100) substrate. The majority spin states in the Ag film, on the other hand, are able to propagate across the interface into bulk states of the Fe substrate, and therefore do not become quantized. The more popular Cu/fcc Co(100) system is not so simple, since states of both spin can propagate from one s,p-band into the other across the interface. Band calculations of the spin-dependent reflectivities are required in this case to obtain the spin-polarization of the observed quantum well states.

After observing quantum well states in the s,p-bands of noble metal spacer layers the question arises whether or not the d-bands of transition metal spacer layers quantize as well. In RKKY theory they should contribute and add extra oscillation periods to the s,p-like periodicities. The latter are rather uniform across the periodic table for a given crystal orientation, which might explain the "universal" periodicity of about 10 Å seen for many systems.¹⁵ In the quantum well picture the d-like parts of the Fermi surface should also quantize, but the energy spacing between quantum well states is going to be smaller (due to the smaller dispersion of d-bands), and their lifetime broadening is increasing (due to the higher density of states available for electron hole pair formation). Therefore, adjacent quantum well states may merge into a bulk-like continuum. We have searched for d-like quantum well systems in a variety of systems (Ru/Co(0001), Cr/Fe(100)), and have found it difficult to discern

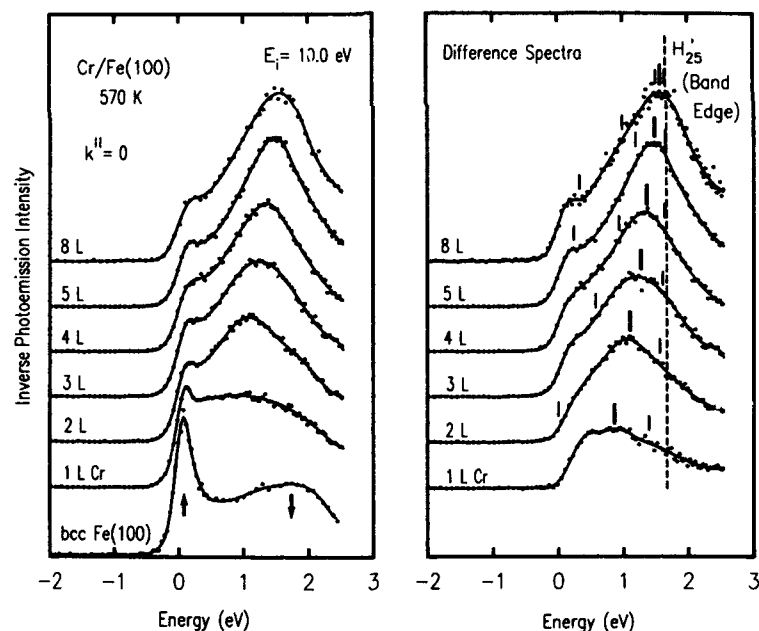


Fig. 4 Inverse photoemission spectra for Cr/Fe(100) grown at 570K, showing the band that contributes strongly to antiferromagnetic coupling (see Fig. 5). Quantum well states calculated from the model in Ref. 10 with estimated phase shifts¹⁹ are shown as thin tickmarks. For the difference spectra the Fe substrate contribution was subtracted, using an attenuation length of two layers that fits the intensity decay at the Fermi level.

discrete states. The main problem so far appears to be not the fundamental lifetime limit outlined above, but the difficulty in producing highly-perfect, flat films, which are necessary to see the short periodicities expected from many transition metal systems. As an example we show data from Cr/Fe(100) in Fig. 4, where a variety of experiments have demonstrated a short, two-layer period reminiscent of antiferromagnetic Cr.¹⁶ This periodicity can be understood in the quantum well picture in a fashion very similar to the arguments¹⁷ given for the bulk antiferromagnetism of Cr (Fig. 5, Ref. 18). There is a pair of d-bands that give nearly identical wavevectors k_{env} for the envelope wavefunctions over a large portion of k^{\parallel} -space. The k_{env} vectors originate in this case from the band minima (dots in Fig. 5), which have a nearly constant spacing from the corresponding Fermi level crossings (lines in Fig. 5). The length of the k_{env} vectors is about half of the Brillouin zone boundary, corresponding to a two layer period. Using the simple model from Ref. 10 we expect majority spin quantum well states at the fine tick marks in Fig. 4.¹⁹ The inverse photoemission data in Fig. 4 show only a single, broad peak (fat tickmarks). It moves upwards with increasing Cr thickness, following roughly the average between the first and second calculated quantum well states. The upwards movement towards the band edge at H'_{25} is analogous to the result for Cu / fcc Fe(100) in Fig. 2. The absence of higher quantum well states in Cr / bcc Fe(100) is probably due to imperfections in the Fe(100) substrate crystal, which lead to inhomogeneous broadening. Highly perfect Fe whiskers might be required to resolve the expected quantum well states, similar to the ones used in the experiments that showed the magnetic oscillations so clearly.¹⁶ Alternatively, there could be additional quantum well states with opposite (minority) spin that fill in between the majority spin states in Fig. 4.

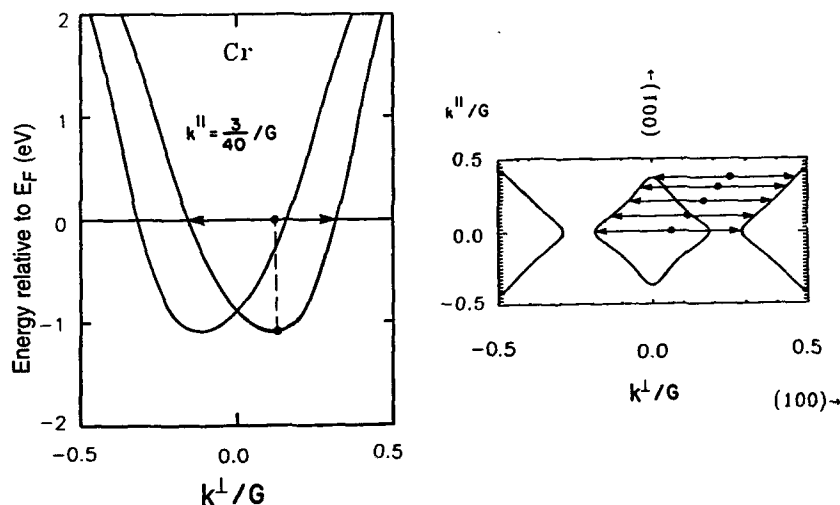


Fig. 5 A portion of the Fermi surface of Cr and the corresponding bands that give rise to antiferromagnetic coupling (from a band calculation by Stiles¹⁸). In the quantum well picture, a magnetic oscillation period of two layers corresponds to envelope wave vectors with a length of half the Brillouin zone boundary momentum (arrows).

MAGNETORESISTANCE

While the magnetic coupling is rather straightforward to explain, either by quantum well states or by RKKY theory, the magnetoresistance is a much more complex phenomenon. To tackle the problem in its full generality requires some 20 parameters,²⁰ whose microscopic origin is sometimes difficult to pinpoint. Instead of treating the problem fully we will focus on phenomena that can be traced directly to the electronic structure. In particular, we will explore how the concept of quantum well states might play a role in explaining giant magnetoresistance. The geometry shown in Fig. 6 is that of a typical trilayer structure. For simplifying the arguments, we take the current perpendicular to the interfaces, as in the experiments of Ref. 21. This differs from most magnetoresistive structures used to date, where the current runs parallel to the layers in order to avoid extremely low resistances. There are indications that the perpendicular geometry reflects the effect in purer form, since it exhibits 3 to 10 times larger magnetoresistance than the parallel geometry for the same combination of materials²¹. This can be rationalized by noticing that, in the parallel geometry, the electrons have to be scattered back and forth between the two magnetic layers in order to sample their relative magnetizations, while they are forced through both layers in the perpendicular geometry. Therefore, additional parameters, such as interface roughness and disorder have been invoked in a number of theories to explain magnetoresistance in the parallel geometry.

Fig. 6 schematically shows a bulk and an interface effect. They both contribute to magnetoresistance, but they may not be the whole story. The bulk effect is based on the shorter mean free path for electrons of minority spin compared to majority spin electrons (dashed versus full arrows in Fig. 6). In a spin valve structure, where

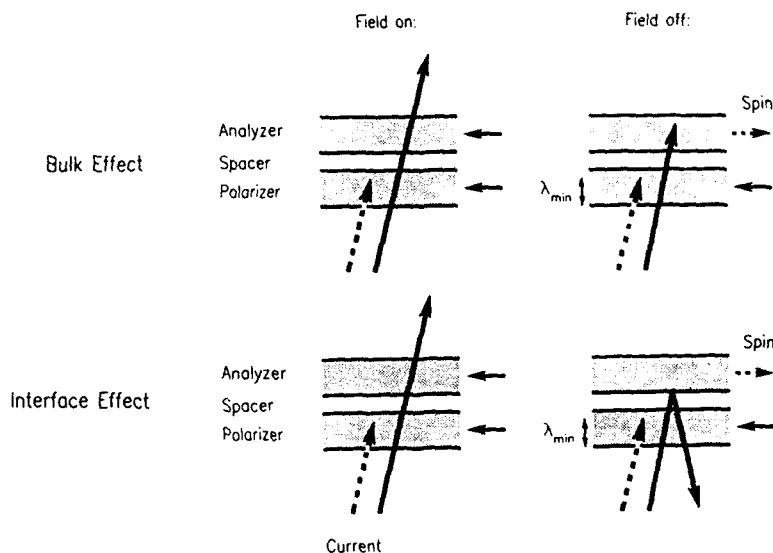


Fig. 6 Two possible effects contributing to the giant magnetoresistance in a spin valve. The bulk effect is based on the shorter mean free path for minority spins, the interface effect is caused by preferential Bragg reflection of minority electrons at the interface.

two magnetic layers are separated by a non-magnetic spacer, an unpolarized current becomes polarized in the majority spin direction after passing the first layer, because more minority spin electrons are absorbed than majority spin electrons. The second magnetic layer then acts as an analyzer, suppressing the injected current if it is antiferromagnetically coupled and transmitting it if aligned ferromagnetically by an external field. Therefore one observes a reduction of the resistance. In order to achieve maximum spin-polarization the magnetic material has to be as thick as the mean free path λ_{min} of minority spin electrons, typically in the 100Å range²¹. The physics of the shorter mean free path for minority spin electrons lies in their band structure. While the majority spin d-bands are filled in ferromagnets, such as Co and Ni, the minority spin d-bands straddle the Fermi level and produce a high density of states that can scatter minority spin electrons by creating electron-hole pairs. (Note that we assume spin-conservation in the scattering process, i.e., the spin-flip scattering length is large compared to all the length scales considered here.) The majority spin electrons see a bandstructure akin to that of a noble metal, with its much longer mean free path. The spin-dependent mean free paths result in typical ratios of 3:1 for the spin-dependent bulk resistances, as extracted from perpendicular magnetoresistance measurements in multilayers.²¹ Even at the vacuum level, i.e. several eV above the Fermi level, the mean free path is still about 20% longer for majority spins than minority spins²².

While the bulk magnetoresistance effect is due to the spin dependence of inelastic scattering, the interface effect shown in Fig. 6 involves elastic scattering. Again, the electron current is first polarized by the first magnetic layer, but then it is analyzed by spin-dependent Bragg-reflection from the second magnetic layer. Such a spin-dependent reflectivity was encountered for Ag/bcc Fe(100) (see above and Refs. 9, 10). In this case minority spin states were totally reflected and thus confined to quantum well states, whereas majority spin electrons kept propagating across the interface. It is not clear yet whether this is a general phenomenon. At least in the case of Ag/Fe(100) it gives rise to a large, yes-or-no effect in the electron transmission across the interface. This may explain the large interface effects found in the analysis of magnetoresistance measurements, e.g. a strong sensitivity of magnetoresistance to additional interface layers⁴ and ratios as high as 12:1 for the interface resistances of minority and majority spins²¹. It should be noted that this spin-dependent Bragg reflection coefficient is really a property of the bulk band structure of the ferromagnet, i.e. it depends on the existence of bulk states in the ferromagnet that match the energy, momentum and spin of the incoming electrons. Despite the crucial role of bulk band gaps, the actual reflection of the electron wave function takes place in a very narrow region at the interface. The width of this region is determined by the imaginary part of the perpendicular momentum k^{\perp} , which describes the decay of the evanescent wavefunction into the ferromagnet. It is given by the energy distance ΔE from the nearest band edge, and takes on the simple form $\text{Im}(k^{\perp}) = \sqrt{2m\Delta E}/\hbar = 0.51\text{\AA}^{-1}\sqrt{\Delta E/\text{eV}}$ for a free electron. Putting in a typical energy offset $\Delta E = 1\text{eV}$ we obtain a decay constant $1/\text{Im}(k^{\perp}) = 2\text{\AA}$, which is comparable to the decay constants of 1.5-3Å reported from magnetic interlayer experiments.⁴ (For the example Ag/bcc Fe(100) we have $\Delta E = \Gamma_{121} - E_{\text{F}} = 1.5\text{eV}$).²³

In the future it would be interesting to explore geometries with the current perpendicular to the interfaces in order to produce higher magnetoresistance, as in Ref. 21. In order to avoid extremely low resistivities and superconducting technology, one could try alternating stripes of magnetic and non-magnetic materials, with the current parallel to the thin film but perpendicular to the stripes. In order to get stripes with

well-defined width, e.g. 5, 12, or 17 atomic layers for the antiferromagnetic coupling maxima in Cu/Co, one could use stepped, high-index surfaces as substrates, where the step spacing determines the stripe width.

Acknowledgement We would like to acknowledge M. D. Stiles for providing the band calculation results on Cr shown in Fig. 5.

REFERENCES

1. M. N. Baibich, J. M. Broto, A. Fert, F. Nguyen van Dau, F. Petroff, P. Etienne, G. Creuzet, A. Friederich and J. Chazelas, *Phys. Rev. Lett.* **61**, 2472 (1988).
2. G. Binasch, P. Grünberg, F. Saurenbach, and W. Zinn, *Phys. Rev. B* **39**, 4828 (1989).
3. S. S. P. Parkin, N. More, and K. P. Roche, *Phys. Rev. Lett.* **64**, 2304 (1990); S. S. P. Parkin, R. Bhadra, and K. P. Roche, *Phys. Rev. Lett.* **66**, 2152 (1991).
4. S. S. P. Parkin, *Appl. Phys. Lett.* **61**, 1358 (1992) and to be published.
5. B. Dieny, P. Humbert, V. S. Speriosu, S. Metin, B.A. Gurney, P. Baumgart, and H. Lefakis, *Phys. Rev. B* **45**, 806 (1992).
6. For an overview see: Chapter "Recording Heads" by R.E. Jones and C.D. Mee, in "Magnetic Recording: Volume 1: Technology", ed. by C. Denis Mee and E.D. Daniel, McGraw Hill 1987, p.244.
7. Z. Q. Qiu, J. Pearson, and S. D. Bader, *Phys. Rev. B* **46**, 8659 (1992).
8. M. T. Johnson, S. T. Purcell, N. W. E. McGee, R. Cochoorn, J. aan de Stegge, and V. Hoving, *Phys. Rev. Lett.* **68**, 2688 (1992); see also J. J. de Miguel, A. Cebollada, J. M. Gallego, R. Miranda, C. M. Schneider, P. Schuster, and J. Kirschner, *J. Magn. Magn. Mater.* **93**, 1 (1991); F. Petroff, A. Barthélemy, D. H. Mosca, D. K. Lottis, A. Fert, P. A. Schroeder, W. P. Pratt, Jr., and R. Loloee, *Phys. Rev. B* **44**, 5355 (1991); W. R. Bennett, W. Schwarzacher, and W. F. Egelhoff, *Phys. Rev. Lett.* **65**, 3169 (1990).
9. J. E. Ortega and F. J. Himpsel, *Phys. Rev. Lett.* **69**, 844 (1992); see also F. J. Himpsel, *Phys. Rev. B* **44**, 5966 (1991).
10. J. E. Ortega, F. J. Himpsel, G. J. Mankey, and R. F. Willis, *Phys. Rev. B* **47**, 1540 (1993) and *J. Appl. Phys.* **73**, May 15 (1993).
11. G. Bastard, *Wave Mechanics Applied to Semiconductor Heterostructures* (Les Editions de Physique, Les Ulis, France, 1988), Chap. III.
12. See, e.g. P. Bruno and C. Chappert, *Phys. Rev. Lett.* **67**, 1602 (1991), and *ibid* **67**, 2592 (1991).
13. D.M. Edwards, J. Mathon, R.B. Muniz, and M.S. Phan, *Phys. Rev. Lett.* **67**, 493 (1991) and *J. Phys. Condens. Matter* **3**, 4941 (1991); M.D. Stiles, to be published.
14. J. Unguris, R. J. Celotta, and D. T. Pierce, *J. Appl. Phys.*, in press; Z. Celinski, B. Heinrich, and J. F. Cochran, *J. Appl. Phys.*, in press.
15. S. S. P. Parkin, *Phys. Rev. Lett.* **67**, 3598 (1991).
16. P. Grünberg, R. Schreiber, Y. Pang, M. B. Brodsky, and H. Sowers, *Phys. Rev. Lett.* **57**, 2442 (1986); J. Unguris, R. J. Celotta, and D. T. Pierce, *Phys. Rev. Lett.* **67**, 140 (1991); J. Unguris, R. J. Celotta, and D. T. Pierce, *Phys. Rev. Lett.* **69**, 1125 (1992); P. Grünberg, S. Demokritov, A. Fuss, R. Schreiber, J.A. Wolf, and S.T. Purcell, *J. Magn. Magn. Mat.* **104-107**, 1734 (1992).

17. W. Koehler, R. M. Moon, A. L. Trego, and A. R. Mackintosh, *Phys. Rev. Lett.* **151**, 405 (1966); E. Fawcett, *Rev. of Mod. Phys.*, **60**, 209 (1988).
18. The band calculation results are from M. D. Stiles, private communication.
19. In order to calculate the quantum well state energies with the formulae in Ref. 10 we used an empirical band structure, matched to the Fermi surface and to our inverse photoemission value of 1.7eV for the H'_{25} point of Cr. For the phase we used the phase shift from Ag/Fe(100) in Ref. 10, which, strictly speaking, applies to states of a different symmetry. Therefore, the absolute positions of the calculated quantum well states are unreliable, but their spacing is insensitive to the phase.
20. A. Barthelemy and A. Fert, *Phys. Rev. B* **43**, 13124 (1991); R. Q. Hood and L. M. Falicov, *Phys. Rev. B* **46**, 8287 (1992).
21. W. P. Pratt, Jr., S.-F. Lee, J. M. Slaughter, R. Loloee, P. A. Schroeder, and J. Bass, *Phys. Rev. Lett.* **66**, 3060 (1991); S. F. Lee, W. P. Pratt, Jr., R. Loloee, P. A. Schroeder, and J. Bass, *Phys. Rev. B* **46**, 548 (1991); W.P. Pratt, Jr, S.-F. Lee, P. Holody, Q. Yang, R. Loloee, J. Bass, and P.A. Schroeder, to be published.
22. D.P. Pappas, K.-P. Kämper, B.P. Miller, H. Hopster, D.E. Fowler, C.R. Brundle, A.C. Luntz, and Z.-X. Shen, *Phys. Rev. Lett.* **66**, 504 (1991); H.C. Siegmann, *J. Phys. Condens. Matter* **4**, 8395 (1992).
23. A. Santoni and F. J. Himpsel, *Phys. Rev. B* **43**, 1305 (1991).

QUANTUM WELL STATES IN Fe(100) ULTRATHIN FILMS OBSERVED BY MAGNETO-OPTICAL EFFECT

Yoshishige Suzuki* and Toshikazu Katayama

Electrotechnical Laboratory, Umezono 1-1-4, Tsukuba, Ibaraki 305, Japan.

*National Institute for Advanced Interdisciplinary Research, Higashi 1-1-4, Tsukuba, Ibaraki 305, Japan.

ABSTRACT

We report on the magneto-optical Kerr rotation(ϕ_K) spectra of ultrathin Fe films on Au or Ag (100) substrates and the ϕ_K oscillation due to interlayer thickness in Fe/Au/Fe sandwich films. In 3.5-4.5 eV, a new ϕ_K peak appears in the bcc-Fe(100) ultrathin films on the fcc-Au(100) surface and it shifts towards the higher energy side with increasing Fe layer thickness. The absolute value of ϵ_{xy} for 3Å(2ML) thick Fe layers is twice as large as that of bulk Fe at 3.7 eV. The thickness dependence of the transition energy of this new peak in the spectra is well explained by the concept of quantum well states in the Fe ultrathin layers, attributing the new transition to a transition from the majority spin Δ_5 band ($\{p_x \pm i p_y\}, \{d_{xz} \pm i d_{yz}\}; m=\pm 1$) to the Δ_1 quantum well states ($s, p_z, d_{z^2}; m=0$). The new peak is also observed in the Fe/Au(100) artificial superlattices. Using the ϵ_{xy} obtained experimentally for the Fe ultrathin films and the ϵ_{xx} of literature, we can reproduce the experimental ϕ_K spectra of the artificial superlattices by optical calculation. On the other hand, we cannot observe the same behavior for the ultrathin Fe films grown on a fcc-Ag(100) surface and covered by a Au(100) ultrathin film, although the ϵ_{xy} of Fe is different from that of the bulk and shows some structures in 2-3 eV. These structures around 2.5 eV are thought to be due to polarized Au atoms adjacent to an Fe layer.

An oscillation of ϕ_K as a function of interlayer thickness, d , was observed in photon energy region between about 2.5 and 3.8 eV for the Fe(6Å)/Au(d Å)/Fe(6Å) sandwiched film. The oscillation period was about 10Å (5ML) of Au. The oscillation is thought to be closely related with a formation of spin polarized quantum well states of Δ_1 band in Au layers sandwiched by magnetic layers.

1. INTRODUCTION

In this decade, a considerable attention has been focused to 3d-ferromagnetic transition metal/noble metal multilayers, because they have a novel potential to provide a method to control a band structure of magnetic materials and then new interesting phenomena like giant magnetoresistance [1] and oscillating interlayer exchange coupling [2]. Many theoretical and experimental works have been done on the electronic structures of 3d-magnetic ultrathin

films[3-7]. Measurements of magneto-optical (M-O) effect is very sensitive and useful method [8-10]. Especially, a spectroscopic measurement of magneto-optical effects can provide an information on magnetic band structures. However, only a few works have been done in the field of the spectroscopy of the magneto-optical effect of ultrathin ferromagnetic films[11].

Recently, we have found a new magneto-optical transition in the ultrathin films of bcc-Fe deposited on the Au (100) plane [12]. The new peak in the ϕK spectra appears in the thickness range between 2 and 10 Å and shifts from about 2.9 to 4.3 eV with increasing Fe layer thickness. Meanwhile, Himpsel observed a formation of quantum well states for the Fe ultrathin layers embedded on the Au(100) using inverse photoemission spectroscopy (IPES) [6]. By taking into account this result, the new ϕK peaks could be explained by a formation of quantum well states in the Fe (100) layers[13].

On the other hand, Bennett *et al.* reported an oscillation behavior of the saturation Kerr rotation with a change of the Cu interlayer thickness, d , in the Fe/Cu(d Å)/Fe sandwiched films [9]. However, since their measurements were performed at only one wavelength(633nm), no electronic contributions to magneto-optical properties have been discussed. While Brooks *et al.* and Ortega *et al.* have also reported a formation of quantum well states in ultrathin noble metal layers which were deposited on magnetic films[7]. This phenomenon is worth to notice because such confined states with spin polarization around Fermi surface can be a mediator of the oscillating interlayer exchange coupling [7,14].

In this paper, we report on the spectroscopic studies of magneto-optical polar Kerr effect in the several kinds of samples which contain Fe ultrathin layers. For the bcc-Fe(100) ultrathin films grown on the fcc-Au(100) and the fcc-Ag(100) surfaces, we will discuss the formation of quantum well states in the Fe ultrathin layers. For the Fe/Au(100) artificial superlattices, we report also a formation of quantum well states in the Fe layers and discuss on the role of Au barriers. Finally, we report on the behavior of saturation magneto-optical polar Kerr rotation spectra and its oscillation due to the interlayer thickness, d , in Fe/Au(d Å)/Fe sandwiched films.

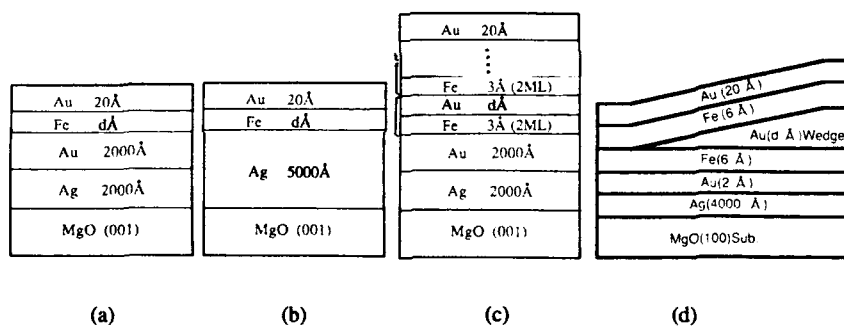


Fig.1 Schematic drawings of cross section of samples. (a) Fe ultrathin film on Au. (b) Fe ultrathin film on Ag. (c) Fe/Au artificial superlattice. (d) Fe/Au/Fe sandwiched film.

II. EXPERIMENTAL PROCEDURES

All the samples were deposited by means of a molecular beam epitaxy (MBE) technique using electron gun sources for Fe and Au and a Knudsen cell for Ag. During the deposition, the vacuum in the MBE chamber was in the range of 10^{-10} Torr. A (100) cleaved MgO single crystal was used as a substrate. After a thermal flashing of the substrate at 900°C, a fcc-Ag(100) buffer layer of 2000Å was deposited on the substrate at room temperature (R.T). This Ag buffer layer was annealed at 450°C for 1 minute. After cooling down to R.T, Fe ultrathin films, Fe/Au artificial superlattices, and Fe/Au/Fe sandwiched films were deposited at room temperature (see Fig.1). A fcc-Au(100) seed layer of 2000Å thick was deposited for the case of Fe ultrathin films on Au(100) and Fe/Au artificial superlattices. The Au seed layer was annealed at 350°C for 1 minute. For the case of Fe/Au/Fe sandwiched films, 2 or 4Å thick Au seed layers were used. All the samples were covered by 20Å thick Au layer to prevent oxidation. In Fe/Au/Fe sandwiched films, a wedge-shaped Au layer was prepared for the accurate measurements of the nonmagnetic interlayer thickness dependence of the Kerr rotation. The wedge layers were formed by means of a moving shutter method.

The thicknesses and growth rates (0.1-0.2 Å/sec) of Fe and Au films were measured and controlled by quartz thickness monitors (INFICON IC-6000) combined with a shutter system. The growth modes were monitored by an observation of reflective high energy electron diffraction (RHEED) patterns and its oscillations.

Saturation polar Kerr rotation (ϕ_K) spectra at room temperature were measured with a Kerr rotation spectrometer using a Faraday modulator (JASCO J-250) in the photon energy range from 1.55 to 5.3 eV. The incident angle of light was 10 degree from normal to the sample plane. Kerr ellipticity (η_K) spectra were calculated from the ϕ_K spectra using Kramers-Kronig (K-K) relation [15]. In the calculation, the integration was only performed in the measured range and no extrapolation was used. Off-diagonal elements of the dielectric tensor (ϵ_{xy}) in Fe layers were calculated using the values of diagonal elements of the dielectric tensor (ϵ_{xx}) of literature [16,17] and under the assumption of no ϵ_{xy} in noble metal layers.

III. M-O EFFECT IN ULTRATHIN FILM AND SUPERLATTICE

In general, the magneto-optical properties are expressed by the dielectric tensor, ϵ , of the materials. For the materials with cubic symmetry and a magnetization normal to the film surface,

$$\epsilon = \begin{pmatrix} \epsilon_{xx} & \epsilon_{xy} & 0 \\ -\epsilon_{xy} & \epsilon_{xx} & 0 \\ 0 & 0 & \epsilon_{zz} \end{pmatrix}, \quad (1)$$

in which z-axis parallel to the magnetization. The polar Kerr effect for a normal incidence is expressed as [18],

$$\phi_K + i\eta_K = \frac{\epsilon_{xy}}{(1 - \epsilon_{xx})\sqrt{\epsilon_{xx}}}, \quad (2)$$

where ϕ_K Kerr rotation and η_K Kerr ellipticity. For the artificial superlattices with a period much shorter than wavelength of the incident light, the complex Kerr rotation, $\phi_K + i\eta_K$, is described also by the equation (2), using effective dielectric constants, $\langle\epsilon_{xx}\rangle$ and $\langle\epsilon_{xy}\rangle$. From the classical electromagnetic calculation, the effective dielectric constants should be an average of each dielectric constant weighted by their thicknesses[19].

$$\langle\epsilon\rangle = \frac{d_1 \cdot \epsilon_1 + d_2 \cdot \epsilon_2 + \dots}{d_1 + d_2 + \dots} \quad (3)$$

From equation (3), it is clear that complex Kerr spectra should be identical for the all artificial superlattices of the same composition but of different period, if there is no change in electronic structure.

The complex Kerr rotation for the ultrathin films ($d \ll \lambda$) is [12],

$$\phi_K + i\eta_K = i \frac{4\pi d}{\lambda} \frac{\epsilon_{xy}}{1 - \epsilon_{xx}^S}, \quad (4)$$

where d thickness of a magnetic layer, λ wavelength of the incident light, and ϵ_{xx}^S dielectric constant of the substrate. If there is no change in the electronic structure, normalized complex Kerr rotation, $(\phi_K + i\eta_K)/d$, should not be affected by a change in thickness of a magnetic layer.

IV. EXPERIMENTAL RESULTS AND DISCUSSIONS

IV-1. Fe(100) ultrathin films on Au

Fig.2 (a) and (b) shows the changes of the (a) ϕ_K and (b) η_K spectra for several Fe layer thicknesses, d , in the Fe ultrathin films grown on the Au(100) surfaces (see Fig.1 (a)). The vertical axis means a normalized value of ϕ_K or η_K by the Fe film thickness. A large negative peak of the Kerr rotation spectrum at 2.5 eV is observed in all the samples, which is due to coupled plasma edge of Au. At this energy, the denominator of the equation (2) has a local minimum and enhances Kerr rotation optically. This phenomenon, so called "plasma enhancement effect," was first pointed out for a bulk material[20] and then multilayers[11].

A new ϕ_K peak appears in 3.5-4.5 eV for the Fe films thinner than 10 Å and shifts toward

higher energy's side with increasing Fe layer thickness. Using equation (4) and dielectric constants of bulk Au [16], off-diagonal element of dielectric tensor of Fe ultrathin films can be calculated. Fig.3 shows absolute value of the off-diagonal dielectric constants, ϵ_{xy} , of the Fe ultrathin films. The ϵ_{xy} spectra show a peak at around 4 eV. For a 10 Å thick Fe, a new peak appears at 4.5 eV. A peak is also observed at the same energy for a 7 Å thick Fe layer. It shifts to lower energy side for Fe films thinner than 5 Å. The center of the peak for a 3 Å thick Fe is about 3.6 eV. The absolute value of ϵ_{xy} of 3 Å thick Fe is about two times as large as that of bulk Fe at 3.6 eV. A separate observation of a real part and an imaginary part of ϵ_{xy} shows dispersion type spectra for the real part, absorptive part, and a single peak for the imaginary part [12]. Such dispersion of ϵ'_{xy} indicates a diamagnetic type transition [21] in the materials.

In Fig.4 the energy of the new transition is shown as a function of Fe layer thickness, where the transition energy is determined from the peak position in the spectra of the absolute value of ϵ_{xy} . An energy shift of up to 2 eV is shown. Such a large shift of the energy level of an empty state was observed also for the same system by Himpsel using inverse photoemission spectroscopy (IPES) [6]. He attributed this new state to a Δ_1 quantum well state in the Fe ultrathin layers. Fig. 5 shows band structures of fcc-Au [22] and bcc-Fe [23] along film normal. Since Au has an energy gap of Δ_1 dispersion above the X'_4 point, electronic states in an Fe layer with Δ_1 symmetry can not connect to states in Au layer in this energy gap

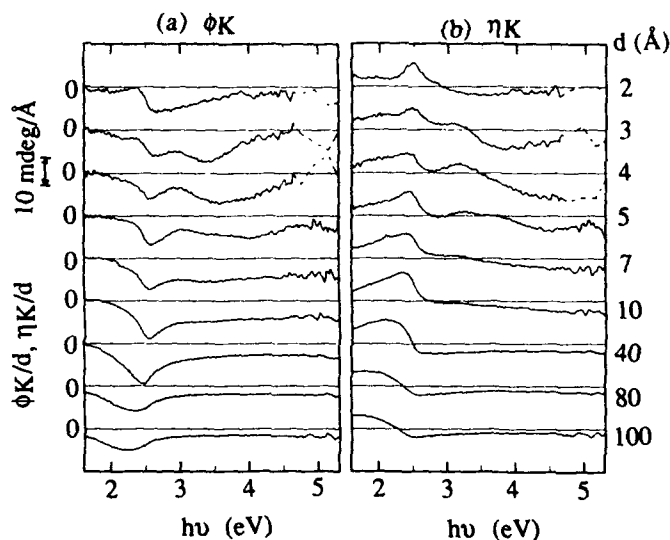


Fig.2 Magneto-optical polar Kerr rotation (ϕ_K) spectra as a function of Fe layer thickness (d) in Au(20Å)/Fe(d Å)/Au(2000Å)/Ag(2000Å)/MgO(100) films at room temperature. (a) Kerr rotation (ϕ_K) spectra, (b) Kerr ellipticity (η_K) spectra. The vertical axis means a normalized values of ϕ_K by the Fe film thickness.

and confined in the Fe layer [6]. The Δ_1 quantum well state is made from s , p_z , and d_{z^2} ($m=0$) orbitals with k -vector near the H point of bcc-bulk Fe [6]. Therefore, only Δ_5 bands ($m=\pm 1$) can be initial states of a dipole transition made by in-plane polarization of the light. Since the minority spin Δ_5 bands are empty for large k_z , only the majority spin Δ_5 bands can contribute to the absorption of the light. The majority spin doubly degenerate Δ_5 band splits into two separate bands corresponding to the angular momentum ($J=3/2, 1/2$) by the spin-orbit interaction, and majority spin Δ_5 to Δ_1 quantum well states transition will yield a diamagnetic-type magneto-optical effect. In Fig. 4, the expected thickness dependence of the transition energy from the majority spin Δ_5 to Δ_1 quantum well state transition is also shown. The characteristics of the Δ_1 quantum well states were obtained from the IPES data [6], and a dispersion of the majority spin Δ_5 bands were taken from the calculated band structure of bulk Fe [23]. The two curves in Fig. 4 have essentially the same properties. The difference between two curves is not large, if we allow experimental errors and some changes of majority spin Δ_5 bands in the ultrathin films. From these results, we can assign the new transition to a transition from majority spin Δ_5 bands to Δ_1 quantum well states in the Fe ultrathin films.

IV-2. Fe/Au Superlattice

Fig 6 shows the Kerr ellipticity spectra of $\text{Fe}(3\text{\AA})/\text{Au}(4\text{\AA})$ and $\text{Fe}(3\text{\AA})/\text{Au}(8\text{\AA})$ artificial superlattices. Both spectra show a single broad peak at 3.8 eV. This energy is close to the

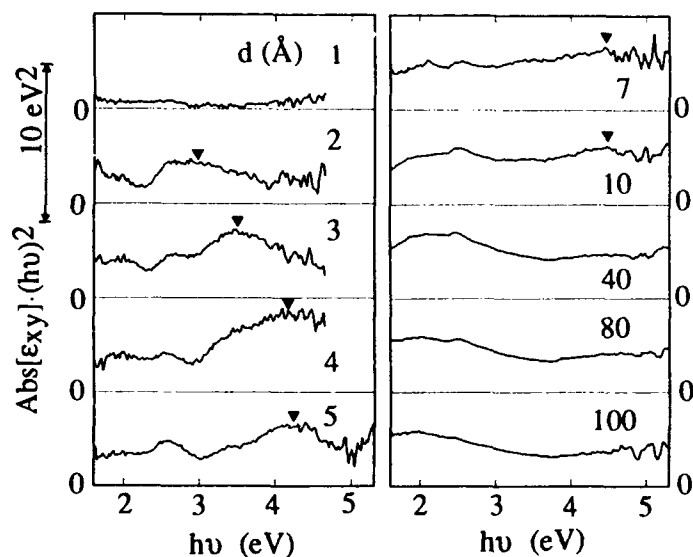


Fig.3 Changes of the spectra of off-diagonal elements (ϵ_{xy}) of the dielectric tensor as a function of Fe layers thickness(d) in $\text{Au}(20\text{\AA})/\text{Fe}(d\text{\AA})/\text{Au}(2000\text{\AA})/\text{Ag}(5000\text{\AA})/\text{MgO}(100)$ films. (a) real part of ϵ_{xy} , (b) imaginary part of ϵ_{xy} .

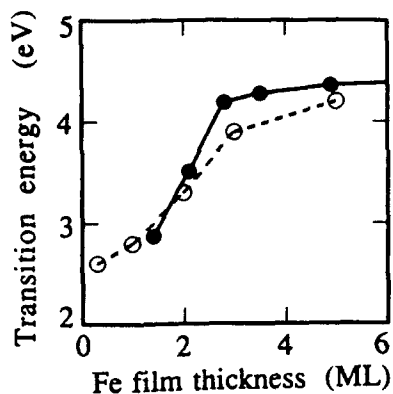


Fig. 4 Thickness dependence of the transition energy observed in the Fe ultrathin films grown on Au(100) (closed circles). Open circles show the transition energy from majority spin Δ_5 [23] to the Δ_1 quantum well state measured by Himpsel [6].

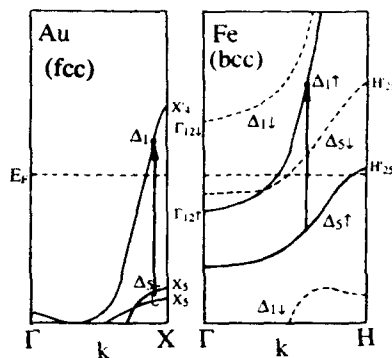


Fig. 5 A schematic drawing of the band structures of bulk bcc-Fe [23] and fcc-Au [22] near the Fermi energy along the film normal.

transition energy for a 3 Å Fe ultrathin film sandwiched by Au, i.e. 3.6 eV. To confirm a contribution of the quantum well states, the Kerr ellipticity spectrum of the Fe(3Å)/Au(4Å) artificial superlattice is examined by optical calculations. In Fig. 7, an experimental ellipticity spectrum of the superlattice is shown with two theoretical curves. Curve A was calculated from equation (2) and (3) using the dielectric constants of bulk Fe [17] and Au [16]. The curve A shows plasma enhancement at 2.5 eV, but does not reproduce an experimental spectrum. The curve B is calculated using the diagonal parts of dielectric tensor of bulk Fe and Au and an experimental off-diagonal element of dielectric constant of 3 Å thick Fe ultrathin films sandwiched by Au that was obtained in section IV-1. The latter curve agrees well with the experimental ellipticity spectrum and indicates an appearance of the quantum well states in Fe/Au artificial superlattices. The transition energies are almost identical for both the artificial superlattices with different Au layer thicknesses. This fact agrees well with a concept of a quantum well states in Fe layers, since those levels are independent from Au layer thicknesses. Only two atomic layers of Au (4 Å) is necessary to work as a barrier of the wells.

IV-3. Fe Ultrathin Films on Ag

In Fig. 8 (a), (b) the changes of ϕ_K and η_K spectra as a function of d in Au(20Å)/Fe(d Å)/Ag(5000Å)/MgO(100) films are shown. A negative large plasma enhanced ϕ_K peak is also observed at 3.8 eV. We can not confirm any new peaks in 3.5-4.5 eV contrary to the Au cases. However, it seems to exist in the 2-3 eV range some ϕ_K structures for the Fe layers thinner than 8 Å. Such kinds of ϕ_K structures were not observed in the Fe

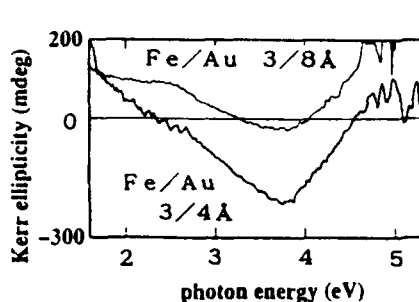


Fig.6 Polar Kerr ellipticity spectra for the Fe(3Å)/Au(dÅ) artificial superlattices.

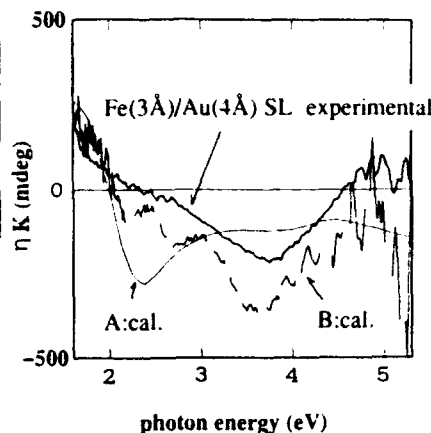


Fig.7. Comparison between experimental polar Kerr ellipticity and two calculations. A: Calculation using dielectric tensor of bulk [16,17]. B: Calculation using diagonal parts of dielectric tensor of bulk [16,17] and off-diagonal part of the 3Å thick Fe ultrathin film obtained here.

layer above 10Å.

In Fig.9 (a), (b) are shown the spectra of real part (ϵ'_{xy}) and imaginary part (ϵ''_{xy}) as a function of d in Au(20Å)/Fe(d Å)/Ag(5000Å)/MgO(100) films. The theoretical ϵ'_{xy} and ϵ''_{xy} spectra of bulk Fe [24] are shown as a composition. The bump in ϵ_{xy} spectra near 3.8 eV is an analytical error caused by an ambiguity of the optical constants of Ag [16]. The whole shape of the ϵ'_{xy} spectrum has a tendency to approach towards that of the bulk Fe with increasing Fe thickness.

To investigate a reason why a new peak at 3.5-4.5 eV does not appear in the Fe on Ag, we measured RHEED intensity during the growth. In Fig.10 the RHEED intensity oscillations during the growth of Fe layer on Au and Ag (100) surfaces are shown. In the case of Fe layer on Au, the RHEED intensity oscillation continues for a long time. On the other hand for the growth of Fe on Ag the oscillation is not so clearly observed. This result suggests that the Fe layer on Ag has a poor layer-by-layer growth different from that of Fe layer deposited on Au, which in turn suggests why the quantum well states are not formed in Fe layer on Ag [13].

The shape of ϵ_{xy} spectra of Fe films less than 8Å deposited on Ag are different from that of Fe bulk state. This suggests that the electronic structure of Fe film less than 8Å is different from that of bulk. In the Fe films thinner than 8Å on Ag, there are some structures of ϵ_{xy} in 2-3 eV. The ϵ_{xy} structure is thought to be related with polarized Au atoms adjacent to the Fe layer from the following two reasons; 1). Schnatterly reported that a magneto-optical transition of polarized Au atoms near the plasma edge where an optical transition between s, p and d bands occurs in Au [25]. 2). The ϵ'_{xy} spectra change with Au layer thickness (x) in Au(20Å)/Ag(10Å)/Fe(3Å)/Au(x Å)/Ag(4000Å)/MgO(100) films.

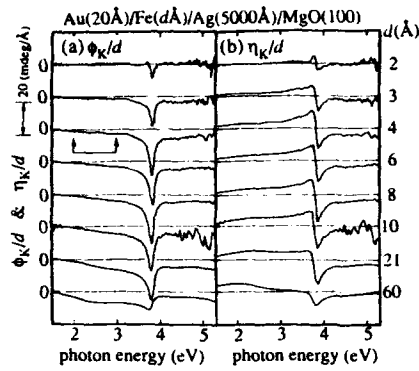


Fig.8 Magneto-optical polar Kerr spectra as a function of Fe layer thickness(d) in $\text{Au}(20\text{\AA})/\text{Fe}(d\text{\AA})/\text{Ag}(5000\text{\AA})/\text{MgO}(100)$ films at room temperature. (a) Kerr rotation (ϕ_K) spectra, (b) Kerr ellipticity (η_K) spectra. The vertical axis means a normalized values of ϕ_K and η_K by Fe film thickness.

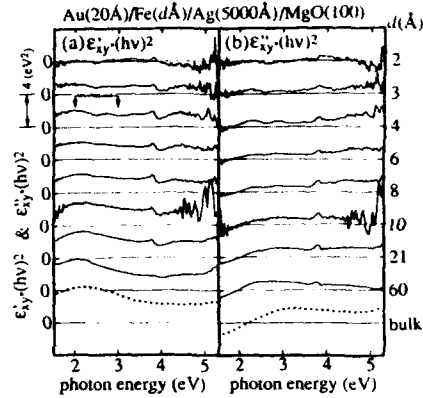


Fig.9 Changes of the spectra of off-diagonal elements (ϵ_{xy}) of the dielectric tensor as a function of Fe layers thickness (d) in $\text{Au}(20\text{\AA})/\text{Fe}(d\text{\AA})/\text{Ag}(5000\text{\AA})/\text{MgO}(100)$ films. The theoretical spectra of Fe bulk are shown as a comparison [24]. (a) real part of ϵ_{xy} , (b) imaginary part of ϵ_{xy} .

IV-4. Fe/Au/Fe Sandwiched Film

We have also prepared several kinds of $\text{Fe}/\text{Au}(d\text{\AA})/\text{Fe}$ sandwiched films and measured saturation polar Kerr rotation (ϕ_K) as a function of the Au interlayer thickness (d) in the sandwiched films. As a sandwiched structure, we employed the $\text{Au}(20\text{\AA})/\text{Fe}(5\text{\AA})/\text{Au}(d\text{\AA})/\text{Fe}(5\text{\AA})/\text{Au}(4\text{\AA})/\text{Ag}(4000\text{\AA})$ structure with a Au wedge whose schematic drawing of cross section is shown in Fig.1 (d)

As pointed out by Ortega *et al.* [7], according to the bulk band structures of bcc-Fe and fcc-Au near the Fermi energy along the film normal [001] [22,23], in the case of Au/Fe system, since an energy gap of minority spin Δ_1 branch exists below the Γ_{121} point of Fe, the majority Δ_1 band of Au couple with Δ_1 band in Fe, but the minority Δ_1 band of Au does not couple with that of Fe layer near the Fermi level. Therefore, a discrete quantum well state will be produced in the minority Δ_1 band of Au around Fermi level. These are spin polarized quantum well states. In that energy region, a propagating wave along the film normal in the Au layer is reflected by Fe barrier at the interfaces because the wave can not propagate in to the Fe layers. So, an interference between the propagating and the reflecting waves makes an envelope function (standing wave). According to a simple approximation in which the phase change of

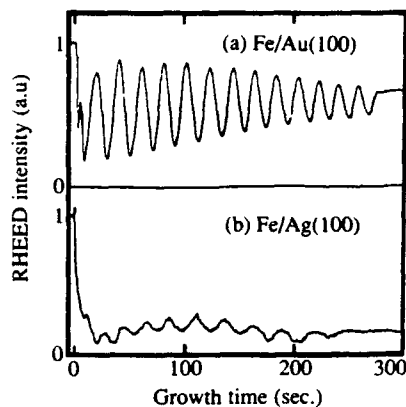


Fig.10 The RHEED intensity oscillations (specular spot intensity) during the growth of Fe layer on (a) Au(100) and (b) Ag(100) surface at room temperature. The primary energy was 20 keV, and glancing angle was 0.3 degree.

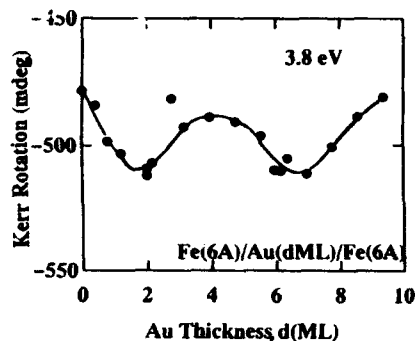


Fig.11 The Au interlayer thickness, d , dependence of ϕ_K at 3.8 eV in $\text{Au}(20\text{\AA})/\text{Fe}(6\text{\AA})/\text{Au}(d\text{ML})/\text{Fe}(6\text{\AA})/\text{Au}(2\text{\AA})/\text{Ag}(4000\text{\AA})$ film. $1\text{ML}=2.0\text{\AA}$.

the wave was neglected, at Fermi Level, the wave number k_z ($k_z = k_F$) can be expressed as [7],

$$k_z = k_F = k_{zB} - n\pi/L \quad (5)$$

where, k_{zB} the wave vector at zone boundary, and k_z the wave vector of the plane wave, L the film thickness of Au, n an integer.

The quantum well states with different integer, n , should cross the Fermi level one after another along the Δ_1 band energy dispersion with the increasing Au thickness. Namely, an empty down spin state will be formed periodically just above Fermi level with the increasing film thickness of Au. Therefore, the period (ΔQ) in which quantum well state appears at the Fermi level is expressed as $\Delta Q = \pi/(k_{zB} - k_F)$ [7]. Ortega and Himpsel found quantum well states in ultrathin noble metal layers such as Ag, Cu grown on Fe and Co by using IPES method and found that, when the energy was fixed, for example at Fermi energy, the inverse photoemission intensities oscillate by every 5 ML's of Ag [7].

It is expected also that a new magneto-optical transition, where the spin polarized quantum well states in noble metals behave as a final state, will occur and its intensity (MO effect) will oscillate periodically by the formation of the quantum well state at Fermi level. The ΔQ is thought to correspond to the period, Λ , of the ϕ_K oscillation. In the cases, it is considered that an optical transition from minority spin Δ_5 bands to the Δ_1 spin polarized quantum well states in Au or Ag is a possible mechanism of the oscillation of saturation ϕ_K in $\text{Fe}/\text{Au}(d\text{\AA})/\text{Fe}$ and $\text{Fe}/\text{Ag}(d\text{\AA})/\text{Fe}$ sandwiches.

In Fig.11 the Au interlayer thickness (d) dependence of saturation polar Kerr rotation (ϕ_K) at 3.8 eV in $\text{Au}(20\text{\AA})/\text{Fe}(6\text{\AA})/\text{Au}(d\text{\AA})/\text{Fe}(6\text{\AA})/\text{Au}(2\text{\AA})/\text{Ag}(4000\text{\AA})$ sandwiched film is shown.

The vertical axis shows a ϕ_K per Fe 1\AA (ϕ_K/d_{Fe}), which was normalized by the total Fe thickness (12\AA). Similar oscillations of ϕ_K were observed in the energy region of 2.5 to 3.8 eV, no oscillations were found at the energies 2.0, 4.0 and 4.5 eV. The oscillation periods (Λ) are about 5ML (10\AA). Similar result was also seen for Fe/Ag/Fe sandwiched film in the energy range from 2.8 to 4.5 eV. The oscillation period (Λ) of Fe/Ag/Fe sandwiched film is in good agreement with IPES experiments of Ortega et al [7].

In these cases, most possible energy range in which such kinds of ϕ_K oscillation should be occur is from the energy corresponds to Δ_5 to Fermi surface transition to the energy of X_5 to X'_4 transition. From the band structures [22], these ranges are 2.0-4.7 eV for Au and 4.0-6.3 eV for Ag. However, as mentioned above, the energy ranges in which the ϕ_K oscillations were observed were 2.5-3.8 eV for the Fe/Au/Fe system and 2.8 to 4.5 eV for Fe/Ag/Fe system. As the energy regions are rather wide, especially for the Fe/Ag/Fe case, another mechanism might be responsible for the observed effect: such as an optical transition in the Fe or an interband transition between a band in Fe and the quantum well states in the Au layers. The oscillation of the MO effect as a function of d in the sandwich films is also thought to be closely related with oscillatory magnetic couplings observed in magnetic multilayers [2, 14].

V. SUMMARIES

We measured the magneto-optical polar Kerr effects on (100) ultrathin Fe films deposited on Au or Ag buffer (100) surfaces. In the photon energy region between 3.5 and 4.5 eV, a new ϕ_K peak appears in the Fe layers deposited on Au, and shifts towards higher energy side with increasing Fe layer thickness, whereas we can not observe the new peak in Fe layers deposited on Ag. The thickness dependence of the transition energy of the new peak in the spectra is well explained by the transition from the majority spin Δ_5 band ($\{p_x \pm i p_y\}, \{d_{xz} \pm i d_{yz}\}; m=\pm 1$) to the Δ_1 quantum well states ($s, p_z, d_{z^2}; m=0$). The new peak is also observed in the Fe/Au(100) artificial superlattices. By comparing the RHEED intensity oscillation for Fe on Au and Fe on Ag, it is concluded that incomplete layer-by-layer growths exclude a formation of quantum well states in Fe layers. On the other hand, Fe ultrathin films deposited on Ag and covered by Au show some structures of ϵ_{xy} in the range of 2-3 eV for the Fe films thinner below 8\AA . These structures are tentatively attributed to spin-polarized Au atoms adjacent to the Fe layer.

We also report on the saturation polar Kerr rotation (ϕ_K) spectra and its oscillation due to interlayer thickness, d , in Fe/Au/Fe and Fe/Ag/Fe films. As a result, the oscillation of ϕ_K as a function of interlayer thickness d was observed between about 2.5 and 3.8 eV for Fe(6\AA)/Au($d\text{\AA}$)/Fe(6\AA) films. The oscillation period Λ is about 5ML (10\AA) of Ag layer corresponding to the IPES results. The oscillation is thought to be closely related with the formation of spin polarized quantum well states of Δ_1 down spin band in Au layers which is the carriers of the oscillatory magnetic coupling.

Acknowledgments The authors would like to express their gratitude to Prof. K.Sato of Tokyo University of Agriculture and Technology for ellipticity measurements, and to Mr. M.Hayashi of Nihon University for Kerr rotation measurements. The authors also would like to acknowledge to Dr. K.Ando, Dr. W.Geerts, Dr. A.Thiaville, and Dr. S.Yoshida of Electrotechnical Laboratory, and Dr.K.Tanaka of National Institute for Advanced Interdisciplinary Research for useful discussions.

References

- [1]. M.N.Baibich, J.M.Brato, A.Fert, F.Nguyen Van Dau, F.Proff, P.Eitenne, G.Creuzet, A.Friederich, and J.Chazelas, Phys. Rev. Lett., **61**, 2472 (1988).
- [2]. S.S.P.Perkin, N.More, and K.P.Roche, Phys. Rev. Lett., **64**, 2304 (1990).
- [3]. C.L.Fu, A.J.Freeman, and T.Oguchi, Phys. Rev. Lett., **54**, 2700 (1985), and Roy Richter, J.G.Gay, and John R.Smith, **54**, 2704 (1985).
- [4]. Chun Li, A.J.Freeman, and H.J.F.Jansen, Phys. Rev., **B42**, 5433 (1990).
- [5]. B.T.Jonker, K.-H.Walker, E.Kisker, G.A.Prinz, and C.Carbone, Phys. Rev. Lett., **57**, 142 (1986).
- [6]. F.J.Himpsel, Phys. Rev. (B) **44**, 5966 (1991).
- [7]. N.B.Brookes, Y.Chang and P.D.Johnson, Phys. Rev. Lett., **67**, 354 (1991) and J.E.Ortega and F.J.Himpsel, Phys. Rev. Lett., **69**, 844 (1992), J.E.Ortega and F.J.Himpsel, to be published in Phys. Rev. B.
- [8]. S.D.Bader, J. Magn. Magn. Matt., **100**, 440 (1991), and references in this report.
- [9]. W.R.Bennett, W.Schwarzacher and W.F.Egelhoff, Phys. Rev.Lett., **65**, 3169 (1990)
- [10]. J.Ferré, G.Pénissard, C.Marliere, D.Renard, P.Beauvillain, and J.P.Renard, Appl. Phys. Lett., **56**, 1588 (1990).
- [11]. T.Katayama, H.Awano, and Y.Nishihara, J. Phys. Soc. Jpn., **55**, 2539 (1986), and T.Katayama, Y.Suzuki, H.Awano, Y.Nishihara, and N.Koshizuka, Phys. Rev. Lett., **60**, 1426 (1988), and K.Sato, H.Kida, and T.Katayama, Jpn. J. Appl. Phys., **27**, L237 (1988).
- [12]. Y.Suzuki, T.Katayama, K.Sato, S.Yoshida and K.Tanaka, Phys. Rev. Lett., **68**, 3355 (1992).
- [13]. Y.Suzuki, T.Katayama, A.Thiaville, K.Sato, M.Taninaka, and S.Yoshida, J. Magn. Magn. Matt., in print, Y.Suzuki and T.Katayama, To be published in Proc. of MORIS'92, [Supplement of J. Magn. Soc. Jpn (1993)], M.Hayashi, T.Katayama, Y.Suzuki, M.Taninaka, A.Thiaville, and W.Geerts, Proceedings of MML '92 Kyoto, to be published in J. Magn. Magn. Matt., T.Katayama, Y.Suzuki, M.Hayashi, and A.Thiaville, Proceedings of MML '92 Kyoto, to be published in J. Magn. Magn. Matt..
- [14]. D.M.Edwards, J.Mathon, R.B.Muniz, and M.S.Phan, Phys. Rev. Lett., **67**, 493 (1991), and P.Bruno and C.Chappert, Phys. Rev. Lett., **67**, 1602 (1991).
- [15]. D.Y.Smith, J. Opt. Soc. Am., **66**, 547 (1976).
- [16]. P.B.Johnson and R.W.Christy, Phys. Rev. **B6**, 4370 (1972).
- [17]. P.B.Johnson and R.W.Christy, Phys. Rev. **B9**, 5056 (1974), and G.S.Krinchik and V.A.Artem'ev, Zh. Eksp. Teor. Fiz., **53**, 1901 (1967) [Sov. Phys. JETP **26**, 1080 (1967)].
- [18]. P.N.Argyres, Phys. Rev., **97**, 334 (1955).
- [19]. This can be easily derived assuming the virtual optical index of the whole system is not affected by an addition/subtraction of one period of the layers.
- [20]. H.Feil and C.Haas, Phys. Rev. Lett., **58**, 65(1987).
- [21]. W.Reim and J.Schoenes, in Handbook of Ferromagnetic Materials, vol.5, eds. E.P.Wohlfahrt and K.H.J.Bushow (North-Holland, Amsterdam, 1990), pp.147-153.
- [22]. H.Eckardt, L.Fritsche, and J.Noffke, J. Phys. F: Mat. Phys., **14**, 97 (1984), and R.Lässer, N.V.Smith, and R.L.Benbow, Phys. Rev., **B24**, 1895 (1981).
- [23]. J.Callaway and C.S.Wang, Phys. Rev. **B16**, 2095 (1977).
- [24]. P.M.Oppeneer, T.Mayrer, J.Sticht, and J.Kuber, Phys. Rev., **B45**, 10924 (1992).
- [25]. Schnatterly, Phys. Rev. **183**, 664, (1969).

QUANTUM-WELL CONTRIBUTIONS TO THE RKKY COUPLING IN MAGNETIC MULTILAYERS

B. A. JONES* AND C. B. HANNA**

*IBM Research Division, Almaden Research Center, K31/802, 650 Harry Road, San Jose, CA 95120-6099

**IBM Research Division, T. J. Watson Research Center, P.O. Box 218, Yorktown Heights, NY 10598

ABSTRACT

We study the effects of quantum-well states on the calculated RKKY coupling. We find that the bound states of a finite-size potential well of depth V give an added oscillation period of size $\pi\hbar/\sqrt{2mV}$. For the simplest case of a spherical free-electron Fermi surface, thus two periods appear: the original, "fast," π/k_F oscillation, and the quantum-well one $\pi\hbar/\sqrt{2mV}$. The quantum-well contributions have larger amplitude, and are in fact the predominant oscillation. For physically reasonable V (tenths of an eV) this period is around 8-10Å. We discuss evidence for these effects in experimental systems.

INTRODUCTION

We wish to discuss an issue concerning the coupling in magnetic multilayers. The experimental fact of this coupling is by this point well-established. (See papers in these proceedings and references therein for an up-to-date review.) Layers of magnetic material, some tens of Angstroms thick, magnetically couple across a nonmagnetic transition metal spacer, with a magnitude which oscillates with the width of the spacer material. The average oscillation period is around 10Å, although a second, smaller period has been seen in some samples,¹ and for a few spacers, such as Cr, the period is near 18Å.²

Oscillating magnetic exchange coupling suggests an RKKY interaction, with the coupling mediated by the spin-polarization of the spacer conduction electrons. There have been several theoretical efforts in this direction,³⁻⁷ and the conclusion of these has been that although a free-electron Fermi surface gives a period, π/k_F , of only 3Å, adding the periodicity of the spacer lattice to give a realistic band structure, and the periodicity of the multilayer to give a beating, "aliasing,"^{3,6,7} effect, results in longer periods which match well with experiment. These long periods are thus essentially an effect of the bulk spacer-material band structure.

One can see from the expression for the RKKY interaction where these oscillation periods arise. In its simplest form, the RKKY interaction is the perturbative effect of a collection of "local moment" spins interacting with the spins of the conduction electrons. If the nonmagnetic conduction electron states can be represented by some single-particle energies $\{\epsilon_k\}$ and wave functions $\{\psi_k(\mathbf{r})\}$, then the effect of a magnetic interaction of the form

$$H_{int} = J \sum_{\substack{\text{conduction} \\ \text{sites}}} \vec{s}_c(\mathbf{r}_i) \cdot \vec{S}_i, \quad (1)$$

($\vec{s}_c(\mathbf{r}_i)$ the spin of the conduction electrons at local moment site i), is to give a leading

order correction to the ground state total energy

$$\Delta E = -\left(\frac{J}{n}\right)^2 \sum_{i,j} \sum_{\substack{\mathbf{k}, \mathbf{k}' \\ \epsilon_{\mathbf{k}} > \epsilon_F \\ \epsilon_{\mathbf{k}'} < \epsilon_F}} \frac{\frac{1}{2} \{ \psi_{\mathbf{k}'}^*(\mathbf{r}_i) \psi_{\mathbf{k}}(\mathbf{r}_i) \psi_{\mathbf{k}}^*(\mathbf{r}_j) \psi_{\mathbf{k}'}(\mathbf{r}_j) + \text{h.c.} \}}{\epsilon_{\mathbf{k}} - \epsilon_{\mathbf{k}'}} \tilde{S}_i \cdot \tilde{S}_j. \quad (2)$$

If one thinks of the product of wave functions ψ as cosine-like, then when $\epsilon_{\mathbf{k}} = \epsilon_{\mathbf{k}'}$ on the Fermi surface, there is a logarithmic singularity which, when integrated against the cosine continuum, gives oscillations with wave vector equal to the singularity wave vector. For a free-electron Fermi sphere the singularity has $\Delta k = \sqrt{2m\epsilon_F}/\hbar = k_F$, and for more complex shapes other Δk are possible.³

We propose to consider additional contributions to the RKKY coupling, namely those from bound states arising from effective quantum wells in these systems. There has been increasing evidence⁸ that quantum-well states exist in some of these materials, arising from differences in environment between magnetic and non-magnetic layers. By use of a simple model, we show that bound states can give a contribution to the RKKY coupling which oscillates with a period dependent only on the height of the well, and independent of any features of the Fermi surface. (Secondary oscillations have period π/k_F , indicative of the continuum contributions. The bound states thus do not change the π/k_F period, but rather are an additional large-amplitude contribution on top of the Fermi surface terms.) Since values of the well height of around a few tenths of an eV give periods $\pi\hbar/\sqrt{2mV}$ in the range of 9 Å, the implications are that in some multilayer systems, some subset of the oscillation periods may have contributions from quantum-well states in addition to the normal Fermi surface effects. Since the physics of these two contributions are different, it may make sense to look for evidence of these effects experimentally in multilayer systems.

METHOD AND RESULTS

Our calculation is straight-forward.⁹ As the simplest case of a quantum well, we start with a free-electron, spherical Fermi surface system, and add a potential for the conduction electrons in the \hat{z} direction (perpendicular to the planes). Such a potential, a quantum-well for the spacer layer, is illustrated in Fig. (1).

(We have also examined other forms of the potential such as delta functions for the interfaces or a "negative well" for the spacer, and we discuss these results elsewhere.¹⁰) The wave functions $\psi_{\mathbf{k}}(\mathbf{r})$ can be calculated exactly for this case, and they are plane waves in the \hat{x} and \hat{y} directions. In the \hat{z} direction the states are solutions of a potential well: a continuum of states for $k_z > \sqrt{2mV}/\hbar$ (sines and cosines with a change of wave vector at the interface), and a set of bound states for $k_z < \sqrt{2mV}/\hbar$. The number of bound states increases as $d\sqrt{2mV}/\pi\hbar$. Even for a piece-wise constant potential, the eigenstate energy $\epsilon_{\mathbf{k}}$ still has the free-electron form, $\epsilon_{\mathbf{k}} = \hbar^2(k_x^2 + k_y^2 + k_z^2)/2m$, where energy is measured from the bottom of the well. We then substitute these $\psi_{\mathbf{k}}(\mathbf{r})$ and $\epsilon_{\mathbf{k}}$ in Eq. (2), and do the $\{\mathbf{k}\}$ and $\{i\}$ sums.

The S_i are taken as constant within each ferromagnetic slab, and so $S_i \cdot S_j$ factors out of the $\{i, j\}$ sum in Eq. (2) as $S_{left} \cdot S_{right}$. We write Eq. (2) as

$$\Delta E = -\left(\frac{J}{n}\right)^2 I(d) \tilde{S}_l \cdot \tilde{S}_r, \quad (3)$$

and calculate $I(d)$ for various well-heights V . We plot a representative result in Fig. (2).

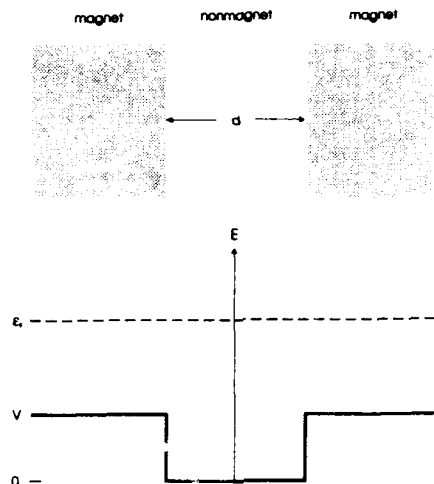


Fig. 1. Model potential used for the calculations of Fig. 2. Note the zero of energy; ϵ_F is measured from the bottom of the well.

This case illustrates the effects of even small well height. (The amplitude of the quantum-well oscillations increases with V .) Compared to no well (Fig. (2a)), the oscillatory period is lengthened considerably by a well of only one-tenth the Fermi energy (Fig. (2b)). The new period is $\lambda \approx \pi\hbar/\sqrt{2mV}$, which one can check by substituting the values given in the caption.

Evidence of what is happening can be obtained by separating $I(d)$ into contributions from continuum and discrete states. The continuum contribution shows small perturbations as a result of resonances from a finite well, but overall the period of oscillations is π/k_F . The quantum-well state contribution, in contrast, has a periodicity of π/k_V , where $\hbar^2 k_V^2/2m \equiv V$. Every time the spacer-layer width d increases by $\pi\hbar/\sqrt{2mV}$, a new quantum-well state appears. States with k_z near $\sqrt{2mV}/\hbar$ have a sharp maximum in their overlap amplitude with the magnetic states; hence, as states periodically pass through this regime, there is a corresponding oscillation in the RKKY interaction. This is thus an effect of sharp modulations in the numerator of the expression in Eq. (2), as opposed to the continuum contribution, which is an effect of zeros in the denominator.

The total RKKY coupling is the sum of the continuum and quantum-well (discrete) contributions. It is important to note that since the quantum-well states are confined to the spacer, their weight, via the $\psi_{k_z}(z)$ in Eq. (2) which go as $1/\sqrt{d}$, sums (the number of bound states goes as d) to a number of order one. The continuum states, normalized to the entire sample, have $\psi_{k_z}(z) \sim 1/\sqrt{L}$, where L is the size of the system. There are of course a large number, of order L , of continuum states (in the z -direction); hence the contributions from bound and continuum states are of the same size. The amplitude of the bound states turns out in fact to be slightly larger, so that when all contributions are added together, two periods are seen, π/k_F and $\pi\hbar/\sqrt{2mV}$, with the predominant one being $\pi\hbar/\sqrt{2mV}$.

Generalizing this result to the case of a more realistic band structure, one can

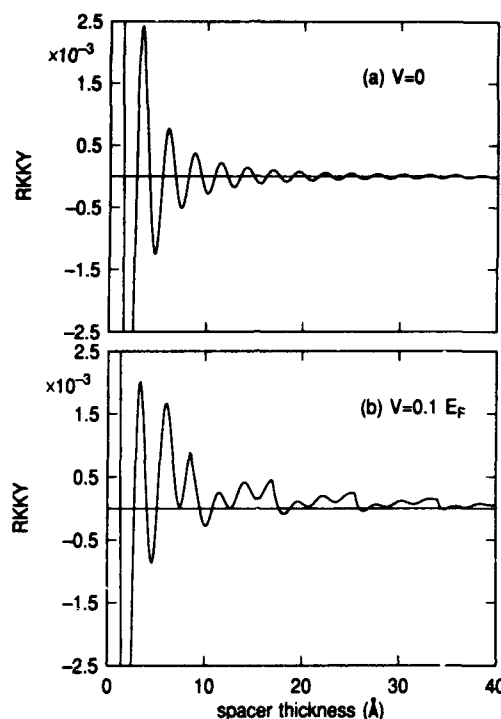


Fig. 2. RKKY coupling of two planes of spins in a sea of conduction electrons as a function of interplanar distance. (The effective filled band width is $\epsilon_F = 5.2$ eV in these plots.) (a) $V = 0$, no scattering potential; (b) $V = 0.10 \epsilon_F$. Note that the $\pi\hbar/\sqrt{2mV}$ oscillations are evident even for this very shallow well. (Positive RKKY is ferromagnetic; negative, antiferromagnetic.)

see that the various periods will add separately, with the predominant period being the one corresponding to the largest amplitude. (Roughness averaging and aliasing will of course smooth out the shorter periods, so the oscillation period seen experimentally may reflect more the largest amplitude terms in a certain range.⁵) Since quantum-well contributions do not interfere with the Fermi-surface-based periods and are merely an additive effect, one might suppose that the ratio of quantum-well to Fermi-surface effects might vary among different systems, and among different oscillation periods in a given system. (If one defines the well as a difference of paramagnetic (filled) band widths, then of course some systems might not display quantum-well, but rather "quantum-wail" (negative V) effects¹⁰.) The fact that a V of 0.3–0.6 eV, a not-unreasonable band-width difference, gives a period of 8–11 Å, indicates that one might look for these effects among the low-end oscillation periods seen experimentally. Quantum-well states of the type considered in our model give a ferromagnetic bias (as seen in Fig. (2b)), which might serve as a check of quantum-well effects.

In summary, we have found an additional physical mechanism for producing oscillation periods in an RKKY interaction. The bound states of a quantum well contribute

a period of $\pi a_0/\sqrt{V}$ (a_0 the Bohr radius and V in Rydberg). The amplitude of this oscillation can be quite large, and for well depths around 0.03 Ry, the oscillation period is near 10 Å, suggesting that quantum-well states might be contributing to the oscillation period in some magnetic multilayer systems.

ACKNOWLEDGEMENTS

We acknowledge helpful discussions with S. Parkin, F. Herman, J. R. Schrieffer, J. Slonczewski, M. Stiles, and V. Kalmeyer. This research was supported in part by the Aspen Center for Physics, and by the National Science Foundation under Grant No. PHY89-04035.

REFERENCES

1. J. Unguris, R. J. Celotta, and D. T. Pierce, *Phys. Rev. Lett.* **67**, 140 (1991).
2. The following work covers study of several spacer materials. S. S. P. Parkin, N. More, and K. P. Roche, *Phys. Rev. Lett.* **64**, 2304 (1990); S. S. P. Parkin, R. Bhadra, and K. P. Roche, *Phys. Rev. Lett.* **66**, 2152 (1991); S. S. P. Parkin, *Phys. Rev. Lett.* **67**, 3598 (1991).
3. P. Bruno and C. Chappert, *Phys. Rev. Lett.* **67**, 1602 (1991); C. Chappert and J. P. Renard, *Europhys. Lett.* **15**, 553 (1991).
4. Y. Wang, P. M. Levy, and J. L. Fry, *Phys. Rev. Lett.* **65**, 2732 (1990); J. L. Fry, E. C. Ethridge, P. M. Levy, and Y. Wang, *J. Appl. Phys.* **69**, 4780 (1991).
5. F. Herman, J. Sticht, and M. Van Schilfgaarde, *J. Appl. Phys.* **69**, 4783 (1991); F. Herman and R. Schrieffer, *Phys. Rev. B*, to be published.
6. D. M. Deaven, D. Rokhsar, and M. Johnson, *Phys. Rev. B* **44**, 5977 (1991).
7. R. Coehoorn, *Phys. Rev. B* **44**, 9331 (1991).
8. J. E. Ortega and F. J. Himpsel, *Phys. Rev. Lett.* **69**, 844 (1992). See also contributions in these proceedings.
9. Details of the calculations appear in B. A. Jones and C. B. Hanna, preprint.
10. See Ref. 9. Delta functions or finite-width barriers for the interfaces give a phase slip; that is, the whole RKKY curve is shifted to the left or to the right. However, no new oscillation periods appear (because the number of bound states, if present, does not vary with the width of the spacer layer). A "negative well" shows similar phase slip effects.

EFFECT OF HYBRIDIZATION ON EXCHANGE COUPLING IN MAGNETIC MULTILAYERS

J. MATHON*, M.A. VILLERET*, J.M. MANDER*, D.M. EDWARDS**, AND R.B. MUNIZ***

*City University, Department of Mathematics, London EC1V 0HB, UK.

**Imperial College, Department of Mathematics, London SW7 2BZ, UK.

***Federal University Fluminense, Department of Physics, Niteroi, RJ24020, Brazil.

ABSTRACT

An earlier theory of the exchange coupling between two ferromagnets separated by a nonmagnetic transition metal spacer was based on size quantization of the electron energies in the spacer. It is now generalized to include the effect of hybridization between the conduction and d bands both in the ferromagnet and in the spacer. The new theory thus unifies the approach based on coupling via d electrons, valid for transition metal spacers, with RKKY-type theories for noble and simple metals which rely on coupling via conduction electrons. The theory is applied to calculate the period and strength of the long-period oscillatory coupling in (001) Co/Cu trilayer.

The oscillatory exchange coupling between magnetic layers separated by a nonmagnetic spacer and the related giant magnetoresistance effect have attracted much attention.¹ It is found experimentally that the magnetic layer moments align themselves ferromagnetically (FM) or antiferromagnetically (AF) depending on the thickness of the nonmagnetic spacer. Multilayers which exhibit such an oscillatory coupling are based on ferromagnetic transition metals and the nonmagnetic spacer layers are usually transition, noble, or simple metals.

The initial theoretical effort was directed toward explaining the observed long oscillation periods. Two mechanisms have been proposed: a theory based on size quantization of magnetic carriers² (complete confinement model) and an RKKY-type approach based on perturbation theory.^{3,6} In both approaches oscillation periods are linked to the shape of the spacer Fermi surface (FS).

However, a true test of any of these theories is whether they can predict not only the period but also the overall strength of the oscillatory coupling for any particular combination of the ferromagnet-spacer materials. RKKY-type theories fail this test because they treat the ferromagnetic layer only as a magnetic plane characterized by one or more adjustable parameters. Moreover, examination of the bulk band structure of the layers in systems based on transition metals shows that magnetic carriers are often completely confined in the spacer region.⁴ The resultant bound states cannot be described within an RKKY approach based on perturbation theory.

At the other extreme, the original version of the complete confinement theory² assumes for the FM configuration that magnetic carriers of one spin orientation travel freely across the whole structure and those of the opposite spin are completely confined in the spacer region. These conditions are fulfilled for Fe/Cr and Co/Ru structures but they are not satisfied even approximately for most other systems. Certainly, the theory of Ref.4 is not applicable to noble and simple metal spacers with conduction electrons mediating the coupling. They can feel the magnetization in the ferromagnetic layers only through hybridization with the ferromagnet d bands but this effect was not included in the theory of Ref.4.

Clearly, what is needed to describe correctly multilayers with transition, noble, and simple metal spacers is a unified nonperturbative theory which can treat bound and propagating states on the same footing and includes hybridization between sp and d bands. The theory should be based on a fully realistic electronic structure of the multilayer constituents and should not contain any adjustable parameters. The purpose of this contribution is to describe such a theory and illustrate its detailed application in the case of (001) Co/Cu trilayer.

The interlayer exchange coupling J is defined as the total energy difference between the ferromagnetic (FM) and antiferromagnetic (AF) configurations of the magnetic layers. It might, therefore, seem that the best way to determine J is to perform first-principle total energy calculations for the FM and AF configurations. This requires the summation of all electron energies in the multilayer below the

Fermi level E_F . However, for a Co/Cu/Co trilayer with a spacer of some $N \approx 20$ atomic planes of Cu the exchange coupling $J(N)$ per surface atom is only $\approx 10^{-6} E_F$. It follows that such a "brute force" approach would require an accuracy which, at present, is computationally not attainable. We, therefore, propose an alternative approach based on a generalization of the theory of Ref. 4. The principal idea is to formulate a total energy calculation in which the summation over one-electron energies is performed analytically rather than numerically. It will be shown that this is possible for multilayers with thick spacer layers ($N \geq 5-6$) in which the interlayer exchange coupling is dominated by just a few "extremal" states at E_F .

Although the proposed method is applicable to any multilayer, we consider here trilayers with thick ferromagnetic layers and describe their electronic structure by canonical tight-binding bands.

We first express $J(N)$ in terms of the thermodynamic potentials Ω^S for electrons of spin s in the FM and AF configurations of the trilayer

$$J(N) = [(\Omega_\uparrow(N) + \Omega_\downarrow(N))_{FM} - (\Omega_\uparrow(N) + \Omega_\downarrow(N))_{AF}] / A, \quad (1)$$

where N is the number of atomic planes in the spacer and A is the cross-sectional area. The thermodynamic potential for a given magnetic configuration at temperature T is given by

$$\Omega^S(N) = -k_B T \int_{-\infty}^{\infty} \ln(1 + \exp((\mu - E)/k_B T)) \mathcal{D}^S(E, N) dE \quad (2)$$

where μ is the chemical potential and $\mathcal{D}^S(E, N)$ is the total density of states (DOS) for particles of spin s in the trilayer having that configuration. Because of the translational invariance in the direction parallel to the layers, we can express $\mathcal{D}^S(E, N)$ as

$$\mathcal{D}^S(E, N) = \sum_{k_\parallel} \mathcal{G}^S(E, k_\parallel, N) \quad (3)$$

where $\mathcal{G}^S = -(1/\pi) \sum_i \text{Tr} \text{Im} G_{ii}(E, k_\parallel, N)$ is the partial DOS, G_{ii} is the local one-particle Green function, the summation over i is over all atomic planes in the trilayer, the trace is over all atomic orbitals, and the wave vector k_\parallel parallel to the layers is from the first two-dimensional Brillouin zone.

For any fixed k_\parallel the calculation of \mathcal{G}^S thus reduces to an effective one-dimensional problem. Within the canonical tight binding scheme, the spacer layer differs from the ferromagnetic layers only by its atomic potentials and hopping integrals, and its effect on magnetic carriers of a given spin is, therefore, equivalent to the effect of a quasi-one-dimensional potential well. Because there is a finite exchange splitting between the majority and minority bands in the ferromagnetic layers, up- and down-spin carriers moving across the structure experience different potential wells in the FM and AF configurations of the trilayer. We clearly have two symmetric wells of different depths for up- and down-spin carriers in the FM configuration and two equivalent asymmetric wells for particles of either spin in the AF configuration.

At this stage, the numerical evaluation of Ω^S for a fully realistic tight-binding band structure is as difficult as in any direct total energy calculation, i.e., computationally not feasible. The key observation which allows us to carry out the k_\parallel and energy sums in Ω^S analytically, and thus render the problem tractable, is that \mathcal{G}^S oscillates as a function of N . The physical origin of the oscillations is easy to understand. All states in the trilayer can be classified into propagating states and bound states localized in the spacer

potential well. The bound states are associated with delta function peaks in \mathcal{G}^S , and they cross any fixed energy E one by one as the thickness N of the spacer is varied, thus leading to oscillations in \mathcal{G}^S . In fact, this is the mechanism we originally proposed to explain the oscillatory exchange coupling. The propagating states do not differ qualitatively from the bound states since they can be regarded as resonances in the well region having a finite lifetime. When the spacer thickness N is varied, the resonances crossing any fixed energy E give rise again to oscillations in \mathcal{G}^S . Such bound states and resonances have been observed using inverse photoemission in Fe/Ag and Co/Cu systems.

The essential mathematical device, which allows us to treat the bound states and resonances on the same footing, is the representation of the average partial DOS $(1/N)\mathcal{G}^S(E, k, N)$ by a Fourier series in N (see Ref.9). Using the Fourier series representation, Eq.(2) becomes

$$\Omega^S(N) = -\frac{k_B T A}{4\pi^3} \sum_n \operatorname{Re} \int_{-\infty}^{\infty} dE \int_{BZ} dk_{\parallel} c_n^S(E, k_{\parallel}) \ln[1 + e^{(\mu - E/k_B T)}] \exp[2in\pi\beta(E, k_{\parallel})] \quad (4)$$

where $\pi/\beta(E, k_{\parallel})$ is the oscillation period and $c_n^S(E, k_{\parallel})$ is the Fourier component of \mathcal{G}^S/N . The $n=0$ term gives a bulk contribution $\propto N$ which will cancel in Eq.(1).

For $n \neq 0$ and large spacer thickness N , the imaginary exponential in Eq.(4) oscillates rapidly as a function of k_{\parallel} and the dominant contribution to the integral with respect to k_{\parallel} comes only from the vicinity of the points k_{\parallel}^0 at which the period reaches an extremum as a function of k_{\parallel} . As in Ref.4, we can, therefore, evaluate both the k_{\parallel} and E integrals in Eq.(4) using the stationary phase approximation. This leads to the following asymptotic formula for the oscillatory part of Ω^S , valid for large spacer thickness

$$\Omega^S(N) = -\frac{k_B T}{8\pi N a^2} \sum_n \operatorname{Re} \frac{\sigma c_n^S(\mu, k_{\parallel}^0) \exp[2in\pi\beta(\mu, k_{\parallel}^0)]}{n^2 \sinh[2Nan\pi(\partial\beta/\partial E)k_B T]} \left| \frac{\partial^2 \beta \partial^2 \beta}{\partial k_x^2 \partial k_y^2} \right|^{-1/2} \frac{\partial E}{\partial \beta} \quad (5)$$

Here, $\sigma=i$ when both second derivatives in Eq.(5) are positive, $\sigma=-i$ when they are negative, and $\sigma=1$ when the two derivatives have opposite signs. All the derivatives are taken at the stationary point $k_{\parallel}=k_{\parallel}^0$, for $E=\mu$, and contributions of all the stationary points must be included in Eq.(5). It should be noted that the oscillation periods and the temperature dependence of each Ω^S are determined, as before, by the spacer FS. It follows from Eq.(1) that $J(N)$ oscillates with the same common periods and has the same temperature dependence as each component Ω^S .

The result of substituting Eq.(5) into Eq.(1) is identical with the asymptotic formula obtained in Ref.4 except for the appearance of the factors $c_n^S(\mu, k_{\parallel}^0)$. However, the change this new term brings is fundamental since we have now removed the constraints of complete confinement and perfect alignment of down-spin bands across the trilayer imposed in Ref.4. Moreover, since Eq.(5) is valid for an arbitrary tight-binding band structure, and that includes sp-d hybridization, not only transition but also noble and simple metal spacers can be treated by the same unified method.

The great advantage of calculating $J(N)$ from Eq.(5) is that we have a nonperturbative total energy calculation but the prohibitive computational effort involved in evaluating the Brillouin zone and energy sums has been completely eliminated. In fact, we only need to know the one-particle states of the trilayer at $E=\mu$ in a small neighborhood of the parallel wave vector k_{\parallel}^0 at which the oscillation period of \mathcal{G} reaches its extremum.

First of all, we need to determine the oscillation period $\pi/\beta(\mu, k_{\parallel}^0)$. It can be proved quite generally that the period is a property of the spacer, independent

of the ferromagnetic layers. For example, for the (001) Co/Cu long-period oscillations used here to illustrate our theory, $\beta(\mu, k_{\parallel}^0)$ is simply the extremal dimension of the Cu FS in the direction perpendicular to the layers associated with the FS extremum at $k_{\parallel}^0=0$ (see Ref.5). It follows that the mixed second derivative in Eq.(5) can be obtained from the FS curvature at $k_{\parallel}^0=0$ which is readily available for bulk Cu. For more complicated systems for which the extremal period is not known in advance, $\beta(\mu, k_{\parallel}^0)$ can be always determined numerically together with its local dependence on k_{\parallel} from a slab electronic structure calculation.

The next problem is to calculate the Fourier components $c_n^s(\mu, k_{\parallel}^0)$ of the partial DOS \mathcal{G}^s which contains all the information about hybridization and matching of the bands across interfaces. It is this term which controls the overall coupling strength for each ferromagnet-spacer combination. To determine \mathcal{G}^s , we only need to examine for both FM and AF configurations how the extremal states with $E=\mu$, $k_{\parallel}=k_{\parallel}^0$, and $s=\uparrow, \downarrow$ evolve across the trilayer in the direction perpendicular to the layers. It is important to note that well away from the spacer-ferromagnet interface the trilayer extremal states must evolve into the bulk states in the spacer (ferromagnet) having the same energy, k_{\parallel} , spin, and symmetry.

We can now proceed with our calculation of $J(N)$ for (001) Co/Cu trilayer. There is only one Cu band in the [001] direction intersecting the FS. It hybridizes with the d band of Δ_1 symmetry and it follows from the above argument that it is only these two bands in Cu and the two bands of the same symmetry in fcc Co that determine the coupling. We can, therefore, describe the electronic structure of the (001) Co/Cu trilayer by two hybridizing tight-binding bands. The atomic levels E_s , E_d , hopping integrals t_s , t_d and hybridization parameters t_{sd} are, of course, different for the Co and Cu layers and they also have different values for \uparrow and \downarrow spin bands in Co. We have assumed the same set of tight-binding parameters for all atomic planes within each layer which amounts to the assumption of an abrupt interfacial potential. This assumption can be easily relaxed and self-consistent potentials can be used in a future calculation. In the present calculation, the tight-binding parameters for each layer were determined from the best fit to the bulk bands of Cu and fcc Co. (Geometric means were used for all interfacial hoppings.) The bands employed in our calculation of $J(N)$ are shown in Fig.1.

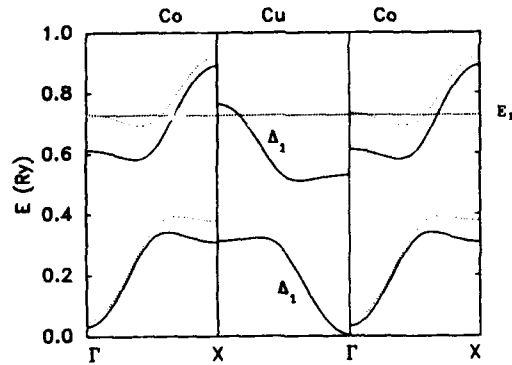


Fig.1. Bands in Co_{\uparrow} (solid line), Co_{\downarrow} (broken line), and Cu which determine the exchange coupling in (001) Co/Cu trilayer.

Given the local tight-binding parameters, the one-electron Green function in each atomic plane was determined by the method of adlayers.¹¹ The sum of its diagonal matrix elements $G_{11}^S(\mu, k_{||}^0, N)$ over the two orbitals and over all the atomic planes in the spacer was then taken to obtain the average partial DOS $(1/N)g^S$. As expected, $(1/N)g^S$ is a periodic function of N and we Fourier-analyzed it in the interval $500 \leq N \leq 600$ to obtain the Fourier components $c_n^S(\mu, k_{||}^0)$. (Large N was chosen to eliminate interfacial contributions $\propto N^{-1}$.) The FS curvature at $k_{||}^0=0$ for Cu was determined using the data of Ref.12 and the derivative $\partial E/\partial k_{||}$ was evaluated analytically for the two-orbital band structure of Cu. With all these quantities now available it is easy to determine $\Omega(N)$ from Eq.(5) for both the FM and AF configurations of the (001) Co/Cu trilayer. These partial Ω^S at zero temperature are shown in Fig.2. As predicted, they all oscillate with the same period of $\approx 10.5\text{\AA}$.

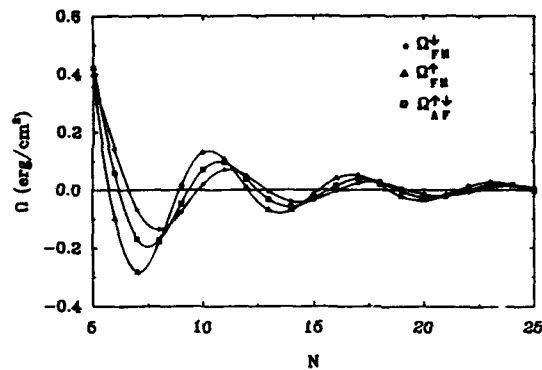


Fig.2. Dependence of the partial Ω^S on the number of (001) Cu planes.

which is somewhat shorter than the observed period¹³ of $\approx 14\text{\AA}$. Finally, the dependence of the exchange coupling $J(N)$ on the number of Cu (001) planes was obtained from Eq.(1) and is shown in Fig.3.

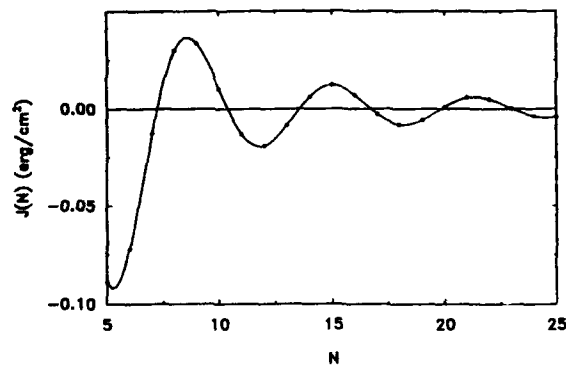


Fig.3. Exchange coupling for (001) Co/Cu trilayer associated with $k_{||}=0$ extremum.

Apart from the assumption of an abrupt interface, the calculation we have described is asymptotically exact for a thick spacer with noninteracting electrons. In particular, our approximation of the electronic structure of Co and Cu by two hybridized bands is asymptotically exact for the purpose of calculating the interlayer coupling. However, it would be premature to expect perfect agreement between our preliminary calculation and the experiment.¹³ We have included only the contribution to $J(N)$ of the Cu FS extremum at $k_{\parallel}=0$ (belly) leading to a long oscillation period but there should be comparable contributions from the other four extrema associated with the FS necks⁵ which lead to a shorter oscillation period. It is, therefore, not surprising that the maximum coupling strength we obtain ($\approx 0.1 \text{ erg/cm}^2$) is about 1/5 of the observed strength ($\approx 0.6 \text{ erg/cm}^2$). New calculation including the neck contributions as well as calculations for the (011) and (111) orientations are now in progress.

Finally, it is interesting to note that all the partial $\Omega^S(N)$ have a much larger amplitude ($\approx 0.4 \text{ erg/cm}^2$) than the final coupling $J(N)$ which is the result of a delicate balance between the $\Omega^S(N)$ in the FM and AF configurations. It is conceivable that the balance may change somewhat when self-consistent interfacial potentials (rather than our abrupt interface model) are used and that could alter both the strength and phase of the exchange coupling. We intend to investigate this factor as well as the related effect of interfacial roughness on the coupling.

REFERENCES

1. P. Grünberg, R. Schreiber, Y. Pang, M.B. Brodsky, and H. Sowers, Phys. Rev. Lett. **57**, 2442 (1986).
2. S.S.P. Parkin, N. More, and K.P. Roche, Phys. Rev. Lett. **64**, 2304 (1990).
3. M.N. Baibich, J.M. Broto, A. Fert, F. Nguyen van Dau, F. Petroff, P. Etienne, G. Creuzet, A. Friederich, and J. Chazelas, Phys. Rev. Lett. **61**, 2472 (1988).
4. D.M. Edwards, J. Mathon, R.B. Muniz, and M.S. Phan, Phys. Rev. Lett. **67**, 493 (1991); J. Phys.: Condens. Matter **3**, 4941 (1991).
5. P. Bruno and C. Chappert, Phys. Rev. Lett. **67**, 1602 (1991).
6. Y. Wang, P.M. Levy, and J.L. Frey, Phys. Rev. Lett. **65**, 2732 (1990).
7. D.A. Papaconstantopoulos, Handbook of the Band Structure of Elemental Solids (Plenum Press, New York, 1986).
8. J.F. Ortega and F.J. Himpsel, Phys. Rev. Lett. **69**, 844 (1992).
9. J. Mathon, Murielle Villeret, and D.M. Edwards, J. Phys.: Condens. Matter **4**, 9873 (1992).
10. V.L. Moruzzi, J.F. Janak, and A.R. Williams, Calculated Electronic Properties of Metals (Pergamon Press, Oxford 1978).
11. J. Mathon, J. Phys.: Condens. Matter **1**, 2505 (1989).
12. M.R. Halse, Proc. R. Soc. London A **265**, 53 (1969).
13. R. Coehoorn, M.T. Johnson, W. Folkerts, S.T. Purcell, N.W.E. McGee, A. De Veirman, and P.J.H. Bloemen, in: Magnetism and Structure in Systems of Reduced Dimension (to be published).

Section A—Multilayers and Surfaces

PART V

Giant Magnetoresistance in Multilayers I

INCREASE IN PERIOD OF OSCILLATORY COUPLING IN Cu BY DOPING WITH Ni

S.S.P. PARKIN, C. CHAPPERT[†] and F. HERMAN

IBM Research Division, Almaden Research Center,
650 Harry Road, San Jose, CA 95120-6099.

[†]Institut d'Electronique Fondamentale, Universite Paris-Sud, Orsay, France.

ABSTRACT

The origin of oscillatory interlayer coupling via Cu is explored in sputtered Co/Cu multilayers by varying the hole concentration in the copper layers by doping with elements of different valence. Detailed studies were carried out for a series of Cu-Ni alloys. The oscillation period of pure Cu is observed to increase monotonically with increasing Ni concentration and is almost doubled for 40 atomic % Ni. The increase in oscillation period can be accounted for by considering changes in the topology of the Fermi surface of the alloy resulting from the change in band filling.

INTRODUCTION

The detailed origin of the magnetic coupling of thin magnetic layers via intervening thin metallic spacer layers is a subject of considerable interest[1-9]. For many transition and noble metal spacer layers the magnetic exchange coupling is found to oscillate back and forth between ferromagnetic and antiferromagnetic coupling as the spacer layer thickness is increased[2-4]. Whether or not the coupling can be accounted for within the well known Ruderman-Kittel-Kasuya-Yosida (RKKY) model[10, 11] is a subject of considerable debate.

In RKKY models the oscillation period is related to the inverse magnitude of wave-vectors along the multilayer direction connecting states at the Fermi surface with antiparallel Fermi velocities. Certain experimental results are difficult to reconcile within simple RKKY models. Firstly a common oscillation period of ~ 8 to 12\AA [4] is observed in most metals with the exception of Cr[2, 5-7] even though the topology of the Fermi surface varies considerably from metal to metal. Secondly the interlayer coupling strength is found to increase systematically with d band filling of the spacer layer metal for the 3d, 4d and 5d transition metals[4], although within RKKY treatments the strength of the coupling is also expected to depend on the detailed Fermi surface topology.

Theoretical predictions of the oscillation period and coupling strength along principle crystallographic axes, based on experimentally determined bulk Fermi surfaces, have been carried out for the noble metals, Cu, Ag and Au within a simple RKKY treatment[12, 13]. Such predictions can be tested by examining the oscillation period and coupling strength along different crystallographic orientations of multilayers containing these metals. This requires the growth of single crystal or highly oriented multilayers along several different crystal axes. Cu is the only spacer layer for which the orientation dependence of the coupling has been studied in detail. The coupling has been measured in experiments on crystalline Fe/Cu and Co/Cu multilayers oriented along [100][9, 14, 15] and [110][16]. Similar long oscillation periods of

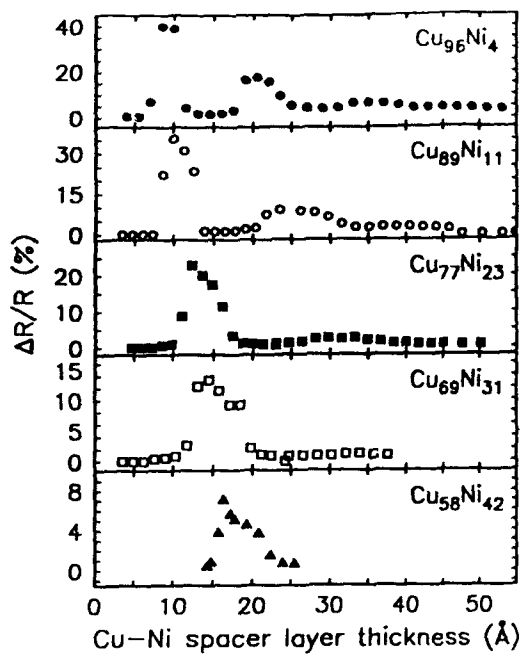


Figure 1:

Saturation magnetoresistance versus spacer layer thickness for series of multilayers of the form, $\text{Si}(100)/50\text{\AA Fe}/[10\text{\AA Co}/\text{Cu}_{1-x}\text{Ni}_x]_n/10\text{\AA Co}/25\text{\AA Cu}_{1-x}\text{Ni}_x$, for $x = 4, 11, 23, 31$ and 42 atomic %.

≈ 11 to 12\AA are found which, while in reasonable agreement with the calculated periods, are not sufficiently dissimilar to provide a stringent test of the theory.

A more stringent test of predictions of RKKY theory is provided by experiments in which the electron concentration in Cu is varied by substituting Cu with elements with lower or higher valence electron concentrations. This is expected to lead to substantial changes in the oscillation period. In this paper we discuss coupling via several different Cu alloys but in particular Cu-Ni alloys.

EXPERIMENTAL DETAILS

The samples in this study were prepared by dc magnetron sputtering. The samples were deposited at $\approx 40^\circ\text{C}$ onto chemically etched 1 inch diameter $\text{Si}(100)$ wafers which had a native oxide $\approx 10 - 20\text{\AA}$ thick. The samples were sputter-deposited in 3.2mTorr Argon at $\approx 2\text{\AA/s}$. The Cu alloy composition was measured on nominally 1000\AA thick calibration films using electron microprobe analysis with an accuracy of $\approx \pm 5$ atomic%. The composition of the films was found to be uniform across the one inch wafers used and no composition variation was found, to within experimental accuracy, from run to run. A wide range of $\text{Cu}_{1-x}\text{Ni}_x$ alloy spacer layers were studied

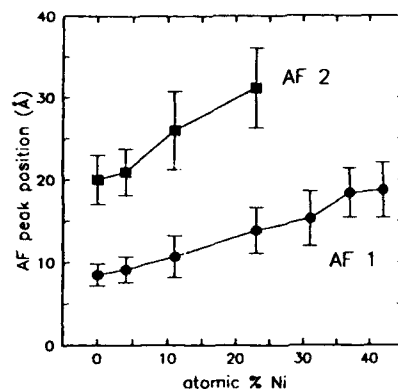


Figure 2:

Position of the first and second AF peaks versus Ni concentration derived from the data in Figure 1. The vertical bars correspond to the full width at half maximum of the AF peaks.

including alloys with Al, Mn, Fe, Co, Ni, Ge, Ru, Rh, Pd, Ag, Pt and Au. Results will be discussed only for multilayers containing magnetic layers of Co. Antiferromagnetic coupling of the Co layers was observed for each of these alloys up to a maximum concentration which varied widely with the different elements. The multilayers were deposited on $\approx 50\text{\AA}$ thick Fe buffer layers, which we have previously shown enhances the structural perfection of the multilayers for these growth conditions[17]. The resistance of the samples was measured using a four in-line contact geometry with gold-plated spring contacts and a low frequency ac lock-in method. The saturation magnetoresistance, MR is defined as the maximum resistance variation observed in the field range examined (typically $\pm 16\text{kOe}$, which was sufficient in all cases to saturate the change in resistance) divided by the high field resistance[2]. The MR was measured with the field in-plane and aligned orthogonal to the sensing current.

EXPERIMENTAL RESULTS

Substitution of Cu with elements from the same column in the periodic table, Ag and Au, should not substantially alter the electron concentration of Cu. Thus no significant effect on the oscillation period is expected. Oscillatory coupling was observed for Cu doped with substantial Au concentrations exceeding 25 atomic % Au. Well defined oscillations in magnetoresistance are observed similar to those found for samples prepared under similar conditions with pure Cu spacer layers[3]. No significant change in the oscillation period in Cu-Au alloys was observed. In contrast significant increases in the oscillation period was found by doping Cu with Ni which has one less electron. Even larger increases in the oscillation period per atomic % dopant were obtained by doping Cu with Fe which has a lower valence still.

The Cu-Ni system was studied in detail for the following reasons. First, Cu and Ni are both fcc and have similar lattice parameters. Second, Cu and Ni are completely soluble in one another over the complete composition range from pure Cu to pure Ni.

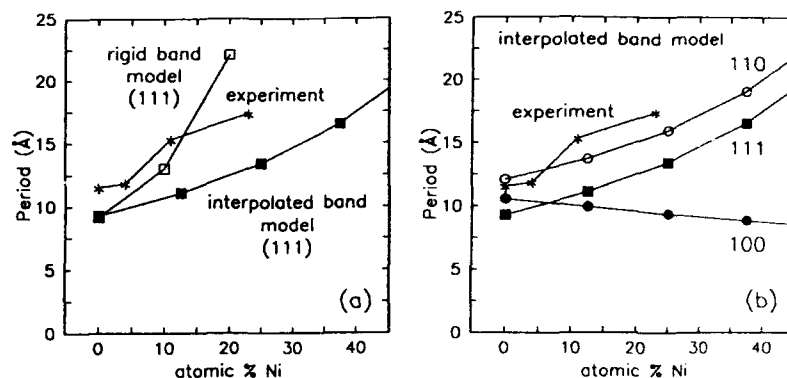


Figure 3:

(a) Oscillation period versus Ni concentration along the (111) orientation, calculated in the rigid band and interpolated band approximations, and comparison with the measured period.

(b) Oscillation period, calculated within the interpolated band approximation, along the (111), (110) and (100) orientations.

Finally Cu-Ni alloys remain paramagnetic for Ni concentrations up to ~ 55 at.% in bulk alloys [18, 19]. In contrast Fe is only weakly soluble in Cu and moreover develops a magnetic moment even for dilute Fe concentrations [19].

The dependence of MR on spacer layer thickness is shown in Fig. 1 for multilayers containing $\text{Cu}_{1-x}\text{Ni}_x$ alloys with x ranging from 0 to 42 at.%. For dilute Ni concentrations three oscillations in MR are observed, for up to ~ 25 at.% Ni two oscillations are observed and for still higher Ni concentrations only one AF peak is found. The data clearly show that the position of the first and second AF peaks are systematically shifted to thicker spacer layers with increasing Ni concentration. The position of the center of these peaks is shown versus Ni concentration, x , in Fig. 2. Defining the oscillation period P , as the difference in position of these peaks, P is found to increase monotonically with x (see Fig. 3). Also included in fig. 2 is the full width at half maximum of the AF peaks. As expected, as P increases the width of the peaks also increases.

THEORETICAL RESULTS

The band structures and Fermi surfaces of fcc $\text{Cu}_{1-x}\text{Ni}_x$ solid substitutional solutions were calculated using two approximations, a rigid band model and a simple interpolation scheme between paramagnetic Ni and Cu bulk band structures. Since a Ni atom has one less valence electron than a Cu atom, the effect of replacing Cu by Ni atoms is to change the detailed nature of the band structure, at the same time lowering the Fermi level. For relatively small concentrations of Ni, the change in band structure can be ignored (rigid band model), and only the lowering of the Fermi level can be taken into account. This model is likely to be a reasonable approximation for very

small Ni concentrations, but for higher Ni concentrations the rigid band model breaks down[20].

A more realistic model was used in which the Fermi surfaces were calculated by linearly interpolating between the paramagnetic band structures for Ni and Cu reported by Papaconstantopoulos[21]. Using his empirical tight-binding band structures, that were fitted to first-principles band calculations[21], the Fermi surface was generated over a very fine mesh (≈ 1000 points in a plane). Fermi surface cross-sections were calculated in the [110] plane for pure Ni, pure Cu, and several intermediate compositions ($x = 25, 50$ and 75 at.%). The Fermi surfaces, which arise predominantly from the sp band, are similar. In the Ni-rich region, there are also small contributions from the d bands, but these are ignored since the experiments are focussed on non-ferromagnetic Cu-rich alloys. Adjacent dog-bone orbits touch for Ni but are separated for Cu due to the necking in the [111] directions. To illustrate the difference between rigid-band and virtual-crystal models, we note that the necks disappear at about 40 at.% Ni in the former and at 100 at.% Ni in the latter.

Before discussing our theoretical predictions, we note that the electronic structure of substitutional alloys can be described by more rigorous models, e.g., the average t -matrix approximation (ATA) and the coherent potential approximation (CPA)[20, 22]. However, these more elaborate treatments would lead to essentially the same physical pictures as does the interpolated band model in the present application, and so were not pursued further. Moreover, our calculated variation of the neck diameter is in unexpectedly good agreement with that of the much more elaborate KKR-CPA calculations of [20]. Note also that our model is applicable only to the non-magnetic range of alloy compositions.

The oscillation periods are obtained from the calculated band structure as described elsewhere[12, 23]. The calculated periods for the (111) orientation versus Ni concentration are displayed in Fig. 3(a) for the rigid band and interpolated band approximations, together with the experimental results of Fig. 2. Apart from a nearly constant offset, the experimental results are in good agreement with the interpolated band approximation predictions. As expected the rigid band model gives poor results for Ni rich compositions. Fig. 3(b) shows results calculated within the interpolated band approximation for the long periods in the three orientations, (111), (100) and (110). The largest variation in P is found along the (111) orientation, for which P increases rapidly with Ni concentration.

The variation of oscillation period with x in the (110) direction is predicted to be similar to that for (111) although the rate of increase is slightly smaller. Moreover, in this case, the strength of the coupling is not expected to be significantly effected by the change in the Fermi surface topology, since the Fermi velocity remains collinear to the spanning wave-vector. In contrast to the (111) and (110) orientations, the calculation predicts only a slow decrease of the period for the [100] orientation with increasing Ni concentration.

CONCLUSIONS

In summary we have shown that the period of oscillatory coupling via Cu in sputtered (111) textured Co/Cu multilayers is significantly increased by doping Cu with Ni or Fe. These elements which have lower valences than Cu cause significant changes in the average Fermi surface of the alloy. In contrast substitution of Cu with elements of the same valence such as Au have much smaller effects on the oscillation period,

consistent with the small differences in Fermi surfaces of these metals. The Fermi surface of several Cu-Ni alloys were calculated within an interpolated band approximation. The oscillation period in the (111) orientation derived from the calculated Fermi surfaces are in good agreement with the experimental observations.

Acknowledgements

We thank K.P. Roche for technical support and R. Savoy for carrying out electron microprobe analysis. We are also grateful to Dr. Papaconstantopoulos for providing us with his band structure codes. We thank Dr. P. Bruno for enlightening discussions.

References

- [1] P. Grünberg, R. Schreiber, Y. Pang, M.B. Brodsky and H. Sowers, *Phys. Rev. Lett.* **57**, 2442 (1986).
- [2] S.S.P. Parkin, N. More and K.P. Roche, *Phys. Rev. Lett.* **64**, 2304 (1990).
- [3] S.S.P. Parkin, R. Bhadra and K.P. Roche, *Phys. Rev. Lett.* **66**, 2152 (1991).
- [4] S.S.P. Parkin, *Phys. Rev. Lett.* **67**, 3598 (1991).
- [5] S.T. Purcell, S.T. Purcell, W. Folkerts, M.T. Johnson, N.W.E. McGee, K. Jager, J. aan de Stegge, W.B. Zeper, W. Hoving, and P. Grünberg, *Phys. Rev. Lett.* **67**, 903 (1991).
- [6] S. Demokritov, J.A. Wolf and P. Grünberg, *Euro. Phys. Lett.* **15**, 881 (1991).
- [7] J. Unguris, R.J. Celotta and D.T. Pierce, *Phys. Rev. Lett.* **67**, 140 (1991).
- [8] A. Fuss, S. Demokritov, P. Grünberg and W. Zinn, *J. Mag. Mag. Mat.* **103**, L221 (1992).
- [9] M.T. Johnson, R. Coehoorn, J.J. de Vries, N.W.E. McGee, J. aan de Stegge, and P.J.H. Bloemen, *Phys. Rev. Lett.* **69**, 969 (1992).
- [10] C. Kittel, in *Solid State Physics*, edited by F. Seitz, D. Turnbull and H. Ehrenreich (Academic Press, 1968) Vol. 22, p. 1.
- [11] Y. Yafet, *Phys. Rev. B* **36**, 3948 (1987).
- [12] P. Bruno and C. Chappert, *Phys. Rev. Lett.* **67**, 1602 (1991).
- [13] P. Bruno and C. Chappert, *Phys. Rev. B* **46**, 261 (1992).
- [14] W.R. Bennett, W. Schwarzacher and W.F. Egelhoff, *Phys. Rev. Lett.* **65**, 3169 (1990).
- [15] A. Cebollada, R. Miranda, C.M. Schneider, P. Schuster and J. Kirschner, *J. Mag. Mag. Mat.* **102**, 25 (1991).
- [16] M.T. Johnson, S.T. Purcell, N.W.E. McGee, R. Coehoorn, J. aan de Stegge, and W. Hoving, *Phys. Rev. Lett.* **68**, 2688 (1992).
- [17] S.S.P. Parkin, Z.G. Li and D.J. Smith, *Appl. Phys. Lett.* **58**, 2710 (1991).
- [18] C.G. Robbins, H. Claus and P.A. Beck, *Phys. Rev. Lett.* **22**, 1307 (1969).
- [19] R.M. White, *Quantum Theory of Magnetism* (Springer Verlag, 1983).
- [20] B. Gordon, W.M. Temmerman, B.L. Gyorffy, G.M. Stocks, in *Transition Metals- 1977*, (Institute of Physics, 1978) Vol. 39, p. 402.
- [21] D.A. Papaconstantopoulos, *Handbook of the Band Structure of Elemental Solids* (Plenum Press, 1986).
- [22] Y. Nakao and S. Wakoh, *J. Phys. Soc. Jap.* **56**, 3983 (1987).
- [23] M.R. Halse, *Phil. Trans. Roy. Soc.* **A265**, 507 (1969).

GIANT MAGNETORESISTANCE IN SPUTTERED NiFe/Ag MULTILAYERS

B. RODMACQ*, A. MALLON* and Ph. GERARD**

*CEA/Département de Recherche Fondamentale sur la Matière Condensée, SP2M/MP, CEN Grenoble, BP 85X, 38041 Grenoble Cédex, France

**CEA/Laboratoire d'Electronique et de Technologie de l'Instrumentation, MEL-SMEM, CEN Grenoble, BP 85X, 38041 Grenoble Cédex, France

ABSTRACT

The magnetoresistive properties of sputtered $\text{Ni}_{81}\text{Fe}_{19}/\text{Ag}$ multilayers have been investigated as a function of both Ag and NiFe layer thicknesses and thermal treatments. For the virgin sample, the magnetoresistance (MR) ratio at room temperature goes through a maximum of 17% for a Ag thickness of about 11 Å. In addition, the $R(H)$ curve is found to be perfectly linear and reversible. Contrary to the MR ratio, the saturation field is observed to decrease continuously as the Ag thickness increases, leading to an increasing slope of the $R(H)$ curves. Upon annealing, we observe both an increase of the MR ratio and a decrease of the saturation field, leading to a three fold increase of the MR slope for annealing temperatures of 280°C. Such a behavior appears to be highly dependent on the layer thicknesses.

INTRODUCTION

The possible use of magnetically coupled multilayers as magnetoresistive read heads has stimulated a large amount of work in the recent years. In all these systems, there exists a critical thickness of the non-magnetic layer through which antiferromagnetic coupling takes place between magnetic layers [1,2]. Under the action of a magnetic field, this coupling can be overcome, the relative orientations of the magnetic moments in successive layers being changed from anti-parallel to parallel. Such a rotation of the magnetizations modifies the spin dependent scattering of the conduction electrons and leads to a decrease of the electrical resistivity [3-5]. As far as applications are concerned, such structures must present large resistance changes at low fields with a $R(H)$ characteristic curve as linear and reversible as possible. In addition, these structures must also be thermally stable. None of the different systems studied up to now seem to meet all these requirements, as for example the NiFe/Cu multilayers in which large field sensitivities have been obtained but with a rather poor thermal stability [6].

We present here results obtained on $\text{Ni}_{81}\text{Fe}_{19}/\text{Ag}$ multilayers prepared by sputtering. We show that replacing 19% nickel by iron leads to a very large enhancement of the magnetoresistance (MR) effect at room temperature compared to Ni/Ag multilayers [7], the MR ratio reaching 17% with a saturation field as small as 300 Oe, corresponding to a $d(\Delta R/R)/dH$ slope of 56% per kOe. Even larger initial slopes can be obtained for samples in which the Ag layer thickness does not correspond to the maximum MR ratio. In addition, the $R(H)$ curve is found perfectly linear and reversible in the whole range of applied fields. Annealing treatments improve the MR properties, through both increase of the MR ratio and decrease of the saturation field. This leads to a three-fold increase of the MR slope for annealing temperatures of 280°C [8].

EXPERIMENTAL SECTION

The samples were prepared by dc sputtering, by depositing sequentially Ag and $\text{Ni}_{10}\text{Fe}_{10}$ layers onto glass substrates kept at a temperature of 100 K, the thicknesses of individual layers being controlled by a quartz monitor. Samples were prepared in the form of ribbons 3×25 mm with a total thickness of either 0.5 or 5 μm , the thin samples being adherent to their glass substrate, whereas the thick ones detached spontaneously from the substrate after heating to room temperature. The structural quality and periodicity were checked by both small-angle and large-angle X ray diffraction in symmetric reflection geometry using λ_{Co} radiation. Diffraction spectra were found typical of (111) textured samples, with a coherence length along the growth direction larger than 200 Å.

The electrical resistivity was measured with a standard four-probe method, the connecting wires being spot-welded on the sample. The magnetic field was applied in the plane of the layers, perpendicular to the current direction. Finally, the magnetization curves were measured using a SQUID magnetometer between 4.2 and 300 K with the field applied parallel to the sample plane.

AS-PREPARED SAMPLES

Figure 1 presents the variations of the MR ratio and saturation field with silver thickness at room temperature. The MR ratio is defined as the resistance change between zero and high field divided by the resistance at high field. The peak in magnetoresistance is quite sharp (FWHM = 3.5 Å) and gives a maximum MR ratio of about 17% for 11 Å of silver. This position is similar to the one observed in pure Ni/Ag multilayers [7,9], but the amplitude is much larger here, since Ni/Ag multilayers with the same thickness of the magnetic layer give a maximum MR ratio of about 5% at room temperature. On the contrary, the saturation field does not go through a maximum for 11 Å of silver, but rather monotonously decreases as the Ag thickness increases, from about 460 Oe for 10 Å to 135 Oe for 12 Å.

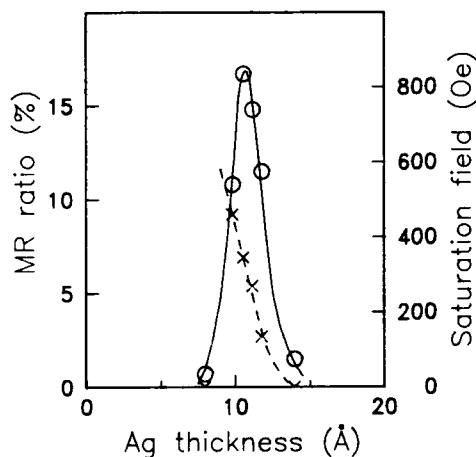


Figure 1: Maximum magnetoresistance ratio (open circles) and saturation field (crosses) as a function of Ag layer thickness for a (NiFe 12.5 Å/Ag t_{Ag}) sample at 300 K.

This leads to a maximum slope of the $R(H)$ curves which is shifted towards larger thicknesses compared to the maximum MR ratio. The same behaviour is observed at low temperature. Taking into account the small width of the MR peak, experiments with a much smaller step in Ag thickness are underway in order to confirm such a behaviour.

Figure 2 compares the field variations of magnetization and magnetoresistance for a (NiFe 12.5 Å / Ag 10.5 Å) sample at 4.2 and 300 K. At room temperature, the magnetization curve (Fig. 2a) saturates in a field of about 300 Oe, the saturation field increasing to 900 Oe at 4.2 K. At this temperature the magnetization curve, although as reversible as was the case at 300 K, does not start from zero at zero field. This supplementary contribution has been recently studied in details by means of magnetization and neutron scattering experiments [10]. The obtained results are to be in very good agreement with a model in which a supplementary biquadratic contribution to the total energy is considered in addition to the conventional bilinear one. From this model one finds that the equilibrium spin configuration at low temperature corresponds to an angle of about 140° between the magnetic moments in adjacent NiFe layers, this angle reaching 180° beyond 100 K. It thus appears that such a zero field contribution to the magnetization at low temperature does not arise from macroscopic inhomogeneities, but rather from some sort of competition between ferromagnetic and antiferromagnetic interactions at a microscopic scale.

The variation of the electrical resistance with applied field (Fig. 2b) is totally consistent with the magnetization results, since it is also reversible and gives saturation fields which agree with those measured on the magnetization curves. An important point is that the field dependence is found to be practically linear, especially at room temperature. Finally, the MR ratio is found to decrease from 50% at 4.2 K to 17% at 300 K. This corresponds to a MR slope of 56% per kOe for both temperatures, more than twice the highest reported one in magnetically coupled NiFe/Cu multilayers [6].

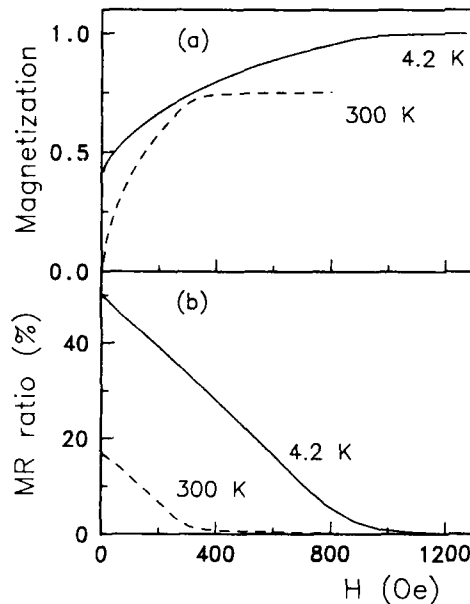


Figure 2: Magnetization (a) and magnetoresistance (b) curves for a (NiFe 12.5 Å / Ag 10.5 Å) sample at 4.2 K (full lines) and 300 K (dashed lines).

ANNEALING EFFECTS

In order to characterize the thermal evolution of the magnetoresistance properties, we have measured the field variation of the electrical resistance at room temperature after annealing for 5 min. at different temperatures up to 340°C. The variation of the MR ratio and saturation field with annealing temperature are very different, as shown in Figure 3 for a (NiFe 12.5 Å / Ag 10.5 Å). The saturation field is almost constant up to 100°C, and then starts decreasing monotonously down to zero for annealing temperatures of about 340°C. On the contrary, the MR ratio goes through a maximum of 24.1% at 240°C, before it drops down to about zero at 340°C. It must be noted that the $R(H)$ curves are found perfectly linear and reversible whatever the annealing temperature.

Figure 4 gives the variation with annealing temperature of the $d(\Delta R/R)/dH$ slope for two samples, the first one with a Ag thickness corresponding to the maximum MR ratio before annealing (NiFe 12.5 Å / Ag 10.5 Å), and the second one to thicker Ag and NiFe layers, that is (NiFe 17 Å / Ag 12.5 Å). For the first sample, the slope (determined from the results given in Fig. 3) is almost constant up to about 150°C, and then starts increasing sharply up to 165% per kOe for annealing temperatures of 280°C. This maximum is shifted to higher temperature with respect to the one of the MR ratio (Fig. 3) because of the decrease of the saturation field. These results show that the MR properties of the NiFe/Ag multilayers are not only stable against temperature, but improve up to quite high annealing temperatures. In addition, because of the parallel thermal variations of both MR ratio and saturation field, it must be noted that the sensitivity is practically independent of temperature, from well below room temperature up to 280°C for annealed samples.

The behaviour of the second sample is found different. The initial slope is larger than that of the first sample (because of the larger Ag thickness) and the maximum value is also larger (around 200% per kOe instead of 165). Nevertheless it appears to be less thermally stable, the maximum slope being obtained at about 180°C instead of 280°C for the first sample. Such a behavior is quite unexpected since our previous investigations on Ni/Ag multilayers have shown an increased thermal stability with increasing layer thicknesses. We are currently investigating samples in which NiFe and Ag layer thicknesses are varied independently in order to understand such an unusual behaviour.

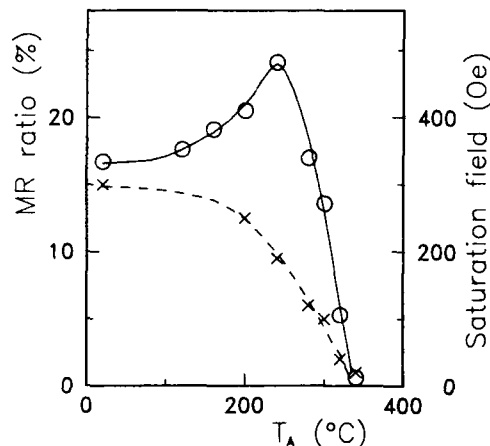


Figure 3: Variation with annealing temperature of the MR ratio (open circles) and saturation field (crosses) measured at room temperature on the same sample as in Figure 2.

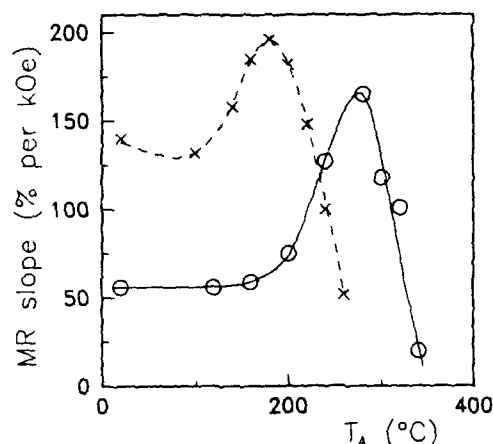


Figure 4: Variation with annealing temperature of the magnetoresistance slope measured at 300 K on a (NiFe 12.5 Å / Ag 10.5 Å) sample (open circles) and on a (NiFe 17 Å / Ag 12.5 Å) one (crosses).

CONCLUSION

The results presented in this paper show that NiFe/Ag multilayers possess very interesting magnetoresistive properties. They exhibit large resistance variations in small applied fields at room temperature, with a $R(H)$ curve perfectly linear and reversible. This leads to quite high magnetoresistance slopes, the highest one being obtained for Ag thicknesses slightly larger than the one corresponding to the maximum MR ratio. Moreover, these properties improve with annealing and reach an optimum value for annealing temperatures as high as 280°C. These properties, as well as the observed temperature independent $R(H)$ slopes, make these structures good candidates for technological applications.

REFERENCES

1. G. Binasch, P. Grunberg, F. Saurenbach, and W. Zinn, Phys. Rev. B **39**, 4828 (1989)
2. S.S.P. Parkin, N. More and K.P. Roche, Phys. Rev. Lett. **64**, 2304 (1990)
3. M. N. Baibich, J. M. Broto, A. Fert, F. Nguyen Van Dau, F. Petroff, P. Etienne, G. Creuzet, A. Friederich and J. Chazelas, Phys. Rev. Lett. **61**, 2472 (1988)
4. D.H. Mosca, F. Petroff, A. Fert, P.A. Schroeder, W.P. Pratt, Jr. and R. Loloee, J. Magn. Magn. Mater. **94**, 11 (1991)
5. S.S.P. Parkin, R. Bhadra and K.P. Roche, Phys. Rev. Lett. **66**, 2152 (1991)
6. S.S.P. Parkin, Appl. Phys. Lett. **60**, 512 (1992)
7. B. Rodmacq, B. George, M. Vaezzadeh and Ph. Mangin, Phys. Rev. B **46**,

1206 (1992)

8. B. Rodmacq, G. Palumbo and Ph. Gérard, J. Magn. Mater. **118**, L11 (1993)
9. C.A. Dos Santos, B. Rodmacq, M. Vaezzadeh and B. George, Appl. Phys. Lett. **59**, 126 (1991)
10. B. Rodmacq, K. Dumesnil, Ph. Mangin and M. Hennion, to be published

GIANT MAGNETORESISTANCE IN Co/Ag MULTILAYERS

M. TAN*, J. A. BARNARD*, M. R. PARKER**, and D. SEALE**

The University of Alabama, *Department of Metallurgical and Materials Engineering,

**Department Of Electrical Engineering, Tuscaloosa, AL 35487-0202

ABSTRACT

The magnetoresistance (MR), magnetic properties, and crystal structure of dc magnetron sputtered Co/Ag periodic multilayers have been investigated. The Co layer thickness was fixed at ~ 30 Å while the thickness of the Ag layer was systematically varied. 'Giant' magnetoresistance was observed. The MR ratio has been found to decline monotonically with increasing Ag thickness in the range 30 Å to 107 Å. Although the maximum room temperature MR ratio is a modest 4.78%, a more technologically significant measurement of field sensitivity (MR ratio/FWHM of the MR vs. H peak) is a promising 0.1%/Oe at its best. The effect of the number of bilayer units has also been examined and no substantial differences were noted between multilayers containing 8, 9, and 10 bilayer units. Coercivities as determined by both magnetometer and the splitting of the MR peaks are in agreement and increase from 25 to 38 Oe with increasing Ag thickness. Evidence for antiferromagnetic coupling is apparent in the hysteresis loops. High angle X-ray diffractometry (HXRD) in the θ -2 θ mode revealed a strong Ag(111) texture in the film, with satellite peaks indicating a layered structure. Low angle XRD (LXRD) also yielded broad superlattice peaks in all samples at least to the second order.

1. INTRODUCTION

Giant magnetoresistance (GMR) in multilayer magnetic thin films has been under intensive study since the first report on GMR behavior associated with antiferromagnetic (AFM) coupling in the Fe/Cr single crystal multilayer system in 1988[1]. Multilayers composed of Fe or Co and one of a number of transition metals have been found to exhibit GMR that is potentially useful for the recording industry[2-7]. MR dependence on the Ag thickness in Co/Ag multilayers has been shown to be very different by different workers[5,6]. The MR ratio in sputtered samples was found to increase with Ag thickness and reach a maximum of 5.1% at room temperature for 60 Å of Ag[5], while molecular beam epitaxy deposited samples showed an oscillatory MR dependence on Ag thickness varying from 4 to 35 Å, with a maximum of 16% at 25 Å[6]. The field required to saturate the sample in [5] was below 1 kOe and in [6] was of the order of 10 kOe. For the thickness range of Ag spacer layer (30 Å and beyond) studied in this work, the MR ratio decreases with an increase in the Ag spacer thickness. Although the absolute value of the MR ratios in the films studied here are not large they are achieved in comparatively low fields (an important issue for technological applications). In this work Co/Ag multilayers were made by dc magnetron sputtering, with fixed Co layer thickness and changing Ag layer thickness. Structure characterization, MR measurement and magnetic property measurements were conducted.

2. EXPERIMENTAL METHODS AND MATERIALS

Sequential dc magnetron sputtering (Vac-Tec Model 250 Batch Side Sputtering System) was used to deposit all the films. Base pressure in the chamber

was $\sim 5 \times 10^{-7}$ torr. Both cobalt and silver were sputtered from 4" diameter targets (99.97% pure) onto Corning 7059 glass substrates. Sputtering was conducted at ambient temperature. Sputtering conditions were 100W power control and 2 mTorr Ar (99.99%) pressure. Sputtering rates were calculated from HXRD satellite peaks and compared with thickness measurements of reference films made with a Dektak Ila surface profilometer. Crystal and microstructural information was obtained by X-ray diffractometry (XRD) using a Rigaku D/Max-2BX X-ray diffractometer with Cu K α radiation. Both LXR and HXR (both in θ - 2θ mode) X-ray scans were run for the multilayers. The MR measurements were made with a linear 4-point probe with both current and magnetic field in the film plane but perpendicular to each other. The measurement was taken on a strip with aspect ratio of roughly 5:1, the long axis of the strip is perpendicular to the magnetic field, and therefore, parallel to the current. A vibrating sample magnetometer (VSM) was utilized for magnetic property determination. All measurements were made at room temperature on as-deposited samples. The properties to be discussed below are: (1) saturation MR ratio (%): $\Delta R/R = (R_{\max} - R_{\text{sat}})/R_{\text{sat}} \times 100\%$ where R_{\max} is the electrical resistance at its peak value, and R_{sat} the resistance when the sample is magnetically saturated; (2) ΔH is the full width at half maximum (FWHM) of the MR-H plot; (3) H_c is the coercivity; and (4) dH is the FWHM of the dM/dH loop.

3. EXPERIMENTAL RESULTS AND DISCUSSIONS

3.1. Structure

The geometry of the Co/Ag multilayers is: glass/(Co t_{Co} /Ag t_{Ag}) N , with t_{Co} and t_{Ag} denoting the Co and Ag layer thickness, respectively, and N is the number of bilayer units. Table I identifies the samples, lists the geometry, and summarizes the experimental results. Multilayer structure was seen in both LXR peaks and HXR

Table I. Summary of Co/Ag multilayer geometries and experimental results.

Sample	t_{Ag} (Å)	N	MR (%)	ΔH (Oe)	MR/ ΔH	H_c (Oe)	dH
CA28	30	8	4.009	47.54	0.0843	25.27	8.7712
CA29		9	4.784	48.91	0.0978	23.58	11.389
CA210		10	4.499	59.11	0.0761	26.32	12.123
CA38	46	8	3.620	56.19	0.0644	27.36	11.103
CA39		9	3.501	78.62	0.0446	31.68	18.593
CA310		10	3.776	65.71	0.0575	27.51	14.575
CA48	61	8	3.489	78.14	0.0447	30.04	17.955
CA49		9	3.381	87.77	0.0385	32.57	16.855
CA410		10	3.303	97.69	0.0338	31.36	17.944
CA58	77	8	2.815	109.40	0.0257	33.40	20.277
CA59		9	2.853	88.16	0.0324	33.07	19.597
CA510		10	3.098	94.13	0.0329	31.92	18.798
CA68	92	8	2.263	81.653	0.0277	33.92	21.093
CA78	107	8	1.746	91.517	0.0191	37.60	29.621
CA79		9	2.011	99.022	0.0212	36.43	26.397

satellite peaks. Multilayer periodicity and sputtering rate were calculated using the HXRD satellite peaks[9]. The Ag sputtering rate by HXRD agrees with what was calibrated by profilometer very well, while the Co rate from HXRD method is higher than the thickness measurement. HXRD patterns showed a strong Ag(111) peak in all the samples. Well defined satellite peaks were observed around the main structure peak up to third or fourth order. The preferred crystal orientation gets stronger with increasing Ag thickness, indicated by the slight yet consistent narrowing of the 'rocking' curve. Figure 1 shows both high angle and low angle XRD spectra for the sample CA29.

3.2. Magnetoresistance and other Magnetic Properties

The number of bilayer units, N , was varied from 8 to 10 for the purpose of studying the influence of bilayer number on MR, magnetic properties, and structure in Co/Ag multilayers. In this narrow range of bilayer numbers our study shows no systematic dependence on N .

In Fig. 2a (the insert) the MR ratio vs. field H loop is plotted for sample CA29 which yields the largest and sharpest MR loop (4.78%). Some evidence for AFM coupling is found in the asymmetry of the two arms of MR- H plot. It takes a much larger magnetic field to re-saturate the sample after the magnetic moments in portion of the adjacent ferromagnetic layers have relaxed from the forced alignment state of the initial saturation and tend to align antiparallel, due to AFM coupling. This phenomenon can be found to varying degrees in all the samples throughout the t_{Ag} spectrum. The appearance of the MR- H and the saturation field are similar to those in [5]. From Table I it is clear that there is a monotonic decrease in MR ratio with increasing Ag thickness in the range studied. However, in order to describe the combination of the magnitude of MR ratio and the sharpness of the MR- H relationship, the expression $MR/\Delta H$ is used. $MR/\Delta H$ versus t_{Ag} is plotted in Fig. 2b. A monotonic decrease in MR sensitivity with increasing t_{Ag} is noted.

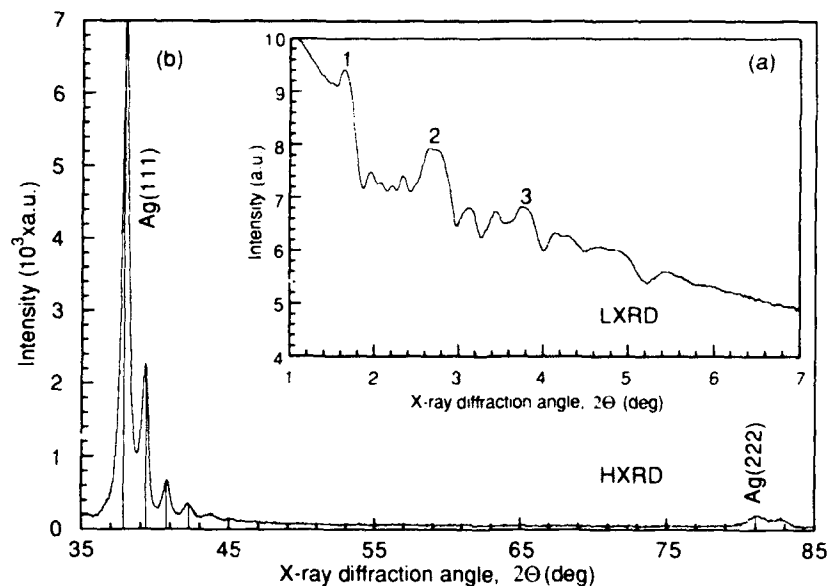


Figure 1. X-ray diffraction spectra for CA29, (a) LXRD (insert), (b) HXRD.

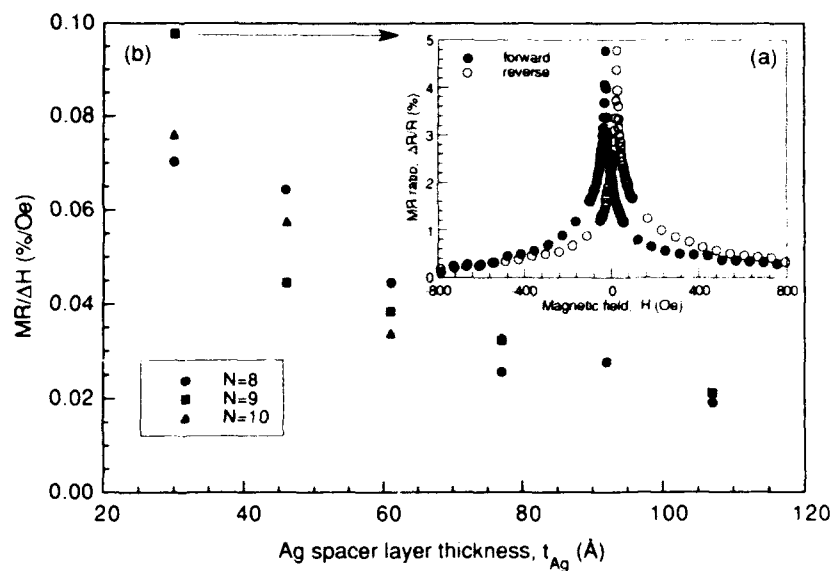


Figure 2. (a) MR ratio vs. magnetic field, CA29 (insert), (b) $MR/\Delta H$ vs. t_{Ag} .

Figure 3 shows the hysteresis loops of two samples (CA29 and CA79), representing the thinnest and thickest Ag spacers used. The form of the M-H curve before and after the reversal again shows the AFM features. Since MR behaves similar to the first derivative of the M-H hysteresis loop, this led us to try to correlate the change in the shape of MR vs. H to the M-H loop. As defined previously, dH is a

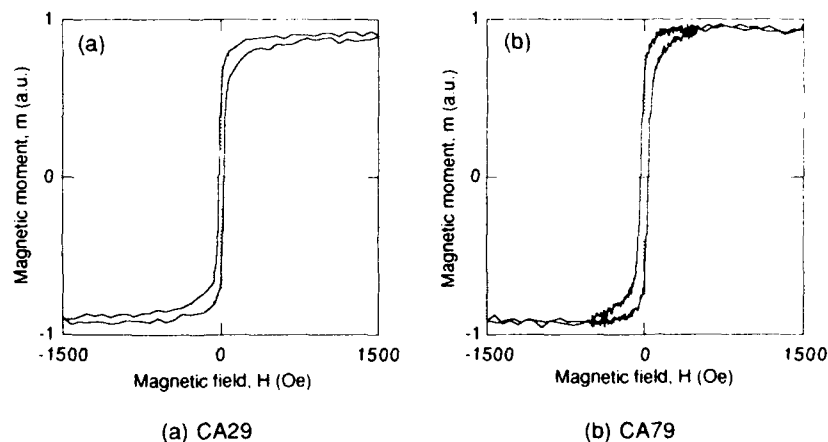


Figure 3. VSM M-H loops for thin (a) CA29, and thick (b) CA79 Ag spacer layers.

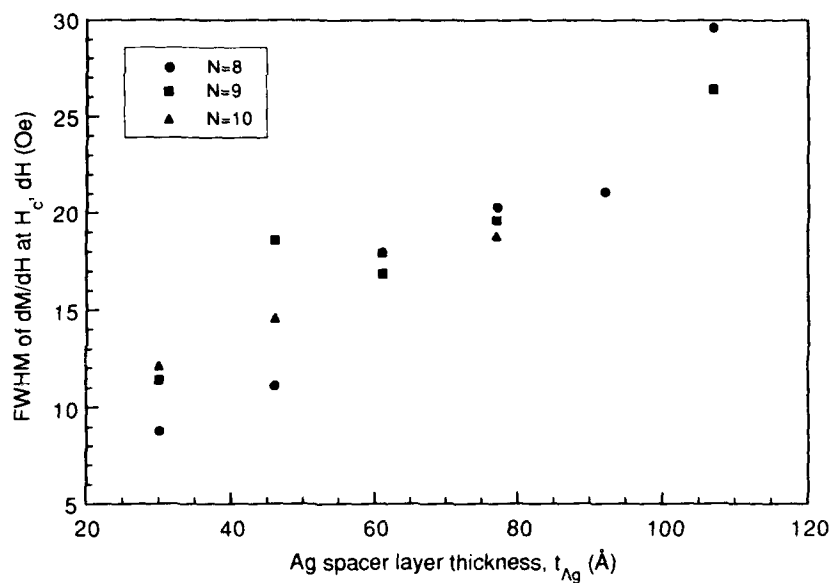


Figure 4. FWHM of dH/dM , dH vs. Ag spacer layer thickness, t_{Ag} .

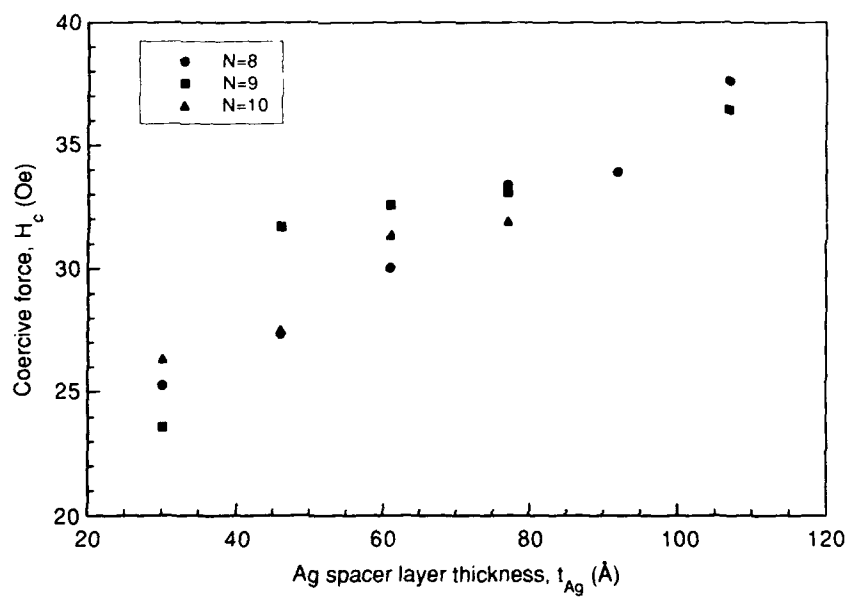


Figure 5. Coercivity, H_c vs. Ag layer thickness, t_{Ag} .

measure of the abruptness of the magnetization reversal. In Fig. 4 dH is plotted against t_{Ag} . Therefore by combining Figs. 2b and 4 the change in MR can be related to the abruptness of the magnetization reversal as a function of t_{Ag} : large MR occurs when the reversal is abrupt (small dH value). Meanwhile, the coercivity, H_c , of the samples shows an increase with Ag thickness (Fig. 5). The coercive field coincides very well with the field at which R_{max} occurs. Figs. 4 and 5 show a similar trend. Further investigation is needed to fully understand this phenomenon. We believe the reduction of AFM coupling due to the increase of t_{Ag} together with domain activities are responsible for the decrease of reversal abruptness and the increase of H_c with increasing t_{Ag} .

4. SUMMARY

Magnetoresistance due to antiferromagnetic coupling has been found in the Co/Ag multilayer system. The best MR in this work is about 5% and coincides with the largest MR/ ΔH value ($\sim 0.1\%/Oe$). It is obvious that our thinnest Ag thickness is beyond the second oscillation[6]. An attempt was made to reduce the Ag thickness so that the first oscillation would be realized. This effort has not been successful so far due to the fact that the sputtering rate for Ag is very high and the deposition time is manually controlled. The MR vs. H plots and the hysteresis loops both suggest antiferromagnetic coupling. The samples were found to be strongly textured with Ag(111) orientation. The correlations between the microstructure, interface structure and the MR, magnetic properties after annealing are under study.

ACKNOWLEDGEMENTS

Acknowledgement is made to the National Science Foundation (grants DMR-8918403 and DMR-9157402) and the MINT Center at The University of Alabama for support of this research.

References

- [1] M. N. Baibich, J. M. Broto, A. Fert, F. Nguyen Van Dau, F. Petroff, P. Eitenne, G. Creuzet, A. Friederich, and J. Chazelas, *Phys. Rev. Lett.*, 61(21), 2472(1988).
- [2] S. S. P. Parkin, N. More, and K. P. Roche, *Phys. Rev. Lett.*, 61(19), 2304(1990).
- [3] J. A. Barnard, A. Wakis, M. Tan, E. Hattek, M. R. Parker, and M. L. Watson, *J. Mag. Mag. Mat.*, 114, 203(1992).
- [4] E. E. Fullerton, D. M. Kelly, J. Guimpel, Z. K. Schuller, and Y. Bruyaseraede, *Phys. Rev. Lett.*, 68(6), 859(1992).
- [5] D.H. Mosca, A. Barthelemy, F. Petroff, A. Fert, P.A. Schroeder, W.P. Pratt, Jr., R. Laloe, and R. Cabanel, *J. Mag. Mag. Mat.*, 93, 480(1991).
- [6] S. Araki, K. Yasui, and Y. Narumita, *J. Phys. Soc. Jpn.*, 60(9), 2827(1991).
- [7] B. Heinrich, Z. Celinski, J. F. Cochran, W. B. Muir, J. Rudd, Q. B. Zhong, A. S. Arrott, K. Myrtle, and J. Kirschner, *Phys. Rev. Lett.*, 64(6), 673(1990).
- [8] R. E. Camley and J. Bunas, *Phys. Rev. Lett.*, 63(6), 664(1989).
- [9] M. Sugawara, M. Kondo, S. Yamazaki, and K. Nakajima, *Appl. Phys. Lett.*, 52(9), 742(1988).

GIANT MAGNETORESISTANCE IN ANNEALED Fe/Cr MULTILAYERS

Noa More Rensing * and Bruce M. Clemens **

*Department of Applied Physics, Stanford University, Stanford CA 94305

**Department of Materials Science and Engineering, Stanford University, Stanford CA 94305

ABSTRACT

The giant magnetoresistance effect in antiferromagnetically coupled Fe/Cr multilayers has been attributed to spin dependent scattering at the interfaces between the constituents. One possible source of this spin dependent scattering is chromium impurities in the iron layers due to intermixing at the interfaces. Annealing the films can promote the diffusion of the components, increasing the impurity concentration and therefore the magnetoresistance. For this study Fe/Cr multilayers were annealed at several temperatures and for several durations. Annealing at moderate temperatures ($\sim 350^\circ\text{C}$) increases the magnetoresistance, while higher temperature anneals ($\sim 600^\circ\text{C}$) cause the magnetoresistance to disappear completely. Long anneals at 330°C (> 100 hours) also reduce the magnetoresistance. VSM measurements indicate that the antiferromagnetic coupling is reduced in the annealed samples but show no evidence of magnetically "dead" alloy layers. Low angle X-ray diffraction indicates that the structural effect of annealing is very subtle in comparison to the significant magnetic effect.

INTRODUCTION

The influence of the structure of the interfaces on the magnetoresistance in antiferromagnetically coupled multilayers and spin valves has been a subject of discussion since the effect was discovered. Baibich *et al.*[1] pointed out that perfectly smooth interfaces could not contribute to the in-plane magnetoresistance, but that steps and other imperfections in the surfaces could contribute to a spin dependent resistance. Camley and Barnas[2] parameterized the interface scattering without attributing its origin, and more detailed theories have attempted to incorporate the possibility of both bulk and interfacial spin dependent scattering[3, 4, 5]. Fits to experimental data, however, largely indicate that interface scattering dominates. The importance of interface scattering was proven by Baumgart *et al.*[6] in a study of doping interfaces of Fe/Cr multilayers by different spin scatterers. They found that when the interfaces were doped with elements that have the same spin scattering asymmetry as chromium, the magnetoresistance was unchanged, but that elements with the opposite asymmetry reduced the magnetoresistance, in effect canceling the influence of some of the chromium scattering sites.

Experimental data on the effect of interface structure has thus far been inconclusive. Petroff *et al.*[7] reported that MBE grown Fe/Cr samples grown under conditions that roughened the interfaces had increased magnetoresistance over smooth samples, increasing from 14% to 33%. Additionally, annealing the smooth sample at 300°C increased in magnetoresistance to 27.3%, but when it was annealed at 350°C the effect decreased to 1.15%. These results were attributed to thermally induced interdiffusion between the two components of the system. They concluded that while some roughening is helpful, overly rough interfaces destroy the antiferromagnetic coupling necessary for GMR.

Fullerton *et al.*[8] roughened the interfaces of Fe/Cr multilayers in several ways, including varying the deposition pressure, sputter gun power, and number of bilayers. They

found that for all cases the magnetoresistance increased with interface roughness. Parkin[9] has reported that the magnetoresistance of Co/Cu multilayers grown on a buffer layer on (001) silicon is higher for iron buffer layers than for copper buffer layers. This difference was attributed to smoother interfaces in the case of the iron underlayer. In a previous paper[10], we reported on the effect of roughening Fe/Cr by increasing the sputtering gas pressure. While the magnetoresistance was found to decrease for rougher films, this could be attributed entirely to an increase in the saturation resistance and not to a change in the spin dependent scattering. In this paper we report the results of annealing Fe/Cr multilayers in order to increase the number of Cr asymmetric scatterers through interdiffusion at the interfaces. While relatively low temperature anneals do increase the magnetoresistance, longer and hotter anneals cause the magnetoresistance to fall.

EXPERIMENT DESCRIPTION

For the purpose of comparing the effect of anneal temperatures and duration, single thickness Fe/Cr multilayers with 42Å bilayer period for resistance measurements and 65Å bilayer period for x-ray measurements were sputtered onto polished silicon(001) substrates. The thicker bilayer period makes it possible to see up to four orders of low angle superlattice peaks with a laboratory diffractometer. The films have (110) out of plane texture and are polycrystalline. A 30Å platinum protective overlayer was sputtered onto the films used for transport measurements, to prevent oxidation from interfering with good electrical contact with the film. This protective overlayer was not used with the X-ray films, because it would interfere with small angle diffraction. The films were cleaved into approximately 5 mm square sections for annealing. Annealing was done in a tube furnace under flowing argon. Before the heater was turned on, the furnace was evacuated to 100 mTorr and backfilled with argon 3 times. The furnace has significant heating and cooling time constants (1 hour and 20 minutes respectively for 350°C). The data has not been corrected for this.

The resistance was measured using a 4-point in-line probe and a low noise dc current source. All magnetic measurements were made at room temperature in a 12 inch magnet capable of 18 kGauss field. Resistance baseline scans were measured on each sample before it was annealed, and the scatter in the magnetoresistance measurements for segments of a single film was about 0.25%. Differences in the saturation resistance of the unannealed samples were attributed to the difference in the area of the different segments. In analyzing the data, we have defined the magnetoresistance as the ratio of the field dependent resistance to the high field saturation resistance, $GMR = (R_s - R_0)/R_s$.

RESULTS AND DISCUSSION

Figure 1 shows the magnetoresistance of an Si(001)/12ÅCr/20*(30ÅFe/12ÅCr)/12ÅCr/-30ÅPt film that had been annealed for 1 hour at several temperatures. The unannealed film had 7.1% magnetoresistance. The magnetoresistance increased with annealing temperature, peaking at 9.5% for the film annealed at 350°C, and then decreased until it disappeared for the film annealed at 650°C.

Magnetoresistance and magnetization data for the films annealed at selected temperatures is shown in figure 2. The increase in magnetoresistance at low temperature anneals is not accompanied by a significant change in the saturation field, so the change cannot be attributed to a change in the antiferromagnetic coupling. In fact, the magnetization loop for the film annealed at 350°C is somewhat more square than for the unannealed film, a feature usually associated with reduced coupling and therefore reduced magnetoresis-

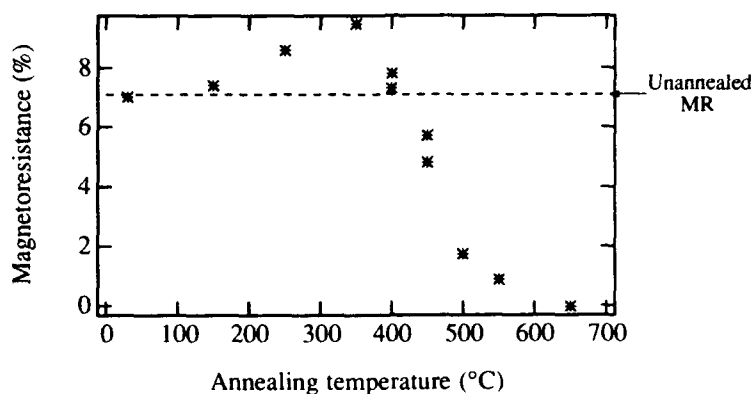


Figure 1: Magnetoresistance as a function of anneal temperature for an Si(001)/12ÅCr/20*(30ÅFe/12ÅCr)/12ÅCr/30ÅPt film.

tance. Thus we conclude that the change in magnetoresistance is due only to an increased spin asymmetry in the electron scattering. On the other hand, the saturation field decreases significantly for the higher temperature anneals, and their magnetization loops are quite square. The magnetoresistance curves for higher temperature anneals also display decreased saturation fields, and the peaks are cusp shaped. In this case the reduced magnetoresistance may be due to incomplete antiferromagnetic alignment at zero field, resulting from decreased antiferromagnetic coupling or increased ferromagnetic coupling between the iron layers. The saturation magnetization of the films does not change significantly upon annealing, indicating that at most less than 5% of the iron had lost its magnetic moment. Dilute alloys of iron in Cr are non-magnetic, so this indicates that there is no significant migration of iron into the spacer layers. There is no evidence of a magnetically dead layer

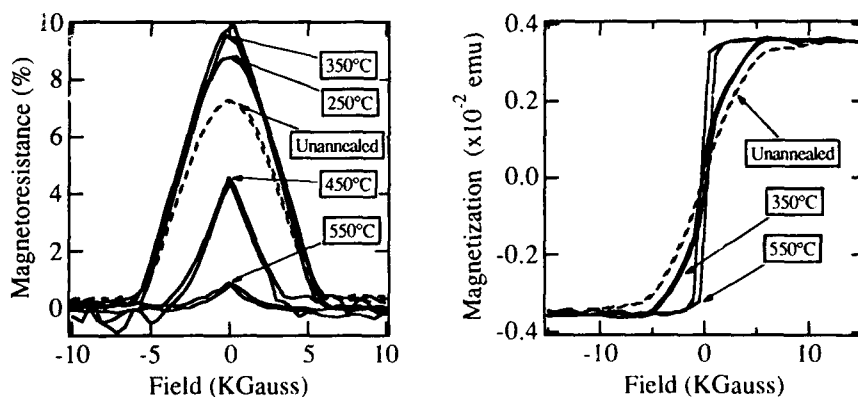


Figure 2: Magnetoresistance and magnetization curves for an Si(001)/12ÅCr/20*(30ÅFe/12ÅCr)/12ÅCr/30ÅPt annealed for one hour at several temperatures. The dashed line is the curve for the unannealed film.

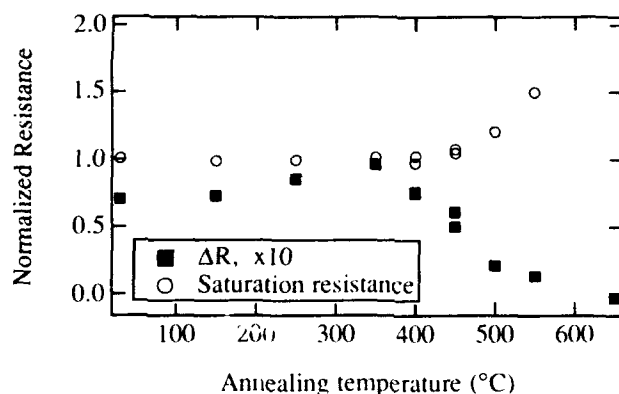


Figure 3: Saturation resistance and field dependent resistance for an $\text{Si}(001)/12\text{\AA Cr}/20^*(30\text{\AA Fe}/12\text{\AA Cr})/12\text{\AA Cr}/30\text{\AA Pt}$ annealed for one hour at several temperatures. The measured values have been normalized to the unannealed saturation resistance to eliminate sample size effects.

at the interface.

A decrease in magnetoresistance can be caused either by an increase in the saturation resistance or by a decrease in the field dependent resistance. The two components are shown separately in figure 3. The increase in magnetoresistance below 350°C is due entirely to a change in ΔR ; the saturation resistance is unchanged at these temperatures. For temperatures above 350°C and less than about 500°C the drop in magnetoresistance is due to a drop in ΔR , whereas for even higher anneal temperatures changes in both the saturation resistance and ΔR contribute to the decrease in the GMR. This indicates that the peak is not due to a crossover between temperature regimes where different processes dominate, a GMR reducing effect at high temperatures and a GMR enhancing effect at lower temperatures, but rather to an optimum point in the effect of annealing on the structure.

Another way to demonstrate this is to anneal at a constant temperature for various durations. Figure 4 shows data for a different film of nominally the same structure as before. In this case, the unannealed GMR was 8.1%. Because the chromium thickness used is very close to the peak in the first oscillation of the GMR, the magnetoresistance of the film is very sensitive to small variations in the chromium thickness, and the difference between the two films is due to a slight change in the sputtering rates. One segment of the film was annealed at 330°C at periods up to 151 hours. The maximum magnetoresistance for this temperature, 9.5%, was reached for anneals as short as 1 hour. A sample which was brought up to temperature and then immediately cooled had 9.3% magnetoresistance. For anneals longer than 3 hours, the magnetoresistance starts to decrease, and after 150 hours, the magnetoresistance has dropped to 7.3%, less than the unannealed film. Another segment of the same film was annealed at 250°C. The magnetoresistance rose to 8.7% for a 10 minute anneal, and continued to rise for longer anneals. After 70 hours it had not yet reached the maximum 9.5% MR achieved by the hotter anneal, but it may do so for even longer anneals. This data also supports the assertion that while the magnetoresistance peaks, the structural changes are continuing.

X-ray diffractin scans of the low angle superlattice lines were used to investigate the degree of intermixing in the multilayers. An $\text{Si}(001)/20^*(10\text{\AA Fe}/25\text{\AA Cr})$ film was used

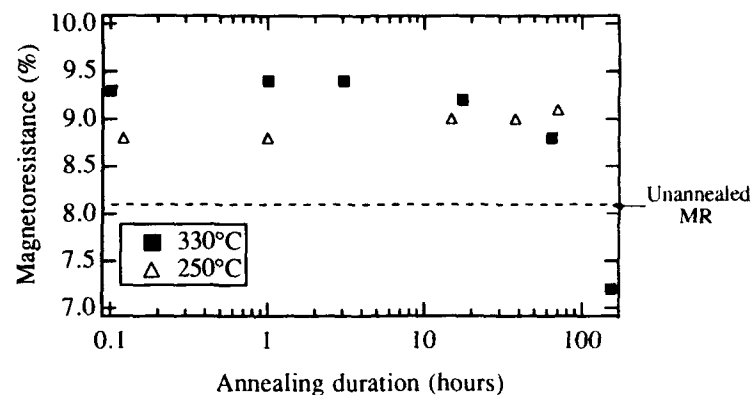


Figure 4: Magnetoresistance of an $\text{Si}(001)/12\text{\AA}\text{Cr}/20\text{\AA}(30\text{\AA}\text{Fe}/12\text{\AA}\text{Cr})/12\text{\AA}\text{Cr}/30\text{\AA}\text{Pt}$ annealed at 330°C and at 250°C for different time periods. The unannealed magnetoresistance was 8.1%, indicated on the left axis.

for the x-ray measurements, shown in figure 5. The unannealed film shows four orders of superlattice peaks, indicating relatively smooth interfaces. Finite size oscillations persist to 3.5 degrees 2θ , so the overall surface of the film is quite smooth. Both high order peaks and oscillations persist through anneals up to 450°C , so the structural effect of the anneal is quite mild. The film annealed at 550°C lacks the two highest order peaks and has weaker finite size oscillations, implying both overall roughening and that intermixing has occurred at the interfaces. However, since two orders of superlattice peaks remain even for the film annealed at 550°C , it is clear that the structural changes are quite subtle, and that significant electron density modulation remains in the film.

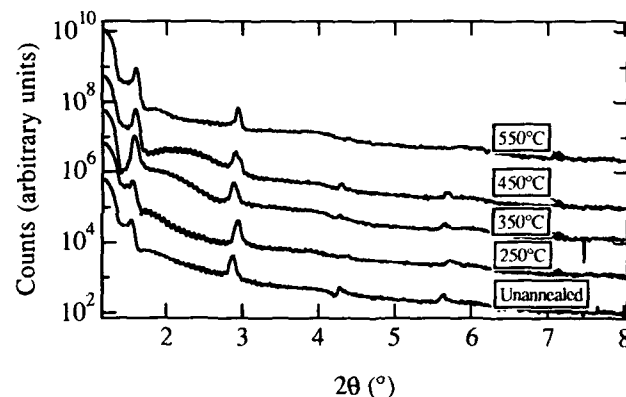


Figure 5: Low angle x-ray diffraction scans of an $\text{Si}(001)/20\text{\AA}(40\text{\AA}\text{Fe}/25\text{\AA}\text{Cr})$ film annealed for one hour at several temperatures. The scans have been offset for clarity.

CONCLUSIONS

Some degree of annealing clearly increases the magnetoresistance of Fe/Cr multilayers: the effect is maximized at 350°C and 1 hour. The increase is probably due to a slight interdiffusion of the two components, increasing the number of chrome scattering sites that differentially scatter the two spin currents. For longer or hotter anneals, the magnetoresistance starts to drop, accompanied by a drop in the saturation field. The magnetic moment is not changed significantly by the anneal, so most of the iron atoms retain their magnetic moment even if interdiffusion does occur. There is no evidence of a dead layer. The structural effects are subtle; the low angle superlattice lines are unchanged for anneals up to 450°C, but for the sample annealed at 550°C there is evidence of intermixing or roughening at the interfaces. We believe that the increase in magnetoresistance is due to interdiffusion at the interfaces, increasing the number of asymmetric Cr impurity scattering sites. The decrease in magnetoresistance and saturation field at higher anneal temperatures or longer time, along with the change in the shape of the curves, is due to a decrease in the antiferromagnetic coupling or an increase in ferromagnetic coupling between the iron layers.

REFERENCES

1. M. N. Baibich, J. M. Broto, A. Fert, F. N. V. Dau, F. Petroff, P. Etienne, G. Creuzet, A. Friedrich, and J. Chazelas. *Phys. Rev. Lett.*, **61**:2472-2475, 1988.
2. R. E. Camley and J. Barnas. *Phys. Rev. Lett.*, **63**:664-667, 1989.
3. P. Levy, S. Zhang, and A. Fert. *Phys. Rev. Lett.*, **65**:1643-1646, 1990.
4. B. Johnson and R. E. Camley. *Phys. Rev. B*, **44**:9997-1002, 1991.
5. P. Bruno and C. Chappert. *Phys. Rev. B*, **46**:261-70, 1992.
6. P. Baumgart, B. A. Gurney, D. R. Wilhoit, T. Nguyen, B. Dieny, and V. S. Speriosu. *J. Appl. Phys.*, **69**:4792-4794, 1991.
7. F. Petroff, A. Barthelemy, A. Hamzic, A. Fert, P. Etienne, S. Lequien, and G. Creuzet. *J. Mag. Mag. Mat.*, **93**:95-100, 1991.
8. E. E. Fullerton, D. M. Kelly, J. Guimpel, I. K. Schuller, and Y. Bruynseraede. *Phys. Rev. Lett.*, **68**:859-62, 1992.
9. S. S. P. Parkin, R. Bhadra, and K. P. Roche. *Phys. Rev. Lett.*, **66**:2152-5, 1991.
10. N. Rensing, A. Payne, and B. Clemens. *J. Mag. Mag. Mat.*, **121**:436-439, 1993.

Section A—Multilayers and Surfaces

PART VI

Structure and Magnetism I

GRAIN BOUNDARY DIFFUSION IN Co/Cu AND Co/Cr MAGNETIC THIN FILMS

JOHN G. HOLL-PELLERIN, S.G.H. ANDERSON, P.S. HO*, K.R. COFFEY, J.K. HOWARD**, AND K. BARMAK***

*Materials Laboratory for Interconnect and Packaging, University of Texas at Austin, BRC/MER Mail Code 78650, Austin, TX 78712-1100

**IBM, ADSTAR Division, 5600 Cottle Rd, 808/282, San Jose, CA 95193

***Department of Materials Science and Engineering, Lehigh University, Whitaker Laboratory, 5 East Packer Ave., Bethlehem, PA 18015-3195

ABSTRACT

X-ray photoelectron spectroscopy (XPS) has been used to investigate grain boundary diffusion of Cu and Cr through 1000 Å thick Co films in the temperature range of 325°C to 400°C. Grain boundary diffusivities were determined by modeling the accumulation of Cu or Cr on Co surfaces as a function of time at fixed annealing temperature. The grain boundary diffusivity of Cu through Co is characterized by a diffusion coefficient, $D_{0,gb}$, of 2×10^{-4} cm²/sec and an activation energy, $E_{a,gb}$, of 2.4 eV. Similarly, Cr grain boundary diffusion through Co thin films occurs with a diffusion coefficient, $D_{0,gb}$, of 6×10^{-2} cm²/sec and an activation energy, $E_{a,gb}$, of 1.8 eV. The Co film microstructure has been investigated before and after annealing by x-ray diffraction and transmission electron microscopy. Extensive grain growth and texturing of the film occurred during annealing for Co deposited on a Cu underlayer. In contrast, the microstructure of Co deposited on a Cr underlayer remained relatively unchanged upon annealing. Magnetometer measurements have shown that increased in-plane coercivity H_c , reduced remanence squareness S , and reduced coercive squareness S^* result from grain boundary diffusion of Cu and Cr into the Co films.

INTRODUCTION

The increasing demands on thin film magnetic media continue to be focused on improving the signal-to-media noise (S/N) ratio in order to achieve ever higher areal recording densities, with particular emphasis placed on reducing noise.¹ Recent studies have shown that the use of a Cr interlayer between magnetic layers can affect the magnetic properties by influencing the grain orientation and the crystallographic texture of CoCr-based thin films.^{1,2,3} For example, Cr templates 150 Å and 1500 Å thick caused the grain size of CoPtCr films to double and created voids between the grains. The films produced with the thicker interlayer exhibited improved noise properties, which were attributed to either a reduction in exchange coupling between the grains or by a loss in preferred c-axis in-plane orientation.³ Significantly, the intergrain exchange coupling could also be reduced by compositional segregation of non-magnetic materials to the grain boundaries.¹ Segregation from a Cr interlayer into the grains and grain boundaries of a CoNiCr magnetic thin film has been proposed to explain the observed increase of in-plane coercivity H_c as a function of time at constant temperature. However, direct evidence for grain boundary diffusion was not presented.⁴

To investigate the nature of grain boundary diffusion in magnetic thin films, we have measured and modeled the surface accumulation of Cu and Cr diffusants through 1000 Å thick Co films with x-ray photoelectron spectroscopy (XPS). By measuring the accumulation

of diffusant on the Co free surface as a function of time at a fixed temperature, the grain boundary diffusivity has been determined using a model developed by Hwang and Balluffi.⁵ In addition, the effects of annealing on the Co thin film microstructures and magnetic properties have been investigated.

METHODS

Experimental

The 1000 Å Co / 100 Å Cu and 1000 Å Co / 100 Å Cr bilayer thin film structures were prepared by UHV evaporation; Co and Cu films were electron beam evaporated while the Cr films were resistively evaporated. All bilayers were deposited onto sputtered 700 Å SiO₂ / Si (100) substrates at a rate of 0.2 Å/sec at ambient temperature. Preparation of the as-received Co/Cu and Co/Cr samples prior to permeation experiments consisted of Ar⁺ sputtering to remove ~44 Å of native CoO formed by exposure to air.⁶ Sputter cleaning was done in a sample introduction/preparation chamber at an Ar pressure of 5×10^{-5} Torr, with 30 mA ion gun emission current and 1 kV Ar⁺ beam energy.

Permeation experiments were performed in a UHV system consisting of three chambers. A turbomolecular-pumped sample introduction chamber (base pressure = 1×10^{-8} Torr) allows annealing and/or sputtering of samples before they are transferred into the XPS analysis chamber. The analysis chamber operates in a pressure range of 5×10^{-11} to 1×10^{-10} Torr with a 400 l/s ion pump. Photons are generated by a non-monochromatized Al/Mg dual anode x-ray source running at 280 W for Mg K_α x-rays ($h\nu = 1253.6$ eV, linewidth = 0.7 eV). Photoelectrons emitted from the sample are measured with a Leybold EA-11 single channel hemispherical analyzer operating at 150 eV pass energy, yielding a energy resolution of ~2.4 eV. Higher resolution measurements (50 eV pass energy yielding ~1.0 eV energy resolution) were made before and after each permeation experiment to check for surface oxidation. All binding energies are referenced to the Au 4f_{7/2} core level peak at -83.9 eV. To enhance surface sensitivity, the permeation experiments were performed with the sample oriented so that the angle between the surface normal direction and the analyzer was ~80°. Samples are annealed to temperatures of 425°C on a heating module that is mounted to the sample manipulator within the XPS analysis chamber.

Permeation experiments were performed by measuring the areas of the 2p_{3/2} core level peaks of Co and Cu or Cr at -779.6, -934.9 and -575.5 eV binding energies, respectively. An inelastic background subtraction routine is used to calculate the core level peak areas during the data acquisition process.⁷ Each of the core level peak areas are normalized to the acquisition time to quantitatively monitor the accumulation profile.

All magnetization measurements were performed with a Quantum Design MPMS superconducting quantum interference device (SQUID) at 300K with the applied field lying in the plane of the Co/Cu and Co/Cr films. Sample sizes were approximately 5 mm wide, 17 mm long and 0.34 mm thick. Hysteresis loop measurements were made with applied fields up to 3 kOe.

Analysis of Grain Boundary Diffusion

The accumulation of diffusant on a surface as a result of grain boundary diffusion has been modeled by Hwang and Balluffi.⁵ Their model was developed within the conditions of type C kinetics where the barrier to bulk diffusion is high and mass transport within the thin

film occurs only along grain boundaries.⁸ As a coarse approximation, type C kinetics apply at temperatures less than ~35% of the film's melting point.

Hwang and Balluffi applied Fick's 2nd law to the grain boundaries and the film's exit, or free, surface where diffusant accumulates and equated the material fluxes at the intersections of the grain boundary with both the diffusant source and exit surfaces. Two assumptions allow direct calculation of the grain boundary diffusivity from the measurement of surface accumulation as a function of annealing time and constant temperature. First, the diffusion of material on the exit surface is assumed to be much faster than diffusion in the grain boundary, so the amount of material accumulated on the exit surface is solely a function of time. Second, the capacity of the grain boundary is assumed to be much less than that of the exit surface. Consequently, a steady state concentration profile in the grain boundary is established and maintained. Combining these assumptions with that of an infinite diffusant source, the following expression for the surface concentration of permeated diffusant material as a function of time was derived:

$$C_s(t)/C_s(\infty) = 1 - \exp(-h(t-t_0)) \quad (1)$$

where C_s is the average surface concentration at annealing time t , t_0 is the time before permeated material reaches the surface, and h is a factor proportional to the grain boundary diffusivity. The factor h consists of the following terms:

$$h = (w_b/w_s)(2/dl) D_b \quad (2)$$

where w_b is the grain boundary width, w_s is the thickness of the accumulated layer on the exit surface, d is the grain diameter, l is the film thickness, and D_b is the grain boundary diffusivity. While these equations have been successfully applied to a wide variety of materials systems, there is little information available for Co thin films.^{9,10}

RESULTS AND DISCUSSION

Permeation of Cu through Co

Permeation experiments for the 1000 Å Co/100 Å Cu thin film structures were carried out at temperatures of 325, 350, 375 and 400°C. Background subtracted peak areas for Cu and Co 2p_{3/2} emission are plotted in Fig. 1 as a function of time at 350°C. The Cu 2p_{3/2} emission rises sharply as Cu emerges from the exit surface and gradually reaches a plateau, while the Co signal attenuates exponentially as the accumulation of Cu on the surface saturates. Measurements at the other temperatures exhibited similar behavior. Superimposed on the Cu surface accumulation profile is a fitted curve in the form of Eq. (1) from which h can be found. Grain boundary diffusivities can then be calculated once the remaining terms in Eq. (2) are known.

In order to determine the grain boundary diffusivity using values of h in Eq. (2), four geometric parameters of the thin film must be known. First, the as-deposited film thicknesses of 1000 Å were assumed to remain unchanged during annealing. The thickness of the saturated Cu overlayer after annealing was estimated by two methods. First, the exponential attenuation of the Co signal was equated to a Cu overlayer thickness of 5 Å where the inelastic mean free path length for 474 eV kinetic energy Co photoelectrons is 13 Å.¹¹ Alternately, by evaporating incremental Cu layers onto a sputtered Co surface and observing the Cu thickness where the attenuated Co signal equaled that of the permeation

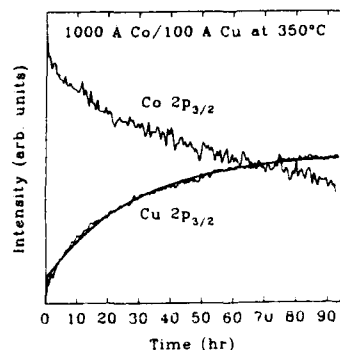


Figure 1. Background subtracted peak areas of the Co $2p_{3/2}$ (upper curve) and Cu $2p_{3/2}$ (lower curve) as a function of annealing time at 350°C.

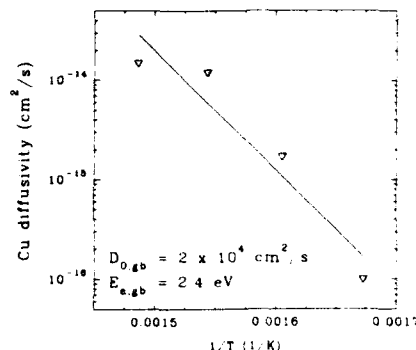


Figure 2. Calculated grain boundary diffusivities of Cu through 1000 Å Co films.

experiment, the Cu overlayer thickness was also found to be 5 Å. The grain boundary width, w_b , was estimated to be equal to the saturated Cu overlayer thickness, $w_s = 5$ Å.

The Co film grain size is the last parameter that must be determined before Eq. (2) can be solved for D_b . Transmission electron microscopy (TEM) and x-ray diffraction have been used to estimate Co grain size on as-deposited and annealed Cu/Co bilayers. Prior to annealing, analysis of diffraction peak widths and TEM revealed the as-deposited Co grain size to be approximately 135 Å with near random orientation on the Cu underlayer. After annealing, substantial grain growth occurred accompanied by preferential texturing of the Co film with a (0001) orientation. The mechanism for grain growth in this case is surface energy enhanced grain growth where the Cu underlayer may promote the growth of Co grains with the lowest surface energy configuration; in this case, grains with the (0001) planes largely parallel to the film surface.¹² The annealed grain size was estimated from the plan view TEM micrographs using the Heyn linear intercept method.¹³ In this analysis, the grain size was calculated to be 3500 Å \pm 750 Å for the annealed film based on an average of 38 line measurements of 40 Co grains. The actual temperature regime where grain growth occurred could not be determined from these measurements since the x-ray diffraction and TEM analyses were done after the samples were subjected to multiple permeation experiments at different temperatures. Similarly, the time necessary for grain growth at the various annealing temperatures was not determined, although this would affect the measured values of h from the least squares fitting of the permeation experiments.

In Fig. 2, the calculated diffusivities are plotted versus $1/T$ for experiments conducted between 325 and 400°C. A straight line fit to the data yields a $D_{0,gb}$ of 2×10^4 cm²/sec and an activation energy $E_{a,gb}$ of 2.4 eV. The bulk diffusion of Cu through Co has a $D_{0,bulk}$ of ~ 1 cm²/sec and an $E_{a,bulk}$ of 2.86 eV.¹⁴ As a general rule of thumb, the activation energy for grain boundary diffusion is approximately half of the energy required for bulk diffusion. The violation of this criteria for the 1000 Å Co / 100 Å Cu bilayer is attributed to extensive grain growth during the annealing process.

Diffusion of Cr through Co

Similar permeation experiments were performed on 1000 Å Co / 100 Å Cr bilayers

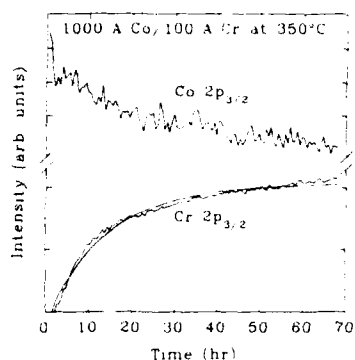


Figure 3. Background subtracted peak areas of the Co $2p_{3/2}$ (upper curve) and Cr $2p_{3/2}$ (lower curve) as a function of annealing time at 350°C .

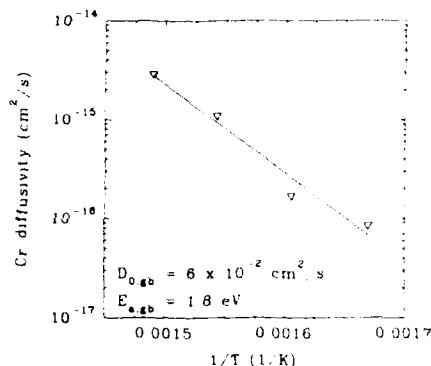


Figure 4. Calculated grain boundary diffusivities of Cr through 1000 Å Co films.

for the same temperatures as the Co/Cu bilayers discussed above. Figure 3 illustrates the behavior of the integrated and background subtracted Co and Cr $2p_{3/2}$ core level peak areas versus time at 350°C including the fitted curve using Eq. (1) for the Cr accumulation. Permeation measurements for the other temperatures yielded similar Cr accumulation behavior and could also be fitted with Eq. (1). The attenuation of the Co $2p_{3/2}$ peak signal with Cr accumulation obeys an exponential decay indicating that the Cr also forms a uniform overlayer saturating at ~ 5 Å thick. This observation is supported by separate measurements of the exponential decrease in the Co emission with incremental Cr evaporations onto a sputtered Co surface.

The Co film microstructures were also compared before and after the Cr permeation experiment at 350°C using x-ray diffraction and TEM. The grain size of the Co film deposited on the Cr underlayer exhibited minimal grain growth from 125 Å to 170 Å upon annealing, in contrast to the Co films deposited on Cu underlayers. The Co grains remained randomly oriented after annealing.

Grain boundary diffusivities for Cr were calculated according to Eq. (2) assuming grain boundary widths and surface layer thicknesses of 5 Å. The grain size was 170 Å for all samples independent of annealing temperature since grain growth was minimal. The calculated grain boundary diffusivities of Cr through Co are summarized in Fig. 4. For temperatures between 325°C and 400°C we have determined a diffusion coefficient, $D_{0,gb}$, of $6 \times 10^{-2} \text{ cm}^2/\text{sec}$ and an activation energy, $E_{a,gb}$, of 1.8 eV.

In summary, we can compare our measured values for Cu and Cr permeation through Co to that for grain boundary self diffusion in Co having an $E_{a,gb} = 1.46 \text{ eV}$ and $D_{0,gb} = 7 \times 10^{-3} \text{ cm}^2/\text{sec}$.¹⁵ Again, we have determined that grain boundary diffusion of Cr through Cu is characterized by an $E_{a,gb} = 1.8 \text{ eV}$ and $D_{0,gb} = 6 \times 10^{-2} \text{ cm}^2/\text{sec}$, in contrast to Cu diffusion through Co exhibiting an $E_{a,gb} = 2.4 \text{ eV}$ and $D_{0,gb} = 2 \times 10^4 \text{ cm}^2/\text{sec}$. The deviation for Co films on Cu underlayers has been explained by observed grain growth which occurred during annealing.

Magnetic Property Measurements of Co/Cu and Co/Cr Bilayers

Magnetization measurements on as-deposited and annealed bilayers have been made to

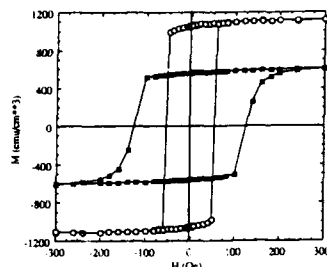


Figure 5. Hysteresis loops for a 1000 Å Co / 100 Å Cr bilayer in the as-deposited case (open circles) and annealed at 400 °C (filled squares).

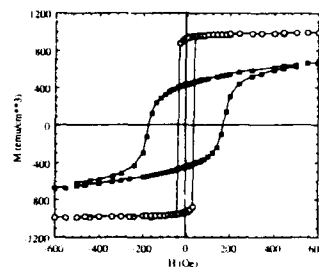


Figure 6. Hysteresis loops for a 1000 Å Co / 100 Å Cu bilayer in the as-deposited case (open circles) and annealed at 400 °C (filled squares).

observe how Cu and Cr grain boundary diffusion affected the magnetic properties of the Co films. Magnetization curves for Co/Cu and Co/Cr bilayers annealed at 400°C were measured after accumulation of the diffusant on the Co surface was complete. Of particular interest are changes in the in-plane coercivity H_c , saturation magnetization M_s , remanence squareness S , and coercive squareness S^* before and after annealing.

For the as-deposited 1000 Å Co / 100 Å Cr bilayer, the magnetization hysteresis loop is shown in Fig. 5 by the open circles where $H_c = 55$ Oe, $M_s = 1100$ emu/cm³, $S = 0.92$, and $S^* = 0.90$. The magnetization behavior after annealing is shown by the filled squares in Fig. 5 yielding an $H_c = 123$ Oe, $M_s = 650$ emu/cm³, $S = 0.86$, and $S^* = 0.76$.

The increase in H_c and reductions in S and S^* with annealing are attributed to the diffusion of Cr into Co grain boundaries separating the Co grains and reducing the magnetostatic coupling among the grains. In addition, a reduction in intergrain exchange coupling with annealing also contributes to increasing H_c and reductions in squareness.¹⁶ The squareness of the hysteresis loop for the as-deposited case is dominated by shape anisotropy of the Co film where the easy magnetization lies in the film plane which is parallel to the applied field direction. For the annealed Co/Cr bilayer, the Co grain size and orientation remain relatively unchanged with annealing as observed by TEM and x-ray diffraction. Therefore, the squareness of the hysteresis loop remains high due to shape anisotropy of the thin film. Overall, the enhancement of H_c and reductions in S and S^* are solely attributed to Co grain boundary stuffing with Cr atoms since little change in the Co film microstructure was observed.

The hysteresis loop for a 1000 Å Co / 100 Å Cu bilayer in the as-deposited condition exhibits a $H_c = 35$ Oe, $M_s = 1000$ emu/cm³, $S = 0.94$ and $S^* = 0.85$ (Fig. 6, open circles). After annealing, H_c increased to 165 Oe, S decreased to 0.48, S^* decreased to 0.78 and M_s remained relatively constant at 910 emu/cm³ as indicated by the filled squares in Fig. 6.

Annealing the Co/Cu bilayers, however, has been shown by x-ray diffraction and TEM to cause extensive grain growth and recrystallization texturing with the c-axis (easy magnetization direction) of the Co grains pointing out of the film plane and, therefore, perpendicular to the applied field direction in the magnetization measurements. Thus, the shape of the hysteresis loop for the annealed Co/Cu sample represents a competition between the shape anisotropy induced by the film geometry and the crystalline anisotropy induced by recrystallization during annealing.

Surface accumulation measurements indicate that Cu diffuses through the Co grain boundaries for the temperatures studied. The enhancement in H_c between the as-deposited and annealed Co/Cu bilayers is likely to be dominated by a reduction in Co intergrain

exchange coupling as in the case of Co/Cr bilayers. However, the additional role of microstructural changes on the magnetic properties is unclear.

CONCLUSIONS

Permeation experiments made over the temperature range of 325°C to 400°C indicate that grain boundary diffusion of Cu and Cr through Co does occur. Thin films of Co on Cu underlayers exhibit extensive grain growth and texturing during annealing which introduce uncertainty into the diffusivity calculations for this bilayer system. Chromium underlayers are observed to preserve the as-deposited Co film microstructure with annealing. For both bilayer systems, improvements in in-plane coercivity H_c and reductions in coercive squareness S^* are attributed to reduced intergranular magnetic coupling by separating Co grains with Cu and Cr in the grain boundaries.

ACKNOWLEDGMENTS

The authors thank Chris Wooten of the Univ. of Texas Physics Dept. for magnetometer measurements. This work was sponsored by the IBM SUR program under Agreement No. SJ92407.

REFERENCES

1. K.E. Johnson, J. Appl. Phys. **69**, 4932 (1991).
2. T. Coughlin, J. Pressesky, S. Lee, N. Heiman, R.D. Fisher, and K. Merchant, J. Appl. Phys. **67**, 4689 (1990).
3. K.E. Johnson, P.R. Ivett, D.R. Thomas, M. Mirzamaani, S.E. Lambert, and T. Yogi, J. Appl. Phys. **67**, 4686 (1990).
4. S.L. Duan, J.O. Artman, K. Hono, and D.E. Laughlin, J. Appl. Phys. **67**, 4704 (1990).
5. J.C.M. Hwang and R.W. Balluffi, J. Appl. Phys. **50**, 1339 (1979).
6. L. Smardz, U. Köbler, and W. Zinn, J. Appl. Phys. **71**, 5199 (1992).
7. A. Proctor and P.M.A. Sherwood, Anal. Chem. **54**, 13 (1982).
8. L.G. Harrison, Trans. Faraday Soc. **57**, 1191 (1961).
9. D. Gupta, D.R. Campbell, and P.S. Ho in Thin Films - Interdiffusions and Reactions, edited by J.M. Poate, K.N. Tu, and J.W. Mayer (Wiley, New York, 1978), p. 161.
10. I. Kaur and W. Gust, Fundamentals of Grain and Interphase Boundary Diffusion (Ziegler Press, Stuttgart, 1989).
11. M.P. Seah and W.A. Dench, Surf. Interface Anal. **1**, 2 (1979).
12. J.A. Venables, G.D.T. Spiller, and M. Hanbücken, Rep. Prog. Phys. **47**, 399 (1984).
13. G.F. Van der Voort, Metallography Principles and Practice (McGraw-Hill, New York, 1984), p.449.
14. Landolt-Börnstein Numerical Data and Functional Relationships in Science and Technology, edited by O. Madelung and H. Mehrer (Springer-Verlag, Berlin, 1990), Group III, Vol. 26, p. 52.
15. S.D. Gertsriken, T.K. Yatsenko, and L.F. Slastnikova, Prob. Phys. Met. Metall. (Voprosy Fiz. Met. Metallov.), Akad. Nauk SSSR **9**, 154 (1959).
16. J. Zhu and H.N. Bertram, J. Appl. Phys. **63**, 3248 (1988).

QUANTITATIVE ANALYSIS OF POLARIZED NEUTRON SPECULAR REFLECTIVITY FROM A Co/Cu(111) SUPERLATTICE AT THE SECOND ANTIFERROMAGNETIC MAXIMUM

J.F. Ankner*, A. Schreyer**, C.F. Majkrzak*, K. Brühl**, Th. Zeidler**, P. Bödeker**, and H. Zabel**

*National Institute of Standards and Technology, Gaithersburg, MD 20899

**Ruhr Universität Bochum, D-4630 Bochum, Federal Republic of Germany

ABSTRACT

We have used polarized neutron reflectivity to prove the existence of oscillatory coupling in MBE-grown Co/Cu(111) superlattices. For a sample of composition $[3.4 \text{ nm Co}/2.0 \text{ nm Cu}]_{10}$, we find that only a small fraction of the sample volume exhibits coherent antiferromagnetic order, with the structure of the remainder of the film being attributable to ferromagnetic domains and small disordered structures.

THE Co/Cu(111) CONTROVERSY

The magnetic coupling of ferromagnetic cobalt layers across nonmagnetic copper interlayers is an extensively studied phenomenon and consequently the field is characterized by a certain amount of disharmony. The first observations of antiferromagnetic (AF) coupling [1] and coupling dependent on Cu interlayer thickness [2] were made on films grown in the (100) orientation (cobalt assumes the fcc structure of copper). Oscillatory coupling with a period of about 1.0 nm was first seen [3, 4] in sputtered (111) multilayers. Subsequent attempts to observe oscillations in single-crystal (111) superlattices grown by molecular-beam epitaxy (MBE) have generally yielded negative or ambiguous results [5-8]. A recent paper [9] reports oscillatory coupling between isolated cobalt monolayers in a copper matrix, but with a much longer period than in the sputtered multilayers.

We have grown a series of Co/Cu(111) superlattices by MBE and have measured oscillations in saturation field as a function of Cu interlayer thickness with peaks around $d_{\text{Cu}} = 1.0, 1.9$, and 2.8 nm [10], in agreement with theoretical predictions [11]. Similar results have subsequently been obtained by Dupas, et al [12] from magnetoresistance measurements. Using polarized neutron diffraction, we have determined that the films exhibit coherent AF order at the first two maxima and no measurable AF order at an intermediate thickness [10]. In this paper, we will present a detailed investigation of the nature of the magnetic order present in a superlattice with $d_{\text{Cu}} = 2.0 \text{ nm}$ and characterize this order by means of quantitative refinement of polarized neutron specular reflectivity data. Combining this information with x-ray and magneto-optic Kerr effect (MOKE) measurements, we will comment on the influence of structural disorder on the observed magnetic behavior.

MEASURING MAGNETIC STRUCTURE

The nature of the magnetic order in Co/Cu(111) films grown by molecular-beam epitaxy (MBE) has been controversial because of the coexistence of remanent ferromagnetism with a generally small or nonexistent antiferromagnetic volume fraction. Our samples were grown by MBE on $\text{Al}_2\text{O}_3(1120)$ substrates with a Nb(110) buffer layer (see refs. [10, 13, 14] for details). The MOKE loop from a sample of similar composition to the one discussed below ($d_{\text{Cu}} = 2.0 \text{ nm}$), shown in Fig. 1a, is typical. At zero field, there exists a large remanent magnetization containing more than half of the total sample moment, preceded by a gradual upward slope to saturation above 1500 Oe. The strength of the antiferromagnetic coupling is commonly determined from the magnitude of the saturation field. What more can be said about the magnetic structure?

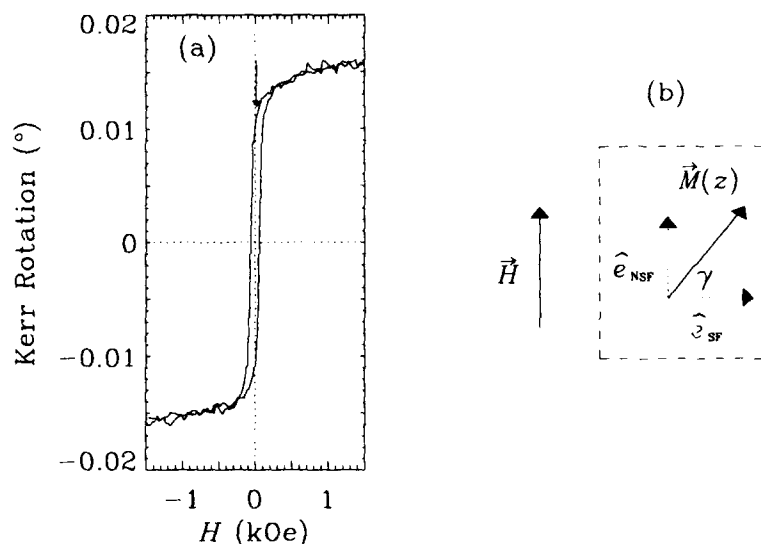


Figure 1: MOKE loop and important vectors. (a) MOKE loop from sample with $d_{\text{Cu}} = 2.0$ nm. At zero field, there is a large remanent magnetization, preceded by a gradual slope to saturation above 1500 Oe. The value of the saturation field is related to the strength of the coupling. The arrow, at $H = 14$ Oe, indicates where neutron data were taken. (b) Axis definitions for scattering. Neutrons, spin-polarized either parallel or anti-parallel to an applied field \vec{H} , interact with nuclei and unpaired electrons in the sample. The orientation of the average magnetization $\vec{M}(z)$ (in general a function of depth z below the surface) with respect to \vec{H} determines the character of the scattering. Magnetization components normal to \vec{H} cause the neutron spin to flip (SF processes), while nuclear scattering and parallel moment components produce intensity in the non-spin-flip (NSF) channel.

In order to move beyond the measurement of bulk properties, our aim has been to construct a quantitative portrait of the magnetic character of these superlattices using polarized neutron reflectivity. In a specular reflectivity measurement (angle of incidence equal to angle of reflection), one can determine the distribution of scattering material with depth below the sample surface [15]. Since thermal neutrons interact with both nuclei and unpaired electron spins, they are an ideal probe of magnetic structure. For magnetic moments lying in the plane of the surface, one can describe the reflectivity qualitatively in terms of spin-dependent refractive indices (see refs. [16, 17] and references therein for the exact formalism),

$$n_{\pm\pm} \approx 1 - \frac{\lambda^2}{2\pi} N [b \pm p \sin \gamma], \quad (1)$$

$$n_{\pm\mp} \approx 1 - \frac{\lambda^2}{2\pi} N p |\cos \gamma|, \quad (2)$$

where λ is the wavelength of the neutrons, N the number density of the scatterers, b the nuclear scattering amplitude, and p the magnetic scattering amplitude [proportional to the magnetic

Table I: Nuclear and magnetic scattering density depth profiles. The data in this table were used in the model: l is the layer number, the second column is a brief description, Nb is the nuclear scattering density, d the layer thickness, σ the Gaussian roughness, and Np the magnetic scattering density. The most significant feature in this list is the presence of significant mixing of the Co and Cu as evidenced by the non-zero magnetic moment of the nominal Cu layers.

l	Type	Nb (10^{-4} nm^{-2})	d (nm)	σ (nm)	Np (10^{-4} nm^{-2})
1	CoO _x	2.0	4.56	0.43	0
2, 4, ..., 20	Cu	4.8	2.03	0.86	1.1
3, 5, ..., 19	Co	3.2	3.45	0.86	2.2
21	Nb	3.9	5.16	0.43	0
22	Al ₂ O ₃	5.2		0.21	0

moment $\bar{\mu}$ per atom: $p \equiv (2.695 \times 10^{-4} \text{ nm}/\mu_B)|\bar{\mu}|$, where μ_B is the Bohr magneton]. The refractive indices depend on the angle γ of the sample magnetization \vec{M} with respect to the neutron quantization axis defined by the applied field \vec{H} (see Fig. 1b). The subscripts refer to neutrons polarized parallel (+) and anti-parallel (-) to the quantization axis before (first subscript) and after (second subscript) reflection from the sample. Each of the quantities N , b , p , and γ may vary with depth below the surface, with the magnetization $\vec{M}(z)$ sampled by the neutrons being the average of the atomic magnetic moments $\bar{\mu}$ at a given depth z . From elementary quantum mechanics, we can describe two types of scattering: magnetization components normal to \vec{H} cause spin-flip (SF) scattering [(+-) and (-+) in equation (2)], while nuclei and parallel magnetic components scatter in the non-spin-flip (NSF) channel [(++) and (--) in equation (1)]. From the reflectivities measured as a function of specular reflection angle θ for these four cross sections, we can extract the depth profiles of both nuclear and magnetic scatterers.

ANTIFERROMAGNETISM AT THE SECOND MAXIMUM

Our neutron reflectivity measurements from the [3.4 nm Co/2.0 nm Cu]₁₀ superlattice unambiguously reveal the presence of coherent antiferromagnetic order at the second maximum of the saturation field. Fig. 2a shows the reflectivity from this film in the four cross sections [(+-) and (-+) are equal and have been added together to improve counting statistics] in an applied field of 14 Oe. The data are plotted as a function of wavevector transfer $Q = 4\pi \sin \theta / \lambda$, where θ is the specular angle and λ the wavelength of the neutrons (0.237 nm). Before being mounted on the BT-7 reflectometer at NIST, the sample was placed in a 700 Oe field parallel to the eventual 14 Oe quantizing field. This procedure aligns the ferromagnetic domains parallel to \hat{e}_{NSF} and orients antiferromagnetic domains by "spin-flop" along \hat{e}_{SF} . There are several significant features visible in the data. The splitting at the first-order superlattice peak [$Q \approx 2\pi/(5.4 \text{ nm}) \approx 1.2 \text{ nm}^{-1}$] between (++) and (--) intensities reveals the presence of significant ferromagnetic (FM) order parallel to the 14 Oe quantizing field, consistent with the MOKE measurement (Fig. 1a). The most important feature, however, is the broad peak in the SF cross sections centered around 0.6 nm^{-1} . This peak indicates that the sample possesses magnetic structure with twice the periodicity of the chemical superlattice. Antiferromagnetic order, with adjacent Co layer moments oppositely aligned, characteristically produces this type of scattering.

The observations outlined above can be quantified by using the exact solution of the spin-1/2 Schrödinger equation for a stratified medium to model the depth profile of the superlattice (see ref. [15] for a description of the fitting process and the references cited in ref. [16] for the polarized neutron formalism). The solid lines in Fig. 2a were generated from the profiles shown in Figs. 2b and 2c, described in Tables I and II. The data exhibit a smaller critical angle for total reflection in the (++) cross section than would be expected if the Co were completely

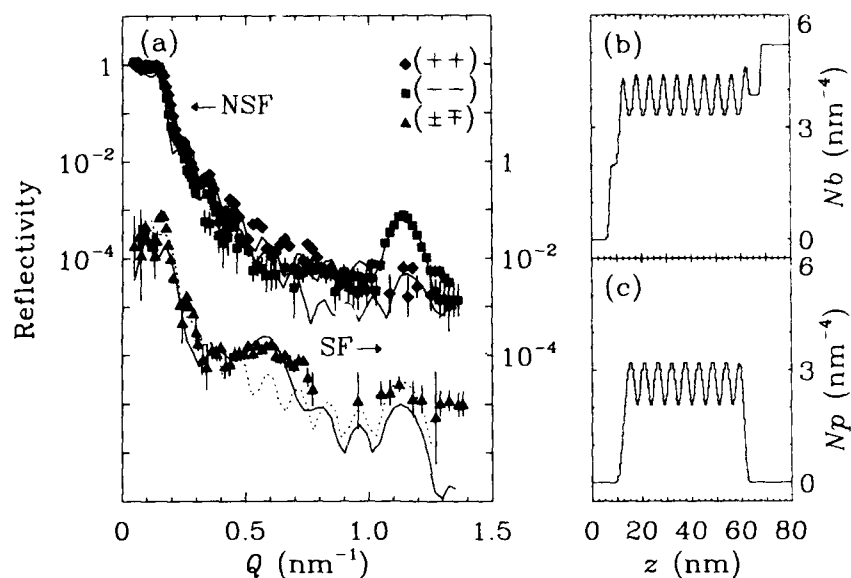


Figure 2: Polarized neutron reflectivity and scattering density profiles. (a) Spin-flip (SF) and non-spin-flip (NSF) reflectivities are plotted as a function of wavevector transfer $Q = 4\pi \sin \theta / \lambda$. The strong splitting at $Q \approx 2\pi / (5.4 \text{ nm}) \approx 1.2 \text{ nm}^{-1}$ in the NSF indicates ferromagnetic order, while the weaker and broader peak at 0.6 nm^{-1} in the SF is the signature of AF structure. The missing data points in the SF scan near $Q \approx 0.85 \text{ nm}^{-1}$ result from subtraction of a non-specular background. The points adjacent to this region should therefore be taken as upper limits on the intensity that was subtracted away. The solid lines represent a model calculation including a 15% AF domain occupancy, while the dashed line was obtained from a completely FM model. The SF data have been offset by two orders of magnitude and are plotted versus the scale on the right axis. (b) Nuclear scattering density depth profile. Proceeding inward from vacuum ($z = 0$), one encounters Co oxide, the Cu/Co superlattice ($12 \text{ nm} < z < 64 \text{ nm}$), the Nb buffer layer, and the Al_2O_3 substrate. (c) Magnetic scattering density depth profile. This curve essentially tracks the presence of Co, which we observe to be present in the non-magnetic Cu layers (minima).

Table II: Magnetic domain populations. The model fits are produced from coherent (amplitude) sums of different magnetic domains, weighted by their occupancies. Most of the sample resides in ferromagnetic (FM) domains, both aligned with the field ($\gamma = 90^\circ$) and normal to it ($\gamma = 0^\circ$). The FM domains are coherent through all 10 bilayers, while the antiferromagnetic (AF) domains are only coherent through about 4 bilayers.

Type	γ	Occupancy	Coherence Length
FM	90°	65%	> 50.0 nm
FM	0°	20%	> 50.0 nm
AF	$0^\circ/180^\circ$	15%	~ 20.0 nm

remanently magnetized. This reduced critical angle implies that the magnetic domains scatter coherently—we must calculate the average magnetic moment from these domains *before* squaring the reflectivity amplitude to obtain the intensity. Employing such a procedure, we find that only 65% of the Co is in remanence. The broad peak in the SF intensity at $Q \approx 0.6 \text{ nm}^{-1}$ (see Fig. 2a) can be reproduced by assuming that 15% of the Co moment resides in AF domains which are coherent over about four bilayers (~ 20.0 nm). The remaining 20% of the Co moment is found in FM domains with net projections along the direction normal to the quantizing field. The solid lines in Fig. 2a were calculated using this model, which is described in Figs. 2b, 2c, and Tables I and II. The dashed line plotted with the SF data was calculated by assuming that all 35% of the non-remnant moment is ferromagnetic and oriented in the SF direction. The poor fit of this model (dashed line) to the SF intensity near $Q \approx 0.6 \text{ nm}^{-1}$ demonstrates that the observed scattering cannot be reproduced by purely FM domains.

DISCUSSION AND CONCLUSION

We have determined the magnetic structure in the growth direction of an MBE-grown Co/Cu(111) superlattice ($d_{\text{Cu}} = 2.0$ nm) and find multiple domains, strong remanent ferromagnetism, and a small but significant antiferromagnetic structural component. Based on x-ray specular reflectivity measurements, we have found it necessary to include in our model a substantial amount of mixing of the Co and Cu layers (see in particular Fig. 2c). The exact nature of this mixing is an important issue that cannot be addressed solely by a specular reflectivity measurement. One must separate out the contributions of atomic steps (caused by, e.g., substrate mis-cut), true diffusion, and uncorrelated interfacial roughness before making any statement about the possible existence of pinholes (see ref. [18]). However, our observation of substantial structural disorder and multiple magnetic domains is consistent with a very recent scanning tunneling microscopy study of Co/Cu(111) growth [19]. This study finds islands of Co and Cu with gaps between, allowing for Co bridges through Cu and vice versa. Such a structure would explain the large ferromagnetic component seen in these films. We are currently at work on an analysis of diffuse and Bragg scattering which we hope will further elucidate the extent of the pinhole phenomenon and its consequences for magnetic structure.

In conclusion, we have given definitive proof of the existence of oscillatory coupling in MBE-grown Co/Cu(111) superlattices by observing antiferromagnetic order for $d_{\text{Cu}} = 2.0$ nm. By studying such an ill-behaved system as epitaxial Co/Cu(111), we can better understand the general interaction between growth, structure, and magnetism. Our ongoing effort is to further this work by improved x-ray and neutron structural characterization.

ACKNOWLEDGMENTS

We would like to thank J.A. Borchers for a skeptical appraisal of some of these ideas and N. Metoki for helpful discussions. The work in Bochum was supported by the Deutsche Forschungsgemeinschaft through SFB 166 and the Bundesministerium für Forschung und Technologie through grant 03-ZA3BOC. Furthermore, we would like to acknowledge travel support from the North Atlantic Treaty Organization through grant CRG 901064.

REFERENCES

1. A. Cebollada, J.L. Martinez, J.M. Gallego, J.J. de Miguel, R. Miranda, S. Ferrer, F. Batallán, G. Fillion, and J.P. Rebouillat, *Phys. Rev. B* **39**, 9726 (1989).
2. D. Pescia, D. Kerkmann, F. Schumann, and W. Gudat, *Z. Phys. B* **78**, 475 (1990).
3. S.S.P. Parkin, R. Bhadra, and K.P. Roche, *Phys. Rev. Lett.* **66**, 2152 (1991).
4. D.H. Mosca, F. Petroff, A. Fert, P.A. Schroeder, W.P. Pratt, and R. Laloe, *J. Magn. Magn. Mater.* **94**, L1 (1991).
5. W.F. Egelhoff, Jr. and M.T. Kief, *Phys. Rev. B* **45**, 7795 (1992).
6. S.S.P. Parkin, R.F. Marks, R.F.C. Farrow, G.R. Harp, Q.H. Lam, and R.J. Savoy, *Phys. Rev. B* **46**, 9262 (1992).
7. J.P. Renard, P. Beauvillain, C. Dupas, K. Le Dang, P. Veillet, E. Vélú, C. Marlière, and D. Renard, *J. Magn. Magn. Mater.* **115**, L147 (1992).
8. M.T. Johnson, R. Coehoorn, J.J. de Vries, N.W.E. McGee, J. aan de Stegge, and P.J.H. Bloemen, *Phys. Rev. Lett.* **69**, 969 (1992).
9. J. Kohlhepp, S. Cordes, H.J. Elmers, and U. Gradmann, *J. Magn. Magn. Mater.* **111**, L231 (1992).
10. A. Schreyer, K. Bröhl, J.F. Ankner, Th. Zeidler, P. Bödeker, N. Metoki, C.F. Majkrzak, and H. Zabel, *Phys. Rev. B* **47**, in press.
11. P. Bruno and C. Chappert, *Phys. Rev. B* **46**, 261 (1992).
12. C. Dupas, E. Kolb, K. Le Dang, J.P. Renard, P. Veillet, and E. Vélú, submitted to *J. Magn. Magn. Mater.*
13. P. Bödeker, A. Abromeit, K. Bröhl, P. Sonntag, N. Metoki, and H. Zabel, *Phys. Rev. B* **47**, 2353 (1993).
14. K. Bröhl, P. Bödeker, N. Metoki, A. Stierle, and H. Zabel, *J. Crystal Growth* **127**, 682 (1993).
15. J.F. Ankner and C.F. Majkrzak, in *Neutron Optical Devices and Applications*, edited by C.F. Majkrzak and J.L. Wood, volume 1738 of *Proc. SPIE*, page 260, Bellingham, Wash. 1992, SPIE.
16. J.F. Ankner, A. Schreyer, Th. Zeidler, C.F. Majkrzak, H. Zabel, J.A. Wolf, and P. Grünberg, in this volume.
17. C.F. Majkrzak, *Physica B* **173**, 75 (1991).
18. J.F. Ankner, J.A. Borchers, R.F.C. Farrow, and R.F. Marks, *J. Appl. Phys.* **73**, 6427 (1993).
19. R. Miranda, private communication.

SPIN POLARIZED LOW ENERGY ELECTRON MICROSCOPY (SPLEEM) OF SINGLE AND COMBINED LAYERS OF Co, Cu, AND Pd ON W(110)

HELMUT POPPA,* HEIKO PINKVOS**, KARSTEN WURM**, AND ERNST BAUER**

*IBM Research, Almaden Research Center, 650 Harry Rd., San Jose, CA 95120

**Physikalisches Institut, Universitaet Clausthal, 3392-Clausthal-Zellerfeld, Leibnizstrasse 4, Germany

ABSTRACT

In-situ recording of ultra-thin film growth by Low Energy Electron Microscopy (LEEM) results in accurate determinations of monolayer metal deposition rates for difficult to calibrate deposition geometries. Deposition rates and growth features were determined for Cu and Co on W(110) allowing for thickness control at the submonolayer level. Also, the transparencies of non-magnetic overlayers of Pd(111) and Cu(111) to very low energy spin polarized electrons were compared and qualitatively explained by band structure considerations. Cu(111) is much more transparent than Pd(111) so that magnetic domain structures can be observed through at least 4 nm of Cu(111). This suggests the use of Cu(111) and other metals of suitable band structure as protective layers for surface magnetic studies.

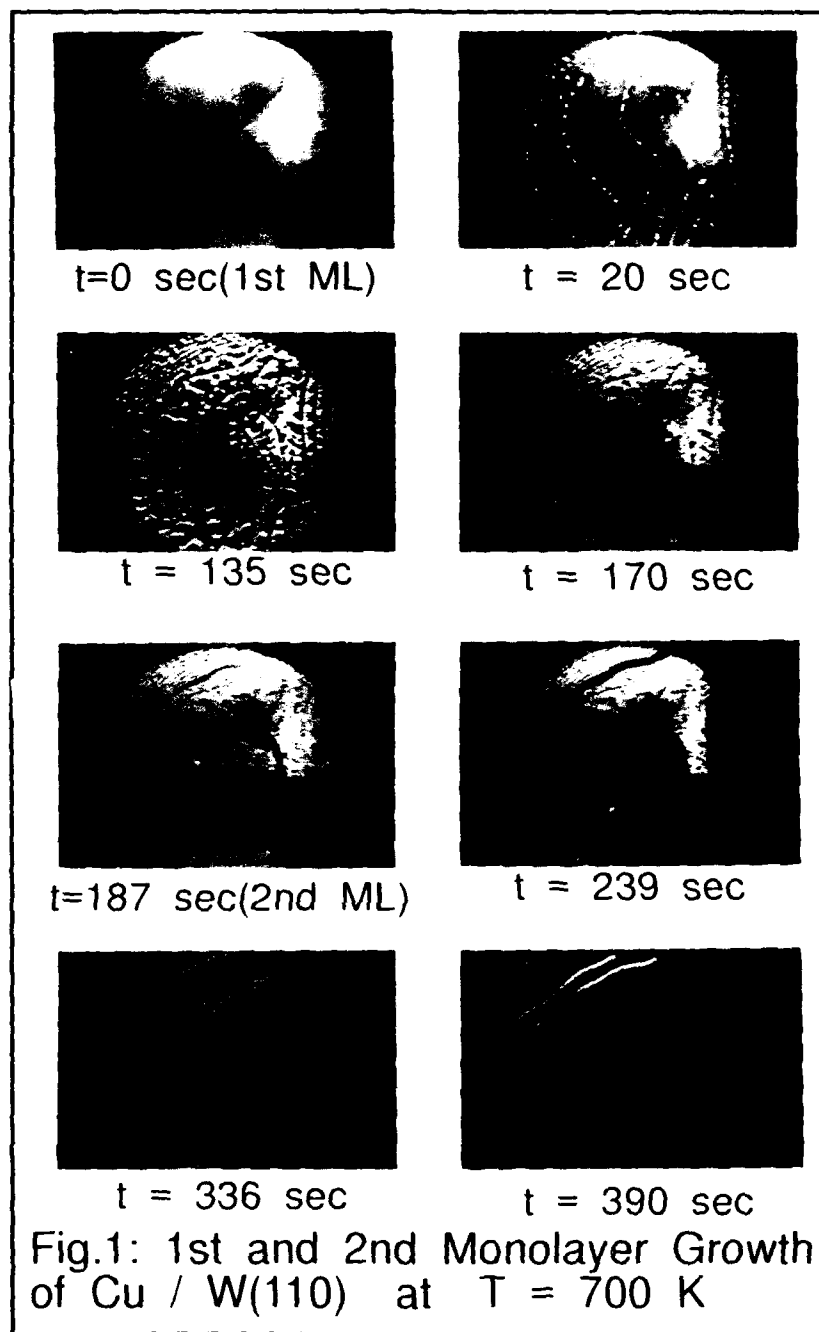
INTRODUCTION

Multilayer sandwiches of magnetic and non-magnetic materials have recently been studied in much detail owing to interest in their basic properties and in potential technological applications [1 - 9] using a variety of experimental approaches. Direct imaging of domain structures on magnetic surfaces and in magnetic thin films grown on magnetic or nonmagnetic metallic supports has been accomplished with varying degrees of lateral resolution by Kerr microscopy [10], magnetic X-ray microscopy [11], and Scanning Electron Microscopy with Polarization Analysis [12 - 14]. We have recently demonstrated the usefulness for surface magnetic imaging of a new experimental approach abbreviated as SPLEEM (Spin Polarized Low Energy Electron Microscopy) [15,16] the main attraction of which is its imaging speed [17] and its integrated use with LEEM/LEED methods [18].

SPLEEM is, therefore, particularly well suited for the in-situ investigation of epitaxial growth processes when appropriate vapor deposition facilities are incorporated into the UHV-based SPLEEM instrument, and the fabrication of multilayer thin film sandwiches by the sequential deposition of magnetic and non magnetic metals becomes possible. The thickness of both the magnetic layers and the non-magnetic spacers can be, however, of critical importance and an exact determination of the respective metal deposition rates is required. Demonstrating the ease of monolayer rate determinations by LEEM (a video clip will be presented at the Conference) for Cu and Co growing on a W(110) substrate crystal is the main objective of this paper. In addition it will be shown that relatively thick epitaxial overlayers of (111) Cu are magnetically transparent to imaging electrons of very low energy in contrast to (111) Pd layers.

RESULTS AND DISCUSSIONS

Co, Pd and Cu were deposited from rate controlled evaporation sources located in a separate evaporation chamber attached to the main microscope and resulting in a shallow angle of incidence to the W(110) substrate. The tungsten substrate crystal is usually cleaned by low pressure oxygen treatment and by repeated flashing to about 2000 K (followed by brief secondary flashes to 1400 K) just before cooling to the deposition temperature, which in the



cases reported here was either about 700 K or room temperature (RT). The energy of the imaging electrons ranged between 1 and 5 eV and was adjusted so as to maximize the (diffraction) image contrast for the metal structures under observation (see later).

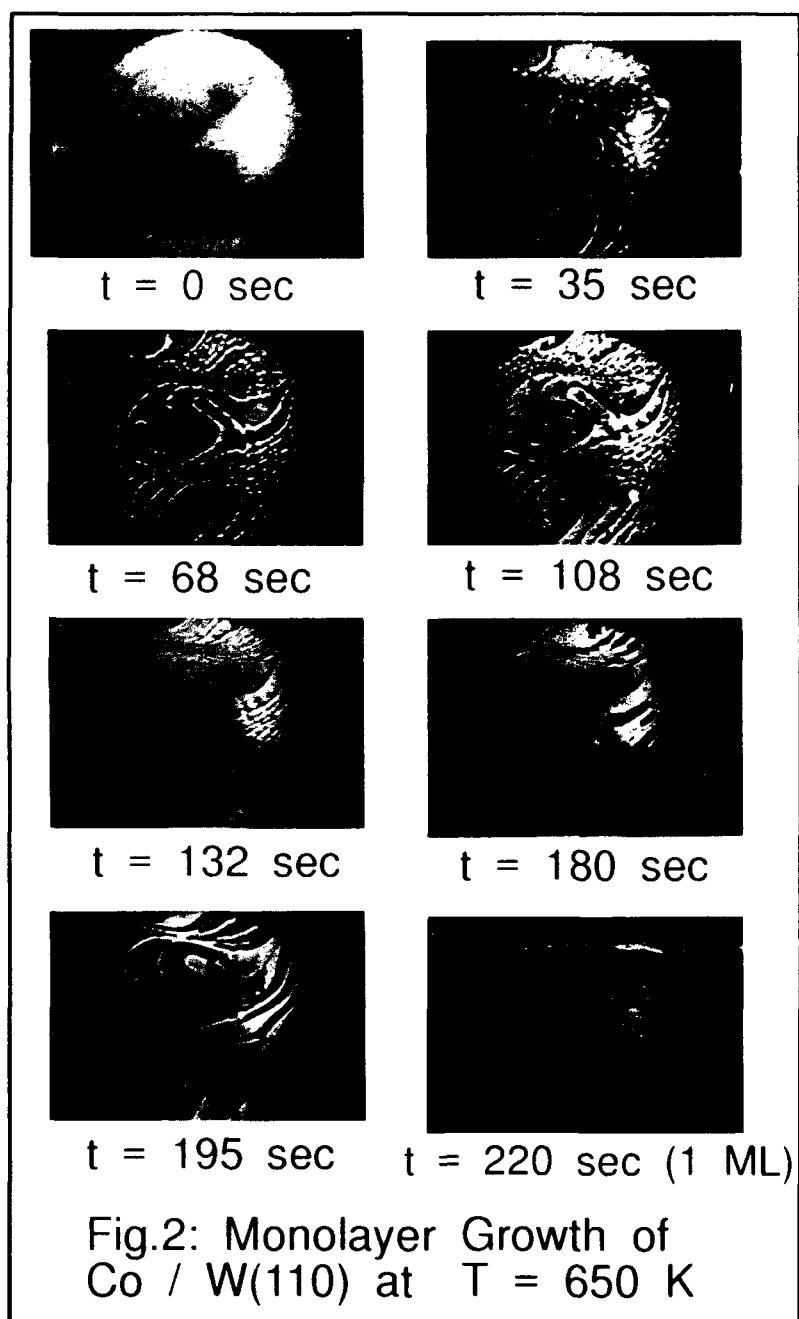
The growth processes at the elevated deposition temperatures were recorded by video-rate taping. Growth sequences captured from the video recordings are displayed in the first two figures where the image magnifications are defined by the circular field of view the diameter of which is 14 microns. Fig. 1 depicts the first and second monolayer (ML) growth of Cu. At the time $t = 0$ the 1st monolayer starts growing and at $t = 187$ sec the 2nd monolayer has just started although the 1st monolayer is not quite complete. At $t = 390$ sec the 2nd monolayer is almost complete. With growth times of 185 and 396 seconds for the end of the first and second ML and considering the respective atomic surface densities of 14 and $30 \times 10^{14} \text{ cm}^{-2}$ [22], a deposition rate of $7.57 \times 10^{12} \text{ cm}^{-2} \text{ sec}^{-1}$ is determined.

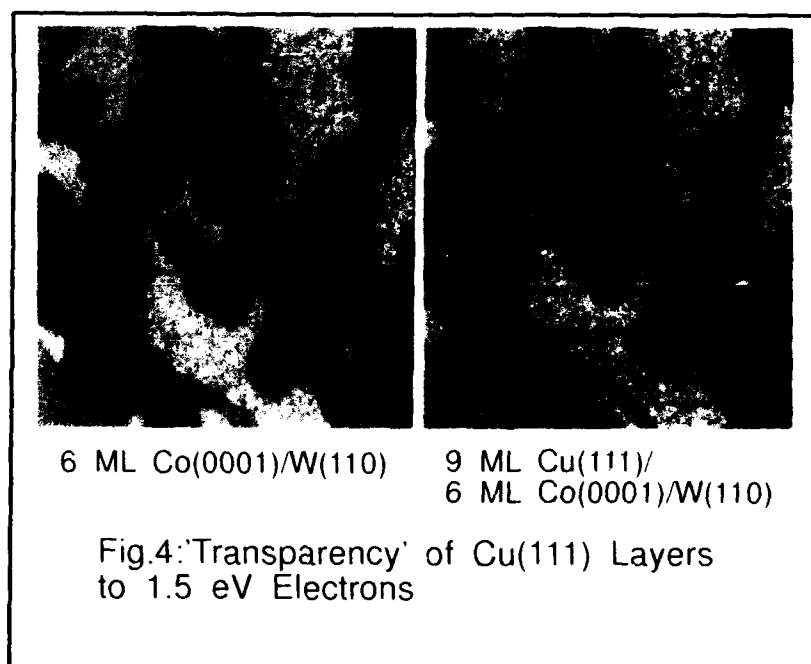
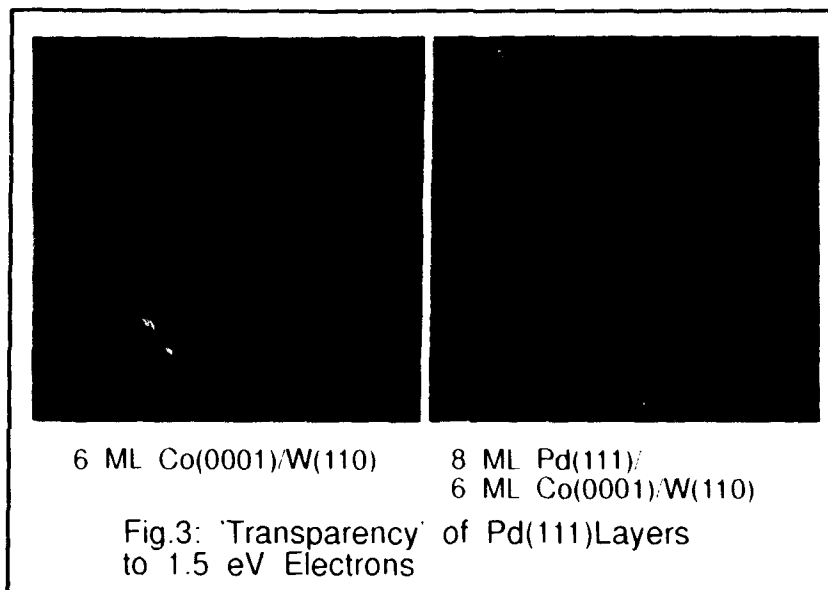
It is also of interest to focus on the different growth modes and image contrast effects that are obvious in these growth images of the first and second monolayer of Cu. As pointed out previously [19 - 21], the growth of a low free surface energy metal like Cu on a high free surface energy metallic substrate like W at elevated substrate temperature will lead to Stranski-Krastanov growth which is monolayer-by-monolayer growth followed by the formation of three-dimensional crystals due to increasing strain. The images at $t = 20, 135$, and 170 seconds in fig. 1 show details of this growth in the first monolayer. Substrate surface steps that are hardly distinguishable at $t = 0$ are well decorated at $t = 20$ sec. Thereafter, the bright contrasted Cu areas exhibit 2-dimensional dendritic growth patterns until only a few (dark) holes remain at $t = 187$ sec when second layer growth, exhibiting dark image contrast features is initiated. This proceeds in a 'step flow' like mode as was previously described for Cu/Mo(110) [21].

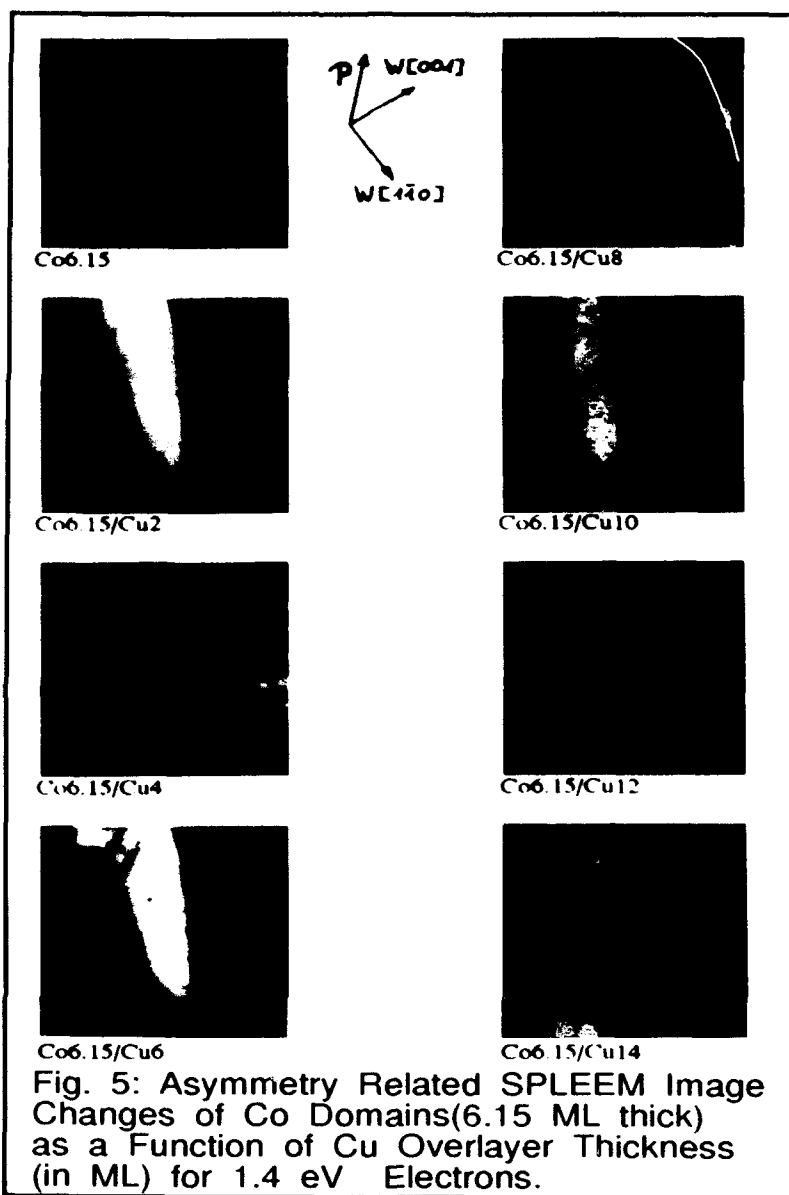
The first two layers of Cu can be distinguished easily by LEEM because they have different crystallographic structures causing "diffraction contrast", the usually dominating contrast mechanism in LEEM. The first layer is a pseudomorphically strained Cu layer whereas the second layer is a misfitting double layer [22]. (More specifically, we are seeing the effects of "bright-field diffraction contrast" here, which is only one of three different modes of diffraction contrast. The other two modes are "tilted bright field" and "dark field" contrast and both find application when surface structural differences do not show up as differences in the intensity of the reflected (00) imaging beam [23]). The surface steps seen in images of clean single crystal W or other substrates are due to a different type of LEEM image contrast; they are "phase contrast" images caused by interference effects of electron beams reflected from substrate areas of different height and are, therefore, strongly dependent on electron energy and on focusing conditions. Under the focusing conditions used in figs. 1 and 2, diffraction and not phase contrast was maximized.

Fig. 2 shows a video-captured growth sequence for Co on the same W(110) substrate but at slightly lower temperature. This sequence is shown not only because we routinely prepare epitaxial Co layers as magnetic test layers with well defined domain patterns (see later) but also because here structural changes occur within a single monolayer that show up as distinct contrast differences in LEEM images. From $t = 0$ to $t = 132$ sec the continuing growth of the pseudomorphic Co layer with bcc structure can be observed up to a coverage of 0.775 ($t = 170$ sec). At this point, the addition of more Co causes the gradual transition to the hexagonal Co structure which results in different diffraction contrast. This hexagonal Co layer continues to spread until a complete monolayer of hexagonally structured Co is reached at $t = 219$ sec. A deposition rate of $1.544 \times 10^{13} \text{ cm}^{-2} \text{ sec}^{-1}$ follows, and additional layers of Co of the same structure can now be grown on top of this Co monolayer at RT for magnetic test purposes.

Such a test layer of epitaxial Co with well delineated magnetic domains is shown on the left of fig. 3. It is being used in this case to study the transparency of a number of non-magnetic overlayers to low energy imaging electrons in SPLEEM. The right side of fig. 3 demonstrates







the effect of 8 monolayers of Pd(111) at the same imaging energy. In spite of strong contrast enhancement during image processing, the domain structures are only just recognizable and the effect was almost as drastic with 4 monolayers of Pd. A very different behavior was, however, found for Cu(111) overlayers. Here up to at least 14 monolayers were highly transparent to magnetic information from the underlying Co (see fig. 4 for the case of 9 monolayers of Cu at the same imaging energy of 1.5 eV). Care has to be taken, however, when interpreting these results because of a strong dependence of the reflected (00) beam intensity asymmetry for spin polarized electrons on their energy. Quantitative results for Cu(111) are forthcoming [24] but similar intensity oscillations for Cu(100) films and 12 eV energy have been measured [25] and related to interference between electrons reflected from the film/vacuum and film/substrate interface, i.e. phase contrast or quantum size contrast [26,23] effects are responsible. As a consequence, asymmetry related contrast variations are found when changing the imaging energy in SPLEEM. This effect is demonstrated in fig. 5 for Cu(111) overlayers of varying thickness acquired at a constant imaging energy of 1.4 eV. In principle, similar contrast variations can be seen for Pd overlayers too but the absolute asymmetry changes are substantially reduced when compared to Cu.

How can such different degrees of attenuation of asymmetry between Cu and Pd be interpreted? They are not so much due to different inelastic mean free paths in the two metal layers but mainly caused by differences in elastic backscattering. At the very low energies used (1.5 eV above vacuum level corresponding to about 6 - 7 eV above the Fermi level) inelastic scattering is weak compared to elastic scattering (see e.g. [27]). Elastic backscattering in crystals is governed by the band structure. At the energy of maximum asymmetry in Co, Pd has a band gap along the Γ/L (111) direction so that the electron wave which is incident along this direction is strongly damped. In Cu, however, allowed states are available at this energy which results in considerable penetration. Thus the observed difference in the transparency of Cu(111) and Pd(111) layers is easy to understand qualitatively. Quantitative comparisons will have to wait for dynamical LEED calculations.

Acknowledgements

This work was partially supported by the Deutsche Forschungsgemeinschaft and by the Volkswagen Foundation. Thanks are due to Thomas Mueller for image processing support.

References

- [1] S.S.S. Parkin, Phys.Rev.Lett. 67(1991), 3598
- [2] R.F.C. Farrow, C.H. Lee, R.F. Marks, G. Harp, M. Toney, T.A. Rabedeau, D. Weller, H. Braendle, in "Magnetism and Structure in Systems of Reduced Dimension", NATO ASI Series, Plenum Publishing Corp., NY / NY (1993)
- [3] M.T. Johnson, R. Coehorn, J.J. de Vries, N.W.E. McGee, J. van de Stegge, P.J.H. Bloemen, Phys. Rev. Lett., 69 (1992), 969
- [4] S.D. Bader, C. Liu, J.Vac.Sci.Technol., A9 (1991), 1924
- [5] W.F. Egelhoff, Jr., M.T. Kief, Phys. Rev. B45 (1992), 7795
- [6] J.J. de Miguel, A. Cebollada, J.M. Gallego, R. Miranda, C.M. Schneider, P. Schuster, J. Kirschner, J. Magn. Magn. Mater. 93 (1991), 1
- [7] J. Unguris, R.J. Celotta, D.T. Pierce, Phys. Rev. Lett. 69 (1992), 1125
- [8] G.A. Prinz, Ultramicroscopy 47 (1992), 346
- [9] J. Kohlhepp, H.J. Elmers, S. Cordes, U. Gradmann, Phys. Rev. B45 (1990), 12287
- [10] R. Schaefer, A. Hubert, phy.stat.sol (a) 118 (1990), 271
- [11] J. Stöhr, c.f. the contribution in this volume
- [12] J. Unguris, M.R. Scheinfein, R.J. Celotta, D.T. Pierce, Appl.Phys.Lett 55 (1989), 2553

- [13] R. Allenspach, M. Stampanoni, A. Bischof, *Phys. Rev. Lett.* 65 (1990), 3344
- [14] H.P. Oepen, *J. Magn. Magn. Mater.* 93 (1991), 116
- [15] M.S. Altman, H. Pinkvos, J. Hurst, H. Poppa, G. Marx, E. Bauer, *Mater. Res. Soc. Symp. Proc.* 232 (1991), 125
- [16] H. Pinkvos, H. Poppa, E. Bauer, J. Hurst, *Ultramicroscopy* 47 (1992), 339
- [17] H. Pinkvos, H. Poppa, E. Bauer, G.-M. Kim, in "Magnetism and Structure in Systems of Reduced Dimension", NATO ASI Series, Plenum Publishing Corp., NY / NY (1993)
- [18] E. Bauer, in: "Chemistry and Physics of Solid Surfaces VIII", R. Vanselow, R. Howe, ed., Springer, Berlin (1990), p. 267
- [19] E. Bauer, H. Poppa, *Thin Solid Films* 12 (1972), 167
- [20] E. Bauer, *Ber. Bunsenges. Phys. Chem.* 95 (1991), # 11
- [21] E. Bauer, *Mat. Res. Symp. Proc.* 198 (1990), 353
- [22] E. Bauer, H. Poppa, G. Todd, F. Bonczek, *J. Appl. Phys.* 45 (1974), 5164
- [23] E. Bauer, M. Mundscha, W. Swiech, W. Telieps, *Ultramicroscopy* 31 (1989), 49
- [24] to be published
- [25] D. Kerkmann, D. Pescia, J.W. Kremer, E. Vescovo, *Z. Phys. B* 85 (1991), 311
- [26] B. T. Jonker, N.C. Bartelt, R.L. Park, *Surf. Sci.* 127 (1983), 183
- [27] E. Bauer, *J. Vac. Sci. Technol* 7 (1970), 3.

OBSERVATION OF X-RAY ABSORPTION MAGNETIC CIRCULAR DICHROISM IN WELL-CHARACTERIZED IRON-COBALT-PLATINUM MULTILAYERS

A.F. JANKOWSKI, G.D. WADDILL and J.G. TOBIN

Lawrence Livermore National Laboratory, Chemistry & Materials Science Department,
P.O. Box 808, Livermore, California 94550 U.S.A.

ABSTRACT

Magnetic circular dichroism in the Fe 2p x-ray absorption is observed in multilayers of $(\text{Fe}9.5\text{\AA}/\text{Pt}9.5\text{\AA})_{92}$. The magnetization and helicity are both in the plane of this multilayer which is prepared by magnetron sputter deposition. This sample is part of a study to examine magnetization in the ternary multilayer system of FeCo/Pt. Lattice and layer pair spacings are measured using x-ray scattering. The atomic concentration profiles of the multilayer films are characterized using Auger electron spectroscopy coupled with depth profiling. Conventional and high resolution transmission electron microscopy are used to examine the thin film, growth morphology and atomic structure.

INTRODUCTION

The observation of perpendicular magnetic anisotropy in the Co/Pt^[1-4] and Fe/Pt^[5] multilayer systems proves to be of interest for magnetic and magneto-optic recording applications. The magnetic properties of Fe/Pt multilayer films are strongly dependent on the relative as well as absolute layer thicknesses.^[6] X-ray absorption spectroscopy (XAS) is used for elemental analysis and magnetic circular dichroism (MCD) measurements. It is shown that MCD can be a useful technique for monitoring changes in the orientation of sample magnetization.^[7] An in-plane magnetization of a $(\text{Fe}9.5\text{\AA}/\text{Pt}9.5\text{\AA})_{92}$ multilayer thin film is found using both MCD and conventional magnetometry.^[8] The MCD technique has the potential to follow the magnetic axis orientation in FeCo/Pt magnetic thin films as well as provide elemental specific determination of the magnetic moment.

SAMPLE PREPARATION

The FeCo/Pt multilayer samples are prepared using magnetron sputter deposition. The deposition chamber is cryogenically pumped to a base pressure of 1.3×10^{-5} Pa. A circular array of magnetron sources is situated 20 cm beneath an oxygen-free copper platen. The magnetron sources are operated in the dc mode at a 330-390 Volt discharge. An argon working gas pressure of 0.40 Pa is used at a flow rate of 15.5 cc min^{-1} . The substrates are sequentially rotated over each source at 1.0 rev min^{-1} . The target materials are >0.9994 pure. The polished Si substrates are cleaned with a procedure consisting of a detergent wash,

deionized water rinse, alcohol rinse and a N_2 gas drying prior to deposition. The substrates remain at a temperature between 293 and 306 K during the deposition. The sputter deposition rates, between 0.02 and 0.50 nm sec^{-1} , are monitored using calibrated quartz crystals. The quartz crystals indicate the component layer thicknesses (Sample column of Table I) and the layer pair thicknesses, $d_{FeCo/Pt}^{XTC}$. The multilayer films are grown to a 0.2 μm thickness.

CHARACTERIZATION METHODS AND RESULTS

X-Ray Diffraction

The lattice and layer pair spacings of the FeCo/Pt multilayers are measured using x-ray diffraction. A powder diffractometer equipped with a graphite monochromator is operated in the $\theta/2\theta$ mode at both grazing incidence and high angle using $Cu K\alpha$ radiation. The grazing incidence scans of the multilayer films (XRD column of Figs. 1a-f) reveal the satellite reflections about (000) attributable to the composition modulation in the multilayer growth direction. The first three satellite peak positions ($n = 1, 2, 3$) are corrected for refraction and fitted to compute a layer pair spacing $d_{FeCo/Pt}^{XRD}$ (Table I). The layer pair spacings $d_{FeCo/Pt}^{XRD}$ are in agreement to within 0.01 nm of the crystal monitor values $d_{FeCo/Pt}^{XTC}$. The high angle Bragg reflections indicate that the thin film samples are all oriented along the [111] direction of a face-centered-cubic (fcc) lattice. The interplanar spacing, $d_{(111)}^{XRD}$ (Table I), is generally intermediate to the values of pure Pt(111) at 0.2266 nm and $\gamma Fe(111)$ at 0.2106 nm. A first-order satellite reflection below the Bragg reflection in the $\theta/2\theta$ scans indicates layer pair spacings, from the relationship $[s_{(111)} - s_{satellite}]^{-1}$ where $s = d^{-1}$, for the films consistent with the grazing incidence measurements.^[6]

Table I. Layer Pair and Interplanar Spacings (nm) of FeCo/Pt(111) Multilayers

Sample	$d_{(111)}^{XRD}$	$d_{FeCo/Pt}^{XRD}$	$d_{FeCo/Pt}^{XTC}$
(Co3.9Å/Pt9.1Å) ₁₃₅	0.2223	1.295	1.294
(Fe1.7ÅCo1.8Å/Pt9.7Å) ₁₃₅	0.2246	1.288	1.313
(Fe9.5Å/Pt9.5Å) ₉₂	0.2193	2.008	1.895
(Fe3.0Å/Pt9.7Å) ₁₃₅	0.2252	1.280	1.267
(Fe3.1Å/Pt19.4Å) ₇₆	0.2270	2.228	2.245
(Fe3.1Å/Pt38.8Å) ₄₄	0.2274	4.238	4.187

Auger Electron Spectroscopy

Atomic concentration profiles of the multilayer thin films are measured using Auger electron spectroscopy (AES) coupled with depth profiling. A 3 keV, 10 μA electron beam is used to generate the Auger electrons. The measured intensities of the 1.967 keV platinum peak (Pt MNN), the 703 eV iron peak (Fe LMM), the 272 eV carbon peak (C KLL) and the 503 eV oxygen peak (O KLL) from data accumulated in the derivative mode are used to compute the

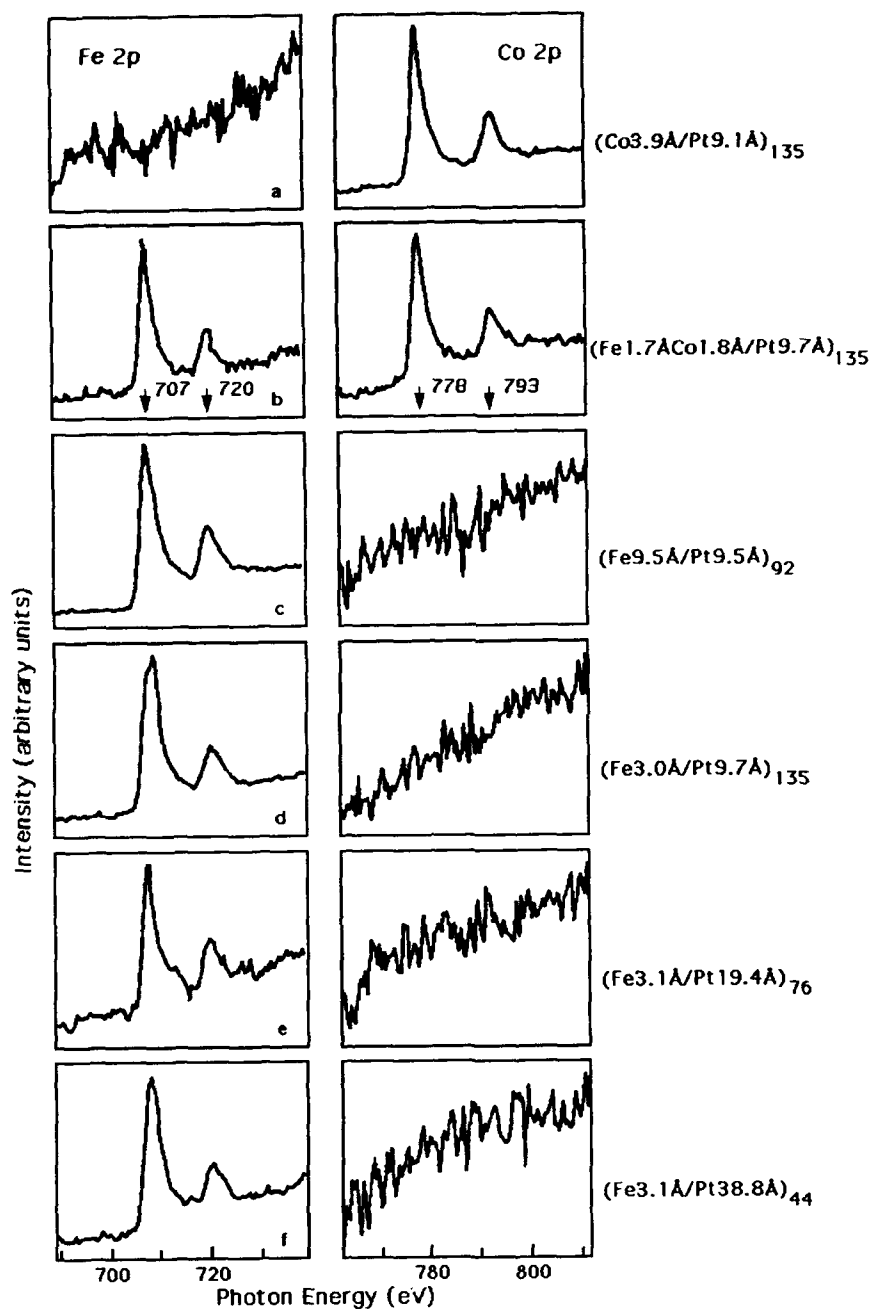


Figure 1. The columns correspond to the x-ray absorption at the Fe 2p and Co 2p edges using linear polarization and normal incidence measurement of the FeCo/Pt multilayer samples.

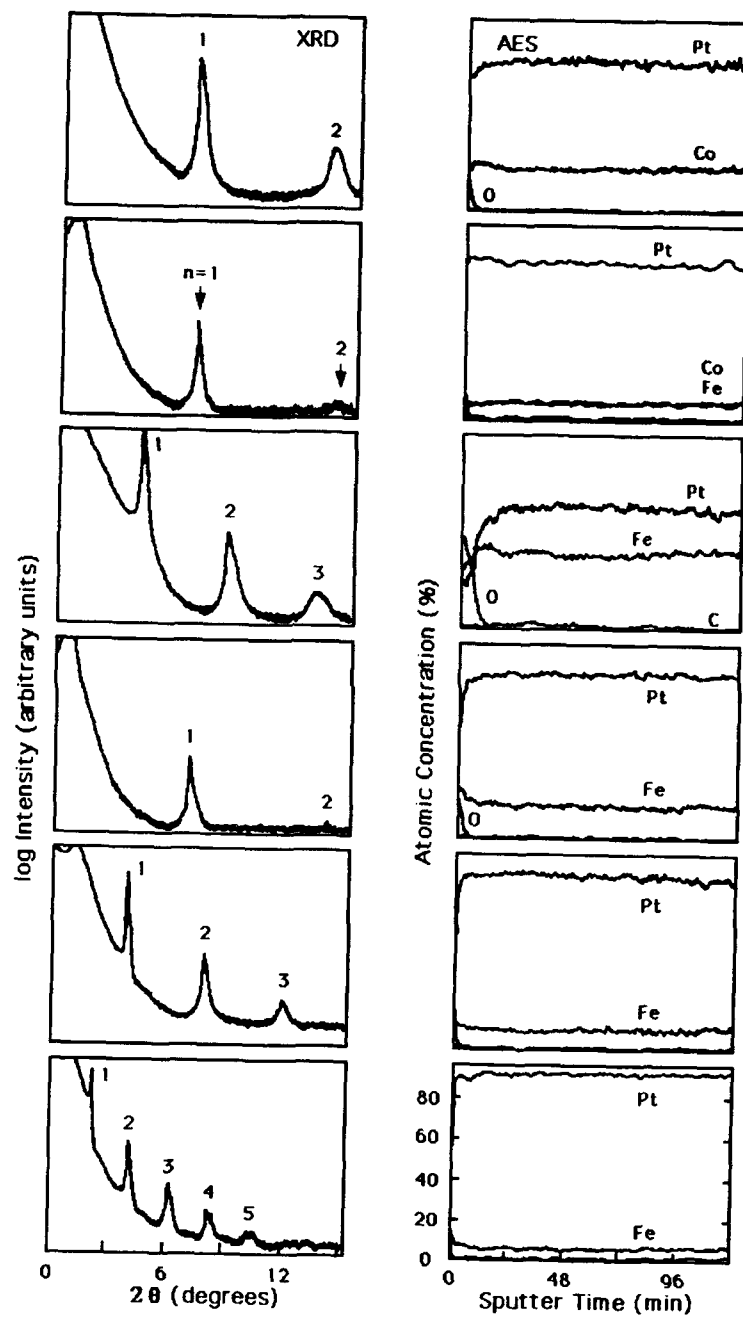


Figure 1.(continued) The columns correspond with grazing incidence x-ray diffraction (XRD) scans and Auger (AES) depth profiles of the FeCo/Pt multilayer samples, as listed in (a-f).

atomic concentrations. A 2 keV, 0.92 μ A argon ion beam is used to sputter etch a 25 mm² area of the sample surface. The gas pressure for the sputter etch is 4×10^{-3} Pa whereas the Auger system base pressure is 6.7×10^{-8} Pa. Once the surface oxide is sputtered through, the film composition is shown to be uniform and free of any C or O contamination (AES column of Figs. 1a-f). The concentration analysis of the films using AES are in agreement to within 10% of the absolute concentration value for each component as determined from the calibrated quartz crystal monitor readings of component layer thicknesses.

Transmission Electron Microscopy

Transmission electron microscopy (TEM) and high resolution imaging reveal the multilayer film morphology and lattice structure. The FeCo/Pt films, as imaged in both plan view (Fig. 2a) and cross-section (Fig. 2c), are typified by a dense columnar growth. The plan view electron diffraction patterns reveal the polycrystalline, in-plane nature of the films. The ring pattern (Fig. 2b) of this fcc phase is indexed to a lattice parameter of 0.3848 nm. This lattice spacing corresponds quite well with the high angle diffraction data that gives a lattice parameter of 0.3798 nm. Diffraction patterns, taken from the multilayer as viewed in cross-section, reveal a 5-8° mosaic of the lattice planes perpendicular to the [111] growth direction. Selected area diffraction patterns of individual grains, viewed in cross-section (Fig. 2d), clearly show the [111] growth direction of an fcc phase in this [110] pole projection. The FeCo/Pt thin film samples are therefore [111] textured in the growth direction but randomly oriented in-plane. The average grain size is 27-30 nm, as measured from the bright field images (as Fig. 2a). Lattice images, recorded at the Scherzer defocus condition using a 400 keV electron beam, show each grain to consist of a single-phase fcc structure (Fig. 3).

X-ray Absorption Spectroscopy and Magnetic Circular Dichroism

The XAS and MCD measurements are performed on a spherical grating monochromator with the ability to generate soft x-rays with a high degree of linear or circular polarization.^[9,10] The absorption measurements are made in a partial electron yield mode with a kinetic energy window centered around 50 eV. The XAS spectra (Fe 2p and Co 2p columns in Fig. 1a-f) are for normal incidence (i.e. 0° from the sample normal). The curves correspond to linear polarization scans for elemental analysis. The presence of Fe as well as Co is detected for even the smallest film concentrations, e.g. 7 at.% Fe in sample (Fe3.1 Å/Pt38.8 Å)₄₄. For the MCD measurements, the samples are magnetized in-situ with a pulse coil capable of generating a 3 kOe field. MCD in x-ray absorption is observed as a circular polarization dependent intensity variation in the L₂ and L₃ edges for 3d transition metals. The polarization dependence requires that the incident x-ray helicity (either parallel or anti-parallel to the direction of propagation) be aligned or anti-aligned with the sample magnetization.^[7,11] The polarization dependence vanishes when these vectors are perpendicular. An intensity difference for the L₂ and L₃ white lines is apparent for sample (Fe9.5 Å/Pt9.5 Å)₉₂ demonstrating a remnant, in-plane magnetization of the film (Fig. 4).

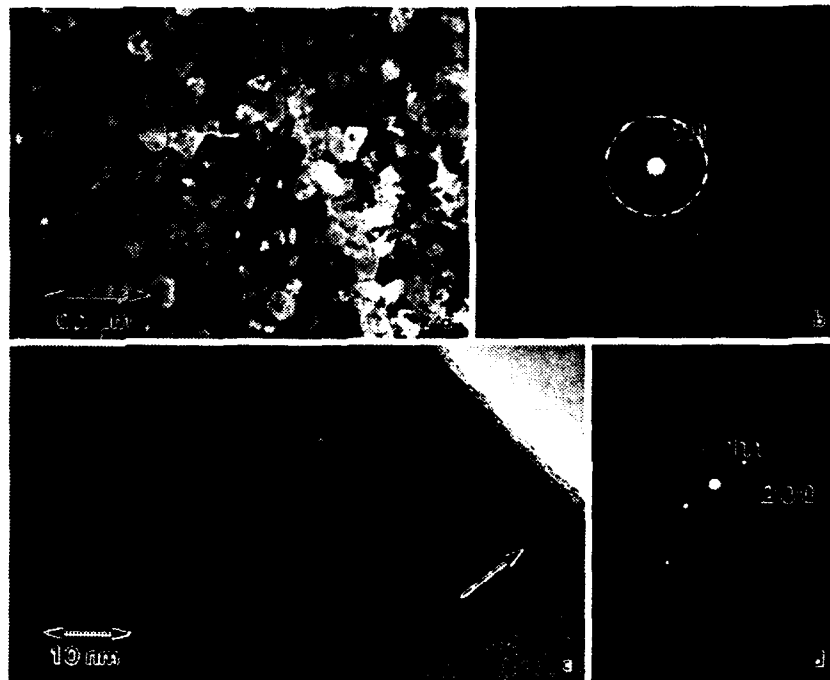


Figure 2. Conventional transmission electron microscopy of sample $(\text{Fe}9.5\text{\AA}/\text{Pt}9.5\text{\AA})_{92}$, as imaged in plan view, reveals (a) the fine grain size in the bright field image and (b) the preferred (111) texture in the electron diffraction pattern of the film. Imaging of sample $(\text{Co}3.9\text{\AA}/\text{Pt}9.1\text{\AA})_{135}$, as prepared in cross-section, reveals (c) layering perpendicular to the growth direction (indicated with an arrow) and (d) a [111] oriented, single-phase structure as seen in the [110] pole projection of this face-centered cubic, selected area diffraction pattern.

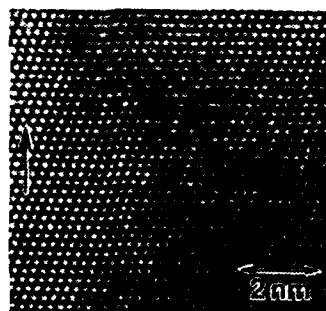


Figure 3. High resolution electron micrograph of the sample $(\text{Fe}9.5\text{\AA}/\text{Pt}9.5\text{\AA})_{92}$, as imaged in cross-section. The growth direction is indicated with an arrow.

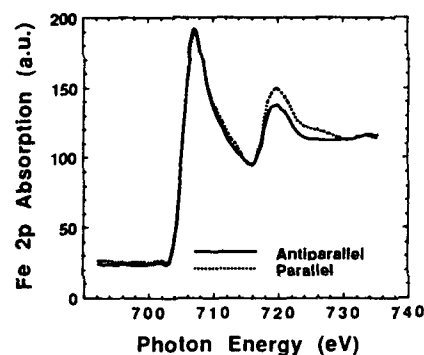


Figure 4. Fe L-edge absorption spectra of the $(\text{Fe}9.5\text{\AA}/\text{Pt}9.5\text{\AA})_{92}$ multilayer for the x-ray helicity and majority d-electron spin nearly parallel (---) and antiparallel (—). This is an illustration of magnetic circular dichroism using circularly polarized x-rays.

DISCUSSION & SUMMARY

The relative strengths of the L_2 and L_3 absorption edges contain information about the spin-dependent density of states near the Fermi level and the spin-orbit splitting in the d-bands. Therefore, information is available about the spin and orbital magnetic moments of the material.^[7,12-14] The spin moment analysis^[7] applied to sample $(\text{Fe}9.5\text{\AA}/\text{Pt}9.5\text{\AA})_{92}$ yields a value of $1 \pm 0.5 \mu_B/\text{Fe}$. The analysis is complicated, however, by the polycrystalline surface. If the sample is not of a single domain, then MCD will average the domains yielding a moment that reflects the average projection of magnetization along the photon propagation direction.

In summary, we have studied the microstructure of FeCo/Pt multilayer films using x-ray diffraction and transmission electron microscopy, the composition using x-ray absorption and Auger spectroscopy, and the magnetic behavior using MCD. The correlation of structural properties with magnetic anisotropy requires detailed and elemental sensitive characterization. MCD enables the study of multi-element films, as FeCo/Pt, where the local moments can be determined for each component material.

ACKNOWLEDGMENTS

The MCD measurements were performed at the Stanford Synchrotron Radiation Laboratory. We thank Mark Wall for the transmission electron microscopy images. This work was performed under the auspices of the United States Department of Energy by Lawrence Livermore National Laboratory under contract W-7405-Eng-48.

REFERENCES

- 1 P.F. Carcia, A.D. Meinhardt and A. Suna, Appl. Phys. **47**, 178 (1985).
- 2 P.F. Carcia, J. Appl. Phys. **63**, 5066 (1988).
- 3 Z. Zhang, P.E. Wigen and S.S.P. Parkin, J. Appl. Phys. **69**, 5649 (1991).
- 4 B.D. Hermsmeier, R.F.C. Farrow, C.H. Lee, E.E. Marinero, C.J. Lin, R.F. Marks and C.J. Chien, J. Appl. Phys. **69**, 5646 (1991).
- 5 T. Katayama, Y. Suzuki, Y. Nishihara, T. Sugimoto and M. Hashimoto, J. Appl. Phys. **69**, 5658 (1991).
- 6 E. Devlin, V. Psycharis, A. Kostikas, A. Simopoulos, D. Niarchos, A. Jankowski, T. Tsakalakos, H. Wan and G. Hadjipanayis, J. Magn. Magn. Mater. **120**, 236 (1993).
- 7 J.G. Tobin, G.D. Waddill and D.P. Pappas, Phys. Rev. Lett. **68**, 3642 (1992).
- 8 A.F. Jankowski, G.D. Waddill and J.G. Tobin, Bull. Amer. Phys. Soc. **38** (1), 831 (1993).
- 9 K.G. Tirsell and V. Karpenko, Nucl. Instrum. Meth. A **291**, 511 (1990).
- 10 L.J. Terminello, G.D. Waddill and J.G. Tobin, Nucl. Instrum. Meth. A **319**, 271 (1992).
- 11 J.L. Erskine and E.A. Stern, Phys. Rev. B **12**, 5016 (1975).
- 12 B.T. Thole and G. van der Laan, Phys. Rev. A **38**, 1943 (1988); B **42**, 6670 (1990).
- 13 B.T. Thole, P. Carra, F. Sette and G. vander Laan, Phys. Rev. Lett. **68**, 1943 (1992).
- 14 P. Carra, B.T. Thols, M. Altarelli and X. Wang, Phys. Rev. Lett. **70**, 694 (1993).

Section A—Multilayers and Surfaces

PART VII

Structure and Magnetism II

MAGNETIC PROPERTIES OF EPITAXIAL 6 ML fcc-Fe/Cu(100) FILMS

L. J. Swartzendruber, L. H. Bennett, M. T. Kief, and W. F. Egelhoff, Jr.
National Institute of Standards and Technology
Gaithersburg, MD 20899

ABSTRACT

A study has been made of the magnetic properties of epitaxial 6 monolayer (ML) fcc-Fe films on Cu(100) with various thicknesses of epitaxial Cu deposited on top of the Fe. It was found that the magnetic properties undergo striking changes as a function of the Cu thickness. The easy axis of magnetization goes from being in-plane for the bare Fe to perpendicular upon the deposition of 1 ML Cu. Concurrently there is a dramatic decrease in the Kerr signal intensity at saturation. Upon depositing a second ML of Cu the Kerr signal intensity more than doubles, and the easy axis remains perpendicular. For Cu overlayers of 3 ML to 10 ML the Kerr signal intensity at saturation gradually diminishes to below the level of detectability, as if the Fe were nonmagnetic. A superlattice consisting of 60 ML Cu/(6 ML ^{57}Fe / 10 ML Cu) \times 5/Cu(100) was fabricated and studied at room temperature by conversion electron Mössbauer spectroscopy. The results confirmed that the Fe is indeed nonmagnetic. The four inner Fe layers of the 6 ML film have the same isomer shift as bulk fcc-Fe in precipitates in Cu, and the two boundary Fe layers exhibit an asymmetric quadrupole doublet.

INTRODUCTION

The study of ultrathin films of fcc-Fe on Cu(100) has been the subject of much interest and some controversy in recent years.[1-10] Such films have served as a testing ground for theories of epitaxial growth and of fundamental magnetic interactions.[1-10] These films are also of interest as building blocks for nanocomposite materials consisting of epitaxially-grown layered structures which exhibit novel and technologically important properties such as the giant magnetoresistance effect.[11] There are several reasons for interest in novel materials based on the Fe-Cu system. First, Fe and Cu have low solubilities in one another, implying greater thermal stability with respect to interdiffusion than would be the case for structures of, say, Ni-Cu which are miscible. Second, the excellent lattice match between fcc-Fe and Cu means that structures with coherent interfaces may readily be grown. Third, small fcc-Fe atom clusters (2 - 10 atoms) in Cu have a large moment, and this effect is often manifested in ultrathin epitaxial films of fcc-Fe. Fourth, an enhancement of a factor-of-two in the Kerr rotation (important for magneto-optical data storage applications) have been found for the Fe/Cu system due to coupling of the photon with the plasma edge of the Cu.[12] A further enhancement is associated with an exchange interaction in Fe/Cu/Fe structures.[9]

EXPERIMENTAL

The molecular beam epitaxy system in which the samples were grown has been described in previous publications.[13-15] Briefly, it consists of a growth chamber which operates in the 10^{-10} torr range and is equipped with four K-cells,

two thin film thickness monitors, a mass spectrometer, reflection high-energy electron diffraction (RHEED), and spot-profile-analysing low-energy electron diffraction (SPA-LEED). The growth chamber is attached to an x-ray photoelectron spectrometer (XPS) system which operates in the 10^{-11} torr range and is used to monitor sample cleanliness and film crystallinity (via photoelectron diffraction). Attached to a port on the XPS system is a quartz tube which passes between the pole faces of an external electromagnet. The vacuum inside the tube is the same as in the XPS chamber. Magneto-optic Kerr-effect measurements are made by directing HeNe light onto the sample through a 6 mm hole drilled in one pole face. The 50 kHz photoelastic modulator technique is used to obtain the Kerr rotation and ellipticity via lock-in amplifiers. During Kerr rotation measurements a Vedet glass disc is placed between the pole face and the quartz tube to cancel the Kerr rotation of the quartz tube. A manipulator permits translation of the sample along the length of the growth chamber, through the XPS chamber, and into the quartz tube.

The conversion electron Mössbauer chamber is a separate instrument. It is equipped with a mylar window to admit the γ -rays at normal incidence on the sample and a channel electron multiplier which is biased at +67 V (at the entrance) to attract the emitted low-energy secondary electrons. An ion pump maintains the system in the 10^{-6} torr range. To protect the samples during the transfer from the growth chamber to the Mössbauer chamber a 60 ML Cu overlayer was always deposited as the final step. In previous work, this thickness was found to be adequate.

The Cu(100) single crystals used in this work were oriented, polished, and cleaned by well established techniques.[15]

All Fe films reported in this work were grown using the approach of Ref. 13, in which the Cu(100) substrate is cooled to approximately 80 K before depositing the Fe film. Following the Fe deposition the sample is annealed gently, usually to approximately 350 K for about 20 s. This two-step procedure largely suppresses the extensive intermixing that otherwise occurs during room temperature deposition of Fe, as Cu atoms initially segregate onto the deposited Fe and then gradually get left behind in the growing Fe film.[13,16,17] During low temperature deposition the growth is not random or amorphous.[13,14] Instead, the Fe atoms roll down into the four-fold hollows of the (100) surface and reside in lattice sites, as shown by LEED and XPS diffraction. However, in the absence of thermal diffusion the surface is very rough, and this is corrected by gently annealing the films, which allows only the surface atoms to diffuse, and this effect smooths out the surface. The atomic sharpness of the buried Fe/Cu interface is unaffected since the onset of bulk diffusion is above 700 K.[18]

Surface segregation is not a problem during deposition of Cu on Fe since Cu, the lower surface free energy metal, prefers to wet the Fe surface. The Cu films were generally deposited on the Fe at 350 K, immediately after the gentle annealing.[13]

The Kerr effect measurements on these films were all made at 150 K, well below the Curie temperatures so that the saturation values of the signal were not subject to any significant thermal effect. The Kerr rotation in all of the samples reported here was an order of magnitude smaller than the Kerr ellipticity. For this reason, only the ellipticity loops are reported here.

RESULTS AND DISCUSSION

One of the motivating factors behind the research presented here was an apparent conflict between the results of Ref. 6, in which a 6 ML fcc-Fe film deposited on Cu(100) was reported to be strongly ferromagnetic, and the results of Ref. 19, in which a 6 ML fcc-Fe film on Cu(100) covered by 60 ML Cu was reported to be nonmagnetic. An essential question was whether there was a genuine conflict here,

as seemed likely, or whether the Cu overlayer was somehow destroying the ferromagnetism in the entire Fe film. The apparent conflict was made all the more dramatic since in the work of Ref. 6 the Kerr signal intensity increased monotonically with Fe thickness in the range of 2 to 8 ML, while in the Cu-covered Fe films of Ref. 19 both the Kerr signal intensity and neutron scattering measurements indicated that the magnetization decreased monotonically as the Fe film thickness increased from 3 to 8 ML.

The data obtained in the present studies indicate that the conflict was not real, and that Cu overlayers indeed have a surprising and profound effect on the magnetism of 6 ML fcc-Fe films on Cu(100). In Fig. 1 we present a representative series of the polar Kerr ellipticity loops obtained in this work. The 6 ML Fe films with no Cu overlayer have their easy axis in-plane, in agreement with the magnetic-anisotropy phase diagram of Ref. 6. When 1 ML Cu is deposited on the Fe film the easy axis changes to perpendicular with near 100 % remanence. There appears to be no precedent for such an effect in the literature, although we have recently become aware of work in preprint form reporting somewhat similar effects.[20-22] This work indicates that strong changes can occur in the magnitude of the anisotropy of a ferromagnetic film upon depositing a nonmagnetic overlayer.

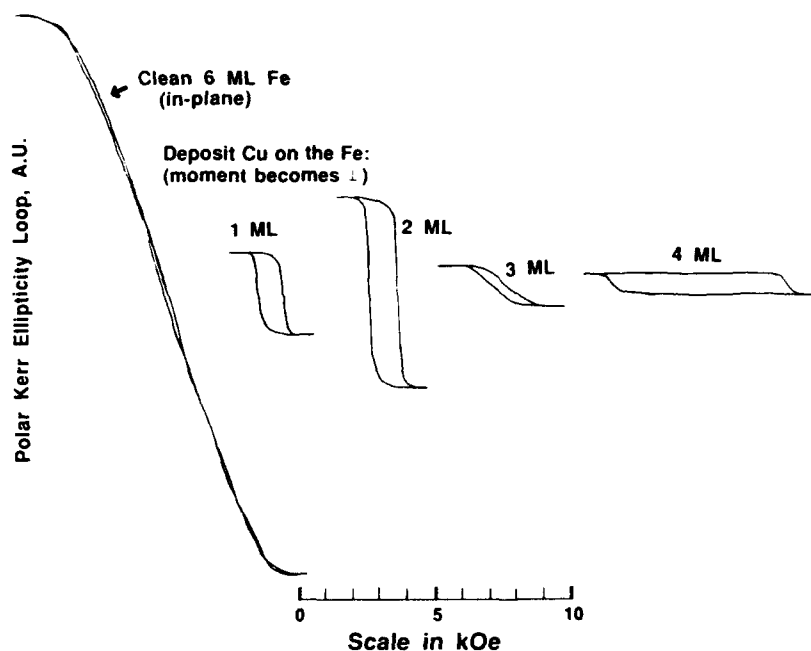


Figure 1 Polar Kerr ellipticity loops for a clean 6 ML Fe film on Cu(100) and for the same Fe film covered with epitaxial Cu films of the indicated thickness.

Also without precedent in the literature is the marked reduction in the saturation value of the Kerr signal upon depositing 1 ML Cu on the Fe film. Although this value is not invariably proportional to the magnetization of a sample, it often is. For example, in the case mentioned above the monotonic decrease from 3 ML Fe to 8 ML Fe was seen in both the neutron measurements (of absolute magnetization) and in the Kerr signal strength.

Perhaps even more remarkable is the unprecedented increase of the Kerr signal strength (by more than a factor-of-two) in these films in going from an overlayer of 1 ML Cu to one of 2 ML Cu. The magnetization of the Fe is apparently very sensitive to the thickness of the Cu overlayer. For 3 ML and 4 ML Cu the Kerr signal strength decreases and the coercivity increases. This increase in coercivity would be surprising if, in these films, the coercivity were governed by domain wall pinning at structural defects. The addition of Cu should not modify these defects. Instead, it seems more likely that, for the 4 ML Cu case, the switching occurs by coherent rotation, and anisotropy governs the switching, not pinning at defects.[22] Thus the primary role of the Cu seems to be to change the magnetization of the Fe film and its anisotropy.

Upon increasing the thickness of the Cu overlayer above 4 ML the strength of the Kerr signal fades away below the detectable limit above about 10 ML Cu. No recovery is seen upon depositing 60 ML Cu, which is used to protect the samples exposed to air.

It seems that these effects might due to electronic interactions between the Cu and the Fe, however structural changes in the Fe cannot easily be ruled out as a possible cause. Although there is some controversy about the structural details of this system, probes such as LEED, RHEED, STM, XPS diffraction, and EXAFS have generally found that in 6 ML Fe/Cu(100) the deviations from fcc-Fe are relatively small.[2,10,23-31] Therefore, a magnetovolume instability producing a first-order phase transition from a ferromagnetic state to a nonmagnetic state, which is theoretically possible as a cause of our results,[32,33] cannot be confirmed or ruled out at this time.

It may be of importance here that the thickness range in which the most dramatic changes occur (0 - 4 ML Cu) is just the range in which the first quantum well state of Cu has been reported to move through the range of binding energies that correspond to the d-band of Fe.[34-37] Interactions between this quantum well state and the Fe d-bands seem plausible as a cause of the effects we report here.

In view of the complexity of the behavior of this system, it seemed worthwhile to make a more definitive examination of the magnetic state of the 6 ML Fe. In particular, an assessment of whether Cu overlayers truly quench the ferromagnetism in this system seemed to be in order. Mössbauer spectroscopy is one of the most informative techniques for investigating such issues. Accordingly, a superlattice sample was grown using ^{57}Fe by depositing alternating 6 ML Fe and 10 ML Cu films. A total of five Fe segments were deposited, and the sample was capped with 60 ML Cu for protection from air. The SPA-LEED diffracted beam profiles showed that the crystalline order of the sample after growth of the superlattice was just as good as that of the Cu(100) substrate. Thus any defects in the crystal structure during the epitaxial growth of the superlattice were below the detectable limit.

Figure 2 presents the room temperature conversion electron Mössbauer data for the superlattice. The lineshape is a classic example of Fe in a nonmagnetic state. A deconvolution, by standard methods, into the components corresponding to the interior Fe and the interface Fe gives, as the solid line in Fig. 2 shows, a reasonable fit to the data. For a more exact fit a third line may be added. Its position is somewhat arbitrary. The fit becomes more definite if it is assumed that the spectrum consists of a single central line with the same isomer shift as low-moment fcc-Fe, and an asymmetric quadrupole doublet consisting of two lines of equal width. The intensity asymmetry of the two lines in the quadrupole doublet is 3.0, indicating an axially symmetric electric-field-gradient tensor with the principal axis parallel to the γ -ray direction, consistent with the geometry of the film. The area ratio of approximately 2:1 is consistent with the expected ratio if the singlet is associated with the four interior Fe atoms of the 6 ML film, and the doublet with the two interface Fe atoms of the 6 ML film. The isomer shift of the singlet is the same as that found for

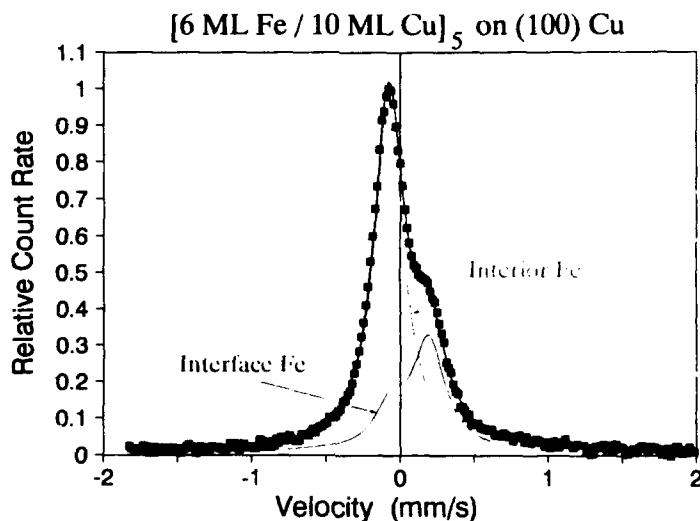


Figure 2 The conversion electron Mössbauer data for a superlattice based on 6 ML Fe films.

low-moment fcc-Fe precipitates in Cu.[38] This low-moment state ($\sim 0.2 m_B$) Fe orders antiferro- magnetically with a Néel temperature below 80 K.[39] No Kerr effect would be expected for this Fe. The effect on the Mössbauer line is to broaden it significantly below the Néel temperature.[40] Thus the room temperature Mössbauer data is entirely consistent with a nonmagnetic state of 6 ML Fe surrounded by Cu(100). Additional details are provided in Table I.

TABLE I

Parameters of the fit shown in Fig. 2. The isomer shifts are relative to pure α -Fe at 300 K.

	Isomer Shift mm/s	FWHM mm/s	Splitting mm/s	Relative Area
Central peak:	-0.079	0.0242	--	0.66
Quadrupole doublet:	0.064	0.251	0.252	0.34

it may be noted that the range of velocities displayed in Fig. 2 does not extend to the ~ 5 mm/s region in which the most intense peaks of high-spin ferromagnetic Fe are normally found. However, a separate measurement was made to ± 7 mm/s and no such peaks were found. To within a few percent the sample contains no magnetically aligned Fe atoms, consistent with the Kerr effect observations. Figure 2 displays only the central portion of the data in order for the details of the lineshape to be visible.

CONCLUSIONS

The major conclusions of this work are the following.

- 1) The 6 ML Fe on Cu(100) is strongly ferromagnetic when the surface is exposed in vacuum.
- 2) Upon deposition of Cu on this surface major changes are induced in the magnetization and the anisotropy.
- 3) The most dramatic effect occurs for 1 ML Cu, which reduces the Kerr signal strength by a factor of ~6 and reorients the easy axis from in-plane to perpendicular.
- 4) Perhaps more remarkable is that upon going from 1 ML to 2 ML Cu the Kerr signal strength increases by more than a factor of two.
- 5) Kerr effect measurements suggest that in the overlayer thickness range of 4 - 10 ML Cu, the ferromagnetism of the Fe is eliminated.
- 6) Mössbauer measurements confirm that in a superlattice composed of 6 ML Fe and 10 ML Cu films the Fe is nonmagnetic.

REFERENCES

- [1] M. F. Onellion, C. L. Fu, M. A. Thompson, J. L. Erskine, and A. J. Freeman, *Phys. Rev. B* 33, 7322 (1986).
- [2] A. Amiri Hezaveh, G. Jennings, D. Pescia, R. F. Willis, K. Prince, M. Surman, and A. M. Bradshaw, *Solid State Comm.* 57, 329 (1986).
- [3] P. A. Montano, et al. *Phys. Rev. Lett.* 59, 1041 (1987).
- [4] D. Pescia, M. Stamparoni, G. L. Bona, A. Vaterlaus, R. F. Willis, and F. Meier, *Phys. Rev. Lett.* 58, 2126 (1987).
- [5] W. A. A. Macedo and W. Keune, *Phys. Rev. Lett.* 61, 475 (1988).
- [6] C. Liu, E. R. Moog, and S. D. Bader, *Phys. Rev. Lett.* 60, 2422 (1988).
- [7] D. P. Pappas, K.-P. Kämper, H. Hopster, *Phys. Rev. Lett.* 64, 3179 (1990).
- [8] W. A. A. Macedo, W. Keune, and E. D. Ellerbroch, *J. Mag. Magn. Mat.* 93, 552 (1991).
- [9] W. R. Bennett, W. Schwarzacher, and W. F. Egelhoff, Jr., *Phys. Rev. Lett.* 65, 3169 (1990).
- [10] J. Thomassen, F. May, B. Feldmann, M. Wuttig, and H. Ibach, *Phys. Rev. Lett.* 69, 3831 (1992).
- [11] D. H. Mosca, F. Petroff, A. Fert, P. A. Schroder, W. P. Pratt, Jr., and R. Laloe, *J. Mag. Magn. Mat.* 94, L1 (1991).
- [12] T. Katayama, Y. Suzuki, H. Awano, Y. Nishihara, and N. Koshizuka, *Phys. Rev. Lett.* 60, 1425 (1988).
- [13] D. A. Steigerwald, I. Jacob, and W. F. Egelhoff, Jr., *Surface Sci.* 202, 472 (1988).
- [14] W. F. Egelhoff, Jr. and D. A. Steigerwald, *J. Vac. Sci. Technol. A* 7, 2167 (1989).
- [15] W. F. Egelhoff, Jr., I. Jacob, J. M. Rudd, J. F. Cochran, and B. Heinrich, *J. Vac. Technol. A* 8, 1582 (1990); W. F. Egelhoff, Jr. and M. T. Kief, *Phys. Rev. B* 45, 7795 (1992).
- [16] A. Brodde and H. Neddermeyer, to be published.
- [17] D. D. Chambliss, R. J. Wilson, and S. Chiang, *J. Vac. Sci. Technol. A* 10, 1992 (1992).
- [18] W. F. Egelhoff, Jr., *J. Vac. Sci. Technol. A* 7, 2060 (1989).
- [19] W. Schwarzacher, W. Allison, R. F. Willis, J. Penfold, R. C. Ward, I. Jacob, and W. F. Egelhoff, Jr., *Solid State Comm.* 71, 563 (1989); and unpublished results.
- [20] B. N. Engel, M. H. Wiedmann, R. A. Van Leeuwen, and C. M. Falco, *J. Appl. Phys.*, in press.

- [21] M. W. Wiedmann, B. N. Engel, R. A. Van Leeuwen, and C. M. Falco, *Mater. Res. Soc. Symp. Proc.* 313 (in press, 1993).
- [22] S. Ould-Mahfoud, R. Mégy, N. Bardoux, B. Bartenlian, P. Beauvillain, C. Chappert, J. Corno, B. Lecuyer, G. Sczigel, P. Veillet, and D. Weller, *Mater. Res. Soc. Symp. Proc.* 313 (in press, 1993).
- [23] A. Clarke, P. J. Rous, M. Arnott, G. Jennings, and R. F. Willis, *Surface Sci.* 192, L843 (1987).
- [24] M. Onellion, M. A. Thompson, J. L. Erskine, C. B. Duke, and A. Paton, *Surface Sci.* 179, 219 (1987).
- [25] S. A. Chambers, T. J. Wagener, and J. H. Weaver, *Phys. Rev. B* 36, 8992 (1987).
- [26] Y. Darici, J. Marcan, H. Min, and P. A. Montano, *Surface Sci.* 182, 477 (1987).
- [27a] W. Daum, C. Stuhlmann, and H. Ibach, *Phys. Rev. Lett.* 60, 2741 (1988).
- [27b] S. H. Liu, J. Quinn, D. Tian, F. Jona, and P. M. Marcus, *Surface Sci.* 209, 364 (1989); F. Jona and P. M. Marcus, *Surface Sci.* 223, L8978 (1989).
- [28] P. Xhonneux and E. Courtens, *Phys. Rev. B* 46, 556 (1992).
- [29] C. Stuhlmann, U. Beckers, J. H. Thomassen, M. Wuttig, H. Ibach, and G. Schmidt, in *The Structure of Surfaces III*, S. Y. Tong, M. A. Van Hove, K. Takayanagi, and X. D. Xie, Eds., Springer-Verlag, Berlin, 1993.
- [30] H. Magnan, D. Chanderis, B. Villette, O. Heckmann, and J. Lecante, *Phys. Rev. Lett.* 67, 859 (1991); and W. Schwarzacher, to be published.
- [31] M. T. Kief and W. F. Egelhoff, Jr., *Phys. Rev. B* 47, 10795 (1993).
- [32] V. L. Moruzzi, *Phys. Rev. Lett.* 57, 2211 (1986).
- [33] V. L. Moruzzi, P. M. Marcus, and J. Kübler, *Phys. Rev. B* 39, 6957 (1989).
- [34] J. E. Ortega, F. J. Himpsel, *Phys. Rev. Lett.* 69, 844 (1992).
- [35] J. E. Ortega, F. J. Himpsel, G. J. Mankey, and R. F. Willis, *Phys. Rev. B*, in press (see curve 2 in Fig. 3b).
- [36] J. E. Ortega, F. J. Himpsel, G. J. Mankey, and R. F. Willis, *Mater. Res. Soc. Symp. Proc.* 313 (in press, 1993).
- [37] P. D. Johnson, *Mat. Res. Soc. Symp. Proc.* 313 (in press, 1993).
- [38] L. H. Bennett and L. J. Swartzendruber, *Acta Metall.* 18, 485 (1970).
- [39] S. C. Abrahams, L. Guttman, and I. S. Kasper, *Phys. Rev.* 127, 2052 (1962); R. J. Weiss, *Phil. Mag.* 9, 361 (1964) and *Proc. Phys. Soc.* 82, 281 (1963).
- [40] W. Keune, R. Halbauer, U. Gonser, J. Lauer, and D. L. Williamson, *J. Appl. Phys.* 48, 2976 (1977).

CRYSTALLOGRAPHIC STRUCTURE OF COBALT FILMS ON CU (100)

O. HECKMANN, H. MAGNAN *, P. LE FEVRE AND D. CHANDESIS

LURE, Université de Paris Sud F-91405 ORSAY France

* and SRSIM, CEA Saclay F-91191 GIF sur YVETTE France

ABSTRACT

The stable structure of cobalt is hexagonal closed packed (hcp), but cobalt can be stabilized in the face centered cubic structure (fcc) by epitaxy on Cu (100). These films are ferromagnetic with [110] in plane easy axis. The magnetic anisotropies of these films strongly depend on their structure, and in particular to the possible deviation from the isotropic fcc structure. We have studied these films by surface EXAFS. By recording the spectra both in normal incidence and in grazing incidence we have shown that the Co/Cu(100) films have a *face centered tetragonal structure*: the mean nearest neighbour distance parallel to the surface is 2.55 Å (same value as in bulk copper) and the interlayer bonds length is 2.50 Å (same value as in bulk cobalt). We conclude that the films are in perfect epitaxy on copper (100) with a contraction of the lattice parameter perpendicular to the surface of 4%. A constant tetragonalization is observed for films of 2 to 15 monolayers.

INTRODUCTION

Thin metastable films of cobalt grown on Cu (100) are the subject of many magnetic and structural studies. MEED oscillations combined with in situ STM experiments¹ show that cobalt grows layer by layer on Cu (100) except for the first two layers. The films are always ferromagnetic, independent of the film thickness, and the remanent magnetization is always parallel to the interface², with a strong in-plane anisotropy: the [110] direction is the easy axis^{3,4}. The Curie temperature of films evaporated at 450 K is strongly increasing with the film thickness from 130 K for 1.5 ML to 500 K for 2.5 ML³. LEED results indicate that cobalt epitaxially grows on Cu (100) with an fcc tetragonal structure^{2,5}.

Surface EXAFS⁶ is a very attractive technique to measure the crystallographic structure of metastable thin films. It gives to a high precision the shape of the first neighbour shell⁷, including its possible asymmetry⁸ and its thermal broadening^{9,10} which is related to the elastic force constant between nearest neighbours (nn) in the film. Moreover, the linear polarization of the synchrotron radiation reveals information about the anisotropy of the crystallographic structure. EXAFS is a selective method: by measuring the EXAFS oscillations above the K edge of cobalt we are sure to be sensitive only to the local order in the cobalt film. Then, films of any thickness, coated films and multilayers can be characterized with the same precision.

EXPERIMENTAL PROCEDURE

The EXAFS experiments were performed at the Laboratoire pour l'Utilisation du Rayonnement Electromagnétique (LURE) on the surface EXAFS set-up using a Si (311) double crystal monochromator installed on the wiggler beam line of DCI storage ring. The samples Co/Cu (100) were prepared in a UHV chamber connected to the X-ray beam line. Cobalt is evaporated from a high purity wire heated by electron bombardment in a vacuum better than 5×10^{-10} mbar (base pressure is 2×10^{-10} mbar). It is deposited at a rate of about 1 ML per min. on a clean Cu surface checked by LEED and Auger spectroscopy. The evaporation rate is calibrated prior to the evaporation with a quartz microbalance. The thickness of the film is controlled by Auger spectroscopy and by measuring the X-ray absorption edge jump of the sample at the K edge of cobalt. Using this calibration, we estimate the thickness of the grown film with an accuracy of 10%. The local atomic structure of the films is then studied in situ.

The variations of the X-ray absorption coefficient of the samples are measured above the K edge of cobalt (7709 eV) in the total yield mode. Quantitative analysis of the EXAFS data is done using the general formula giving the EXAFS modulation function, χ , in the case of a linear polarized light and for a K edge^{7,10}:

$$\chi(k) = \sum_i (N_i^* / k r_i^2) \exp(-2r_i/\lambda) \exp(-2\sigma_i^2 k^2) B_i(k) \sin[2kr_i + \Phi_i(k)] \quad (1)$$

where the sum runs over all the shells i of neighbours situated at the distance r_i of the absorbing atom, $B_i(k)$ their backscattering amplitude, λ is the mean free path of the photoelectron, k its wave number; $[2kr_i + \Phi_i(k)]$ is the total phase shift taking into account atomic potentials. σ_i^2 is the mean square relative displacement between the absorbing atom and the neighbours i (including static and thermal disorder) and N_i^* is the effective number of atoms of the shell situated at the distance r_i :

$$N_i^* = \sum_j 3 \cos^2 \alpha_j \quad (2)$$

where α_j is the angle between the electric field vector of the X-rays and the direction of the bond between the absorbing atom and the neighbour j of the shell i .

The backscattering amplitude $B_i(k)$ and phase shift $\Phi_i(k)$ amplitude are determined experimentally from reference EXAFS spectra measured on bulk cobalt.

TETRAGONAL DISTORTION

The X-ray absorption coefficient of thin films of cobalt of thicknesses between 2 and 15 monolayers grown at room temperature have been measured above the K edge of cobalt (7709 eV) both in grazing incidence and in normal incidence. Due to the two-dimensional character of thin films, we can expect nearest neighbour bonds of different type if they are in-plane bonds (parallel to the interface plane) or out-of-plane bonds. The linear polarization of the synchrotron radiation allows to separate these two contributions since the contribution of each bond is weighted by a factor $\cos^2 \alpha$ (equation 2) where α is the angle between the bond and the polarization direction of the X-rays. In our case, if we assume a perfect fcc epitaxy, every cobalt atom has 4 nn in its plane, 4 above (missing for the top layer) and 4 below. When the polarization of the light is perpendicular to the surface (grazing incidence) only the interlayer bonds contribute to the EXAFS signal but in normal incidence (polarization parallel to the surface) both interlayer bonds and intralayer bonds are contributing with the same weight.

Some raw EXAFS spectra of cobalt films are reproduced on figure 1. On figure 1a, we directly see the tetragonal distortion of the 3 ML thick film: the frequency of the main EXAFS oscillations is higher in normal incidence than in grazing incidence which means a longer nearest neighbour (nn) distance for intralayer bonds. On the other hand, on figure 1b, we clearly see that in normal incidence, the frequency of the EXAFS oscillations is the same for a 3 ML and an 8 ML thick films.

The Fourier transforms of the EXAFS spectra of the 3 ML and 15 ML thick films are shown on figure 2: in normal incidence it is characteristic of an fcc well ordered structure (position and relative intensities of the different shells of neighbours), but in grazing incidence there is a displacement of the fourth peak to which contribute the fourth neighbours. In a perfect fcc structure the fourth neighbours are aligned with the first ones and the focusing effect¹¹ of the first shell is responsible for the anomalous high intensity of this shell. Its modification in grazing incidence must also be related to the structural anisotropy of these films.

The spectra were then filtered in real space to isolate the first peak of the Fourier transforms and finally back-transformed in k -space. Quantitative parameters are then obtained by an analysis of these spectra using a plane-wave approximation and experimental phaseshifts and backscattering amplitudes. The first shell radial distribution function (RDF) gaussian parameters are reported in table 1 for samples of different thicknesses. The measured coordination numbers are compared to the effective coordination numbers calculated for a perfect epitaxial fcc thin film of the same thickness, $N^* = \sum_j 3 \cos^2 \alpha_j$. The grazing incidence

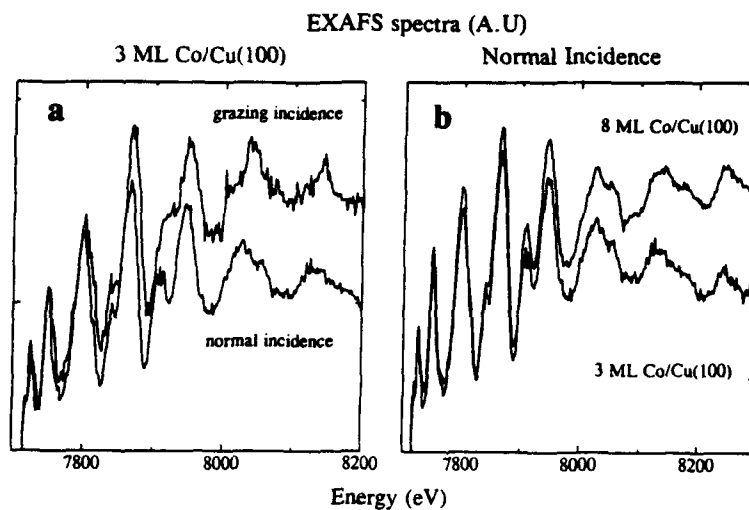


Figure 1: EXAFS spectra recorded at 77 K at the cobalt K edge
a) for 3 ML Co/Cu (100) grown at 300K in normal incidence and in grazing incidence.
b) for 3 ML Co/Cu (100) and 8 ML Co/Cu (100) grown at 300K in normal incidence.

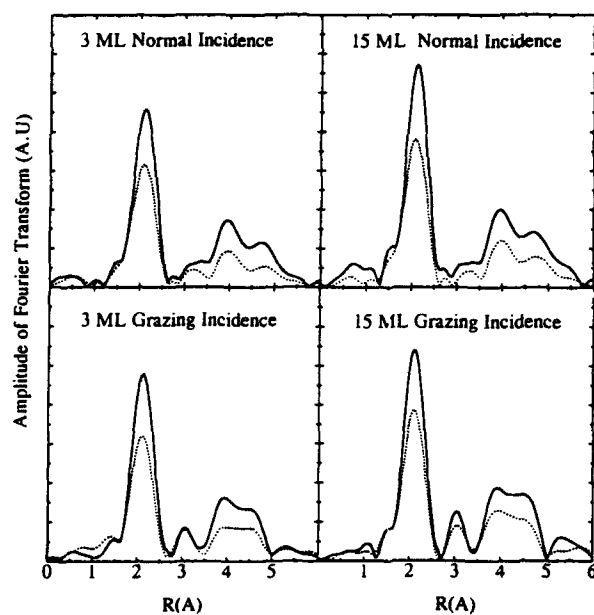


Figure 2: Fourier Transforms between $k = 2.55 \text{ \AA}^{-1}$ and $k = 11.64 \text{ \AA}^{-1}$ for EXAFS spectra recorded at 77 K (full line) and 300K (dotted line), in normal incidence and in grazing incidence, for 3 ML and 15 ML Co/Cu (100) grown at 300 K.

Thickness ($\pm 10\%$)	Incidence		N*	R (\AA) (± 0.01)	$\sigma^2(77\text{K})(\text{\AA}^2)$ $\pm 0.5 \times 10^{-3}$	$\Delta\sigma^2(\text{\AA}^2)$ $\pm 0.5 \times 10^{-3}$
3 ML	Normal	in plane:	6	2.55	3.6	4
		out of plane:	5	2.51	2	
	Grazing	in plane:	0			4.5
		out of plane:	10	2.51	2	
5 ML	Normal	in plane:	6	2.55	1.2	3.6
		out of plane:	5.4	2.50	3.3	
	Grazing	in plane:	0			4.2
		out of plane:	10.8	2.50	3.3	
6 ML	Normal	in plane:	6	2.55	2.5	3.9
		out of plane:	5.5	2.51	2.6	
	Grazing	in plane:	0			3.6
		out of plane:	11	2.51	2.6	
8 ML	Normal	in plane:	6	2.55	1.8	3.6
		out of plane:	5.6	2.50	2.8	
	Grazing	in plane:	0			4.1
		out of plane:	11.2	2.50	2.8	
15 ML	Normal	in plane:	6	2.55	1	3.3
		out of plane:	5.8	2.51	2.3	
	Grazing	in plane:	0			3.3
		out of plane:	11.6	2.51	2.3	

Table I: Structural parameter results of least square fits of the first shell of neighbours for different films of Co/Cu (100). N* is the effective coordination number for a perfect fcc epitaxial film calculated for the in plane bonds and out of plane bonds in normal and grazing incidence. R is the mean nn distance determined by the fits for the in plane bonds and the out of plane bonds, $\sigma^2(77\text{K})$ the width of the RDF, and $\Delta\sigma^2$ the variation of the Debye-Waller factor between 300K and 77 K.

spectra give a precise measure of the out of plane nn distance. We then deduce the in plane nn distance from the normal incidence EXAFS spectra where the intralayer bonds and the interlayer ones contribute with the same weight. For all the samples, the in plane nn distance is 2.55 \AA ($\pm 0.01 \text{ \AA}$) which is exactly the nn distance in bulk copper, and the out-of plane nn distance is 2.50 \AA ($\pm 0.01 \text{ \AA}$) which is the nn distance of bulk cobalt. So the tetragonal deformation of the films appears to be an expansion parallel to the interface to adapt exactly the in-plane nn distance of the film to substrate's one, but the out of plane nn distances keep the same value than in bulk cobalt. These values give an in-plane lattice parameter $a_{\parallel} = 3.61 \pm 0.02 \text{ \AA}$ and an out of plane lattice parameter $a_{\perp} = 3.46 \pm 0.02 \text{ \AA}$. Then the lattice parameter perpendicular to the interface is contracted by $\approx 4\%$ with respect to the parallel one. This tetragonal deformation of 4 % is the same for all the thicknesses up to 15 ML. All these films are well ordered : the static disorder coefficient, $\sigma^2(77\text{K})$, is between $1 \times 10^{-3} \text{ \AA}^2$ and $3.6 \times 10^{-3} \text{ \AA}^2$. In bulk cobalt, it is $2.7 \times 10^{-3} \text{ \AA}^2$. The shape of the Fourier Transforms of the EXAFS spectra confirms this result : the peaks corresponding to the third and fourth shells of neighbours are well defined, as in bulk samples. A lack of local order should decrease rapidly these peaks. Moreover, conversely to other systems (Fe/Cu (100)¹² for example), there is about no change of the local order in the film when its thickness increases.

Can this tetragonal distortion be seen as a simple elastic accommodation of the cobalt film to the strain imposed in the plane parallel to the interface by the copper substrate? The nn distance in bulk cobalt is 2.50 \AA ($\pm 0.01 \text{ \AA}$). In the cobalt films epitaxially grown on Cu (100), the in-plane nn distance of cobalt atoms is 2.55 \AA : the strain imposed by the substrate induces a lateral expansion $\Delta a_{\parallel} / a_{\parallel} = 2\%$ of the lattice parameter. Since the surface of the film is free, we can assume no stress in the cobalt film in the direction perpendicular to the interface. So, the

relative contraction of the lattice parameter in this direction $\Delta a_{\perp}/a_{\perp}$ can be related to the in plane expansion by the relation¹³

$$\frac{\Delta a_{\perp}}{a_{\perp}} = -2 \frac{C_{12}}{C_{11}} \frac{\Delta a_{\parallel}}{a_{\parallel}}$$

where C_{12} and C_{11} are the standard elastic coefficient in a cubic crystal. In cubic cobalt, we can assume the ratio C_{12}/C_{11} equal to $0.6 \pm .05$ ¹³ and we should have $\Delta a_{\perp}/a_{\perp} = -2.4\%$. The experimental value is $2\% \pm 0.5\%$ and we can say that the tetragonal deformation present in the cobalt films is the elastic accommodation of the film to the lateral strain induced by the epitaxy on the monocrystal of copper.

ELASTIC PROPERTIES

Since the structure is not isotropic, one can expect anisotropic elastic properties in these films, as it was observed in metastable iron films grown on Cu (100)¹². Temperature dependent EXAFS measurements give the amplitude of the thermal vibrations along the different bonds which are related to the effective force constants between nearest neighbours¹⁰. We have compared the filtered first shell EXAFS signals recorded on the same samples at room temperature, $\chi(k, 300K)$, and at 77K, $\chi(k, 77K)$. Between these two temperatures we do not observe any structural change: the Fourier transform profiles have the same shape and the nearest neighbour distances are the same. Then we measure the variation of the Debye-Waller factor between these two temperatures, $\Delta\sigma^2 = \sigma^2(300K) - \sigma^2(77K)$ by the relation^{9,10}:

$$\ln[\chi(k, 77K)/\chi(k, 300K)] = 2k^2\Delta\sigma^2 \quad (3)$$

The results are displayed in table I last column. Once more, we can say that all the films have a very similar behaviour: the anisotropies are small and the measured $\Delta\sigma^2$ values are not far from the bulk ones. In bulk cobalt, $\Delta\sigma^2 = 3.6 \times 10^{-3} \text{ \AA}^2$ and in bulk copper $\Delta\sigma^2 = 4.7 \times 10^{-3} \text{ \AA}^2$. The tetragonal deformation does not induce a strong anisotropy of the elastic properties in these cobalt films. The evolution that we can mention is a decrease of $\Delta\sigma^2$ in grazing incidence when the thickness of the film increases: $\Delta\sigma^2 = 4.5 \times 10^{-3} \text{ \AA}^2$ for the 3 ML thick film, and $\Delta\sigma^2 = 3.3 \times 10^{-3} \text{ \AA}^2$ for the 15 ML thick film. It means that the interlayer bonds become stiffer in the thicker films, but this increase is slow and can explain why the films do not relax to their bulk structure even for quite high thicknesses: the tetragonal deformation is elastic and the force constants between nearest neighbours are not significantly modified.

CONCLUSION

In summary, this EXAFS study shows that we observe about always the same structure when growing cobalt on copper (100) between 2 and 15 monolayers: a tetragonally distorted fcc structure. The cobalt is in perfect epitaxy on the substrate with an in-plane expanded nearest neighbour distance equal to that of bulk copper, and a contraction in the other direction. The tetragonal deformation is the elastic accommodation of the film to the lateral strain induced by the epitaxy on the monocrystal of copper. This distortion means that there is an evident loss of symmetry: there is no more [111] symmetry axis. All the films are well ordered, and their elastic properties are neither strongly anisotropic, nor very different from those of bulk cobalt: this is coherent with the fact that the deformation is elastic. The constant magnetic properties measured in these films (always ferromagnetic and in-plane easy axis) are certainly due to this unique structure.

REFERENCES

1. C. M. Schneider, A.K. Schmid, H.P. Oepen and J. Kirschner in *Structure and Magnetism in Low Dimensional Systems*, eds R.F.C. Farrow, M. Donath, B. Dieny, A. Fert, B. Hermsmeier (Plenum Press, New York 1993)
2. M. Stamparoni, *Appl. Phys. A* **49**, 449 (1989).
3. C. M. Schneider, P. Bressler, P. Schuster, J. Kirschner, J. J. de Miguel, and R. Miranda, *Phys. Rev. Lett.* **64**, 1059 (1990).
4. H. P. Oepen, M. Benning, H. Ibach, C. M. Schneider, and J. Kirschner, *Journal of Magn. Mat.* **86**, L 137 (1990).
5. B. Heinrich, J.F. Cochran, M. Kowalewski, J. Kirschner, Z. Celinski, A.S. Arrott, and K. Myrtle, *Phys. Rev. B* **44**, 9348 (1991) and M. Kowalewski, C.M. Schneider and B. Heinrich, *Phys. Rev. B* **47**, (1993)
6. A. Clarke, G. Jennings, R. F. Willis, P. J. Rous, and J. B. Pendry, *Surf. Sci.* **187**, 327 (1987).
7. J. Stöhr, D. Denley, and P. Perfetti, *Phys. Rev. B* **18**, 4132 (1978); P. H. Citrin, P. Eisenberger, and R. C. Hewitt, *Phys. Rev. Lett.* **41**, 309 (1978).
8. D. E. Sayers, E. A. Stern and F. W. Lytle, *Phys. Rev. Lett.* **27**, 1204 (1971).
9. G. Bunker, *Nucl. Instr. Meth.* **207**, 437 (1983); H. Magnan, D. Chandesris, G. Rossi, G. Jezequel, K. Hricovini, and J. Lecante, *Phys. Rev. B* **40**, 9989 (1989).
10. R. B. Greegor and F. W. Lytle, *Phys. Rev. B* **20**, 4902 (1979).
11. P. Roubin, D. Chandesris, G. Rossi, J. Lecante, M. C. Desjonquères, and G. Tréglia, *Phys. Rev. Lett.* **56**, 1272 (1986); P. Roubin, D. Chandesris, G. Rossi, and J. Lecante, *J. Phys. F* **18**, 1165 (1988).
12. P. A. Lee and J. B. Pendry, *Phys. Rev. B* **11**, 2795 (1975).
13. H. Magnan, D. Chandesris, B. Villette, O. Heckmann and J. Lecante, *Phys. Rev. Lett.* **67**, 859 (1991).
14. using the standard definition of the elastic constants for cubic crystals. From the American Institute of Physics Handbook, the ratio C_{12}/C_{11} is respectively 0.59 and 0.64 for cubic Fe and Ni and is 0.54 for hexagonal cobalt.

**IN SITU RHEED AND MAGNETO-OPTIC STUDY OF ULTRATHIN
COBALT FILMS ON (111) GOLD SUBSTRATE :
EFFECT OF A METALLIC OVERLAYER**

OULD-MAHFOUD S., MEGY R., BARDOU N., BARTENLIAN B., BEAUVILLAIN P.,
CHAPPERT C. ** CORNO J., LECUYER B., SCZIGEL G., VEILLET P. and
***WELLER D.

Institut d'Electronique Fondamentale and ** Institut d'Optique, Laboratoires associés au
CNRS, Université Paris-Sud, 91405 Orsay Cedex.

*** IBM Almaden Research Center, 650 Harry Road, San José CA 95120-6099.

ABSTRACT

We present a comparative in situ RHEED and Polar Magneto-optic Kerr Effect study of the first stages of the growth of a Au overlayer on top of a (111) Co ultrathin film. Drastic behaviours are evidenced on the RHEED diagram, magnetic anisotropy and coercive force, around 1.5 ML of Au coverage.

INTRODUCTION

A lot of work has been devoted in the last few years to the study of the magnetic anisotropy in ferromagnetic ultrathin films [1]. Besides the magnetocrystalline interface anisotropy introduced by L. Néel [2], strain induced magnetoelastic anisotropy [3], or spin polarization of the interface layer in the non magnetic substrate [4], have been proposed to explain the observed behaviours of anisotropy versus the ferromagnetic film thickness, or for different non magnetic metal substrate. To shed new light on the respective importance of those phenomena, we performed a comparative in situ RHEED and Polar Magneto-optical Kerr Effect (PMOKE) study of a Co ultrathin film deposited on a Au (111) substrate, during the first stages of the growth of the second Co/Au interface with a Au coverage layer.

EXPERIMENTAL

Details of our sample preparation method have been already published [5]. First a 300 Å thick Au buffer layer is grown on a float glass platelet, and annealed to give a polycrystalline, (111) textured, atomically flat film. Co is then deposited at room temperature from an e-beam source, at a rate of about 0.01 Å/s. During all evaporation and characterization steps the pressure in the system remains well within the 10^{-10} mbar range (mostly residual H_2). Thicknesses are measured using a quartz microbalance, calibrated against Grazing X rays Reflectivity (GXR) measurements performed on test films. GXR was also used as a powerful tool to optimize the quality of the Au buffer layer [6]. We can perform RHEED measurements (up to 30 keV) during film growth. For PMOKE studies, the sample is tilted to face a liquid N_2 cooled solenoid, producing a field up to 1.4 kOe, perpendicular to the sample. PMOKE measurements are performed through the clear bore of the coil.

To achieve maximum precision and reliability in our study of the magnetic properties versus films thicknesses, we made stepped samples using a moving shutter between sample and evaporation sources. For each sample, up to ten 2mm-wide steps were made, with varying Co or Au coverage thicknesses (resp. t_{Co} and t_{Au}). To minimize shadow effects, the shutter slides less than 1 mm below the sample surface, while the sources are more than 450 mm away, with incidence angles less than 8 degrees.

In both RHEED and PMOKE measurements the sample is precisely moved with a fixed incident e⁻ or laser beam, in order to scan the different steps. Moreover, the Au overlayer is grown in successive thin layers, and for each new layer complete RHEED and PMOKE scans are performed. The RHEED diagram of the Au buffer layer displays narrow lines with a good contrast [7], in agreement with the known good quality of the surface. With Co deposition the lines get wider, with a clear evolution towards a 3D structure, as the Co doesn't grow in a layer by layer mode on Au.

A striking phenomenon occurs during the first stages of the Au overlayer growth. Figure 1 shows the intensity variation, along the [111] direction, of the diffraction line near the central line of the diagram in [1-10] azimuth.

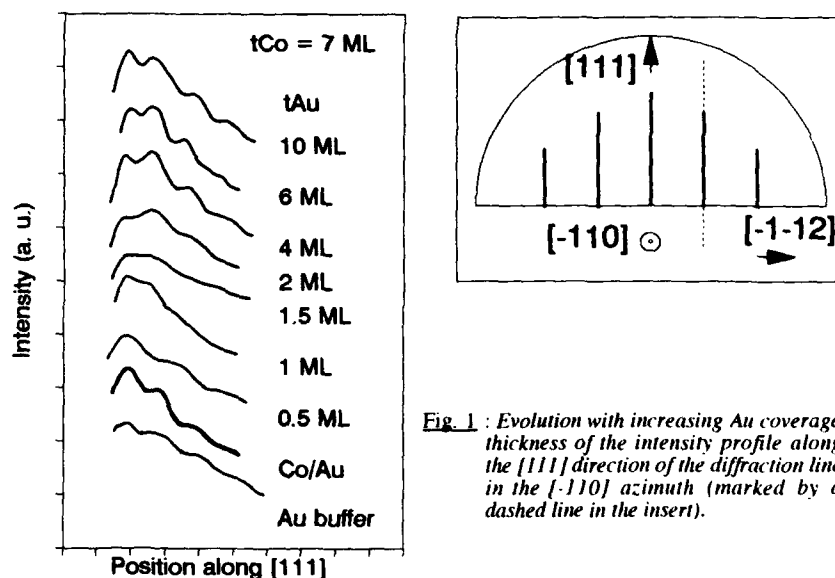


Fig. 1 : Evolution with increasing Au coverage thickness of the intensity profile along the [111] direction of the diffraction line in the [-110] azimuth (marked by a dashed line in the insert).

For the 7 ML thick Co film surface, the line shows marked intensity variations, characteristic of a rough surface. With increasing Au coverage, the variations amplitude first decreases, and vanishes totally for 1.5 ML of Au, where the diagram is again a line diagram characteristic of a flat surface. This drastic smoothing of the Co free surface by 1-2 ML of Au coverage can be attributed to a surfactant effect of Au: indeed, the [111] surface energy of Au is lower than the (0001) Co one. This is a major phenomenon, that involves an important reorganization of the Co layer to rub out at least short range roughness.

Figure 2 displays PMOKE hysteresis loops taken at room temperature in perpendicular field at steps with Co thicknesses of 8, 10, 12, and 14 ML, and Au overlayer thicknesses of 0.5, 1.5 and 4 ML. The anisotropy clearly displays a drastic behaviour. Indeed, while at these Co thicknesses the uncovered Co film is magnetized in plane, covering by only 1.5 ML of Au is enough to get perpendicular magnetization with square hysteresis loops up to t_{Co} about 10 ML (20 Å). Also very interesting is the fact that subsequent increase in Au coverage thickness reduces the anisotropy. Such a behaviour has been evidenced recently [9] on Co films with Cu coverage.

Our deposition system so far is not equipped to measure in situ the magnetic anisotropy coefficients of the samples. Moreover, for Co thin films the two first anisotropy coefficients K_1 and K_2 have comparable amplitude (K_1 and $K_2 > 0$), and the change with Co thickness in easy axis from perpendicular to in plane is not simple, with the occurrence of an intermediate phase where the easy direction lies on a cone of half angle γ . Provided the sample remains in a single domain state, which is likely at least for low to intermediate values of γ , the ratio of the remanent on saturated Kerr rotations θ_R/θ_S should be equal to $\cos(\gamma)$, given by :

$$\cos(\gamma) = \left(\frac{-2\pi M_S^2 + K_1 + 2K_2}{2K_2} \right)^{1/2} \quad (1)$$

where M_S is the saturation magnetization. In the hypothesis where K_2 doesn't change much with t_{Co} , which to our knowledge has always been observed, a good characterization of the dependence of K_1 versus t_{Co} is given by the crossover thickness t^* where for instance $\gamma = 45^\circ$.

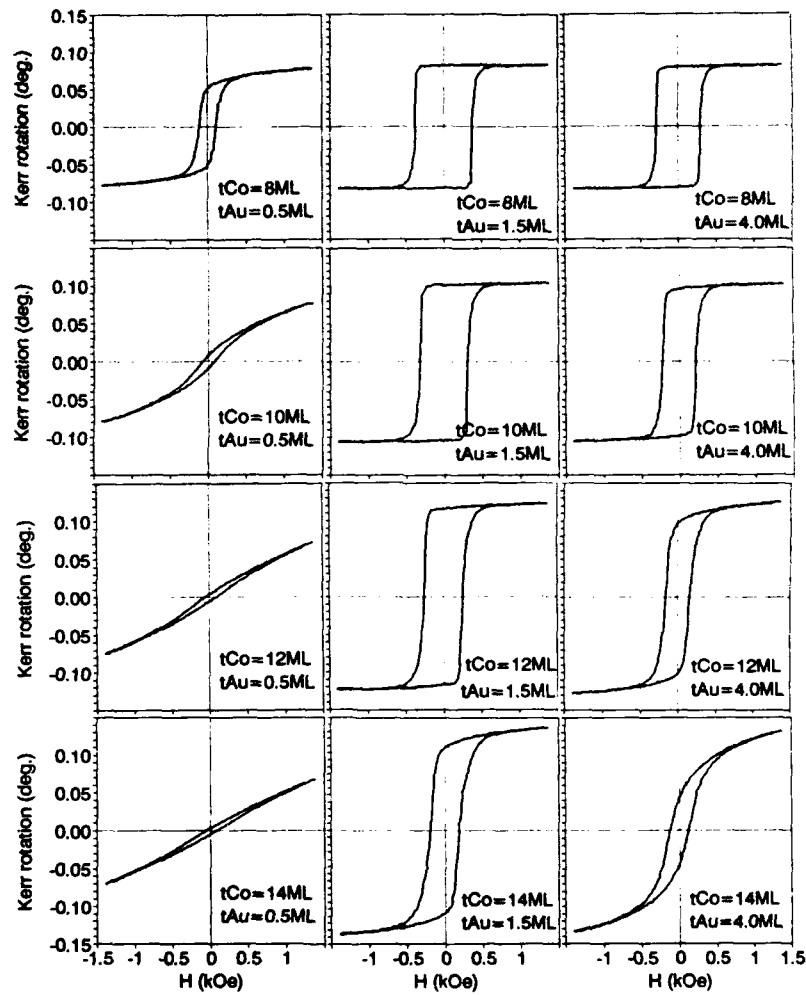


Fig. 2 : PMOKE hysteresis loops at room temperature measured "in situ" on steps of the samples with different Co thicknesses t_{Co} at successive stages of the Au overlayer deposition t_{Au} .

By introducing for K_1 the usual expression with interface anisotropies K_{S1} and K_{S2} respectively for the first (Co/Au) and second (vacuum/Co or Au/Co) interfaces, and volume anisotropy K_V , one gets the expression

$$K_{S1} + K_{S2} = t^* (2\pi M_s^2 - K_V - K_2) \quad (2)$$

The maximum magnetic field in our set up is too low to allow precise determination of θ_S for t_{Co} values where the loop is not perfectly square. However, in this last case, the θ_S values that we measure vary linearly with t_{Co} (cf. Figure 3).

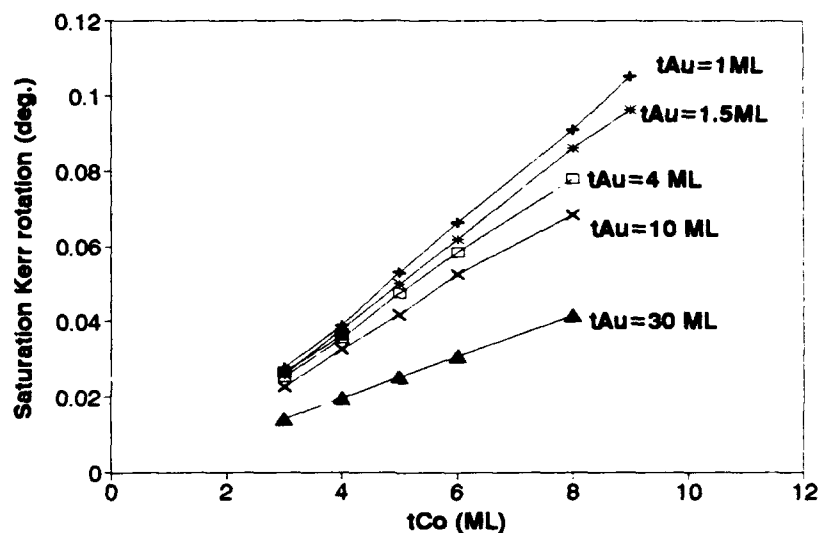


Fig. 3 : Saturation Kerr rotations deduced from the PMOKE hysteresis loops, versus Co thicknesses t_{Co} , for various values of the Au overlayer thickness t_{Au} .

To evaluate θ_S we thus extrapolate this linear variation to higher t_{Co} values. The variation of t^* versus t_{Au} is thus given in figure 4. We observe a very fast increase in t^* at the very beginning of the Au overlayer growth, with a narrow peak around $t_{Au} = 1.5$ ML, followed by a subsequent decrease of t^* towards saturation. Note that the value of t^* that we measure on uncovered Co film ($t^* = 4.3$ ML) is in very good agreement with that already reported [9].

An other interesting behaviour visible in figure 2 is the important variations of the coercive force H_c . As we had already reported [7], we observe a fast increase in H_c with decreasing t_{Co} . In agreement with reference [8], we also observe a peak of H_c around $t_{Au} = 1.5$ ML, relatively all the more enhanced that t_{Co} gets closer to t^* . This behaviour is displayed on figure 5.

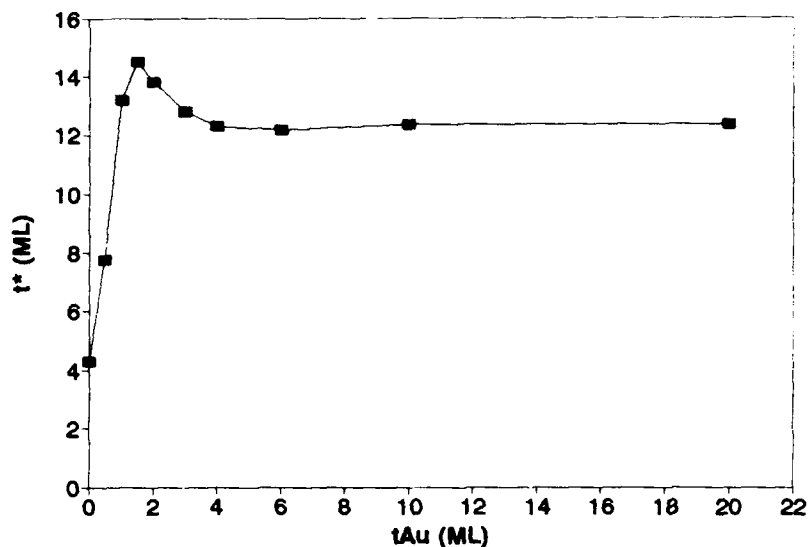


Fig. 4 : Variation with Au overlayer thickness t_{Au} of the Co thickness t^* where the remanent Kerr rotation is equal to $(1/\sqrt{2})$ of the saturation Kerr rotation.

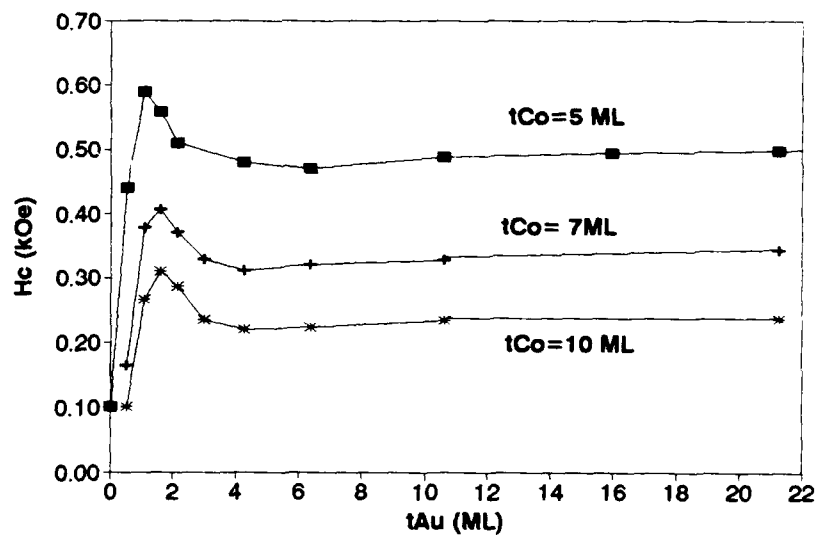


Fig. 5 : Variation with Au overlayer thickness t_{Au} of the coercive force H_c for various Co thicknesses t_{Co} .

DISCUSSION

The variation observed in I_{lc} versus t_{Au} closely follows that of t^* . Indeed, as was recently pointed out [10], in such high quality Au/Co/Au films with very square hysteresis loops the coercive field is a nucleation field, and certainly depends on the anisotropy. The clear relation between H_c and t^* could then be expected. We are pursuing now a more complete experimental and theoretical study of this relation.

The behaviour of the anisotropy with t_{Au} is more surprising. We think that strain induced magnetoelastic anisotropy (MEA) is unlikely to be at the origin of this behaviour. Even if a contribution of MEA cannot be ruled out, going with the surface reorganisation evidenced by RHEED, it would at most give an increase in $(K_{S1} + K_{S2})$ by a factor of 2, too low to account for the observed increase in t^* from 4.3ML to 14.5ML at the peak near $t_{Au}=1.5$ ML, not even $t^*=12$ ML at thick Au coverages. A simple effect of smoothing, linked to the surfactant effect of Au, can neither explain the experimental results.

The abruptness of the behaviour would rather lead to point out to an electronic effect. Supposing that K_{S1} and K_{S2} take similar positive values for high t_{Au} values, the increase in anisotropy can be explained by giving a negative value to the Co/vacuum interface anisotropy, in agreement for instance with theoretical predictions of reference [11] and discussion of reference [12]. In a similar argument, the peak around $t_{Au}=1.5$ ML could be attributed to a change in K_{S2} , linked to a change in the electronic band structure of the Au interface layer. As evidenced in our RHEED results, this layer clearly has a marked 2-dimensionnal character around $t_{Au}=1.5$ ML, and the interface anisotropy is expected to show a strong dependence on band structure [11,13]. Using in equation 2 bulk values for M_s , K_1 and K_2 as in reference [9], we can evaluate K_S values of 0.8 erg cm^{-2} , $-0.24 \text{ erg cm}^{-2}$, and 1.08 erg cm^{-2} , respectively for interfaces Co/Au, Co/vacuum, and Co/Au (1.5 ML).

Finally, even if nothing in our PMOKE data confirms that, we cannot completely rule out the occurrence of a small spin polarization in the Au monolayer on Co, as has been theoretically predicted at the Au/Fe interface [14]: given the strong spin orbit coupling in Au, this would lead to a contribution to the anisotropy.

REFERENCES

- [1] W.J.M. de Jonge, P.J.H. Bloemen and F.J.A. den Broeder in Ultrathin Magnetic Structures, Vol.1.3: Experimental Investigations of Magnetic Anisotropy, edited by B. Heinrich and J.A.C. Bland (Springer Verlag), to be published.
- [2] L. Néel, J. de Phys. et le Rad. **15**, 225(1954).
- [3] C. Chappert and P. Bruno, J. Appl. Phys. **64**, 5736(1988).
- [4] D. Weller, Proceedings of the NATO workshop on Magnetism and structure in systems of reduced dimension (1993), to be published in NATO Advanced Science Institute Series.
- [5] D. Renard and G. Nihoul, Phil. Mag. **B55**, 75(1987).
- [6] L. Nevot, Acta Electronica **24**, 255(1981/82).
- [7] C. Chappert, P. Beauvillain, P. Bruno, J.P. Chauvineau, M. Galtier, K. Le Dang, C. Marlière, R. Mégy, D. Renard, J.P. Renard, J. Seiden, F. Trigui, P. Veillet and E. Vélú, J. Mag. Mat. **93**, 319(1991).
- [8] B.N. Engel, M.H. Wiedemann, R.A. Van Leeuwen and C.M. Falco, MORIS 92, to be published in J. Mag. Soc. Japan (1993).
- [9] R. Allenspach, M. Stambanoni and A. Bischof, Phys. Rev. Letters **65**, 3344(1990).
- [10] J. Pommier, P. Meyer, G. Pénissard, J. Ferré, P. Bruno and D. Renard, Phys. Rev. Letters **65**, 2054(1990).
- [11] P. Bruno, Phys. Rev. B **39**, 865(1989).
- [12] B.N. Engel, M.H. Wiedemann, R.A. Van Leeuwen and C.M. Falco, Kyoto Symposium on Metallic Multilayers (March 1993).
- [13] G.H.O. Daalderop, P.J. Kelly and M.F.H. Schuurmans, Phys. Rev. **B42**, 7270(1990).
- [14] G. Li, A.J. Freeman, H.J.F. Jansen and C.L. Fu, Phys. Rev. B **42**, 5433(1990).

THEORETICAL STUDIES ON THE MAGNETIC MOMENTS OF IRON NITRIDES INCLUDING Fe_{16}N_2

AKIMASA SAKUMA AND YUTAKA SUGITA*

Magnetic and Electronic Materials Research Laboratory, Hitachi Metals, Ltd., Mikajiri 5200, Kumagaya 360, Saitama, Japan

*Central Research Laboratory, Hitachi Ltd., 1-280, Higashi-Koigakubo, Kokubunji, Tokyo, 185, Japan

ABSTRACT

The spin-polarized band calculations for the iron nitrides, Fe_3N , Fe_4N and Fe_{16}N_2 , have been performed with use of LMTO-ASA method in the frame of local spin density functional formalism. The results show that the most distant Fe atoms from N have the largest magnetic moment. The central role of the N atom is to bring about the large magnetic moments through the lattice expansion. Concurrently, the N atoms promote an itinerancy of electrons and then in turn prevent the exchange-splitting. This results in an Fe_{16}N_2 with the lowest N concentration having the largest magnetic moments. Quantitatively, the obtained magnetic moments are in fair agreements with the experimental results except for Fe_{16}N_2 . The calculated magnetic moment of Fe_{16}N_2 is about $2.4 \mu_B/\text{Fe}$, while the measured value is reported as $3.5 \mu_B/\text{Fe}$. The orbital magnetic moment of Fe_{16}N_2 is about $0.07 \mu_B$, which is too small to make up for the difference from the experimental value.

INTRODUCTION

Until the early 1970's, iron nitrides had been investigated in terms of the itinerant electron magnetism of the transition metals including interstitial non-magnetic atoms [1-9]. The aim of the studies was focused on the establishment of the relationship between ferromagnetism and metal-nonmetal bonding. Since Kim and Takahashi [10] found a giant magnetic moment in the Fe-N film in 1972, the elements such as N, C and B in the transition metals have attracted concerns not only in the physical aspect but also in the development of magnetic materials for technological applications. They reported that the film consists of Fe and Fe_{16}N_2 whose structure was discovered previously by Jack [11]. Ever since, many attempts have been made to prepare the single phase Fe_{16}N_2 with several techniques. Recently, Komuro et al. [12] have first grown a single crystal Fe_{16}N_2 film on InGaAs epitaxially by MBE technique and demonstrated B_s of the Fe_{16}N_2 to be 2.8-3.0T. Concurrently, Nakajima et al. [13,14] succeeded to construct the Fe_{16}N_2 film by ion implantation and measured the average magnetic moment of Fe atom is about $2.5 \mu_B$. Although the data reported by several workers scatters so far, it is convincing that the magnetic moment of Fe_{16}N_2 exceeds one of bcc-Fe by far. The current controversial problems are the mechanism of the occurrence of such a large magnetic moment and how the magnetism of the Fe_{16}N_2 is related to that of both Fe-N with no site order of N atoms and other iron nitride compounds.

There are four phases in the iron nitrides, $\zeta\text{-Fe}_3\text{N}$, $\epsilon\text{-Fe}_x\text{N}$ ($2 < x \leq 3$), $\gamma\text{-Fe}_4\text{N}$ and $\alpha\text{-Fe}_{16}\text{N}_2$ whose structures were determined by Jack [11,15] previously. $\epsilon\text{-Fe}_x\text{N}$ exhibits

hexagonal structure in the range $2 < x \leq 3$ and transfers into orthorhombic structure just above $x = 2$, where $\zeta\text{-Fe}_x\text{N}$ is established. Deducing from the previous investigations [1-4], the magnetic moment decreases from about $2 \mu_B$ at $x = 3$ with decreasing x , and drops sharply into about $0.2 \mu_B$ at $x = 2$. In Fig.1, we show the crystal structure of $\epsilon\text{-Fe}_3\text{N}$ together with that for $\gamma\text{-Fe}_4\text{N}$ and $\alpha\text{-Fe}_{10}\text{N}_7$. $\gamma\text{-Fe}_4\text{N}$ has been experimentally investigated [5-9] precisely since older times because of its thermal stability and relatively large magnetic moments. The crystal structure is simple cubic composed of fcc iron and N atom at the body center position. As for iron atoms, there are two different sites, one is cornered FeI and another is face centered FeII site. According to the neutron diffraction measurement [6], the magnetic moments on FeI and FeII sites are $2.98 \mu_B$ and $2.01 \mu_B$, respectively. The data agree well with the Mössbauer spectroscopy reported by Wiener et al [5]. $\alpha\text{-Fe}_{10}\text{N}_7$ forms bct structure and consists of three different Fe sites. This phase has been believed to be metastable state, which makes the preparation difficult. According to Sugita et al. [16], the average magnetic moment per Fe atom reaches about $3.5 \mu_B$ at -268°C . The data is apparently projected from ones of other iron nitrides.

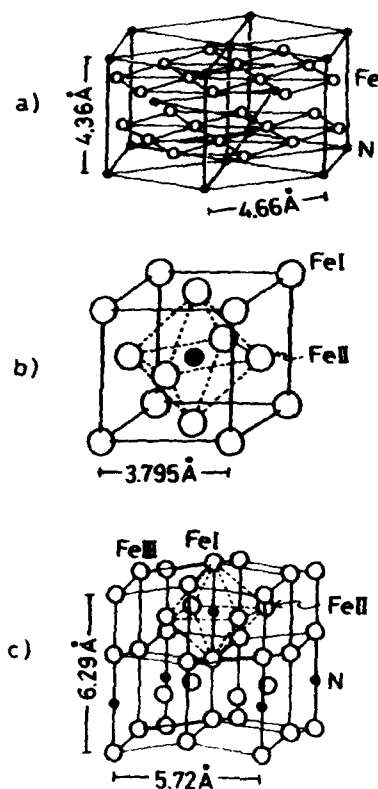


Fig.1 Crystal structures of a) Fe_3N , b) Fe_4N and c) Fe_{10}N_7 , deduced from the results by Iwak [11,15].

Theoretically, the band calculation for γ -Fe₄N has been carried out by Wei Zhou et al. [17], followed recently by the present author [18] with the spin-polarized band calculation. Afterwards, the calculations for the Fe₁₆N₃ have been performed by many authors [19-22], leading a result that the average moment per Fe atom is about 2.4-2.5 μ_B . Though the current band calculations seem to be inadequate to give a quantitative explanation to the high B_s of the Fe₁₆N₃, it may be desired to have a more microscopic foundation derived from the band theory for the subsequent analysis of the magnetism. In this report, we will review the results of the band calculations for the series of iron nitrides, Fe₃N, Fe₄N and Fe₁₆N₃, in order to obtain the systematic understand about the effects of interstitial N atom and its concentration on the magnetic structures of these compounds. In addition, further inspection for the magnetism of the Fe₁₆N₃ will be presented in this paper.

METHOD OF CALCULATION

The linearized muffin-tin orbital (LMTO) method [23,24] has been employed to perform a semi-relativistic band calculation in the frame of the local spin density (LSD) functional theory. The exchange-correlation term takes the form deduced by von Barth and Hedin [25] with parameters given by Janak [26]. For the band calculation, the atomic sphere approximation (ASA) and the combined correction term for the use of ASA are adopted. The core charge density is calculated with the Dirac equation for a free atom and the result is used in the band calculation as a so-called frozen core. For valence electrons, we have employed s, p and d basis functions for Fe atoms and s and p for N atoms. The densities of states (DOS) are evaluated by tetrahedron method. The atomic sphere radius for N atom is set at 1.7 a.u. and radii of Fe are chosen so as to satisfy $V=(4\pi/3)\sum S_i^3 Q_i^3$, where V is the volume of a primitive cell, and S_i is the atomic radius of equivalent Q_i atoms in the cell.

RESULTS AND DISCUSSION

Density of states

We first make a comparison of the calculated density of states (DOS) of Fe-N with the experimental results of the x-ray photoemission spectroscopy (XPS) data obtained by Ertl et al. [9]. In Fig.2, the DOS of Fe₄N in paramagnetic (spin-less) state is shown. The dashed line in the figure is that of the fcc-Fe which leads to Fe₄N with inclusion of N atom at the body center. Comparing these two results, it is easily seen that the structure around -0.6 to -0.4 Ry in the DOS of Fe₄N is attributed to the N atom, which belongs mainly to the 2p states. Roughly speaking, both the energy position and the intensity of the N 2p state coincide with the observed XPS peak around -0.5 Ry which grows with increasing N concentration. The gross feature of the spectrum are also agreeable with the DOS with reasonable accuracy. It should be noted, however, that the peaked feature of the DOS of Fe₄N at the Fermi level, E_F , is a consequence of the paramagnetic state, which means that the system will be stabilized with the help of spin-polarization.

Calculated results of the spin-polarized DOS of each compound are shown in Fig.3. In each plane, the upper half part indicates the up (majority) spin states while the lower half part is for down (minority) spin states. It can be seen that the key features are common for all compounds as follows.

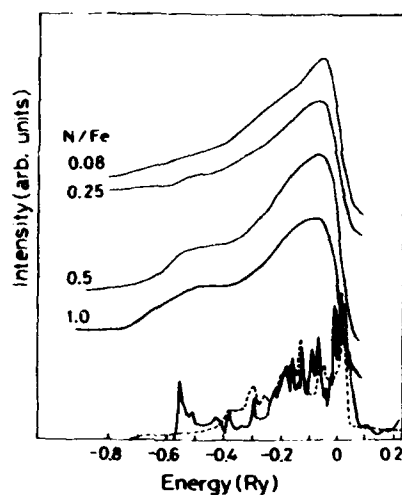


Fig.2 Comparison of the density of states of paramagnetic Fe_xN (solid line) and fcc-Fe (dashed line) and the photoemission data by Ertl et al [9]. The zero on the energy scale corresponds to the Fermi energy, E_F .

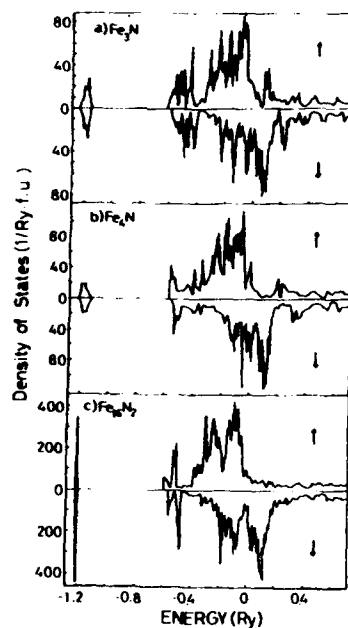


Fig.3 Total density of states for up spin states (↑) and down spin states (↓) of a) Fe_3N , b) Fe_4N and c) Fe_{16}N_2 . The energy is measured with respect to the E_F (ref.[19])

The isolated structures located around -1.2 Ry are mainly due to $2s$ states of N. The main structures around the Fermi energy, E_F , are almost composed of $3d$, $4s$ and $4p$ states of Fe. The E_F 's are pinned at around the dip position in down spin electron density of states, which makes these states stable with a help of spin-polarization. As mentioned previously, the N $2p$ bands are found at about -0.6 Ry to -0.4 Ry below the $3d$ bands, which can be observed in XPS. Furthermore, Ertl's experimental results that no change in the $3d$ bands occurs during nitrition can be understood by noting that the gross features of $3d$ bands look same for all compounds.

Magnetic moments

As we have shown in ref.[19], the features of local densities of states of each Fe in Fe_4N and Fe_{16}N_2 are considerably different depending on the site. It should be marked that the most distant Fe atoms from the N atom, FeI for Fe_4N and FeIII for Fe_{16}N_2 , have the intensive $3d$ hole in the down spin states just above the E_F , while the up spin states of the sites are almost occupied. Actually the local magnetic moments of these sites are the largest as shown in Table I which gives the electron numbers and magnetic moments estimated within

Table I Electron numbers and magnetic moments calculated within each atomic sphere. (ref.[19])

		S		nf	ni	nf+ni	m(μ_B)
Fe_4N	Fe	2.731	3d	4.37	2.40	6.77	1.94
			4s	0.29	0.30	0.59	
			4p	0.48	0.51	0.99	
			total	5.14	3.21	8.35	
	N	1.7	2s	0.57	0.57	1.14	-0.08
			2p	1.34	1.42	2.76	
			total	1.89	1.99	3.90	
Fe_{16}N	FeI	2.749	3d	4.77	1.66	6.42	3.07
			4s	0.29	0.30	0.60	
			4p	0.36	0.39	0.76	
			total	5.42	2.35	7.78	
	FeII	2.749	3d	4.43	2.37	6.80	2.03
			4s	0.30	0.31	0.61	
			4p	0.49	0.51	1.00	
			total	5.22	3.19	8.41	
	N	1.7	2s	0.56	0.57	1.13	-0.01
			2p	1.39	1.40	2.79	
			total	1.95	1.97	3.92	
Fe_{16}N_2	FeI	2.719	3d	4.44	2.14	6.58	2.27
			4s	0.33	0.33	0.66	
			4p	0.44	0.48	0.93	
			total	5.21	2.95	8.17	
	FeII	2.719	3d	4.46	2.18	6.64	2.25
			4s	0.32	0.32	0.64	
			4p	0.43	0.46	0.90	
			total	5.21	2.96	8.18	
	FeIII	2.719	3d	4.68	1.81	6.49	2.83
			4s	0.31	0.32	0.63	
			4p	0.37	0.41	0.78	
			total	5.36	2.54	7.90	
	N	1.7	2s	0.61	0.62	1.23	-0.07
			2p	1.41	1.48	2.89	
			total	2.02	2.10	4.12	

each atomic sphere. The electron numbers of these sites are found to be smaller about 0.3 to 0.6 than that of other sites. So it can be considered that the large moments of these sites are attributed mainly to the shortage of down spin electrons rather than the receipt of the up spin electrons. The variations of these charge distribution on each Fe site can be regarded as an effect of N atom. Thus the present result that the moments of FeI and FeII in Fe_{16}N_4 are nearly the same seems to come from the fact that the distances from the N atom are almost the same for these sites.

From the above results, we have realized the feature that the most distant Fe atoms from the N atom have the largest magnetic moments for Fe_4N and Fe_{16}N_4 . This is related to the bonding nature between N atom and surrounding Fe atoms. Actually, the variance of the moments on each Fe site has been proved to be brought about by the redistribution of the down spin electrons due to the electronic interference by the interstitial N atoms. It can be said that this event reflects the relative arrangement of the Fe atoms against the N atoms in these compounds. According to Kanamori [27], the elements such as B, C and N enhance the magnetic moments of the next nearest neighboring Fe atoms. That is, the 3d levels, especially the down spin state of the nearest neighbor (n.n.) Fe atoms to the N atoms (Fe_{1st} in Fig.4) are lowered through the hybridization with a part of the N 2p state located around

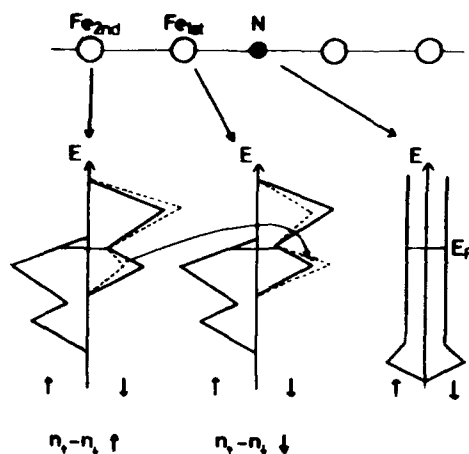


Fig.4 The local DOS of Fe atoms are changed from solid lines to dashed lines with the inclusion of N atom and, then the electrons mainly of the down spin states transfer from the Fe_{1st} to the Fe_{2nd} . As a result, the local magnetic moment of Fe_{2nd} is raised while one of Fe_{1st} lowers its moment.

the E_F , and in turn the 3d down spin state of the next n.n. Fe atoms (Fe_{2nd} in Fig.4) are raised conversely. As a consequence, the electrons mainly of the down spin states transfer from the next n.n. Fe atom to the n.n. Fe atoms (see Fig.4). This electronic bonding feature is strongly responsible for the variation of the local magnetic moments of each Fe site in the iron nitride system. Actually, for Fe_4N , the Mössbauer and neutron diffraction measurements support the above picture and the magnetic structure can be reproduced quantitatively by the present calculation.

As for the average moments, the present results indicate that the lattice expansion due to N atoms plays a central role for the enhancement of the magnetic moments. In Fig.5, we give the average magnetic moment of each compound as a function of N concentration.

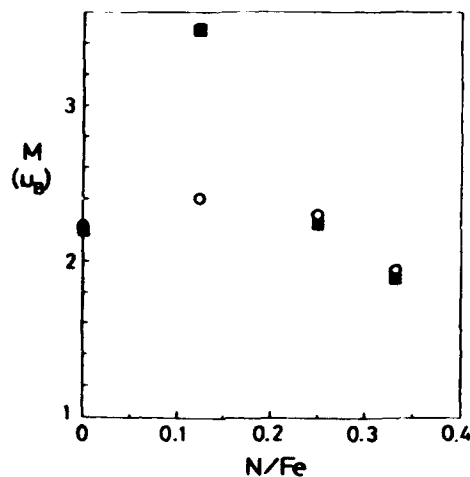


Fig.5 N concentration dependence of the average magnetic moments of iron nitrides. The open circles indicate the calculates results (ref.[19]), and the closed squares are from the measured values (from the data denoted by $\mu(\text{Fe}_i^{-1})$ in ref.[4] for Fe_3N , ref.[6] for Fe_4N and ref.[16] for Fe_{16}N_2).

Our calculated result for bcc Fe is also shown in the figure. Though the quantitative agreement with the experiments can not be reached for Fe_{16}N_2 , the dependence of the moments on the N concentration can be proved qualitatively. The behavior that the lower concentration of N atoms leads larger magnetic moment may be understood by the following interpretation. An interstitial N atom expands the inter-atomic distance not only of the nearest neighboring Fe atoms but also of the next nearest neighboring and more distant Fe atoms for avoiding the lattice distortion. This certainly enhances the moments of the system even though the low concentration of N atom. Additionally, as have been mentioned in the previous section, the N atoms play a role of hopping site for the electrons, which in turn prevent the exchange splitting concurrently. (Note that this may be inseparable from the charge redistribution which gives the variance of the local magnetic moments.) Eventually, it comes to the result that the lower concentration of N atom is preferable for the large magnetic moments.

Effects of Fe lattice expansion on the magnetic moments

In Figs.6, 7 and 8, we show the unit cell volume dependence of the local magnetic moments on each Fe site of Fe_3N , Fe_4N and Fe_{16}N_2 , respectively. The calculations have been made with S_N/S_{Fe} being constant during the volume change. Except for Fe_4N , the moments increase monotonously with lattice expansion through the magnetovolume effect. In the case of Fe_4N , we have undergone the metamagnetism in the range of volume around

$53 - 55 \text{ \AA}^3$, that is, the two solutions are found in this region. One is given by the solid lines and another is by the dashed lines in Fig.7. This magnetic feature can be ascribed to the intricate structure of the density of states at around the F_1 where the density of states of down spin electron has multiple minima. We have taken the state given by the solid lines as a density of states of Fe_4N in Fig.3 since this state is found to be more stable as much as about 3 mRy than that by dashed lines at the measured volume.

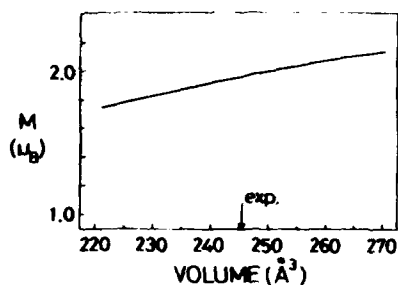


Fig.6 Unit cell volume dependence of the magnetic moment of Fe_4N . The arrow indicates the measured volume. (ref.[19])

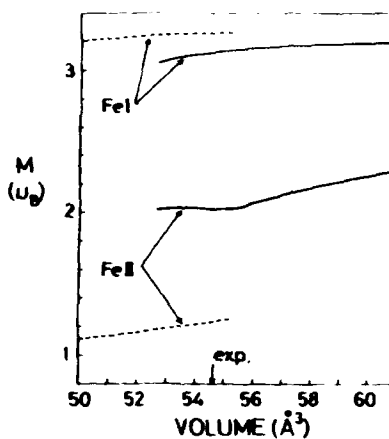


Fig.7 Unit cell volume dependence of the local magnetic moments of Fe_4N . The solid line indicate the high moment state and the dashed lines are for the low moment state. (ref.[19])

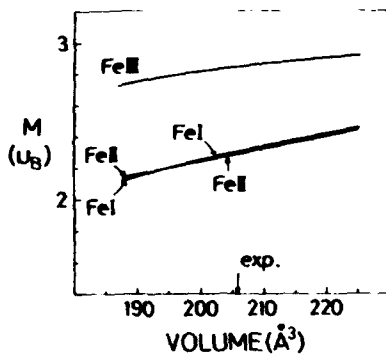


Fig.8 Unit cell volume dependence of the local magnetic moments of Fe_{16}N_7 . (ref.[19])

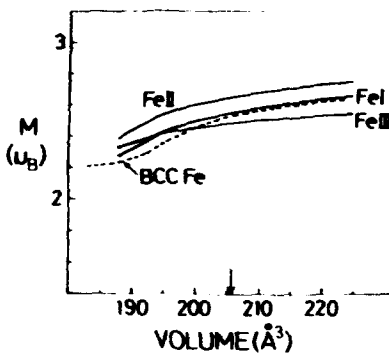


Fig.9 Volume dependence of the local moments of the same volume as Fe_{16}N_7 with no N (solid lines) and of bcc-Fe with eight unit cell(dashed line). The arrow indicates the measured volume of Fe_{16}N_7 . (ref.[19])

To understand the possible effects of the N atom on these system, we have further performed the band calculations for the same structures as each compound with no N atoms. For the calculations, the atomic sphere radii of each atom have been kept by introducing the empty spheres instead of N atoms. The obtained magnetic moment for ϵ -phase iron with the same volume as Fe_3N is about $2.7 \mu_B$ per Fe atom. The result for γ -phase iron with the same volume as Fe_4N is also about $2.7 \mu_B$. The density of states of this γ -phase had been presented in the previous paper [18]. Noting that both ϵ and γ -irons at equilibrium volume exhibit anti-ferromagnetism with the magnetic moment less than $0.7 \mu_B$, these results demonstrate that the lattice expansion with the inclusion of N atoms has enormous influence on the magnetic moments. Thus it is possible to consider that the occurrence of the comparatively large moments of Fe_3N and Fe_4N are brought about predominately by the lattice expansion due to the interstitial N atoms. Notice, however, that the obtained values of $2.7 \mu_B$ for expanded ϵ and γ -irons are fairly larger than that for Fe_3N and Fe_4N . The reduction of the moments with the inclusion of the N atoms can be understood by noting that the N atoms promote an itinerancy of electrons, which eventually prevent the exchange-splitting.

For α' -phase, the calculated magnetic moments of the corresponding structure in the absence of N atoms are given in Fig.9 as a function of unit cell volume. It can be seen that the order of the magnitude of the local magnetic moments is changed and the variation is reduced. This convinces ourselves that the large variance of the local moments in Fe_{16}N_2 is caused by the N atoms through the electronic bonding with the surrounding Fe atoms. Nevertheless, the average magnetic moment does not differ so much from one of Fe_{16}N_2 , which turns out to be about $2.55 \mu_B$ at the measured volume of Fe_{16}N_2 . In addition, the calculated result for the relaxed structure free from strain in α' -phase is also shown in the figure in order to examine the effect of strain on the magnetic moments. This turns out to be bcc Fe with eight unit cells. As for this structure, starting from about $2.2 \mu_B$ at equilibrium volume of 8 unit cells, $\sim 189 \text{ \AA}^3$, the moment reaches about $2.5 \mu_B$ at the measured volume of Fe_{16}N_2 . These results indicate that the occurrence of the calculated magnetic moments for Fe_{16}N_2 are dominated mainly by the lattice expansion as well as for Fe_3N and Fe_4N and the strain in Fe_{16}N_2 has little influence on the average magnetic moment, so far as the band calculations are concerned.

Inspections for the magnetism of Fe_{16}N_2

For Fe_{16}N_2 , the calculated result of the magnetic moment is considerable smaller than the measured value. Recently, Sugita et al. [16] reported that the average moment of Fe_{16}N_2 extends to $3.5 \mu_B$ at -268°C with the measurement of the magnetization. Thus the magnetic aspect of Fe_{16}N_2 seems to be quite outstanding in the series of iron nitrides. In this section, we try the further inspection for the magnetism of the Fe_{16}N_2 .

Table II Spin and orbital magnetic moments (μ_B) of Fe_{16}N_2 and bcc-Fe

Fe_{16}N_2		spin	orbital
	FeI	2.27	0.082
	FeII	2.26	0.066
	FeIII	2.82	0.082
bcc-Fe		2.23	0.062

In Table II, we present the orbital moments of Fe_{16}N_2 calculated by introducing the spin-orbit interaction in the LMTO-Hamiltonian. The result for bcc-Fe is also shown for comparison. Though the orbital moment of Fe_{16}N_2 is slightly larger than that of bcc-Fe, it is still small as is the case with usual transition metal systems. So it is found that the orbital moment can not make up for the difference from the experiments. Actually, the g -value of this film has been measured to be almost 2.0 [28].

Further we tried a non-local correction to the local density approximation with use of generalized gradient approximation (GGA) [29] and obtained an increase of magnetic moment as much as about $0.1 \mu_B$ per Fe atom. Thus the non-local correction is also minor contribution to the magnetic moment.

Looking into an influence of the local atomic structure on the magnetic moment, we attended to the octahedron structure of FeI and FeII atoms surrounding the N as a central atom. From view point that this octahedron is a unit basis of the corresponding martensite, we examine the relation between the elongation ratio and the variation of the local magnetic moments. Fig. 10 gives the calculated local magnetic moments of each Fe site as a function of distance, d_{FeII} , between the neighboring FeII atoms. The moments of the FeII sites increase with increasing d_{FeII} while the moments of the FeI and FeIII sites decrease. As a result, moments of the FeII site and the FeI site split as d_{FeII} increases. This result predicts that the variation of the local moment is strongly correlated with the elongation ratio of the Fe octahedron. On the other hand, the average moment exhibits few change with the elongation ratio and then is expected not to be affected so much by the local atomic arrangements.

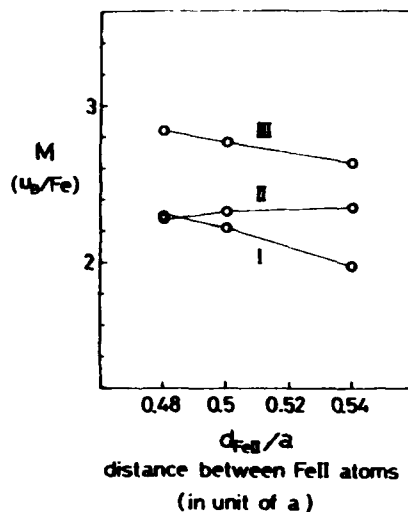


Fig. 10 Local magnetic moments of Fe_{16}N_2 as a function of the distance between the FeII atoms.

Finally, we have performed the calculation for Fe_{16}N_2 ($X=\text{B}, \text{C}, \text{N}, \text{O}$ and vacancy) to obtain systematically the effects of the non-metal atom on the Fe moments. Fig. 11 shows the calculated magnetic moments for each Fe_{16}X_2 . The average moment is found to be increased with the increase of the atomic number and the moment reaches the maximum value when X takes the vacancy. The results can be considered to reflect the fact that the charge distributions of the valence electrons of these elements are getting shrunk as the

atomic number increases (Fig.12). That is, the lower the atomic number is, the more the wavefunction is delocalized and then the itinerancy of the valence electrons is getting enhanced. This in turn suppresses the exchange splitting.

Fig.11 Local magnetic moments and the average magnetic moments of Fe_{16}X_3 ($\text{X}=\text{B}, \text{C}, \text{N}, \text{O}$ and vacancy)

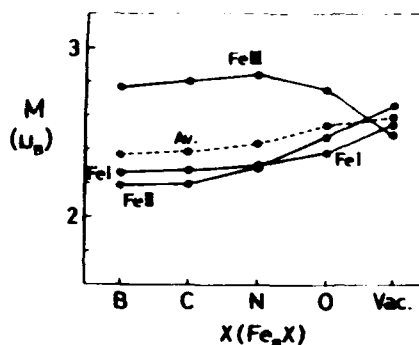
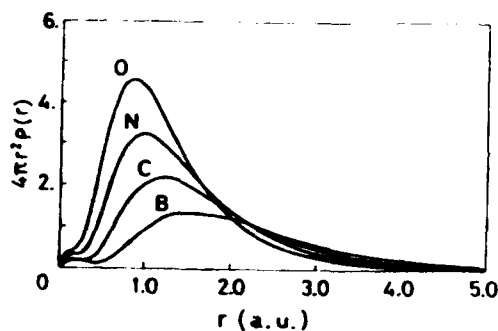


Fig.12 Valence (2s and 2p states) charge densities of atomic states of the elements, B, C, N and O.



SUMMARY

We have performed the spin-polarized band calculations for the iron nitrides, Fe_3N , Fe_4N and Fe_{16}N_2 , with LMT0-ASA method within the frame of local spin density formalism. As for the local magnetic moments, the most distant Fe atoms from N have the largest magnetic moment. The central role of the N atom is to expand the Fe lattice to give the enhancement of the magnetic moments. It should be noted, however, that the N atoms help a hopping of the electrons and then prevent the exchange-splitting. As a consequence, the lower concentration of the N atom gives the larger magnetic moment. Quantitatively, the calculated moments are in good agreement with the experimental results except for Fe_{16}N_2 , whose magnetic moment is quite outstanding. We insist that a new theoretical concept is required to give a quantitative explanation for the giant moment of Fe_{16}N_2 . Experimentally, more refined analysis for the crystal structure such as local arrangement of Fe and N atoms and the magnetic data such as Mössbauer and neutron diffraction are also desired.

ACKNOWLEDGMENTS

The authors thank Dr. Mitsuoka, Mr. Komuro and Mr. Takahashi in Hitachi, Ltd. for useful discussions.

REFERENCES

- [1] A. Wold, R.J. Arnott and N. Menyuk: *J. Phys. Chem.* 65(1961)1068.
- [2] M. Mekata, H. Yoshimura and H. Takaki: *J. Phys. Soc. Jpn.* 33(1972)62.
- [3] M. Robbins and J.G. White: *J. Phys. Chem. Solids* 25(1964)717.
- [4] K.H. Eickel and W. Pitsch: *phys. stat. sol.* 39(1970)121.
- [5] G.W. Wiener and J.A. Berger: *J. Met.* 7(1955)360.
- [6] B.C. Frazer: *Phys. Rev.* 112(1958)751.
- [7] G. Shirane, W.J. Takei and I. Ruby: *Phys. Rev.* 126(1962)49.
- [8] S. Nagakura: *J. Phys. Soc. Jpn.* 25(1968)488.
- [9] G. Ertl, M. Huber and N. Thiele: *Z. Naturforsch.* 34a(1970)30.
- [10] T.K. Kim and M. Takahashi: *Appl. Phys. Lett.* 20(1972)492.
- [11] K.H. Jack: *Proc. Roy. Soc. London*, A208(1951)216.
- [12] M. Komuro, Y. Kozono, M. Hanazono and Y. Sugita: *J. Appl. Phys.* 67(1990)5126.
- [13] K. Nakajima and S. Okamoto: *J. Appl. Phys.* 65(1989)4357.
- [14] K. Nakajima and S. Okamoto: *Appl. Phys. Lett.* 56(1990)92.
- [15] K.H. Jack: *Proc. Roy. Soc. London*, A195(1948)34.
- [16] Y. Sugita, K. Mitsuoka, M. Komuro, H. Hoshiya, Y. Kozono and M. Hanazono: *J. Appl. Phys.* 70,5977(1991).
- [17] Wei Zhou, Li-jia Qu and Qi-ming Zhang: *Phys. Rev.* B40(1989)6393.
- [18] A. Sakuma: *J. Phys. Soc. Jpn.* 60(1991)2007.
- [19] A. Sakuma, *J. Magn. Magn. Mater.* 102,127(1991).
- [20] S. Ishida, K. Kitawatase, S. Fujii and S. Asano, *J. Phys. Condens. Matter*, 4, 765(1992).
- [21] B.I. Min, *Phys. Rev. B* 46,8232(1992).
- [22] R. Cochoom, G.H.O. Daalderop and H.J.F. Jansen, submitted to *Phys. Rev.*
- [23] O.K. Andersen: *Phys. Rev. B* 12(1975)3060.
- [24] H.L. Skriver: *The LMTO Method*, ed. M. Cardona, P. Fulde and H.-J. Queisser (Springer, Berlin, 1984).
- [25] U. von Barth and L. Hedin: *J. Phys.* C5(1972)1629.
- [26] J.F. Janak: *Solid State Commun.* 25(1978)53.
- [27] J. Kanamori: *Proc. 10th Int. Workshop on Rare-Earth Magnets and Their Applications*, Kyoto, 1989 (The Society of Non-Traditional Technology, Tokyo, 1989) Vol.1, p.1.
- [28] H. Takahashi, K. Mitsuoka, M. Komuro and Y. Sugita, to be published in *J. Appl. Phys.* (1993).
- [29] J.P. Perdew and Y. Wang, *Phys. Rev. B* 33,8822(1986): 34,7406(1986).

Section A—Multilayers and Surfaces

PART VIII

**Giant Magnetoresistance in Low Fields:
Multilayers and Spin Valves**

GIANT MAGNETORESISTANCE AND SOFT MAGNETIC PROPERTIES OF NiFeCo/Cu MULTILAYERS

S. TSUNASHIMA, M. JIMBO*, T. KANDA, S. GOTO, AND S. UCHIYAMA

Nagoya University, Nagoya, 464-01 Japan.

*Daiko Institute of Technology, Nagoya, 457 Japan.

ABSTRACT

Giant magnetoresistance(GMR) and soft magnetic properties together with their structural characteristics were investigated for $\text{Ni}_{56}\text{Fe}_{16}\text{Co}_{18}/\text{Cu}$ multilayers. The multilayers were prepared by the conventional rf sputtering method on glass or Si substrates using various buffer layers including Fe, NiFeCo, NiFe and CoZr. Although most of the multilayers exhibited (111) preferred orientation, Fe buffered multilayers showed a considerable (200) X-ray diffraction peak at Cu thicknesses around 1 nm and 2.2 nm which corresponded to the peak positions of GMR. By using fcc or amorphous underlayers the (200) diffraction intensity decreased while antiferromagnetic coupling strength was much reduced. Cross-sectional transmission electron micrograph revealed that the (100) oriented multilayer was grown on the (100) oriented Fe underlayer. By controlling the crystal orientation and the layer structure, significantly large magnetoresistance ratio of more than 10 % can be achieved in a field as low as 30 Oe.

INTRODUCTION

Since the giant magnetoresistance(GMR) effect has been found in Fe/Cr and Co/Cu multilayers(MIs), many efforts have been made to achieve small saturation fields while maintaining large MR[1-6]. Magnetic multilayers with the GMR that consist of soft magnetic layers are of technological interest for the application of magnetoresistance heads.

Shinjo and Yamamoto [1] obtained an MR ratio of 6% with a field change of 50-100 Oe by using NiFe/Cu/Co/Cu MIs; NiFe layers are soft magnetic, while Co layers are hard. When the field strength is in between the coercive fields of the Co and NiFe layers and the exchange coupling is low enough, antiferromagnetic ordering occurs during the magnetization process. Sakakima and Satomi[2] examined similar structure of NiFeCo/Cu/Co/Cu MIs, and obtained an MR ratio of 15% in a field as low as 100 Oe.

Another approach is the so-called spin-valve structure[3], where two soft magnetic layers, one of which is constrained by exchange anisotropy, are separated by a noble metal layer. The magnetic layers are not coupled antiparallel, giving large changes of resistance at low fields.

Multilayers with a simple structure of NiFe/Cu were examined by Parkin[4] and by Nakatani et al[5]. They both found oscillation in saturation magnetoresistance as a function of Cu spacer layer thickness. The MR ratio at the first peak of the oscillation was 16 to 19 % at room temperature with saturation fields of 600 to 2 kOe. These fields seem still too high for the MR heads. Since the saturation fields become exponentially smaller with increasing spacer layer thickness, it is worthwhile to try the second peak as is in the case of the spin-valve. In case of NiFe/Cu MIs, however, the GMR becomes smaller than 10% and sometimes does not appear[4]. This may be due to the very weak antiferromagnetic coupling between NiFe layers.

The authors have examined NiFeCo/Cu MIs[6-9], expecting a larger GMR than those of NiFe/Cu MIs. As shown in the diagram of Fig. 1[10,11], the zero-magnetostriction and the zero-magneto crystalline anisotropy coexist at two compositions at the same time. The composition with higher Co content, namely $\text{Ni}_{56}\text{Fe}_{16}\text{Co}_{18}$ is supposed to exhibit a larger GMR and a larger uniaxial anisotropy[12]. A large uniaxial anisotropy is effective in defining

the direction of the moment in each magnetic layer and thus the magnetization process becomes a coherent rotation desirable for a good high frequency response.

In the previous paper, the authors reported that $\text{Ni}_{60}\text{Fe}_{16}\text{Co}_{18}/\text{Cu}$ MLs with Fe buffer layers prepared by rf magnetron method exhibit an MR ratio of 35% and 15% at the first and the second peak, respectively. The interlayer antiferromagnetic coupling constant is as low as 0.05 and 0.003 erg/cm² for the first and the second peak, respectively[6]. We also found that the interlayer coupling at the second peak was reduced one third by using NiFeCo buffer layers[8,9].

In this paper we will describe the GMR and the structure of soft magnetic NiFeCo/Cu MLs prepared on various buffer layers. We will discuss effect of buffer layers on the microstructure and on the interlayer coupling strength. We will also show the thermal stability of the MLs.

EXPERIMENTAL

NiFeCo/Cu Multilayered films and NiFeCo single layered films were prepared using the magnetron sputtering method at an Argon pressure of 5 mTorr. Films were deposited at a rate of about 0.1 nm/s both for NiFeCo and Cu. When not notified the substrates were microscope glass slides. The target for the NiFeCo was a composite type where Fe and Co chips were placed on a Ni plate. Since Ni is relatively soft-magnetic, the magnetic flux from the magnet behind the target was almost shunted through the Ni target.

To induce uniaxial anisotropy in the magnetic layers, a magnetic field of about 40 Oe was applied parallel to the film plane by NdFeB magnets placed above the NiFeCo target. This field also influenced the discharge, enhancing the sputtering rate of NiFeCo about two times. As described in ref.[8], good layer structure resulting in a large MR ratio was obtained only when the field was applied.

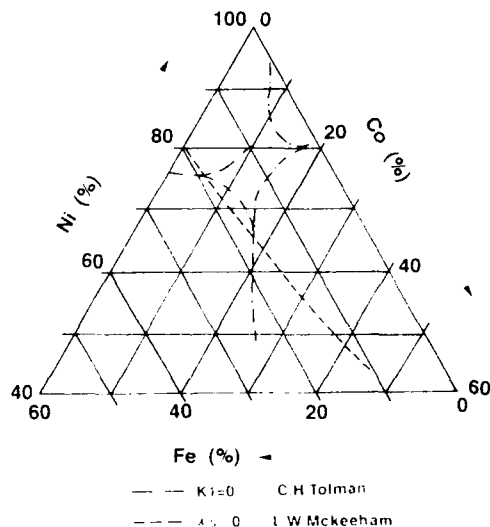


Fig.1 Zero-magnetostriction and zero-magnetocrystalline anisotropy composition for $\text{Ni}_{60}\text{Fe}_{16}\text{Co}_{18}$ alloy system.

Multilayers with a construction of $\{\text{NiFeCo}(1.5\text{nm})/\text{Cu}(t_{\text{Cu}})\}_{30}$ were deposited on substrates with or without bufferlayers. The buffer layers were 5 nm thick; Fe, $\text{Fe}_{70}\text{Co}_{30}$, $\text{Ni}_{66}\text{Fe}_{16}\text{Co}_{18}$, $\text{Ni}_{82}\text{Fe}_{18}$ or $\text{Co}_{92}\text{Zr}_8$ were deposited at room temperature. The crystal structure of Fe and FeCo buffer layers were found to be bcc and CoZr was amorphous.

Structural analysis was done by conventional X-ray diffractometry using the Cu-K α radiation. For typical samples, high resolution transmission electron microscopy (TEM) observation was done with a H-9000UHR electron microscope at an acceleration voltage of 300 kV. To study the thermal stability, isochronal annealing was carried out at successively higher temperatures of up to 400 °C for 1 hour in a vacuum of 10^{-5} Torr.

RESULTS AND DISCUSSION

Soft magnetic properties of NiFeCo single layered films

$\text{Ni}_{66}\text{Fe}_{16}\text{Co}_{18}$ single layered films of 240 nm in thickness were prepared under the same condition as the MLs except the substrate holder fixed above the NiFeCo target. Figure 2 shows the magnetization curves by applying fields parallel and perpendicular to the easy axis. The coercivity in the easy axis loop is as low as 1.3 Oe, but that of hard axis is a little higher. The film shows an anisotropy field of about 20 Oe which is several times larger than conventional permalloy ($\text{Ni}_{82}\text{Fe}_{18}$) films. We have confirmed that the single layered films exhibit a saturation magnetostriction smaller than 1×10^{-6} .

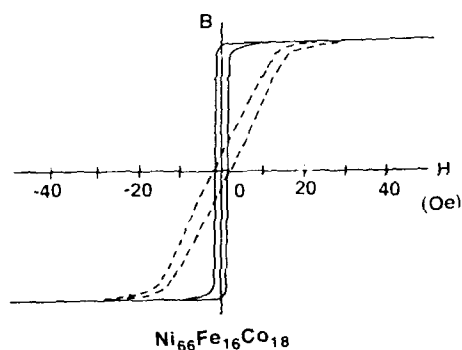
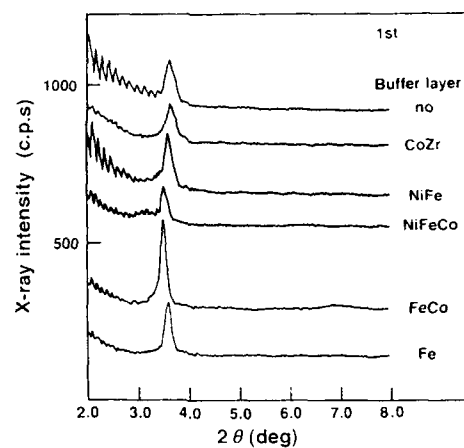


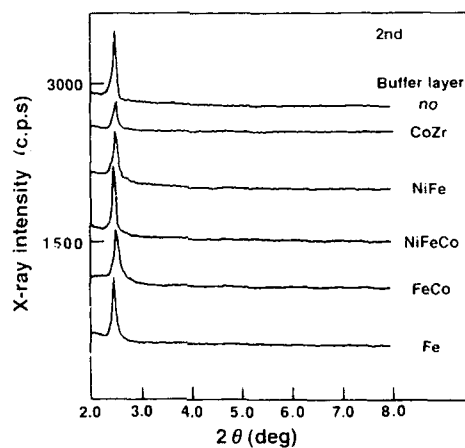
Fig. 2 Magnetization curves for a 240 nm thick NiFeCo alloy film prepared by rf sputtering. Full and broken lines respectively show the curves measured with a field parallel and perpendicular to the easy axis.[10,11]

Structure of NiFeCo multilayers

Figures 3(a) and (b) show the low angle diffraction patterns for NiFeCo/Cu MLs with $t_{\text{Cu}} = 0.9$ and 2.2 nm, which correspond to the first and the second peaks of MR ratios, respectively. According to the figure, there were some differences in the intensity of the first order low angle diffraction peak for both $t_{\text{Cu}} = 0.9$ and 2.2 nm. The differences however were not systematically dependent on the structure of the buffer layers. As far as the low angle diffraction pattern is concerned, the difference in layer structure is not clear.



(a)

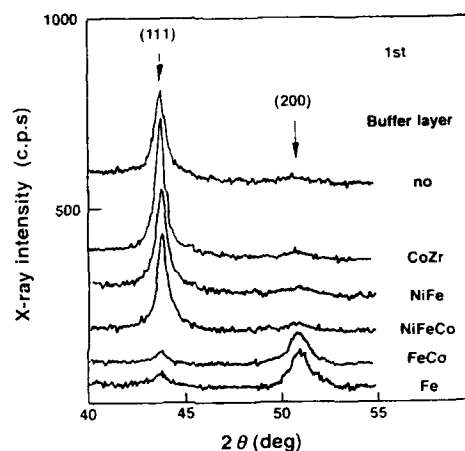


(b)

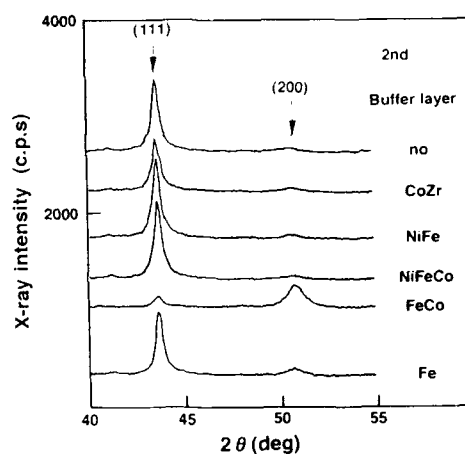
Fig. 3 Low angle XRD patterns for $[\text{NiFeCo/Cu}]_{30}$ multilayers prepared on various buffer layers, where the thickness of Cu layers are about 0.9 and 2.2 nm for (a) and (b), respectively.

High angle diffraction patterns are shown in Figs. 4(a) and (b) for the same MLs with Figs. 3(a) and (b), respectively. As seen in Fig. 4(a), the NiFeCo, NiFe, CoZr buffered and nonbuffered MLs showed (111) preferred orientation while Fe and FeCo buffered MLs were unstable or uncontrollable in crystal orientation: some times (111) intensity is stronger than (200) and some times vice versa. In the samples of Fig. 4(a), Fe and FeCo buffered MLs show (200) diffraction peak intensities even higher than (111) intensities. At the second peak of $t_{\text{Cu}} = 2.2\text{nm}$, although (111) intensities become much higher than those of the first peak, the tendency in the orientation is similar to that of the first peak.

As shown in Fig. 4(b), the (200) intensities in Fe and FeCo buffered MLs are higher than others. Thus we consider that bcc Fe and FeCo buffer layers are effectively nucleating and developing the (100) oriented crystallites in the MLs.



(a)



(b)

Fig. 4 High angle XRD patterns for $[\text{NiFeCo/Cu}]_{30}$ multilayers prepared on various buffer layers, where the thickness of Cu layers are about 0.9 and 2.2 nm for (a) and (b), respectively.

Figure 5(a) and (b) show cross-sectional TEM views of Fe(5nm) buffered [NiFeCo(1.5nm)/Cu(1nm)]₃₀ ML prepared on a Si(100) substrate. In the low magnification bright field view in Fig. 5(a), a well defined and reasonably flat layer structure is seen for the NiFeCo/Cu ML and for the Fe buffer layer although the chemical contrast between Cu and NiFeCo is generally lower than grain contrast. From this view, columnar structure is also observed parallel to the film normal direction. In the high resolution image of Fig. 5(b), lattice images are seen both in the NiFeCo/Cu ML and the Fe buffer layer. A flat Fe layer is seen on an oxidized Si layer, where {110} lattice fringes are 45° from the film normal. This shows that the Fe buffer layer has <100> axis mostly normal to the film plane. In the ML region, (111) lattice planes are 40 to 80 degree angles in relation to the film plane. They can scarcely be seen in the direction parallel to the film plane. Instead, on the right side of the photograph lattice fringes corresponding to (200) planes are seen parallel to the film plane. These results are consistent with the results of XRD measurements. The ML has a random or weak <100> orientation. The lattice misfit for bcc-Fe[001] || fcc-Ni[011] epitaxial growth is as large as 11%, but both Fe(001) and Ni(001) planes are simple square lattices. Such an epitaxis is likely to occur at the interface between Fe buffer and NiFeCo/Cu MLs.

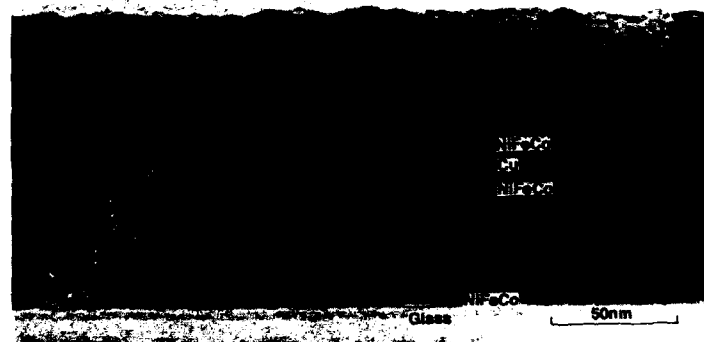
Figures 6(a) and (b) show cross-sectional views of NiFeCo(5nm) buffered [NiFeCo(1.5nm)/Cu(2.1nm)]₃₀ ML prepared on a glass substrate. The low magnification bright field view which is slightly defocused shows clear layer structure. The flatness of layer interfaces is slightly less than that of the Fe buffered ML shown above while the columnar structure is more pronounced. The average diameter of the columns is about 25 nm on the film surface. In the high resolution image, (111) lattice fringes are seen in various directions for both the buffer and the ML. Many of them are at low angles with respect to the film plane. Here it is noted that on the upper right side (200) lattice plane are also seen in a direction nearly parallel to the film plane. Although it is a problem whether the cross sectional TEM image shows structures equal to those averaged in the whole film, this image suggests that the film has a weakly (111) oriented texture and is consistent with the XRD results.

The difference between the samples in Figs. 5 and 6 is not only in the buffer layer but also in the substrate and the Cu layer thickness (consequently the total thicknesses of the films are different). However for the crystal orientation, the buffer layer will be most responsible. The relation between the crystal orientation and the flatness of the layer interface is still not known. The mixture of (111) and (100) oriented grains may suppress the columnar grain growth and result in very flat interfaces.

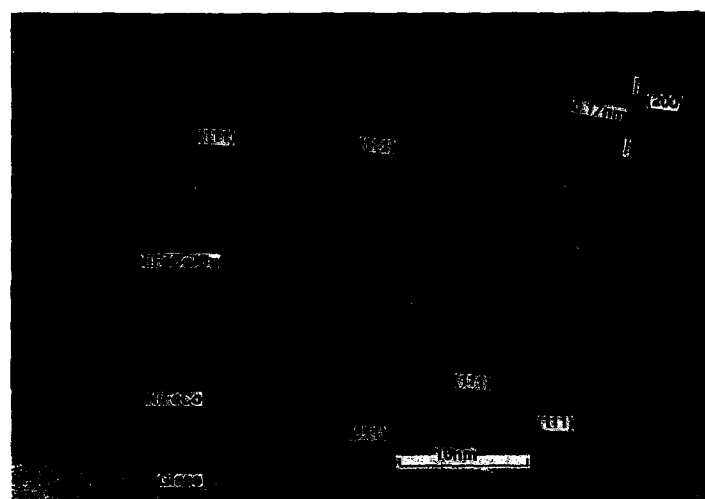
Magnetoresistance

Typical magnetoresistance curves are shown in Figs. 7(a) and (b) for the MLs with tCu around the 1st and the 2nd peak, respectively, grown on various buffer layers. In the 1st peak, Fe and FeCo buffered MLs show larger MR ratios and higher saturation fields than others. The saturation fields of other MLs are not reduced much, so the field sensitivities dR/dH of all the MLs are nearly the same. For the 2nd peak, the MR curves are much different in shape. The MLs with NiFeCo, NiFe, CoZr and without buffer layers show much smaller saturation fields than MLs with Fe and FeCo buffer layers. It should be noted here that NiFeCo buffered ML shows a saturation field as low as 30 Oe keeping a larger MR ratio of 12% which is nearly the same as Fe buffered ML. As a result, NiFeCo buffered ML exhibit a field sensitivity as high as 0.5 %/Oe on the easy axis. When the field is applied in the hard direction, the MR varies smoothly with the applied field, reflecting the magnetization process with magnetization rotation. However, the trace of minor loops are slightly different from the major loop; the minor loops show some hysteresis. The field sensitivity for a small ac field was about 0.3 %/Oe, which was almost constant up to 1 MHz.

The multilayers with NiFe, CoZr and no buffer layers also showed very small saturation fields but we have not yet succeeded to get high MR ratio.



(a)



(b)

Fig. 6 Cross-section transmission electron micrographs of NiFeCo(5nm) buffered [NiFeCo(1.5nm)/Cu(2.1nm)]₃₀ multilayers on glass substrate at (a) low and (b) high resolution.

Figure 8 shows Cu layer thickness dependence of the MR ratio and the saturation field for $[\text{NiFeCo}(1.5\text{nm})/\text{Cu}(t_{\text{Cu}})]_{30}$ MLs with various buffer layers. Although the data are not sufficient for buffer layers other than Fe, all the MLs with different buffer layers seem to exhibit the same oscillation behavior as a function of t_{Cu} . It is seen from the figure that Fe and FeCo buffered MLs show MR ratios slightly larger than others and the large MR ratio in wider range of t_{Cu} . The latter point indicates that Fe and FeCo, namely bcc buffered MLs have a more perfect layer structure than the others. Waved structure seen near the surface of NiFeCo buffered ML [Fig.6(b)] will disturb the complete antiferromagnetic coupling. It makes a mixture of antiferromagnetic and ferromagnetic coupling. These results in a narrower range of t_{Cu} for antiferromagnetic ordering.

From the lower figure it is seen that NiFeCo, NiFe, CoZr buffered and non-buffered MLs exhibit smaller saturation fields than Fe and FeCo buffered MLs, especially in the second peak. The saturation fields for fcc and amorphous buffer layers are less than one third of Fe

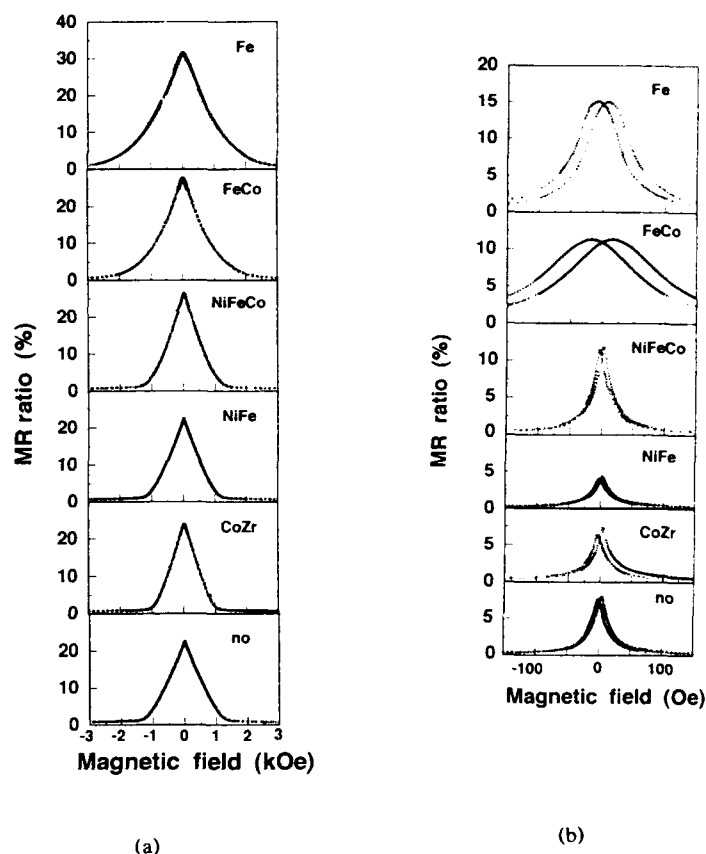


Fig. 7 Magnetoresistance curves for (a) $[\text{NiFeCo}(1.5\text{nm})/\text{Cu}(1.0\text{nm})]_{30}$ and (b) $[\text{NiFeCo}(1.5\text{nm})/\text{Cu}(2.1\text{nm})]_{30}$ multilayers prepared on various buffer layers of 5 nm thick.

and FeCo buffered MLs. According to the argument of Egelhoff and Kief[13], the str. antiferro coupling in Fe and FeCo buffered MLs could be a result of a minority constituent (100) oriented grains. Their argument was based on the fact that the GMR was hardly found in MBE grown (111) Co/Cu superlattices. Recently several groups have found large MR in (111) oriented MBE films for Cu thicknesses less than 1 nm[13,14]. Furthermore Renard et al.[15] found a large GMR even with Cu thickness in the second peak with relatively low saturation field of about 1 kOe. They pointed out that the low roughness of the Co/Cu interface is crucial to the large MR effects.

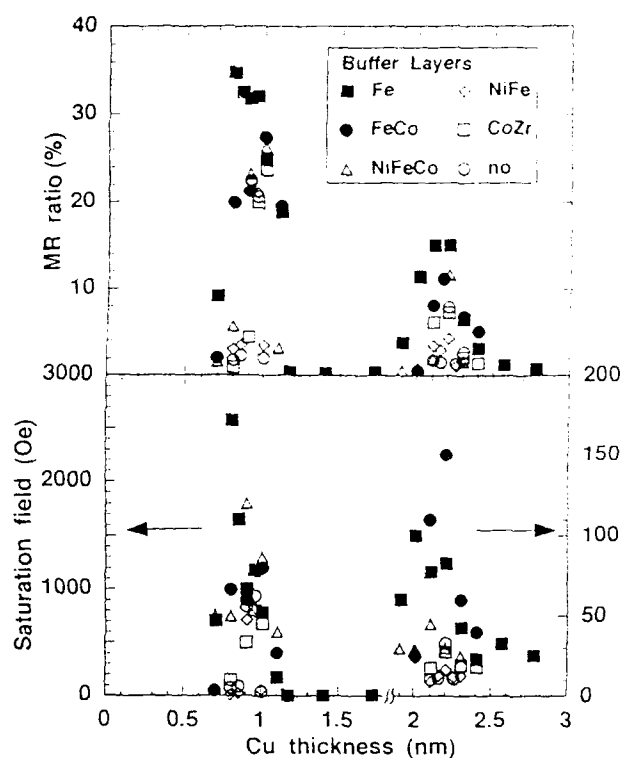


Fig. 8 Magnetoresistance ratio and saturation field for $[\text{NiFeCo}(1.5\text{nm})/\text{Cu}]_{30}$ multilayers prepared on various buffer layers as a function of Cu layer thickness.

At present we are not sure whether lower saturation fields in fcc and amorphous buffered MLs came from the (111) preferred orientation or from the rougher layer structure. As for as the 1st peak of the low angle diffraction is concerned, we have not found systematic relation between the layer structure and the saturation field strength. For further discussion, we need more precise low angle XRD measurements and/or more systematic cross sectional TEM observation.

Thermal stability

Finally we present preliminary results of annealing experiments. In the low angle XRD measurement, both MLs with t_{Cu} in the 1st and 2nd peaks showed no significant change in the intensity of the 1st peak after annealing up to 400 °C. In the high angle XRD, the MLs showed slight growth of crystallites in the film normal direction after annealing at above 300 °C.

Figures 9(a) and (b) show the MR curves for NiFeCo buffered MLs with Cu thickness for the 1st and 2nd peaks, respectively. In the 1st peak, considerable degradation was seen in the MR ratio after annealing at 250 °C and GMR almost disappeared at 300 °C. The saturation fields didn't appear to be influenced by the annealing.

For the 2nd peak, the MR ratio was almost constant or slightly increased by the annealing up to 250 °C. Degradation began after annealing at 300 °C in the MR ratio. The saturation field was also constant or slightly increased after annealing up to 300 °C. Comparing Figs. (a) and (b), one can see that the ML structure of the 2nd peak is more stable to thermal agitation than the 1st peak, and probably more suitable for applications.

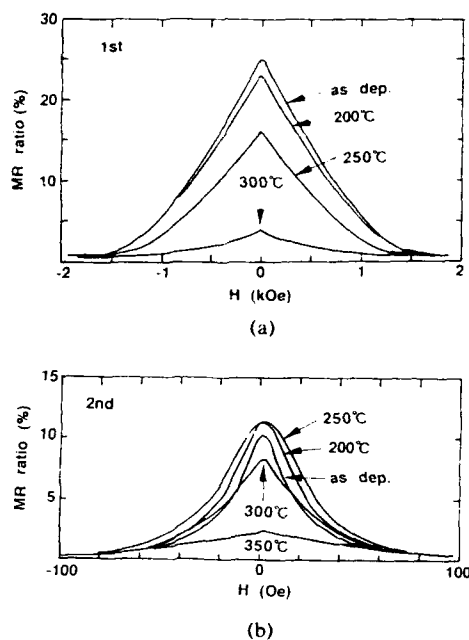


Fig. 9 Magnetoresistance curves for NiFeCo buffered (a) [NiFeCo(1.5nm)/Cu(1.0nm)]₃₀ and (b) [NiFeCo(1.5nm)/Cu(2.1nm)]₃₀ multilayers after annealing at various temperatures.

CONCLUSION

Giant magnetoresistance and antiferro coupling have been investigated for NiFeCo/Cu multilayers grown on various buffer layers. The multilayers have random or (100) preferred orientation when prepared on bcc Fe or FeCo, while (111) orientation prepared on fcc NiFe, NiFeCo, amorphous CoZr, or glass. NiFeCo, NiFe, CoZr buffered and non-buffered MLs exhibit smaller saturation fields than Fe and FeCo buffered MLs, especially at the second peak. Although samples are limited and not systematic, cross sectional TEM observation revealed that the Fe buffer layer has (100) an orientation normal to the film plane and NiFeCo/Cu crystallites often grow epitaxially on Fe (100) a plane with [100] axis normal to the film plane. This seems to be the reason why the Fe buffered ML has often (100) orientation. The mixture of (100) oriented crystallites with (111) oriented ones may suppress the columnar grain growth and make the interface flatter.

In NiFeCo buffered MLs at the second peak a considerably high field sensitivity of about 0.5 %/Oe was obtained at room temperature. This is comparable to or higher than MR ratios in conventional anisotropic magnetoresistance materials. Further improvement in the soft magnetic properties will make this material promising for practical applications.

ACKNOWLEDGEMENT

We thank Drs. N. Tanaka and S. Iwata of Nagoya University, and Drs. Y. Sugita and R. Nakatani of Central Research Lab., Hitachi, Ltd. for useful discussion. We also thank Mr. K. Meguro for experimental assistances and Mr. Y. Adachi for EPMA measurements. This work was partly supported by Grant-in-Aid for Scientific Research from Ministry of Education, Science and Culture of Japan.

REFERENCES

- [1] T. Shinjo and H. Yamamoto, *J.Phys.Soc.Jpn*, 59, 3061(1990)
- [2] H. Sakakima and M. Satomi, *Jpn.J.Appl.Phys.* 31, L484(1992)
- [3] B. Dieny, V.S. Speriou, S.S.P. Parkin, B.A. Gurney, D. R.Wilhoit and D. Mauri, *Phys. Rev. B*, 43, 1297(1991)
- [4] S.S.P. Parkin, *Appl. Phys. Lett.* 60, 27(1992)
- [5] R. Nakatani, T. Dei, T. Kobayashi and Y. Sugita, *IEEE Trans.Magn.* 28, 2668(1992)
- [6] M. Jimbo, T. Kanda, S. Goto, S. Tsunashima and S. Uchiyama, *Jpn. J. Appl. Phys.*, 31, L1348(1992)
- [7] S. Tsunashima, M. Jimbo, T. Kanda, S. Goto and S. Uchiyama, *J. Magn. Magn. Mater.* (in press)
- [8] T. Kanda, M. Jimbo, S. Goto, K. Kumazawa and S. Uchiyama, *J. Mag. Soc. Jpn.* 17 (in press)
- [9] M. Jimbo, T. Kanda, S. Goto, S. Tsunashima and S. Uchiyama, *Proc. the first Intnat.Symp. on Metallic Multilayers, Kyoto,1993* (to be published in *J. Magn. Magn. Mater.*)
- [10] L.W. McKeehan, *Phys.Rev.* 51, 136(1937)
- [11] C.H. Tolman, *J.Appl.Phys.* 38, 3409(1967)
- [12] T. Fujii, S. Uchiyama, M. Takayasu, and K. Takahashi, *Memoire of Faculty of Engng. Nagoya Univ.*, 26, 109(1974)
- [13] W.F. Egelhoff Jr. and M.T. Kief, *Phys.Rev. B*, 45, 7795(1992)
- [14] A. Kamiyo and H. Igarashi, *Jpn.J. Appl.Phys.* 31, L1058(1992)
- [15] J.P. Renard, P. Beauvillain, C. Dupas, K.Le. Dang, P. Veillet, E. V lu, C. Marli re and D. Renard, *J.Magn.Magn.Mater.*, 115, L147(1992)

COMBINED SPIN VALVE AND ANISOTROPIC MAGNETORESISTANCE IN NiFe/Cu/NiFe LAYERED THIN FILMS

Th.G.S.M. RIJKS^{a,b}, R. COELHOORN^b AND W.J.M. DE JONGE^a

^aEindhoven University of Technology, P.O. Box 513, 5600 MB Eindhoven, The Netherlands

^bPhilips Research Laboratories, P.O. Box 80000, 5600 JA Eindhoven, The Netherlands

ABSTRACT

We present a theoretical study of the combined effect of spin valve and anisotropic magnetoresistance in NiFe/Cu/NiFe layered thin films, using an extended form of the semiclassical Camley and Barnás model for electron transport. The anisotropic magnetoresistance is treated by introducing spin-dependent anisotropic mean free paths in the NiFe layers. From calculations of both magnetoresistance effects as a function of NiFe and Cu thickness, we discuss the validity of a description of the combined effect in terms of a simple summation of spin valve and anisotropic magnetoresistance.

INTRODUCTION

Recently Dieny et al. reported on the magnetotransport properties of $\text{Ni}_{80}\text{Fe}_{20}/\text{Cu}/\text{Ni}_{80}\text{Fe}_{20}/\text{Mn}_{50}\text{Fe}_{50}$ layered thin films^{1,2}. The low field magnetoresistive behaviour of these layered systems may be advantageous for application in magnetoresistive readback heads, which are an important element of high density magnetic recording³. Recent measurements on this type of layered thin films show a combination of two magnetoresistance effects⁴, viz. the spin valve magnetoresistance ("Giant Magnetoresistance", GMR), depending on the angle between the magnetization vectors of the $\text{Ni}_{80}\text{Fe}_{20}$ layers, and anisotropic magnetoresistance (AMR), depending on the angle between current and magnetization in each permalloy layer.

In this paper we present a theoretical study of the magnetoresistance of $t_{\text{NiFe}}/\text{Cu}/t_{\text{NiFe}}$ layered thin films. We calculate the GMR and AMR as a function of the thickness of the NiFe layers (t_{NiFe}) and the Cu interlayer (t_{Cu}), and we will discuss the validity of a description of the combined effect in terms of a simple summation of the GMR and AMR, as proposed by Miller et al.⁵:

$$R(\varphi_1, \varphi_2) = R_0 - \frac{1}{2} \Delta R_{\text{AMR}} (\sin^2 \varphi_1 + \sin^2 \varphi_2) + \frac{1}{2} \Delta R_{\text{GMR}} (1 - \cos(\varphi_1 - \varphi_2)) \quad (1)$$

In this equation φ_1 and φ_2 are the angles of the magnetizations of the two NiFe layers with respect to the current direction and R_0 is the resistance for $\varphi_1 = \varphi_2 = 0^\circ$.

Fig. 1 shows the geometry of the system. Magnetizations and current are directed

in the plane of the layers. The magnetization vector of the lower NiFe(1) layer can be rotated with respect to the top NiFe(2) layer magnetization, as in the case of exchange biased systems, enabling one to create a transition between a parallel and antiparallel arrangement of the two layers, yielding the GMR. In our calculation of the AMR the current direction is rotated with respect to the direction of the magnetization of both magnetic layers, contrary to the experiments of Miller et al.⁵.

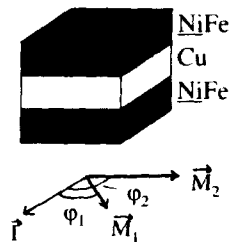


Figure 1: Geometry of the sample. \vec{M}_1 and \vec{M}_2 are the NiFe magnetization vectors and \vec{I} is the current.

THE MODEL

We have carried out model calculations of the resistance, using the semiclassical model for electron transport in magnetic multilayers that has been proposed by Camley and Barnás⁶. This model is based on the Boltzmann transport equation. In the original version the model parameters were chosen to describe mainly interfacial spin-dependent scattering, as it was applied to multilayers of pure elements. In our case, being interested in layered thin films involving a ferromagnetic alloy, we expect a large additional contribution of bulk spin-dependent scattering, as was already indicated by Jaoul et al.⁷ and Dieny et al.². In the present model calculations we assume only bulk spin-dependent scattering in the ferromagnetic layers, and neglect effects at the interfaces. At the outer boundaries we assume a perfectly diffusive scattering of electrons. Calculations are carried out for $T=0$ K, where spin flip scattering can be neglected: the spin up and spin down contributions to the current are independent.

In order to treat the AMR, we have extended the Camley and Barnás model, by adding a dependence of the mean free paths in the NiFe on the angle ϑ between the electron velocity vector \vec{v} and the NiFe magnetization vector \vec{M} . This intrinsically anisotropic mean free path for majority(\uparrow) and minority(\downarrow) spin electrons is given by:

$$\lambda^{\uparrow(\downarrow)}(\vartheta) = \lambda_0^{\uparrow(\downarrow)}(1 - a^{\uparrow(\downarrow)}\cos^2\vartheta - b^{\uparrow(\downarrow)}\cos^4\vartheta) \quad (2)$$

This expression can be derived when taking spin-orbit interaction in the NiFe 3d bands into account (after McGuire and Potter⁸). Neglecting the $\cos^4\vartheta$ -term, a set of $a^{\uparrow(\downarrow)}$ parameters can be derived which is consistent with the experimental spin

and angular resolved resistivity data, obtained by Dorleijn⁹, for dilute bulk NiFe:

$$\frac{i^{\uparrow}}{i} = 0.92, \quad \left(\frac{\rho_{\uparrow} - \rho_{\downarrow}}{\rho_{\uparrow}}\right)^{\uparrow} = 14\%, \quad \left(\frac{\rho_{\uparrow} - \rho_{\downarrow}}{\rho_{\uparrow}}\right)^{\downarrow} = -2.2\%, \quad (3)$$

where ρ_{\uparrow} is the resistivity in the case of $M\parallel i$ and ρ_{\downarrow} is the resistivity in the case of $M\perp i$, i^{\uparrow} is the current due to spin up electrons and i is the total current. Dorleijn's data show that the conductivity of NiFe is mainly due to majority spin electrons, and that the AMR is governed by the anisotropic scattering of majority spin electrons. The results for NiFe, with small concentrations of Fe in Ni, are: $a^{\uparrow}=0.327$, $a^{\downarrow}=-0.055$, corresponding to $\Delta\rho/\rho_{\uparrow}=12.9\%$ for bulk alloys at 4.2 K⁴. The data of eq. (3) apply only to dilute systems, and at present no values of a^{\uparrow} and a^{\downarrow} can be derived for more concentrated alloys, such as $\text{Ni}_{80}\text{Fe}_{20}$ in which $\Delta\rho/\rho_{\uparrow}=15.2\%$ at 4.2 K. Therefore we used the $a^{\uparrow(i)}$ for dilute alloys in our model calculations. Furthermore we used $\lambda_0^{\uparrow}(\text{NiFe})=120\text{ \AA}$, $\lambda_0^{\downarrow}(\text{NiFe})=6\text{ \AA}$ and $\lambda(\text{Cu})=135\text{ \AA}$. As shown by Dieny¹⁰ these are quite realistic values for $\text{Ni}_{80}\text{Fe}_{20}/\text{Cu}/\text{Ni}_{80}\text{Fe}_{20}$ systems.

RESULTS AND DISCUSSION

Fig. 2a shows the calculated values of the giant magnetoresistance ratio as a function of t_{Cu} and t_{NiFe} , defined as:

$$\text{GMR}(M\parallel i) \equiv \frac{R(\text{AP}, M\parallel i) - R(\text{P}, M\parallel i)}{R(\text{P}, M\parallel i)} \quad (4)$$

the magnetizations being colinear to the current direction. Fig. 2b shows the calculated anisotropic magnetoresistance ratio as a function of t_{Cu} and t_{NiFe} , defined as:

$$\text{AMR}(\text{P}) \equiv \frac{R(\text{P}, M\parallel i) - R(\text{P}, M\perp i)}{R(\text{P}, M\parallel i)} \quad (5)$$

the magnetizations being mutually parallel. From fig. 2a we can see that the maximum in GMR is achieved at very low thicknesses for $t_{\text{Cu}} \approx 0\text{ \AA}$ and $t_{\text{NiFe}} \approx 20\text{ \AA}$. For larger t_{Cu} the GMR is reduced because of shunting effects. For large t_{NiFe} it is also shunting that determines the reduction in GMR. For very small t_{NiFe} diffuse scattering of the spin up electrons at the boundaries reduces the asymmetry in the scattering of spin up and spin down scattering and therefore the GMR. The dashed line in fig. 2a marks the t_{NiFe} with the highest GMR, as a function of t_{Cu} . It shows that, in order to maximize the GMR, t_{NiFe} must be enlarged with increasing t_{Cu} , thereby preventing the current from running mainly through the Cu layer. In fig. 2b it can clearly be noticed that shunting by the Cu interlayer gives a considerable reduction of the AMR. For $t_{\text{NiFe}}=200\text{ \AA}$ and $t_{\text{Cu}} \approx 0\text{ \AA}$ the assumed bulk value of 12.9% for the AMR is almost reached.

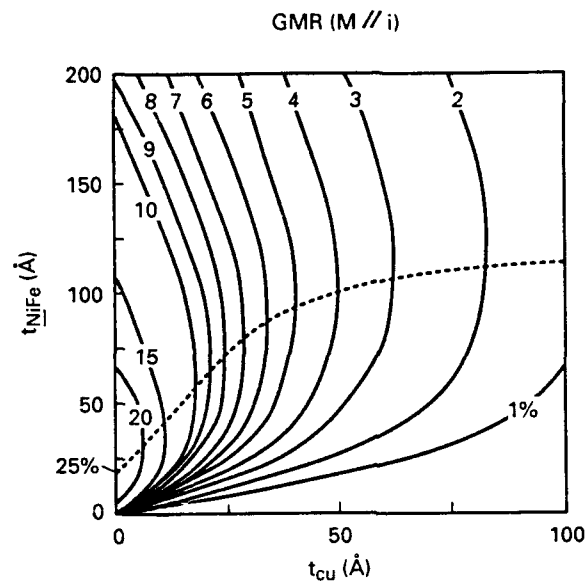


Figure 2a: Calculated GMR (%), with magnetizations parallel to the current direction, as a function of t_{NiFe} and t_{Cu} . The dashed line connects points, for each Cu thickness, of optimal NiFe thickness.

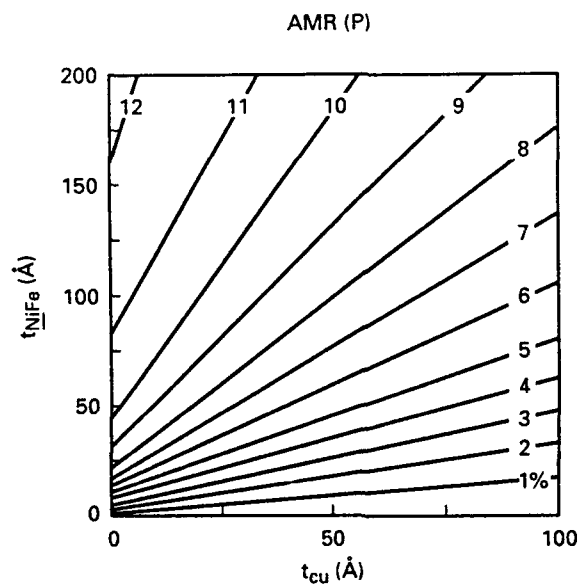


Figure 2b: Calculated AMR (%), with parallel magnetizations, as a function of t_{NiFe} and t_{Cu} .

In fig. 3 the difference Δ_{GMR} , which is defined as:

$$\Delta_{\text{GMR}} = \frac{[R(\text{AP}, \text{M} \parallel \text{i}) - R(\text{P}, \text{M} \parallel \text{i})] - [R(\text{AP}, \text{M} \perp \text{i}) - R(\text{P}, \text{M} \perp \text{i})]}{R(\text{P}, \text{M} \parallel \text{i})} \quad (6)$$

is plotted as a function of t_{NiFe} and t_{Cu} . Δ_{GMR} represents the influence of anisotropic scattering on the GMR. Comparison of fig. 2a and 3 shows that $\Delta_{\text{GMR}}/\text{GMR}(\text{M} \parallel \text{i})$ can reach at least 10 to 20% in areas where GMR is very small and Δ_{GMR} is large enough, e.g. for $t_{\text{Cu}} \approx 10 \text{ \AA}$ and t_{NiFe} very small. Trends in fig. 3 can be understood when taking the following three points into account. (i) According to eq. (2) the average value of $\lambda^{\uparrow}(\text{NiFe})$ for electrons colinear to the direction of the current is smallest in the case of $\text{M} \parallel \text{i}$. This reduces the spin-dependence of the scattering and gives a negative contribution to Δ_{GMR} . This effect is most important for small NiFe thicknesses, for which (due to the diffusive scattering at the boundaries) most of the current is carried by electrons with a velocity vector close the current direction. (ii) In the case of $\text{M} \parallel \text{i}$, the enhanced scattering of spin up electrons parallel to the current direction results in a relatively larger contribution to the current from electrons with a large velocity component perpendicular to the plane of the layers. This results in a positive contribution to Δ_{GMR} , which is most important for large NiFe thicknesses. In this case diffusive scattering at the boundaries does not severely limit the contribution to the current of electrons with a large perpendicular velocity component. (iii) When the GMR decreases, the absolute value of Δ_{GMR} decreases.

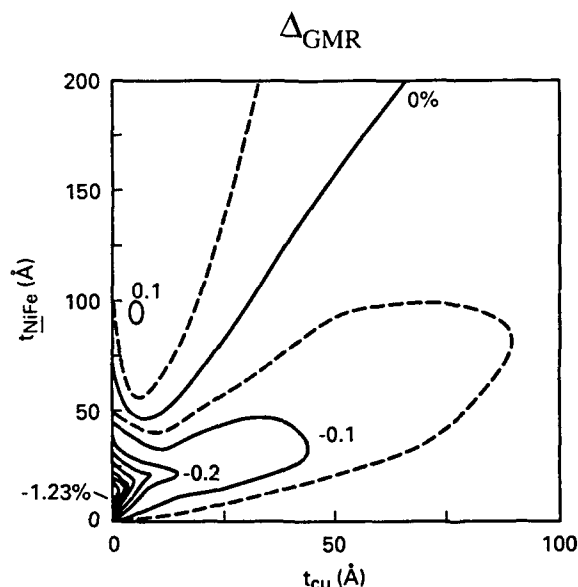


Figure 3: $\Delta_{\text{GMR}}(\%)$ as a function of t_{NiFe} and t_{Cu} , representing the influence of anisotropic scattering on the GMR.

The dependence of the AMR on the mutual alignment of the magnetic layers follows

from the quantity Δ_{AMR} , which is defined as:

$$\Delta_{\text{AMR}} = \frac{[R(\text{P}, \text{M} \parallel \text{i}) - R(\text{P}, \text{M} \perp \text{i})] - [R(\text{AP}, \text{M} \parallel \text{i}) - R(\text{AP}, \text{M} \perp \text{i})]}{R(\text{P}, \text{M} \parallel \text{i})} \quad (7)$$

From comparison of eqs. (6) and (7) it follows that $\Delta_{\text{AMR}} = -\Delta_{\text{GMR}}$. Therefore the quantity Δ_{AMR} does not contain new information.

CONCLUSIONS

Our calculations have revealed that the spin valve and anisotropic magnetoresistance in NiFe/Cu/NiFe layered thin films cannot in all cases be treated as independent phenomena. Consequently, the description of the combined effect in terms of a summation of a GMR and an AMR term (eq. (1)) is not strictly valid. In a limited range of NiFe and Cu thicknesses, the dependence of the giant magnetoresistance ratio on the current direction is larger than 10%. However, predictions of the total resistance, based on eq. (1), are in almost the entire thickness region studied precise within a few tenths of a percent.

It can be shown that our calculations of the AMR, based on intrinsically anisotropic mean free paths in the NiFe layers, provide an alternative for the postulate of extrinsically anisotropic scattering by grain boundaries, as was proposed by Dieny¹⁰. A more extensive discussion of this issue and a comparison with the experimental results will be published elsewhere¹.

REFERENCES

- ¹ B. Dieny, V.S. Speriosu, S. Metin, S.S.P. Parkin, B.A. Gurney, P. Baumgart and D.R. Wilhoit, *J. Appl. Phys.* **69**, 4774 (1991).
- ² B. Dieny, V.S. Speriosu, S.S.P. Parkin, B.A. Gurney, D.R. Wilhoit and D. Mauri, *Phys. Rev. B* **43**, 1297 (1991).
- ³ D.A. Thompson, L.T. Romankiw and A.F. Mayadas, *IEEE Trans. on Magn.* **MAG-11**, 1039 (1975).
- ⁴ Th.G.S.M. Rijks, R. Coehoorn, W. Folkerts and W.J.M. de Jonge, to be published.
- ⁵ B.H. Miller, E. Youjun Chen, and E. Dan Dahlberg, presented at MMM in Houston, USA (1992).
- ⁶ R.E. Camley and J. Barnás, *Phys. Rev. Lett.* **63**, 664 (1989).
- ⁷ O. Jaoul, I.A. Campbell, and A. Fert, *J. Magn. Magn. Mat.* **5**, 23 (1977).
- ⁸ T.R. McGuire, and R.I. Potter, *IEEE Trans. on Magn.* **MAG-11**, 1018 (1975).
- ⁹ J.W.F. Dorleijn, *Philips Res. Repts* **31**, 287, (1976).
- ¹⁰ B. Dieny, *Europhys. Lett.* **17**, 261, (1992).

ANNEALED Cu/Co/Cu/NiFe/FeMn SPIN VALVES : NANOSTRUCTURE AND MAGNETISM

C. MENY*, J.P. JAY*, P. PANISSOD*, P. HUMBERT*, V.S. SPERIOSU*,
H. LEFAKIS*, J.P. NOZIERES*+ AND B.A. GURNEY*

*IPCMS, UMR 46 CNRS, 4 rue Blaise Pascal, 67070 Strasbourg, France

*IBM Research Division, Almaden Research Center, 650 Harry Road, San Jose, CA 95120-6099, USA

+Present address: Laboratoire de Magnétisme Louis Néel, UPR 5051 CNRS, BP 166X, 38042 Grenoble, France.

ABSTRACT

Magnetic, magnetotransport and structural properties of Cu/Co/Cu/NiFe/FeMn spin-valve structures were studied before and after sequential annealing in the temperature range 240-360°C. Since no extended interdiffusion is observed, the overall deterioration of the magnetic and magnetoresistive properties of the spin valve is believed to originate from morphological and structural changes. In particular, annealing was found to decrease the magnetoresistive properties of Co as a result of structural changes within the Co layer and at the Co/Cu interface. These changes are accompanied by modifications of the magnetic properties. For annealing temperatures above 240°C, strong grain growth within the Co layer and increasing amount of fcc Co explain the increased magnetic hardness of this layer.

INTRODUCTION

Since its discovery, many efforts have been made to understand the fundamental mechanisms of giant magnetoresistance. Its origin is now widely believed to be spin dependent scattering (SDS) [1-8]. The influence of the detailed bulk and interface structure of metallic multilayers and sandwiches is well accepted too. The nature of the SDS was shown to be either interfacial [1,2,5-7], bulk [3,4] or both [7], depending on the materials involved. In systems with interfacial SDS, the structural properties of the interface such as interface roughness or compositional intermixing play a dominant role. In Fe/Cr multilayers for example, the magnetoresistance amplitude is increased by interface roughening [8,9]. In sputtered NiFe/Cu/NiFe/FeMn spin valves, the role of compositional intermixing at the NiFe/Cu interfaces has been recently studied by systematically increasing the thickness of the intermixed regions through successive annealings [10-14]. In contrast to Fe/Cr, interface roughening decreases the magnetoresistance amplitude. The observed decrease was attributed to the presence of high resistivity compositionally intermixed layers at the NiFe/Cu interfaces. Spin independent scattering within these non-magnetic, Cu-rich, intermixed layers reduces both the number and the mean free path of the electrons exchanged between the two ferromagnetic layers.

In this paper, we report the effect of annealing on the magnetic, magnetotransport and structural properties of Co/Cu/NiFe/FeMn spin valves. The results were obtained by conventional magnetometry and transport measurements and by zero field ^{59}Co NMR. They were interpreted in the light of measurements of nonferromagnetic interfacial layers on annealed Cu/Co/Cu structures [10], of extensive studies of annealed NiFe/Cu/NiFe/FeMn spin valves [11-15] and of a recent investigation of non-annealed Co/Cu/NiFe/FeMn spin valves by NMR [16]. By comparing the annealing effect on Co/Cu/NiFe/FeMn and NiFe/Cu/NiFe/FeMn spin valves, we show that structural changes within the Co layer and at the Co/Cu interface decrease the magnetoresistive properties of Co. For annealing temperatures above 240°C, we note an increased hardness of the Co layer which can be related to grain growth with fcc structure within this layer. Since no extended interdiffusion is observed, it is believed that deterioration has its origin in morphological and structural changes, accompanied by modifications of the magnetic properties, in particular within the Co layer and at the Co/Cu interface.

EXPERIMENTAL

A series of Ta 50Å/Cu 30Å/Co 75Å/Cu 22Å/NiFe 50Å/FeMn 80Å/Ta 50Å spin-valve structures were grown on Si(100) wafers during the same deposition run in a computer controlled DC magnetron sputtering system with a base pressure of $5 \cdot 10^{-8}$ Torr and an Ar plasma pressure of 3 mTorr. The films have a columnar structure with a strong $\langle 111 \rangle$ texture and an average grain diameter of about 100Å [12]. Annealing was carried out in a high vacuum furnace (10^{-7} Torr) under a constant magnetic field of 500 Oe in order to maintain the pinned layer constrained by exchange anisotropy. Consecutive annealings for 6.5h were performed at four temperatures : 240, 280, 320 and 360°C.

Magnetization loops were measured using a commercial B-H loop or a Vibrating Sample Magnetometer. Different magnetic and transport properties were monitored at room temperature after each anneal : magnetoresistance ($\Delta R/R$), sheet resistance (R_{\square}), saturation magnetic flux (Φ_s), coercivity (H_c), coupling field (H_i) and exchange bias (H_{ex}). $\Delta R/R$ and R_{\square} were measured with standard four point probes with an in-plane field applied along the easy axis defined by exchange anisotropy and the current perpendicular to the field. Bulk and interface structure as well as magnetic properties of the Co layer were investigated by zero field NMR. The ^{59}Co spectra were measured at 1.5°K using an automated frequency-scanning broadband spectrometer with phase coherent detection. The rf field was applied in the plane of the layers, perpendicular to the easy axis. In order to compare absolute intensities, all spectra were normalized to the total surface area of the Co resonance peaks, which represents the total number of magnetic Co atoms.

RESULTS AND DISCUSSION

Figure 1a shows the magnetic moment versus applied field for an as-deposited sample. The curve consists of two well-separated hysteresis loops. The loop at about 15 Oe corresponds to the reversal of the magnetization of the Co layer, while the loop shifted by exchange anisotropy to about 220 Oe corresponds to the reversal of the pinned NiFe layer. The values of the different magnetic and transport properties measured on two as-deposited samples are listed in Table I.

The ^{59}Co NMR spectrum of an as-deposited sample is shown in Figure 2. The spectrum can be separated into three parts : a main line at 215 MHz, a large shoulder at higher frequencies and a set of lines below 200 MHz. These different features respectively correspond to bulk fcc Co, bulk hcp Co and Co atoms with at least one Cu among their nearest neighbors. In particular, the satellite line at 165 MHz which corresponds to Co atoms with three Cu nearest neighbors, is characteristic of perfect $\langle 111 \rangle$ interfaces. In addition,

Table I - Magnetic and transport properties of two as-deposited (AD) and annealed Si/Ta 50Å/Cu 30Å/Co 75Å/Cu 22Å/NiFe 50Å/FeMn 80Å/Ta 50Å spin-valve structures : magnetoresistance ($\Delta R/R$), sheet resistance (R_{\square}), saturation magnetic flux (Φ_s), coercivity (H_c), coupling field (H_i) and exchange bias (H_{ex}).

	$\Delta R/R$ (%)		R_{\square} (Ω)		Φ_s (nWb)		H_c (Oe)		H_i (Oe)		H_{ex} (Oe)	
sample	1	2	1	2	1	2	1	2	1	2	1	2
AD	4.63	4.65	9.87	9.47	0.475	0.505	20.2	20.3	14.7	13.4	220	225
240°C	3.80	3.74	10.12	9.86	0.476	0.500	17.3	17.1	15.0	14.5	224	224
280°C	2.41	2.52	11.38	11.04	0.466	0.460	4.1	4.9	39.2	39.1	155	167

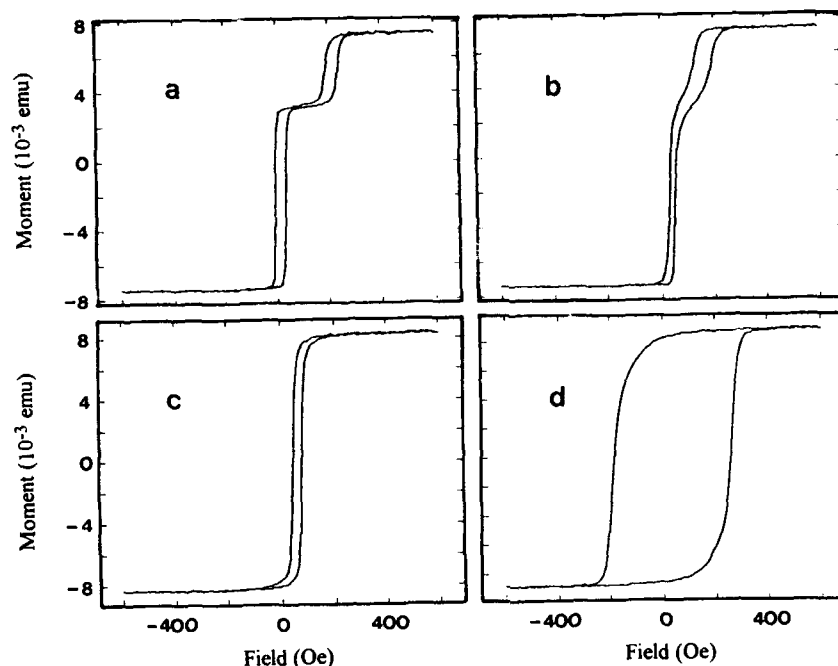


Fig. 1 - Magnetization curves measured with the field along the easy axis for Si/Ta 50Å/Cu 30Å/Co 75Å/Cu 22Å/NiFe 50Å/FeMn 80Å/Ta 50Å spin-valve structures (a) as-deposited and after sequential annealing up to (b) 280°C, (c) 320°C and (d) 360°C.

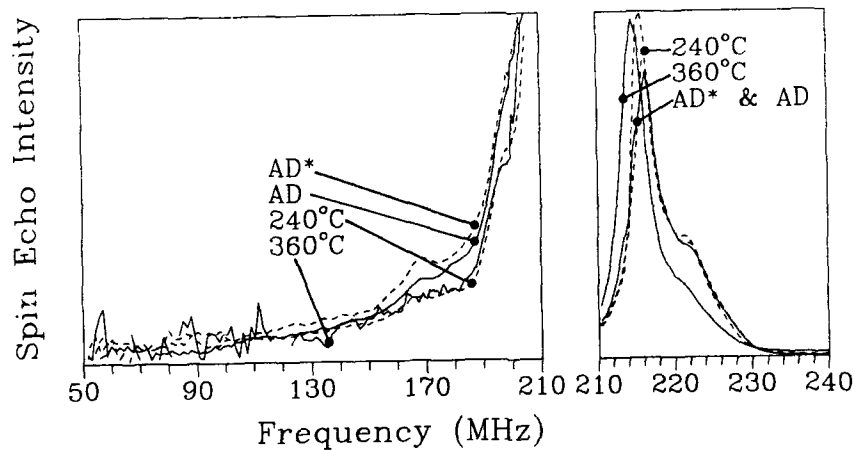


Fig. 2 - ^{59}Co NMR spectra of the Cu/Co/Cu/NiFe/FeMn spin-valve structure as-deposited (AD) and after sequential annealing. The label AD* refers to an as-deposited sample studied previously [16]. Spectra are normalized to the peak surface area and the magnification factor of the low frequency side is 33.

we reported the presence of a contribution between 200 and 210 MHz which we showed to originate from Co atoms located at the grain boundaries of the columnar grains [16]. Whereas the spectra obtained for the as-deposited samples of the present batch are superimposed, slight differences can be noted when compared to similar samples studied in our previous work [16]. This is illustrated in Figure 2. The overall number of Co atoms at the interface is lower and the three-Cu nearest neighbor contribution is smaller for the present samples. Whereas the Co/Cu interfaces of the previous samples were composed of a small number of wide islands with perfect interfaces separated by slightly intermixed regions, the present samples have fewer and/or smaller flat areas but also lower compositional intermixing in between.

Apart from a slight decrease of the coercivity of the Co layer, magnetic measurements did not show significant changes after annealing at 240°C. Magnetoresistance however decreased by about 20% although the sheet resistance increased only by about 3% (Table I). This small variation in R_{\square} cannot solely account for the drop in $\Delta R/R$. As pointed out in previous studies on the annealing of NiFe/Cu/NiFe/FeMn spin-valves [12-14], this drop is due to the presence of high resistivity, non-magnetic, Cu-rich intermixed layers at the NiFe/Cu interfaces. Spin independent scattering within these layers indeed decreases the flow of polarized electrons exchanged between the two ferromagnetic layers. Magnetic measurements showed that the thickness of the non-magnetic layer per NiFe/Cu interface increases from 2.0 to 4.0 Å after annealing at 240°C [12]. The drop of $\Delta R/R$ for a NiFe 75 Å/Cu 22 Å/NiFe 50 Å/FeMn 110 Å spin valve in these conditions is about 20% as well. Measurements on Cu/Co/Cu structures showed that the non-magnetic layer thickness per Co/Cu interface is 1.0 Å and increases only slightly after annealing at 240°C. Since the same drop of $\Delta R/R$ is observed for Co/Cu/NiFe/FeMn and NiFe/Cu/NiFe/FeMn spin valves although in the former case no resistivity change is expected at the Co/Cu interface, we conclude that annealing lowers the intrinsic magnetoresistive properties of Co. The NMR spectrum after annealing at 240°C shows a lower intensity in the range 160-190 MHz, corresponding to Co atoms surrounded by three Cu nearest neighbors at most (Fig. 2). This is explained by an interface smoothening due to thermally activated local atomic rearrangement. On the other hand, magnetic measurements show a slight increase of the thickness of the nonmagnetic layer. A possible explanation would be that some Co atoms remain in the Cu layer. Due to an increased number of Cu neighbors, their magnetic moment and their Curie temperature are then lowered as pointed out by Schneider et al. [17]. At 1.5°K, their NMR spectral contribution would be shifted toward and spread over the lower frequency range. At RT, nonmagnetic layer thickness measurements would be the result of an approximate balance between lower interface roughness and slight diffusion into the Cu layer. Finally we believe that the decrease of the magnetoresistive properties of Co after annealing is related to the modification of the Co/Cu interface structure since no other magnetic or morphological changes were observed. This relation can be explained by the interfacial SDS properties of Co [18].

After subsequent annealing at 280°C, the hysteresis exhibits noticeable changes although the loops corresponding to the free and to the pinned layer are still separated (Fig. 1b). On one hand the exchange anisotropy field of the NiFe layer decreases to about 160 Oe. On the other hand the loop of the free Co layer shifts to about 39 Oe together with a strong drop of coercivity and lower coercivity squareness (Table I). After the same thermal treatment, magnetic measurements show that the thickness of the magnetically inactive layer increases from 4.0 to 5.0 Å per NiFe/Cu interface in the case of NiFe/Cu/NiFe/FeMn spin valves [13] and from 1.6 to 2.0 Å per Co/Cu interface in the case of Cu/Co/Cu structures. Considering these low thickness variations, we believe that the origin of the coupling field increase is not a thickness decrease of the Cu layer due to interdiffusion. This coupling field behavior could be related to the deterioration of the anisotropy exchange field. Figure 3 represents the frequency dependence of the NMR signal on the optimum rf field strength. This quantity is proportional to the local magnetic moment stiffness. First we note that the hardness of the Co layer increased after the 280°C anneal, in agreement with the RT magnetic measurements. Furthermore, the feature at about 210 MHz fades due to an increased stiffness of the Co atoms at the grain boundaries. Grain boundary and interface Co atoms have now almost comparable magnetic moment stiffness. Figure 4 is a topographic view of the spin echo intensity versus resonance frequency and optimum rf field strength. As indicated by arrow 1, the spectral region corresponding to grain boundaries atoms (200-215 MHz) shows lower intensity. The smaller amount of Co atoms at the grain boundaries can be

explained by grain growth within the Co layer. Moreover we note an increase of intensity around 215 MHz at high rf field strength (arrow 2). This effect is related to grain growth as well. As the size of the grains increases, the number of bulk Co atoms increases and the core of the grains becomes magnetically harder. Also this intensity increase only concerns Co atoms in an fcc environment. This observation is confirmed by the fcc/hcp ratio which increases from about 1.0 before annealing to 1.5 after annealing at 280°C. These different structural changes in the bulk of the Co layer coincide with strong modifications of the magnetic properties of the spin valve whereas only slight changes are observed at the Co/Cu interface.

After annealing at 320°C, we observe a general breakdown of the magnetic and magnetoresistive properties of the spin valve structure. Hysteresis (Fig. 1c) now only consists in one single loop centered at about 60 Oe with a coercivity of about 16 Oe. As a consequence of the inability to rotate separately the magnetizations of the Co and the NiFe layers, the magnetoresistance strongly dropped from 2.47 to 0.65%. The sheet resistance increased by about 20%, mainly due to the growth of the high resistivity intermixed layer at the NiFe/Cu interface. Indeed, in the same annealing conditions, the nonmagnetic layer thickness is 8.3 Å for the NiFe/Cu interface [13] and only 2.4 Å for the Co/Cu interface. The changes observed by NMR consist in a continuing development of the phenomena described for the 280°C anneal (Fig. 3 and 4). The main characteristics are a further increase of the hardness of the Co layer, a further and stronger grain growth and a still increasing amount of bulk fcc Co. The measured fcc/hcp ratio is now about 1.9. In addition we observed a small peak in the intensity versus frequency spectrum at about 290 MHz. From reference data charts of NMR shifts in metallic alloys [19], this resonance line is likely to arise from Mn in NiFe (≈ 320 MHz) rather than from Co. Further experiments are however needed to clarify this point.

The final anneal at 360°C again led to deep changes of the magnetic properties (Fig. 1d) and to a definitive drop of $\Delta R/R$ to a near zero value. The single hysteresis loop, centered at about 40 Oe, presents now a very large coercivity of about 230 Oe. A further

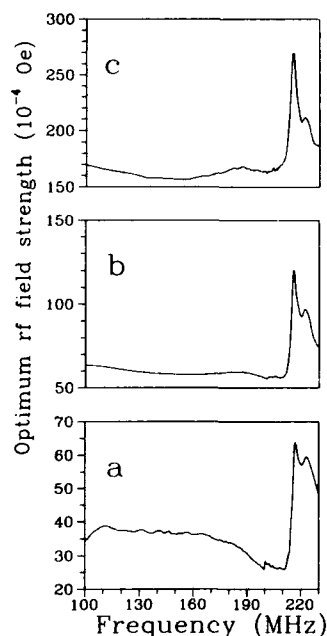
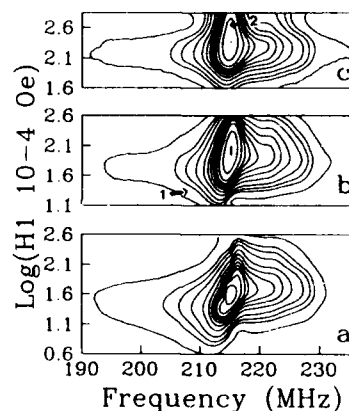


Fig. 3 (left) - Optimum rf field strength (i.e. local magnetic moment stiffness) versus resonance frequency for the Cu/Co/Cu/NiFe/FeMn spin-valve structure (a) as-deposited and after sequential annealing up to (b) 280°C and (c) 320°C.

Fig. 4 (below) - Topographic view of the spin echo intensity versus resonance frequency and optimum rf field strength for the Cu/Co/Cu/NiFe/FeMn spin-valve structure (a) as-deposited and after sequential annealing up to (b) 280°C and (c) 320°C. Arrow 1 and 2 as explained in the text.



strong increase of the hardness of the Co layer is observed by NMR too. The additional peak at 290 MHz still increases, which confirms that it originates from some diffusion phenomenon between the sandwich layers. The fcc/hcp ratio increases to a value of 2.3 : about 70% of the Co atoms are now in a bulk fcc Co environment. Since low temperature annealing is expected to favor the growth of the stable hcp phase, we believe that the top part of the Co layer, which is more hcp-like [17], transforms into fcc Co during annealing due to the influence of the overlying Cu layer, in a similar way the underlying Cu layer determines the initial growth of fcc Co during deposition.

CONCLUSIONS

We have shown that annealing leads to a decrease of the magnetoresistive properties of Co which can be explained by structural changes at the Co/Cu interface and in the bulk of the Co layer. Since no extended interdiffusion is observed, the deterioration of the magnetoresistive properties of the spin valve is believed to originate from morphological and structural changes, in particular within the Co layer and at the Co/Cu interface. Whether similar effects occur in the NiFe or in the FeMn layer is not known. These changes are accompanied by modifications of the magnetic properties. For annealing temperatures above 240°C, the hardness of the Co layer increases as a result of grain growth within this layer together with a strong increase of the amount of fcc Co. This can be explained by a combined effect of the two adjacent Cu layer which favors the growth of the fcc structure during annealing to the detriment of hcp Co.

REFERENCES

1. G. Binasch, P. Grünberg, F. Saurenbach and W. Zinn, *Phys. Rev. B*, **39**, 4828 (1989).
2. M.N. Baibich, J.M. Broto, A. Fert, F. Nguyen Van Dau, F. Petroff, P. Etienne, G. Creuzet, A. Friederich and J. Chazelas, *Phys. Rev. Lett.*, **61**, 2472 (1988).
3. B. Dieny, V.S. Speriosu, S.S.P. Parkin, B.A. Gurney, D.R. Wilhoit and D. Mauri, *Phys. Rev. B*, **43**, 1297 (1991).
4. B. Dieny, P. Humbert, V.S. Speriosu, S. Metin, B.A. Gurney, P. Baumgart and H. Lefakis, *Phys. Rev. B*, **45**, 806 (1992).
5. R.E. Camley and J. Barnas, *Phys. Rev. Lett.*, **63**, 664 (1989).
6. P.M. Levy, S. Zhang and A. Fert, *Phys. Rev. Lett.*, **65**, 1643 (1990).
7. B. Dieny, V.S. Speriosu, J.P. Nozières, B.A. Gurney and D.R. Wilhoit, submitted to *J. Mag. Mag. Mat.* (1992).
8. F. Petroff, A. Barthélémy, A. Hamzic, A. Fert, P. Etienne, S. Lequien and G. Creuzet, *J. Mag. Mag. Mat.*, **93**, 95 (1991).
9. E.E. Fullerton, D.M. Kelly, J. Guimpel, I.K. Schuller and Y. Bruynsraede, *Phys. Rev. Lett.*, **68**, 859 (1992).
10. to be published.
11. T.C. Huang, J.P. Nozières, V.S. Speriosu, H. Lefakis and B.A. Gurney, *Appl. Phys. Lett.*, **60**, 1573 (1992).
12. J.P. Nozières, V.S. Speriosu, B.A. Gurney, T.C. Huang, R.H. Geiss and H. Lefakis, to be published.
13. V.S. Speriosu, J.P. Nozières, B.A. Gurney, B. Dieny, T.C. Huang and H. Lefakis, accepted in *Phys. Rev. B, Rap. Comm.*, (1993).
14. J.P. Nozières, V.S. Speriosu, B.A. Gurney, B. Dieny, H. Lefakis and T.C. Huang, to be published.
15. T.C. Huang, J.P. Nozières, V.S. Speriosu, B.A. Gurney and H. Lefakis, *Appl. Phys. Lett.*, April (1993).
16. C. Mény, P. Panissod, P. Humbert, J.P. Nozières, V.S. Speriosu, B.A. Gurney and R. Zehringer, *J. Mag. Mag. Mat.*, **121**, 406 (1993).
17. C.M. Schneider, P. Bressler, P. Schuster, J. Kirschner, J.J. de Miguel and R. Miranda, *Phys. Rev. Lett.*, **64**, 1059 (1990).
18. S.S.P. Parkin et al., submitted to *Phys. Rev. Lett.*.
19. G.C. Carter, L.H. Bennett and D.J. Kahan, *Metallic Shifts in NMR*, Progress in Materials Science Vol.20 (Pergamon Press, Oxford, 1977), Part II p. 966; Part III p.1648.

Section A—Multilayers and Surfaces

PART IX

**Magnetism and Structure in
Ultrathin Films**

A TIGHT-BINDING STUDY OF VERY THIN TRANSITION METAL FILM MAGNETIC ANISOTROPY

Š. PICK¹ and H. DREYSSE²

¹ J. Heyrovský Institute of Physical Chemistry and Electrochemistry, Academy of Sciences of the Czech Republic, CS-182 23 Prague 8, Czech Republic

² Laboratoire de Physique du Solide, B.P. 239, 54506 Vandœuvre-les-Nancy, France

ABSTRACT

We discuss shortly some problems that have been met in recent systematic calculations of the magnetic anisotropy energy (MAE) performed by the present authors as well as in studies of other investigators. As an example, we present MAE for ferromagnetic (001) bilayers with antiferromagnetic inter-plane coupling and for an antiferromagnetic (001) monolayer. It appears that antiferromagnetism can invoke specific effects and under certain conditions, both MAE and magnetic orbital moment are strongly enhanced.

Due to the symmetry lowering at transition metal surfaces and in films, the magnetic (magnetocrystalline) anisotropy energy (MAE) is enhanced with respect to its bulk value. It is, nevertheless, small enough (10^{-4} - 10^{-3} eV) to make its evaluation difficult. Recently, the present authors completed an extensive semi-empirical study^{1,2} of MAE in transition metal mono- and bilayers, respectively. Into the common tight-binding d-band Hamiltonian for magnetic films the spin-orbit coupling (SOC) operator was introduced to account for the magnetic anisotropy and the relevant quantities were evaluated by using the recursion method. The model parameters were fitted to reproduce the data for the iron overlayer at the Au(001) surface (large exchange splitting case) or for the free-standing Ni(001) monolayer (small exchange splitting). With the above parameters, MAE has been calculated for a number thin films as a function of the d-electron occupation N_d . Simultaneously a formal analysis of the Hamiltonian moments $m_k = \text{Tr } H^k$ has been performed. By using a mathematical theorem we have shown that MAE changes its sign four-times at least as N_d varies from 0 to 10. It appears, however, that a number of oscillatory features are imposed on the MAE curve that in some cases mask completely the "canonical" form suggested by the moment analysis.

Presently, there are strong indications^{1,4} showing that the irregular features on the MAE curve originate from the energy-band crossings at the Fermi level E_F removed by the SOC. According to ref. 4 such contributions to MAE are of order $\xi \cdot A$ where ξ is the SOC parameter and A is the area in the 2-dim Brillouin zone where the quasidegenerate perturbation theory is valid. Since for the band crossing in an isolated point generally $A \sim \xi^2$ the authors of ref. 4 conclude that the contribution is small in comparison with the 2nd order perturbation theory terms and the irregular features come from numerical errors. Let us stress, nevertheless, that our calculations are free

from the possible sources (special integration grid and E_F independent of ξ) of numerical inaccuracy listed in ref. 4. Actually, for $\xi \approx 0$ the bands of different symmetry cross also along numerous curves²; at the energy extrema on these curves we easily get the guess $A \sim \xi^{3/2}$ which makes the above criticism less clear. Generally, the problem does not seem to be fully understood; it is interesting that a model substrate which breaks the symmetry and reduces essentially the number of band crossings has a smoothing effect on the MAE curve².

Apart from these complex questions some MAE features seem to admit a more straightforward interpretation. In this short study we discuss some simple trends in systems with anti-ferromagnetic (AF) coupling which have not been paid sufficient attention in our previous papers. Let us first consider MAE for the ferromagnetic free-standing (001) monolayer in the large exchange splitting regime and let us compare it with the results for free-standing (001) bilayers with the fcc and bcc geometry, respectively (Fig. 1). The bilayers consist of two ferromagnetic planes coupled anti-ferromagnetically. At the first sight there is a striking similarity between the three curves presented. The explanation is simple: due to a considerable energetical separation between parallel spin bands in the two planes (AF arrangement) the layers behave roughly like isolated ones. We find even a quantitative accord between the monolayer and fcc bilayer gross MAE features, whereas the fine irregular structure is more sensitive to the geometry change as it is expected from the previous discussion. We observe a similar effect when the (111)

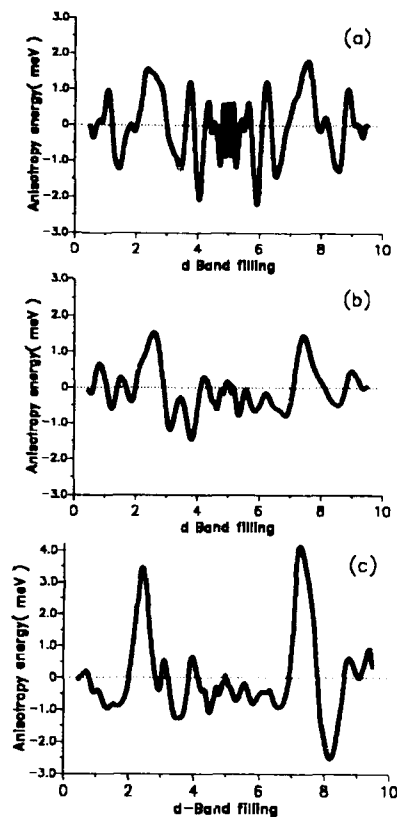


Figure 1. Magnetic anisotropy energy (MAE) per atom (meV) versus the d-band filling in the large exchange splitting regime for:
 (a) (001) monolayer
 (b) fcc-like (001) bilayer
 (c) bcc-like (001) bilayer
 Negative values correspond to favorable perpendicular direction of the magnetization.

monolayer and fcc bilayer are compared. In this case, however, the situation is more obscured by the presence of oscillations.

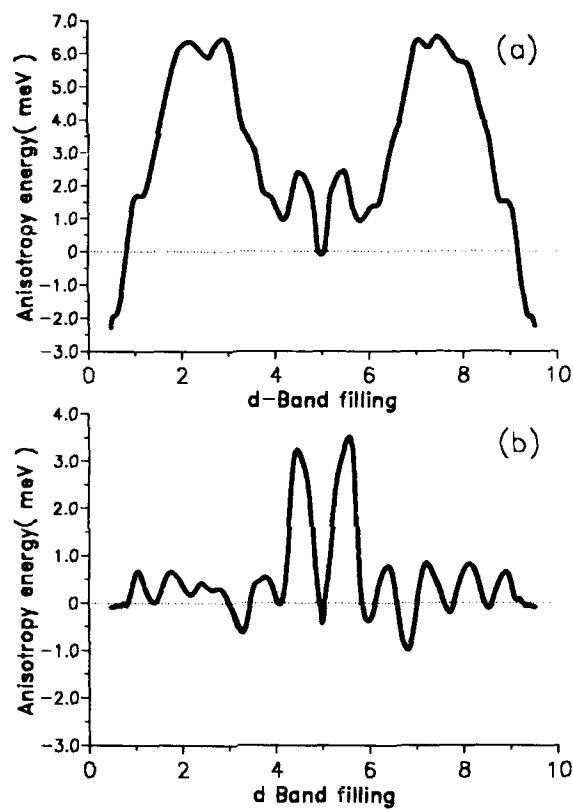


Figure 2:

Magnetic anisotropy energy (MAE) per atom (meV) versus the d-band filling for (001) monolayer supposing anti-ferromagnetic in-plane order. Negative values correspond to favorable perpendicular direction of the magnetization.

- (a) in the large exchange splitting regime
- (b) in the small exchange splitting regime

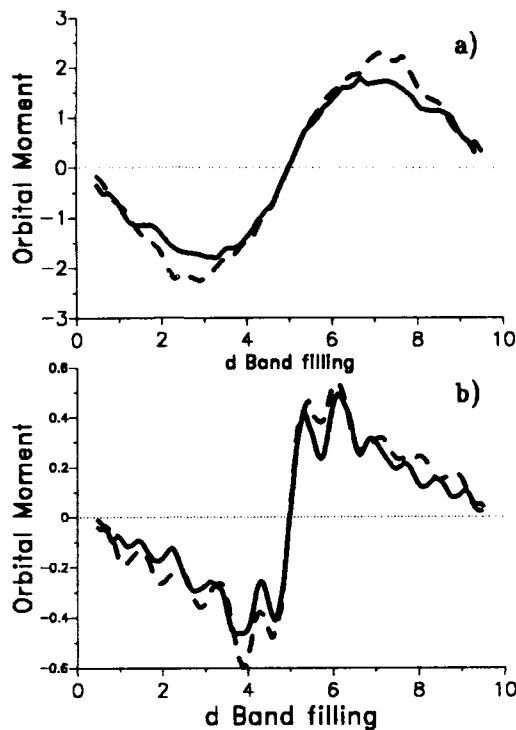


Figure 3:

Magnetic orbital moment (in Bohr magnetons) versus the d-band filling for (001) monolayer supposing anti-ferromagnetic in-plane order. Full (dashed) line corresponds to perpendicular (in-plane) component parallel to the magnetization:

- (a) in the large exchange splitting regime
- (b) in the small exchange splitting regime

For the bcc (001) bilayer, the amplitude of the MAE curve is bigger; the reason is that now we treat the in-plane nearest neighbors as 2nd nearest neighbors in the bulk and hence, the in-plane hopping integrals are reduced twice. The doubling of the magnitude of gross features follows immediately from the 2nd order perturbation theory arguments⁴⁻⁵; however, the oscillating features do not conform with this picture. Let us note that a similar "free-standing layer" behavior can be anticipated also for thicker films with interlayer AF coupling supposing that the exchange splitting (or magnetization) is sufficiently large.

As another example let us study the free-standing (001) monolayer with an AF arrangement of spins forming the $c(2 \times 2)$ structure which might have been observed experimentally⁶ for Cr/Ag(001) recently and which has been predicted theoretically for some transition metals on noble metal^{7,8}. To this goal let us glance once more on the result for the ferromagnetic (001) monolayer (Fig. 1a). An outstanding feature on the MAE curve are the peaks pointing to the preferred in-plane magnetization in the middle of the majority ($N_d \sim 2.5$) and minority ($N_d \sim 7.5$) spin bands, respectively. These features can be related to the XY-orbital peak in the local density of electronic states in the centre of the d-band: the hybridization of these states with (XZ,YZ) states with the same spin orientation via SOC explains the MAE sign¹. (To avoid a confusion, let us note the this mechanism need not be operative when the coupling with e_g states is effective, e.g. due to large crystal-field splitting or for another geometry). Unlike in ferromagnetic materials, there is no separation between opposite spin bands in AF structures; instead of it, the bands split at the boundary of the new Brillouine zone. The splittings occur mainly in the d-band central part. For small exchange splitting the XY-peak lies at $N_d \sim 5$ and is split into two parts. We see the corresponding effect on the MAE curve (Fig. 2b). When the exchange splitting is large, the separation of the two peaks the MAE curve grows as well as their width does (Fig. 2a). Note that the 1a. case is especially unfavorable for the perpendicular magnetic anisotropy.

The fact that for the AF $c(2 \times 2)$ structure the magnitude of MAE can be rather large and increases with the growing exchange splitting is caused by the energetical separation between parallel spin states at neighboring atoms which reduces the intensity of interactions and leads to the band narrowing. In this situation SOC becomes more important (cf. small denominators in the 2nd order perturbation theory). Let us remark that in systems where a large MAE is possible, the projection of the orbital moment on the spin direction can, as a rule, attain considerable values (cf. refs. 1,2,5). For the AF $c(2 \times 2)$ monolayers we obtain extremal values of the orbital moment as large as about $0.6\mu_B$ and $2.3\mu_B$ for the small and large exchange splitting, respectively (Fig. 3). The orbital moment contribution enhances/quenches the local magnetic moment when the d-band is more/less than half-filled.

In conclusion, we have found that in AF superstructures specific effects can take place including large enhancement of MAE or magnetic orbital moment. One can speculate that analogous effects could occur also for appropriate magnetic alloy surfaces and films.

Acknowledgements: S. Pick would like to thank the Laboratoire de Physique du Solide for kind hospitality. The Laboratoire de Physique du Solide de Nancy is Unité Associée au CNRS 155.

References

- ¹ S. Pick and H. Dreyssé, Phys. Rev. B 46, 5802 (1992).
- ² S. Pick and H. Dreyssé, Solid State Commun. 84, 627 (1992); Appl. Surf. Sci. 64-65, 140 (1993) and to be published.
- ³ G.H.O. Daalderop, P.J. Kelly, and M.F.H. Schurmans, Phys. Rev. B 41 11919 (1990).
- ⁴ D.-s. Wang, R. Wu, and A.J. Freeman, Phys. Rev. Lett. 70, 869 (1993) and to be published.
- ⁵ P. Bruno, Phys. Rev. B 39, 865 (1989).

- ⁶ C. Krembel, M.C. Hanf, J.C. Peruchetti, D. Bolmont and G. Gewinner, Phys. Rev. B 44, 8407 (1991).
- ⁷ A.J. Freeman and C.L. Fu, J. Appl. Phys. 61, 3356 (1987).
- ⁸ S. Blügel, M. Weinert and P.H. Dederichs, Phys. Rev. Lett. 60, 1077 (1988).

SPIN WAVE PROPAGATION AND BRILLOUIN LIGHT SCATTERING ON ANTIFERROMAGNETICALLY COUPLED BILAYERS

R. L. STAMPS AND R.E. CAMLEY

Department of Physics, University of Colorado at Colorado Springs, Colorado Springs, CO 80933-7150

ABSTRACT

The ground state spin configuration of antiferromagnetically coupled ferromagnetic thin films is determined by competition between anisotropies, interlayer exchange and the applied magnetic field. It is shown that many details of a ground state spin configuration can be obtained by studying the behavior of the spin wave frequencies as functions of propagation direction and applied field strength. A sensitive dependence on the relative film thicknesses is found for small applied field strengths.

I. INTRODUCTION

Recent theoretical and experimental studies have examined some of the unusual ground state spin configurations possible in antiferromagnetically coupled bilayer structures with strong uniaxial and four-fold anisotropies [1-5]. The present work is motivated by magnetometry measurements and Brillouin light scattering results which clearly indicate a series of transitions between various spin configurations [4,5]. Knowledge of the exact ground state spin configuration is important not only to measuring the nature and strength of the antiferromagnetic coupling mechanism and anisotropies of thin film structures, but also for understanding phenomena that depend on the relative orientation of spins in neighboring films. This is especially important for the giant magnetoresistance effect which depends on the antiparallel alignment of ferromagnetic films in a multilayer and is therefore sensitive to the ground state spin configuration.

In this paper a theory for the lowest energy spin wave excitations in antiferromagnetically coupled bilayers is presented. The spin wave frequencies are studied for equilibrium configurations of the magnetizations determined by four-fold anisotropies with arbitrary orientations of an externally applied static in-plane magnetic field. The aim is to provide a framework for describing results from resonance and Brillouin light scattering experiments. It is shown that the spin wave frequencies are strongly nonreciprocal ($\omega(q) \neq \omega(-q)$) in certain spin configurations.

II. THEORY

The geometry of the two layer system is shown in Fig. 1 for an arbitrary angle between the equilibrium directions of the magnetizations of the films. The thickness of the films are d_1 and d_2 and they are separated by a distance s . An applied magnetic field H_0 is placed along the z direction. A wavevector q is defined which makes an angle ϕ with the z axis and lies in

the xz plane. The frequencies of traveling waves will in general depend on the magnitude and direction of the wavevector q because of both exchange and dipolar interactions. All fields and magnetizations are treated as continuously varying functions of position. The magnetizations are separated into a static part whose orientation is specified by α and a small dynamic part m .

The equilibrium direction of the magnetization in each film depends on the strength of the applied magnetic field, the antiferromagnetic coupling as well as the anisotropy energies present in the material. In general the canting angles α_1 and α_2 are not the same for arbitrary orientations of the applied field relative to the easy anisotropy axes. A four-fold anisotropy energy K is assumed with one easy axis an angle θ away from the field direction and another easy axis normal to the film plane. The magnetization is assumed to lie in the film plane. The total energy of the two layer system is:

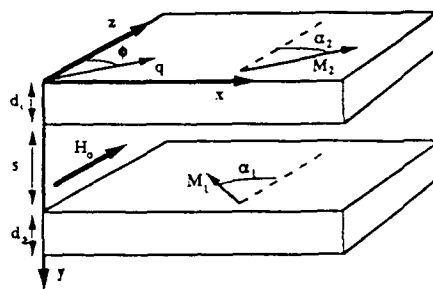


Figure 1. Geometry for the bilayer.

$$E = \frac{K}{4} [\sin^2(2(\theta + \alpha_1)) + \sin^2(2(\theta - \alpha_2))] - H_0 M_s (\cos \alpha_1 + \cos \alpha_2) + \lambda M_s \cos(\alpha_1 + \alpha_2) \quad (1)$$

Here λ is a constant that measures the strength of the interlayer exchange. The direction of the equilibrium magnetization can be found by minimizing E with respect to α_1 and α_2 . This can be done using simple numerical techniques.

Spin wave frequencies are calculated from the Bloch equations of motion. For the magnetization in film 1, these are:

$$\frac{d}{dt} \vec{M}_1 = \gamma \vec{M}_1 \times (\hat{z} H_0 + D_{ex} \nabla^2 \vec{m}_1 - \hat{K} \vec{m}_1 - \vec{K}_{1s} - \vec{h}_{dip}) \quad (2)$$

The various terms are as follows: H_0 is the applied magnetic field, D_{ex} is a measure of the strength of the exchange interaction within the film and h_{dip} are the dipolar fields acting on the magnetization of film 1. \hat{K} is a matrix containing anisotropy terms such that $\hat{K} \vec{m}_1$ are the

effective dynamic anisotropy fields acting on the magnetization of film 1 and K_s is the static anisotropy field acting on the magnetization of film 1 (for the case where the magnetization does not lie in a direction of symmetry). Similar expressions can also be written for M_2 .

Electromagnetic theory can be used to relate h_{dip} to m_1 and m_2 . Since the system has translational invariance in the x and z directions, Fourier transforms can be used to eliminate x and z dependencies in all the fields and magnetizations. The goal is then to have an expression which gives h_{dip} acting on a plane at position y due to the magnetization in a plane at position y' . A functional relationship is then sought of the form:

$$\bar{h}_{dip}(q, y) = \int dy' \bar{g}(q, y - y') \bar{m}(q, y') \quad (3)$$

The wavevector q lies in the xz plane. The Maxwell equations can be used to obtain \bar{g} [6]. This integral representation of h_{dip} gives the Fourier transform of the dipolar field at a plane located at y due to a spin wave travelling with wavevector q in a plane located at y' .

When Eq. (3) is used in the equations of motion one obtains after linearization a set of integral equations involving m_1 and m_2 . All of these equations are coupled and must be solved for ω . This is in fact a difficult task for thick ferromagnetic films but can be done relatively simply for the lowest energy modes of coupled systems of very thin ferromagnetic films. The reason is that the lowest energy mode of a thin film is the uniform mode where the time varying magnetization is essentially constant across the thickness of the film. This in turn allows one to average the dipolar fields over the thicknesses of the films and simplifies the calculation considerably [7].

In order to perform this averaging process, the effective fields are integrated over y. Each of the integrals can be evaluated as follows. Since the magnetization is assumed not to vary across the thickness of a film, m_1 and m_2 may be taken outside the integrals. The resulting surface terms are evaluated using the Hoffmann boundary conditions in the limit of small qd .

The resulting set of six coupled equations can be put in the form of an eigenvalue equation which can be solved for the eigenvalues ω and eigenvectors m_1 and m_2 . The solutions can be found numerically or in some special cases simple analytical forms can be derived. In general there will be two modes: One due to an in-phase precession of m_1 and m_2 and one due to out-of-phase precession of m_1 and m_2 . These modes are referred to as acoustic and optic, respectively.

It is assumed for the moment that $d_1 = d_2$. In the case of propagation perpendicular to field direction, the acoustic mode frequency is (to first order in qd):

$$\omega_1^2 = \gamma^2 H_O (H_O + 4\pi M_s \cos \alpha) + \gamma^2 \frac{1}{2} (4\pi M_s)^2 qd (1 + e^{-qs}) \cos^2 \alpha \quad (4)$$

The anisotropy is set to zero in this example. The canting angle

α is then simply $\cos \alpha = -H_0 / (2 \lambda)$. When $\alpha=0$ and $s=0$, Eq. (4) gives the frequency of the Damon-Eshbach surface mode on a thin ferromagnetic film of thickness $2d$.

III. RESULTS

A great deal of information about the spin configurations can be obtained by studying spin wave frequencies for different directions of propagation. The dependence of the frequencies on propagation angle ϕ is shown in Fig. 2 for a case where the applied field is aligned along an easy axis ($\theta=0$). The parameters are $2K/M_s = 580$ G, $H_{ex} = -150$ G, $4\pi M_s = 19$ kG, $d_1 = d_2 = 38$ Å and $q = .006$ cm⁻¹. The applied field is $H_0 = 100$ G and the magnetizations are canted symmetrically about the field direction (i.e. $\alpha_1 = \alpha_2$).

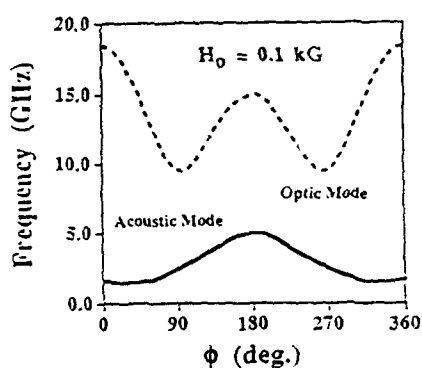


Figure 2. Frequencies as functions of propagation direction. The field is along an easy direction.

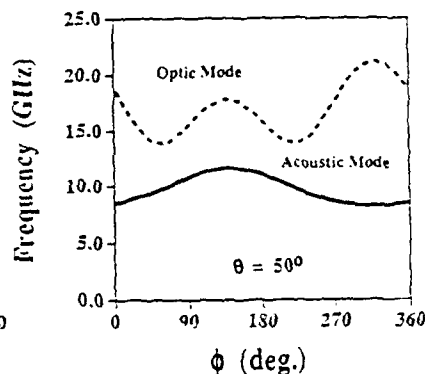


Figure 3. Frequencies as functions of propagation direction. The field is 5° from a hard direction.

The frequencies as functions of ϕ are shown in Fig. 3 with the field aligned 5° from a hard axis. The field is again 100 G but now $\alpha_1 \neq \alpha_2$ so that there is a small net magnetization in a direction 40° from the applied field. Note that $\omega(q) \neq \omega(-q)$ for propagation perpendicular to the field direction ($\phi \approx 90^\circ$ and 270°). This nonreciprocal behavior can be understood from symmetry considerations.

This nonreciprocity of the frequency between $+q$ and $-q$ should be of interest for Brillouin light scattering. Nonreciprocity occurs in two cases: (1) For propagation in the direction of the applied field for canting angles $\alpha > 0$; and (2) when the canting angles of the two films are different such that the vector sum of the static magnetizations has a component perpendicular to the field direction. This means that the nonreciprocal behavior of the spin wave frequencies can be used to provide information on the direction of the average static

magnetization of the two film system.

Another way of understanding the dependence of ω on ϕ is to view the dipolar interaction as similar to a q dependent anisotropy. A symmetry axis of the dipolar "anisotropy" fields is the direction of the net magnetization.

There is a surprising dependence on relative film thicknesses for bilayers constructed from very thin film ferromagnets. The reason is that a slight difference of thickness results in a different net magnetic moment for each film. This leads to a unique spin configuration in small applied fields where the larger magnetic moment is nearly aligned along the field direction and the smaller magnetic moment is nearly aligned anti-parallel to the field direction.

This is illustrated in Fig. 4 where the average magnetization in the field direction is shown as a function of field strength for the case of (a) equal film thicknesses and (b) a 7% difference between film thicknesses. In Fig. 4(a) $\alpha_1 = \alpha_2$ and the magnetization is always symmetrically canted away from the field for small fields. The magnetizations jump into the field direction at about 250 G.

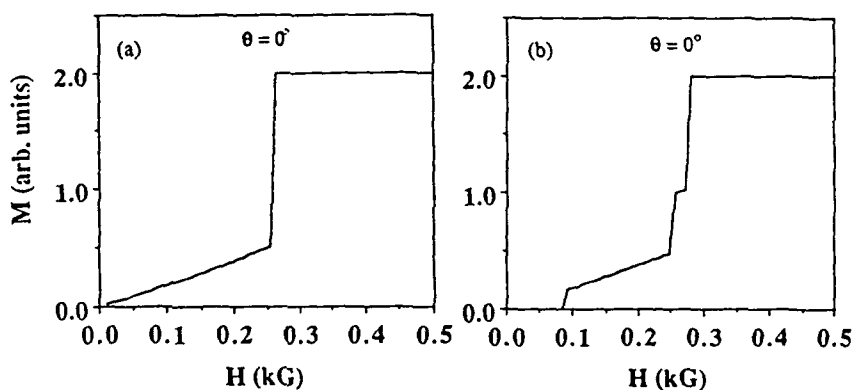


Figure 4. Static magnetization in the field direction as a function of field. In (a) the thicknesses of the two films are the same. In (b) the thicknesses differ by 7%.

In Fig. 4(b) however, $\alpha_1 \neq \alpha_2$ for fields below 87 G and the net magnetization is nearly zero. Between 87 G and 250 G, $\alpha_1 = \alpha_2$ again and the magnetizations are symmetrically canted away from the applied field. Between 250 G and 280 G, the larger magnetization is aligned nearly along the field direction while the smaller magnetization remains canted away from the field. Above 280 G, both magnetizations are aligned along the field.

This behavior is reflected in the spin wave frequencies. The acoustic mode frequency is shown in Fig. 5 as a function of applied field for the case $d_1 \neq d_2$ described in Fig. 4(b). Discontinuities appear at 87 G, 250 G and 280 G, corresponding to changing spin

configurations described above. Note the large nonreciprocity in frequencies for $\phi = \pm 90^\circ$ at small fields. There is again a small nonreciprocity for fields between 250 G and 280 G. The nonreciprocity is larger for the small field case because the net magnetization is nearly 90° from the field direction in this configuration.

In conclusion, nonreciprocal properties of spin waves on magnetic bilayers are very sensitive to the spin configuration and can provide a great deal of information on the anisotropies in the magnetic films and the exchange coupling between the films. Even slight variations in layer thicknesses can lead to large effects in the spin wave frequencies.

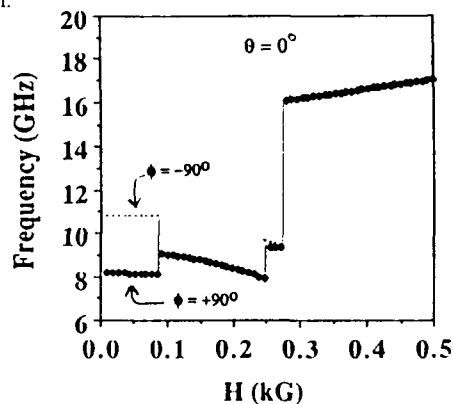


Figure 5. Frequencies as functions of field. The thicknesses of the two films differ by 7% as in Fig. 4(b).

ACKNOWLEDGEMENTS: This work was supported by the US Army Research Office under Grant No. DAAL0391-G-0229.

REFERENCES:

1. Dieny and J.P. Gavigan, J. Phys. C **2**, 187 (1990); B. Dieny, J.P. Gavigan and J.P. Rebouillat, J. Phys. C **2**, 159 (1990).
2. P. Grünberg, R. Schreiber, Y. Pang, and U. Walz, J. Appl. Phys. **61**, 3750 (1987); M. Vohl, J. Barnas and P. Grünberg, Phys. Rev. B **39**, 12003 (1989).
3. J.F. Cochran, J. Rudd, W.B. Muir, B. Heinrich and Z. Celinski, Phys. Rev. B **42**, 508 (1990).
4. B. Heinrich, J. Kirschner, M. Kowalewski, J.F. Cochran, Z. Celinski, and A.S. Arrott, Phys. Rev. B **44**, 9348 (1991); J.J. Krebs, P. Lubitz, A. Chaiken and G.A. Prinz, J. Appl. Phys. **67**, 5920 (1990).
5. M.O. Dima, D.B. Church, P. Kabos and C.E. Patton, proceedings of the 37th Annual MMM Conference.
6. R.E. Camley and R.L. Stamps, in *Spin Waves and Nonlinear Excitations in Magnetic Thin Films and Superlattices* (World Scientific, to be published).
7. R.L. Stamps and B. Hillebrands, Phys. Rev. B **44**, 12417 (1991).

MAGNETIC ANISOTROPY IN EPITAXIAL Ni/Cu (100) THIN FILMS

G. BOCHI, C. A. BALLENTINE, H. E. INGLEFIELD, S. S. BOGOMOLOV, C. V. THOMPSON, and R. C. O'HANDLEY

Massachusetts Institute of Technology, Cambridge MA 02139

ABSTRACT

Epitaxial Ni/Cu (001) films grown on Si (001) by Molecular Beam Epitaxy were studied *in-situ* using the Surface Magneto-optic Kerr Effect (SMOKE) and *ex-situ* with a Vibrating Sample Magnetometer (VSM). Perpendicular magnetization is observed for Ni thicknesses $15 \text{ \AA} \leq h \leq 60 \text{ \AA}$ and fully in-plane magnetization for $h \geq 70 \text{ \AA}$ when the films are characterized *in-situ*. The reversal in magnetic anisotropy observed *in-situ* at 60 \AA shifts to 125 \AA when the films are exposed to air. 100 \AA Ni films deposited on $\text{Cu}_{1-x}\text{Ni}_x$ alloy substrates also show a reversal in magnetic anisotropy as x is changed. These results suggest that changes in magnetic anisotropy correlate with misfit strain accommodation.

INTRODUCTION

Since the theoretical predictions of Gay and Richter [1], considerable experimental effort has been focused on the issue of perpendicular magnetic anisotropy in ultrathin ferromagnetic films grown epitaxially on non-magnetic substrates. The systems that have been investigated most extensively are Fe/Ag (100) [2-5] and Fe/Cu (100) [6-10]. For Fe/Ag (100) at 100 K, the magnetization switches from perpendicular to in-plane above 2 monolayers (ML) of Fe [5]. In the case of Fe/Cu (100) the switching behavior has been observed even at $T=300 \text{ K}$ where the magnetization goes from perpendicular to in-plane at a thickness of 6 ML [7].

The change in magnetic anisotropy in the Ni/Cu (100) system has received less attention than in the Fe/Cu and Fe/Ag systems. SMOKE measurements [11] at $T=100 \text{ K}$ indicate that the easy axis of magnetization lies in the plane of the film for Ni thicknesses up to 3.1 ML and a preference for perpendicular magnetization is observed above 4.7 ML. An interesting reversal in magnetic anisotropy has also been observed in epitaxial Cu/Ni/Cu (100) sandwiches (Cu thickness= 1000 \AA) deposited on Si (100) and characterized *ex-situ* by VSM [12]. The magnetization was found to lie in plane for Ni thicknesses $h \geq 500 \text{ \AA}$ and out-of-plane for $h=50 \text{ \AA}$ with a transition thickness $h \approx 100 \text{ \AA}$.

In the present paper, we report on the behavior of magnetic anisotropy in epitaxial Ni/Cu/Si (100) at $T=300 \text{ K}$ characterized under UHV conditions by SMOKE and in air by VSM. The Ni film thicknesses extend from 15 \AA to 200 \AA . We also present preliminary results showing the correlation between magnetic anisotropy changes and misfit strain in the

magnetic film. With lattice parameters of 3.52 Å and 3.61 Å for Ni and Cu, respectively, the misfit between the film and the substrate is $\eta \approx 2.5\%$. The misfit can be reduced to 1.5 % by depositing Ni on $\text{Cu}_{1-x}\text{Ni}_x/\text{Cu}$ alloy substrates, where x is varied between 0 and 0.4 (above $x=0.6$ bulk Ni-Cu alloys exhibit a ferromagnetic order). Even though the importance of strain has already been pointed out by Chappert and Bruno [13], very few papers establish a direct connection between the onset of misfit dislocations [10] or misfit strain [14] and the behavior of the magnetic anisotropy.

EXPERIMENTAL PROCEDURE

The metal films were deposited on Si (100) wafers by Molecular Beam Epitaxy (MBE). The base pressure of the chamber was 5×10^{-11} Torr and the pressure never exceeded 1×10^{-8} Torr during deposition. The Si wafers were dipped in a 10 % HF-deionized water solution to remove the native oxide layer but were not heat cleaned in UHV before growth. The deposition rates for Cu and Ni were 3 Å/s and 0.5 Å/s respectively. The thickness of the Cu layer was 3000 Å in the Ni/Cu/Si samples. In the $\text{Ni/Cu}_{1-x}\text{Ni}_x/\text{Cu/Si}$ samples, the Cu layer thickness was 1000 Å and the alloy layer thickness was 2000 Å. The depositions were carried out at room temperature. The crystallographic quality of the films was studied *in-situ* by RHEED and *ex-situ* by X-ray diffraction and TEM. The results indicate that the films are epitaxial and grow with an (001) orientation. The purity of the films was studied *in-situ* by Auger electron spectroscopy.

The magnetic properties of the films were studied *in-situ* by SMOKE. The maximum fields that can be applied are 220 Oe perpendicular to the film and 650 Oe in-plane. The light source is a polarized 10 mW He-Ne laser. The laser beam makes an angle of 45° with the film normal. The intensity of the laser light is monitored by a photodiode which is connected to the data acquisition system through a lock-in amplifier. Finally, the samples were removed from the MBE chamber and studied again with a VSM. All magnetic characterizations were done at room temperature.

RESULTS

The longitudinal and polar M-H loops for 150 Å, 35 Å and 15 Å Ni/Cu/Si measured by SMOKE are shown in Figs. 1-3 respectively. The M-H loops measured *in-situ* for 100 Å Ni/Cu/Si and 75 Å Ni/Cu/Si are similar to those shown in Fig. 1. As expected, the magnetization of our films lies in plane at large Ni thicknesses. For 35 Å Ni (Fig. 2), the SMOKE loops show the magnetization to prefer an orientation perpendicular to the film plane; the polar loop is square and the longitudinal signal is negligible. The loops for 50 Å and 25 Å Ni films are very similar to that for 35 Å. For 15 Å of Ni (Fig. 3), a strong in-plane component coexists with the out of plane component. At $T=100$ K, it has been observed [11] that the magnetization is fully in plane for $h \leq 5.5$ Å and out of plane for $h > 8.3$ Å.

The strong longitudinal signal in our films at $h=15$ Å suggests that this is the lower anisotropy switching thickness corresponding to that observed at $h \approx 6$ Å for 100 K. Further measurements on films of thickness $h < 15$ Å have so far failed to clarify the nature of this transition.

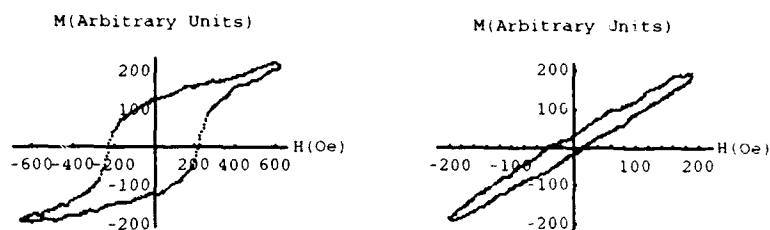


Fig.1: Longitudinal (left) and polar (right) M-H loops for 150 Å Ni/3000 Å Cu/Si(100).



Fig.2: Longitudinal (left) and polar (right) M-H loops for 35 Å Ni/3000 Å Cu/Si(100).

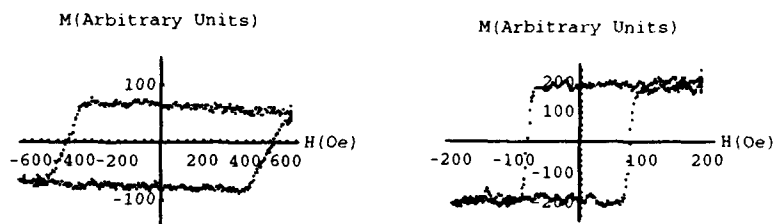


Fig.3: Longitudinal (left) and polar (right) M-H loops for 15 Å Ni/3000 Å Cu/Si(100).

The variations with Ni film thickness of the perpendicular remanence normalized to the saturation magnetization is summarized in Fig. 4. This figure includes *in-situ* SMOKE and *ex-situ* VSM data. The most striking

and interesting feature of Fig. 4 is the existence and the extent of the region where perpendicular anisotropy is observed: from 15 Å to 60 Å for films kept under UHV conditions; from 25 Å to 125 Å for films exposed to air. This range of perpendicular easy axis is large compared to that observed in the Fe/Cu (100) system where the perpendicular to in-plane switching thickness does not exceed 10 Å at $T=300$ K [7]. The switching of the magnetic anisotropy observed *in-situ* at 60 Å shifts to 125 Å when the samples are exposed to air. This shift is most likely due to oxidation of the Ni film. In fact, samples with 100 Å and 75 Å Ni films which have been exposed to air and placed back in the MBE chamber show loops similar to the VSM loops, indicating an out of plane magnetization.

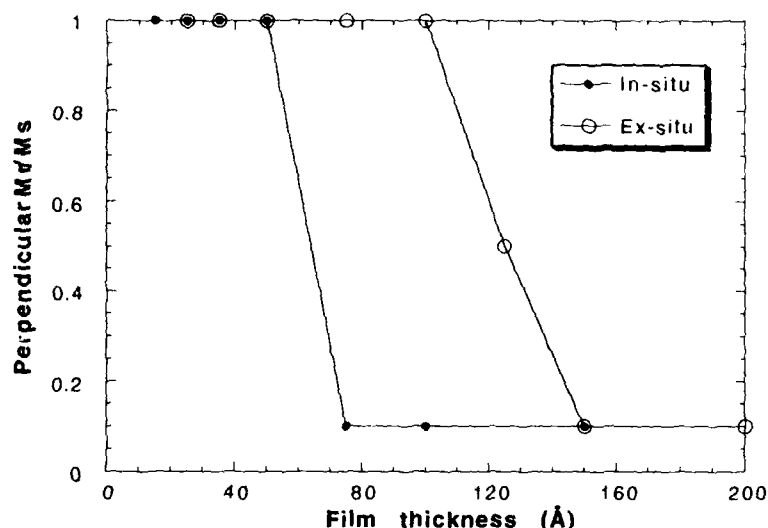


Fig.4: Variation of the perpendicular remanence (normalized to the saturation magnetization) with Ni film thickness in Ni/3000 Å Cu/Si(100).

The results for the magnetic properties of 100 Å Ni films on alloy substrates ($\text{Cu}_{1-x}\text{Ni}_x/\text{Cu/Si}$) characterized by VSM are summarized in Fig. 5 where the perpendicular remanence, normalized to the saturation magnetization, is plotted as a function of Ni content in the substrate. The $\text{Cu}_{1-x}\text{Ni}_x/\text{Cu/Si}$ substrates were shown to be non-magnetic by VSM measurements. The *ex-situ* magnetization is perpendicular to the film plane when a 100 Å Ni film is deposited on pure Cu and falls in-plane when the Ni concentration in the substrate exceeds 25 %. This switching of the magnetization easy axis with film-substrate misfit, for a film with a relatively large thickness, is very interesting because it shows a qualitative correlation between the change in magnetic anisotropy and magneto-elastic effects in thin films.

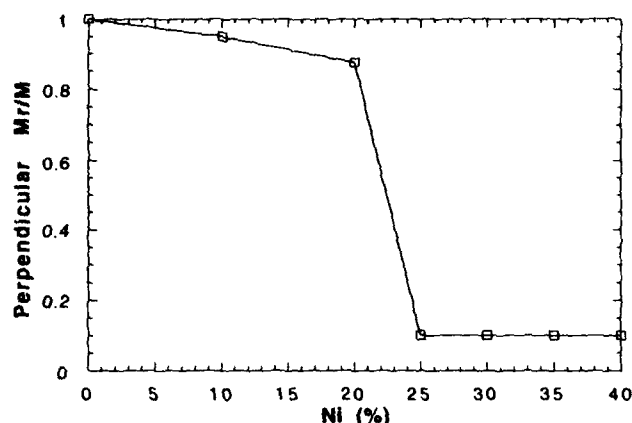


Fig.5: Variation of the perpendicular remanence (normalized to the saturation magnetization) with x in 100 Å Ni/2000 Å $\text{Cu}_{1-x}\text{Ni}_x$ /1000 Å Cu/Si(100).

DISCUSSION

It has been emphasized by many research groups [2,6,8,9] that perpendicular magnetic anisotropy in ultrathin films is expected whenever a uniaxial anisotropy energy K_s , arising from the reduced symmetry at interfaces, overcomes the magneto-static (MS) energy $2\pi M_s^2$ of the film. At 300 K, perpendicular anisotropy is observed up to 10 Å in Fe/Cu (100) [7] and up to 60 Å in our Ni/Cu (100) films. The ratio of the MS energy of Fe to that of Ni is approximately equal to 10/1. It is therefore very tempting to associate the larger switching thickness in Ni/Cu (100) with the lower MS energy of Ni. However, this argument overlooks the surface and interface anisotropies which could also be quite different in the Ni/Cu (100) and the Fe/Cu (100) systems. We believe that the switching of the magnetization from perpendicular to in-plane is instead determined by a competition between the MS energy, the surface anisotropy energy and the magneto-elastic (ME) energy of the film. The Ni film, which has a smaller lattice parameter than the Cu substrate, is under an in-plane biaxial tensile strain. Since the first order (bulk) ME coupling coefficient of Ni is positive ($B_1 = 6.21 \times 10^7$ erg/cm³), ME energy favors a perpendicular anisotropy. We have measured the dislocation spacing and the in-plane biaxial strain ϵ in the Ni film as a function of thickness in epitaxial Ni/3000 Å Cu/NaCl (100) structures [15]. We can then get an estimate of K_s by solving the following equation at the transition thickness $h=60$ Å where $\epsilon=1.1\%$ (Fig. 4, ref. 15):

$$2B_1\epsilon - 2\pi M_s^2 + 2K_s/h = 0 \quad (1)$$

With $2\pi M_s^2 \approx 1.47 \times 10^6$ erg/cm³ for Ni, we obtain $K_s = 0.03$ erg/cm². This argument is semi-quantitative since the strain was measured *ex-situ* and may differ slightly from the strain for a film kept under UHV. Moreover,

the bulk values of the coefficient B_1 and of M_s might not be adequate for 60 Å films and thinner.

The reversal in magnetic anisotropy observed in 100 Å Ni on alloy substrates $\text{Cu}_{1-x}\text{Ni}_x$ by VSM can also be understood based on the interplay between ME and MS energies. For Ni/Cu samples exposed to air, the switching thickness of the magnetization is $h \approx 125$ Å (Fig. 4). As the Ni content in the substrate is increased from 0 to 40%, the misfit between the film and the substrate is reduced from 2.5% to 1.5%. This reduction in misfit is significant and could lower the ME energy $B_1\epsilon$ enough to make the magnetization switching thickness decrease to 100 Å for films exposed to air. We plan to make a more quantitative study of misfit effects by measuring the strain in the films as a function of x , extending these measurements over a broader range of Ni thicknesses and characterizing the films *in-situ* by SMOKE.

ACKNOWLEDGMENTS

This work is supported by grants from NSF and ARO. Two of the authors G. B. and H. E. I. would like to thank NSERC of Canada and the Claire Boothe-Luce Foundation, respectively, for the financial support through graduate fellowship grants.

REFERENCES

- [1] J. G. Gay and Roy Richter, Phys. Rev. Lett. **56**, 2728 (1986).
- [2] N. C. Koon, B. T. Jonker, F. A. Volkening, J. J. Krebs, and G. A. Prinz, Phys. Rev. Lett. **59**, 2463 (1987).
- [3] M. Stampanoni, A. Vaterlaus, M. Aeschlimann, and F. Meier, Phys. Rev. Lett. **59**, 2483 (1987).
- [4] B. Heinrich, K. B. Urquhart, A. S. Arrott, J. F. Cochran, K. Myrtle, and S. T. Purcell, Phys. Rev. Lett. **59**, 1756 (1987).
- [5] C. A. Ballentine, R. L. Fink, J. Arayat-Pochet, and J. L. Erskine, Appl. Phys. A **49**, 459 (1989).
- [6] D. Pescia, M. Stampanoni, G. L. Bona, A. Vaterlaus, R. F. Willis, and F. Meier, Phys. Rev. Lett. **59**, 933 (1987).
- [7] C. Liu, E. R. Moog, and S. D. Bader, Phys. Rev. Lett. **60**, 2422 (1988).
- [8] D. P. Pappas, K. P. Kamper, B. P. Miller, H. Hopster, D. E. Fowler, A. C. Luntz, C. R. Brundle, and Z.-X. Shen, J. Appl. Phys. **69**, 5209 (1991).
- [9] R. Allenspach and A. Bischof, Phys. Rev. Lett. **69**, 3385 (1992).
- [10] J. Thomassen, F. May, B. Feldmann, M. Wuttig, and H. Ibach, Phys. Rev. Lett. **69**, 3831 (1992).
- [11] C. A. Ballentine, Ph. D. Thesis, University of Texas at Austin, 1989.
- [12] Chin-An Chang, J. Appl. Phys. **68**, 4763 (1990).
- [13] C. Chappert and P. Bruno, J. Appl. Phys. **64**, 5736 (1988).
- [14] C. H. Lee, Hui He, F. J. Lamelas, W. Vavra, C. Uher, and Roy Clarke, Phys. Rev. B **42**, 1066 (1990).
- [15] H. E. Inglefield, C. A. Ballentine, G. Bochi, S. S. Bogomolov, R. C. O'Handley, and C. V. Thompson, Mater. Res. Soc. Proc. **308** (in press, 1993).

Magnetization Reversal in CoPt Magneto-optic Recording Alloys

T. Kleinfeld*, W.S. Kim*, J. Valentin* and D. Weller**

* Universität Duisburg, FB 10/ Angewandte Physik, Postfach 101503, D-4100 Duisburg, Germany

** IBM Research Division, Almaden Research Center, 650 Harry Road, San Jose, CA 95120-6099, USA

ABSTRACT

High resolution Kerr microscopy has been used to study newly developed Co₂₅Pt₇₅ alloy films with perpendicular magnetic anisotropy. In particular, the dynamics of magnetization reversal processes were investigated by means of time resolved domain pattern analysis. Domain wall motion dominated magnetization reversal as well as nucleation dominated processes were observed. Magnetic aftereffect phenomena were confirmed by relaxation measurements of magnetic domains. The fractal dimension of the observed domains is correlated to the macroscopic coercivity determined from hysteresis loop measurements.

INTRODUCTION

Thin metallic films of alloys of Co and Pt have recently been discussed as promising new materials for magneto-optic recording applications [1]. The advantages of these alloys compared with other recording materials were clearly pointed out in recent publications [1-3]. The process of magnetization reversal is of particular interest because of its important role in thermomagnetic recording. Special interest is focused on the formation of magnetic domains and the stability of the domain shape after reversal of the magnetization in the writing laser spot. Therefore the magnetic aftereffect is considered to be one of the limiting factors in magneto-optic recording applications.

In this paper we present a study of the magnetization dynamics using Kerr microscopy and successive image processing. In addition, quasi static hysteresis loops for the present Co₂₅Pt₇₅ samples with uniaxial perpendicular anisotropy could be determined with this method. The shape of these hysteresis loops basically coincide with that from conventional polar MOKE loops [5].

EXPERIMENTAL

The determination of domain patterns is based on a polarisation microscope setup described elsewhere [6]. The imaging is based on the polar Kerr effect. Image acquisition is performed with a highly resolving CCD-Camera with linear response in intensity. By using frame data averaging in a fast real-time image processor we were able to reduce the noise and drastically enhance the contrast in the domain imaging. Subtracting background images further improves the quality of the data.

Co₂₅Pt₇₅ alloy films were prepared by e-beam evaporation in high vacuum with a base pressure of $\sim 10^{-8}$ mbar at a typical deposition temperature of about 220°C. Polished Si(100) substrates were used with 400 Å thick SiN_x etched buffer layers [7]. Alloys were obtained by subatomic layering of Pt and Co as described previously [1-2]. The final composition was determined with x-ray fluorescence. Typical film thicknesses cover the range from $d=100$ Å to $d=300$ Å. All measurements were carried out at room temperature in a high field magnet arrangement (up to 1 T) especially designed for microscopic applications. The characterisation of the film structure yields for the alloy samples cubic symmetry with fcc(111) orientation predominantly parallel to the film plane [1-3]. The films are polycrystalline and average grain sizes based on x-ray diffraction measurements and surface topography characterization in the order of 100-200 Å have been observed [5].

RESULTS AND DISCUSSION

Figure 1 shows hysteresis loops of two Co₂₅Pt₇₅ alloy samples with $d=100$ Å and $d=200$ Å thicknesses. All data points were obtained from domain images at the respective field steps by determining the ratio of up and down magnetised areas after background subtraction and normalized with respect to the field of view.

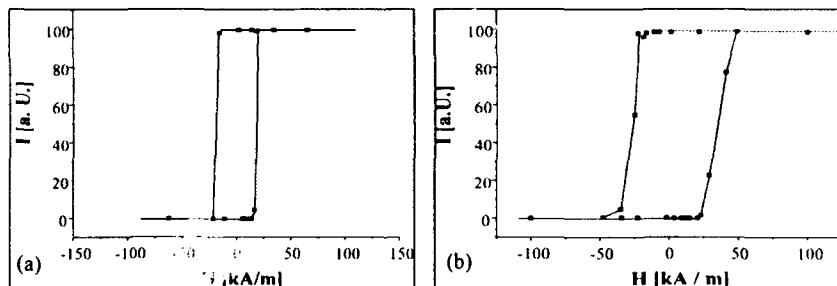


Fig.1: Hysteresis loop of Co₂₅Pt₇₅ alloy film with (a) $d = 100$ Å and (b) $d = 200$ Å determined from domain pattern analysis.

The images were acquired after relaxation of the domain pattern to obtain quasi-static hysteresis loops. Systematic investigation of the magnetization curves of films with different varying film thicknesses yields an increase in coercivity H_c with growing film thickness. In all

samples ($d=100,200,300\text{\AA}$), we found $M_r/M_s = 1$. With increasing thickness the nucleation points in the hysteresis loops become less well defined and their shape becomes rounded. A detailed analysis of domain shapes at the nucleation field is shown in Fig. 2. We find in general, that with increasing film thickness an increasing number of small sized domains is being formed at the nucleation field

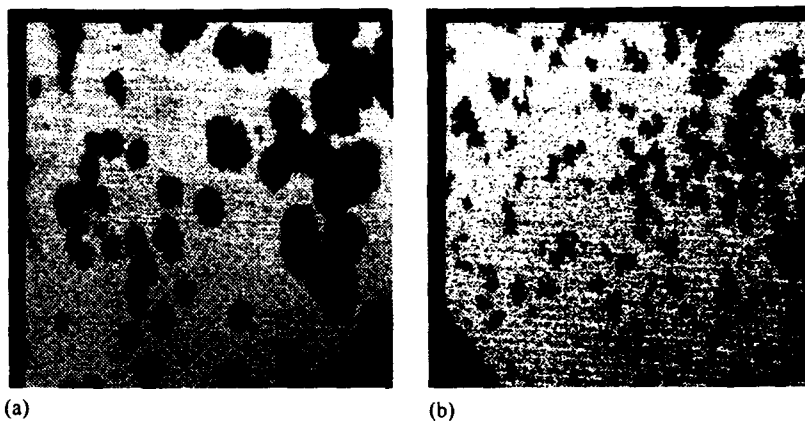


Fig. 2: Typical domain shapes at the nucleation points of two different $\text{Co}_{25}\text{Pt}_{75}$ alloy films (a) $H=15.5\text{ kA/m}$ and $d=100\text{\AA}$ (b) 20.5 kA/m , $d=200\text{\AA}$. The white area represents up and the dark area down domains, respectively.

At a film thickness of 100\AA the magnetization reversal is dominated by domain wall motion while at larger thicknesses nucleation of domains seems to prevail. An analysis of the wall structure with respect to the domain area yields evidence for a correlation between the fractal dimension of the domains and the film coercivity. In general we find, that the fractal dimension increases with H_c . Figure 3 displays a series of domain pattern images from a $\text{Co}_{25}\text{Pt}_{75}$ alloy film of $d=100\text{\AA}$ after application of a reverse field step, i.e. a magnetic field opposite to the actually saturated magnetization state. The field is stepped to a given negative field value near the nucleation field within one second and kept constant thereafter. Domain pattern images are gathered subsequently in time intervals of a few seconds. One can easily follow the growth of the dark shaded down domains. After a few minutes complete relaxation into saturation is obtained. The area of magnetization collinear with the external field is plotted in Fig. 4 for two different field steps of $H=15.5\text{ kA/m}$ and 16.8 kA/m , respectively. The experiment obviously indicates that the slope of the magnetization curve vs. time becomes steeper as the negative field step is increased. Small field amplitudes result in magnetization curves with very flat initial slope. Refined analysis in this time regime shows evidence for a noisy Barkhausen type change of the magnetization.

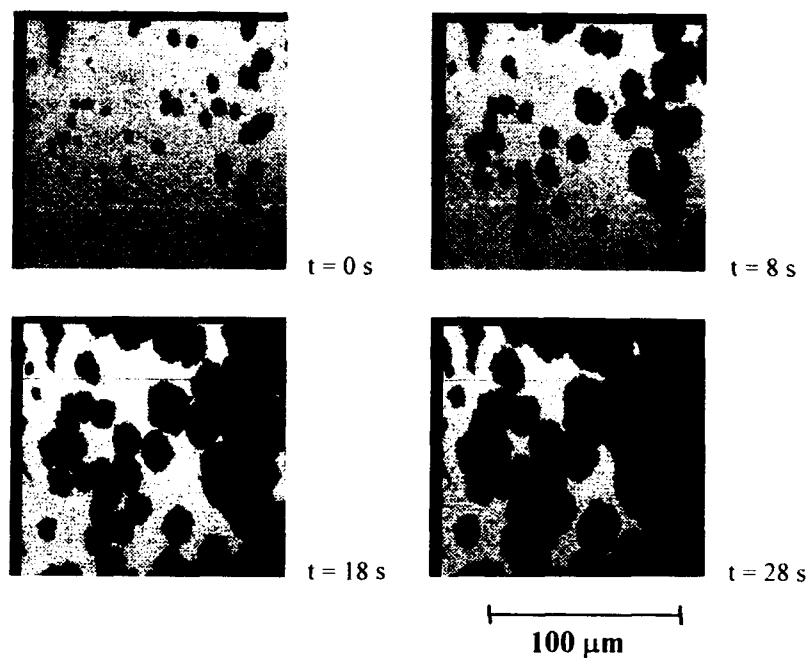


Fig.3: Time evolution of the domain shape after application of reverse field of $H = 15.5\text{ kA/m}$ in a 100\AA thick $\text{Co}_{25}\text{Pt}_{75}$ alloy film.

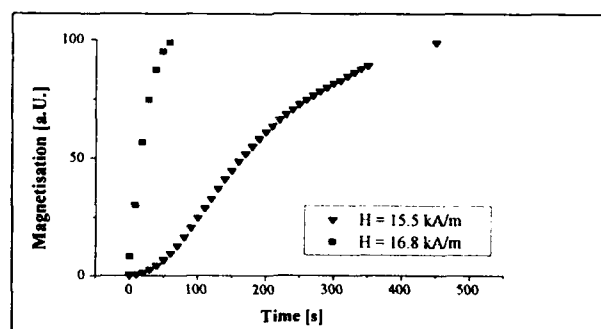


Fig.4: Time dependence of magnetization after application of reverse magnetic field

Similar results for the field dependence of relaxation time were reported for Co/Au ultrathin films [2]. A first analysis of our results in terms of the Fatuzzo model [8] shows that this cannot be applied in all cases to the present samples. Additional work has to be done to determine the ratio of nucleation- and domain-wall-dominated reversals.

CONCLUSION

We have investigated a series of $\text{Co}_{25}\text{Pt}_{75}$ alloy samples with various film thicknesses. The coercivity of these alloys increases with total film thickness. The magnetization reversal mechanism changes from a wall-motion-dominated type to a nucleation-dominated type as the film thickness increases. Magnetic aftereffect measurements show a relaxation behaviour which is only partly in accordance with the Fatuzzo model. Although a correlation between the fractal dimension of the domains and the coercivity is indicated, this clearly needs to be investigated in further detail.

REFERENCES

- [1] D. Weller, H. Brändle, G. Gorman, C.-J. Lin, H. Notarys *Appl. Phys. Lett.* 61,2726(1992)
- [2] D. Weller, H. Brändle, C. Chappert *J. Magn. Magn. Mater.* 121,461(1993)
- [3] D. Weller, J. Hurst, H. Notarys, H. Brändle, R.F.C. Farrow, R. Marks, G. Harp *J. Magn. Soc. Jpn. Suppl.* 51,72(1993)
- [4] J. Pommier, P. Meyer, G. Penissard, J. Ferré, P. Bruno, D. Renard *Phys. Rev. Lett.* 65,2054(1990)
- [5] V. Harzer, B. Hillebrands, I.S. Pogosova, M. Herrmann, G. Güntherodt, D. Weller *MRS'93 San Francisco*, April 12-16 (1993)
- [6] S. Botermann, W. Kleemann, T. Kleinfeld, M. Schlusen, Y. J. Wang *Proc. of ISPM'92, Beijing*
- [7] D. Weller, H. Notarys, T. Suzuki, G. Gorman, T. Logan, I. McFadyen, C.J. Chien *IEEE Trans. Mag.* 28,2500(1992) and references herein
- [8] E. Fatuzzo *Phys. Rev.* 127,1999(1962)

VANADIUM AS OVERLAYER ON Ag(001)

H. NAIT-LAZIZ *, C. DEMANGEAT * and A. MOKRANI **

* IPCMS, Université Louis-Pasteur, 4, rue Blaise Pascal, 67070 Strasbourg, France

** Laboratoire de Physique du Solide, 2, rue de la Houssinière, 44072 Nantes, France

ABSTRACT

The electronic and magnetic structure of small vanadium clusters adsorbed on Ag(001) is studied as a function of the exchange integral J of the Hubbard Hamiltonian and cluster size with bcc structure. For each topological arrangement, the transition from nonmagnetic to magnetic order is characterized. As in the case of films (1 or 2 layers thick) epitaxially grown on Ag(001), antiferromagnetic coupling between V atoms is usually obtained. However, because the symmetry is lower in the present case, various magnetic configurations are displayed.

INTRODUCTION

Since a long time, vanadium has attracted interest for its specific magnetic properties: the isolated atom has a permanent moment of $3\mu_B$; however it is well known that bulk V is paramagnetic. Very recently, Bouarab et al [1] and Dorantes-Davila et al [2] have discussed respectively the onset of magnetic moments of vanadium free standing layers or as overlayer on Ag(001) and of free standing clusters of vanadium. The local magnetic moment, magnetic order and average magnetic moment are calculated for $T=0K$ as a function of the intra-atomic exchange integral J . In the present communication we will consider clusters of vanadium adsorbed on Ag(001). A one-layer cluster of 21 atoms and a two-layers cluster of 33 atoms are considered (figure 1). Free standing V clusters have been shown to become magnetic when the number of atoms is not too high [2, 3]. Two contradictory effects appear to be in work for these clusters: a supermagnetic effect [4] leading to a cancellation of the magnetic moment in the case of small size of the vanadium cluster and a coordination number effect which tends to cancel the moment of the cluster when the size is too great [2, 3]. Through Stern-Gerlach measurements, Douglas et al [4] have shown that the maximum true moment consistent with uncertainty is considerably below the calculated values of Dorantes-Davila et al [2] and Feng-Liu et al [3]. The small value may indicate that the lattice spacing is less than the bulk value. In order to stabilize the lattice parameter, experimentalist do perform growth of V on Ag(001). As an example, Moodera and Meservey [5] have recently observed through surface impedance measurements, that small clusters of vanadium on Ag(001) do present interesting magnetic properties. Moreover, they have observed that these magnetic properties do depend drastically on the size of the adsorbed cluster. Recently, Dorantes-Davila and Dreyssé [2] have pointed out that a first-order transition appears for a critical value J_c , for all sizes of the cluster. Therefore, one have to be very cautious in the study of this type of systems. Christensen et al [6] have determined through Linear-Muffin-Tin-Orbital

(LMTO) method the values of the exchange integrals for the transition metal elements. However this is a bulk calculation and thus the values of the exchange integral may vary with the size of the cluster. Moreover it has been shown by Stollhof et al [7] that the local density approximation (LDA) used by Christensen et al largely neglects correlation. For this reason, in the present communication, we derive the magnetic moments of small clusters of V adsorbed on Ag(001) in terms of J .

RESULTS

The cluster of 21 atoms displays strong peaks in the local density of states (LDOS). These peaks are related to the low coordination number of the V atoms and are more pronounced than in the case of V overlayer on Ag(001) [1]. We report in figure 2 the polarization of the nanostructure of 21 V atoms on Ag(001); the polarization of the silver atoms is negligible so that we do not report on it here. The calculations have been performed in the framework of the tight-binding method in the unrestricted Hartree-Fock approximation to the Hubbard Hamiltonian [1, 2]. In a previous paper [9], we reported the polarization of the V atoms for $J=0.35$ eV. Here we extend it to different values of J because the exact value of J is not well known.

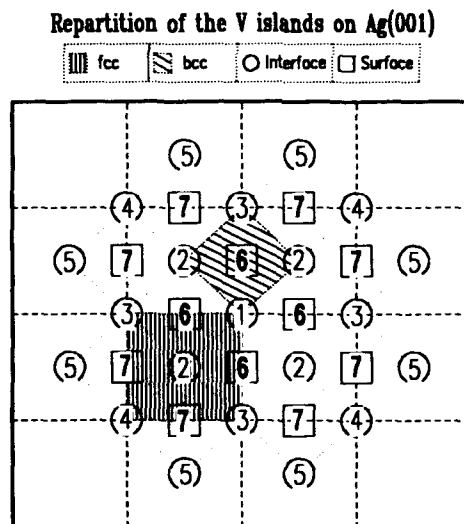


Fig 1: Disposition of the V atoms in the two nanostructures adsorbed on Ag(001). The two hatched regions correspond to a (001) cut of the fcc Ag (big region) and bcc V (small region) rotated by 45° . The atoms numbered 1,2,3,4 and 5 are in the V-layer adjacent to Ag and consist of 21-atoms nanostructure. The atoms 6 and 7 are on the top V-layer, located in symmetrical positions above the 21 V-atoms nanostructure. Atoms numbered from 1 to 7 are part of a 33 V-atoms nanostructure.

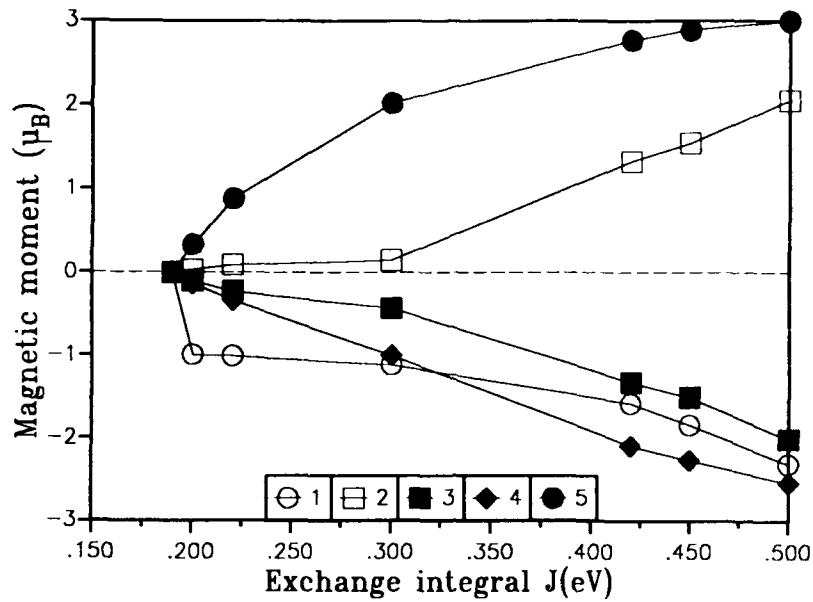
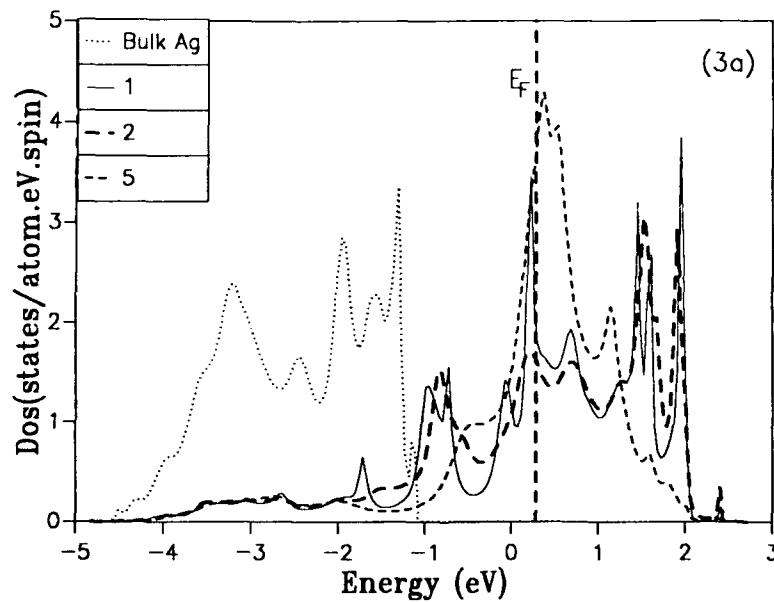


Fig 2: Magnetic moment $\mu(\mu_B)$ per atom, on the 5 inequivalent V atoms in the 21 atoms nanostructure on Ag(001)



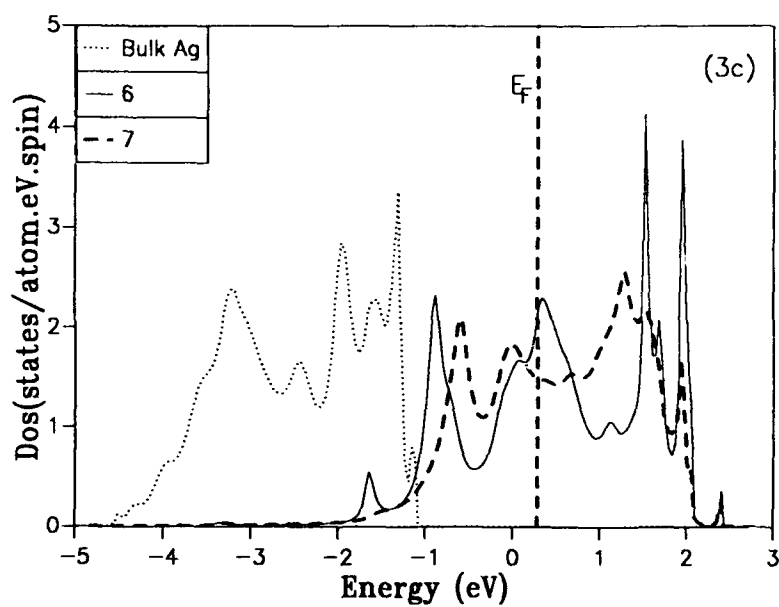
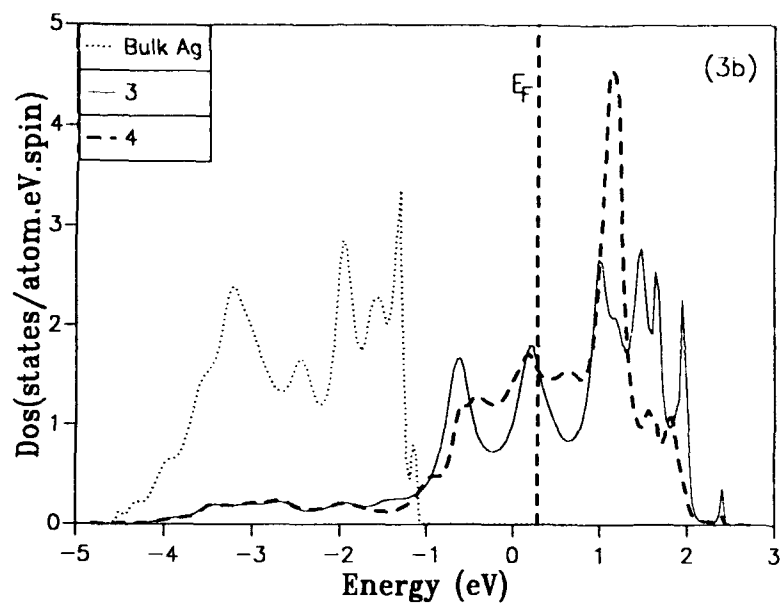


Fig 3(a,b,c): Local density of states for the 7 inequivalent V atoms in the 33 atoms nanostructure on Ag(001).

On figure 2 it can be shown that in-plane antiferromagnetism is present in the one-layer cluster. For reasonable values of J (i.e. J of the order of 0.4-0.5 eV), the less coordinated atom (only V atoms count for this number because the Ag d-bands are far apart so that the effect of the hybridization is small), has the strongest magnetic moment. The high magnetic moment of this external atom of type 5 can be explained through Stoner criterion because it presents the highest LDOS at the Fermi level.

In figure 3, we report the LDOS for the cluster of 33 V atoms. This structure consists of 12 atoms adsorbed on the previously discussed 21 atoms structure (see fig. 1). The LDOS of the V atoms are less peaky than in the case of the 1-layer cluster of 21 atoms. This arises from the fact that the V atoms are more coordinated as before (less atomic-like). Also at the Fermi level, the LDOS are smaller and consequently the onset of magnetism is for higher values of J (figs 2 and 4). Figure 4 displays the magnetic moments for the cluster of 33 atoms: atoms of type 6 and 7 have two nearest V neighbors with a positive polarization and two others with an opposite polarization. Therefore, they are frustrated and thus they display a low magnetic moment for J values less than 0.45 eV.

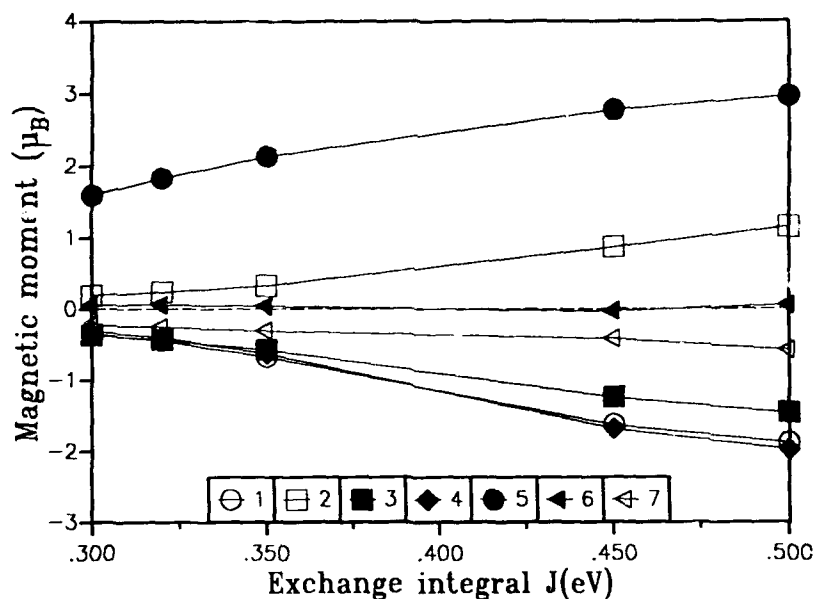


Fig 4: Magnetic moment $\mu(\mu_B)$ per atom, on the 7 inequivalent V atoms in the 33 atoms nanostructure on Ag(001)

CONCLUSION

This calculation has clearly shown that the vanadium atoms with a small coordination are clearly magnetic. This is in agreement with the experimental result of Moodera and Meservey [5]. However, the polarization map obtained is very complicated and similar to the results obtained by Dorantes Davila et al [2] in the case of free-standing vanadium clusters. For the 1-layer nanostructure of 21 atoms on Ag(001) an in-plane AF solution may not be unique [9] and detailed calculations have to be done for particular values of J . Moreover, a total energy calculation have to be performed [8]. The 2-layer nanostructure of 33 V atoms is no more AF but presents some frustration which decreases the value of the considered V atoms.

REFERENCES

1. S. Bouarab, H. Nait-Laziz, C. Demangeat, A. Mokrani and H. Dreyssé, Phys. Rev. **B,46**, 889 (1992); and references therein.
2. J. Dorantes-Davila and H. Dreyssé, Phys. Rev. **B,46**, 3857 (1993); and references therein.
3. Feng Liu, S. N. Khanna and P. Jena, Phys. Rev. **B,43**, 8179 (1991).
4. D. C. Douglas, J. P. Bucher and L. Blomfield, Phys. Rev. **B,45**, 6341 (1992).
5. J. S. Moodera and R. Meservey, Phys. Rev. **B,40**, 8541 (1989).
6. N. E. Christensen, O. Gunnarsson, O. Jepsen and O. K. Andersen, J. Physique (Paris) **49**, C8-17 (1988).
7. G. Stollhof, A. M. Oles and V. Heine, Phys. Rev. **B,41**, 7028 (1990).
8. H. Nait-Laziz, PhD thesis, University Louis-Pasteur, Strasbourg, (1993); unpublished.
9. H. Nait-Laziz, C. Demangeat and A. Mokrani, J. Magn. Magn. Mat. **121**, (1993), in press.

STRONG INFLUENCE OF Tb CONCENTRATION ON DOMAIN STRUCTURE AND KERR EFFECT OF $\text{Tb}_x\text{Fe}_{1-x}$ THIN FILMS

V. FLORESCU, C. RAU AND N. J. ZHENG

Rice University, Department of Physics and Rice Quantum Institute,
Houston, Texas 77251 - 1892.

ABSTRACT

Amorphous TbFe films with perpendicular magnetic anisotropy are attracting wide attention as promising candidates for erasable high - density magneto - optical recording and thermomagnetic printing. $\text{Tb}_x\text{Fe}_{1-x}$ thin films with $0 \leq x \leq 0.37$ are deposited on glass substrates using r.f. sputtering. The magnetic remanent domain structures are studied at room temperature using the longitudinal and polar Kerr effect. Samples with $0 \leq x \leq 0.23$ exhibit magnetic in-plane anisotropy, while samples with $0.26 \leq x \leq 0.37$ possess uniaxial anisotropy with easy axis perpendicular to the film plane. The remanent domain structures depend strongly on Tb content. High remanence and high coercivity are found for samples with $0.27 \leq x \leq 0.34$ which is confirmed by additional vibrating sample magnetometer (VSM) measurements.

INTRODUCTION

Amorphous rare-earth-transition metal alloys are widely investigated for the use as magneto-optical recording media.^{1,2} Moreover it has been suggested that TbFe films could provide suitable media for magnetic printing.^{3,4} In magnetic printing, latent images are produced thermomagnetically and developed using magnetic toner particles.⁵ For such an application, films with high remanence and/or sufficient thickness are required in order to create a strong force on the toner particles. The domain structure and magnetic properties (anisotropy energy) depend strongly on the composition⁶ and on preparation parameters (substrate temperature).⁷

In this paper, we report the influence of Tb concentration on the remanent domain structure and on the magnetic properties (saturation magnetization, coercivity and remanence) of thin TbFe films.

EXPERIMENTAL

In our experiments, we use $\text{Tb}_x\text{Fe}_{1-x}$ thin films with a Tb content x between 0 and 0.37. The deposition was performed by co-sputtering in a pure argon atmosphere (99.997 %) using a target-substrate (glass) distance of 35 mm. These deposition parameters are used for all samples. Details about the sputtering conditions are reported elsewhere.^{8,9} The composition of the films is determined by using X-ray fluorescence analysis (XFA) where values of $x=0, 0.17, 0.23, 0.26, 0.27, 0.30, 0.31, 0.34, 0.37$ are found. Film thicknesses, t , are about 150 nm. All the samples are coated with a thin Al_2O_3 protective layer. The size of the sample is 30 x 30 mm². For further measurements, the samples are cut to a size 15 x 15 mm². Each set of

samples is used for different measurements in order to obtain reliable data. Auger electron spectroscopy (AES) measurements are performed in order to check composition data obtained by using XFA and to obtain data about films homogeneity in the growth direction. Using a DRON - 2 diffractometer, the angular distribution of X - ray diffracted intensities is measured using Mo K α radiation up to :

$$K_{\max} = 4\pi \sin\theta_{\max} / \lambda = 15 \text{ \AA} \quad (1)$$

The radiation is monochromatized by using a concave quartz crystal placed in front of a scintillation counter. Computerized data processing allowed for corrections of X-ray scattering in air and in the glass substrate as well as absorption in the film. The first two contributions are estimated by measuring, under the same experimental conditions an annealed Au foil and a clean substrate respectively. The absorption $\mu \cdot t$ in the film (μ = linear absorption coefficient) is measured with Mo K α radiation in transmission geometry with reference to a clean substrate. The remanent magnetic domain structure is directly observed by using the Kerr - effect and a digital contrast enhancement scheme.¹⁰ The local hysteresis loops are studied by using a He-Ne laser in the longitudinal and polar Kerr - effect configuration. Additional magnetization (M) versus magnetic field (H) loop measurements were made with a vibrating sample magnetometer (VSM), calibrated with a Ni standard in a 20 kOe applied field. All the samples are measured in two position, perpendicular and parallel to applied field.

RESULTS AND DISCUSSION

AES depth profile analyses shows that our films are homogeneous in the growth direction. The Fe and Tb concentration does not change with increasing film depth and the values are similar to those determined by XFA. X - ray diffractograms show that films with $0.17 \leq x \leq 0.37$ are perfectly amorphous. The diffractogram patterns are quite similar to those reported in ref 9 for TbFe amorphous alloys, showing a main peak at $K = 1.43 \text{ \AA}$ and further weaker details. For films with x ranging between 0.17 and 0.27, the ratio K_2/K_1 is around 1.56. For films with $x = 0$, the X - ray diffraction patterns indicates, as expected the presence of polycrystalline Fe. Fig. 1 shows, for $x=0$ four different remanent domain structures obtained with MOKE. Using longitudinal Kerr effect conditions various domain pattern are observed after reducing an applied magnetic field from saturation value to zero and by selecting four different in-plane directions. (see Figs. 1A-1D). The single domain state at saturation breaks up into a multidomain configuration after demagnetizing the films by a reducing the applied magnetic field to zero. No perpendicular magnetization could be observed. However, there is hard to establish an orientation of the spontaneous magnetization of the domains versus crystallographic directions because of polycrystalline Fe sample. The domain structures presented in Fig. 1 are very close to those reported in ref. 11 (domains size of 2000 \AA thick, for a 81 - Permalloy film). We notice that for Permalloy film demagnetized in a c magnetic field along the easy axis, the obtained patterns are similar to those presented in our Fig 1A. However, Permalloy films demagnetized in a c magnetic field along the hard axis, the obtained patterns are near identical to those shown in our Fig. 1C. This comparison suggests for our polycrystalline Fe sample a sort of hierarchy for the in - plane easy directions : not all are really easy directions. Fig. 2 shows the characteristic remanent domain structure for samples with $x = 0.23$ (A), 0.26 (B), 0.34 (C) and 0.37 (D). The patterns from Fig. 2A are obtained by using longitudinal Kerr effect, while Fig. 2 B-2 D, by using polar Kerr effect. The type of remanent domain structure in Fig. 2 B-2 D are very different from the domains in Fig. 2A and Fig. 1. It is clear that we have now a structure with free magnetic poles, that can be led into a magnetic

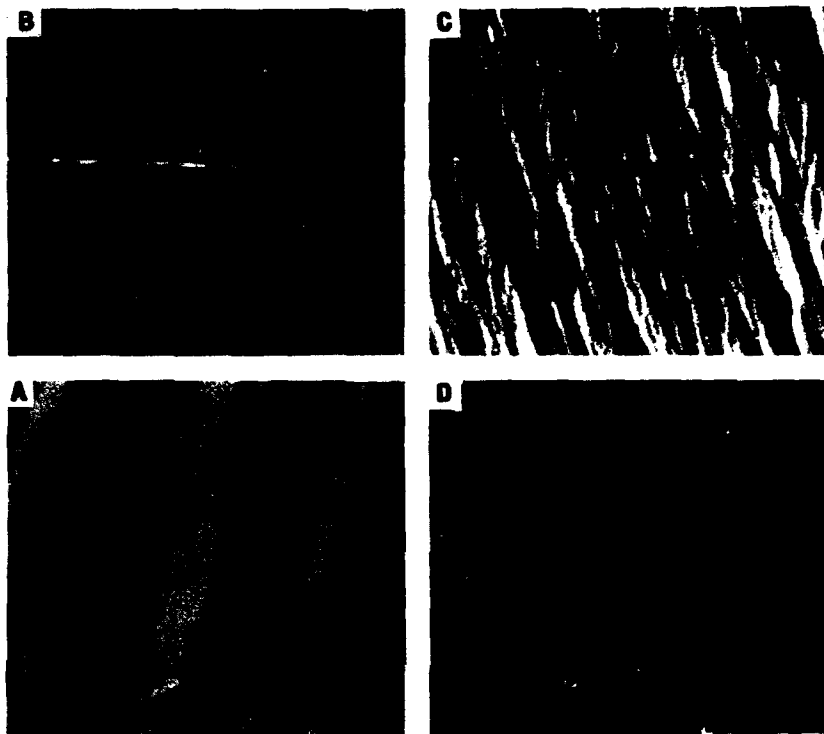


Fig. 1 : Four different remanent domain structures of Fe sample. (All photographs have the same magnification)

applied field to a bubble structure. Furthermore, in Fig. 2B there are two big domains one black and one white. Inside of the white one there is possible to be notice the circular black domains with different diameters. Some of them seems to have the bubble dimensions. There is also interesting to point out the differences between Fig. 2A and 2B which represented the two remanent patterns before and over composition with compensation temperature near room temperature.¹² In general the domain structure depends strongly on the direction of the uniaxial anisotropy and the magnitude of magnetization which is influenced by the compensation temperature.¹³ This statement is also confirmed by our domain observations, Fig. 2B-2D, where the domain dimensions are gradually decreasing with increasing the Tb content far away to the composition with compensation temperature near room temperature. One of the main conclusion results from the domain observation is that samples with $0 \leq x \leq 0.23$ show in plane anisotropy, while the sample with $0.26 \leq x \leq 0.37$ show uniaxial anisotropy with the easy axis perpendicular to the film plane. A typical example of a local hysteresis loop obtained by using a He-Ne laser in the longitudinal Kerr effect for the Fe polycrystalline sample is shown in Fig. 3. Similar curves have been obtained for the sample with $0 \leq x \leq 0.23$, proving that easy axis is lying in the plane of samples. For all the samples additional M-H loop measurements, using a VSM with the magnetic field applied perpendicular and parallel to the film surfaces were carried out. Fig. 4 shows the dependence of coercivity (H_c) versus saturation magnetization (M_s). The sample with $x = 0$ has the lowest value of H_c and the

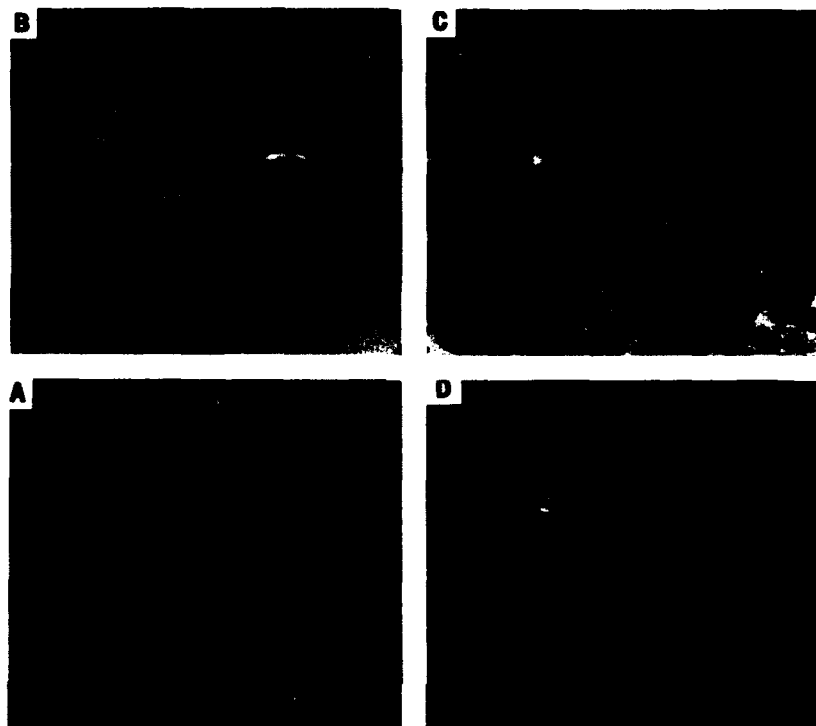


Fig. 2 : The remanent domain structures for the samples $x=0.23$ (A), 0.26 (B), 0.34 (C), and 0.37 (D). (All photographs have the same magnification)

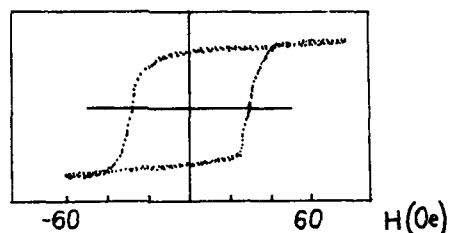


Fig. 3 : Local hysteresis loop for the sample with $x=0$

maximum value of M_s . For the samples with $0.27 \leq x \leq 0.34$ the H_c always has value over 1.26 kOe with the maximum of 4.27 kOe . The quite exponential decrease of coercivity with increasing the saturation magnetization in the condition of Tb content variation has also reported by Higashi.⁴ In order to check if our Tb-Fe films with uniaxial anisotropy are suitable for obtaining high remanence magnetization required for magnetic printing we show Fig. 5. It is evident from this that samples with $0.26 \leq x \leq 0.34$ have a very high remanence

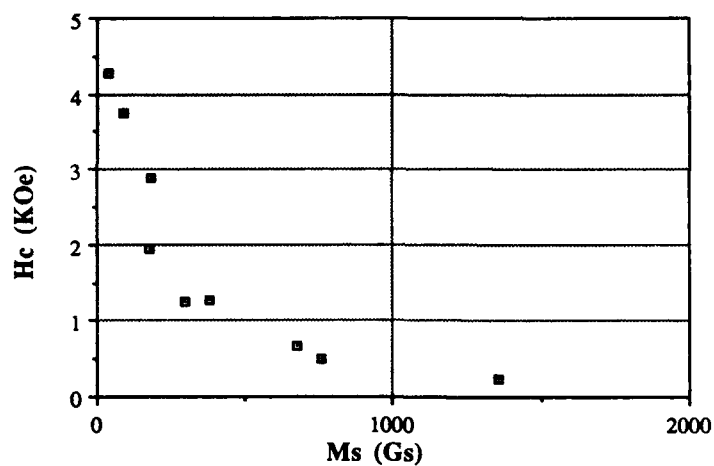


Fig. 4 : The dependence of coercivity (H_c) versus saturation magnetization (M_s) for Tb-Fe serie samples.

magnetization with M_r / M_s between 84% and 100%. It is also possible in this Fig. to make the distinguish between samples with in- plane and uniaxial anisotropy and to confirm the domain structure observations .

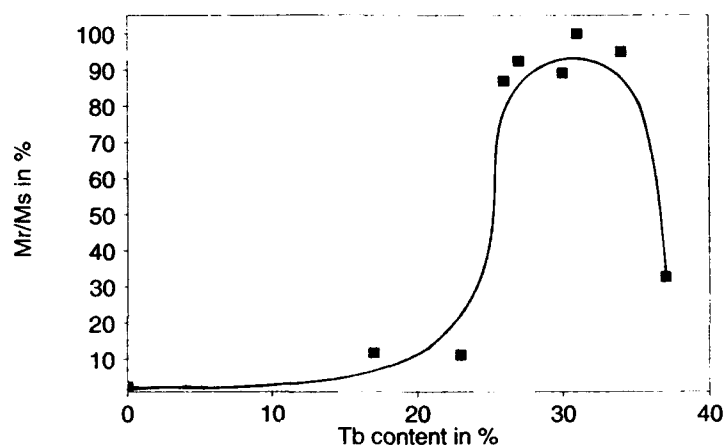


Fig. 5 : The dependence of M_r / M_s ratio versus Tb content for Tb-Fe serie samples.

CONCLUSIONS

- Demagnetized $\text{Fe}_x\text{Tb}_{1-x}$ films show strongly different domain patterns below and above composition with $x=0.23$.
- The magnetic domain observation and additional magnetic measurements show that samples with $0 \leq x \leq 0.23$ exhibit in-plane anisotropy, while samples with $0.26 \leq x \leq 0.37$ possess uniaxial anisotropy with easy-axis oriented perpendicular to the film plane.
- High magnetic remanence is found for samples with $0.27 \leq x \leq 0.34$.

ACKNOWLEDGMENTS

We thank Prof. A. Hubert for using the magnetic domain observation equipment and Mr. M. Haidl for his assistance in VSM measurements. This work was supported by the National Science Foundation, the Welch Foundation, the Texas Higher Education Coordinating Board and the Alexander von Humboldt Foundation.

REFERENCES

1. P. Hansen and H. Heitmann, IEEE Trans. Magn. **MAG - 25**, 4390 (1989).
2. N. Imamura, S. Tanaka, F. Tanaka and Y. Nagao, IEEE Trans. Magn. **MAG-21**, 1607 (1985).
3. M. Komori, T. Numata, K. Tsutsumi, S. Inokuchi and Y. Sakurai, IEEE Trans. Magn. **MAG-20**, (1984).
4. J. Higashi, T. Numata, S. Inokuchi and Y. Sakurai, Japan J. Appl. Phys., **26**, 1262 (1987).
5. J. J. Eltgen and J. G. Maguenet, IEEE Trans. Magn. **MAG - 16**, 961 (1980).
6. C. J. Lin, J. C. Suit and R. H. Geiss, J. Appl. Phys. **63**, 3835 (1988).
7. Y. Takeno, M. Suwabe, T. Sakurai and K. Goto, Japan J. Appl. Phys. **25**, L 657, (1986).
8. V. Florescu, Zaki AL - Tamimi, M. D. Serbanescu, R. Manaila and W. A. Grant, IEEE Trans. Magn. **MAG -24**, 1734 (1988).
9. V. Florescu, M. D. Serbanescu, R. Manaila, W. A. Grant, J. Magn. Mag. Mat., **92**, 137 (1990).
10. F. Schmidt, W. Rave and A. Hubert, IEEE Trans. Magn. **MAG - 21**, 1596 (1985).
11. B. D. Cullity, Introduction to Magnetic Materials (Addison - Wesley Publishing Comp. Inc., 1972) p. 436.
12. P. Hansen, C. Clausen, G. Much, M. Rosenkranz and K. Witter, J. Appl. Phys. **66**, 756 (1989).
13. P. Hansen, J. Appl. Phys. **63**, 2364 (1988).

NEUTRON AND X-RAY SCATTERING STUDIES OF $(\text{FeF}_2)_m(\text{CoF}_2)_n$ MULTILAYERS

D. LEDERMAN^{a,b}, D. P. BELANGER^c, J. WANG^c, S.-J. HAN^c,
C. PADUANI^{c,d}, C. A. RAMOS^{b,e}, AND R. M. NICKLOW^f

^aDept. of Physics, University of California, San Diego, La Jolla, CA 92093-0319

^bDept. of Physics, University of California, Santa Barbara, CA 93106

^cDepartment of Physics, University of California, Santa Cruz, CA 95064

^dDepartment of Physics, Univ. Fed. de Santa Catarina, Florianopolis, Brazil

^eCentro Atómico Bariloche, 8400 Bariloche, Río Negro, Argentina

^fSolid State Division, Oak Ridge National Laboratory, Oak Ridge TN 37831

ABSTRACT

We have performed elastic neutron scattering measurements of the staggered magnetization in $(\text{FeF}_2)_m(\text{CoF}_2)_n$ superlattices. Thermal expansion measurements, which are proportional to the magnetic contribution to the specific heat, were also carried out using high resolution x-ray diffraction. One of the two measured samples has thicknesses of $m = n \approx 4.5$ and the other $m = 26$ and $n = 28$ monolayers, as determined from high angle x-ray $\theta - 2\theta$ scans. In the $m = n = 4.5$ sample, only one transition is observed at $T_N = 62.9\text{K}$. Analysis of the neutron data, including the rounding effects, indicates an effective $\beta \approx 0.42$. This does not compare well with the 3D Ising exponent $\beta = 0.325$. The X-ray data also show the existence of only one specific heat anomaly at $T = 62.8\text{K}$. For the $m = 26, n = 28$ sample, dips in the staggered magnetization and peaks in the thermal expansion were observed at $T \approx 40\text{K}$ and 74K . The higher temperature anomaly, associated primarily with the FeF_2 layers, is sharper than the lower one, which is presumably rounded by the staggered ordering field imposed by the long range order in the FeF_2 regions on the CoF_2 regions.

INTRODUCTION

Multilayered epitaxial insulating antiferromagnetic films are promising systems for the study of a variety of physical models. Since they can be fabricated with overall thicknesses of a few microns, they can be used to obtain extinction-free Bragg scattering results. This has been demonstrated[1] using a single $0.8\text{ }\mu\text{m}$ thick layer of FeF_2 grown on a ZnF_2 substrate to obtain the critical behavior of the staggered magnetization for reduced temperatures of $0.002 < |t| < 0.025$. In the same manner, *multilayer* thin films can be used to obtain the staggered magnetization near phase transitions using neutron scattering techniques. Additional information may be obtained from high resolution x-ray techniques. For example, the thermal expansion coefficient of a film α , which is proportional to the magnetic contribution to the specific heat, may be measured with x-rays, thus providing the specific heat critical behavior[2, 3, 4].

Bulk crystals of the isomorphous FeF_2 and CoF_2 antiferromagnets have been well characterized[7, 8]. Both antiferromagnets are Ising-like in their critical behavior because of the large anisotropies which force the spins to align along the c-axis. The effective exchange interaction strength in CoF_2 is much weaker than that of FeF_2 . In both cases the dominant exchange is between the body-center and body-corner next-nearest-neighbor ions. The corresponding transition temperatures are $T = 78\text{K}$ and $T = 38\text{K}$ for FeF_2 and CoF_2 , respectively. The FeF_2 - CoF_2 *mixed* system can be well modeled by Ising spins for which the next-nearest-neighbor interactions are equal to the geometric mean of the interaction strengths of the two materials[9].

Epitaxial *single* thin films made of these materials have been studied using a variety of techniques and their behaviors have been described in some detail[10]. An important result of these measurements is that the fundamental magnetic interactions in single thin films, ranging from

0.25 μm to 3 μm in thickness, do not measurably change from their bulk values.

Conversely, epitaxially grown *multilayers* in many instances have unique properties. For example, antiferromagnetic layers separated by nonmagnetic layers are useful for studying the crossover from three-dimensional (3D) to two-dimensional (2D) critical behavior[3, 4]. Alternatively, multilayers consisting of antiferromagnetic materials with differing nonzero exchange interactions may be fabricated to study the effects of a modulating exchange interaction along one direction.[2, 5, 6]

In the study described here, we investigated the dependence of cooperative Ising phase transitions in periodic multilayered structures, composed of two antiferromagnetic materials which have considerably different next-nearest-neighbor exchange interactions. This was done using x-ray diffraction and neutron Bragg scattering intensity measurements of antiferromagnetic $(\text{FeF}_2)_m(\text{CoF}_2)_n$ multilayered structures, whose superlattice period is composed of m monolayers of FeF_2 and n monolayers of CoF_2 . The results obtained from the x-ray and neutron scattering techniques are consistent with each other. We find that for a $m = n = 4.5$ sample only one transition is observed, while for a $m = 26, n = 28$ sample two anomalies are detected. The anomaly at the higher temperature, which is associated with the long-range ordering of the FeF_2 regions, is sharper than the lower one, which is presumably rounded by the long range order imposed by the FeF_2 on the CoF_2 regions.

PREPARATION AND STRUCTURAL CHARACTERIZATION

The details of the multilayer growth technique have been described elsewhere[10]. Briefly, the samples were grown along the c-axis direction via MBE at a base pressure $< 5 \times 10^{-9}$, a substrate temperature of 300° C, and a rate of approximately 3 Å/sec. Polished ZnF_2 single crystal discs, 1 cm in diameter and oriented along the [001] direction, were used as substrates because ZnF_2 is both non-magnetic and has an excellent lattice match with both FeF_2 and CoF_2 . Two samples were studied, with $m = n = 4.5$ and $m = 26, n = 28$, as determined from X-ray $\theta - 2\theta$ scans. The sample thicknesses are 0.29 μm and 0.91 μm , for the $m = n = 4.5$ and $m = 26, n = 28$ samples, respectively. A detailed x-ray analysis of these samples[3] indicates the presence of interface step disorder ≈ 1 monolayer in the $m = n = 4.5$ sample and ≈ 3.5 monolayers in the $m = 26, n = 28$ sample, with negligible interdiffusion. The widths of the main superlattice peaks indicate superlattice structural coherence lengths of 900 Å for the $m = n = 4.5$ sample and 2200 Å for the $m = 26, n = 28$ sample.

EXPERIMENTAL TECHNIQUES

X-rays were also used to study the specific heat critical behavior. The thermal expansion coefficient, $\alpha = \Lambda^{-1} \Delta\Lambda / \Delta T$, where Λ is the superlattice modulation length, which is proportional to the magnetic specific heat, was determined from the position of the main superlattice peak as a function of temperature. The specific details of this technique may be found elsewhere[2, 3, 4].

The staggered magnetization was independently studied using elastic neutron scattering techniques. The neutron scattering measurements were made at the Oak Ridge National Laboratory High Flux Isotope Reactor on a triple-axis spectrometer. The scattering took place in the horizontal plane about the (100) magnetic peak. The data of the $m = n = 4.5$ sample were taken with a pyrolytic graphite monochromator and analyzer at an energy of 14 meV. One graphite filter was used to reduce contamination from high energy neutrons. For the $m = 26, n = 28$ sample, a graphite monochromator and beryllium analyzer were used. Two graphite filters were used to reduce the background signal. Transverse peaks were resolution limited for both crystals, indicating a large crystalline coherence in the directions perpendicular to the film planes.

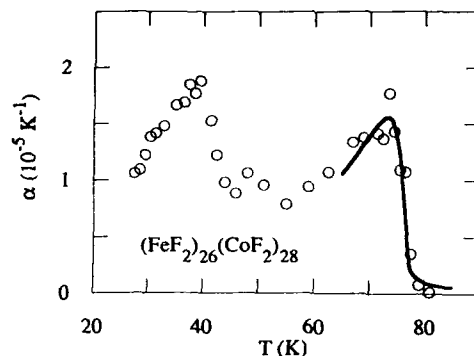


Figure 1: Thermal expansion coefficient α along the $[001]$ direction of the $m = 26, n = 28$ sample, determined from x-ray scattering measurements. The solid curve represents a fit to a rounded transition. This rounding is presumed to be caused by the step disorder in the superlattice, resulting in a distribution of layer thicknesses.

EXPERIMENTAL RESULTS

Using the x-ray and neutron scattering techniques described above, we characterized the Ising-like magnetic ordering taking place in two regimes of layer thickness. For the $m = 26, n = 28$ sample, a phase transition takes place at $T \approx 74K$ which can be associated with the ordering in the FeF_2 layers. This can be seen in Fig. 1 for the x-ray scattering, which shows the thermal expansion coefficient versus T , and in Fig. 2 which shows the neutron scattering behavior of the staggered magnetization. The x-ray data shown in Fig. 1 clearly have two peaks, both of which are rounded. In order to obtain $T_N \approx 74K$, the higher temperature peak was fit to a rounded 3D-Ising specific heat function. This function is represented by the solid curve. The rounding was presumed to arise from the step disorder present in the samples, causing different macroscopic FeF_2 regions to have different transition temperatures due to finite-size scaling.[3, 5]. The basic form $\alpha(T) = A_{\pm}|t^{-a}|$, with $t = 1 - T/T_N$, $a = 0.11$, and the amplitude ratio $A_+/A_- = 0.54$, corresponding to the 3D Ising model, was utilized.

The neutron Bragg scattering intensity is well described by the power law

$$I \sim M_s^2 = M_o^2 |t|^{2\beta} \quad (1)$$

where M_s is the staggered magnetization, $t = T/T_N - 1$, $T_N = 72.5$, and $\beta = 0.325$, as shown near the upper transition by the solid curve in Fig. 2. The slight discrepancy between the T_N values determined from x-rays and neutrons is probably due to the uncalibrated thermometer used in the neutron scattering experiment. We also show, with a dashed curve, what the second rise in intensity would look like if it were sharp and simply added to the intensity from the higher transition. The observed rise at lower temperatures, primarily from the ordering of the CoF_2 layers with the staggered field from the FeF_2 layers imposed at the layer interfaces, is rounded over a range of temperature of approximately 15 K.

The $m = n = 4.5$ sample shows only one clear anomaly, at an intermediate temperature $T = 69.2K$. The thermal expansion coefficient is shown in Fig. 3 and the neutron Bragg scattering intensity versus T is shown in Fig. 4. This sample is clearly near the limit in which the two kind of layers are strongly coupled. There is some rounding of the transition, presumably due to different macroscopic regions with slightly different values of m and n , each independently going through their phase transitions at slightly different temperatures. It is worth noting that

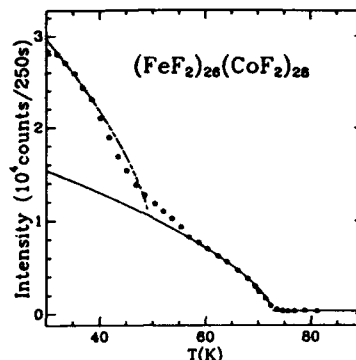


Figure 2: Neutron scattering intensity of the (100) magnetic peak for the $n = 26$, $m = 28$ sample. The solid curve represents a fit to $I \propto |t|^{2\beta}$ with $t = T/T_N - 1$ and $\beta = 0.325$. The dashed curve represents a second sharp transition added to the intensity of the solid curve.

the rounding of the neutron scattering data cannot be due to background fluctuations, since it has been experimentally shown that critical fluctuations are negligible[1]. For both the neutron and x-ray data, the solid curves are fits to appropriate power law behaviors with a Gaussian distribution in the transition temperature. From the thermal expansion data, the rounding was found to be $\delta T = 2.2$ K, while from the neutron scattering data $\delta T = 2.3$ K. Both fits yield a value of $T_N = 69.2$. However, the fitted value $\beta \sim 0.42$ is not in agreement with the well-known 3D Ising value $\beta = 0.325$. This disagreement could be explained if the order parameter in the FeF_2 and CoF_2 layers tended to grow at different rates below T_N . In this case, the intensity would not follow the expected power law behavior, except close enough to T_N so that the correlation length spans the entire superlattice period. This hypothesis is being tested via computer modeling of these multilayers, with the magnetic interactions at the interfaces equal to the geometric mean of the two intra-layer interactions.[11]

DISCUSSION

Clearly the FeF_2 layers attempt to order first as the temperature is lowered since bulk FeF_2 has a higher T_N than bulk CoF_2 . If the FeF_2 layers are sufficiently thick, the CoF_2 regions will only weakly affect the critical behavior in FeF_2 layers. In this case, the value of T_N will be lowered only slightly by the presence of the more weakly interacting CoF_2 layers. On the other hand, the CoF_2 layers cannot order independently of the FeF_2 regions, since the already well ordered FeF_2 layers will act on the Co^{++} spins near the interfaces, thus producing an effective staggered ordering field on the CoF_2 layers. Just as in the case of a ferromagnet with an applied uniform field, the antiferromagnetic layers with the effective staggered field on the surface spins will *not* experience a sharp phase transition, since the ordering field induces spin order above T_N . Since the strength of the effect of one kind layer on the other will depend upon the number of interface spins relative to the spins within layers, sufficiently thick CoF_2 layers will be only slightly affected by the FeF_2 . Hence, one would expect a slightly rounded transition only slightly elevated in temperature (with respect to T_N for bulk CoF_2) for thick CoF_2 layers.

As the layer thicknesses decrease, the behavior of the two kinds of layers will become more interdependent. In the extreme limit in which the thicknesses become one atomic layer ($m = n = 1$), the system can be considered to be a new crystalline structure with a single magnetic exchange interaction. Thus, only a single phase transition occurs, with no remnant of a second

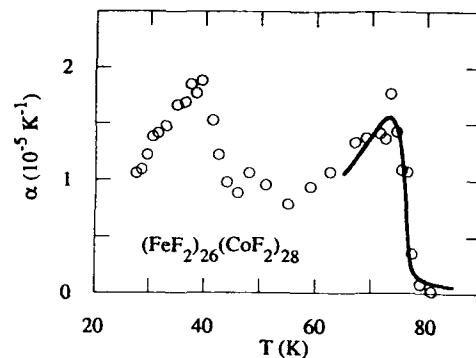


Figure 1: Thermal expansion coefficient α along the [001] direction of the $m = 26$, $n = 28$ sample, determined from x-ray scattering measurements. The solid curve represents a fit to a rounded transition. This rounding is presumed to be caused by the step disorder in the superlattice, resulting in a distribution of layer thicknesses.

EXPERIMENTAL RESULTS

Using the x-ray and neutron scattering techniques described above, we characterized the Ising-like magnetic ordering taking place in two regimes of layer thickness. For the $m = 26$, $n = 28$ sample, a phase transition takes place at $T \approx 74\text{ K}$ which can be associated with the ordering in the FeF_2 layers. This can be seen in Fig. 1 for the x-ray scattering, which shows the thermal expansion coefficient versus T , and in Fig. 2 which shows the neutron scattering behavior of the staggered magnetization. The x-ray data shown in Fig. 1 clearly have two peaks, both of which are rounded. In order to obtain $T_N \approx 74\text{ K}$, the higher temperature peak was fit to a rounded 3D-Ising specific heat function. This function is represented by the solid curve. The rounding was presumed to arise from the step disorder present in the samples, causing different macroscopic FeF_2 regions to have different transition temperatures due to finite-size scaling.[3, 5]. The basic form $\alpha(T) = A_{\pm}|t|^{-\alpha}$, with $t = 1 - T/T_N$, $\alpha = 0.11$, and the amplitude ratio $A_+/A_- = 0.54$, corresponding to the 3D Ising model, was utilized.

The neutron Bragg scattering intensity is well described by the power law

$$I \sim M_s^2 = M_0^2 |t|^{2\beta} \quad (1)$$

where M_s is the staggered magnetization, $t = T/T_N - 1$, $T_N = 72.5$, and $\beta = 0.325$, as shown near the upper transition by the solid curve in Fig. 2. The slight discrepancy between the T_N values determined from x-rays and neutrons is probably due to the uncalibrated thermometer used in the neutron scattering experiment. We also show, with a dashed curve, what the second rise in intensity would look like if it were sharp and simply added to the intensity from the higher transition. The observed rise at lower temperatures, primarily from the ordering of the CoF_2 layers with the staggered field from the FeF_2 layers imposed at the layer interfaces, is rounded over a range of temperature of approximately 15 K.

The $m = n = 4.5$ sample shows only one clear anomaly, at an intermediate temperature $T = 69.2\text{ K}$. The thermal expansion coefficient is shown in Fig. 3 and the neutron Bragg scattering intensity versus T is shown in Fig. 4. This sample is clearly near the limit in which the two kind of layers are strongly coupled. There is some rounding of the transition, presumably due to different macroscopic regions with slightly different values of m and n , each independently going through their phase transitions at slightly different temperatures. It is worth noting that

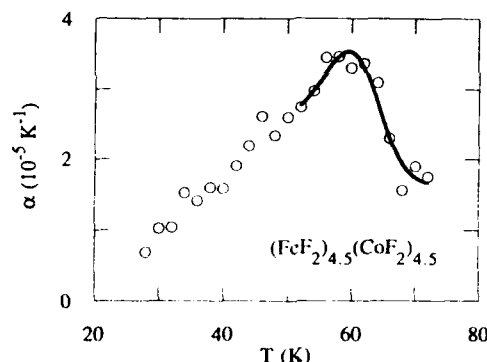


Figure 3: Thermal expansion coefficient α along the [001] direction of the $m = n = 4.5$ sample, determined from x-ray scattering measurements. The solid curve represents a fit to a rounded transition. This rounding is presumed to be caused by different macroscopic regions, with slightly different values of m and n , going through their transition at slightly different temperatures.

one, and the transition temperature should be intermediate between the bulk ones.

At intermediate layer thicknesses, one would expect the system to have two anomalies, as long as the strength of the FeF_2 layers' magnetic interactions is not strong enough to overcome the disorder in CoF_2 regions. If this is not the case, a single transition for the $m = n \neq 1$ system could be observed for sufficiently small values of m . The evolution of the behavior from large to small layer thickness has been described previously [3, 5, 12].

In the case of the present study, we find that for the $m = 26$, $n = 28$ sample, the neutron scattering data indicates that the higher temperature dip is much sharper than the lower temperature one. However, the position of the thermal expansion peak and the neutron scattering dip ($T \approx 74$ K), which is about 4 K lower than the transition temperature of bulk and single thin film FeF_2 , indicates that the CoF_2 layers indeed affect the ordering of the FeF_2 regions. On the other hand, the $m = n = 4.5$ sample clearly shows a single rounded transition, indicating that at this value of $m = n$, the FeF_2 and CoF_2 regions order simultaneously. Hence, the $m = 26$, $n = 28$ sample belongs to the intermediate layer regime. Conversely, the $m = n = 4.5$ sample is clearly in the thin layer regime.

CONCLUSIONS

We have presented neutron and x-ray scattering data for multilayer thin films $(\text{FeF}_2)_m(\text{CoF}_2)_n$ for two layer thickness regimes. The $m = 26$, $n = 28$ sample shows a relatively sharp transition which can be associated with the ordering of the FeF_2 layers and, at lower T , a rounded transition from the CoF_2 layers. The rounding is from the staggered field imposed by the ordered FeF_2 layers. The sample with thin layers, $m = n = 4.5$, shows only one transition at an intermediate temperature, but does not yield the correct value for the exponent β , which may indicate that the order parameter grows at different rates in the two layers for $T \ll T_N$.

ACKNOWLEDGEMENTS

We would like to thank A. R. King and V. Jaccarino for discussions and for support of this work. This work was supported by the Department of Energy grant No. DE-FG03-87ER45324.

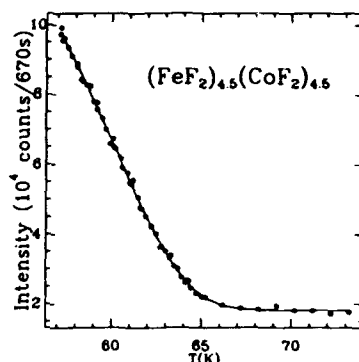


Figure 4: Neutron scattering intensity of the (100) magnetic peak for the $n = m = 4.5$ sample. The solid curve represents a fit to a rounded phase transition with $\beta = 0.42$.

DOE-Martin Marietta contract No. DE-AC05-84OR21400 and NSF Grant No. DMR 88-15560.

REFERENCES

1. D. P. Belanger, M. Lui, and R. W. Erwin, these proceedings.
2. C. A. Ramos, D. Lederman, A. R. King, and V. Jaccarino, *Phys. Rev. Lett.* **65**, 2913 (1990).
3. D. Lederman, Ph.D. Thesis, University of California, Santa Barbara, unpublished (1992).
4. D. Lederman, C. A. Ramos, V. Jaccarino, and J. L. Cardy, to be published.
5. D. Lederman, C. A. Ramos, and V. Jaccarino, presented at the Seventh Latin-American Symposium on Surface Physics, Bariloche, Argentina, 1992 (to be published).
6. For work done on antiferromagnetic oxides, see, for example, M. J. Carey, F. E. Spada, A. E. Berkowitz, W. Cao, and G. Thomas, *J. Mater. Res.* **6**, 2680 (1991) and J. A. Borchers, M. J. Carey, R. W. Erwin, C. F. Majkrzak, and A. E. Berkowitz, *Phys. Rev. Lett.* **70**, 1878 (1993).
7. R. A. Cowley, W. J. L. Buyers, P. Martel, and R. W. H. Stevenson, *J. Phys. C* **6**, 2997 (1973).
8. M. T. Hutchings, B. D. Rainford and H. J. Guggenheim, *J. Phys. C* **3**, 307 (1970).
9. A. E. Nash, C. A. Ramos, and V. Jaccarino, *Phys. Rev. B* **47**, 5805 (1993).
10. For a review, see V. Jaccarino, A. R. King, D. Lederman, M. Lui, and C. A. Ramos in *Heteroepitaxy of Dissimilar Materials*, edited by R. F. C. Farrow, J. P. Harbison, P. S. Peercy, and A. Zangwill (*Mater. Res. Soc. Proc.* **221**, Pittsburgh, PA, 1991) pp. 3-14.
11. M. B. Viani, D. P. Belanger and D. Lederman, unpublished.
12. For theoretical calculations based on mean field models, see A. S. Carrico and R. E. Camley, *Phys. Rev. B* **45**, 13117 (1992) and R. W. Wang and D. L. Mills, *Phys. Rev. B* **46**, 11681 (1992).

MAGNETIC PROPERTIES AND CRYSTAL STRUCTURE OF HIGH MOMENT FeTaN THIN FILMS

G. QIU*, E. HAFTEK*, J. C. CATES**, C. ALEXANDER, JR.**, and J. A. BARNARD*
The University of Alabama, *Department of Metallurgical and Materials
Engineering and **Department of Physics and Astronomy,
Tuscaloosa, AL 35487-0202

ABSTRACT

High moment single layer FeTaN films with excellent soft magnetic properties have been grown by high rate reactive dc magnetron sputtering. The best combination of properties (easy and hard axis coercivities < 1 Oe, saturation magnetization > 1650 emu/cc, anisotropy field of 5 Oe, and initial permeability of 4800) are found in films containing ~ 3.2 a/o Ta and ~ 7.5 a/o N after 400°C annealing in a 200 Oe dc field for two hours. These properties are associated with a single phase, random, nanocrystalline structure consisting of α -Fe crystallites (grain size of $\sim 100\text{\AA}$) whose lattice is expanded by both Ta and N.

1. INTRODUCTION

Materials for thin film recording heads must exhibit a difficult to achieve combination of physical properties including high saturation magnetization (M_s), low coercivity (H_c), high permeability at high frequency, and near zero magnetostriction (λ). Thermal stability and corrosion and wear resistance are also important. FeN-based films have received considerable recent attention because Fe itself has an M_s (1710 emu/cc) higher than that of the presently used permalloy, sendust, and Co-based amorphous alloys. The incorporation of nitrogen into Fe films refines the grain size, inhibits grain growth, and expands the bcc α -Fe lattice, which in turn are associated with low H_c , high M_s films[1]. Grain growth (accompanied by an increase in H_c) can still be a problem when annealing simple FeN films (those without third element additions). The addition of Ta is also found to inhibit grain growth even at high annealing temperatures. Ta has been added to FeN-based films in both small (~ 2 a/o[2]) and large (8 - 13 a/o[3]) amounts and found to improve soft magnetic properties and enhance corrosion resistance. In this study, the effects of nitrogen flow rate and annealing treatment on the structure and magnetic properties of FeTaN films containing 3.2 a/o Ta grown by high rate dc magnetron reactive sputtering are examined. The soft magnetic properties of these films are very promising for magnetic head applications and are significantly better than those found in our previous study[4] of FeTaN films containing 1.6 a/o Ta and are comparable to the best single layer FeN-based films in the literature[5-7].

2. EXPERIMENTAL METHODS AND MATERIALS

Single layer FeTaN films were grown at ambient temperature by reactive dc magnetron sputtering (Vac-Tec Model 250 Sputtering System). A hot-pressed Fe-10 w/o Ta target which produces films containing 3.2 atomic percent Ta was used. All films were made at a fixed sputtering power of 300W, fixed Ar pressure of 3 mtorr, but variable N_2 flow rate (in sccm). The nitrogen content of the films varies linearly with flow rate in the range studied (~ 0.36 a/o N per sccm N_2). These conditions produced growth rates of $\sim 1000\text{\AA}$ / minute; films were sputtered for 5

minutes. Si(111) wafers with a base layer of $\sim 34\text{\AA}$ of sputtered SiO_2 were used as substrates. Films were grown in an aligning field of ~ 70 Oe to induce a uniaxial anisotropy. We report on both as-deposited and field-annealed samples ($\sim 400^\circ\text{C}$ for 2 hours in a 200 Oe aligning field at 10^{-6} torr). Magnetic properties were measured with a Digital Measurement Systems VSM Model 880 and a SHB Instruments Model 106 loop tracer. Permeability was measured by a swept frequency-type permeameter. Composition was determined by x-ray fluorescence. X-ray diffraction was performed on a Rigaku D/Max-2BX XRD System.

3. EXPERIMENTAL RESULTS

3.1. Magnetic Properties

Figure 1a illustrates the dependence of coercivity on N_2 flow rate in easy and hard axis directions. Coercivity decreases with increasing N_2 flow rate. Nitrogen flow rates of 15 and 20 sccm produce the softest films (consistently < 1 Oe). Previous work[4] has shown that FeTa films with no nitrogen exhibit coercivities > 10 Oe (which do not improve on annealing) and that soft magnetic properties deteriorate at flow rates above 20 sccm. The well defined uniaxial anisotropy caused by an external field should reduce magnetization dispersion effects and improve soft magnetic properties. In addition, the smoothness of the surface of the substrate also has a considerable effect on the magnetic properties[8]. Relatively small decreases in coercivity are noted following the annealing for the films with N_2 addition, however for the films with no nitrogen, H_c increases from 5 Oe to 12 Oe, which indicates that the thermal stability of FeTaN films were improved due to the combined effect of N and Ta atoms in the films. The effect of nitrogen flow rate on the anisotropy field, H_K , is plotted in Fig. 1b. H_K increases from 7 to 12 Oe with nitrogen flow in the as-deposited state. Annealing in a 200 Oe field has a much larger effect on H_K than on H_c . Following the annealing an H_K of 4-5 Oe is found which is basically insensitive to nitrogen flow rate (in the range examined here). The decrease of H_K after annealing is probably related to the ease of nitrogen diffusion and the relaxation of the film stress.

Figure 2a illustrates the dependence of saturation magnetization, M_s , on N_2 flow rate. Note that in the as-deposited state M_s consistently exceeds that expected for pure Fe (~ 1710 emu/cc). This effect has been observed repeatedly and may be associated with expansion of the Fe lattice[1]. Uncertainty in film thickness and film area measurement can lead to a maximum error in M_s of $\pm 10\%$. After annealing the magnetization is reduced but still exceeds 1650 emu/cc for the 15 and 20 sccm nitrogen flow rates. The initial permeability and f_{50} , the frequency at which initial permeability drops to 50% of its low frequency value is plotted in Figure 2b. The permeability at high N_2 flow rate is strongly influenced by annealing. There is a trend of increasing μ with nitrogen flow rate for annealed samples reaching a maximum of 4800 for 20 sccm N_2 . The frequency response of permeability can not be fully explained by the classical eddy current model, which is probably due to domain wall movement process. f_{50} for the best film is 160 MHz. We have recently reported on the magnetostriction, λ_s , of FeTaN films in a separate paper[9] and therefore only summarize the trends observed for this set of films. This issue is also addressed in a companion paper in these proceedings[10]. In as-deposited films λ_s increases roughly linearly with nitrogen flow from -3×10^{-6} (at 0 sccm N_2) to $+8 \times 10^{-6}$ (at 20 sccm N_2). Unfortunately, near zero λ_s occurs at lower flow rates (~ 5 sccm) than those needed for optimization of other soft magnetic properties. λ_s is surprisingly insensitive to annealing at temperatures up to $\sim 400^\circ\text{C}$.

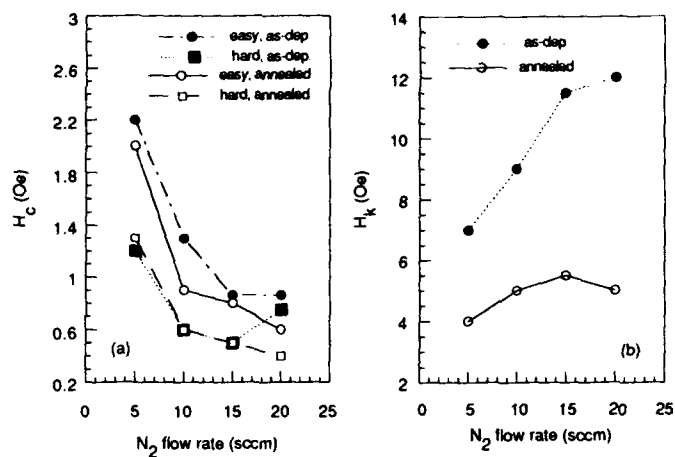


Figure 1. Magnetic properties of FeTaN films as a function of N_2 flow rate in as-deposited and annealed states; a) coercivity, H_c , and b) anisotropy field, H_k .

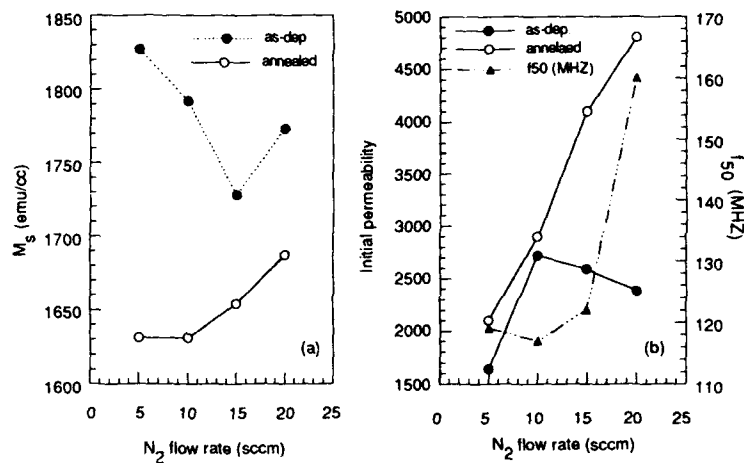


Figure 2. Magnetic properties of FeTaN films as a function of N_2 flow rate in as-deposited and annealed states; a) saturation magnetization, M_s , and b) initial permeability, μ , and roll of frequency at 50% of initial permeability, f_{50} .

3.2. Structure

Representative θ - 2θ XRD scans for annealed FeTa (0 sccm N_2) and FeTaN (20 sccm N_2) are plotted in Fig. 3a and 3b, respectively. Without nitrogen (Fig. 3a) FeTa films exhibit strong (110) growth texture. The films are single phase bcc with Ta dissolved substitutionally in the α -Fe lattice. Note that 3.2 % Ta exceeds the equilibrium stability of less than 1 %, but this is not unusual in sputtered films. No evidence was found for Fe-Ta compounds. In the insert of Fig. 3a a texture analysis (TA) scan[11] is plotted which quantifies the degree of (110) texture by measuring the angular distribution of (110) crystallite poles about the normal to the substrate. A scan with 2θ fixed on the (211) peak while the incidence angle α is varied is used in this experiment. The width of the observed 'peak' indicates that most of the textured FeTa crystallites are oriented within $\sim 8^\circ$ of the ideal position (expected at $\alpha = 10.2^\circ$). When nitrogen is added to the films (Fig. 3b) the (110) peak shifts to lower angles (due to lattice expansion) and decreases in intensity and broadens (attributed primarily to a decrease in grain size). No evidence is found for Fe-Ta, Fe-N, or Ta-N compounds despite the annealing treatment at 400°C . The insert in Fig. 3b shows very little evidence of (110) texture. Also, the position of the shallow 'peak' in the TA scan is far from the expected maximum at 10.8° . XRD analyses at intermediate N_2 flow rates show a systematic decrease in (110) growth texture with increasing N_2 flow.

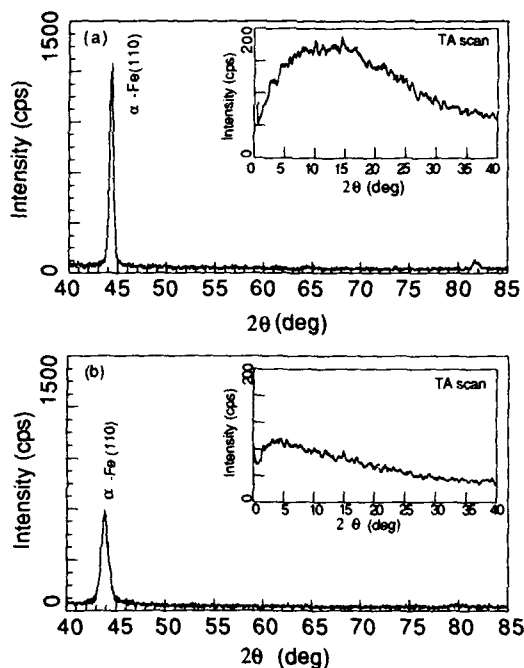


Figure 3. θ - 2θ XRD patterns and texture analysis scans (inserts); a) annealed FeTa film (no nitrogen), and b) annealed FeTaN film (20 sccm N_2).

It has been found that the soft magnetic properties of Fe-based nitride films are attributed to the decrease in the effective magnetic anisotropy caused by small grain size and an appropriate amount of lattice strain which are correlated with the addition of N[12]. Figure 4a illustrates the dependence of the lattice spacing of (110) planes, d_{110} , on nitrogen flow rate calculated from (110) peak positions on θ -2 θ XRD scans. A roughly linear increase in d_{110} with nitrogen flow is noted, which indicates the incorporation of nitrogen in the films. Annealing causes a systematic, uniform reduction in lattice spacing. This contraction is most likely associated with stress relaxation and miscellaneous defect annihilation processes. The average grain size estimated from the FWHM of the (110) peaks is plotted as a function of N_2 flow rate in Fig. 4b. The calculated grain size should be viewed as a minimum (i.e., all broadening is assumed to be due to grain size decrease). The grain size of annealed samples reaches a minimum of $\sim 100\text{\AA}$ at 20 sccm. The apparent increase in grain size on annealing is due at least in part to peak sharpening arising from defect annihilation and stress relief and may not indicate true grain growth.

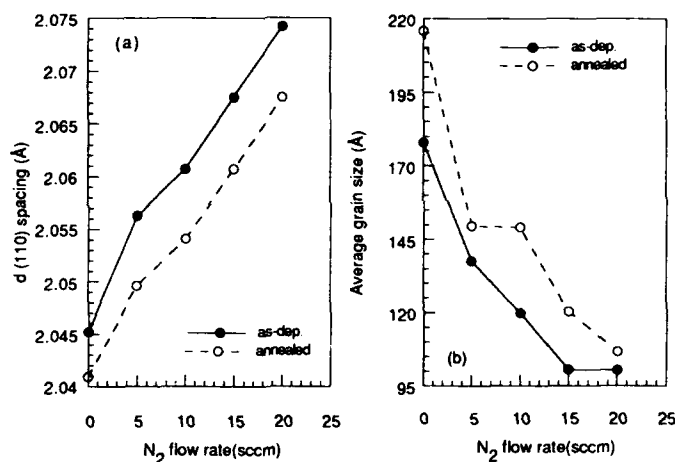


Figure 4. Structure of FeTaN films as a function of N_2 flow rate in as-deposited and annealed states; a) lattice spacing of (110) planes, d_{110} , and b) grain size.

4. CONCLUSIONS

High moment single layer FeTaN films with excellent soft magnetic properties have been successfully grown from a hot-pressed Fe - 10 w/o Ta by high rate reactive dc magnetron sputtering onto Si(111) wafers precoated with 34 \AA of sputtered SiO_2 . Soft magnetic properties in FeTaN films depend strongly on the nitrogen content in the films and on the annealing process. The coexistence of N and Ta atoms play an important role in improving the soft magnetic properties and thermal stability of FeTaN films. The best combination of properties (easy and hard axis coercivities < 1 Oe, saturation magnetization > 1650 emu/cc, anisotropy field of 5 Oe, and initial permeability of 4800) are found in films containing ~ 3.2 a/o Ta

and ~7.5 a/o N after 400°C annealing in a 200 Oe dc field for two hours. X-ray diffraction studies suggest that these properties are associated with a single phase, random, nanocrystalline structure consisting of α -Fe crystallites (grain size of ~100Å) whose lattice is expanded by both Ta and N. Well defined magnetization induced anisotropy as well as the smoothness of the substrate are also important in improving the soft magnetic properties of the films.

ACKNOWLEDGEMENTS

Acknowledgement is made to the National Storage Industry Consortium - Advanced Technology Program, the NSF (DMR-9157402), the Data Storage Systems Center of Carnegie Mellon University (NSF-ECD-8907068), IBM, and the MINT Center at The University of Alabama for support of this research. Thanks also to Mr. Peng Tang for his help with permeability measurements.

References

- [1] M.A. Russak, C.V. Jahnes, E. Klokholm, J-W. Lee, M.E. Re, and B.C. Webb, J. Magn. and Mag. Mater. **104-107**, 1851 (1992).
- [2] Y. Watanabe, H. Oura and N. Onozato, IEEE Trans. Magn. **Mag-26**, 1500 (1990).
- [3] N. Ishiwata, C. Wakabayashi, and H. Urai, J. Appl. Phys. **69**, 5616 (1991).
- [4] G. Qiu, E. Haftek, and J.A. Barnard, J. Appl. Phys., in press
- [5] N. Terada, Y. Hoshi, N.Naoe, and S. Yamanaka, IEEE Trans. Magn. **Mag-20**, 1451 (1984).
- [6] Y. Nagai, A. Tago, K. Yanagisawa, and T. Toshima, J. Appl. Phys. **61**, 3841 (1987).
- [7] S. Wang, and M.H. Kryder, J. Appl. Phys. **67**, 5134 (1990).
- [8] K. L. Chopra, Thin Film Phenomenon, (Robert E. Krieger Publishing Company, Inc., Malabar, Florida, 1985), p. 672.
- [9] J.C. Cates, C.A. Alexander, Jr., E. Haftek, and J.A. Barnard, submitted IEEE Trans. Mag.
- [10] J.C. Cates, G. Qiu, E. Haftek, C.A. Alexander, Jr., and J.A. Barnard, this proceedings.
- [11] P.A. Flinn and G.A. Waychunas, J. Vac. Sci. Technol. **B6**, 1749 (1988).
- [12] T. Shimatsu, H. Shoji, M. Kyyoho, Migaku Takahashi and T. Wakiyama, J. Magn. Soc. Jpn. **15**, 63 (1991).

MAGNETOSTRICTION AND STRESS IN HIGH MOMENT FeTaN FILMS

J. C. CATES*, G. QIU**, E. HAFTEK**, C. ALEXANDER, JR.*, and J. A. BARNARD**
The University of Alabama, *The Department of Physics and Astronomy and **The
Department of Metallurgical and Materials Engineering,
Tuscaloosa, AL 35487-0202

ABSTRACT

Magnetostriction and thin film stress have been studied in high moment single layer FeTaN films deposited by high rate reactive dc magnetron sputtering. Low magnetostriction (magnitude less than 1×10^{-6}) can be obtained over a fairly large range of nitrogen flow rates during film deposition by vacuum annealing at 500°C. After annealing at 500°C for two hours, all films were found to be in a state of tensile stress. Stress versus temperature measurements up to 400°C show film stress in as-deposited films to be highly hysteretic during the first temperature cycle reflecting the films' processing history. Stress-temperature cycles on annealed samples indicate that extremely stable films are produced in an intermediate range of nitrogen content.

1. INTRODUCTION

As coercivities in recording media increase, a growing emphasis has been placed on developing materials with a high saturation magnetization for high density magnetic recording heads. Potential materials must also exhibit a low coercivity, high permeability, small magnetostriction, and suitable corrosion and thermal properties. Because of their high moment, FeN-based materials have been examined and show considerable potential for application in high-density thin film recording heads. The addition of small amounts of Ta to the FeN films has been shown to improve the soft magnetic properties and enhance corrosion resistance in these films[1-3].

Domain structure is extremely important in optimizing the performance of the thin film recording head. The magnetoelastic anisotropy, which is proportional to the product of the magnetostriction and film stress, is used to control the domain structure in thin film heads. The interrelationship and importance of stress and magnetostriction has recently been addressed[4]. In this paper, the dependence of magnetostriction and film stress on deposition conditions and annealing are examined in FeTaN films. In a companion paper[5] we report on the very promising soft magnetic properties of a similar set of FeTaN films.

2. EXPERIMENTAL METHODS

Single layer FeTaN films were deposited on glass substrates at ambient temperature by dc magnetron reactive sputtering in a Vac-Tec Model 250 Batch Side Sputtering System. The hot pressed Fe target contained approximately 10 w/o Ta which produced films containing 3.2 a/o Ta. The thickness of the films in this study is ~420 nm; deposition rates were 1-1.5 nm/sec. The Ar flow rate was set at 60 sccm and the N₂ flow rate varied from 0 to 25 sccm. The N content in the films increased linearly with N₂ flow rate (approximately 0.36 a/o N per sccm N₂). Vacuum annealing at 500°C was performed at $\sim 10^{-6}$ torr. Magnetostriction was measured in an AC magnetostriction tester based on a design by Tam and Schroeder[6]. Film stress was measured on a FLEXUS 2320 thin film stress

measurement system with built in annealing capabilities. Film structure was studied by x-ray diffraction on a Rigaku D/Max-2BX XRD System.

3. EXPERIMENTAL RESULTS

3.1 Structure

Details of the structure of FeTaN films can be found in a companion paper in these proceedings[5]. In the as-deposited state FeTaN films consist of single phase polycrystalline α -Fe with Ta and N in solution, which changes from (110) preferred growth texture for FeTa films (at 0 sccm N_2) to a more random, finer grained structure as the N_2 flow rate increases. An increase in the d(110) lattice spacing with N_2 flow rate is attributed to the incorporation of nitrogen in the films. After annealing at 500°C for 2 hours, grain growth occurs. d(110) spacing decreases due to film densification and redistribution of N atoms. Iron nitrides were observed after annealing for films prepared at high nitrogen flow rates of 20 and 25 sccm. Films prepared at 20 sccm consist predominantly of α -Fe with small amounts of ϵ -Fe_{2.3}N. For films prepared at 25 sccm, one diffraction peak appears ($2\theta=44.05^\circ$) which cannot be unequivocally associated with a particular Fe-N compound. This peak could be attributed to partially ordered martensite. Small amounts of amorphous TaN might also form in the annealed films which is not detected by XRD. Fig. 1 illustrates the effect of annealing on a high nitrogen FeTaN film.

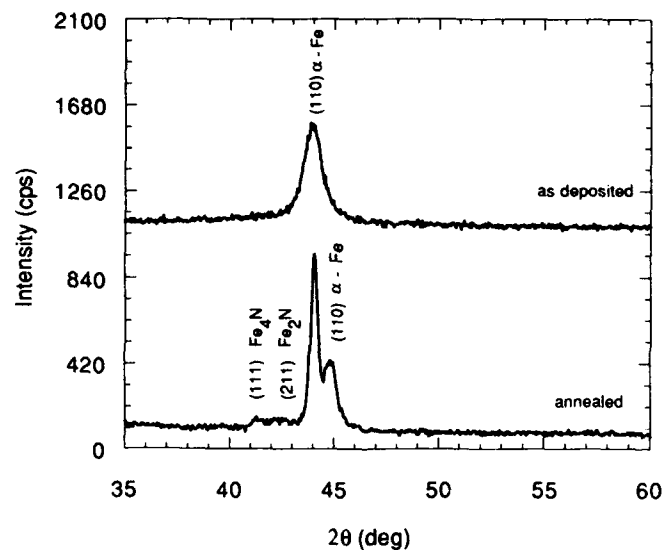


Figure 1. X-ray diffraction scan of FeTaN film prepared at 25 sccm N_2 .

3.2 Magnetostriction

In previous work[7], we have shown that the saturation magnetostriction in as-deposited FeTaN films is dependent on film thickness and increases linearly from negative to positive with increasing nitrogen content, passing through zero magnetostriction at a nitrogen flow rate of approximately 5 sccm for films of thickness 400 nm. Annealing at 300°C in vacuum did not affect the magnetostriction in these films. Unfortunately, this zero point in the magnetostriction does not coincide with the optimal conditions for coercivity which occurs at the higher nitrogen flow rates[5]. In an effort to improve the range of low magnetostriction, high temperature annealing at 500°C was conducted on the FeTaN films.

The effect of the annealing on magnetostriction is shown in Fig. 2. Magnetostriction in as-deposited films passes through zero at nitrogen flow rates of less than 5 sccm. The range of low magnetostriction (less than 1×10^{-6}) occurs only over a very narrow range of nitrogen flow rates. After annealing, the magnetostriction is shifted downwards and the slope decreased. This has the effect of moving the zero point of magnetostriction to higher nitrogen flow rates and greatly increasing the range of low magnetostriction.

The change in magnetostriction with annealing may be due to grain growth that occurs at the higher annealing temperatures. This growth might increase the amount of crystalline grains with (110) orientation which have an average negative magnetostriction at the expense of randomly oriented grains and the disordered material at the grain boundaries which has a more positive magnetostriction. Magnetostriction could also be affected by nitrogen leaving the iron lattice during annealing and migrating to grain boundaries or being incorporated into small amounts of Fe-N or Ta-N phases that may not be detectable by x-ray measurements. In high nitrogen flow rate samples a solid state reaction is noted on annealing in Fig. 1.

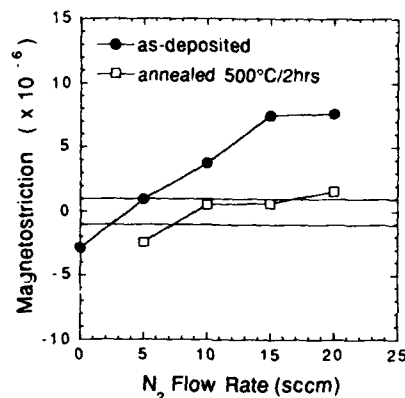


Figure 2. Magnetostriction versus nitrogen flow rate for FeTaN films (as-deposited and annealed). Lines mark the region where the magnitude of the magnetostriction is less than 1×10^{-6} .

3.3 Film Stress

Room temperature film stress versus nitrogen flow rate in both as-deposited and annealed FeTaN films is plotted in Fig. 3. As-deposited films gradually change from a state of tension to compression with increasing N content. This trend is associated with the systematic increase in lattice parameter as N is incorporated in the Fe(Ta) lattice. Following anneal all films are in a state of tension. The change in stress due to annealing is roughly proportional to the as-deposited nitrogen flow rate. It has been suggested that annealing in this temperature range promotes the formation of TaN thus removing some of the interstitial N from the Fe lattice[4].

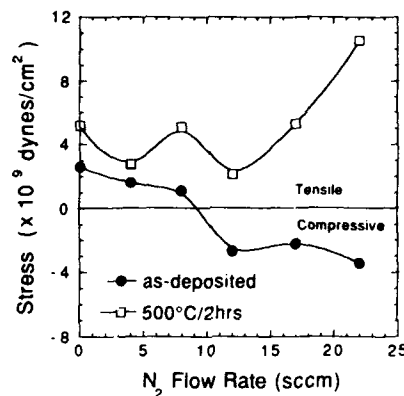


Figure 3. Film stress versus nitrogen flow rate for FeTaN films (as-deposited and annealed).

3.4 Stress versus Temperature

Stress versus temperature (σ -T) experiments utilize the difference in thermal expansion between the film and substrate to study the mechanical properties of thin films. The interpretations presented here rely on an excellent general review of thin film mechanical properties by Nix[8]. σ -T plots for as-deposited films exhibit features which are characteristic of the processing history of the sample (i.e., they say as much about the effects of sputtering as about the inherent properties of the films). In the top row of Fig. 4 the effect of N content on as-deposited σ -T cycles is illustrated. The large stress relaxations beginning in the range 270-300°C are related to densification (perhaps combined with plastic deformation) of the as-deposited films. There is a notable and systematic decrease in the magnitude of the slope $d\sigma/dT$ on heating with increasing N. The large spike in the σ -T plot for a high N film (25 sccm) may be related to a phase transformation. Cooling of all the as-deposited films leaves them in a state of tension.

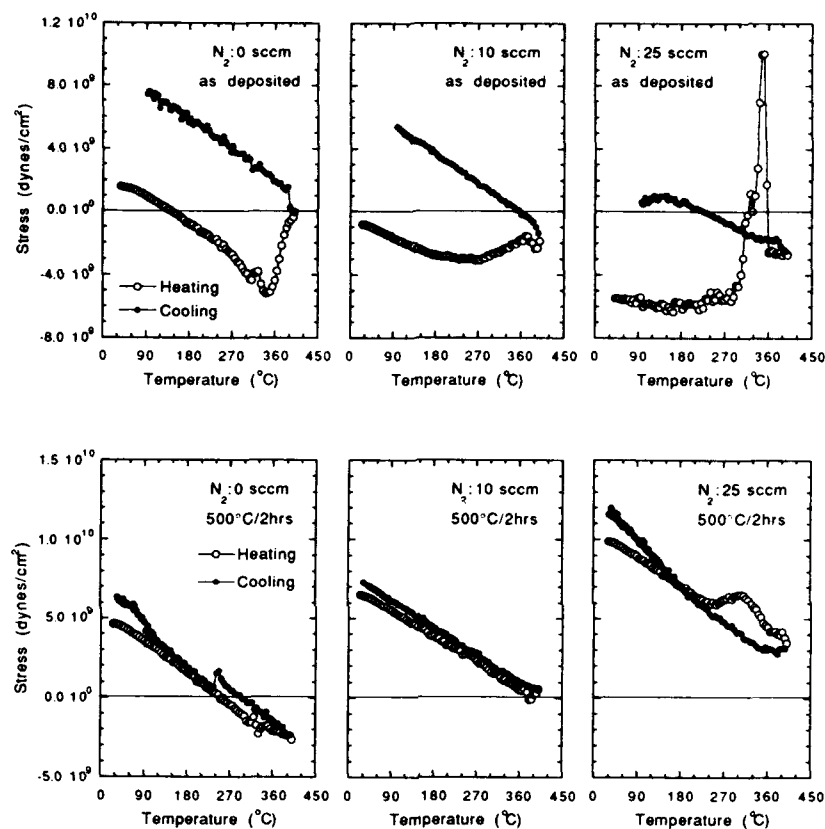


Figure 4. Film stress as a function of temperature for as-deposited and annealed FeTaN films. Open circles: stress during heating. Closed circles: cooling.

By contrast, the σ - T plots for *pre-annealed* films (bottom row) are very different and are related more directly to the intrinsic properties of the films. Notice that all pre-annealed films are in a state of tension which increases with N. Without N, simple FeTa films deform elastically on heating to ~330°C. Slight yielding in compression begins at roughly -2×10^9 dynes/cm². On cooling the difference in thermal expansion is accommodated elastically (ignoring the discontinuity at ~240°C) until strengthening occurs at ~100°C. At moderate nitrogen flow rates (10 sccm) the film deforms completely elastically. This film is extremely stable. Note that the elastic portions of the heating and cooling curves for both 0 and 10 sccm films are parallel. For high nitrogen flows (25 sccm) very different and complex behavior is observed. The change in slope at 270°C on heating that occurs as the film tension is being *relieved* is difficult to explain. It may be related to formation of a phase with a smaller molar volume than the rest of the film. Continued heating

above $\sim 330^\circ\text{C}$ further relieves the tensile stress. On cooling of the high nitrogen film $d\sigma/dT$ is very different from that found on heating, most likely reflecting a permanent change in Young's modulus due to solid state phase change. The high nitrogen content FeTaN film is significantly less stable than the film with a moderate N content (10 sccm).

4. SUMMARY

The influence of nitrogen content and annealing treatment on the magnetostriction and stress in FeTaN films has been studied. Low values of magnetostriction over a broad nitrogen content can be achieved by annealing at 500°C . As-deposited FeTaN films exhibit highly hysteretic σ -T plots which are strongly affected by nitrogen content. Annealing at 500°C effectively stabilizes the mechanical properties of FeTaN films with intermediate N contents. These films exhibit essentially perfectly elastic behavior in temperature cycling to 400°C .

ACKNOWLEDGEMENTS

Acknowledgement is made to the National Storage Industry Consortium - Advanced Technology Program, the NSF (DMR-9157402 and EHR - 9108761, EPSCoR-Alabama), the Data Storage Systems Center of Carnegie Mellon University (NSF-ECD-8907068), IBM, and the MINT Center at The University of Alabama for support of this research.

References

- [1] Y. Watanabe, H. Oura and N. Onozato, IEEE Trans. Magn., **Mag-26**, 1500 (1990).
- [2] N. Ishiwata, C. Wakabayashi, and H. Urai, J. Appl. Phys. **69**, 5616 (1991).
- [3] G. Qiu, E. Haftek, and J.A. Barnard, J. Appl. Phys., in press
- [4] N. Ishiwata, Y. Takeshima, T. Konehara, and H. Urai, presented at the 6th International Conference on Ferrites, in press.
- [5] G. Qiu, J.C. Cates, E. Haftek, C. Alexander, Jr., and J.A. Barnard, this proceedings.
- [6] A. Tam and H. Schroeder, IEEE Trans. Magn., **25**, 2629 (1989).
- [7] J.C. Cates, C.A. Alexander, Jr., E. Haftek, and J.A. Barnard, submitted IEEE Trans. Mag.
- [8] W.D. Nix, Metall. Trans. A **20A**, 2217 (1989)

FERRIMAGNETIC COBALT FERRITE FILMS PREPARED BY THE SOL-GEL PROCESS

EVA M. WONG^{*}, HAIXING ZHENG^{*}, JOHN D. MACKENZIE^{*} AND T. TSUCHIYA^{**}

^{*}University of California, Los Angeles, Department of Materials Science and Engineering, 405 Hilgard Avenue, Los Angeles, California 90024

^{**}Science University of Tokyo, Department of Materials Science and Technology, Tokyo, Noda, Chiba 278 Japan.

ABSTRACT

Ferrimagnetic oxide films have been shown to have potential for use as magneto-optical information storage materials. Cobalt ferrite films are particularly interesting for magneto optical information storage due to their high magneto optical rotation [1]. In this work, synthesized soluble cobalt (II) and iron (III) methoxyethoxides were mixed in stoichiometric ratios for use as Co and Fe precursors in the preparation of CoFe_2O_4 ferrimagnetic films. The decomposition of the precursors was characterized by thermogravimetric analysis.

CoFe_2O_4 films were prepared by the dip coating technique using fused silica substrates. These films were then heat treated at temperatures ranging from 200°C to 600°C to study the transformation from an amorphous film to a crystalline film as determined by x-ray diffraction. The magnetic hysteresis behavior of the films as a function of heat treating temperature and hence crystallinity was also studied. As a general trend, films having a greater degree of crystallinity exhibited larger values of saturation magnetization and remanent magnetization. The amorphous film was found to exhibit the highest coercive field, but low values of saturation and remanent magnetization. The effect of heat treating under the influence of a magnetic field of 1.88 kOe was found to enhance crystallization only slightly and had very little effect on the magnetic properties of the film.

INTRODUCTION

Materials generally used for magneto optical recording are amorphous rare earth-transition metal compounds, but these materials exhibit low polar Kerr contrast ($\theta_K < 0.4^\circ$) when compared to cobalt ferrite films ($\theta_K > 0.5^\circ$) [2,3]. Advantages are that oxide films have greater corrosion resistance, are very reproducible and are typically less expensive. Amorphous oxide films offer the additional advantage that the absence of grain boundaries reduces media noise [2].

Ferrimagnetic thin films are of interest for a number of novel applications including, but not limited to magneto-optical recording, spatial light modulators and magneto elastic devices. Many deposition methods have been investigated including epitaxial growth [4], spray pyrolysis [3], sputtering [5] and double source evaporation [6], however these methods require expensive and elaborate equipment, continual atmosphere control and long deposition times. NiO and CoO have recently been sputtered by Berkowitz [7] and Fe_3O_4 and NiO using reactive MBE by Lind [8] with relatively high deposition rates of 2.0-2.5 Å/sec. However, these techniques are still limited to single component systems. Multicomponent systems with controlled stoichiometry can not be easily made. Conversely, sol gel processing can overcome many of the problems associated with the synthesis of multicomponent systems. Sol gel processing routes offer several advantages over conventional processing routes

including improved homogeneity by mixing at the molecular level in solution, reduced processing temperatures which allow for the synthesis of novel materials, and an economical means by which to achieve films of desired composition with the added benefit of ease of fabrication.

In this work, sols obtained by the controlled hydrolysis and condensation of a metal alkoxide precursor solution were used to dip coat thin films of CoFe_2O_4 onto fused silica substrates. The decomposition of the precursor was studied using thermogravimetric analysis. In addition, the effects of the application of a 1.88 kOe magnetic field during firing and increasing the heat treating temperature from 200°C to 600°C on the crystallinity of the films were studied using x-ray diffraction. The results of magnetic property measurements are reported for these films.

EXPERIMENTAL

Co (II) and Fe (III) methoxyethoxides, synthesized and characterized in earlier work [9], were used as the starting precursors. The metal ion concentration in the Co (II) solution was determined by the gravimetric method described by Kodama [10]. Using this method, the Co concentration was found to be 0.0075 g/ml solution. Because it is more difficult to determine Fe (III) concentration in solution via the gravimetric method, an oxidation-reduction titration using potassium permanganate as the titrant was performed as described by Skoog and West [11]. The concentration of Fe (III) in solution was found to be 0.0174 g/ml solution.

The Fe-Co coating solution was prepared by mixing the Fe and Co alkoxides in a 2:1 stoichiometric molar ratio followed by refluxing for two hours. The resulting solution, after cooling, was stored in a tightly sealed container at room temperature and did not gel over a 3 month period. This solution was used for coating.

Films were prepared by dip coating fused silica or silicate glass slides in the solution with a withdrawal rate of approximately 7 cm/min. The film was dried at 110°C for 1 hour after each coat and the procedure was repeated to obtain films of the desired thickness. The films were then fired in air with a heating and cooling rate of 2°C/hour after multiple coats. Films used in this study were dip coated a total of ten times.

Thermogravimetric analysis (TGA) of the Fe and Co precursors was performed using a Perkin Elmer thermal analysis data system. The temperature was increased from 50°C to 900°C at a rate of 10°C/minute.

The crystallinity of the films was determined by x-ray diffraction. All spectra were collected with a diffractometer using $\text{Cu K}\alpha$ radiation ($\lambda = 1.5418 \text{ \AA}$). The x-ray intensity was collected for 50 seconds at steps of 0.04 degrees from $25^\circ < 2\theta < 70^\circ$.

The magnetic properties of the films were measured with a Riken Electric Company vibrating sample B-H curve tracer using an applied field of 5 kOe oriented parallel to the film. All measurements were made at room temperature.

RESULTS AND DISCUSSION

Thermal decomposition of the precursor solutions was followed using thermogravimetric analysis. The gravimetric data indicates that the majority of solvent and organic components are removed by 400°C as shown in Figure 1. In the case of the Co-methoxyethoxide, weight loss at approximately 110°C corresponds to the removal of solvent. Total weight loss for the Co-Fe precursor was approximately 25%. The weight of the precursors is stable over the temperature range of 400°C to 800°C. At 800°C a small weight

loss is observed and is an indication of a change of oxidation state of the metal ions thereby changing the oxygen-metal stoichiometry although measurements to confirm this have not been made. It has been reported in the literature that changes in stoichiometry effect the magnetocrystalline anisotropy [12].

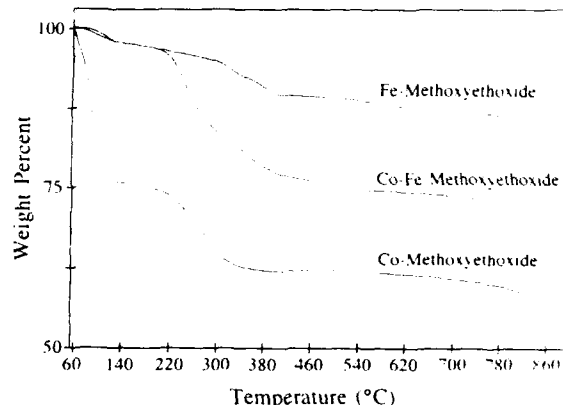


Figure 1. TGA data of precursor solutions collected using a heating rate of $10^{\circ}\text{C}/\text{min}$.

Glass slides were used as substrate material initially because the thermal expansion coefficient of CoFe_2O_4 ($\alpha = 8.7 \times 10^{-6}/^{\circ}\text{C}$) [13] is very similar to that of slide glass ($\alpha = 6 \times 10^{-6}/^{\circ}\text{C}$) [14]. It was found, however, that they were not suitable substrates as the coatings reacted with the glass during firing. Fused silica substrates were therefore used for film crystallization studies since the precursor solution did not react with the substrate and ferrite films were easily formed. A disadvantage to using fused silica is the difference in the expansion coefficients of fused silica ($\alpha = 0.5 \times 10^{-6}/^{\circ}\text{C}$) [15] and CoFe_2O_4 . This difference could cause some residual stress to develop in the film which could in turn lead to cracking during heat treating.

The films were transparent and orange-brown in color upon dipping and became dark brown after firing, but maintained transparency. The films were homogeneous and when examined with an optical microscope did not show signs of cracking. The film thickness was measured to be approximately $0.4 \mu\text{m}$.

The evolution of the film from the amorphous state to the crystalline state is shown in Figure 2 by the collected x-ray spectra of the films. After being heat treated at temperatures from 300°C to 600°C for 1 hour in air, the films were found to be polycrystalline, with an amorphous fraction of less than 20%. Increasing the heat treatment temperature, but maintaining the time at 1 hour, resulted in increasing crystallinity. A small peak at $2\theta = 45^{\circ}$ in the XRD pattern of the sample heated to 600°C may indicate the presence of carbon. Heat treating the film at 200°C for 1 hour resulted in an amorphous film, however, as can be seen from Figure 1, some residual organic remains in this film. The effects of heat treating for longer times were not investigated in this study.

The effect of applying a magnetic field during heat treatment on crystalline orientation was studied by firing samples to 400°C for one hour while simultaneously applying a magnetic field of 1.88 kOe in a solenoid. The x-ray diffraction spectrum of a film prepared in this manner, is compared to a film prepared with the same heat treatment time and temperature without the influence of an applied magnetic field in Figure 3. It can be seen that the film fired in the presence of a magnetic field exhibits some enhanced crystallization, but no enhanced orientation effects are observed.

Magnetic hysteresis loops were obtained for the heat treated films. The values of saturation and remanent magnetization and coercive field are shown in Table I. In this table, the values of both σ_s and σ_r were calculated from the magnetization values assuming that the film was completely dense and was uniformly thick. The hysteresis loop of the sample prepared at 500°C/1 hour is shown in Figure 4 as an example of the hysteresis behavior of a crystalline film. The crystalline films exhibited similar hysteresis behavior, with saturation and remanent magnetization values as summarized in Table I. As a general trend, increasing the heat treating temperature, and hence the crystallinity, was accompanied by an increase in both σ_s and σ_r .

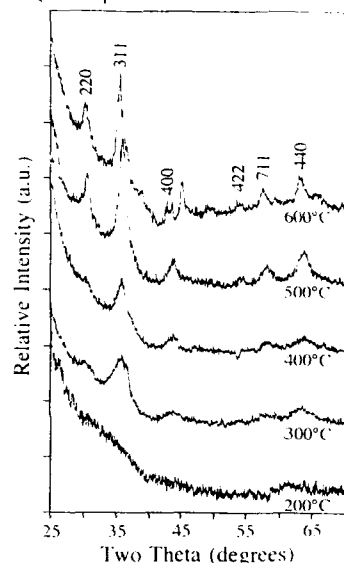


Figure 2. XRD spectra of samples fired at temperatures ranging from 200°C to 600°C for 1 hour. Note the evolution from an amorphous film to an increasingly crystalline film.

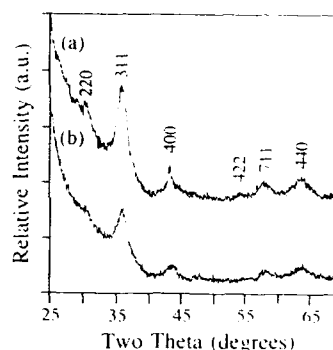


Figure 3. Comparison of the XRD spectra of films fired at 400°C for 1 hour (a) with and (b) without an applied magnetic field of 1.88 kOe.

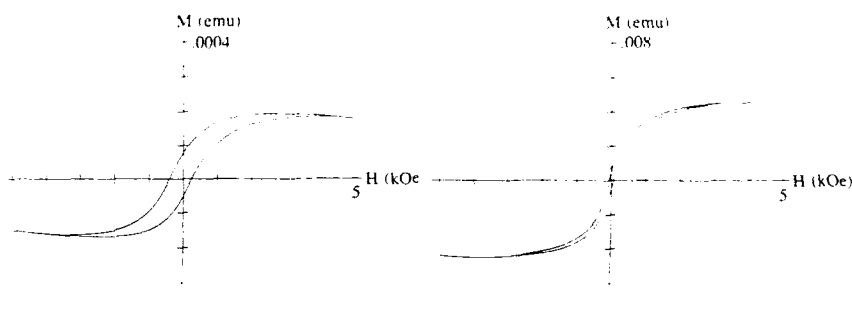


Figure 4. Magnetic hysteresis loop of crystalline film heat treated at 500°C for 1 hour.

Figure 5. Magnetic hysteresis loop of amorphous film heat treated at 200°C for 1 hour.

Table I. Summary of Magnetic Properties of CoFe_2O_4 Films with Various Heat Treatments

Sample	Saturation Magnetization σ_s (emu/cc)	Remanent Magnetization σ_r (emu/cc)	Coercive Force H_c (Oe)
Single Crystal Film [3]	280 Gauss	---	6 kOe
Bulk Powder [16]	198 Gauss	---	3.09 kOe
200°C/1hr	4.24	1.79	330
300°C/1hr	61.16	10.33	40
400°C/1hr	92.27	4.55	20
400°C/1hr w/field	81.94	1.98	20
500°C/1hr	122.87	7.98	30
600°C/1hr	182.54	30.75	100

The measured hysteresis loop of the amorphous sample heat treated at 200°C for 1 hour is shown in Figure 5. The amorphous film shows a slightly shifted hysteresis loop (which is often seen with exchange biasing) with small values of σ_s and σ_r , but a considerably larger value of H_c when compared with the crystalline films. Despite the lack of structural order on the microscopic scale, it is postulated that a type of "ferrimagnetic order" exists as in the amorphous magnets of transition metal-rare earth systems [14] such that a spontaneous magnetization occurs.

From Table I, it can be seen that firing the film while applying a magnetic field of 1.88 kOe had little effect upon the magnetic properties of the film. A field of 1.88 kOe is very small compared to the applied field used in obtaining the hysteresis curves and is a value much lower than the field required to reach saturation magnetization. This may indicate that the field strength displaces the domain boundaries in a reversible fashion, hence no large effect was observed in the hysteresis behavior as compared to a film that had not been exposed to this field during heat treatment. This may also explain why no preferred crystalline orientation was observed in the diffraction spectra of the film heat treated with a 1.88 kOe applied field.

CONCLUSION

Ferrimagnetic CoFe_2O_4 films prepared from metal alkoxide solutions were characterized. X-ray diffraction studies of the films showed that increasingly crystalline films could be obtained by heat treating at temperatures above 300°C for 1 hour. Films heat treated at 200°C for 1 hour were found to be amorphous. Heat treating films under an applied field of 1.88 kOe did not appreciably enhance crystalline orientation.

Magnetic hysteresis loops of the crystalline films demonstrated a general trend of increasing saturation and remanent magnetization with increasing heat treatment temperature. The amorphous film exhibited hysteresis behavior defined by low values of σ_s and σ_r , but a relatively large value of coercive force. Heat treating of the film on a fused silica substrate at 400°C for 1 hour under an applied field of 1.88 kOe did not appreciably enhance the magnetic properties of the film.

Ongoing work is directed toward the preparation of single crystal films and the study of the effects of annealing time and atmosphere (i.e. O_2) on crystal growth. Scanning electron microscopy to observe grain sizes and morphology, and measurements to confirm stoichiometry (i.e. SIMS) and the effects on magnetocrystalline anisotropy are planned for future work.

ACKNOWLEDGEMENTS

The authors would like to gratefully acknowledge the *Air Force Office of Scientific Research* for the support of this work.

REFERENCES

1. J.W.D. Martens and W.L. Peeters, *J. Magn. and Mag. Matls.* **61**, 21-23 (1986).
2. M. Abe and M. Gomi in *Advances in Magneto-Optics* (Proc. Int. Symp. Magneto-Optics **11** suppl. S1, 1987) pp. 299-304.
3. J. Martens, A. Voermans, *IEEE Trans. Magn.* **20** (5), 1007-1012 (1984).
4. N. Evtihiev, N. Economov, A. Kreba and N. Zamjatina, *IEEE Trans. Magn.* **12** (6), 773-775 (1976).
5. M. Kawasaki, M. Gomi and M. Abe, Digests 10th Ann. Conf. Magn. Jpn., 26 (1986).
6. M. Sugimoto and N. Hiratsuka, *Advances in Ceramics* **16**, 207-211 (1985).
7. W. Cao, G. Thomas, M.J. Carey, and A.E. Berkowitz, *Scripta Metallurgica et Materialia* **25** (12), 2633-2638 (1991).
8. D.M. Lind, S.D. Berry, G. Chern, H. Mathias, and L.R. Testardi, *Phys. Rev. B* **45** (4), 1838-1850 (1992).
9. E.M. Wong, H. Zheng and J.D. Mackenzie, unpublished work.
10. K. Kodama, *Methods of Quantitative Inorganic Analysis*, (Interscience Publishers, John Wiley & Sons, New York, 1973) p. 269.
11. D.A. Skoog and D.M. West, *Fundamentals of Analytical Chemistry*, (Holt, Rinehart and Winston, New York, 1963) p. 742.
12. Z. Kakol and J.M. Honig, *Phys. Rev. B* **40** (13), 9090-9097 (1989).
13. A. Goldman, *Modern Ferrite Technology*, (Van Nostrand Reinhold, New York, 1990).
14. W.D. Kingery, H.K. Bowen, and D.R. Uhlmann, *Introduction to Ceramics*, 2nd ed. (John Wiley and Sons, New York, 1976), p. 595.
15. T. Kanyoshi, *Amorphous Magnetism*, (CRC Press, Boca Raton, Florida, 1984), p. 3.
16. Landolt-Börnstein, *Numerical Data and Functional Relationships in Science and Technology*, vol. 4 part b, edited by K.H. Hellwege (Springer Verlag, 1970) p.370.

DEVELOPMENT OF CRYSTALLOGRAPHIC TEXTURE IN RF SPUTTER DEPOSITED CoCrTa/Cr THIN FILMS

Y. C. FENG, D. E. LAUGHLIN and D. N. LAMBETH*,

Department of Materials Science and Engineering,

*Department of Electrical and Computer Engineering,

Data Storage System Center, Carnegie Mellon University, Pittsburgh, PA 15213

ABSTRACT

It is well known that Cr sputtered on glass or NiP/Al substrates has either the (002) or (110) crystallographic texture (depending on the substrate temperature) and that the Co-alloy layers which are deposited on the Cr underlayers have either the (1120) or (10 $\bar{1}$ 1) textures respectively. However, the dependence of the crystallographic textures on other sputtering parameters is not clear. We report here on the study of the dependence of crystallographic textures of CoCrTa/Cr films on substrate bias. It is found that both Cr (110) and Cr (002) textures can form at elevated temperature, depending on the substrate bias. The development of the crystallographic texture is discussed with a model. It is also found that the epitaxy of CoCrTa layer depends on the sputtering conditions of both the Cr and the CoCrTa layers. The extrinsic magnetic properties (such as H_c, S and S*) of thin films with various textures are also presented. By controlling the sputtering procedure, the effects of crystallographic textures on magnetic properties were separated from the effects of film morphology.

I. INTRODUCTION

Sputtered CoCrTa thin films on Cr underlayers are one of the most promising candidates for longitudinal recording media,^{1,2} due to their high in-plane coercivity and low recording noise.³ It is believed that the Cr underlayer enhances the magnetic properties by facilitating the growth of Co-alloy grains with a crystallographic plane of either hcp (1120) or (10 $\bar{1}$ 1) parallel to the film surface.⁴ This causes the c-axis to lie nearly in the film surface. Therefore, understanding the dependence of crystallographic texture of CoCrTa/Cr thin films on sputtering condition is of great importance.

Previous work regarding the crystallographic texture of Co-alloy/Cr has been summarized by T. Ohno *et al.*⁵ It is well known that sputtered Cr thin films have either (110) or (002) texture,⁵⁻⁷ depending on the substrate temperature. When deposited without substrate preheating, the Cr layers have the (110) texture, while when deposited at elevated temperatures they tend to have the (002) texture. However, the dependence of crystallographic texture on other sputter parameters is not clear. In this work, we have studied the dependence of the crystallographic texture of RF sputter deposited Cr underlayer on substrate bias. We find that when it is deposited at room temperature, the Cr layer always has the (110) texture and when deposited at elevated temperature, the Cr layer has either the Cr (002) or the Cr (110) texture depending on the substrate bias. The dependence of crystallographic texture of Cr on substrate bias is discussed with a model.⁸

It is also well known that when Co alloys are deposited on Cr with the (110) texture, they have the (10 $\bar{1}$ 1) texture and when they are deposited on Cr of the (002) texture, they have the (1120) texture.^{4,5} This is believed due to grain to grain epitaxy.^{9,10} However, the effect of various sputtering conditions on this epitaxy has not been fully studied. In this work, we find that the epitaxy depends on the sputtering conditions of both the Cr and Co-alloy layer.

The extrinsic magnetic properties of thin films depend on their microstructure. To investigate the effects of each microstructural feature on the magnetic properties, it is critical to vary each microstructural feature independently. Y. Shen *et al.*¹¹ have tried to separate the effects of substrate heating, which has been thought to cause grain boundary segregation of Ta atoms, from the crystallographic texture effects. However, the substrate temperature also influences the morphology of the film.¹² In this work, the magnetic properties of films with various crystallographic textures are studied. By controlling the sputtering procedure, we try to separate the effects of crystallographic texture on the extrinsic magnetic properties from the effects of other microstructural features.

II. EXPERIMENTAL

CoCrTa/Cr thin films were RF sputter deposited on Corning 7059 glass substrates in an Leybold-Heraeus Z-400 sputtering system with a background pressure of 7.0×10^{-7} Torr. The composition of the CoCrTa layers is Co-12 at% Cr-2 at% Ta. The density of forward sputtering power was 1.6 Watts/cm² and the Ar pressure was 10 mTorr during the deposition of the film. The preheated substrate temperature, the Ar pressure and the substrate bias were varied, and will be specified in the text. The rate of deposition was determined by step profilometry measurements and these rates were used to calculate the various thicknesses of the films. The crystallographic texture was studied by x-ray diffraction using Cu K α radiation. The magnetic properties of these films were measured using a Vibrating Sample Magnetometer.

III. RESULTS AND DISCUSSION

1. The crystallographic texture of the Cr underlayer

In this work, the Cr layers were deposited with various substrate biases on glass substrates at either room temperature or preheated to 260 °C. The films deposited at room temperature all show the (110) texture. However, films deposited at 260 °C have either the (002) or the (110) texture, depending on the substrate bias. To investigate the effects of applying substrate bias during the RF sputtering deposition at elevated temperature, four films were deposited, each with a 1000 Å Cr underlayer and 400 Å CoCrTa magnetic layer. For all four films, the CoCrTa layer was deposited with the same sputtering conditions, (forward sputtering power, 100 Watts; Ar pressure, 10 mTorr; preheating substrate temperature, 260 °C; substrate bias, -150 V) but the Cr underlayer was deposited with different biasing procedures, as listed in Table 1. Other sputtering parameters were fixed (100 Watts; 10 mTorr; 260 °C).

Table 1. Bias on the Cr underlayer of sample A, B, C and D

sample	bias on the first 200 Å Cr	bias on the remaining 800 Å
A	0 V	0 V
B	-200 V	-200 V
C	0 V	-200 V
D	-200 V	0 V

The X-ray diffraction spectra of these films are shown in Figure 1. In sample A, the (002) texture is dominant in the Cr underlayer, which was deposited without applying substrate bias, and the CoCrTa layer has the (11 $\bar{2}$ 0) texture. This is consistent with previous work.^{5,7} On

the other hand, in sample B, the Cr underlayer, which is deposited with -200 V substrate bias, has the (110) texture and the CoCrTa layer has the (10 $\bar{1}$ 1) texture correspondingly. Comparing sample A and B, it seems that the substrate bias promotes the Cr (110) texture even at elevated substrate temperature. However, it is interesting to note that for sample C, for which the first 200 Å of Cr was deposited without applying substrate bias but the remainder 800 Å Cr was deposited with -200 V bias, the Cr underlayer has a very strong (002) texture, even stronger than that in the sample A. Comparing sample A and C shows that applying substrate bias for the remainder 800 Å Cr, promotes the continuation of the growth of the (002) texture. On the other hand, as seen by comparing sample A and D, applying substrate bias at the initial stage of film formation prevents the (002) texture formation and produces films with the (110) texture.

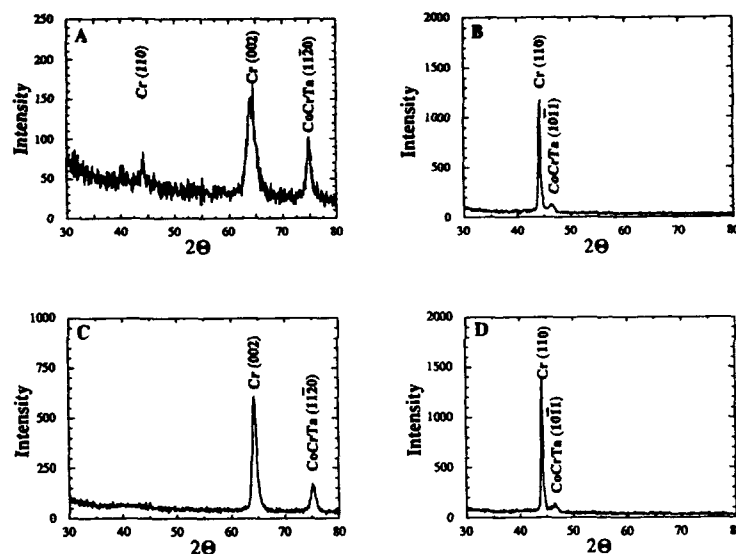


Figure 1, X-ray diffraction spectra of samples A, B, C and D

The films form by a nucleation and growth process. Based on the minimization of surface energy, we have proposed a model for the formation mechanism of crystallographic texture of sputter deposited Cr films.⁸ From this model, the (002) and (110) textures are shown to form by different mechanisms. The (002) texture forms at the very beginning of the film deposition, when the "film" is composed of separated islands. Each single island prefers the (002) orientation, due to minimization of surface energy. On the other hand, the (110) texture is developed by a faster grain growth mechanism after the film become continuous. The higher the concentration of nucleation centers, the sooner the films become continuous. Therefore the (110) texture develop faster.

At room temperature, the nucleation rate is always high, so that the (110) texture always forms very early in the growth of the film. However, heating the substrate reduces the nucleation rate. The nucleation rate also depends on other sputtering parameters. Applying substrate bias increases the bombardment energy of the Ar⁺ ions onto the substrate. At the initial stage of deposition, the concentration of nucleation centers increases with this bombardment because the sites of impingement will become sites for preferential nucleation.¹³

Thus, applying a substrate bias at the initial stage of deposition, promotes the (110) texture. On the other hand, applying substrate bias increases the mobility of surface atoms. When the film becomes continuous, bias promotes surface diffusion. This helps some grains to grow faster than others. Grains with low energy crystalline planes, such as (110) and (002), which are parallel to the film surface, grow faster than others. Therefore, applying substrate bias after the film become continuous promotes the growth of whichever texture is present initially.

2. The crystallographic texture of the CoCrTa layer

It is believed that Co-alloy layers grow epitaxially on the Cr underlayers. Therefore, the crystallographic texture of the Co-alloy layer depends only on the crystallographic texture of Cr underlayer. As shown in Figure 1, comparing spectra A and C, the intensities of the CoCrTa (11 $\bar{2}$ 0) peaks are proportional to the intensities of the Cr (002) peaks. Similarly, comparing spectra B and D, the intensities of the CoCrTa (10 $\bar{1}$ 1) peaks are seen to be proportional to the intensities of the Cr (002) peaks. However, these relationships are not always observed. For example, as shown in Figure 2, three films in which the Cr underlayer have similar crystallographic texture, have different crystallographic texture in their CoCrTa layers. The sputtering conditions of these films are listed in Table 2.

Table 2. Sputtering conditions of samples E, F and G

sample	Cr layer				CoCrTa layer			
	Ts (°C)	P (Watt)	Ar (mT)	Vb (V)	Ts (°C)	P (Watt)	Ar (mT)	Vb (V)
E	R.T	100	2	0	R.T	100	10	-150
F	R.T	100	10	-200	R.T	100	10	-150
G	260	100	10	-200	260°C	100	10	-150

Ts--substrate temperature, P--Sputtering power, Ar--Ar pressure, Vb--Substrate bias

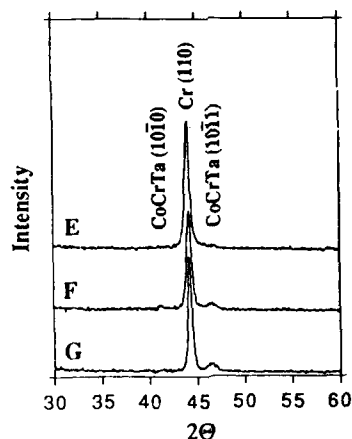


Figure 2. X-ray diffraction spectra of samples E, F and G

Comparing samples E and F, their CoCrTa layers were deposited with the same conditions, but the Cr underlayer of sample E was deposited without applying substrate bias

and the Cr underlayer of sample F was deposited with -200 V substrate bias. As shown in Figure 2, the spectrum E does not show clearly any peaks from the CoCrTa layer, while in the spectrum F does show the (1011) and (1010) peaks from CoCrTa layer, even though spectra E and F show similar Cr (110) textures. The (1011) texture is believed due to the epitaxial growth of Co-alloy on the Cr (110) plane, but it is not clear how the (1010) texture develops.⁴ Comparing samples F and G, both of which were deposited with the same conditions except for the substrate temperature, it can be seen that sample G, which was deposited at elevated temperature, shows stronger (1011) texture and less (1010) texture than F. This means that epitaxial growth at elevated temperature is easier. From these results, it is seen that elevated substrate temperature and applying substrate bias during the deposition of Cr underlayer promotes epitaxial growth.

3. Magnetic properties and crystallographic texture

The extrinsic magnetic properties of magnetic thin films depend on their microstructure. The crystallographic texture describes the orientation of the grains and the surface roughness describes the surface morphology of the film. By applying a substrate bias, we can obtain either the (110) or the (002) texture at the same elevated temperature. On the other hand, applying substrate bias also changes the film morphology. Due to resputtering, when the film is deposited with applied substrate bias, the film is denser (lesser voids between the grains) and its surface is smoother.¹² By controlling the sputtering process, we try to separate the effects of crystallographic texture from that of surface morphology. The magnetic properties and microstructure features of samples A, B, C and D are listed in Table 3.

Table 3. The magnetic properties and microstructure features of samples A, B, C and D

	Hc (Oe)	S	S*	Texture (CoCrTa/Cr)	Roughness
A	1950	0.79	0.78	(1120)/(002)	large
B	1550	0.74	0.74	(1011)/(110)	small
C	1790	0.76	0.85	(1120)/(002) (strong)	small
D	1570	0.72	0.76	(1011)/(110)	large

Hc--Coercivity, S--Remanence squareness, S*--Coercivity squareness

Comparing samples A and D, which have different crystallographic textures but may have similar morphology because they were deposited with the same conditions except for the first 200 Å Cr, the Hc and S of sample A are larger than those of sample D. This is understood because the CoCrTa layer of sample A has the (1120) texture, which brings the c-axis into the plane of the film, while the CoCrTa layer of sample D has the (1011) texture, for which the c-axis is 28° out of the film surface. Similarly, comparing B and C, which may have similar morphology but different type of texture, sample C, which has the (1120) texture, has the larger Hc and S.

Comparing samples A and C, which have the same type of texture but may have different morphologies, the Hc of sample A is larger, even though sample C has a stronger (1120) texture. This may due to their different morphologies. The Cr layer of sample A was deposited without applying substrate bias, therefore, the surface of the Cr layer is rougher due to the effects of shadowing.¹² This rough surface helps to separate the CoCrTa grains which grow on that surface. The related smaller S* of sample A supports this argument.¹⁴

IV. SUMMARY

1) The dependence of crystallographic texture of CoCrTa/Cr thin films deposited by RF sputtering on deposition conditions has been investigated. Cr layers deposited without preheating have the (110) texture. However, when Cr is deposited at elevated temperatures, the texture of the Cr layer depends on the substrate bias. Either the (110) or the (002) texture can be obtained at elevated temperature. We explain this by a simple model.

2) For the CoCrTa layers, the epitaxial growth depends on the microstructure of the Cr layer and the deposition conditions of CoCrTa layer. Applying substrate bias during the deposition of the Cr layer and increasing the substrate temperature during the deposition of CoCrTa promotes epitaxial growth.

3) By controlling the sputtering procedures, the crystallographic texture and morphology can be varied independently. The extrinsic magnetic properties depend on the crystallographic texture and the morphology of the CoCrTa films.

ACKNOWLEDGMENT

This work is supported by the Department of Energy, Grant DE-FG02-90-ER45423. The facilities used for this research are supported in part by the DSSC of CMU under a grant from NSF, No. ECD-8907068.

REFERENCES

- ¹J. C. Allen and R. D. Fisher, *IEEE Trans. Magn.*, **MAG-23**, 122 (1987).
- ²R. D. Fisher, J. C. Allen and J. L. Pressesky, *IEEE Trans. Magn.*, **MAG-22**, 352 (1986).
- ³J. A. Christner, R. Ranjan, R. L. Peterson and J. I. Lee, *J. Appl. Phys.*, **63**(8), 3260 (1988).
- ⁴Y. Hsu, J. M. Sivertsen and J. H. Judy, *IEEE Trans. Magn.*, **MAG-26**, 1599 (1990).
- ⁵T. Ohno, Y. Shiroishi, S. Hishiyama, H. Snzuki and Y. Matsuda, *IEEE Trans. Magn.*, **MAG-23**, 2809 (1987).
- ⁶H. J. Lee, *J. Appl. Phys.*, **57**, 4037 (1985).
- ⁷S. L. Duan, J.O. Artman, B. Wong and D. E. Laughlin, *J. Appl. Phys.*, **67**(9), 4913 (1990).
- ⁸Y. C. Feng, D. E. Laughlin and D. N. Lambeth, submitted to *J. Appl. Phys.*
- ⁹J. Daval and D. Rabdet, *IEEE Trans. Magn.*, **MAG-5**, 768 (1970).
- ¹⁰D. E. Laughlin and B. Y. Wong, *IEEE Trans. Magn.*, **MAG-27**, 4713 (1991).
- ¹¹Y. Shen, D. E. Laughlin and D. N. Lambeth, *IEEE Trans. Magn.*, **MAG-28**, 3261 (1992).
- ¹²J. A. Thornton, *J. Vac. Sci. Technol.*, **A 4**(6), 3059 (1986).
- ¹³L. Eckertova, *Physics of Thin Films*, p.130, New York: Plenum Press (1986).
- ¹⁴J. G. Zhu and H. N. Bertram, *IEEE Trans. Magn.*, **MAG-24**, 2706 (1988).

IN SITU ANALYSIS OF MAGNETIC AND STRUCTURAL PROPERTIES OF EPITAXIAL AND POLYCRYSTALLINE $\text{Ni}_{80}\text{Fe}_{20}$ THIN FILMS

I. Hashim and H.A. Atwater
Thomas J. Watson Laboratory of Applied Physics
California Institute of Technology, Pasadena, CA 91125

ABSTRACT

We have investigated structural and magnetic properties of epitaxial $\text{Ni}_{80}\text{Fe}_{20}$ films grown on relaxed epitaxial $\text{Cu}/\text{Si}(001)$ films. The crystallographic texture of these films was analyzed *in situ* by reflection high energy electron diffraction (RHEED), and *ex situ* by x-ray diffraction and cross-sectional transmission electron microscopy (XTEM). In particular, RHEED intensities were recorded during epitaxial growth, and intensity profiles across Bragg rods were used to calculate the surface lattice constant, and hence, find the critical epitaxial thickness for which $\text{Ni}_{80}\text{Fe}_{20}$ grows pseudomorphically on $\text{Cu}(100)$. XTEM analysis indicated that the epitaxial films had atomically-abrupt interfaces which was not the case for polycrystalline Cu and $\text{Ni}_{80}\text{Fe}_{20}$ film interfaces. The magnetic properties of these epitaxial films were measured *in situ* using magneto-optic Kerr effect magnetometry and were compared with those of polycrystalline films grown on SiO_2/Si . Large H_c (~ 35 Oe) was observed for epitaxial $\text{Ni}_{80}\text{Fe}_{20}$ films less than 3.0 nm thick whereas for increasing thickness, H_c decreased approximately monotonically to a few Oersteds. Correlations were made between magnetic properties of these epitaxial films, the strain in the film and the interface roughness obtained from XTEM analysis.

INTRODUCTION

Permalloy ($\text{Ni}_{80}\text{Fe}_{20}$) heterostructures are of great interest for magnetoresistive devices based on anomalous antiferromagnetic (AF)-coupling and giant magnetoresistance (GMR) in $\text{Ni}_{80}\text{Fe}_{20}/\text{Cu}$ multilayers[1] and spin-valves[2]. To date, all investigations of such $\text{Ni}_{80}\text{Fe}_{20}$ heterostructures have employed polycrystalline films with atomically rough interfaces where the interface roughness is of the same order as the nonmagnetic spacer layer thickness[1, 2]. Since AF-coupling and GMR depend sensitively on $\text{Ni}_{80}\text{Fe}_{20}/\text{Cu}$ interface structure and the film morphology, the magnetotransport properties of atomically-abrupt epitaxial films should more clearly elucidate the underlying physics. Furthermore, with atomically-abrupt film interfaces, it would be possible to fabricate thinner nonmagnetic spacer layers without the interface roughness being the limiting factor. Finally, the growth of epitaxial single layer $\text{Ni}_{80}\text{Fe}_{20}$ films on silicon is potentially of great interest for studying magnetotransport and for applications to magnetoresistive devices because of reduced interfacial and grain-boundary scattering[3].

Epitaxial $\text{Ni}_{80}\text{Fe}_{20}(100)$ films were grown on a relaxed $\text{Cu}(001)$ seed layer, epitaxially grown on $\text{Si}(001)$. The epitaxy of Cu at room temperature on H-terminated $\text{Si}(001)$ has been the object of earlier investigations[4, 5, 6] and has been successfully demonstrated to occur in high-vacuum and UHV conditions. The mode of this epitaxy was found to take place by occlusion of non-(100) grains by (100) grains in the Cu film[6]. The crystallographic orientation of the film is $\text{Cu}(001) \parallel \text{Si}(001)$ with $\text{Cu}[100] \parallel \text{Si}[110]$. The lattice mismatch between Cu and Si for this orientation is 6% whereas for Cu and $\text{Ni}_{80}\text{Fe}_{20}$, it is 3%.

EXPERIMENTAL PROCEDURES

Films were grown in a custom-designed, load lock-equipped ultrahigh vacuum ion beam sputtering system with base pressure in the mid- 10^{-10} Torr regime. Prior to sample insertion into the vacuum system, samples were cleaned by sequential chemical oxidation in a 5:1:1 solution of $\text{H}_2\text{O}:\text{HCl}:\text{H}_2\text{O}_2$ at 80°C , followed by etching in a buffered HF solution. Upon insertion into the sputtering system chamber, reflection high energy electron diffraction (RHEED) at 15 keV was used to confirm (1×1) surface reconstruction of the (001) Si that is commonly observed on HF-dipped Si (001), and which corresponds to dihydride termination of the surface[7]. The as-inserted Si (001) substrates were heated to $T = 200^\circ\text{C}$ for approximately two hours and cooled to room temperature at a cooling rate of $3^\circ\text{C}/\text{minute}$, prior to sputter deposition of Cu. $\text{Ni}_{80}\text{Fe}_{20}$ was grown on this Cu seed layer, which ranged in thickness from 10-300 nm. The $\text{Ni}_{80}\text{Fe}_{20}$ was deposited in the presence of a magnetic field of 20 Oe to induce a uniaxial anisotropy[8]. The deposition rate was approximately 0.10 nm/s. The film thickness, estimated during growth using an oscillating-crystal thickness monitor, was confirmed afterwards with Rutherford backscattering spectrometry. Information about the evolution of the film microstructure during growth was also obtained using *in situ* RHEED measurements, which were recorded on video tape and later analyzed using an image analysis computer program to find the intensity profile across the Bragg rods and hence calculate the surface lattice constant.

Crystallographic texture of the $\text{Ni}_{80}\text{Fe}_{20}/\text{Cu}$ films on Si was confirmed by x-ray diffraction. Measurements were performed using a $\text{Co } K_\alpha$ x-ray source with fixed incident beam angles in the range from 5° - 45° in 5° intervals, along both the [100] and [110] azimuths of the Si surface. Scattered x-rays were measured using a parallel detection and data acquisition instrument simultaneously over an angular range of 120° with 0.05° angular resolution. Cross-sectional transmission electron microscopy (XTEM) analysis was performed on a Philips EM430 microscope operating at 300 keV. TEM samples were prepared using adhesives which did not require any high-temperature curing. The samples were ion-milled using Ar^+ immediately prior to electron microscopy. Magnetic properties were measured using magneto-optic Kerr effect (MOKE) magnetometer after sample transfer to a quartz tube interfaced to the UHV-sputtering system. A 670 nm semiconductor diode laser beam polarized by a Glan-Thompson polarizer was used as the incident beam, whose rotation in polarization after reflection from the magnetic sample was detected using a Wollaston prism and a photodiode pair. The sum and difference voltage signals from the photodiodes were amplified and acquired on a 386 computer. The angle of incidence was approximately 70° from the normal. A pair of Helmholtz coils were used to magnetize the sample such that the Kerr rotation measured was longitudinal[9]. The sample holder geometry allows rotation about the surface normal of the sample so that the in-plane easy and hard axis Kerr loops could be measured for NiFe films down to thicknesses of 1.0 nm.

RESULTS & DISCUSSION

From surface lattice constant measurements shown in Fig. 1, the $\text{Ni}_{80}\text{Fe}_{20}$ films were observed to be pseudomorphic with the Cu film up to a thickness of 2.3 nm, followed by growth of a relaxed film with bulk lattice parameter. The critical epitaxial film thickness h_c for a lattice misfit f , is obtained by solving the transcendental equation[10]:

$$h_c = \frac{b}{8\pi f \cos \lambda} \left[\frac{1 - \nu \cos^2 \beta}{1 + \nu} \right] \ln \left(\frac{4h_c}{b} \right) \quad (1)$$

where b is the misfit dislocation Burger's vector, ν is the Poisson's ratio, β and λ are the

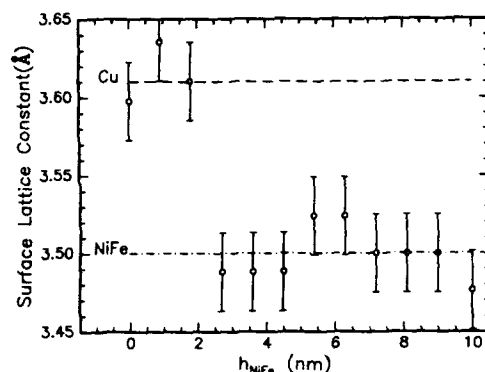


Figure 1: Surface lattice constant of $\text{Ni}_{80}\text{Fe}_{20}$ film grown on $\text{Cu}(100)$ calculated from RHEED measurements as a function of $\text{Ni}_{80}\text{Fe}_{20}$ film thickness.

angles that the Burger's vector makes with the dislocation line and the direction normal to the dislocation line lying within the plane of the interface, respectively. Substituting the lattice constant of $\text{Ni}_{80}\text{Fe}_{20}$ for b , $\lambda = \beta = 60^\circ$ which is often the case for fcc crystals, ν of 0.31 for Ni, h_c was found to be 2.1 nm from solving eq. (1), which agrees well with the experimentally-determined critical epitaxial thickness for $\text{Ni}_{80}\text{Fe}_{20}$.

Figure 2 shows an x-ray scan for $\theta_i = 30^\circ$ for a $\text{Ni}_{80}\text{Fe}_{20}$ (30 nm)/ Cu (30 nm)/ $\text{Si}(001)$ film which indicates that the (100) texture in the films is 2-3 orders of magnitude stronger than other fcc textures, notably (111). Furthermore, the lattice constants calculated from the diffraction spectrum confirm that the Cu and the $\text{Ni}_{80}\text{Fe}_{20}$ films are strain-relieved; i.e., have the bulk lattice constants. XTEM was used to analyze the $\text{Ni}_{80}\text{Fe}_{20}$ /Cu interface roughness, which was found to depend on the Cu seed layer thickness. For Cu thicknesses ≤ 100.0 nm, the interface was smooth and atomically-abrupt. Figure 3 shows XTEM image of a $\text{Ni}_{80}\text{Fe}_{20}$ /Cu/Si(001) film. The NiFe/Cu interface cannot be clearly seen in Fig. 3 due to lack of Z-contrast between NiFe and Cu. However, it is discernible in high resolution XTEM images by the presence of Moiré fringes and misfit dislocations to accommodate lattice mismatch between Cu and $\text{Ni}_{80}\text{Fe}_{20}$ [11]. Nevertheless, from the NiFe film surface and the Cu/Si interface in Fig. 3, the r.m.s. roughness of the film was estimated to be ≤ 0.7 nm. For Cu seed layer thicknesses of 300 nm, the interface had a roughness of 9.3 nm. The development of this roughness with epitaxial Cu thickness is currently under investigation and is probably related to film deposition conditions[11].

Magnetic properties of the epitaxial and polycrystalline $\text{Ni}_{80}\text{Fe}_{20}$ films, 1.5-20.0 nm thick, were measured using MOKE magnetometry. As can be observed from Kerr loops shown in Fig. 4, for epitaxial and polycrystalline $\text{Ni}_{80}\text{Fe}_{20}$ films 3.0 nm thick, H_c is considerably higher for epitaxial films. It is plausible that dislocations generated due to misfit in the epitaxial film cause domain wall pinning and hence, an increase in H_c . No well-defined uniaxial anisotropy was observed for epitaxial films with thicknesses ≤ 3.0 nm, whereas that was not the case for film thicknesses ≥ 10.0 nm. For a 20 nm thick epitaxial $\text{Ni}_{80}\text{Fe}_{20}$ film, H_{ce} , H_{ch} , and H_k were comparable to that of a soft polycrystalline $\text{Ni}_{80}\text{Fe}_{20}$ film (see Fig. 4), indicating that the 20.0 nm thick epitaxial film is relatively strain-free and devoid of defects or pinning sites for domain walls. Figure 5 shows the variation of H_{ce} as a function of epitaxial $\text{Ni}_{80}\text{Fe}_{20}$ film thickness for various Cu seed layer thicknesses. Notice that even though the film has no coherent strain for thicknesses greater than $h_c = 2.5$ nm, H_{ce}

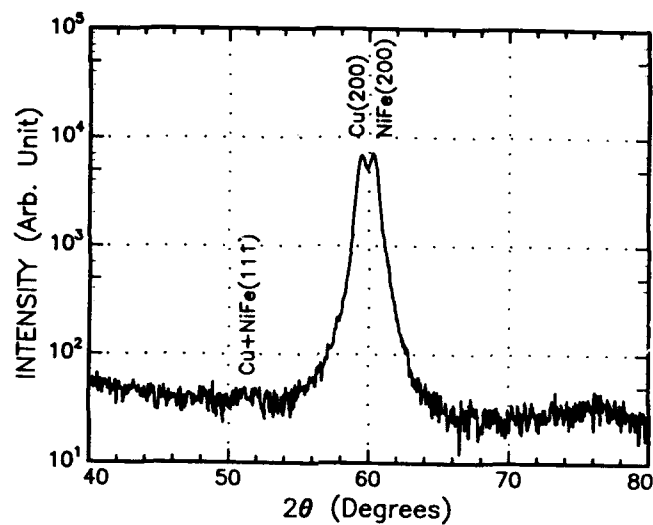


Figure 2: Co- K_α x-ray diffraction spectrum of NiFe(30nm)/Cu(30nm)/Si(001) film for beam incidence angle of 30° .

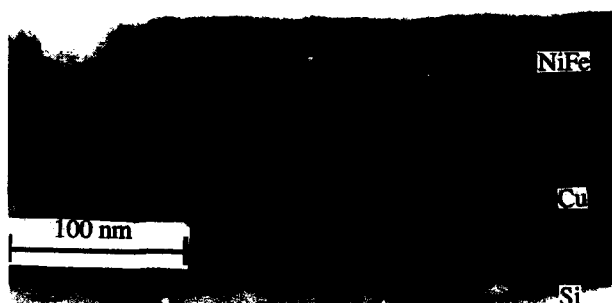


Figure 3: Electron micrograph of epitaxial NiFe/Cu/Si(001) film.

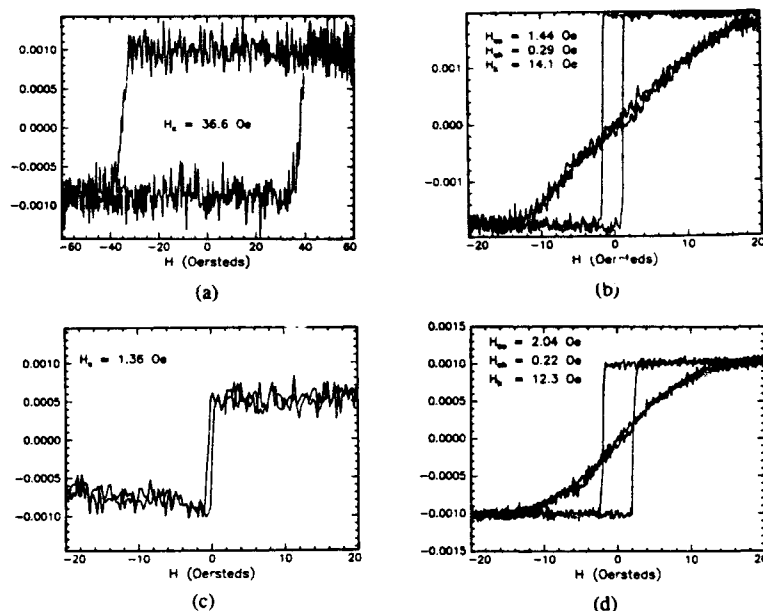


Figure 4: Kerr loops for epitaxial NiFe/Cu/Si(001) film (a) 3.0 nm and (b) 20.0 nm thick, and for polycrystalline NiFe/SiO₂/Si films (c) 3.0 nm and (d) 20.0 nm thick.

is still significantly high for $h \approx 4 * h_c$. This may be due to the presence of localized strain fields caused by misfit dislocation networks associated with lattice mismatch between Cu and Ni₈₀Fe₂₀. Magnetostriction measurements were made for 20.0 nm thick polycrystalline Ni₈₀Fe₂₀ films on glass with a saturation field of 20 Oe, and was found to be $+2.4 \times 10^{-6}$. The concentration for which magnetostriction is zero for (100) and (111) textured NiFe films, is $x_{Ni}=0.83$ and $x_{Ni}=0.81$ [12], respectively. Therefore, it is likely that the epitaxial (100) Ni₈₀Fe₂₀ films have higher magnetostriction than the polycrystalline films on SiO₂/Si which generally possess (111) texture[11]. Efforts are under way to measure the magnetostriction of epitaxial NiFe films *in situ*, and observe its variation with the misfit strain relaxation.

CONCLUSIONS

Epitaxial Ni₈₀Fe₂₀/Cu/Si(001) films were observed to have atomically-abrupt interfaces and roughness significantly less than that for polycrystalline Ni₈₀Fe₂₀ films. The critical thickness for which Ni₈₀Fe₂₀ grows pseudomorphically on Cu(100) was found to be 2.3 nm. Magnetic properties of these films were investigated *in situ* and were found to be sensitive to the misfit strain between the Ni₈₀Fe₂₀ film and the Cu seed layer. H_c was observed to be significantly higher for less than 10 nm thick epitaxial Ni₈₀Fe₂₀(100) films as compared with polycrystalline films of same thickness. However, relatively strain-free epitaxial Ni₈₀Fe₂₀ films (~ 20 nm thick) had soft magnetic properties comparable to those of polycrystalline films, suggesting that they could be used for epitaxial NiFe heterostructures such as spin-valves, and for studying magnetotransport in NiFe/Cu multilayers.

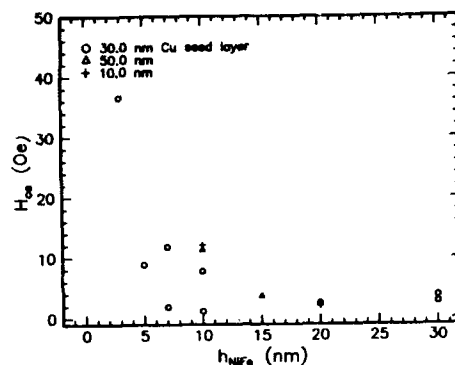


Figure 5: Variation of H_c with epitaxial NiFe film thickness for various Cu seed layer thicknesses.

ACKNOWLEDGEMENTS

This work was supported by NSF and IBM. We would also like to acknowledge DOE grant DEFGO589ER75511 which made the use of Inel Thin Film Diffractometer possible for x-ray analysis. We thank Kirill Shcheglov and Wurzel Keir for assistance with MOKE software and hardware development, Carol Garland for assistance with electron microscopy, Ken Kung and Bob Valetta for making magnetostriction measurements at IBM Almaden, Bruce Gurney for helpful advice in the design of the MOKE magnetometer, Byungwoo Park for help with the earlier part of this project and lastly, Selmer Wong for help with preparing the poster for this paper. The RHEED video images were analyzed using Image 1.40 public domain software, copyright National Institute of Health.

References

- [1] S.S.P. Parkin, Appl. Phys. Lett. **60**, 512 (1992).
- [2] B. Dieny, V.S. Speriosu, B.A. Gurney, S.S.P. Parkin, D.R. Wilhoit, P. Roche, S. Metin, D.T. Peterson, and S. Nadimi, J. of Magn. and Magn. Mater. **93**, 111 (1991).
- [3] A.F. Mayadas and M. Shatzkes, Phys. Rev. B **1**, 1382 (1970).
- [4] C.A. Chang, Appl. Phys. Lett. **55**, 2754 (1989).
- [5] J. Li and Y. Shacham-Diamand, J. Electrochem. Soc. **139**, L37 (1992).
- [6] I. Hashim, B. Park and H.A. Atwater, Mater. Res. Soc. Proc. Vol. 280, (1992).
- [7] J.A. Schaefer, Physica **B170**, 45 (1991).
- [8] M. Takahashi, J. Appl. Phys. **33**, 1101 (1962).
- [9] M.J. Freiser, IEEE Trans. Mag. **Mag-4**, 152 (1968).
- [10] J.W. Matthews and A.E. Blakeslee, J. Cryst. Growth. **27**, 118 (1974).
- [11] I. Hashim and H.A. Atwater, (unpublished).
- [12] E. Klokholm and J.A. Aboaf, J. Appl. Phys. **52**, 2474 (1981).

EPITAXIAL GROWTH OF fcc FE AND CU FILMS ON DIAMOND

D.P. PAPPAS, J.W. GLESENER, V.G. HARRIS, J.J. KREBS, Y.U. IDZERDA, A.A. MORRISH, AND G.A. PRINZ

NAVAL RESEARCH LABORATORY, WASHINGTON, DC 20375

ABSTRACT

The growth of iron and copper films and multilayers on the (100) face of diamond has been achieved and studied by reflection high energy electron diffraction (RHEED), extended x-ray absorption fine structure (EXAFS), ferromagnetic resonance (FMR), and SQUID magnetometry. RHEED and AES studies show that 2-3 atomic layers (AL) of Fe on C(100) forms a continuous film. The films as deposited at room temperature are disordered, and after a 350° C anneal displays a face-centered cubic structure. Subsequent layers of Cu on this epitaxial Fe film grow as an oriented, single crystal fcc film. FMR and SQUID signals have been observed from the Fe films, showing that they are ferromagnetic.

INTRODUCTION

Stabilization of metastable phases of matter by epitaxial growth on lattice matched substrates has opened an entirely new field of experimental and theoretical physics [1]. The use of diamond substrates is appealing due to the extraordinary properties of diamond, i.e. its large band gap, high thermal conductivity, extreme hardness, and desirable optical properties. In the past few years there has been a strong interest in the growth and applications of thin diamond films on various surfaces. Characterization and optimization of the interfacial properties between diamond and various metals is a necessary step in the development of diamond-based electronic devices. An understanding of the magnetic properties of transition metal films on diamond may also provide a means of developing non-volatile magnetic storage devices based on diamond.

The epitaxial growth of transition metals on C(100) is feasible due to the close lattice match ($a=3.57 \text{ \AA}$ for diamond vs. 3.59, 3.52, and 3.61 for fcc-Fe, Ni, and Cu, respectively), and the fact that the symmetry of the (100) face of the diamond and fcc structures is the same. In fact, recent work by Humphreys, *et. al* [2], has shown that it is possible to grow continuous, single crystal films of Ni(100) on C(100) by e-beam epitaxy. Cu(100), on the other hand, is more difficult to grow on C(100) due to its tendency to grow in a polycrystalline fashion at room temperature, and ball up into islands upon annealing [3]. Stabilization of single crystal Cu(100) films on an easily prepared, reusable, and insulating substrate such as diamond would be useful in that it would then be possible to prepare Cu(100) surfaces *in-situ* (rather than resorting to cutting and polishing a Cu single crystal and then sputtering and annealing *in-situ*). In addition, if magnetic films are to be prepared on Cu(100), subsequent *ex-situ* measurements such as ferromagnetic resonance (FMR) and magnetoresistance are more easily conducted when there is only a thin film of Cu rather than a macroscopic single crystal substrate.

The growth of fcc-Fe at low temperature is also an important objective of this work. It is well known that the high temperature, fcc phase (γ -Fe) can be stabilized in films up to 20 \AA thick on single crystal Cu substrates [4]. Due to the similarities in lattice constants of diamond and Cu, it might also be expected that fcc-Fe could be stabilized on C(100). In this work, we show that very thin films of Fe on C(100) exhibit an fcc-like RHEED pattern when prepared properly, and that subsequent films of Cu on the Fe/C(100) also exhibit fcc RHEED patterns which rival the quality of patterns obtained from a single Cu(100) crystal.

The metastable fcc-Fe is interesting from a magnetic point of view as well. While the high temperature γ -phase of Fe is antiferromagnetic, it has been observed that under the proper growth conditions, thin films of fcc-Fe/Cu(100) are ferromagnetic with a strong perpendicular anisotropy

[5]. Theoretical calculations show that fcc-Fe may possibly occur in three different magnetic states, either antiferromagnetic, ferromagnetic with a high moment ($\approx 2.2\mu_B$), or ferromagnetic with a low moment ($\approx 1 - 1.5\mu_B$) [6]. The fcc-Fe is predicted to go from the AFM to a FM state as the lattice constant increases, with the transition happening very close to the lattice constant of Cu. The energy differences between these states are small, and it is difficult to accurately predict the true ground state even with current calculational techniques.

SAMPLE PREPARATION AND STRUCTURAL CHARACTERIZATION

The $3 \times 3 \times 2$ mm C(100) substrates used in this work were cleaned by etching in an aqua regia solution and then boiling in an $H_2O_2 - NH_4OH - H_2O$ solution. The substrate was then loaded into a UHV chamber (base pressure $< 1 \times 10^{-10}$ Torr) and the surface characterized using reflection high energy electron diffraction (RHEED) and Auger electron spectroscopy (AES). The only *in-situ* preparation of the C(100) substrate prior to growth was e-beam bombardment of the face with the 10 keV RHEED beam. Electrical contact was made with the surface in order to reduce charging effects while conducting the RHEED and AES studies. A typical RHEED pattern of the C(100) face is shown in Fig. 1(a). The RHEED pattern is taken along a [110] axis, and has a low diffuse background and the symmetry expected from a (100) cubic face. We report here that there was virtually no evidence of an oxygen peak in the AES spectrum, and therefore conclude that any residual oxygen termination of the surface had been desorbed by the RHEED beam.

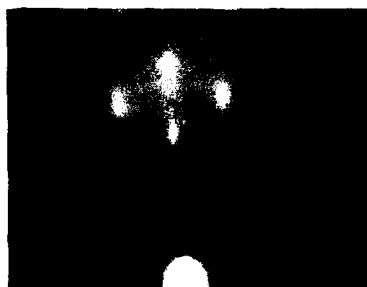
The Fe was deposited by sublimation from an electron beam heated rod, and the pressure stayed below 5×10^{-10} Torr during growth. The thickness was measured with a quartz crystal monitor. During the Fe growth the C(100) substrate was left at room temperature. After ≈ 5 Å of Fe had been deposited, there was a complete loss of the C(100) RHEED pattern, and only a bright diffuse background with a weak specular reflection was observed on the screen. This is strong evidence that the Fe has covered the diamond in a continuous film. We also note that the AES uptake curve up to 20 Å of Fe follows a smooth exponential increase when the substrate is held at room temperature. A fit of the room temperature, normalized Fe signal ($Fe/(Fe+C)$) saturates to 1 with an attenuation constant 10 Å, which is again consistent with a continuous Fe coverage. For comparison, the normalized Fe uptake curve taken with the substrate held at 300° C during deposition saturates at 0.6, and evidence of the sharp C(100) RHEED pattern is still evident up to 20 Å coverage. These effects are characteristic of the Fe agglomerating into islands for the high temperature growth.

Clearly, then, it is possible to obtain a disordered, continuous Fe film on C(100) by deposition at room temperature. We grew the Fe film up to a final thickness of 10 Å, gently annealed it to 350° C, and observed the formation of the fcc-like RHEED pattern shown in Fig. 1(b). We also report that for this annealing temperature there was no change in the AES Fe/C intensity ratio. While the spots are much broader than those from the diamond substrate, the symmetry and spacings of the two patterns are the same, and we conclude that the Fe has assumed a slightly disordered fcc structure.

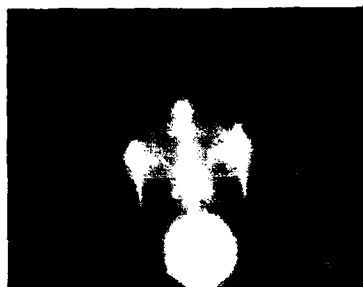
The Cu was evaporated from a W basket at a pressure of 1×10^{-9} Torr, and the thickness was again measured with a quartz crystal thickness monitor. The Fe/C(100) substrate was held at 300° C during the Cu evaporation. A RHEED pattern from the Cu after 100 Å had been deposited is shown in Fig. 1(c), and shows much sharper streaks than the underlying Fe. We attribute the improved RHEED pattern to the high mobility of the Cu atoms, thus defects in the Fe seed are being annealed out as the Cu film thickness increases. In addition, there are superstructure spots appearing at approximately the 3rd order positions, which could be caused by, e.g., a stress in the Cu film. After about 100-200 Å Cu, the reconstruction spots vanish and the quality of the RHEED pattern continues to improve. In Fig. 1(d) and (e) we compare the RHEED pattern of 1350 Å of Cu to that obtained from a Cu(100) single crystal which had been oriented to within 0.5°, polished, and then sputtered and annealed *in-situ*. The quality of the grown Cu(100) surface as determined by the RHEED rivals that of the bulk single crystal.



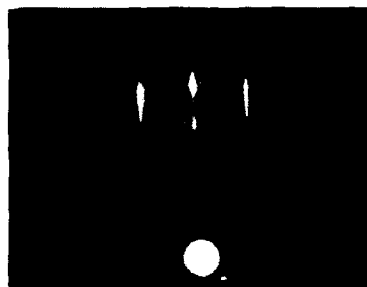
a) Diamond(100) single crystal



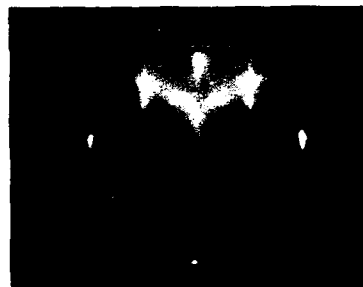
b) 10 Å Fe/Diamond(100)



c) 100 Å Cu/Fe/Diamond(100)



d) 1350 Å Cu/Fe/Diamond(100)



e) Cu(100) single crystal

Figure 1: RHEED patterns of the samples taken in-situ. Panel (a) shows the pattern obtained from the C(100) substrate, while (b) shows the pattern from 10 Å film after it had been annealed to 350°C. Panels (c) and (d) show patterns from 100 and 1350 Å Cu grown on the Fe/C(100) at 300°C. The RHEED pattern in (e) is a reference spectrum from a single Cu crystal.

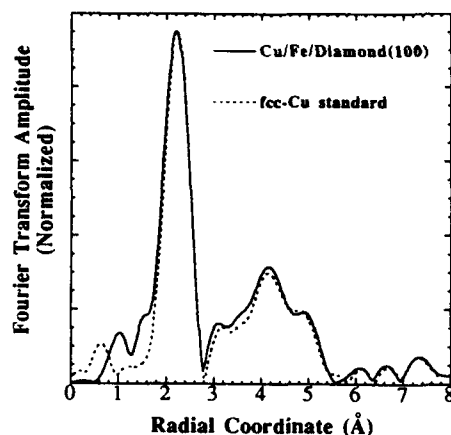


Figure 2: Fourier transformed Cu K-edge EXAFS data for Cu/Fe/Diamond(100) and a 1350 Å Cu film. Both data sets have been analyzed using a k -range of 2.5-11.5 Å⁻¹ and a k^2 -weighting. Data have not been corrected for electron phase shifts.

In order to demonstrate that the Cu is in an fcc structure, we have conducted extended x-ray absorption fine structure spectroscopy (EXAFS) on the Cu K-absorption edge. The details of the data collection and analysis are presented elsewhere [7]. Figure 2 is a plot of Fourier transformed Cu EXAFS data collected from Cu/Fe/Diamond(100) sample and a known fcc-Cu standard. Although these data have not been corrected for electron phase shifts and therefore do not represent true radial distances, both sets have undergone identical analysis procedures which allow direct comparisons to be made. Comparisons between the data sets illustrate a close match in both Fourier amplitude and radial distances of the near neighbor and higher order peaks. It is clear that the Cu in the Cu/Fe/Diamond(100) sample is in an fcc environment. The slight offset in the distance of the nearest neighbor peaks is evidence of a small tetragonal distortion of the Cu lattice which most likely stems from the lattice mismatch between the substrate and the layered structure.

Magnetic characterization

The magnetic properties of the Fe films under the thick (≈ 1000 Å) Cu cap layers were investigated *ex-situ* using both FMR and SQUID magnetometry. Ferromagnetic signals were observed using both techniques, and when the techniques are used in conjunction it is possible to extract the average moment, the coercive field, the in-plane anisotropies, and the strength and sign of the perpendicular anisotropy.

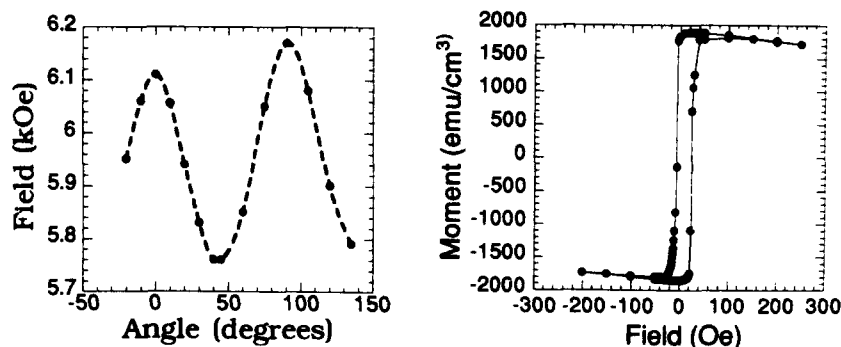


Figure 3: The angle resolved FMR spectrum of a 20 Å Fe/C(100) film taken at 35 GHz and a hysteresis loop of the same film taken in a SQUID magnetometer. The film was capped with ≈ 1000 Å Cu.

The angle resolved FMR signal taken at 35 GHz is shown on the left side of Fig. 3. At zero degrees, the magnetic field is aligned along the [010] axis of the diamond substrate. This angle could be accurately calibrated by monitoring the splitting of the nitrogen electron spin resonance lines. When the field is exactly along the highest symmetry axis, there will be no splitting of the nuclear spin $I = \pm 1$ lines [8]. The minimum resonance field was obtained at 45° , indicating that the easy axis in the plane of the film are along the [011] directions. We note here that the easy axis of both bulk fcc-Fe/Cu(100) and bcc-Fe is along the [001] directions [9, 10]. In addition, since there is a difference in the maxima at 0 and 90 degrees, a small uniaxial anisotropy in the plane of the film is also present. By fitting the FMR data, therefore, the following quantities can be extracted:

$$\begin{aligned} 4\pi M' &= 17.6 \text{ kG} \\ K_1/M_s &= -0.106 \text{ kG} \\ |K_u|/M_s &= 0.022 \text{ kG}, \end{aligned}$$

where $4\pi M'$ is the effective magnetization (including a perpendicular anisotropy field), K_1 is the cubic magnetocrystalline anisotropy, and K_u represents an in-plane uniaxial anisotropy.

The SQUID magnetometer data was obtained with the magnetic field applied in the plane of the film along the [011] easy axis. A hysteresis loop taken at 100 K is shown on the right in Fig. 3. The negative sloping background is due to a diamagnetic contribution from the nitrogen impurities in the diamond substrate. From this data, the absolute magnetization M_s and the coercive field H_c can be obtained:

$$\begin{aligned} M_s &= 1900 \pm 200 \frac{\text{emu}}{\text{cm}^3} \\ H_c &= 12 \pm 2 \text{ Oe}. \end{aligned}$$

The error in the magnetization is primarily due to the uncertainty in the film thickness. Using the identity

$$4\pi M' = 4\pi M_s + \frac{2K_\perp}{M_s}, \quad (1)$$

where K_\perp is the anisotropy perpendicular to the film, and the formula for the magnetic dipole energy E_D of a thin film, we find:

$$\begin{aligned} E_D &= 2\pi M_s^2 = 2.3 \times 10^7 \frac{\text{erg}}{\text{cm}^3} \\ K_\perp &= -6 \times 10^6 \frac{\text{erg}}{\text{cm}^3}. \end{aligned}$$

The negative sign of the perpendicular anisotropy means that it favors a magnetization out of the plane of the film. However, it is smaller in magnitude than the dipole energy of the film, and the magnetization therefore lies in the plane of the film. Dividing K_\perp by the film thickness, we find that this would correspond to a surface anisotropy $K_s \approx 1 \text{ erg/cm}^2$, which agrees roughly with that of, e.g., Fe/Cu(100) [11].

Summary

Evidence is presented that fcc-Fe can be grown on C(100) by deposition at low temperature and subsequent annealing to 300°C . The Fe/C(100) is ferromagnetic, with a different in-plane easy axis than fcc-Fe/Cu(100). The sign and magnitude of the perpendicular anisotropy of these systems is comparable. Further EXAFS and angle resolved AES studies are in progress to understand more completely the structure of the Fe films. The Fe/C(100) films were capped with Cu, which shows single crystal quality fcc RHEED and EXAFS signals. Growth of Cu(100) *in-situ* on a reusable, high resistivity substrate such as diamond will allow, for example, resonance and transport measurements to be conducted more easily on samples grown on such Cu(100) faces.

REFERENCES

1. L.M. Falicov, D.T. Pierce, S.D. Bader, R. Gronsky, K.B. Hathaway, H. Hopster, D.N. Lambeth, S.S.P. Parkin, G. Prinz, M. Salamon, I.K. Schuller, and R.H. Victora, *J. Mater. Res.* **5**, 1299 (1990).
2. T.P. Humphreys, H. Jeon, R.J. Nemanich, J.B. Posthill, R.A. Rudder, D.P. Malta, G.C. Hudson, R.J. Markunas, J.D. Hunn, and N.R. Parikh, *Mat. Res. Soc. Symp. Proc.* **202**, 463, 1991.
3. C. Wan-rong and W.U. Zi-qin, *Chinese Physics* **3**, 299 (1983).
4. S.A. Chambers, T.J. Wagener, and J.H. Weaver, *Phys. Rev. B* **36**, 8992 (1987).
5. C. Liu, E.R. Mooh, and S.D. Bader, *Phys. Rev. Lett.* **60**, 2422 (1988).
6. C.S. Wang, B.M. Klein, H. Krakauer, *Phys. Rev. Lett.* **54**, 1852 (1985).
7. In *X-Ray Absorption Principles, Applications, Techniques of EXAFS, SEXAFS, and XANES*, ed. by C.C. Koningsberger and R. Prins (Wiley, New York 1988).
8. W.V. Smith, P.P. Sorokin, I.L. Gelles, G.J. Lasher, *Phys. Rev.* **115**, 1546 (1959).
9. See, for example, C. Kittel, *Introduction to Solid State Physics*, (Wiley, New York 1976).
10. R. Allenspach and A. Bischof, *Phys. Rev. Lett.* **69**, 3385 (1992).
11. J.R. Dutcher, B. Heinrich, J.F. Cochran, D.A. Steigerwald, and W.F. Egelhoff, *J. Appl. Phys.* **63**, 3464 (1988).

**THE INFLUENCE OF QUANTIZING MAGNETIC FIELD ON THE MAGNETIC
SUSCEPTIBILITIES IN ULTRA THIN FILMS OF DILUTE MAGNETIC MATERIALS**

KAMAKHYA P GHATAK* AND S. N. BISWAS**

*Department of Electronics and Tele-communication Engineering,
Faculty of Engineering and Technology, Jadavpur University,
Calcutta 700032, INDIA.

**Institut für Halbleitertechnik, RWTH, 5100 Aachen, WSH.
Sommerfeld Strasse, GERMANY.

ABSTRACT

In this paper we have studied the dia and paramagnetic susceptibilities of the holes in ultrathin films of dilute magnetic materials in the presence of a quantizing magnetic field and compared the same with that of the bulk specimens under magnetic quantization for the purpose of relative comparison. It is found, taking $\text{Hg}_{1-x}\text{Mn}_x\text{Te}$ and $\text{Cd}_{1-x}\text{Mn}_x\text{Se}$ as examples, that both the susceptibilities increase with decreasing film thickness and increasing surface concentration in oscillatory manners. The numerical values of the susceptibilities in ultrathin films of dilute magnetic materials are greater than that of the bulk and the theoretical analysis is in agreement with the experimental data as reported elsewhere.

Introduction

The interest in epitaxial films of $\text{Cd}_{1-x}\text{Mn}_x\text{Te}$ arises from the novel magnetic properties due to the Mn atoms and the close lattice match and chemical compatibility with $\text{Hg}_{1-y}\text{Cd}_y\text{Te}$, an ideal material for long wave length infrared detectors. It is worth remarking that the close lattice match and chemical compatibility of CdMnTe with HgCdTe are important because it is possible to monolithically integrate devices such as CdTe transistors ($\text{Hg}, \text{Cd}, \text{Mn}$) [1,2], the heterojunction lasers [3,5] and other optical and electronic devices with HgCdTe infrared focal plane arrays. Recent advances in molecular beam epitaxy techniques have made possible the controlled substitutional doping of CdTe [6], CdMnTe [7] and CdMnTe-CdTe superlattices [8]. The combined compatibility of controlled substitutional doping and heterostructure of dilute magnetic materials make possible magnetically tuned lasers, magnetic field sensor and magnetic field sensitive transistors [9]. Though considerable work has already been done nevertheless it appears from the literature that the dia and paramagnetic susceptibilities of the holes in ultrathin films of dilute magnetic materials have yet to be investigated. In this paper we shall study both the susceptibilities for the more interesting case which occurs from the presence of a quantizing magnetic field, taking $\text{Hg}_{1-x}\text{Mn}_x\text{Te}$ and $\text{Cd}_{1-x}\text{Mn}_x\text{Se}$ as examples.

In ultrathin films the restriction of the motion of the carriers along the direction normal to the film of the layer (say, the z-direction) may be viewed as carrier confinement in a one-dimensional potential well leading to the quantization of the wave-vector of the carriers (known as quantum size effect) in the z-direction. In the presence of a quantizing magnetic field along the z-direction, the free motion parallel to the film is also quantized forming Landau levels and leading to diamagnetism. Moreover, the spinning motion of the electrons leads to paramagnetism due to the spin-splitting of Landau

levels. In this work we shall study the doping and film thickness dependences of both the susceptibilities of the holes in ultrathin films of $\text{Hg}_{1-x}\text{Mn}_x\text{Te}$ and $\text{Cd}_{1-x}\text{Mn}_x\text{Se}$ respectively in the presence of broadening of Landau levels.

Theoretical Background

The hole energy spectra in bulk specimens of dilute magnetic materials are given by [10]

$$E_{\pm \frac{3}{2}}(k) = (\hbar^2/2) [(3/4m_{lh} + 1/4m_{hh})(k_x^2 + k_y^2) + (k_z^2/m_{hh})] \pm 3A_0 \quad (1)$$

$$\text{and } E_{\pm \frac{1}{2}}(k) = (\hbar^2/2) [(1/4m_{lh} + 3/4m_{hh})(k_x^2 + k_y^2) + (k_z^2/m_{lh})] \pm A_0 \quad (2)$$

where the notations have been defined in the above reference. In the presence of a quantizing magnetic field B along z -direction, the modified hole dispersion laws in ultrathin films of dilute magnetic materials of width d_0 can be expressed as

$$E_{\pm(3/2)}(k) = (n_1 + \frac{1}{2})\hbar\omega_1 + (\hbar^2 t_1^2 \pi^2 / 2m_{hh} d_0^2) \quad (3)$$

$$\text{and } E_{\pm(1/2)}(k) = (n_2 + \frac{1}{2})\hbar\omega_2 + (\hbar^2 t_2^2 \pi^2 / 2m_{lh} d_0^2) \quad (4)$$

where $n_i = 0, 1, 2, \dots$, $i=1, 2$, $\omega_i = eB/m_i$

$$(m_1)^{-1} = ((3/4m_{lh}) + (1/4m_{hh}))^{-1}, \quad (1/m_2) = ((1/4m_{lh}) + (3/4m_{hh}))^{-1},$$

and $t_i = 1, 2, 3, \dots$

The free energy of the holes, including broadening, is given by

$$F(B) = p_0 E_F - (2eBk_B T / \hbar d_0) [D_1 (A_{1,+} + A_{1,-}) + D_2 (A_{2,+} + A_{2,-})] \quad (5)$$

where p_0 , the total hole concentration, can be written as

$$p_0 = (2eB/\pi \hbar d_0) [D_1 (t_{1,+} + t_{1,-}) + D_2 (t_{2,+} + t_{1,-})] \quad (6)$$

$$D_i = \sum_{n_i=0}^{n_{i\max}} \sum_{t_i=1}^{t_{i\max}}, \quad t_{i,t} = a_{i,t} (a_{i,t} + \cos C_{i,t}) / A_{i,t},$$

$a_{i,t} = \exp [(k_B T)^{-1} (E_F - E_{i,t})]$, k_B is Boltzmann constant, E_F is the Fermi energy in the present case, $E_{i,t}$ are the roots of (3) and (4) respectively, $C_i = p_{i,t} / k_B T$, $p_{i,t}$ are the respective broadening parameters and

$$A_{i,t} = 1 + (a_{i,t})^2 + 2(a_{i,t}) (\cos C_{i,t})$$

The equation for diamagnetic susceptibility is

$$\chi_d = -\mu_0 F''(B) \quad (7)$$

where μ_0 is the permeability of free space, $F''(B)$ denotes the double differentiation with respect to B . Thus combining (5) to (7) we can determine χ_d . When spin splitting is considered, the free energy can be written as

$$f(B) = p_0 E_f - (2eBk_B T / \hbar d_0) [D_1 (G_{1,+} + G_{1,-}) + D_2 (G_{2,+} + G_{2,-})] \quad (8)$$

where E_f is the Fermi energy when spin splitting is considered and can be determined from the equation

$$p_0 = (2eB/d_0 \pi \hbar) [D_1 (H_{1,+} + H_{1,-}) + D_2 (H_{2,+} + H_{2,-})] \quad (9)$$

$$H_{i,t} = \bar{a}_{i,t} (\bar{a}_{i,t} + \cos C_{i,t}) / G_{i,t},$$

$$\bar{a}_{i,t} = \exp [(k_B T)^{-1} (E_f - E_{i,t})],$$

$E_{i,t} + E_{i,t} \pm (B \beta g_{i/2})$, g_1 and g_2 are the magnitudes of the effective g factors at the valence bands whose dispersion relations are given by (3) and (4) respectively and

$$G_{i,t} = 1 + (\bar{a}_{i,+})^2 + 2(\bar{a}_{i,t}) (\cos C_{i,t})$$

$$\text{Thus using the equation } \chi_p = -\mu_0 f''(B) \quad (10)$$

and combining (8) and (10) we can determine the paramagnetic susceptibility.

Results and Discussion

Using the appropriate equations and taking the parameters given in [10] we have plotted χ_d and χ_p versus d_0 and n_0 in ultrathin films of $\text{Hg}_{1-x}\text{Mn}_x\text{Te}$ and $\text{Cd}_{1-x}\text{Mn}_x\text{Se}$ as shown in Figs. 1 and 2 respectively where the same dependences have also been plotted for bulk specimens under magnetic quantization for the purpose of relative comparison. The circular plots in Fig. 2 exhibit the same dependences in accordance with the experimental results [11].

The influence of size quantization is immediately apparent from Fig. 1 since both χ_p and χ_d in ultrathin films oscillate with d_0 . The humps occur when the quantum numbers change from one fixed value to another allowed one. For the corresponding bulk materials, both the susceptibilities are d_0 invariant. From Fig. 2 it appears that the values of χ_p and χ_d increases with increasing p_0 and $\chi_d = K_0 \chi_p$ where K_0 is a constant.

With varying magnetic field a change is reflected in χ_p and χ_d through the redistribution of the holes in magnetosize quantized levels. In the presence of broadening, the holes motion is possible in the broadened sub-bands. In the absence of broadening, the 3D quantization will lead to completely discrete energy levels which can produce sharp oscillatory changes. This follows from the inherent nature of the 3D quantization of the hole gas, since under such quantization, there remain no free hole states between any two allowed sets of magneto-size quantized levels, in contrast to what has been found for the present case considering the influence of broadening. Consequently, the crossing of the Fermi level by the magneto-size quantized subbands would have much greater impact on the redistribution of the holes among the allowed sets, as found in the present case under broadening. It may be stated that p_0 increases very much with the consequent rise of the Fermi level

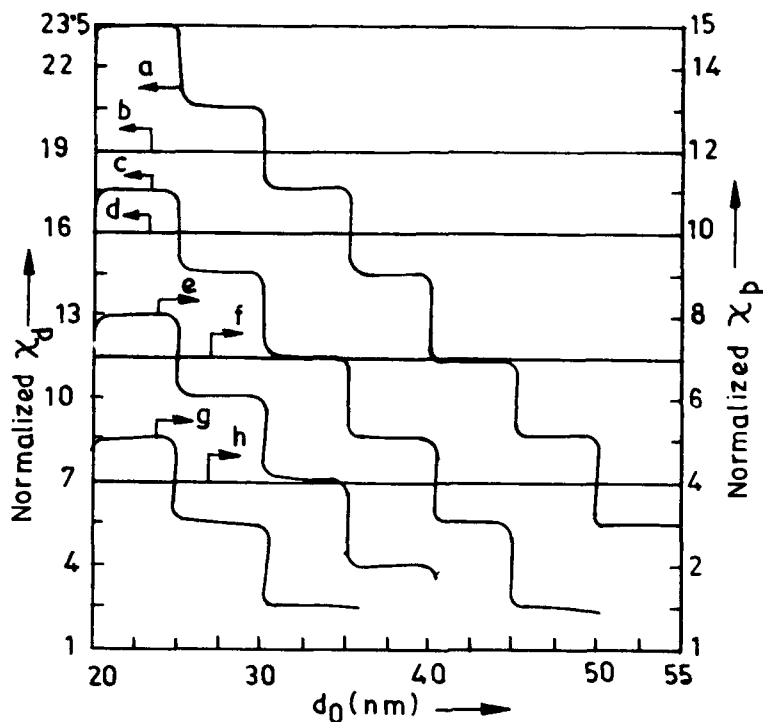


Fig. 1 Plot of χ_d versus d_0 in (a) ultrathin films of $\text{Hg}_{1-x}\text{Mn}_x\text{Te}$ (b) bulk specimen of $\text{Hg}_{1-x}\text{Mn}_x\text{Te}$ (c) ultrathin film of $\text{Cd}_{1-x}\text{Mn}_x\text{Se}$ and (d) bulk specimen of $\text{Cd}_{1-x}\text{Mn}_x\text{Se}$. The plots e, f, g and h exhibit the variations of χ_p as functions of d_0 in $\text{Cd}_{1-x}\text{Mn}_x\text{Se}$ for the above cases.

with respect to the bottom of the lowest Landau level resulting in the occupation of a large number of Landau levels even under strong magnetic quantization. Thus the magnetic quantum number becomes very large for large p_0 , leading to the picture assumed in the well-known Landau theory. Finally, it may be noted that though the mixing of holes and many body effects should be taken into account, this simple analysis exhibit the basic qualitative features of the magnetic susceptibilities in ultrathin films of dilute magnetic materials and theoretical results are in agreement with the experimental data as given elsewhere [11].

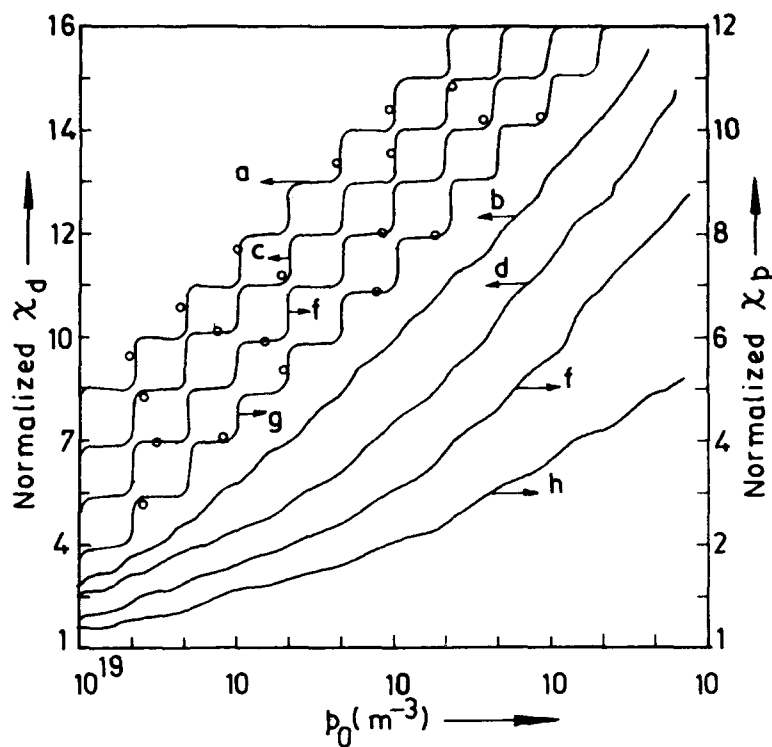


Fig. 2 Plot of X_p versus p_0 for all the cases of Fig. 1. The circular plots exhibit the experimental results [11].

1. D. L. Dreifus, R. M. Kobylous, K. A. Harris, R. N. Bicknell, N. C. Giles and J. F. Schetzina, *Appl. Phys. Letts.* **51**, 931 (1987).
2. D. L. Dreifus, R. M. Kolbus, J. R. Tassitino, R. L. Harper, R. N. Bickness and J. F. Schetzina, *J. Vac. Sci. Tech.* **6A**, 2722 (1988).
3. R. N. Bicknell, N. G. Giles-Taylor, J. F. Schetzina, N. G. Anderson and W. D. Laidig, *J. Vac. Sci. Tech.* **4**, 2126 (1986).
4. R. N. Bicknell, N. C. Giles, J. F. Schetzina, N. G. Anderson and W. D. Laidig, *Appl. Phys. Letts.* **46**, 238 (1985).
5. P. Becla, *J. Vac. Sci. Tech.* **6A**, 2725 (1988).

6. R. N. Bicknell, N. G. Gales and J. F. Schetzina, Appl. Phys. Letts 49, 1095 (1986).
7. R. N. Bicknell, N. C. Giles, J. F. Schetzina and C. Hitzman, J. Vac. Sci. Tech. 5A, 3059 (1987).
8. R. L. Harper, S. Hwang, N. C. Giles, R. N. Bickness, J. F. Schetzina, Y. R. Lee and A. K. Ramdas, J. Vac. Sci. Tech. 6A, 2627 (1988).
9. D. L. Dreifas and R. M. Kolbous, Appl. Phys. Letts. 53, 1279 (1988).
10. J. K. Furdyna, J. Appl. Phys. 64, 29 (1988).
11. A. L. Elfros and B. Kakanov, J. Exp. Theo. Phys. 96, 218 (1992).

MAGNETIC ORDERING OF Mn OVERLAYERS ON Fe(100)

T. G. WALKER AND H. HOPSTER

Department of Physics and Institute for Surface and Interface
Science, University of California, Irvine, CA 92717

ABSTRACT

Spin polarized electron energy loss spectroscopy (SPEELS) was used to probe the magnetic state of Mn overlayers on Fe(100). Non-zero exchange asymmetries are measured and found to oscillate with a two monolayer period as the Mn overlayer thickness is varied, proving that the surface layer of the Mn overlayers has a net magnetic moment and that these (100) magnetic layers are aligned antiferromagnetically. The average exchange splitting of the Mn surface layer is found to be 2.9 eV, indicating that the Mn surface has a magnetic moment of the order $3 \mu_B$. In addition, oxidized Mn overlayer surfaces have been studied, and the spectral features in the range 0 to 6 eV energy loss can be assigned to 3d-3d transitions of Mn^{2+} . No indication of magnetic ordering of the MnO overlayer has been observed.

INTRODUCTION

Magnetic multilayer coupling can be described by an RKKY type interaction when the spacer layers are paramagnetic materials¹. However, a more interesting situation arises when the spacer layer itself exhibits magnetic ordering. In the Fe/Cr/Fe(100) system two-monolayer period oscillations were observed². Direct measurements of the magnetic order of Cr overlayers on an Fe(100) surface have shown long range order both below³ and above⁴ the Néel temperature of bulk Cr, with a layer-by-layer antiferromagnetic structure similar to the near two monolayer spin density wave of bulk Cr. In this paper we report magnetic studies of Mn overlayers on Fe(100). Bulk Mn is a complicated system that can exist in various structures and magnetic states. We find that Mn on Fe does show long range magnetic order and that this order is very similar to the Cr/Fe system.

EXPERIMENT

Spin polarized electron energy loss spectroscopy (SPEELS) studies were used to probe the magnetic state and structure of the Mn overlayers. The experimental arrangement is reported elsewhere^{3,5}. Clean Fe substrates were obtained by evaporating 60 to 70 Å of Fe onto a Cr(100) crystal. The subsequent Mn evaporations were performed from an Al_2O_3 crucible at sample temperatures between 90°C and 145°C, pressures of about 1×10^{-9} Torr and rates of 0.2 to 2 Å/min. All thickness measurements were obtained by comparing Auger peak intensities, with calibration

performed using a quartz microbalance thickness monitor. Both LEED and Auger electron spectroscopy were used to monitor sample quality. Prolonged exposure to the base pressure during the Mn thickness sweeps brought oxygen contaminations up to 10%, however the spectra observed contain features that are associated with Mn and are decidedly different than the spectra for the heavily oxidized Mn films. The Mn spectra were sensitive to contamination, and leaving the sample idle for 1 hour destroyed the magnetic ordering. Thus we believe that the magnetic features observed result from the magnetic ordering of the Mn overlayers and are not induced by the sample contamination.

The SPEELS experiment performed consists of scattering incident spin polarized electrons off the sample and collecting scattered electrons in the off-specular (20°) geometry. The scattered electrons are then energy and spin analyzed using a 180° hemispherical energy analyzer with an energy resolution of 300 meV and a 100 keV Mott detector, respectively. Primary electrons of 31.5 eV generated in a GaAs photocathode were used. Both the intensity and polarization were measured for scattered electrons from incident beam polarizations both up and down relative to the remanent magnetic state of the Fe substrate. One defines the exchange asymmetry as the normalized difference between scattering intensities for incident up and incident down electron spins.

RESULTS

The exchange asymmetry of the Mn overlayers was found to be critically dependent on the method of sample preparation. Detailed anneal studies reported elsewhere⁵ indicated that at temperatures between 50°C and 100°C an atomic smoothing of the surface occurs, and that at 150°C intermixing begins. All data reported here are for films grown between 90°C and 145°C . The measured asymmetry of the Mn overlayers was also found to be sensitive to the temperature during measurement. Fig. 1 shows the measured exchange asymmetry as the temperature is varied. It is clear that long range order exists only at lower temperatures.

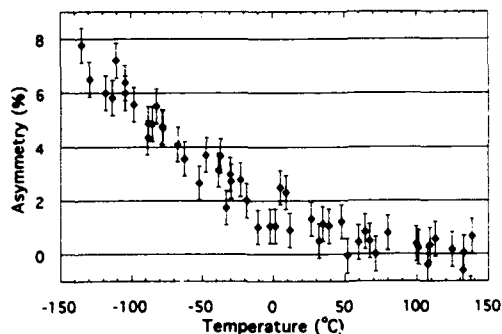


Fig. 1. The exchange asymmetry of 2 ML Mn/Fe(100) vs measurement temperature.

The exchange asymmetry spectra for the bare Fe film as well as 3 ML Mn/Fe are shown in Fig. 2a. The large negative values of the Fe asymmetry are typical of a ferromagnet magnetized to saturation⁶. Since all spin polarizations are defined with respect to the Fe majority-spin direction, the positive values of the Mn

overlayer asymmetry indicates that the Mn surface layer is aligned antiferromagnetically to the Fe substrate. Also shown are the spin-flip and non-flip (spin conserving) partial scattering rates for incident up and down electrons. Spin-flip scattering consists of an incident electron filling a vacant state and scattering out an electron from a filled state of opposite spin. Thus the flip scattering cross section probes a convolution of empty states of one spin with filled states of the opposite spin. Generally, the energy loss of the spin-flip scattering maximum corresponds to the average exchange splitting⁶, which in turn correlates with the magnetic moment with a relationship of roughly $1 \text{ eV}/1 \mu_B$. Thus the location of the spin-flip scattering maximum at 2.9 eV loss indicates that the surface of the Mn overlayer on Fe(100) has an average exchange splitting of 2.9 eV, and this corresponds to a magnetic moment of the order of $2.9 \mu_B$. While Mn films of different thicknesses showed different values of the asymmetries, all Mn films measured showed spin-flip scattering maxima at 2.9 eV loss.

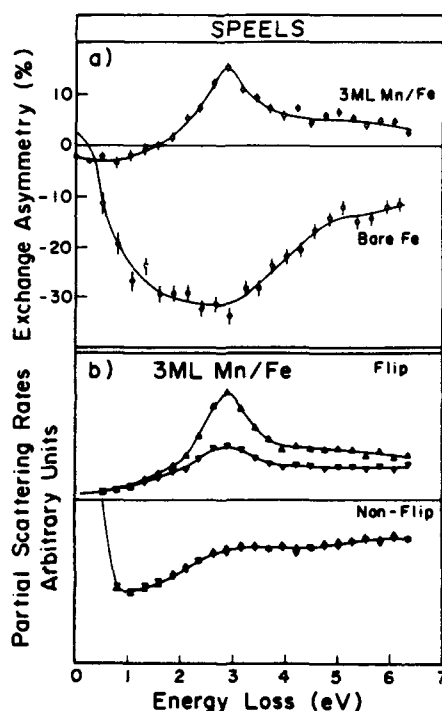


Fig. 2(left). (a) The exchange asymmetry vs electron energy loss for 3 ML Mn/Fe(100) for incident electrons of spin parallel (\blacktriangle) and antiparallel (\blacktriangledown) to the Fe substrate majority spin direction.

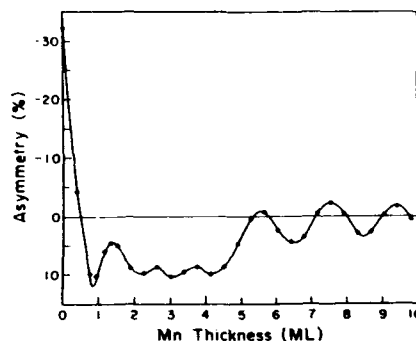


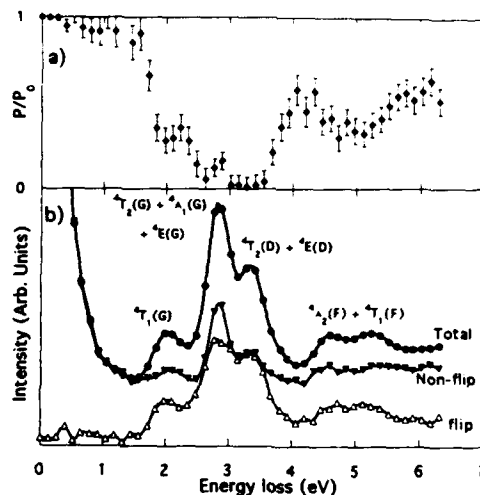
Fig. 3(above). The exchange asymmetry at 2.9 eV loss vs Mn overlayer thickness. Statistical errors are contained within the symbol size.

In order to probe the magnetic structure of these Mn overlayers, thickness dependent data were taken with the energy loss held constant at the Mn asymmetry peak of 2.9 eV (Fig. 3). Since the probing depth of our experiment is only about a monolayer, the measured asymmetry represents the magnetic state of

the surface layer for the given thickness³. The thickness sweeps are very similar to the Cr/Fe(100) SPEELS studies reported earlier, with two-monolayer oscillations providing strong evidence for layer-by-layer antiferromagnetic ordering of the Mn overlayers. Although substrate and sample quality did affect the measurements, all samples showed the same features. Measurements were taken between each successive Mn evaporation, giving a cycle time of 10 to 13 minutes per data point. Asymmetry oscillations as large as 10% (Fig. 3) and oscillations out to 21 ML Mn were observed⁵.

The effects of exposure to oxygen were also observed. Fig. 4 shows the scattered beam polarization as well as the flip and non-flip scattering intensities for a 10 ML Mn/Fe sample, exposed to about 20 langmuirs of oxygen. The spectrum shows several loss features, all showing an enhancement of the spin-flip type scattering. The loss features all correspond to the energies of Mn^{2+} 3d-3d transitions^{7,8}. Since the ground state of the Mn^{2+} ion has a half filled 3d-shell, $S = 5/2$ to $S = 3/2$ transitions are the only 3d-3d transitions that can be induced by electron scattering. These transitions would involve significant spin flip components to the scattering. Thus the energies and spin character of the loss features of the exposed films are consistent with a surface stoichiometry of MnO rather than Mn_2O_3 . The feature locations also correspond to recent unpolarized EELS studies of bulk MnO⁸. We found no detectable exchange asymmetries in the MnO surface data, and thus conclude that no long range order was present.

Fig. 4. MnO SPEELS data. (a) The scattered beam polarization vs energy loss. (b) The intensities for spin-flip and non-flip scattering as well as the total scattered intensity. Statistical errors are contained within the symbol size. The corresponding 3d-3d Mn^{2+} transitions are shown.



DISCUSSION

The magnetism of Mn is complicated. As the structure of Mn is varied, the magnetic structure predicted from calculations runs through paramagnetic, ferromagnetic and antiferromagnetic states⁹. Additionally, the crystal structure of Mn is by itself a very complicated system. Room temperature bulk Mn forms a complex structure with a unit cell of 58 atoms¹⁰. Epitaxial Mn layers on Fe(100)¹¹ have been found to grow in a face centered tetragonal (fct) structure with $c = 3.3 \text{ \AA}$ and the in plane spacing of the Fe

substrate, $a = 2.87 \text{ \AA}$. This structure can be regarded as either bct with $c/a = 1.15$ or fct with $c/a = 0.81$.

While many calculations have been performed for various bulk structures of Mn, none have been performed for the particular structure of Mn overlayers on Fe(100). Calculations for the correct atomic volume but a bcc structure predict a moment of $2.6 \mu_B$, while calculations for the fct structure but slightly smaller atomic volume predict moments of 2.3 to $2.5 \mu_B$ for various c/a ratios, including 0.81¹². Additionally, the spin dependent density of state curves shown with these calculations show apparent average exchange splittings of 2.9 to 3.3 eV^{9,12,13}. These values are remarkably close to our measured value of 2.9 eV.

It is interesting to compare our thickness dependent measurements with previous results for the Cr/Fe, Fe/Cr/Fe and Fe/Mn/Fe systems. In the case of the Fe/Cr system, for Cr thicknesses greater than 5 ML, it has been established both experimentally^{2,4} and theoretically¹⁴ that the Cr overlayers form ferromagnetic (100) sheets aligned antiferromagnetically and that Fe/Cr/Fe sandwiches show two monolayer coupling oscillations as the Cr thickness is varied, implying that the Fe coupling is mediated by the magnetic state of the Cr spacer layer. For Mn films thicker than 5 ML we find that the Mn overlayers form ferromagnetic (100) sheets aligned antiferromagnetically, as the Cr overlayers do. Since the Mn overlayers on Fe form a layer-by-layer antiferromagnet very similar to the Cr overlayers, one would expect that the Fe/Mn/Fe system would oscillate just as in the Fe/Cr/Fe system. However, this is in contradiction with the recent studies of Purcell et al., who observed only antiferromagnetic couplings for Mn thicknesses greater than 4 to 7 ML, with oscillatory modulations in the coupling strength¹¹.

We believe that this discrepancy results from differences in sample growth temperatures and measurement temperatures. Our previously reported anneal studies⁵ showed that annealing above 50°C provided smoother films and an enhancement of the magnetic signal by a factor of 3. Additionally, temperature studies clearly show (Fig. 1) that measurements at low temperatures provide a magnetic signal much larger than room temperature measurements. The Fe/Mn/Fe samples of Purcell et al. were grown at 50°C and measured at room temperature. These films would have reduced magnetic ordering due to increased surface roughness and higher temperatures of measurement. If the Fe-Fe coupling is mediated by the Mn layers, then one would expect that the reduced ordering of the Mn layers would reduce the superlattice coupling between the Fe layers. Since the dipole interactions of the Fe films would favor an antiferromagnetic alignment, a reduction in the coupling strength would provide precisely the results of the Purcell group: a dipole dominated antiferromagnetic alignment with two monolayer coupling strength oscillations due to the Mn magnetic effects. Thus one would expect that smoother films with low temperature measurements would provide coupling oscillations in the Fe/Mn multilayers.

CONCLUSION

We have performed detailed SPEELS studies of the surface layer of Mn overlayers on Fe(100) and found the value of the average

exchange splitting to be 2.9 eV. This value corresponds to a surface magnetic moment of the order $2.9 \mu_B$, comparing well with calculated values. The exchange asymmetry on the surface of Mn overlayers on Fe(100) was measured, providing strong evidence for a layer-by-layer antiferromagnetic structure coupled to the Fe substrate. The magnetic ordering of the Mn is found to be temperature dependent, indicating that Fe/Mn superlattices should show two monolayer period coupling oscillations at low temperatures. Oxidized Mn overlayers show several loss features that are consistent with a MnO surface, although no evidence for long range magnetic order was found.

This project was supported by the NSF through grant No. DMR 9119815.

REFERENCES

- [1] P. Bruno and C. Chappert, Phys. Rev. Lett. 67, 1602(1991); Baitensperger and J. S. Helman, Appl. Phys. Lett. 57, 2954 (1990); D. M. Edwards, J. Mathon, R. B. Muniz, and M. S. Phan, Phys. Rev. Lett. 67, 493 (1991).
- [2] P. Grunberg, S. Demokritov, A. Fuss, R. Schreiber, J. A. Wolf, and S. T. Purcell, J. Magn. Magn. Mater. 104, 1734 (1992); J. Unguris, R. J. Celotta, and D. T. Pierce, Phys. Rev. Lett. 67, 140 (1991).
- [3] T. G. Walker, A. W. Pang, H. Hopster, and S. F. Alvarado, Phys. Rev. Lett. 69, 1121 (1992).
- [4] J. Unguris, R. J. Celotta, and D. T. Pierce, Phys. Rev. Lett. 69, 1125 (1992).
- [5] T. G. Walker and H. Hopster, Submitted to Phys. Rev. B.
- [6] H. Hopster and D. L. Abraham, Phys. Rev. B 40, 7054 (1989); Phys. Rev. Lett. 62, 1157 (1989); A. Venus and J. Kirschner, Phys. Rev. B 37, 2199 (1988).
- [7] S. Sugano, Y. Tanabe, and H. Kamimura, Multiplets of Transition-Metal Ions in Crystals (Academic Press, New York, 1970), p. 124.
- [8] S. Jeng and V. Henrich, Solid State Comm. 82, 879 (1992).
- [9] S. Fujii, S. Ishida, and S. Asano, J. Phys. Soc. Jpn. 60, 1193 (1991).
- [10] R. S. Tebble and D. J. Craik, Magnetic Materials (Wiley, New York, 1969), pp 61-63.
- [11] S. T. Purcell, M. T. Johnson, N. W. E. McGee, R. Coehoorn, and W. Hoving, Phys. Rev. B 45, 13064 (1992).
- [12] T. Oguchi and A. J. Freeman, J. Magn. Magn. Mater. 46, L1 (1984).
- [13] J. Yamashita, S. Asano, and S. Wakoh, J. Appl. Phys. 39, 1274 (1968).
- [14] Z. Shi, P. M. Levy, and J. L. Fry, Phys. Rev. Lett. 69, 3678 (1992).

STRUCTURAL AND MAGNETIC PROPERTIES OF e-BEAM PREPARED Co_xPt_{1-x} ALLOY FILMS

J.V. HARZER*, B. HILLEBRANDS*, I.S. POGOSOVA*, M. HERRMANN*, G.
GÜNTHERODT* AND D. WELLER**

*2. Physikalisches Institut, Rheinisch-Westfälische Technische Hochschule Aachen,
Templergraben 55, W-5100 Aachen, Germany.

**IBM Almaden Research Center, San Jose, CA 95120, U.S.A.

ABSTRACT

We have investigated structural and magnetic properties of CoPt alloy films with strong perpendicular magnetic anisotropy in the thickness range between 100Å and 400Å. From a detailed x-ray analysis we find highly (111)-textured CoPt microcrystallites in all samples. STM studies reveal a granular topography with grain diameters of up to 250Å. Measurements of hysteresis loops yield a saturation field which increases with thickness, and which is consistent with a freely mobile domain model. Brillouin light scattering measurements of the frequencies of the surface and standing spin wave modes yield a bulk exchange constant, which is strongly dependent on the Pt content.

INTRODUCTION

Polycrystalline Co_{1-x}Pt_x alloy films have recently been demonstrated as attractive media for magneto-optical storage applications [1-4]. All magnetic parameters are strongly dependent on the film composition, the film thickness and the growth conditions. For alloys evaporated in high-vacuum at $\approx 200^\circ\text{C}$ a perpendicular easy magnetization axis has been reported in a broad composition range of 50-90 at.% Pt [1].

From the application viewpoint, alloy films have several advantages compared to corresponding Co/Pt multilayers of the same composition ratio. Their fabrication is easier and the Kerr effect is larger, particularly in the UV region, which makes them particularly attractive for future magneto-optical storage applications [2,4].

The microstructure of CoPt alloy films is mainly determined by granular growth and its importance for magnetic properties has been recognized. For instance, Kitada and Shimizu [5] reported for sputtered Co_{1-x}Pt_x alloys ($x=0-50\text{at.}\%$) a linear correlation between grain sizes and the coercive field strength. The exchange interaction, which is strongly related to the particular microstructure, was identified as one of the most important factors in controlling magnetic properties [6,7]. Murayama et al. [8] measured the exchange interaction in sputtered Co_{1-x}Pt_x alloy films ($x=0-14\text{at.}\%$) and showed that magnetic inhomogeneities caused by the distribution of grain size and their separation are closely related to the Pt content [8]. For sputtered CoNiPt alloy films the exchange constant was found to be strongly reduced compared to evaporated CoNiPt films [9].

In this paper we present for the first time data on the bulk exchange interaction constant, A_{ex} , for perpendicularly magnetized alloy films investigated by Brillouin light scattering experiments. A structural analysis yields data on the (vertical and lateral) average grain size and the texture of Co₂₅Pt₇₅ alloy films. We discuss the thickness dependence of hysteresis properties within the framework of a stripe domain model [10], and present evidence for a correlation between the domain wall mobility and the average grain size.

EXPERIMENTAL

The investigated alloy films were e-beam evaporated in a 10^{-8} mbar vacuum system on polished Si (100) substrates covered with an etched SiN_x buffer layer (see Ref. [11]). For some samples (see further below), an additional 40 Å Pt buffer layer was used. The deposition temperature was $\approx 220^\circ\text{C}$ and subatomic layering or coevaporation of Co and Pt was employed in order to obtain large values for the perpendicular anisotropy, K_u . The composition was measured with x-ray fluorescence (XRF), and structural information was investigated by x-ray diffraction (XRD). The hysteresis loops were obtained with the polar Kerr effect and the Brillouin light scattering experiments were performed using a computer-controlled Sandercock-type (3+3)-pass tandem Fabry-Perot interferometer in backscattering geometry [12].

RESULTS AND DISCUSSION

Since magnetic properties depend strongly on the microstructure, (i.e., grain sizes and their orientation, defect structure) an analysis of the latter is eminently important. Here we briefly review some of the main results obtained by x-ray diffraction and scanning tunneling microscopy (STM).

The film structure is of cubic symmetry with the fcc (111) lattice planes preferentially oriented parallel to the film plane. Strong texturing is indicated by a weak fcc (200) reflection, which is only about 3% of the (111) reflection, and the degree of texturing increases if a Pt buffer is introduced (see below) [1]. From the width of the CoPt(111) reflection in the θ - 2θ XRD geometry we infer average vertical grain sizes of 90 Å, 140 Å and 160 Å for film thicknesses $d = 100, 200$ and 300 Å, respectively. These studies were complemented by STM surface topography measurements. The granular structure is clearly resolved. The lateral grain size is similar in all samples and shows a variation typically of the order of 100 to 250 Å.

Magnetic hysteresis properties were characterized with polar Kerr loops. For all samples the remanence is 100% and the coercivity H_c is independent on d . Films with $d=100$ Å show almost perfect square loops. With increasing film thickness the hysteresis loops are sheared and the perpendicular saturation field, H_s , at which magnetization reaches saturation, increases strongly.

Draaisma et al. [10] calculated the shape and the properties of perpendicular magnetization curves of single magnetic layers and multilayers with strong perpendicular anisotropies within the framework of a stripe domain model. The model assumes freely mobile domain walls (no coercivity) and is based on minimizing the total free energy of the system taking into account field, wall and demagnetization energy contributions. For details see also the work of Kooy and Enz [13]. Within this model the dependence of H_s on the film thickness can be calculated with the domain wall mobility, characterized by a characteristic length, $\tau = \sigma_w / F_D$, as a fit parameter. Here σ_w is the domain wall energy density and $F_D = \mu_0 M_s^2 / 2$ is the demagnetizing energy.

Fig. 1 shows the dependence of H_s on the reduced film thickness d/τ (solid line) for a single magnetic layer using the model of Draaisma et al. [10]. The circles are the measured values of H_s for $\text{Co}_{25}\text{Pt}_{75}$ alloy films with thicknesses as indicated. The experimental data can be well reproduced by choosing a value for τ of 120 ± 15 Å. For smaller film thicknesses only stripe domains were observed in auxiliary Kerr microscopy investigations [14].

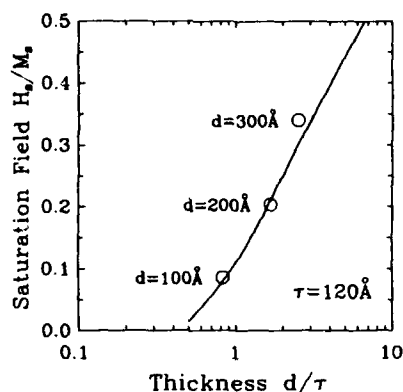


Fig. 1: Perpendicular saturation field, H_s , vs. reduced film thickness d/τ . The circles denote the measured values of H_s . The solid line is a fit using a model of Draaisma et al. (see text) and the characteristic length τ is a free parameter.

The experimental value of $\tau = 120 \text{ Å}$ can be compared to an estimate obtained from the domain wall energy σ_w . With $\sigma_w \approx \sqrt{A_{ex} K_u}$ and with the exchange constant $A_{ex} = 0.43 \cdot 10^{-11} \text{ J/m}$, the saturation magnetization $M_s = 370 \text{ kA/m}$ and the uniaxial anisotropy $K_u = 0.2 \text{ MJ/m}^3$, we obtain a value of $\tau = 320 \text{ Å}$ which is of the same order of magnitude as the experimental value. Here we used values for A_{ex} , M_s and K_u obtained by Brillouin light scattering as discussed below. We would like to point out that for both cases τ is of the order of the grain sizes. Magnetic inhomogeneities at the grain boundaries (see below) might therefore determine the domain wall mobility (coercivity) in these films.

We now turn to the determination of the exchange interaction in the alloy films. For a detailed study we prepared three additional sets of $\text{Co}_{1-x}\text{Pt}_x$ alloy films with $x = 45, 60, 74 \text{ at.}\%$ and of thicknesses $d = 100, 200, 300$ and 400 Å each. Contrary to the samples discussed so far ($x = 75 \text{ at.}\%$), the new sample sets have a 40 Å Pt buffer layer in between the etched SiN_x buffer layer and the alloy film and were deposited by coevaporation rather than subatomic layering.

The exchange interaction is obtained by measuring the frequencies of inelastically scattered light from spin waves using the Brillouin light scattering technique [15-18]. Two types of spin wave modes contribute to the scattering cross section. First, the Damon-Eshbach (DE) mode, which is a dipolar mode localized at the film surface, and which is sensitive to the magnetization and anisotropy contributions. Second, the so-called standing spin wave (SSW) modes, which are in addition sensitive to the bulk exchange constant, A_{ex} . Apart from the crossing regime with the Damon-Eshbach mode the standing spin waves are characterized by a wavevector $q = n\pi/d$ with n the integer mode order; their frequency ν is given by $2\pi\nu/\gamma = Dq^2$ with γ the gyromagnetic ratio and $D = 2A_{ex}/M_s$ the spin-wave stiffness constant. The magnetic properties are obtained by a fit of a suitable model [18], which contains all details of the spin-wave dispersion, to the experimentally obtained spin wave dispersion properties. Here we used the saturation magnetization, M_s , the uniaxial anisotropy constant, K_u , and the exchange constant, A_{ex} , as fit parameters [15,18]. The results for M_s and A_{ex} are listed in Table I.

All measured alloy films show well-defined spin wave spectra, i.e., the Damon-Eshbach mode and the first standing spin wave of the film. The width of the observed modes is much broader than the experimental resolution which is indicative of large magnetic inhomogeneities caused by the granular structure [9,8].

The standing spin waves were identified by their characteristic $1/d^2$ dependence on the film thickness, d . This is demonstrated in Fig. 2. The measured (squares) and fitted (full lines) spin wave frequencies are shown for $\text{Co}_{55}\text{Pt}_{45}$ alloy films as a function of the film thickness in an applied field of 20 kOe . The results of A_{ex} and D for all four sets of samples are listed in Table I.

Table I:

Exchange constant A_{ex} and spin wave stiffness constant D for the present $Co_{1-x}Pt_x$ alloy films (#1-4) obtained by a least-squares fit to the measured spin wave frequencies. For comparison literature data of a sputtered $Co_{86}Pt_{14}$ film and bulk hcp Co are given.

#	Pt content	Pt buffer	M_s	A_{ex}	D
	[at.%]	[Å]	[kA/m]	[10^{-11} J/m]	[10^{-17} Vs]
1	75	0	370	0.43	2.32
2	74	40	390	0.77	3.95
3	60	40	580	0.99	3.41
4	43	40	780	1.38	3.54
Ref.[8]	14	0	1060	1.59	3.0
bulk Co	0		1400	2.85	4.07

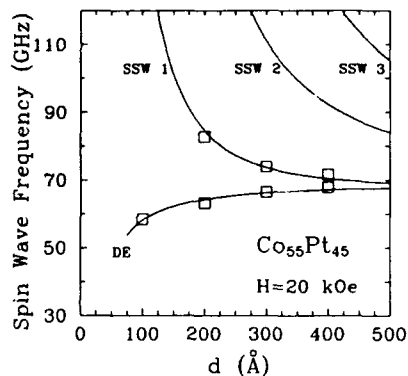


Fig. 2:

Measured (squares) and calculated (solid line) spin wave frequencies for $Co_{55}Pt_{45}$ alloy films of up to 500 Å thickness in an applied magnetic field of 20 kOe. The parameters for the calculation are: $M_s=780$ kA/m, $A_{ex}=1.55 \cdot 10^{-11}$ J/m, and $K_u=0.1$ MJ/m³. The Damon-Eshbach mode (DE) and the standing spin wave modes (SSW) are indicated.

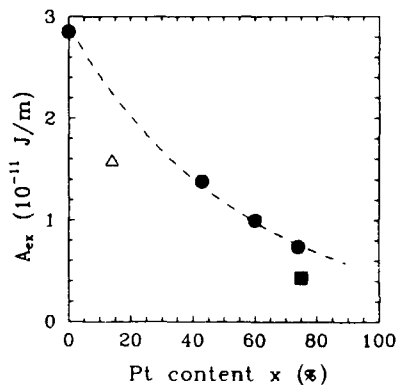


Fig. 3:

Bulk exchange constant A_{ex} as a function of the Pt content of $Co_{1-x}Pt_x$ alloys. The full dots (square) denote data of alloy films with (without) a 40 Å-thick Pt buffer layer. The value for $x=0$ (bulk hcp Co) was taken from Ref. [19]. The triangle represents a sputtered $Co_{86}Pt_{14}$ film [8].

The results for the exchange constant, A_{ex} , are plotted in Fig. 3 as a function of the Pt content. The full dots denote the values for $Co_{1-x}Pt_x$ alloy films with a 40 Å Pt buffer. The value for $x=0$ is the value of bulk hcp Co, which $2.85 \cdot 10^{-11}$ J/m. Clearly a strong dependence of A_{ex} on the Pt content is observed. We would like to mention that the observed dependence is mainly due to the reduction of the saturation magnetization with increasing Pt content [1]. The obtained values for the spin-wave stiffness constant, D , do not vary as a function of Pt content within the error bars of $\pm 8\%$ (see Tab. I). This might be indicative of a structurally uniform growth of the system independent of the Pt content. For comparison, the obtained exchange constant for a $Co_{25}Pt_{75}$ alloy film without a Pt buffer layer is shown in Fig. 3 as a square. This value is reduced by almost a factor of 2 compared to the same sample with a Pt buffer layer. It is likely that this finding is due to the reduced degree of (111) texturing in the films without Pt buffer layer. As already pointed out by Murayama et al. [8] for sputtered $Co_{1-x}Pt_x$ films ($x=0-14$ at.%) of 250 Å thickness, any reduction in the degree of texture improves the formation of grain separations by non magnetic Pt, which, in turn, will

reduce the inter-grain exchange coupling and thus the effective exchange parameter of the film as tested by the standing spin waves.

CONCLUSIONS

The exchange interaction in $\text{Co}_{1-x}\text{Pt}_x$ alloy films with large perpendicular anisotropies was measured with Brillouin light scattering experiments. A_{ex} rapidly decreases with increasing Pt content and is strongly dependent on the degree of (111) texture of the films. Microstructural properties of $\text{Co}_{25}\text{Pt}_{75}$ alloy films have been studied with XRD and STM methods. The observed grain sizes were found to be independent on the film thickness and of the order of 100 to 250 Å. The perpendicular saturation fields of the samples, as determined by polar Kerr measurements, increase strongly with thickness. The observed behavior is consistent with a stripe domain model yielding a characteristic length describing the domain wall mobility, τ , of 120 Å which is of the order of the grain sizes of the film. This result corroborates the importance of granular growth on the magnetic properties of the films.

ACKNOWLEDGMENTS

We like to thank F. Lauks for the Kerr measurements. Support by the Deutsche Forschungsgemeinschaft through SFB 341 is gratefully acknowledged.

REFERENCES

- [1] D. Weller, H. Brändle, C.-J. Lin, H. Notarys, Appl. Phys. Lett. **61**, 2726 (1992).
- [2] D. Weller, H. Brändle, C. Chappert, Symp. Mag. Ultrathin Films, Multilayers and Surfaces, Lyon, Sept. 1992, J. Magn. Magn. Mat., **121**, 1993, 461.
- [3] D. Weller, J. Hurst, H. Notarys, H. Brändle, R.F.C. Farrow, R. Marks, G. Harp, "MO signal in Co-Pt and Co-Pd alloy disks: comparison to respective multilayers and TbFeCo", Proc. of MORIS'92, Tucson, to be published.
- [4] C.-J. Lin and G. Gorman, Appl. Phys. Lett. **61**, 1600 (1992).
- [5] M. Kitada, N. Shimizu, J. Appl. Phys. **54**, 7089 (1983).
- [6] T. Chen, T. Yamashita, IEEE Trans. Magn. **MAG-24**, 2700 (1988).
- [7] J.G. Zhu, H.N. Bertram, J. Appl. Phys. **63**, 3248 (1988).
- [8] A. Murayama, M. Miyamura, K. Nishiyama, K. Miyata, Y. Oka, J. Appl. Phys. **69**, 5661 (1991).
- [9] A. Murayama, M. Miyamura, S. Ishikawa, Y. Oka, J. Appl. Phys. **67**, 410 (1990).
- [10] H.J.G. Draaisma, W.J.M. de Jonge, J. Appl. Phys. **62**, 3318 (1987).
- [11] D. Weller, H. Notarys, T. Suzuki, G. Gorman, T. Logan, I. McFadyen, C.J. Chien, IEEE Trans. Mag. **MAG-28**, 2500 (1992), and references therein.
- [12] R. Mock, B. Hillebrands, and J.R. Sandercock, J. Phys. E **20**, 656 (1987).
- [13] C. Kooy und U. Enz, Philips Res. Rep. **15**, 7 (1960).
- [14] T. Kleinfeld, W.S. Kim, D. Weller, (these proceedings).
- [15] B. Hillebrands, A. Boufelfel, C.M. Falco, P. Baumgart, G. Güntherodt, E. Zirngiebl, J.D. Thompson, J. Appl. Phys. **63**, 3880 (1988).
- [16] B. Hillebrands, G. Güntherodt, in: *Ultrathin Magnetic Structures Vol II*, J.A.C. Bland, B. Heinrich (eds.), Springer Verlag (Heidelberg, Berlin, London, New York, Tokyo, 1993).
- [17] P. Grünberg, *Light Scattering in Solids V*, M. Cardona, G. Güntherodt (eds.), Springer Ser. Topics Appl. Phys. **66**, 303 (1989).
- [18] B. Hillebrands, Phys. Rev. B **41**, 530 (1990).
- [19] E.P. Wohlfarth, in: *Ferromagnetic Materials. A handbook on the properties of magnetically ordered substances*, E.P. Wohlfarth (editor), North-Holland New York (1980).

MAGNETORESISTANCE AND STRUCTURE OF GRANULAR Co/Ag THIN FILMS

MARY BETH STEARNS AND YUANDA CHENG*

Arizona State University, Department of Physics and Astronomy, Tempe, Arizona, 85287

ABSTRACT

Several series of $\text{Co}_x\text{Ag}_{1-x}$ granular thin films ($\sim 3000\text{\AA}$) were fabricated by coevaporation of Co and Ag in a dual e-beam UHV deposition system at varying substrate temperatures. These films have low field magnetoresistance values as large as 31% at room temperature and 65% at liquid N_2 temperature. The structure of the films was determined using magnetization measurements as well as x-ray and various electron microscopy techniques. The composition was determined using Rutherford backscattering spectroscopy. The magnetoresistance was measured at both room and liquid N_2 temperatures.

We deduce from the magnetization and RBS measurements that the films consist of Co globules embedded in a Ag matrix and that there is no appreciable mixing of the Co and Ag atoms in the films deposited at substrate temperatures $\geq 400^\circ\text{K}$. The size of the Co globules is seen to increase with increasing Co concentration and the maximum magnetoresistance occurs in those films having the smallest Ag thickness which provides magnetic isolation of the Co globules.

We suggest that the large magnetoresistance of these films arises from the same mechanism which causes the low field magnetoresistance in pure ferromagnets, namely, the scattering of the highly polarized d conduction electrons of the Co at magnetic boundaries. The large increase in the room temperature magnetoresistance of the Co/Ag films as compared to those of pure 3d ferromagnetic films is due to the distance between the magnetic boundaries being reduced to a few nanometers, because of the small size of the single domain Co globules, as compared to a few microns in 3d ferromagnets.

INTRODUCTION

Recently it has been found that granular as well as layered structures have a large magnetoresistance, MR, at room temperature^{1,2}. In particular the $\text{Co}_x\text{Ag}_{1-x}$ system³ was found to have MR values of $\sim 30\%$ at room temperature. It is known that Co and Ag are immiscible and the surface free energy of Co (2.71 J/m^2) is more than twice that of Ag (1.30 J/m^2). We find that the films deposited at substrate temperatures which are high enough so that the adatoms have appreciable mobility are completely segregated. The $\text{Co}_x\text{Cu}_{1-x}$ system is much less favorable for complete segregation since the surface free energy of Cu (1.93 J/m^2) is closer to that of Co.

Here we study the correlation between the microstructure and magnetic and resistive properties of Co/Ag granular films. Because of the simpler structure, the magnetoresistance behavior of the well segregated Co/Ag granular structures are more amenable to modeling than the complex structure of multilayers. TEM micrographs of many multilayer systems have shown that usually only the first few bilayers are of good quality with strong columnar growth and severe intermixing occurring in the layers further from the substrate.

We consider that the magnetoresistance in the Co/Ag granular films is due to the same mechanism causing magnetoresistance in pure ferromagnets, namely, scattering of the highly polarized d conduction electrons of the Co at magnetic boundaries. In the granular structures the room temperature magnetoresistance is much larger than that of the pure ferromagnets because the domain size has been greatly reduced from the micron range, typical of pure ferromagnets, into the nanometer range. This small domain size is achieved in the $\text{Co}_x\text{Ag}_{1-x}$

system because there is essentially complete segregation of the Co and Ag and at Co concentration of <37 at.% Co the single domain Co globules are magnetically isolated by the non-magnetic Ag matrix.

EXPERIMENTAL DETAILS

Several series of $\text{Co}_x\text{Ag}_{1-x}$ and pure element films were prepared by evaporation of Co and Ag in a dual e-beam gun UHV deposition system. The nominal thickness of the films was $\sim 3000\text{\AA}$. High purity single crystal Si wafers with an oxidized surface layer were used as the substrates. The deposited samples consisted of a square of $\sim 2\text{ cm}$ on a side and a dumbbell pattern with a small neck of $\sim 0.2\text{ mm} \times 5\text{ mm}$ for resistance measurements. In order to study changes in the microstructure the substrate temperature, T_s , was varied from room temperature (RT) to 500°K . The deposition rate of Co was kept constant at 0.6 \AA/sec while the Ag rate was varied from 0.5 to 2 \AA/sec in order to change the composition of the films.

A Rigaku D/Max-IIIB x-ray diffractometer with $\text{CuK}\alpha$ radiation was used to study the grain size and crystal orientation of the films. The Co and Ag were found to be fcc with preferential growth in the $\langle 111 \rangle$ direction. Studies of the morphology of the films were made, and are still in progress, using cross-sectional electron microscopy as well as a number of other electron microscopy techniques. The atomic compositions were determined using Rutherford Backscattering (RBS).

The magnetization curves were measured on a small rectangle using a vibrating sample magnetometer whose maximum field was 10 KOe . The magnetoresistance was measured on the dumbbell shaped samples using the four-probe method in a field varying up to 14 KOe . The four probes were gold plated stop balls which were connected to a digital voltmeter which supplied a constant current of 10 mA through the sample. The resistivity was found to be independent of the size of the current. Resistance measurements were made at both room and liquid N_2 temperatures. The magnetoresistance (MR) measurements were made for the applied field, H , in-plane and perpendicular to the film and with the current both transverse (TMR) and parallel (LMR) to the field.

MAGNETIZATION MEASUREMENTS

For each series of films, made at a fixed T_s , those with less than $\sim 35\text{ at.}\%$ Co were superparamagnetic indicating that the Co atoms are clustered together into magnetically isolated globules. The magnetization curves began to open up near zero field for compositions between $35\text{--}40\text{ at.}\%$ Co. With increased Co concentration the non-reversible hysteresis loop continued to grow and the coercive fields of the films increased. The average moment, $\bar{\mu}$, and number of the Co globules, N_g , were obtained from fitting the magnetization curves to a Langevin function using Kaleidagraph.

$$M = N_g \bar{\mu} [\coth(\bar{\mu} H/kT) - 1/(\bar{\mu} H/kT)], \quad (1)$$

where $M_s = N_g \bar{\mu}$. Assuming that each Co atom in the globules has a full RT moment, $\mu_{\text{Co}} = 1.72\text{ }\mu_B$, we obtained the number of Co atoms per globule, $N_{\text{Co}} = \bar{\mu} / \mu_{\text{Co}}$. If we know the average volume per Co atom, V_{Co} , we can then obtain the average volume of the globules, $V_g = N_{\text{Co}} V_{\text{Co}}$.

We found that the V_{Co} values are quite different from the bulk value. They were obtained in the following way: On measuring the magnetization curves of pure Co films deposited at the various substrate temperatures we found that the saturation magnetizations were about $75\text{--}80\%$ that of the bulk value. We attributed this to voids in the films and from the measured M_s values calculated V_{Co} of the Co atoms in the films. This assumption was

confirmed by RBS measurements in two ways: Using RBS we determined the atomic fractions of Co and Ag and number of atoms per cm^2 , N_s , of each film. The average volume for each atom could be deduced from the known film thicknesses (from profilometer measurements) and the N_s values; again assuming that any variation from the bulk values was due to voids. The average volumes could also be deduced from the measured atomic volumes and the volume fractions known from the deposition rates. Both of these determinations agreed well with the values obtained from the pure Co films. Upon viewing the granular films with cross-sectional TEM micrographs we indeed saw that they contain voids as well as spherically shaped Co particles. For the granular films near optimum conditions the saturation magnetizations were the same as in the pure Co films indicating that the Co and Ag have a negligible fraction of mixed regions.

The volume fractions, f_v , of the granular films were also obtained from $f_v = N_g V_g$. These agreed well with those obtained from the deposition rates and RBS. Taking the globules to be spherical, as seen by XTEM, we obtained the average radius of the Co spheres, r_0 . These values are shown plotted as a function of Co at.% in Fig. 1a. The Co globules in the films deposited at 400°K and above are seen to have average radii of 23-26Å. The average volume

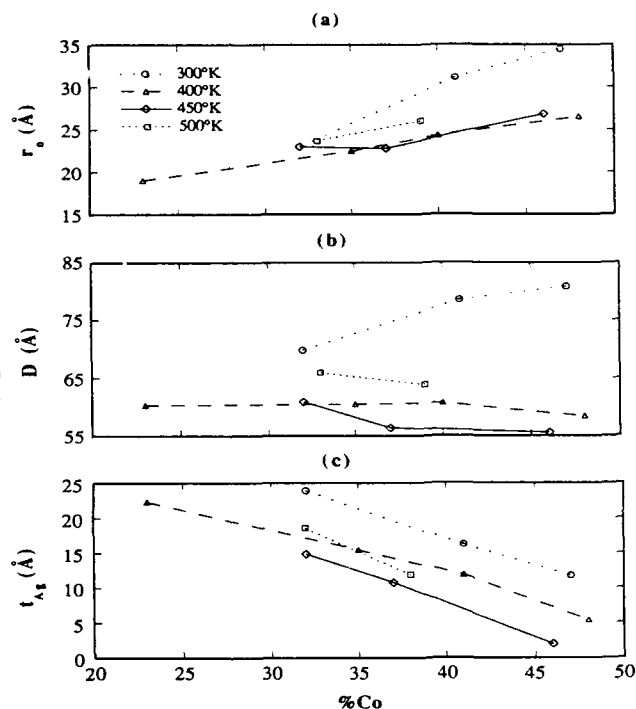


Fig. 1. Variation of the (a) average Co globule radius, r_0 , (b) cell size, D , and (c), the minimum Ag thickness, t_{Ag} , as a function of at.% Co.

of a cell containing a Co globule and its surrounding Ag matrix is given by $V_c = V_g / f_v$. Assuming that this volume is in the shape of a cube we can obtain the average cube side, D . These values are shown in Fig. 1b. We see that for the better films these are in the range of 55-65Å. Thus we conclude that the Co/Ag granular films deposited at $T_s \geq 400^\circ\text{K}$ consist of segregated Co globules embedded in a matrix of pure Ag. From previous experience of observing XTEM micrographs of the structure of metallic films of many different materials which are deposited by evaporation at various substrate temperatures we know that usually the films deposited at RT are of very poor quality⁴. This is due to the small surface mobility of the adatoms at RT so that the crystallites are small and jagged. The quality of the films

improves greatly for films deposited at 400°K and above. The x-ray spectra confirm this behavior.

A quantity of interest in determining the magnitude of the MR effect is the average minimum thickness of the Ag, $t_{Ag} = D - 2r_0$, between the Co globules. These values are shown in Fig. 1c. It is significant that the appearance of the non-reversible open hysteresis loop sets in at $t_{Ag} \sim 10\text{\AA}$ for all the series with $T_s \geq 400^\circ\text{K}$ and that at all Co concentrations t_{Ag} is the smallest at the optimum substrate temperature, $T_s = 450^\circ\text{K}$.

MAGNETORESISTANCE MEASUREMENTS

The resistance variation with applied field, H , was measured at RT and liquid NT with H both in-plane and perpendicular to the films. For the superparamagnetic films the transverse magnetoresistance (TMR) was independent of the orientation of the field with respect to the film. For an in-plane field the longitudinal magnetoresistance, LMR (the current and H in the same direction) was slightly different than the TMR in agreement with there being an increase in resistance with H due to the anisotropic shape of the electronic cloud of the d electrons being visible because of spin-orbit coupling^{6,7}. For these granular films the anisotropic magnetoresistance, $AMR = LMR - TMR$, was found to have a maximum value of about the same as for pure Co films; i.e., $\sim 1\%$.

In the rest of this paper we will consider only the TMR. The magnetoresistance is defined here to be $MR = R(H) - R_{min} / R_{min} = \rho(H) - \rho_{min} / \rho_{min} = \Delta\rho / \rho_{min}$. Since for many of the samples our maximum field, 14KOe, is not quite sufficient to reach R_{min} we determined its value by fitting the magnetoresistance curves with two Lorentzian functions using KaleidaGraph. Typical fits to both the magnetization and the magnetoresistance curves are shown in Fig. 2. The dashed curves through the data points are the fitted curves. In this way

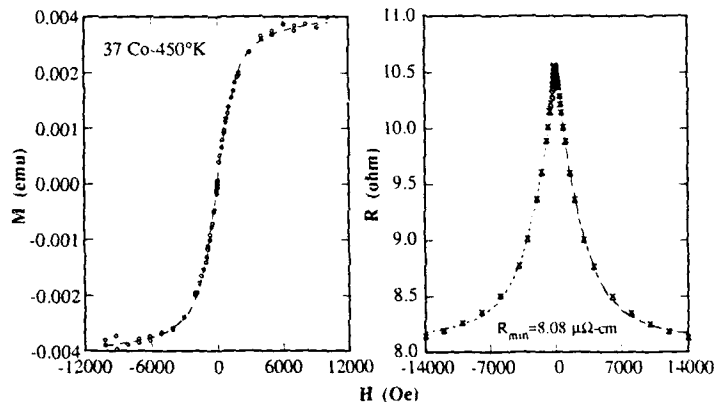
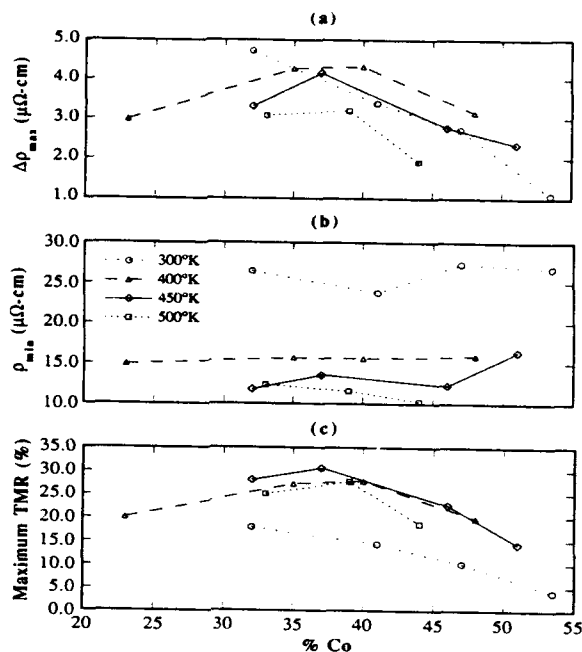


Fig. 2. Typical fits to the magnetization and the magnetoresistance curves are shown for 37 at.% Co film deposited at 450°K.

we determined $R_{max} - R_{min}$ or the more fundamental quantity $\Delta\rho_{max}$. Its variation with % Co is shown in Fig. 3a. We see that for each substrate temperature above 300°K $\Delta\rho_{max}$ increases with at.% Co up to where $t_{Ag} \sim 10\text{\AA}$ where the films start developing some coupling between the Co globules. This coupling was also strikingly evident in the relaxation behavior of these films. In measuring the magnetoresistance curves it was observed that at fields near the coercive field and in the open magnetization loop it took extraordinarily long times for the resistance to come to equilibrium; --in some films several minutes.

We show the variation of ρ_{min} with % Co in Fig. 3b. It is seen to be quite independent

Fig. 3. Variation of (a) $\Delta\rho_{\max}$, (b) ρ_{\min} , and (c) the maximum TMR with at.% Co.



of at.% Co and decreases with increased substrate temperatures. Thus increasing the amount of the higher resistivity element Co does not increase the resistivity of the films. The poorer quality 300°K films are seen to have significantly higher resistivity. In Fig. 3c we show the variation of the maximum TMR with %Co. It is seen that 450°K is the optimum substrate temperature giving the largest TMR value of 31% at RT. The TMR of the optimum 37 at.%-450°K film at 77°K was 65% with $\Delta\rho$ increasing from 4.2 $\mu\Omega\text{-cm}$ to 6.6 $\mu\Omega\text{-cm}$ and ρ_{\min} decreasing from 13.6 $\mu\Omega\text{-cm}$ to 10.2 $\mu\Omega\text{-cm}$.

A quantity of interest for device development is the full-width at half-maximum, FWHM, of the MR curves. Its value is ~4000 Oe for the optimum films. This large value occurs because the small size of the Co globules requires a rather high field to align the single particle domains. These FWHM values would decrease if the superparamagnetic Co globules could be increased in size.

Annealing studies were made for the optimum film of 37 at.% Co -450°K and two of the poorer films, 32at.% -300°K and 41 at.% -300°K. They were annealed for 30 min. at 300°C. Upon the first anneal $\Delta\rho_{\max}$ decreased for all three samples. For the optimum films, ρ_{\min} decreases in the same ratio leaving the TMR unchanged. However for the poorer films, annealing increased the quality of the films as evidenced by a large drop in ρ_{\min} . $\Delta\rho_{\max}$ also decreased but not as much as for ρ_{\min} so that the TMR values increased. The second anneal however had the net effect of decreasing the TMR of the 32-300 film from 26 to 21% but leaving the 41-300 film the same, at 16%.

It has long been observed that the TMR decreases less rapidly than the magnetization approaches saturation⁷. We find that for these films the variation of the relative TMR with the relative magnetization M/M_s does not follow the functional form $(1-M/M_s)^n$ very well. However, if forced to fit this functional form the best fits were with $n \sim 1.4$ -1.6. Since M is a measure of the net projected volume of domains oriented in a particular direction and the TMR is a measure of the scattering from magnetic boundaries and depends on their shape it is expected that the two quantities can have quite different functional forms with no simple relation between them.

DISCUSSION AND CONCLUSIONS

We first consider the behavior of room temperature ρ_{\min} . For the 450°K series its value is $\sim 13 \mu\Omega\text{-cm}$ and it is essentially independent of Co concentration. There are three main contributions to ρ_{\min} : (1) One is due mainly to phonons and, to a lesser extent, magnons, ρ_{ph} . Assuming that the decrease in ρ_{\min} in going to LN temperature is mainly due to this term and that it varies inversely with temperature we estimate its value to be $\sim 4.6 \mu\Omega\text{-cm}$. This is reasonable value since the RT resistivities of the pure elements are 5.8 and $1.6 \mu\Omega\text{-cm}$ respectively for Co and Ag. We would expect that the value of this term would increase slightly with increasing %Co. (2) A second contribution is due to the interfacial scattering, ρ_{if} , of the electrons because of the step potential seen by the conduction electrons at a Ag/Co interface. The conduction electrons of pure Ag have about 77% sp-like and 23% d-like character⁸ with a Fermi energy of $E_F \sim 6.0 \text{ eV}$ and Fermi wave-vector of $k_F \sim 1.2 \text{ \AA}^{-1}$. The Fermi energy of the majority electrons for Co is $\sim 3\text{-}4 \text{ eV}$ so the step potential at a Co/Ag interface can be estimated to give a resistivity comparable to that of ρ_{ph} . As seen from the variation of the values of r_0 and the number of globules/cm³, N_g in Fig. 2 for any given series the interfacial area increases with % Co. Thus we expect that this resistivity should also increase with % Co. (3) The third contribution to the resistivity, ρ_{void} , comes from the large fraction of voids in the films. It is expected that the fraction of voids is rather constant since the pure Co films have about the same fraction as the granular films so this contribution should be independent of the % Co. Thus the constancy of ρ_{\min} with % Co is not understood. The magnitude of ρ_{void} is seen to be about the same as ρ_{ph} and ρ_{if} .

The magnetization and RBS measurements show that the Co and Ag atoms in the films deposited at substrate temperatures $\geq 400^\circ\text{K}$ are essentially completely segregated. Thus any explanation of the large MR effect as being due to the spin dependent scattering from Ag solute atoms in Co is not applicable to these films. We suggest that the MR effect in these granular films is due to the same scattering mechanism that gives rise to the MR effect in pure 3d ferromagnets. Namely the scattering of the highly polarized d conduction electrons of the 3d magnetic material at magnetic boundaries⁵. It was shown that the magnitude of $\Delta\rho_{\text{max}}$ varies inversely with the distance between magnetic boundaries, $\Delta\rho_{\text{max}} \sim 1/D$. When there is a spatial gap between the sequential domains each of the other scattering mechanism decreases the number of electrons that retain their memory of the magnetization orientation between the domains. Thus the optimum geometry for a large $\Delta\rho_{\text{max}}$ is that of a small cell size with the largest globules which still remain isolated from adjacent cells. We see from Figs. 2 and 4a that indeed the largest $\Delta\rho_{\text{max}}$ values are obtained for the smallest cell size having the largest non-touching globules. Once they touch, as indicated by the appearance of a hysteresis loop or coercive field, the domain size increases causing $\Delta\rho_{\text{max}}$ to decrease rapidly as seen in Fig. 4a. The magnitude of $\Delta\rho_{\text{max}}$ in the granular films agrees well with that obtained from the derived expression for $\Delta\rho_{\text{max}}$ in pure Fe with each of the above three scattering mechanism, ρ_{ph} , ρ_{if} and ρ_{void} attenuating the $\Delta\rho_{\text{max}}$ of pure Fe by about 30%.

We wish to thank C.H. Lee for measuring the magnetization curves of these films.

* Presently at Akashic Memories Corporation, San Jose CA 95134.

1. A.E. Berkowitz, J.R. Mitchell, M.J. Carey, A.P. Young, S. Zhang, F.E. Spada, F.T. Parker, A. Hutten and G. Thomas, Phys. Rev. Lett. **68**, 3745 (1992).
2. J.Q. Xiao, J. S. Jiang and C.L. Chien, Phys. Rev. Lett. **68**, 3749 (1992).
3. J.A. Barnard, A. Wakis, M. Tan, E. Haftek, M.R. Parker and M.L. Watson, Jour. Magn and Magn. Matls., **114**, 204 (1992).
4. M.B. Stearns, C-H. Chang and D.G. Stearns, J. Appl. Phys. **71**, 187 (1992).
5. M.B. Stearns, Internat. Conf. on Magnetism, Edinburgh, Scotland, September, 1991; J. Magn. and Magn. Matls. **104-107**, 1745 (1992) and Internat. Workshop on Spin-Valve Layered Structures, Madrid, Spain, September, 1991.
6. M.B. Stearns, APS March Meeting, Seattle WA, 1993.
7. R.M. Bozorth, *Ferromagnetism*, p. 745, D. Van Nostrand Company, Inc., Princeton, N.J. (1961).
8. D.A. Papaconstantopoulos, "Band Structure of Elemental Solids", Plenum Press, New York, 1986.

GIANT MR IN GRANULAR SYSTEMS PREPARED BY MELT-SPINNING AND SPUTTERING

B.DIENY, S.R.TEIXEIRA, B.RODMACQ, A.CHAMBEROD, J.B.GENIN,
S.AUFFRET.

CEA/Département de Recherche Fondamentale sur la Matière Condensée, SP2M-MP,
85X, 38041 Grenoble Cedex, France.

P.GERARD

CENG, LETI/MEM, 85X, 38041 Grenoble Cedex, France

O.REDON, J.PIERRE, R.FERRER, B.BARBARA

Laboratoire Louis Néel, CNRS, BP166X, 38042 Grenoble Cedex.G

ABSTRACT

We report the observation of giant magnetoresistance in granular systems prepared by either melt-spinning or sputtering. For melt-spun $\text{Co}_x\text{Cu}_{1-x}$ alloys, with x varying between 5 and 30%, magnetoresistance amplitudes of 20% in 50 kOe at 5 K were obtained, similar to those reported for the same alloys prepared by sputtering. For sputtered $(\text{Ni}_{80}\text{Fe}_{20})_x\text{Ag}_{1-x}$ alloys, three different contributions to the magnetoresistance have been clearly identified: The spin-valve (or giant) magnetoresistance, scattering on magnetic fluctuations, and anisotropic magnetoresistance. These three contributions have their own dependences on the size of the magnetic particles, on the degree of intermixing between NiFe and Ag, and on the temperature. In the third series of samples, sputtered $(\text{Co}_{70}\text{Fe}_{30})_x\text{Ag}_{1-x}$, very large magnetoresistance amplitude has been observed ($\Delta R/R$ as high as 20% at room temperature in 10 kOe and 60% at 10 K).

INTRODUCTION

Recently, giant magnetoresistance (GMR) has been reported in heterogeneous alloys ($\text{Co}_x\text{Cu}_{1-x}$ ^[1,2], $\text{Co}_x\text{Ag}_{1-x}$ ^[3], $\text{NiFe}_x\text{Ag}_{1-x}$ ^[4]) prepared by sputtering and also by melt-spinning^[5]. These alloys comprise two immiscible metallic components, one magnetic, the other non-magnetic. For sputtered samples, depending on the substrate temperature during deposition, the samples are homogeneous metastable alloys (if deposited at liquid nitrogen temperature) or granular alloys consisting of single domain ferromagnetic particles embedded in a metallic matrix. The size of the magnetic particles can be increased by subsequent annealings. By melt-spinning, the size of the particles is obviously much larger than in sputtered samples (especially for samples prepared at LN₂ temperature). However, this size is smaller than the optimal size of grains required for largest MR.

The physical origin of GMR in granular alloys is the same as in multilayers, namely interplay between neighboring magnetic grains of spin dependent scattering of conduction electrons occurring at interfaces between ferromagnetic and nonmagnetic regions or in the bulk of the single domain magnetic regions. In most cases, electrons having spins antiparallel to the magnetization of the ferromagnetic regions are more strongly scattered than those having spins parallel to the magnetization. So, at low magnetic fields, since the ferromagnetic regions are randomly oriented both spin orientations should experience strong scattering. However, at high magnetic fields, the ferromagnetic regions are aligned parallel to the direction of the applied field. Electrons with spins parallel to the magnetization do not experience the strong scattering at the interfaces or in the bulk of the ferromagnetic regions resulting in a low resistance for this spin orientation. Since the two types of electrons (spins ↑ or ↓) carry the current in parallel, the low resistance dominates at high magnetic fields, leading to GMR effect. For each couple of magnetic/non-magnetic materials, the largest possible MR is not easily predictable since a large number of parameters such as grain sizes, shapes and

distances between magnetic grains are broadly distributed and influence its amplitude. From the point of view of fundamental physics the transport properties of these alloys are much more complex and difficult to interpret quantitatively than in multilayers. However, from the point of view of applied physics, these alloys are quite interesting since their magnetoresistance amplitude may be potentially larger than in multilayers in the usual in-plane current^[6] (CIP) geometry. Moreover they are easier to prepare and have good thermal stability (annealed samples).

In this paper, we give an overview of our recent results on giant magnetoresistance in as-quenched and annealed heterogeneous alloys prepared by sputtering or melt-spinning. Three series of alloys have been investigated : melt-spun $\text{Co}_x\text{Cu}_{1-x}$, sputtered $\text{NiFe}_x\text{Ag}_{1-x}$ and sputtered $(\text{Co}_{70}\text{Fe}_{30})_x\text{Ag}_{1-x}$ alloys with x varying between 5 and 40%.

MELT-SPUN SAMPLES

The melt-spun samples are prepared in an argon atmosphere^[5]. They consist of granular $\text{Co}_x\text{Cu}_{1-x}$ alloys in the form of long ribbons 5mm wide, 50 μm thick, tens of meters long. In the as-quenched ribbons, X-ray spectra show the formation of Co-rich precipitates (containing about 10% of Cu) embedded in a Cu-rich matrix. The width of the line associated with the Co-rich phase corresponds to a size of magnetic particles of about 120 \AA . After 10 minutes annealing at 950K, this size has increased up to 250 \AA . Fig. 1 shows the magnetoresistance of a melt-spun ribbon of composition $\text{Co}_{0.2}\text{Cu}_{0.8}$ at 4K after 10 minutes annealing at various temperatures. The amplitude of the magnetoresistance goes through a maximum for the samples annealed at 480°C. The saturation field decreases with increasing annealing temperature which is consistent with an increase of the size of the magnetic grains. The results of figure 1 can be directly compared with previously published results on sputtered $\text{Co}_{0.2}\text{Cu}_{0.8}$ alloys^[1,2]. The amplitude of the GMR is as large (almost 20% at 4K in 50kOe) in the present melt-spun ribbon as in the sputtered samples. This method of preparation opens the prospect of new applications of GMR at high currents in electrical engineering or electrotechnique.

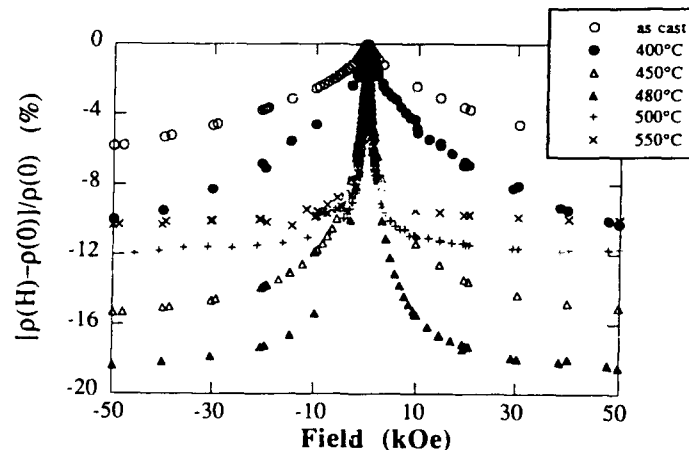


Figure 1 : Magnetoresistance of melt-spun $\text{Co}_{0.2}\text{Cu}_{0.8}$ metallic ribbons at 4K after successive annealings for 10 minutes at various temperatures

SPUTTERED SAMPLES

The sputtered $(\text{Ni}_{0.81}\text{Fe}_{0.19})_x\text{Ag}_{1-x}$ alloys were prepared at room or LN₂ temperatures. The X-ray analysis shows that the samples consist of NiFe rich precipitates embedded in a Ag matrix. Some alloying formation between the NiFe and Ag has been observed which results in a ramified gradient of concentration from the Ag matrix to the inner part of NiFe grains. So NiFe particles consist of a ferromagnetic core surrounded by a ramified paramagnetic envelope, the thickness of which decreases with temperature (gradient of magnetic ordering temperature associated with the gradient of concentration). We carried out a detailed study of structural, transport and magnetic properties of these alloys^[6]. Fig. 2a, b, c show the observed magnetoresistance curves of three as-deposited alloys prepared at R.T. with NiFe concentration of 20, 30 and 40% respectively. These curves are quite different. Their analysis point out the existence of three main physical contributions to the MR in these systems as will be discussed below.

Fig. 2a shows the MR curves in the low NiFe concentration limit ($\text{NiFe}_{0.25}\text{Ag}_{0.75}$). The grains are in large proportion paramagnetic down to 110K^[6]. A ferromagnetic order within the grains appears below 110K. The magnetoresistance is consequently dominated by the scattering on paramagnetic fluctuations above 110K (round shaped MR(H) curve) as in bulk ferromagnets (De Gennes-Friedel, 1958)^[7]. Below 110K, the MR curves exhibit a singularity around zero field, reflecting the change in the magnetic behavior. The steep decrease of the MR in relatively low fields is due to the onset of spin-valve MR (rotation of the magnetic moments of individual grains) resulting from the decreasing spin-flip scattering on magnetic fluctuations. The amplitude of this MR contribution increases with decreasing temperature. The long MR tail at high fields (the amplitude of which decreases with decreasing temperature in contrast to the spin-valve contribution) is still associated with scattering on magnetic fluctuations.

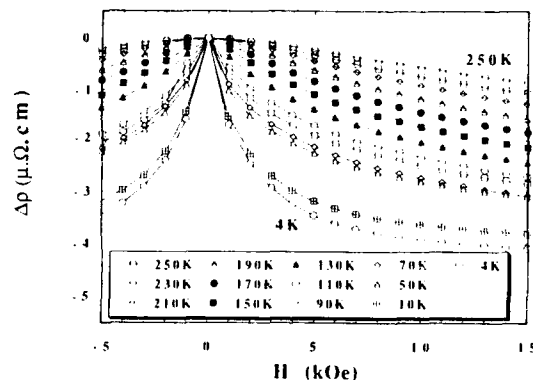


Figure 2a : Magnetoresistivity of as-sputtered $\text{NiFe}_{0.25}\text{Ag}_{0.75}$ at various temperatures.

In the opposite limit of high concentration ($\text{NiFe}_{0.40}\text{Ag}_{0.60}$, Fig 2b), two points must be underlined. Firstly, the MR curve also exhibits a reversible shape characterized by two symmetrical maxima. Secondly, in contrast to the low concentration limit, the MR is maximum at room temperature and not at 4K. Since we are here at 40 at.% of NiFe, the GMR hardly plays any role at this concentration because of strong ferromagnetic coupling between magnetic grains. It should be pointed out that the MR measurements have been carried out with current parallel to the applied field. In this geometry, as the field is increased from 0 Oe, the anisotropic MR (AMR), determined by the average cosine square of the angle between the magnetizations of the NiFe grains and current, leads to an increase in resistivity. In contrast, the scattering on magnetic-

fluctuations decreases as the field is increased resulting in a negative MR. In low fields (between 0 and about 300 Oe) the AMR dominates the decreasing scattering on magnetic fluctuations leading to a positive MR. At higher fields, the magnetic moments of the grains do not rotate any more (saturation of the ferromagnetic part of the magnetization) leading to a saturation of the AMR. As a result only the scattering on magnetic fluctuations still contributes to the MR. The MR is then negative as observed in Fig. 2a. Furthermore the fact that the amplitude of the MR decreases as the temperature is decreased, is consistent with a reduction of the magnetic fluctuations in the magnetic grains since the Curie temperature of the magnetic grains in this alloy is above room temperature[6].

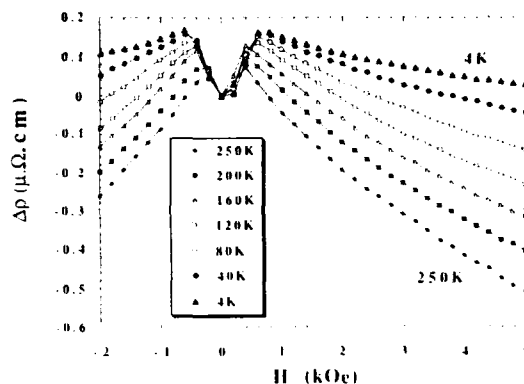


Figure 2b : Magnetoresistivity of as-sputtered $\text{NiFe}_{0.40}\text{Ag}_{0.60}$ at various temperatures.

Fig. 2c corresponds to an intermediate NiFe concentration (30%). Three successive behaviors are observed in this case as the temperature is decreased. Above 200K the envelope of the NiFe grains is paramagnetic. The MR has a round shape as in the low concentration limit (see Fig. 2a above 110K). Below 200K, the envelopes of the magnetic grains begin to order ferromagnetically. The anisotropic magnetoresistance (AMR) is still small. The main contributions to the MR are still scattering on magnetic fluctuations and rising spin-valve MR. This leads to an angular MR shape around zero field (as in Fig. 2a below 110K). Below 150K, the AMR has significantly increased so that a double maximum appears as in the previous case.

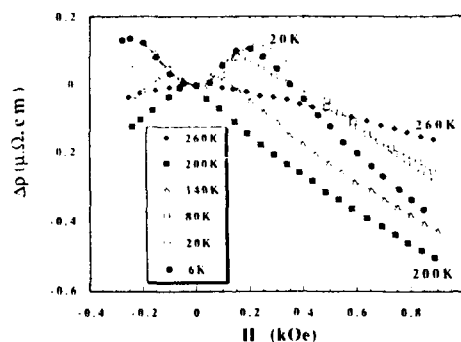


Figure 2c : Magnetoresistivity of as-sputtered $\text{NiFe}_{0.30}\text{Ag}_{0.70}$ at various temperatures.

During annealing, demixing between NiFe and Ag takes place as observed by X-ray diffraction. As a result, the relative role of the three contributions to the MR change dramatically. The Curie temperature of the magnetic grains raises much above room temperature leading to a decrease of the role of scattering on magnetic fluctuations. The increase in the size of magnetic grains and the improved interfaces sharpness result in a large enhancement of the role of the GMR (up to an optimal grain size related to the mean free paths in the magnetic grains). The AMR also increases with grain size. Fig. 3 shows a comparison of magnetoresistance in an as-sputtered and annealed sample of composition $\text{NiFe}_{0.35}\text{Ag}_{0.65}$. The shape and temperature dependence of the MR before and after annealing are quite different as a result of the increase of GMR upon annealing. In this series of NiFeAg alloys, we have obtained MR amplitudes as large as 50% at 5K in 5kOe after annealing at 550°C for 20 minutes (maximum for NiFe concentration of 25%) which is comparable to the results of ref 4.

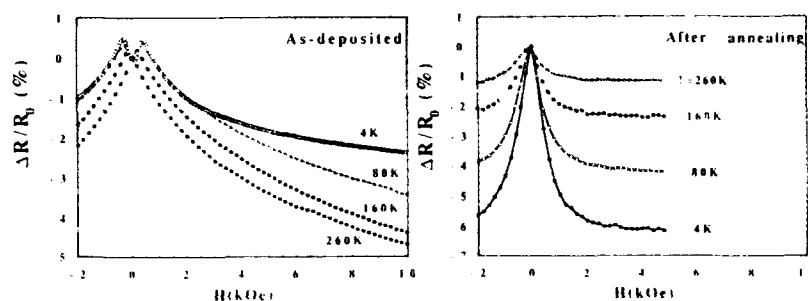


Figure 3 : Comparison of magnetoresistance in as-sputtered and annealed $\text{NiFe}_{0.35}\text{Ag}_{0.65}$ alloys at various temperatures (annealed at 550°C for 10 minutes).

The third series of granular systems investigated was sputtered $(\text{Co}_{0.70}\text{Fe}_{0.30})_x\text{Ag}_{1-x}$ alloys. The samples were prepared at room or LN_2 temperatures with composition varying between 20 and 47 at% of CoFe. Fig. 4a shows the measured GMR at room temperature as a function of CoFe concentration in the as deposited samples. The GMR shows a maximum for 38 at% of CoFe, with MR amplitudes of 15 and 10 % for samples prepared at room and LN_2 temperatures respectively. This difference of MR amplitudes reflects the difference in the nanostructure of the samples due to different substrate temperature during growth. It is interesting to note that the position of the maximum occurs at relatively high magnetic concentration (38 at% CoFe) in comparison to other granular alloys (closer to 25% in NiFeAg, CoCu or CoAg alloys^[1-4]). The decrease of MR at large magnetic concentration is mainly due to the increase in ferromagnetic coupling between magnetic grains preventing a change with applied field in the relative orientation of the magnetic moments of neighboring grains. The onset of ferromagnetic coupling only at 38 at% of magnetic element in $(\text{Co}_{0.70}\text{Fe}_{0.30})_x\text{Ag}_{1-x}$ suggests that the grains have more compact shapes than in other alloys^[1-4] (may be due to a difference in structure between the bcc magnetic grains and the fcc matrix) or that antiferromagnetic couplings between magnetic grains through Ag exist in these alloys.

Regarding the MR amplitude in this series, we observed one of the largest magnetoresistance ever reported at room temperature in these granular materials (18% at room temperature in 10 kOe after annealing at 600K for 10 mn.), see Fig. 4b. This MR is larger than in $\text{Co}_x\text{Ag}_{1-x}$ at room temperature^[9]. It is interesting to note that in Co/Ag multilayers, in CIP geometry, the MR does not exceed 30% at low temperature^[8]

compared to 84% in CoAg granular alloys^[4]. The larger MR observed in CoAg alloys than in Co/Ag multilayers with current flowing in the plane of the layers indicates the potential very large MR amplitude that one can expect from granular systems (without considering the values of saturation fields).

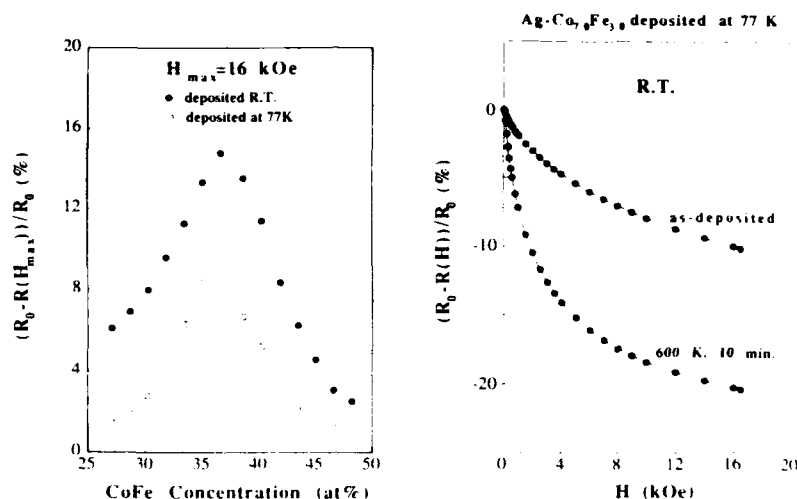


Figure 4: a) Room temperature magnetoresistance at 16kOe of CoFeAg versus concentration of CoFe. b) Magnetoresistance of $\text{CoFe}_{0.38}\text{Ag}_{0.62}$ as-deposited at 77K and after annealing at 600K during 10 minutes.

To our point of view, this larger MR in granular systems results from the relative geometry of the current lines in the system and of the magnetic inhomogeneities (grains or layers) which give rise to the GMR. The situation of granular systems is in fact intermediate between the situation of multilayers with current flowing in the plane of the layers (layers in parallel) and multilayers with current perpendicular to the interfaces (layers in series)^[6]. One may therefore expect magnetoresistance amplitudes in granular alloys intermediate between the magnetoresistance of multilayers with current flowing in the plane or perpendicular to the layers.

REFERENCES

- [1]-A.E.Berkowitz, J.R.Mitchell, M.J.Carey, A.P.Young, S.Zhang, F.E.Spada, A.Hutten, G.Thomas, *Phys.Rev.Lett.* **68** (1992) 3745.
- [2]-J.Q.Xiao, J.S.Jiang, C.L.Chien, *Phys.Rev.Lett.* **68** (1992) 3749.
- [3]-P.Xiong, G.Xiao, J.Q.Wang, J.Q.Xiao, J.S.Jiang, C.L.Chien, *Phys.Rev.Lett.* **69** (1992) 3220.
- [4]-J.S.Jiang, J.Q.Xiao, C.L.Chien, *Appl.Phys.Lett.* **61** (1992) 2362.
- [5]-R.Ferrer, B.Barbara, B.Dieny, A.Chamberod, C.Cowache, J.B.Genin, S.R.Teixeira, submitted to *Appl.Phys.Lett.* (Feb.93).
- [6]-B.Dieny, S.R.Teixeira, B.Rodmacq, C.Cowache, O.Redon, J.Pierre, submitted to *J.Mag.Mag.Mater.* (April 93).
- [7]-P.G.De Gennes, J.Friedel, *J.Phys.Chem.Sol.* **4** (1958) 71.
- [8]-S.Araki, K.Yasui, Y.Narumiya, *J.Phys.Soc. of Japan*, **60** (1991) 2827.
- [9]-M.J.Carey, A.P.Young, A.Starr, D.Rao, A.E.Berkowitz, *Appl.Phys.Lett.* **61** (24), 2935.

GIANT MAGNETORESISTANCE IN GRANULAR $\text{Ni}_{81}\text{Fe}_{19}/\text{Ag}$ FORMED FROM ANNEALED MULTILAYERS

X. Bian*, A. Zaluska*, Z. Altounian*, J.O. Ström-Olsen*, Y. Huai** and R.W. Cochrane***

* Centre for the Physics of Materials and Department of Physics, McGill University, 3600 University St., Montréal, Québec, Canada H3A 2T8

** INRS-Énergie et Matériaux, 1650 Montée, St-Julie, Varennes, Québec, Canada J3X 1S2

*** Département de Physique, Université de Montréal, C.P.6182, Succ. A, Montréal, Québec, Canada H3C 3J7

ABSTRACT

We have observed giant magnetoresistance (GMR) in $\text{Ni}_{81}\text{Fe}_{19}/\text{Ag}$ granular structures synthesized by the annealing of artificial multilayers made by sputtering. The size and morphology of the magnetic precipitates can be controlled by adjusting the magnetic layer thickness in the initial stage. Magnetoresistance as large as 30% was found at 4.2 K with a rather small saturation field. Giant magnetoresistance in this alloy system essentially depends on the magnetic precipitate size, annealing temperature and the $\text{Ni}_{81}\text{Fe}_{19}$ concentration. The temperature dependence of the magnetoresistance in these films is discussed.

1. INTRODUCTION

The recent discovery of giant magnetoresistance (GMR) for ferromagnetic granules in a non-magnetic metal matrix [1,2] adds a new dimension to the phenomenon of GMR in magnetic multilayer[3]. Substantial MR of these immiscible granular alloy systems, such as Co-Cu[1,2], and Co-Ag[4], have increased our fundamental understanding of GMR effects, as well as increased their potential for applications. However, to be useful as for magnetoresistive sensor devices, thin film materials require much lower saturation field H_S than have hitherto been found.

In this paper we report the synthesis of $\text{Ni}_{81}\text{Fe}_{19}/\text{Ag}$ granular films based on the heat treatment of the multilayered samples containing ultrathin NiFe layers. The permalloy/Ag system was chosen because of the relative insolubility of the two components over a wide composition range[5], thus guaranteeing a phase separated granular alloy. The extraordinary soft magnetic properties of $\text{Ni}_{81}\text{Fe}_{19}$ combined with the large electronic mean free path in Ag, should lead to small saturation fields and enhanced MR. Also, the magnetic concentration and particle size can be controlled by adjusting the permalloy layer thickness during the sputtering process. We will show that giant magnetoresistances are observed in these alloy films with significantly lower saturation fields than in other similar systems, leading to relatively high field sensitivity.

2. EXPERIMENTAL

The $\text{Ni}_{81}\text{Fe}_{19}/\text{Ag}$ multilayers with individual NiFe layers ranging from 4 Å to 7 Å and Ag layers of 20 Å to 22 Å were prepared by dc magnetron sputtering from separate targets of $\text{Ni}_{81}\text{Fe}_{19}$ alloy and Ag onto glass substrates at room temperature. The background pressure was $<2 \times 10^{-7}$ torr. With a sputtering pressure of 7.5 mtorr of argon, the deposition rates (determined from the measured thicknesses of single films by low-angle x-ray reflectivity measurements) were 1.4 Å/s for $\text{Ni}_{81}\text{Fe}_{19}$ and 1.6 Å/s for Ag. The individual layer thicknesses of $\text{Ni}_{81}\text{Fe}_{19}$ and Ag were adjusted to yield films of composition between 20 and 45 at.% NiFe. Total film thicknesses were 600-1000 Å. All the samples were examined

both before and after heat treatment under a vacuum of $< 2 \times 10^{-6}$ Torr.

The structural characterization of the samples was performed by low and high angle x-ray diffraction using $\text{Cu-K}\alpha$ radiation [6] and transmission electron microscopy (TEM). The film compositions, as determined by electron microprobe measurements, were found to be within 4% of the nominal values. The magnetoresistance measurements were carried out using a four-terminal geometry and a high-resolution ac bridge [7]. The current was in the plane of the film with the magnetic field either in or perpendicular to the plane.

3. RESULTS AND DISCUSSION

The low-angle x-ray reflectivity spectra reveal sharp superlattice peaks for all the as-deposited samples down to a bilayer thickness of $\Lambda = 26 \text{ \AA}$ (with a 4 \AA layer of $\text{Ni}_{81}\text{Fe}_{19}$), indicating a well-defined composition modulation along the growth direction. The corresponding high-angle x-ray diffraction and electron diffraction for these samples show that the multilayer films have coherent interfaces and a highly textured structure with (111) orientations normal to the film plane (Fig.1(a)). However, after annealing the samples at 450 $^{\circ}\text{C}$ for 20 minutes, both low and high-angle x-ray results show that the superlattice structures were washed out, indicating significant interdiffusion during the annealing

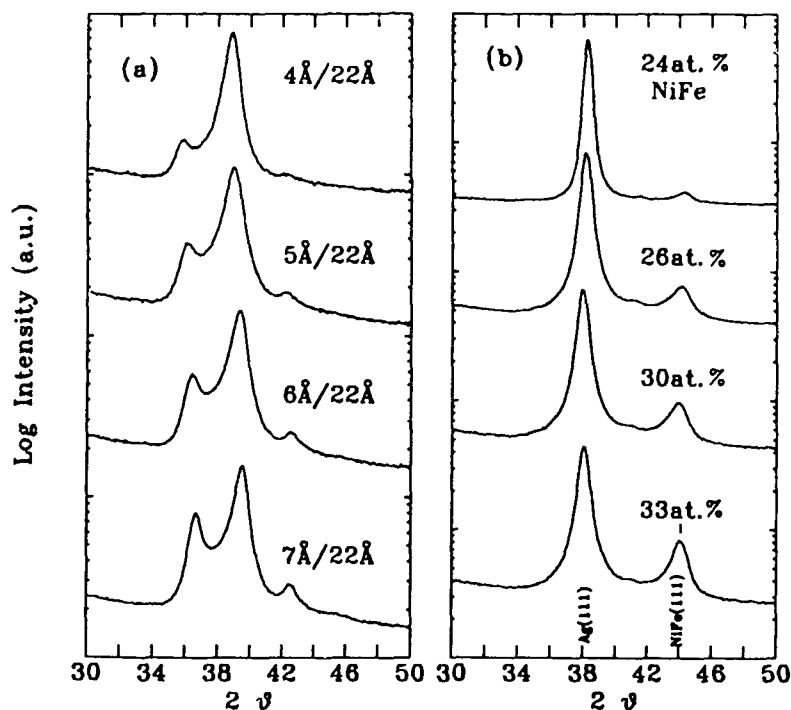


Figure 1. High-angle x-ray diffraction measurements for the as-deposited multilayers (a) and annealed (450 $^{\circ}\text{C}$, 20 minutes) NiFe/Ag alloy films (b), for different NiFe-compositions. The vertical lines indicate the position of permalloy (111) peak.

stage. Highly (111) textured structures can still be seen in the annealed samples as demonstrated by the two peaks in fig.1 (b) for the annealed samples, which are indexed as Ag(111) and NiFe(111), respectively. It is to be noted that the intensity of the smaller peak at $2\theta=44.4^\circ$ in Fig.1(b) increases and becomes sharper as the NiFe concentration is increased from 20 at.% to 37 at.% NiFe, confirming the assignment of the (111) peak to NiFe. The NiFe particle sizes, observed from TEM images, were 60 to 100 Å at this annealing temperature depending on the original thickness of the NiFe layers. Fig.2(a) shows high-angle x-ray diffraction scans for one sample at different annealing temperatures during which it transforms from a superlattice structure to a phase separated alloy. As the annealing temperature is increased, the superlattice coherence is lost and the peak intensity at $2\theta=44.4^\circ$ increases and becomes sharper with the growth of NiFe precipitates.

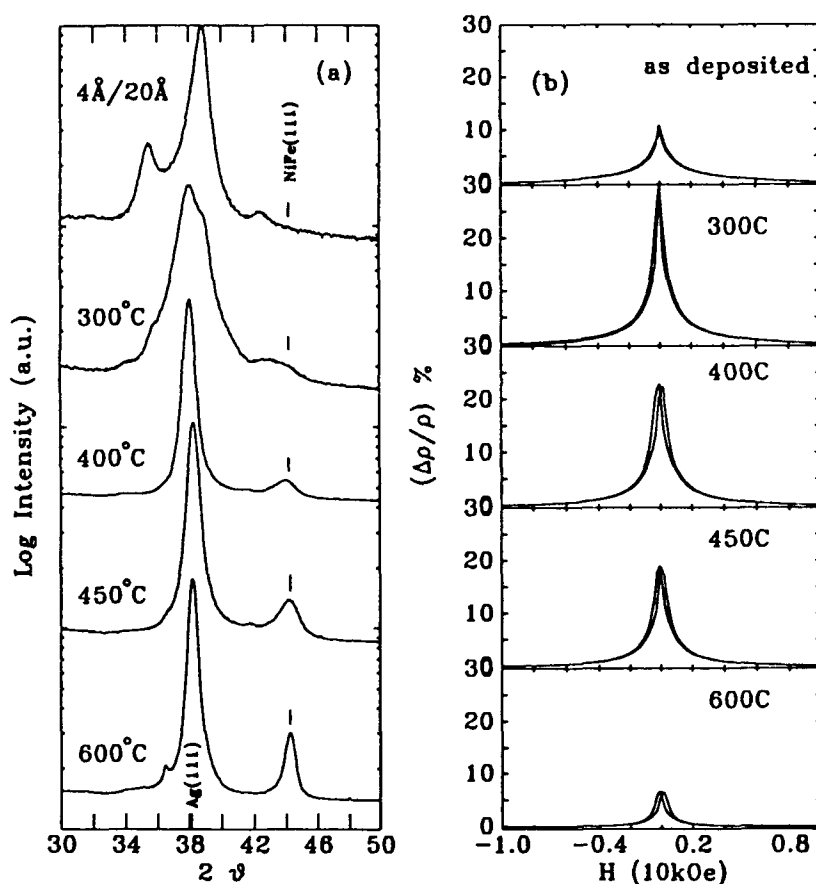


Figure 2. (a) High angle x-ray scans for the NiFe(4Å)/Ag(20Å) alloy as-deposited and after 30 minute annealings at 300 °C, 400 °C, 450 °C and 600 °C; (b) magnetoresistance curves measured at 4.2 K after each annealing listed in (a).

Magnetoresistance measurements were performed between 4.2 and 300 K in magnetic fields of up to 10 kOe. Fig.2(b) shows the MR values measured at 4.2 K for the 24 at.% NiFe sample as-deposited and after successive annealings. The as-deposited multilayer has a small MR values of less than 10% at 4.2 K and less than 2% at 300 K, with no evidence of antiparallel spin alignment between the NiFe layers across the Ag spacer. Upon annealing an appreciable increase of $\Delta\rho (= \rho_{(H=0)} - \rho_{(H=H_s)})$ up to 85% was observed; the resistivity ρ , however, decreases by about a factor of 1.25 to 4.6 Ohm-m, giving an even large enhancement in $\Delta\rho/\rho$ after heat-treatment. An MR value as large as 30% was found for the sample annealed at 300 °C. It is also noted that the high temperature (> 450 °C) annealing substantially decreased the MR, this may be due to the extreme growth of NiFe grains or a decrease in surface to volume ratio. However, the important property of our alloy films is the small saturation fields, as shown in Fig.2(b). A saturation field of 2-2.5 kOe can be deduced which is about 5-10 times smaller than those found in co-sputtered Co/Cu[1] and Co/Ag[4] granular alloy systems. The small H_s in this system may be ascribed to the shape anisotropy of the magnetic particles. The MR curves, in fact, are broader for the field perpendicular to the film plane and narrower for the field in the plane of the film, implying the existence of some plate-like particles.

Selecting and controlling the structural parameters in order to maximize MR and minimize H_s are important aspects for producing granular alloy systems. Fig.3 shows the composition dependence of the MR and the saturation field H_s for several annealed alloys at 4.2 K. $\Delta\rho/\rho$ increases from low NiFe concentration to such a maximum at about 24 at.% NiFe and then gradually decreases. H_s decreases more rapidly with NiFe concentration before reaching a constant value for concentrations above 33 at.% NiFe. $\Delta\rho$ versus composition shows a similar behavior, a maximum found at 24 at.% NiFe. At a certain annealing temperature below 450 °C, low magnetic concentrations imply small particle sizes and a large surface/volume ratio. It has been suggested[8] that the spin dependent scattering in this case is dominated by the scattering at the interface rather than bulk and that this is the reason for the GMR. As particle sizes become comparable with the mean free path, the effective surface/volume ratio is reduced lowering the contribution of the spin dependent interfacial scattering, and the MR is reduced. The

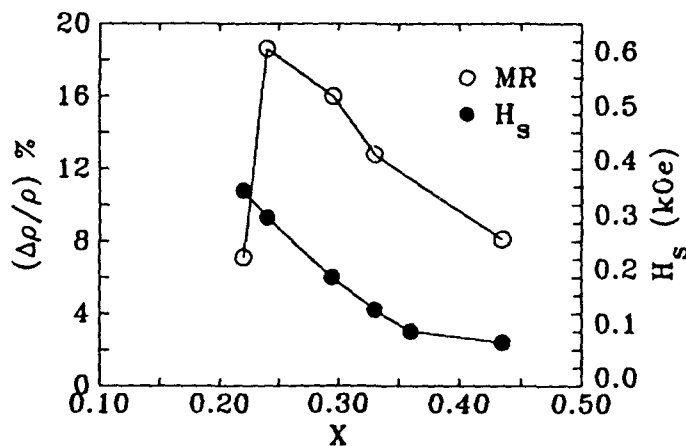
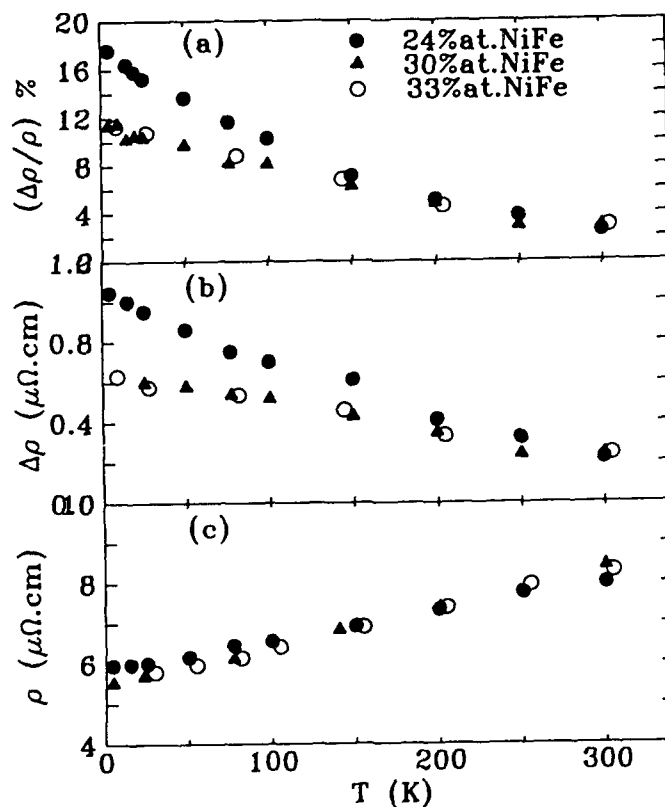


Figure 3. Magnetoresistance and saturation field, measured at 4.2 K, as a function of NiFe concentration, $(\text{NiFe})_x\text{Ag}_{1-x}$.

small value of the MR at NiFe concentrations below 20 at.%, however, may simply reflect the diminished level of magnetic particles. The saturation field H_s , as shown in Fig.3 is also related to the concentration of the magnetic alloy. Saturation fields less than 1 kOe for NiFe concentrations above 35 at.% are found. The temperature dependences of $\Delta\rho/\rho$, $\Delta\rho$ and ρ for alloy films annealed at 450 °C for 30 minutes are presented in Fig.4. For samples with NiFe concentrations above 30 at.%, $\Delta\rho/\rho$ decreases linearly with temperature, while for samples with NiFe below 24 at.% both $\Delta\rho/\rho$ and $\Delta\rho$ decrease more rapidly at low temperatures. The sheet resistivities ρ , however, show a nearly linear decrease with the temperature for all the samples at this annealing temperature. The fact that $\Delta\rho$ changes by a factor of 4.8 between 300 K and 4.2 K, for the sample with 24 at.% NiFe, compared to $\Delta\rho$ changes of 2.5 times for NiFe concentrations above 30 at.%, indicate that the contributions to GMR for the first sample arises mainly from the increased $\Delta\rho$ at low temperature, while for the second it is due mainly to the reduced sheet resistivity. As the temperature increases, inelastic scattering events from phonons and magnons give rise[8] to a decrease in $\Delta\rho$ and an increase in ρ . In addition, the interface, which gives the most important contribution to the MR, may have a considerably lower effective Curie



4. Figure 4, Temperature dependences of (a) $\Delta\rho/\rho$, (b) $\Delta\rho$ and (c) ρ for three NiFe concentrations.

temperature due to the so-called softening of the magnetization at the interface[9] The large temperature dependence of MR at low magnetic concentration samples may also be attributed to superparamagnetism. As the magnetic anisotropy of the particles is proportional to their size, thermal activation will cause a spontaneous rotation of the magnetic moments for small particles[10]. The rather moderate temperature behavior of high magnetic concentration samples has been shown to be more magnetically stable. However, the relatively strong temperature dependence of MR in a granular alloy system may prevent its technological application.

4. CONCLUSIONS

We have synthesized phase separated $\text{Ni}_{81}\text{Fe}_{19}/\text{Ag}$ alloy films by annealing of the multilayered structures containing ultrathin NiFe layers. The magnetic concentration and precipitate size can be controlled by adjusting the NiFe layer thickness in the deposition stage as well as by subsequent heat-treatment. The alloy films display giant magnetoresistance with a maximum value of 30% at 4.2 K for NiFe concentration near 24 at.%, and a relatively small saturation field of 2 kOe. The strong temperature dependence of MR is shown to be related to the composition, size and thermal stability of the magnetic particles. Even lower saturation fields should be possible by varying the NiFe concentration and the annealing temperature.

ACKNOWLEDGEMENTS

We acknowledge the financial support from the NSERC, Canada, FCAR, Quebec and Martinex Science, Inc.

References

- [1] A.E. Berkowitz, M.J. Carey, J.R. Mitchell, A.P. Young, S. Zhang, F.E. Spada, F.T. Parker, A. Hutten, and G. Thomas, *Phys. Rev. Lett.* **68**, 3745 (1992).
- [2] J.Q. Xiao, J.S. Jiang and C.L. Chien, *Phys. Rev. Lett.* **68**, 3749 (1992).
- [3] M.N. Baibich, J.M. Broto, A. Fert, F. Nguyen van Dau, F. Petroff, P.E. Etienne, G. Creuzet, A. Friederich, and J. Chazelas, *Phys. Rev. Lett.* **61**, 2472 (1988).
- [4] J.Q. Xiao, J.S. Jiang and C.L. Chien, *Phys. Rev.* **B46**, 9266 (1992).
- [5] T.B. Massalski, *Binary Alloy Phase Diagrams*, Vol.1 p25, 48 (1986).
- [6] Y. Huai, R.W. Cochrane, Y. Shi, H.E. Fischer and M. Sutton. *Mat. Res. Soc. Symp. Proc.* Vol.238, 671 (1992).
- [7] R.W. Cochrane, J. Destry and M. Trudeau, *Phys. Rev.* **B27**, 5955 (1983).
- [8] Shufeng Zhang, *Appl. Phys. Lett.* **61**, 1855 (1992).
- [9] Shufeng Zhang and P.M. Levy, *Phys. Rev.* **B43**, 11048 (1991).
- [10] A.H. Morrish, *Physical Principles of Magnetism* (Wiley, New York 1965).

GIANT MAGNETORESISTANCE AND STRUCTURE OF PHASE-SEGREGATED EPITAXIAL METALS *

R.F. Marks, R.F.C. Farrow, G.R. Harp, S.S.P. Parkin, T.A. Rabedeau, M.F. Toney,
A. Cebollada, IBM Research Division, Almaden Research Center, 650 Harry Road,
San Jose, CA 95120-6099;

N. Thangaraj, Kannan M. Krishnan, National Center for Electron Microscopy,
Lawrence Berkeley Laboratory, Cyclotron Road, Berkeley, CA 94720

* This work was supported in part by ONR.

ABSTRACT

Giant magnetoresistance, GMR, in thin metal films elicits attention due to its technological potential as well as its relevance to theory of exchange coupling. Epitaxial, phase-segregated ferromagnet/paramagnet mixtures have been grown by UHV evaporation. Such films show spontaneous formation of ferromagnetic clusters, leading to large values of GMR (40% at room temperature) as grown. The growth of Co-Cu, Co-Ag, Fe-Ag and Permalloy-Ag films are described. Structural analysis by grazing-incidence small angle X-ray scattering (GISAXS) provides a measure of cluster size and characteristic spacing. Effects of growth temperature and subsequent annealing on GMR and film structure are described. Preliminary results of TEM examination of (001) Fe-Ag and Co-Ag granular films are presented for the first time.

1. INTRODUCTION

Following active research in GMR of multilayer material systems, important GMR effects have been reported for phase-segregated films of Co-Cu [1,2] and Co-Ag [2] prepared by magnetron sputtering. Because of mutual immiscibility of components, Co-Cu, Co-Ag, Ni-Ag and Fe-Ag alloy films are presumed to contain small magnetic particles embedded in a nonmagnetic host matrix. To achieve a high magnetoresistance (MR) for sputtered alloy films, post-growth annealing was necessary to induce this phase segregation. In contrast, we report large values of magnetoresistance for as-deposited films of (111) and predominantly (001) oriented Co-Cu and Co-Ag grown at $\approx 250^\circ\text{C}$ as well as for Fe-Ag, NiFe-Ag and NiFeCo-Ag. By selecting optimal growth temperature, epitaxial films with considerably larger GMR than that of comparable sputtered films can be realized, without additional annealing steps[3].

Both Co-Cu and Co-Ag are mutually insoluble (solubility $<0.01\%$) with even lower solubility for Fe and Ni in Ag at temperatures below $\approx 400^\circ\text{C}$. Under UHV conditions there should be ample surface diffusion to permit phase segregation during epitaxy. The characteristic size and separation of ferromagnetic clusters are controlling parameters in the GMR of phase-segregated metals [1,2,4,5] and a better understanding of GMR in phase-segregated materials requires analysis of microstructure in these systems. Additionally, one needs to identify underlying mechanisms of GMR, including the relative importance of interfacial and volume spin dependent electron scattering in these materials. This work examines the effects of alloy composition, post-growth anneal and growth temperature on GMR and relates these to structural determination by TEM and GISAXS.

2. EPITAXY AND CHARACTERIZATION

The crystalline films were grown in a VG80M (V.G. Semicon) molecular beam epitaxy (MBE) system equipped with LEED and RHEED. Electron-beam sources, with feedback control of flux, were used for Co, Fe and NiFe (permalloy) and temperature-stabilized effusion cells were used for Cu and Ag. Typical growth rates were ~ 0.05 to 0.3 \AA/s .

Films with (111) orientation and uniform composition could be prepared up to seven at a time on one inch diameter sapphire (0001) disks. Multiple sample runs of this type provided consistent nucleation and growth conditions for comparative studies of the relationship between anneal temperature, ferromagnetic cluster size and GMR. For surveys of the effect of composition on GMR, special, 50mm-long (0001) sapphire strips were employed. By growing on these without substrate rotation, the growth geometry resulted in a nearly linear variation in composition along the strip. After growth the pre-scribed strip was cleaved into samples of appropriate size for MR measurements.

The (111) crystalline orientation was nucleated by thin Pt seed layers, $\sim 30 \text{ \AA}$ thick, which were deposited at 600°C . The Pt seed layer grows epitaxially on sapphire with $[6] \text{ Pt}(111) \parallel \text{Al}_2\text{O}_3(0001)$ and $\text{Pt}(110) \parallel \text{Al}_2\text{O}_3(10\bar{1}0)$. Two twin orientations of Pt, differing by a rotation of 180° about the $[111]$ axis, were observed. A final capping film of 30 \AA Pt was deposited on most samples. Samples intended primarily for X-ray analysis were capped by 20 \AA of Cu.

Films with (100) orientation were grown directly onto air-cleaved NaCl wafers ($12 \times 12 \text{ mm}$ in size), which were cleaned before growth by heating to 300°C in UHV. During growth the temperature was held at 250°C .

GISAXS involves intensity measurements near the specularly reflected beam. The use of this technique to characterize Co cluster size in a Cu matrix is described in detail in reference [4]. In this study, five films (800 \AA of $\text{Co}_{16}\text{Cu}_{84}(111)$) were grown simultaneously at 200°C . After growth, one sample was removed from the MBE chamber and the remaining samples were annealed in ultra high vacuum for 10 minutes at maximum temperatures of 250°C . The removal/anneal sequence was repeated at successive temperatures of 350°C , 450°C , and 550°C . To minimize oxidation, the samples were always maintained in UHV or in inert gas (except during brief transfers) throughout the anneal sequence and during subsequent GISAXS measurements.

The crystallographic order of these films was later studied by X-ray diffraction using a laboratory X-ray source. This confirmed the films to be epitaxial with $\sim 0.5^\circ$ surface normal and in-plane mosaics. There was little effect of post growth anneal on the crystal coherence length. The inverse half width at half maximum of the (111) peaks range from 150 \AA (550°C film) to 200 \AA (250°C film).

Reflection high energy electron diffraction (RHEED) showed, for Co-Ag films, two distinct diffraction patterns; one set of streaks corresponding to the Ag lattice and a second set of elongated spots to a lattice constant close to, but $\sim 2\%$ larger than that of bulk fcc Co. These observations are consistent with spontaneous phase separation during growth and suggest that the Co islands are strained.

3. EXPERIMENTAL RESULTS

The dependence of saturation magnetoresistance, $\Delta R/R$ as a function of composition for Co-Cu and Co-Ag films has been reported elsewhere[3]. To summarize, for films grown at 250°C , the GMR shows a broad peak near 25% Co for Co-Cu and 30% Co for Co-Ag. The respective peak GMR values are 50%

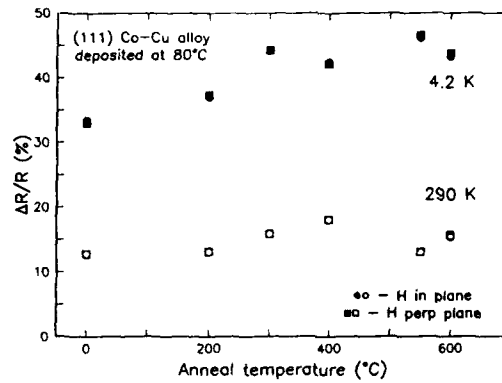


Figure 1. Anneal temperature dependence of the GMR for a set of $\text{Co}_{15}\text{Cu}_{85}$ films grown simultaneously on sapphire at 80°C .

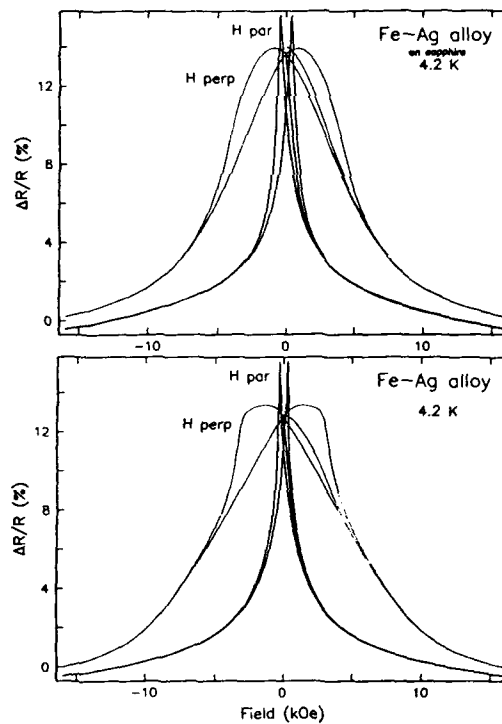


Figure 2. Field dependence of saturation magnetoresistance, at 4.2K, for Fe-Ag films (~29at% Fe):
 (a) (111) film grown on sapphire (0001)
 (b) (001) film grown on NaCl.

(4.2K), 21%(300K) for Co-Cu and 71% (4.2K), 38% (300K) for Co-Ag. On annealing Co-Cu films sequentially to 550°C, the GMR decreased. However, for films grown at 80°C, the GMR increased with sequential annealing, to 550°C, as shown in Figure 1. It is interesting to note that this property of the Co-Cu films grown at lower temperature is similar to the effect of post-growth annealing on sputter-deposited films. Co-Cu films grown at $\approx 80^\circ\text{C}$ showed almost no magnetic anisotropy either before or after annealing. Co-Ag films grown at 250°C exhibited significant anisotropy as we have described earlier[3]. When measured at 4.2K these films exhibited perpendicular anisotropy with perpendicular remanence.

The size of Co clusters and their distribution were investigated using GISAXS on Co-Cu films grown on sapphire (0001) at 200°C. From a fit of the GISAXS data one can extract an accurate measure of both the characteristic Co cluster size and the Co-Co cluster nearest neighbor separation. The data are presented elsewhere[3,4]; here we simply note that a theory relating characteristic cluster size and separation with GMR has been proposed by Zhang et al[5]. We find[4] that our data are in reasonable agreement with the theory when it is assumed that interfacial, spin-dependent electron scattering is the predominant scattering mechanism responsible for GMR.

Epitaxial Co-Cu, Co-Ag and Fe-Ag films were grown on (001) NaCl for both GMR and TEM studies. A motivation for this was that (unlike the films on sapphire) films grown on NaCl were rather easily removed for TEM studies. 500Å-thick films of composition $\text{Co}_{0.15}\text{Cu}_{0.85}$ and $\text{Co}_{0.21}\text{Ag}_{0.79}$ displayed room temperature saturation magnetoresistance values of $\approx 7\%$ and $\approx 21\%$, respectively. Figures 2(a) and (b) show the 4.2K GMR of epitaxial Fe-Ag films (~ 29 atomic % Fe) nucleated on sapphire and on NaCl. Two striking results are evident for this system. The magnitude of the GMR is equivalent for the two growth orientations. Also this system shows substantial anisotropy, the largest we have observed for any phase-segregated system grown by UHV co-evaporation.

We have also examined films of $\text{Ni}_{87}\text{Fe}_{13}$ particles in Ag grown in a (111) orientation. Room- and helium temperature measurements of GMR show 14% and 35% respectively. The addition of $\leq 10\%$ cobalt to the ferromagnet regions results in some reduction of the saturation field (to about 15 kOe) but has little effect on GMR.

Transmission electron microscopy studies have been carried out on the Fe-Ag and Co-Ag films grown onto NaCl substrates. Here we report preliminary results and a full analysis will be reported elsewhere. Figure 3(a) shows a bright-field image from the Fe-Ag film. The mesostructure shows two regions, light and dark grey with some internal structure. The light regions are Fe-rich with about 10 at% Ag and are preferentially thinned during TEM sample preparation. The grey region is Ag-rich and contains about 25% Fe. In some regions there are pure Ag particles. The internal structure seen in the grey region (Figure 3(a)) actually arises from Ag twins formed during the growth of the film. The electron diffraction pattern from the light regions do not show any additional reflections. This indicates that bcc Fe is formed with (001) parallel to Ag(001). In this setting, the bcc spots replicate the Ag(001) spots. This assertion is under further investigation to examine the nature of the microstructure from the Fe-rich region.

Figures 3 (b) and (c) show selected-area diffraction patterns from the grey region of the mesostructure. In (b) the electron beam is along the film normal i.e. Ag[001]. In (c) the beam is close to the [112] direction of the Ag-rich grey region. One can see extra spots (indicated) due to Ag twins. There are 4 variants of the (111)

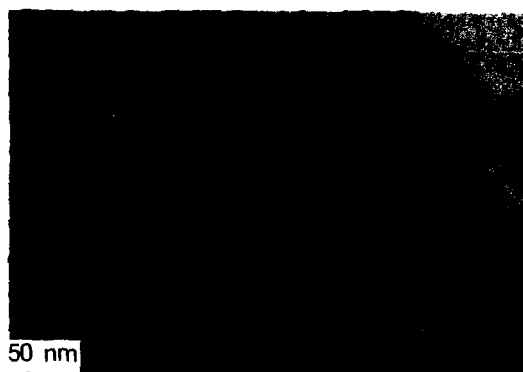


Figure 3(a). TFM bright-field image of an $\sim 500\text{\AA}$ -thick film of (001) $\text{Fe}_{0.29}\text{Ag}_{0.71}$ after removal from the NaCl substrate and removal of the Pt overlayer by ion milling.



Figure 3(b). Transmission electron diffraction pattern from the film with the beam along the film normal i.e. along Ag[001]. Ag(200) indicated.



Figure 3(c). Transmission electron diffraction pattern with the beam tilted about 8° away from the normal. [110] tilt axis. Additional features (indicated) are seen near the Ag(200) spot.

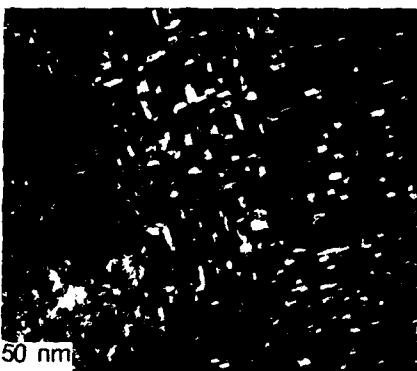


Figure 3(d). Dark-field image formed using the two additional spots near Ag(200). Here, the image reveals precipitates with their boundaries close to Ag(110) or (110) planes.

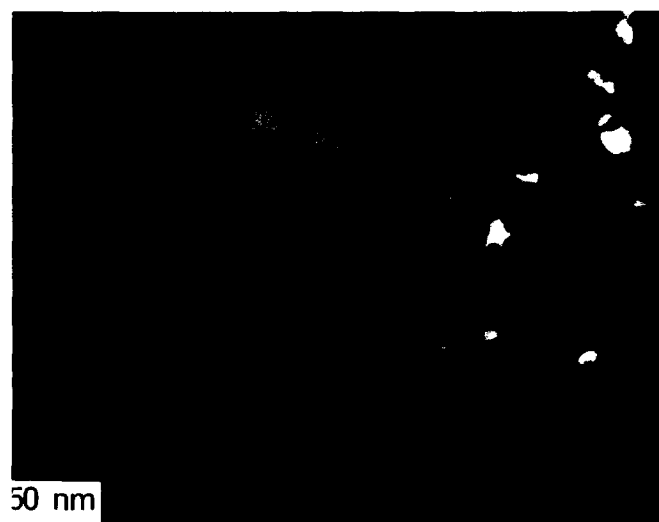


Figure 4(a). Bright-field image of an $\approx 500\text{\AA}$ -thick film of (001) $\text{Co}_{0.21}\text{Ag}_{0.79}$ after removal from the NaCl substrate and removal of the Pt overlayer by ion milling.

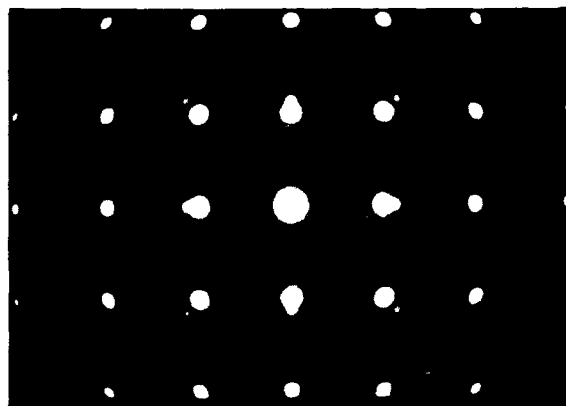


Figure 4(b) shows the corresponding transmission electron diffraction pattern. The pattern is a superposition of patterns from fcc Co(001) and fcc Ag(001), with Co (100) parallel to Ag (100) i.e. no relative rotation of the two unit cells. The splitting of the (220)-type spots is clearly seen, confirming phase separation.

twins of Ag present in the film, which is typical of fcc metal films grown on rocksalt. The dark-field image shown in Figure 3(d) is formed using these spots and orthogonal orientations of twins, each consisting of two variants, are present.

Figure 4(a) shows a bright-field image of a ≈ 500 Å-thick film of (001) $\text{Co}_{0.21}\text{Ag}_{0.79}$ after removal from the NaCl substrate and removal of the Pt overlayer by ion milling. The mesostructure is quite similar to the Fe-Ag film. The light regions are Co-rich and the grey regions are Ag-rich with 10-15 at% Co. The structure in the grey region also shows the growth twins observed for the Fe-Ag film. The electron diffraction pattern from the film (Figure 4(b)) shows that the Co is stabilized in the fcc form. The pattern is a superposition of patterns from fcc Co (001) and fcc Ag(001), with Co(100) parallel to Ag(100). Splitting of the (220)-type reflections confirms phase separation.

4. CONCLUSIONS

GMR, as a function of Co concentration has been studied in a series of crystalline epitaxial structures. Large values of GMR are reported for the as-grown films. For Co-Cu films deposited at 80°C, the GMR increased with subsequent annealing, as for sputtered films.

GISAXS studies of Co-Cu films have given a characteristic size and separation of Co clusters. A relationship between cluster size and GMR has been observed. For example, with progressive annealing, the Co cluster diameter increased from ~ 20 Å to ~ 250 Å with a concomitant drop in the 4.2K GMR from $\sim 35\%$ to 1%.

The best fit of these data to phenomenological theory indicates that interfacial spin dependent electron scattering is the predominant scattering mechanism affecting the GMR for cluster diameters up to ~ 250 Å.

Magnetic anisotropy in Co-Cu, Co-Ag and Fe-Ag alloys is discussed and preliminary TEM studies of the Fe-Ag and Co-Ag films are described.

ACKNOWLEDGEMENTS

This work was partially supported by the Director, Office of Energy Research, Office of Basic Energy Sciences, Materials Sciences Division of the US Department of Energy under Contract No. DE-AC03-76SF00098.

REFERENCES

1. A.E. Berkowitz, J.R. Mitchell, M.J. Carey, A.P. Young, S. Zhang, F.E. Spada, F.T. Parker, A. Hutten and G. Thomas, Phys. Rev. Lett. **68**, 3745 (1992).
2. (a) J.Q. Xiao, J.S. Jiang and C.L. Chien, Phys. Rev. Lett., **69**, (1992).
(b) J. Samuel Jiang, John Q. Xiao and C.L. Chien, in "Magnetism and Structure in Systems of Reduced Dimension". NATO ASI Series, Plenum Publishing Corporation, New York (1993).
3. S.S.P. Parkin, R.F.C. Farrow, T.A. Rabedeau, R.F. Marks, G.R. Harp, Q. Lam, C. Chappert, M.F. Toney, R. Savoy and R. Geiss, Europhys. Lett. accepted, (1993).
4. T.A. Rabedeau, M.F. Toney, R.F. Marks, S.S.P. Parkin, R.F.C. Farrow and G.R. Harp, (preprint) (1993).
5. (a) S. Zhang, Appl. Phys. Lett., **61**, 1855 (1992).
(b) S. Zhang and P.M. Levy, J. Appl. Phys. (in press).
6. R.F.C. Farrow, G.R. Harp, R.F. Marks, T.A. Rabedeau, M.F. Toney, R. Savoy, D. Weller and S.S.P. Parkin, J. Crystal Growth, submitted (1993).

GIANT MAGNETORESISTANCE IN SINGLE LAYER AND MULTILAYER PHASE SEPARATING ALLOY FILMS

S. HOSSAIN*, A. WAKNIS**, D. SEALE*, M. TAN**, M.R. PARKER*, and J.A. BARNARD**

The University of Alabama, *Department of Electrical Engineering and **Department of Metallurgical and Materials Engineering, Tuscaloosa, AL 35487-0202

ABSTRACT

The phenomenon of giant magnetoresistance (GMR), previously measured only in multilayer films comprising ferromagnetic layers separated by nonmagnetic spacers, has recently been observed in single layer 'granular' alloy thin films prepared by co-sputtering a ferromagnet and a nonmagnet which tend to phase separate (cluster) under equilibrium conditions. We have systematically studied the magnetoresistance of two new phase separating GMR systems ($\text{Ni}_{66}\text{Fe}_{16}\text{Co}_{18}\text{-Ag}$ and $\text{Co}_{90}\text{Fe}_{10}\text{-Ag}$) both of which exhibit large room temperature GMR (>11% and >14%, respectively). We have also attempted to influence the details of the field dependence of the magnetoresistance in the previously studied Co-Ag system by employing novel processing methods including interrupted sputtering and layering of the Co-Ag alloy with Cu spacers.

1. INTRODUCTION

In the last year, remarkably large GMR ratios have been unexpectedly observed (both in our lab [1-3] and elsewhere [e.g., 4-6]) in *single layer films* variously described as 'granular', 'metastable alloys', and 'heterogeneous', but which are, in every case so far reported, prepared by co-sputtering a ferromagnet and a nonmagnet which phase separate (cluster) under equilibrium conditions (e.g., Co-Cu, Co-Ag). Single layer GMR is apparently restricted to those alloy systems which exhibit extremely small mutual solid solubilities at equilibrium. The occurrence of GMR is associated with a microstructure which can be crudely described as consisting of very small ferromagnetic clusters in a 'nonmagnetic' matrix. There is evidence[1,2], however, that a rapid quench process such as sputtering can suppress complete phase separation leaving the matrix in a supersaturated metastable solid solution alloy state. Based on the condition that only strongly phase separating metal-metal systems containing a ferromagnet will exhibit GMR, a very limited number of binary systems are available for study. We have reviewed the equilibrium binary temperature - composition phase diagrams containing Co, Fe, and Ni and have found that Ag, Au, and Cu are the only elements yielding immiscible binary phase diagrams (Cu-Ni is an exception). It is also interesting to examine the possibility of alloying the magnetic components, i.e., Co-Fe, Co-Ni, and Fe-Ni. Co-Fe and Co-Ni are both miscible systems while Fe and Ni are completely miscible at high temperature but exhibit compound formation (FeNi_3) at lower temperatures. In Fig. 1 the characteristics of the binary phase diagrams of interest in single layer GMR are summarized.

Both the magnitude of the magnetoresistance ratio and the details of the magnetic field dependence of the resistivity in single layer GMR materials are extremely sensitive to 'metallurgical' factors (composition, annealing treatments, growth parameters, microstructural features, texture, etc.). These factors influence the size distribution, shape, number density, and relative orientation of the ferromagnetic clusters, the composition of the matrix, as well as the nature of the interface between the clusters and the matrix. Here we survey our recent experimental results on GMR in new materials systems and report on the effects of novel processing of 'granular' GMR alloy systems.

	Co	Fe	Ni	Ag	Au
Ag	I	I	I		
Au	I	I	I	M	
Cu	I	I	M	E	C
Co		M	M		
Fe			C		

I - immiscible
M - completely miscible
C - compounds
E - eutectic

Figure 1. Characteristics of the temperature-composition binary phase diagrams of interest in single layer GMR.

2. EXPERIMENTAL METHODS AND MATERIALS

All of the films discussed below were grown on Corning 7059 glass or thermally oxidized Si wafers at ambient temperature by dc magnetron sputtering (Vac-Tec Model 250 Sputtering System). Magnetic properties were measured with a Digital Measurement Systems VSM Model 880. Composition was determined with a JEOL 8600 Electron Probe Microanalyser. X-ray diffraction (XRD) was performed on a Rigaku D/Max-2BX XRD System. MR measurements were made by 4-point probe with both current and field in the film plane but perpendicular to each other. All measurements were made at room temperature. To obtain a broad range of compositions under identical conditions a split target assembly described in detail elsewhere[1] was used in making all of the alloy systems discussed.

3. EXPERIMENTAL RESULTS

3.1. New materials systems: $\text{Ni}_{66}\text{Fe}_{16}\text{Co}_{18}\text{-Ag}$ and $\text{Co}_{90}\text{Fe}_{10}\text{-Ag}$

The soft magnetic alloy permalloy-Co has recently yielded promising GMR properties in the multilayer geometry[7]. It thus seemed sensible to explore the use of this alloy in a granular format. $\text{Ni}_{66}\text{Fe}_{16}\text{Co}_{18}\text{-Ag}$ alloy films were prepared over a broad range of Ag compositions (the Ni/Fe/Co ratio is fixed) and sputtering conditions. This system yields comparatively large room temperature MR ratios which are sensitive to annealing at modest temperatures. In Fig. 2 the MR ratio versus magnetic field for as-deposited and annealed films with Ag content of 64 a/o is plotted. The increase in the magnitude of the MR ratio with post-deposition annealing may be the result of both Co clusters approaching an optimal size and an overall decrease in film resistivity presumably due to elimination of defects and diffusion of Co remaining in the essentially Ag matrix to the Co clusters. The sharpening of the field dependence of the MR ratio is most logically related to larger, more easily saturated Co clusters which have grown on annealing. Note that the films are far from saturation in the modest fields available in our lab. The difficulty in saturating granular GMR films is a generic but not well understood feature of these materials. In an extreme case 20T was found insufficient in the Co-Au system[8]. In the insert of Fig. 2 the compositional dependence of the MR ratio in this system is plotted. Again, the films are not fully saturated. The peak in the MR ratio near 65 a/o non-magnetic matrix element has also been observed in as-deposited Co-Ag[1] and may be most

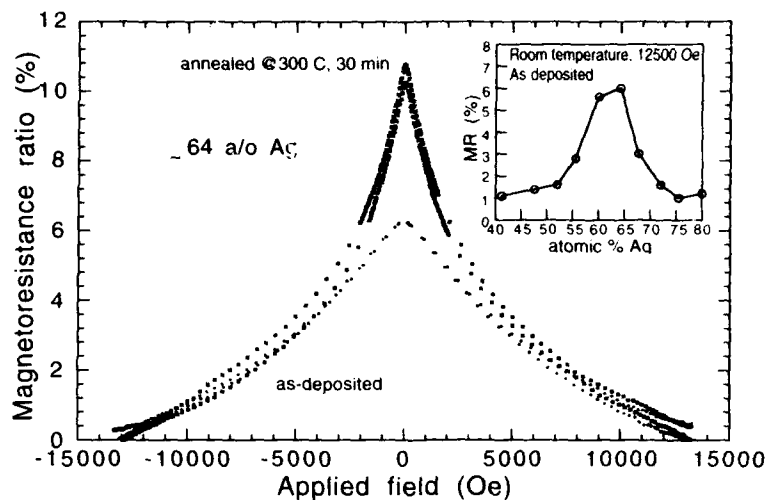


Figure 2. Magnetoresistance in granular $\text{Ni}_{66}\text{Fe}_{16}\text{Co}_{18}\text{-Ag}$ films.

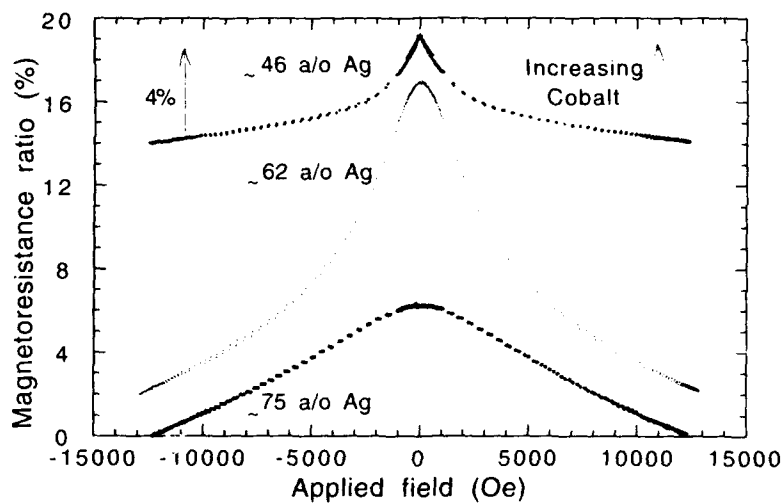


Figure 3. Magnetoresistance in granular $\text{Co}_{90}\text{Fe}_{10}\text{-Ag}$ films.

logically related to a type of percolation limit, $\text{Co}_{90}\text{Fe}_{10}$ has also received recent attention in the multilayer format[9]. $\text{Co}_{90}\text{Fe}_{10}\text{-Ag}$ alloy films were prepared, once again, over a broad range of Ag compositions and sputtering conditions. Very large room temperature ratios were found in this system. Representative MR loops as a function of composition are plotted in Fig. 3 for as deposited samples.

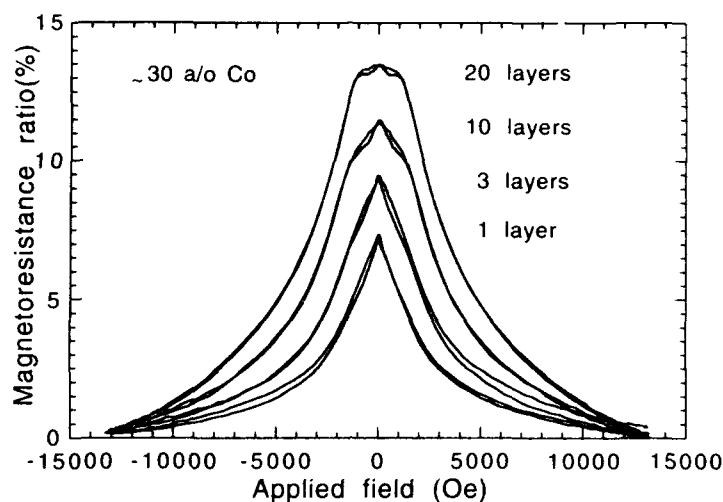


Figure 4. Magnetoresistance of 'layered' Co-Ag granular films prepared by interrupted sputtering (see text)

As the proportion of the ferromagnetic component increases so should the average cluster diameter (for similar growth conditions). This is reflected in the shape of the MR loops. Small clusters at relatively low number densities yield a broad, difficult to saturate MR plot. As the proportion of ferromagnet increases an optimum cluster size and spacing is reached which gives a maximum MR ratio. At even higher concentrations the magnitude of the MR ratio is reduced although the peak is comparatively sharp due to the presence of more easily saturated larger clusters. The precise position of the maximum in the MR ratio as a function of composition is likely to depend somewhat on the maximum field at which the measurements were made. The general trend, however, should remain. The structural features of both of the new systems are similar to those found previously for Co-Ag[1,2]. These films are nanocrystalline and exhibit strong (111) crystallographic growth texture. A systematic change in the lattice parameter is observed which is consistent with metastable solid solution behavior.

3.2. The Effect of 'Layering' on Co-Ag Granular Films

The largest MR ratios found in granular films have been in the Co-Ag system (~28% at room temperature for $\text{Co}_{38}\text{Ag}_{62}$ [2]). In order to try to reduce the field required to saturate the samples (i.e., to increase the MR sensitivity) by influencing the cluster shape a growth method involving pseudo-layering by systematically interrupted sputtering has been undertaken in this alloy system. Six samples were grown with a total thickness of ~1200Å. Each sample, however, was 'layered' by pausing the sputtering periodically for ~5 seconds. In this way samples with $N = 1, 2, 3, 5, 10$, and 20 'layers' were prepared. The thickness of each 'layer' is given by $1200\text{Å}/N$. All other conditions are identical (e.g., sputtering parameters, composition). A remarkable effect on the MR loops has been observed and plotted in Fig. 4 for a representative composition of ~30 a/o Co. Quite clearly GMR is systematically enhanced by this specialized growth method, i.e., the MR ratio increases with the number of 'layers' (which is, of course, inversely related to 'layer' thickness). However, the MR sensitivity

declines with increasing N . The thinner layers also exhibit a low field structure in their MR loops which may be related to the presence of perpendicular anisotropy. There is no evidence of anisotropic magnetoresistance. Pausing the sputtering may allow time for surface rearrangements to occur by surface diffusion while also lowering the average substrate temperature in comparison with continuous growth. Although no direct evidence for contamination during the pause has been found, it cannot be ruled out. The details of the structure and growth mode of these films are under investigation. Preliminary studies show no substantial difference in XRD patterns with increasing layer number.

3.3 Co-Ag Granular Films Layered with Cu

In order to more directly influence the Co cluster shape and to explore very thin granular layers, a set of periodic multilayer films of the form $(20\text{\AA Co-Ag granular alloy}/17\text{\AA Cu})_{x10}$ were grown with variable Co-Ag composition. Representative MR loops from this experiment (as-deposited films) are plotted in Fig. 5. Unlike single layer Co-Ag films[2] which exhibit an onset of coercivity for films with $> \sim 30$ a/o Co, these MR loops indicate no appreciable coercivity in the composition range studied (~ 30 -55 a/o Co in the Co-Ag alloy layers) even for the most Co-rich sample (the uppermost curve). A gradual increase in both the magnitude of the MR ratio and the sharpness of the field response (as measured by the change in MR % per 1000 Oe in the linear portion of the curve which increases from 0.21 to 3.20) is noted. The low field MR sensitivity of the most Co-rich sample is better than that previously reported in as-deposited single layer Co-Ag films[1]. It should be pointed out that part of the MR effect is lost in this system because of the shunting of current through the Cu spacer. However, this effect may be reduced by using a Cu spacer of optimum thickness or by choosing a better spacer material. Although this granular alloy has been placed in a 'layered' geometry, there is no evidence that conventional multilayer GMR is contributing to the observed behavior.

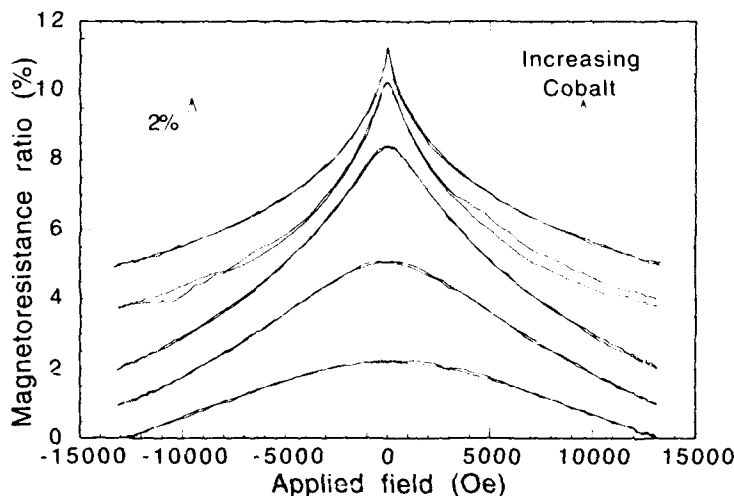


Figure 5. Magnetoresistance in Co-Ag/Cu multilayers $(20\text{\AA Co-granular alloy}/17\text{\AA Cu})_{x10}$.

4. CONCLUSIONS

GMR in single layers appears to be restricted to those alloy systems which exhibit extremely small mutual solid solubilities. We have identified and reported on two new granular GMR systems, $\text{Ni}_{66}\text{Fe}_{16}\text{Co}_{18}\text{-Ag}$ and $\text{Co}_{90}\text{Fe}_{10}\text{-Ag}$ whose ferromagnetic components are immiscible in Ag at equilibrium. New growth methods including pseudo-layering of Co-Ag alloy by interrupted sputtering and growth of Co-Ag/Cu multilayers have been studied. Pseudo-layering of Co-Ag dramatically increases the magnitude of the MR but does not improve field sensitivity. Co-Ag/Cu multilayers do exhibit increased MR sensitivity in the low field regime (<1000 Oe) when compared with single layer Co-Ag[1]. Clearly, novel processing which influences the ferromagnetic cluster size, shape, and distribution in granular materials can dramatically affect the field dependence of the magnetoresistance.

ACKNOWLEDGEMENTS

Acknowledgement is made to the National Science Foundation (grants DMR-8918403 and DMR-9157402), the National Storage Industry Consortium Advanced Technology Program, and the MINT Center at The University of Alabama for support of this research.

References

- [1] J.A. Barnard, A. Waknis, M. Tan, E. Haftek, M.R. Parker, and M.L. Watson, J. Mag. Mat. **114**, L230 (1992).
- [2] J.A. Barnard, S. Hossain, M.R. Parker, A. Waknis, and M.L. Watson, J. Appl. Phys., in press.
- [3] M.L. Watson, J.A. Barnard, S. Hossain, and M.R. Parker, J. Appl. Phys., in press.
- [4] A.E. Berkowitz, J.R. Mitchell, M.J. Carey, A.P. Young, S. Zhang, F.E. Spada, F.T. Parker, A. Hutten, and G. Thomas, Phys. Rev. Lett. **68**, 3745 (1992).
- [5] J.Q. Xiao, J.S. Jiang, and C.L. Chien, Phys. Rev. Lett. **68**, 3749 (1992).
- [6] J.S. Jiang, J.Q. Xiao, and C.L. Chien, Appl. Phys. Lett. **61**, 2362 (1992).
- [7] M. Jimbo, T. Kanda, S. Goto, S. Tsunashima, and S. Uchiyama, Jpn. J. Appl. Phys. **31**, L1348 (1992).
- [8] J.A. Barnard, M.R. Parker, D. Seale, and J. Yang, submitted IEEE TRANS. MAG.
- [9] Y. Saito and K. Inomata, Jpn. J. Appl. Phys. **30**, L1333 (1991).

A Microstructural Study of Iron Carbides Formed by Plasma-Enhanced Chemical Vapor Deposition (50-800 nm thick)

H. Siriwardane,* W.J. James,* O.A. Pringle* and J.W. Newkirk†

*Departments of *Physics, *Chemistry, and †Metallurgical Engineering and the *Graduate Center for Materials Research, University of Missouri-Rolla, Rolla, MO 65401 (U.S.A.)*

Thin mirror-like iron carbide films were prepared by introducing iron pentacarbonyl $[\text{Fe}(\text{CO})_5]$ and hydrogen $[\text{H}_2]$ into a glow discharge. The deposition temperatures were varied from 200-500°C. The iron to carbon ratios of the resulting films were controlled by adjusting the gas flow ratios. The microstructure and phase transformations occurring in these films were studied before and after annealing at 400°C for four hrs. Characterization techniques used included x-ray diffraction, electron diffraction, Auger spectroscopy and atomic force microscopy.

X-ray diffraction data of plasma-deposited films on glass substrates maintained at 400°C showed the presence of only Fe_3C . However, the x-ray diffraction data of films on carbon coated glass, and transmission electron microscopy selected area diffraction patterns of films on carbon coated copper grids indicated the presence of a second phase, the closely related metastable Fe_7C_3 , as well as small amounts of Fe_3O_4 . Atomic force microscopy of crystallites on the surface of films deposited at 400°C and annealed at 400°C for four hours revealed a periodic structure of oblate spheroids. The measured spacings and angle, when compared to projected models of high reticular density planes, suggested the surface to have a structure corresponding to that of bulk Fe_3C or Fe_7C_3 . However the data were not of sufficient quality to unambiguously determine such.

1. INTRODUCTION

Thin iron-carbide films of Fe_7C_3 and Fe_3C are readily deposited in a cold plasma by introducing the vapor of iron pentacarbonyl and H_2 into a glow discharge.^{1,2} Possible applications of these films are in wear and corrosion resistant coatings, and magnetic storage.³ The conventional bulk forms of these phases are produced at pressures of thousands of atmospheres and temperatures of thousands of degrees centigrade.⁴ On the other hand, the plasma-formed analogues are produced at low temperatures and low pressures, typically 200°-400°C and 50-100 milli Torr. To exploit the potential uses of plasma deposited films, it is necessary to understand how the film microstructure, atomic structure, and magnetic structure relate to its properties. The aim of the present study is to understand the microstructure of these Plasma Enhanced Chemical Vapor Deposited (PECVD) films.

2. EXPERIMENTAL

The Fe_7C_3 and Fe_3C films were prepared by introducing iron pentacarbonyl $[\text{Fe}(\text{CO})_5]$, and H_2 vapor into an inductively coupled glow discharge tubular reactor. The reactor system was the same as that used by Lin et al.⁵ The starting materials were, iron pentacarbonyl from the Alpha division of Morton Thiokol Inc., and H_2 from the Matheson Gas Group Inc.. Iron pentacarbonyl was degassed prior to use. Films discussed in this paper were grown on microscope glass slides, carbon coated glass, and carbon coated copper grids, at elevated temperatures (200-500°C). Substrates were put on a heater plate which was located in the reactor with its leading edge 2 cm from the vapor inlet. The distance from the vapor inlet to the leading edge of the substrate was approximately 5 cm. Iron pentacarbonyl vapor and

H₂ gas were introduced into the reactor simultaneously, by carefully adjusting metering valves to the desired flow rates. Films were deposited using pre-determined gas flow rates, substrate temperatures, substrate locations, and rf power.⁶

Films deposited on the above mentioned substrates at different temperatures, and their in-situ annealed counterparts were collected, and their microstructures were characterized. The annealing temperature and time were 400°C and 4 hrs. respectively. Film compositions were analyzed by Auger electron spectroscopy (AES). The microstructure and crystallinity of the films were analyzed by transmission electron microscopy (TEM), scanning electron microscopy (SEM), atomic force microscopy (AFM), and x-ray diffraction (XRD).

3. RESULTS AND DISCUSSION

3.1 TEM, AES and XRD Characterization.

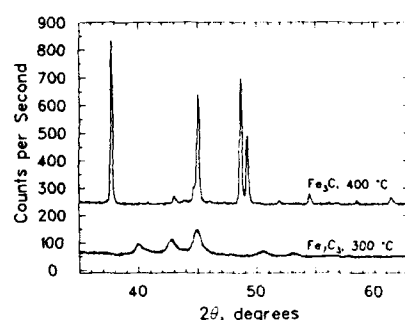


Figure 1. XRD patterns of iron carbide films deposited on glass substrates at 300° & 400°C.

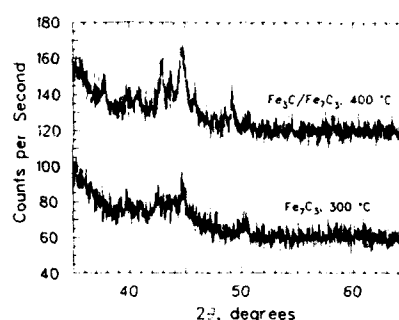


Figure 2. XRD patterns of iron carbide films deposited on carbon coated glass substrates.

The XRD patterns from PECVD iron carbide films grown on glass substrates evidenced single phases of Fe₇C₃ and Fe₃C at substrate temperatures of 300° and 400°C, respectively (see Fig. 1). The XRD of films grown on carbon coated glass showed the presence of Fe₇C₃ at 300°C, and both Fe₇C₃ and Fe₃C at 400°C (see Fig. 2). The presence of a carbide phase in these films was confirmed by the AES C1s carbon satellite peaks. The presence of the carbon-rich metastable Fe₇C₃ deposited at 400°C on carbon coated glass (not evidenced on glass at the same deposition temperature) probably results from the carbon provided by the carbon support film on the copper grids. The annealed films, deposited under identical experimental conditions showed the same phases as their un-annealed counterparts. The only noticeable effect of annealing was a decrease in the line widths of the x-ray spectra, due to grain growth and stress release.⁶ The grain growth of these films was also observed by SEM, TEM and AFM. The SEM micrographs shown in Figure 3 clearly indicate grain growth due to annealing. The TEM samples were prepared using the same plasma operating parameters as the films grown on glass, except they were grown on carbon coated copper grids. Deposition times for these films were only 20-30 minutes in order to obtain films sufficiently thin (~500Å) for examination by TEM. Selected area diffraction (SAD) patterns (see Figure 4) of these films showed the presence of both Fe₃C and Fe₇C₃ at substrate temperatures of both 300° and 400°C in accord with the XRD results obtained from the carbon coated glass substrates. The presence of some Fe₃O₄ was also seen in the SAD patterns. The AES data (obtained from the films deposited on glass and carbon coated grids) showed the amount of oxygen present in these films to be less than one atomic % after two

minutes of sputtering at 35 Å/min. This indicates that the amount of Fe_3O_4 present in these films is small. The in-situ annealed grid samples evidenced spottier diffraction rings, once again indicating the presence of larger grains in the annealed samples.⁶

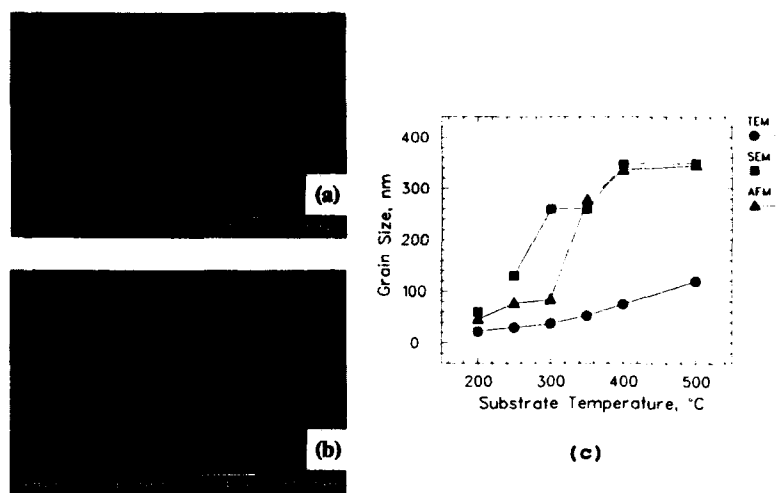


Figure 3. (a) A SEM micrograph of a PECVD Fe_7C_3 film before annealing. (b) A SEM micrograph of 3(a) after annealing at 400°C for 4 hrs. (c) The grain size of carbide films as a function of substrate temperature.



Figure 4. A TEM micrograph and its SAD pattern of (a) a film deposited at 300°C, (b) a film deposited at 400°C. The substrates were carbon coated copper grids.

3.2 AFM Characterization.

Both un-annealed and annealed films deposited on glass were investigated on an atomic scale using AFM. These films were argon ion etched for 30 minutes in a glow discharge plasma with an input power of 50 W (S.W.R. ~ 1), in order to clean the surface prior to observations. All physisorbed contaminants (CO_2 , H_2O) on the surface of these films were expected to sputter away during this process. When observed in the AFM, none of these films showed periodicities on an atomic scale. These films gave pronounced XRD peaks as

shown in Figure 1, indicating their bulk to be well ordered. This indicates that either the surfaces of PECVD iron carbide films were not ordered enough to see their periodicities by the AFM, or else the nanocrystalline size grains could be the reason for not seeing the periodicities in the AFM. The measured grain sizes of the PECVD iron carbide films, as a function of substrate temperature, are shown in Figure 3c. The grains may be too small for the AFM tip to focus on and scan a sufficient area before it sees the effects of the surrounding grains. Upon annealing these films, the grain size increased and the surface became more ordered, providing larger grains for the AFM study.^{7,8,9}

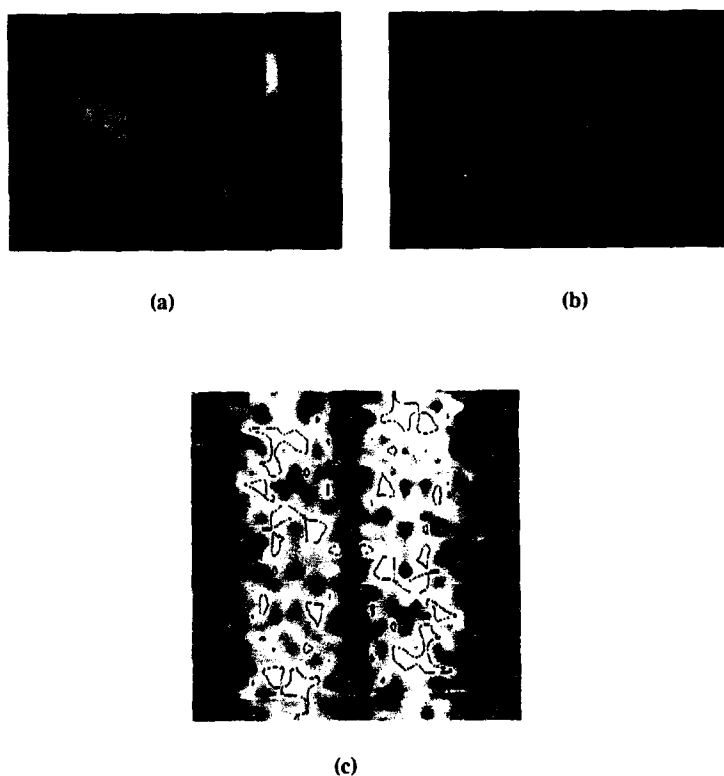


Figure 5. (a) An AFM image of a PECVD carbide film deposited at 400°C and annealed at 400°C for 4 hrs. (b) A 3D AFM image of Fig. 5a, at a higher magnification. (c) A Fourier spectrum of image 5b.

An AFM micrograph of an annealed film is shown in Figure 5a, and its 3D image after filtering its high frequencies is shown in Figure 5b. The observed periodicities in these images, at an atomic scale level remained fixed at different magnifications, which led us to further pursue investigations of these data. Knowing that the AFM system is capable of producing false structure on images due to time-domain instabilities of the microscope and its environment and also due to the scan tip, it was decided that these images should be analyzed more carefully.

Direct measurements made on the surface structure gave approximate periodicities of 5.5 Å and 6.1 Å, and an interplanar angle of 56°. In order to verify the zone axis, the periodicities of Fe_7C_3 and Fe_3C were modeled¹¹⁻¹³ along the first six highest reticular density planes. The crystal systems for both carbides are orthorhombic.¹⁴ The obtained spacings and interplanar angles along the highest reticular density planes are listed in Table I. Figures 6a and 6b show how the values given in Table I were obtained. The obtained spacings and the angles from modeling did not match well with the measured AFM data, although some data did correspond to the reticular density planes of both Fe_3C and Fe_7C_3 .

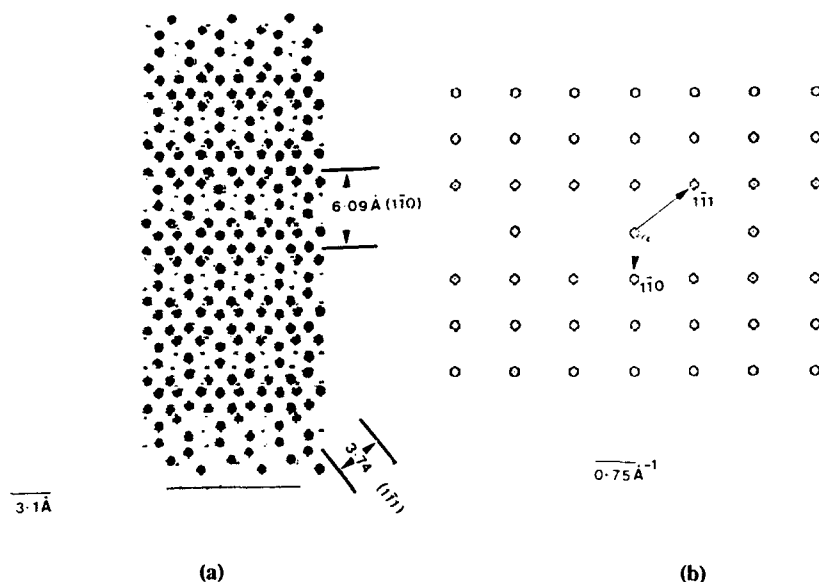


Figure 6. (a) A projection of the bulk structure of Fe_7C_3 along the $\langle 110 \rangle$ zone. (b) A single crystal diffraction pattern of Fig. 6(a).

Table I. The High Reticular density plane spacings & interplanar angles for Fe_7C_3 and Fe_3C .

zone	Fe_7C_3 (d_1, d_2) Å	α	zone	Fe_3C (d_1, d_2) Å	α
$\langle 001 \rangle$	(3.74, 6.09)	127	$\langle 011 \rangle$	(4.06, 3.05)	41
$\langle 011 \rangle$	(4.19, 3.62)	31	$\langle 100 \rangle$	(3.94, 3.35)	54
$\langle 100 \rangle$	(5.94, 3.64)	54	$\langle 111 \rangle$	(4.06, 3.35)	58
$\langle 110 \rangle$	(6.09, 4.33)	101	$\langle 010 \rangle$	(3.35, 2.68)	36
$\langle 111 \rangle$	(6.09, 3.44)	31	$\langle 021 \rangle$	(2.79, 2.39)	32
$\langle 101 \rangle$	(6.38, 3.62)	35	$\langle 211 \rangle$	(4.06, 3.01)	77

Since a mixture of phases was observed in the TEM specimens, an attempt was made to match the obtained spacings and the angle with any of the possible phases. This was done by using a crystallographic matching program "SX."^{11,12} The spacings obtained by AFM did not match well with any of the phases known to exist in these films.

It was then decided to determine the spacings from the Fourier spectrum of the AFM micrographs. A Fourier spectrum obtained from an image similar to Figure 5b is shown in Figure 5c. Every combination of spacings and angles obtained from the peaks in the Fourier spectrum were compared to the modeled data in Table I, and were re-examined using the "SX" program. On the basis of the measured spacings and the angles, when compared to the projected models of high reticular density planes, we were unable to unambiguously determine the surface structure of the carbide films. This could be a direct result of the time-domain instabilities of the microscope and its environment and the tip structure which we generally refer to as "tip noise" dominating over the structure of the PECVD films.¹⁰

4. CONCLUSIONS

X-ray diffraction data of plasma-deposited films on glass substrates deposited at 300°C and 400°C showed the presence of only Fe_3C and Fe_7C_3 respectively. However, XRD data obtained on films on carbon coated glass substrates at 400°C indicated the presence of Fe_7C_3 and Fe_3C . The TEM SAD patterns of films deposited on carbon coated copper grids at 300°C and 400°C indicated the presence of a mixture of metastable Fe_7C_3 , Fe_3C and a small amounts of Fe_3O_4 . These results indicate that, at high substrate temperatures carbon containing substrates favor the deposition of the metastable Fe_7C_3 over Fe_3C .

Atomic force microscopy of a single crystallite on the surface of a film deposited at 400°C and annealed at 400°C for 4 hours revealed a periodic structure of oblate spheroids. The measured spacings and angle, when compared to projected models of high reticular density planes, suggested the surface to have a structure corresponding to either that of bulk Fe_3C or Fe_7C_3 . However the large contributions of noise to the AFM Fourier spectrum resulted in data, which were not of sufficient quality to unambiguously determine the surface structure of the carbide films.

REFERENCES

1. J. L. Li, T. J. O'Keefe and W. J. James, *Mat. Sci. Eng.* **B7**, 15-23 (1990); **B7**, 5-13 (1990).
2. H. Siriwardane, W. J. James, O. A. Pringle and J. Newkirk (to be published in Scripta Met.).
3. P. J. Grundy, *J. Magn. Magn. Mater.* **21**, 1 (1980).
4. A. A. Putyatin, *Sverkhtrudye Materialy* **12**, 22-29 (1990).
5. T. J. Lin, T. J. O'Keefe and W. J. James, *Mat. Sci. Eng.* **B5**, 359-370 (1990).
6. H. Siriwardane, J. Newkirk, W. J. James and O.A. Pringle (to be published in Thin Solid Films).
7. B. A. Movchan and A. V. Demchishin, *Fiz. Met. Metalloved.* **28**, 83 (1969).
8. J. A. Thornton, *Ann. Rev. Mat. Soc.* **7**, 239 (1969).
9. C. R. M. Govenor, H. T. G. Hentzell and D. A. Smith, *Acta Metall.* **32**, 773 (1984).
10. H. Siriwardane, P. Fraundorf, L. Fei, W. J. James, J. W. Newkirk and O. A. Pringle accepted for publication in MSA'93 proceedings.
11. A. Bourret, J. Thibault-Desseaux and D. N. Seidman, *J. appl. Phys.* **55**, 825 (1984).
12. P. Fraundorf, *Ultramicroscopy* **22**, 225-230 (1987).
13. T. J. Bernatowicz, "Lattice" - A Crystallography Utilities Program, Washington University, (1989).
14. J.P. Bouchaud, *Ann.Chim.* **2**, 353-365 (1967).

DYNAMICAL SCATTERING OF POLARIZED NEUTRONS BY THIN MAGNETIC FILMS

V. NUNEZ*, C.F. MAJKRZAK AND N.F. BERK
NIST, Gaithersburg, MD 20899.

*and University of Maryland, College Park, MD 20742

ABSTRACT

Using Larmor precession as a clock, Büttiker¹ identified theoretical times for the scattering of particles from an opaque slab coincident with a magnetic field. The subsequent model generated interesting predictions for the influence of opaque regions on the magnetic polarization of the transmitted and reflected beams. Previous attempts to verify these predictions were unable to do so unambiguously². Here, Büttiker's formulae are extended to more general geometries. An experiment has been devised to test the theory by measuring neutron beam polarization in both reflection from and transmission through magnetic films below the critical angle for external reflection.

INTRODUCTION

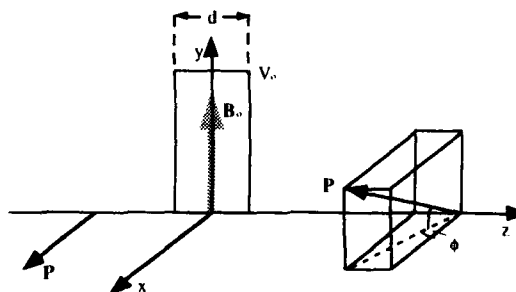
In recent years there has been considerable interest in the notion of tunneling time: the amount of time particles spend in classically inaccessible regions of space. Büttiker introduced the idea of the Larmor clock to determine quantities that he called transmission (traversal), reflection and dwell time. Very little experimental work has been done to verify these controversial ideas. Indeed, only two attempts to produce a Larmor clock have been recorded^{3,4}. However, the theory remains to be verified.

In order to investigate the Larmor clock, there are two aspects to be considered. The first is how the polarization of particles changes as they tunnel through a potential barrier (as shown in Fig. 1), and the second is how this change in polarization is related to time (if at all). Here, we concentrate on the first of these, in particular, the interesting predictions for the influence of opaque regions on the magnetic polarization of the transmitted and reflected beams, and the method for verifying them.

THE LARMOR CLOCK

In the Larmor clock, a particle moves along some axis (z in Fig. 1). The particle has kinetic energy $E = \hbar^2 k^2 / 2m$, spin $S = 1/2$ and is polarized (along x in Fig. 1). The particle interacts with a potential barrier of height $V_0 = \hbar^2 k_0^2 / 2m$ and width d , in which there is a magnetic field, B_0 , directed along y . As the particle tunnels through the barrier its polarization changes. Baz⁵ and Rybachenko⁶ believed this change to be a precession of the polarization around the field direction. They used this precession angle ϕ to define a traversal time τ given by $\phi = \omega_L \tau$.

Fig. 1 Schematic diagram of Büttiker's Larmor clock. Particles move along z with polarization along x . The field in the potential barrier is along y . Polarization of the transmitted particles precesses about the field and also has a component along the field.



However, Büttiker realised that in addition to the precession there would be a component of polarization along the field direction. This can be considered as a rotation of polarization towards the field or as a partial alignment with the field. He then used the three orthogonal components of polarization of the transmitted beam of particles to define 'times' τ_x , τ_y and τ_z in terms of the Larmor frequency ω_L ($\hbar\omega_L = 2\mu_B B$) such that

$$\langle S_z \rangle = -\frac{\hbar}{2} \omega_L \tau_z, \quad \langle S_y \rangle = \frac{\hbar}{2} \omega_L \tau_y, \quad \langle S_x \rangle = \frac{\hbar}{2} (1 - \omega_L^2 \tau_x^2 / 2). \quad (1)$$

Using the above, Büttiker then defined the following process times:

- traversal time, τ_T (reflection time, τ_R) - the time during which a particle interacts with the potential barrier if it is finally transmitted (reflected) through the barrier;
- dwell time, τ_d - the average time during which a particle interacts with the barrier regardless of whether the particle is reflected or transmitted by the barrier.

Subsequently, for an opaque barrier ($k_0 d \gg 1$) he obtained (to first order in k)

$$\begin{aligned} \tau_T = \tau_Y &= \frac{md}{\hbar k_0} \\ \tau_d = \tau_z &= \frac{k \hbar}{\kappa V_0} = \frac{\hbar}{V_0} \sqrt{\frac{E}{V_0}} \\ \tau_x &= \sqrt{\tau_y^2 + \tau_z^2} \end{aligned} \quad (2)$$

Attempts to verify the theory have been inconclusive², possibly because they have concentrated on electron tunneling, where theory and experiment are complicated by strong charge-dependent interactions. Büttiker mentioned using neutrons, but to our knowledge, no such experiments have been performed.

NEUTRON TUNNELING

In neutron reflectometry, a beam of particles impinges at grazing incidence on a thin film sample which, in our case, is ferromagnetic. Both the transmitted and reflected beams can be measured and the polarization of the neutrons before and after the sample can be analyzed. For specular scattering, the experimental arrangement can be considered equivalent to a 1-dimensional potential barrier along the direction of the momentum transfer (z in Fig. 2). The barrier is the sum of nuclear and magnetic potentials, where the latter results from the Zeeman interaction of the neutron with the film magnetization. Thus, one may consider a particle moving along z with kinetic energy $E = \hbar^2 q^2 / 2m$ where $q = (\mathbf{k}_i - \mathbf{k}_r) / 2 = k \sin \theta$ is the magnitude of the component of momentum transfer perpendicular to the film (see Fig. 2). The incident particles have polarization P_i and the field \mathbf{B} in the sample is restricted to the plane of the film (x - y plane in Fig. 2).

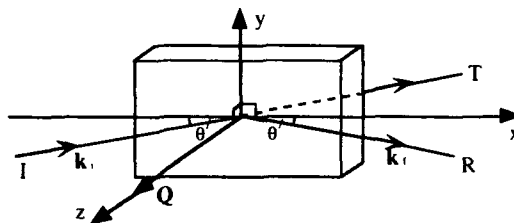


Fig. 2 Schematic diagram of specular scattering, showing the directions of incident, reflected and transmitted neutrons and the vector of momentum transfer \mathbf{Q} for a beam of neutrons incident at some grazing angle θ to a thin film.

Following Büttiker, we treat the scattering as a steady state problem described by the time-independent Schrodinger equation. This is solved using standard transfer matrix techniques which have been generalized to the case of magnetic scattering^{7,8}. Thus, one must solve the equation

$$\begin{bmatrix} T_+ \\ T_- \\ iqT_+ \\ iqT_- \end{bmatrix} = A \begin{bmatrix} I_+ + R_+ \\ I_- + R_- \\ iq(I_+ - R_+) \\ iq(I_- - R_-) \end{bmatrix} \quad (3)$$

where T_{\pm} and R_{\pm} are the transmission and reflection amplitudes for the \pm spin states along the axis of quantization (z) and A is a 4×4 matrix, the elements of which depend on quantities s_1 and s_2 which are related to the refractive indices for the spin states

$$\begin{aligned} s_1 &= (4\pi Nb - q^2 + 4\pi Np)^{1/2} \\ s_2 &= (4\pi Nb - q^2 - 4\pi Np)^{1/2} \end{aligned} \quad (4)$$

where N is the number density of scattering centres per unit volume, b is the average coherent nuclear scattering amplitude and p is the magnetic scattering amplitude ($2\pi\hbar^2 Np/m = -\mu_B|B|$).

To obtain analytical formulae, we replace s_1 and s_2 by the small field approximations

$$s_1 = s_0 + a \quad s_2 = s_0 - a \quad (5)$$

where $s_0^2 = 4\pi Nb - q^2$ and $a = 2\pi Np/s_0$.

In general, the nuclear scattering amplitude b is complex, the imaginary component representing absorption. Consequently, s_0 is also complex. In the absence of absorption, s_0 is purely real below and purely imaginary above the critical angle for reflection.

Note: these approximations require the magnetic scattering amplitude to be small enough that

$$4\pi Np \ll 4\pi Nb - q^2 \quad (6)$$

which prevents one from applying the resulting formulae in the immediate vicinity of the critical angle. (However, we have numerical solutions for all values of the model parameters⁸.)

Using the above, the transmission coefficients T_+ and T_- are calculated, from which the polarization components for the transmitted neutrons are obtained using:

$$P_x = \frac{2\text{Re}(T_+^* T_-)}{|T_+|^2 + |T_-|^2} \quad P_y = \frac{2\text{Im}(T_+^* T_-)}{|T_+|^2 + |T_-|^2} \quad P_z = \frac{|T_+|^2 - |T_-|^2}{|T_+|^2 + |T_-|^2} \quad (7)$$

The polarization components for the reflected neutrons are obtained from similar expressions in terms of the reflection coefficients.

Thus, one finds the compact result

$$P_f = \frac{P_i - c_1 B + c_2 P_i \times B}{1 - c_1 P_i \cdot B} \quad (8)$$

where $P_i = (P_x, P_y, P_z)$, $B = (B_x, B_y, 0)$ and the coefficients c_1 and c_2 are functions of s_0 , d and q . (The coefficients are complicated and cannot be shown here because of space limitations).

Equation (8) is exact to first order in the field (except at the critical angle) and generalizes Büttiker's calculations to arbitrary directions of P_i and B (B in plane of film). Three aspects

should be emphasized:

- (i) if the coefficient c_1 is non-zero, the potential barrier is a transmission polarizer;
- (ii) if the polarization of the incident neutrons is parallel to the field, the polarization will be unchanged upon transmission of neutrons through the barrier;
- (iii) for non-zero c_1 and c_2 , the polarization of the transmitted beam changes in two ways: it has a component in the field direction as well as a component which is the result of precession about the field direction.

Equation (8) gives rise to interesting predictions for the polarization in different limits (some of these are displayed in the appendix), but here we concentrate on the case discussed by Büttiker.

Opaque Limit

In the opaque limit, $s_0 d \gg 1$ (and $q \rightarrow 0$), the polarization of the transmitted neutrons becomes

$$\mathbf{P}_t = \frac{\mathbf{P}_i - c_1 d \mathbf{B} - c_2 q \mathbf{P}_i \times \mathbf{B}}{1 - c_1 d \mathbf{P}_i \cdot \mathbf{B}} \quad (9)$$

where c_1 and c_2 depend only on s_0 ($s_0 \approx \sqrt{4\pi N}b$) and where the surviving d - and q -dependence has been made explicit. In Büttiker's geometry ($\mathbf{B} \parallel y, \mathbf{P}_i \parallel x$)

$$\mathbf{P}_t = \mathbf{P}_i - c_1 d \mathbf{B} - c_2 q \mathbf{P}_i \times \mathbf{B} \quad (10)$$

or, looking at the individual components,

$$\begin{aligned} P_{tx} &= P_{ix} \\ P_{ty} &= -\frac{md}{\hbar s_0} \left(\frac{2\mu_n}{\hbar} \right) B = -\frac{md}{\hbar s_0} \omega_L \\ P_{tz} &= \frac{2qm}{\hbar s_0^2} \left(\frac{2\mu_n}{\hbar} \right) B = \frac{\hbar}{V_0} \sqrt{\frac{E}{V_0}} \omega_L \end{aligned} \quad (11)$$

It follows that P_{ty} and P_{tz} lead to Büttiker's τ_y and τ_z using his prescription, $\tau_j = P_j / \omega_L$ ($j=y, z$). However, his definition of τ_x is inconsistent with the calculated changes in polarization to first order in the field. Note that Büttiker's definition of τ_x was previously criticized by other authors⁹.

Regardless of imposing a Larmor clock interpretation on the polarization of transmitted and reflected beams, the implications of these results are interesting in themselves. In equations (11), the component P_{ty} describes rotation or alignment of the polarization towards the field direction, and depends on the barrier width d . The component P_{tz} describes precession of the polarization about the field and—contrary to classical precession—is independent of the barrier width. As noted in the appendix, classical behaviour is retrieved in the high- q limit where equation (8) becomes equivalent to the gyromagnetic equation. The alignment tendency is arguably an intuitive consequence of Zeeman splitting by the field in the barrier, but the remarkable change in the precession accompanying opacity seems more difficult to rationalize on familiar grounds. Evidently, the non-oscillatory (or 'overdamped') nature of the spatial part of the wave function in an opaque barrier has a profound effect on the response of the beam polarization to the uniform field confined there. Clearly, information is required for the Larmor clock idea which is based on the behaviour of the polarization in the tunneling regime. If measurements were to disagree with equation (8), the fundamental model assumed for the physical system would apparently need re-examination. Below, we describe a method to test these polarization predictions experimentally.

EXPERIMENTAL ARRANGEMENT

The experimental arrangement developed at NIST is described in Fig. 3. The sample is a thin film of an ordered remnant ferromagnet set in a zero field region. The geometry of the sample is such that return fields outside the plane of the sample are negligible. Polarized neutrons are incident at grazing angles to the sample and the reflected and transmitted neutrons are measured. The incident beam can have its polarization set to any required direction and the polarizations of the transmitted and reflected beams are analyzed. From these, the angles of rotation and precession of the polarization can be obtained. To verify equation (8) and the complete numerical predictions, this must be done as a function of incident energy (i.e., by varying the angle of incidence), sample thickness and nuclear potential magnitude.

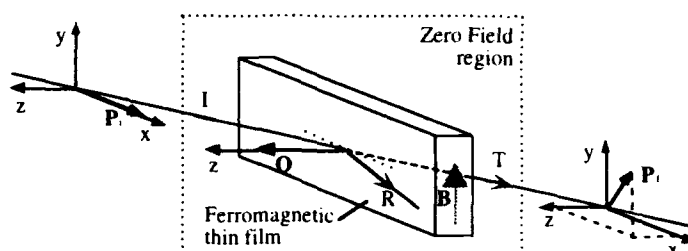


Fig. 3 Schematic diagram of experimental arrangement. The sample is a thin film of remnant ferromagnet placed in a zero-field region. The polarization of the incident neutrons is set to any chosen direction and the polarization of the transmitted neutrons is analyzed.

CONCLUSION

With polarized neutrons it is possible to interpret quantum mechanical tunnelling theory in a relatively uncomplicated formalism from which predictions for polarization vectors of transmitted and reflected neutrons can be made as functions of the barrier potential and field and the incident neutron polarization and energy. Since these predictions are verifiable by experiment, polarized neutrons can be used to test the first part of Büttiker's theory of tunnelling times while avoiding the problematical interpretive layer of time itself. Moreover, as emphasized above, the effects of opacity on polarization are intrinsically interesting. To verify the part which relates these polarization changes to tunneling times, it will be necessary to compare the 'times' calculated from the polarization with direct measurements of the time of passage of neutrons through ferromagnetic samples. Thus polarized neutrons may aid to resolve the controversial issue of tunnelling time and the Larmor clock.

APPENDIX

Kinematic limit

In the high- q limit, the alignment term in equation (8) vanishes, and the transmitted polarization becomes

$$\mathbf{P}_t = \mathbf{P}_i - \frac{2\mu_n}{\hbar} \frac{m}{\hbar q} \mathbf{P}_i \times \mathbf{B} \quad (\text{A1})$$

In this limit, one can consider the neutrons to be travelling with momentum $mv = \hbar q$.

Combining this with (A1) one obtains the gyromagnetic equation for classical precession of the polarization vector in a uniform magnetic field

$$\frac{\partial \mathbf{P}}{\partial t} = (\mathbf{P}_t - \mathbf{P}_i) \frac{v}{d} = -\gamma \mathbf{P}_i \times \mathbf{B} \quad (\text{A2})$$

where $\gamma = \left(\frac{2\mu_B}{\hbar} \right)$.

Reflection

For reflected neutrons, the polarization is given by

$$\mathbf{P}_t = \frac{\mathbf{P}_i + c'_1 \mathbf{B} - c'_2 (\mathbf{P}_i \times \mathbf{B})}{1 + c'_1 \mathbf{P}_i \cdot \mathbf{B}} \quad (\text{A3})$$

where the coefficients c'_1 and c'_2 are not provided here due to space limitations. To first order in q , $c'_1 \approx 0$ so

$$\mathbf{P}_t = \mathbf{P}_i - c'_2 (\mathbf{P}_i \times \mathbf{B}) \quad (\text{A4})$$

This leads to the results of Baz⁵, Rybachenko⁶ and Büttiker for the reflected particles.

Pure absorption

Alloys can be made in which the real part of the nuclear scattering amplitude is zero, leaving only the imaginary component describing absorption. For this special absorption-only case, the polarization of the transmitted neutrons \mathbf{P}_t is given by

$$\mathbf{P}_t = \frac{\mathbf{P}_i - c'_1 d \mathbf{B} - c'_1 d \mathbf{P}_i \times \mathbf{B}}{1 - c'_1 d \mathbf{P}_i \cdot \mathbf{B}}, \quad (\text{A5})$$

where now the polarization precession angle is equal to the rotation angle and the coefficient $c'_1 = ad$, where $a = 2\pi Np/s_0$ and d is the barrier width.

REFERENCES

- 1 M. Büttiker, Phys. Rev. B, **27**, 6178 (1983).
- 2 Eg. see review by R. Landauer, Ber. Bunsenges. Phys. Chem **95**, 404 (1991).
- 3 P. Gueret, A. Baratoff and E. Marclay, Europhys. Lett., **3**, 367 (1987).
- 4 M. Deutch and J.E. Golub, presented at the 1993 APS March Meeting, Seattle, WA, 1993 (unpublished).
- 5 A.I. Baz', Sov. J. Nucl. Phys. **4**, 182 (1967).
- 6 V.F. Rybachenko, Sov. J. Nucl. Phys. **5**, 635 (1966).
- 7 G.P. Felcher, R.O. Hilleke, R.K. Crawford, J. Haumann, R. Kleb and G. Ostrowski, Rev. Sci. Instr. **58**, 609 (1987).
- 8 C.F. Majkrzak and N.F. Berk, Phys. Rev. B **40**, 371 (1989).
- 9 S. Collins, D. Lowe and J.R. Barker, J. Phys. C: Solid State Phys. **20**, 6213 (1987).

STRUCTURAL CHARACTERIZATION OF THIN Co/Cu SUPERLATTICES

DAVID J. SMITH, A.R. MODAK, AND S.S.P. PARKIN*

Center for Solid State Science, Arizona State University, Tempe, AZ 85287

*IBM Almaden Research Center, 650 Harry Rd, San Jose, CA 95120

ABSTRACT

High-resolution electron microscopy has been used to characterize the microstructure of thin Co/Cu metallic multilayers grown on Si(100) substrates by dc magnetron sputtering. The nature of the buffer layer between the silicon wafer and the multilayer had a significant effect on the structural integrity of the multilayer. An increase in grain size was observed as a function of Cu layer thickness, with grain sizes typically being at least 3-4 times the bilayer period. A high degree of structural ordering was observed in superlattices comprised of thicker Cu layers with large grains often spanning the complete multilayer stack. Complementary magnetic measurements enabled the microstructure to be related to the oscillatory exchange coupling and large magnetoresistance exhibited by these thin magnetic films.

INTRODUCTION

Metallic multilayer structures consisting of alternating magnetic and non-magnetic thin films exhibit long-range oscillatory coupling and giant magnetoresistance (GMR) behavior that is intimately related to the occurrence of antiferromagnetic coupling between layers. The GMR effect was first reported in epitaxial, single-crystal Fe/Cr multilayers [1] but it was later also discovered in sputtered, polycrystalline Fe/Cr films [2], and eventually established as a widespread property common to many transition metals [3].

Various theoretical models have been proposed to explain the GMR effect as it relates to these artificially layered structures: better differentiation between (some of) the models is simplified with assistance from electron micrographs that compare microstructural features of the respective thin films. The high-resolution electron microscope (HREM) is nowadays capable of providing atomic-level structural information [4]: it thus represents an excellent tool for characterizing the morphology of magnetic multilayers where layer dimensions and other features of interest approach this scale. In this paper, we describe our recent HREM observations of a variety of Co/Cu metallic superlattices grown on Cu, Fe and Ru buffer layers. Particular attention is given to the relationship between microstructure and magnetic properties, especially the crucial role played by the buffer layers deposited upon the silicon substrate before growth of the multilayer.

EXPERIMENTAL DETAILS

The Co/Cu multilayer samples were deposited on polished and chemically etched Si(100) wafers using a computer-controlled dc magnetron sputtering system having a base pressure of $\sim 2 \times 10^{-9}$ Torr. Samples for electron microscopy were prepared in cross-section in the standard manner [5] by mechanical polishing, dimpling and ionmilling to perforation using 5 keV argon ions with the sample in a liquid-nitrogen milling stage. Electron microscope observations utilized a JEM-4000EX HREM operated at 400 keV. The standard double-tilt specimen holder was used to orient the Si substrate into a [110] projection, with the substrate normal aligned perpendicular to the incident beam direction so that the multilayer stack could be observed in an edge-on configuration. Variations in microstructure as a function of distance from the substrate could then be established. Images were recorded at both the optimum defocus (~ -48 nm), and at a substantial underfocussing condition (~ -200 nm), with typical electron-optical magnifications of 500,000 times. The former defocus provided standard high-resolution micrographs, while the latter defocus enabled better differentiation to be made between the Cu and Co layers. Selected area electron diffraction (SAED) patterns provided details about the extent and development of local texturing in the thin films.

RESULTS AND DISCUSSION

1. Influence of buffer layer.

Our initial electron microscopy observations compared Co/Cu multilayer samples that had 5nm buffer layers of either Fe or Cu interspersed between the Si substrate and the multilayer stack, with the same metals also being used as capping layers[6]. GMR values at room temperature were found to exceed 45% for the Fe buffer but barely reached 20% for the Cu buffer, and later magnetic measurements for an optimised [0.8nm Co/ 0.83nm Cu] multilayer, with Fe buffer layer and Cu capping layer, demonstrated GMR values of greater than 65% at room temperature and 115% at 4.2K. Representative, low-magnification electron micrographs of two Co/Cu multilayers, deliberately underfocussed to heighten contrast differences between the Cu and Co layers, are shown in Fig.1. It is clear that the Cu buffer layer (Fig.1a) has reacted with the Si substrate to depths of greater than 5nm, but there is no indication of any similar reaction for the Fe buffer layer (Fig.1b). Residual diffraction contrast, which is more apparent in low-resolution images and also confirmed in high-resolution lattice images recorded at optimum defocus, suggests the existence of extensive columnar growth extending through several bilayers. It is also interesting to compare the considerable layer buckling that occurs for the Cu buffer layer sample with the comparatively smooth and flat layers observed for the Fe buffer. The disparity in magnetic behavior between these samples has been attributed to these morphological differences that originate from the buffer materials. For example, the layer buckling could result in only partial ferromagnetic alignment of adjacent Co layers, and variations in Cu spacer layer thickness will affect the extent and nature of the magnetic coupling between layers which is known to be very thickness-sensitive [7].

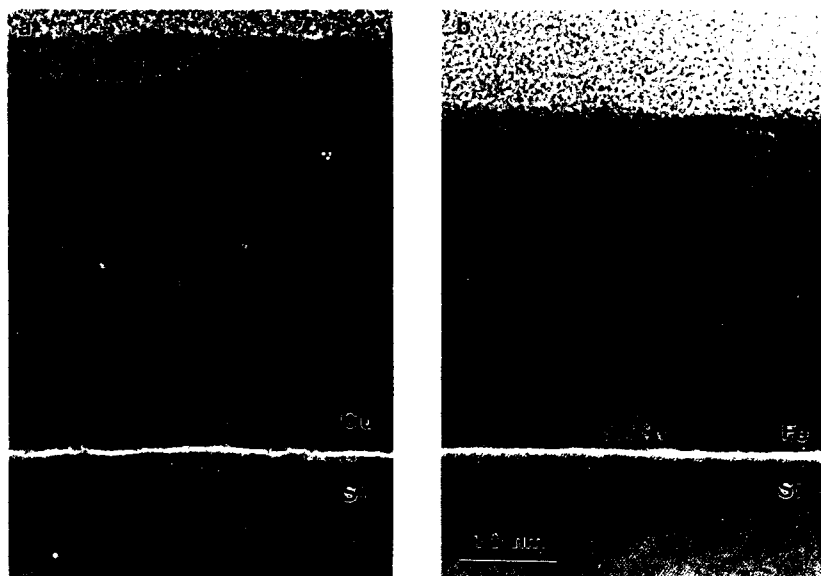


Fig. 1. Cross-sectional electron micrographs of [1.0nm Co/0.9nmCu] multilayers: (a) 5.0nm Cu buffer layer/5.0nm Fe capping layer; (b) 5.0nm Fe buffer layer/5.0nm Cu capping layer. Micrographs recorded at ~ -200 nm to enhance contrast between Co and Cu layers.

2. Effect of Cu layer thickness.

Oscillatory exchange coupling has been observed for Co/Cu multilayers grown on Si substrates as the Cu layer thickness is increased, with an oscillation period of $\sim 1\text{nm}$ [7]. The oscillations dampen out after $\sim 5\text{nm}$ and the related GMR then decays inversely as the Cu spacer layer thickness [8]. We have observed a series of Co/Cu samples with Ru buffer and capping layers, Co magnetic layers of constant 1.0nm thickness, and Cu layer thicknesses varying from 1.0 to 40nm [9]. Compositional contrast was still difficult to achieve in optimum defocus images because of the proximity of Co and Cu in the Periodic Table but images recorded at large underfocus values could again be utilized to provide details of the multilayer topography.

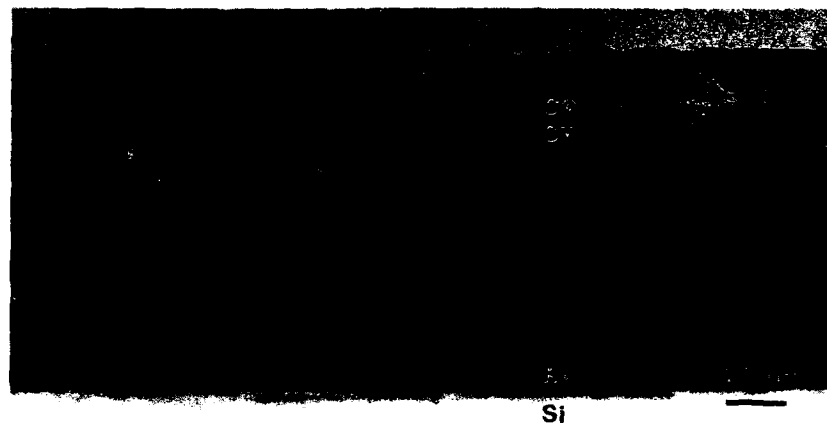


Fig. 2. Cross-sectional electron micrograph of $[1.1\text{nm Co}/17.0\text{nm Cu}]$ multilayer recorded at large underfocus value ($\sim -200\text{nm}$).

As an example, Fig.2 shows an underfocussed image from the sample of nominal structure $\text{Si}(100)/\text{Ru}(5.0\text{nm})[\text{Co}(1.1\text{nm})/\text{Cu}(17.0\text{nm})]_6/\text{Ru}(1.5\text{nm})$. The positions of the Co magnetic layers within the Cu spacer layers are easily discerned on the basis of contrast differences that are accentuated by Fresnel diffraction effects. The "waviness" of the Fresnel fringes, which increases further away from the substrate, serves as an indication that the flatness of the Co layer is also decreasing but there is no obvious direct bridging between consecutive magnetic layers. An overview of a compendium of micrographs confirms that similar observations are applicable to the entire series. Basically, the multilayers have polycrystalline structure, with grain sizes that generally increase with increasing Cu layer thickness. The predominant grain morphology is columnar, with grains usually extending over three or more bilayer periods. Measurements from high-resolution (optimum defocus) images enable the sizes of individual grains to be accurately estimated: the results are summarized in Table I.

Table I
Variation in average grain size with Cu spacer layer thickness

$t_{\text{Cu}}(\text{nm})$	Grain size (nm)
0.9	3-5
4.3	10-20
8.5	20-40
17.0	80-100
34.0	200-300

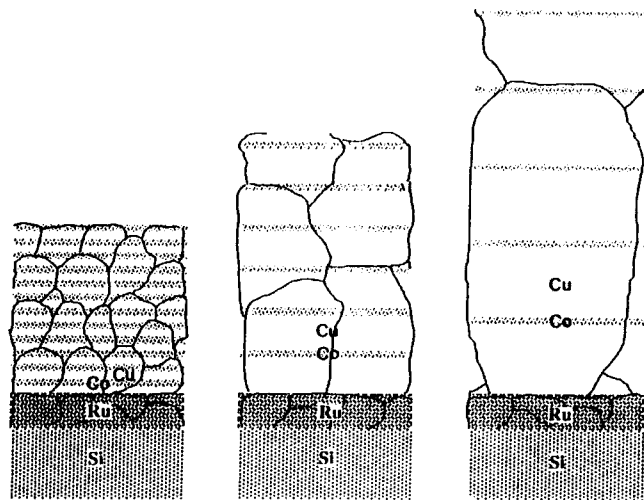


Fig. 3. Schematic drawing to illustrate the variation in multilayer morphology with increasing Cu spacer layer thickness.

Based on these observations, the morphology of the multilayers can be represented schematically as a function of the Cu spacer layer thickness, as shown in Fig. 3. It is also clear from careful study of the high-resolution images, and confirmed by the strong texturing seen in the SAED patterns, that many of these columnar grains have Cu {111} (close-packed) planes parallel, or nearly parallel (to within $\sim 1-2^\circ$), to the substrate surface. An example taken from the sample with a nominal Cu thickness of 17.0 nm is shown in Fig. 4. Overall, most of the grains appear to be well-ordered, although stacking faults and twin boundaries are sometimes seen, and strain contrast associated with the presence of the Co layers is often visible in multilayers with thick Cu spacer layers. Grains of other orientation were also observed but these did not appear to have any well-defined crystallographic relationship with the substrate.

It is not difficult to reconcile these structural characteristics with the corresponding magnetic behavior, particularly in view of the fact that the GMR effect occurs only for structures containing at least two Co layers but not for structures with single Co layers sandwiched between thick Cu layers [8]. Thus, the occurrence of GMR must be related to propagation of conduction electrons from Co layers through Cu layers to adjacent Co layers. It is also clear that GMR must be dependent upon layer smoothness, interlayer bridging, interface roughness, crystal orientation and the presence of defects. The occurrence of large grains in the Co/Cu multilayers implies reduced grain boundary scattering with the primary microstructural feature being the compositional layering. Theoretically, the microstructure could be considered as approaching a single, large Cu grain with periodically interspersed, compositionally different layers (Co). The inverse thickness dependence of the GMR that is observed for large spacer thickness can be explained in terms of its dependence on scattering at Co/Cu interfaces [10]. Thus, the pronounced crystallinity and the strong Co layering effectively mean that there is a dilution of the interfacial scattering effect as the spacer layer thickness is increased. Finally, the crystalline perfection of the individual Cu grains justifies a value for the electron scattering length (~ 30 nm) that is close to the bulk mean free path within Cu, as predicted solely on the basis of the falloff of GMR with increasing Cu thickness [8].

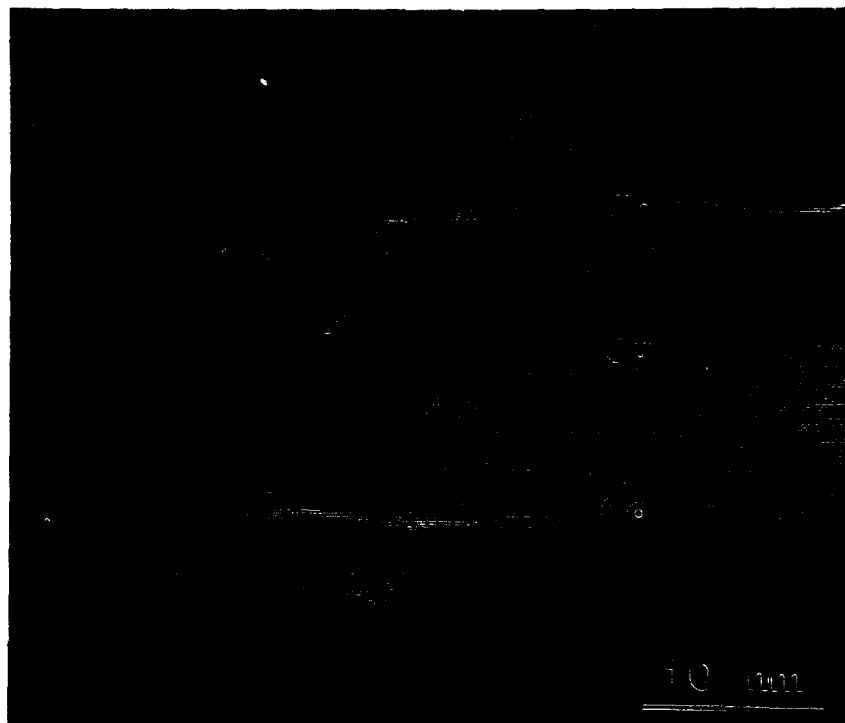


Fig. 4. High-resolution electron micrograph from the [1.1nm Co/17.0nm Cu] multilayer including part of large Cu grain with {111} planes parallel to plane of substrate.

CONCLUSIONS

On the basis of our electron microscopy observations of sputtered Co/Cu metallic superlattices, particularly at high resolution, a number of useful correlations have been made between the magnetic behavior and the microstructure. For thin Cu spacer layers, the quality of the initial buffer layer controlled the subsequent growth of flat Co and Cu layers, with Fe being far superior to Cu both in terms of structural quality and desired magnetic properties. The deposited films had a polycrystalline, columnar structure extending through several bilayer periods but the positions of the Co layers were observed to remain well-defined. It was apparent that grain sizes increased with increasing Cu spacer layer thickness and they were usually at least 3 to 4 times the bilayer period. Those multilayers grown with thicker Cu layers, ($t > 10\text{nm}$) had preferred {111} grain orientations that imparted a pronounced texture to selected area diffraction patterns. These structural characteristics implied that conduction electron scattering at grain boundaries should not play a significant role in developing models for the observed thickness dependence of GMR. Overall, it can be concluded that the microstructural information about the Co/Cu multilayers provided by the electron microscopy enabled better insights to be gained about their magnetic behavior.

ACKNOWLEDGEMENTS

The electron microscopy was conducted at the Center for High Resolution Electron Microscopy at Arizona State University supported by NSF Grant DMR-91-15680. ARM is pleased to acknowledge support from an IBM Graduate Fellowship, and we thank K.P. Roche for technical support.

REFERENCES

1. M.N. Baibich, J.M. Broto, A. Fert, Nguyen van Dau, F. Petroff, P. Etienne, G. Creuzet, A. Friederich and J. Chazelas, *Phys. Rev. Lett.* **61**, 2472 (1988).
2. S.S.P. Parkin, N. More and K.P. Roche, *Phys. Rev. Lett.* **64**, 2304 (1990).
3. S.S.P. Parkin, *Phys. Rev. Lett.* **67**, 3598 (1991).
4. J.M. Cowley and D.J. Smith, *Acta Cryst.* **A43**, 737 (1987).
5. J. Bravman and R. Sinclair, *J. Electron Micr. Tech.* **1**, 53 (1984).
6. S.S.P. Parkin, Z.G. Li and D.J. Smith, *Appl. Phys. Lett.* **58**, 2710 (1991).
7. S.S.P. Parkin, R. Bhadra and K.P. Roche, *Phys. Rev. Lett.* **66**, 2152 (1991).
8. S.S.P. Parkin, A.R. Modak and D.J. Smith, *Phys. Rev.* **B47**, 9136 (1993).
9. A.R. Modak, S.S.P. Parkin and D.J. Smith, *Ultramicroscopy* **47**, 375 (1992).
10. S.S.P. Parkin, *Appl. Phys. Lett.* **61**, 1358 (1992).

Section A—Multilayers and Surfaces

PART X

Surface Magnetism

THEORY FOR THE NONLINEAR MAGNETO-OPTICAL KERR-EFFECT AT FERROMAGNETIC TRANSITION METAL SURFACES

U. PUSTOGOWA, W. HÜBNER, AND K. H. BENNEMANN

Institute for Theoretical Physics, Freie Universität Berlin
Arnimallee 14, 1000 Berlin 33, Germany

ABSTRACT

The nonlinear magneto-optical Kerr-effect (NMOKE) has been proven to be an ultrafast spectroscopic probe of the magnetic and electronic properties of ferromagnetic surfaces. Extending our previous theory we calculate the linear and nonlinear magneto-optical Kerr-spectra of Fe. The results for the nonlinear Kerr spectra are compared with recent experiments on a Fe(110) surface. We derive and discuss general features of the nonlinear Kerr-effect, especially the details of its dependence on exchange interaction and Fermi-level crossings in the Stoner picture and beyond, frequency, and spin-orbit interaction. Furthermore we demonstrate how various electronic material properties, such as d-band width, s-d hybridization or band narrowing due to electronic correlations or caused by geometry (reduced coordination number in thin films), can be extracted from the spectra. As an example, we compare the linear and nonlinear Kerr-spectra of Fe to those of Ni. The extension of our theory to the Kerr spectra of thin magnetic films as well as of hidden magnetic interfaces occurring in sandwiches and multilayers is discussed.

INTRODUCTION

The nonlinear magneto-optical Kerr-effect (NOLIMOKE) describes the rotation of the polarization plane for second harmonic generation (SHG) in reflection from a ferromagnetic sample surface. This effect reflects the symmetry of the surface and allows for the study of two-dimensional ferromagnetic structures at surfaces, interfaces, in thin magnetic films and multilayers. In combination with optical "pump and probe" techniques the nonlinear magneto-optical Kerr-effect allows a time-dependent investigation of 2D-magnetism on the pico- through femtosecond time scale. Since it seems conceivable to apply NOLIMOKE for layer-by-layer magneto-optical recording this effect is interesting for the development of magneto-optical storage media. Note that in contrast to non-optical studies the nonlinear Kerr-effect is destructionless and not restricted to the study of remanent magnetization. As NOLIMOKE is caused by the interplay of spin-orbit and exchange interaction it becomes important for the determination of the spin-orbit induced magnetocrystalline anisotropy.

Motivated by theoretical studies on NOLIMOKE in Ni [1, 2] first experiments on Fe were performed in 1991 (Reif *et al.* [3]).

Besides comparing with these experiments it is of general interest to analyse theoretically the differences between the Kerr-spectra of Fe and Ni. The differences regarding the magnetic properties like exchange splitting, magnetic moments and crystal structure require an extension of our previous theory. For Fe one expects a reduction of electronic many-body effects and at the same time an increase of geometric structure effects. Furthermore, by varying different characteristics of the bandstructure (d-band width, s-band position, exchange splitting), we expect a more-detailed understanding of the parameters

controlling the features of the spectrum. This will be also useful for a systematic understanding of the nonlinear Kerr-effect in different ferromagnetic transition metals and for an extension of our theory to interfaces, thin magnetic films, and magnetic alloys.

THEORY

The linear Kerr susceptibility (bulk effect) is given by the familiar expression ($\mathbf{M} \perp$ surface, incident electric photon field $\parallel \hat{x}$)

$$\chi_{xy}^{(1)}(\mathbf{q}, \omega, \mathbf{M}) = \frac{e^2 \lambda_{s.o.}}{\Omega \hbar \omega} \sum_{\mathbf{k}, l, l', \sigma} \left[\langle \mathbf{k} + \mathbf{q}, l' \sigma | y | \mathbf{k} l \sigma \rangle \langle \mathbf{k} l \sigma | x | \mathbf{k} + \mathbf{q}, l' \sigma \rangle \cdot \frac{f(E_{\mathbf{k}+\mathbf{q}, l' \sigma}) - f(E_{\mathbf{k} l \sigma})}{E_{\mathbf{k}+\mathbf{q}, l' \sigma} - E_{\mathbf{k} l \sigma} - \hbar \omega + i \hbar \alpha_1} \right]. \quad (1)$$

The nonlinear magneto-optical surface susceptibility resulting from theory [2] is

$$\chi_{zzz}^{(2)}(2\mathbf{q}_{\parallel}, 2\omega, \mathbf{M}) = \frac{e^3 q_{\parallel} a \lambda_{s.o.}}{\Omega \hbar \omega} \sum_{\sigma} \sum_{\mathbf{k}, l, l', l''} \left[\langle \mathbf{k} + 2\mathbf{q}_{\parallel}, l'' \sigma | x | \mathbf{k} l \sigma \rangle \langle \mathbf{k} l \sigma | z | \mathbf{k} + \mathbf{q}_{\parallel}, l' \sigma \rangle \langle \mathbf{k} + \mathbf{q}_{\parallel}, l' \sigma | z | \mathbf{k} + 2\mathbf{q}_{\parallel}, l'' \sigma \rangle \cdot \frac{f(E_{\mathbf{k}+2\mathbf{q}_{\parallel}, l'' \sigma}) - f(E_{\mathbf{k}+\mathbf{q}_{\parallel}, l' \sigma})}{E_{\mathbf{k}+2\mathbf{q}_{\parallel}, l'' \sigma} - E_{\mathbf{k}+\mathbf{q}_{\parallel}, l' \sigma} - \hbar \omega + i \hbar \alpha_1} - \frac{f(E_{\mathbf{k}+\mathbf{q}_{\parallel}, l' \sigma}) - f(E_{\mathbf{k} l \sigma})}{E_{\mathbf{k}+\mathbf{q}_{\parallel}, l' \sigma} - E_{\mathbf{k} l \sigma} - \hbar \omega + i \hbar \alpha_1} \right] \cdot \frac{1}{E_{\mathbf{k}+2\mathbf{q}_{\parallel}, l'' \sigma} - E_{\mathbf{k} l \sigma} - 2\hbar \omega + i 2\hbar \alpha_1}. \quad (2)$$

Here, the following symbols are used: The photon wave vector parallel to the surface is denoted by \mathbf{q}_{\parallel} , $\lambda_{s.o.}$ is the spin-orbit coupling constant, $|\mathbf{k} l \sigma\rangle = \frac{1}{\sqrt{\Omega}} u_{\mathbf{k} l \sigma} e^{i \mathbf{k} \cdot \mathbf{r}}$ are Bloch states of wave vector \mathbf{k} and spin σ in the l th band, $E_{\mathbf{k} l \sigma}$ is the bandstructure of the irradiated material and α_1 is the experimental resolution. Ω refers to the volume and a is the lattice constant. For a detailed derivation see [1, 2]. The tensors $\chi_{xy}^{(1)}(\mathbf{q}, \omega, \mathbf{M})$ and $\chi_{zzz}^{(2)}(2\mathbf{q}_{\parallel}, 2\omega, \mathbf{M})$ are tensors of rank two and three, respectively. In centro-symmetric media, $\chi_{zzz}^{(2)}(2\mathbf{q}_{\parallel}, 2\omega, \mathbf{M})$ vanishes exactly due to the product of three parity-changing dipole matrix elements, except for the surface where the crystal symmetry is broken. The photons of frequency ω induce oscillating dipole moments leading to a surface charge of frequency ω which in turn interacts with the incoming photons and becomes the source of the frequency-doubled reflected light. This holds also in the presence of a finite magnetization \mathbf{M} .

RESULTS AND DISCUSSION

We calculate the nonlinear magneto-optical Kerr-susceptibility $\chi^{(2)}(\omega)$ in Fe in order to compare directly with experiment. In order to include the influence of many-body effects, especially the narrowing of the s and d bands due to electronic correlations, we make the following changes of the bandstructure parameters given in ref. [4]: (i) All hopping parameters are reduced to 60 % of their values. This corresponds to the reduction of the d -band width. (ii) The energy of the Γ -point is changed from 1.47 eV to 2.5 eV. Thus, the occupied portion of the s bands is narrowed. All other parameters are taken from ref.

[4], except for the exchange coupling constant $J = 1.7$ eV and the spin-orbit coupling $\lambda_{s.o.} = 0.05$ eV.

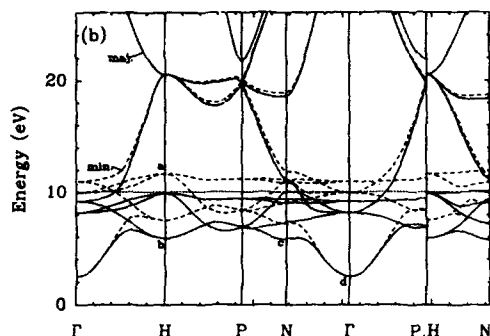


Figure 1: Spin-polarized bandstructure of iron. Solid (dashed) curves refer to the majority- (minority-) spin bands.

To demonstrate the validity of the electronic structure used in our calculations of $\chi^{(1)}(\omega)$ and $\chi^{(2)}(\omega)$, we show in Fig. 1 the resulting ferromagnetic band structure of Fe. It is obvious that the d -band width becomes smaller by the reduction of the tight-binding hopping parameters A_i ($i = 1, \dots, 7$). The points a, b, and c indicate the shift of the respective pure d -like or sd -hybridized high-symmetry points. Similarly, the modification of the energies β of the Γ -point leads to a shift of the s -like symmetry points.

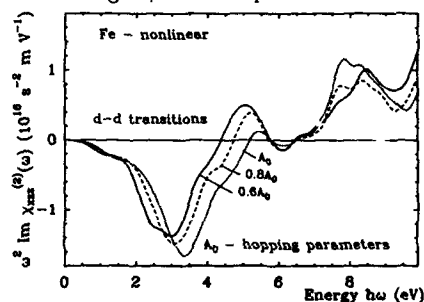


Figure 2: Nonlinear magneto-optical Kerr susceptibility of Fe for different d -band widths as a function of frequency.

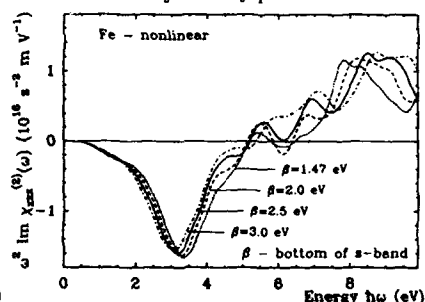


Figure 3: Frequency dependence of the nonlinear magneto-optical Kerr susceptibility of Fe for shifted s bands.

In Fig. 2 we show the nonlinear magneto-optical Kerr-spectra for different values of the Fletcher-Wohlfahrt hopping parameters. For the dotted curves, we use the values of the hopping parameters A_i ($i=1, \dots, 7$) given in ref. [4]. The dashed and solid curves correspond to a reduction of all A_i to 80 % and 60 % of these values, respectively. This reduction of the d - d hopping leads to a narrowing of the d band (see Fig. 1). Due to electron-electron correlations the probability of transitions with lower energies is increased. This essentially leads to a shift of the first structures in the linear and nonlinear Kerr-spectra to lower energies and to a simultaneous reduction of their heights. The shift of the second

structures is due to transitions between the d band and s -like or sd -hybridized bands and is therefore always smaller than the shift of the first structures which predominantly result from transitions between d -like bands close to the Fermi level. The modifications of the third structure in the spectra increasingly correspond to bands far from the Fermi-level and do not show a clear dependence on the d - d hopping elements. Thus, in summary, we may conclude that changes in the d -band width affect different parts of the spectra differently. We expect then such a behavior also with respect to changes in the position of the s band as can be seen in Fig. 3.

Fig. 3 shows the nonlinear magneto-optical spectrum for different values of the bottom of the s band (Γ -point). The position β of the energy at the Γ -point is increased from 1.47 eV via 2.0 eV and 2.5 eV to 3.0 eV. Changing β affects in particular the first peak of the nonlinear spectrum. It is shifted to smaller energies. The peaks at large energies (above 8 eV) however, are shifted to larger frequencies since the top of the s band lies at increasingly higher energies (high above the Fermi-level). Note that the first structure of the nonlinear Kerr-spectrum is mainly independent of β which is in agreement with our previous observation (see Fig. 2) that this peak involves mostly d - d transitions.

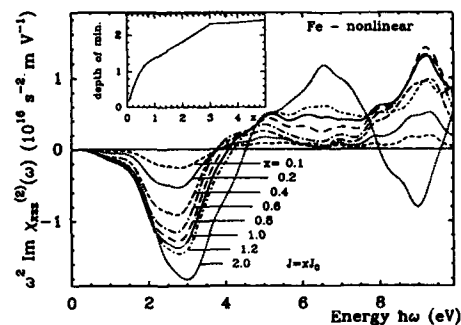


Figure 4: Dependence of the nonlinear magneto-optical Kerr susceptibility of Fe on magnetization as characterized by the exchange splitting $J = xJ_0$, $J_0 = 1.776$ eV. The inset shows the height of the first structure (at 2 eV...3 eV) as a function of splitting.

In Fig. 4, we show the dependence of the nonlinear Kerr-spectra on the exchange coupling constant J . We find for the nonlinear spectrum (at least for energies below 7 eV) a monotonic increase of the structure heights with increasing J . As is shown in the inset, this increase starts linearly in J . For larger values of the exchange interaction, the dependence tends to saturate.

In view of our results it is possible to understand more about the differences in the Kerr-spectrum expected for different ferromagnetic metals.

First, the dependence on J may be understood as follows. The increase of J has basically three effects: (i) Starting with small values of J the difference of allowed majority- and minority-electron dipole transitions at a certain frequency increases linearly in J , see illustration Fig. 5 for an atomic picture. For large J , however, this difference saturates, since the self-consistently determined Fermi-level becomes pinned and moves rigidly upon further increase of J . (ii) As long as the increase of J and the subsequent self-consistent readjustment of the Fermi-level do not cause bands to cross the Fermi-energy, the overall shape and peak structure of the spectrum remains unaltered. As soon as Fermi-level

crossings occur (either gradually for relatively steep bands or more abruptly for rather flat bands), the occupation character of the bands is changed. As a consequence, one may get drastic changes in the structure of the Kerr-spectra. Although the value of J in ferromagnetic Fe is quite large (1.776 eV) this possibility occurs only for energies larger than 7 eV and for a value $J = 2J_0$. Otherwise the features of the spectra appear to be very robust. (iii) As is shown in detail in the Appendix, the increase of J leads also to a small shift of the peak energies to larger values. The reason is that the exchange splitting of the d -like bands affect differently the s -like and sd -hybridized states via sd -hybridization.

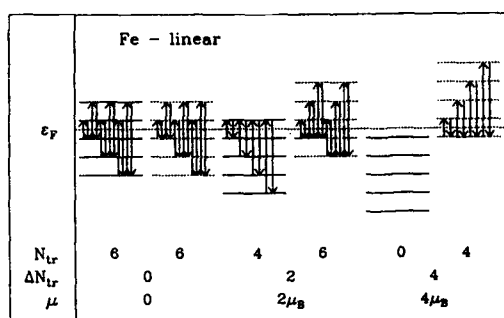


Figure 5: Illustration of the d -band transitions in Fe in an atomic picture. ϵ_F , μ_B , ΔN_{tr} denote Fermi-energy, magnetic moment, number of transitions, and difference of transitions in minority and majority spin bands, respectively.

Secondly, concerning the dependence of the spectra on *spin-orbit* coupling one should note the following: The nonlinear magneto-optical Kerr-spectrum depends linearly on *spin-orbit* coupling. This does not only hold for our perturbational treatment of spin-orbit interaction, but is also true if this interaction is included in the diagonal and off-diagonal matrix elements of the Hamiltonian[5, 6].

These general features of the theory are of interest for a systematic understanding of the Kerr-effect in the transition-metal series and will also be useful for the comparison of the Kerr-spectra of Ni and Fe.

Next, we compare the calculated nonlinear magneto-optical Kerr-spectra of Fe with those obtained previously for Ni. Of course, it matters that the electronic structure of bcc-Fe and fcc-Ni are different. We obtain for Fe and Ni for the structure at 2 eV to 3 eV a height ratio $\frac{P_{Fe}}{P_{Ni}}$ of 2.5. Note, the height ratio is not simply given by the ratio of the exchange couplings (4.5), or that of the magnetic moments (3.8), but also by the difference of spin-orbit coupling which enhances relatively the height of the Ni spectra ($\lambda_{s.o.}[Fe] = 50$ meV and $\lambda_{s.o.}[Ni] = 70$ meV). The larger minima and maxima in the nonlinear magneto-optical Kerr-spectrum of Fe compared with Ni result mainly for two reasons: (i) The exchange splitting is larger in Fe by a factor of 4.5. (ii) The filling of the 3d bands is different. Fe is much closer to half-filling which leads to a larger number of $d-d$ transitions. Furthermore, the peaks and minima in the optical region of Fe are shifted to higher energies compared to Ni because of the larger width of the Fe d band. This discussion shows how the Kerr-spectra change from transition metal to transition metal.

Finally, we should remark on using constant matrix elements for Fe in contrast to Ni. It is more physical to perform the calculations for iron using constant matrix elements to

obtain peak widths in accordance with the experimental peaks.

We use now the previous general theoretical considerations for the comparison of the theory with the experiment of Reif *et al.*[3]. The main experimental results obtained for only one frequency ($\hbar\omega = 2.33$ eV) can be summarized as follows: Upon reversing the direction of the in-plane surface magnetization by the external magnetic field a pronounced change of $\delta = I(\mathbf{M}) - I(-\mathbf{M})$ is observed, where I refers to the SHG intensity and \mathbf{M} to the in-plane magnetization at the surface. Using $I \sim P^2$, $P = \chi^{(2)}E^2$ and $\chi^{(2)} = \chi_{\text{nonmag.}}^{(2)} \pm \chi_{\text{mag.}}^{(2)}$, one may rewrite

$$\frac{\delta}{I_{\text{nonmag.}}} \sim \frac{\chi_{\text{mag.}}^{(2)}}{\chi_{\text{nonmag.}}^{(2)}}.$$

Thus, one finds from experiment a value of 25 % for $\frac{\chi_{\text{mag.}}^{(2)}}{\chi_{\text{nonmag.}}^{(2)}}$. Also experiment supports sensitivity of the nonlinear Kerr-effect for surface magnetization, since δ disappears exponentially with time and since $\chi_{\text{nonmag.}}^{(2)} \approx \text{const.}$ upon CO-chemisorption.

Using our results for Fe we find for

$$\frac{\chi_{\text{mag.}}^{(2)}}{\chi_{\text{nonmag.}}^{(2)}} = \left(\frac{\chi_{\text{mag.}}^{(2)}}{\chi_{\text{nonmag.}}^{(2)}} \right)_{\text{Ni}} \cdot \frac{P_{\text{Fe}}}{P_{\text{Ni}}} \cdot F = 7\% \cdot 2.5 = 17.5\%,$$

where 7 % refers to the corresponding value for Ni[7, 3]. The surface sensitivity of the nonlinear Kerr-effect is in accordance with the theoretical prediction (SHG occurs only for a few atomic layers at the surface where inversion symmetry is broken). Finally, theory permits a nonlinear Kerr-effect in principle also for coated surfaces and for interfaces and, furthermore, does not require saturated magnetization.

In summary, we have presented a theory which may be used for a systematic understanding of the nonlinear magneto-optical Kerr-effect in transition metals. In particular, we have given results for the dependence of the nonlinear Kerr-spectrum on *s*- and *d*-band width, *sd*-hybridization, exchange interaction, spin-orbit coupling, and crystal structure (fcc-Ni vs. bcc-Fe). The theory is used to analyse recent NOLIMOKE experiments in Fe. The theory may be extended to thin films.

References

- [1] W. Hübner, K. H. Bennemann, Phys. Rev. B **40**, 5973 (1989).
- [2] W. Hübner, Phys. Rev. B **42**, 11553 (1990).
- [3] J. Reif, J. C. Zink, C.-M. Schneider, and J. Kirschner, Phys. Rev. Lett. **67**, 2878 (1991).
- [4] S. K. Baker, and P. V. Smith, J. Phys. F **7**, 781 (1977).
- [5] D. K. Misemer, J. Magn. Magn. Mater. **72**, 267 (1988).
- [6] P. M. Oppeneer, J. Sticht, T. Maurer, and J. Kübler, Z. Phys. B **88**, 309 (1992).
- [7] W. Hübner, K. H. Bennemann, Vacuum **41**, 514 (1990).

CANTED MAGNETIC MOMENTS AT THE Gd(0001) SURFACE

Dongqi Li, Jiandi Zhang, and P. A. Dowben
 Department of Physics, Syracuse University, Syracuse, NY 13244
 K. Garrison, and P. D. Johnson
 Physics Department, Brookhaven National Laboratory, Upton, NY 11973
 H. Tang*, T. G. Walker, and H. Hopster
 Department of Physics, University of California, Irvine, CA 92717
 J. C. Scott, D. Weller, and D. P. Pappas†
 IBM Almaden Research Center, 650 Harry Road, San Jose, CA 95120

ABSTRACT

With spin polarized electron spectroscopies, we have investigated ordered Gd(0001) films deposited on W(110). The photoemission features of the gadolinium 5d surface state, the 4f levels, and the background exhibit considerable spin polarization along the same direction in the plane of the film, indicative of ferromagnetic coupling between the surface and the bulk. The 4f spin polarized photoemission data provides strong evidence that the surface 4f polarization differs from the bulk 4f polarization for Gd(0001). Our temperature dependent measurements with spin polarized secondary electron spectroscopy conclusively establishes that the surface of clean Gd(0001) possesses a perpendicular polarization component which persists to an enhanced surface Curie temperature. Small amounts of contamination at the surface result in the disappearance of the perpendicular component and, therefore, a more perfect ferromagnetic coupling between the surface and the bulk.

INTRODUCTION

The issues of surface magnetic anisotropy and the magnetic coupling between the surface and the bulk have attracted considerable attention. The Gd(0001) surface appears to exhibit enhanced magnetic order, i.e., higher Curie temperature at the surface than in the bulk [1]. It is seen to be able to maintain an in-plane remanent magnetization [1, 2, 3, 4], although there is indication that an perpendicular anisotropy exists for ultrathin Gd films [4]. Calculations [5] supported the altered exchange coupling in the surface layer, and the postulate put forward earlier on the basis of experiment [1] that the surface is antiferromagnetically coupled with the bulk. In this paper, we provide evidence that the surface is not antiferromagnetically coupled with the bulk but rather an imperfect ferromagnetic coupling exists between the surface and the bulk as a result of a sizable perpendicular polarization of the surface layer, consistent with earlier work [3, 6, 7]. This effect undoubtedly results in phenomena consistent with the earlier experiment [1] but challenges the simpler models of perfect antiferromagnetic [1, 5] or perfect ferromagnetic [8] coupling between the surface and the bulk.

Our recent photoemission studies [9, 10, 11] of the Gd(0001) band structure have demonstrated the existence of a surface state at $\bar{\Gamma}$ consistent with the theoretical band structure [5]. The surface state is well localized at the surface [11, 12], and is therefore a unique probe of the surface magnetic order without requiring the complex task of separating surface and bulk signals. In addition, the temperature dependence of both the parallel

and perpendicular components can be measured explicitly.

EXPERIMENTAL

The photoemission experiments were undertaken at the U5 beamline at the National Synchrotron Light Source (NSLS). The spectra were taken at low photon energies (typically 43 eV in this work) using a low energy spin polarimeter (described in detail elsewhere [13, 14]) attached to a commercial angle-resolved hemispherical analyzer. The light polarization of the incident light was perpendicular to the applied field and a mixture of s- and p-polarized light (55° incidence angle). All photoelectrons were collected normal to the surface since the Gd surface state is centered at $\bar{\Gamma}$ [5, 9, 10, 11, 12]. The combined energy resolution of the spectra was 300 meV. Spin polarized secondary electron emission experiments were conducted in a separate UHV system [15] equipped with two medium-energy retarding field Mott polarimeters capable of measuring all three components of the spin polarization vector. The secondary electrons were collected around normal emission with the sample negatively biased at -30 V. All spin polarization measurements were performed on remanently magnetized samples.

The gadolinium films were evaporated from a tungsten basket, or crucible, at a rate of 0.5 - 2 Å/min. onto single crystal W(110), following well established procedures that are known to give coherent ordered clean gadolinium films [11, 16]. Following the deposition onto the room temperature substrate to allow layer-by-layer growth, the films were annealed at 450-550°C to reduce the number of defects [17, 18]. The films prepared in this way are flat and yield better remanent magnetization, in contrast to the "island" films grown at the elevated temperature of 450°C. The thickness of the films used in this work was typically 200 - 500 Å.

RESULTS AND DISCUSSION

As seen in Figure 1, the 5d surface state near the Fermi energy is highly spin polarized as is the photoemission background and the Gd 4f levels for Gd(0001) films at 100K (the bulk Curie temperature is 293 K). The polarization for these films is 33 to 52% in the plane of the film. The polarization of both the surface state near E_f which contains only the surface contribution and the 4f photoemission feature with strong contributions from the gadolinium bulk are nearly constant at around 33%. The spin polarization of the 4f feature does not change much ($\pm 10\%$) with photon energy of 43 - 100 eV, while the surface sensitivity changes because the electron mean free path changes with electron kinetic energy. These facts exclude any possibility that the surface is antiferromagnetically coupled to the bulk. These results are consistent with the previously reported results from spin polarized photoemission of the shallow 4f gadolinium core levels and the spin polarized secondary electrons [3, 7].

The "in plane" 4f spin-polarized spectra for clean, well ordered gadolinium films have a maximum for the spin minority peak at a binding energy 300 to 400 meV greater than that of the spin majority peak for gadolinium films at 100K (as seen in Fig. 1 & 2). This binding energy difference diminishes with the adsorption of a very small amount of contamination as seen in Fig. 2. Continued adsorption of contamination leads to a decrease in the net polarization and a diminution of the surface state intensity.

It has been well established that there exists a surface to bulk core level shift for gadolinium [19, 20]. For the 4f photoemission feature the surface component has a binding

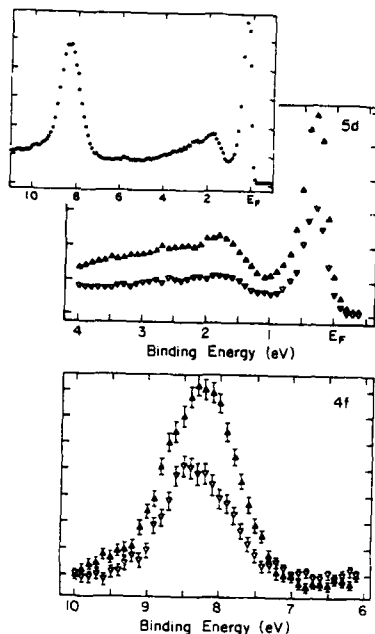


Fig. 1. The spin polarized photoemission spectra for a 300 Å thick gadolinium film on W(110) at 100K. The spin majority signal (Δ) and spin minority signal (∇) were measured in the plane of the film. The photon energy is 43 eV and the photoelectrons were collected normal to the film so the surface state near E_F (200 meV binding energy) can be distinguished from the bulk Gd bands (1 - 4 eV binding energy). The insert shows the spin integrated Gd photoemission spectrum.

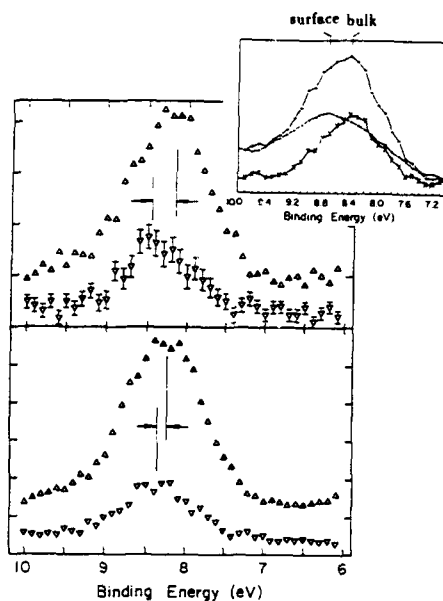


Fig. 2. The in-plane spin polarized photoemission spectra for a 300 Å thick gadolinium film on W(110) at 100K across the Gd 4f levels. At top are shown the spectra of the freshly deposited film and below following exposure to a small amount of contamination. Spin majority (Δ) and spin minority (∇) are indicated, the photon energy is 43 eV. The insert shows the different Gd 4f photoemission spectra for an one monolayer and a ten monolayer film illuminating the different surface (one monolayer, $\bullet-\bullet$) and bulk (the difference spectrum, $\times-a$), contributions to the Gd film (this time deposited on Cu(100)). Data for the insert is described in Ref. 16 and taken with a photon energy of 40 eV.

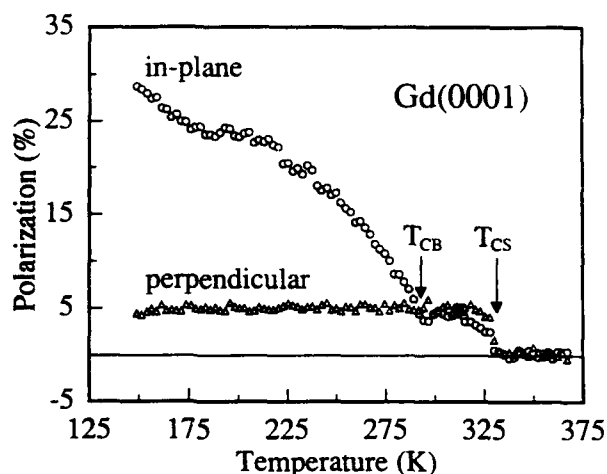


Figure 3: Temperature dependence of the spin polarization of 2 eV secondary electrons from a 400 Å Gd(0001) film grown at 300K annealed to 825K for 3.5 minutes. T_{CB} and T_{CS} indicate the surface and bulk magnetic ordering temperatures, respectively.

energy at least 0.37 ± 0.02 eV greater than the bulk[19]. The different surface layer and bulk contributions to the Gd 4f photoemission signal can be easily seen from the difference spectrum between the spectrum obtained for a 1 monolayer films and the spectra obtained for thicker gadolinium films as seen in insert to Fig. 2. As can be seen from the insert to Fig. 2, the intensity and binding energy of the surface (1 monolayer film) contribution to the 4f levels closely resembles the intensity and peak position of the spin minority contribution to the spin resolved photoemission spectra for gadolinium films at 100K ($T/T_c = 0.34$). While the level of polarization ($>30\%$) and the spin majority polarization of the surface state excludes antiferromagnetic coupling between the surface and the bulk as noted above, this apparently slightly greater binding energy of the in-plane spin minority gadolinium 4f peak indicates that, for the films that are free of contaminations, the surface is slightly less polarized in the plane of the film when compared to the bulk. The Gd 4f moment may be safely assumed to be the same for the surface and the bulk as they are large localized moments [5]. Our results, therefore, suggest that there exists a surface magnetic moment component normal to the surface.

The existence of a perpendicular component in the surface magnetization is clearly shown in the temperature dependent secondary electron polarization data in Fig. 3. The secondary electrons are highly polarized due to significant contributions from the 4f core electrons[3, 7], and clearly show both perpendicular and in-plane polarization. Since the perpendicular component persists to a critical temperature well above (~ 40 K) the bulk Curie temperature (T_{CB}), it can only be identified with the surface polarization, as is the non-vanishing in-plane component above T_{CB} . The complete insensitivity of the perpendicular magnetization to the bulk magnetic transition suggests that the Gd(0001) surface behaves as an independent magnetic entity. We further note that, as best revealed in the perpendicular component, the surface magnetic transition is extremely abrupt, reminiscent of a two-dimensional system or possibly even a first order phase transition[21]. It is important to stress, however, that in the present experiment the sample was left in its remanent state throughout the entire temperature sweep, whereas in the previous

SPLEED[1] experiment the sample was remagnetized at each temperature step. Therefore, the present data contains, in the sign of the polarization, the added information on the relative directions of the in-plane polarizations above and below T_{CH} . The lack of a sign reversal on going through T_{CB} shows that the in-plane surface and bulk moments are ferromagnetically coupled.

The presence of a normal component of the surface magnetization are substantially altered by contamination. Very small amounts of contamination result in a reduction of the out of plane component of magnetization in the surface. As seen in Fig. 2, the binding energies for the spin minority and spin majority contributions to the Gd 4f signal differ by 350 ± 50 meV for a clean Gd film but differ by less than 100 meV following the adsorption of contamination. We noted that the surface state still exists with the level of contamination that results in near perfect ferromagnetic ordering. So this perpendicular component of the magnetization at the surface is more sensitive to surface conditions than the surface state.

CONCLUSION

With spin-polarized spectroscopies, we have shown that the 5d surface state near E_f is a magnetic surface state. The surface magnetization of clean Gd(0001) is canted out of the plane, with its in-plane component ferromagnetically coupled with the bulk magnetization. The existence of a perpendicular component in the surface magnetization indicates an altered surface-bulk coupling and possibly a strong surface anisotropy.

ACKNOWLEDGEMENTS

This work was supported in part by the U.S. Department of Energy (Syracuse University) and the NSF (Univ. of California at Irvine). The NSLS is supported by the DOE under contract # DE-AC02-76CH00016. The authors would like to thank G.A. Mullholland (Univ. of Texas) for his technical assistance and Prof. Erskine (Univ. of Texas) for loan of the dewar.

* Present address: Mail Stop 66, Stanford Linear Accelerator Center, Stanford, CA 94309.

† Present address: Code 6345, Naval Research Laboratory, Washington, DC 20375-5343.

References

- [1] D. Weller, S. F. Alvarado, W. Gudat, K. Schröder and M. Campagna, Phys. Rev. Lett. 54, 1555 (1985); D. Weller and S. F. Alvarado, J. Appl. Phys. 59, 2908 (1986).
- [2] M. Taborelli, R. Allenspach, G. Boffa and M. Landolt, Phys. Rev. Lett. 56, 2869(1986); O. Paul, S. Toscano, W. Hüsch and M. Landolt, J. Magn. Magn. Mater. 84, L7 (1990).
- [3] H. Tang, D. Weller, T. G. Walker, J. C. Scott, C. Chappert, H. Hopster, A. W. Pang, D. S. Dessau, and D. P. Pappas, Phys. Rev. Lett., submitted.
- [4] M. Farle, A. Berghaus, and K. Baberschke, Phys. Rev. B 39, 4838 (1989).

- [5] R. Wu, C. Li, A. J. Freeman and C. L. Fu, *Phys. Rev. B* **44**, 9400 (1991); R. Wu and A. J. Freeman, *J. Magn. Magn. Mater.* **99**, 81 (1991).
- [6] Dongqi Li, Jiandi Zhang, P. A. Dowben, and K. Garrison, *J. Phys.: Condens. Matter*, **5**, L73 (1993).
- [7] H. Tang, T. G. Walker, H. Hopster, D. P. Pappas, D. Weller and J. C. Scott, *Phys. Rev. B*, **47**, 5047 (1993).
- [8] G. A. Mulhollan, K. Garrison, and J. L. Erskine, *Phys. Rev. Lett.* **69**, 3240 (1992).
- [9] Dongqi Li, C. W. Hutchings, P. A. Dowben, C. Hwang, R. T. Wu, M. Onellion, A. B. Andrews, and J. L. Erskine, *J. Magn. Magn. Mater.* **99**, 85 (1991).
- [10] Dongqi Li, C. W. Hutchings, P. A. Dowben, C. Hwang, R. T. Wu, M. Onellion, A. B. Andrews and J. L. Erskine, *J. Appl. Phys.* **70**, 6062 (1991).
- [11] Dongqi Li, Jiandi Zhang, P. A. Dowben and M. Onellion, *Phys. Rev. B* **45**, 7272 (1992).
- [12] Dongqi Li, Jiandi Zhang, P. A. Dowben and M. Onellion, *Phys. Rev. B*, submitted.
- [13] M. R. Scheinfein, D. T. Pierce, J. Unguris, J. J. McClelland, R. J. Celotta and M. H. Kelley, *Rev. Sci. Instrum.* **60**, 1 (1989).
- [14] P.D. Johnson, N.B. Brookes, S.L. Hulbert, R. Klaffky, A. Clarke, B. Sinković, N.V. Smith, R. Cellota, M.H. Kelley, D.T. Pierce, M.R. Scheinfein, B.J. Wacławski, and M.R. Howells, *Rev. Sci. Instrum.* **63**, 1902 (1992).
- [15] D. P. Pappas, K.-P. Kämper, and H. Hopster, *Phys. Rev. Lett.* **63**, 3179 (1990).
- [16] P. A. Dowben, D. LaGraffe and M. Onellion, *J. Phys. Cond. Matt.* **1**, 6571 (1989).
- [17] U. Stetter, M. Farle, K. Baberschke, W. G. Clark, *Phys. Rev. B* **45**, 503 (1992).
- [18] S.D. Barrett, *Surface Science Repts.* **14**, 271 (1992).
- [19] D. LaGraffe, P. A. Dowben, and M. Onellion, *Phys. Rev. B* **40**, 3348 (1989).
- [20] R. Kammerer, J. Barth, F. Gerken, A. Flödstrom and L. I. Johansson, *Solid State Commun.* **41**, 435 (1982).
- [21] D. Weller and S.F. Alvarado, *Phys. Rev. B* **37**, 9911 (1988).

IN-SITU MAGNETO-OPTICAL KERR EFFECT OF EPITAXIAL Gd(0001)

C. Chappert¹⁾, D. Weller, H. Tang²⁾, J.C. Scott, H. Hopster³⁾ and D.P. Pappas¹⁾
 IBM Research Division, Almaden Research Center, 650 Harry Road, San Jose, CA, 95120

¹⁾present address: Institut d'Électronique Fondamentale, Université Paris Sud, 91405 Orsay, France

²⁾ Department of Physics and Institute for Surface and Interface Science, University of California, Irvine, CA.

³⁾present address: Naval Research Laboratory, Washington, DC 20375-5343

ABSTRACT

We have characterized magnetization loops of epitaxially grown Gd(0001) films on W(110) in the temperature range $145 \leq T \leq 300\text{K}$. This was accomplished by measuring magneto-optical Kerr loops in UHV, in the transverse geometry, using a 2×10^{-4} deg sensitivity differential detector and He-Ne laser light.

Films grown in the Stranski-Krastanov (SK) mode (growth temperature 400°C) and films grown in a Frank-van-der-Merwe (FM) like mode (growth temperature 20°C) behave significantly differently. While the room temperature grown films (FM) show square hysteresis behavior only after an annealing cycle to at least 300°C , the higher growth temperature (SK) leads to highly remanent films in the as grown state.

The hysteresis behavior of these films is most important in conjunction with recently reported spin-polarized photoemission results, which showed that the growth temperature and therefore the film morphology has a strong influence on the surface magnetic reconstruction of Gd(0001) [1].

1. INTRODUCTION

Gd is a simple ferromagnet with localized magnetic (4f) moments and a relatively high Curie temperature of $\sim 293\text{K}$. This has made it an ideal model system for the investigation of bulk Heisenberg magnetism. Temperature dependent magnetization and coercivity properties of bulk Gd specimens can be found in the work of Belov et al. [2]. Gd *thin films* have become of particular interest, as they revealed new surface magnetism phenomena which had been predicted in theory in 1971 [3] and have recently been confirmed in several experiments. In 1983, Rau et al. [4, 5] reported an enhanced surface Curie temperature on polycrystalline Gd films as revealed by electron capture spectroscopy. In 1985, Weller et al. demonstrated by spin-polarized low-energy electron diffraction (SPLEED) remanent, ferromagnetic Gd(0001) films on W(110) [6] with a surface Curie temperature of $T_{CS} = 315\text{K}$, 22K above $T_{CB} = 293\text{K}$ and proposed AF surface coupling J_1 , based on the observation of a compensation feature in both temperature dependent SPLEED and low temperature 4f-photoemission data [7]. In 1991, Wu et al. [8] confirmed the possibility of AF surface coupling in FLAPW ab-initio bandstructure calculations. This work also gave theoretical support to the existence of a localized 5d surface state, which had been previously observed by Li et al. in photoemission experiments [9-11]. In 1992, Mulhollan et al. [12] claimed that the surface magnetic coupling in Gd was purely ferromagnetic; however they reported a much reduced spin-polarization of only $\sim 50\%$ at 100K . Tang et al. [13] had earlier reported 50% spin-polarization at 150K and subsequently showed that clean Gd(0001) surfaces can exhibit the phenomenon of surface spin canting by direct observation of an out-of-plane spin-polarization in resonant spin-resolved 4f-photoemission and spin-polarized secondary electron

spectroscopy [1, 13, 14]. The latter result was confirmed by Li et al. [15, 16], who also pointed out the sensitivity to surface contamination. Despite the ongoing interest in surface magnetic properties of epitaxial Gd(0001) films, relatively little work has been devoted to the study of bulk properties, and in particular the hysteresis properties of Gd(0001) films, which provide the basis for the interpretation of photoemission or other (low energy) electron spectroscopic data. The bulk Curie temperature was previously measured using in-situ MOKE [7, 17] and the magnetization reversal in Gd(0001) has just recently been discussed on the basis of biased initial susceptibility and MOKE butterfly loops in UHV, however, at low temperature only [18]. Farle et al. finally discussed in detail the dependence of the Curie temperature on both the Gd film thickness and the film deposition conditions [19].

Here we report bulk properties of the same films which showed the spin-canting phenomenon discussed first by Tang et al. [1], using a high sensitivity in-situ MOKE apparatus. In particular, we discuss the preparation sensitivity of the hysteresis properties and report an interesting feature in the temperature dependent coercivity measurements near T_C , which we interpret in conjunction with the surface spin orientation of these films.

2. EXPERIMENTAL

Gd(0001) films of 300-400 Å thickness were deposited in ultra-high vacuum (UHV) on W(110) substrates, which were kept either at 300K to promote coherent, layer-by-layer film growth or at 725K to induce Stranski-Krastanov (SK) type growth (see [6, 17]). We have consistently used growth rates of $\sim 0.7 \text{ Å/sec}$, which resulted in a pressure increase from 2×10^{-10} to $\sim 1 \times 10^{-9}$ Torr during film growth. The films deposited at 300K were subsequently annealed at 650K or higher for $\sim 3 \text{ min}$. LEED patterns of such thick films are only observed after annealing. They reveal the typical hexagonal basal-plane structure of Gd(0001) films as reported before [17, 20]. Only films of at least 300Å thickness were investigated in order to avoid

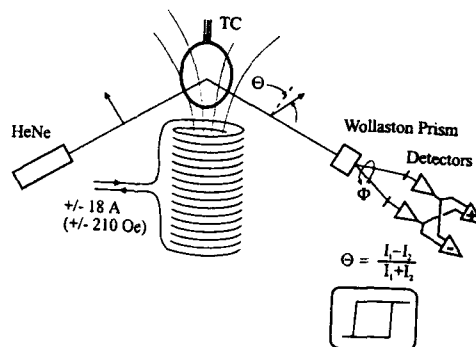


Fig.1: Transverse Kerr arrangement used in the present experiment. The sample was placed near the top of a single UHV compatible magnetic field coil, which provided fields up to $\pm 210 \text{ Oe}$.

the coalescence regime in SK type films, which is between 50 and 100 Å [6, 17]. Thinner films and films grown at lower growth rates can have significantly different properties, especially with respect to their morphology and surface topography (roughness). Furthermore, the films were kept in an in-plane magnetic field of $\sim 100 \text{ Oe}$ during cooling from the deposition/annealing temperature down to the measurement temperatures. This procedure also reportedly has a significant

influence on the surface magnetic properties [21]. Details of the apparatus for UHV growth and characterization have been published elsewhere.[1, 14]

The in-situ MOKE apparatus is shown schematically in Fig.1. We use the transverse geometry, with the magnetic field axis perpendicular to the plane of incidence of the linearly polarized He-Ne laser light beam. The polarization change occurring upon reflection from the sample is transferred into a net rotation using a Wollaston prism and two silicon photodiodes. A low noise difference and sum amplifier yields the output signal $(I_1 - I_2)/(I_1 + I_2)$, which is subsequently converted into the Kerr signal, using a calibration constant determined from the angular sensitivity of the system in the linear regime around the $I_1 = I_2$ setting. A slope of 0.35V/deg was found in a range of $\Phi \sim \pm 5$ deg and with an electronic noise floor of ≤ 0.1 mV we obtained a maximum sensitivity of 0.2mdeg in Kerr rotation. Note that the Kerr effect at the present wavelength of 633nm has a probing depth of $\sim 500\text{\AA}$ and that therefore the whole sample volume within the laser spot size of $\sim 1\text{mm}^2$ is being probed.

3. RESULTS AND DISCUSSION

Fig. 2 shows the result of an annealing study of a 300Å thick Gd(0001) film which was grown at room temperature (FM mode).

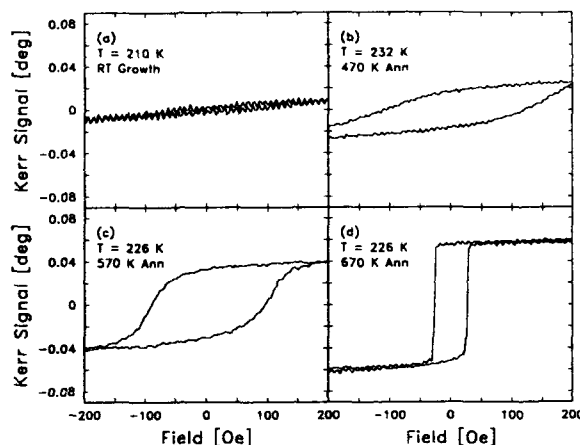


Fig. 2: Transverse Kerr loops, measured in UHV on a 300Å thick Gd(0001) film, which was subjected to three different annealing/cooling cycles as indicated in the figure. Annealing to at least 670K produces "square" loops with high (100%) remanence.

The measurements were carried out at a temperature of 200K after the initial deposition and subsequently after each annealing cycle to temperatures of 460K, 570K and 670K, respectively, at which the sample was kept for 3min each time. Evidently, the as prepared film cannot be magnetized with the available field of $\pm 210\text{Oe}$ and only the reversible initial susceptibility is observed. The loops become hysteretic after the 460K anneal although they still cannot be saturated. Further anneal decreases the coercivity, increases the squareness and reduces the paramagnetic slope, clearly visible in all but the 670K case. Annealing to 670K finally results in a loop, which is indicative of single domain behavior with essentially 100% remanence.

In Fig. 3, we compare loops obtained on two films of 400Å thickness grown under different conditions. The top part of the figure (a & b) shows results for a FM type film grown at room temperature and post-annealed in UHV for 3min at 825K (550°C). The film was cooled in the presence of an in-plane field of $\sim 1000\text{Oe}$ to the first measurement temperature of $\sim 150\text{K}$ and Kerr loops were taken while stepping the temperature up to above room temperature ($\sim 310\text{K}$). Representative loops are shown for $T = 182\text{K}$ and 288K . The main observation is

that these films show essentially square loops with high remanence even close to the Curie temperature $T_{C,B} = 293\text{K}$. A similar procedure was used for a film grown at an elevated substrate temperature of 675K (400°C), which results in the well known SK growth mode. Subsequent cooling again was carried out in the presence of a 100Oe in-plane field. The low temperature loop (c) looks similar to the one discussed above (a), only the coercivity is somewhat smaller, 20Oe for the SK film as opposed to 28Oe for the FM type film. More drastic differences are apparent near the Curie point (d). A distinct slope is observed, suggestive of paramagnetic or hard axis behavior. The remanence is reduced by at least 40% of its saturation value. (The maximum available field, 210Oe , was insufficient to yield complete saturation.) Lastly, in this temperature range the coercivity is now larger for the SK film than for the FM film. The differences between SK and FM films become clearer if we compare temperature dependences.

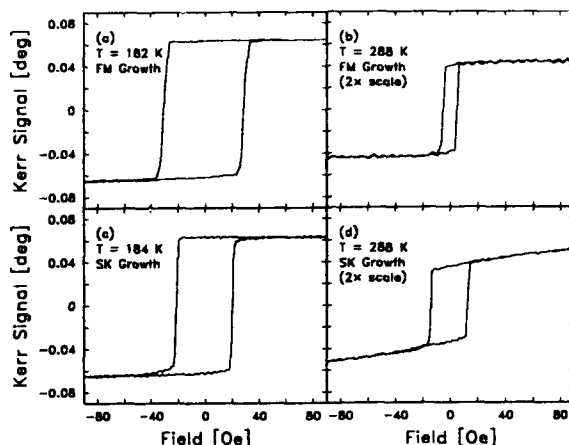


Fig. 3: Transverse Kerr loops of 400\AA thick $\text{Gd}(0001)$ films grown under different condition and at two temperatures far below T_C and near T_C : (a) FM film at $T = 182\text{K}$, (b) same film at 288K , (c) SK type film at 184K and (d) same film at 288K . Note the differences especially at 288K .

Fig. 4 shows a comparison of the remanent Kerr rotations (M_R) and Fig. 5 a comparison of the coercivities (H_C) of the SK and FM films. In both cases we have fitted the low temperature regime ($0 \rightarrow 225\text{K}$) to a $T^{3/2}$ law, according to

$$M_R(T) = M_0(1 - CT^{3/2}) \quad (1)$$

and

$$H_C(T) = H_{C,0}(1 - CT^{3/2}) \quad (2)$$

respectively.

The fit parameters C , M_0 and $H_{C,0}$ are indicated in the figures. Note that C is essentially equal (a) for both the Kerr signal and the coercivity measurements and (b) for both types of films (SK and FM). The main differences in the films are the extrapolated 0K values M_0 and $H_{C,0}$ and especially the coercivity behavior around T_C . We do not attach any particular physical meaning to the slightly reduced M_0 in the case of the annealed film: a thickness difference, the different film morphology etc. could cause this effect. On the other hand, the drastic differences near the Curie temperature certainly deserve attention.

The phenomena of dramatically increased coercivity, reduced remanence and loss of squareness of the SK film loops, relative to those of the FM films within $\sim 10\text{K}$ below $T_{C,B}$, clearly point to a fundamental change in the

magnetization reversal process. We believe that these differences are related to the degree of surface roughness of the two film types, and propose the following explanation, based on our previously reported experimental findings [1] of (i) an out-of-plane surface magnetization component, (ii) a strongly enhanced surface Curie temperature and (iii) ferromagnetic coupling to the subsurface layers. We assume, in addition, that the 300-400Å thick SK type Gd films have greater surface roughness than the corresponding FM films. (This is reasonable, although we haven't carried out surface characterization, e.g. with in-situ STM, which could prove this point.) Briefly, we suggest that the combination of roughness and enhanced perpendicular surface magnetization leads to an inhomogeneous out-of-plane moment.

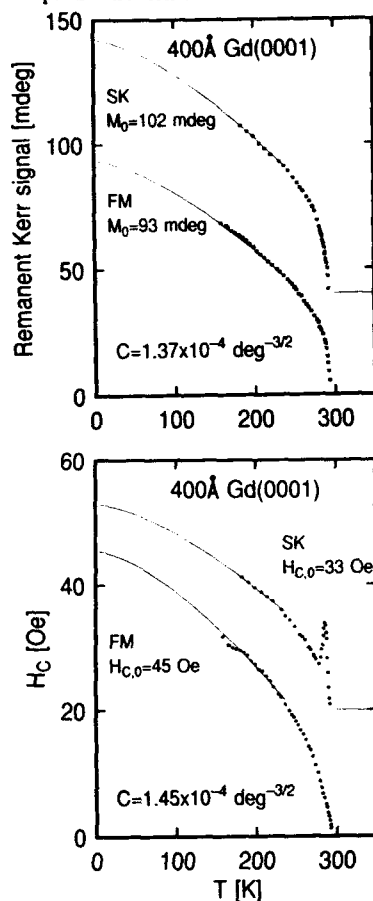


Fig. 4: Temperature dependent Kerr signals of the FM and SK type films discussed in Fig. 3. The low temperature regime can be fitted to a $T^{3/2}$ law according to eq.(1). The parameters C and M_0 are indicated in the figure.

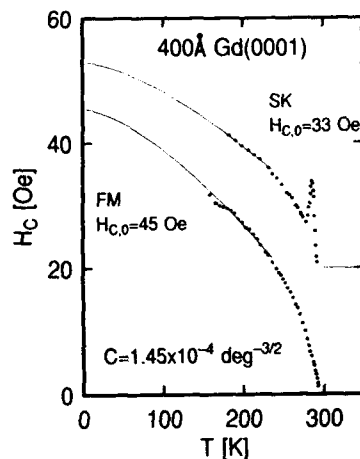


Fig. 5: Temperature dependent coercivity of the FM and SK type films discussed in Fig. 3. The low temperature regime can be fitted to a $T^{3/2}$ law according to eq.(2). The parameters C and $H_{c,0}$ are indicated in the figure.

To elaborate on this picture, recall that surface roughness in general leads to a reduction of the in-plane dipolar (shape) anisotropy near the surface of a (thick) film [22]. Thus an out-of-plane contribution, i.e. that due to the modified electronic structure of the Gd surface with respect to the bulk, becomes an important consideration in the energy balance. At temperatures well below $T_{C,B}$, where the bulk magnetization is large, the shape anisotropy will dominate to maintain in-plane alignment. Near the Curie temperature, the bulk magnetization is reduced, and now the enhanced surface component dominates to yield an

out-of-plane component extending further away from the surface. This may be viewed as a 90 degree domain wall parallel to the film plane and is sometimes referred to as perpendicular surface pinning of the magnetization. Analogous behaviour e.g. is found in the case of perpendicular magnetic anisotropy induced by interface/surface anisotropy in ultrathin films and multilayers. In the absence of roughness the shape anisotropy is not reduced and the energy balance will shift towards in-plane alignment. Moreover, the magnetization near a smooth surface is expected to be more homogeneous, so that coherent rotation about the surface normal can be achieved with minimal cost in anisotropy and exchange energy.

This effect of spin-reorientation as the temperature is swept through the bulk Curie temperature is reflected in the hysteresis properties: as the magnetization rotates increasingly out of the plane, the in-plane remanence is reduced; the squareness of the loop is destroyed as the applied field competes with the net out-of-plane anisotropy; and the coercivity increases as the inhomogeneous surface magnetization pins that of the bulk. These are the phenomena demonstrated in Fig. 3(d).

4. CONCLUSIONS

We have measured in UHV Kerr loops of epitaxial Gd(0001) films grown on W(110) substrates in two deposition modes, the continuous Frank-van-der Merwe (FM) type mode and the more cluster like Stranski-Krastanov (SK) type. For films grown at low temperature (FM), only post annealing to at least 670K establishes rectangular magnetization loops with high remanence. In contrast, films grown at 675K do show this type of loop in the as-grown state. Significant differences in the temperature dependences of the two types of film are observed. The appearance of a coercivity peak near the Curie temperature in the SK film has been related to the recently observed phenomenon of surface spin-canting in these films [1].

5. Acknowledgement

Several interesting discussions with F. Salas, M. Farle and W. Lewis are gratefully acknowledged. We thank T.G. Walker for calibrating the field coil used in the present experiments.

6. REFERENCES

- [1] H. Tang, D. Weller, T.G. Walker, J.C. Scott, C. Chappert, and H. Hopster, A.W. Pang, D.S. Dossau, and D.P. Pappas, Magnetic reconstructions at the Gd(0001) surface, *Phys. Rev. Lett.* (submitted), 1993.
- [2] K.P. Belov, R.Z. Levitin, S.A. Nikitin and A.V. Ped'ko, Magnetic and magneto-elastic properties of Dysprosium and Gadolinium, *Soviet Physics JETP*, 13, 1961, 1096-1101.
- [3] D. Mills, *Phys. Rev. B*, 3, 1971, 3887.
- [4] C. Rau, *J. Magn. Magn. Mater.*, 31-59, 1983, 874.
- [5] C. Rau and S. Eichner, *Phys. Rev. B*, 34, 1986, 6347.
- [6] D. Weller and S.F. Alvarado, Preparation of remanently ferromagnetic Gd(0001), *J. Appl. Phys.*, 59, 1986, 2908.
- [7] D. Weller, S.F. Alvarado, W. Gudat, K. Schröder and M. Campagna, Observation of Surface-Enhanced Magnetic Order and Magnetic Surface Reconstruction on Gd(0001), *Phys. Rev. Lett.*, 54, 1985, 1555.
- [8] R. Wu, C. Li, A.J. Freeman, C.L. Fu, *Phys. Rev. B*, 44, 1991, 9400.
- [9] D. Li, C.W. Hutchings, P.A. Dowben, C. Hwang, R.-T. Wu and M. Onellion, A.B. Andrews and J.L. Erskine, *J. Magn. Magn. Mater.*, 99, 1991, 85.

- [10] D. Li, J. Zhang, P. Dowben, M. Onellion, *Phys. Rev. B*, 1991.
- [11] Dongqi Li, Jiandi Zhang, P.A. Dowben, and M. Onellion, *Phys. Rev. B*, 45, 1992, 7272.
- [12] G.A. Mulhollan, K. Garrison, J.L. Erskine, Surface Magnetism of Gd(0001): Evidence of Ferromagnetic Coupling to Bulk, *Phys. Rev. Lett.*, 69, 1992, 3240-3243.
- [13] H. Tang, D. Weller, T.G. Walker, J.C. Scott, C. Chappert, and H. Hopster, A.W. Pang, D.S. Dessau, and D.P. Pappas, Spin-polarized photoemission study of epitaxial Gd(0001) films on W(110), *J. Appl. Phys.*, 73, 1993, 6769.
- [14] H. Tang, T.G. Walker, H. Hopster, D.P. Pappas, D. Weller, and J.C. Scott, Spin polarization of secondary electrons from Gd(0001), *J. Magn. Magn. Mater.*, 121, 1993, 205-207.
- [15] Dongqi Li, Jiandi Zhang, P.A. Dowben, and K. Garrison, *J. Phys.: Condensed Matter*, 5, 1993, L73.
- [16] Dongqi Li, Jiandi Zhang, P.A. Dowben, K. Garrison, P.D. Johnson, H. Tang, T.G. Walker, H. Hopster, J.C. Scott, and D. Weller, D.P. Pappas, Canted Magnetic Moments at the Gd(0001) Surface, *MRS '93, San Francisco*, April 12-16, 1993 (this proceedings).
- [17] D. Weller, Strukturelle, elektronische und magnetische Eigenschaften von epitaktischen Gd(0001) Filmen auf W(110), *PhD thesis*, 1985 (unpublished).
- [18] F.H. Salas, D. Weller, Magnetization reversal of Gd(0001) thin films: TBIS- and MOKE butterflies in UHV, *J. Magn. Magn. Mater.* (submitted), 1993.
- [19] M. Farle, K. Baberschke, U. Stetter, A. Aspelmeier, and F. Gerhardter, Thickness dependent Curie temperature of Gd(0001)/W(110) and its dependence on the growth conditions, *Phys. Rev. B* (submitted 12/92), 1993.
- [20] U. Stetter, M. Farle, K. Baberschke, W.G. Clark, *Phys. Rev. B*, 45, 1992, 503.
- [21] D. Weller and S.F. Alvarado, *Phys. Rev. B*, 37, 1988, 9911.
- [22] P. Bruno, *Phys. Rev. B*, 39, 1989, 865.

Section A—Multilayers and Surfaces

PART XI

**Magnetic Bilayers, Trilayers
and Multilayers**

MODIFICATION OF MAGNETIC COUPLING IN ANTIFERROMAGNETICALLY COUPLED BILAYERS DUE TO THE EXISTENCE OF FERROMAGNETIC PIN HOLES.

J.F. BOBO, H. FISCHER AND M. PIECUCH

Laboratoire mixte CNRS St Gobain BP 104 54704 Pont à Mousson Cedex France.

ABSTRACT

We have calculated numerical simulations and analytical solutions of the influence of a pin hole on the magnetization curves of multilayer systems. The magnetization curves we obtained can be described by a biquadratic coupling model and are close to the experimental curves.

INTRODUCTION

The growing interest in magnetic coupling between magnetic layers through non magnetic spacers has led in the recent years to several unexpected discoveries like giant magnetoresistance effect [1,2] and biquadratic coupling [3,4]. The question of the origin of this biquadratic coupling remains an open question. Several successful explanations have been proposed for this biquadratic coupling like interface defect [5] or intrinsic band structure effect [6,7]. More recently following the initial remark by Parkin [8] some groups have observed by transmission electron microscopy [9,10] the existence of partial contact between successive magnetic layers, the so called "pin holes". However a detailed study of the magnetic behavior of multilayers or bilayers with this kind of defects is actually lacking, this is the purpose of this paper where we investigate the magnetic properties of bilayers with pin holes.

FORMULATION OF THE PROBLEM

The system we studied is a trilayer consisting of two magnetic layers of thickness t_m separated by a non magnetic layer of thickness t_{nm} . We have considered that the magnetization is the same at each z inside the ferromagnetic layers and that the pinholes are not able to give a perpendicular component of the magnetization and then, that the field is in the plane of the layers. θ_1 and θ_2 are the angles of the magnetizations in the two magnetic layers with respect to H_{app} (in plane applied field). Since the solution is inhomogeneous, θ_1 and θ_2 are function of r , the position in the plane of the layer.

The magnetic energy in each layer is the sum of the Zeeman energy and of the exchange energy (We have neglected the anisotropy energy). The next term is the coupling energy between the two layers. At a particular point r , the sum of these energies can be written:

$$E(r) = At_m(\nabla\theta_1)^2 + At_m(\nabla\theta_2)^2 - H(\cos\theta_1(r) + \cos\theta_2(r)) - J(r) \cos(\theta_1(r) - \theta_2(r)) \quad (1a)$$

A is the usual exchange stiffness parameter, $H = H_{app} M_s t_m$, H_{app} is the external applied field, M_s is the saturation magnetization (per unit volume) and $J(r)$ the value of the magnetic coupling between the two layers at r , $J(r) = -J_c$ (intrinsic antiferromagnetic coupling) at the normal sites and $J(r) = J_h$ at the pinholes ($J_h = 2A/t_{nm}$). We assume a symmetric solution for the two layers $\theta_1 = -\theta_2 = \theta$. Then, the total energy of the system can be written as:

$$E = 2 \int (At_m(\nabla\theta)^2 - J(r) \cos^2\theta(r) - H \cos\theta(r)) d^2r \quad (1b)$$

The demagnetizing and field energy inside the pinhole have been neglected and then equation (1b) is strictly valid for a vanishing concentration of pinholes (but, since the exchange is strong, this approximation is relatively good).

Equation (1b) is difficult to solve and we have slightly modified the problem. We have assumed point like pin holes, writing:

$$J(\mathbf{r}) = -J_i + \sum_h J_h r_h^2 \delta(\mathbf{r} - \mathbf{r}_h) \quad (2)$$

Where $\delta(\mathbf{r} - \mathbf{r}_h)$ is the Dirac delta function and r_h^2 is the size of the pinhole. This expression for the coupling constant leads to nearly the same energy integral as the initial one. The minimization of E with this expression for the coupling constant gives the Euler equation:

$$2A t_m \nabla^2 \theta(\mathbf{r}) = -2J_i \sin \theta(\mathbf{r}) \cos \theta(\mathbf{r}) + H \sin \theta(\mathbf{r}) \quad (3a)$$

With the limiting conditions at each pinhole:

$$-2J_i \sum_j r_{hj} \nabla \theta(\mathbf{r}_h)_j + 2J_h \cos \theta_h \sin \theta_h + H \sin \theta_h = 0 \quad (3b)$$

$\nabla \theta(\mathbf{r}_h)_j$ is the value of the gradient in the hj direction and $J_i = A t_m / r_h^2$. Near the pinhole the gradient of θ is not a continuous function.

The rest of the paper will be divided in two parts, in the first part we have derived an analytical solution for a simplified version of the problem to give some physical insight of the phenomena and in the second part we have solved the problem by numerical simulations on a discrete lattice.

ANALYTICAL SOLUTION

In 1 dimension (and with a regular lattice of linear pinholes distant of d from each other), a first integral of the Euler equation (3a) is immediately obtained:

$$-l_i^2 \left(\frac{d\theta}{dx} \right)^2 + \cos^2 \theta - 2h \cos \theta = C \quad (4a)$$

$$\text{Here: } l_i^2 = \frac{A t_m}{J_i} \text{ and } h = \frac{H}{2J_i} \quad (4b)$$

l_i is the length scale of the problem, C is a constant ($C < 1$), $C = \cos^2 \theta_m - 2h \cos \theta_m$, if $\cos \theta_m$ is the minimum value of $\cos \theta$ where the derivative of θ is zero. The solution of (4) is:

$$\cos \theta = \frac{(1-ab) \operatorname{dn}(y) + (1+ab) \sqrt{1-\mu}}{(1+ab) \operatorname{dn}(y) + (1-ab) \sqrt{1-\mu}} \quad (5a)$$

dn is the delta amplitude Jacobian elliptic function of parameter $\mu = \frac{4ab}{(a+b)^2}$.

$$y = \frac{x - \frac{d}{2}}{l_h} \text{ and } l_h = \frac{2l_i}{\sqrt{(1+c)^2 - h^2} + \sqrt{(1-c)^2 - h^2}} \quad (5b)$$

$$a^2 = \frac{1+c-h}{1-c+h}, b^2 = \frac{1-c-h}{1+c+h} \text{ and } c^2 = h^2 + C = (\cos \theta_m - h)^2 \quad (5c)$$

Equation (3b) is used for the determination of the remaining constant c (or C), this gives (with the use of (4a)):

$$c^2 = (\cos \theta_h - h)^2 - \lambda^2 \sin^2 \theta_h (\cos \theta_h + h_0)^2 \quad (6a)$$

$$\text{with } \lambda = \frac{l_i}{l_0} = \frac{J_h r_h}{2J_i l_i}, l_0 = \frac{2At_m}{r_h J_h} = \frac{l_m l_{nm}}{r_h} \text{ and } h_0 = h \frac{J_i}{J_h} = \alpha h \quad (6b)$$

$\cos\theta_h$ is the value of $\cos\theta$ at the pinhole. The true solution of the problem is the solution of (6a) which has the lowest energy. One may write the energy per unit surface e as :

$$e = (1-c_h)e_{\text{layer}} + c_h e_{\text{pin}} \quad (7a)$$

$$e_{\text{pin}} = - (2(J_h - J_i)\cos^2\theta_h + 8J_i h \cos\theta_h + 2J_i C) \quad (7b)$$

$$e_{\text{layer}} = 4J_i (<M^2> - 2h<M>) - 2J_i \cos^2\theta_m + 4J_i h \cos\theta_m \quad (7c)$$

c_h is the concentration of pinholes, $c_h = r_h/d$. Formula (7c) clearly shows the physics of the calculations: we have the energy of the magnetic moments in the field, $-4J_i h <M>$, the antiferromagnetic coupling energy, $2J_i <M^2>$ and the energy difference between the existing solution and a constant solution corresponding to the maximum angle: $\Delta e = 2J_i (<M^2> - \cos^2\theta_m) - 4J_i h (<M> - \cos\theta_m)$ which is the exchange energy in the layers.

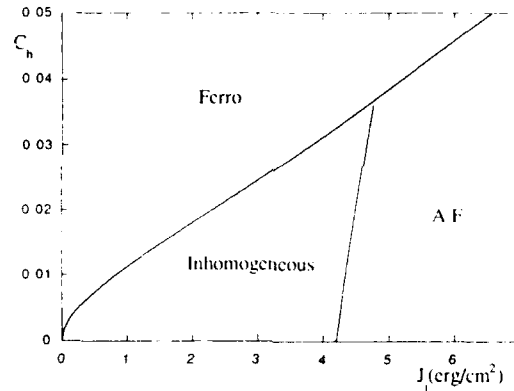


Figure 1: Phase diagram for $r_h = 2 \text{ \AA}$, $t_{nm} = 4 \text{ \AA}$ and $t_m = 13 \text{ \AA}$.

Equation (6a) always has two basic solutions:

a) $c = 1-h$, which gives $\mu = 0$ and $\text{dn}(y)=1$ for all y . ($\cos\theta_h = \cos\theta_m = 1$). This is the ferromagnetic solution of energy:

$$e = 2J_i(1-c_h) - 2J_h c_h - 4J_i h \quad (8)$$

b) $c=0$, which gives $\mu = 1$ and θ_h is given by:

$$(\cos\theta_h - h)^2 - \lambda^2 \sin^2\theta_h (\cos\theta_h + \alpha h)^2 = 0 \quad (9)$$

This solution corresponds to infinitely separated pinholes for which $\cos\theta_m = h$. In this case $\cos\theta$ is expressed simply in terms of hyperbolic functions.

These solutions can be compared for $h=0$. In that case, equation (9) has two solutions (if h is not zero, equation (9) has only one solution). These solutions are either $\cos\theta_h = 0$ or $\sin\theta_h = 1/\lambda$. The first solution gives $c=0$ (this is the normal antiferromagnetic solution). The energy of the other solution can also be calculated analytically and one may derive the concentration of pinholes where the various solutions are stable. Then, one obtains a phase diagram between J_i and c_h at $h=0$ for the stability of these three phases if the size of the pinholes and the different thicknesses are fixed (we have five parameters for the problem but only three are unknown, J_i the intrinsic antiferromagnetic coupling, c_h the concentration of pinholes and r_h their size). Such a diagram is depicted in figure 1. This diagram is a good starting point for the understanding of the solutions under field. The situation is trivial if the ferromagnetic solution is stable (low J_i or high c_h) since in that case the ferromagnetic solution is obviously the most stable also under applied field. The situation is also relatively simple in the case when the inhomogeneous solution is stable at zero field (low J_i and low c_h), since the exact solution under field is also obtained for a very low c and is relatively close to the $c=0$ solution. The situation is a little bit more complicated for the case when the stable solution in zero field is the antiferromagnetic one (high J_i and low c_h) since this solution is no longer valid at non zero field. But, there exists, in that case, a solution with finite c which tends to the antiferromagnetic solution at $h=0$ and this solution remains the lowest energy solution. The magnetization curves can be calculated and are relatively different in the two later cases. Some calculated magnetization curves are presented in figure 2 for the phase diagram of figure 1. One can see the different behaviors of the curves according to the location of the points in the phase diagram. When the inhomogeneous solution is stable at zero field we have a magnetization which starts at a non zero value and tends to 1 at a field lower than the theoretical saturation field (curves a and b of figure 2). When the antiferromagnetic solution remains stable at zero field the magnetization starts at zero and then has a marked curvature with the field and finally saturates slowly (curves c and d of figure 2).

Two others interesting points can be emphasized: First, one can always fit the curves with a biquadratic coupling model. Some examples of such fits are presented in figure 3. The fits are rather good but the fitted values of J are always lower than the real ones, this can be one of the reasons of the low values of J deduced from the experiments. Second, as there exists different solutions for the spatial distribution of the magnetic moments some hysteresis is expected.

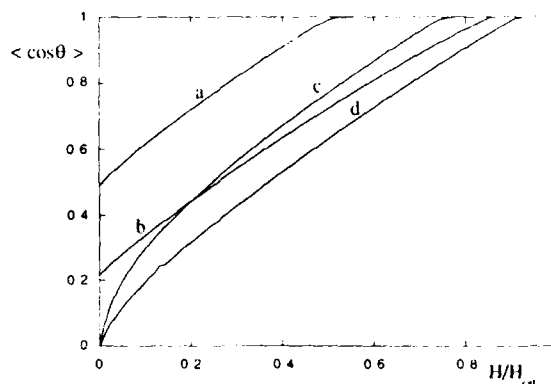


Figure 2: Magnetization curves with the following parameters:

$r_h = 2\text{\AA}$, $t_{nm} = 4\text{\AA}$ and $t_m = 13\text{\AA}$.
 a) $c_h=0.02$ $J=4$ b) $c_h=0.01$ $J=3$ c) $c_h=0.02$ $J=6$ d) $c_h=0.01$ $J=6$

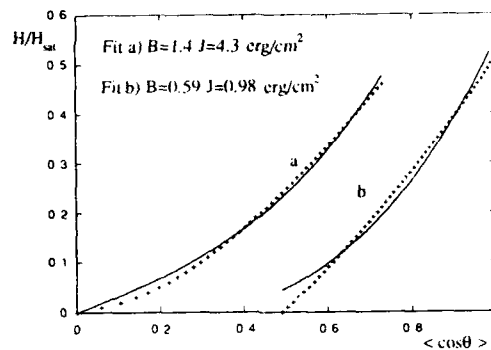


Figure 3: Biquadratic coupling fits of 2 theoretical curves:

$$r_h = 2\text{\AA}, t_{nm} = 4\text{\AA} \text{ and } t_m = 13\text{\AA}.$$

$$a) c_h = 0.02 \text{ J}=6 \text{ b) } c_h = 0.02 \text{ J}=3$$

NUMERICAL SIMULATION

The continuous formula (1b) can be discretized by a finite element method as:

$$e = \frac{E}{S} = -2J_0 \sum_{ij} \cos(\theta_i - \theta_j) + \sum_{i \neq h} 2J_i \cos^2 \theta_i - \sum_h 2J_h \cos^2 \theta_h - \sum_i 2H \cos \theta_i \quad (10)$$

S is the surface of the unit cell in the finite element lattice (the size of the pinholes must be greater than the size of the mesh). The i sites are the ordinary sites where an antiferromagnetic interaction is present and the h sites are the pinholes. J_0 is the ferromagnetic exchange interaction in the layers ($J_0 = At_m/S$). Numerical simulations have been carried out using equations (10). We have taken, again, a periodic repartition of pinholes with a square 2 dimensional lattice. We have used the relaxation method, as described by Arrot et al.[11] to reach the equilibrium configuration. Such a configuration is shown in figure 4 where the pin holes are represented by grey columns. These calculations give simple magnetization curves. Some of them are shown in figure 5, where we have used the same parameters as in the phase diagram of figure 1. One can see that the results qualitatively agree with the simple one dimensional model.

CONCLUSION

We have demonstrated that a simple model of ferromagnetic coupling through pin holes can give a qualitative description of the observed magnetization curves in multilayers. The competition of the local ferromagnetic coupling and of the normal antiferromagnetic coupling leads to inhomogeneous repartitions of the magnetic moments when the concentration of pin holes is weak and can give ferromagnetic alignment when the concentration of such defects is high. The existence of these defects tends also to reduce the apparent value of the antiferromagnetic coupling constant and may be one of the reasons of the discrepancy between theoretical and experimental values of the coupling constant.

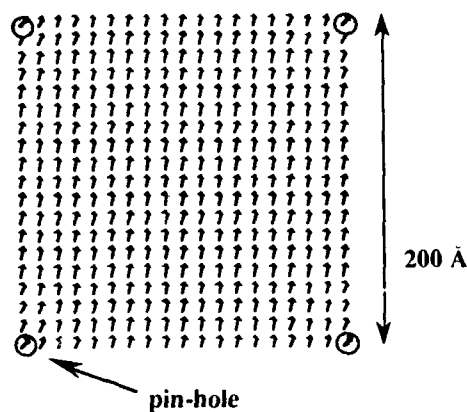


Figure 4: Spatial distribution of the magnetic moments at zero field for one typical case.

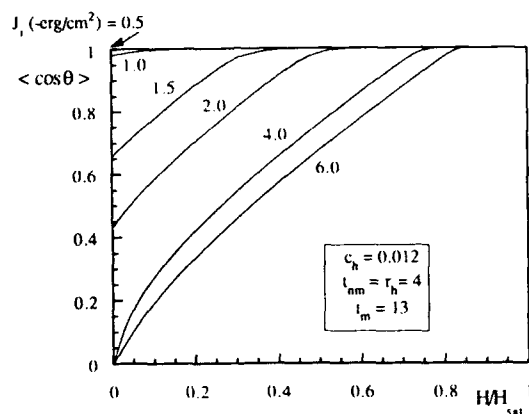


Figure 5: Magnetization curves deduced from the numerical simulations.

References:

1. M.N. Baibich, J.M. Broto, A. Fert, F. Nguyen Van Dau, F. Petroff, P. Etienne, G. Creuset, A. Friederich, G. Chazelas, Phys. Rev. Lett. , **61**, 2472 (1988)
2. S.S.P. Parkin N. More and K.P. Roche Phys. Rev. Lett. **61**, 2472 (1990)
3. P. Grünberg, S. Demokritov, A. Fuss, R. Shreiber, J.A. Wolf and S.T. Purcell, JMMM **104-107**, 1734 (1992).
4. S. Andrieu et al these proceedings.
5. J.C. Slonczewski ,Phys. Rev. Lett , **67** , 3172 (1991)
6. D. Stoeffler Thesis University of Strasbourg (1992)
7. D.M. Edwards, J.M. Ward and J. Mathon to be published (1993)
8. S.S.P. Parkin, Z. G. Li, D.J. Smith Appl. Phys. Lett. **58**, 2710 (1991)
9. N. Mliki and G. Nihoul private communication
10. J.F. Bobo, M. Piecuch and E. Snoeck JMMM in press (1993)
11. A.S. Arrot and B. Heinrich JMMM **93**, 571 (1991)

NEW BCT IRON PHASE IN (100) FeIr SUPERLATTICES

S. ANDRIEU*, J. HUBSCH**, M. PIECUCH*, L. HENNET*, H. FISCHER*

* Laboratoire mixte CNRS-St GOBAIN, 54704, Pont-à-Mousson France

** Laboratoire de Cristallographie, Univ. Nancy I, 54506, Vandoeuvre France

ABSTRACT:

In this paper, the synthesis of a new structure of iron in (100) FeIr superlattices grown by Molecular Beam Epitaxy is reported. Two-dimensional growth up to 4 planes at 400K occurs, as shown by RHEED oscillations. Electron diffraction also gives evidence that the Fe lattice is pseudomorphic to the Ir one during the 2D-growth, and relaxes to the bcc lattice for thicker deposits. An X-Ray analysis shows that the Fe structure is a body centered tetragonal one with a c/a ratio close to 1.25. This phase is observed to be non-magnetic at room temperature, as a weak ferromagnetic behaviour is observed at low temperatures, except at small Ir thicknesses. This is the evidence of the existence of a low spin phase which seems to undergo a second order phase transition with the atomic volume of iron.

INTRODUCTION:

The heteroepitaxy of metals is now usually realised using the Molecular Beam Epitaxy (MBE) technique. The synthesis of 3d metals in new crystallographic structures is thus possible. This opens a new field: the experimental study of the correlation between the structure and the magnetic behavior. Indeed, a comparison of the structures between 3d (magnetic) and 4d or 5d (non-magnetic) metals indicates that the magnetic behavior is probably responsible for the anomalous structures in the 3d series. Between the systems which have been studied up to now, the epitaxy of 3d metals on square lattices seems to be particularly interesting since the growth of tetragonal structures is possible. Indeed, in (100) Co/Cu [1], Cu/Pd [2] and Mn/Pd [3], the mismatch between the interatomic distances leads to body centered tetragonal (bct) structures with c/a ratio different from 1 (bcc) and $\sqrt{2}$ (fcc). In the case of Fe, three systems were studied ((100) FeCu [4], FePd [5] and FeNi [6]) but a largely tetragonized structure was only observed for the FeNi one. The magnetic properties are thus difficult to carry out since Ni is also magnetic. The main goal of this study is to synthesized Fe in a bct phase and to determine its magnetic properties. We want to travel along the Bain path in order to see if there exists some magnetic transition versus the iron volume and (or) the c/a ratio. The choice of Ir as a substrate is motivated by the fact that its distance between first neighbours in the (100) plane (2.715Å) is located between those of bcc (2.866Å) and fcc (around 2.5Å at RT) Fe. We thus expect to be able to vary the volume and c/a ratio and to record the existence and the nature of the magnetic transition.

EXPERIMENTAL RESULTS:

The epitaxies are performed in a MBE chamber with vacuum in the range of 10^{-10} torr. An Ir buffer layer of 200Å is firstly realised at 500°C on (100) MgO substrates. Ir is evaporated by an e-gun at 0.5 Å/s, and Fe using a Knudsen cell heated up to 1350°C at around 0.1 Å/s. RHEED oscillations are thus recorded during the Fe growth, but not during the Ir one since the magnets of the e-gun disturb the e-beam of the RHEED apparatus. The FeIr superlattices (SL) are realised at 100°C in order to avoid interdiffusion. The Fe and Ir thicknesses varied from 2 to 30Å. Transmission Electron Microscopy (TEM) [7] is also used to determine the quality of the SL. A 2-circles θ -2 θ X-Ray diffraction apparatus (XRD) is used to determine the period of the SL and the average distance between planes.

SQUID measurements are performed from 5 to 300K with applied fields from 0 to 40 kOe. As the MgO substrates are found to be paramagnetic, the total system MgO+SL is firstly

measured, and a second measurement is performed on the same MgO substrate after the elimination of the SL by HCl. The difference between both measurements gives the $M(T)$ diagram of the SL.

The surface of the Ir buffer layer grown on MgO is arranged in a 5×1 reconstruction, typical of a bulk like material with a flat and clean surface [7], as confirmed by TEM. This superstructure disappears after Fe deposition, and does not reappear during the growth of the SL. A square surface lattice is observed and remains for unlimited Fe thickness. RHEED oscillations are observed up to more than 10 planes at around 250K and 4 planes at 400K [8]. These oscillations are commonly understood via a layer by layer growth. The growth of Fe on Ir (100) is thus two-dimensional (2D), without interdiffusion since the period of the oscillations is constant. The measurement of the distance between streaks on RHEED pattern shows that Fe is firstly pseudomorphic to the Ir lattice up to around 5 planes at RT and rapidly relaxed to its bcc structure. This shows that several kinds of SL can be obtained [8], but here we are only interested by the pseudomorphic regime.

The distance d_{Fe} between Fe planes in the growth direction can be easily obtained using thickness calibration and RHEED oscillations. The Fe thickness divided by the number of oscillations directly gives $d_{Fe} = 1.70 \pm 0.05 \text{ \AA}$ (if we consider a monoatomic layer by layer growth). This value is confirmed by XRD. Indeed, the principal SL peak corresponds to an average distance $\langle d \rangle$ between Ir and Fe planes as (e_{Fe} is the Fe thickness):

$$\langle d \rangle = \frac{e_{Fe}d_{Fe} + e_{Ir}d_{Ir}}{d_{Fe} + d_{Ir}} \quad (1)$$

Assuming in a first approximation that the distances between planes d_{Fe} and d_{Ir} do not vary with e_{Fe} and e_{Ir} , i.e. are constant from one SL to another, these distances can thus be simply determined using the technique described in ref.9. We find $d_{Fe} = 1.70 \pm 0.05 \text{ \AA}$ in total agreement with the RHEED determination. As the in plane distance given by RHEED is close to the 2.715 \AA Ir distance, and the in plane structure is a square lattice, the Fe structure is a bcc one with a c/a ratio close to 1.25. Moreover, assuming that Ir is infinitely rigid (not strained by Fe) and a uniform in plane stress without out of plane one, the in and out of plane strains ϵ_{xx} and ϵ_{zz} are related by:

$$\epsilon_{zz} = \left(\frac{-2\nu}{1-\nu} \right) \epsilon_{xx} \quad \text{i.e.} \quad \frac{d_{Fe}}{d_0} - 1 = \left(\frac{-2\nu}{1-\nu} \right) \left(\frac{a}{a_0} - 1 \right) \quad (2)$$

where a is the in plane distance, a_0 and d_0 the parameters of the original unstrained cubic Fe phase. As the poisson ratio is always close to 0.3, the equation (2) gives a bcc parameter of 3.08 \AA and a fcc one of 3.6 \AA . This clearly shows that the obtained bcc Fe phase is a distortion of the fcc Fe one.

A more realistic elastic modeling can however be proposed. We now consider that the whole SL is in elastic equilibrium, i.e. Fe and Ir are strained by each other. We thus assume that the in plane parameter is constant all over a SL but is not equal to Ir one since Ir is not infinitely rigid. We neglect the influence of the substrate (at the end of the buffer epitaxy, Ir is actually relaxed). The total elastic energy is the sum of the buffer, N Fe and N Ir layers contributions as:

$$E_n = (A \cdot \epsilon_{xx}^2)_{Ir} (e_b + N e_{Ir}) + (A \cdot \epsilon_{xx}^2)_{Fe} (N e_{Fe}) \quad (3)$$

where e_i is the thickness of i (buffer, Ir or Fe layers) and $A = E/(1-\nu)$ with E the Young modulus. The in plane parameter is thus calculated by minimizing this energy. The out of plane d_{Fe} and d_{Ir} distances are thus calculated using equation (2) and $\langle d \rangle_{th}$ using equation (1). As shown on the figure 1, the calculated and experimental values are in very good agreement using a parameter of the original fcc Fe phase of 3.55 \AA .

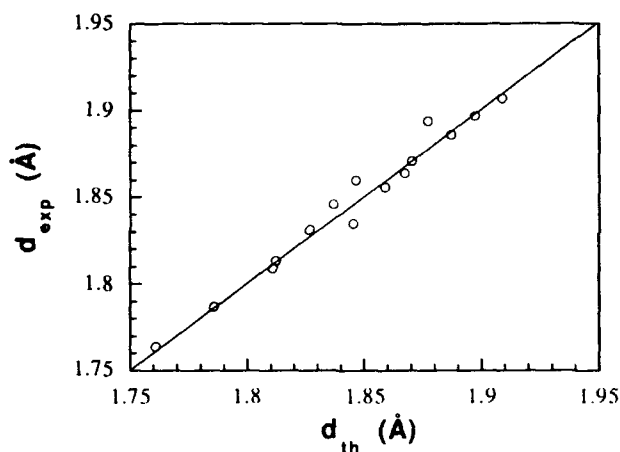


Figure 1 : experimental and theoretical values of the average parameter in the superlattices.

The magnetic hysteresis loops show that this bct Fe structure is not magnetic at RT. A small moment was detected in preliminar experiments [8] but probably comes from magnetic impurities in the MgO substrates. Ferromagnetic loops appears at room temperature when the Fe thickness is greater than 4 planes corresponding to the relaxation in the bcc structure [8].

SQUID measurements are thus performed on a series of SL with $e_{Fe}=4ML$. Typical ferromagnetic $M(T)$ curves (Fig.2) are measured except for the small Ir thickness (3\AA) where a C/T law is observed with $C=0.18 \pm .05$ K (Fig.3). Moreover, the moment extrapolated at $0K$ varies with the iridium thickness and is small (from 0 to $0.8 \mu_B$). Consequently, we have used the equation of states of a weak itinerant ferromagnet to fit the experimental results. The results of the magnetization measurements and of the fits are summarized in table I. T_C and m are deduced from the weak itinerant ferromagnetic fits, p_s from the magnetization at $5K$. θ is deduced from the paramagnetic fit above T_C and p_c from the corresponding Curie constant. $M(H)$ curves at $100K$ are also shown on figure 5.

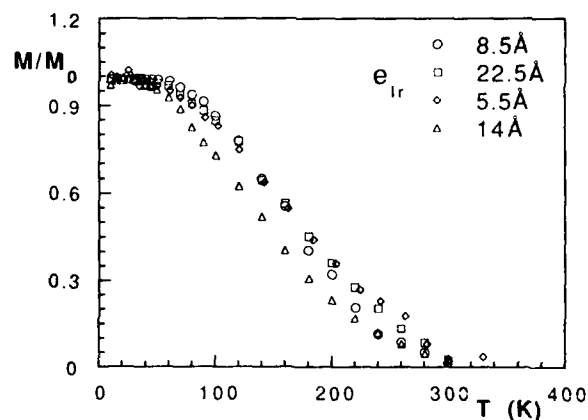


Figure 2: Thermomagnetic curves for several superlattices with a constant iron thickness of 4 ML and various iridium thickness

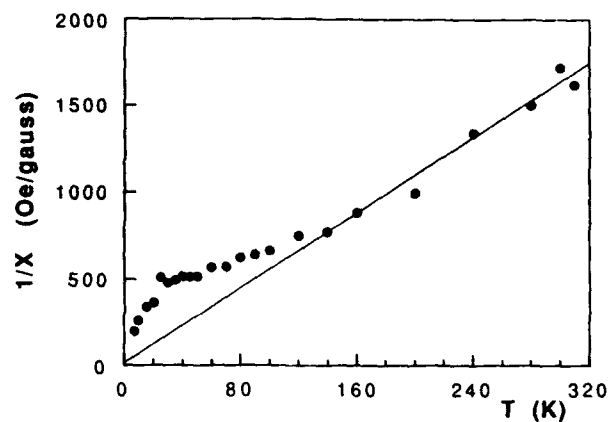


Figure 3 : Reciprocal susceptibility versus temperature for a superlattice with the same iron thickness as the preceding ones but with an iridium thickness of 3 Å.

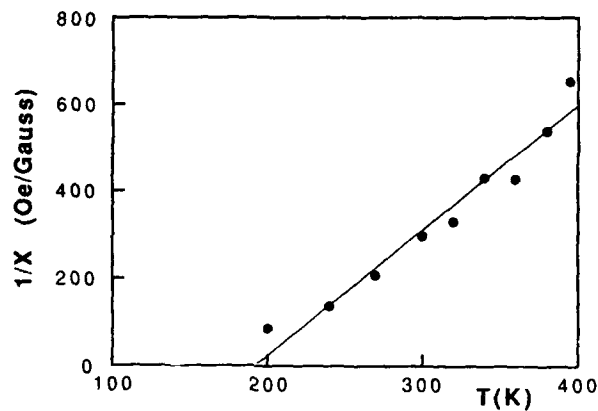


Figure 4 : $1/\chi$ (T) curve for $e_{Ir}=8.5\text{Å}$. The line gives a Curie constant of 0.33 K.

Ir.thick. (Å)	Fe atomic volume (Å ³)	c/a	m Bohr mag.	p_s Bohr mag.	p_c Bohr mag.	T_c K	θ K
3	11.87	1.28	0	0.02	2.3	0	0
5.5	11.91	1.26	0.20 ± 0.02	0.25	2.5	125 ± 43	170
8.5	11.95	1.25	0.36 ± 0.02	0.38	3.5	155 ± 40	185
14	11.98	1.23	0.28 ± 0.04	0.41	2.5	85 ± 38	160
22.5	12.00	1.23	0.71 ± 0.03	0.82	2	145 ± 35	160

Table 1 : Magnetic properties of the measured superlattices (see text).

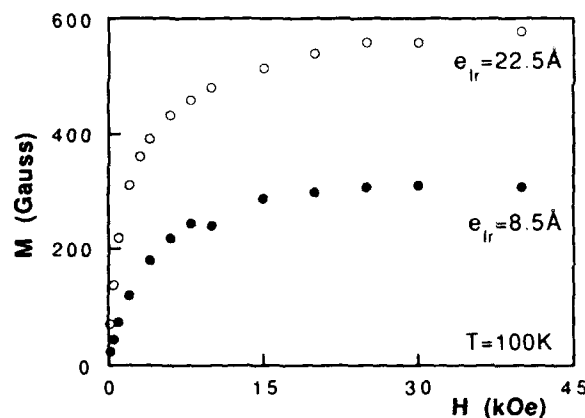


Figure 5 : magnetization curves (H : 40 to 0 kOe) at 100K

DISCUSSION

Several comments can be made on these results. The first one is that the ratio of the iron moment deduced from the Curie constant of the susceptibility p_c and of the iron saturation magnetic moment p_s is large, as expected from the universal Rhodes Wohlfarth correlation [10]. However, the agreement between the experimental data and the weak itinerant ferromagnetic fits is rather poor (which explains the large uncertainty on T_c) and a better determination of T_c and p_c is necessary to compare our results with Rhodes Wohlfarth curve. Moreover, the Curie temperature do not follow a regular law with the iridium thickness and calculated iron volumes, which may be due to the interlayer coupling which oscillate relatively fast in iridium [11]. Moreover, an increase of p_s (magnetic moment at zero temperature) is observed when the Ir thickness is increased. The natural explanation of this increase is the increasing stress imposed by Ir. In that way, d_{Fe} varies with the Ir thickness. On figure 6 is plotted the value of the iron magnetic moment versus the atomic volume of iron calculated using the elastic modeling presented before.

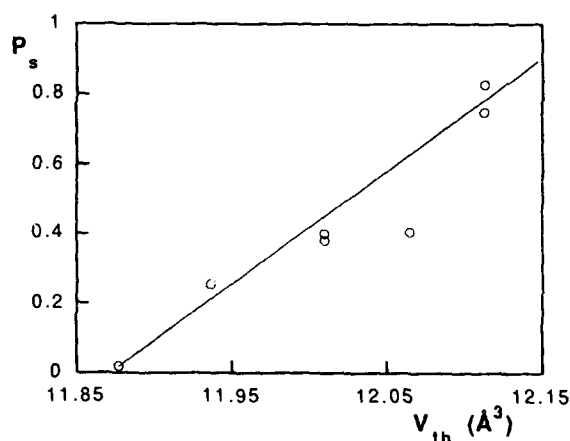


Figure 6 : Variation of the average magnetic moment per Fe atom with the theoretical Fe volume calculated using the elastic modeling.

This is the central result of this paper and the first evidence of a real low spin phase corresponding to a second order phase transition when the iron volume increases. The value of the iron atomic volume corresponding to this transition is close to the theoretical predictions where the critical atomic volume is around 12\AA^3 . However, the phase transition is predicted to be first order and two phases may exist with an iron magnetic moment between 0.02 and 0.1 Bohr magnetons for the first one and between 0.5 and 1.2 Bohr magnetons for the second one [12,13].

CONCLUSION

In conclusion, we have for the first time synthesized a weak ferromagnetic bct Fe structure with a c/a ratio close to 1.25. Such a low spin ferromagnetic Fe state is predicted by theorists [11,12] but has rarely been observed. It is also demonstrated that this bct structure does not result from an elastic deformation of the bcc phase, but rather from the fcc one. However, a paradox appears : if this bct phase is the strained fcc one, why does Fe relax to the bcc structure? Finally, this bct phase is a typical weak itinerant ferromagnet at low temperature, except at small Ir thickness. The variation of the iron magnetic moment with the iron atomic volume seems to indicate a second order transition.

References:

- 1- J.J. de Miguel, A. Cebollada, J.M. Gallego, R. Miranda, C.M. Schneider, P. Schuster, J. Kirschner, J. Magn. Magn. Mat., **93**, 1 (1991)
- 2- H.Li, S.C.Wu, D.Tian, J.Quinn, Y.S.Li, F.Jona, P.M.Marcus, Phys. Rev. B, **40**, 5841 (1989)
- 3- D.Tian, S.C.Wu, F.Jona, P.M.Marcus, Solid State Commun., **70**, (1989), 35
- 4- H.Magnan, D.Chandesris, B.Villette, O.Heckemann, J.Lecante, Surf. Sci., **251/252**, 597 (1991) and ref. therein
- 5- J.Quin, Y.S.Li, H.Li, D.Tian, F.Jona, P.M.Marcus, Phys. Rev. B, **43**, 3959 (1991)
- 6- S.H.Lu, Z.Qwang, D.Tian, H.Li, F.Jona, P.M.Marcus, Surf. Sci., **221**, 35 (1989)
- 7- M.Hallouis, S.Andrieu, M.Piecuch, Electron Microscopy, **2**, 759 (1992),
- 8- S.Andrieu, M.Piecuch, H.Fischer, J.F.Bobo, F.Bertran, PH.Bauer, M.Hennion, J. Magn. Magn. Mat., **121**, 30 (1993)
- 9- S.Andrieu, M.F.Ravet, O.Lenoble, V.Dupuis, M.Piecuch, S.Pizzini, F.Baudelet, A.Fontaine, Europhys. Lett., **18**, 529 (1992)
- 10- P.R. Rhodes, E.P. Wohlfarth Proc. R. Society **273**, 247 (1963)
- 11- S. Andrieu, M. Hennion, M. Piecuch, these proceedings
- 12- V.L.Moruzzi, P.M.Marcus, K.Schwarz, P. Mohn, Phys. Rev. B, **34**, 1734 (1986)
- 13- N. E. Christensen, G. Gunnarsson, O. Jepsen and O.K. Andersen, J. Phys. (Paris) C8, **49**, 17 (1988)

SPIN CONFIGURATIONS AND THE DYNAMIC RESPONSE OF ANTIFERROMAGNETICALLY COUPLED SYSTEMS

F.C. Nörtemann, R.L. Stamps, and R.E. Camley
Department of Physics, University of Colorado at Colorado Springs, Colorado Springs, CO
80933-7150

ABSTRACT

We present a calculation of spin waves in coupled multilayered structures which is based on exact evaluation of both exchange and dipolar fields. The ground state spin configuration in antiferromagnetically coupled multilayers can differ significantly from the uniformly canted ground state usually assumed. This non-uniform ground state is found to radically alter the character of the spin wave modes and sometimes lead to a strong localization of the wave to the outermost magnetic films of the multilayer.

I. INTRODUCTION

The discovery of antiferromagnetic coupling between ferromagnetic films across nonmagnetic layers [1] has raised several important questions and resulted in a number of exciting potential applications. Even though the actual spin configuration often plays a very important role in the most interesting properties of these systems [2-4], to date theoretical investigations [5-7] of giant magnetoresistance and dynamic response of antiferromagnetically coupled systems have assumed only the simplest possible magnetic ground states.

In a recent paper [8], we showed that multilayered systems of antiferromagnetically coupled films will have complicated groundstates that are strongly field dependent. Some of these groundstates are quite different from the groundstate assumed by previous theoretical studies of these systems. In the present work we discuss the effects of the correct groundstate on the linear dynamic magnetic behavior of multilayer systems.

In this paper we present a microscopic calculation of spin wave frequencies in magnetic multilayer structures which makes no restrictions on the allowed ground state magnetic configurations. We will use this model to discuss the effects of complicated ground states on spin wave frequencies and characteristics.

II. THEORY

The geometry of the multilayer is shown in Fig. 1. The axis of the multilayer lies along the y direction, an external applied magnetic field H_0 is directed along the z axis and the magnetizations in each layer lie in the xz plane some angle α from the z axis. The magnetic layers are identified by the integer n and the angle α for the magnetization of each layer by the

subscript n . The number of atomic layers in each magnetic film is N and there are a total of L magnetic layers in the multilayer. The number of atomic layers in each non-magnetic film is N_s . For simplicity we assume that the lattice is simple cubic with spacing a . For future reference, we also define a wavevector q that lies in the xz plane at an angle ϕ from the z axis.

We now review the important features of the ground state configurations. If $|\alpha_n|$ were independent of position then the magnetization of each film would be canted away from the applied field direction by an amount α given by

$$\cos \alpha = -g\mu_B L N H_0 / 4(L-1)J_i \quad (1)$$

Here J_i is the interlayer exchange energy, g is the g factor and μ_B is the Bohr magneton. The strength of this field decreases when the thickness, or number of atomic layers N , of the magnetic films is increased. Note that the sign convention is such that a negative J_i denotes antiferromagnetic coupling. In the remainder of this paper we refer to this angle α as the "bulk" canting angle. This ground state configuration is sketched in Fig. 2a. The arrows represent the net magnetization in each magnetic film. Here the magnetization of each film is canted away from the direction of the field by the angle α calculated according to Eq. (1).

A canted state where every canting angle is given by Eq. (1) is not stable for a finite multilayer [8]. The reason is that in a finite multilayer the outermost films experience only half the interlayer exchange coupling compared to a film inside the multilayer. Because of competition between antiferromagnetic exchange and Zeeman energies, it is energetically favorable to rotate the outermost magnetizations away from the bulk angle given by Eq. (1) in such a way as to lower the net Zeeman energy for the entire structure.

The lowest energy stable states are somewhat complicated and strongly dependent on the

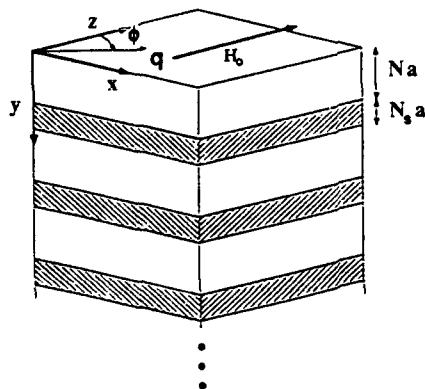


Figure 1. Geometry for the multilayer.

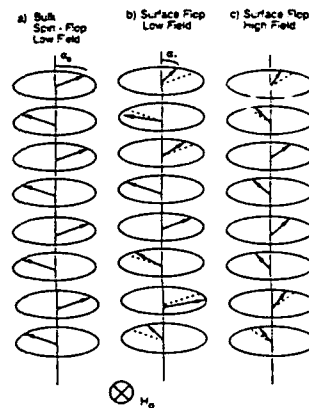


Figure 2. Spin configurations. The uniform "bulk" state is depicted in (a). Nonuniform canted states are shown for low fields in (b) and high fields in (c).

magnitude of the external applied field. These states are depicted in Fig. 2b for small field strengths and in Fig. 2c for larger field strengths. The dotted lines are the bulk α given by Eq. 1 for large L . At high fields, the angles α_n of the outermost spins are less than the bulk α . For low fields, the size of the angles alternate with respect to the bulk α from layer to layer. Note that the equilibrium magnetizations all lie in the field direction for fields greater than $4J/g\mu_B$.

The largest angular deviations from the bulk value occurs for magnetizations in the outermost layers. We find that modes which are localized to the outermost layers are the most strongly affected by the nonuniform canting [9].

We now examine the magnetostatic spin waves for the groundstates shown in Fig. 2. Our theory includes both dipolar and exchange interactions. As in the above discussion, all layer dependent variables are indexed by the integer n . The spins are treated as point dipoles arranged in a cubic lattice structure within each film. A Heisenberg exchange interaction is assumed and the spins are also coupled via dipolar interactions. The dipolar interaction appears in the Hamiltonian as a sum over all lattices sites r :

$$H_{\text{dip}} = (g\mu_B)^2 \sum_{\vec{r}, \vec{r}'} \left[\frac{\vec{S}(\vec{r}) \cdot \vec{S}(\vec{r}')}{|\vec{r} - \vec{r}'|^3} - 3 \frac{(\vec{r} \cdot \vec{S}(\vec{r}))(\vec{r}' \cdot \vec{S}(\vec{r}'))}{|\vec{r} - \vec{r}'|^5} \right] \quad (2)$$

This interaction is long ranged and the sum includes operators S for all spins in the multilayer system.

The equations of motion are calculated from the complete Hamiltonian including a Zeeman energy term due to an external magnetic field H_0 . The long wavelength region is considered where the spin operators can be treated as classical vectors. We are interested in small amplitude excitations so we first linearize the equations of motion. This is accomplished by separating the spin variables into a static part $S(r)$, and a dynamic part $s(r,t)$. Terms of second order in $s(r,t)$ are then neglected in the equations of motion. Plane wave solutions are assumed for $s(r,t)$ and the static part is written as S_n . The particular choice of groundstate enters through the angle α_n as

$$\vec{S}_n = \hat{x} S \sin \alpha_n + \hat{z} S \cos \alpha_n \quad (3)$$

The resultant linearized equations of motion for spins within a film are:

$$\begin{aligned}
 -i\hbar\omega\vec{s}_n = & \vec{s}_n \times \left[g\mu_B (\hat{z}H_0 + \vec{H}_a) + 4J\vec{S}_n + J_{n,n-1}\vec{S}_{n-1} + J_{n,n+1}\vec{S}_{n+1} \right] \\
 & + \vec{S}_n \times \left[g\mu_B \vec{h}_n(\vec{q}) + 2J\vec{S}_n (\cos q_1 a + \cos q_2 a) + J_{n,n-1}\vec{S}_{n-1} + J_{n,n+1}\vec{S}_{n+1} \right]
 \end{aligned}
 \tag{4}$$

Here a is the lattice spacing within a film. The exchange constant $J_{n,m}$ is defined as $J_{n,m} = J$ when n and m are in the same magnetic film; $J_{n,m} = J_i$ when n and m are the outermost layers of neighboring magnetic films; $J_{n,m} = 0$ when n or m is an outermost layer of the multilayer. The dipolar terms are contained in \vec{H}^S and $\vec{h}(\vec{q})$. Fields which are independent of \vec{q} are written in \vec{H}^S and \vec{q} dependent dipolar fields are written in $\vec{h}(\vec{q})$. Both of these fields can be written in terms of \vec{s}_n and \vec{S}_n as rapidly convergent sums [10].

The complete set of coupled equations of motion define a large but straightforward eigenvalue problem. The calculational procedure is as follows: Low temperatures are assumed and the ground state is found using a numerical mean field approach which gives the angles α_n [8]. Next the eigenvalue problem is solved for the eigenfrequencies ω and eigenvectors.

III. RESULTS

The general features of the allowed spin wave modes are most simply illustrated by first examining spin wave propagation assuming the uniform groundstate defined by Eq. (1). Unless otherwise specified, we use the following parameters in all the examples presented in this paper: $N/N_s=2$, $L=10$, $J=10 \text{ J cm}^2$, $J_i=0.001 \text{ J cm}^2$, $qa=0.001$ and $\phi=90^\circ$. The results are given in terms of unitless variables Ω and h which are proportional to the frequency and applied field strength.

The uniform ground state is not stable and some spin wave modes will soften at certain applied field strengths. This can be seen in Fig. 3 where the lowest ten spin wave frequencies are shown as functions of applied field assuming a uniform canted ground state. The spins are canted for fields less than $h=1$ and aligned in the field direction for fields above $h=1$. In Fig. 3 we see that a mode softens for an h near 0.85 and reappears at $h=1$. This gap where the mode disappears indicates that the uniform groundstate is not stable for h values near 1. Finally, the mode labeled 10 is the Damon-Eshbach mode for this structure.

Spin wave frequencies are shown in Fig. 4 as functions of applied field for the stable groundstates shown in Fig. 2b and 2c. Propagation is again perpendicular to the field. At small fields, the groundstate is similar to that of Fig. 2b and at fields near $h=1.0$ the ground state is similar to that of Fig. 2c. For $h>1$, all the spins are aligned in the direction of the field.

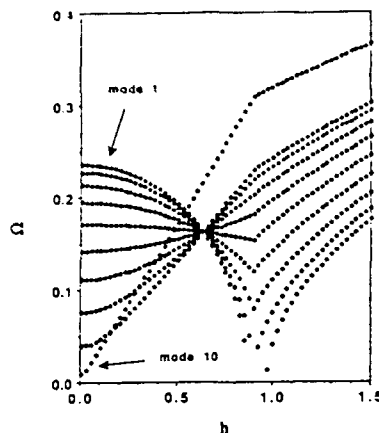


Figure 3. Spin wave frequency functions of field for the uniform state of Fig. 2(a).

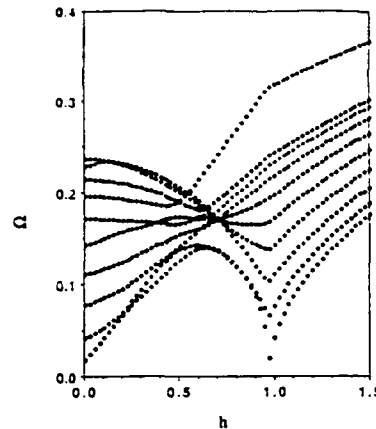


Figure 4. Spin wave frequencies as functions of field for the nonuniform canted states of Fig. 2(b,c).

The main difference between the spin wave frequencies in the nonuniform groundstate and those in the uniform ground state is that there is a great deal of mode mixing. This is clearly seen in Fig. 4 for h near 0.5 where the Damon-Eshbach mode passes through the band of bulk modes. The reason for this is that the symmetry of the structure has been significantly lowered. For example it is no longer possible to define a small unit cell for a groundstate configuration. Here the entire structure is the unit cell. As a result, modes which were orthogonal to one another in the uniform structure are now mixed and mode repulsion is observed. Note that with the correct ground state there is a mode softening at $h=1$ where the magnetization changes from perfectly aligned to canted.

A dramatic example of how the finite structure induces mode mixing is found when the frequencies are studied as functions of wavevector q . In Fig. 5, the uniform ground state is assumed and the frequencies are shown as functions of q . Propagation is perpendicular to the

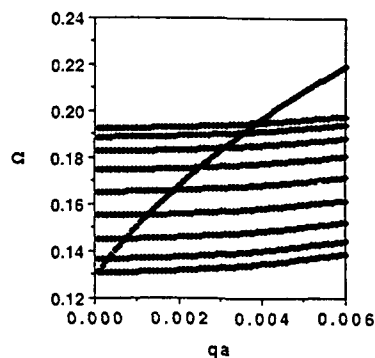


Figure 5. Spin wave frequencies as functions of q for the uniform canted state of Fig. 2(a).

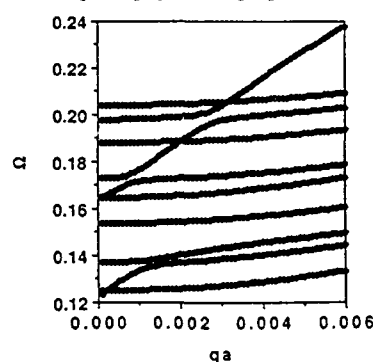


Figure 6. Spin wave frequencies as functions of q for the nonuniform canted states of Fig. 2(b,c).

field ($\phi=90^\circ$). The applied field is $h=0.5$ so that the spins are canted away from the applied field direction. The Damon-Eshbach mode is the most strongly dispersive of the spin wave modes and rises through the band of bulk modes with increasing q . Note that there are no mode repulsions visible on this scale.

In Fig. 6, the frequencies are again shown as functions of wavevector but with the groundstates shown in Fig. 2b and 2c. The applied field is $h=0.5$ as in Fig. 5. Here there are large repulsions as the Damon-Eshbach mode crosses through the spin wave band. This is due to the mixing of modes caused by the nonuniform groundstate.

In conclusion, we have studied the allowed spin wave modes of a finite multilayer with a non-periodic spin configuration. The nonuniform ground states lower the symmetry of the magnetic structure and lead to a large mixing of modes. This mixing appears as gaps in the spin wave dispersions as the Damon-Eshbach mode crosses through the spin wave band.

ACKNOWLEDGEMENTS: This work was supported by the US Army Research Office under Grant No. DAAL0391-G-0229.

REFERENCES:

1. P. Grünberg, R. Schreiber, Y. Pang, M. B. Brodsky and H. Sowers, *Phys. Rev. Lett.*, **57**, 2442 (1986)
2. M. N. Baibich, J. M. Broto, A. Fert, F. Nguyen Van Dau, F. Petroff, P. Etienne, G. Creuzet, A. Friederich, and J. Chazelas, *Phys. Rev. Lett.* **61**, 2472 (1988)
3. G. Binasch, P. Grünberg, F. Saurenbach, and W. Zinn, *Phys. Rev. B* **39**, 4828 (1989)
4. S. S. P. Parkin, N. More, K. P. Roche, *Phys. Rev. Lett.* **64**, 2304 (1990)
5. R. E. Camley and J. Barnas, *Phys. Rev. Lett.* **63**, 664 (1989)
6. P. M. Levy, S. Zhang and A. Fert, *Phys. Rev. Lett.* **65**, 1643 (1990)
7. A. Vedyayev, B. Dieny and N. Ryzhanova, *Europhys. Lett.* **19**, 329 (1992)
8. F. C. Nörtemann, R. L. Stamps, A. S. Carriço, and R. E. Camley, *Phys. Rev. B* **46**, 10847 (1992)
9. F. C. Nörtemann, R. L. Stamps and R. E. Camley, to appear in *Phys. Rev. B*
10. H. Benson and D.L. Mills, *Phys. Rev.* **178**, 839 (1969); R.P. Erickson and D.L. Mills, *Phys. Rev. B* **43**, 10715 (1991); R.P. Erickson and D.L. Mills, *Phys. Rev. B* **44**, 11825 (1991)

MAGNETIZATION LOOPS IN Fe/Ag/Fe/Ni(001) STRUCTURES

B. HEINRICH* Z. CELINSKI* H. KONNO*[†] A. S. ARROTT*
M. RÜHRIG** AND A. HUBERT**

*Physics Department, Simon Fraser University, Burnaby, BC, Canada, V5A 1S6

**Institut für Werkstoffwissenschaften der Universität Erlangen-Nürnberg,
Martensstr. 7, D-91058 Erlangen, Germany

ABSTRACT

The lattice reconstructed bcc Ni(001) in Fe/Ni(001) ultrathin layers allows one to engineer films in which the in-plane 4-fold anisotropies and coercive fields can be varied and adjusted according to specific requirements. Magnetization reversals have been studied in layered structures of Fe/Ag/Fe/Ni(001). For Ag(001) interlayers thicker than 13 ML magnetization reversal can proceed in two steps. In these samples the minor loops switch the magnetization of the Fe(001) layer from the parallel to the antiparallel configurations with respect to the magnetic moment of the Fe/Ni film. Such minor loops exhibit a rectangular behavior with switching fields of 15-25 Oe. The lattice transformed Fe/Ni layers could be useful in spin-valve structures.

INTRODUCTION

Ni can be grown epitaxially on Fe(001). The first 3 monolayers (ML) follow the bcc stacking with the same lateral spacing¹ and the same vertical relaxation² as is observed for Fe(001). After reaching a critical thickness, 3-5 ML, the Ni overlayers transform gradually into a more complicated structure^{2,3,4}. The transformed "bcc Ni" exhibits the same main features of the Reflection High Energy Electron Diffraction (RHEED) patterns along the {100} and {110} azimuths as the Fe(001), but the RHEED patterns corresponding to {110} azimuths show in addition a weak diffraction streak. The additional superlattice streaks are also visible for azimuths away from the {100} and {110} directions. Their complicated angular dependence and SEXAFS⁵ studies by Jiang et al. indicate that the Ni transformation is a rather severe distortion of the basic bcc Ni(001) structure. "bcc Ni" overlayers grown on Fe(001) form a unique structure having magnetic properties which are truly different from those observed for bcc Fe(001) and pure bcc Ni(001).

FMR measurements played a crucial role in determining the magnetic properties of both the pure bcc and lattice transformed Fe/Ni(001) bilayers^{2,6}. The magnetic moment in Fe/Ni bilayers measured by FMR was significantly greater than that of the Fe layer whether the added layer was the pure bcc Ni(001) or the lattice transformed "bcc Ni". The saturation magnetizations of both forms of bcc Ni, ~5 kG, are nearly as large as in fcc Ni⁶. This is in agreement with calculations by Moruzzi and Marcus⁷. The presence of pure bcc Ni does not affect the 4-fold in-plane anisotropy of the Fe(001) layer. However, the lattice transformed "bcc Ni" showed remarkable magnetic properties^{2,4,6}. The 4-fold anisotropies observed in lattice transformed Fe/Ni bilayers far exceeded those observed in regular 3d transition metals and their alloys; e.g., $2K_1/M_s = 2.33$ kOe in a bilayer with 6 ML of Fe and 15 ML of Ni (6Fe/15Ni) compared with 0.55 kOe for bulk Fe.

A clue as to the origin of the large in-plane anisotropies was found from measurements of the angular dependence of the FMR linewidth³. ΔH exhibited a linear dependence on microwave frequency with a zero frequency offset $\Delta H(0)$, as is usual³. The linear slope corresponding to the intrinsic Gilbert damping was found to be isotropic, as it is in all 3d transition metals, but the $\Delta H(0)$ term was found to have a strong angular dependence. The zero-frequency FMR linewidth $\Delta H(0)$ is caused by crystallographic faults generated, in this case, during the Ni overlayer transformation. The angular dependences of the in-plane resonance field and the FMR linewidth follow each other very closely³. This strongly indicates that they have a common origin.

The crystallographic defects created during the Ni layer transformation likely form a network which satisfies the observed in-plane 4-fold symmetry. The electron orbital momentum is quenched in cubic structures and therefore the contribution of the spin-orbit interaction is weak. The situation changes along crystallographic defects where the orbital quenching is lifted. This results in an enhanced spin-orbit interaction and consequently an increased magnetic anisotropy.

It is remarkable that the crystallographic defects triggered by the lattice transformation of metastable bcc Ni can result in well defined 4-fold anisotropies and can be used to engineer new types of magnetic materials.

The defect structure which leads to an increased value of the 4-fold in-plane anisotropy also increases the coercive field of Fe/Ni films. By changing the ratio between the Fe and Ni thicknesses, the coercive field can be adjusted over the range of 2-300 Oe. This feature can be employed in ultrathin trilayers which consist of two magnetic layers separated by a nonmagnetic layer. The purpose of this paper is to demonstrate that by a suitable choice of the individual Fe and Ni layer thicknesses one can create ultrathin structures in which the switching from the parallel to the antiparallel configuration occurs in low magnetic fields. In this paper only results for Fe/Ag/Fe/Ni structures are presented

EXPERIMENTAL RESULTS AND DISCUSSION

Fe/Ni layers were formed by covering a 6 ML Fe(001) film on a Ag(001) substrate with one of several thicknesses (10-18 ML) of lattice transformed "bcc Ni". The hysteresis loops, observed using the longitudinal Magneto-Optical Kerr Effect (MOKE), see details in ref. [8], were rectangular as shown in Fig. 1 for the field along an easy {1,0} axis. The coercivities were much larger than those of single layers of Fe. Single layers of 10 ML of Fe show quite rectangular loops with coercivities of only a few Oe (1-3 Oe).

Sandwiches of Fe, Ag and Fe/Ni were formed by starting with a single 10 ML Fe film grown on a Ag(001) bulk substrate. Then a non-magnetic interlayer of Ag(001) using one of several thicknesses between 10 and 18 ML were grown epitaxially on the Fe. The second ferromagnetic layer, Fe/Ni, was formed next by depositing a 6 ML Fe(001) film which was covered by lattice transformed bcc Ni(001) of a chosen thickness between 10 and 18 ML. All structures were covered by a 20 ML epitaxial Au(001) layer for protection.

For very weakly coupled Fe and Fe/Ni layers one would expect that the magnetization reversal starts in the Fe layer at a slightly negative field which is close to its coercive field. At this field the magnetic moment of the Fe/Ni layer would maintain the direction of the previously applied positive field. The reversal of the magnetic moment in the Fe/Ni layer (complete magnetization reversal) is then expected to occur at a field which is close to the coercive field of the Fe/Ni layer. The magnetization reversal in Fe/Ag/Fe/Ni films depends strongly on the individual layer thicknesses, e.g., the samples showed only simple rectangular magnetization loops for the thinner Ag(001) interlayers. In such cases the coupling between layers is sufficiently strong that the magnetic moments in Fe and Fe/Ni layers maintain their orientation parallel to each other during the process of magnetization reversal. They reverse their orientation together at a field which is between the Fe and Fe/Ni coercive fields. The measured coercive field, 40 Oe, is almost independent of the Ag interlayer thickness between 10 and 13 ML for the structures with a 10Fe layer and a 6Fe/13Ni layer, see Fig.2.

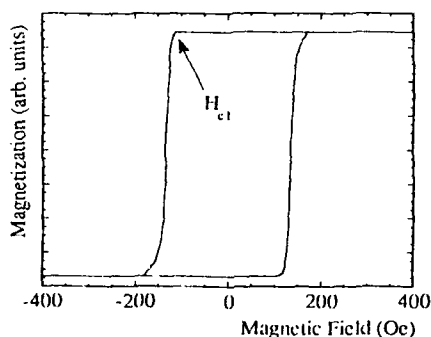


Fig. 1. Hysteresis loop for a 6Fe/15Ni sample along the easy axis {10}. The integers before the elements indicate the number of monolayers (ML).

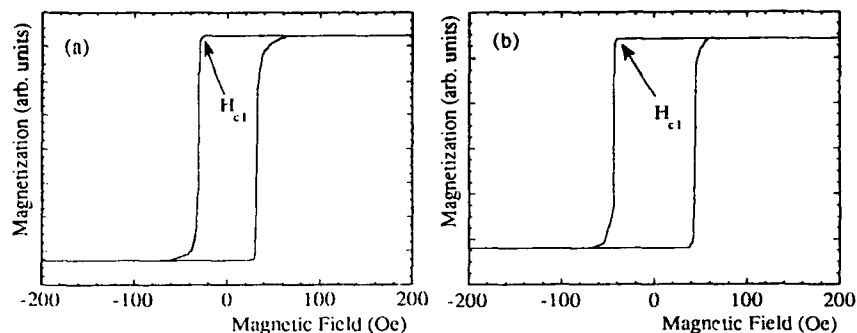


Fig. 2. Hysteresis loops for (a) 10Fe/13Ag/6Fe/13Ni and (b) 10Fe/10Ag/6Fe/13Ni.

The exchange coupling between Fe layers separated by Ag(001) interlayers thicker than 7 ML, when grown at 300 K, is no more than 0.004 ergs/cm² as deduced from FMR⁹. This is too small to account for a 40 Oe coercivity. Therefore the interlayer coupling between Fe and Fe/Ni layers in these samples is not due to the exchange coupling alone but it is caused by the magnetostatic interactions, most likely originating in the lattice defects and the interface roughness of the Fe/Ni and the interface roughness of the Fe layers.

For strong coupling between the Fe and the Fe/Ni layers, the measured coercivity can be related to the coercivity of the individual layers by

$$H_c = \frac{M_{Fe} H_{cFe} + M_{FeNi} H_{cFe/Ni}}{M_{Fe} + M_{Fe/Ni}} \quad (1)$$

where M_{Fe} and $M_{Fe/Ni}$ represent the total magnetic moments in the Fe and Fe/Ni layers, respectively, and H_{cFe} and $H_{cFe/Ni}$ are their respective coercive fields. If one assumes³ that the magnetic moment per Ni atom is 0.5 μ_B then putting the measured value of $H_c=40$ Oe for 10Fe/13Ag/6Fe/13Ni, see Fig. 2, in Eq. 1 gives $H_{cFe/Ni}=80$ Oe. This value is reasonably close to the coercive field for a single 6Fe/13Ni film, $H_c=100$ Oe, found by interpolation. This shows that the coercivity of the Fe/Ni layer is not changed appreciably by inclusion in the sandwich.

For thicker Ag(001) interlayers one can obtain magnetization loops in which the magnetization reversal proceeds in several steps. The crossover from simple hysteresis loops (exhibiting one single magnetization reversal) to more complicated magnetization reversals which involves several distinct steps depends very strongly on the thickness of the Ni layer. Samples with 18 ML Ni (10Fe/13Ag/6Fe/18Ni) show a well defined two step magnetization reversal, see Fig. 3, while samples with 13 ML Ni (otherwise identical structure) show a simple magnetization reversal, see Fig. 2. Films with 13 ML Ni in the Fe/Ni layer require at least 15 ML of Ag(001) to exhibit a multistep magnetization reversal, see Fig. 4.

At this point one would like to identify the process in which the magnetic moments reverse their orientation in reverse applied fields. For the two step magnetization process one expects that the reversal proceeds in very simple manner. At the first critical field, $H_{c1}=20$ Oe, the Fe layer orients antiparallel to the Fe/Ni magnetic moment, see Fig. 3. It takes then a larger field, the second critical field H_{c2} , to reverse the magnetic moment of the Fe/Ni layer. The total magnetic moment after the first magnetization reversal process, at H_{c1} , should be given by the difference $M_{Fe/Ni} - M_{Fe}$. The magnetic moments in 10Fe/13Ag/6Fe/18Ni are expected to be close, $M_{Fe}=M_{Fe/Ni}=22 \mu_B$ (per row of atoms). Therefore one expects to observe a nearly zero magnetic moment at H_{c1} . Fig. 3 shows that the total moment after the first jump at H_{c1} is only 1/10 of the fully saturated sample. This is close to zero. In fact one should expect a slightly positive magnetic moment at H_{c1} since the Kerr effect signal of the Fe layer is partly attenuated by the Ag and Fe/Ni layers.

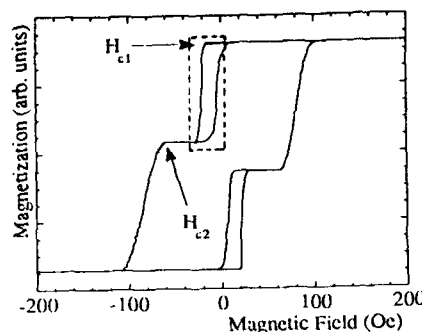


Fig. 3. Magnetization reversal for a 10Fe/13Ag/6Fe/18Ni sample. The minor loop is shown in the dashed frame. Note that below H_{c1} and above H_{c2} the total magnetic moment is close to zero.

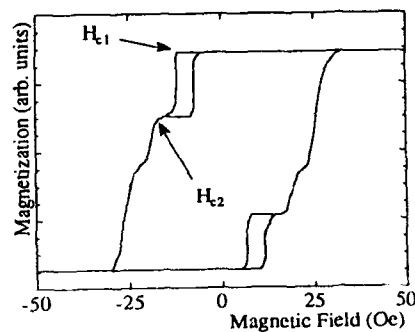


Fig. 4. Magnetization reversal for a 10Fe/15Ag/6Fe/13Ni sample. Note two jumps at H_{c1} and H_{c2} . Only after the second jump the total magnetic moment is close to zero.

The critical field $H_{c1} = 20$ Oe is larger than the coercivity of the Fe layer. This is the effect of the coupling between the Fe layer and the Fe/Ni layer, which one can estimate using the formula

$$J_{AB} = -H_{c1} M_s d, \quad (2)$$

where J_{AB} is the effective layer-layer coupling per unit area, M_s is the magnetization of Fe and d is the thickness of the Fe layer. This leads to $J_{AB} \sim 0.005$ ergs/cm² which is close to that deduced from FMR in Fe/Ag/Fe(001) structures⁹ with comparable Ag thicknesses.

Minor loops, see Fig. 3, show that one can reverse the magnetic moment of the Fe layer with respect to that of the Fe/Ni layer by cycling a small applied field of ~ 18 Oe. This is larger than the coercive field of the individual 10 ML Fe layer. This difference is caused, most likely, by pinning effects of the magnetostatic fields from the Fe/Ni layers.

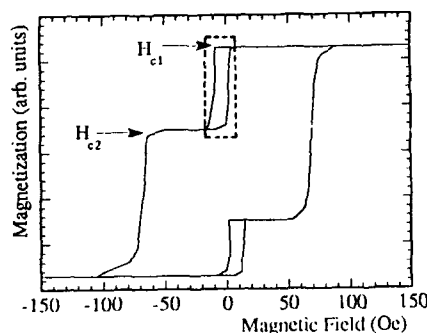


Fig. 5. Magnetization loop of a 10Fe/18Ag/6Fe/13Ni sample. The minor loop is shown in the dashed frame. Note that after the first magnetization reversal (H_{c1}) the total magnetic moment is well above zero.

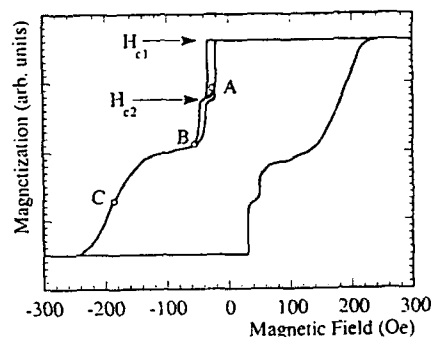


Fig. 6. Magnetization loop of a 10Fe/15Ag/6Fe/18Ni. Note that only after the second magnetization reversal step at H_{c2} the MOKE measurement shows the total magnetic moment to be close to zero.

Even in the case of a two step magnetization reversal process, the magnetic moment in the Fe layer does not have to be oriented *entirely* in the direction antiparallel to the Fe/Ni magnetic moment, see Fig. 5. The total magnetic moment at H_{C1} in Fig. 5 is not close to zero. Here the magnetic moment at H_{C1} was expected to be negative because $M_{Fe/Ni} - M_{Fe} \sim -2 \mu_B$ (per row of atoms). The large positive magnetic moment at H_{C1} indicates that only some parts of the Fe layer reversed their magnetic moments with respect to the Fe/Ni layer. In fact many samples exhibited three step magnetization reversal processes, see Fig. 6. It is the second magnetization reversal step at H_{C2} , see Fig. 6, which leads to the total magnetic moment close to zero.

By using high resolution Kerr microscopy¹⁰, the formation of magnetic domains at various applied fields could be observed, see Fig. 7. The measured contrast allowed identification of all three important magnetic configurations. The two extreme shades correspond to fully saturated regions in which the magnetic moments in the Fe and Fe/Ni layers are parallel. The white regions show domains oriented parallel to the forward applied magnetic field; the dark regions show domains oriented parallel to the reversed magnetic field. In the grey regions the magnetic moment of the Fe layer is antiparallel to the magnetic moment of the Fe/Ni layer. Fig. 7a shows that at the first critical field H_{C1} (the first step in magnetization reversal) a large portion of the Fe layer remains parallel to the moment of the Fe/Ni layer. At the second critical field, H_{C2} , only a small fraction of the Fe layer remains parallel to the Fe/Ni magnetic moment. Thus in this sample the interlayer coupling is mostly distributed around two values which determine the critical fields H_{C1}

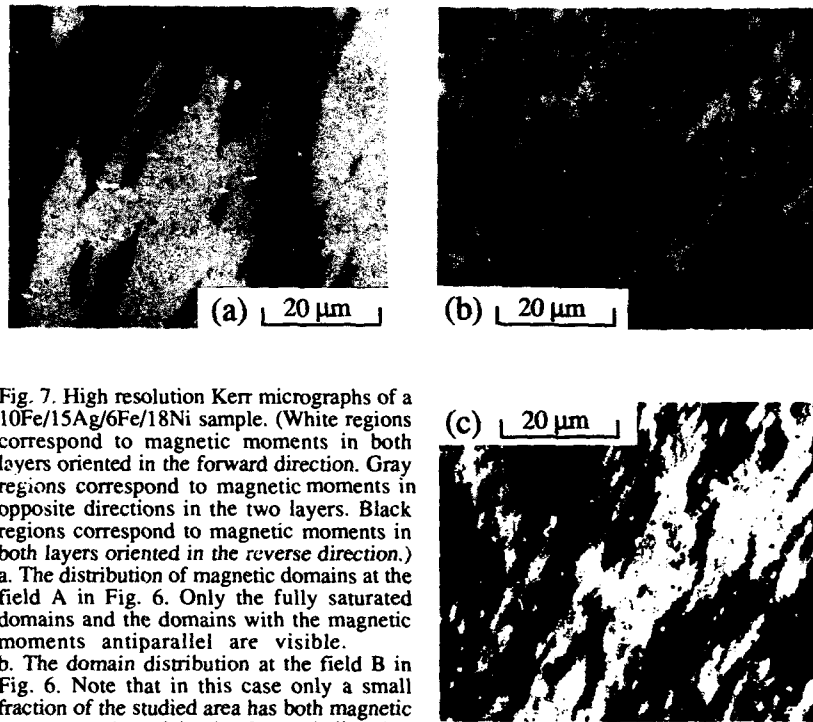


Fig. 7. High resolution Kerr micrographs of a 10Fe/15Ag/6Fe/18Ni sample. (White regions correspond to magnetic moments in both layers oriented in the forward direction. Gray regions correspond to magnetic moments in opposite directions in the two layers. Black regions correspond to magnetic moments in both layers oriented in the reverse direction.) a. The distribution of magnetic domains at the field A in Fig. 6. Only the fully saturated domains and the domains with the magnetic moments antiparallel are visible. b. The domain distribution at the field B in Fig. 6. Note that in this case only a small fraction of the studied area has both magnetic moments oriented in the forward direction (white).

c. The Kerr micrograph for the field C in Fig. 6. The dark domains correspond to completely reversed magnetic moments. Note that some small regions of the sample are still oriented in the forward direction.

and H_{c2} . Figs. 7b and 7c show that even at the fields between H_{c3} and H_{c2} some small regions (5-10 μm wide) are still oriented along the Fe/Ni layer. The interlayer coupling is varying from place to place; small parts of this sample exhibit appreciable spread in its strength.

CONCLUSIONS

We have shown that Fe/Ag/Fe/Ni(001) ultrathin structures can exhibit well-defined magnetization loops in which the magnetization reversal starts in the Fe layer only. Several distinct hysteresis loops were identified. Domain wall nucleation and subsequent domain wall propagation plays an important role in the magnetization reversal of the Fe layer. Fe/Ag/Fe/Ni structures exhibit interlayer coupling that arises partially from magnetostatic interactions between the Fe/Ni and Fe layers. This coupling is comparable in strength to exchange couplings seen in Fe/Ag/Fe structures. Variations in the effective coupling from region to region result in multistep magnetization reversals. The Kerr micrographs show that these variations are on the lateral scale of 10-100 μm . One can obtain also samples in which the Fe layer magnetic moment can be reversed in a single step. In these samples the magnetic moment of the Fe layer can be switched from the parallel to the antiparallel configuration with respect to the magnetic moment of Fe/Ni layer by cycling applied fields of the order of 15 to 25 Oe. The low switching fields in these structures should make these films (when grown on semi-insulating substrates) attractive in applications using the Giant Magnetoresistance effect.

ACKNOWLEDGMENT

The authors would like to thank to the National Research Council of Canada for its financial support.

REFERENCES

+ Visiting Scientist from NEC Corporation, Kawasaki, Kanagawa, 211 JAPAN

1. B. Heinrich, A. S. Arrott, J. F. Cochran, C. Liu and K. Myrtle, *J. Vac. Sci. Technol.* A4 1376 (1986).
2. Z. Q. Wang, Y. S. Li, F. Jona and P. M. Marcus, *Sol. St. Comm.* 61, 623 (1987).
3. B. Heinrich, S. T. Purcell, J. R. Dutcher, K. B. Urquhart, J. F. Cochran and A. S. Arrott, *Phys. Rev. B* 38, 12879 (1988).
4. B. Heinrich, J. F. Cochran, A. S. Arrott, S. T. Purcell, K. B. Urquhart, J. R. Dutcher and W. F. Egelhoff, Jr, *Appl. Phys.* A49, 473 (1989).
5. D. T. Jiang, N. Alberding, A. J. Seary, B. Heinrich, and E. D. Crozier, *Physica B* 158, 662 (1989).
6. B. Heinrich, A. S. Arrott, J. F. Cochran, K. B. Urquhart, K. Myrtle, Z. Celinski and Q. M. Zhong, *Mat. Res. Soc. Symp. Proc.* 151, 177 (1989).
7. V. L. Moruzzi and P. M. Marcus, *Phys. Rev. B* 38, 1613 (1988).
8. B. Heinrich, J. Kirschner, M. Kowalewski, J. F. Cochran, Z. Celinski and A. S. Arrott, *Phys. Rev. B* 44, 9348 (1991).
9. Z. Celinski, B. Heinrich and J. F. Cochran, *J. Appl. Phys.* 73, (1993), in press.
10. A. Hubert and M. Rühlig, *J. Appl. Phys.* 69, 6072 (1991).

Section A—Multilayers and Surfaces

PART XII

Magnetic Anisotropy, Magneto-optics

Magneto Optical Kerr Spectroscopy as a Probe of Chemical Ordering In CoPt

G. R. Harp, D. Weller, T. A. Rabedeau, R. F. C. Farrow, and R. F. Marks
IBM Almaden Research Center, 650 Harry Rd., San Jose, CA 95120-6099

Abstract

We demonstrate that the photon energy dependence of the polar Kerr effect can be used as a sensitive probe of chemical ordering effects in binary intermetallic alloys. We demonstrate this effect in the $\text{Co}_{50}\text{Pt}_{50}$ alloy, which is known to have a L_{10} phase (critical temperature $\sim 825^\circ\text{C}$). Kerr spectra of the ordered and disordered phases of the $\text{Co}_{50}\text{Pt}_{50}$ alloy composition differ drastically from each other and the ordered phase shows an unprecedented, new peak at 2.2eV photon energy. The intensity of this new peak correlates with the degree of chemical ordering and the magnetic anisotropy in these films.

1 Introduction

Magneto-optical spectroscopy has attracted renewed attention as a powerful spin-polarized electronic structure probe in magnetic thin film research. Some of these recent developments include the detection of quantum well states in ultrathin Fe films and multilayers [1] and the observation of chemical environment effects in annealed CoPt alloy films [2]. While other electronic structure probes like spin-polarized photoemission spectroscopy or X-ray magnetic circular dichroism probe more directly either the initial, occupied electron density of states or (even element specifically) the final, unoccupied electronic levels, magneto-optical techniques due to their smaller transition energies (0.5–5.5eV) in general probe a convolution of initial and final states within the valence bands of a material which usually complicates the interpretation of these spectra. On the other hand, neither (ultra-) high vacuum conditions nor synchrotron radiation are required, when measuring magneto-optical spectra, which makes this technique versatile and convenient to use.

In this article, we extend our previous work on the structure dependence of magneto-optical spectra in the Co-Pt intermetallic alloy system [2] and show for the first time that chemical ordering can lead to the development of new "electronic" features in the Kerr spectrum. Near the CoPt composition range, there exists a chemically ordered phase with an order-disorder phase transition temperature of about 850°C . This phase has a site structure corresponding to a tetragonally distorted fcc crystal, where monolayers of pure Co are separated by monolayers of pure Pt along the (001) direction. It is well known that this "natural superlattice" of CoPt has a very large magnetic anisotropy [3], with the (001) axis being the easy axis of magnetization. This motivated our choice of the CoPt system since it is hoped that we might acquire insight to electronic structural origins of magnetic anisotropy.

The other key finding is that we demonstrate how molecular beam epitaxy (MBE) growth of alloys provides a *direct* method for the production of chemically ordered

alloy phases in their thermodynamically equilibrium state. This is because atomic diffusion rates at the growing film surface are higher for a given temperature than bulk interdiffusion rates. Thus, stable alloy phases which are difficult to achieve in the bulk because of kinetic limitations can be fabricated quickly by MBE. In this way, MBE provides a means for the study of a new class of low temperature ordered alloy phases.

Finally we point out that the present work was strongly motivated by the potential use of Co-Pt intermetallic alloys as short wavelength magneto-optical recording materials because of suitable Curie temperatures, large perpendicular magnetic anisotropies and appropriate hysteresis properties in the CoPt[4] and CoPt₃[5, 6] composition range.

2 Experimental

1000Å thick Co₅₂Pt₄₈ films, were simultaneously deposited onto both sapphire(0001) and MgO(001) substrates at 300°C, 500°C and 700°C, following the growth of ~150Å Pt buffer layers at 700°C. This procedure leads to high quality (111) or (001) epitaxial films of the CoPt alloys. Here we shall concentrate on the depositions made in the (001) orientation at 300°C and 500°C, and defer discussion of the other depositions to a future article[7]. The 1000Å alloy thickness was chosen to avoid effects of a possible buffer layer/alloy intermixing zone and/or interference with the substrate itself on the magneto-optical spectra. The deposition chamber was maintained at a pressure $< 4 \times 10^{-10}$ mbar throughout growth. Electron gun sources were used for both Co and Pt, with deposition rates in the range of 0.05–0.2Å/s. The energy dependence of the polar Kerr effect was measured in the presence of saturating magnetic fields using a fully automated, zeroing spectrometer described elsewhere[8], in the photon energy range 0.8–5.3eV at room temperature.

3 Results

Chemical ordering in thin films of CoPt was studied in 1974 by Treves et. al. using co-deposition by a sputtering technique followed by post-growth annealing[4]. Such samples had a {111} texture (using fct miller index designations), so that the CoPt c-axis was tilted 55° from the surface normal, and thus the films had reduced out of plane magnetic anisotropy. This method of sputtering followed by post-growth anneal has been recently revisited by Lairson et. al.[9], where instead of an alloy film, the starting material was a Co/Pt multilayer. The multilayers were deposited on MgO(001) in an attempt to align the c-axis of CoPt with the surface normal and to generate perpendicular magnetic anisotropy. Here we have made a similar attempt to generate CoPt(001) on MgO(001). But in the present case we deposit the films by molecular beam epitaxy (MBE) at elevated temperature, and grow the films *directly* in the ordered phase. Thus, no post-growth annealing is required. The latter technique insures samples of very high quality with regard to crystalline perfection and degree of chemical ordering.

Figure 1 displays a comparison of the specular X-ray diffraction intensity for the CoPt alloys deposited on MgO(001) substrates at 500°C and 300°C. There are distinct

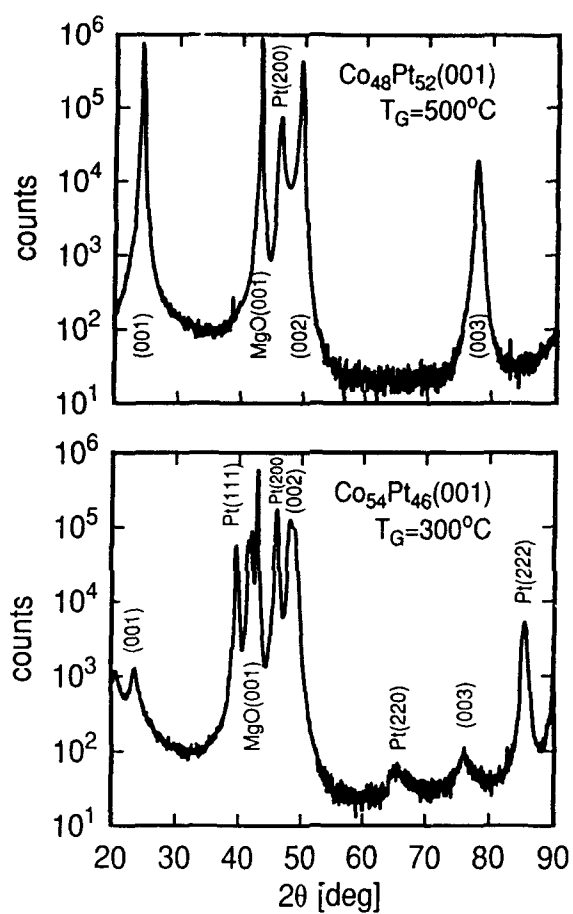


Figure 1: Specular X-ray diffraction intensities of two CoPt(001) films deposited on MgO(001) at (a) 500°C and (b) at 300°C .

differences between their diffracted intensities, which are associated with the presence of chemical ordering in the 500°C film, but not in the 300°C film. In particular, at $\sim 24^\circ$ and $\sim 77^\circ$, we see the (001) and (003) diffraction features. These are forbidden for a disordered fcc alloy but are present in ordered CoPt. These features are present strongly in the 500°C sample but are 2-3 orders of magnitude weaker in the sample deposited at 300°C. At 300°C, the (002) feature at about 49° is split, indicating a superposition of ordered and disordered CoPt. Regarding the extent of the chemical ordering, we estimate that in the 500°C sample the (nominally) pure Co planes of the perfect structure consist of no more than 10% Pt, and vice versa. In contrast to this, we estimate that the 300°C sample contains $<3\%$ of the ordered phase in a disordered matrix. Moreover, for 300°C growth, the (001) and (003) features are shifted slightly to lower angle, relative to the more perfect structure at 500°C. We take this as further evidence of imperfect ordering, that is, the tetragonal distortion which accompanies chemical ordering is not saturated due to intermixing of the Co and Pt layers.

There are a number of other structures which need be identified in these X-ray spectra. For both 300°C and 500°C growth, the MgO(002) and Pt(002) features are strongly evident at $\sim 43^\circ$ and $\sim 47^\circ$, respectively. In the 300°C spectrum, however, the MgO(002) feature shows weaker structures at slightly lower angles. We believe that these structures arise from regions of the substrate which deviate from the 1:1 stoichiometry of MgO. Such features are visible in all MgO substrates (note weak shoulder in the 500°C sample), but with variable intensity. Nucleation on these deviant regions sometimes gives rise to other Pt (and CoPt) orientations such as Pt(111) or (110), and these secondary orientations give rise to scattering features visible in the 300°C sample: Pt(111) and Pt(222) at $\sim 39^\circ$ and $\sim 85^\circ$, and Pt(220) at $\sim 66^\circ$.

The Kerr spectra from these two films are displayed in figure 2. Changes in electronic structure upon ordering give rise to significant changes in the Kerr spectra between these two samples. Firstly we find the uv Kerr rotation strongly enhanced in the ordered phase, which we can take as evidence for the predominant contributions of spin-polarized Pt atoms to the magneto-optical transitions in that spectral range, an effect which is due to the modified Pt-Co coordination in the ordered vs. disordered phase (for details see ref. [2]). The other striking, and so far unprecedented effect is the appearance of a new feature at 2.2eV in the spectrum of the ordered (001) film[10]. This feature has never before been observed in Co-Pt alloys, and we find generally that it is correlated with chemical ordering in CoPt.

We note that neither reflectivity nor direct optical constant measurements indicated the presence of features correlating with the enhanced Kerr rotation around 2.2eV and attribute the observed feature to an enhanced "magneto-optical activity" σ_{xy} . A possible explanation could be a stronger confinement of Co and/or Pt related d-states in the quasi two dimensional superlattice environment, which then accordingly can lead to a large oscillator strength at a transition energy, which in the present case appears to be 2.2eV. Such states should be visible as "localized" d-states, e.g. in photoemission experiments, which could directly confirm this hypothesis.

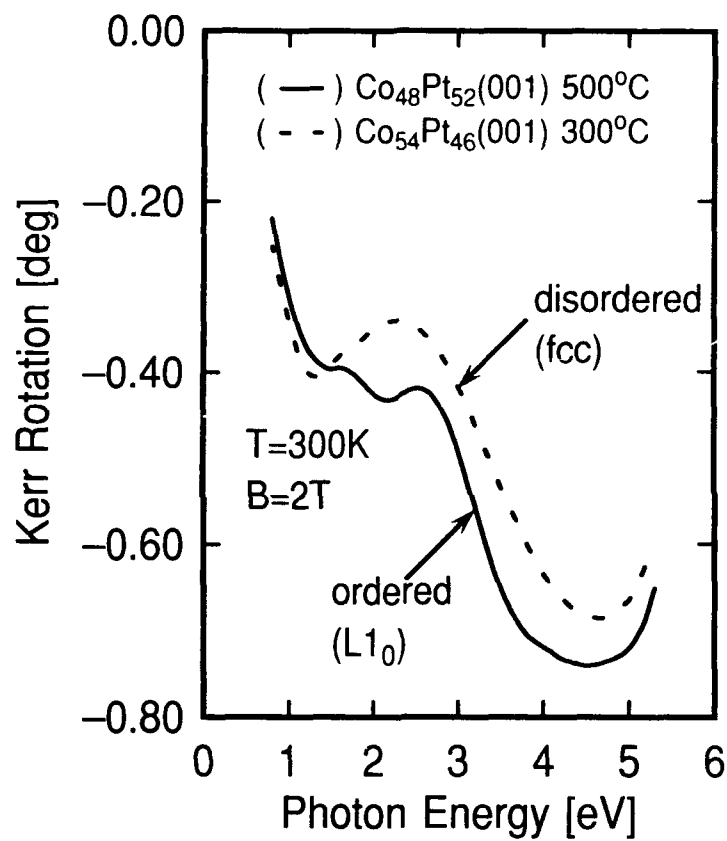


Figure 2: Saturation polar Kerr rotation as a function of photon energy for the two films of the previous figure. This demonstrates how Kerr spectroscopy is sensitive to changes in the local chemical environment in binary alloys.

4 Discussion

This work is distinguished from previous work on CoPt by two important differences. The first is the method of growth, and the second is by the characterization techniques applied. Conventional preparation of chemically ordered alloys involves high temperature annealing to induce bulk diffusion and phase separation. However, high temperatures also lead to alloy disorder, even *below* the order disorder transition. On the other hand, when one lowers the temperature to promote the chemically ordered phase, the rate of diffusion decreases exponentially, so that some ordered phases (e.g. NiFe[11]) may require extremely low cooling rates on cosmological time scales (~ 1 in 10^6 years) for chemical ordering and phase separation below the order-disorder temperature of 320°C .

MBE deposition therefore has an advantage over "bulk" methods in that there is an extra degree of freedom at the developing film surface during growth. Because surface diffusion rates can exceed bulk diffusion rates by orders of magnitude, chemically ordered phases may be established much more easily by MBE than by post-growth annealing techniques. Another advantage of MBE growth is that the surface also introduces an anisotropy axis in the growth of CoPt which is not present in a bulk material. Beginning with a disordered (although crystalline) CoPt alloy, chemical ordering may occur with the *c*-axis aligned along any one of three equivalent axes in the disordered fcc crystal: (100), (010), or (001). However, during MBE growth the (001) axis (surface normal) is clearly inequivalent to the (100) and (010) axes, generating a uniaxial alignment of the *c*-axis in the ordered CoPt phase.

The second important contribution of this work is the demonstration that Kerr spectroscopy is sufficiently sensitive to probe changes in the spin-polarized band structure that accompany chemical ordering and that such changes can be conveniently detected with its use. As mentioned above, Kerr spectroscopy has the advantage of being an *ex-situ* technique, and moreover is no less sensitive to polycrystalline samples than to single crystalline samples (as is e.g. X-ray diffraction).

The Kerr spectrum is directly related to the spin-orbit coupling in electron states involved in the magneto-optical transitions. Likewise is the magneto-crystalline anisotropy a spin-orbit interaction effect and correlations between both measurements have been reported recently[12]. Thus, the energy dependent saturation Kerr rotation may as well give us a window into the important electronic structures which give rise to magnetic anisotropy. We mention that indeed the new structure in the Kerr spectrum at 2.2eV in CoPt is directly correlated with the onset of magnetic anisotropy in this system, and we shall discuss this point in more detail in a forthcoming publication. In order to better understand the microscopic mechanisms which lead to the observed drastic changes in the magneto-optical spectra, first principles band structure and magneto-optical calculations are currently being pursued[13, 14].

5 Conclusion

We have fabricated CoPt films in the (001) orientation on MgO(001) at various temperatures. We find that growth at 500°C leads to highly chemically ordered ($>90\%$) films

of the $L1_0$ phase with the c-axis perpendicular to the film surface. Growth of a similar film at 300°C gives rise to a film which is almost completely disordered. The saturation polar Kerr rotation was measured as a function of photon energy and shows significant differences for these two films. In particular, a new feature at 2.2eV was observed in the chemically ordered CoPt film. Thus changes in spin-polarized band structure which occur upon chemical ordering can be tracked using Kerr spectroscopy. Drawing and analogy with the field of semiconductors, we believe that Kerr spectroscopy can play a crucial role in magnetic film characterization similar to that of photoluminescence spectroscopy of semiconductor films. Both techniques are exquisitely sensitive to both short and long range ordering, as well as to defects and impurities.

Acknowledgments: The authors gratefully acknowledge R. Swope for technical assistance, and H. Brändle for helpful conversations regarding the Kerr spectroscopic measurements.

References

- [1] Y. Suzuki, T. Katayama, K. Sato, S. Yoshida, K. Tanaka Phys. Rev. Lett. **68**, 3355 (1992).
- [2] D. Weller, H. Brändle, R.F.C. Farrow, R.F. Marks, G.R. Harp, in: *Magnetism and Structure in Systems of Reduced Dimensions*, ed. R. F. C. Farrow, NATO ASI Series, Plenum Publishing Corp., New York (1993).
- [3] R.A. McCurrie and P. Gaunt, Proceedings of International Conference on Magnetism, Nottingham (1964).
- [4] D. Treves, J. T. Jacobs, and E. Sawatzky, J. Appl. Phys. **46**, 2760 (1974).
- [5] D. Weller, H. Brändle, C.-J. Lin, H. Notarys, Appl. Phys. Lett. **61**, 2726 (1992).
- [6] R. F. C. Farrow, R. H. Geiss, G. L. Gorman, G. R. Harp, R. F. Marks, E. E. Marinero, J. Magn. Soc. Jpn., 17 Supp. S1, 140 (1993)
- [7] D. Weller, G. R. Harp, R. F. C. Farrow, R. F. Marks, to be published.
- [8] H. Brändle, D. Weller, S. S. P. Parkin, J. C. Scott, P. Fumagalli, W. Reim, R. J. Gambino, R. Ruf, G. Güntherodt, Phys. Rev. B **46**, 13889 (1992).
- [9] B. M. Lairson, M. R. Visokay, E. E. Marinero, R. Sinclair, and B. M. Clemens, J. Appl. Phys., submitted (1993)
- [10] We note, that while writing this manuscript, we were made aware of a similar experiment in ordered FePt, where also a distinct peak, possibly related to chemical ordering was observed: B. Lairson et al., to be published
- [11] J.F. Albertsen, J.M. Knudsen, N.O. Roy-Poulsen, L. Vistisen, Physica Scripta **22**, 171 (1980).
- [12] D. Weller, H. Brändle, C. Chappert, E-MRS Symposium on "Magnetic Ultrathin Films, Multilayers, and Surfaces", Lyon, France Sept. 7-10, 1992; J. Magn. Magn. Mater., in press 1993.
- [13] D. Weller, J. Sticht, G. R. Harp, R. F. C. Farrow, R. F. Marks, this publication.
- [14] J. Sticht et al., to be published.

MAGNETO-OPTICAL SPECTRA OF COPT₃; EXPERIMENTS AND FIRST PRINCIPLES CALCULATIONS

D. Weller, J. Sticht^{*)}, G.R. Harp, R.F.C. Farrow, R.F. Marks and H. Brändle^{***)}

IBM Research Division, Almaden Research Center, 650 Harry Road, San Jose, CA 95120

^{*)}Technical University Darmstadt, Hochschulstraße 6, Darmstadt, Germany;

^{**)}present address: Biosym Technologies Inc., 9685 Scranton Rd., San Diego, CA 92121

^{***)}present address: Balzers AG, FL-9496 Balzers, Liechtenstein.

ABSTRACT

The magneto-optical Kerr effect of CoPt₃ ordered compounds and alloys is investigated experimentally and analyzed theoretically using first principles band structure calculations.

The calculations confirm the experimental results and allow for the first time a detailed, bandstructure based interpretation of the electronic transitions leading to the well known strong uv peak at around 4eV. This feature can be unambiguously attributed to magneto-optical transitions within the Pt p and d bands.

1. INTRODUCTION

CoPt alloys near the CoPt₃ composition have recently been demonstrated as perspective magneto-optical recording materials [1-4]. In particular, their excellent static read-out signal as well as their recording performance at short wavelengths make these new materials attractive alternatives to TbFeCo, which suffers from degrading read-out performance at short wavelengths and has a poor chemical stability.

The reason for the good performance of CoPt alloys as well as respective multilayers [5] rests in the large Kerr rotation, which typically peaks to values up to 0.8deg at room temperature near photon energies of 4eV, i.e. in the uv spectral range [6-8]. Its microscopic origin though, has been discussed somewhat controversially in the recent literature. Based on a strong density of an (initial) states feature near 4eV binding energy in X-ray photoemission experiments, Weller et al. [7] argued that Pt 5d band transitions were mainly responsible. Spin-resolved photoemission work by Weber et al. [9], however, did not provide evidence for a spin-splitting of the occupied Pt 5d levels in Pt/Co sandwiches and it was argued that interface states might contribute. On the other hand, it is well known that Pt carries a substantial, exchange-induced magnetic moment in these structures and its participation in magneto-optical transitions is undisputed. In particular it was found, that the 4eV peak in CoPt alloys is about 3x larger than a respective feature in CoPd and a linear correlation with the spin-orbit coupling parameters of Pt and Pd, respectively, was pointed out [2]. Linearity of the Kerr effect in the spin-orbit coupling strength is expected in theory as pointed out first by Misemer [10] and recently by Oppeneer et al. [11] in first-principles band structure calculations.

Such ab-initio bandstructure and MO calculations have successfully been applied to systems like Fe, Ni and FeCo [11]. They are particularly useful in providing microscopic insight into the electronic nature of the Kerr effect and could define the tuning parameters for high Kerr rotations [12].

We show here that bandstructure calculations can indeed describe the CoPt system quite well and will, in particular, exploit the linear relationship between Kerr effect and spin-orbit coupling to determine the electronic origin of the uv peak in CoPt.

2. EXPERIMENTAL

The films used for the present comparison with theory were deposited in ultrahigh vacuum on sapphire or SiN_x coated Si(111) substrates. All films were at least 1000\AA thick and standard x-ray diffraction and x-ray fluorescence characterization was performed to study their structure and composition. Polar Kerr spectra, in the presence of saturating fields up to 28kOe were measured in the photon energy range $0.8\text{--}5.3\text{eV}$ with a fully automatic spectrometer described elsewhere [13]. Annealing below the disorder-order temperature of CoPt_3 ($\sim 750^\circ\text{C}$) in UHV led to partial chemical ordering of the films and the Kerr effect was tracked as function of the annealing time.

3. RESULTS AND DISCUSSION

We first address the effect of chemical ordering on the Kerr spectra in the CoPt_3 composition range, as the present calculations are restricted to ordered compounds only. In a previous study, it was shown that only minor changes occur in the spectral features of CoPt_3 ; mainly, the room temperature Kerr spectra scale uniformly with the magnetization M_S , which drops toward zero as an increased amount of the ordered phase is produced by annealing [14]. Fig. 1 shows this experimental result.

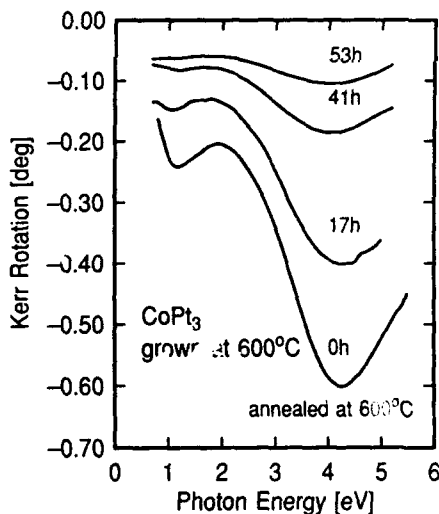


Fig. 1: Polar Kerr spectra at room temperature of a $\text{Co}_{22}\text{Pt}_{18}$ film which was grown at 600°C on basal plane sapphire and subsequently annealed for 17, 41 and 53 hours, respectively, at 680°C in UHV. The strong uv peak shifts to slightly higher energy as the amount of chemically ordered CoPt_3 (L_{12}) phase is increased by annealing. The overall drop of the Kerr rotation is due to a respective reduction of the room temperature magnetization.

By performing a self-consistent spin-polarized band structure calculation [15] for CoPt_3 in the ordered AuCu_3 structure with a lattice constant of $a=3.847\text{\AA}$ we obtain the partial densities of states as shown in Fig. 2. The 3d-states on the Co sites form a 4 eV broad band where the majority states are fully occupied in contrast to the minority states which show a huge density of states at the Fermi energy. This leads to a magnetic moment on the Co sites of $\mu_{\text{Co}}^{\text{tot}}=1.71\mu_B$ and an exchange splitting of about 1.6 eV for the Co-d states. The bandwidth of the Pt-5d states which are shown in Fig. 2(b) is about 8 eV . A small but significant admixture of sp-states to the 5d-states on the Pt sites is obvious. Furthermore we obtain a strong hybridization between Co-3d and Pt-5d

states close to the Fermi energy shown by van Hove singularities in the densities of states for the different sites. Especially the singularities at 1 eV below the Fermi energy for the spin-up state and about 1 eV above for the other spin direction support this result. The induced magnetic moment on the Pt atoms is $\mu_{\text{Pt}}^{\text{spin}} = 0.25\mu_B$ adding up to a total moment of $\mu_{\text{Pt}}^{\text{tot}} = 0.30\mu_B$ if the orbital contribution is included. These results are in general agreement with the calculations reported by Kootte et al. [16].

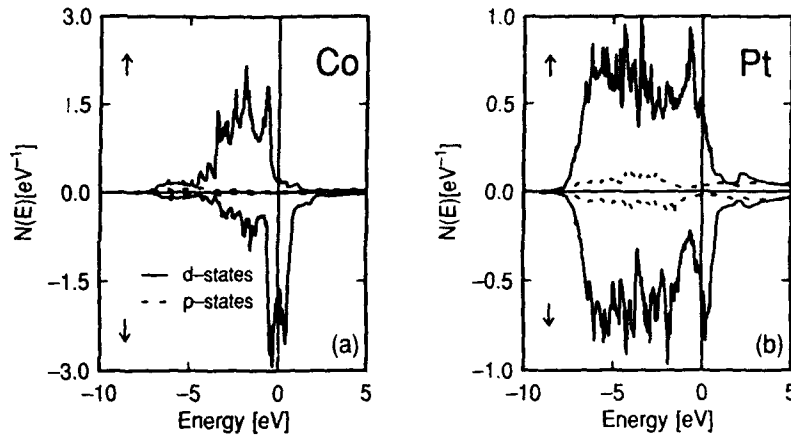


Fig.2: Spin-up and spin-down p- and d- density-of-states curves calculated from first principles for (a) Co sites (3d and 4p) and (b) Pt sites (5d and 6p) in CoPt_3 in the ordered AuCu_3 structure ($a = 3.847\text{\AA}$). Van Hove singularities are observed at $\sim 1\text{eV}$ above and below the Fermi energy, indicative of strong hybridization of Pt and Co d-states in that energy range. These results agree with those reported by Kootte et al. [16].

The exchange splitting of the Pt-d states is found to be 0.16 eV, i.e. one order of magnitude smaller than for the Co-d states. By calculating the macroscopic conductivity tensor $\tilde{\sigma}$ we are able to determine the Kerr rotation spectra from first principles according to:

$$\tilde{\Phi} = \theta_K + i\varepsilon_K = -\frac{\tilde{\sigma}_{xy}}{\tilde{n}\tilde{\sigma}_{xx}} \quad (1)$$

Here $\tilde{\sigma}_{xx}$ and $\tilde{\sigma}_{xy}$ denote the complex diagonal and off-diagonal parts of the conductivity tensor and \tilde{n} is the complex index of refraction, which relates to the diagonal conductivity as $\tilde{n} = \sqrt{1 + i4\pi\tilde{\sigma}_{xx}/\omega}$. The conductivity tensor itself can be related to microscopic optical transitions using the Kubo formula (for details see Wang and Callaway [17]). For the interband contributions to this tensor we obtain [11]:

$$\sigma_{xy}(\omega) = \frac{ie^2}{m^2\hbar} \sum_k \sum_l \sum_n^{\text{occ unocc}} \frac{1}{\omega_n(k)} \times \left\{ \frac{\Pi_{ln}^x \Pi_{nl}^y}{\omega - \omega_n(k) + i\delta} + \frac{(\Pi_{ln}^x \Pi_{nl}^y)^*}{\omega + \omega_n(k) + i\delta} \right\} \quad (2)$$

$$\sigma_{xx}(\omega) = \frac{ie^2}{m^2\hbar} \sum_k \sum_l^{\text{occ}} \sum_n^{\text{unocc}} \times \left\{ \frac{|\Pi_{ln}^x|^2}{\omega - \omega_{nl}(k) + i\delta} + \frac{(|\Pi_{ln}^x|^2)}{\omega + \omega_{nl}(k) + i\delta} \right\}, \quad (3)$$

with δ being a phenomenological lifetime parameter, and ω_{nl} the energy difference between an occupied and an unoccupied state.

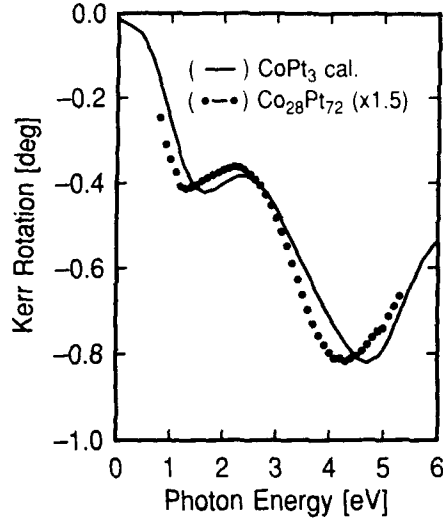


Fig. 3: Calculated (—) and experimental (•) polar Kerr rotation as function of photon energy of CoPt_3 . The experimental data were obtained from a 1000Å thick, polycrystalline and disordered $\text{Co}_{28}\text{Pt}_{72}$ film, UHV grown at 300°C on SiN_x buffered Si(111). Good agreement is obtained by multiplying the spectrum by a scaling factor of 1.5 to take into account the reduced room temperature magnetization at this Co-Pt composition.

The summations are carried out over all occupied and unoccupied states l and n , respectively, within the Brillouin zone. Π are the matrix elements of the momentum operator. Additional intraband contributions to the conductivity tensor are omitted in this paper.

Fig. 3 shows a comparison of the calculated and experimental Kerr rotation as a function of the photon energy. The lifetime parameter in the calculations was chosen to $\delta = 0.2$ eV. We find two maxima in agreement with the experiment, one in the ir region and the other one in the uv region, which shows a Kerr rotation up to 0.8° . The result agrees well with the experimental data (dots in Fig. 3), especially in view of the various parameters that enter both the experiment and the calculation. The ir region, in particular, is expected to be affected by intraband contributions, which are omitted in the present *ab-initio* calculations as stated above. This might explain the blueshift in the theoretical data. The shift in the uv region is most likely due to imperfect chemical ordering of the present sample. The experimental data were multiplied by a constant factor of 1.5, to take into account the temperature dependence of the magnetization, which at the present composition is already considerably reduced at room temperature as compared to low temperatures, where the ground state calculations were carried out.

To study the origin of the maxima we make use of the scaling property of the Kerr rotation with the spin orbit coupling parameter ξ (ref. Oppeneer et al.[12]). This value will normally be determined self-consistently, however, by using the Atomic Sphere Approximation (ASA), we are able to multiply the parameter ξ by a constant factor separately for each atomic site. The result for the Kerr rotation with different spin-orbit coupling parameters for Co and Pt are shown in Fig.4. On the left hand side (Fig.4(a)) we have increased ξ_{Co} by a factor of two keeping ξ_{Pt} constant, whereas the right hand picture (Fig.4(b)) represents the opposite situation. In the ir region (up to 3 eV) we observe for both cases only a

moderate change in the Kerr rotation. This result can be explained by the strong hybridization of Co-d and Pt-d states close to the Fermi energy, so that a non-zero value of the lifetime parameter will wipe out the scaling properties of the Kerr rotation. In the uv region (around 4.5 eV) it is clearly seen that increasing the spin-orbit coupling parameter on the Pt sites leads to an increase of the Kerr rotation, roughly proportional to ξ_{SO}^{Pt} . The Co atoms show no significant contribution in this energy region. Whether the maximum at 4.5 eV has its origin from transitions of occupied Pt-d to unoccupied Pt-p states or vice versa cannot yet be determined from the present analysis.

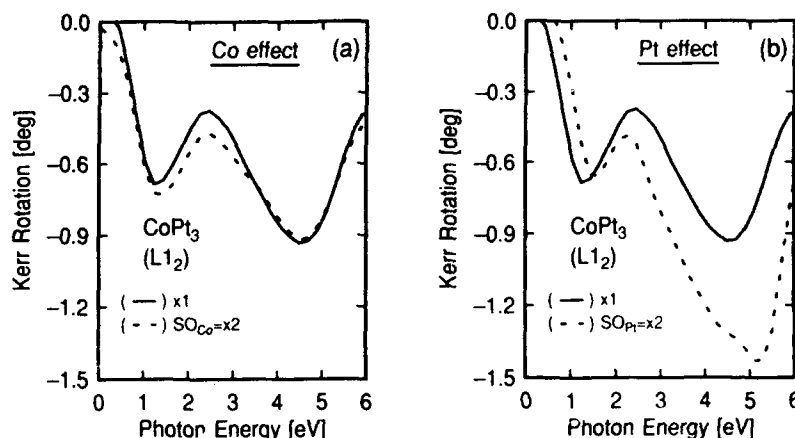


Fig.4: Calculated Kerr rotation spectra of CoPt₃ in the ordered AuCu₃ structure. Compared to Fig.2 we used a smaller number of k-points for the integration. The spin-orbit coupling parameter was selectively enhanced by a factor of 2 for Co sites (a) and Pt sites (b), respectively, to study the scaling behavior with ξ_{SO} and the origin of the strong uv peak in the Kerr spectra.

4. CONCLUSIONS

The calculated Kerr rotation of CoPt₃ shows excellent agreement with experimental data. We have shown, that the Kerr spectra in the uv region are dominated by transitions on the Pt sites. Strong hybridization of Pt and Co d-states near the Fermi level are obvious from density of states calculations, however, no spin-splitting is seen at binding energies around 4eV in agreement with recent spin-polarized photoemission results [9].

5. REFERENCES

- [1] D. Weller, H. Brändle, G. Gorman, C.-J. Lin and H. Notarys, Magnetic and magneto-optical properties of Cobalt Platinum alloys with perpendicular magnetic anisotropy, *Appl. Phys. Lett.*, 61, 1992, 2726-2728.
- [2] D. Weller, H. Brändle, C. Chappert, Relationship between Kerr effect and perpendicular magnetic anisotropy in Co-Pt and Co-Pd alloys, *J. Magn. Magn. Mater.*, 121, 1993, 461.
- [3] D. Weller, J. Hurst, H. Notarys, H. Brändle, R.F.C. Farrow and R. Marks, G. Harp, Mo signal in Co-Pt and Co-Pd alloy disks: comparison to respective multilayers and TbFeCo, *J. Magn. Soc. Jpn.*, 17, Supp. S1, 1993, 72-75.

- [4] R.F.C. Farrow, R.H. Geiss, G.L. Gorman, G. Harp, R.F. Marks and E.E. Marinero, Large Perpendicular Anisotropy, High Coercivity Co-Pt Alloys For Magneto-Optical Recording, *J. Magn. Soc. Jpn.*, 17 Supp. S1, 1993, 140-144.
- [5] W.B. Zeper, F.J.A.M. Greidanus, P.F. Carcia, C.R. Fincher, Perpendicular magnetic anisotropy and magneto-optical Kerr effect of vapor-deposited Co/Pt layered structures, *J. Appl. Phys.*, 65, 1989, 4971-4975.
- [6] K.H.J. Buschow, P.G. van Engen, R. Jongebreur, Magneto-optical properties of metallic ferromagnetic materials, *J. Magn. Magn. Mat.*, 38, 1983, 1-22.
- [7] D. Weller, W. Reim, Spectroscopic study of potential magneto-optic storage layers, *Appl. Phys. A*, 49, 1989, 599-618.
- [8] H. Brändle, D. Weller, S.S.P. Parkin, J.C. Scott, C.-J. Lin, Optical and Magneto-Optical Characterization of Evaporated Co/Pt Alloys and Multilayers, *IEEE Trans. Mag.*, 28, 1992, 2967-2969.
- [9] W. Weber, D.A. Wesner, D. Hartmann, G. Güntherodt, *Phys. Rev. B*, 46, 1992, 6199.
- [10] D.K. Misemer, *J. Magn. Magn. Mater.*, 72, 1988, 267.
- [11] P.M. Oppeneer, T. Maurer, J. Sticht, J. Kübler, *Phys. Rev. B*, 45, 1992, 10924.
- [12] P.M. Oppeneer, J. Sticht, T. Maurer, J. Kübler, Ab initio investigation of microscopic enhancement factors in tuning the magneto-optical Kerr effect, *Z. Phys. B - Condensed Matter*, 88, 1992, 309-315.
- [13] H. Brändle, D. Weller, S.S.P. Parkin, J.C. Scott, and P. Fumagalli, W. Reim, R.J. Gambino, R. Ruf, G. Güntherodt, Magneto-optical properties of CrO₂, *Phys. Rev. B*, 46, 1992, 13889-13895.
- [14] D. Weller, H. Brändle and R.F.C. Farrow, R.F. Marks, G. Harp, in "Magnetism and Structure in Systems of Reduced Dimensions", *NATO ASI series*, eds. R.F.C. Farrow et al. Plenum Publishing Corp., New York, 1993.
- [15] A.R. Williams, J. Kuebler, C.D. Gelatt, *Phys. Rev. B*, 19, 1979, 6094.
- [16] A. Kootte, C. Haas, R.A. de Groot, The electronic structure of ordered binary Co-Pt compounds, *J. Phys.: Condens. Matter*, 3, 1991, 1133-1152.
- [17] C.S. Wang, J. Callaway, *Phys. Rev. B*, 9, 1974, 4897.

EPITAXIAL FERROMAGNETIC MnGa AND $(\text{MnNi})\text{Ga}$ THIN FILMS WITH PERPENDICULAR MAGNETIZATION ON GaAs

M. TANAKA^a), J.P. HARBISON, T.D. SANDS, B.A. PHILIPS^b), J. DE BOECK^c), T.L. CHEEKS, L.T. FLOREZ and V.G. KERAMIDAS

Bellcore, 331 Newman Springs Road, Red Bank, NJ 07701-7040.

^a*On leave from Department of Electrical Engineering, The University of Tokyo, 7-3-1 Hongo, Bunkyo-ku, Tokyo 113, Japan.*

^b*Present address: Materials Science Department, Carnegie Mellon University, Pittsburgh, PA 15213-3890.*

^c*Permanent address: Interuniversity Microelectronics Center (IMEC), Kapeldreef 75, B3001 Leuven, Belgium.*

ABSTRACT

We have successfully grown thermodynamically stable ferromagnetic $\text{Mn}_x\text{Ga}_{1-x}$ ($x=0.55-0.60$) thin films with thicknesses ranging from 3 nm to 60 nm on GaAs substrates by molecular beam epitaxy. The c -axis of the tetragonal structure of the MnGa film is shown to be aligned perpendicular to the substrate. Both magnetization measurements and extraordinary Hall effect measurements indicate perpendicular magnetization of the MnGa films, exhibiting square-like hysteresis characteristics. Furthermore, we have investigated the effect of Ni additions as a substitution for Mn in $(\text{Mn}_{60-y}\text{Ni}_y)\text{Ga}_{40}$ alloy thin films with $y=0-30$ at% Ni. With increasing Ni, the perpendicular component of the magnetization becomes smaller up to $y=18$ where the magnetization is in-plane. At $y=30$, the magnetization is again perpendicular.

INTRODUCTION

Epitaxial growth of ferromagnetic thin films on III-V semiconductors can lead to the integration of magnetic effects with high speed III-V electronics/photonics [1], offering a wide range of possibilities for producing new devices such as non-volatile memory coupled with underlying III-V circuitry. Although most of the magnetic thin films so far obtained have in-plane magnetization due to the shape anisotropy [2], many potential applications of ferromagnetic films require magnetization perpendicular to the substrate, both to allow higher storage density in magnetic storage applications and to allow the use of extraordinary Hall effect (EHE) and magneto-optic Kerr effect (MOKE).

Recently, we have explored the growth of metastable τMnAl on GaAs substrates by molecular beam epitaxy (MBE), and found that heteroepitaxy helps to align the magnetization direction of the MnAl film, which lies along the c -axis of the tetragonal unit cell of τ phase, in an orientation perpendicular to the substrate [3][4]. In this paper, we present our study of the MBE growth of $\text{Mn}_x\text{Ga}_{1-x}$ ($x=0.55-0.60$), the stable ferromagnetic Ga-based phase, compatible with GaAs substrates in epitaxy due to the shared group III atom in the MnGa/GaAs couple. It is shown that the MBE-grown MnGa films indeed have perpendicular magnetization, square-like EHE hysteresis characteristics, and a high value of remanent magnetization, making them a promising candidate for applications in certain non-volatile magnetic memory coupled with III-V optical and/or electronic devices. Furthermore, we have investigated the MBE growth of $(\text{Mn}_{60-y}\text{Ni}_y)\text{Ga}_{40}$ alloy films with $y=0-30$ at % Ni and the dependence of the magnetic properties on the Ni composition.

MBE GROWTH

Unlike metastable τMnAl , $\text{Mn}_x\text{Ga}_{1-x}$ with $x=0.55-0.60$ is a thermodynamically stable ferromagnetic phase in the bulk Mn-Ga system [5][6]. In the bulk, the single phase region was found to extend from 54.5 to 60.0 at% Mn at 450°C [6]. The crystal structure of the MnGa is tetragonal, analogous to that of τMnAl , with an ordered crystal structure of the CuAu type. The Mn-Mn spacing in the basal plane (a_0) is 0.274 nm, independent of the Mn content, and along the c -axis (c_0) is 0.365 nm at 56% Mn and 0.369 nm at 59% Mn, respectively. The easy magnetization direction is along the c -axis. Since a_0 is close to half of the lattice constant of GaAs (0.283 nm) with a lattice mismatch of only 3.8%, the orientation relationship with the c -axis of the MnGa parallel to the surface normal of the (001) GaAs substrates is expected, as

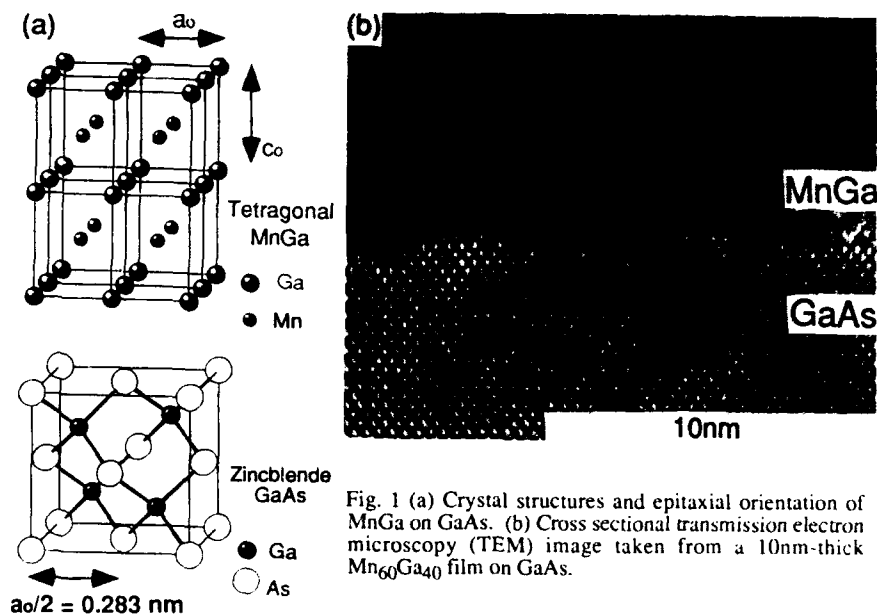


Fig. 1 (a) Crystal structures and epitaxial orientation of MnGa on GaAs. (b) Cross sectional transmission electron microscopy (TEM) image taken from a 10nm-thick $\text{Mn}_{60}\text{Ga}_{40}$ film on GaAs.

shown in Fig. 1 (a).

The growth of MnGa on (001) GaAs was performed with a conventional III-V MBE machine (Riber-2300) with effusion cells for Mn, Ni, Ga and As, using the multistep technique analogous to that employed in the growth of rMnAl/AlAs/GaAs [3][4]. Since the details of the growth have been reported previously [7], we briefly summarize the growth procedure here. After a 100nm-thick GaAs buffer layer was grown at 580°C under conventional III-V growth conditions, the substrate temperature was cooled to 20 - 40°C while completely eliminating the As flux. Then a thin (about 0.9nm-thick) amorphous MnGa template was deposited at 20 - 40°C. The amorphous template was next heated up to 200 - 250°C to form a monocrystalline template by solid phase epitaxy. After the template with the desired epitaxial relation was thus established, Mn and Ga were subsequently codeposited at 150 - 200°C at a growth rate of 0.05 $\mu\text{m/hr}$, to a final $\text{Mn}_x\text{Ga}_{1-x}$ thickness of 3 - 60nm. The Mn content x was set to 55% - 60% in the present study. Finally, postgrowth annealing was performed at 300 - 410°C for 2 minutes. Such annealing at a temperature T_a of at least 300°C was found to be necessary in order to improve the structural and magnetic properties of the MnGa film.

STRUCTURAL AND MAGNETIC PROPERTIES OF MnGa THIN FILMS

The epitaxial MnGa with its c -axis aligned normal to the substrate was confirmed first by *in situ* reflection high energy electron diffraction (RHEED) and also by cross sectional transmission electron microscopy (TEM). Figure 1 (b) shows a $\langle 110 \rangle$ TEM lattice image of the 10nm-thick $\text{Mn}_{60}\text{Ga}_{40}$ film grown on GaAs, indicating that a monocrystalline MnGa layer was indeed grown with the c -axis properly oriented perpendicular to the GaAs substrate. The interface between the MnGa and the GaAs is found to be very smooth and abrupt, and no interfacial transition layer was observed. The horizontal lattice fringes with a spacing of 0.31nm correspond to the (001) planes of the tetragonal structure of the MnGa. This value of the c parameter in the present epitaxial MnGa film is significantly smaller than that of bulk MnGa (0.36-0.37nm) [5][6] and a MBE-grown MnGa film (0.35nm) with greater (30nm) thickness [8]. Although the reason for the reduced tetragonality is not yet clear, the explanation may be that the present MBE film is

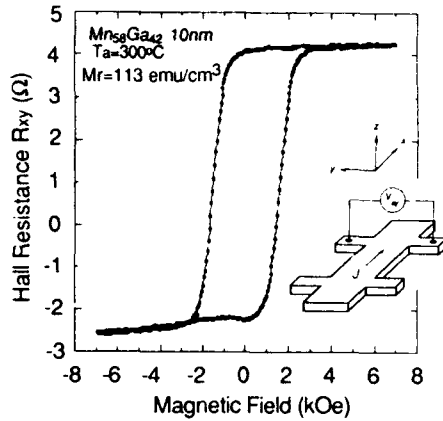


Fig. 2 Extraordinary Hall effect (EHE) as a function of perpendicular magnetic field for a 10nm-thick $\text{Mn}_{58}\text{Ga}_{42}$ film at room temperature. The inset shows the geometry of the measurement. The M_r value perpendicular to the film plane is also shown.

composed of an intermediate phase between the tetragonal phase and cubic phase, stabilized by the coherent epitaxy, as has been shown in the case of MnNiAl [9][10].

To investigate the magnetic properties of the epitaxial MnGa films, we performed vibrating sample magnetometer (VSM) measurements as a function of magnetic field perpendicular to the substrate at room temperature. Fairly square hysteresis loops were observed at room temperature [7], offering direct evidence of the desired perpendicular magnetization. Similar results were obtained in all the samples of MnGa with Mn content ranging from 55% to 60%. The remanent magnetization M_r along the c-axis was estimated to be 113 - 225 emu/cm^3 , and the coercive field H_c was 0.85 - 3.15 kOe.

The Hall effect measured in a ferromagnetic film is known to have an "extraordinary" component resulting from the asymmetric scattering of carriers with magnetic atoms [11]. The extraordinary Hall effect (EHE) is very useful in this case because the Hall resistivity measured in a patterned Hall bar in the MnGa films is proportional to the magnetic moment perpendicular to the film plane. Figure 2 shows an example of Hall resistance R_{xy} vs. perpendicular magnetic field measured at room temperature on a 200 μm -wide Hall bar fabricated in a 10nm-thick $\text{Mn}_{58}\text{Ga}_{42}$ film prepared with $T_a = 300^\circ\text{C}$. One can see a fairly square hysteresis loop with nearly 100% remanence, Hall resistance R_{xy} of 3.5 Ω (corresponding Hall resistivity ρ_{xy} of 3.5 $\mu\Omega\text{cm}$) and H_c of 1.46 kOe. Similar square-like hysteresis loops were observed in the EHE measurements in all the present MnGa samples, indicating a large component of perpendicular magnetization, consistent with the VSM measurement results. The EHE resistivity ρ_{xy} was found to vary from 0.1 $\mu\Omega\text{cm}$ to 4 $\mu\Omega\text{cm}$, depending on the growth parameters.

The magnetic and magnetotransport properties of the MBE-grown MnGa films, such as remanent magnetization M_r , saturation magnetization M_s , coercive field H_c , Hall resistance R_{xy} and Hall resistivity ρ_{xy} , depend on the various growth parameters such as growth temperature T_g , postgrowth annealing temperature T_a , Mn composition x , and thickness of the MnGa film t . Here, we briefly describe the change in the properties of $\text{Mn}_{60}\text{Ga}_{40}$ films grown at $T_g = 200^\circ\text{C}$ and at $T_a = 350^\circ\text{C}$ when the thickness t was varied from 3 nm to 60 nm. Over the entire range of the thickness explored here, perpendicular magnetization was evidenced by both VSM and EHE measurements and electrical continuity in each of the films was confirmed. Figure 3 shows a set of plots of Hall resistance as a function of perpendicular magnetic field at room temperature on the $\text{Mn}_{60}\text{Ga}_{40}$ films with $t = 3\text{nm}$ (a), 10nm (b), and 60nm (c). With the change of film thickness, the value of R_{xy} ($=\rho_{xy}/t$) changes drastically, from about 2 Ω to 0.07 Ω . The value of coercive field H_c was maximum (3.15 kOe) at $t = 10\text{nm}$, and minimum (0.85 kOe) at $t = 60\text{nm}$. The VSM measurement showed that the saturation magnetization M_s of the 60nm-thick film was 394 emu/cm^3 , as high as the bulk value of 390 emu/cm^3 [6], indicating the high quality of the MBE film. This growth parameter dependence can allow us to control the magnetic properties in these MBE-grown films.

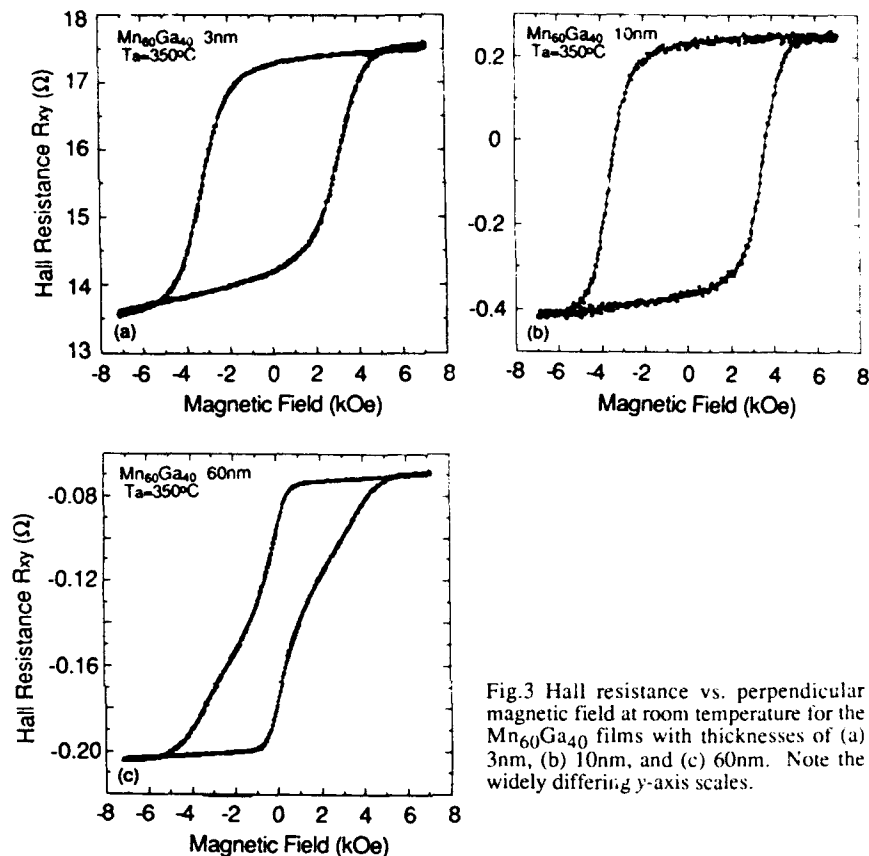


Fig.3 Hall resistance vs. perpendicular magnetic field at room temperature for the $\text{Mn}_{60}\text{Ga}_{40}$ films with thicknesses of (a) 3nm, (b) 10nm, and (c) 60nm. Note the widely differing y-axis scales.

Ni ADDITIONS: $(\text{Mn}_{60-y}\text{Ni}_y)\text{Ga}_{40}$ ALLOY THIN FILMS

The addition of Ni to the MnGa films is expected to lead to the reduction of the tetragonality of the lattice. This should in turn decrease the magnetocrystalline anisotropy, resulting in a change in magnetic properties, as in the case of MnNiAl thin films [9]. In order to explore the effect of Ni additions on the structural and magnetic properties, we have fabricated a series of $(\text{MnNi})\text{Ga}$ samples where Ni was substituted for Mn in $\text{Mn}_{60}\text{Ga}_{40}$ films over the range of 4% to 30% atomic fraction of Ni. The growth procedures and conditions in the MnNiGa films are the same as in the case of MnGa , except that the growth temperature was 200 - 220°C, a little higher than that of MnGa .

Figure 4 shows a series of RHEED patterns along the $\langle 110 \rangle$ azimuth taken from the 10nm-thick $(\text{Mn}_{60-y}\text{Ni}_y)\text{Ga}_{40}$ films with various Ni content ($y=4, 8, 18$ and 30 at% Ni), both for as-grown surfaces and for the surfaces after the postgrowth annealing at 300°C for 2 minutes. These streaky patterns suggest that monocrystalline epitaxial films are obtained with very smooth surface, over the entire range explored here. The postgrowth annealing was found to be effective in improving the RHEED quality. As the value of y increases, the RHEED pattern becomes more streaky and sharper. For the MnNiGa with $y=30$, one can see a (4×4) reconstruction on the as grown surface which changed into a sharp (2×2) reconstruction after the annealing, while (2×2) reconstructions are seen for the MnNiGa with $y < 30$.

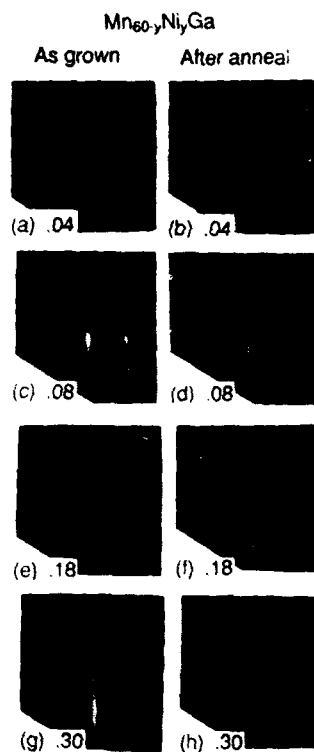
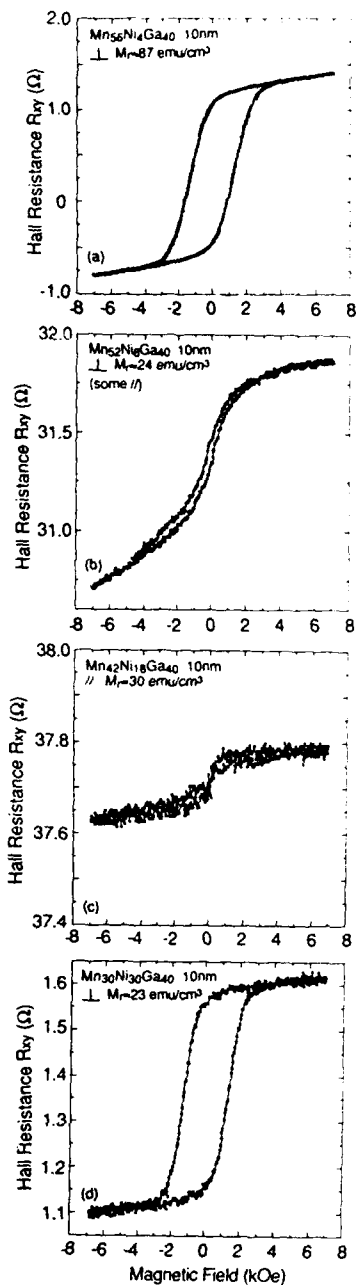


Fig. 4 A series of RHEED patterns along the $\langle 110 \rangle$ azimuth taken of 10nm-thick $(\text{Mn}_{60-y}\text{Ni}_y)\text{Ga}_{40}$ films with various Ni content ($y=4, 8, 18$ and 30 at % Ni as indicated). The left hand pictures are taken from the as grown surfaces, and right hand ones are from the surfaces after the postgrowth annealing at 300°C for 2 minutes.

Fig. 5 EHE characteristics are plotted as a function of applied magnetic field perpendicular to the film plane, and the M_r values are shown with the magnetization directions, where \perp and \parallel denote perpendicular and in-plane magnetization, respectively.



To investigate the magnetic properties, we performed VSM and EHE measurements at room temperature. The results are summarized in Fig. 5, where the EHE characteristics are plotted as a function of magnetic field applied perpendicular to the film plane. The M_r values and the magnetization directions measured by VSM are also shown in the figures. It was found that the perpendicular magnetization decreases and the EHE hysteresis loop becomes smaller with increasing Ni content (y varying from 0 to 18), as shown in Fig. 2 and Figs. 5 (a), (b) and (c). The VSM measurements revealed that the MnNiGa films with $y=4$ and $y=8$ have smaller values of M_r (87 emu/cm³ and 24 emu/cm³, respectively), along the perpendicular direction, than the M_r (> 110 emu/cm³) of MnGa. However, it was found that the MnNiGa film with $y=8$ has some in-plane component of magnetization though the dominant component is perpendicular. It was also found that the MnNiGa film with $y=18$ has almost no perpendicular magnetization, but rather a dominantly in-plane magnetization. This result suggests that the epitaxial relationship of Fig. 1 (a) may not be realized in the Mn₄₂Ni₁₈Ga₄₀/GaAs heterostructure, and the c -axis of the MnNiGa may instead be aligned in the (001) plane of GaAs. Alternatively, the magneto-crystalline anisotropy may be overcome by the shape anisotropy, yielding in-plane magnetization. This could result from the reduced tetragonality of the MnNiGa with such a high Ni content, though a more detailed structural analysis is necessary. Furthermore, it was found that when we further increase the Ni addition up to $y=30$, the MnNiGa shows perpendicular magnetization and a square-like EHE hysteresis loop again, as shown in Fig. 5 (d), though both the values of M_r and ρ_{xy} are significantly smaller than those of MnGa. Thus the Ni content dependence of the magnetic properties of the MnNiGa alloy films was found to be more complex than that of MnNiAl alloy films [9].

CONCLUSIONS

We have successfully grown ferromagnetic MnGa films on GaAs by MBE. The long axis (c -axis) of the tetragonal structure of the MnGa film is aligned perpendicular to the substrate. Both VSM and EHE measurements confirm this perpendicular magnetization, and exhibit square-like hysteresis loops in our MnGa films with thicknesses ranging from 3nm to 60nm at room temperature. The growth and magnetic properties of Mn_{60-y}Ni_yGa₄₀ alloy films on GaAs were also explored. With increasing Ni, the perpendicular component of the magnetization becomes smaller and the alloy film at $y=18$ shows in-plane magnetization, while the film at $y=30$ shows perpendicular magnetization.

ACKNOWLEDGMENTS

The authors thank the cooperation of M.C. Tamargo and H.L. Gilchrist. One of the authors (M.T.) acknowledges the financial support from the Japan Society for the Promotion of Science.

REFERENCES

1. G.A. Prinz, *Science* **250**, 1092 (1990).
2. J.J. Krebs, *Appl. Phys.* **A49**, 513 (1989).
3. T. Sands, J.P. Harbison, M.L. Leadbeater, S.J. Allen, Jr., G.W. Hull, R. Ramesh, and V.G. Keramidas, *Appl. Phys. Lett.* **57**, 2609 (1990).
4. J.P. Harbison, T. Sands, R. Ramesh, L.T. Florez, B.J. Wilkens, and V.G. Keramidas, *J. Crystal Growth* **111**, 978 (1991).
5. T.A. Bither and W.H. Cloud, *J. Appl. Phys.* **36**, 1501 (1965).
6. M. Hasegawa and I. Tsuboya, *Review of Electrical Communication Laboratory* **16**, 605 (1968) and references therein.
7. M. Tanaka, J.P. Harbison, J. DeBoeck, T. Sands, B. Philips, T.L. Cheeks, V.G. Keramidas, *Appl. Phys. Lett.* **62**, 1565 (1993).
8. K.M. Krishnan, *Appl. Phys. Lett.* **61**, 2365 (1992).
9. J.P. Harbison, T. Sands, J. DeBoeck, T.L. Cheeks, P. Miceli, M. Tanaka, L.T. Florez, B.J. Wilkens, H.L. Gilchrist and V.G. Keramidas, *J. Crystal Growth*, in press.
10. T. Sands, J. DeBoeck, J.P. Harbison, A. Scherer, H.L. Gilchrist, T.L. Cheeks, P.F. Miceli, R. Ramesh and V.G. Keramidas, *J. Appl. Phys.*, in press.
11. E.D. Dahlberg, K. Riggs and G.A. Prinz, *J. Appl. Phys.* **63**, 4270 (1988).

STUDIES OF MAGNETO-OPTICAL RECORDING IN MULTI-MAGNETIC-LAYER DISK BY ANALYTIC AND SIMULATING APPROACHES

YOSHIYUKI KAWAZOE, XIAO HU AND SHIGERU HONMA
Institute for Materials Research, Tohoku University,
2-1-1 Katahira, Aoba-ku, Sendai 980, Japan

ABSTRACT

The effect of magnetic coupling in multi-layer system is discussed by an analytic approach and computer simulation. The dependence of the enhancement of external field on the magnetic properties of the relevant materials is studied. Comparison between the theoretical estimate, simulation result and experimental observations are presented.

INTRODUCTION

It is found by experiments that the strength of external field for complete recording in a disk with a recording film capped with an in-plane magnetized film is one-tenth of that for the conventional magneto-optical (MO) disk which consists of single magnetic film[1]. The mechanism of this effect is revealed theoretically first by Hu et al. [2]. The purpose of the present study is to investigate the dependence of the capping effect on the magnetic properties of the relevant materials which is very important in practical point of view such as the field-modulation recording in MO disk.

DEFINITION AND FORMALISM

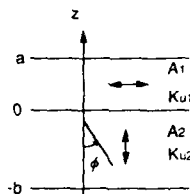


Figure 1: Double-film system studied in the present work[2].

We study a magnetic double-film system, where the easy-axis of the capping film (film-1) is horizontal whereas vertical in the recording film (film-2). We take z -axis perpendicular to the films and its origin at the interface as shown in Fig.1. The angle from the negative direction of z -axis is used to describe the configuration of magnetizations and it is considered to be uniform in x and y directions.

Table I: Magnetic Constants and Film Dimensions[2]

Quantity	film-1	film-2
Material	TbFeCo	PtCo
M_s [emu/cc]	32.4	10.0
A [erg/cm]	1.3×10^{-8}	9.2×10^{-8}
K_u [erg/cc]	3.3×10^4	9.2×10^5
Thickness[Å]	200	350

The total magnetic energy per unit area is

$$\gamma = \int_0^a [A_1 (\frac{d\varphi}{dz})^2 + K_1 \cos^2 \varphi + M_{s1} H_{ext} \cos \varphi] dz + \int_{-b}^0 [A_2 (\frac{d\varphi}{dz})^2 + K_2 \sin^2 \varphi + M_{s2} H_{ext} \cos \varphi] dz \quad (1)$$

with $A_{1(2)}$ and $K_{1(2)}$ standing for the stiffness constant and the anisotropy constant, which consists of the uniaxial anisotropy part and the demagnetization part, for the capping(recording) film. The direction of the magnetization is supposed to be continuous at the interface between the films within the present continuous approximation. The recording field H_{ext} is taken positive if it is applied in the positive direction of z -axis.

In terms of the variational method to the energy (1) we can derive differential equations for the function $\varphi(z)$. We have found that the magnetic coupling between the film can be regarded as a local magnetic field on the magnetizations of the recording film:

$$H_{cap} = \frac{A_1 (d\varphi/dz)^2}{M_{s2} \cos \varphi}, \quad (2)$$

and explicitly

$$H_{cap} = \frac{\sin^2 \varphi}{\cos \varphi} \left[1 - \frac{E_{z2}}{2 \cos^2(\varphi/2)} \right] \times \frac{K_{u2}}{M_{s2}}, \quad (3)$$

where $E_{z2} = M_{s2} H_{ext} / K_{u2}$. The direction of the magnetization $\varphi(z)$ is determined by a single non-linear equation including Jacobian elliptic functions with the magnetic constants, the thickness of the films and the external field as parameters. In other words, the magnetizations in the recording film feels an additional field to the external one from the magnetic coupling with the capping film with horizontal easy-axis.

FIELD ENHANCEMENT

In the present section the field enhancement H_{cap} is investigated quantitatively with emphasis on its profile in the recording film and its dependence on the thickness of the capping film, temperature and the external field.

Configuration of magnetization

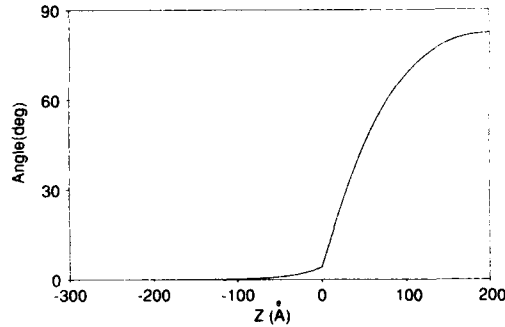


Figure 2: Configuration of magnetizations under the external field of $H_{ext} = 50\text{Oe}$ and temperature of $T = 160^\circ\text{C}$ [2].

Typical configuration of the magnetization is shown in Fig.2. It is found that the direction of magnetization decays very quickly to zero inside the recording film. This

corresponds to the fact that memory can be recorded firmly in the recording film even with an additional film capped on.

Comparison with experiments

Let us first evaluate H_{cap} at typical conditions of experiments and make some comparison between the present theoretical result with experimental observations. Let us study the case of external field $H_{ext} = 50\text{Oe}$ since this is the minimum external field for complete recording in such system[1]. The field enhancement is $H_{cap} \approx 487.00\text{Oe}$.

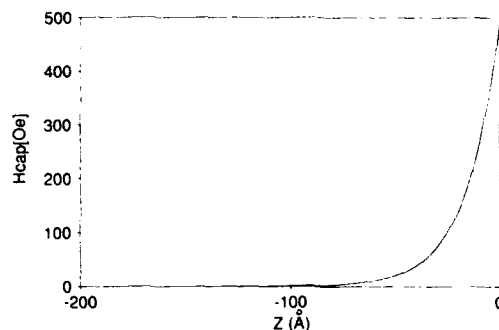


Figure 3: Profile of field enhancement under the same conditions for Fig. 2[2].

Under the uniform external field of $H_{ext} = 50\text{Oe}$, the magnetizations at the interface experience an effective field of about 550Oe. The last digit is near to the minimum field $H_{ext} \sim 600\text{Oe}$ for complete recording in a conventional disk with single magnetic-film[3]. Since the field enhancement assumes its maximum at the interface and drops very quickly inside the recording film as seen in Fig. 3, nucleation of the reversal magnetization takes place at the interface with the highest probability. As the magnetizations at the interface ($z = 0$) are reversed, the locus where the maximum field enhancement is assumed shifts inside the recording film. It in turn results in magnetization reversal at a deeper part of the recording film. Putting it in other words, nucleation occurred at the interface is followed by a movement of magnetic wall. Therefore, the coincidence between our theoretical estimate of field enhancement and the experimental observations provides a numerical evidence for the nucleation and followed by wall-movement mechanism of magnetization reversal in magneto-optical recording.

Dependence on the thickness of the capping film

We have found that the field enhancement shows a strong non-linear dependence on the thickness of the capping film[2]. There is a minimum thickness of the capping film so as to show capping effect; the field enhancement saturates at large film thickness. The behavior at the temperature of $T = 160^\circ\text{C}$ and the external field of $H_{ext} = 50\text{Oe}$ is shown in Fig. 4.

We have found theoretically that minimum thickness corresponds to the bifurcation point of differential equation discussed in the preceding section: below the minimum thickness there is only a trivial solution $\varphi = 0$ in the whole system where no capping effect exists while above it there appears a non-uniform solution as shown in Fig. 2. The analytic expression for the minimum thickness is[2]:

$$a_{min} = \sqrt{A_1/K_{u1}(1 + E_1/2)} \tan^{-1} \frac{\sqrt{A_2 K_{u2}(1 - E_2/2)}}{\sqrt{A_1 K_{u1}(1 + E_1/2)}} \quad (4)$$

The critical thickness is about $a_{min} = 94.8\text{\AA}$ for the system described in Tabel 1. The critical behavior is of the following form:

$$H_{cap} \approx \dot{H}_{cap}(a - a_{min}). \quad (5)$$

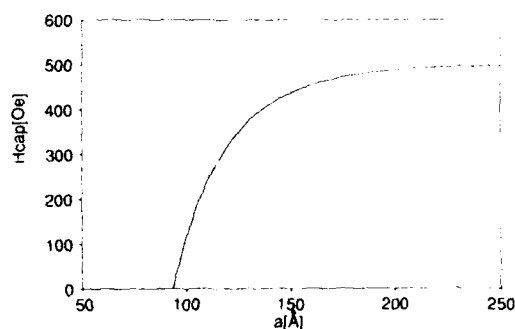


Figure 4: Field enhancement vs thickness of the capping film under the external field $H_{ext} = 50\text{Oe}$ and temperature of $T = 30^\circ\text{C}$ [2].

Dependence on temperature and external field

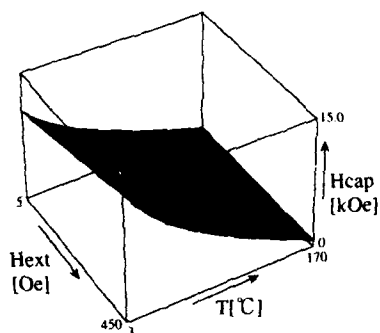


Figure 5: Field enhancement as function of the temperature and the external field for the thickness of the capping film $a = 200\text{\AA}$.

It is found that the enhancement of the external field by the capping film drops as the temperature increases. It is because the Curie point of the capping film is about 170°C [2]. Above this temperature no magnetic coupling is present and no capping effect can be expected.

Simulation

Computer simulation is performed in order to study the capping effect in real-time recording process and the final recorded mark. The dimensions of the region for simulation are $12\mu\text{m}$ in the rotating direction and $8\mu\text{m}$ in the radius direction. By dividing space into nearly 270 thousand $a^2 \approx 0.1\mu\text{m} \times 0.1\mu\text{m}$ meshes and the recording period into 2.5nsec time steps, we have solved the thermal diffusion equation with a specifically developed

computer language DEQSOL (Differential Equation Solver Language) and determined the temperatures at each mesh point at each time step.

We perform magnetic reversals according to the balance between magnetic forces based on the isotherms and the magnetic configuration. There are four forces on the magnetization at a mesh point, namely the Zeeman force H_{ext} from the external field, the demagnetizing force H_d from other dipoles, a force H_w corresponding to the wall energy if a boundary of opposite magnetizations locates at one side of the mesh under study and finally the magnetic coupling with the capping film, namely the enhancement of the external field H_{cap} discussed theoretically in the preceding sections. Dynamical process of magnetizations in the capping film is neglected and the effect of the magnetic coupling between the magnetizations in the two films is approximated by the temperature-dependent H_{cap} derived in the preceding section. We notice that this treatment is the roughest approximation for computer simulation.

The mesh points where the following inequality is satisfied[3]

$$|H_{ext} + H_{cap} + H_d - H_w| > H_c \quad (6)$$

are candidates for magnetic reversals. After the investigation of the above magnetic balances over all the meshes we reverse the magnetizations in the marked meshes simultaneously to produce a new configuration. The simulated recording process is shown in Fig.6.

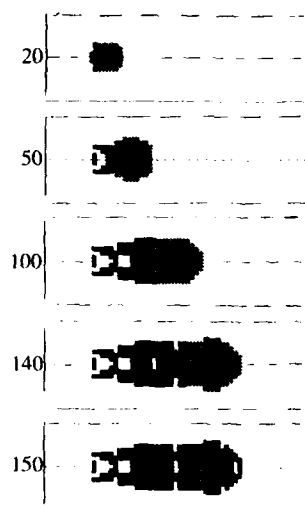


Figure 6: Simulated recording process in the system of $Tb_{28}Fe_{60}Co_{12}/PtCo$. The conditions for recording are as follows: power $P = 9mW$, laser pulse duration 140nsec, linear velocity 22.5m/sec, external field 200Oe.

The comparison between the recorded mark in the double-film system and the single film system is essential to test our theoretical discussions. It is read from Fig.7 that the mark circumference is considerably improved in the double-film system. It is the first observation, by computer simulation, of the capping effect in the magneto-optical recording. In contrast, most of the inner part seems to remain unchanged and some additional unreversed domains appear in the inner part of the mark in the double-film system. The reason is of three-fold: First, as is seen in Fig.5 the enhancement of the external field H_{cap} is very small and vanishes as the temperature exceeds the Curie temperature of the

capping film; Secondly, since the recording process is simulated by discrete time sequence, phenomena take place within a time scale less than the time step cannot be grasped by the present simulation. Thirdly, the demagnetization field is overestimated in the approximation for the present simulation since it is already taken into account partly in the field enhancement H_{cap} . Therefore, the unreversed domain in both (a) and (b) of Fig.7 at the locus, where laser pulse is cut off and thus the temperature drops very quickly, may be fictitious.

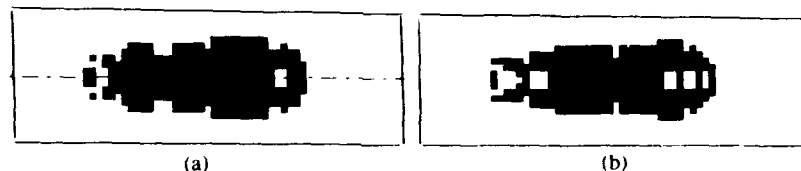


Figure 7: (a) Recorded mark in single film system of $Tb_{28}Fe_{60}Co_{12}$ under the conditions in Fig.6; That in the system of (a) capped on PtCo film.

SUMMARY

We have studied theoretically magnetic-coupled double-film systems. The enhancement of the external field by the capping film is investigated in terms of the magnetic properties of the relevant materials. We have simulated the magneto-optical recording process in double-film system by incorporating the enhancement of the external field into the magnetic force balance equation. We have found that considerable improvement in the mark circumference is achieved by the capping effect.

Acknowledgments

Hu is supported in part by the Scientific Research Fund of the Ministry of Education, Science and Culture of Japan and partially by a grant from Iketani Science and Technology Foundation.

References

- [1] S. Ohnuki, K. Shimazaki, N. Ohta and H. Fujiwara: J. Magn. Soc. Jpn., **15** Supplement No.S1(1991)(Proc. of MORIS'91), 399; S. Ohnuki, K. Shimazaki and N. Ohta: Digest of Optical Memory Symp. '92, 119(in Japanese).
- [2] X.Hu, Y.Kawazoe, T.Yorozu and N.Ohta: submitted to J.Appl.Phys. and references therein; X.Hu, T.Yorozu, Y.Kawazoe, S.Honma, S.Ohnuki and N.Ohta: Proc. of INTERMAG'93 (April 13-16,1993, Stockholm, Sweden), to be published as a transaction of IEEE.
- [3] Y.Kawazoe, X.Hu, S.Honma, T.Yorozu, T.Imazu and N.Ohta: to appear in J.Magn.Soc.Jpn. (Proc. of MORIS'92); S.Honma, X.Hu, T.Yorozu, Y.Kawazoe, T.Imazu and N.Ohta: submitted to J.Magn.Mater..

GROWTH, STRUCTURE AND MAGNETISM OF COBALT-PLATINUM ULTRATHIN FILMS AND SANDWICHES

J.P. DEVILLE, A. BARBIER, C. BOEGLIN AND B. CARRIERE
I.P.C.M.S. Groupe "Surfaces-Interfaces" - UMR 046 du CNRS
4, rue Blaise Pascal, F-67070 STRASBOURG Cedex, France

ABSTRACT

Cobalt-platinum alloys and multilayers are now well known for their potentialities in magneto-optical recording media. The growth of ultrathin layers and sandwiches is thought to be useful to find the relationship between the structural and magnetic properties at an atomic level. Low Energy Electron Diffraction (LEED) and Auger spectroscopy (AES) are used here to study the crystallography and the growth modes of Pt on Co(0001) surfaces. Co/Pt/Co sandwiches are also built and investigated by the same methods. At room temperature we show the evidence of a good epitaxy of platinum on the Co(0001) surface leading to the possibility of obtaining ordered Co/Pt/Co sandwiches. Annealings at moderate temperatures lead to an epitaxial alloy formation. Auger results show that alloying indeed induces a magnetic moment on platinum atoms. This could explain the magnetic properties already observed in Co/Pt (111) multilayers.

1. INTRODUCTION

In the last decade multilayers based on the Co-Pt system have become of interest as potential candidates for magneto-optical perpendicular recording media hoping to take advantage of the large magnetic anisotropy which is well known in the $L1_0$ structure of the PtCo alloy. This magnetic anisotropy could be due to the strong hybridization between the Co3d and Pt5d levels and the large spin-orbit coupling [1]. Lee et al. [2] have indeed studied multilayers based on this system: they concluded that the magnetic anisotropy was dependent on the growth direction and they showed that the argument given earlier by Néel [3], based on broken symmetry effects, was not sufficient to explain satisfactorily the observed magnetic anisotropies in the multilayers.

More recently, multilayers based on alloys have been investigated [4,5]. They show a larger static signal level than multilayers based on the alternance of Co and Pt layers, Curie temperatures around 200°C (for $\text{Co}_{22}\text{Pt}_{78}$) and a good chemical stability. Annealing processes on ultrathin Pt/Co layers and sandwiches built at different temperatures allow one to get a good model to study the alloy formation and its influence on the magnetic properties of the samples.

2. EXPERIMENTAL

All experiments were performed in a conventional UHV chamber with a base pressure better than $5 \cdot 10^{-11}$ Torr. Auger spectra used to check the substrate cleanliness and to establish growth kinetics were obtained with a MAC2 RIBER analyzer working in the derivative mode. The LEED structural studies were done with an OMICRON Spectaleed optics allowing us to measure precise surface parameters. The cobalt single crystal surfaces were cleaned with conventional argon-ion bombardments at 300°C followed by a final annealing process at temperatures not higher than 350°C to avoid the martensitic phase transition. Platinum was then evaporated from a Joule heated Pt wire at a very slow rate (≈ 1 monolayer/20 minutes).

3. GROWTH MODE AND STRUCTURE OF PLATINUM ULTRATHIN LAYERS

3.1. Growth mode at room temperature of platinum on Co(0001)

It is now well established [6] that Auger Electron Spectroscopy allows one to determine the growth mode of binary systems. A careful analysis of the substrate and adsorbate Auger peak intensities may indeed discriminate between the different growth modes which can occur without diffusion either at equilibrium : - Frank-Van der Merwe (FM : layer by layer), Stranski-Krastanov (SK : layer(s) followed by islands), Volmer-Weber (VW : islands) - or out of equilibrium - simultaneous multilayers (SM) -. The corresponding analytical expressions for the Auger adsorbate and/or substrate intensities can be easily derived [6]. As we did in a previous study on the Pt/Co(10.0) interface [7] we use systematically several graphs (intensity vs. time, adsorbate/substrate ratio vs. time, intensity of substrate vs. intensity of adsorbate) to interpret the experimental Auger data. This is necessary because of the large number of non independent parameters and one avoids misinterpretations due to wrong values of the inelastic mean free paths (IMFP's). Taking into account the possible growth processes with diffusion needs a further analytical step in which many parameters have to be considered. This part is beyond the scope of this paper.

Figure 1 shows the evolution of the cobalt substrate Auger peaks (CoMVV at low kinetic energy and CoLVV at high kinetic energy) and the platinum adsorbate Auger peaks (PtN₆₇VV) vs coverage (equiv. ML). The crossed lines correspond to a layer by layer growth model derived with the IMFP's used for these lines in Ref. 7. Even when using other sets of representations or other values for the IMFP's, there is no agreement for a FM growth mode, at least for coverages smaller than 4ML. One should point out that the IMFP of the CoLVV transition is rather large ($\approx 11\text{\AA}$) and thus, this peak is not sensitive to small changes in the growth mode. The straight lines correspond to the growth of a high density of pyramidal islands with small spatial extension. They coalesce for a high of 4 layers. The agreement is fairly good in the first stages of growth. Than one could imagine that the accumulated stress is relaxed by island formation.

After 4ML the coalescence of the film is fully completed and the growth mode is similar to a Frank - van der Merwe one.

3.2. Structure of platinum on Co(0001) for room temperature deposition

The LEED patterns remain always well contrasted during platinum deposition except a small background increase with coverage. We never observed any superstructures, i.e. the repulsive energy for Pt-Pt bonds must be very small in regard to the attractive one in Co-Pt bonds. For all thicknesses we observe a sixfold symmetry of the pattern over the whole

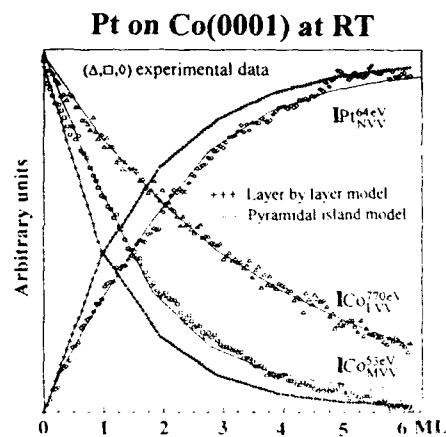


Figure 1 : Co and Pt Auger intensities as a function of platinum equivalent coverage.

observed energy range (0 - 1000 eV). This indicates either a hcp stacking of platinum or a two-domain twinned fcc structure. The peaks in the so-called I - V curves, shown in figure 2 for the (0,0) spot, can only be indexed for a hcp stacking and they are clearly located at different energies than for the clean fcc Pt(111) surface described by Stair *et al.* [8]. However, due to the coherence length of low energy electrons (< 50 nm), the addition of smaller domains with different fcc stackings (such as ABABabc + ABABcba...) are not ruled out. Such stacking sequences have recently been clearly demonstrated for the Co/Cu(111) system which exhibits, also, a six-fold LEED pattern[9]. Work is in progress to perform a complete LEED dynamical calculation on the Co/Pt system.

The in-plane parameters have been measured on the LEED patterns and the parameter along the normal to the surface has been determined through the I - V curves. These results are summarized in the left-hand side in figure 3. No relaxation in the c direction has been observed although the observed interplane distance (2.04 Å) is smaller than the Pt-Pt distance along the (111) direction (2.26 Å). For room temperature deposited layers and up to 4 ML, Pt fully accommodates the Co lattice. This is very surprising since the lattice mismatch between the two metals is about 10% leading to a very large strain in the layer. Relaxation is only observed for layer thicknesses larger than 4 ML. This is in agreement with the Auger results: in the first stages of growth, small and well ordered Pt crystallites in epitaxy with the substrate having a small lattice parameter store a large amount of the elastic energy induced by the strain. A full platinum layer with these parameters is in fact energetically very unstable. However superdensification of (111) surfaces of noble metals has been demonstrated, the stress being accommodated by interface dislocations. So, after 4ML, coalescence occurs with an increasing in-plane relaxation of the layer, allowing the spreading of the overlayer.

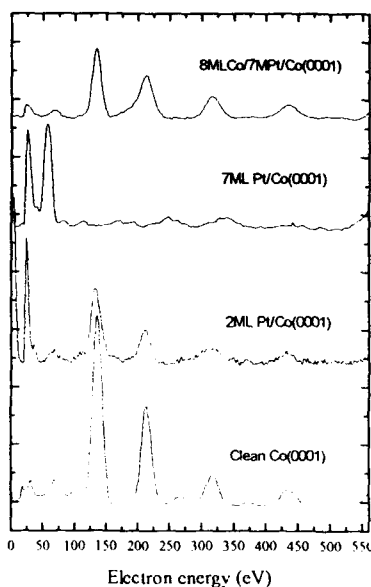


Figure 2 : I - V curves of the (0,0) spot for various Pt and Co + Pt coverages

Indeed, after 6 ML Pt deposition, the film is not fully relaxed to the Pt (111) fcc parameter. This is only the case after a short annealing at 650K during several minutes (Fig. 3, middle).

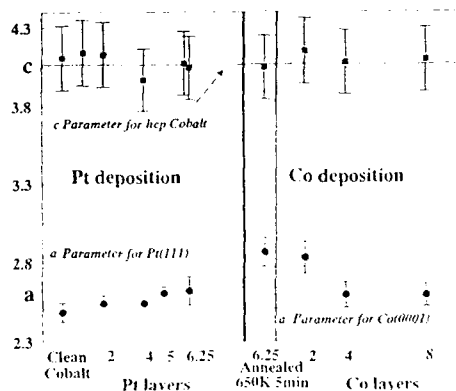


Figure 3 : Evolution of the lattice parameters a and c of the layers as determined by LEED

3.3. Temperature effect on the RT deposited film

In order to check the possibility to obtain better ordered films by heat treatments, we performed annealings for several layer thicknesses varying the temperature and the annealing time. We present in figure 4 the effect of annealing on 1 and 6 ML Pt deposited on Co(0001). Annealings up to 300°C do not improve drastically the LEED pattern, this is only the case for higher annealing temperatures. They induce a relaxation of the in-plane parameter reaching finally the Pt one (Fig. 3, right-hand side).

In the monolayer range (Fig. 4a), annealing at 200°C and 350°C during several minutes induces an increase of the Pt Auger signal. This means that the apparent surface coverage in platinum increases : this can be explained by a progressive spreading of the islands as already described in section 3.1. Under 350°C and for small platinum deposits there is neither diffusion nor alloy formation, unlike to what is observed for thicker layers.

For these thicker layers (more than 4ML) no decrease of the CoM_{VV}/PtN₇VV ratio has been observed under 300°C. In this case, the island spreading does not occur anymore since coalescence has already took place and a FM growth is now started. For annealings at 350°C, the LEED pattern improves, the six-fold symmetry remains over the whole range of energy and one observes an increase of the CoM_{VV}/PtN₇VV ratio. This is characteristic of the formation of an ordered compound or of a surface alloy, the composition of which being still not well determined since AES by itself does not allow to evaluate the concentration profile within these layers. Fig. 4b shows that the alloy is rich in Pt and we see also that during the alloy formation the N₇VV/N₆VV ratio increases up to the maximal observed ratio during the growth. This should indicate a hcp alloy in which Pt shows a magnetic moment as it will be seen in section 5.

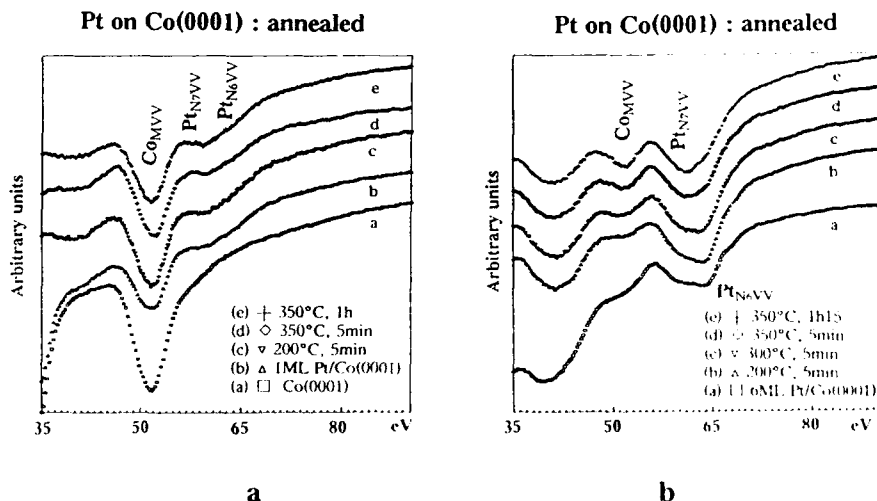


Figure 4 : Evolution of the CoM_{VV}, PtN₆VV and PtN₇VV Auger transitions for various annealings of (a) : 1 Pt ML on Co(0001), (b) : 6 Pt ML on Co(0001)

4. Co/Pt/Co SANDWICH FORMATION

As discussed in section 3 the growth of thick platinum layers on Co(0001) is well described : the Pt overlayer is flat and has well defined epitaxial relationships with the substrate. Thus it was interesting in this case to investigate the formation of Co/Pt/Co sandwiches. As a matter of fact the growth of cobalt on a relaxed Pt layer (*i.e.* annealed at 650K) can be considered as a symmetrical situation to the one where platinum is deposited on Co(0001). Of course such a surface cannot be compared with a single crystal Pt(111) substrate. Because of the greater corrugation of the surface there is no reason that the growth would be the same as the one observed on Pt(111)[10]. In our case the influence of the substrate is not known and could be determining. Here the misfit is again about 10%, but with an opposite strain. So we may expect that the cobalt layer will be expanded in the same manner as the platinum one was contracted.

In figure 3 (right-hand side) we show the results obtained for a fractional deposition of Co on a relaxed 6.25 ML Pt overlayer. It has been verified by AES that no cobalt diffusion towards the surface had occurred. We see effectively that the parameter of the thin cobalt layers (up to 2 ML) is expanded and equal to the platinum one. The full relaxation of the cobalt layer is obtained for a 4 ML deposit. For this thickness the Pt_{6,7}VV Auger peak is undistinguishable from the background and, from escape depth arguments, we can conclude that the cobalt layer is continuous. No further relaxation has been observed for thicker layers.

All along the cobalt deposition the LEED pattern has the six-fold symmetry, characteristic for a hcp or twinned fcc stacking. The adsorbate (now Co) accommodates the substrate lattice (now Pt).

The final situation, obtained for a Co(8ML)/Pt(6ML)/Co(0001) sandwich, is more probably hcp and epitaxial. Its in-plane parameter is the same as in the case of the 2ML Pt on Co(0001), and the corresponding LEED *I-V* curves are also identical. These two structures are evidently the same but one with Co on top and the other with Pt on top.

5. AES AS A LOCAL PROBE FOR MAGNETISM ?

To clarify the relationship between the spin polarization of the Pt valence band, which has been recently confirmed by spin polarized photoemission [11], and the relative behaviour of the intensities of the N₆VV and N₇VV Auger lines, a very simple approach based on the spin dependent transition probabilities of the Auger process can be used. It allows to show that the PtN_{6,7}VV behaviour is a valence band effect due to the induced magnetic moment on Pt atoms.

In the L-S coupling scheme one can finally find the following Auger probabilities P_↑ (initial excited electron "up") and P_↓ (initial excited electron "down") :

$$\begin{aligned} P_{\uparrow} &= 2\pi/h \cdot (D - E)^2 \{ 16 n_{\downarrow}(E)_f + n_{\uparrow}(E)_f \} \\ P_{\downarrow} &= 2\pi/h \cdot (D - E)^2 \{ 16 n_{\uparrow}(E)_f + n_{\downarrow}(E)_f \} \end{aligned}$$

where D and E are respectively the coulombian and exchange matrix elements, and $n_{\uparrow\downarrow}(E)_f$ the spin dependent electronic state densities at the Fermi level.

This calculation must be taken with some caution since, except the "s" levels, the other levels are not pure spin ones. They are only spin polarized. In all cases for a ferromagnet the transition probability from the minority spin level should be always the largest for any given level. So the transition probability depends essentially on the number of spin-down electrons in the level. Since the N₇ level has more spin-down electrons than the N₆ one, a progressive magnetization of the Pt adatoms should induce a relative increase of the N₇VV/N₆VV ratio.

In fact this effect is illustrated in figure 5 where the normalized N_{7VV} and N_{6VV} Auger intensities are plotted. The maximum difference between the intensities of the two Auger N_{7VV} and N_{6VV} lines occurs between the first and the second Pt layers. The first platinum layer bears an induced magnetic moment and for the following layers this is no longer the case. This phenomenon is also observed for annealed platinum layers. Fig. 5 shows clearly an evolution of the N_{7VV}/N_{6VV} ratio. This demonstrates that interdiffusion at temperatures higher than 300°C leads to an alloy where the platinum atoms bear a magnetic moment.

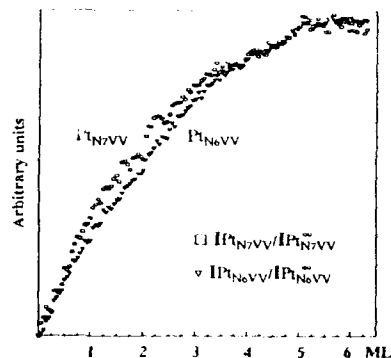


Figure 5 : Evolution of the intensity of the platinum N_{67VV} Auger lines (normalized to bulk Pt) as a function of Pt coverage.

6. CONCLUSION

At room temperature, the growth mode of ultrathin layers of platinum on Co(0001) can be characterized by the progressive coalescence of small islands which is completed for 4 monolayers. Platinum is in epitaxy on Co(0001) and accommodates the substrate lattice parameters up to a 4 ML coverage and then relaxes to its own in-plane parameter. The LEED patterns show that platinum is in a hcp stacking. Annealings at 650K induce a better crystallisation of the platinum overlayer with some interdiffusion of cobalt leading to the formation of an interfacial Co-Pt alloy. On top of these annealed layers, it is possible to grow epitaxially cobalt overlayers and to realize well structurally defined Co/Pt/Co sandwiches. In both cases (ultrathin platinum layers and sandwiches) it is possible to evidence, through modifications of the transition probabilities of the N_{67VV} Auger lines, that the platinum atoms bear a magnetic moment.

REFERENCES

1. S. Hashimoto, A. Maesaka, K. Fujimoto and K. Bessho, Appl. Surf. Sci., in press
2. A. Koote, C. Haas and R.A. de Groot, J. Phys.:Condens. Matter 3, 1133 (1991)
3. C.H. Lee, R.F.C. Farrow, C.J. Lin, E.E. Marinero and C.J. Chien, Phys. Rev. B 42, 11384, 1990
4. L. Néel, J. Phys. Rad. 15, 255 (1954)
5. D. Weller, H. Brändle, G. Gorman, C. J. Lin and H. Notaris, Appl. Phys. Lett. 61, 2726 (1992)
6. D. Weller, H. Brändle and C. Chappert, J. Magn. Magn. Mat. 121 (1993), in press
7. C. Argile and G.E. Rhead, Surf. Sci. Rep. 10, 277 (1989)
8. A. Barbier, V. Da Costa, P. Ohresser, B. Carrière and J.P. Deville, J. Magn. Magn. Mat. 121, 73 (1993)
9. P.C. Stair, T.J. Kaminska, L.L. Kesmodel and G.A. Somorjai, Phys. Rev. B 11, 623 (1975)
10. J.de la Figuera, J.E.Pietro, C.Ocal and R.Miranda, Phys. Rev. B47 (in press)
11. N.W.E.McGee, M.T.Johnson, J.J.de Vries, J.ann de Siegge, J. Appl. Phys. 7, 2424 (1993)
12. W. Weber, D.A. Wesner, D. Hartmann, U.A. Effner and G. Güntherodt, J. Magn. Magn. Mat. 121, 156 (1993)

ROUGHNESS AND MAGNETIC PROPERTIES OF Pt/Co MULTILAYERED FILMS

S.Sumii, Y.Kusumoto, Y.Teragaki and K.Torazawa
Sanyo Electric Co.,Ltd., Anpachi-cho, Gifu 503-01, Japan

S.Tsunashima and S.Uchiyama
Dept. of Electronics, Nagoya University, Nagoya 464-01, Japan

ABSTRACT

Magnetic properties and roughness of sputter-deposited Pt/Co films strongly depend on preparation conditions such as rf-input power, underlayers and their etching. Large coercivity was obtained by using suitable underlayers such as ZnO and adjusting input power higher for Co and lower for Pt. The coercivity in Pt/Co films seems to depend on the roughness of the surface and/or the layer interface as well as the perpendicular anisotropy.

INTRODUCTION

The relationship between the magnetic properties and the structure is always a very attractive problem in magnetic thin films. In particular, multilayered films such as Pt/Co will present a new idea since they consist of columnar crystallites with multilayered structure which is essential to the perpendicular magnetic anisotropy [1][2]. Therefore, the magnetic properties of the multilayered films have been considered to be much influenced by the surface roughness and the film morphology [3][4][5]. It is well known that Pt/Co films with large perpendicular magnetic anisotropy and enhanced Kerr effect at the shorter wavelength [6] are one of the promising materials for a high density magneto-optical recording medium. However, since lower media noise as well as higher stability of the recorded domains are required for such materials, it is still important for Pt/Co films to achieve both higher coercivity and better surface flatness [7].

Since the (111) orientation as well as the layer interface are important for the perpendicular anisotropy of Pt/Co films [8], it is of much interest to investigate the relationship between the structures and the magnetic properties. We have already reported that the sputter etching of SiN underlayers flatten the film surface [9] and that the hcp(002) orientation of ZnO underlayers enhance the fcc(111) orientation of Pt/Co films [10]. It was also reported that in the reactive sputtering of ZnO with Ar+O₂ gas and a ZnO target, the crystal orientation depended on the O₂ pressure [11]. According to these facts, we further tried to control the structures of Pt/Co films, namely, the roughness of the film surface and interface and the crystal orientation, by adjusting preparation parameters in the etching of underlayers, the reactive sputtering of ZnO underlayers and the sputtering of Pt/Co films.

In this paper, we report that the magnetic and structural properties of the Pt/Co sputtered films strongly depend on the properties of underlayers and on the input powers for Pt and Co targets, and discuss the relationship between the structure and the magnetic properties of the films.

EXPERIMENTAL PROCEDURE

Pt/Co films consisting of (17Å Pt/5Å Co)x9 bilayers were prepared by rf magnetron sputtering onto glass substrates placed on a rotating table. The sputtering system has a transfer table and shutters controlled by a microcomputer, and is able to prepare the films with varying input power for Pt and Co targets, independently of each other. Pt and Co were sputtered with an input power in the range of 20–200 W, which resulted in a deposition rate of 0.1–2.1 Å/sec for Pt and 0.1–2.0 Å/sec for Co. SiN and ZnO underlayers (800Å thick) were prepared by the rf sputtering from SiN and ZnO targets using Ar and (Ar+O₂), respectively. The pressures of the Ar and (Ar+O₂) were kept at 5 mTorr throughout the sputtering process.

The coercivity H_c and effective perpendicular anisotropy K_{eff} were measured with a Kerr loop tracer and a torque magnetometer, respectively. The structure of the films was examined with X-ray diffractometry (XRD), and the surface roughness (rms) was estimated from scanning tunneling microscope using DI NanoScope II with a mechanical polished Pt-Ir tip.

RESULTS

Etching of SiN underlayers

As previously reported [9][12], the sputter etching of dielectric underlayers prior to the Pt/Co deposition improves the magnetic properties

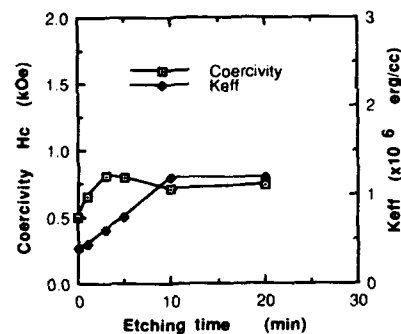


Fig. 1 H_c and K_{eff} of (17Å Pt/5Å Co)x9 with SiN underlayers as a function of etching time of the underlayer.

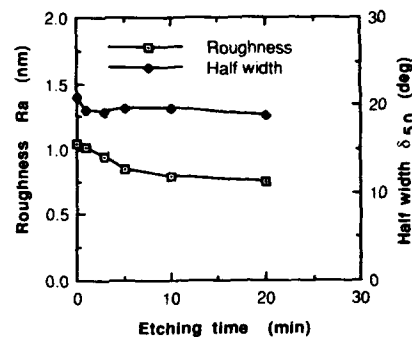


Fig. 2 Etching time dependence of surface roughness R_a and half width δ_{50} of (111) rocking curves for (17Å Pt/5Å Co)x9.

of the films. Figure 1 shows H_c and K_{eff} of Pt/Co films with SiN underlayers as a function of the etching time of the underlayers. The SiN underlayers were etched by back sputtering at an rf power of 300 W, which resulted in an etching rate of 5 Å/min. K_{eff} increased remarkably with the etching time and became saturated at around 10 min, while H_c increased at the beginning of the etching and exhibited the maximum value at several minutes.

From the XRD results, the Pt/Co films with etched underlayers showed much stronger XRD intensity for both the low-angle 1st peak and the high angle Pt/Co(111) peak [9]. This indicates that the underlayer etching improves the flatness of the layer interface and the (111) orientation. Figure 2 shows surface roughness R_a and half width δ_{50} of rocking curve for Pt/Co(111) as a function of the etching time of the underlayers. Surface roughness R_a lowered with the sputter etching and half width δ_{50} also decreased slightly. These results consistent with the previous ones, showing that the underlayer etching improves the flatness of the film surface and layer interface, as well as the (111) orientation of crystallites.

ZnO underlayer

We have found that Pt/Co films prepared on ZnO underlayers exhibit a large perpendicular anisotropy because of the epitaxial growth of Pt/Co(111) on ZnO(002) [10]. On the other hand, it is known that, in the reactive sputtering of ZnO with Ar+O₂, the crystal orientation changes depending on the partial pressure of O₂ [11]. Thus, we expect that the preferred orientation of Pt/Co(111) as well as ZnO(002) can be achieved by adjusting various sputtering conditions.

Figure 3 shows surface roughness R_a and half width δ_{50} of rocking curve for Pt/Co(111) in the films prepared on ZnO underlayers as a function of the partial pressure of O₂ during the preparation of ZnO layer. Both surface roughness R_a and half width δ_{50} show the minimum values at around a partial O₂ pressure of 5%. The rocking curves for ZnO(002) behaved in the same manner as those for Pt/Co(111).

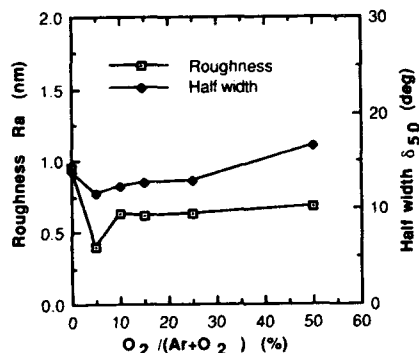


Fig. 3 O_2 partial pressure in the reactive sputtering of ZnO underlayers vs surface roughness R_a and half width δ_{50} of (111) rocking curves for (17Å Pt / 5Å Co)x9.

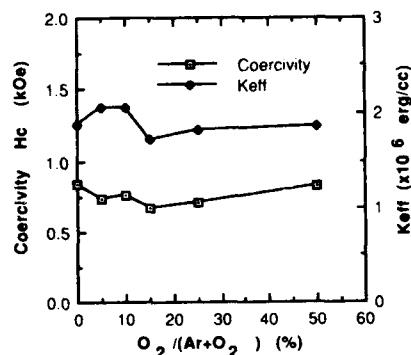


Fig. 4 H_c and K_{eff} of (17Å Pt / 5Å Co)x9 as a function of partial pressure $O_2 / (Ar + O_2)$ in the reactive sputtering of ZnO underlayers.

Figure 4 shows coercivity H_c and effective perpendicular anisotropy K_{eff} as a function of partial pressure of O_2 . Both H_c and K_{eff} changed slightly with increasing O_2 pressure, showing a small minimum in H_c at O_2 ratio of 15 % and a maximum in K_{eff} at O_2 ratio of 5 to 10 %.

Input power dependence

Since the interface between Pt and Co layers are essential to the perpendicular anisotropy [1], we tried to change the interface roughness and magnetic properties by varying Pt and Co input power, independent of each other.

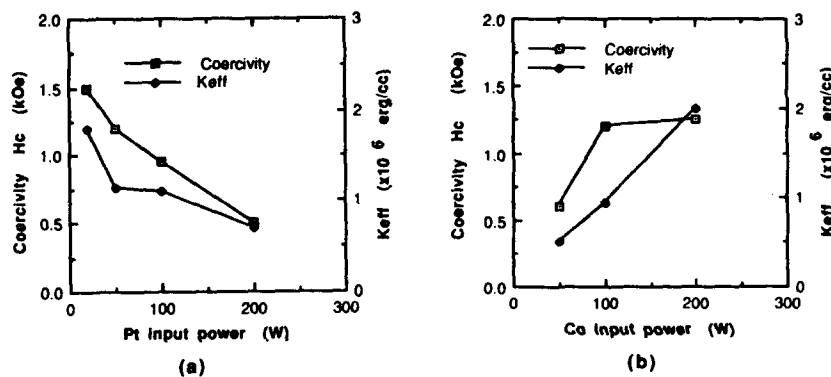


Fig. 5 Coercivity H_c and perpendicular magnetic anisotropy K_{eff} as a function of (a) Pt input power and (b) Co input power, where Co input power was 100 W and Pt 50 W, respectively.

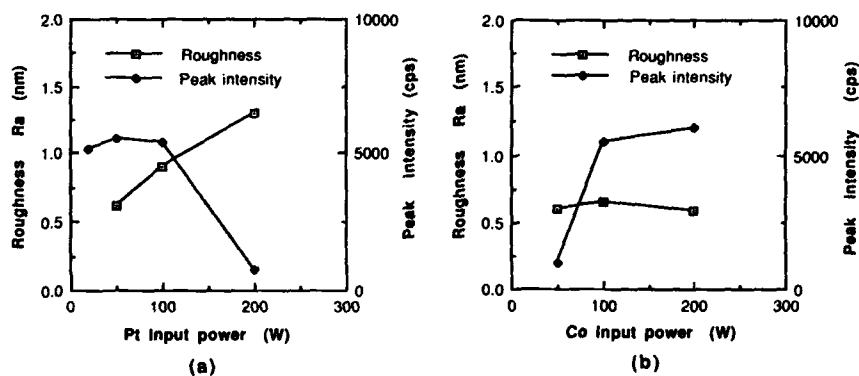


Fig. 6 Roughness R_a and 1st order peak intensity of low-angle XRD as a function of (a) Pt input power and (b) Co input power, where Co input power was 100 W and Pt 50 W, respectively.

Figures 5(a) and (b) show (a) Pt and (b) Co input power dependence of H_c and K_{eff} , where Co and Pt input powers are 100 W and 50 W for (a) and (b), respectively. Both H_c and K_{eff} decreased considerably with increasing Pt input power but increased with increasing Co input powers. The Pt/Co films showed large H_c when they prepared with lower input power for Co but higher input power for Pt. The anisotropy changed also in the same manner as the H_c .

Figure 6(a) and (b) show surface roughness R_a and 1st peak intensity of low-angle XRD as a function of (a) Pt and (b) Co input power, respectively. The surface of Pt/Co films sputtered with lower Pt input power was smoother than that of films with higher Pt input power. The 1st peak intensity that becomes higher for lower Pt input power indicates the improvement of the multilayered structural order. On the other hand, with lowering Co input power, the surface roughness did not change but the 1st peak intensity drastically decreased.

According to the results of Figs 5 and 6, both the flatness of the films and well defined multilayered structure are thought to be important for large anisotropy as well as for high coercivity. Lower input power for Pt and higher input power for Co are favorable to obtain such structures.

DISCUSSION

As seen in the previous sections, the magnetic properties and the roughness of Pt/Co films strongly depended on preparation conditions such as input power, underlayers and their etching.

In the case of the SiN underlayer etching, the coercivity H_c was proportional to the perpendicular anisotropy K_{eff} at the beginning of the etching. However, the H_c saturated earlier than the K_{eff} . On the other hand, the surface roughness lowered gradually with increasing etching time. We speculate that, in the beginning of the etching, the coercivity is related to the anisotropy field $H_k = 2K_{eff}/M_s$ or the nucleation field H_n of the reverse domains which is closely related to the anisotropy. If we assume that the wall is pinned at the defects generated from the surface roughness, the H_c will saturate and decrease again with prolonged etching, because the films with a smoother surface might have less defects, and the wall motion will become easier. Thus, although, the smooth surface and interface with the etching may bring the large anisotropy to the films [9], it will be difficult to obtain a high coercivity that is proportional to the large anisotropy.

For the film with ZnO underlayers, the anisotropy K_{eff} was obtained as large as 2.0×10^6 erg/cc which was two times larger than the films with SiN underlayers, while the coercivity H_c was nearly the same. Judging from the results of Figs 3 and 4, the coercivity is determined by neither the anisotropy nor the surface roughness. Since the films with ZnO underlayers have distinct column boundaries and fine layered structures [10], the wall might be pinned at the position of the boundaries. So the surface roughness R_a does not seem to be so important to the H_c as in the case of SiN underlayers.

As for the rf power dependence, the largest coercivity was obtained at a lower Pt input power of 20 W and a higher Co input power of 200 W. Lower Pt input power improves the Pt/Co(111) orientation and makes the surface smoother. As a result, the films exhibit higher anisotropy. On the other hand, higher Co input power enhances the anisotropy and the coercivity. Comparing Fig. 6(b) with Fig. 5(b), the coercivity is seen to change parallel to the 1st peak intensity but not always to the anisotropy. The reasons for the higher coercivity in films with the higher Co input power are not clear but they may be related to the wall pinning at the interface between Pt and Co layers.

As described above, the coercivity seems to depend often on the roughness of the film surface and the interface rather than the anisotropy. For the application to the magnetooptical recording materials, smoother surface, higher coercivity and larger anisotropy are required. Then, for the

Pt/Co films, it seems to be important to achieve both the smooth surface and the well defined interface as well as the (111) preferred orientation. These futures can be achieved by optimizing preparation conditions.

CONCLUSIONS

The magnetic properties and the roughness of Pt/Co films strongly depended on the preparation conditions such as input power, underlayers and their etching. Large coercivity was obtained by using suitable underlayers such as ZnO and adjusting input powers higher for Co and lower for Pt. However, the films with large perpendicular anisotropy did not always show large coercivity. The coercivity in Pt/Co films seemed to depend strongly on the roughness of the film surface and the interfaces. The smooth surface and interface seem to be important for good recording properties.

ACKNOWLEDGEMENT

The authors would like to thank Y.Ishii, General Manager of Information & Communications Systems Research Center, for his continuous encouragement and many helpful discussions.

This works have been done at the Center for Cooperative Research in Advanced Science and Technology (CCRAST) Nagoya University.

REFERENCES

1. P.F.Carcia: J.Appl.Phys., 63, 5066(1988).
2. S.Tsunashima, M.Hasegawa, K.Nakamura and S.Uchiyama:
J. Magn. Magn. Mat., 93, 465(1991).
3. W.B.Zeper, H.W.van Kestern, B.J.Jacobs, J.H.M.Spruit and P.F.Carcia:
J.Appl.Phys., 70, 2264(1991).
4. T.Suzuki, H.Notarys, D.C.Dobbertin, C-J.Lin, D.Weller,
D.C.Miller and G.Gorman: IEEE Trans.Magn., 28, 2754(1992).
5. S.Hashimoto, Y.Ochiai and K.Aso: J.Appl.Phys., 67, 4429(1989).
6. S.Hashimoto, H.Matsumoto and Y.Aso: Appl.Phys.Lett., 56, 1069(1990).
7. S.Sumii, Y.Kusumoto, Y.Teragaki, K.Torazawa, S.Tsunashima and
S.Uchiyama: presented at MML'93, Kyoto, Japan, 1993
(to be published in J.Magn.Magn.Mat.).
8. C.-J.Lin, G.L.Lee, R.F.C.Farrow, E.E.Marinero, H.V.Do and H.Notary:
J.Magn.Magn.Mat., 93, 194(1991).
9. S.Sumii, K.Tanase, Y.Teragaki, K.Torazawa, S.Tsunashima and S.Uchiyama:
Jpn.J.Appl.Phys., 31, 3328(1992).
10. S.Sumii, Y.Kusumoto, Y.Teragaki, K.Torazawa, S.Tsunashima and
S.Uchiyama: Proc. of ICF 6, Kyoto, Japan, 1992.
11. C.R.Arita, A.J.Purdes and P.D.Funkenbush: J.Appl.Phys., 51, 5533(1980).
12. P.F.Carcia, M.Reilly, W.B.Zeper and H.W.van Kestern:
Appl.Phys.Lett., 58, 191(1991).

ANOMALOUS PERPENDICULAR ANISOTROPY IN ULTRA-THIN Co FILMS

MICHAEL H. WIEDMANN,* BRAD N. ENGEL,* ROBERT A. VAN LEEUWEN,*
KO MIBU**, TERUYA SHINJO** AND CHARLES M. FALCO*

*Physics Department and Optical Sciences Center, University of Arizona, Tucson, AZ 85721

**Institute for Chemical Research, Kyoto University, Uji 611, Japan.

ABSTRACT

We have used *in situ* polar Kerr effect measurements to study the magnetic coercivity and anisotropy of MBE-grown Pd(111)/Co/X and Au(111)/Co/X trilayers, where X is the non-magnetic noble or transition metal overlayer Ag, Cu or Pd. Polar hysteresis curves were measured *in situ* for systematically varied Co and overlayer thicknesses $2 \text{ \AA} \leq t_{\text{Co}} \leq 20 \text{ \AA}$ and $0 \text{ \AA} \leq t_{\text{X}} \leq 50 \text{ \AA}$. We find the coercivity and total anisotropy display a strongly peaked perpendicular contribution at ~ 1 atomic layer (2 \AA) non-magnetic metal coverage. For Cu, where the effect is strongest, the total anisotropy energy rapidly decreases by a factor of 3 from its peak value after a total coverage of ~ 2 atomic layers (4 \AA) of Cu.

INTRODUCTION

Multilayers of Pd/Co and Pt/Co are potential material systems for magneto-optical data storage applications, since they can be produced with an easy-axis of magnetization oriented perpendicular to the film plane. This perpendicular anisotropy is thought to arise from the interfaces between Co and the non-magnetic metal layers. For sufficiently thin Co layers this interface anisotropy dominates the in-plane shape anisotropy of the Co film resulting in a perpendicular magnetization.

In this paper we describe studies of this interface anisotropy using *in situ* Kerr effect measurements in our molecular beam epitaxy (MBE) system. We have studied the evolution of the magnetic behavior of ultra-thin Co films during the progressive formation of interfaces with the three different non-magnetic overlayers, Ag, Cu and Pd. The Co films were epitaxially grown on Pd(111) and Au(111) surfaces and the structural and magnetic behavior systematically studied as a function of overlayer coverage and material species.

EXPERIMENT

The results reported here are for Co films in the thickness range $2 \text{ \AA} \leq t_{\text{Co}} \leq 20 \text{ \AA}$ deposited on 600 \AA thick buffer layers of both Pd (111) and Au(111). The buffer layers were grown on suitably prepared Co-seeded GaAs (110) substrates.¹ We used effusion cells for Ag and Pd deposition at 0.1 $\text{\AA}/\text{s}$ and 0.15 $\text{\AA}/\text{s}$ respectively, and optical-feedback-controlled electron-beam evaporators to deposit the Au (0.1 $\text{\AA}/\text{s}$), Co (0.25 $\text{\AA}/\text{s}$) and Cu (0.1 $\text{\AA}/\text{s}$). All deposition rates were determined from Rutherford backscattering spectrometry (RBS) analysis of thick calibration films. The background pressure during deposition was $\leq 5 \times 10^{-10}$ torr and consisted mostly of hydrogen. The crystalline quality of the films was monitored during growth with Reflection High Energy Electron Diffraction (RHEED). The RHEED images were captured with a digital camera system capable of resolving changes in surface lattice spacings $\sim 1\%$.

A sample can be transferred between the deposition chamber of our MBE system and another connected ultra-high vacuum chamber ($P < 2 \times 10^{-10}$ torr) where it is aligned between the poles of an external electro-magnet for *in situ* Kerr effect measurements. The magnetic field is applied along the sample normal with a maximum field of ± 2.2 kOe. We use a 50 kHz photo-elastic modulator and lock-in amplifier based detection scheme with a HeNe-laser to measure the polar Kerr ellipticity of the sample as a function of applied field. Measuring

the ellipticity rather than the Kerr rotation eliminates the background Faraday rotation from the quartz vacuum window. Optical access is provided by a hole along the axis of one of the magnet poles. The sample can be moved repeatedly between the measurement and the deposition chambers without need for optical realignment.

After deposition of the thick Pd or Au buffer layer and ultra-thin Co film, *in situ* polar Kerr hysteresis curves were measured from the initially uncovered sample. Kerr measurements were then repeated after each of the many overlayer depositions spanning the coverage range $0 \leq t_x \leq 50 \text{ \AA}$ in small 1–10 \AA steps. The entire deposition/measurement cycle for each coverage step required less than ten minutes in a pressure $P < 2 \times 10^{-10}$ torr. Therefore, surface contamination was insignificant.

RESULTS AND DISCUSSION

Coercivity Measurements

The perpendicular hysteresis curves of the uncovered Co grown on Pd buffer layers are nearly square for $t_{\text{Co}} \leq 6 \text{ \AA}$ with coercive fields of $H_c \leq 200 \text{ Oe}$. In contrast, the Co films grown on Au surfaces show nearly square curves for $t_{\text{Co}} \leq 12 \text{ \AA}$. Above these thicknesses, the easy-axis becomes in-plane with a resulting linear hysteresis curve when measured in the perpendicular direction. The difference in perpendicular anisotropy observed for the Pd and Au buffer layers is likely dominated by differences in the quality of Co growth on these two surfaces. However, for a particular range of Co film thicknesses where the initial easy-axis is strongly in-plane, deposition of approximately one atomic monolayer (ML = 2 \AA) of any of the metals Ag, Cu, or Pd results in strongly perpendicular square hysteresis loops. This surprising phenomenon indicates that a large change in the perpendicular anisotropy results from a very small amount of overlayer material.

To investigate the influence of the overlayer interface as it is progressively formed, we measured hysteresis curves as a function of overlayer coverage. Figure 1 is a plot of the coercive field H_c versus Cu coverage of a 6 \AA Co film deposited on Pd (111). The most striking feature is the pronounced peak in the coercivity at $\sim 2 \text{ \AA}$ coverage which, to within our resolution and control, is located at $\sim 1 \text{ ML}$. For slightly higher coverage, the coercivity rapidly drops to a minimum by $\sim 5 \text{ \AA}$. We have measured the coercive field H_c versus Cu

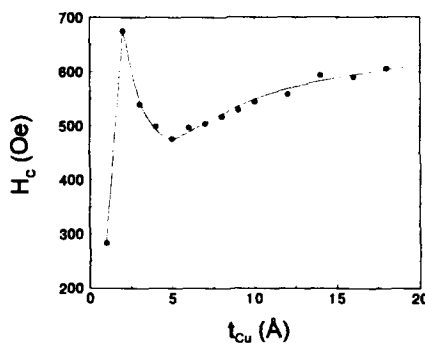


Figure 1 Coercive field H_c vs. Cu overlayer coverage t_{Cu} of a 6 \AA Co film deposited on Pd (111). The pronounced peak at 2 \AA is at one monolayer coverage to within our resolution.

overlayer coverage for four different Co thicknesses 4, 6, 8, and 10 Å. The pronounced peak with overlayer coverage is evident for all four Co thicknesses and is located at the same 2 Å coverage. However, the peak-to-valley change of the coercivity varies somewhat, increasing with Co thickness. The behavior of Ag overlayers is very similar to that of Cu.

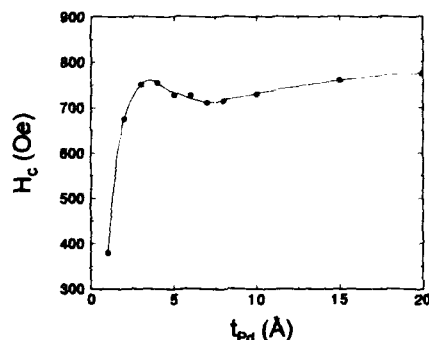


Figure 2 Coercive field, H_c , vs. Pd overlayer coverage t_{Pd} of an 8 Å Co film deposited on Pd (111). The peak near one monolayer coverage is less pronounced than for Ag or Cu.

Figure 2 is a plot of the coercive field H_c versus Pd coverage of an 8 Å Co film deposited on Pd (111). The behavior is similar to that observed for the Cu overlayers. However, Pd overlayers do not display such a prominent coercivity peak as shown in Figure 2. Deposition of 2 Å of Pd greatly increases the coercivity of the Co film compared to that of the bare Co. However, above 2 Å Pd coverage, the coercivity decreases much less than for Cu and Ag overlayers.

We have simultaneously measured the remanent ellipticity ϵ_k to search for any change in the total magnetic moment coincident with the large observed change in coercivity. Figure 3

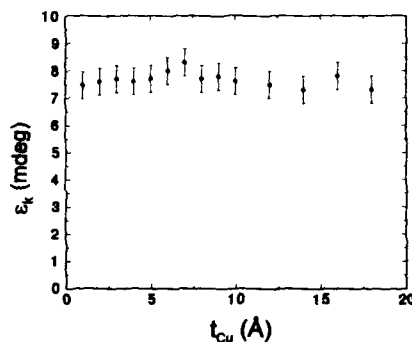


Figure 3 Remanent Kerr ellipticity, ϵ_k , vs. Cu coverage, t_{Cu} , of the 6 Å Co film from Figure 1. The ellipticity does not show any anomalous behavior near one monolayer coverage.

is a plot of ellipticity *versus* Cu coverage for the 6 Å Co on Pd sample of Figure 1. In contrast to the coercivity, ϵ_k is constant near 1 ML and hence there is no abrupt change in magnetization with Cu coverage.

There is also no evidence from our simultaneously measured RHEED data of any large discontinuous structural changes for any of the overlayer materials. We cannot, however, rule out any subtle structural changes below our $\sim 1\%$ resolution. In addition, RHEED measures only the in-plane lattice spacing and is not sensitive to any changes in the perpendicular atomic spacings.

Anisotropy Measurements

The pronounced peak in the perpendicular coercivity we observe at ~ 1 ML suggests a large change in anisotropy with overlayer coverage. However, coercivity is the result of the interaction of several parameters rather than being a fundamental magnetic quantity. For this reason we have directly measured the uniaxial anisotropy of Co films *in situ* as a function of metal coverage. To accomplish this, we measured hard-axis magnetization curves and deduced the anisotropy field by extrapolating the linear curves to saturation. Because our MBE system is equipped with only a 2.2 kOe perpendicular magnetic field, we are limited to making these measurements on films with in-plane easy-axes of moderate anisotropy strength. However, we can create films of this type by selecting the proper Co film thickness that we grow on the Pd or Au buffer layers. Using this idea of designing samples which balance the relatively strong shape and interface anisotropies against each other allows us to very easily observe small changes in the total anisotropy energy due to overlayer deposition. Figure 4 is a schematic of this measurement technique.

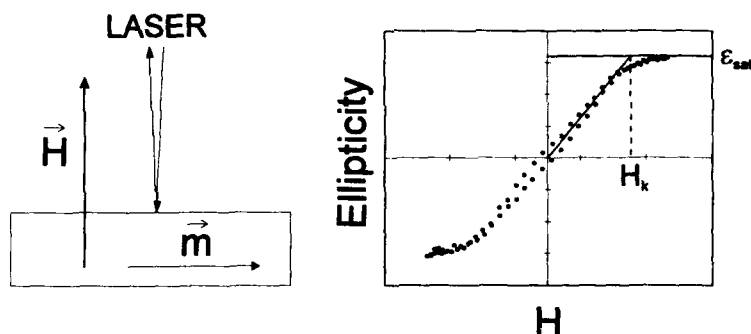


Figure 4 Schematic of the *in situ* anisotropy energy measurement. The magnetization \mathbf{m} lies in the plane of the sample while the applied field \mathbf{H} is perpendicular to the film plane.

The properly chosen Co thickness allows saturation of the magnetization by our 2.2 kOe field after overlayer coverage, while still maintaining an in-plane easy-axis. In this way we can directly determine the anisotropy field from extrapolation of the hard-axis curves to saturation and calculate the total anisotropy energy from the relation

$$K_1 = H_k M_s / 2 \quad (1)$$

where $M_s = 1422 \text{ emu/cm}^3$ is the bulk saturation magnetization of Co. To assure the validity of this technique, after completing our complete set of *in situ* measurements we removed representative samples and verified the bulk magnetization behavior of the Co with a

vibrating sample magnetometer. We also verified the saturation ellipticity ϵ_{sat} with an *ex situ* Kerr measurement to 10 KOe.

Figure 5 is a plot of the anisotropy constant K_1 vs. Cu coverage for 12 Å Co on Pd(111) and 18 Å Co on Au(111), respectively. The total anisotropy energy displays the same peaked behavior with Cu coverage we observed in the coercivity of the perpendicular films discussed earlier. The overall negative anisotropy values of Figure 5 indicate an in-plane easy-axis was maintained throughout the coverage range. Here we have adopted the convention used by many researchers, where a positive K_1 indicates perpendicular anisotropy.

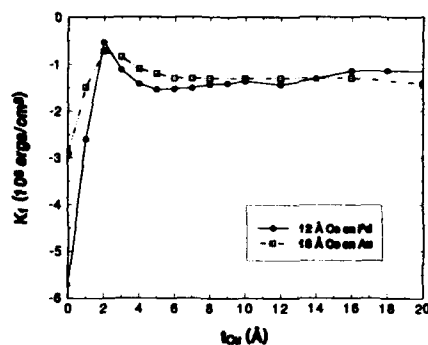


Figure 5 The total anisotropy energy K_1 vs. Cu overlayer coverage of 12 Å Co on Pd(111) and 18 Å Co on Au(111).

In Figure 5, the initial total anisotropies of the two uncovered Co films are strong and in-plane, but with different magnitudes for the Pd and Au buffer layers. As the Cu coverage is increased from 0 to 2 Å, the magnitude of this anisotropy energy rapidly approaches zero, indicating the presence of an increasing perpendicular contribution. This large increase in perpendicular anisotropy after Cu coverage is surprising in light of the very weak interface anisotropy displayed in Co/Cu multilayers.² One possibility is the existence of a large, in-plane Co/vacuum interface anisotropy that is being replaced by a perpendicular contribution from the forming Co/Cu interface. Such a large in-plane vacuum interface anisotropy has recently been observed in fcc Co (100) films.³ However, this picture is not entirely consistent with our data since there is a large behavioral difference between Co grown on Pd and Au buffer layers. More work is needed to separate the substrate and morphological effects on the anisotropy in this low coverage regime.

Above 2 Å Cu coverage, the total anisotropy becomes increasingly negative indicating a reduction of the perpendicular contribution. A possible explanation of this phenomenon is the existence of a structural change in the Co film due to the overlayer. However, there is no evidence from our simultaneously measured RHEED data of any abrupt in-plane structural changes within our resolution of ~1%. The RHEED streak spacings change continuously from those of the Co surface to those of bulk Cu (~2% difference) by 6 Å Cu coverage. Unfortunately, we cannot say at present whether the Cu grows in a layer-by-layer mode, and hence it is difficult to uniquely determine the presence of strain at the interface. However, as discussed earlier, the behavior of Ag and Cu overlayers on Co is very similar. These overlayers have very different lattice mismatches with Co (~14% for Ag and ~2% for Cu) and hence it is unlikely that the presence of localized strain at the interface can entirely explain the observed behavior.

Another possibility is that the magnetic interface anisotropy is very sensitive to details of the electronic band-structure.⁴ Recent photoemission measurements^{5,6} of Cu monolayers deposited on ferromagnetic metals have found electronic states that deviate significantly from

bulk behavior. This variation of the overlayer electronic structure in the monolayer limit may be related to our observed peak in perpendicular anisotropy at 1 ML coverage.

SUMMARY AND CONCLUSIONS

In conclusion, we have used *in situ* polar Kerr effect measurements to study the perpendicular magnetic behavior of MBE-grown Pd/Co/X and Au/Co/X sandwich structures where X = Ag, Cu, and Pd. For these overlayers, we find an enhanced perpendicular contribution to the coercivity and total anisotropy peaked at a coverage of ~1 ML. The coverage dependence reported here will provide a rigorous test for theoretical explanations of the magnetic anisotropy at interfaces and in layered metallic systems.

ACKNOWLEDGEMENTS

This work was supported by the U.S. Department of Energy Grant No. DE-FG02-87ER45297 and the Optical Data Storage Center at the University of Arizona. The authors greatly acknowledge J. Leavitt for RBS measurements. We also thank the Japan Society for the Promotion of Science and NSF INT-90-16752 for a travel grant.

REFERENCES

1. C. D. England, B. N. Engel, and C. M. Falco, *J. Appl. Phys.* **69**, 5310 (1991).
2. F.J.A. den Broeder, W. Hoving, P.J.H. Bloemen, *J. Magn. Magn. Mat.* **93**, 562 (1991).
3. P. Krams, F. Lauks, R.L. Stamps, B. Hillebrands, and G. Güntherodt, *Phys. Rev. Lett.* **69**, 3674 (1992).
4. A.J. Freeman and R. Wu, *J. Magn. Magn. Mater.* **100**, 497 (1991).
5. D. Hartmann, W. Weber and G. Güntherodt, *Ultra Thin Films, Multilayers and Surfaces*, edited by F.J.A. den Broeder (MRS, Pittsburgh, in press). Symposium held 7-10 September 1992. Lyon, France.
6. J. E. Ortega, F. J. Himpsel, G. J. Mankey and R. F. Willis, *Phys. Rev. B* **47**, 1540 (1993).

Section B—Interfaces and Characterization

PART I

Theories and Spin Polarized Spectroscopies

Magnetism and Magnetic Interactions at Transition Metal Surfaces and Interfaces

Ruqian Wu¹, Dingsheng Wang^{1,2} and A.J. Freeman¹

¹Department of Physics & Astronomy, Northwestern University, Evanston, IL 60208-3112

²Institute of Physics, Academia Sinica, Beijing 100080, P.R. China

ABSTRACT

In the exciting field of low dimensional magnetic systems including surfaces, interfaces and thin-films, local spin density (LSD) functional *ab initio* electronic structure calculations have played a key role by not only providing a clearer understanding of the experimental observations but also predicting new systems with desired properties. Our extensive calculated results demonstrate that: (i) magnetic clean surfaces or interfaces with inert substrates undergo strong magnetic moment enhancements; (ii) the strong interaction with nonmagnetic transition metals diminishes (completely in some cases) the ferromagnetism and usually stabilizes the antiferromagnetic configuration. By including spin-orbit coupling as a perturbation, (i) reliable results for the magneto-crystalline anisotropy of ultra-thin films can be obtained using the state-tracking procedure, although the anisotropy energy is a few tenths of a meV; (ii) spectra of the magneto-optical Kerr effects and magnetic circular dichroism in the soft x-ray region can be determined.

INTRODUCTION

During the course of the last decade, low-dimensional magnetism of surfaces, interfaces and thin-films has matured into a major branch of modern condensed matter physics and is likely to open vast vistas for practical applications. [1, 2] The abrupt termination of the lattice or composition in these systems leads to a variety of exotic phenomena such as localized electronic states, magnetic moment enhancement, perpendicular magneto-crystalline anisotropy (MCA), complex magnetic ordering, etc. Fortunately today, it is possible to synthesize and study thin films with either stable or metastable phases, and this has dramatically and importantly increased the range of materials that are magnetic and hence the challenges for understanding magnetism in low dimensional systems.

It is known that *ab initio* numerical energy band methods (mainly the full-potential linearized augmented plane wave (FLAPW) method) based on local spin density (LSD) functional theory have played a very important role in the development of lower-dimensional magnetism. [3] Theoretical calculations predicted the large enhancement of the magnetic moment for 3d transition metal (TM) surfaces or TM ultrathin films deposited on inert substrates, [4] and possible magnetism in some normally non-magnetic materials [5]; some of these predictions have been already verified experimentally. [6, 7]. Stable magnetic structures, especially some antiferromagnetic (AFM) configurations, can now be predicted by comparing total energies and, in the same way, equilibrium atomic geometries and lattice relaxation (including surface and interface) can also be determined. Very recently, we proposed and implemented a state-tracking procedure to treat the effects of spin-orbit coupling (SOC) into our FLAPW method. As a result, we can obtain (i) reliable MCA energies (although it is as small as a few tenths of an meV/atom) for real complex systems and (ii) magneto-optical Kerr effect (MOKE) and magnetic soft x-ray circular dichroism (MCD). Model analyses have been shown to provide a clear physical picture for these important phenomena previously thought to be very complex.

Results surveyed here include predicted surface and interfacial effects on the magnetic moment, magnetic ordering and the effects of SOC on MCA, MOKE and MCD.

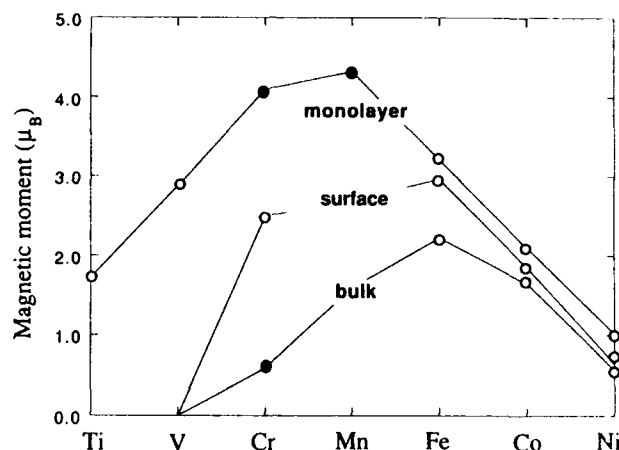


Figure 1: The calculated magnetic moment of 3d transition metals in their bulk, surfaces and monolayers. Open (filled) circles denote the ferromagnetic (antiferromagnetic) ground state.

MAGNETIC MOMENT ENHANCEMENT IN LOW-DIMENSIONAL SYSTEMS

Surprisingly, early studies [8] reported that Ni, Fe and Co surface layers were magnetically "dead" (later investigations traced these results to surface contamination). Now it is well recognized that, as expected, environments with few nearest neighbors and hence weaker interatomic hybridization are conducive to enhanced magnetization. [3] As shown in Fig. 1, a general trend is clearly demonstrated that the magnetic moment of 3d transition metals increases with decreasing dimensionality of the system from bulk, surface to monolayer according to the first principles calculations.

When first found, the prediction of enhanced magnetism at transition metal surfaces was thought to be unusual. Wimmer et al. [9] attributed the large surface magnetic enhancement (23%) for Ni(001) to two additive effects: (i) *sp-d* dehybridization at the surface and (ii) electrostatic shifts required to maintain layer-by-layer neutrality. Since the magnetism of Ni is determined by the number of 3d holes and thus by the *sp-d* charge transfer, it reacts very strongly to changes in the environment due to the large spatial extension of the *sp* wave functions. For the Ni monolayer, *s, p* states become more occupied in the vacuum region to lower the kinetic energy, which creates more minority spin 3d holes and thus enhances the magnetic moment to 1.02 μ_B . The same amount of change for the magnetic moment is expected for Co and Fe. Indeed, as shown in Fig. 1, the three curves become almost parallel for Co and Ni (top two curves for Fe, Co and Ni). For Fe bulk, it is known that part of antibonding majority spin band becomes unoccupied which, of course, diminishes the magnetic moment drastically (reflected also by a large percentage of magnetic moment enhancement on Fe surfaces). [10]

Still today, few directly measured magnetic moment exist. A technique to obtain surface M by fitting SPLEED "rocking curves" [6] has been developed recently but there still exists some uncertainty because the results were deduced from only one spectral feature. For example, the reported magnetic enhancement for Fe(110) [6] is 36%-40%, which is about two times larger than our theoretical result (19%). For Ni(001), the experimental value is definitely lower than that predicted theoretically; good agreement was found, however, for Ni(111) [11].

Note that non-magnetic elements, namely Ti and V, also possess magnetism in their monolayers with sizable magnetic moments ($1.7 \mu_B$ and $2.9 \mu_B$, respectively) due to the reduced coordination number. Physically, the narrowed 3d band width results in a giant density of states at the Fermi level for the paramagnetic (PM) case, and thus induces much stronger Stoner magnetic instability in the lowered dimensions. For example, the Stoner factor for the PM V(001) surface layer is 0.68, a value still far from 1.0 (a critical value for a PM to FM phase transition), thus, V(001) is magnetically "dead." For the V monolayer, with only 4 second neighboring atoms, the Stoner factor increases to 2.19. This induced ferromagnetism in a free standing monolayer geometry has also been predicted for some 4d elements as Pd, Rh and Ru etc. (with magnetic moments of $0.35 \mu_B$, $1.45 \mu_B$ and $2.12 \mu_B$, respectively). [13] The density of states at E_F of PM Ru and Rh monolayers are found to increase by 450% over their corresponding bulk values, which results in a large Stoner factor (1.45 and 1.89 for Ru and Rh monolayers, respectively) and thus a Stoner instability.

INTERFACIAL EFFECTS

An important development in the last decade is the ability to study 2D (monolayer) magnetism by the synthesis of ultrathin magnetic films on various kinds of substrates. The lively interplay of theory and experiment has already yielded unusual results. [3] In general, interfacial effects with inert substrates (noble metals and ceramics) do not affect significantly the magnetism of free monolayers (except Ni), while strong *d* band interaction with transition metal substrates (except Pd) diminishes the overlayer ferromagnetism substantially and usually leads to some kind of AFM configuration.

3d Overlayers On Inert Substrates

In Fig. 2, the calculated magnetic moment for 3d metal monolayers on Ag(001) and Cu(001) substrates are presented. For Fe and Co, the Ag substrate reduces their free monolayer magnetic moment only negligibly, by 0.1 - $0.2 \mu_B$. This is expected since Ag lacks electronic states at the Fermi energy, which minimizes the overlayer-substrate hybridization and thus enhances the overlayer magnetism. By comparison, Cu(001) exhibits stronger proximity effects since, as shown in Fig. 2, the overlayer magnetic moments on Cu(001) are $0.3 \mu_B$ smaller than on Ag(001). Physically, the reduction of the overlayer magnetic moment results from (i) less (more) occupation in the 3d band for majority (minority) spin due to the overlayer-substrate *d*-band hybridization and (ii) the feedback of *sp* electrons into the overlayer region (also explained as a charge transfer from the substrate [14]) which usually give a negative contribution to that from *d* electrons. The proximity effects are especially important for Ni because of its small magnetic moment. As shown in Fig. 2, the Ni magnetic moment decreases by $0.5 \mu_B$ in Ni/Ag(001) and $0.7 \mu_B$ in Ni/Cu(001) – about 50% or more of the value for the free standing monolayer, $1.02 \mu_B$. It is not surprising that, as predicted in FLAPW calculations [15] and also confirmed in experiments [16], Ni monolayer becomes truly magnetically dead when sandwiched by Ag.

Mn and Cr monolayers exhibit AFM coupling of their giant magnetic moments for both the isolated and adsorbed cases. Surprisingly, the greatly enhanced moment of Cr/Au is only moderately reduced when Cr is itself covered by an additional Au layer. [17] The Cr magnetic moment is as large as $2.90 \mu_B$, and a stable in-plane AFM coupling occurs for a Au/Cr/Au(001) superlattice.

Whereas an isolated V monolayer is ferromagnetically ordered, the coupling changes dramatically to antiferromagnetic ordering when deposited on a Ag(001) substrate. As revealed in our recent studies, this phase transition can be attributed primarily to interfacial *sp-d* hybridization (with a charge transfer from both Ag and V sites to the interfacial region). While most of the recent experiments failed to detect unambiguous manifestations of ferromagnetism in V/Ag(001), [18] one group claims to have done so. [19] The reason for this difference is still a point of

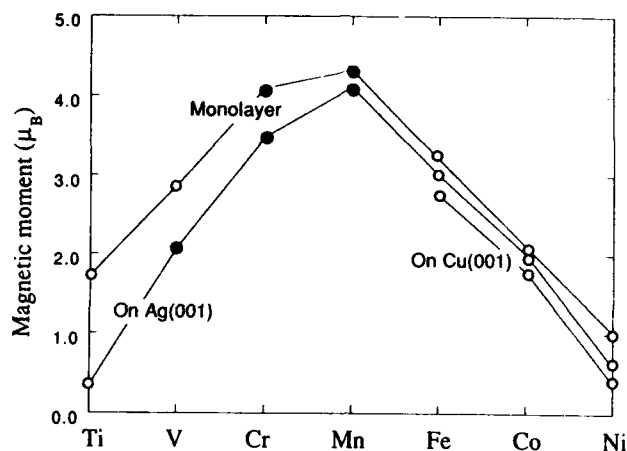


Figure 2: The calculated magnetic moment of 3d transition metal monolayers on the Ag(001) and Cu(001) substrates. Open (filled) circles denote the ferromagnetic (antiferromagnetic) ground state.

controversy.

3d Overlayers On Transition Metal Substrates

Due to the strong interfacial *d* band hybridization between magnetic overlayers and transition metal substrates, large overlayer relaxations and their strong interplay with the magnetism have been found for these systems. As illustration, we cite here two examples (i) Fe/Ru(0001) and (ii) Fe/W(001).

The Fe(111)_n/Ru(0001) overlayer system [20] and the hcp Fe_n/Ru_m [21] superlattice were reported to be "magnetically dead" when the number "n" of Fe layers is less than 2 (on the surface) or 4 (in the superlattice). Strikingly, the ferromagnetism of the first 2 (4) Fe layers can not be activated by deposition of successive FM Fe layers, as deduced from a thickness-dependent extrapolation. [20] The calculated total energy difference and the magnetic moment for the Fe/Ru(0001) system (using the FLAPW method) [22] are plotted in Fig. 3 with respect to the nearest Fe-Ru distance. Obviously, (i) the in-plane AFM state lies lowest in energy and thus becomes the stable ground state for Fe(111)/Ru(0001) – which explains the origin of the observed "magnetically dead layers"; [20, 21] (ii) the magnetization affects the overlayer relaxation strongly, from a 6% contraction for PM case to a 1% expansion for the FM and AFM cases; and (iii) the magnetic moment becomes a strong function of the Fe-Ru distance, especially for the FM phase. At the equilibrium position, the local magnetic moment of AFM Fe/Ru(0001) is 2.2 μ_B – about reduced 30% from that of the free standing Fe monolayer (with the same pseudomorphic geometry), 2.9 μ_B . Calculations carried out for Fe_n/Ru_m superlattices [23] found that Fe is magnetically dead when n=1. For thicker Fe films, the antiferromagnetic coupling through the intervening Ru layers becomes more favorable.

By contrast, the interfacial interaction for Fe/W(001) is even stronger because of the roughness of the bcc W(001) surface. Our FLAPW calculation results indicated that, although the free Fe monolayer shows strong ferromagnetism with a large magnetic moment (3.1 μ_B), Fe/W(001) has

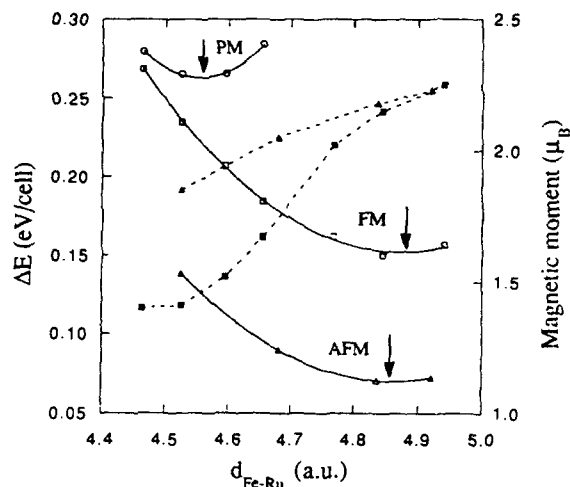


Figure 3: The calculated total energy difference (solid lines) and magnetic moment (dashed lines) for Fe/Ru(0001). Circles, squares and triangles represent results for paramagnetic, ferromagnetic and antiferromagnetic states, respectively.

no stable or even metastable FM state. More importantly, the AFM state, with a magnetic moment of $0.7 \mu_B$ at the equilibrium position, is about 0.01 eV/cell lower than the PM state. As was also the case for Fe/Ru(0001), [22] we found that a strong overlayer-substrate d band hybridization usually leads to AFM coupling. Very interestingly, the FM of the previous "dead" Fe layer can be activated by an additional Fe overlayer and the moments in the interface and surface layers increase to $1.68 \mu_B$ and $2.43 \mu_B$, respectively. Therefore, the observation of magnetism in Fe/W(001) should vary dramatically between one and two layers.

Possibility of Magnetism in Non-magnetic 4d Elements

Since the $4d$ wave function is more spatially extended compared to the $3d$'s, their magnetic properties are expected to be more sensitive to any small change of the environment. Indeed, Pd(001) and Pd(111) are predicted to be magnetically dead despite the expectation of magnetic moment enhancement at the surface. A Pd monolayer was found to lose its magnetism on the Ag(001) surface and even on MgO(001), which is found to be an almost perfect substrate (no chemical interaction) for Fe overlayer magnetism. [24]

Strikingly, the magnetism of the free Rh monolayer is found to remain on the Ag(001) and Au(001) substrates. [13] However, verification experiments failed to find any evidence of ferromagnetism in Rh/Ag(001) at temperatures down to 40 K. [25] To verify this discrepancy, FLAPW calculations, including total energy determinations of the overlayer relaxation, were carried out for the Rh/Ag(001), Ru/Ag(001), Ag/Rh/Ag(001) and Ag/Ru/Ag(001) systems. We found that: (i) the overlayer relaxation is less than 2% for both Ru/Ag(001) and Rh/Ag(001); (ii) FM ordering is confirmed to be the ground state for Rh/Ag(001) with a sizable magnetic moment of $0.96 \mu_B/\text{atom}$, but that an additional Ag overlayer diminishes the magnetic moment to $0.46 \mu_B/\text{atom}$, and more importantly, reduces drastically the energy of magnetization from 0.039 eV/atom to almost zero - explaining the lack of a FM signal in the SMOKE experiments; [25] (iii) considerable charge redistributions for all the systems (accumulated in the interfacial region) suggests a strong

4d overlayer-substrate interaction; (iv) by contrast, the FM state lies much lower in energy than the PM state for both Ru/Ag(001) and Ag/Ru/Ag(001) – which thus provides a more suitable system for experimental verifications of 4d ferromagnetism than does Rh.

X-RAY MAGNETIC CIRCULAR DICHROISM

It is known that SOC induces orbital magnetic moments in magnetic materials. The calculated orbital magnetic moment, $\langle L_z \rangle$, was found to enhance significantly at the Ni(001) surface ($0.08 \mu_B$) and in the free Ni monolayer ($0.10 \mu_B$) compared to that for bulk Ni ($0.036 \mu_B$). For Co monolayer, a more drastic enhancement for L_z has been found ($0.16 \mu_B$ vs $0.04 \mu_B$ for bulk Co). In fact, the perturbation of SOC on the wave functions is inversely proportional to the band width, thus the enhancement of $\langle L_z \rangle$ in low dimensions is expected due to the band narrowing.

Now the problem is how to isolate the small orbital contribution from the predominant spin magnetic moment for 3d transition metal systems. The recent development of x-ray magnetic circular dichroism (MCD) [26] sheds some light since an MCD sum rule has been proposed, [27] which builds up a direct connection between $\langle L_z \rangle$ and the features of the MCD spectra as

$$\frac{\int_{L_3+L_2} \sigma_m dE}{\int_{L_3+L_2} (\sigma_t + \sigma_0) dE} \approx -\frac{\langle L_z \rangle}{2N_h} \quad (1)$$

Here $\sigma_m = \sigma_+ - \sigma_-$ and $\sigma_t = \sigma_+ + \sigma_-$, with σ_+ , σ_- and σ_0 representing the cross sections for left-, right-circularly polarized and parallel polarized (along the direction of magnetization) incident light. Compared to other techniques, the high element selectivity of MCD is especially useful for identifying the magnetism from different specific atoms (e.g., impurity, surface or interface, etc.). We carried out highly precise first principles calculations (based on the FLAPW method) and a tight binding analysis and found that the MCD sum rule is valid only at high symmetry points in the Brillouin zone (BZ). Thus, it cannot be applied to 3d transition metal systems for which strong interatomic hybridization is involved.

To calculate the MCD spectra from first principles theory, one actually determines the energy dependence of the difference between σ_+ and σ_- . For electric dipole transitions,

$$\sigma_{\pm}(E) = \int_k |\langle \psi_c | p_{\pm} | \psi_v \rangle|^2 \delta(E_v - E_c - E) dk \quad (2)$$

Integrations of the angular and spin momentum parts result in the selection rules

$$\Delta l = \pm 1; \Delta m = \pm 1; \Delta s = 0 \quad (3)$$

We calculated the cross sections from both a first principles and a tight binding analytical way. While the results obtained from these ways agree with each other and serve as a check of the validity of the complex first principles calculations, we found that the MCD sum rule is the natural result of our calculations for the $\bar{\Gamma}$ point. Away from the high-symmetry k points, the LCAO wave functions with different angular and magnetic quantum numbers are mixed up, and the validity of the MCD sum rule becomes a question. Our highly precise FLAPW calculations indicate that this MCD sum rule holds to within 5-10% for transition metal systems if the contributions from the high-lying s and p states are excluded in the integrations in Eq (1). This can be done by cutting the upper-limit of integrations for total absorption and N_h when the MCD spectrum approaches zero (cf. Fig. 4) for both L_3 and L_2 peaks.

Fig. 4 presents the k -integrated σ_t (dotted lines) and σ_m (solid lines) for the Ni monolayer; of course, only the values above E_F are detectable in absorption experiments. Physically, we found that SOC plays the key role in MCD phenomena. SOC enhances (reduces) the L_3 (L_2) absorption peak for the unoccupied states, and reduces (enhances) the L_3 (L_2) absorption peak for the occupied states. MCD measurements for the occupied states (spin-resolved emission experiments) are highly desired to verify our other theoretical predictions.

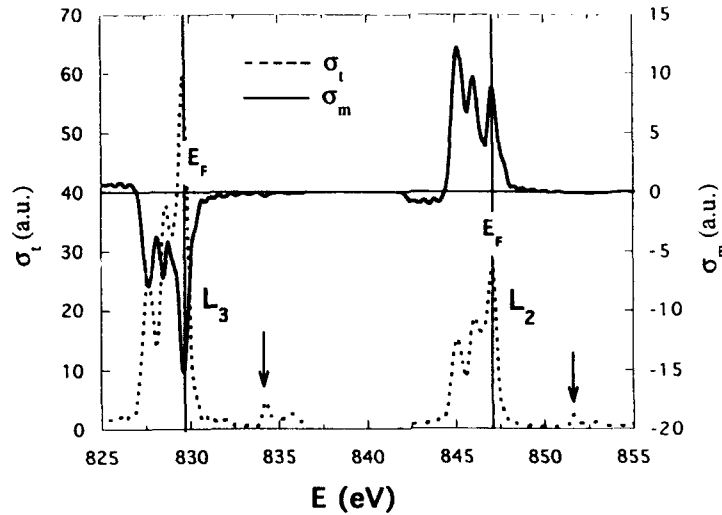


Figure 4: The k -integrated σ_m (solid lines) and σ_l (dotted lines) for a Ni(001) free standing monolayer. The vertical E_F lines separate the occupied and empty states. Arrows in panel point out the position of side peaks.

MAGNETO-CRYSTALLINE ANISOTROPY

To determine the MCA, the SOC ($H^{\text{sl}} = \xi \vec{\sigma} \cdot \vec{L}$) must be included into the Hamiltonian. In transition metal systems, since the SOC is much weaker compared to the crystalline field, a perturbative (rather than self-consistent) treatment based on a force theorem [28] is usually adopted in MCA calculations, in which the SOC induced change of total energy is given by $E^{\text{sl}} = \sum_{O'} \epsilon'_i - \sum_O \epsilon_i$. Now the problem is how to define the set $\{O'\}$ of occupied states after SOC is introduced. In all previous calculations, [29, 30] $\{O'\}$ was defined solely by comparing the eigen-energies, ϵ'_i , regardless of any information about their wave functions (Fermi filling). This definition (i) results in a strong stochastic MCA energy distribution in the BZ and with respect to the charge filling [30] and (ii) violates its basic assumption, i.e., minimal change of the charge and spin densities required by the correct application of the force theorem. [28] This is why previous first principles theoretical studies of MCA actually resulted in seemingly more controversy than success. [30]

Very recently, we proposed a state tracking technique [31] to determine the set of occupied states $\{O'\}$ which can ensure the stability of the calculated MCA energy with respect to the number of k points, electron filling and even the SOC scaling factor. We treat the H^{sl} in a second variational way employing the eigenvalues and wave functions, Ψ_i , obtained for the unperturbed Hamiltonian, H^0 , using the regular FLAPW method as basis. Whether the state Ψ_i should be considered occupied is determined by tracking its projection onto the occupied states Φ_j by defining

$$P_i^{\text{occ}} = \sum_{j \in \{\text{occ}\}} |C_j^i|^2 \quad (4)$$

rather than using its energy ϵ'_i . Since H^{sl} is very weak, this definition does not introduce any ambiguity, i.e., the value of P_i^{occ} is either $>99\%$ or $<1\%$ (excluding degenerate state pairs which have no contribution to MCA). In this sense, the newly occupied states give almost the same

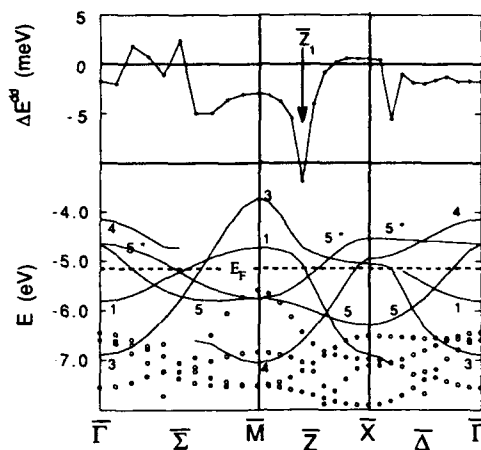


Figure 5: The calculated band structure (bottom panel, lines for minority spin states, circles for majority spin states) and the distribution of the magneto-crystalline anisotropy energy along high symmetry lines for the Co(001) monolayer. Numbers denote the symmetry properties of states. The arrow points out the position of the surface pair coupling.

spatial distribution of the charge and spin densities – which ensures the correct application of the force theorem. Furthermore, such a state-tracking procedure is done independently at each k point; hence, the randomness in the BZ can also be removed.

We applied this state-tracking procedure to study the magnetic anisotropy of the Fe, Co and Ni monolayers, Co/Cu(001) overlayer system and Cu/Co/Cu sandwiches. Stable calculated results allow us to reveal important background physics and to provide general trend for the MCA. For a simple demonstration, here we will discuss why Co (in plane) and Fe (perpendicular) ultra thin films, favor different MCA directions.

The calculated band structure for the Co(001) monolayer is presented in the bottom panel of Fig. 5. There are two important SOC contributions, i.e., (i) states 5 and 5^* through L_z and (ii) states 1 and $5(5^*)$ through L_x . As clearly shown in the top panel of Fig. 5, SOC between 5 and 5^* contributes a positive MCA energy along the Σ direction. However, in most parts of the Brillouin zone, SOC between 1 and $5(5^*)$ becomes stronger (resulting in a negative MCA energy) because of either the occupation of both 5 and 5^* (around \bar{M}) or $|\epsilon_1 - \epsilon_5| < |\epsilon_5 - \epsilon_{5^*}|$ (along $\bar{\Delta}$). The calculated total MCA energy (integrated over the BZ) is -1.35 meV/atom for the free Co monolayer – indicating an in-plane magnetization. Note that in the middle of the Σ line, states 1 and 5^* become almost degenerate at E_F , which results in a singularity of the MCA energy as pointed out by an arrow. This so-called surface pair coupling requires special treatment in some cases [31, 32]. For Fe, the Fermi level shifts down by 0.5 eV. As a result, the predominant SOC pair will be $5 - 5^*$ (especially in the area around \bar{M}) and the MCA energy becomes positive in most of the BZ for the Fe monolayer. The calculated MCA energy for Fe monolayer (with the same lattice constant as that for the Co(001) monolayer) is 0.42 meV/atom – indicating a perpendicular magnetization.

MAGNETO-OPTICAL EFFECTS

SMOKE

The surface magneto-optic Kerr effect (SMOKE) has recently been demonstrated to be a powerful *in situ* characterization probe of the magnetic and magneto-optic properties of magnetic films during the growth process. [33] Now it is well accepted that the Kerr effect results mainly from the combined action of SOC and exchange interaction in the process of interband transitions. [34] SOC acts as a magnetic field and thus breaks the symmetry between the absorption for left- and right-handed circularly polarized photons. The exchange interaction, on the other hand, separates the majority and minority spin states and allows a net rotation of the polarization plane of the incident light. Since the Kerr effect is determined by SOC perturbations on the wave functions (including states lying 10-20 eV above E_F), a very accurate treatment of both the semi-relativistic ground state properties (magnetic moment and band structures, etc.) and SOC perturbation are essential to obtain correct results theoretically.

For the most important physical case of SMOKE, i.e., the polar Kerr effect, both the magnetization and the incident wave vector are perpendicular to the surface. Recently, we developed an approach and a computer code to calculate Kerr effects for both bulk and thin film materials based on the FLAPW method. Our goal is to explore the physical origin of the Kerr effects on the microscopic level and, hopefully, to predict ultimately new magneto-optic materials. First results obtained for the Ni(001) surface (simulated by 1, 3 and 5 layer slabs) and bulk Ni show that the agreement between the calculated and measured curves for bulk Ni is acceptable considering that the existing experimental values are highly scattered. [35] In addition, we found that there is no simple (e.g., proportional) relationship between the intensity of the SMOKE signal and the magnetic moment for a given photon energy.

CONCLUSIONS

In summary, state-of-the-art *ab initio* LSD electronic structure calculations have achieved great success in the exciting field of thin film magnetism, in both explaining existing phenomena and, more importantly, in predicting the properties of new systems. Illustrative results demonstrate that: (1) the lowered coordination number at clean metal surfaces leads to enhanced magnetic moments; (2) inert substrates do not affect the magnetism in most cases, but show significant effects on 4d overlayers; (3) the strong interaction (hybridization) with nonmagnetic transition metals diminishes (entirely in some cases) the ferromagnetism and usually leads to AFM ordering; (4) the magnetic anisotropy can be predicted correctly using the state-tracking procedure; and (5) magneto-optical Kerr effect and magnetic circular dichroism can be explained in the framework of single particle interband transitions. In the future, electronic structure theory is expected to continue play a more predictive role by considering more complex systems, by eliminating the limitation of the local spin density approximation and developing more efficient and precise methods.

ACKNOWLEDGEMENTS

Work was supported by the National Science Foundation (Grant No. DMR 91-17818).

REFERENCES

1. See review papers in "Magnetism in the Nineties", J. Magn. Magn. Mater. **100** (1992).

2. L.M. Falicov, D.T. Pierce, S.D. Bader, R. Gronsby, K.B. Hathaway, H.J. Hopster, D.N. Lambeth, S.P. Parkin, G. Prinz, M. Salamon, I.K. Schuller and R.H. Victora, *J. Mater. Res.* **5** (1990) 1299.
3. A.J. Freeman, R. Wu, *J. Magn. Magn. Mater.* **100** (1991) 497.
4. C.L. Fu, A.J. Freeman and T. Oguchi, *Phys. Rev. Lett.* **54** (1985) 2700.
5. S. Blügel, *Phys. Rev. Lett.* **68** (1992) 851.
6. E. Tamura, R. Feder, G. Waller and U. Gradmann, *Phys. Stat. Sol. (b)* **157** (1990) 627.
7. H.J. Elmers, G. Liu and U. Gradmann, *Phys. Rev. Lett.* **63** (1989) 566; T. Beier, D. Pescia, M. Stampanoni, A. Vaterlaus and F. Meier, *Appl. Phys. A* **47** (1988) 73.
8. L.M. Liebermann, D.R. Fredkin and H.B. Shore, *Phys. Rev. Lett.* **22** (1969) 539; L.M. Liebermann, J. Clinton, D.M. Edwards and J. Mathon, *ibid.* **25** (1970) 232.
9. E. Wimmer, A.J. Freeman and H. Krakauer, *Phys. Rev. B* **30** (1984)
10. S. Ohnishi, A.J. Freeman and M. Weinert, *Phys. Rev. B* **28** (1983) 6741.
11. U. Gradmann, *J. Magn. Magn. Mater.* **100** (1991) 481.
12. S. Ohnishi, C.L. Fu and A.J. Freeman, *J. Magn. Magn. Mater.* **50** (1985) 161.
13. M.J. Zhu, D.M. Bylander and L. Kleinman, *Phys. Rev. B* **42** (1990) 2874; O. Eriksson, R.C. Albers and A.M. Boring, *Phys. Rev. Lett.* **66** (1991) 1350; M.J. Zhu, D.M. Bylander and L. Kleinman, *Phys. Rev. B* **43** (1991) 4007; R. Wu and A.J. Freeman, *Phys. Rev. B* **45** (1992) 7222.
14. D.S. Wang, A.J. Freeman and H. Krakauer, *Phys. Rev. B* **26** (1982) 1340.
15. S.C. Hong, A.J. Freeman and C.L. Fu, *Phys. Rev. B* **39** (1989) 5719.
16. M.A. Thompson, M. Onellion and J.L. Erskine, *Bull. Am. Phys. Soc.* **31** (1986) 675.
17. T. Oguchi and A.J. Freeman, *J. Magn. Magn. Mater.*, **54-57** (1986) 797.
18. M. Stampanoni, A. Vaterlaus, D. Pescia, M. Aeschlimann, F. Meier, W. Dürr and S. Blügel, *Phys. Rev. B* **37** (1988) 10380; R.L. Fink, C.A. Ballentine, J.L. Erskine and J.A. Araya-Pochet, *Phys. Rev. B* **41** (1990) 10175.
19. C. Rau, G. Xing, C. Liu and M. Robert, *Phys. Lett. A* **135** (1989) 227; J.S. Moodera and R. Meservey, *Phys. Rev. B* **40** (1989) 8541.
20. C. Liu and S.D. Bader, *Phys. Rev. B* **41** (1990) 553.
21. M. Maurer, J.C. Ousset, M. Piecuch, M.F. Ravet and J.P. Sanchez, *Mat. Res. Soc. Symp. Proc. Vol. 151* (1989) 99; M. Maurer, J.C. Ousset, M. Piecuch and M.F. Ravet, *Europhys. Lett.* **9**, (1989) 803.
22. R. Wu and A.J. Freeman, *Phys. Rev. B* **44** (1991) 4449.
23. D. Knab and C. Koenig, *Phys. Rev. B* **43** (1991) 8370.
24. C. Li and A.J. Freeman, *Phys. Rev. B* **43** (1991) 780.
25. G.A. Mulhollan, R.L. Fink and J.L. Erskine, *Phys. Rev. B* **44**, 2393 (1991); C. Liu and S.D. Bader, *Phys. Rev. B* **44** (1992) 12056.

26. B.T. Thole, G. van der Laan and G.A. Sawatzky, Phys. Rev. Lett. **55**, 2086 (1985); G. van der Laan, B.T. Thole, G.A. Sawatzky, J.B. Goedkoop, J. Fuggle, G. Schütz, W. Wagner, W. Wilhelm, P. Kienle, R. Zeller and G. Materlik, Phys. Rev. Lett. **58**, 737 (1987); C.T. Chen, F. Sette, Y. Ma and S. Modesti, Phys. Rev. B **42**, 7262 (1990); C.T. Chen, N.V. Smith and F. Sette, Phys. Rev. B **43**, 6785 (1991); L. Baumgarten and C.M. Schneider, H. Petersen F. Schäfers and J. Kirschner, Phys. Rev. Lett. **65**, 492 (1990); J.G. Tobin and G.D. Wadill and D.P. Pappas, Phys. Rev. Lett. **68**, 3642 (1992), and references therein.
27. B.T. Thole, P. Carra, F. Sette and G. van der Laan, Phys. Rev. Lett. **61**, 1943 (1992); P. Carra, Synch. Rad. News **5**, 21 (1992); M. Altarelli, Phys. Rev. B **47**, 597 (1993).
28. M. Weinert, R.E. Watson and J.W. Davenport, Phys. Rev. B **32** (1985) 2115, and references therein.
29. H. Brooks, Phys. Rev. **58** (1940) 909; A.J. Bennett and B.R. Cooper, Phys. Rev. B **3** (1971) 1642; N. Mori, Y. Fukuda and T. Ukai, J. Phys. Soc. Jpn. **37** 1263 (1974); P. Bruno, Phys. Rev. B **39** (1989) 865.
30. J.G. Gay and R. Richter, Phys. Rev. Lett. **56** (1986) 2728; C. Li, A.J. Freeman, H.J.F. Jansen and C.L. Fu, Phys. Rev. B **42** (1990) 5433; R. Richter and J.G. Gay, Mat. Res. Soc. Symp. Proc. **151** (1989) 3; P. Strange, J.B. Staunton, B.L. Gyorffy and H. Ebert, Physica B **172** (1991) 51; G.H.O. Daalderop, P.J. Kelly, M.F.H. Schuurmans, Phys. Rev. B **41** (1990) 11919.
31. D.S. Wang, R. Wu and A.J. Freeman, Phys. Rev. Lett. **70** (1993) 869.
32. E.I. Kondorskii and E. Straube, Soviet Physics JETP **36** (1973) 188.
33. S.D. Bader, Proc. IEEE **78** (1990) 909; J. Magn. Magn. Mater. **100** (1991) 440.
34. H.S. Bennett and E.A. Stern, Phys. Rev. **137** (1965) A448; B.R. Cooper, *ibid* **137** (1965) A1504; J.L. Erskine and E.A. Stern, Phys. Rev. B **8** (1973) 1239; C.S. Wang and J. Callaway, *ibid* **9** (1974) 4897; P.M. Oppeneer, T. Maurer, J. Sticht and J. Kübler, Phys. Rev. B **45** (1992) 10924.
35. K.H.J. Buschow, in *Ferromagnetic Materials*, ed. by E.P. Wohlfahrt and K.H.J. Buschow (North-Holland, Amsterdam, 1988), Vol. 4, pp. 493; J.L. Erskine, Physica **89B** (1977) 83.

MECHANISM FOR THE MAGNETORESISTANCE OF PURE BULK FERROMAGNETS AND COMPOSITE THIN FILM STRUCTURES

MARY BETH STEARNS

Department of Physics and Astronomy, Arizona State University, Tempe, Arizona, 85287

ABSTRACT

A unified explanation is given of the long-standing question of the origin of the low-field magnetoresistance, MR, behavior in pure ferromagnetics and the large magnetoresistance effects seen in magnetic layered and granular structures. It is shown that the main contributions to these effects are due to the scattering that occurs at the magnetic boundaries between non-aligned magnetic regions. This scattering occurs because the predominant conduction electrons in 3d ferromagnetics are the highly polarized itinerant d electrons. As a result of this polarization the majority-band d electrons are strongly reflected at an antiparallel magnetic boundary due to a lack of available states for occupancy. The traversing electrons are further scattered as they cross the boundary due to a discontinuity in the potential caused by the interchange of their kinetic and exchange energies at the boundary. Expressions for the magnetoresistance due to these scattering mechanisms are derived and shown to describe very well the wide variety of magnetoresistance values and other features found in the literature for both pure Fe and nano-structures of Fe or Co with non-magnetic materials. The MR magnitude is seen to vary inversely with the domain size. Thus the domain size and sample purity are seen to be the main factors that determine the magnitude of the MR effect in pure ferromagnets. The large MR values seen in layered and granular magnetic structures arise from the small effective domain size attainable in these structures. This is achieved by introducing a non-magnetic material into these structures which allows the effective domain size to be decreased from the micron range of the pure ferromagnetic elements into the nanometer range.

INTRODUCTION

The low field magnetoresistance (MR) of the 3d ferromagnetic elements was extensively studied in the 1960's and 1970's. It was found that at liquid He temperatures Fe had huge magnetoresistance effects¹⁻⁶. For example, at 4.2K, a transverse MR effect of magnitude 15 was reported in Ref. 1 and longitudinal magnitude of 7.8 along the $\langle 111 \rangle$ direction was reported in Ref. 2. It was found¹ that the largest MR values were obtained in the purest samples.

More recently several series of experiments in various laboratories have found that sandwiches⁷⁻¹¹ or granular¹²⁻¹⁵ nano-structures containing magnetic and non-magnetic materials have "large" low-field magnetoresistance values ranging up to ~ 1 . Several highly parameterized versions of a theoretical explanation^{7,16-17} based on the assumption that the spin-up and spin-down electrons of the ferromagnet have appreciably different scattering amplitudes for solute atoms of the non-magnetic element, have been proposed to explain these results. However, the spin-dependent scattering rates used in these calculations for the solutes in Fe have recently been shown¹⁸ to be incorrect by a large factor and furthermore the systematics of the magnitude of the measured MR effects do not correlate well with the measured scattering rates; so these theories do not explain the experimental data well.

The earlier MR effect in Fe had been attributed to scattering in the domain walls, e.g., due to a spin-orbit interaction of the conduction electrons with the magnetic inhomogeneities in the domain walls. However, no satisfactory theory was ever developed to explain the data although one of the papers¹⁹ contained a scattering mechanism which is very similar to one of those discussed here and previously presented elsewhere²⁰. However, in Ref. 19 it was concluded that this mechanism would not give a large MR effect, because the authors presumed, in keeping with the popular belief at that time, that the conduction electrons were essentially unpolarized s-like electrons.

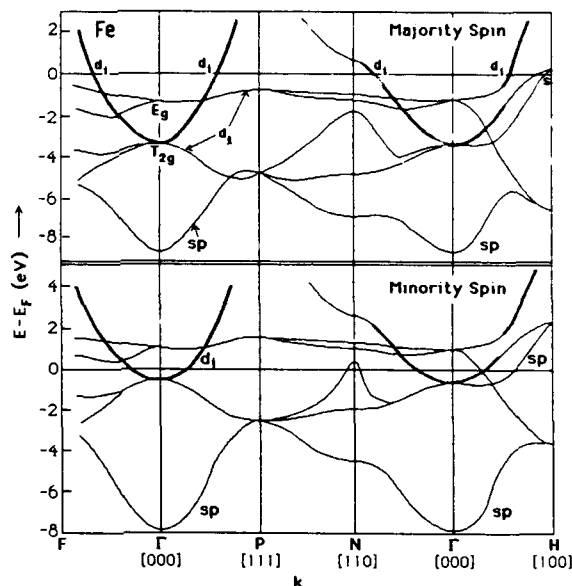
Here it is shown that the MR behavior for both the pure materials and the nanostructures can be explained by the scattering of the itinerant d electrons, d_i , as they cross unaligned magnetic boundaries. These are the predominant conduction electrons in 3d ferromagnetic transition metals²¹.

CAUSE OF MAGNETORESISTANCE OF PURE FERROMAGNETS

The MR effect is defined as $MR = [R(H) - R_{sat}] / R_{sat}$, where $R(H)$ is the resistance of the film with an applied field, H , and R_{sat} is the film resistance at a sufficiently high H value to give magnetic saturation of the sample but not so high that there is an appreciable component of the normal high-field galvanomagnetoresistance. The maximum MR effect, MR' , is then $MR' = (R_{max} - R_{min}) / R_{min}$. The salient features of the MR effect are that it reaches its maximum when the net magnetization is zero, i.e., when there is the maximum amount of antiparallel alignment in the sample. It then decreases to zero monotonically as the magnetization increases.

A central point for understanding the MR effect is the realization that the conduction electrons in ferromagnetic Fe are predominantly the highly polarized d-like (itinerant) conduction electrons, d_i . These are the same electrons that cause the ferromagnetic coupling of the local moments through the RKKY interaction²¹. The fact that the major portion of the Fe conduction electrons are itinerant d's is seen from the Fe band structure²² depicted in Fig. 1.

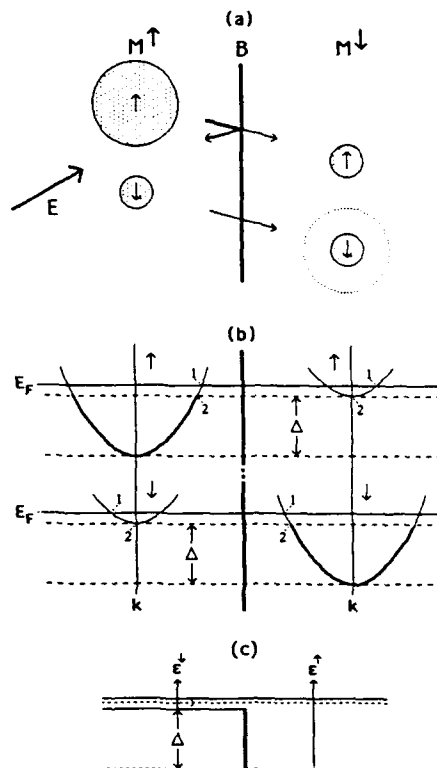
Fig.1. The band structure of Fe in several crystallographic directions.



The lowest bands are the 4sp-like electrons and the other five bands are the d electrons. It is seen that four of the d-bands are rather flat corresponding to the localized d levels; in some regions they have curvature due to hybridization with the 4sp-like electrons. The fifth d-band, shown darkened for each spin, has a parabolic behavior with a curvature corresponding to an effective mass of about that of a free electron. These are the itinerant d-like electrons. We have labeled the orbital character of each band which crosses the Fermi level; d_i for the itinerant d's and sp or s for the 4sp-like electrons. It is seen that the sp-like bands seldom cross the Fermi level and so contribute very little to the conductivity. That this is so was strikingly seen in a series of tunneling experiments between various ferromagnets and a superconductor by Meserve et al.²³ which measured the spin-polarization of the tunneling electrons. It was found that the spin polarization was proportional to the ferromagnetic moments. It was shown²⁴ that this proportionality occurred because the d_i electrons are the main conduction electrons. In contrast with tunneling from a normal metal, due to the d_i electrons converting their exchange energy into kinetic energy as they enter the tunneling region the values of the Fermi level k_F vectors in the ferromagnetic state explicitly appear in the expression of the tunneling current. These k_F values directly reflect the d_i band-splitting which is proportional to the ferromagnetic moments.

As is well-known, the domains in a ferromagnetic material have the full magnetization; i.e., the band splitting in all regions of a ferromagnetic material is always the full splitting. Reduced magnetization of a sample only corresponds to the magnetization direction not being the same for all domains. Thus, incomplete magnetization should be considered as the sample being composed of varying amounts of parallel and antiparallel regions. This allows the use of the simplified model for the magnetic boundaries, depicted in Figs. 2a and 2b, for derivin-

Fig.2. Schematic depiction of the main contributions to the magnetic boundary scattering in Fe. (a) Scattering due to the lack of states for occupancy. (b) and (c) Scattering from the step potential seen by the d_i 's in crossing a magnetic boundary.



expressions for the resistivity arising from the scattering mechanisms discussed here.

The scattering giving rise to the MR of Fe is due to two effects. One contribution comes from the reflection of majority electrons at an antiparallel magnetic boundary because the occupied Fermi spheres for the spin-up and spin-down electrons differ greatly in size. This is depicted schematically in Fig. 2a where we show a realistically scaled version of the size of the *Fermi spheres in Fe* for the majority and minority d_i electrons. Where majority (minority) are defined as the spins parallel (antiparallel) to the direction of magnetization. As indicated, many of the occupied majority states no longer exist in going from a region of parallel to antiparallel magnetization since here the spin-up states are the minority states. Thus, as the majority d_i 's encounter a boundary, B, between M^\uparrow and M^\downarrow a fraction R_d are reflected. In contrast, the spin-down electrons crossing the same boundary undergo no reflection from this effect since there are sufficient available spin-down states in the M^\downarrow region to accommodate them. However, for Fe, Co and less so for Ni the conduction electrons are predominantly majority spins.

Note that, in contrast to the behavior of the spin of a traversing neutron, an electron spin does not follow the spin rotation in crossing a domain wall. This occurs for two reasons: First, the wavelength of thermal neutrons is of the order of the atom separation while that of the electrons at the Fermi surface is $\sim 6\text{\AA}$ for majority and $\sim 16\text{\AA}$ for minority d_i electrons. Second, the transit time for thermal neutrons to cross a domain wall of 500\AA is $\sim 2 \times 10^{-11}$ sec while that the electrons at the Fermi level is $\sim 1 \times 10^{-13}$ sec for minority electrons and $\sim 4 \times 10^{-14}$ sec for majority electrons. Thus, while neutrons are able to adiabatically follow the spin direction in the wall, the sudden approximation applies for the electrons and they do not change spin direction in crossing a wall.

A second contribution to the scattering occurs at B for both majority and minority electrons due to a change in the potential caused by the interchange of the kinetic and exchange energies at the boundary as indicated in Fig. 2b and 2c. In crossing B the total energy of the electrons remains the same but the kinetic energy, KE, of all majority spin electrons is reduced by the amount of the exchange energy splitting, Δ . Thus in crossing B the majority electrons at the Fermi level remain at E_F but with a reduced k_F value corresponding to that of the minority spin. Such electrons are denoted by 1 in Fig. 2b. In a similar manner majority electrons with a $KE = \Delta$ end up at the bottom of the minority bands as they cross B. Such electrons are denoted by 2 in Fig. 2b. All the majority electrons having a KE less than Δ have no states available for occupancy as they attempt to cross B; so they are reflected at B. These states are depicted by the darkened curves in Fig. 2b. In contrast all minority states have an increase in KE equal to Δ upon crossing B. So they go into states near the top of the majority bands leaving unoccupied lower k-value states. Corresponding minority states that traverse B at E_F and the bottom of the minority band are also labeled 1 and 2 respectively.

The reflectivity from this scattering contribution due to the discontinuous potential at an antiparallel boundary for both the majority and minority electrons is given by the well-known expression for the reflectivity from a step potential depicted in Fig. 2c.

$$R_s = [(1 + \Delta/\epsilon^\downarrow)^{1/2} - 1] / [(1 + \Delta/\epsilon^\downarrow)^{1/2} + 1] \quad (1)$$

Where Δ is the exchange splitting of the d_i bands and ϵ^\downarrow is the normal energy component of the minority state when the incident electron is either entering or leaving the step potential.

Due to the random orientation of the domains at $M=0$ the current which is parallel to the domain walls in bulk Fe samples is small. Thus considerations of whether the scattering is specular or non-specular at the magnetic boundaries is unimportant here.

CALCULATION of MR for PURE FERROMAGNETS

The maximum resistivity occurring for complete antiparallel alignment, $\rho^{\uparrow\downarrow}$, is the sum of the magnetic boundary scattering, ρ_{MB} , and all the other types of scattering which are present when there are no magnetic boundaries, $\rho^{\uparrow\uparrow}$, thus $\rho^{\uparrow\downarrow} = \rho_{MB} + \rho^{\uparrow\uparrow}$. We assume that the various types of scattering are independent and $\rho^{\uparrow\uparrow} = \rho_{\text{impurity}} + \rho_{\text{magnon}} + \rho_{\text{phonon}}$. Thus the maximum MR value is given by

$$\text{MR} = (\rho^{\uparrow\downarrow} - \rho^{\uparrow\uparrow}) / \rho^{\uparrow\uparrow} = \rho_{MB} / \rho^{\uparrow\uparrow}. \quad (2)$$

Many of the derivations made to obtain the resistivity giving rise to the low field MR have used the Boltzmann-equation approach^{16,25} to justify the use of the semiclassical kinetic free-electron expression for the resistivity. Here we assume that this is valid, and applies well to the parabolic bands of the d_i 's, so that we use the well-known expression $\rho = m/(ne^2\tau)$ to derive the resistivity ρ_{MB} .

Let us calculate ρ_{MB} for pure Fe at low temperatures where ρ_{MB} is the predominant contribution to the resistivity at $M=0$. Consider the hypothetical case where all adjacent domains are aligned antiparallel, as shown in Fig. 2. Let n^{\uparrow} and n^{\downarrow} be the number of majority and minority d_i electrons per unit volume respectively and $\tau^{\uparrow,\downarrow}$ be the collision times corresponding to the transit time between antiparallel magnetic boundaries. We then have $\rho^{\uparrow,\downarrow} = m/(n^{\uparrow,\downarrow}e^2\tau^{\uparrow,\downarrow})$. Since here we are concerned only with the maximum MR' value corresponding to no net magnetization, the system is completely symmetric for \uparrow and \downarrow spins. Thus the mean-free-path, mfp, is given by $\lambda = v_F\tau^{\uparrow} = v_F\tau^{\downarrow}$. Substituting $n = k_F^3/12\pi^2$ for bcc Fe, the resistivities in terms of the Fermi wave vectors are given by

$$\rho^{\uparrow,\downarrow} = 12\pi^2\hbar / (e^2\lambda k_F^{\uparrow,\downarrow 2})$$

We must now decide how the two spins channels should be added in order to obtain ρ_{MB} . There are two extreme cases, one where the two channels are completely mixed so that ρ^{\uparrow} and ρ^{\downarrow} should be added in series first and then in parallel giving

$$\rho_{MB} = \rho^{\uparrow} + \rho^{\downarrow} = (6\pi^2\hbar/e^2\lambda_{MB})(1/k_F^{\downarrow 2} + 1/k_F^{\uparrow 2}). \quad (3)$$

The other extreme is no mixing so that ρ^{\uparrow} and ρ^{\downarrow} should be added in parallel, giving

$$\rho_{MB} = \rho^{\uparrow}\rho^{\downarrow}/(\rho^{\uparrow} + \rho^{\downarrow}) = (12\pi^2\hbar/e^2\lambda_{MB})/(k_F^{\downarrow 2} + k_F^{\uparrow 2}). \quad (4)$$

Where the mfp, λ_{MB} , for scattering is the average distance traveled by the conduction electrons between being scattered by magnetic boundaries. Note that all quantities in Eqs. 3 and 4 are known except λ_{MB} . The degree of mixing depends on the magnitude of the reflectivity at the boundaries.

It is of interest to comment on the difference between the two spin channel model for this resistivity and that used to derive the spin-dependent scattering cross-sections of solute atoms in ferromagnetic hosts^{18,26}. In that case, in order to avoid effects due to the magnetoresistance, the measurements are made in applied fields which are strong enough to remove all the domains. The zero field resistivity values used to determine the spin-dependent

cross-sections are then obtained by extrapolating the measured resistivities back to zero field²⁶. The applied field thus prevents the mixing of the spin up and down channels by the domains and under these conditions at low temperatures the observed resistivity is due to the spin up and down channels conducting independently in parallel.

Estimate of λ_{MB}

In order to estimate the mfp for a sample at $M=0$ we idealize the system to be an array of volumes with average linear dimension of D where each volume is surrounded by volumes having antiparallel alignment. In Fig. 3 we depict the possible scattering processes for both

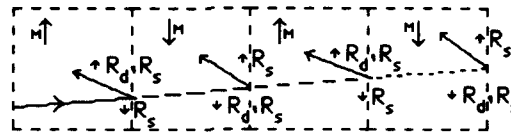


Fig. 3. Schematic diagram for calculation of λ_{MB} .

majority and minority electrons in crossing the antiparallel boundaries of such an array. We obtain the average mfp, λ_{MB} , by summing over all possible weighted λ_{MB} values.

Consider an electron that has just been scattered at boundary (1). At the next magnetic boundary (2) a spin up (majority) electron has a probability of reflection of R_M given by $R_M = R_d + T_d R_s$ or $R_s + T_s R_d = R_d + R_s - R_d R_s$ while a spin down (minority) electron has a probability of reflection of R_S due only to the step potential at the boundary. T is the probability of transmission, equal to $1-R$. As indicated in Fig. 3 if an electron is not reflected at a magnetic boundary it switches roles between majority and minority in the next domain so the probability of reflection at the next boundary (3) is R_S for a spin up electron and R_M for a spin down electron. Summing over all the possibilities the average mfp for a majority electron starting at boundary (1) is thus given by

$$\lambda_M = DR_M + 2DT_MR_S + 3DT_MT_S R_M + 4DT_M^2 T_S R_S + 5DT_M^2 T_S^2 R_M + \dots$$

$$\text{or} \quad = D(R_M + 2R_S T_M) \sum_{n=1}^{\infty} (2n-1) (T_M T_S)^{n-1}.$$

By expanding and dividing $1/(1-T)^2$ it is easily seen that

$$\sum_{n=1}^{\infty} n T^{n-1} = 1/(1-T)^2; \quad \text{also using} \quad \sum_{n=1}^{\infty} T^{n-1} = 1/(1-T),$$

we obtain

$$\lambda_M = D(R_M + 2R_S T_M) [2/(1-T_M T_S)^2 - 1/(1-T_M T_S)]$$

In a similar manner it can be shown that the mfp for a minority electron starting at boundary (1) or the majority electron starting at boundary (2) is given by

$$\lambda_m = D(R_S + 2R_M T_S) \sum_{n=1}^{\infty} (2n-1) (T_M T_S)^{n-1}$$

Since the mfp, λ_{MB} , for boundary scattering in a ferromagnet of with an equal number of antiparallel domains of average size D is completely symmetric for majority and minority electrons it is given by $\lambda_{MB} = (\lambda_M + \lambda_m)/2$ so we finally get

$$\lambda_{MB} = D[3(R_M + R_S)/2 - 2R_S R_M] [2/(1-T_M T_S)^2 - 1/(1-T_M T_S)] \quad (5)$$

The actual magnetization of the domains in polycrystalline Fe samples at $M=0$ is composed of a complex array of regions magnetized in various directions. This can be taken into account by multiplying ρ_{MB} by a factor, A , obtained by averaging $(1-\cos\theta)/2$ over all directions, where θ is the angle between the magnetization directions of two adjacent domains. Thus $A = \int (1-\cos\theta)/2 \cdot p(\theta) d\Omega / 4\pi$, where $p(\theta)$ is the probability distribution of θ . The value of A is 1 for a system where all the adjacent domains are antiparallel [$p(\theta) = \delta(\pi)$] and 1/2 for completely random orientation of the domains [$p(\theta) = 1$]. Thus

$$MR' = A \rho_{MB} / \rho^{\uparrow\uparrow} \quad (6)$$

For an incompletely aligned sample having magnetization, M , less than the saturation magnetization, M_s , the resistivity, ζ_{MB} , is given by $\zeta_{MB} = A f(M/M_s) \rho_{MB}$. For $M < M_s$ in the region of domain wall motion the size of the domains is no longer equal so the value of λ_{MB} differs from that derived above. In general it has been found experimentally that the magnetoresistance varies less rapidly than M and the functional form of $f(M/M_s)$ has been taken to vary as $[1 - (M/M_s)^n]$ with $n > 1$. Since here we are only concerned with the maximum MR values the exact dependence on M is not considered further.

For Fe at low temperatures, where ρ_{magnon} and ρ_{phonon} are negligible, we have $MR' = A \rho_{MB} / \rho_{purity}$. In this case MR' becomes very large for the pure samples and strongly depends upon the purity, as observed¹. At room temperature ρ_{phonon} generally dominates and is much larger than ρ_{MB} so MR' is less than a percent.

EVALUATIONS of MR' for Fe

We can evaluate MR' for Fe as follows. The average k_F^\uparrow and k_F^\downarrow values from band calculations and de Haas-van Alphen measurements²⁷ for Fe are 1.1\AA^{-1} and 0.42\AA^{-1} respectively. This corresponds to the number of majority and minority d_i electrons of 0.26 and 0.015 electrons per atom respectively.

The density of states or the number of minority d_i states in a shell of thickness ΔE at the Fermi level is $\sim 38\%$ of the number of majority states. Thus the reflectivity due to the lack of states for occupancy in crossing a magnetic boundary is $R_d \sim 62\%$. An estimate of the reflectivity due to the step potential at a magnetic boundary, R_s , can be made using Eq. 1. The minimum reflectivity of the electrons is obtained for incident angles perpendicular to the boundary with $\epsilon^\perp = \epsilon_F^\perp$. From band calculations²² $\Delta/\epsilon_F^\perp \sim 3.5$ for Fe so the minimum reflectivity from the step potential at the boundary is $R_s(\text{min}) \sim 0.3-0.4$. In order to calculate the mean R_s more accurately a complex average over the incident angles and energies for the actual domain structure must be made. However it can be seen that from Eq. 5, that λ_{MB}/D is quite insensitive to the value of R_s . This is shown in Fig. 4 where we show the dependence of λ_{MB}/D of the value of R_s for the values of R_d corresponding to Fe, Co and Ni. Since λ_{MB}

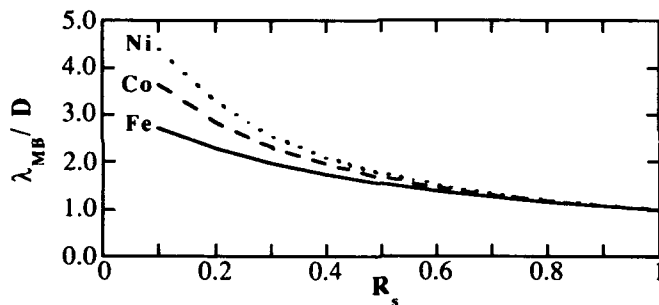


Fig. 4. Variation of λ_{MB}/D with R_s for values of $R_d = 0.62, 0.47$ and 0.38 for Fe, Co and Ni respectively.

is not strongly dependent on R_s we assume $R_s \sim 0.5$ which gives $R_M \sim 0.81$ and $\lambda_{MB} \sim 1.5D$ for Fe. Using the Fe k_F values given above we obtain for the two extreme cases of Eqs. 3 and 4

$$\rho_{MB} = 1.6/\lambda_{MB} \quad (\text{mixed}) \quad \text{and} \quad \rho_{MB} = 0.4/\lambda_{MB} \quad (\text{no mixing}).$$

Where ρ_{MB} is in $\mu\Omega\text{-cm}$ and λ_{MB} is in μm . Taking ρ_{MB} to be the average of the two extreme cases we have $\rho_{MB} \sim 1/\lambda_{MB}$. The maximum magnetoresistance is thus given by

$$MR' \sim A/(1.5D \rho^\uparrow),$$

Defining MR' to be $\Delta\rho/\rho^{\uparrow\uparrow}$ we have $\Delta\rho = A/\lambda_{MB}$. To the extent that D and $p(\theta)$ are temperature independent, $\Delta\rho$ is independent of temperature. However, D may vary somewhat with temperature since at lower temperatures there may be more nucleation centers which give rise to smaller domains.

Since at $M=0$ for polycrystalline Fe the domains are aligned randomly we take $A=1/2$. We thus get an estimate of the average domain size from the expression

$$\Delta\rho (\mu\Omega\text{-cm}) \cong 1/(3D(\mu\text{m})). \quad (7)$$

We now evaluate and compare the quantities derived above with data given in the literature and summarized in Table I. Since $\Delta\rho$ is determined experimentally the only

Table I. Calculated $\Delta\rho$ and the average domain size, D , from $D=1/(3\Delta\rho)$ for several Fe samples from the ρ_{\min} and MR' values given in the literature. W indicates that the sample was an Fe whisker.

Size Lxw (mm)	ρ_{\min} (4.2°) ($10^{-3}\mu\Omega\text{-cm}$)	MR' (4.2°)	$\Delta\rho$ (4.2°) ($10^{-2}\mu\Omega\text{-cm}$)	$D(\mu\text{m})$	$MR'(RT)$ meas calc (%)		Ref.
n.a.	1.76	15	2.6	19			1
~5x0.2 ^W	4.85	9	4.4	11			1
25x3.1	5.0	7.2	3.6	14			6
~20x0.4 ^W	11	0.88	1.0	50			5
~40x4	15	1.5	2.3	22			4
25x3.1	19	1.3	2.5	20			6
~6x0.24 ^W	22.0	1.2	2.6	19	≥0.1	0.27	2
~6x0.3 ^W	20.0	0.8	1.6	31	≥0.14	0.17	2
~23x1	~27	0.43	~1.2	~42			2
25x3.1 ^a	229	0.16	3.7	14			6
25x3.1 ^b	429	0.07	3.0	17			6
25x3.1 ^c	910	0.033	3.0	17			6
25x3.1 ^d	850	0.07	6.0	8			6
25x3.1 ^e	1600	0.038	5.7	9			6
25x3.1 ^f	1950	0.02	3.9	13			6

a. 0.25 wt% Co

b. 0.50 wt% Co

c. 0.92 wt% Co

d. 0.25 wt% Cr

e. 0.54 wt% Cr

f. 0.70 wt% Cr

undetermined quantity in our formulation is the average domain size in the samples. The domain size for Fe samples described in the literature has been roughly estimated^{3,28} in the literature to be $D \sim 10 \mu\text{m}$ (the domain wall thickness in Fe is $\sim 0.05 \mu\text{m}$). As a check on the model we derive the domain sizes to compare to the estimated size. The lengths and average rectangular widths of a number of Fe samples are listed in the first column of Table I. The measured values of $\rho^{\uparrow\uparrow}$ and MR' at 4.2K are given in the second and third columns. The values for $\Delta\rho = \text{MR}'\rho^{\uparrow\uparrow}$ are listed in column four. Using these values the D values obtained from Eq. 7 are listed in column five of Table I. We see that most of the samples have average D values between $10\text{--}20 \mu\text{m}$. Considering that the samples differ widely in shape and purity, the D values obtained are satisfactorily close to the estimated domain size. Since the $\Delta\rho$ values, $(1\text{--}6) \times 10^{-2} \mu\Omega\text{-cm}$, are similar for all the samples, we see that the MR' values at 4.2K for these samples are mainly determined by the purity of the sample, with the purest samples having the largest MR' values.

In two cases the MR' values were also measured at room temperature so we have calculated these values assuming that $\Delta\rho$ is the same at RT as at 4.2K and using a room temperature resistivity value, $\rho^{\uparrow\uparrow} = 9.7 \mu\Omega\text{-cm}$. We see that the estimated values for MR' at room temperature are in good agreement with the measured values.

From Table I we see that the alloy samples tend to have smaller domain sizes. This trend is expected since the solute atoms act as nucleation centers for domains and thus the domain sizes in the alloys should be smaller than in pure Fe. Surprisingly this is a small effect here which may be due to segregation of the solute atoms at grain boundaries. However, it is seen that the solute atoms strongly increase the $\rho^{\uparrow\uparrow}$ values which causes the MR' values to decrease rapidly with the increasing solute concentration. Thus the two mechanisms causing magnetic boundary scattering of the highly polarized d_j electrons account very well for the wide variety of behavior seen for the magnetoresistance of pure Fe.

For device application it is of great interest to maximize the MR effect at room temperature. We now see that the way to do this is by decreasing the domain size, or distance between magnetic boundaries. If it were possible to decrease the effective domain size to a distance of 10 nm for pure Fe we would have $\Delta\rho \sim 33 \mu\Omega\text{-cm}$ or an achievable MR' value of the order of ~ 3 at room temperature. We will see that the layered and especially the granular structures are favorable structures in which this occurs.

MR of LAYERED OR GRANULAR NANO-STRUCTURES

We make the reasonable assumption that the mechanism of the MR effect is the same in these structures as in pure Fe, namely the existence of magnetic boundaries between unaligned magnetic regions in the structures. However here the magnetic regions are also separated by non-magnetic regions. The non-alignment in these structures can be caused by a variety of mechanisms besides domain boundaries, such as: exchange coupling between neighboring magnetic layers which are separated by non-magnetic layers, different coercive fields in nearby regions which give rise to complex hysteresis loops of the sample, and random orientation of non-interacting magnetic globules as in granular structures. In real films, especially the multilayer structures, the MR effect is often a combination of these mechanisms and thus they are very difficult to analyze. Moreover, upon viewing many of these structures with high resolution cross-section transmission electron microscopy it has been found that the multilayer films are often of very poor structural quality. They frequently appear to be more a granular rather than a layered structure; especially after the first few layers.

The $\text{Co}_x\text{Ag}_{1-x}$ granular structures are an ideal prototypical system for the model presented here. The Co and Ag are immiscible since the surface free energy of Co is about twice that of Ag²⁹ and the Co and Ag are poorly lattice matched. Thus the Co atoms are found to form single domain particles which are embedded in a Ag matrix. Recent experiments, which are reported elsewhere in this conference, have shown that for this system all the Co

atoms have essentially the full moment of 1.7 Bohr magnetons and reside in pure Co single domain globules. At Co concentrations lower than ~37 at.% the Co particles are magnetically isolated and the films are superparamagnetic. The average size of the single domain globules is determined independently from the superparamagnetic behavior and found to have radii of ~23-26 Å. The globules are embedded in volumes of ~60 Å on a side. The same model as used to describe the pure ferromagnetic magnetoresistance, modified only to take into account the additional scattering due to a potential step at the Co-Ag interfaces and in the non-magnetic regions, fits the data excellently. Due to the small distance between magnetic boundaries, ~60 Å, the MR values are large; e.g., 31% at RT and 65% at NT for a film with 37 at.% Co.

REFERENCES

1. W.A. Reed and E. Fawcett, *Phys. Rev.* **136**, A422 (1964); *Proceedings of the International Conference on Magnetism, Nottingham, 1964* (The Institute of Physics and The Physical Society, London, 1965), p. 120.
2. A. Isin and R. V. Coleman, *Phys. Rev.* **142**, 372 (1966); R.V. Coleman and A. Isin, *J. Appl. Phys.* **37**, 1028 (1966); P.W. Shumate, Jr., R.V. Coleman and R.C. Fivaz, *Phys. Rev.* **B1**, 394 (1970).
3. A.M. Sudovtsov and E.E. Semenenko, *Z. Eksperim. i Teor. Fiz.* **35**, 305 (1958); **47**, 486 (1964); [English transl.: *Soviet Phys.-JETP* **8**, 211 (1958); **20**, 323 (1965)].
4. A. Schindler and B.C. La Roy, *J. Appl. Phys.* **37**, 3610 (1966).
5. P.N. Dheer, *Phys. Rev.* **156**, 637 (1967).
6. A.K. Majumbar and L. Berger, *Phys. Rev.* **B7**, 4203 (1973).
7. M.N. Baibich, M.M. Broto, A. Fert, Nguyen Van Dau, F. Petroff, P. Etienne, G. Creuzet, A. Friederich and J. Chazelas, *Phys. Rev. Lett.* **61**, 2472 (1988); A. Barthélémy, G. Creuzet, *J. Appl. Phys.* **67**, 5908 (1990).
8. G. Binasch, P. Grünberg, F. Saurenbach and W. Zinn, *Phys. Rev.* **B39**, 4828 (1989).
9. B. Kieny, V.S. Speriosu, S. Metin, S.S.P. Parkin, B.A. Gurney, P. Baumgart and D.R. Wilhoit, *J. Appl. Phys.* **69** (8), 4774 (1991).
10. S.S.P. Parkin, N. More and K.P. Roche, *Phys. Rev. Lett.*, **64**, 2304 (1990).
11. P. Grünberg, R. Schreiber, Y. Pang, M.B. Brodsky and H. Sowers, *Phys. Rev. Lett.* **57**, 2442 (1986); P. Grünberg, S. Demokritov, A. Fuss, M. Vohl, and J.A. Wolf, *J. Appl. Phys.* **69** (8), 4789 (1991); S. Demokritov, J.A. Wolf, and P. Grünberg, submitted to *Europhysics Letters*.
12. A.E. Berkowitz, J.R. Mitchell, M.J. Carey, A.P. Young, S. Zhang, F.E. Spada, F.T. Parker, A. Hutten and G. Thomas, *Phys. Rev. Lett.* **68**, 3745 (1992).
13. J.Q. Xiao, J. S. Jiang and C.L. Chien, *Phys. Rev. Lett.* **68**, 3749 (1992).
14. J.A. Barnard, A. Wakis, M. Tan, E. Haftek, M.R. Parder and M.L. Watson, *Jour. Magn. and Magn. Mats.*, **114**, 204 (1992).
15. M.B. Stearns and Y. Cheng, APS March Meeting 1993, Seattle, WA; MRS Spring 1993 Meeting, San Francisco, CA.
16. R.E. Camley and J. Barnas, *Phys. Rev. Lett.* **63**, 664 (1989).
17. P.M. Levy, K. Ounadjela, S. Zhang, Y. Wang, C.B. Sommers and A. Fert, *J. Appl. Phys.* **67** (9), 5914 (1990).
18. M.B. Stearns, *J. Appl. Phys.* **72**, 5354 (1992).
19. G.G. Cabrera and L.M. Falicov, *Phys. Stat. Sol.* **61**(b), 539 (1974).
20. M.B. Stearns, Internat. Conf. on Magnetism, Edinburgh, Scotland, September, 1991; *J. Magn. and Magn. Mats.* **104-107**, 1745 (1992) and Internat. Workshop on Spin-Valve Layered Structures, Madrid, Spain, September, 1991.

21. M.B. Stearns, Phys. Rev. **B6**, 3326 (1972); **B8**, 4383 (1973); **B13**, 1183 (1976).
22. K.J. Duff and T.P. Das, Phys. Rev. **B3**, 192 (1971); R.A. Tawil and J. Callaway, Phys. Rev. **B7**, 4242 (1973); D.A. Papaconstantopoulos, "Band Structure of Elemental Solids", Plenum Press, New York, 1986.
23. P.M. Tedrow and R. Meservey, Phys. Rev. Lett. **26**, 191 (1971); Phys. Rev. **B7**, 318 (1973); R. Meservey, D. Paraskevopoulos and P.M. Tedrow, Phys. Rev. Lett. **37**, 858 (1976); R. Meservey, P.M. Tedrow and J.S. Moodera, J. Magn. Magn. Mater. **35**, 1 (1983). The spin polarization value of ~ 0.22 for the tunneling electrons from Ni found in later work is significantly different from the earlier value of 0.11. This difference was attributed by the authors as due to the ferromagnetism at the Ni surface being degraded from OH ions in the earlier experiments.
24. M.B. Stearns, Jour. Magn and Magn. Mats., **5**, 167 (1977).
25. R.Q. Hood and L.M. Falicov, Phys. Rev **B46** 8287 (1992).
26. J.W.F. Dorleijn and A.R. Miedema, AIP Proc. **34**, 50 (1976); J.Phys. F: Metal Phys. **5**, 487 (1975); Philips Res. Rep. **31** 287 (1976); I.A. Campbell and A. Fert, *Ferromagnetic Materials*, edited by E.P. Wohlfarth (North-Holland, Amsterdam, 1982) Vol. III, p. 747.
27. For a discussion of the evaluation of these quantities see M.B. Stearns, p. 24 (Landolt and Börnstein, New Series, III/19a, Springer-Verlag, New York, Ed. by H.P.J. Wijn, 1986)
28. C. Kittel and J.F. Galt, Solid State Phys. Vol. **3**, 437 (1956).
29. L.Z. Mezey and J. Giber, Jpn. J. Appl. Phys. **21**, 1569 (1982).

Spin Polarized Electron Spectroscopies of 3d and 4f Systems

H. HOPSTER

Department of Physics and Institute for Surface and Interface Science, University of California, Irvine, CA 92717

Abstract

Recent results from spin polarized electron spectroscopic studies of surfaces and ultrathin films are presented. The magnetic coupling of 3d transition metals (Cr, Mn) to the Fe(100) surface is studied by spin polarized electron energy loss spectroscopy. The first atomic layer of Cr and Mn aligns antiparallel to the Fe. For larger thicknesses we find evidence for layer-by-layer antiferromagnetic order. In the range of 1-6 atomic layers the behavior is more complex with the surface of the Cr films showing preferential ferromagnetic alignment while the Mn surface aligns antiparallel to the Fe substrate. Secondary electrons from Gd(0001) surfaces are shown to be highly spin polarized. However, no enhancement mechanism at low kinetic energy as in the 3d transition metals is observed indicating the absence of strongly spin dependent inelastic scattering in Gd. Temperature dependent spin polarized 4f photoemission results show almost complete polarization demonstrating ferromagnetic surface coupling. However, a perpendicular surface magnetization component is found indicating surface spin canting. A large enhancement of the surface Curie temperature is also present.

I. Introduction

Spin polarized electron spectroscopies have played a major role in the studies of magnetism of surfaces and ultrathin films[1]. One of the main advantages of electron spectroscopies is their intrinsic surface sensitivity due to the short mean free path of low-energy electrons in solids.

This paper reviews recent results using three different spin polarized electron techniques. Spin polarized electron energy loss spectroscopy (SPEELS) was used to study the magnetic structure of ultrathin epitaxial 3d transition metal layers (Cr and Mn) on Fe(100) substrates. The intriguing magnetic properties of the Gd(0001) surface were studied by spin polarized secondary electron emission spectroscopy (SPSEES) and spin polarized photoemission spectroscopy (SPPEES) on thick epitaxial Gd films on W(110).

II. The magnetic order of 3d transition metal overlayers on Fe(100) studied by SPEELS

In spin polarized electron energy loss spectroscopy (SPEELS) a polarized electron beam is scattered off a surface and the intensity and polarization of the scattered electrons are measured as a function of energy loss. In the case of a ferromagnetic surface the scattering intensity depends on the alignment between the surface majority-spin direction and the incident beam polarization. One defines a scattering asymmetry A as the normalized difference between scattering intensities for beam

polarization parallel and antiparallel to the sample majority spin direction: $A = (1/P_0)(I_{\uparrow} - I_{\downarrow}) / (I_{\uparrow} + I_{\downarrow})$. SPEELS experiments on elemental 3d ferromagnetic surfaces (Ni, Fe, Co) have shown large negative asymmetries in the range of small energy losses [2-4]. This means that spin-down electrons undergo inelastic scattering with a higher probability than spin-up electrons. Although the absolute values of the scattering asymmetries cannot be directly interpreted e.g. in terms of surface magnetization (for instance Ni shows a larger scattering asymmetry than Fe) the existence of non-zero scattering asymmetries reveals the presence of a net surface magnetic moment. The scattering asymmetries in SPEELS have been shown to be caused mainly by spin-flip scattering of incoming spin-down electrons (spin-down flip processes). Spin polarization analysis of the scattered electrons allows one to directly determine the individual spin resolved scattering rates, in terms of flip and non-flip processes.

For the study of magnetic properties the flip-down scattering processes (i.e. incoming spin-down, scattered spin-up electron) are the most interesting ones. The mechanism (proceeding via exchange scattering) is indicated in a schematic exchange-split density of states in Fig. 1. The incoming spin-down electron falls into an empty minority-spin state above E_F and a spin-up electron from an occupied level is emitted. Experiments have shown rather broad spin-flip energy loss spectra on the ferromagnetic metals with the maximum of the flip-down energy loss spectrum corresponding to the average exchange splitting. Thus one can approximately correlate the maximum of the flip-down intensity spectrum with the surface exchange splitting and thereby get an indirect estimate of the the surface magnetic moments.

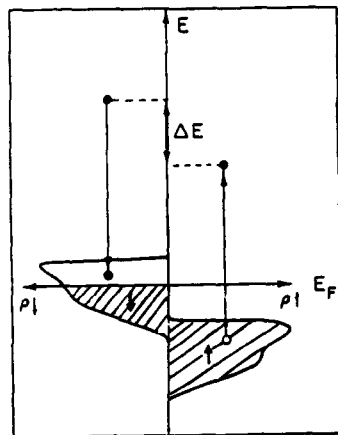


Fig. 1
Schematic of the flip
process for a spin-down
electron

In our experiments the polarized electron beam is derived from a GaAs source which provides spin polarizations in the range of $P_0 = 25\%$. A transversely polarized beam is created by deflecting the emitted electrons electrostatically by 90° . The spin polarization can be easily switched between up and down by changing the helicity of the exciting light from a AlGaAs laser diode between left and right circular polarization by a Pockels cell. The kinetic energy of the electron beam for the SPEELS experiment is usually set at around 30 eV. At these low energies exchange effects are large leading to large spin-flip scattering intensities. The scattered electrons are energy analyzed in a 180° hemispherical analyzer and their polarization is then measured in a 100 kV Mott detector. The total energy resolution is about 300 meV. The total scattering angle in the experiment is fixed at 90° .

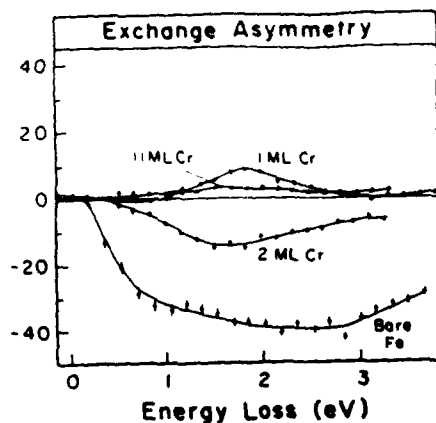


Fig. 2
Asymmetry spectra for various
Cr layer thicknesses on Fe(100)

with the moments pinned at the Fe interface. We therefore decided to study the surface of free Cr films deposited on Fe(100). The coupling of Cr monolayers on Fe(100) had been studied before by spin polarized core level photoemission spectroscopy and was shown to be antiferromagnetically aligned to the Fe moments[8]. In our experiments we followed the evolution of the spin dependence in the SPEELS measurements as the thickness of the Cr layers was slowly increased in sub-monolayer increments. The Cr films were evaporated onto an Fe(100) surface

SPEELS data are taken in off-specular geometry (20°) in order to suppress the spin independent dipole scattering events which dominate the loss spectrum in specular direction[5].

The magnetic coupling of Cr to Fe has been of particular interest as a model system due to the magnetoresistance effects encountered in Fe/Cr/Fe sandwiches and superlattices. Two-monolayer period oscillations were found in the magnetic coupling in well-prepared epitaxial Fe/Cr/Fe sandwich structures[6,7]. This behavior suggests that the Cr films exhibit ferromagnetic (100) sheets with subsequent layers aligned antiferromagnetically (as in the bulk

magnetic structure of Cr) which was itself an epitaxial film grown on a bulk Cr(100) crystal. The thick Fe film (30-50 layers) could be magnetized remanently in-plane by a current pulse through a magnetizing coil below the sample. The films were evaporated at 200° and the SPEELS measurements were taken at lower temperatures (around -50° C). Sample quality was checked by LEED and Auger spectroscopy. For more details on the preparation process see Ref. 9). Fig. 2

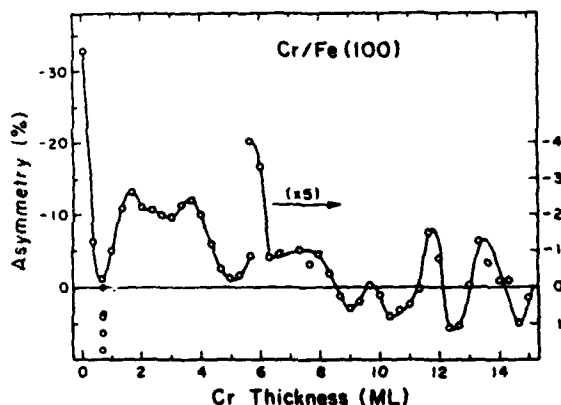


Fig. 3
Thickness dependence of the asymmetry at 1.9 eV energy loss

shows a few representative asymmetry spectra starting with the bare Fe(100) surface. The large negative asymmetry values on the bare Fe prove that the Fe films are magnetized to saturation. With the addition of a monolayer Cr the asymmetries change sign and the spectral distribution changes dramatically (see below) with the asymmetry maximum shifting to smaller energy losses around 1.9 eV. The change in sign directly demonstrates the antiferromagnetic alignment of the Cr monolayer in agreement with the polarized photoemission results. We followed the evolution of the scattering asymmetries as a function of Cr thickness by tuning the spectrometer to 1.9 eV energy loss and adding Cr in submonolayer quantities. The asymmetries are shown in Fig. 3. One clearly sees a two-monolayer period oscillation in the data demonstrating the layer-by-layer antiferromagnetic structure of the Cr films. However, in the thickness range of 1-6 layers the

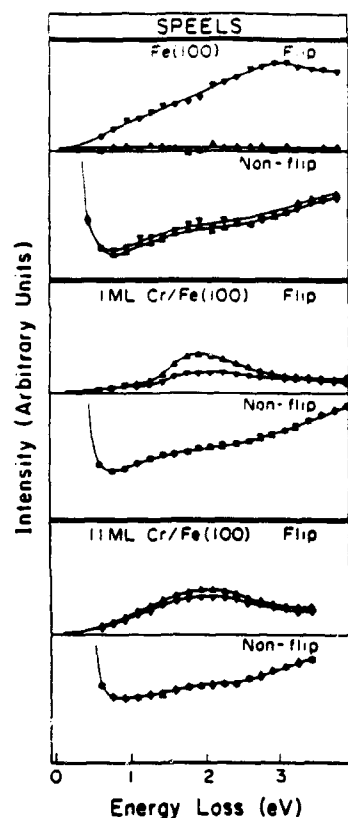


Fig. 4
Spin resolved energy loss
spectra for Cr on Fe(100)

behavior is more complex. This might be due to changes in the electronic structure for these very thin films which are not yet described by the bulk electronic structure. One has to stress also that the SPEELS experiment is sensitive to the surface magnetization only.

The asymmetry maximum around 1.9 eV energy loss is caused mainly by spin-flip excitations as shown in Fig. 4 where we show a few representative spin resolved energy loss spectra. The flip channel shows an intensity maximum around 1.9 eV energy loss. In accordance with the general picture we interpret this as the average exchange splitting at the surface of the Cr film. From (unpolarized) photoemission spectra on bulk Cr(100) surfaces a surface moment of $2.4 \mu_B$ was deduced[10] in agreement with theoretical predictions of a greatly enhanced surface moment of $2.5-3 \mu_B$ as compared to the maximum of $0.55 \mu_B$ in the bulk. The calculations show an average surface exchange splitting on the order of 3 eV[11]. Thus, while our data qualitatively support an enhanced surface moment the magnitude of our measured exchange splitting points to a value somewhat lower than the calculations.

As a first step toward a systematic study of the coupling of other 3d metals to Fe we investigated the magnetic structure of Mn films on Fe(100) in a similar manner. Bulk manganese has a complicated magnetic structure. Fe/Mn/Fe sandwiches have recently been studied by Purcell et

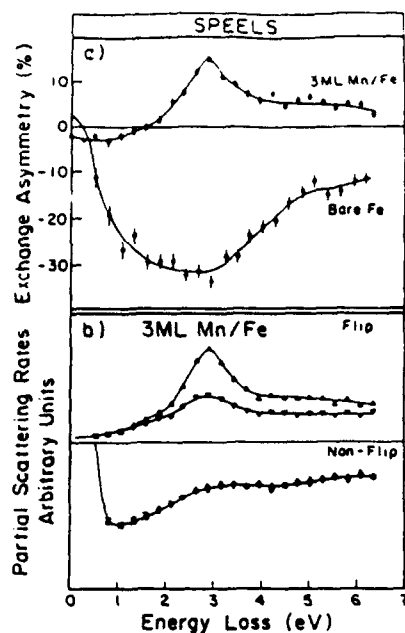


Fig. 5
Asymmetry (a) and spin resolved SPEELS spectra (b) for three atomic layers of Mn on Fe(100)

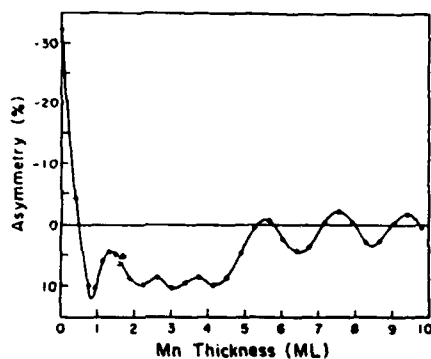


Fig. 6
Thickness dependence of the scattering asymmetry for Mn on Fe(100) at -100°C

al.[12] who found antiferromagnetic Fe-Fe coupling for Mn interlayers thicker than 6-8 layers. The coupling strength was reported to show two-layer oscillation period, however. We grew Mn films on Fe(100) at about 100°C . The Mn grows in a tetragonally distorted bcc structure (bct). For details of the sample preparation and characterization see Ref. 13. The SPEELS spectra taken at -100°C are shown in Fig. 5 for a three monolayer film. We see a strong spin-flip structure around 2.9 eV energy loss. For this thickness the asymmetry is opposite to the bare Fe asymmetry, showing the antiferromagnetic alignment of the Mn surface moments. The average exchange splitting of 2.9 eV compares well with theoretical electronic structure calculations which yield magnetic moments of 2.5-3 μB and exchange splittings of 2.5-3 eV for Mn structures similar to the ones encountered in the present films (for more details see Refs. 13 and 14).

The thickness dependence of the asymmetry at 2.9 eV energy loss is shown in Fig. 6 over the range 0-10 layers. As in the case of Cr, the Mn monolayer couples antiferromagnetically. Two-layer oscillations are clearly visible suggesting a layered antiferromagnetic structure. Interestingly, the very thin layers again behave differently. In the case of Mn the surface moments are aligned preferentially antiparallel to the Fe substrate in the range up to 5 layers while the Cr surface showed parallel alignment.

We want to stress here that the presence of non-zero asymmetries proves the existence of a macroscopic net magnetic moment over the diameter of the electron beam which is a few mm

wide. Another interesting point is the sensitivity to the over-layer thickness in the SPEELS experiment compared to other electron spectroscopic techniques. Obviously a high surface sensitivity is required in order not to average out the signal over perpendicular layers. Unguris et al. [15] were able to detect the surface magnetic moments in wedge shaped Cr films on Fe(100) whiskers using scanning electron microscopy with polarization analysis (SEMPA). The accepted probing depth (exponential decay function) in secondary electron emission spectroscopy on 3d transition metals is about 3 atomic layers. This is consistent with their reported decay of the spin polarization as Cr is deposited on the Fe substrate. From the decay of the SPEELS asymmetry in Fig. 4 an exponential probing depth of only about one layer is apparent. We attribute this extremely short probing depth to the fact that in SPEELS the scattered electrons have to penetrate into and exit from the sample while for secondary electrons the probing depth is determined by the attenuation length of the outgoing electrons only. In addition, in SPEELS the electrons enter and exit at an angle (about 45°) to the surface normal whereas secondary electrons are usually collected for normal emission. Thus, these two factors explain the difference in the effective probing depth of SPEELS and SEMPA. Photoemission is expected to have a surface sensitivity similar to SEMPA. The failure to observe the layered antiferromagnetic ordering in polarized core level spectroscopy [8] might have been due to insufficient surface sensitivity. A probing depth of one layer in SPEELS has also been reported by Zhang et al. in experiments on Mo/Cu(100) [16].

III. Spin polarized secondary electron emission spectrum from Gd(0001)

Low energy secondary electrons are emitted from a solid surface upon the bombardment by energetic electrons. The spin polarization of the low-energy secondary electrons has been used to study the magnetism of surfaces and thin films of 3d transition metals. As in SPEELS, a direct interpretation of the magnitude of the measured polarization in terms of the surface magnetization is difficult for two reasons. First, the polarization is an average over the probing depth (three atomic layers in the 3d transition metals). Second, the low-energy electron spin polarization is in general not equal to the net magnetization. Instead, it is well established that the polarization from ferromagnetic 3d transition metal surfaces is enhanced over the 3d band polarization by a significant amount (2-3 times) at very low secondary electron energies (<10 eV). Only at higher energies (10-20 eV) does the polarization gradually approach the net magnetization value. The polarization enhancement is attributed to spin dependent inelastic scattering due to Stoner excitations (spin flip scattering). While this model gives a qualitative account of the observed spin polarization in all the 3d metals the situation is less clear for other systems, e.g. the rare earth. Paul et al. [17] showed that secondary electrons from Gd are indeed spin polarized.

We have studied the spin polarization spectrum from the Gd(0001) surface. The first question of interest was how much do the 4f levels, which carry the bulk of the magnetic moment, but are

well below (8 eV) the Fermi level, actually contribute to the secondary electron emission. The second question concerns the presence and magnitude of possible polarization enhancement mechanisms. Due to the very different electronic structure of the rare earths compared to the 3d metals one might expect very different scattering mechanisms to be at work in these materials.

Our studies were carried out on thick (400 Å) epitaxial Gd(0001) films grown on W(110). The studies were performed in a UHV system previously used in the studies of the magnetic reorientation transition in ultrathin Fe films on Cu(100) and Ag(100)[18]. The secondary electrons were excited by an unpolarized 1 keV primary electron beam impinging on the surface at an angle of about 45°. Secondary electrons are extracted in normal emission geometry by applying a negative bias voltage to the sample. After energy analysis in a 90° spherical electrostatic energy analyzer spin polarizations are measured in a medium-energy (25-30 kV) retarding-field Mott detector. The Gd films were grown in UHV on a W(110) substrate by evaporation from a W crucible. The films were remanently magnetized in-plane by a magnetic field pulse. The growth mode of Gd on W is critically dependent on the growth conditions. At elevated temperature the films grow in a three dimensional Stranski-Krastanov mode. While these films show sharp LEED patterns it is believed that they exhibit a significant amount of surface roughness. The other growth method which is believed to yield smoother surfaces is to deposit the film at room temperature and then anneal to 630 K for a few minutes. It was found that the room temperature grown films show higher spin polarizations than the high temperature films[19].

Therefore, we are concerned only with the "better" low temperature grown films for the moment. The hysteretic properties of the films was studied by in-situ magneto-optical Kerr loops to ensure full remanence[20].

Fig. 7 shows a spectrum of the secondary electron intensity and the spin polarization as a function of kinetic energy at a sample temperature of 150 K. The intensity shows the typical distribution with the strong maximum at low energies. The spin polarization is almost constant at a value of 30-32% in the energy range 1.5-7 eV. At lower energies, however, the polarization drops significantly. This polarization behavior is drastically different from that of the 3d transition metals. First, the constancy of the polarization suggests that no significant enhancement mechanism due to

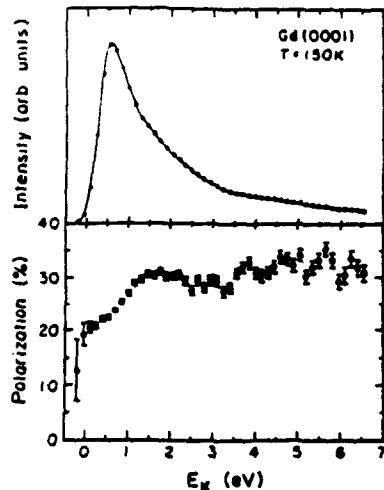


Fig. 7
Intensity and polarization
spectrum of secondary
electrons from Gd(0001)

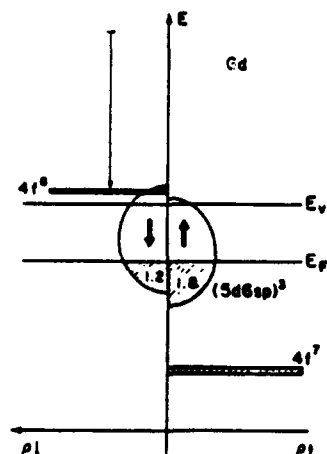


Fig. 8
Schematic of the electronic structure of Gd

character which is located just above the vacuum level. The proposed mechanism is indicated in Fig. 8. Excited electrons scatter into the $4f^8$ states from which they are emitted into vacuum. This scattering channel is available only for minority spin electrons and therefore leads to the observed reduced polarizations just above E_{vac} .

IV. Magnetic reconstruction of the Gd(0001) surface

The discussion of the spin polarization from Gd in the previous section assumed that the magnetic moments at the Gd(0001) surface are all ferromagnetically aligned. However, the magnetic structure of the Gd(0001) surface has been of interest for a long time since the observation of an enhanced surface ordering temperature[22] and the proposal of an antiferromagnetically aligned surface layer[23]. An antiferromagnetic surface layer was also favored in recent ab-initio electronic structure calculations[24]. The existence of a surface state was also predicted by the calculations, in agreement with (spin integrated) photoemission spectra[25]. However, recent spin polarized photoemission spectroscopy on Gd(0001) found the surface state to be of majority-spin character[26,27], as opposed to the predicted minority-spin character. Spin polarized photoemission spectroscopy from the 4f levels found spin polarizations of about 50% at 100K [26] which was interpreted as evidence for a ferromagnetic surface structure. The reduced polarization from the expected complete polarization for fully aligned 4f moments was attributed to depolarization of the photoelectrons due to spin flip scattering.

We have performed temperature dependent measurements of the 4f polarization using a photon energy of 149 eV at an undulator beam line at the Stanford Synchrotron Radiation Laboratory. At

spin dependent inelastic scattering is at work. In the absence of polarization enhancement the polarization should then reflect the surface magnetization. The magnetic moment of Gd at zero temperature is 7.6 μ_B of which 7 μ_B is carried by the 4f shell and 0.6 μ_B is due to conduction band polarization. A schematic of the electronic structure of Gd is shown in Fig. 8. The conduction band polarization is 20%. The expected secondary electron polarization then depends on the relative contributions from the 4f states and the conduction bands. The observed value of 32% at 150 K extrapolates into about 45% at zero temperature [21]. This implies that there is a significant contribution to the secondary yield from the 4f levels. The drop of the spin polarization below 1.5 eV kinetic energy is attributed to the presence of the empty $4f^8$ state of minority spin

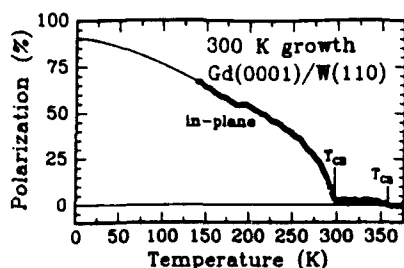


Fig. 9
Temperature dependence of
the 4f spin polarization

annealed, since they yield higher polarization values. The temperature dependence of the 4f polarization is shown in Fig. 9. In these experiments we measured the in-plane polarization component only. The bulk Curie temperature T_{CB} (293 K) is clearly visible in the data. There is however a small non-zero spin polarization component that persists above T_{CB} and vanishes only at much higher surface Curie temperature T_{CS} of about 350 K. We found that the surface temperature depends critically on the surface conditions. Also we see a kink in the data at 187 K. We interpret this as being connected to the spin reorientation transition which occurs at 225 K in bulk Gd. In order to get an estimate of the zero temperature polarization we extrapolated the low temperature polarization to $T=0$ using a $T^{3/2}$ law. The polarization reaches values of about 90% which is within the accuracy of the polarization measurements (estimated to be $\pm 5\%$).

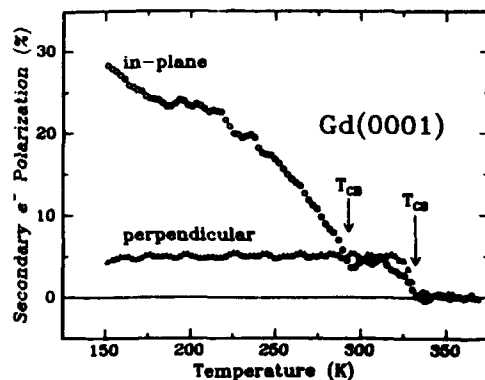


Fig. 10
Temperature dependence of
secondary electron polarization

this energy the photoemission process proceeds mainly through a 4d-4f resonance which yields an order of magnitude increase in the 4f intensity, thus enabling us to perform complete temperature sweeps between 150 K and the Curie temperature in one hour. It was experimentally verified that the spin polarizations obtained in the resonant emission process are identical to the polarizations obtained in direct (non-resonant) photoemission. Again, here we only report data on Gd films which were grown at room temperature and were then

almost complete polarization. Thus, this clearly proves the predominant ferromagnetic surface alignment. We further investigated the surface transition by performing temperature dependent spin polarized secondary electron measurements. The secondary electron energy was set to 2 eV for these experiments. In these experiments we also measured the spin polarization component perpendicular to the film plane. The results are shown in Fig. 10. Again, we see a clearly non-vanishing spin polarization persisting above the bulk T_C .

In addition, there is a significant perpendicular polarization component which is constant until it rather abruptly vanishes at T_{CS} . Thus, even though the surface is clearly coupled mainly ferromagnetically as seen from the large in-plane 4f polarizations we propose that the magnetic state of Gd(0001) is a canted spin configuration. We attribute the spin canting to an intrinsic surface anisotropy. The temperature dependence of the perpendicular component is characteristic of a two-dimensional phase transition. Thus, it appears that the surface acts as almost decoupled from the bulk. It is interesting to note that the perpendicular component is more readily detected in secondary electron spectroscopy than in the photo-emission data. This points to a very small electron mean free path in Gd at low energies.

V. Conclusions

We have shown that spin polarized electron spectroscopies can be used to yield information on the magnetic structure and the electronic structure of surfaces of novel magnetic systems. Spin polarized electron energy loss spectroscopy was shown to be able to detect the surface magnetization on epitaxial films of Cr and Mn on Fe(100). An estimate of the average surface exchange splitting is derived from the spin-flip energy loss spectrum. Spin polarized photoemission from the 4f levels from Gd(0001) surfaces shows almost complete polarization. A perpendicular spin polarization component of secondary electrons from Gd(0001) suggests a canted spin state at this surface.

This work was performed in collaboration with S.F. Alvarado, C. Chappert, D.S. Dossau, A.W. Pang, D.P. Pappas, J.C. Scott, H. Tang, T.G. Walker, and D. Weller. Support from the National Science Foundation and IBM Almaden Research Center is gratefully acknowledged. The photoemission experiments were performed at the Stanford Synchrotron Radiation Laboratory.

References

1. H. Hopster, in *Ultra-thin Magnetic Structures*, Vol. I, edited by B. Heinrich and A. J. Bland, Springer Verlag (1993)
2. D.L. Abraham and H. Hopster, *Phys. Rev. Lett.* 62, 1159 (1989)
3. A. Venus and J. Kirschner, *Phys. Rev.* B37, 2199 (1988)
4. K.-P. Kamper, D.L. Abraham, and Hopster, *Phys. Rev.* B45, 14335 (1992)
5. H. Hopster and D.L. Abraham, *Phys. Rev.* B40, 7054 (1989)
6. P. Grunberg, S. Demokritov, A. Fuss, R. Schreiber, J.A. Wolf, and S.T. Purcell, *J. Magn. Magn. Mater.* 104, 1734 (1992)
7. J. Unguris, R.J. Celotta, and D.T. Pierce, *Phys. Rev. Lett.* 67, 149 (1991)
8. R. Jungblut, Ch. Roth, F.U. Hillebrecht, and E. Kisker, *J. Appl. Phys.* 70, 5923 (1991)
9. T.G. Walker, A.W. Pang, H. Hopster, and S.F. Alvarado, *Phys. Rev. Lett.* 69, 1121 (1992)
10. L. E. Klebanoff, S.W. Robey, G. Liu, and D.A. Shirley, *Phys. Rev.* B31, 6379 (1985)

11. R.H. Victora and L.M. Falicov, Phys. Rev. B31, 7335 (1985);
C.L. Fu and A.J. Freeman, Phys. Rev. B33, 1755 (1985)
12. S.T. Purcell, M.T. Johnson, N.W.E. McGee, R. Coehorn, and
W. Hoving, Phys. Rev. B45, 13064 (1992)
13. T.G. Walker and H. Hopster, MRS Spring Meeting 1993, this
proceedings
14. T.G. Walker and H. Hopster, submitted to Phys. Rev. B
15. J. Unguris, R.J. Celotta, and D.T. Pierce, Phys. Rev. Lett.
16. X. Zhang, H. Hsu, F.B. Dunning, and G.K. Walters, Phys. Rev.
B44, 9133 (1991)
17. O. Paul, S. Toscano, and M. Landolt, to be published;
O. Paul, Ph. D. Thesis, ETH Zurich (1990)
18. D.P. Pappas, K.-P. Kamper, and H. Hopster, Phys. Rev. Lett.
64, 3179 (1990)
19. H. Tang, D. Weller, T.G. Walker, J.C. Scott, C. Chappert,
H. Hopster, A.W. Pang, D.S. Dessau, and D.P. Pappas, sub-
mitted to Phys. Rev. Lett.
20. C. Chappert, D. Weller, H. Tang, J.C. Scott, H. Hopster,
and D.P. Pappas, MRS Spring Meeting 1993, this proceedings
21. H. Tang T.G. Walker, H. Hopster, D.P. Pappas, D. Weller, and
J.C. Scott, Phys. Rev. B47, 5049 (1993)
22. C. Rau and S. Eichner, Phys. Rev. B34, 6347 (1986)
23. D. Weller, S.F. Alvarado, W. Gudat, K. Schroder, and
M. Campagna, Phys. Rev. Lett. 54, 1555 (1985)
24. R. Wu, C. Li, A.J. Freeman, Phys. Rev. B44, 9400 (1991)
25. Dongqi Li, Jiandi Zhang, P.A. Dowben, and M. Onellion, Phys.
Rev. B45, 7272 (1992)
26. G.A. Mulhollan, K. Garrison, and J.L. Erskine. Phys. Rev.
Lett. 69, 3240 (1992)
27. Dongqi Li, Jiandi Zhang, P.A. Dowben, K. Garrison, P.D.
Johnson, H. Tang, T.G. Walker, H. Hopster, J.C. Scott,
D. Weller, and D.P. Pappas, MRS Spring Meeting 1993, this
proceedings

PROBING THE SURFACE-VACUUM INTERFACE WITH SPIN-SENSITIVE METASTABLE ATOM DEEXCITATION, ELECTRON CAPTURE AND ELECTRON EMISSION SPECTROSCOPIES

G. K. WALTERS AND C. RAU

Physics Department and Rice Quantum Institute, Rice University, Houston, TX 77251-1892

ABSTRACT

Spin-Polarized Metastable Atom Deexcitation (SPMDS) and Electron Capture (ECS) Spectroscopies probe the exponential tails of electronic wavefunctions extending from the surface into the vacuum, and are consequently extremely sensitive to the surface-vacuum interface. The use of SPMDS to probe the near-surface vacuum magnetization of Ni(110) and Fe(110) and the dramatic changes that result upon exposure to ambient gases is discussed, as is the use of ECS and Spin-Polarized Electron Emission Spectroscopy (SPEES) to determine the ferromagnetic and critical behavior of surfaces and ultra-thin epitaxial systems.

INTRODUCTION

Particle (atoms, ions)-surface scattering experiments provide a powerful means to study the topmost surface-layer electronic and magnetic properties of magnetic materials. This can be achieved by keeping the energy component E_{\perp} of the incident particles normal to the probed surface below 10 - 20 eV, thus preventing their penetration into the surface and assuring top layer specificity in their interaction with target surfaces. Spin-polarized metastable (atom) deexcitation spectroscopy (SPMDS), electron capture spectroscopy (ECS), and spin-polarized electron emission spectroscopy (SPEES) have emerged as extremely surface specific probes of magnetic properties at the surface-vacuum interface.¹ The physical processes underlying each of these spectroscopies are briefly described below and selected experimental results are presented to illustrate the insights into surface magnetic behavior that they provide.

SPIN-POLARIZED METASTABLE DEEXCITATION SPECTROSCOPY (SPMDS)

In SPMDS surface electronic and magnetic structure and the near-surface magnetic environment are probed by investigating spin dependences in the interaction of thermal-energy (~ 0.03 eV) electron-spin-polarized He(2^3S) metastable atoms with a magnetized surface. The energy distributions and polarization of electrons ejected from the surface as a result of metastable-atom deexcitation are measured as is (for a magnetized surface) any spin dependence in the total ejected-electron signal.^{2,3}

The apparatus is shown schematically in Fig. 1 and is described in detail elsewhere.^{2,4} Briefly, a fraction of the atoms contained in a ground-state helium atom beam are collisionally excited to the 2^1S levels by a coaxial electron beam. The 2^1S atoms are removed from the beam by illuminating it with $2.06\text{-}\mu\text{m}$ radiation from a helium discharge which excites $2^1S \rightarrow 2^1P \rightarrow 1^1S$ transitions. A weak (~ 0.5 G) magnetic field is applied perpendicular to the beam to preserve a well-defined quantization axis. Circularly polarized $1.08\text{-}\mu\text{m}$ $2^3S \rightarrow 2^3P$ resonance radiation from a high-power rf-excited helium lamp is incident along the magnetic field direction and is used to optically pump the 2^3S atoms to increase the relative populations in the $M_J(M_S) = +1$ or -1 magnetic sublevels. The resultant beam polarization is defined as

$$P_{He} = \frac{F_+ - F_-}{F_+ + F_0 + F_-} \quad (1)$$

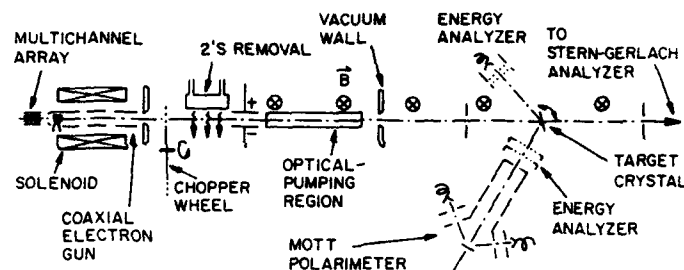


Fig. 1. Schematic diagram of the SPMDS apparatus.

where F_+ , F_0 , and F_- are the fluxes of $\text{He}(2^3\text{S})$ atoms with $M_S = +1, 0$ and -1 , respectively. The beam polarization, $P_{\text{He}} \sim 0.4$, is measured by a Stern-Gerlach analyzer⁴ and can be simply reversed ($P_{\text{He}} \rightarrow -P_{\text{He}}$) by changing the sense of circular polarization of the optical pumping radiation.

The energy distribution of the electrons ejected from the target surface is measured using a simple retarding grid energy analyzer, and those electrons with sufficient energy to overcome the retarding potential barrier are detected by a channeltron. The number of electrons with energies in some particular interval is determined by switching the potential applied to the retarding grid between the appropriate limits and observing the resultant *change* in the detected electron signal. The energy analyzer is also used to investigate spin dependences in the total number of electrons ejected with energies greater than the cut off determined by the potential V applied to the retarding grid. Such spin dependences are characterized by an asymmetry parameter $A(V)$ defined as

$$A(V) = \frac{1}{|P_{\text{He}}|} \frac{I_+ - I_-}{I_+ + I_-} \quad (2)$$

where I_+ and I_- are the ejected electron currents observed with the incident beam polarized parallel and antiparallel, respectively, to the majority spin direction in the (magnetized) target.

A second independent experimental parameter, the polarization of the ejected electrons, can also be measured. This is accomplished using a compact Mott polarimeter equipped with a retarding potential energy analyzer.⁵ The average polarization of those ejected electrons with energies greater than the cut off set by the retarding potential V applied in the energy analyzer is determined by measuring the asymmetry in the count rates of electrons quasielastically scattered (at 20 keV) through $\pm 120^\circ$ at a gold target. The electron polarization, which depends both on the helium atom polarization and the retarding potential, is defined by

$$P_e(P_{\text{He}}, V) = \frac{I_p - I_A}{I_p + I_A} \quad (3)$$

where I_p and I_A are the currents of electrons ejected with spins parallel and antiparallel, respectively, to the majority spin direction in the target.

Values of the asymmetry $A(V)$ measured for an atomically clean Ni(110) surface² and for an Fe(110) surface with residual carbon ($\sim 9\%$) and oxygen ($\sim 4\%$)³ -- the cleanest achievable and henceforth referred to as the "clean" Fe surface -- are shown in Figs. 2 and 3. Fig. 3 also

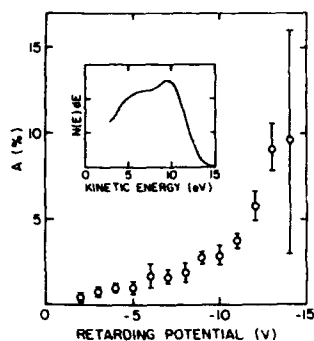


Fig. 2. Polarization asymmetry A as a function of retarding potential for a clean, magnetized Ni(110) sample at -130°C . The inset shows the measured secondary-electron energy distribution.

shows the changes in $A(V)$ that result when the Fe(110) surface is exposed to oxygen. The ejected electron energy distributions for the clean surfaces, and for Fe(110) following 8 L exposure to oxygen, are shown in insets. Fig. 3 also includes values of the asymmetry expected for an atomically clean Fe(110) surface obtained by linear extrapolation of the asymmetries measured at different oxygen coverages as inferred from Auger analysis. (Tests revealed that the presence of small amounts of carbon on the surface had a negligible effect on the measured asymmetries.)

The asymmetries shown in Figs. 2 and 3 can be interpreted in terms of the theory of spin polarized metastable atom deexcitation at magnetic surfaces recently developed by Penn and Apell (PA).⁶ A $\text{He}(2^3\text{S})$ atom incident upon a clean, relatively high-work-function surface such as Ni(110) or Fe(110) first undergoes resonance ionization (RI) in which the excited $2s$ electron tunnels into an unfilled level above the Fermi surface. The resulting He^+ ion continues toward the surface where it undergoes Auger neutralization (AN) in which a conduction electron from the metal tunnels into the $1s$ hole, the released energy being communicated to a second (Auger) conduction electron which may escape the metal. The energy available to the escaping electron depends on the energy of the He^+ $1s$ hole and this decreases as the ion approaches the surface due to the He^+ image potential. Thus the farther from the surface that the AN event occurs, the greater the energy (on the average) of the escaping electron. PA show that the

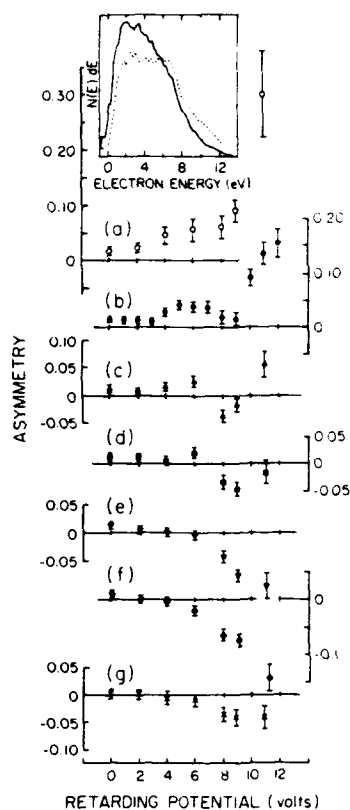


Fig. 3. Values of the asymmetry $A(V)$ for (a) an atomically clean Fe(100) surface (obtained by extrapolation, see text); (b) a sputtered and annealed Fe(110) surface; and (c), (d), (e), (f), and (g) an Fe(110) surface following exposure to 1, 2, 4, 8, and 16 L of oxygen, respectively. The inset shows the ejected electron-energy distributions for a clean Fe(110) surface (---) and following an 8-L exposure to oxygen (—).

measured asymmetries arise as a consequence of a non-zero magnetization in the vacuum well outside the surface where AN occurs.

The AN rate at some distance z from the target surface is proportional to the number density of conduction electrons at z that are available to fill the He^+ 1s hole. For incident $\text{He}(2^3\text{S})$ atoms, and hence He^+ ions, with positive (negative) polarizations (i.e., spins parallel (antiparallel) to the majority spin direction in the magnetized target) neutralization can only occur with minority (majority) conduction electrons (the helium ground state is a spin singlet). Thus the average distance at which AN occurs, and hence the average energy available to the Auger electron, will depend on the spin orientation of the incident $\text{He}(2^3\text{S})$ atoms because the majority and minority spin densities in the vacuum are in general unequal for a ferromagnetic target.

Using this model, PA have shown that the sign of the asymmetry parameter $A(V)$ will be positive (negative) if the conduction electron density in the vacuum outside the target surface is predominantly minority (majority). Their analysis of the $\text{Ni}(110)$ asymmetry yields a magnetization of $\sim -20\%$ at the Fermi energy and 4.5 \AA from the surface.⁶ The negative magnetization in the vacuum is consistent with band calculations of Wimmer et al. who show that the nickel s-p electrons, which through s-d hybridization are polarized oppositely from the d electrons that dominate the total magnetic moment in the bulk, spill out into the vacuum region and are dominant beyond $\sim 2.5 \text{ \AA}$.⁷ Negative magnetization in the vacuum above $\text{Ni}(110)$ has also been reported by Rau, based on electron capture experiments.⁸ Exposure of the $\text{Ni}(110)$ surface to 4 Langmuirs of CO reduces the measured asymmetry to zero, suggesting that the vacuum magnetization is quenched to $\pm 2\%$ within experimental uncertainty.²

The data in Figure 3 show that $A(V) > 0$ for a clean $\text{Fe}(110)$ surface, requiring on the basis of the PA theory that, as for $\text{Ni}(110)$, minority electrons are dominant at distances $\sim 3\text{--}5 \text{ \AA}$ outside the surface where AN occurs. However, the measured asymmetry is extremely sensitive to the presence of oxygen on the surface, reversing sign and becoming strongly negative for exposures above about 4 L. According to the PA theory this requires that the vacuum magnetization at distances where AN occurs change from negative to positive upon oxygen adsorption. This result is consistent with subsequent *ab initio* electronic structure calculations by Wu and Freeman, which reveal that the $\text{Fe}(110)$ vacuum magnetization at distances where AN occurs is indeed negative, strongly so for states near the Fermi energy that are responsible for the large asymmetry observed at the highest ejected electron energies.⁹ The calculations also agree with experiment in showing that the vacuum magnetization is positive for the $\text{O}/\text{Fe}(110)$ surface.

The polarizations $P_e(P_{\text{He}}, V)$ of electrons ejected from clean and oxygen-exposed $\text{Fe}(110)$ surfaces were also measured. The data are summarized in Table I for several values of the retarding potential V . Table I includes data obtained using an unpolarized incident beam, and an incident beam polarized either parallel or antiparallel to the majority spin direction in the (magnetized) sample. Since the polarizations of both the incident $\text{He}(2^3\text{S})$ atoms and ejected electrons are defined relative to the target majority spin direction, the measured values of P_e should remain unchanged upon reversal of the magnetization of the target ($M\uparrow \rightarrow M\downarrow$), as is observed. In contrast to the marked sensitivity of the asymmetry $A(V)$ to oxygen exposure, both the ejected-electron energy distribution and polarization of electrons ejected by an unpolarized incident $\text{He}(2^3\text{S})$ beam are essentially unchanged by oxygen exposure.

The data in Table I also reveal a significant spin correlation favoring the ejection of electrons with the same spin orientation as the incident metastable atoms. This spin correlation, which amounts to $\sim 20\%$, i.e., the change in polarization of the ejected electrons is $\sim 20\%$ that of the incident atoms, is similar to that observed from paramagnetic targets¹⁰ for which it has been demonstrated that metastable deexcitation occurs via $\text{RI}+\text{AN}$ exclusively.¹¹ Indeed, this unexpected $\geq 20\%$ spin correlation in Auger neutralization of He^+ ions at surfaces has been observed for every target investigated, both paramagnetic and ferromagnetic.

The ejected electron polarizations resulting from the deexcitation of an unpolarized $\text{He}(2^3\text{S})$ beam at both a clean $\text{Fe}(110)$ surface, and following oxygen exposure, are positive, i.e., the ejected electron polarization is parallel to the majority spin direction and reflects the conduction band polarization. This requires that, on average, the ejected electrons originate

TABLE I. Measured spin polarization $P_e(V)$ of electrons ejected by both unpolarized $\text{He}(2^3\text{S})$ atoms and by $\text{He}(2^3\text{S})$ atoms polarized parallel and antiparallel to the majority-spin direction in the target. Data for the clean $\text{Fe}(110)$ surface after reversing the target magnetization ($M \uparrow \rightarrow M \downarrow$) are included. The majority-spin direction in the target is taken to be the direction of positive P_{He} and $P_e(V)$. The uncertainty in each measured value of P_e is $\sim \pm 0.03$.

	V	$M \uparrow$ P_{He}			$M \downarrow$ P_{He}		
		-0.40	0	+0.40	-0.40	0	+0.40
		$P_e(V)$			$P_e(V)$		
(a) Clean $\text{Fe}(110)$	0	0.07	0.12	0.21	0.004	0.10	0.21
	3	0.02	0.08	0.18	0.04	0.09	0.15
	6	-0.01	0.07	0.14	0.02	0.04	0.19
	9	-0.06	0.10	0.22	0.02	0.11	0.21
(b) $\text{O}/\text{Fe}(110)$ (8-L exposure)	0	0.04	0.10	0.15			
	3	-0.03	0.07	0.14			
	6	-0.02	0.08	0.15			
	9	-0.03	0.09	0.21			

deeply enough within the target surface that their polarizations are not significantly affected by the presence of an oxygen adlayer. Photoemission¹² and electron bombardment¹³ studies of magnetized iron surfaces also have shown that the ejected electron polarization mirrors the band polarization, but the measured polarizations are much greater than observed in the present work. The present data are, however, in reasonable agreement with the results of Kirschner et al. who studied the polarization of electrons ejected (by potential ejection) when 1 keV He^+ or Ar^+ ions are neutralized at a magnetized $\text{Fe}(110)$ surface.¹⁴ They attribute the generally low polarizations of the ejected electrons to a reduction in the band polarization in the near surface region, where the ejected electrons originate, because of the spill-out of negatively polarized s-p electrons above the surface. Alternately, matrix element effects favoring Auger ejection from the s-p band could account for the low measured polarizations.

In summary, measurements and analysis of asymmetry and spin-polarization of electrons ejected from magnetic surfaces by $\text{He}(2^3\text{S})$ metastable-atom deexcitation demonstrate that SPMDS is an extraordinarily sensitive probe of the surface magnetic environment and the pronounced changes that can result upon exposure to ambient gases.

ELECTRON CAPTURE AND SPIN-POLARIZED ELECTRON EMISSION SPECTROSCOPIES

Electron capture spectroscopy (ECS) and spin-polarized electron emission spectroscopy (SPEES) utilize capture and emission of spin-polarized electrons during grazing-angle surface reflection of fast ions at magnetic surfaces. These spectroscopies provide a powerful means for study of two-dimensional (2D) magnetic properties (critical behavior, element-specific ferromagnetic order, magnetic anisotropies, etc.) both of bulk surfaces and of ultra-thin films, with unprecedented surface sensitivity.^{15,16}

The fundamental physical process in ECS is the capture of one or two spin-polarized electrons during small-angle surface reflection of fast ions, enabling the study of both long-range and short-range order at surfaces of ferromagnetic materials.^{17,18} For 150 keV deuterons and for an ion angle of incidence of 0.2° the distance of closest approach of the ions to the reflecting surface is about 0.1 nm (see Fig. 4, full line). Therefore, the ions probe spin-polarized local electron densities of state at the topmost surface layer. For the measurement of long-range surface ferromagnetic order, one electron capture processes ($\text{D}^+ + e^- = \text{D}^0$) are exploited by determining the spin polarization of the captured electrons; details are presented elsewhere. For the measurement of short-range ferromagnetic order, protons or deuterons are used to study

two-electron capture processes (e.g., $D^+ + 2e^- = D^-$).¹⁷ The only stable bound state of H^- or D^- is the $1s^2\ ^1S$ state. Therefore, stable H^- or D^- ions can only be formed by capture of two electrons with oppositely oriented spins. In the ESP experiments reported here, 25 keV protons or 150 keV deuterons are used. For this energy range, the distance within which 2 electrons are captured by a single ion is in the range 0.5-2 nm. Thus, two-electron capture processes are sensitive to short-range ferromagnetic order existing within a range of only a few atomic neighbors. It is obvious that two-electron capture will be strongly suppressed by the presence of short-range ferromagnetic order where predominantly electrons with parallel oriented spins are available for capture by a single ion. The reduction in the H^-/H^+ or D^-/D^+ ratio measured after beam reflection at the surface of a magnetic sample, relative to that for a nonmagnetic target such as Cu, provides a direct measure of the short-range ESP at a magnetic surface.

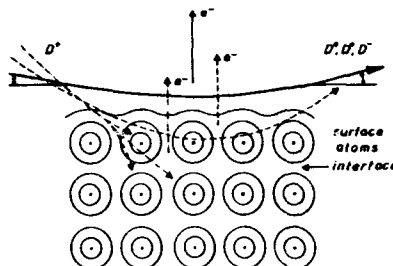


Fig. 4. Scheme illustrating ion trajectories for various scattering angles, the emission of ion-induced electrons and the surface potential plotted on a plane perpendicular to the reflecting surface.

In angle- and energy-resolved, spin-polarized electron emission spectroscopy (SPEES), small angle surface scattering of energetic (5 - 150 keV) ions (H^+ , He^+ or Ne^+) is used to study the emission of spin-polarized electrons as a measure of long-range surface ferromagnetic order. Fig. 1 illustrates ion trajectories for various scattering angles, the ion-induced emission of electrons, and the surface potential plotted on a plane perpendicular to the reflecting surface. Varying the ion scattering angle from 0.2° up to 45° results in an increase of the probing depth of the incident ions from the topmost surface layer to interface and deeper layers. Electrons emitted along the surface normal (emission cone angle 8°) of a nonmagnetic or remanently magnetized target are both energy- and spin analyzed.

Ultra-thin magnetic films are deposited by electron beam evaporation. The thickness of the films is determined with a calibrated quartz oscillator, calibrated Auger electron signals and with RHEED oscillations. The island-free growth of the films is checked by monitoring the ion reflectivity and the energy distribution of the specularly reflected deuterons. At the surface of all films studied so far, the reflectivity is not reduced from its initial value of 95% measured at the carefully prepared substrate surfaces which have been shown by scanning tunneling microscopy to be atomically flat over distances of 150 - 200 nm. Furthermore, the presence of islands would yield an additional energy loss of the deuterons caused by penetration of the ions through islands by planar channeling, which is not observed.

Ultra-thin (5 nm) hcp Tb(0001) films which are epitaxially and homogeneously deposited at 300 K on bcc W(110) substrates provide a striking example of the use of ECS for studies of long-range ferromagnetic order with top layer specificity.¹⁹ The electron spin polarization (ESP) of the captured electrons is measured. Their polarization

$$P = \frac{n_+ - n_-}{n_+ + n_-} \quad (4)$$

is defined relative to the direction of the magnetic field H applied at the target, and n^+ and n^- are the numbers of majority- and minority-spin electrons detected.¹⁷ In the case of rare-earth metals such as Tb and Gd, the measured polarization P is attributed to the polarization of the 5d-6s surface electrons¹⁷ which is proportional to the surface magnetization of the localized 4f

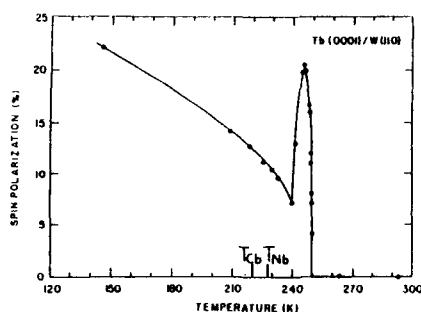


Fig. 5 Electron spin polarization $P(\%)$ of the topmost surface layer of 5 nm thin Tb(0001)/W(110) films as function of temperature. T_{Cb} denotes the bulk Curie temperature, and T_{Nb} denotes the bulk Néel temperature of Tb.

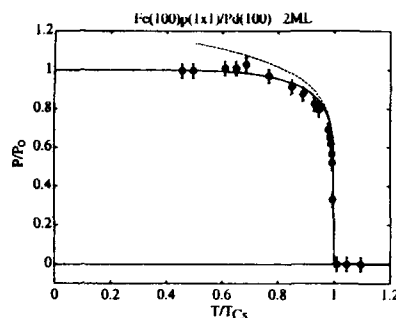


Fig. 6. Electron spin polarization P/P_0 as function of T/T_{Cs} for the surface of a 2 ML thin bct Fe(100)p(1x1)/Pd(100) film. The solid and dashed lines represent, respectively, the exact solution of the 2D Ising model and the power law approximation for $T \rightarrow T_{Cs}$.

electrons, the predominant carriers of the magnetization. P is measured in magnetic fields ranging between 25 and 600 Oe, the samples being magnetized along the W[100] direction and the temperature being kept constant within 0.02° . Such applied fields have been shown to have a negligible effect on the electron spin polarization in the investigated temperature range.²⁰

In Fig. 5, the temperature dependence of P at Tb(0001)/W(110) surfaces is shown for $H=250$ Oe. H was varied between 25 Oe and 600 Oe, and no significant influence on the polarization data was detected. Nonzero P values establish that the surfaces of the films are ferromagnetically ordered up to 248 K, which lies above both the bulk Curie and Néel temperatures, T_{Cb} and T_{Nb} , as indicated in Fig. 5. With increasing temperature, P decreases from 22% at 146 K, reaching a value of 7% at about 240 K, which lies slightly above T_{Cb} and T_{Nb} . As T increases further, P increases very steeply to 21% at 243 K, then drops suddenly to zero at a surface Curie temperature $T_{Cs} = 249.96$ K. In more recent ECS experiments, it has been found that the short-range ESP extends up to temperatures of about 300 K.

From the measured temperature variation of P the critical exponent β is determined simultaneously with T_{Cs} by a linear least-square fit. For $(T_{Cs} - T)/T_{Cs}$ ranging between 2×10^{-2} and 10^{-4} , a value $\beta = 0.348 \pm 0.01$ is obtained.

Previous magnetic studies of surface critical behavior have been restricted to the case $T_{Cs} = T_{Cb}$, for which β has been measured to be 0.75 ± 0.05 ²¹ for several systems. The only other experimental determination of β for the case T_{Cs} larger than T_{Cb} was for ultra-thin films of V(100) on Ag(100) substrates,²² for which $T_{Cb} = 0$. For that system ECS measurements yielded $\beta = 0.125$, a value identical to that of the two-dimensional Ising ferromagnet. In the present case, T_{Cs} lies close to T_{Cb} , and one does not expect 2D Ising critical behavior. The fact that $T_{Cs} \neq T_{Cb}$ indicates that the magnetic couplings between the surface spins are strongly anisotropic, which may explain why the measured $\beta = 0.348$ is much smaller than the value $\beta = 0.75$ expected in the absence of anisotropy.²³

In other ECS experiments, ultra-thin (1-4 ML) bct Fe(100) films were deposited on atomically flat Pd(100) substrates. For a substrate temperature of 293 K and an evaporation rate of 0.002 nm/s, homogeneous and island-free growth of the Fe films is obtained.²⁴ The samples are magnetized in fields up to 75 Oe, the temperature of the samples being kept constant within 0.05° . Such applied fields have a negligible effect on the ESP in the investigated temperature range and it was found that, within experimental errors, the remanent magnetization is equal to the saturation magnetization. Fig. 6 shows the normalized long-range electron spin polarization

P/P_0 at the surface of a 2 ML Fe(100) film on Pd(100), as a function of T/T_{Cs} , with $T_{Cs} = 613.1$ K being the measured surface Curie temperature and $P_0 = -33\%$ the calculated electron spin polarization at $T = 0$. The full line in Fig. 6 represents the temperature dependence of the magnetization as predicted by Yang for the 2D Ising model,²⁵ and the dashed line gives the best fit in the asymptotic power law approximation with $\beta = 0.125$. It is obvious that the experimental data are precisely described by the exact solution of the 2D Ising model given by Yang.

For the SPEES experiments discussed here, surface scattering of 25 keV Ne^+ ions was used to study the emission of spin-polarized electrons produced as a consequence of the particle-surface interaction. Figure 7a shows for an angle of incidence $\alpha = 1^\circ$ the energy distribution (relative to the vacuum level) and the ESP of electrons emitted along the surface normal from clean (solid line) and O-covered (dashed line) polycrystalline Fe surfaces.¹⁹ At this incidence angle the Ne^+ ions are specularly reflected and do not penetrate the Fe surfaces. For both clean Fe and O/Fe, the energy distribution of the emitted electrons peaks at around 4 eV. However at O/Fe a strong increase in the intensity of emitted electrons is found as compared to that of clean Fe.

The ESP of electrons emitted from the topmost surface layer of clean Fe is $P = (33 \pm 2)\%$ for $E = 10$ eV but increases to $P = (48 \pm 2)\%$ for $E = 4$ eV. These values are far above the 28% average bulk magnetization value of Fe. For Fe surfaces with one monolayer of O, the average ESP of electrons at $E = 10$ eV remains nearly unchanged ($32 \pm 2\%$), but for electrons with $E = 4$ eV the ESP drops from $(48 \pm 2)\%$ to $-(14 \pm 2)\%$ indicating the presence of a magnetically active surface layer.

It is of considerable interest to determine whether the measured ESP of the emitted electrons reflects the layer-dependent net magnetization of a material. From ion-^{16,25,26} and electron-induced electron spectra,²⁷ there is evidence that the ESP of electrons emitted at high energies (≈ 10 eV above the vacuum level) scales roughly with the average net magnetization.

For $\alpha = 8^\circ$, E_\perp is 32.8 eV, and the ions can penetrate the topmost surface layer and excite electrons from the second layer. The shape of the energy distributions of the emitted electrons are similar to those of Fig. 7a with the peak maximum shifted upwards to about 5 eV (see Fig. 7b). In this case the average ESP of the electrons emitted from clean Fe increases from $P = 29\%$ at $E = 10$ eV to $P = 50\%$ at $E = 4$ eV. For the

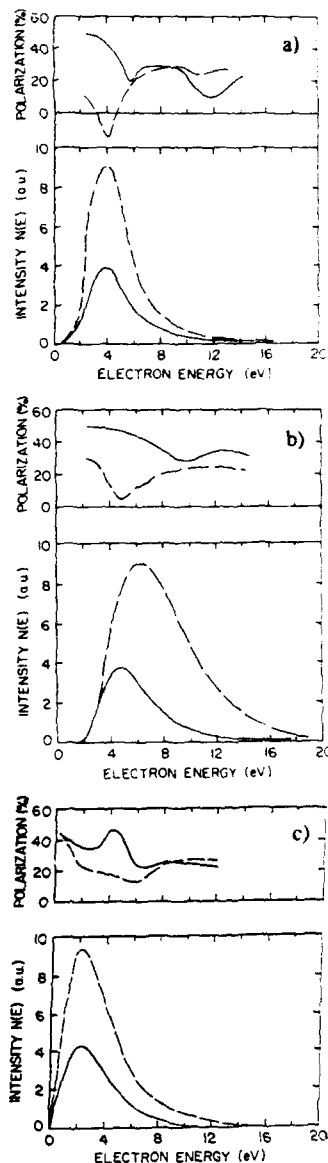


Fig. 7. Energy distribution and ESP as function of the energy E of electrons emitted from clean (solid line) and O-covered (dashed line) Fe surfaces by incident 25 keV Ne^+ ions and with incidence angles of 1° (a), 8° (b) 45° (c).

O/Fe surface the average ESP of electrons with $E=10$ eV remains unchanged ($32\pm 2\%$), whereas for electrons with $E=4$ eV the ESP decreases from ($50\pm 2\%$) to ($14\pm 2\%$) eV.

Fig. 7c shows for the energy distributions and the ESP's of electrons emitted from clean (solid line) and O/Fe (dashed line) surfaces for $\alpha = 45^\circ$. For this incidence angle E_i is 12.5 keV and the ions can penetrate deeply into the solid and excite electrons from bulk layers. In this case the energy distributions of clean and O-covered Fe surfaces are similar to those obtained in electron-induced secondary electron emission experiments,²⁶⁻²⁸ peaking at 2 eV. For O/Fe surfaces, however, a strong increase in the intensity of the emitted electrons is again observed. For electrons excited in bulk layers electron cascading and multiple scattering are the dominant processes occurring during electron transport to the surface, which causes the well-known 2 eV peak in electron- or ion-induced electron spectra. This is consistent with the data for $\alpha=1^\circ$ and $\alpha=8^\circ$ where the energy distributions of the emitted electrons peak at higher energies (around 4-5 eV) showing that electron cascading and multiple scattering processes are less pronounced. As regards the average ESP of the electrons emitted from clean Fe, an increase from $P=(25\pm 2)\%$ for $E=10$ eV to $P=(45\pm 2)\%$ for $E=4$ eV is observed. For the O/Fe surface, the average ESP of electrons with $E=10$ eV remains unchanged ($25\pm 2\%$), whereas for electrons with $E=4$ eV the ESP drops to ($15\pm 2\%$) eV.

Changing α from 45° to 1° , which corresponds to a reduction in the probing depth from deep lying layers, where bulk physical properties are probed, to the topmost surface layer, results in an increase in the ESP of "high-energy" electrons from 25% to 33%. This would imply that for polycrystalline Fe surfaces the net magnetization increases in going from the bulk to the surface. Assuming that the ESP of electrons emitted at high energies (≈ 10 eV) scales roughly with the average net magnetization, it is tempting to interpret this surface enhancement of the ESP in terms of theoretically predicted magnetic surface states which cause enhancements of the magnetization at Fe(100) and Fe(110) surfaces.^{29,30}

For low emitted electron energies, the measured ESP's from clean Fe are substantially enhanced above the bulk polarization values, as has been observed also for electron- and ion-induced emission. This enhancement can be attributed to Stoner excitations across the ferromagnetic exchange gap which occur during inelastic exchange scattering of minority electrons.^{31,32} The fact that the enhancements are observed to be approximately the same for electrons emitted from the surface layer ($\alpha = 1^\circ$) and from subsurface and deeper layers ($\alpha = 8^\circ$ and 45°) suggests that the mean free path for Stoner excitation is of order one monolayer or less.

Finally, the substantial polarizations of electrons emitted from O/Fe, and the pronounced dependence of the ESP at low energies on the incidence angle of the ion beam clearly demonstrate the absence of a magnetically dead layer at the surface and are consistent with the existence of spin-split electronic bands in the occupied and unoccupied parts of the band structure of O/Fe surfaces.³³

In conclusion, the experiments discussed here provide clear evidence that ECS and SPEES are powerful techniques for the study of topmost and interface layer magnetic properties.

This work was supported by the National Science Foundation, the Department of Energy, the Welch Foundation and the Texas Higher Education Coordinating Board.

References

1. F.B. Dunning, C. Rau and G.K. Walters, *Comm. on Solid Physics*, **12**, 17 (1985).
2. M. Onellion, M.W. Hart, F.B. Dunning and G.K. Walters, *Phys. Rev. Lett.*, **52**, 380 (1984).
3. M.S. Hammond, F. B. Dunning, G. K. Walters and G.A. Prinz, *Phys. Rev B*, **45**, 3674 (1992).
4. T.W. Riddle, M. Onellion, F.B. Dunning and G.K. Walters, *Rev. Sci. Instrum.*, **52**, 797 (1981).

5. F.-C. Tang, X. Zhang, F.B. Dunning and G.K. Walters, *Rev. Sci. Instrum.*, **59**, 504 (1988).
6. D.R. Penn and P. Apell, *Phys. Rev. B*, **41**, 3303 (1990).
7. E. Wimmer, A.J. Freeman and H. Krakauer, *Phys. Rev. B*, **30**, 3113 (1984).
8. C. Rau, *J. Magn. Magn. Mater.*, **30**, 141 (1982).
9. R. Wu and A.J. Freeman, *Phys. Rev. Lett.*, **69**, 2867 (1992).
10. M.W. Hart, M.S. Hammond, F. B. Dunning and G.K. Walters, *Phys. Rev. B*, **39**, 5488 (1989).
11. D.M. Oró, Q. Lin, P.A. Soletsky, X. Zhang, F.B. Dunning and G.K. Walters, *Phys. Rev. B*, **46**, 9893 (1992).
12. E. Kisker, W. Gudat and K.S. Schröder, *Solid State Commun.*, **44**, 591 (1982).
13. J. Unguris, D. T. Pierce, A. Galejs and R.J. Celotta, *Phys. Rev. Lett.*, **49**, 72 (1982).
14. J. Kirschner, K. Koike and H.P. Oepen, *Vacuum*, **41**, 518 (1990); *Phys. Rev. Lett.*, **59**, 2099 (1987).
15. C. Rau, *Appl. Phys. A*, **49**, 579 (1989).
16. C. Rau, K. Waters, and N. Chen, *Phys. Rev. Lett.*, **64**, 1441 (1990).
17. C. Rau, *J. Magn. Magn. Mater.*, **30**, 141 (1982).
18. C. Rau and S. Eichner, *Phys. Rev. Lett.*, **47**, 939 (1981).
19. C. Rau, C. Jin and M. Robert, *Phys. Lett. A*, **138**, 334 (1989).
17. C. Rau, P. Mahavadi, and M. Lu, *J. Appl. Phys.* (1993), in print.
18. N. Yang, *Phys. Rev.*, **85**, 808 (1952).
19. C. Rau, N. J. Zheng and M. Lu, *J. Magn. Magn. Mat.*, (1993), in print.
20. J. Balberg and J. S. Helman, *Phys. Rev. B*, **18**, 303 (1978).
21. S. F. Alvarado, M. Campagna, and H. Hopster, *Phys. Rev. Lett.*, **48**, 51 (1982); B. H. Dauth, S. F. Alvarado, and M. Campagna, *Phys. Rev. Lett.*, **58**, 2118 (1987).
22. C. Rau, G. Xing, C. Liu and M. Robert, *Phys. Lett.*, **135**, 227 (1989).
23. H. W. Diehl and E. Eisenriegler, *Phys. Rev. B*, **30**, 300 (1984).
24. J. Quinn, Y.S. Li, H. Li, D. Tian, F. Jona and P.M. Marcus, *Phys. Rev. B*, **43**, 3959 (1991).
25. J. Kirschner, in Surface and Interface Characterization by Electron Optical Methods, ed. by A. Howie and U. Valdre (Plenum Publ. Co., 1988), p. 297.
26. J. Kirschner, K. Koike, and H.P. Oepen, *Phys. Rev. Lett.*, **59** (1987) 2099.

27. M. Landolt, in "Polarized Electrons in Surface Physics", ed. by R. Feder (World Sci. Publ. Co., 1985), Chap.9; and Refs. cited therein.
28. R.A. Baragiola, E.V. Alonso, and A. Oliva-Florio, *Phys. Rev.* B61, 121 (1979).
29. C.L. Fu, A.J. Freeman, and T. Oguchi, *Phys. Rev. Lett.* 54, 2700 (1985).
30. J.W. Krewer and R. Feder, *Physica B* (1991) 135; and Refs. cited therein.
31. D. Penn and P. Apell, and S.M. Girvin, *Phys. Rev. Lett.* 55, 518 (1985).
32. J. Glaser and E. Tosatti, *Sol. Stat. Comm.* 52, 905 (1984).

SPIN-RESOLVED PHOTOEMISSION STUDY OF $n = 2$ CORE LEVELS OF IRON

L.E. KLEBANOFF*, D.G. VAN CAMPEN, and R.J. POULIOT

Lehigh University, Department of Chemistry and Zettlemoyer Center for Surface Studies, Sinclair Laboratory, 7 Asa Drive, Bethlehem, PA 18015

ABSTRACT

The first spin-resolved x-ray photoelectron spectroscopy (SRXPS) study of the $n = 2$ core levels of ferromagnetic Fe are reported. The $2p_{3/2}$, $2p_{1/2}$ and $2s$ core levels all display interesting spin-dependent structures and splittings. The spectral complexity predicted by a purely atomic picture is not observed in the data. The results indicate that theories incorporating the delocalization of the $3d$ valence band are more applicable to the description of core-level photoemission in iron.

Introduction

Spin-resolved photoemission has played an important role in elucidating the nature of interface magnetism. The majority of such studies have been spin-resolved ultra-violet photoemission (SRUPS) investigations of the valence-band structure of metallic surfaces [1-4]. These studies have provided a wealth of information concerning the valence electronic structure of ferromagnetic metals. SRUPS has also been used to measure the spin dependence of the rather shallow $3s$ and $3p$ core levels of Fe [5-8] and the $3p$ level of Co [1]. A disadvantage of using SRUPS for core-level study is that the low-energy ultra-violet radiation can photoionize only very shallow core levels, leaving the more tightly bound $n = 2$ levels of the $3d$ ferromagnets inaccessible. While SRUPS is ideal for valence-band study, valence-band investigations do not usually afford the element specificity that is often required to investigate heterogeneous magnetic interfaces.

We present here the first spin-resolved photoemission study employing a high photon energy (1253.6 eV) often used in x-ray photoelectron spectroscopy (XPS) studies of core levels. Spin-resolved XPS (SRXPS) results for the Fe $2p_{3/2}$, $2p_{1/2}$, and $2s$ levels are reported. The results show that intra-atomic exchange effects are important for these tightly bound levels, despite their small radial extent. The SRXPS data also clarify the nature of core-level initial states involved in soft x-ray magnetic circular dichroism (MCD) spectroscopic studies [9-11] of Fe.

Experimental

Our Fe sample was a thin film prepared by evaporating high-purity Fe in ultra-high vacuum onto the surface of a sputter-cleaned cobalt-based ferromagnetic metallic glass of composition $\text{Co}_{66}\text{Fe}_4\text{Ni}_{14}\text{B}_{14}\text{Si}_{15}$ [12]. The glass substrate consisted of a loop that was easily magnetized to saturation by passing current through coils wrapped around the legs of the loop. This arrangement allowed the preparation of high-purity polycrystalline Fe films with thicknesses of 20-30 Å with very little oxygen contamination [13]. The ferromagnetic exchange coupling between the Co metallic glass substrate and the Fe thin film conveniently leads to an in-plane magnetically saturated Fe film (with negligible stray magnetic field) that is required for SRXPS study. A fresh

Fe film was prepared every 12-24 hours as needed. The very surface sensitive 30 eV secondary electron spin polarization of Fe showed excellent reproducibility and stability throughout all measurements.

Our SRXPS spectrometer combines a VG MkII hemispherical electron energy analyzer with an electron spin detector based on the low-energy diffuse scattering method [14]. The photon source is an unmonochromatized $\text{MgK}\alpha$ ($h\nu = 1253.6$ eV) x-ray source operating at 510W power. The instrumental energy resolution was 1.6 eV full width at half maximum. The spectrometer vacuum during measurement was 5×10^{-10} Torr.

Results

The spin-resolved data were collected into four channels N_L^+ , N_L^- and N_R^+ , N_R^- . Here, N_L^+ represents the number of electrons diffusely scattered to the left (L) from the Au target in the spin detector when the sample magnetization is positive (+). N_R^- is the number of electrons scattered to the right (R) from the Au target when the sample magnetization has been reversed to the negative (-) direction. The electron beam polarization, P , can then be expressed as [15]:

$$P = \frac{1}{S} \left(\frac{\sqrt{N_L^+ N_R^-} - \sqrt{N_L^- N_R^+}}{\sqrt{N_L^+ N_R^-} + \sqrt{N_L^- N_R^+}} \right) \quad (1)$$

where S is the analyzing power of the spin detector, known as the Sherman Function. The value of S for our measurements was 0.04. SRXPS measurements using both (+) and (-) magnetizations (Eq.(1)) removes from the polarization data apparatus asymmetry effects unrelated to the spin of the electron beam [15]. Figure 1 displays

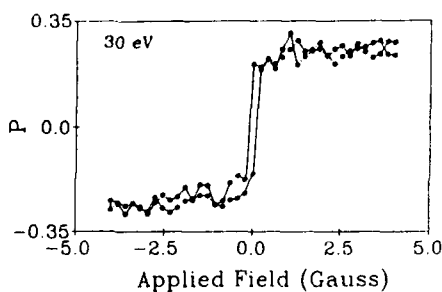


Fig. 1. A hysteresis curve for the Fe film generated by measuring the spin polarization of the x-ray-excited 30 eV Fe secondary electrons as a function of the magnetic field applied to the metallic glass substrate.

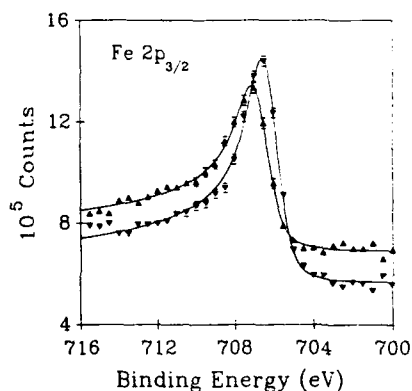


Fig. 2. Separate N_\uparrow and N_\downarrow SRXPS spectra for the Fe $2p_{3/2}$ majority-spin (\blacktriangle) and minority-spin (\blacktriangledown) photoelectrons, respectively. The lines through the data are the result of a simplex fit to each spin component using a single Doniach-Sunjić lineshape convoluted with a Gaussian of 1.6 eV FWHM.

a hysteresis curve acquired with x-ray excited spin-polarized 30 eV secondary electrons. The hysteresis loop is quite sharp, with a 30 eV spin polarization ($P = 0.27$) consistent with the known Fe magnetic moment of $2.2 \mu_B$. Count rates (summed over both detectors) for the $2p_{3/2}$, $2p_{1/2}$, and $2s$ levels were approximately 2700 s^{-1} , 2290 s^{-1} , and 1560 s^{-1} [16].

The polarization data can be separated into individual $N\uparrow$ and $N\downarrow$ SRXPS spectra for the majority-spin (\uparrow -spin) and minority-spin (\downarrow -spin) photoelectrons, respectively [17]. The $N\uparrow$ and $N\downarrow$ components for the Fe $2p_{3/2}$ level are shown in Fig. 2. The lines through the raw data are simplex fits to the individual $N\uparrow$ and $N\downarrow$ spectra using a single Doniach-Sunjić (DS) lineshape [18] convoluted with a 1.6 eV FWHM Gaussian representing the instrumental response.

The $N\uparrow$ and $N\downarrow$ Fe $2p_{3/2}$ spectra are both fitted very well with a single DS line. The $N\uparrow$ DS component has a binding energy of $706.69 \pm 0.03 \text{ eV}$ [19]; the $N\downarrow$ Fe $2p_{3/2}$ DS component has binding energy of $706.21 \pm 0.03 \text{ eV}$. Thus an apparent "exchange splitting" of $0.48 \pm 0.05 \text{ eV}$ is observed. Baumgarten and coworkers [9], using the photoemission MCD technique to probe the Fe $2p_{3/2}$ level, estimated a splitting of $0.5 \pm 0.2 \text{ eV}$, with the majority-spin component possessing the higher binding energy. The two measurements are therefore in excellent agreement for the Fe $2p_{3/2}$ level. The $N\uparrow$ and $N\downarrow$ SRXPS DS lineshapes have very similar values for the singularity index α : 0.46 ± 0.05 and 0.42 ± 0.05 , respectively. The $N\uparrow$ $2p_{3/2}$ component has a larger FWHM Lorentzian broadening ($0.56 \pm 0.04 \text{ eV}$) than the $N\downarrow$ component ($0.44 \pm 0.04 \text{ eV}$). The $N\uparrow/N\downarrow$ Fe $2p_{3/2}$ integrated intensity ratio is 0.77 ± 0.05 .

It should be noted that the DS lineshape, which has found considerable success in describing core-level XPS lineshapes in metals requires that the true binding energy of the photoelectron peak (i.e., the peak position in the absence of intrinsic Fermi sea excitations) differs from the spectral peak maximum when Lorentzian broadening and intrinsic Fermi sea excitations are present [18]. Since the singularity index, α , accounting for these low-energy electron-hole pair excitations is sizeable for the Fe core levels, and the core holes are naturally lifetime (Lorentzian) broadened, the reported DS binding energies appropriately lie to somewhat lower binding energy than the apparent peak maxima. The spectral peak maximum is not a reliable indicator of peak binding energy for these metallic XPS lineshapes [18].

Figure 3 presents $N\uparrow$ and $N\downarrow$ SRXPS spectra for the Fe $2p_{1/2}$ level. Neither the $N\uparrow$ $2p_{1/2}$ component nor the $N\downarrow$ $2p_{1/2}$ component can be reasonably fit with a single DS line. The $N\downarrow$ component seems to consist of a main peak accompanied by a broad shoulder on the high binding energy side. The spectral complexity of the $2p_{1/2}$ SRXPS spectra makes it difficult to view the Fe $2p_{1/2}$ level as simply an exchange-split doublet. The interpretation [9,10] of photoemission MCD measurements of the Fe $2p_{1/2}$ level suggests a $2p_{1/2}$ $N\uparrow$, $N\downarrow$ doublet split in energy by $0.3 \pm 0.2 \text{ eV}$. However, the SRXPS results for the $2p_{1/2}$ level suggest additional spectral complexity not resolvable in the photoemission MCD studies.

The Fe $2s$ SRXPS data are shown in Fig. 4. The Fe $2s$ level is a challenging SRXPS measurement because the $2s$ line is quite broad and lies on a large spectral background. The $2s$ $N\uparrow$ and $N\downarrow$ components are adequately fit by single DS lineshapes. The Fe $2s$ $N\uparrow$ peak is located at $843.0 \pm 0.1 \text{ eV}$ with a Lorentzian width of $7.4 \pm 0.3 \text{ eV}$ and a singularity index of $\alpha = 0.65 \pm 0.05$. The Fe $2s$ $N\downarrow$ component has a binding energy of $841.8 \pm 0.1 \text{ eV}$, with $\alpha = 0.56 \pm 0.05$ and a Lorentzian width of $5.8 \pm 0.3 \text{ eV}$. Thus a $2s$ "exchange splitting" of $1.2 \pm 0.2 \text{ eV}$ is observed. Although the $N\uparrow$ component has a larger singularity index and lifetime broadening than the $N\downarrow$ component, the two Fe $2s$ spin-resolved components have very similar lineshapes. This is in contrast to the Fe $3s$ level, which displays drastically different

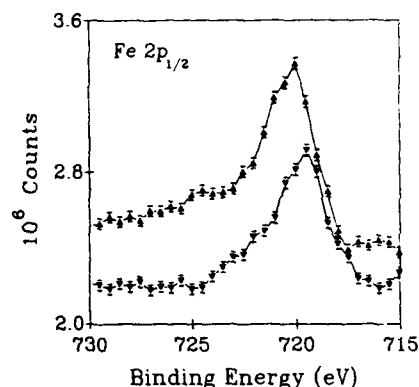


Fig. 3. Separate $N\uparrow$ and $N\downarrow$ SRXPS spectra for the Fe $2p_{1/2}$ majority-spin (Δ) and minority-spin (∇) photoelectrons, respectively. The graph lines connect the experimental data points.

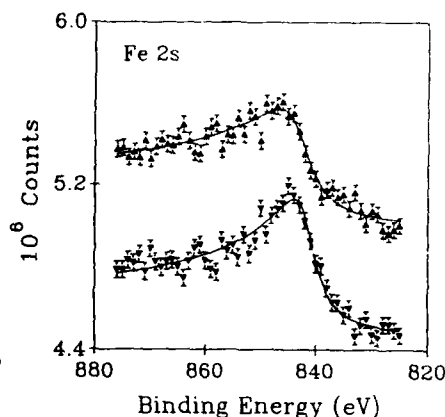


Fig. 4. $N\uparrow$ (Δ) and $N\downarrow$ (∇) spectra for the Fe 2s peak. The lines through the data are the result of a simplex fit to each spin component using a single Doniach-Sunjić lineshape convoluted with a Gaussian of 1.6 eV FWHM.

lineshapes for the $N\uparrow$ and $N\downarrow$ components [5]. It may be that a form of intra-shell electron correlation [20] is responsible for the unusual Fe 3s lineshapes. Electron correlation should affect the 2s level to a much smaller degree due to the increased radial separation of the 2s and 3d orbitals. The Fe 2s $N\uparrow/N\downarrow$ intensity ratio is 1.0 ± 0.1 .

Discussion

The SRXPS data for the $n = 2$ core levels are particularly revealing in regard to the nature of core-valence coupling in metallic Fe. Intra-atomic core-valence exchange is clearly important despite the small radial extent of the $n = 2$ levels. If one were to qualitatively describe the $2p_{3/2}$, $2p_{1/2}$ SRXPS data from a purely atomic viewpoint, one could start by considering a hypothetical $4s^2 3d^6$ Fe atom with two unpaired electrons in a 3H ground state (i.e., a $2\mu_B$ Fe atom). In a pair coupling (jK coupling) scheme [21], the 2p electron spin is coupled first to its own orbital angular momentum to form a resultant 2p total angular momentum j with quantum number $j = 3/2, 1/2$. The spin-orbit splitting into $2p_{3/2}$ and $2p_{1/2}$ states is the strongest interaction. The total 2p angular momentum j can then couple to the orbital angular momentum of the valence shell L to form a resultant total momentum K ($j + L = K$), which can in turn be coupled to the electron spin S in the valence shell to form a resultant total angular momentum J ($K + S = J$) with quantum number J . This atomic picture predicts a $2p_{3/2}$ manifold composed of 12 discrete states and a $2p_{1/2}$ manifold composed of 6 discrete states. Within each manifold the states would be separated in energy according to the J . Atomic calculations suggests that such separations would be sizeable, up to a few electron volts [22].

The level of complexity predicted by this purely atomic view is inconsistent with the relative spectral simplicity of the SRXPS data. For example, the finding that the Fe

$2p_{3/2}$ $N\uparrow$ and $N\downarrow$ components are both reasonably fit by single-component DS lineshapes strongly suggest that an atomic complexity does not exist in the data, even when one takes into consideration the nonzero energy resolution of the SRXPS measurement. The jK coupling estimate above is also a lower limit of atomic complexity, because only a single final-state valence configuration has been assumed. The 2s and 3s [5] $N\uparrow/N\downarrow$ intensity ratios found experimentally are inconsistent with an atomic view that would suggest a ratio of $S/(S+1)$ [23]. Thus, we do not believe the SRXPS data for metallic Fe can be successfully interpreted by atomic theories that consider the 3d valence shell to be purely atomic-like, or by solid-state theories [11] that consider valence spin polarization to be localized rather than itinerant.

Kakehashi and coworkers [23] have developed a theory that attempts to describe core-level photoemission while interpolating between the purely atomic and purely delocalized valence limits. They predict that photoemission of an \uparrow -spin core electron produces a singlet final state; photoemission of a \downarrow -spin core electron produces a triplet final state. The energy splitting between the singlet and triplet final states is theoretically proportional to the valence magnetization. The intensity ratio between the two components is thought to depend on the degree of valence-band delocalization. These theoretical predictions are in qualitative accord with the SRXPS data. The experimentally observed $N\uparrow/N\downarrow$ intensity ratios suggest a rather delocalized 3d valence-band limit. The assumptions inherent in the theory preclude a quantitative comparison to experiment.

These results suggest that SRXPS studies of the deep core levels will provide a wealth of information regarding surface, interface and thin-film magnetism. SRXPS measurements of the $2p_{3/2}$ level of the 3d transition metals should be particularly useful. Such measurements are highly element-specific due to the large energy differences between $2p_{3/2}$ binding energies in the 3d transition series. The $2p_{3/2}$ peaks are the most intense in the XPS spectrum, and the kinetic energies of the $2p_{3/2}$ photoelectrons endow them with a good level of surface sensitivity. Further experimental and theoretical work is required to reveal the extent to which quantitative information regarding the atomic magnetic moment can be extracted from the $2p_{3/2}$ SRXPS spectra. However, the facts that the spin-orbit interaction is large (and easily identified) for the 2p spectra, that the $N\uparrow$ and $N\downarrow$ $2p_{3/2}$ components have a large exchange splitting, and that the $N\uparrow$ and $N\downarrow$ lineshapes are single components all suggest that a quantitative interpretation will be possible.

In summary, the first SRXPS study of the deep core levels in Fe is presented. The results clarify the nature of the core-level initial states often involved in MCD spectroscopies. The relative simplicity of the SRXPS spectra indicates that a purely atomic picture is incapable of describing the SRXPS data, and that theories incorporating the delocalization of the 3d valence band are more applicable.

Acknowledgements

The authors thank Prof. Michael Scheinfein for his generosity and enthusiasm during our valuable discussions of electron spin detector design. Thanks are also extended to Prof. David Shirley and Dr. John Unguris for helpful discussions. This paper is based upon work supported by the National Science Foundation under Grant No. CHE-9117138. Acknowledgement is made to the donors of the Petroleum Research Fund, administered by the American Chemical Society, for partial support of the research. Financial support also came from the Camille and Henry Dreyfus Foundation, The

Charles A. Dana Foundation and Lehigh University. R.J.P. acknowledges support from a USDE fellowship.

References

* Author to whom correspondence should be addressed.

1. W. Clemens, E. Vescovo, T. Kachel, C. Carbone and W. Eberhardt, Phys. Rev. B **46**, 4198 (1992).
2. K.-P. Kamper, W. Schmitt, and G. Guntherodt, Phys. Rev. B **42**, 10696 (1990).
3. P.D. Johnson, A. Clarke, N.B. Brookes, S.L. Hulbert, B. Sinkovic and N.V. Smith, Phys. Rev. Lett. **61**, 2257 (1988).
4. E. Kisker, K. Schröder, W. Gudat and M. Campagna Phys. Rev. B **31**, 329 (1985).
5. F.U. Hillebrecht, R. Jungblut and E. Kisker, Phys. Rev. Lett., **65**, 2450 (1990).
6. B. Sinkovic, P.D. Johnson, N.B. Brookes A. Clarke and N.V. Smith Phys. Rev. Lett. **65**, 1647 (1990).
7. C. Carbone, T. Kachel, R. Rochow and W. Gudat Sol. St. Commun. **77**, 619 (1991).
8. C. Carbone, and E. Kisker, Sol. St. Commun. **65**, 1107 (1988).
9. L. Baumgarten, C.M. Schneider, H. Petersen, F. Schäfers and J. Kirschner, Phys. Rev. Lett. **65**, 492 (1990).
10. H. Ebert, L. Baumgarten, C.M. Schneider and J. Kirschner Phys. Rev. B **44**, 4406 (1991).
11. B.T. Thole and G. Van der Laan, Phys. Rev. B **44**, 12424 (1991).
12. Allied Signal MetGlas Alloy # 2714A.
13. XPS analysis indicated an O/Fe stoichiometric ratio of 0.09. Assuming oxygen contamination exists as Fe_2O_3 [8], 6% of the Fe atoms exist as Fe^{3+} . This oxidation produces very small peaks chemically shifted by 4.5 eV to higher binding energy in the $\text{N}\uparrow$ Fe $2p_{3/2}$, Fe $2p_{1/2}$ spectra.
14. M.R. Scheinfein, D.T. Pierce, J. Unguris, J.J. McClelland, R.J. Celotta, and M.H. Kelly, Rev. Sci. Inst. **60**, 1 (1989).
15. J. Kessler, in Polarized Electron (Springer Verlag, Berlin, 1985), p. 234.
16. Count rates reflect the total photoelectric signal (peak + background).
17. The $\text{N}\uparrow$ and $\text{N}\downarrow$ spectra are calculated from the polarization P by the relations: $\text{N}\uparrow = 2N_{\text{TOT}}(1+P)$; $\text{N}\downarrow = 2N_{\text{TOT}}(1-P)$, where $N_{\text{TOT}} = (N_L^+ + N_L^- + N_R^+ + N_R^-)/4$. Statistical error bars ($\pm \delta\text{N}\uparrow\downarrow$) shown in the figures are calculated via the expression $\delta\text{N}\uparrow\downarrow = \text{N}\uparrow\downarrow(1/S\sqrt{4N_{\text{TOT}}})$.
18. S. Doniach and M. Sunjic, J. Phys. C: Sol. St. Phys. **3**, 285 (1970).
19. The error indicates binding energy precision, not accuracy.
20. P.S. Bagus, A.J. Freeman and F. Sasaki, Phys. Rev. Lett. **30**, 850 (1973).
21. R.D. Cowan in The Theory of Atomic Structure and Spectra (U. of California, Berkeley, 1981), p. 130.
22. R.P. Gupta and S.K. Sen, Phys. Rev. B **10**, 71 (1974).
23. Y. Kakehashi, Phys. Rev. B. **32**, 1607 (1985), and references therein.

SPIN-POLARIZATION IN ULTRATHIN Rh LAYERS ON Fe(001)

A. CHOUAIRI*, H. DREYSSE *, H. NAIT-LAZIZ** AND C. DEMANGEAT**

*Laboratoire de Physique de Solide, BP 239, 54506 Vandœuvre-les-Nancy, France.

**IPCMCS, Université Louis Pasteur, 4 rue Blaise Pascal, 67070 Strasbourg, France.

ABSTRACT

The origin of the Rh polarization at the interface with Fe is discussed within a self-consistent mean-field parameterized tight-binding model. Since experimentally it is not yet known how Rh grows on Fe(001), in this paper we consider both fcc and bcc growth. When Rh grows in the fcc structure, it expands its lattice parameter and a polarization is present up to 3 layers, whereas in the bcc case only the Rh atoms at the interface are polarized. The results obtained are compared to recent spin- and angle-resolved photoelectron spectroscopy experiments. Good agreement with experiment is obtained in the case of a fcc Rh configuration.

INTRODUCTION

Kachel et al. [1] have recently shown through spin-resolved valence-band and core level spectroscopy that very thin films of Rh coated on Fe(001) are ferromagnetically ordered at room temperature. Through ab-initio calculations using the full-potential linear augmented-plane wave (FLAPW) method [1] they found that a perfect Rh monolayer is polarized ferromagnetically with Fe with a magnetic moment of $0.82 \mu_B$. Nothing is said however, in this calculation, about the spin-polarization of a small number of Rh layers grown on Fe. Therefore it is difficult to say 'a-priori', as suggested in the paper by Kachel et al. [1], that the Rh overlayers are ferromagnetically ordered at room temperature. In fact, as discussed recently by different authors, Rh may present some antiferromagnetic (AF) polarization near the (001) surface [2], in thick Rh films (3 to 6 layers) [3] or as Rh clusters adsorbed on Ag(001) [4]. The origin of this AF-like coupling is unclear. Heine and Samson [5] have discussed the type of magnetism which may appear in the transition-metal series and proved that AF coupling is favored in the middle of the series whereas ferromagnetic (F) coupling can be present at the beginning and the end. However only 3D systems were studied in their work. For thin films, the geometry of the problem has a great influence on the spin-polarization.

There are in fact two possible reasons for the onset of magnetism in Rh films coated on Fe(001). The first reason is a purely d-d hybridization where the d-band splitting of Fe induces a polarization in the d-bands of Rh. This is usually a short-range effect and has been observed in the case of $\text{Pd}_n/\text{Fe}(001)$ [6]: the Pd atoms in the film are found to be polarized in contrast with Pd atoms and Pd bulk crystals where no magnetic moments are present. The second reason is related to the so-called coordination effect which relates the magnetic moment of a given atom to the number of its nearest-neighbor (n.n.) atoms: the lower the number of n.n. atoms, the higher the magnetic moment. For example, a perfect monolayer of Rh on Ag(001) has been found to be ferromagnetically coupled in all calculations [7-10]. For sake of simplicity this contribution will be called henceforth "intrinsic" magnetism. Indeed, because bulk Rh is non-magnetic, there must exist a transition between the ferromagnetic monolayer and the bulk paramagnet. In this paper we will show that there is no smooth decrease of the magnetic moment versus the thickness of the slab but an oscillatory behavior of the polarization. We propose a method which can discriminate between the d-d interface hybridization and the thickness effect. To determine the polarized Local Density of States (LDOS), we use a self-consistent tight-binding derivation of the Hubbard Hamiltonian in the unrestricted Hartree-Fock approximation. In this work we study the magnetic moment versus the exchange integral of Rh, allowing us to discuss clearly the physical origins of the Rh polarization. For a precise discussion on the value of the magnetic moment of Rh thin films, a value of 0.50 eV is taken for the Rh exchange integral. This value is deduced from a LMTO derivation [11] taking into account that a calculation using the Local Density Approximation, as in ref [11], overestimates the final value by 20% [12].

The differences between the free-standing Rh_3 film and the 3 layer slabs of Rh on Fe(001) are the following : i) the "intrinsic" magnetism appears for smaller values of J_{Rh} in the case of the interface with Fe; ii) the paramagnetic (P) - F transition is first-order for the free-standing film whereas it is second order in $\text{Rh}_3/\text{Fe}(001)$: this is due to the d-d hybridization; iii) for large values of J_{Rh} , there is a faster saturation of the magnetic moment in the case of Rh_3 films because the coordination number is lower compared to the $\text{Rh}_3/\text{Fe}(001)$ case.

In Table 1 we report the results (for $J_{\text{Rh}} = 0.50$ eV) concerning the magnetization of $n = 1$ to 6 layers of Rh in the fcc phase on Fe(001). Our results (for the fcc phase) are in agreement with the FLAPW results and the experimental results for the Rh monolayer on Fe(001) : the Rh atoms bear a magnetic moment of $0.90 \mu_B$ which is ferromagnetically coupled to its Fe neighbors. The polarization of the fcc-like $\text{Rh}_n/\text{Fe}(001)$ decreases strongly for $n > 3$ as shown experimentally; a noticeable polarization remains only near the interface with Fe and near the free surface of Rh. However, contrary to the claim of Kachel et al.[1], the polarization of the Rh layers over Fe(001) does not seem to present a ferromagnetic polarization but an oscillatory one.

	Fe_{I-1}	Fe_I	Rh_I	Rh_{I+1}	Rh_{I+2}	Rh_{I+3}	Rh_{I+4}	Rh_{I+5}
$\text{Rh}_1/\text{Fe}(001)$	2.08	2.10	0.90					
$\text{Rh}_2/\text{Fe}(001)$	2.22	2.03	0.12	-0.80				
$\text{Rh}_3/\text{Fe}(001)$	2.18	2.08	0.36	-0.94	-1.04			
$\text{Rh}_4/\text{Fe}(001)$	2.20	2.03	0.30	-0.38	0.05	0.43		
$\text{Rh}_5/\text{Fe}(001)$	2.20	2.05	0.33	-0.45	-0.21	0.48	0.81	
$\text{Rh}_6/\text{Fe}(001)$	2.19	2.05	0.37	0.31	-0.12	0.08	0.27	0.41

Table 1 : Magnetic moment distribution for fcc-like Rh_n ($n = 1, 2, \dots, 6$) layers adsorbed on Fe(001) for $J_{\text{Rh}} = 0.50$ eV. Index I stands for atoms at the Rh/Fe interface.

In Table 2, we report the magnetic moment distribution for the bcc phase. We restrict ourselves to $n = 1$ to 3 because the decrease of the magnetic moments versus the thickness of the slab is much more rapid than for the fcc-like Rh film. Clearly the bcc-like Rh on Fe(001) does not present any long range magnetic order. The main difference between fcc-like and bcc-like film is the distance between nearest-neighbors Rh atoms : for bcc-like, this distance is too small to have an onset of "intrinsic" magnetism.

	Fe_{I-1}	Fe_I	Rh_I	Rh_{I+1}	Rh_{I+2}
$\text{Rh}_1/\text{Fe}(001)$	2.32	1.68	0.37		
$\text{Rh}_2/\text{Fe}(001)$	2.47	2.25	0.23	-0.13	
$\text{Rh}_3/\text{Fe}(001)$	2.31	2.25	0.35	0.00	0.06

Table 2 : Magnetic moment distribution for bcc-like Rh_n ($n = 1, 2$, and 3) layers adsorbed on Fe(001) for $J_{\text{Rh}} = 0.50$ eV. Index I stands for atoms at the Rh/Fe interface.

RESULTS

Experimentally, it is not yet possible to discriminate between fcc and bcc growth of Rh on Fe(001) [1]. Therefore we will present results for both geometries. Fcc and bcc epitaxial growth of Rh on Fe(001) are considered. The distance between the Rh monolayer in the fcc phase and the Fe(001) substrate is higher than in the bcc growth. The distances are given by: $d^{\text{fcc}} = (a_{\text{Fe}} + a_{\text{Rh}}(\text{fcc}))/2$ and $d^{\text{bcc}} = (a_{\text{Fe}} + a_{\text{Rh}}(\text{bcc}))/2$, where the a 's are given by $a_{\text{Rh}}(\text{fcc}) = \sqrt{2} a_{\text{Fe}}$ and $a_{\text{Rh}}(\text{bcc}) = a_{\text{Fe}}$. As in [13], we restrict this calculation to local neutrality for the determination of the magnetic moments versus the exchange integral J_{Rh} , the exchange integral J_{Fe} being adjusted in order to recover the Fe bulk magnetic moment. In the case of the fcc monolayer of Rh on Fe(001), a magnetic moment of $0.90 \mu_B$ is obtained for $J_{\text{Rh}} = 0.50$ eV, in agreement with the FLAPW calculation of the perfect Rh monolayer on Fe(001) [1].

In Figures 1 we report the results obtained for 3 layers of Rh on Fe(001). Fig. 1a displays the polarization for Rh in an fcc configuration whereas Fig. 1b concerns Rh in a bcc configuration. The difference is obvious: for $J_{\text{Rh}} > 0.40$ eV the three layers of Rh are polarized for the fcc phase whereas in the bcc configuration only the interface Rh layer remains polarized. These results can be easily explained because the Rh-Rh distance is much smaller in the bcc phase [14]. At first sight the polarization of the Rh layers is very striking because there appears an AF-like coupling between the interface Rh layer and the subsurface Rh layer. However, these results are in line with previous calculations [2-4].

In the fcc phase, the two contributions to the magnetism i.e. the d-d hybridization and the thickness of the film can be easily separated if we consider the result concerning the polarization of a 3 layer Rh slab (Figure 2) with the same lattice parameter as the Rh films on Fe(001). The d-d hybridization can be assumed to give a slowly increasing nearly linear contribution. For $\text{Rh}_3/\text{Fe}(001)$, the thickness effect or the "intrinsic" magnetism appears for a value of J_{Rh} equal to 0.40 eV. Magnetization in Rh_3 free-standing film appears only for a value of J_{Rh} roughly equal to 0.55 eV.

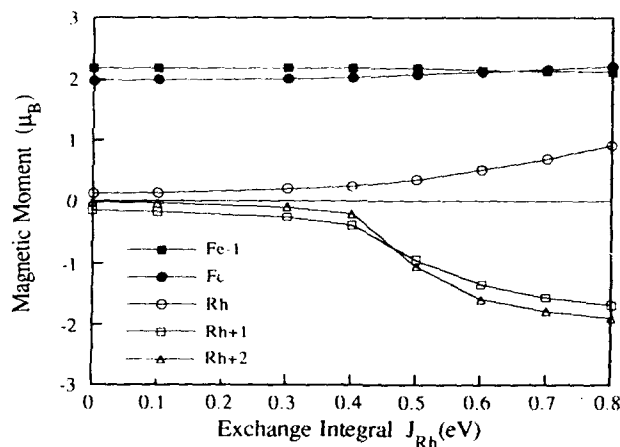


Figure 1a: Magnetic moment per atom (μ_B) for 3 layers of fcc-like Rh adsorbed on Fe(001) versus the exchange integral of Rh.

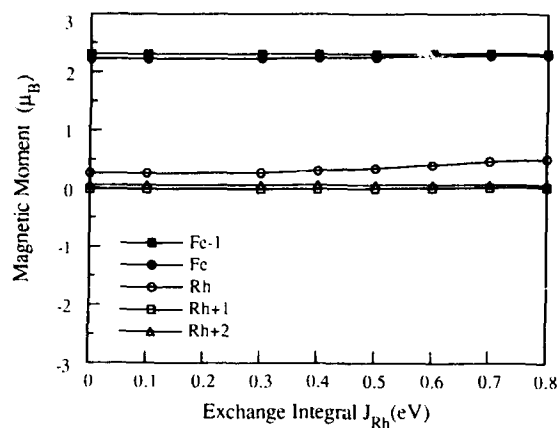


Figure 1b: Magnetic moment per atom (μ_B) for 3 layers bcc-like Rh adsorbed on Fe(001) versus the exchange integral of Rh.

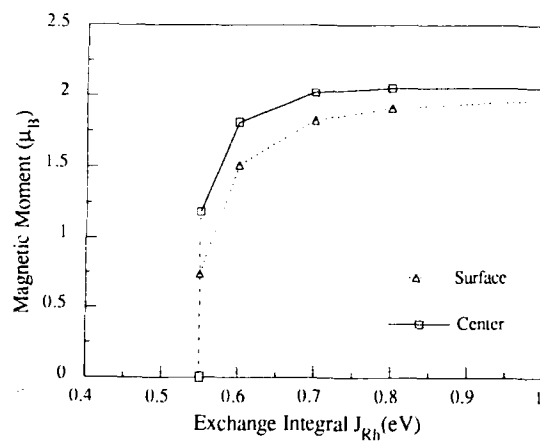


Figure 2: Magnetic moment per atom (μ_B) for the surface and the central layers of 3-layer slabs of fcc-Rh(001) with the epitaxial parameter $\sqrt{2} a_{Fe}$, versus of the exchange integral of Rh.

Let us consider the fcc-Rh/Fe system. Clearly our results indicate that the d-d hybridization at the interface is short ranged: mainly the Rh atoms near the interface, over 3 planes, are affected. Moreover the value of this magnetic moment at the interface is lower than the magnetic moment at the free surface for $n \leq 5$. Thus the final magnetic moment distribution of the Rh film can be related to some boundary conditions (possibly giving a polarization) and a central part which tends to have no magnetic moment. These boundary conditions are not symmetric: a clear trend exists to give a magnetic moment = $0.35 \mu_B$ at the fcc-Rh/Fe interface independently of the Rh thickness, whereas for $J = 0.50$ eV, the (001) Rh surface will not display a magnetic order. Thus the boundary condition for the free surface is a function of the thickness.

CONCLUSION

In this short communication we have obtained results for the Rh_n/Fe(001) systems that are consistent with both FLAPW (for the Rh monolayer on Fe(001)) and with experimental results when we consider the epitaxial growth of fcc Rh on Fe(001). A new effect is observed: *n* Rh overlayers on Fe(001) are not ferromagnetically ordered but present an oscillatory polarization which is short ranged. There remains however some long-range polarization for $n > 3$ but the magnetic moments are much lower than for $n < 4$. Let us recall that our calculation has been performed at $T = 0$ K. Nevertheless, some unresolved problems remain because the LEED results of Kachel et al. [1] revealed layer by layer but non-epitaxial overlayer growth. Another difficulty is the fact that we have considered fcc and bcc epitaxial growth which increases (fcc) or decreases (bcc) the atomic volume of Rh. Therefore, it appears to be of interest to extend this calculation to fct and bct configurations in order to keep a constant atomic volume in the growth process of Rh. The polarization of such configurations is presently under investigation.

References

1. T. Kachel, W. Gudat, C. Carbone, E. Vescovo, S. Blügel, U. Altkemper and W. Eberhardt, Phys. Rev. B46, 12888 (1992).
2. A. Mokrani and H. Dreyssé, submitted to J. Magn. Magn. Mat.
3. A. Chouairi, Ph.D. Thesis, University of Nancy (1993), unpublished.
4. W. Hergert, P. Rennert, S. Bouarab, C. Demangeat and H. Dreyssé, Communication at MML' 93 to appear in J. Magn. Magn. Mat.
5. V. Heine and J. H. Samson, J. Phys. F13, 2155 (1983).
6. Z. Celinski and B. Heinrich, J. Magn. Magn. Mat. 99, L25 (1991).
7. O. Eriksson, R. C. Albers and A. M. Boring, Phys. Rev. Lett. 66, 1351 (1991).
8. S. Blügel, Europhys. Lett. 18, 257 (1992).
9. R. Wu and A. J. Freeman, Phys. Rev. B45, 7222 (1992).
10. A. Mokrani, H. Dreyssé, S. Bouarab and C. Demangeat, J. Magn. Magn. Mat. 113, 201 (1992).
11. N. E. Christensen, O. Gunnarsson, O. Jepsen and O. K. Andersen, J. Physique (Paris) 12 C8, 17 (1988).
12. G. Stollhoff, A. M. Oles and V. Heine, Phys. Rev. B41, 7028 (1990).
13. H. Nait-Laziz, S. Bouarab, C. Demangeat, A. Mokrani and H. Dreyssé, J. Magn. Magn. Mat. 118, 365 (1993).
14. V. L. Moruzzi and P. M. Marcus, Phys. Rev. B39, 471 (1989).
D. Stoeffler and H. Dreyssé, Solid State Com 79, 645 (1991).

MAGNETIC ORDER OF Fe AND Co ON Cu(001)

A. HAROUN*, A. CHOUAIRI*, S. OUANNASSER*, P.J. JENSEN**,
K.H. BENNEMANN**, AND H. DREYSSE*

*Laboratoire de Physique du Solide. BP 239, F-54506 Vandoeuvre-les Nancy, France.

** Institut für Theoretische Physik, Freie Universität Berlin. Arnimallee 14, D-1000 Berlin 33, Germany.

ABSTRACT

We determine the initial growth mode of Co and Fe on Cu(001). In the monolayer range Co and Fe present a clear trend to form clusters on Cu (001). Supposing a perfect epitaxy and fcc lattice, the magnetic moment distribution is determined by using a tight binding Hubbard-like Hamiltonian. The influence of the temperature is taken into account in order to compare the theoretical predictions with experimental results.

INTRODUCTION

The skill of elaboration process and the development of experimental techniques have revealed the complexity of epitaxially grown transition metal systems. In this work we concentrate on the magnetic properties of very thin Co and Fe films on a Cu(001) substrate. These systems show controversial experimental results. At room temperature for a Co monolayer on Cu(001), Pescia et al.[1] found a long range ferromagnetic order, while Schneider et al.[2] have shown that the Curie temperature is below 50K. For Iron conflicting results have been reported [3]. The key quantity is the preparation temperature: for low preparation temperature, five monolayers of fcc-Fe(001) show a large magnetic moment, while after annealing at temperatures above 500K a transition to state with a low moment is observed [4].

Concerning the growth mode of Co on Cu(001) substrate, A.Schmid[5] showed by using STM that roughly 30% of the Cu surface is still not covered by the first layer of Co when 10% of the second layer is already present on top of the first layer islands, in agreement with the results of Li and Tonner [6]. For the Fe/Cu system, the situation is confusing. Layer by layer growth mode has been found [7,8], whereas Chambers et al. [9] observed that at room temperature the first monolayer of Fe does not adsorb uniformly, but forms two-layer thick clusters. At 300K Thomassen et al. [10] have observed a layer by layer growth mode for thickness above 5 ML, but below this thickness the film is characterized by iron agglomeration.

In this short paper we intend to study the growth mode of Fe, Co, and Ni on Cu(001), and to discuss the influence of the temperature on the magnetic behavior of these systems. A more complete discussion of the magnetic properties of Co and Fe layers on Cu(001) is in progress and will be reported elsewhere.

INITIAL GROWTH MODE OF Co AND Fe ON Cu(001).

The initial growth mode of Co and Fe on Cu(001) can be estimated with a simple approach. Consider in the monolayer range, on top of the Cu(001) semi-infinite crystal, a binary alloy (adsorbed atoms and vacancies) on a square lattice. Similarly to the bulk alloy phase stability studies [11] this alloy problem can be transformed to a two-dimensional "Ising-like" problem. Hence, each lattice site p is associated with a pseudo-spin variable σ taking the values $+1$ (if an adsorbate occupies the site p), -1 (if the site p is not occupied). Any configuration on the lattice can be specified by a N -dimensional vector $=\{\sigma_1, \sigma_2, \dots, \sigma_N\}$. Thus any function of configuration $f(\sigma)$ can be expanded in terms of an orthonormal

set of cluster functions. In particular, the internal energy can be expanded in terms of Effective Cluster Interactions (ECI's):

$$E = V_0 + \sum_{\alpha} \xi_{\alpha} V_{\alpha}$$

where V_{α} are the ECI's for a given cluster α with n_{α} sites, V_0 is the empty cluster, and ξ_{α} are the correlation functions, given by the ensemble average:

$$\xi_{\alpha} = \langle \sigma_1 \cdot \sigma_2 \dots \sigma_{n_{\alpha}} \rangle$$

This model has been used successfully to determine the phase stability in the substitutional alloys [11,12], and more recently to calculate the surface segregation phenomena [13,14]. It has been shown that few ECI's are necessary to get satisfactory convergence: pairs and triples are generally sufficient.

In general, there are two different averaging schemes to determine the ECI's. In the canonical model the ECI's depend explicitly on the concentration of the adsorbed atoms, while for the grand-canonical averaging they do not depend on it. In our calculations, we have considered only the later scheme which correspond to a concentration $c = 50\%$ of the adsorbate atoms. In this paper, the ECI's are calculated by the method of direct configurational averaging (DCA) [15], within the framework of Linearized-Muffin-Tin-Orbital (LMTO) Hamiltonian cast into tight-binding form. Some of the advantages of the DCA method are that it avoids the CPA (Coherent Potential Approximation), permits a calculation in the real space (using the recursion method), and allows to take into account s, p and d orbitals on the same footing. Knowledge the values of ECI's allows to search for the minimum of the energy with respect to variation in the Ising-model configurations. These ECI's have been determined from the electronic structure by averaging over 20 randomly selected configurations, and using 10 levels in the continued fraction.

In the present work we have computed Effective-Pair-Interactions (EPI's) and Effective-Triplet-Interactions (ETI's), supposing a paramagnetic state for Fe, Co and Ni. Ni has also been considered in order to check the existence of a general trend. For all these cases the trends are very clear: table 1 shows that the nearest-neighbor (n.n) EPI is strongly attractive. Thus all these metals will form clusters on Cu(001). Furthermore by checking the ETI's, the linear one is found to be repulsive: the Fe, Co and Ni atoms will form compact clusters, as observed experimentally [5,10].

Metal	V_1	V_2	O_1	O_2	L
Fe	-0.5572	-0.0040	0.0023	-0.0016	0.0394
Co	-0.4816	-0.0052	0.0003	-0.0004	0.0253
Ni	-0.3961	-0.0054	0.0005	0.0001	0.0066

Table 1 : Effective Cluster Interactions for 2D Co, Fe and Ni submonolayer film on Cu(001). V_1 and V_2 are the nearest neighbors (n.n) and next-nearest-neighbor (n.n.n) Effective Pair Interactions, O_1 and O_2 are the Effective Cluster Interactions corresponding to a triangle with two nn and two nnn bounds, L corresponds to linear ETI's.

MAGNETIC ORDER

First the ground state ($T = 0\text{K}$) for Co and Fe on Cu(001) is determined. We suppose a perfect epitaxy of Co and Fe on Cu(001) and a perfect fcc lattice for Co and Fe, neglecting any relaxation or reconstruction [16]. We use a self-consistent tight-binding Hubbard-type Hamiltonian in the unrestricted Hartree-Fock approximation including s , p and d electrons. The calculations are performed in real space by means of the recursion method. Since the Co bulk magnetic moment is known, the value of the exchange integral J_{Co} can be deduced, whereas for the fcc Fe the situation is more delicate. The bulk magnetic moment versus J_{Fe} (or equivalently the lattice parameter) presents a first order transition. In this work we have taken $J_{\text{Fe}} = 1.10\text{ eV}$, and we found an A.F bulk ground-state for fcc Fe with a magnetic moment of $1.89\mu_{\text{B}}$, in agreement with the calculation of Freeman et al.[17]. This value of J_{Fe} can be considered as an upper limit, but a systematical study has shown [18] that the general trends for thin Fe films are rather insensitive to the value of J_{Fe} . Similar behavior is also observed for $J = 1.00\text{ eV}$, but for this value the bulk fcc-Fe ground state is paramagnetic.

For a perfect monolayer of Co on Cu(001) we obtain $1.80\mu_{\text{B}}$, whereas on a 6×6 square cluster, the inequivalent magnetic moments are found to increase slightly when the coordination number decreases as shown in figure 1. For 2 ML Co on Cu (001), the surface (interface) magnetic moment is $1.80\mu_{\text{B}}$ ($1.62\mu_{\text{B}}$). For thicker film, the values of magnetic moment tend fastly to the bulk values, with the exception of the surface magnetic moment which is around $1.75\mu_{\text{B}}$.

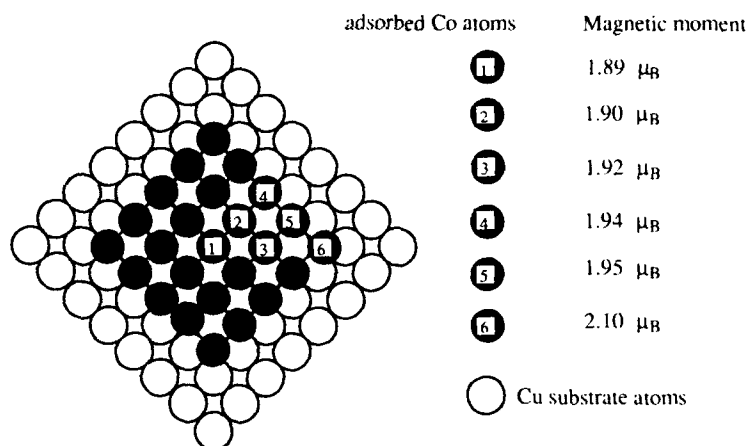


Figure 1 : Magnetic moment distribution for the non equivalent atoms in the 6×6 Co cluster on Cu(001) substrate.

The ground state of the Fe monolayer on Cu(001) is clearly ferromagnetic, with a large magnetic moment $3.00\mu_B$. For the 2ML Fe/Cu(001) we found two solutions, the ferromagnetic solution has the surface and interface magnetic moment, respectively, $2.62\mu_B$ and $2.93\mu_B$, and the antiferromagnetic one has a magnetic moment $2.40\mu_B$ and $-2.84\mu_B$ for interface and surface respectively. These values are in accordance with the ab-initio calculation carried out by C. L. Fu and J. Freeman [17]. We can note that the surface magnetic moment of one monolayer and two layers with the ferromagnetic interplane coupling is the same in the both cases. For thicker film, we obtain multiple solutions for the local magnetic moment (table 2). Let us note the comparable magnetization on the surface layer for the different solutions and for different thickness, and the large values of the other magnetic moments are obtained when only ferromagnetic coupling is present. An antiferromagnetic coupling induces a decrease of local magnetic moments. These trends seem to be quite general. However, a full calculation is needed to obtain quantitative results. Finally we should like to mention that for a two- and three- layer film of fcc-Fe on Cu (001) we obtain all possible combinations of different couplings between planes parallel to the (001) direction. For a four- layer Fe film on Cu (001), two possibilities of coupling do not exist. In a general manner for n- layer Fe film, 2^{n-1} solutions exist a priori.

System	$\mu(S) (\mu_B)$	$\mu(S-1) (\mu_B)$	$\mu(S-2) (\mu_B)$	$\mu(S-3) (\mu_B)$	$T_c/T_c(\text{bulk})$
Fe ₁ /Cu(001)	3.00				0.46
Fe ₂ /Cu(001)	2.93	2.62			1.35
	-2.84	2.40			1.20
Fe ₃ /Cu(001)	2.88	-1.60	2.50		1.03
	-2.84	2.10	2.60		1.28
	-2.95	-2.22	2.46		1.35
	2.94	2.44	2.61		1.49
Fe ₄ /Cu(001)	2.94	2.39	2.38	2.59	1.50
	-2.94	-2.22	2.13	2.58	1.35
	-2.89	1.68	-1.85	2.49	1.04
	-2.92	-2.36	-2.06	2.46	1.38
	2.94	2.22	-1.86	2.47	1.28
	2.86	-1.73	2.17	2.58	1.16

Table 2 : Magnetic moment per atom in unit of Bohr magneton of fcc Fe_n/Cu(001) film; 2^{n-1} solutions are obtained. It is also reported the ordering temperature (T_c) in units of the bulk critical temperature. (S) denotes the free surface, whereas the index (S-n+1) denotes the Fe plane at the Cu interface.

In a recent study, the temperature effects has been described in a mean-field approach by considering Ising- or Heisenberg-type spins and thermal fluctuations [19]. A perfect layer-by-layer growth mode is found to exhibit a ferromagnetic order for a coverage of one ML. By considering non perfect layer-by-layer growth as observed experimentally, the onset of a long-range ferromagnetic order is obtained for Co at coverage larger than one monolayer in agreement with ref[2]. Stampanoni et al.[20] have reported the thickness dependence of the Curie temperature for fcc Fe film on Cu (001). A maximum for T_C is found in the range of 2-3 ML (500 K), then T_C decreases to 300K till 15 ML, when the transition to bcc phase occurs. According to our calculation reported in table 2, this behavior corresponds to the ferromagnetic solution.

In the monolayer range, another problem arises. For finite systems like magnetic islands a sharp transition from an ordered to a disordered state no longer exists. In this case an internal ordering temperature T_C^{int} can be defined giving a rough estimate whether the finite system is ordered or not. This case leads to an ensemble of superparamagnetic particles. By increasing the magnetic atoms coverage, the whole film becomes coherently ordered. Generally in this case a sharp phase transition at an extended ordering temperature T_C^{ext} exists. For almost complete layer these two temperatures should merge, otherwise T_C^{ext} is lower than T_C^{int} .

The determination of the magnetic moment distribution is not easy. The ordering temperature corresponding to the onset of a long-range magnetic order is the relevant quantity which allows to compare experimental results and theoretical predictions.

A way to test this approach is to determine T_C at given thickness for a different preparation temperature. As shown before for increasing preparation temperature in the monolayer range, Co forms more compact clusters. Then the experimental ordering temperature decreases, corresponding to a decrease of T_C^{ext} . This behavior has clearly observed by M. T. Kief et al.[21].

In conclusion, in this short communication, we have determined the initial growth mode of Co, Fe and Ni on Cu (001). In agreement with experimental results, these atoms tend to form clusters. The influence of the temperature has been taken into account. The determination of the ordering temperature allows a comparison with experimental results. The importance of the preparation temperature have been also emphasized. For Co on Cu(001) a clear description can be proposed. However, for Fe/Cu(001), the situation is much more complex. A complete study should include relaxation and reconstructions.

ACKNOWLEDGEMENTS

We like to thank Prof. D. de Fontaine, Drs C. Scheinder, M. Kief and C. Wolverton for fruitful discussions. This project was partially supported by the french-german cooperation grant PROCOPE.

REFERENCES

1. D. Pescia, M. Stampanoni, G.L. Bona, A. Vertalaus, R. F. Willis and F. Meier, Phys. Rev. Lett. 58, 2126 (1987)
2. C. M. Schneider, P. Bressler, P. Schuster, J. Kirschner, J. J. de Miguel and R. Miranda, Phys. Rev. Lett. 64, 1059 (1990)
3. J.F. Himpsel, Phys. Rev. Lett. 67, 2363 (1991)
4. W. Keune, E. D. Ellerbrock, S. Dunkhorst, A. Fuest, A. Schatz and R. A. Brand, MML'93 (Kyoto, march 1993), to appear in J. M. M. M.
5. A. Schmid, PhD Dissertation (Freie Universitat Berlin, 1991)
6. Hong. Li and B. P. Tonner, Surf. Science 237, 141 (1990)

7. U.Gradmann and P. Tillmann, *Phys. Stat. Sol (a)* 44, 539 (1977)
8. A. Clarke, P.J. Rous, M. Amott, G. Jennings, R.F Willis, *Surf. Sci.* 192, 843 (1977)
9. S. A. Chambers, T.J. Wagener and J. H Weaver, *Phys. Rev. B* 36, 8992 (1987)
10. J. Thomassen, B. Feldmann and M.Wuttig, *Surf. Sci.* 264, 406 (1992)
11. M. Asta, C. Wolverton, D. de Fontaine and H.Dreyssé, *Phys. Rev. B* 44, 4907 (1991)
12. C. Wolverton, M. Asta, H. Dreyssé and D. de Fontaine, *Phys. Rev. B* 44, 4914 (1991)
13. H. Dreyssé, L. T. Wille and D. de Fontaine, *Phys. Rev. B* 47, 62 (1993)
14. C. Wolverton, M. Asta, S. Ouannasser, H. Dreyssé and D. de Fontaine, *J. Chim. Phys.* 90, 249 (1993)
15. H.Dreyssé, A. Berera, L.T. Wille and D. de Fontaine, *Phys. Rev. B* 39, 2442 (1989)
16. H. Magnan, D. Chandesris, B. Vilette and J. Lecante, *Surf. Sci.* 251, 597 (1991)
17. P. Khonneux, E. Courtens, *Phys. Rev. B* 46, 556 (1992)
18. C. L. Fu and A.J. Freeman, *Phys. Rev. B* 35, 925 (1987)
19. A. Haroun, (PhD thesis, Nancy 1993, unpublished)
20. P. J. Jensen, H. Dreyssé and K.H. Bennemann, *Europhys. Lett.* 18, 463 (1992)
21. M. Stampanoni, A. Vaterlaus, M. Aeschliman, F. Meier and D. Pescia, *J. Appl. Phys.* 64, 5321 (1988)
22. M. T. Kief, G.J. Mankey, R. F. Willis, *J. Appl. Phys.* 69, 5000 (1991)

Section B—Interfaces and Characterization

PART II

**Applications of Synchrotron
Radiation Techniques to Magnetic Materials**

SPIN POLARIZED PHOTOEMISSION STUDIES OF QUANTUM WELL STATES IN THIN FILMS

P.D. JOHNSON, N.B. BROOKES,[†] Y. CHANG, and K. GARRISON
 Physics Dept., Brookhaven National Laboratory, Upton, NY 11973.

ABSTRACT

Spin polarized photoemission is used to study the electronic structure of noble metals deposited on ferromagnetic substrates. Studies of Ag deposited on an Fe(001) substrate reveal a series of minority spin interface or quantum well states with binding energies dependent on the thickness of the silver. Similar behavior is observed for Cu films deposited on a fcc Co(001) substrate. Tight-binding modeling reproduces many of the observations and shows that hybridization of the sp-bands with the noble metal d-bands cannot be ignored.

INTRODUCTION

Surfaces, thin films and multilayers may all display unique and interesting magnetic properties.[1] Theoretical studies indicate that enhanced magnetic moments may exist both in the surface and in the interface region between two elemental systems.[2] Magnetic multilayers display oscillatory exchange coupling which is currently the subject of a large amount of research. Dependent on the thickness of some intervening non-magnetic layer, adjacent ferromagnetic layers may align either ferromagnetically or antiferromagnetically.[3] Straightforward application of RKKY theory with a period length λ given by π/k_F , where k_F is the free electron Fermi wave vector, has been shown not to be applicable to these systems. Indeed if we consider copper as the intervening layer, RKKY theory would predict a period length of between one and two atomic layers. In reality the period length is often found to be of the order of 5-6 monolayers. Theoretical studies have shown that a more realistic description of the oscillation periods may be obtained by consideration of Fermi surface spanning vectors that reflect the correct nearly free electron Fermi surface of copper.[4] These theories consider the intervening layer in terms of the bulk band structure and predict oscillation periods given by $2\pi/q$ where q is effectively $2k_F - G$ with G the appropriate reciprocal lattice vector.

The finite dimensions of a thin film will lead to a quantization of the bulk band structure in the direction normal to the film. This results in the observation of a series of discrete states with binding energies dependent on the thickness of the film rather than the continuum of states characterizing the bulk. In experimental studies the observed discrete states have been termed interface states in the ultrathin regime[5] and quantum well states in the case of thicker films.[6] In the latter study it has been observed that the states cross the Fermi level with a periodicity comparable to that found for the period length of the exchange coupling in the multilayers. This observation leads to the suggestion that these states are in fact involved in the coupling between adjacent ferromagnetic layers, which is not unreasonable because the states effectively define the Fermi surface which is invoked in the RKKY like theories of the coupling.[4]

Photoemission studies of these different systems are limited by the mean free path or escape depth of the photoelectrons. It is therefore not possible to study the electronic structure of the multilayer systems directly. However it is possible to explore the properties of thin films and extrapolate the observations from those systems to the multilayer problem. In this paper we use spin polarized photoemission to study the electronic structure of the noble metals Ag and Cu deposited on the ferromagnetic substrates, Fe(001) and fcc Co(001) respectively. For both systems we observe quantum well states that display the finite size effects. Our spin polarization measurements indicate that in all cases the states show

minority spin polarization. Tight-binding calculations provide similar results to these observations and show that the states have sp and d character. The spin polarization observed for the states is also shown to reflect the hybridization in the interface.

EXPERIMENTAL

The experimental studies in this paper were carried out on a spin polarized photoemission facility developed on beamline U5 at the National Synchrotron Light Source (NSLS).[7] This system exploits the large photon flux provided by a UV undulator source. The spin polarization is measured with a low energy spin detector described in detail elsewhere.[8] Briefly the photoemitted electrons pass through a commercial hemispherical analyzer before scattering of a polycrystalline gold surface at an incident energy of 150 eV. An asymmetry in the scattering provides a measure of the spin polarization of the electrons. The experimental facility was also equipped with Auger Electron Spectroscopy (AES) and Low Energy Electron Diffraction (LEED) for monitoring chemical composition and crystallographic order respectively.

The silver films were grown by evaporating silver onto an iron picture frame cut in the $\langle 001 \rangle$ direction. The copper films were grown by evaporation onto a fcc Co(001) substrate previously grown on a Cu(001) substrate. Elsewhere it has been shown that Co films grown in this manner have a tetragonal distortion perpendicular to the film.[9] Evaporation rates were monitored both by AES and quartz crystal monitors. LEED studies indicated that for silver deposition on Fe(001) it was possible to grow a good $p(1 \times 1)$ structure out to several layers. LEED studies also indicated that for both Co growth on the Cu(001) substrate and the subsequent growth of Cu on the Co substrate the structure was again a $p(1 \times 1)$. This observation confirms earlier structural studies of this system.[9,10]

Spin polarized photoemission studies of the Co(001) film, grown to a thickness of the order of 20 monolayers, confirmed the spectra found in earlier studies and also confirmed the bulk ferromagnetic band structures calculated for this material.[11] As a secondary check on the thickness of the copper thin films, a second Co film was deposited on the outside of the copper film. The exchange coupling between the two cobalt layers was then measured by monitoring the spin polarization in the photoemission from the outer layer. These latter measurements found similar results to those found in an earlier surface magneto-optic Kerr-effect study of the coupling in Cu/Co multilayers.[10]

RESULTS

Photoemission studies of the silver overlayers deposited on Fe(001) reveal a series of states that have discrete binding energies dependent on the thickness of the silver film.[5,12] As shown in fig. 1, these states are observed to step up towards and through the Fermi level at a film thickness of the order of three or four monolayers. The zero coverage or clean surface spectrum shows a minority spin feature at a binding energy of 2.4 eV that has previously been shown to be a surface state.[13] Inverse photoemission studies of this same system indicate that this trend continues with the states having passed through the Fermi level eventually converging on the X_4' critical point, characteristic of bulk Ag.[14] Also shown in fig. 1, spin polarization measurements indicate that these states carry minority spin polarization at all thicknesses measured.[5]

Similar behavior is found in studies of copper films deposited on Co(001).[15] Shown in fig. 2, a series of states is again observed in the vicinity between the copper 3d bands and the Fermi level. The incident light was p-polarized with an energy of 24 eV for these spectra. Spin polarized photoemission measurements show that in all cases the quantum well states again carry minority spin polarization. A comparison of the Fermi surface crossing for these states, fig. 3, confirms the observation of Himpsel and co-workers[6,14] that the crossings occur with a frequency, 5-6 monolayers, comparable to that observed for the oscillatory exchange coupling in the magnetic multilayers.[10]

The frequency of Fermi surface crossings for the quantum well states may simply be derived within the context of a phase model.[16-18] Here the states are considered to be

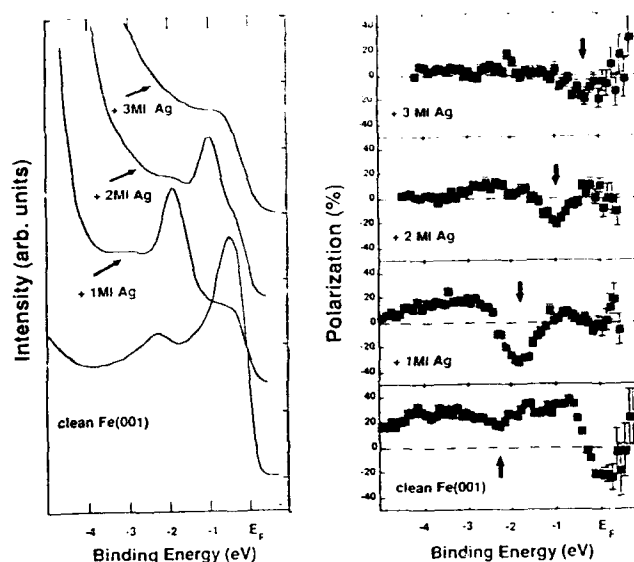


Fig. 1. The photoemission spectra (left panel) and spin polarization (right panel) measured from silver films deposited on Fe(001) as a function of silver thickness. The spectra show interface or quantum well states stepping up to the Fermi level. The incident photons are p-polarized with an incident photon energy of 52 eV.

confined within the quantum well defined by the metal-metal interface on one side and the solid-vacuum interface on the other. If the total phase change on reflection at the solid-solid interface and at the solid-vacuum interface is given by ϕ , the binding energy of the different states will be given by

$$\phi + 2kma = 2\pi n, \quad n=1,2,3,\dots \quad (1)$$

where k describes the wavevector of the state, m is the number of layers in the film, a is the interlayer thickness and n takes integer values. With each new layer the series of states given by equation (1) is redefined through the addition of an extra 2π to the right hand side, reflecting the presence of the additional layer. If we consider the phase changes appropriate to the Fermi level, then it is easy to show that two successive states with the same spin will cross the Fermi level at a separation in layers Δm given by

$$\Delta m = \frac{\pi}{\pi \cdot k_F a} = \frac{k_{BZ}}{k_{BZ} - k_F} \quad (2)$$

Here, the zone boundary wave vector k_{BZ} is given by π/a . Recognizing again that $k_{BZ} - k_F$ is equal to $q/2$, with q the zone boundary Fermi surface spanning vector, equation (2) reduces to a period length $\Delta m a$ equal to $2\pi/q$, i.e. the same as that found in the RKKY like theories discussed earlier.[4]

CALCULATIONS AND DISCUSSION

In order to better understand the results presented in the previous section, we have developed a spin dependent tight-binding scheme in a slab formulation that allows us to calculate the electronic structure of the different thin film systems. These tight-binding calculations were carried out using an approach based on the use of a Hubbard Hamiltonian. Thus

$$H = \sum_k E(k) n_k + \frac{U}{N} \sum_{k,k'} n_{k\uparrow} n_{k'\downarrow} \quad (3)$$

where the first term reflects the paramagnetic bandstructure and the second term represents the modification due to an on-site spin dependent potential, U . This "exchange" potential leads to a spin dependent splitting of the electronic states with the resulting formation of local moments. We associate U with the effective Stoner parameter for the different elements. It has been demonstrated elsewhere that the latter parameter is essentially an atomic property showing little variation from one environment to another.[19]

Our approach is to assume in the case of the transition metals, that the moments are carried almost entirely by the more localized d electrons. Thus we take the parameters associated with a tight-binding fit to the appropriate paramagnetic or non-magnetic band structure, split the on-site spin dependent energies for the d-blocks by an amount Δ and, in the case of a non-orthogonal fit, make appropriate adjustments to the associated off-diagonal elements. We then integrate the spin-dependent densities of states up to the Fermi-level to obtain the resulting layer dependent moments. A self-consistent solution is sought such that for each layer

$$\Delta_i = U_i m_i \quad (4)$$

where Δ_i is the layer dependent splitting introduced into the d-block, U_i the layer dependent Stoner parameter and m_i the calculated moment for each layer.

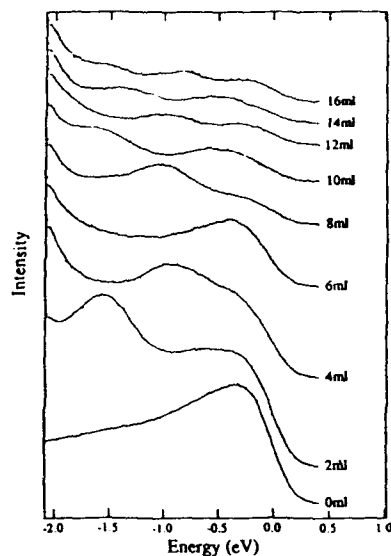


Fig. 2. The photon emission spectra recorded from copper films deposited on an Co(001) substrate. The spectra show the region between the copper d-bands and the Fermi level as a function of the copper thickness as indicated. The incident photon energy is 24 eV.

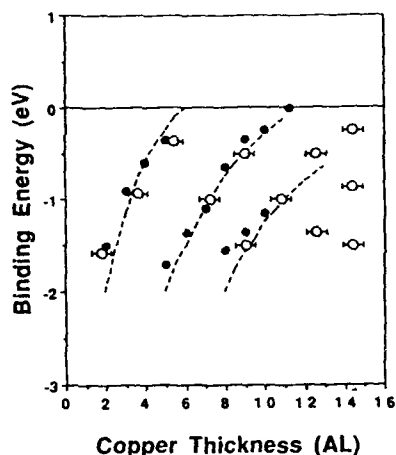


Fig. 3. Comparison of observed binding energies for quantum well states of the Cu/Co(001) system from the present experiment (o), an earlier photoemission study (●) (ref. 13) and the extrapolation of lines modelling inverse photoemission observations of the same states above the Fermi level. (dashed lines) (ref. 13). The copper thickness is given in atomic layers.

Initially a small ferromagnetic moment is applied to every site to move away from the trivial solution $m_i=0$. Charge neutrality for the system as a whole is maintained throughout the calculation. Two center tight binding parameters are taken from the compilation of Papaconstantopoulos[20] and values for U were taken from Local Spin Density calculations of the susceptibility and related Stoner parameters.[21] The total density of states was calculated for each overlayer system by summing over 28 k-points evenly distributed throughout the irreducible surface Brillouin zone.

Applying this method to the growth of thin films, we consider first a Ag film grown on the Fe(001) substrate. The silver-iron interaction parameters were taken as the mean of the silver and iron parameters. Where required the scaling scheme of Anderson and coworkers was used.[22] The on-site energies were adjusted to align the Fermi levels of the two metals. The lattice constants were taken as the bulk values and for the interfacial separation the mean of the two elemental interlayer spacings was used.

As noted earlier, the presence of finite boundary conditions in a thin film will result in a quantization of the bands in the direction perpendicular to the film. We illustrate this in fig. 4 by examining the calculated eigenvalues with eigenvectors of predominantly sp_z symmetry in the region of the Fermi level for silver slabs of different thicknesses. As the thickness of the slab increases the eigenvalues, indicated by the dashed lines, will converge because we sample the sp band with increasing frequency.

We also show in the same figure our spin dependent calculations of these same states for 1, 2 and 3 monolayers of silver placed on a Fe(001) substrate. The states now display magnetic character with both minority and majority spin states appearing in the calculation. A first principles FLAPW calculation of the monolayer Ag/Fe(001) system also finds both majority and minority spin interface states.[23] In agreement with the results of the same calculation our model predicts that deposition of the initial monolayer reduces the surface moments of the iron from 2.94 μ_B to 2.5 μ_B . With subsequent deposition of silver layers the Fe surface moments show little change in our calculation.

The experimental observations from the spin polarized photoemission study of the interface states[5] and the results of an Inverse Photoemission study[13] of the same states

observed above the Fermi level are also shown in fig. 4. Examination of the figure shows that reasonable agreement is obtained between both sets of experimental observations and the results of the calculation. In particular we note the good agreement between the calculated minority spin states and the experimental observations in the low coverage regime. Both the experiment and the model suggest that the minority spin states cross the Fermi level at a coverage of between three and four layers of silver.

The minority spin states dominate the experimental spectrum with only the smallest indication of a possible majority state for the silver monolayer coverage. An examination of the eigenvectors in our tight-binding model suggests that the minority spin states are more localized in the interface region than the majority spin states which display weight back into the bulk of the Fe. This result is not inconsistent with the idea discussed elsewhere that the presence of a band gap at E_F in the even symmetry states of minority spin character for the Fe substrate should produce a dominance of minority spin polarization for the states in the silver.[13]

We now apply the same method to the Cu/Co(001) system. However now, rather than plotting the layer dependent eigenvalues and in order to make a more direct comparison with the photoemission spectra recorded along the surface normal, we show in figure 5, the calculated density of states in a narrow region around Γ , the Brillouin Zone center. The layer dependent charge densities, corresponding to the different eigenvalues are weighted by factors reflecting the relative photoionization cross-sections for copper and cobalt[24] and for the mean free path of the photoemitted electrons. For the present calculations a representative mean free path of 6.5 Å was used. The figure shows both majority and minority spin "spectra" as a function of copper thickness. For both spin components, peaks corresponding to the main copper d bands are observed at a binding energy of 2.75 eV. However the minority spin spectra also show peaks moving up to and through the Fermi level with a frequency comparable to that observed in the experiment. Similar structure is apparent in the majority spin channel but at a much reduced intensity. Indeed in the experiment no clearly defined majority spin peaks are observed.

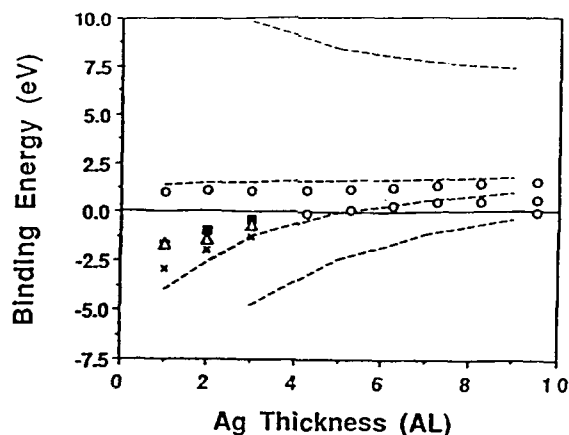


Fig. 4. Calculated states of sp symmetry for silver slabs of different thicknesses (dashed lines). Calculated minority spin states (Δ) and majority spin states (x) for silver layers deposited on an Fe(001) substrate. Experimentally observed minority spin states observed in photoemission studies (\blacksquare) (ref. 5) and the same states (o) observed above the Fermi level in an Inverse Photoemission study (ref. 13)

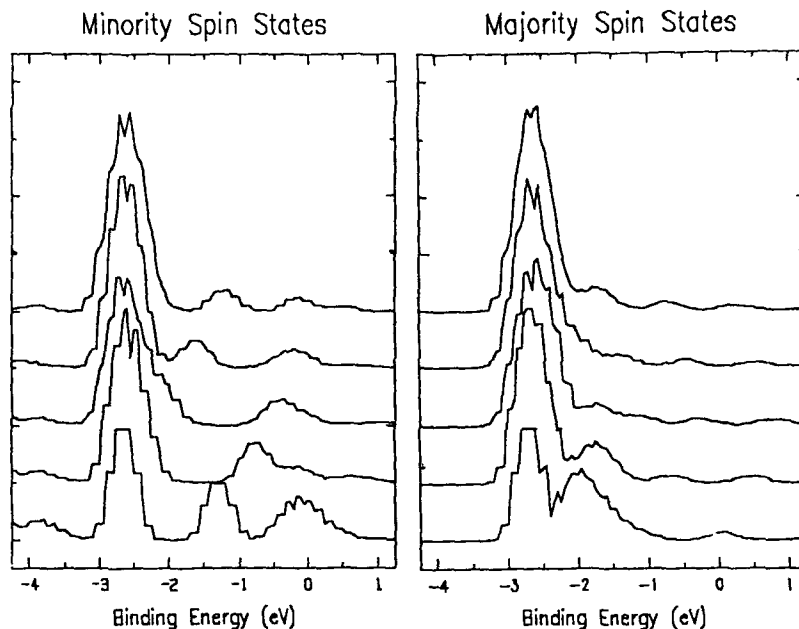


Fig. 5. Calculated "photoemission spectra" as a function of copper thickness for copper layers deposited on a fcc Co substrate. The spectra on the left hand side correspond to minority spin densities of states and those on the right hand side to majority spin states. The spectra are calculated for two to six monolayers of copper running from bottom to top of each panel in steps of one monolayer.

Examination of the eigenvectors or charge densities associated with the eigenvalues calculated for the Cu/Co(001) system reveals two important observations. First, the states contain a substantial copper d-component as well as sp-component reflecting hybridization between the copper sp and d bands. This hybridization occurs throughout the Brillouin zone, up to and through the Fermi level. Secondly the minority spin states all show a significant interfacial component with a large substrate d-component. Indeed because atomic photoionization cross-sections were used in the modeling, the spectra in fig. 5 essentially represent thickness dependent d band density of states for the system.

The layer by layer charge densities of d symmetry for a minority spin state calculated to be at the center of the zone for six layers of Cu deposited on a cobalt substrate are shown in fig. 6(a). The figure clearly shows the peaking in the interface and the rapid decay into the bulk of the Co. This localization in the surface region reflects the presence of an even symmetry band gap for the substrate at this particular binding energy. For comparison we show in fig. 6(b) the same charge densities but now for a state calculated again at the center of the zone for six layers of copper sandwiched between two Co films ferromagnetically aligned with respect to each other. Again we observe the same peaking in the interface with strong localization in the surface region of the Co layers. The binding energies calculated for these two states are 1.19 eV and 1.17 eV with respect to the Fermi level respectively.

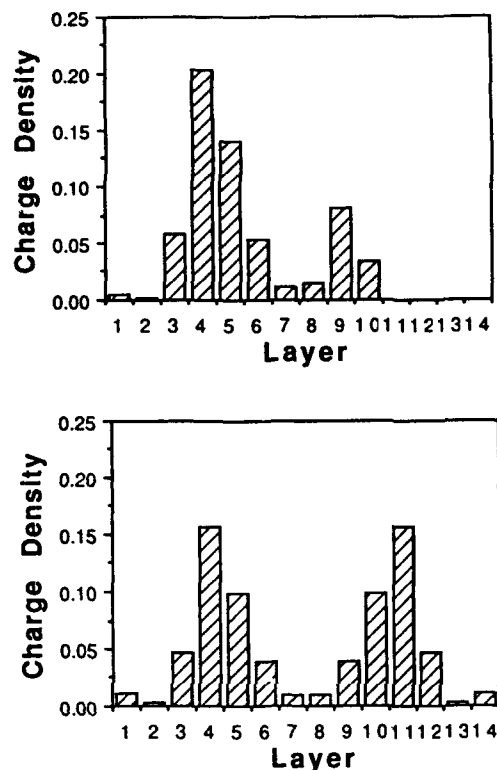


Fig. 6. Layer dependent charge densities with d_{zz} symmetry for a minority spin state calculated for (a) six monolayers of coppers (layers 5 to 10) deposited on a Co(001) substrate and (b) six monolayers of copper (layers 5 to 10) sandwiched between two ferromagnetic Co layers.

SUMMARY

Our spin polarized photoemission studies of the noble metals Ag and Cu deposited on an Fe(001) and Co(001) substrate respectively, show that quantum well states exist for both systems and that certainly in the latter case, they pass through the Fermi level with a periodicity comparable to the oscillatory exchange coupling observed for the equivalent multilayer systems. Our observation that they are highly polarized and that they also show a localized spin polarization in the interface region offers strong support to idea that they mediate the coupling between adjacent ferromagnetic layers. Finally we would comment that our experiment clearly shows the presence of spin polarized states associated with the copper crossing through the Fermi level. This observation suggests that the copper atoms will carry a small magnetic moment. However the use of angle resolved photoemission will not provide us with sufficient information for a determination of the magnitude of the moment. Further our calculation probably does not have the sophistication required to accurately predict the magnitude of a small moment.

ACKNOWLEDGEMENTS

The authors would like to acknowledge useful discussions with M. Weinert and N.V. Smith. This work has been supported in part by the Department of energy under contract DE-AC02-76CH00016 and in part by the NSF under contract No. DMR-86-03304.

REFERENCES

- † Present Address: ESRF, BP 220, F38043 Grenoble Cedex, France.
1. e.g. Magnetic Surfaces, Thin Films, and Multilayers, ed. S.S.P. Parkin, H.Hopster, J-P Renard, T. Shinjo and W. Zinn, MRS Proceedings **231**, (Pittsburg,1992).
 2. A.J. Freeman and Ru-qian Wu, J. Magn. Mater., **100**, 497 (1991).
 3. S.S.S. Parkin, Phys. Rev. Lett. **67**, 3598 (1991).
 4. e.g. P. Bruno and C. Chappert, Phys. Rev. Lett. **67**, 1602 (1991).
 5. N. B. Brookes, Y. Chang, and P. D. Johnson, Phys. Rev. Lett. **67**, 354 (1991). 6.
 6. J.E. Ortega and F.J. Himpsel, Phys. Rev. Lett. **69**, 844 (1992).
 7. P. D. Johnson, S. L. Hulbert, R. Klaffky, N. B. Brookes, A. Clarke, B. Sinkovic, N.V. Smith, R. Celotta, M. H. Kelly, D.T. Pierce, M. R. Scheinfein, B. J. Wacławski and M.R. Howells, Rev. Sci. Instr. **63**, 1902 (1992).
 8. J. Unguris, D.T. Pierce, R.J. Celotta, Rev. Sci. Instrum., **57** (1986) p. 1314 ; M.R. Scheinfein, D.T. Pierce, J. Unguris, J.J. McClelland, R.J. Celotta, and M.H. Kefley, Rev. Sci. Instrum. **60**(1), 1 (1989).
 9. A. Clarke, G. Jennings, R.F. Willis, P.J. Rous and J.B. Pendry, Surf. Sci., **187**, 327 (1987); J.J. de Miguel, A. Cebollada, J.M. Gallego, R. Miranda, C.M. Schneider, P. Schuster and J. Kirschner, J. Magn. Magn. Mat. , **93**, 1 (1991)
 10. Z.Q. Qiu, J. Pearson, and S.D. Bader, Phys. Rev. B **46**, 8659 (1992).
 11. C.M. Schneider, J.J. de Miguel, P. Bressler, P. Schuster, R. Miranda, and J. Kirschner, J. Elect. Spect., **51**, 263 (1990).
 12. P.D. Johnson, N.B. Brookes, Y. Chang, A. Clarke, and N.V. Smith, to be submitted.
 13. N. B. Brookes, A. Clarke, P. D. Johnson, and M. Weinert, Phys. Rev. **B41**, 2643 (1990).
 14. J.E. Ortega, F.J. Himpsel, G.E. Mankey and R.F. Willis, Phys. Rev. B **47**, 1540 (1993).
 15. K. Garrison, Y. Chang, and P.D. Johnson, to be published.
 16. P.D. Loly and J.B. Pendry, J. Phys. C **16**, 423 (1983).
 17. A.L. Wachs, A.P. Shapiro, T.C. Hsieh, and T.-C. Chiang, Phys. Rev. B **33**, 1460 (1986).
 18. S.A. Lindgren and L. Wallden, Phys. Rev. Lett. **61**, 2894 (1988).
 19. S. Ohnishi, C.L. Fu and A.J. Freeman, J. Magn. Mater., **50**, 161 (1985).
 20. D.A. Papaconstantopoulos, Handbook of the Band Structure of Elemental Solids (Plenum Press 1986).
 21. J.F. Janak, Phys. Rev. B **16**, 255 (1977).
 22. e.g. O.K. Andersen and O. Jepsen, Physica, **B 91**, 317 (1977).
 23. S. Ohnishi, A.J. Freeman and M. Weinert, Phys. Rev. B **30**, 36 (1984)
 24. J.J. Yeh and I. Lindau, Atomic Data and Nuclear Data Tables, **32**, 1 (1985).

Magnetic Circular Dichroism in X-Ray Absorption and Core-Level Photoemission

J.G. Tobin, G.D. Waddill, T.H. Gouder, and C.A. Colmenares

*Chemistry and Materials Science Department, University of California, Lawrence Livermore
National Laboratory, P.O. Box 808, Livermore, CA 94550 USA*

D.P. PAPPAS

Naval Research Laboratory, Washington, DC 20375 USA

ABSTRACT

Here is reported observation of magnetic circular dichroism in both x-ray absorption and core-level photoemission of ultra thin magnetic films using circularly polarized x-rays. Iron films (1–4 ML) grown on a Cu(001) substrate at 150 K and magnetized perpendicular to the surface show dramatic changes in the $L_{2,3}$ absorption branching ratio for different x-ray polarizations. For linearly-polarized x-rays perpendicular to the magnetic axis of the sample the branching ratio was 0.75. For films ≥ 2 ML, this ratio varied from 0.64 to 0.85 for photon spin parallel and anti-parallel, respectively, to the magnetic axis. This effect was observed either by changing the x-ray helicity for a fixed magnetic axis, or by reversing the magnetic axis for a fixed x-ray helicity. Our observation can be analyzed within a simple one-electron picture, if the raw branching ratios are normalized so that the linear value becomes statistical. Furthermore, warming the films to ~ 300 K eliminated this effect, indicating a loss of magnetization in the film over a temperature range of ~ 30 K. Finally, reversing the relative orientation of the photon spin and the magnetic axis from parallel to anti-parallel allowed measurement with photoemission of the exchange splitting of the Fe 2p and 3p core levels which were found to be 0.3 eV and 0.2 eV, respectively. These results are consistent with earlier studies, but the use of off-plane circularly-polarized x-rays from a bending magnet monochromator offers ~ 2 orders of magnitude greater intensity than typical spin-polarization measurements. Finally, we have performed preliminary x-ray absorption studies of UFe_2 , demonstrating the feasibility of MCD measurements in 5f as well as 3d materials.

One of the basic thrusts of the investigation of nanoscale magnetic structures, whether it be ultrathin monolayer films, multilayers, or clusters, is the establishment of structure-property relationships. (For examples of this in the case of Fe/Cu(001), see references 1–4 and references therein.) To be more specific, the determination of the interconnections between geometric, electronic, and magnetic structure is the fundamentally important but intermediate goal, with an eye towards the ultimate manipulation and application of this understanding. Ordinarily, efforts to measure nanoscale magnetic properties in conjunction with atomistic geometric and electronic structures runs headlong into the same problem: The magnetic perturbation tends to be a small component of the overall effect. In contrast to this, here we report *giant circular dichroism* in the near-edge core-level x-ray absorption of a near-monolayer metal film. An example of our data^{4,5} is shown in Fig. 1. The essential effect is the relative amplification of the $2p_{1/2}$ peak where the magnetization and helicity are parallel, regardless of whether the magnetization is into or out of the surface plane. (Because the magnetization and x-ray incidence are normal to the surface, we call it perpendicular dichroism.) This is a direct measurement of the spin polarization and the density of the unoccupied states near E_F in a ferromagnetic system.

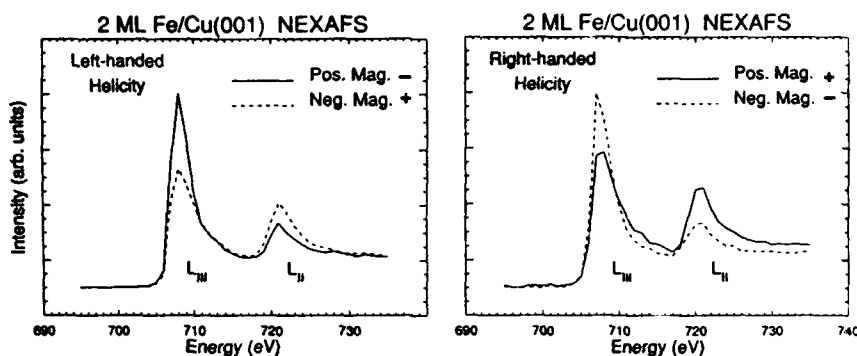


Figure 1. The near-edge x-ray absorption fine structure (NEXAFS) dichroism of 2 ML of Fe/Cu(001). These are plots of absorption versus photon energy. The left panel shows the effect of reversing the magnetization while maintaining the left-handed helicity of x-rays. Similarly, for the right panel and right-handed helicity x-rays. Samples are perpendicularly magnetized either into (pos. mag.) or out of (neg. mag.) the surface. The symbol +(-) means that helicity and magnetization are parallel (anti-parallel). The $2p_{3/2}$ peak is at the LIII edge and the $2p_{1/2}$ peak is at the LII edge. The spectra were normalized to each other by equating the pre-edge intensity, at energies below approximately 700 eV.

The temperature dependence of the perpendicular magnetization can also be followed with this technique. Figure 2 illustrates the behavior for 4 ML of Fe/Cu(001). Here, we are using branching ratio (BR) as a measure of the dichroism. BR is defined in Eq. (1). I is the integrated intensity of the white line peak at each edge jump.

$$BR = I(2p_{3/2}) / [I(2p_{3/2}) + I(2p_{1/2})] \quad (1)$$

We have developed a simple, one-electron picture to analyze our results, which can be summarized into the closed form analytic expression shown in Eq. (2).

$$BR = \frac{3 + 2(1-\alpha)\beta + 2(1-\beta)\alpha}{6} = \frac{2}{3} - \frac{(P_{\parallel})(P_{\perp})}{6} \quad (2)$$

Previously⁴, we expressed this equation in terms of α and β . α is the spin down alignment of the unoccupied 3d states and β is the degree of right circular polarization. We have now derived a more compact form, using the classical definitions of polarization. See Table I for details.

To use a one-electron picture, it is necessary to "normalize-out" the non-statistical (e.g., many-body effects). To do this we multiply all BR values by $2/3/BR_{\text{EXP}}(\text{lin})$. This allows us to concentrate upon the effects of helicity variation. The results of our analysis, assuming $2\mu_B/\text{Fe}$ atom ($\alpha = 25\%$ and 75%) is shown in Table II.

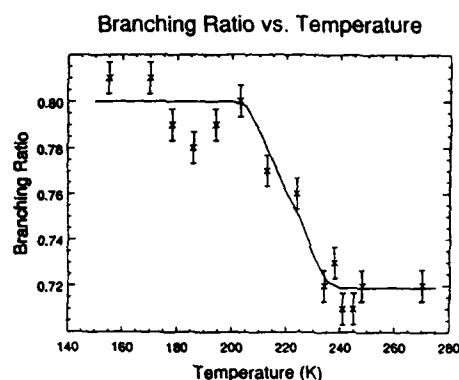


Figure 2. The temperature dependence of the magnetization of 4 ML Fe/Cu(001) using NEXAFS magnetic circular dichroism as the probe. Because of the imperfect placement of the thermocouple on the sample plate, the sample temperature may be slightly higher than that shown. Error bars of approximately $\pm 1\%$ are included for comparison but the true time error estimate is probably higher (about 4%). A branching ratio near 0.72 corresponds to an unmagnetized sample.

	Empty Valence States		
	Pure Down	Pure Up	Random
$\alpha = \frac{N_{\text{UNOCC}}^{\downarrow}}{N_{\text{UNOCC}}^{\downarrow} + N_{\text{UNOCC}}^{\uparrow}}$	1.0	0.0	0.5
$P_e = \frac{N_{\text{UNOCC}}^{\downarrow} - N_{\text{UNOCC}}^{\uparrow}}{N_{\text{UNOCC}}^{\downarrow} + N_{\text{UNOCC}}^{\uparrow}} = 2\alpha - 1$	1.0	-1.0	0.0
	Photon Helicity		
	Pure Right Circular	Pure Left Circular	Linear
$\beta = \frac{I_R}{I_R + I_L}$	1.0	0.0	0.5
$P_w = \frac{I_R - I_L}{I_R + I_L} = 2\beta - 1$	1.0	-1.0	0.0

Table I: N_{UNOCC} is the number of empty d valence states. The symbols \uparrow and \downarrow denote spin up and down, respectively. α is the spin alignment of the d valence states. P_e is the polarization of the d valence states. β is the degree of right circular helicity of the x-rays. P_w is the circular polarization of the x-rays. $I_R(I_L)$ is the intensity of the right (left) circularly-polarized component of the x-ray beam.

Table II.

P versus M	BR _{EXP}	BR' _{EXP}	BR _{TH}
+	0.645	0.585	0.60
-	0.83	0.75	0.73
lin	0.74	0.67	0.67

P = polarization

M = magnetization direction

P vs M: relative directions of helicity and magnetization

+ = parallel

- = anti-parallel

BR = branching ratio

BR_{EXP} = raw experimental resultsBR'_{EXP} = experimental results, normalized to the linear statistical predictionBR_{TH} = atomic theory prediction, 2 μ B/Fe atom, α = 25%, 75% and β = 10%, 90% pol.

We have also used MCD with core-level photoemission to measure the exchange splitting of the 2p_{3/2} and 2p_{1/2} peaks of 4ML of Fe/Cu(001)⁶ as well as the Fe3p peak of 2 ML of Fe/Cu(001). The spectra are shown in Figures 3 and 4. The exchange splitting of 2p_{3/2} peak is 0.22 ± 0.10 eV. The apparent change in the spin-orbit splitting between the two peaks is 0.33 ± 0.14 eV. The exchange splitting of the Fe3p is approximately 0.2 eV. There are less than those observed in the bulk (see Reference 6 and references therein). It should be noted that these measurements are complicated by broadening of the individual components which compose the internal structure of each observed peak. All measurements were made in remanence and with perpendicular magnetization.

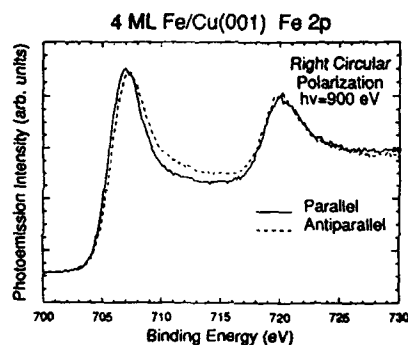


Figure 3 Fe 2p spectra taken with $h\nu = 900$ eV and positive photon helicity. The solid lines are for parallel orientation of photon spin and sample magnetization and the broken lines for an anti-parallel orientation. The two orientations were achieved by fixing the photon helicity and reversing the magnetization of the sample. The spectra are as collected and show the differences in binding energy for the 2p_{3/2} and 2p_{1/2} levels for the two helicity and magnetization orientations.

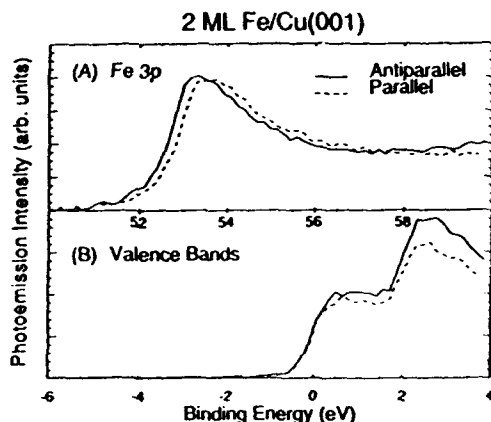


Figure 4 Magnetic circular dichroism in photoemission of the fcc-Fe 3p core level. The bottom panel shows the alignment of the Fermi edge, which allows for a direct comparison of the 3p binding energies in the top panel. The sample was 2 ML Fe/Cu(001), with perpendicular magnetization.

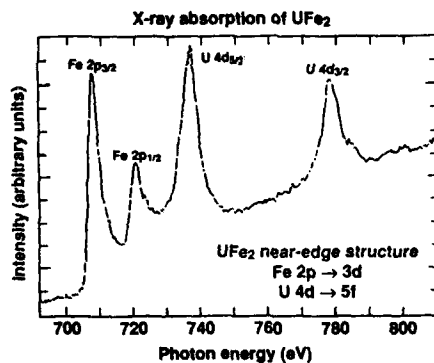


Figure 5 The near-edge x-ray absorption fine structure (NEXAFS) spectrum of UFe_2 , taken with linearly-polarized x-rays, is shown here. Note the strong transitions for both the Fe2p and U4d states.

Recently we began a series of experiments using near-edge-x-ray-absorption-fine structure (NEXAFS) looking for magnetic-circular-dichroism (MCD) in the magnetic actinide materials UFe_2 and U-S . These and our previous experiments were performed at SSRL using the University of California/National Laboratories PRT beamline 8-2⁷. This SGM beamline permits us to access the $2p \rightarrow 3d$ transition of Fe ($B^F = 707, 720$ eV) and the $4d \rightarrow 5f$ transition of U ($B^F = 736, 778$ eV). Absorption experiments with circularly-polarized x-rays should allow direct, elementally-specific interrogation of the magnetic and related electronic structure of these materials, in analogy with the results from magnetic x-ray scattering⁸. Our initial experiments

utilized NEXAFS, but in the future they will also be expanded to include core-level photoemission as well. We expect that the orders-of-magnitude improvement in brightness at the ALS will open the door for an unprecedented opportunity for both basic science using 5f elements, as well as improving the overall understanding of the physical and chemical properties of uranium compound materials.

We have performed magnetic circular dichroism (MCD) experiments upon Fe/Cu(001), using both core-level photoemission and near-edge absorption fine structure. A simple, one electron picture worked well to explain normalized branching ratio measurements. We plan to continue and expand this work, including pursuing the measurement of MCD effects in 5f systems.

Acknowledgments

Work performed under the auspices of the U.S. Department of Energy by the Lawrence Livermore National Laboratory under contract No. W-7405-ENG-48. D.P. Pappas was supported by IBM Almaden when this experimental work was done. These measurements were made on Beamline 8-2 at the Stanford Synchrotron Radiation Laboratory. Beamline 8-2 is part of the UC/National Laboratories Participating Research Team (PRT) facilities⁷. The authors wish to thank Ms. Karen Clark for clerical support of this work.

References

1. S.A. Chambers, T.J. Wagener, and J.H. Weaver, *Phys. Rev. B.*, **36**, 8992 (1987)
2. C. Liu, R. Moog, and S.D. Bader, *Phys. Rev. Lett.* **60**, 2422 (1988).
3. D.P. Pappas, K.P. Kämper, and H. Hopster, *Phys. Rev. Lett.* **64**, 3179 (1990).
4. J.G. Tobin, G.D. Waddill, and D.P. Pappas, *Phys. Rev. Lett.*, **68**, 3642 (1992) and references therein.
5. G.D. Waddill, J.G. Tobin, and D.P. Pappas, *J. Appl. Phys.*, In press, 1993.
6. G.D. Waddill, J.G. Tobin, and D.P. Pappas, *Phys. Rev. B*, **46**, 552 (1992).
7. L.J. Terminello, G.D. Waddill, and J.G. Tobin, *Nucl. Instrum. Meth.* **A319**, 271 (1992); J.G. Tobin, G.D. Waddill, Hua Li, and S.Y. Tong, *MRS Symp. Proc.* (1993), in press; K.G. Tirsell, and V.P. Karpenko, *Nucl. Instrum. Meth.*, **A291**, 511 (1990).
8. D.B. McWhan, C. Vettier, E.D. Isaacs, G.E. Ice, D.P. Siddons, J.B. Hastings, C. Peters, and D. Vogt, *Phys. Rev. B* **42**, 6007 (1990).

EVIDENCE FOR SPIN POLARIZATION OF METALLIC COPPER IN Co/Cu AND Fe/Cu MULTILAYERS

S. PIZZINI*, C. GIORGETTI*, A. FONTAINE*, E. DARTYGE*, G. KRILL*,
J.F. BOBO**, M. PIECUCH*

*LURE, CNRS, CEA, MESR Bat. 209D, Université Paris-Sud, 91405 Orsay, France

**Laboratoire CNRS Pont-à-Mousson Saint Gobain, Pont-à-Mousson, France

ABSTRACT

Magnetic circular x-ray dichroism measurements on Co/Cu and Fe/Cu multilayers at the K edge of copper show that the $4p$ -states of copper are significantly spin-polarized by the adjacent magnetic layers. In relation to the phase opposition of the copper thickness-dependent magnetoresistance of Co/Cu and Fe/Cu multilayers it is of prime importance to notice that the polarization of the conduction electrons of copper follows specifically the polarization of the conduction electrons of the adjacent magnetic element.

INTRODUCTION

Fe/Cu and Co/Cu multilayers are extensively studied because of the oscillatory dependence (AF-FM-AF) of the magnetic coupling between magnetic layers as a function of the thickness of the copper spacer [1,2]. The period of the oscillations (12Å) is roughly the same in the two systems but the phases are opposite. The magnetoresistance corresponding to the first AF peak is much larger for Co/Cu than for Fe/Cu multilayers (78% vs. 12%) [2].

The interpretation of the oscillatory coupling in terms of RKKY oscillations equivalent to those found in rare-earths materials, fails to predict the right periods ($\approx 2\text{Å}$ for most transition metals). A variety of more complex models, which in addition take into account the properties of the Fermi surface of the spacer, are able to predict at least the periods of the coupling oscillations [3,6]. In particular, the treatment by Edwards [4] which deals with the confinement of d electrons in the spacer layer by the exchange potential, leads to size-quantization of electron energies. Using the analogy with the de Haas-van Alphen effect the authors explain the periodic oscillations and the temperature dependence of the exchange coupling.

To explain the oscillatory magnetic coupling and their phase difference in Fe/Cu and Co/Cu multilayers, an analog model, but based on the confinement of the conduction electron, has been recently developed by Ortega and Himpsel [7]. Again for spacer's thicknesses corresponding to resonant conditions, each spacer acts as a "quantum well" for only one of the spin components of the conduction (sp) electrons of the spacer, leading to a thickness-dependent oscillations of the density of states close to the Fermi level. The results of inverse photoemission show that layers thicknesses giving maxima of the density of states correspond to the maxima of the AF coupling between the magnetic layers.

It is now clear that the conduction electrons of the spacer metal (Cu) have an essential role in the transport of the magnetic polarization across the ferromagnetic layers. This paper presents a direct experimental proof of the essential role of the spin-polarization of the conduction electrons for the magnetic coupling in Co/Cu and Fe/Cu multilayers.

To experimentally demonstrate the presence of spin polarization of the p -bands of copper we have performed magnetic circular x-ray dichroism (MCXD) measurements at the Cu K edge.

MCXD is the difference between the absorption of right ($\mu+$) and left ($\mu-$) circularly polarized photons of a ferro (ferri) magnetic material. In a model simplified to a one-electron picture, MCXD can be viewed as the result of the emission of a spin-polarized and angular-moment polarized photoelectron into an outer shell, acting as a spin or angular-moment resolving detector [8]. If no angular moment is involved, the MCXD signal, defined as $\mu c = (\mu+ - \mu-)/(\mu+ + \mu-)$, can be expressed by:

$$\mu_c = P_E P_C \Delta\rho/\rho$$

where P_E is the spin-polarization of the photoelectron, P_C is the rate of circular polarization of the incident x-ray beam,

$$\Delta\rho = \rho\uparrow - \rho\downarrow \text{ and } \rho = \rho\uparrow + \rho\downarrow.$$

This picture is rather misleading since the MCXD signal requires the presence not only of exchange splitting in the valence band, but also of spin-orbit interaction either in the excited core level or of the host band of the photoelectron, both in the final state. The absence of spin-orbit interaction in the $1s$ core level leads to a smaller spin-polarization and therefore much smaller MCXD signals for K-edge absorption, compared with L and M edges. However K-edge absorption spectroscopy presents the following advantages: (i) it probes directly the conduction electrons which are expected to mediate the magnetic interactions in Co/Cu multilayers and (ii) it avoids the limitation brought by soft x-rays whose sensitivity is restricted to a few layers close to the surface.

The amplitude of K-edge MCXD signals is not, in general, proportional to the magnetic moment of the ferromagnetic sample [9]. This is the case of Fe, Co and Ni. In the case of Co however, Stähler *et al.* have shown that the MCXD signal is correlated to the p -moment. Theoretical evaluations by Schwartz *et al.* [10] have shown that p and d moments have opposite signs for Fe and Co and estimated the p component to be of the order of $0.05\mu_B$.

The information obtained from MCXD measurements benefits from the double selectivity of x-ray absorption spectroscopy: (i) thanks to the *atom* selectivity, the signal can be probed independently for each chemical species in the sample (ii) the electric dipole selection rules determine the *symmetry* of the final state. Measurements at both the K and $L_{2,3}$ edges allow the spin-polarization of p -like electrons (sp bands) and d -like electrons to be obtained independently.

In the following we will show the results of K-edge MCXD measurements on a series of sputtered Co/Cu multilayers [11]. These will be discussed along with the results obtained for $L_{2,3}$ edge MCXD measurements which will be presented in a future paper [12].

EXPERIMENTAL METHODS AND RESULTS

The Co/Cu and Fe/Cu multilayers were prepared by magnetron sputtering. $\text{Co}_{9\text{\AA}}\text{Cu}_{8\text{\AA}}$, $\text{Co}_{10\text{\AA}}\text{Cu}_{9\text{\AA}}$, $\text{Co}_{10\text{\AA}}\text{Cu}_{13\text{\AA}}$, $\text{Co}_{12\text{\AA}}\text{Cu}_{8\text{\AA}}$ and $\text{Fe}_{12\text{\AA}}\text{Cu}_{8\text{\AA}}$ multilayers (total thickness 700\AA) were prepared starting from a 50\AA Fe buffer deposited on a $7\mu\text{m}$ thick kapton substrate. The samples are polycrystalline and untextured and have good interface quality [13]. The crystallographic structure of the multilayers is fcc for Co/Cu and bcc for Fe/Cu. All the samples present oscillatory coupling and large magnetoresistance. The magnetoresistance of the kapton-deposited samples is smaller than that of the Si-deposited samples (6% vs 45% for the sample with nominal composition 50\AA Fe - $(\text{Co}_{9\text{\AA}}\text{Cu}_{8\text{\AA}})_{38}$ - 12\AA Cu).

K-edge MCXD measurements were carried out at LURE-DCI synchrotron radiation source, at the energy dispersive x-ray absorption beam-line. Right circularly polarized light was selected by using a slit positioned at about 0.3 radians below the orbital plane of the storage ring. The multilayer samples were positioned in grazing geometry (10°) with respect to the propagation direction of the x-rays. X-ray absorption spectra were measured in an applied magnetic field of 0.3 T, whose direction was alternatively switched from parallel to anti-parallel to that of the x-ray beam. The details of the experimental methods are described elsewhere [14]. Spectra with good statistics at the Cu K-edge ($S/N \approx 10^5$) were obtained with acquisition times of about 8 hours. The S/N ratio for the MCXD data is of the order of 10 since the difference ($\mu_+ - \mu_-$) is as small as 10^{-4} .

The Cu K-edge MCXD spectra measured for a series of Co/Cu multilayers is presented in Fig. 1. The spectra are normalized to an absorption edge step equal to 1.

The MCXD signal is present as a negative peak in the vicinity of the Cu K edge absorption edge (the zero energy in the figure corresponds to the first maximum of the derivative the

rising edge of copper). To confirm that the signal is not a result of artefacts or spurious signals, we have shown that the spectrum of pure copper metal, measured in the same experimental conditions, does not show any MCXD signal. As expected, no signal is obtained when the same spectrum is measured without inversion of the magnetic field.

The Cu K edge MCXD spectrum of the $\text{Co}_{12}\text{ÅCu}_8\text{Å}$ multilayer, which was measured with a better statistics than the spectra shown in Fig. 1 (about 12hrs of acquisition time and a thicker sample), is presented in Fig. 2 where it is compared with the Co K edge measured for the same sample. The Co K edge spectrum is typical of close-packed bulk cobalt even if some details, and in particular the presence of a positive peak before the main negative peak, would have to be confirmed with higher quality data. The Cu K and Fe-K edge MCXD spectra of the $\text{Fe}_{12}\text{ÅCu}_8\text{Å}$ multilayer are shown in Fig. 3.

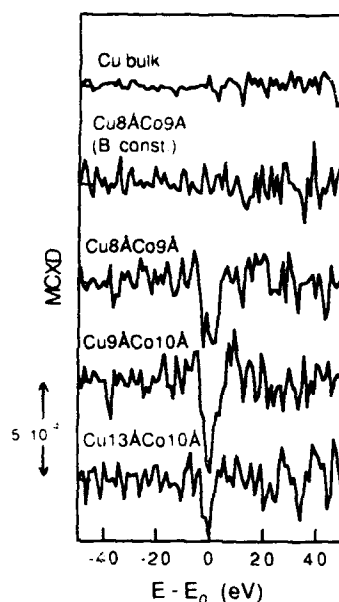


Figure 1: Cu K-edge MCXD signal for a series of sputtered Co/Cu multilayers. These are compared with the spectrum obtained for Cu metal and the spectrum measured for the $\text{Co}_9\text{ÅCu}_8\text{Å}$ multilayer without inverting the magnetic field, for which the MCXD signal is zero.

DISCUSSION

The presence of a MCXD at the K-edge and at $L_{2,3}$ -edges of copper in the Co/Cu multilayers is the indication of spin-polarization respectively of *p*- and *d*-like states in copper.

Figure 1 shows that the amplitude of the Cu K-edge MCXD signal is thickness dependent and decreases as the copper thickness increases. This behaviour suggests that the signal mainly derives from copper atoms close to the interface, i.e. in the vicinity of cobalt atoms.

Figure 2 shows the comparison between Co K-edge and Cu K-edge data in the $\text{Co}_{12}\text{ÅCu}_8\text{Å}$ multilayer. The Co K-edge spectrum is similar to that typical of cobalt metal, both in shape and in amplitude. This shows that the cobalt layer is fully polarized and that the coupling

between layers is ferromagnetic. The Cu K-edge MCXD spectrum is narrower than the Co K-edge and exhibits a small positive contribution before the main negative peak.

The physical nature of this positive structure is still the subject of speculation. Our study of Co-Fe alloys [15] and the results of Refs. 9 and 16 for Fe-Ni alloys indicate that the appearance of a positive peak in K-edge MCXD spectra corresponds to the transition from a strong to a weak ferromagnet i.e. to the availability of holes in majority spin bands. Theoretical explanations [17] invoke the presence of p - d hybridization to explain the difference between the K-edge MCXD spectrum of iron, which presents a positive and a negative peak, and the spectra of cobalt and nickel, which only show a negative peak.

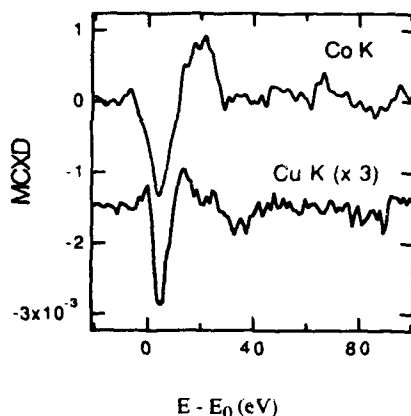


Figure 2: Cu K-edge and Co-K edge MCXD spectra of the $\text{Co}_{12}\text{\AA}\text{Cu}_8\text{\AA}$ multilayer. The Cu K edge signal has been multiplied by 3.

The maximum and integrated amplitudes of the main negative peak of the Cu K-edge MCXD spectrum are respectively $1/3$ and $1/5$ of those of the Co K-edge. If we admit that the amplitude of the MCXD signal is proportional to the p -like magnetic moment on the probed atomic species, as Stähler *et al.* have demonstrated in the case of cobalt, we could then conclude that the p -like moment on copper, averaged over the copper thickness (4ML), is about one fifth of the p -moment on cobalt. The sign of the copper K edge signal, which is the same as in cobalt, indicates that the p -moments on copper and cobalt are aligned. If we assume that only the copper layer in contact with cobalt is spin-polarized, the relevant p -moment of this copper interface layer amounts to 40% of that of cobalt ($\approx -0.02\mu_B$).

The results of the $L_{2,3}$ edges of Co and Cu on a similar multilayer can be summarized as follows [12]:

- (i) holes are present in the d -band of copper.
- (ii) the copper $L_{2,3}$ MCXD signals are weak with respect to cobalt. According to the sum rules proposed by Carra *et al.* [18] the orbital contribution of the Cu d -band is almost zero. This is consistent with the branching ratio of the total absorption cross section which is close to 2.
- (iii) the quantitative interpretation of the individual L_2 and L_3 MCXD signals in terms of d moments is still rather unsure. A possible estimation, which unfortunately relies on an estimation of the number of copper d -holes, could be obtained by comparison with the Co $L_{2,3}$ -edge data. This will be the subject of a forthcoming paper [12].
- (iv) the signs of the Co and Cu $L_{2,3}$ MCXD signals are consistent with a parallel alignment of d -moments in Cu and Co.

In conclusion, the spin-polarization of the d -band of copper appears to be extremely small

compared with that of cobalt. On the other hand the spin-polarization of each of the two p -bands appears to be of the same order of magnitude.

Whether the net moment of copper will be dominated by the contribution of the conduction electrons ($4p$ and $4s$) or by the $3d$ contribution is still an open question which requires a refined analysis and theoretical support. Since the p -moment is relatively strong and the d -moment is weak and of opposite direction, the net polarization is left very weak.

The presence of a positive pre-peak in the K edge MCXD of copper is consistent with a weak polarization of the almost full d -band of copper containing d holes with both spin polarizations. The small relative size of the positive peak indicates that fewer holes are present in the majority band. The polarization of the conduction electrons of the Cu layer is due to the adjacent layer since the polarization of the Cu $3d$ bands is very small.

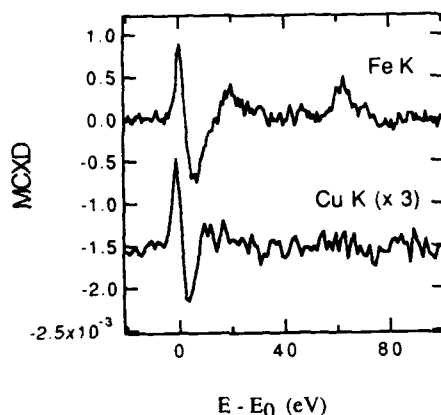


Figure 3: Cu K-edge and Fe-K edge MCXD spectra of the $\text{Fe}_{12}\text{ÅCu}_8\text{Å}$ multilayer. The Cu K edge signal has been multiplied by 3.

When copper is sandwiched between iron layers in the $\text{Fe}_{12}\text{ÅCu}_8\text{Å}$ multilayer (Fig. 3) the shape of the Cu K edge MCXD spectrum is very similar to that of Fe and its amplitude is three times smaller. The reduction of the width of the negative peak is analogous to that observed for the $\text{Co}_{12}\text{ÅCu}_8\text{Å}$ multilayer.

In the $\text{Co}_{12}\text{ÅCu}_8\text{Å}$ multilayer the maximum amplitude is reduced by three and, due to the narrowing of the signal, the total area is five times smaller than the Co K data. In the $\text{Fe}_{12}\text{ÅCu}_8\text{Å}$ multilayer the integrated positive area of the Cu MCXD signal dominates the integrated negative area. In line with the present understanding of the K-edge, this indicates that copper layers are weak ferromagnetic with a significant p -polarization. By comparison with Fe and Co K-edge MCXD signals, one can see that in Co/Cu and Fe/Cu multilayers the p -bands of copper have spin polarization of opposite character.

The dependence of the Cu-MCX signal on the crystallographic structure (bcc/fcc) cannot be at the origin of this behaviour. The weak ferromagnetic behaviour is not systematically related to the bcc structure, as seen in fcc Fe-Ni alloys where the Fe-K edge MCXD signal still exhibits the characteristic structure with a positive and a negative peak [16].

The dependence of the spin-polarization of copper on the nature of the ferromagnetic atom may be useful to help the understanding of the phase difference in the magnetic oscillations of Co/Cu and Fe/Cu multilayers. Within the model developed by Ortega and Himpsel [7] the phase of the magnetic oscillations is determined exclusively by the nature of the magnetic material.

REFERENCES

- [1] S.S.P. Parkin, R. Bhadra, K.P. Roche, *Phys. Rev. Lett.* 66 (1991) 2152
- [2] F. Petroff, A. Barthélemy, D.H. Mosca, D.K. Lottis, A. Fert, P.A. Schroeder, W.P. Pratt, R. Loloee, S. Lequien, *Phys. Rev. B* 44 (1991) 5355
- [3] P. Bruno, C. Chappert, *Phys. Rev. B* 46 (1992) 261
- [4] D.M. Edwards, J. Mathon, R.B. Muniz, M.S. Phan, *Phys. Rev. Lett.* 67 (1991) 493
- [5] F. Herman, J. Sticht, M. Van Schikfgaarde, *J. Appl. Phys* 69 (1991) 4783
- [6] P. Bruno, *J. Mag. Mag. Mat.* 121 (1993) 248
- [7] J.E. Ortega, F.J. Himpsel, *Phys. Rev. Lett.* 69 (1992) 844; J.E. Ortega, F.J. Himpsel, G.J. Mankey, R.F. Willis, *Phys. Rev. B* 47 (1993) 1540
- [8] J. Stohr, Y. Wu, *Proc. Nato Advanced Study Institute*, to be published by Kluwer Academic Publishers, Netherlands.
- [9] S. Stähler, G. Schütz, H. Ebert, *Phys. Rev. B* 47 (1993) 818
- [10] K. Schwartz, P. Mohn, P. Blaha, J. Kubler, *J. Phys. F: Met. Phys.* 14 (1984) 2659
- [11] S. Pizzini, F. Baudelet, E. Dartyge, A. Fontaine, J.F. Bobo, M. Piecuch, C. Marlière, *J. Mag. Mag. Mat.* 121 (1993) 208
- [12] M. Knulle, S. Pizzini, F. de Groot, P. Fischer, A. Fontaine, S. Stähler, G. Schütz, C.T. Chen, H. Ebert, F. Bobo, M. Piecuch, to be published
- [13] J.F. Bobo, M. Piecuch, E. Snoeck, to be published in *J. Mag. Mag. Mat.* 1993
- [14] F. Baudelet, E. Dartyge, A. Fontaine, C. Brouder, G. Krill, J.P. Kappler, M. Piecuch, *Phys. Rev. B* 43 (1991) 5857
- [15] S. Pizzini, F. Baudelet, A. Fontaine, C. Giorgetti, E. Dartyge, J.P. Kappler, to be published
- [16] H. Sakurai, F. Itoh, M. Nakamura, H. Maruyama, A. Koizumi, H. Yamazaki, Y. Tanji, T. Iwazumi, M. Sato, H. Kawata, Photon Factory, Tsukuba, 1993 Report
- [17] C. Brouder, M. Hikam, *Phys. Rev. B* 43 (1991) 3809
- [18] P. Carra, B.T. Thole, M. Altarelli, X. Xindong Wang, *Phys. Rev. Lett.* 70 (1993) 694

MAGNETIC SPECTRO-MICROSCOPY USING MAGNETO-DICHOIC EFFECTS IN PHOTON-INDUCED AUGER ELECTRON EMISSION

C.M. SCHNEIDER^{1,2}, K. MEINEL², K. HOLLDACK³, H.P. OEPEN⁴, M. GRUNZE³,
AND J. KIRSCHNER²

¹ Surface Physics Laboratory, Simon Fraser University, Burnaby, B.C., V5A 1S6, Canada

² MPI f. Mikrostrukturphysik, Weinberg 2, O-4050 Halle/Saale, Germany

³ Inst. f. Angew. Phys. Chemie, Universität Heidelberg, Im Neuenheimer Feld 253,
D-6900 Heidelberg, Germany

⁴ Inst. f. Grenzflächenforschung u. Vakuumphysik, KFA Jülich, Postfach 1915,
D-5170 Jülich, Germany

ABSTRACT

We have imaged the magnetic domain structure on the surface of Fe(100) single crystals using energy resolved photoemission microscopy with circularly polarized soft x-rays. The contrast between different domains arises due to magneto-dichroic effects in the emitted Auger electrons. This new approach offers a surface sensitive way to combine chemical and magnetic information on a microscopic scale.

INTRODUCTION

Within the last decades photoelectron spectroscopy has matured into a powerful tool in surface science. Even the photoelectron spin has been successfully made accessible to experimental investigations on both non-magnetic and ferromagnetic materials [1]. Spin-split electronic states in ferromagnets may be studied in great detail either by an explicit analysis of the photoelectron spin [2], or by means of the recently reported magnetic circular dichroism in photoemission (MCDAD) [3]. Both approaches add magnetic sensitivity to conventional photoelectron spectroscopy. The present photoemission experiments are usually hampered by sampling a rather large surface area ($\sim \text{mm}^2$), as determined by the size of the illuminated spot and the characteristics of the electron optics. The investigation of electronic and magnetic microstructures, however, requires lateral resolution capabilities. The combination of lateral resolution and magnetic sensitivity in photoemission techniques can be used in two ways: magnetic sensitive spectroscopy on well-defined areas on the surface (micro-spectroscopy), and imaging of magnetic domains with electrons of a selected kinetic energy (spectro-microscopy).

EXPERIMENTAL DETAILS

Our experimental approach to the problem employed a so-called ESCASCOPE, which has been described in detail by Coxon et al. [4]. Briefly, the set-up features a hemispherical energy analyzer (HMA) in combination with an electrostatic input lens system. The instrument can be operated either in a spectroscopic mode as a conventional electron spectrometer, or in an imaging mode. The latter allows the acquisition of photoelectron images with a spatial resolution $\Delta d < 10 \mu\text{m}$, using electrons of a well defined kinetic energy. Our experiments were performed in a UHV system (base pressure 1×10^{-10} mbar) at the German storage ring BESSY, using elliptically

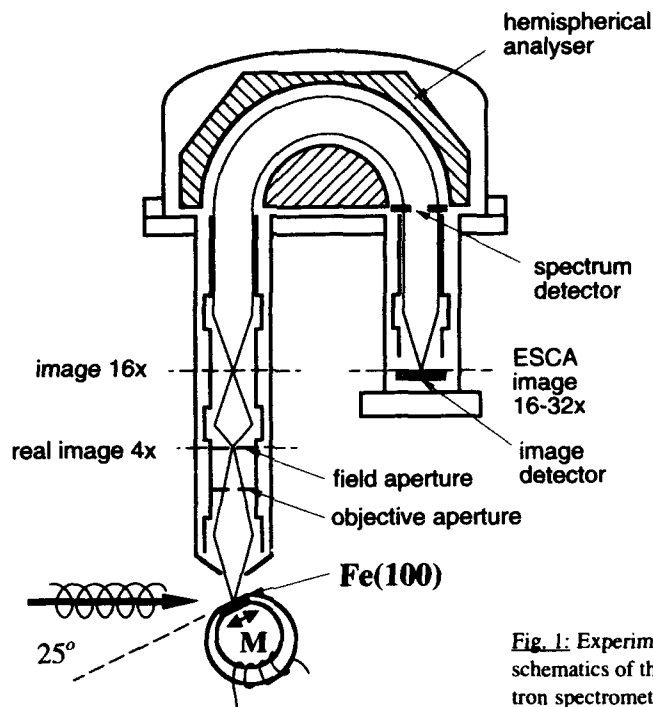


Fig. 1: Experimental set-up and schematics of the imaging electron spectrometer (see also ref. 4).

polarized off-plane radiation dispersed by the SX-700-3 monochromator [5]. The light was incident at 65° with respect to the surface normal of the specimen. The photoemitted electrons were collected perpendicular to the photon beam within the plane of incidence. The experiments were performed on several Fe(100) whiskers and an Fe(100) single crystal. The latter was mounted onto a soft iron yoke equipped with a wire coil, which allowed us to bring the crystal into a defined state of magnetization.

MAGNETIC CIRCULAR DICHROISM IN AUGER ELECTRON EMISSION

In order to introduce magnetic sensitivity into the imaging process, we exploited the effect of x-ray magnetic circular dichroism in the emitted photoelectrons (MCDAD). In MCDAD, magnetic samples exhibit a difference in the intensity spectra recorded with circularly polarized light of opposite helicities. The specific form and structure of the energy distribution curve depends on the relative orientation of the sample magnetization \mathbf{M} with respect to the direction of the incident light (or equivalently, the photon spin σ) and the wavevector of the emitted photoelectrons [6]. The dichroic signal is calculated from intensity spectra $I(E)$ taken at opposite \mathbf{M} or σ as the so-called intensity asymmetry A

$$A(E) = \frac{I^+(E) - I^-(E)}{I^+(E) + I^-(E)} \quad (1)$$

Domains with different orientation relative to the incoming photon beam will thus give rise to a

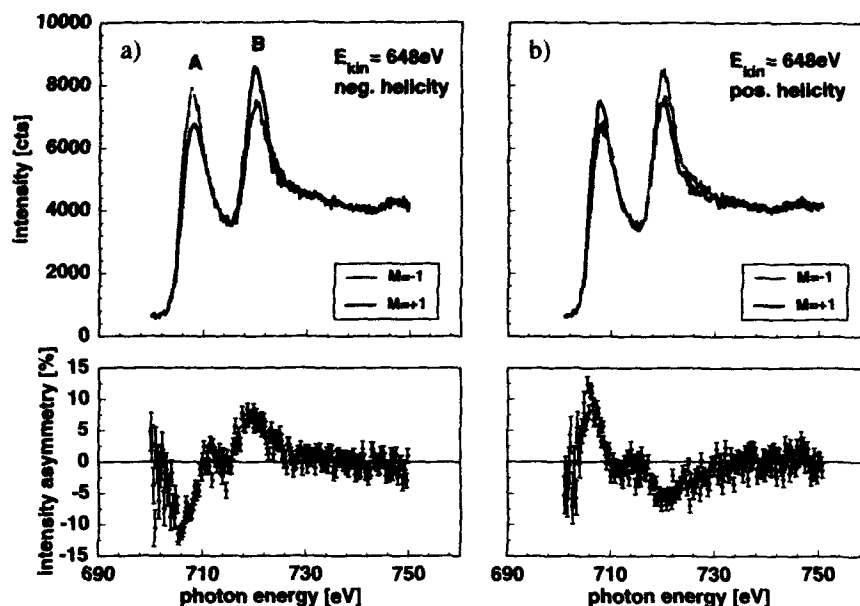


Fig. 2: Magnetic circular dichroism in the Fe $L_3M_{23}V$ Auger electrons as a function of photon energy. Constant final state spectra (upper panels) as taken with circularly polarized light for opposite sample magnetizations ($M=-1$) and ($M=+1$). The intensity asymmetry (lower panels) is calculated according to eq. (1).

spatial variation of the energy resolved photocurrent. This contrast may be optimized by tuning the energy filter to the maximum value of A. Maximum experimental asymmetries for photoemission from the Fe 2p levels range from 2% to 10%, depending on the geometry [7]. A further important finding is that magneto-dichroic effects are not limited to the direct photoelectrons, but also appear in true secondaries such as Auger electrons. This is demonstrated in Fig. 2, displaying the intensity of the $L_3M_{23}V$ Auger transition in Fe as a function of photon energy. The ESCASCOPE was operated in the spectroscopy mode and tuned to an electron energy of 648 eV with a bandwidth $\Delta E=2$ eV. The two peaks at 708 (A) and 720 eV photon energy (B) correspond to the photoexcitation thresholds of the $2p_{3/2}$ and $2p_{1/2}$ core levels, respectively. Magnetic circular dichroism causes the peak height of the spectral features to depend strongly on the direction of the Fe crystal's remanent magnetization \vec{M} with respect to the photon spin \vec{g} . For negative helicity (Fig. 2a), $M=-1$ (shaded curve) corresponds to a magnetization direction with a large component antiparallel to \vec{g} , whereas $M=+1$ (solid curve) has a large component along \vec{g} . The intensity differences give rise to pronounced features in the asymmetry function (Fig. 2, lower panels). The dichroic signal $A(E)$ has approximately the same size, but an opposite sign for the excitation with 708 and 720 eV photons, yielding a peak-to-peak asymmetry of $\sim 20\%$. Switching the helicity of the light leads to a sign reversal in the asymmetry function (Fig. 2b). A qualitatively similar situation is observed at kinetic energies of 598 eV and 703 eV, corresponding to the $L_3M_{23}M_{23}$ and L_3VV Auger transitions in iron, respectively.

IMAGING OF MAGNETIC DOMAINS

The intensity asymmetry $A(E)$ observed in electron spectroscopy forms the basis of a magnetic contrast in photoelectron images taken from magnetic surfaces. It will cause magnetic domains, which are oriented parallel and antiparallel to the photon spin, to appear with different intensities, i.e. with different grey levels in an grey scale representation. Fig. 3a shows an image of the Fe(100) surface taken from an area close to the edge of the crystal. The image has been acquired (acquisition time ~5min) with electrons of 648eV kinetic energy, corresponding to the Fe $L_{3/2}$ V Auger transition. Prior to the measurement, the Fe crystal has been demagnetized by driving the coil with an ac current, which was then gradually reduced to zero. The photon energy was tuned to 708eV, corresponding to the $2p_{3/2}$ excitation resonance (peak A), the light having positive helicity. The image will therefore be referred to as \mathcal{A}^+ . The raw data in \mathcal{A}^+ contain a combination of magnetic and chemical/topographic contrast. The latter is responsible for the number of dark spots which are scattered across the surface. As a local XPS analysis of these spots excluded the contrast to be of chemical origin, it is tentatively attributed to the surface topography. It is well known that transition metal single crystals, which have undergone an extensive sputter cleaning and annealing procedure, usually exhibit a large number of small pits and hillocks on the surface. The magnetic contribution to the contrast appears in Fig. 3a as a pattern of differently shaded areas. In order to separate magnetic and topographical/chemical information in the image, a second image with inverse magnetic contrast is needed. This image can be obtained, for instance, by switching the helicity of the light (\mathcal{A}^-). Yet, the photon energy dependence of the contrast (Fig. 2) suggests a more elegant solution to the problem. Since the asymmetry $A(E)$ at the $2p_{3/2}$ ($h\nu=708\text{eV}$) and $2p_{1/2}$ ($h\nu=720\text{eV}$) resonances is essentially of the same magnitude, but of opposite sign, images taken $h\nu=720\text{eV}$ (\mathcal{B}^+) contain an inverted magnetic contrast. The asymmetry image $A_E(x,y)$ is then calculated from the original images \mathcal{A}^+ and \mathcal{B}^+ in analogy to eq. (1) as

$$A_E(x,y) = \frac{\mathcal{A}^+ - \mathcal{B}^+}{\mathcal{A}^+ + \mathcal{B}^+} \quad (2)$$

The result of this operation is displayed in Fig. 3b, showing the domain structure of the Fe(100) crystal. Essentially only three grey levels are observed: the black (white) areas correspond to domains with their magnetization vector parallel (antiparallel) to the direction of light incidence. Domains with \mathbf{M} oriented perpendicular to the photon spin show up in a medium grey level. The domains are found to be rather small, i.e. considerably less than $100\mu\text{m}$, in agreement with observations by scanning electron microscopy with spin-polarization analysis (SEMPA) [8]. Only in the region close to the edge, some larger domains are located. These are presumably determined by defects at the crystal edge. Performing the operation in eq. (2) with images \mathcal{A}^+ and \mathcal{A}^- , instead of \mathcal{A}^+ and \mathcal{B}^+ , yields the same domain pattern as shown in Fig. 3b. Thus, the experiment proves our approach in eq. (2) to be equivalent to a change of the light helicity. It must be noted, however, that this equivalence follows from the particular photon energy dependence of the asymmetry in iron. For other materials, the corresponding "working points" may be established by further spectroscopic investigations.

Similar experiments as described above have been carried out on Fe(100) whiskers. These crystals usually have very well defined domain structures, which are determined mostly by the shape of the sample. The ideal domain pattern in a long narrow whisker, for instance, consists of only two domains separated by a 180° wall, and closure domains with 90° walls at each end of the specimen [9]. The domain image displayed in Fig. 4 has been obtained from an "L"-shaped sample, using $L_{3/2}$ VV Auger electrons (703 eV kinetic energy). Again three distinct grey levels, corresponding to the four magnetization directions in Fe(100) are observed. The image shows the elbow region of the whisker, which exhibits a relatively complicated domain pattern. In fact, the

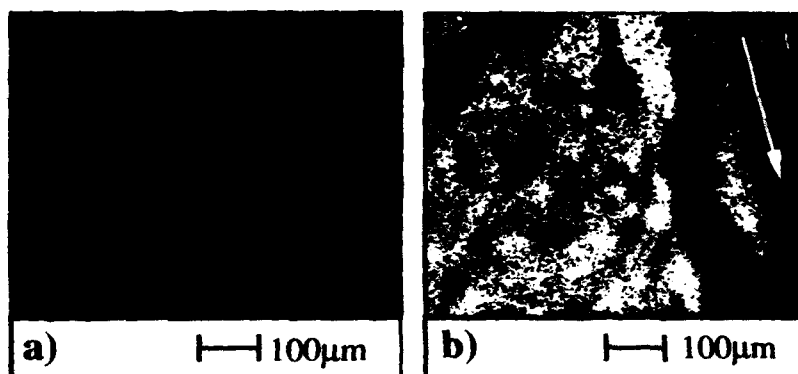


Fig. 3: Spectro-microscopy from an Fe(100) surface using $L_3M_{23}V$ Auger electrons. (a) raw image recorded with left hand circularly polarized light of $h\nu=708\text{eV}$. (b) magnetic domain pattern obtained by forming the asymmetry (eq. 2) from images taken at $h\nu=703\text{eV}$ and $h\nu=720\text{eV}$.

horizontal leg, which extends to the right border of the image, exhibits a domain distribution close to the case described above. The two oppositely oriented domains are both perpendicular to the incoming light and thus indistinguishable. This leads to the extended area of a medium grey level in the right hand part of the image. Only a small rotation of the sample is required to produce a sizable projection of the magnetization along the photon spin, causing these domains to show up with a different contrast. The deviations from the ideal domain pattern in the elbow region are very likely due to some defects along the lower edge of the crystal. These may give rise to local demagnetizing fields, and thus to a complex pattern of closure domains. Furthermore, the whisker may be subject to residual strain due to its fixation to the specimen holder, which is also likely to influence the formation of domains. Similar domain images as in Fig. 4 have been recorded with the directly emitted photoelectrons of the 2p and 3p core levels.



Fig. 4: Domain image from an "L"-shaped Fe(100) whisker using L_3VV Auger electrons (703 eV kinetic energy). Photon energies and helicity as in Fig. 3. Arrows mark the orientation of magnetization in individual domains.

CONCLUSIONS AND OUTLOOK

We have imaged magnetic domains on various Fe(100) surfaces by means of magneto-dichroic effects in the emitted Auger electrons. With its presently limited spatial resolution, this experimental approach does not intend to compete with other well-established domain imaging techniques, such as SEMPA or optical Kerr microscopy. It should rather be seen as a complementary method, with its main advantage being the unique combination of spectroscopic (i.e. elemental and chemical specificity) and magnetic information on a microscopic scale. Compared to a very recent experiment, in which magnetic domains were imaged by photo-emission microscopy using the total electron yield [10], the above energy-resolved approach has several advantages. First, it can exploit magneto-dichroic effects in the direct photoemission channel as well as in the emitted secondary electrons. By tuning the electron energy from direct photoelectrons through Auger excitations down to low-energy secondary electrons, one obtains a very detailed picture of the individual contributions to the magnetism. Secondly, the different angular dependences of MCDAD and MCD can be used to compensate for possible geometrical restrictions of the experimental set-up. Thirdly, one may intentionally introduce a depth selectivity into the measurements by analyzing electrons of very different kinetic energy. These virtues suggest that magnetic spectro-microscopy on the basis of magneto-dichroic phenomena will become an interesting and versatile new tool in surface and thin film magnetism.

We are indebted to Drs. B. Heinrich and Z. Celinski for providing us with the iron whiskers. This work was supported by the Bundesminister f. Forschung u. Technologie through grants Nos. 05 5 EFAA 1 5 and FKZ 055VHFX1. C.M.S. acknowledges financial support of the Deutscher Akademischer Austauschdienst (No. 516-401-514-3) during his stay at Simon Fraser University.

REFERENCES

1. U. Heinzmann and G. Schönhense, in: *Polarized Electrons in Surface Physics*, edited by R. Feder (World Scientific, Singapore, 1985)
2. E. Kisker, in: *Metallic Magnetism*, edited by H. Capellmann (Springer-Verlag, Berlin, 1987)
3. C.M. Schneider, D. Venus, J. Kirschner, Proceedings VUV 10, Paris 1992 (published by World Scientific, Singapore, 1993)
4. P. Coxon, J. Krizek, M. Humpherson, I.R.M. Wardell, J. Electron Spectrosc. Rel. Phenom. **51/52**, 821 (1990)
5. J. Bansmann, Ch. Ostertag, G. Schönhense, F. Fegel, C. Westphal, M. Getzlaff, F. Schäfers, H. Petersen, Phys. Rev. B **46**, 13496 (1992)
6. L. Baumgarten, C.M. Schneider, H. Petersen, F. Schäfers, J. Kirschner, Phys. Rev. Lett. **65**, 492 (1990); C.M. Schneider, D. Venus, J. Kirschner, Phys. Rev. B **45**, 5041 (1992)
7. D. Venus, C.M. Schneider, J. Kirschner, L. Baumgarten, C. Boeglin, J. Phys.: Condens. Matter **5**, 1239 (1993)
8. H.P. Oepen, J. Kirschner, Scanning Microsc. **5**, 1 (1991)
9. D.J. Craik and R.S. Tebble: *Ferromagnetism and Ferromagnetic Domains* (Wiley, New York, 1965)
10. J. Stöhr, Y. Wu, M.G. Sarmant, B.D. Hermsmeier, G. Harp, S. Koranda, D. Dunham, B.P. Tonner, Science **259**, 658 (1993), and these proceedings

MCD OBSERVED BY PHOTOEMISSION ON THE 2p LINES OF IRON FILMS UNDER AN EXTERNAL APPLIED FIELD.

C. Boeglin*, E. Beaupaire*, B. Carrière*, K. Hricovini** and G. Krill**.

*IPCMS-CNRS, Université Louis Pasteur, F-67070 Strasbourg, France.

**LURE, LP CNRS, Université de Paris-Sud, F- 91405 Orsay, France.

ABSTRACT

Circular Dichroic X-ray Photoemission Spectroscopy (CDXPS) experiments have been performed on the 2p core level spectra of polycrystalline Fe film which was magnetized by a low excitation field. The ability to perform the CDXPS experiments in a non remanent mode at a photon energy of 2100 eV opens new and interesting possibilities for the MCD technique in the study of surface and interface magnetism. Our work on this polycrystalline iron gives some new insights into the understanding of the MCD mechanism. First results show a similar angular variation for the measured asymmetry, as those observed on a Fe bcc (100) single crystal remanently magnetized in the [100] direction. Our results make clear that the parameters governing the behaviour of the asymmetry factor (A) are not completely described by the relative direction of the magnetization (M) with the polarization vector of the incident beam (q) and the direction of detection of the photoelectrons (z). The specific outcome of this work is to clearly show that this behaviour of A is not connected to the crystalline structure of the film for our geometries.

INTRODUCTION.

Magnetic circular dichroism (MCD) is now widely used to study the local magnetic properties of atoms in any magnetic materials. If the absorption experiments are now rather well described for localized and itinerant magnetic systems [1 - 6], the MCD effect observed by photoemission is to first order explained by a simple extended "absorption model" [3] where the emission direction is not explicated.

Recently new experiments showed interesting results on a Fe(110) single crystal face since a magnetic asymmetry was observed on the Fe2p levels in a "forbidden geometry" considering absorption measurements [7]. On the contrary to absorption experiments, where the electrons produced by the absorption process are not analysed, photoemission experiments involve the detection of photoelectrons with a well-defined direction with respect to the magnetization M, the surface normal and the wave vector q of the photon. Thus, the asymmetry factor $A = [I(-M) - I(+M)] / [I(-M) + I(+M)]$ can be shown to be strongly dependent on the detection angle [7,8,12].

Recently, a CDXPS experiment has been performed on the Ni 3p core level from a Ni(110) surface [9]: the importance of the orbital magnetic moment on the surface layer has been invoked in order to explain the large discrepancy concerning the magnitude of the asymmetry, within the above mentioned model.

Analytical calculations [13] has shown that the asymmetry A is dependent on both, the rate of the circularly polarized light and the rate of the linearly polarized light.

For this reason we choose in this paper to discuss differences of the photoemission intensity $I(-M) - I(+M)$ where the linear term is suppressed. Therefore we are able to compare them to the theoretically calculated differences for various collection angles.

We also demonstrate in this paper, that our results on a thick polycrystalline Fe film (100 Å) deposited on a Ni₃Fe (μ -metal) substrate reproduce fairly well those obtained on Fe(100) single crystal [8], and we conclude about the absence of influence on the measurements stemming from the crystallographic state of the surface.

A limitation of CDXPS is related with the fact that in principle such experiments have to be done in the remanent mode, i.e. the magnetic field has to be switched off during the experiments in order to avoid any disturbance of the photoelectron itself by the excitation field. Obviously this limits its use to those cases where the sample has a strong remanence at $H=0$. This is not the general situation encountered in surface and interface magnetism. Thus, it seemed important to us to investigate the possibility to use CDXPS in a less restrictive case, i.e. when the remanent induction is zero and when the sample is polycrystalline.

EXPERIMENTAL CONDITIONS.

The experiments were performed at the LURE - SuperACO synchrotron ring using the circularly polarized light produced by an asymmetric Wiggler. Monochromatic light was obtained from a Si(111) two crystal monochromator. The data were obtained using a constant photon energy of 2100 eV and recorded with a high resolution hemispherical energy analyzer. (The experimental resolution was estimated to be 0.4 eV (HWHM) in the present work). Fe2p photoelectrons ($E_B = 700$ eV) are therefore detected with a high kinetic energy; this is of interest both for the data processing (the background, due to secondary electrons is significantly reduced) and also for the smaller influence of stray magnetic field on the photoelectron.

Obviously, our experimental conditions are less favorable than those used in previous CDXPS experiments. The use of a two-crystal monochromator, instead of a grating optics, is really penalizing for flux consideration and especially for the loss in the circular polarization rate ($\tau < 0.3$). Nevertheless it presents several advantages related with the fact that almost all core-level spectra (for instance the $3d^{5/2}$, $3d^{3/2}$ of the rare earth) may be studied. Moreover, the fact that the kinetic energy of the photoelectron can be changed significantly may be of trivial interest for the study of surface magnetism, via the well known dependence of the mean free path of the photoelectron with its kinetic energy.

As seen in fig.1, a yoke made of μ -metal insured a closed guide for magnetic field, and the polished side of the yoke plays the role of substrate for the iron evaporated film. The iron film (thickness = 100 Å) was evaporated after a careful in situ cleaning of the μ -metal by argon sputtering at room temperature.

At least 8 hours were necessary to collect the XPS data for each direction of the magnetization. The experiments were done under UHV conditions ($P = 5.10^{-10}$ hPa) and the sample cleanliness was periodically checked by monitoring the O_{1s} and the C_{1s} XPS spectra (recorded using a conventional Al K α X-ray source).

For this experiment we need to maintain the magnetic field (a few mTeslas for the excitation field) during the measurements. In fact no remanence persists in the evaporated iron film as seen by the absence of any dichroic signal. This is coherent with the fact that the film is polycrystalline. The external magnetic field provided in the iron film a

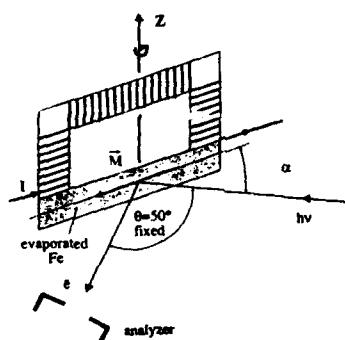


Fig. 1: Experimental condition: The iron film is directly evaporated on a flat side of the yoke, made of μ -metal. The in-plane excitation field of $H = 10$ Gauss lies in the incidence plane and is switched on during the data acquisition. Different emission angles are obtained by a rotation of the sample around the Z axis (The sample normal lies in the incidence plane).

magnetization direction lying in the incidence plane. The angle between the incident photon beam and the analyzer was fixed to 50° . Instead of changing the helicity (which implies to move up and down the optics by 0.6 mrad) we simply change the direction of the magnetization M for a given helicity to extract the Fe2p asymmetry.

This procedure is widely used and is equivalent to the one used by Baumgarten [8] where an angular analysis has been performed on Fe(100) single crystal within an equivalent experimental geometry.

Magnetic circular dichroism obtained by reversing the applied magnetic field with fixed helicity has been followed for different incidence (and emission) angles. The most important problem to solve for variable geometry is the energy shift of the photoelectron lines when M is changed; this shift is strongly emission angle dependent and is due to the distribution of the stray field around the sample. For each emission angle the value of the shift to introduce has been measured on the Fe2p lines by reversing the magnetization direction using linearly polarized light (where the magnetic stray fields are the unique origin of the shifts). This value never exceeded 50 meV. The resolution of the spectra allows us to fix the shift with a total incertitude better than 10 meV. Looking for 100 meV to 200 meV exchange shifted Fe2p $_{3/2}$ peaks this seems to be a reasonable way to extract correct values of asymmetry.

EXPERIMENTAL RESULTS.

In fig.2 we present the difference spectra $I(+M) - I(-M)$ obtained for different geometry [(a) normal emission, (b) 15° off-normal and (c) 25° off normal] when circularly polarized light of negative helicity is used. The energy step of the data shown in fig.2 is 0.24 eV.

The two photoemission spectra are compared after an adjustment of their backgrounds which have to match on both sides of the pair feature by averaging over several data points.

As shown in this figure, there is a significant dependence of the asymmetry factor with the emission angle.

The dependence of this difference on the experimental geometry can be given by [7]:

$$\sigma^+ - \sigma^- = \tau \cdot [4q \cdot M - 6(z \cdot q)(z \cdot M)] \quad (1)$$

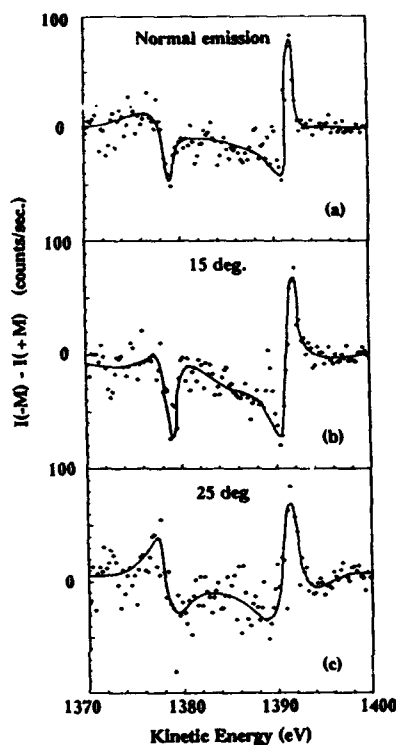


Fig. 2: Evolution of the intensity difference $I(-M) - I(+M)$ for different angles when circularly polarized light of negative helicity is used. (a) Data for the normal emission geometry with an incidence angle of $\alpha = 40^\circ$ with respect to the magnetization vector M . (b) Data for the 15° off normal emission angle with an incidence angle of $\alpha = 55^\circ$. (c) Data for the 25° off normal emission angle with an incidence angle of $\alpha = 65^\circ$.

where z , q and M are the unit vectors respectively of the direction of the photoelectron emission, the photon polarization vector and the magnetization. Whereas τ is the rate of circularly polarized light:

$$(I_{\text{left}} - I_{\text{right}}) / (I_{\text{left}} + I_{\text{right}}) = \tau$$

In our experiment the polarization rate is estimated to 20%. For the three different experimental geometries of fig.2 the predicted values using (1) are : 0.61 for the normal emission geometry (a), 0.65 for the 15° off normal (b), and 0.67 for the 25° off normal emission geometry.

The smooth evolution toward higher values of this calculated values is in clear opposition with our experimental data. If we scale our value on fig.2a (measured on the $2p_{3/2}$ line) with 0.61, we obtain in the case (b) 0.71 and for case (c) 0.51. The evolution of the experimental value is not coherent with the calculated ones and could not have his origin in a surface related component because of the high kinetic energies of the detected photoelectrons.

The same specific behaviour has been measured on Fe(100) single crystal [8], which demonstrates that the crystalline state is not the origin of the effect.

Our results make clear that the parameters governing the behaviour of the asymmetry factor are not completely described by the relative direction of the magnetization M with the polarization vector of the incident beam q and the direction of detection of the photoelectrons z .

In order to compare our data with those of Baumgarten [8] we subtract the background from the photoemission spectra as seen in fig.3 and normalize them to a signal to background ratio of 2. Below the total photoelectron spectrum (sum of two spectra taken with $+M$ and $-M$) we display in fig.3b the normalized intensity asymmetry $(I^+ - I^-)/(I^+ + I^-)$. The same normalization of the photoemission spectra has been made by Baumgarten [8]. This allows to compare the asymmetry values for both systems.

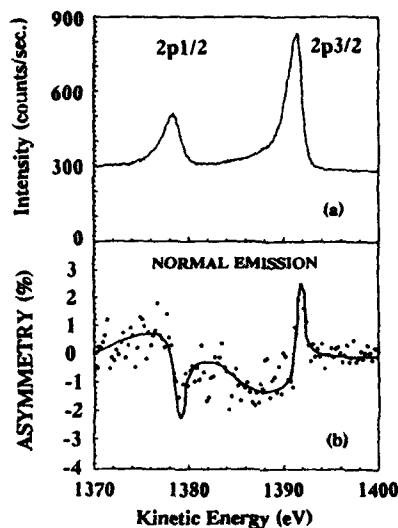


Fig. 3: (a) Normalized spectra after background subtraction (for details see text), average for +M and -M magnetization direction, when circularly polarized light of negative helicity is used. (b) The normalized intensity asymmetry $A = (I^+ - I^-)/(I^+ + I^-)$ after the above mentioned correction on the photoemission spectra. This value can directly be compared to ref.8.

The data presented in fig.3 were recorded when circularly polarized light of negative helicity is used in the geometry where the angle of incidence for the light is 50° with respect to the surface normal (or $\alpha = 40^\circ$ in fig.1) and consequently the emission is along the sample normal. The obtained peak to peak value for the $2p_{3/2}$ asymmetry is about 3.5%. Previous data of Baumgarten for Fe(100) taken in the same geometry shows a 12% asymmetry on the $2p_{3/2}$ line.

Our value is clearly reduced by a factor 3. The values for the 15° off normal emission ($\alpha = 55^\circ$) and for the 25° off normal emission ($\alpha = 65^\circ$) are respectively 6% and 4.5%. Also for these two angles the data of Baumgarten for Fe(100) are corresponding by a factor 3 (respectively 19% and 13%).

This difference can not be caused by an imperfectly magnetized sample since we estimate the applied field to be 10 times the saturation field for metal. The presented data have been recorded with a resolution of 0.4 eV to minimize the reduction of the asymmetry due to line broadening. This excludes an artificial reduction of our data to be the origin of the smaller values found.

This difference originates simply from the lower circular polarization rate in our experiment ($\approx 20\%$) as compared to that obtained with a grating optics in ref. 8 ($\approx 70\%$). In fact, the evolution observed presents qualitatively the same angular dependence of the asymmetry as in ref.8 for a Fe(100) single crystal. The angular variation of the asymmetry is therefore independent of the crystalline state of the magnetic material (implicit in formule (1)).

The origin of the strange behaviour of the asymmetry can be corelated to a crystal field effect, which could be superimposed to the classical effect. A detailed analysis of the photolines shows an intensity difference for the $2p_{3/2}$ lines taken for +M and -M, in addition to the observed shift which is in our case of 150 meV. This observation is clearly connected with the difference in intensity (in the opposite direction) energetically located between the $2p_{1/2}$ and $2p_{3/2}$ lines and is obviously connected to the angular dependence as observed on our data. Considering that the total integrated signal for the $2p_{3/2}$ photoelectron intensity has to be constant by reversing the magnetic field, the loss of intensity at 1391 eV is compensated by an enhancement at higher binding energies. In the framework of the atomic picture [10,11], Imada and Jo introduced crystal field and Coulomb interaction which give rise to a multiplet structure selectively excited by circularly

polarized light. The crystal field related photoelectron lines are energetically located between the 2p_{3/2} and 2p_{1/2} line.

This multiplet structure induced terms in the MCD signal could be partially responsible for our observed angular dependence, especially on the left part of the 2p_{3/2} MCD signal.

In order to draw definitive conclusions about the mechanism responsible for this angular variations, it is necessary to improve the data quality in order to discuss the fine structure of the MCD signal.

CONCLUSION.

The CDXPS results presented in this paper demonstrate the possibility to carry out such experiments on polycrystalline compounds in the non-remanent mode. The experimental results for Fe films are almost identical to those obtained in the remanent mode on Fe(100) single crystal. Such a similarity of the data shows that it is possible to overcome the difficulty, related with the presence of stray magnetic field during the experiments, and opens the possibility to study all the systems where the remanent magnetization is zero.

In particular we show that the variations of the asymmetry are not related to the crystalline state of the sample as suggested in [7]. Nevertheless the angular variation of the CDXPS asymmetry still remains poorly understood and requires further experimental and theoretical studies.

1. C. Brouder and M. Hikam, Phys. Rev. B 43, 3809 (1991)
2. G. Schütz, W. Wagner, W. Wilhelm, P. Kieule, R. Frahm and G. Materlik Phys. Rev. Lett. 58, 737 (1987)
3. H. Ebert, P. Strange and B.L. Gyorffy, Z. Phys. B 73, 77 (1988)
4. C.T. Chen, F. Sette, Y. Ma and S. Modesti, Phys. Rev. B 43, 7262 (1990)
5. G. van der Laan, B.T. Thole, G.A. Sawatzky, J.B. Goedkoop, J.C. Fuggle, J.M. Esteve, R. Karnatak, J.P. Remeika and H.A. Dabkoska, Phys. Rev. B 34, 6529 (1986)
6. J.B. Goedkoop, B.T. Thole, G. van der Laan, G.A. Sawatzky, F.M.F. de Groot and J.C. Fuggle, Phys. Rev. B 37, 2086 (1988)
7. C.M. Schneider, D. Venus, J. Kirschner Phys. Rev. B 45, 5041 (1992)
8. L. Baumgarten, PhD Thesis (1992)
9. G. van der Laan, M.A. Hoyland, M. Surman, C.F.J. Flipse and B.T. Thole, Phys. Rev. Lett. 69, 3827 (1992)
10. S. Imada and T. Jo, J. Phys. Soc. Jpn. 60, 2843 (1991)
11. G. van der Laan Phys. Rev. Lett. 66, 2527 (1991)
12. D. Venus, L. Baumgarten, C.M. Schneider, C. Boeglin and J. Kirschner, J. Phys.: Condensed Matter 5, 1239 (1993)
13. C. Brouder (privat communication).

STRONG MAGNETIC CIRCULAR DICHROISM IN 4f PHOTOEMISSION

KAI STARKE, E. NAVAS, L. BAUMGARTEN, AND G. KAINDL
Institut für Experimentalphysik, Freie Universität Berlin, Arnimallee 14,
W-1000 Berlin 33, Germany

ABSTRACT

We report on strong magnetic circular dichroism (MCD) in 4f photoemission (PE) from magnetized Gd(0001)/W(110) films. The shape of the $4f^{6-7}F_J$ final-state PE multiplet depends on the relative orientation between photon spin and sample magnetization and can be described within an atomic model. The spectra rule out antiferromagnetic alignment of the (0001) surface layer and the bulk of Gd. This MCD in 4f-PE from rare-earth materials opens new perspectives in the analysis of surface and thin-film magnetism and as a sensor for circular polarization of soft x-rays.

The availability of intense circularly polarized x-ray beams has recently led to a number of studies of magnetic circular dichroism (MCD) in photoabsorption and photoemission¹⁻⁷ of ferromagnetic materials. In case of MCD, the photoabsorption and photoemission (PE) processes depend on the relative orientation between photon spin and sample magnetization. MCD in PE was first observed in 2p core-level spectra from ferromagnetic Fe(110)¹ and was explained in terms of spin-selective dipolar transitions in the presence of spin-orbit coupling^{1,2}. Several theoretical treatments of the observed MCD effects in PE have been given^{2,6,7}.

In the present contribution we report on the observation of MCD in 4f PE from magnetized Gd(0001) films grown epitaxially on W(110). The shape of the $4f^{6-7}F_J$ final-state PE multiplet exhibits a strong dependence on the relative orientation between photon spin and sample magnetization. Even with the circular polarization of the synchrotron radiation beam amounting to only 55%, a 30-% MCD effect has been observed. Due to the localized nature of the 4f states in Gd, this MCD in PE can be explained within an atomic model making use of the dipole-selection rules. From MCD spectra recorded with high surface sensitivity at $h\nu=48$ eV, antiferromagnetic alignment of the (0001) surface layer and the bulk of Gd can be ruled out⁸. This strong MCD in 4f PE carries a substantial potential as an analytical tool in surface and thin-film magnetism and for an absolute determination of the degree of circular polarization of soft x-rays.

The experiments were performed with circularly polarized soft x-rays from two different monochromators at the Berliner Elektronenspeicherring für Synchrotronstrahlung (BESSY): the plane-grating SX700/III at a bending magnet⁹ and the U2-FSGM at the crossed undulator¹⁰.

Epitaxial Gd(0001) films with a thickness of 80 ± 10 Å were prepared by vapor deposition of Gd onto a clean and well-ordered W(110) substrate at room temperature (base pressure $< 8 \cdot 10^{-11}$ mbar); this results in a layer-by-layer growth of the first few layers of Gd^{8,11}. As confirmed by LEED, a well-ordered Gd film was obtained by a subsequent brief annealing at 870 K¹¹. The thickness of the film was monitored by a quartz micro balance and calibrated via the relative intensities of the 4f PE lines from Gd and W. Chemical cleanliness was checked by monitoring the O-2p PE intensity, which has been found to be sensitive to O₂ exposures as low as 0.01 L. Gd(0001) films are known to be magnetized entirely in plane¹² with only few magnetic domains, which was checked *in situ* by magneto-optical Kerr-effect (MOKE). The PE spectra were taken with the

Gd(0001) film remanently magnetized in the plane of incidence of the photon beam, achieved by magnetizing pulses of $H_{\text{max}}=360$ A/cm applied through a closely solenoid. The circularly polarized light was incident at an angle of 15° with respect to the film plane and the photoelectrons were collected around the surface normal using a hemispherical electron-energy analyzer with moderate angular resolution ($\pm 10^\circ$); the experimental geometry is given in the inset of Fig. 1

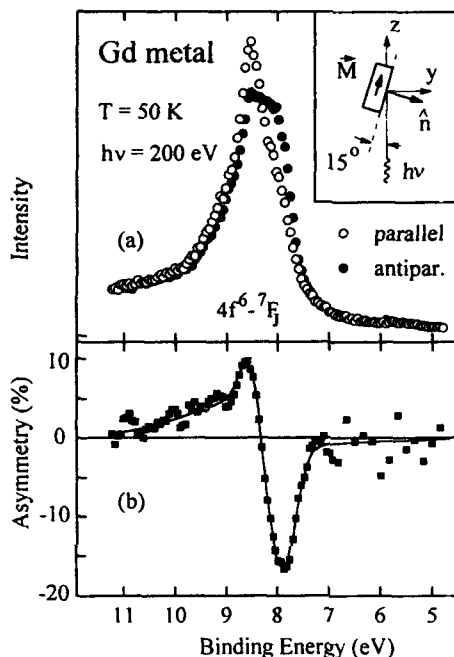


FIG. 1. (a) Gd-4f PE spectra ($h\nu=200$ eV) of a remanently magnetized Gd(0001)/W(110) film. The open (filled) dots are for parallel (antiparallel) orientation of photon spin and sample magnetization. (b) Asymmetry $(I_{\uparrow\uparrow} - I_{\uparrow\downarrow}) / (I_{\uparrow\uparrow} + I_{\uparrow\downarrow})$ calculated from the raw experimental spectra in (a). The inset gives schematically the experimental geometry.

ing use of the dipole selection rules, $\Delta J=0, \pm 1$ and $\Delta M_J=\pm 1$, that connect the fully magnetized ground state, $^8S_{7/2} (J=7/2, M_J=7/2)$, with final states $|J', M_J'\rangle$; the latter are formed by coupling the angular momenta of the PE final states (7F_J multiplet) with those of the detected photoelectron. For the photoelectron only $4f \rightarrow \epsilon g$ transitions were considered since contributions from $4f \rightarrow \epsilon d$ are estimated to be negligibly small in the present context.

The results of this atomic calculation for the relative contributions of the 7F_J multiplet components are presented graphically in Fig. 2(a) for parallel orientation ($\Delta M_J=+1$) and in Fig. 2(b) for antiparallel orientation ($\Delta M_J=-1$). The energy spacings between the multiplet sublevels were chosen according to the Landé-interval rule. Also shown in Fig. 2 are the experimental spectra from Fig. 1, however, normalized to 100% circular polarization of the photon beam in order to facilitate a comparison with the theoretical multiplets. Note

Fig. 1

Fig. 1(a) shows Gd-4f PE spectra obtained with circularly polarized light from the SX700/III for a remanently magnetized Gd(0001)/W(110) film at ≈ 50 K for parallel (open dots) and antiparallel (full dots) orientation of photon spin and sample magnetization, respectively. For both orientations, the spectral shapes deviate markedly from the well-known shape of the paramagnetic $4f^6-^7F_J$ final-state multiplet⁸. For parallel orientation, the 4f spectrum (open dots) yields a sharp "fir-tree-like" structure, which changes to a broad and rounded structure (filled dots) upon reversal of magnetization. The asymmetry $(I_{\uparrow\uparrow} - I_{\uparrow\downarrow}) / (I_{\uparrow\uparrow} + I_{\uparrow\downarrow})$, calculated from the raw experimental data, is plotted in (b); it amounts to $\approx 30\%$, which is by far the strongest MCD effect in PE observed so far.

Due to the localized nature of the 4f states in Gd, the 4f PE process can be described within an atomic model mak-

the good *qualitative* agreement of the peak shapes of the normalized spectra with the theoretical multiplet shapes.

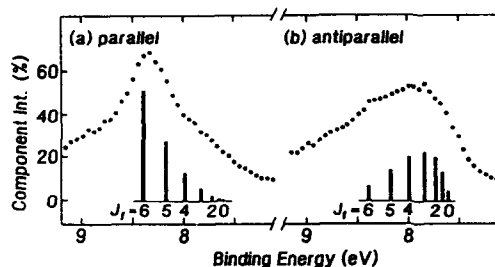


Fig. 2. Calculated relative intensities of the $4f^{6.7}F_j$ final-state PE multiplet components for (a) parallel ($\Delta M_j = +1$) and (b) antiparallel ($\Delta M_j = -1$) orientation between photon spin and sample magnetization. For comparison, the experimental spectra from Fig. 1, normalized to 100% circular polarization, are also given.

(0001) surface of Gd and the bulk¹⁴. (3) The circular polarization of the photon beams used was incomplete: the residual light is linearly polarized in the storage-ring plane in

case of the SX700/III positioned at a bending magnet⁹, while it is unpolarized in case of the crossed undulator¹⁰.

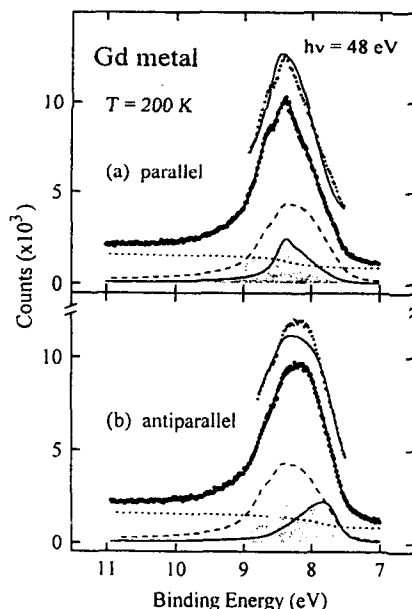


FIG. 3. Gd-4f PE spectra taken with circularly polarized 48-eV photons from the crossed undulator at BESSY. The (0001) surface layer (grey-shaded components) is ferromagnetically aligned to the bulk of Gd (solid subspectra). The dashed components, which are identical in spectra (a) and (b), represent the sum of the paramagnetic bulk and surface signals due to unpolarized light and the finite sample temperature. The solid curves through the peaks displaced vertically represent the best fit results for hypothetical antiferromagnetic alignment of surface layer and bulk.

In this way the spectra of Fig. 1(a) can be simultaneously least-squares fitted with a common parameter set assuming theoretical relative intensities of the $7F_j$ multiplet lines for parallel and antiparallel orientation and Doniach-Sunjić line shapes; due to the finite

angle between the light-propagation direction and the surface plane of the sample, the magnetization has a non-vanishing component M_y parallel to the linear polarization vector (see inset in Fig. 1), which leads to weak transitions with $\Delta M_J=0$. In addition, bulk PE contributions with opposite ΔM_J were included in each case, caused by the incomplete circular polarization of the photon beam, as well as surface core-level shifted components from a ferromagnetically aligned outermost surface layer. Significantly worse fits were obtained when an antiferromagnetically aligned or a paramagnetic outermost surface layer was assumed. For reasons of space, these fits of the MCD PE spectra taken at the SX700/III are not shown¹⁵.

In order to enhance the surface contribution, MCD PE spectra were also taken at $h\nu=48$ eV (see Fig. 3). In this case circularly polarized light from the crossed undulator was employed to avoid $\Delta M_J=0$ contributions to the spectra. The two spectra for parallel and antiparallel orientation exhibit clearly visible shoulders on the high binding-energy sides, which are a consequence of relatively strong surface contributions (surface-to-bulk intensity ratio \approx about 1.1 to 1); such shoulders have not been resolved with unpolarized light^{8,13,14}.

The subspectra in Fig. 3 are again the results of a simultaneous fit of the two spectra with a common parameter set, assuming ferromagnetic alignment of the (0001) surface layer and the Bulk of Gd.

Antiferromagnetic coupling, as shown in the vertically displaced peaks in Fig. 3, led to significantly larger misfits; similarly large misfits were obtained under the assumption of a paramagnetic surface layer (results not shown here). Thus MCD in 4f PE provides a further strong evidence for ferromagnetic alignment of the (0001) surface layer of Gd and the bulk.

Due to the strength of the observed effect MCD in 4f-PE from Gd - and also from other rare-earth elements - will enable studies of surface and thin-film magnetism with the ease of conventional PE measurements. The possibility to exploit 3d \rightarrow 4f and 4d \rightarrow 4f resonant PE allows studies with substantially increased sensitivity as well as in an element specific way. In addition, the magnitude of the 4f-PE MCD effect offers particularly attractive perspectives for magnetic imaging applications.

The atomic description of the observed MCD effect in 4f PE provides a way to quantitatively measure the degree of circular polarization in the soft x-ray region over a wide range of photon energies from about 40 eV up to well beyond the 3d \rightarrow 4f threshold (at \approx 1190 eV for Gd). Further work in this direction, both with different Gd systems and with other rare-earth elements, is in progress in our laboratory.

Acknowledgements:

This work was supported by the Bundesminister für Forschung und Technologie, project No. 05-5KEAXI-3/TP01, and the Sfb-290/TPA6 of the Deutsche Forschungsgemeinschaft.

References:

- ¹ L. Baumgarten, C.M. Schneider, H. Petersen, F. Schäfers, and J. Kirschner, Phys. Rev. Lett. **65**, 482 (1990).
- ² H. Ebert, L. Baumgarten, C.M. Schneider, and J. Kirschner, Phys. Rev. B **44**, 4406 (1991).

- 3 C.M. Schneider, M.S. Hammond, P. Schuster, A. Cebollada, R. Miranda, and J. Kirschner, Phys. Rev. B **44**, 12066 (1991).
- 4 C.M. Schneider, D. Venus, and J. Kirschner, Phys. Rev. B **45**, 5041 (1992).
- 5 G.D. Waddill, J.G. Tobin, and D.D. Papas, Phys. Rev. B **46**, 552 (1992).
- 6 B.T. Thole and G. van der Laan, Phys. Rev. B **44**, 12424 (1991).
- 7 S. Imada and T. Jo, J. Phys. Soc. Jap. **60**, 2843 (1991).
- 8 D. Weller, S.F. Alvarado, W. Gudat, K. Schröder, and M. Campagna, Phys. Rev. Lett. **54**, 1555 (1985).
- 9 M. Willmann, H. Petersen, F. Schäfer, M. Mast, B.R. Müller, and W. Gudat, BESSY Jahresbericht (1991).
- 10 J. Bahrdt, A. Gaupp, W. Gudat, M. Mast, K. Molter, W.B. Peatman, M. Scheer, Th. Schroeter, and Ch. Wang, Rev. Sci. Instrum. **63**, 339 (1992).
- 11 U. Stetter, M. Farle, K. Baberschke, and W.G. Clark, Phys. Rev. B **45**, 503 (1992).
- 12 M. Farle, A. Berghaus, and K. Baberschke, Phys. Rev. B **39**, 4838 (1989).
- 13 R. Kammerer, J. Barth, F. Gerken, A. Flodström, and L.I. Johansson, Sol. State Commun. **41**, 435 (1982).
- 14 G. A. Mulhollan, K. Garrison, and J. L. Erskine, Phys. Rev. Lett. **69**, 3240 (1992).
- 15 K. Starke, E. Navas, L. Baumgarten, and G. Kaindl, Phys. Rev. B **48** (in print).

Section B—Interfaces and Characterization

PART III

**Structural and Interfacial
Characterization**

MAGNETIC AND STRUCTURAL ANALYSIS OF ULTRA-THIN MAGNETIC FILMS, MULTILAYERS, AND SUPERLATTICES BY MÖSSBAUER SPECTROSCOPY

J. FREELAND, D. KEAVNEY, D. STORM, AND J. CALVIN WALKER
Johns Hopkins University, Department of Physics and Astronomy, Baltimore,
Maryland 21218

In the study of thin films and surfaces as well as the examination of superlattices, the careful characterization of these systems including their structural, magnetic, transport, and other properties has been absolutely crucial to the advancement of the field. As means of sample preparation have progressed, techniques for evaluating the flatness, continuity, crystallinity, etc. of thin films and surfaces have become ever more necessary to understand the resulting magnetic and electronic properties. Because iron is often a constituent of *magnetic* thin films and because the isotope ^{57}Fe shows a strong Mössbauer Effect over a wide temperature range the technique of Mössbauer Spectroscopy offers much to the study of surfaces, thin films, and superlattices.

Mössbauer spectroscopy depends on the achievement in a very special way of nuclear resonance fluorescence. In the case of nuclear transitions, photon energies are typically in the range from tens of thousands to millions of electron volts. Typically recoil energies in both the emission and absorption processes are greater than linewidths and very little resonance fluorescence takes place. Mössbauer was studying this unlikely phenomenon when he made his discovery: when nuclear photon energies aren't too high (~ 10 -100 keV) and the atom containing the excited nucleus is firmly bound in a stiff solid at moderate-to-low temperatures, there is a significant probability that the only lattice-vibrational normal mode excited as a result of the photon emission is the zero-frequency ($\omega=0$) mode. This implies that the recoil momentum is taken up by the entire lattice, not just the recoiling nucleus. In this case there is negligible recoil energy loss. The same process can also occur in resonance absorption. An additional bonus - very important for Mössbauer spectroscopy - is the fact that the first order doppler line-broadening caused by thermal vibration of the emitting nucleus disappears in the Mössbauer Effect.

For ^{57}Fe , with a 14.4 keV nuclear transition energy to the ground state, a recoil-free fraction of gamma emissions in Fe metal is .81 at room temperature. This high fraction can be attributed to the rather low nuclear transition energy and to the significant lattice stiffness associated with Fe metal.

As mentioned above, the doppler-broadening of the emitted or absorbed gamma line-width cancels out to first order in v/c . Here v is speed of the emitting or absorbing nucleus associated with thermal vibrations. This eliminates the major source of gamma line-broadening and for a high quality crystalline source and absorber the gamma line width will be close to the value given by the uncertainty principle. Using the 100ns lifetime of the 14.4 keV level of ^{57}Fe as the measurement time uncertainty: $E \sim 10^{-6}\text{eV}$. This implies a resolution $E/\Delta E$ of about 10^{12} which offers an explanation for the efficacy of Mössbauer spectroscopy for looking in small energy shifts associated with solid-state systems.

Mössbauer spectroscopy makes use of gamma ray emission from an excited nucleus bound in a solid. As the gamma transitions are usually very short-lived, (^{57}Fe is long at 100ns.) the excited nuclear state which normally decays to the nuclear

ground state is usually fed by a conveniently long-lived beta-emitting state which decays to the relevant gamma emitting state. In the case of ^{57}Fe the beta-emitting parent, ^{57}Co , decays primarily to the 136 keV state of ^{57}Fe (Figure 1). This second excited state decays very rapidly primarily to the 14.4 keV first excited state with the emission of a 122 keV gamma ray. The subsequent decay of the 14.4 keV state provides the gamma rays used for Mössbauer spectroscopy in ^{57}Fe . It should be noted that only 2.17% of natural Fe is ^{57}Fe . The rest of the Fe, consisting mainly of ^{56}Fe , shows no Mössbauer effect. This can be exploited in a very interesting way as we demonstrate below.

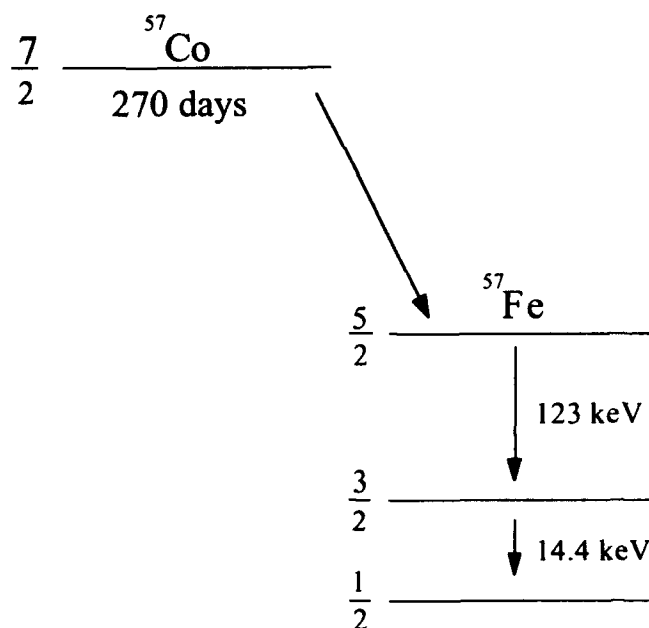


Figure 1. Decay scheme for ^{57}Co to ^{57}Fe

In the case of ^{57}Fe the 14.4 keV transition is from a $J = 3/2$ nuclear level to a $J = 1/2$ ground state. The nuclear moments, magnetic and electric quadrupole, associated with these levels interact with magnetic and electric fields at the nucleus to produce a hyperfine splitting of the nuclear levels. Because these moments are independently known, a determination of the hyperfine splittings for a particular sample determines the magnetic field and electric field gradient at the nucleus. Both of these quantities provide very useful information when studying thin films, surfaces, or superlattices. The magnetic hyperfine interaction produces a nuclear Zeeman effect with equal spacing of the magnetic sublevels of the $J = 3/2$ excited state (Figure 2).

To obtain maximum information about a magnetic system using Mössbauer spectroscopy requires the ability to take spectra with the sample kept accurately at temperatures ranging from 4.2 (normal liquid He) to 600-700 K (temperatures above which irreversible changes in thin film or superlattice systems can occur.) Various techniques have been devised to deal with this matter. Flow cryostats with resistance heaters, thermal sensors, and electronic temperature controllers can hold temperatures to ± 0.1 K indefinitely at significant cost for liquid coolants (particularly at the lower temperatures). We have found the most satisfactory solution in a helium gas refrigerator system¹ that requires no liquid coolants and includes temperature control as good or better than flow cryostats. Refrigerator systems can have vibration problems due to vigorous motion of the displacer piston in the cooling head. This can cause serious line-broadening in the Mössbauer spectra. Modern commercial units have overcome this completely by isolating the cooling station from the mechanical part of the system and conducting heat away from the station using cold helium gas. No mechanical connection means no line broadening in the system and the operator can easily stabilize any temperatures between 10 K and 400 K. For higher temperatures a specialized temperature-controlled oven is used.

Information Obtainable From Mössbauer Spectra

A typical Mössbauer spectrum shown in Figure 2 contains a great deal of information. The nuclear transition from the $j = 3/2$ 14.4 keV excited state to the $j = 1/2$ ground state is an M1 (magnetic dipole) transition with selection rules $m = 0, \pm 1$. In the case in which a magnetic splitting of the $3/2$ level into $m = \pm 3/2$ and $m = \pm 1/2$ levels and the $1/2$ level into $m = \pm 1/2$ levels occurs, six of the possible eight transitions are allowed. This shows in the spectrum as six lines. The transitions included by magnetic dipole selection rules $m = +3/2 \rightarrow m = -1/2$ and $m = -3/2 \rightarrow m = +1/2$ do not appear. The relative intensities of the transitions are also very interesting. The transition probabilities are the *squares* of Clebsch-Gordon coefficients appropriate to these angular momentum states. They depend not only on the j and m values but also on the angle between the direction of the detected gamma ray and the direction of the magnetic field producing the Zeeman splitting of the nuclear levels. For an *unmagnetized* Fe absorber in which the direction of the magnetic field at the nucleus is random (due to domains) the six lines have intensity ratios 3:2:1:1:2:3. Of course the *unmagnetized* Fe is still magnetically ordered within a domain so that the nucleus still "sees" a net magnetic hyperfine field produced by the surrounding electrons. Bulk Fe shows this magnetic order below the Curie temperature of 1040 K.

Our thin films and superlattices usually involve magnetized films of Fe thinner than 100 layers which have single domains and in the absence of significant surface anisotropy are magnetized in-plane. In this case the ratios of Mössbauer spectral lines are 3:4:1:1:4:3. When large surface anisotropy effects overcome the dipolar shape effects and lead to a magnetization perpendicular to the film surface (and therefore parallel to the gamma ray direction in a transmission Mössbauer measurement) the transition probabilities for the $+1/2 \rightarrow +1/2$ and $-1/2 \rightarrow -1/2$ $\Delta m = 0$ transitions become zero. In this interesting case the line intensities become 3:0:1:1:0:3.

In general the line intensity relation is given by:

$$3:x:1:1:x:3 \quad x = 4 \sin^2(\theta/2) / (1 + \cos^2\theta)$$

where θ is the angle between the gamma ray and the direction of the magnetization M . In pure bulk Fe the magnetic hyperfine field is 341 kilo-oersteds at 4.2K and 333 kilo-oersteds at 295K. Because the magnetic moments of the nuclear ^{57}Fe and ^{59}Fe levels are independently known, the Mössbauer spectrum shown in Figure 2 yields values for the hyperfine fields from an appropriate least-squares fit to the spectrum.

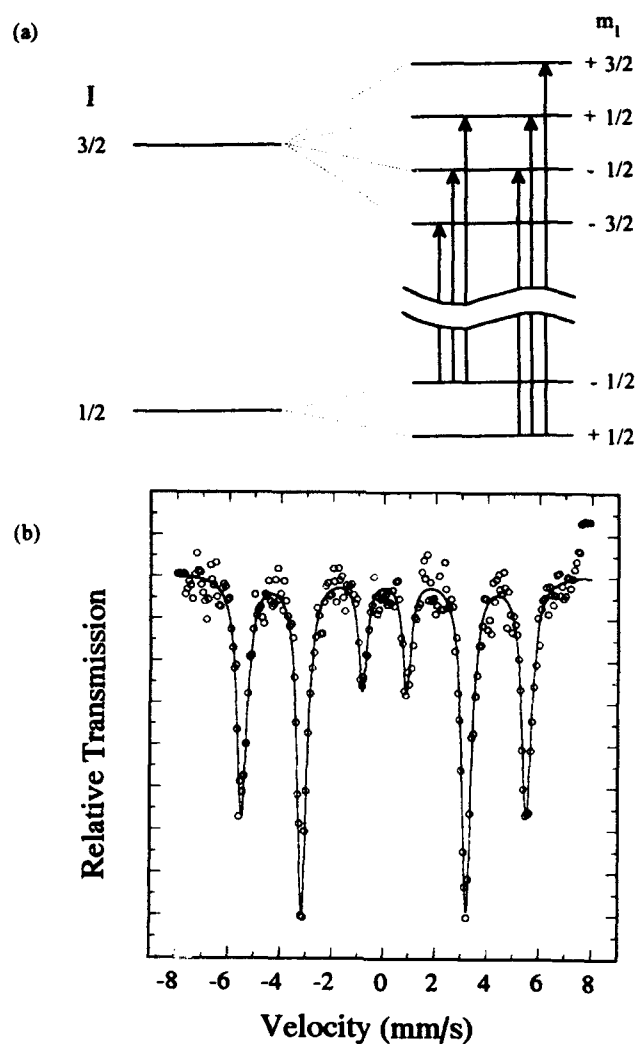


Figure 2. (a) Magnetic hyperfine splittings of the ground state and first excited state of ^{57}Fe . The six allowed $M1$ transitions are indicated. A typical absorption spectrum from transmission Mössbauer spectroscopy is shown in (b).

The magnetic hyperfine field at the nucleus depends in a complicated way on the magnetic properties of host lattice. In a paramagnetic metal or alloy the hyperfine field at the nucleus rapidly relaxes in spatial direction due to the spin-spin relaxation associated with the thermal lattice energy kT . This results in no *net* magnetic field at the nucleus over the time comparable to the Larmor precession period of the nuclear moment in the (non-static) magnetic field produced by the electrons around the nucleus. In making a ^{57}Co radioactive source for obtaining the initial resonant gamma rays for Mössbauer spectroscopy this is used to produce a magnetically "unsplit" single line gamma source. Typically ^{57}Co is diffused into Rhodium. The resulting paramagnetic alloy also has cubic symmetry so that the source line is "unsplit" either by magnetic or electric quadrupole hyperfine interactions.

Conversion Electron Mössbauer Spectroscopy - CEMS

In this variant of conventional transmission Mössbauer spectroscopy, advantage is taken of the fact that nature provides a means of de-excitation of the 14.4 keV nuclear excited state of ^{57}Fe other than photon emission. An excited nucleus may de-excite by transferring its energy to one of the inner electrons which have some appreciable density at the nucleus (typically s-electrons). In the case of ^{57}Fe this "internal conversion" occurs *nine* times more often than emission of a 14.4 keV photon.

This forms the basis for Mössbauer spectroscopy in cases in which the thin film or superlattice system is not transparent to 14.4 keV gammas. This occurs, for example with very dense or thick single crystal substrates such as tungsten or GaAs. A scattering geometry is appropriate with 14.4 keV gammas from a ^{57}Co source incident on the Mössbauer scatterer which is often much smaller than a transmission geometry absorber. When the source is doppler-shifted into resonance with the scatterer, a recoilless Mössbauer absorption takes place, temporarily leaving some ^{57}Fe nuclei in the scatterer in an excited state. These nuclei de-excite primarily by "internal conversion" which results in the ejection of a κ -electron of about 7 keV energy. The resulting excited atom with a κ -shell hole will de-excite by emitting a 6.4 keV x-ray or (about 50% of the time) by emitting a number of outer-shell electrons by the Auger process. The spectrum of electrons from these processes is not sharply defined in energy, but tends to have lower energy than "noise" electrons from photoelectric or Compton processes. More sophisticated Conversion Electron Mössbauer Spectrometers (CEMS) pass these electrons through a rather broad-band electron spectrometer before they are detected by a channeltron or other suitable electron detector. The signal-to-noise ratio for such a sophisticated system can be very high, although dense substrates such as tungsten can produce significant noise problems. The high sensitivity and large signal-to-noise ratios have permitted Mössbauer spectroscopy of Fe films of mono-layer thickness, while the thinnest films for which transmission spectra are reported are about two monolayers. Because electrons in this energy range are not very penetrating, the entire spectrometer must be evacuated, while transmission experiments don't usually require vacuum except as part of the absorber cooling system. The need for a vacuum for CEMS has been turned to advantage by some groups by having the film production inside the same vacuum system as the Mössbauer spectrometer. In principle this might mean that no protective covering layer would have to be put over the Fe before Mössbauer measurements. In practice a great deal of time (~15 hrs.) must elapse before enough

counts are recorded to provide a Mössbauer spectrum with good counting statistics. It is not possible to keep a bare Fe surface free of contamination during such a time.

Because one is counting electrons which cannot escape from very deep in the sample, CEMS is more surface sensitive than transmission experiments. In practice, however, surface sensitivity is achieved by making Fe films from isotopically pure ^{56}Fe which shows no Mössbauer effect and then depositing one or two atomic layers of isotopically pure ^{57}Fe at or near the Fe film surface.² In this way genuine surface sensitivity is achieved by both Mössbauer spectroscopy geometries.

Example of Mössbauer Spectroscopy Applied to the Study of Magnetic Thin Films, Surfaces, and Superlattices

We conclude our discussion of Mössbauer spectroscopy applied to the study of magnetic thin films, superlattices, and surfaces with a discussion of our experiment in which Mössbauer spectroscopy provided the critical information about the interlayer coupling in Fe(110)/Ag(111) multilayers grown by molecular beam epitaxy (MBE). Previous work by this group has shown the existence of interlayer coupling in this multilayer system.³ In that work, the existence of interlayer coupling was inferred from the observation of a dimensional crossover in the spin-wave spectrum of 3 ML Fe(110) layers from quasi 2-D to 3-D as the Ag(111) interlayer thickness decreased. Because of that dimensional crossover, it was not possible to detect oscillations in coupling strength. To see such oscillations, it is necessary to compare samples which exhibit the same dimensionality in their spin-wave behavior.

In this experiment we have used the surface sensitive technique to detect interlayer exchange coupling of thick Fe layers through the nonmagnetic Ag layers. To do so we use the fact that the spin wave spectrum exhibited by an interfacial Fe atom is different from that of a bulk Fe atom. Since Fe atoms at the interface have a lower coordination number, it is easier for thermal fluctuations to deflect their spins, resulting in a softer spin wave spectrum. This is observable in the temperature dependence of the hyperfine magnetic field. As long as one stays within the spin wave regime (typically $0.3 T_c$), the hyperfine fields at both the interface and the bulk will follow the Bloch ($1-BT^{3/2}$) form very closely. The interfacial Fe atoms will have a larger $T^{3/2}$ prefactor than the bulk, and the hyperfine field at the interface will fall off faster. Mills and Maradudin⁴ have shown that the value of B , called the spin wave stiffness parameter, at a free ferromagnetic surface is twice that of the bulk. For the case of an Fe/Ag multilayer, the interfacial Fe atoms will experience a bulk exchange J_0 with nearest neighbors within an Fe bilayer component, and a weaker interaction J_1 with Fe atoms in adjacent Fe bilayers. The strength of that interlayer exchange can then be investigated by the surface sensitive technique described above.

In this work all the films were grown by MBE on a thick, single-crystal Ag(111) substrate which was grown *in situ* on a mica substrate. The Fe bilayer thickness was kept fixed at 22 ML, and the Ag interlayer thickness was varied between 0 and 40 ML. Of the 22 ML Fe layers, 20 ML were composed of natural Fe, and the 2 ML at the interface was composed of 95.7% enriched ^{57}Fe . Given the relative abundance of ^{57}Fe in natural Fe, and assuming no interdiffusion, this results in 92% of the ^{57}Fe in the sample being separated to the interface. We have found that when the 2 ML probe layer is placed at a "free" Fe/Ag interface, the measured spin-wave spectrum at the probe layer follows a surface spin-wave spectrum very closely. This indicates that the interdiffusion of ^{57}Fe into the 20 ML natural Fe layer is negligible.

Therefore the Mössbauer spectra obtained from such samples correspond to the interface region. In this way we can measure the spin wave spectrum *only* at the interface. It is worthwhile to note that this technique does not require the presence of an external field, which makes it a very powerful technique for studying weak antiferromagnetic interactions between Fe layers. In addition, traditional magnetometry techniques would provide no information on coupling strength in *ferromagnetically* coupled layers.

All the samples discussed in this paper followed the Bloch law very closely, as would be expected for a 22 ML Fe film. The temperature dependent hyperfine fields were then fit to a $(1-BT^{2/3})$ form. The results of these fits are shown in Figure 3 (dashed line) and indicate clear oscillations with a period of 6 ML in the surface spin-wave stiffness parameter $B(y)$ superimposed upon the expected increase from the bulk value $B(0)$ to twice $B(0)$. Also shown in Figure 3 is a prediction of $B(y)$ based on the RKKY model of ref. 4, with a period of 6 ML (solid line). The lines in this figure are meant only as guides to the eye to show that at every dip in the data, the prediction has a corresponding dip. This oscillating behavior can be understood in the framework of an oscillating J_1 and a J_0 which remains fixed. Using this model, Green's function calculations can be performed in the spin-wave approximation to obtain $B(y)$ from $J_1(y)$.⁵ As J_1 passes through zero, $B(y)$ must increase to its free interface value, and as J_1 reaches an extremum, the Fe spins at the interface become more "bulk-like", resulting in a drop in $B(y)$ toward the bulk value. It is this feature which makes this technique very sensitive to weak oscillations in coupling strength. The observed periodicity of 6 ML compares very favorably with the prediction of 5.94 ML for Ag(111) from recent theoretical efforts.⁶ It should be pointed out that the magnitude of the oscillations predicted by the RKKY theory does not match the observations very closely. This can be very sensitive to the overall quality of the interface, with reduced oscillation amplitudes resulting from interfacial roughness. Since the RKKY theory used above does not account for any roughness, the real test should be whether the oscillation periods are accurately predicted.

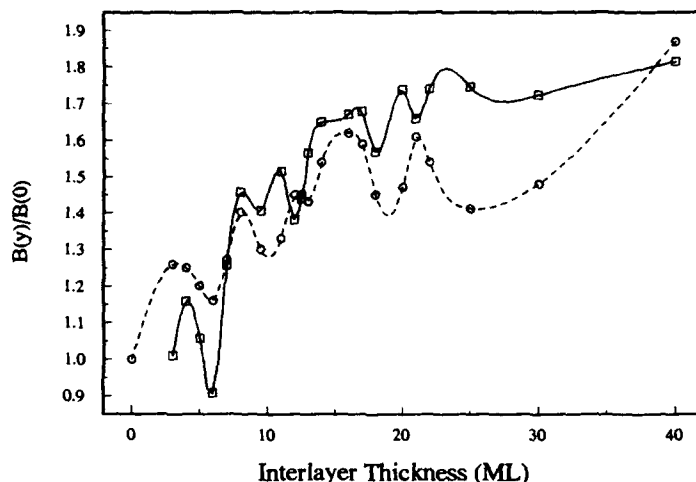


Figure 3. Spin-wave stiffness parameter for Fe(110)/Ag(111) multilayers. Oscillations show variations in interlayer coupling strength J_1 . The dashed line is experimental data, and the solid line is a fit based on the extended RKKY model.

1. ADP Cryogenics, Inc. 1833 Vultee St., Allentown, PA.
2. J. Tyson, A. Owens, J.C. Walker, *J. Mag. Magn. Mat.* **35** (1983) p. 126-129.
3. C.J. Gutierrez, Z.Q. Qui, M.D. Wiecsorek, H. Tang with J.C. Walker, *Phys. Rev. B* **44** (1991-I) p.2190.
4. D.L. Mills and A.A. Maradudin, *J. Phys. Chem. Solids*, **28**, 1855 (1967).
5. M. Maccio, M.G. Pini, P. Politi and A. Rettori, *Phys. Rev. B* **44** (1991-I) p.2190.
6. P. Bruno and C. Chappert, *Phys. Rev. B* **26**, 261 (1992); P. Bruno, *J. Magn. Magn. Meter* **116**, L13 (1992).

AUGER ELECTRON AND PHOTOELECTRON DIFFRACTION IN MAGNETIC THIN FILMS

Y.U. IDZERDA* and D.E. RAMAKER**

*Naval Research Laboratory, Washington, D.C. 20375

**Dept. of Chemistry, George Washington University, Washington, D.C. 20052

ABSTRACT

The role of the final-state character of the emitted electron in Auger electron diffraction (AED) and x-ray photoelectron diffraction (XPD) is examined with respect to magnetic materials. Single scattering cluster calculations with the inclusion of the spherical wave character and the final-state character of the emitted electron (both angular momentum quantum number and magnetic quantum number) show that selective emission from different m-levels, generated by a non-statistical distribution of initial m-levels or by an m-selective excitation process, results in distinctly different emission patterns.

INTRODUCTION

X-ray photoelectron diffraction (XPD) and Auger electron diffraction (AED) have been used extensively over the last decade to determine the structure of ultra-thin films¹⁻⁴. At high electron kinetic energies (>300 eV), these closely related techniques have found successful application for ultra-thin films and overlayers in determining the complete structure (in-plane and out-of-plane lattice constants)¹⁻⁴, the film growth mode^{5,6}, and even to resolve surface reconstructions⁷. The measured experimental spectra can be accurately reproduced by quantum mechanical electron scattering theories¹⁻⁴. Complete angular intensity mappings can also be successfully Fourier transformed under appropriate conditions to form electron holograms⁸⁻¹¹.

One of the early successes of XPD was the investigation of the growth and structure of Fe/Cu(001)^{12,13} lending insight into the complicated and controversial magnetic behavior of the Fe overlayers¹⁴. Many subsequent studies have demonstrated the utility of high energy AED and XPD in resolving structural problems which impact thin film magnetic properties. For example, AED studies have confirmed the single-crystal growth of both bcc Fe/GaAs and bcc Co/GaAs¹⁵, and have provided convincing evidence for the body-centered tetragonal (bct) phase of Mn/Ag¹⁶, thought to be responsible for the absence of ferromagnetism in the Mn^{17,18}. A growth mode determination for the Ni/Cu(001) system⁶ confirmed the layer-by-layer growth of the Ni required for an understanding of the thickness dependent curie temperature¹⁹. Most AED and XPD studies on magnetic systems have focussed on the structural and morphological aspects of the magnetic thin films, inferring implications for their observed magnetic behavior.

A recent development in the understanding of AED and XPD, which has ramifications for magnetic thin films, is the recognition of the importance of the wave-function character of the emitted electron. Early works demonstrated the

importance of including the spherical nature of the outgoing electron in the scattering process²⁰. After the inclusion of the spherical wave, calculations showed that the angular momentum character of the emitted electron plays a significant role in the scattering process, especially at lower electron kinetic energies^{21,22}. In mapping the intensity of low energy Auger electrons from a variety of materials, Frank *et al.*²³ experimentally found angular distributions in stark contrast to the "forward scattering" picture applicable to high energies. Instead of intensity maxima along inter-nuclear directions, they detected intensity minima. To describe these minima, they proposed a physical model utilizing a more classical approach of electron attenuation. In this "blocking" model, atoms lying between the detector and the atomic site of the electron emission block transmission of the electron. The angular intensity pattern consists of "silhouettes" of atoms, "back-lit" by the electron emission.

This model was counter to the widely accepted forward scattering picture, especially at higher energies, and produced strong objections²⁴. To investigate this apparent controversy, Terminello and Barton²⁵ examined isoenergetic Auger electrons and photoelectrons in an attempt to isolate the source of the phenomena observed by Frank *et al.* Interestingly, they found that the angular distribution pattern for the $M_{23}M_{45}M_{45}$ Auger electron and the Cu $3p_{3/2}$ photoelectron, taken from a Cu(001) substrate at nearly the same energy (56.6 eV), were strikingly different: The Auger emission showed an intensity minimum in the surface normal direction while the photoemission showed an intensity maximum. It has since been determined by a variety of investigators^{11,21,22,26,27} that the reason for these different angular distributions is the different character (final-state) of the emitted electron.

In this report, we continue to examine the role of final-state effects and how they relate to the intensity patterns from magnetic materials. We demonstrate that not only is the angular momentum quantum number, ℓ , important in the understanding of the scattering, but the magnetic quantum number, m , is also (in some cases, dominating the influence on the intensity patterns).

DATA REPRESENTATION

Although only calculated results are reported here, it is useful to describe the typical data acquisition and data representation of the angular dependence of the emitted electron intensities. Typically the data is acquired as single line scans either in the polar (θ) or azimuthal (ϕ) configuration, although display analyzers are also in use²⁵. Although the line scans are sufficient for determining crystal structure parameters, significantly more information can be displayed and understood using a full 2π -hemispherical intensity plot. There are many projections available for displaying a hemispherical intensity pattern as a flat display using a gray-scale or false-color^{28,29}. The two used regularly in the AED and XPD literature are the azimuthal equidistant polar projection (used in this work), where equal increments in the polar angle (θ) are represented by equal increments in the radial direction (see figure 1a-b) and the stereographic projection (see figure 1c) where the radial distance is equal to $2 \times \tan(\theta/2)$ ²⁹. The azimuthal equidistant polar projection accurately reproduces the center of the intensity pattern, but enhances the displayed area around the border of the pattern. The stereographic projection is a more balanced representation at the loss of direct correspondence with the line scans.

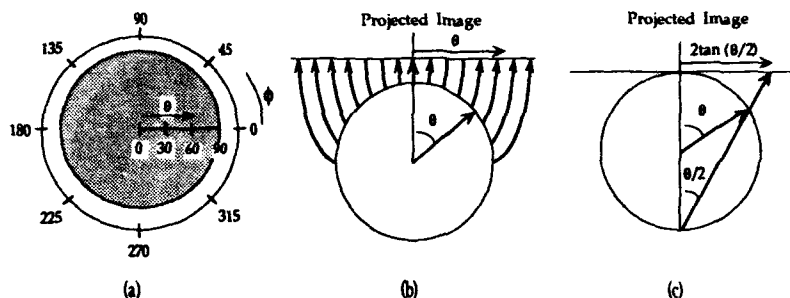


FIGURE 1: Data representation. (a) 2π hemispherical representation of data, equivalent to an azimuthal equidistant polar projection (b) where radial distances are equivalent to the θ -value. (c) Stereographic projection where the radial distances are equivalent to $2 \times \tan(\theta/2)$.

FINAL-STATE EFFECTS

To investigate the role of final-state effects in the AED and XPD spectra, we have separately calculated the full 2π emission patterns for each electron emission character (ℓ and m). The calculational scheme employed is the well developed and successful single scattering cluster (SSC) method^{1,2} with the inclusion of spherical wave corrections²⁰. The calculations use the Rehr-Albers formalism³⁰, which is a general electron scattering formalism beginning with the separable free-electron Green's-function propagator. The formalism has been encoded by Friedman and Fadley²³ for monoenergetic, single scattering electrons. The program has been altered to allow for the separate calculation of the intensity pattern for each electron emission character, ℓ and m , for either photon excitation (of various polarizations) or electron excitation (for electron induced AED).

The importance of the character of the final-state on the intensity distribution patterns for low energy electron emission has been demonstrated by ourselves and others^{11,21,22,26,27}. The most insightful example is obtained from the calculated angle-dependent intensity map for low energy emission from Pt(111) and Cu(001)²⁶, the systems studied by Frank and by Terminello. In figure 2a and 2b we compare the 56.6 eV $3p_{3/2}$ photoelectron intensity mapping (where both $\ell=0$ and $\ell=2$ final-state momenta contribute equally) with the calculated 56.6 eV, $M_3M_{45}M_{45}$ Auger electron intensity profile (where we determine the final-state angular momentum to be mostly f-character, $\ell=3$). In this case, we have summed over each of the allowed m -levels equally. The photoemission selection rules dictate that the allowed magnetic sublevels are $m_f=m_i$ (assuming the quantization axis is along the incident photon polarization vector) for the $\ell=2$ Cu $3p$ photoemission. For the Auger transition, all of the $2\ell+1$ magnetic sublevels contribute equally ($m=+3$ to -3 for the $\ell=3$ Auger emission). For the photoemission calculation, the unpolarized photons are represented by two polarization vectors, one along the detector direction and one orthogonal

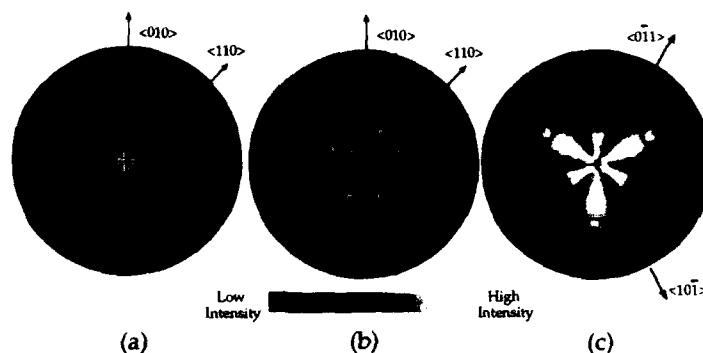


Figure 2: Calculated angle-dependent 56.6 eV electron intensity profiles for (a) Cu 3p photoemission (with $\ell=0$ and 2) and (b) $M_3M_{45}M_{45}$ Cu Auger emission (with $\ell=3$) for Cu(001). (c) $N_{67}O_{45}O_{45}$ Pt Auger emission (65 eV) from Pt(111) with $\ell=3$. Sample orientation is indicated by the arrows.

and within the surface plane. As discussed earlier, the inclusion of the appropriate angular momentum character of the electron source accounts for the striking differences experimentally observed by Terminello and Barton. For the Cu 3p photoemission (final-state character $\ell=0,2$) there is an intensity maximum in the surface normal direction, whereas for Cu Auger emission of the same energy (final-state character $\ell=3$) there is an intensity minimum. Shown in figure 2c is the calculated intensity pattern for the 65 eV $N_{67}O_{45}O_{45}$ Pt Auger emission from a Pt(111) single crystal. In this case, we again calculate that the emission character is dominated by $\ell=3$ (90% f-character, $\ell=3$, with the remainder being p-character, $\ell=1$). Again, the pattern is in excellent agreement with the measured spectra of Frank *et al.*

MAGNETIC MATERIALS

When magnetic materials are examined by AED and XPD, there are two additional aspects present in including final-state effects. The global magnetic moment defines a natural quantization axis for the expansion of the spherical harmonics, and, due to spin-orbit and exchange interactions, the magnetic quantum number, m , is not equally populated for all m values. When examining the final-state effects on the intensity patterns from non-magnetic materials, all $2\ell+1$ magnetic sublevels are equally populated in the initial state, and the quantization axis could be arbitrarily defined (usually aligned with the incident photon polarization direction so that $m_i=m_f$). In magnetic materials with an orbital contribution to the total moment, all of the magnetic sublevels are not equally populated, so that there will be an angular dependence to the electron emission from the source, proscribed by the local magnetization direction. For magnetic materials, not only will the scattering depend on the ℓ and m value, but the electron emission now has a strong angular character.

The angular dependence of the emission is most easily seen from the intensity patterns calculated for a single atom (shown in figures 3 and 4). To simplify the discussion, we will examine only two quantization directions corresponding to

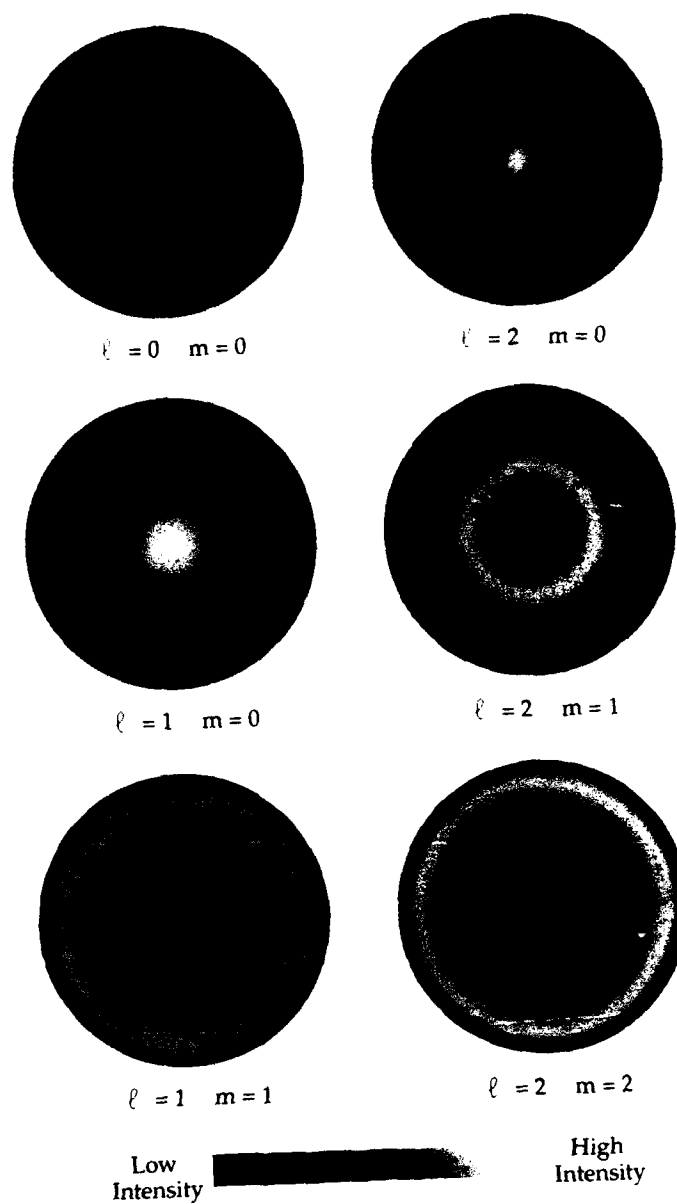


Figure 3: Single atom emission patterns for particular final states with the quantization direction along the z-axis (perpendicular). Angular momentum value, ℓ , and magnetic quantum number, m , as indicated.

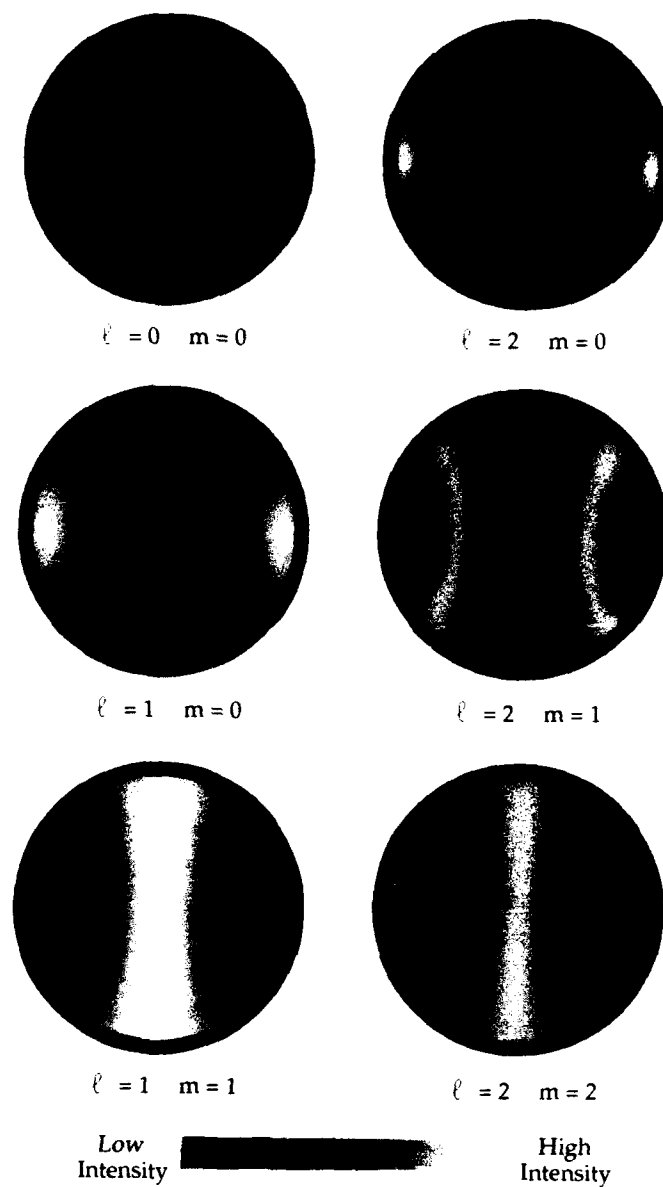


Figure 4: Single atom emission patterns for particular final states with the quantization direction along the x-axis (in-plane). Angular momentum value, ℓ , and magnetic quantum number, m , as indicated.

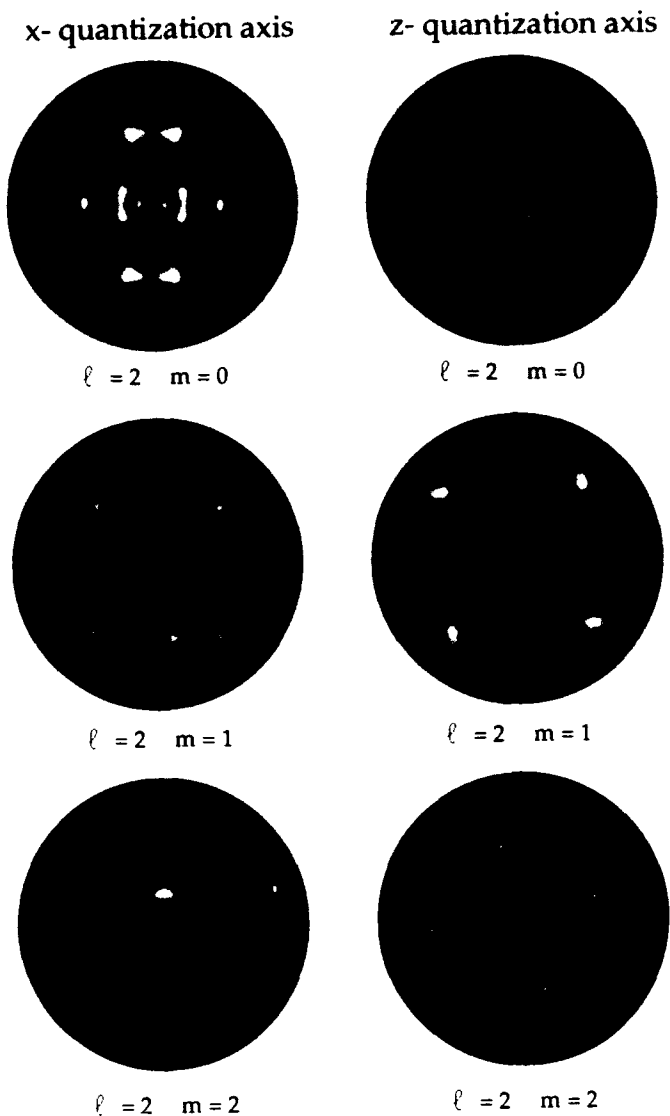


Figure 5: Calculated angle-resolved intensity patterns for electron emission from bcc Fe(001) at 47 eV for particular final-states. The quantization axis for an in-plane moment is along the $\langle 100 \rangle$ direction (x-axis) and for a perpendicular moment along the $\langle 001 \rangle$ direction (z-axis). Only the non-negative m -sublevels for the $\ell=2$ state are shown. Intensity patterns for negative m -sublevels can be obtained from the corresponding positive m patterns by allowing $\phi \rightarrow (-\phi)$.

the z-axis, $\langle 001 \rangle$ direction, and the x-axis, $\langle 100 \rangle$ direction. In thin films, this will correspond to a perpendicular remnant moment and an in-plane remnant moment, respectively. More complex magnetic orientations and structures can also be considered. The patterns in figures 3 and 4 simply represent the spherical harmonic as viewed on-end (z-axis) where the quantization axis is parallel to the surface normal, or on-side (x-axis) where the quantization axis is perpendicular to the surface normal.

The emission from the $\ell=0$, $m=0$ state is spherically symmetric as is the emission from the summation over all equally populated m -sublevels of a given ℓ . Already, some interesting features are apparent. For the z-axis emission patterns, only the $m=0$ state contributes to emission in the surface normal direction, and the large $|m|$ values contribute to emission at the exterior. For the in-plane quantization axis (x-axis) the reverse occurs. These emission patterns are independent of the electron energy.

It is interesting to see how this emission character is reflected in the electron intensity patterns for an atom imbedded in a crystal structure when the electron is allowed to scatter off the surrounding atoms. For these calculations, we have used a ~ 1500 atom bcc Fe(001) cluster (10 ML slab) with the bulk Fe lattice spacing of 2.86 Å. The calculations are performed at low energies (referenced to outside the material) corresponding to the low energy Auger transition at 47 eV. The quantization axis was chosen to be either the $\langle 100 \rangle$ or the $\langle 001 \rangle$ direction. The resulting intensity patterns for 47 eV electrons emitted with d-character ($\ell=2$) are shown in figure 5. (Note that for later comparison, we have used $\ell=2$ even though we have determined that $\ell=3$ dominates for the Fe Auger emission.) Only spectra for positive magnetic quantum numbers are shown. The spectra for the negative m -levels can be obtained by letting $\phi \rightarrow (-\phi)$. The angular dependence of the source emission is clearly reflected in the intensity patterns. In addition to the gross features from the angular dependence of the source emission, there are also distinct features due solely to scattering of the emitted electron. For the x-axis data, there is a distinct asymmetry for features above and below the centerline representing the quantization axis. Similarly, in the z-axis data, a distinct chirality of the spectra is evident. (Changing m to $-m$ results in a reversal of the asymmetries.) As in the case of the angular momentum final-state effects, the features in the magnetic final-state are due to the relative phase difference of the scattered and directly emitted waves.

There is clear evidence that the intensity pattern for a given m has unique features. But these features are only present if there is a non-statistical distribution in m -levels of the emitted electron. This non-statistical distribution of emitted m -levels can be generated by a number of mechanisms. If the initial-state m -levels are non-statistical, then the final-state m -levels will reflect the non-statistical weighting of the initial state. The redistribution of initial state m -levels can be magnetic in origin, or arise from chemical bonding at an interface, or, as we have suggested³¹, from the direct and secondary excitation process. The case of magnetic systems is particularly interesting because of the possibility of determining from the measured intensity patterns, the m -level populations, and therefore the magnetic state of the thin film (direction and moment).

In figure 6 we show the anticipated emission pattern for three m -level populations for both perpendicular and in-plane magnetization directions. For equal m -level populations (the first set of patterns), the pattern is symmetric and equal for the two quantization directions, as expected. This would correspond to

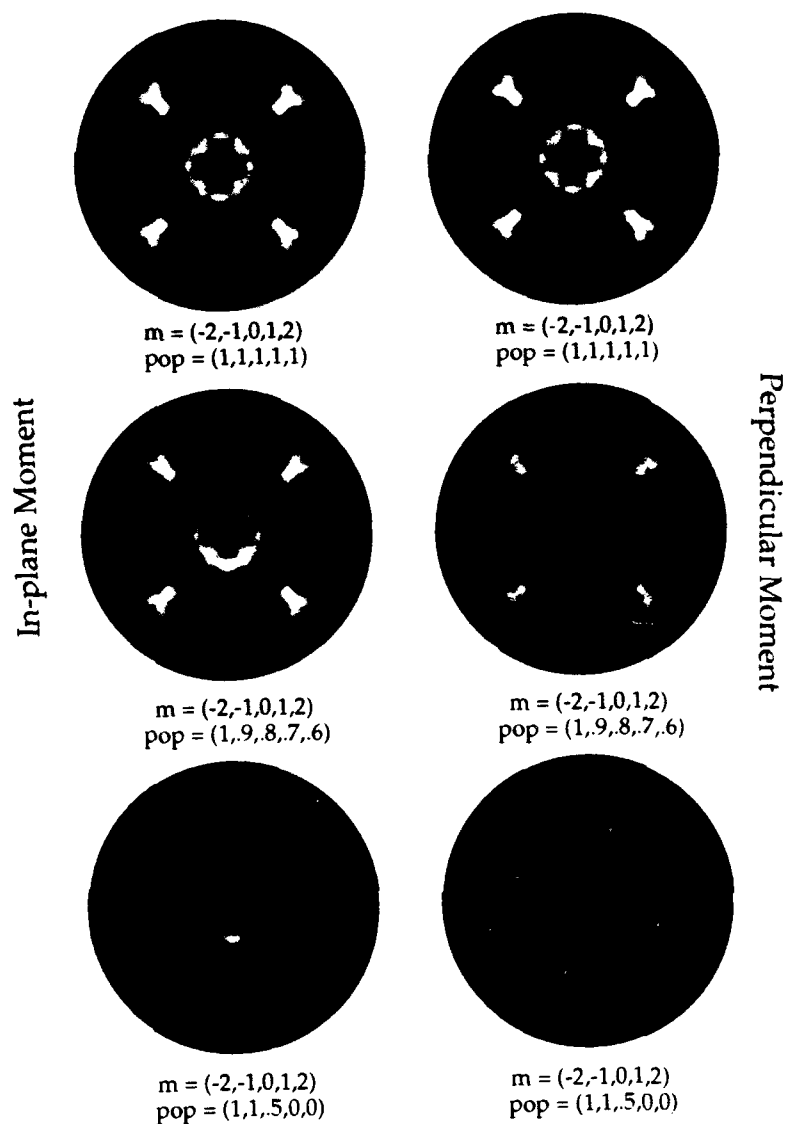


Figure 6: Calculated angle-resolved intensity pattern for electron emission with d-character ($\ell=2$) from bcc Fe(001) at 47 eV. The m-sublevel populations are shown below each figure for both in-plane (x-axis) and perpendicular (z-axis) moments. (TOP) is an equal population of all m-sublevels, (MIDDLE) is a realistic spin-orbit re-population of the m-sublevels, and (BOTTOM) corresponds to a severe spin-orbit re-population.

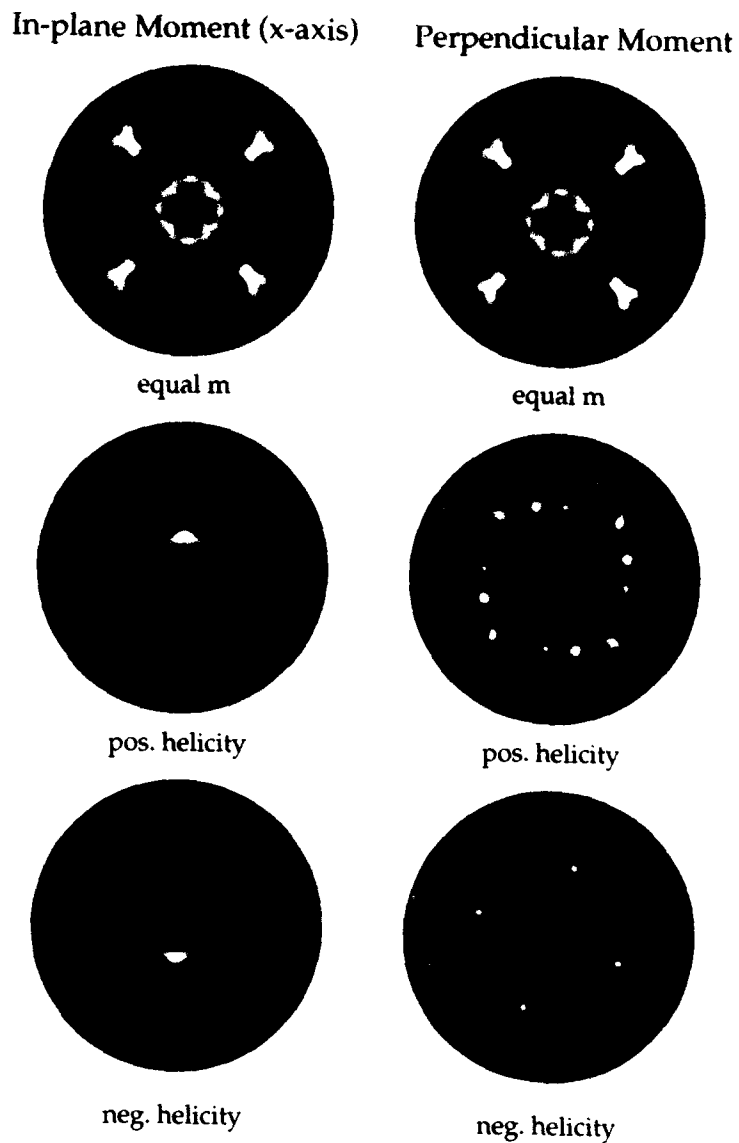


Figure 7: Calculated angle-resolved intensity pattern for photoelectron emission with d-character ($\ell=2$) from bcc Fe(001) at 47 eV using circularly polarized photons incident along either the in-plane (x-axis) or perpendicular (z-axis) moment direction. (TOP) equal emission from all $2\ell+1$ m-sublevels, (MIDDLE) emission from 100% positive helicity light, and (BOTTOM) emission from 100% negative helicity light.

the emission pattern for bcc Fe(001) with no orbital moment. Because all m-levels are equally populated, the emission is spherically symmetric and the quantization axis is irrelevant. As we turn on the spin-orbit interaction and populate the lower lying m-levels more strongly, slight, but measurable differences are observed in the patterns. (A realistic m-level population is shown in the middle set of patterns.) For the x-axis spectra, there is an increasing top-bottom asymmetry. For the z-axis, a chirality of the spectra develops. These asymmetries, of order 10-20%, are small but measurable. For a severely distorted m-level population (shown in the bottom set), the asymmetries are very distinct.

Instead of relying on a non-statistical population of initial-state m-levels, these magnetic final-state effects can also be generated by using an excitation source which preferentially excites particular m-levels. One method for generating electron emission from selected m-sublevels is photoemission using circularly polarized light. For a circularly polarized photon incident along the remnant magnetization direction, in addition to the typical dipole selection rule ($\Delta\ell=\pm 1$) for the angular momentum quantum number, there is a selection rule for the m-sublevels ($\Delta m=\pm 1$), depending on the helicity of the circularly polarized light. For the photo-excitation of p-levels (initial m-sublevels $m=0,\pm 1$), the transition is dominated by transitions to states with d-character ($\ell=2$). For positive helicity light, the selection rule ($\Delta m=+1$) dictates that only electrons with magnetic quantum numbers $m=0, 1$, and 2 will be emitted. For negative helicity light, the selection rule ($\Delta m=-1$) dictates that only electrons with magnetic quantum numbers $m=0, -1$, and -2 will be emitted. Figure 7 shows the calculated intensity pattern for electron emission with the allowed m-sublevels equally represented in the emission; photoemission from positive helicity light, and photoemission from negative helicity light for both in-plane and perpendicular remnant moment directions. The emission patterns are dramatically different, showing 70% intensity variations upon helicity reversal. This has serious implication for angle-resolved photoemission using circularly polarized light, termed magnetic circular dichroism (MCD).

CONCLUSIONS

We have shown that the final-state character of the emitted electron plays an important role in the AED and XPD angle-resolved intensity distributions. Inclusion of the final-state angular momentum of the emitted electron in single scattering cluster (SSC) calculations reproduces the experimentally observed patterns. Extension to magnetic systems shows that similar, large effects in the angle-resolved intensity patterns can be expected for systems with non-statistical m-sublevel populations, or when an excitation source which is m-selective is employed (eg. photoemission using circularly polarized light).

ACKNOWLEDGMENTS

We are grateful for the use of the Univ. of Washington EXAFS code (FEFF 3.0, see J.J. Rehr, J. Mustre de Leon, S.I. Zabinsky, and R.C. Albers, J. Am. Chem. Soc. 113, 5135 (1991)) for generating our atomic potentials and to D.J. Friedman and C.S. Fadley for providing us with the general-purpose single scattering diffraction computer program used for these calculations. This work is supported by the Office of Naval Research.

REFERENCES

1. C.S. Fadley, *Prog. Surf. Sci.* **16**, 275 (1984): C.S. Fadley, in Synchrotron Radiation Research: Advances in Surface Science, ed. R.Z. Bachrach (Plenum, New York, 1990), and references therein.
2. W.F. Egelhoff, Jr., *Crit. Rev. Solid State Mater. Sci.* **16**, 213 (1990).
3. S.A. Chambers, *Advances in Physics* **40**, 357 (1991).
4. S.A. Chambers, *Surf. Sci. Report*, **16**, 261 (1992).
5. D. Naumovic, A. Stuck, T. Greber, J. Osterwalder, and L. Schlapbach, *Surf. Sci.* **269**, 719 (1992).
6. Y.U. Idzerda and G.A. Prinz, *Surf. Sci. Lett.* **284**, L394 (1993).
7. S.A. Chambers and T.T. Tran, *Phys. Rev. B*, May 15, (1993) (to be published).
8. J.J. Barton, *Phys. Rev. Lett.* **67**, 3106 (1991).
9. S. Thevuthasau, G.S. Herman, A.P. Kaduwela, R.S. Saiki, Y.J. Kim, W. Niemczura, M. Burger, and C.S. Fadley, *Phys. Rev. Lett.* **22**, 469 (1991).
10. G.K. Harp, D.K. Saldin, and B.P. Tonner, *Phys. Rev. Lett.* **65**, 1012 (1990).
11. P. Hu and D.A. King, *Nature* **353**, 831 (1991).
12. S.A. Chambers, T.J. Wagner, and J.H. Weaver, *Phys. Rev. B* **36**, 8992 (1987).
13. D.A. Steigerwald, I. Jacob, and W.F. Egelhoff, Jr., *Surf. Sci.* **202**, 472 (1988).
14. S.H. Lu, J. Quinn, D. Tian, F. Jona, and P.M. Marcus, *Surf. Sci.* **209**, 364 (1989), and references therein.
15. B.T. Jonker, G.A. Prinz, and Y.U. Idzerda, *J. Vac. Sci. Tech. B* **9**, 2437 (1991).
16. W.F. Egelhoff, Jr. (unpublished).
17. T. Oguchi and A.J. Freeman, *J. Magn. Magn. Mater.*, **46**, L1 (1984).
18. Y.U. Idzerda, B.T. Jonker, W.T. Elam, and G.A. Prinz, *J. Appl. Phys.* **67**, 5385 (1990).
19. L.H. Tjeng, Y.U. Idzerda, P. Rudolf, F. Sette, and C.T. Chen, *J. Magn. Magn. Mat.* **109**, 288 (1992).
20. M. Sagurton, E.L. Bullock, R. Saiki, A. Kaduwela, C.R. Brundle, C.S. Fadley, and J.J. Rehr; *Phys. Rev. B* **33**, 2207 (1986).
21. D.J. Friedman and C.S. Fadley, *J. Elect. Spectrosc. Related Phenom.* **51**, 689 (1990).
22. R.N. Lindsey and C.G. Kinneburgh, *Surf. Sci.* **63**, 162 (1977).
23. D.G. Frank, N. Batina, T. Golden, F. Lu, and A.T. Hubbard; *Science* **247**, 182 (1990): D.G. Frank, N. Batina, J.W. McCargar, and A.T. Hubbard; *Langmuir* **5**, 1141 (1989).
24. S.A. Chambers, *Science* **248**, 1129 (1990): W.F. Egelhoff, Jr., J.W. Gadzuk, C.J. Powell, and M.A. Van Hove; *Science* **248**, 1129 (1990): X.D. Wang, S.L. Han, B.P. Tonner, Y. Chen, and S.Y. Tong; *Science* **248**, 1129 (1990): D.P. Woodruff, *Science* **248**, 1131 (1990).
25. L.J. Terminello and J.J. Barton, *Science* **251**, 1218 (1991).
26. Y.U. Idzerda and D.E. Ramaker, *Phys. Rev. Lett.* **69**, 1943 (1992).
27. T. Greber, J. Osterwalder, D. Naumovic, A. Stuck, S. Hufner, and L. Schlapbach, *Phys. Rev. Lett.* **69**, 196 (1992).
28. see: G.R.P. Lawrence, Cartographic Methods (Methuen, London, 1979).
29. D. Naumovich, A. Stuck, T. Grber, J. Osterwalder, and L. Schlapbach, *Phys. Rev. B* **47**, 7462 (1993).
30. J.J. Rehr and R.C. Albers, *Phys. Rev. B* **41**, 8139 (1990).
31. D.E. Ramaker, H. Yang, and Y.U. Idzerda, *Fall MRS Proceedings, Boston* (1992) (to be published).

PERPENDICULAR MAGNETIC ANISOTROPY IN ULTRATHIN Fe(110) FILMS ON Cr(110)

HELMUT FRITZSCHE AND ULRICH GRADMANN

Physikalisches Institut, Technische Universität Clausthal, D 3392 Clausthal-Zellerfeld,
Germany.

ABSTRACT

In contrast to Fe(110)-films on W(110), which are magnetized always in the plane as a result of easy-plane magnetic surface anisotropies (MSA), Fe(110)-films on Cr(110) show perpendicular magnetization up to a thickness of roughly 3 monolayers, as a result of a perpendicular MSA of the Fe(110)/Cr(110) interface. Accordingly, Fe(110)-films on W(110), covered with Cr(110), show asymmetric MSA, the easy-plane MSA of the W(110)/Fe(110)-interface opposing the perpendicular one of the Fe(110)/Cr(110)-interface. It turns out that MSA is asymmetric too in Fe(110) films on W(110) covered by Cu, Ag, Au or UHV.

INTRODUCTION

Extended experimental work on (out-of-plane) magnetic surface anisotropy (MSA) of bcc α -Fe [1-6] shows perpendicular MSA for Fe(100)-interfaces with Ag, Au and UHV [1-5], but easy-plane MSA in Fe(110)-films on W(110), covered with Ag, Au, Cu and UHV [6]. Surprisingly, despite of the extraordinary interest in the Fe/Cr-system in connexion with indirect coupling phenomena observed in it [7-11], experimental work on MSA of Fe/Cr-interfaces is missing. The present work will close part of this gap. Following the examples given above, one might guess that the sign of MSA is determined by the ferromagnetic film itself (its material and its orientation) and is independent on the nonmagnetic substrate or coverage material. An inspection of Ni(111), which shows always easy plane MSA for Cu, Ag, Pd and UHV coverages [12], and of Co(111), which shows always perpendicular MSA [13-15] for interfaces with Ag, Au, Cu, Ir, Mo, Pd and Pt, apparently confirms this rule that the sign of MSA is independent on the contact material (for a general review of ultrathin magnetic films and MSA in them see [16]). We were surprised to find that this rule is broken by Fe(110) on Cr(110), which shows perpendicular MSA in contrast to the easy-plane MSA of Fe(110) on W(110). Even more, MSA is of perpendicular type for all known interfaces of Fe(110), with the only exception of the Fe(110)/W(110)-interface, which shows easy-plane MSA with an exceedingly large magnitude of 1.7 mJ/m² which dominates in all films prepared on W(110) and makes them easy plane. All Fe(110)-films on W(110) therefore show an asymmetric MSA, perpendicular in one interface and easy plane in the other one, a phenomenon which has not been reported before.

PREPARATION

Experiments were done using sandwiches of type $W(110)/Fe(110)/X$ and $W(110)/Cr(110)/Fe(110)/X$, X representing a final Cr-coverage or UHV. The films were prepared in UHV by evaporation ($p < 10^{-10}$ Torr) onto atomically smooth and clean $W(110)$ -surfaces, with growth rates of the order of 0.5 ML/min, at substrate temperatures of 300 K, except for Cr base layers, which were prepared with temperatures raising up to 570 K. Growth modes and surface defect structures were tested by Auger electron spectroscopy (AES) and low-energy electron diffraction with high angular resolution spot-profile analysis (SPA-LEED, see [17]); details will be published elsewhere [18]. The main defects of the interfaces consist of atomic steps along [001] with mean distances of about 10 and 30 atomic rows on Fe and Cr, respectively. As estimated from a previous analysis of step anisotropies [17], this causes only minor corrections to the MSA determined below. Film thickness was measured using quartz-crystal oscillators with a resolution of 5% and checked both the completion of the pseudomorphic monolayer, sensitively detected by SPA-LEED, and using magnetometry of thick films.

MAGNETOMETRY

Torsion oscillation magnetometry (TOM, [19,20]) was done in situ immediately after or even during evaporation. Only room temperature magnetometry is reported in the present paper. The advantage of our TOM is to provide both magnetic moments and anisotropies

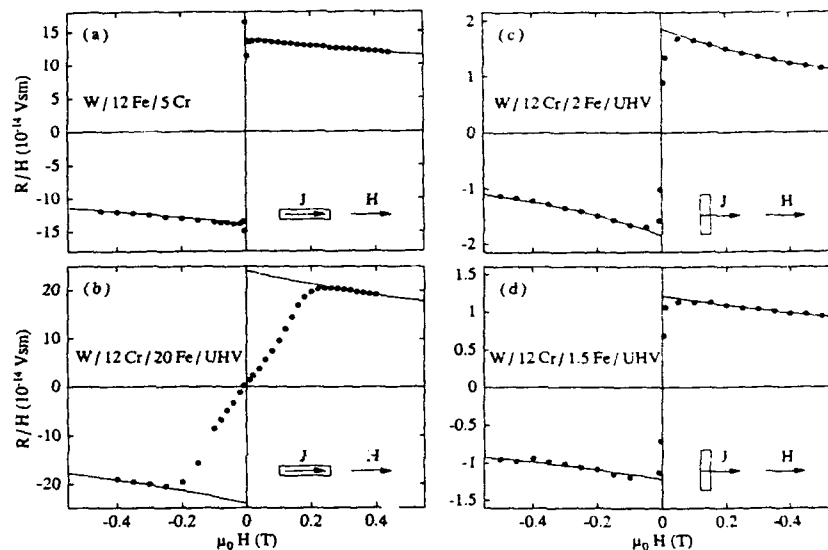


Figure 1: Magnetization loops R/H versus H (see Equ. 1) for Fe/Cr epitaxial films on $W(110)$. The external field is along $[1\bar{1}0]$. (a) Easy-axis in-plane loop for a sample $W(110)/12Fe/5Cr$ (film thickness by monolayers). (b) Hard-axis in-plane loop for a sample $W(110)/20Fe/UHV$. (c) and (d) Easy axis perpendicular loops for $W(110)/2Fe/UHV$ and $W(110)/1.5Fe/UHV$, respectively.

with submonolayer resolution from one combined measurement in situ in UHV. We measure the period of torsion oscillations of the sample, suspended in a magnetic field H . The dependence of this period on H is expressed by a torque constant $R = -dT/d\phi$ (torque T per angle ϕ). We represent magnetic anisotropy by the leading terms of the free energy F per volume V , $F/V = L \cdot \cos^2\vartheta + K_p \cdot \sin^2\vartheta \cdot \cos^2\varphi$, where ϑ is the polar angle of the magnetization direction with respect to the surface normal and φ an in-plane azimuth with respect to $[001]$. L and K_p are out-of-plane and in-plane anisotropy constants, respectively. The magnetic field is applied along $[1\bar{1}0]$. For the case of magnetic saturation in the plane ($\varphi = 90^\circ$), we analyse small amplitude oscillations near an equilibrium with the film plane parallel to the field. R is then connected with the saturation moment $m = J_s V$ and with the anisotropy field $H_L = 2L/J_s$ by

$$R/H = J_s V \cdot [H_L / (H + H_L)] \quad (1)$$

Figure 1 shows magnetization loops of the quasi-moment R/H versus H for three samples. Figure 1a is taken from a sample W/12Fe/5Cr, consisting of 12 atomic layers of Fe(110) on W(110), covered by 5 atomic layers of Cr; it shows an easy axis loop, indicating $K_p > 0$, in which R/H follows the saturation hyperbola of equation (1) down to zero field, with a low coercive field < 2 mTesla (not resolved). $J_s V$ and H_L can easily be determined. For comparison, Figure 1b shows the hard-axis loop of the sample W/12Cr/20Fe/UHV, with magnetic saturation for $\mu_0 H \geq 0.2$ Tesla only; H_L and $J_s V$ result as before from the saturation branch; K_p , which is now negative, results in the usual way from the initial slope. The deviations from linearity indicate higher order terms of the in-plane anisotropy which will be discussed elsewhere. We were surprised to observe that 2 monolayers Fe on Cr(110) oriented themselves spontaneously at right angles to the field, that means that they showed perpendicular magnetization ($L < 0$). For this case, the appropriate mode of TOM is to observe torsion oscillations near the new equilibrium with the film at right angles to the field; easy axis loops of this type are shown in Figure 1c and d, respectively.

EVALUATION OF MAGNETIC SURFACE ANISOTROPIES

For the anisotropies determined from standard loops as in Figure 1, the separation of volume and surface contributions was done as usual by plotting total film anisotropy fields $H_L = 2L/J_s$ versus $1/D$, the inverse of the number of atomic layers in the ferromagnetic component, $D = t/d$ (film thickness t , distance of atomic layers d). Assuming $\mu_0 H_L$ to be a superposition of a volume contribution ($J_s + \mu_0 H_v$), composed of shape anisotropy J_s and a crystalline volume component $\mu_0 H_v$, and of a surface contribution $(1/D)(\mu_0 H_s^{(1)} + \mu_0 H_s^{(2)})$, with surface anisotropy fields $H_s^{(1,2)}$ which can be thought of acting on the topmost magnetic layer only in both interfaces, we make the usual Ansatz

$$\mu_0 H_L = (J_s + \mu_0 H_v) + (1/D)(\mu_0 H_s^{(1)} + \mu_0 H_s^{(2)}). \quad (2)$$

The surface anisotropy fields $H_s^{(i)}$ are connected with the usual surface anisotropy constants by $K_s^{(i)} = (1/2)J_s \cdot H_s^{(i)}d$. Note that we use, as in previous papers [6, 12, 16, 17], the original Néel notation $\sigma = K_s \cos^2\vartheta$, which differs in sign of K_s from part of the literature. Figure 2 shows a plot of H_L versus $1/D$ for sample-series of type W/Fe/UHV, W/Fe/Cr, W/Cr/Fe/UHV and W/Cr/Fe/Cr, respectively, all containing D atomic layers of Fe(110) in different surroundings. The straight fitting lines for the first

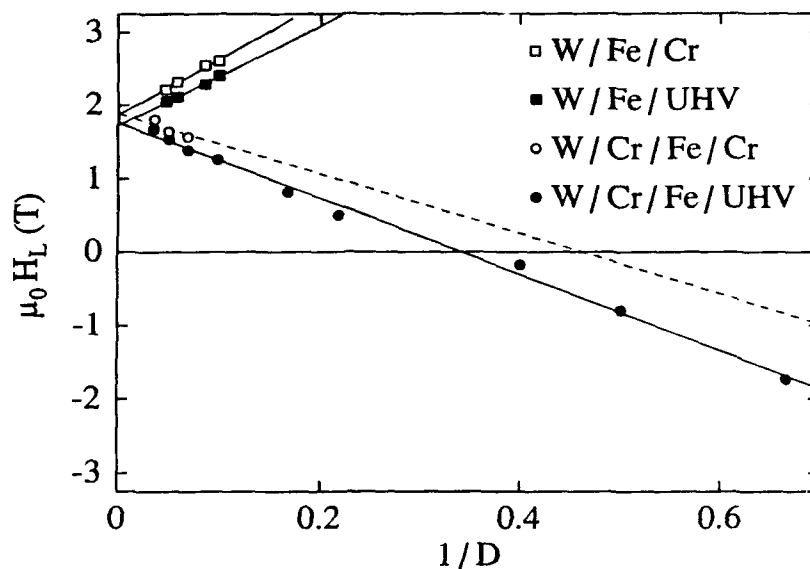


Figure 2: Total out-of-plane anisotropy-fields $\mu_0 H_L$ versus $1/D$, for film series W/Fe/Cr, W/Fe/UHV, W/Cr/Fe/Cr and W/Cr/Fe/UHV, all containing D atomic layers of Fe(110) in different environments.

Table 1: Single interface MSA constants K_s of Fe(110)-interfaces. The first three values are determined from the measurements of the present paper, the following three using previous work on W/Fe/X-films [6]. All data are for room temperature, except the last one, Fe/Au*, which comes from low-temperature at 10 K of Au(111)/Fe(110)/Au sandwiches [21], unstable at room temperature. The error is generally of the order 0.1 mJm^{-2} .

Interface	Fe/UHV	Fe/Cr	Fe/W	Fe/Cu	Fe/Ag	Fe/Au	Fe/Au*
K_s/mJm^{-2}	-0.51	-0.35	+1.70	-0.24	-0.60	-0.53	-0.69

three series confirm the existence of surface anisotropies. For W/Cr/Fe/Cr, a strong in-plane anisotropy with [001] as an easy axis prevented the saturation hyperbola, see Figure 1b, and therefore the determination of H_L for the thinner films; we abstain from a linear fit to the three remaining points. Instead, we include the dotted line, the slope of which results from the MSA determined from the other series. It fits well to the W/Cr/DFe/Cr data. Note that the straight line for W/Cr/Fe/UHV connects data from samples with $H_L > 0$ which oscillated near parallelly to the external field with data from samples with $H_L < 0$ which oscillated near perpendicular orientation. The good linear fit connecting these quite different situations of measurement confirms the concept of our analysis. From the total surface anisotropies for the three series, resulting from the slopes of the full lines, the anisotropies of the three involved single interfaces could be determined. They are collected in Table 1.

Data for Fe(110)-interfaces with Cu, Ag and Au are included which were obtained using total film surface anisotropies from previous work [6]. Obviously, all interface anisotropies are negative (perpendicular) except $K_s^{W/Fe}$, which is positive and exceedingly large. We found surprisingly good agreement of our room temperature value for $K_s^{Fe/Au}$ with the low-temperature value of Lugert and Bayreuther [21].

DISCUSSION

In Figure 2, the remarkable agreement of the axial sections which represent volume type anisotropies, for series with quite different slopes, which in turn represent surface anisotropies, confirm the MSA concept. The common volume anisotropy of the series W/Fe/UHV and W/Cr/Fe/UHV, $(J_s + \mu_0 H_v) = 1.75$ Tesla, can be compared with the standard bulk value of $(J_s - 2\mu_0 K_1/J_s) = 2.10$ Tesla (standard 4th order crystalline anisotropy K_1). The difference of 0.35 Tesla is not unreasonable and can roughly be explained by an effective size-effect-type reduction of J_s by about 0.2 Tesla and a strain contribution of 0.15 Tesla corresponding to a residual strain of 1% [6], which in turn is not unreasonable for the film thicknesses used and the misfit $\epsilon_{Fe/W} = -9.6\%$. We note that the subsequent coverage by Cr rather changes the axial section than the slope. Apparently, the Cr-coverage induces a transition between two neighbouring coincidence structures with resulting minor changes of volume type strain anisotropy. Second order in-plane anisotropy fields H_p could be determined from the initial slope of hard axis loops (like Figure 1b); they are reported elsewhere [22].

What is the origin of the exceptional sign and magnitude of $K_s^{W/Fe}$? One might suppose a surface-type contribution of residual epitaxial strain anisotropies. However, this is of wrong sign, as can be seen qualitatively from Figure 2: Residual strain anisotropy is negative, and its magnitude certainly increases with increasing $1/D$, so its surface contribution is negative, too. Clemens et al. [22] recently made this argument more quantitative in a magnetoelastic analysis of interface misfit dislocation relaxation in Mo(110)/Fe(110)-samples (because of the negligible difference of 0.001 nm of the W and Mo lattice parameters, the result can be applied to the present case). They obtain a strain contribution to K_s of -0.36 mJ/m². The inclusion of this contribution would even increase the true interface MSA to $+2.1$ mJ/m². One might further suggest that the broken symmetry in the misfit dislocation cores could be the origin of an additional contribution to MSA, specific for the misfitting W/Fe-interface and therefore missing for the other interfaces. This is improbable in view of the out-of-plane anisotropy of the pseudomorphic monolayer W(110)/1Fe/Ag [23], $\mu_0 H_L = +5$ Tesla (at 220K), which is not far away from the $+7$ Tesla which result from the data of Table 1 in a certainly very simple model of the pseudomorphic monolayer as a system with a W/Fe and a Fe/Ag-interface, and a reduced shape anisotropy of about 1 Tesla. Because dislocations are absent in the pseudomorphic monolayer, this argument contradicts the idea of misfit dislocation cores as origin of the outstanding interface anisotropy. We conclude that $K_s^{Fe/W}$ is of intrinsic electronic nature and should be accessible to first principles calculations.

In conclusion, we have shown that iron-films on Cr(110) are magnetized perpendicularly, up to roughly 3 monolayers. Fe-films on W(110), with free surface or covered by Cu, Ag, Au or Cr, are asymmetric with respect to their out-of-plane MSA, which is easy plane and of outstanding magnitude for the W/Fe-interface but perpendicular for the other interfaces. For coverage with Cr, the films are asymmetric with respect to the in-plane MSA, too. New static and dynamic magnetic properties can be expected for such films with asymmetric MSA. The magnitude of MSA in the W/Fe-interface, $K_s^{W/Fe} = 1.7$

mJ/m², exceeds all values of MSA reported before. Apparently, it is of electronic origin. It is a challenge for first principles calculations and may be a clue in the search for strong interface anisotropies in general.

ACKNOWLEDGEMENTS

This work was supported by the Deutsche Forschungsgemeinschaft.

REFERENCES

1. B.T. Jonker, K.H. Walker, E. Kisker, G.A. Prinz and C. Carbone, *Phys. Rev. Lett.* **57**, 142 (1986).
2. N.C. Koon, B.T. Jonker, F.A. Volkening, J.J. Krebs and G.A. Prinz, *Phys. Lett.* **59**, 2463 (1987).
3. M. Stampanoni, A. Vaterlaus, M. Aeschlimann and F. Meier, *Phys. Rev. Lett.* **59**, 2483 (1987).
4. B. Heinrich, K.B. Urquhart, R.R. Dutcher, S.T. Purcell, J.F. Cochran and A.S. Arrott, *J. Appl. Phys.* **63**, 3863 (1988).
5. J.R. Dutcher, J.F. Cochran, B. Heinrich and A.S. Arrott, *J. Appl. Phys.* **64**, 6095 (1988).
6. H.J. Elmers and U. Gradmann, *Appl. Phys. A* **51**, 255 (1990); H.J. Elmers, T. Furubayashi, M. Albrecht and U. Gradmann, *J. Appl. Phys.* **70**, 5764 (1991).
7. P. Grünberg, R. Schreiber, Y. Pang, M.B. Brodsky and H. Sowers, *Phys. Rev. Lett.* **57**, 2442 (1986).
8. P. Grünberg, J. Barnas, F. Saurenbach, J.A. Fuß, A. Wolf and M. Vohl, *J. Magn. Magn. Mat.* **93**, 58 (1991).
9. S.S.P. Parkin, N. More and K.P. Roche, *Phys. Rev. Lett.* **64**, 2304 (1990).
10. M.N. Baibich, J.M. Broto, A. Fert, F. Nguyen Van Dau, F. Petroff, Etienne, G. Creuzet, A. Friederich and J. Chazelas, *Phys. Rev. Lett.* **61**, 2472 (1988).
11. J. Unguris, R.J. Celotta and D.T. Pierce, *Phys. Rev. Lett.* **67**, 140 (1991).
12. U. Gradmann, *J. Magn. Magn. Mat.* **54**, 313 (1986).
13. P. Bruno and J.P. Renard, *Appl. Phys. A* **49**, 499 (1989).
14. P.F. Carcia, *J. Appl. Phys.* **63**, 5066 (1988).
15. F.J.A. den Broeder, W. Hoving and P.J.H. Bloemen, *J. Magn. Magn. Mat.* **93**, 562 (1991).
16. U. Gradmann, *Magnetism in Transition Metal Films*, in K.H.J. Buschow (ed), *Ferromagnetic Materials*, Volume 7, Elsevier 1993.
17. M. Albrecht, T. Furubayashi, M. Przybylski, J. Korecki and U. Gradmann, *J. Magn. Magn. Mat.* **113**, 207 (1992).
18. H. Fritzsche, M. Albrecht and U. Gradmann, to be published.
19. U. Gradmann, *Ann. Physik (Leipzig)* **17**, 91 (1966).
20. R. Bergholz and U. Gradmann, *J. Magn. Magn. Mat.* **45**, 389 (1984).
21. G. Lugert and G. Bayreuther, *Thin Solid Films* **175**, 311 (1989).
22. H. Fritzsche and U. Gradmann, to be published.
23. B.M. Clemens, R. Osgood, A.P. Payne, B.M. Lairson, S. Brennan, R.L. White and W.D. Nix, preprint 1992.
24. U. Gradmann, M. Przybylski, H.J. Elmers and G. Liu, *Appl. Phys. A* **49**, 563 (1989).

MICROSTRUCTURAL DEPENDENCE OF THE PERPENDICULAR MAGNETIC ANISOTROPY IN Co-Pt ALLOYS

E. E. Marinero, R. F. C. Farrow, G. R. Harp, R. H. Geiss, IBM Research Division, Almaden Research Center, 650 Harry Road, San Jose, CA 95120-6099;
J. A. Bain and B. Clemens, Department of Materials Science and Engineering, Stanford University, Stanford, CA 94305.

ABSTRACT

To establish the structural origins of the perpendicular magnetic anisotropy in Co-Pt alloys, a variety of magnetic and structural characterization techniques have been utilized. We have determined that the development of out-of-plane magnetization in these alloys, strongly depends on growth temperature and in contrast to Co/Pt multilayers, the highest anisotropies and coercivities are observed in polycrystalline alloys with negligible preferred crystallographic orientation. Lattice strain measurements, surface roughness determination and crystal growth studies indicate that contributions from magnetostrictive and magnetostatic contributions to the perpendicular anisotropy in these alloys are not significant. HRTEM and synchrotron-based x-ray diffraction experiments, on the other hand, confirm the existence of ordered CoPt_3 at elevated temperatures. We suggest that the strong temperature dependence of the perpendicular anisotropy is correlated to the onset of spontaneous chemical ordering during the growth which results in anisotropic pair ordering. A tentative model explaining this strong temperature dependence is described.

1. INTRODUCTION

The presence of perpendicular anisotropy in Co-Pt alloys was first demonstrated by Treves et al⁽¹⁾. In their work they demonstrated that the formation of the tetragonally ordered $\text{Co}_1\text{Pt}_1\text{-L1}_0$ phase was key to the development of perpendicular anisotropy. Ordering was obtained by annealing at 600°C their-sputter deposited alloy films. More recently, Lin and Gorman⁽²⁾ reported perpendicular anisotropy in evaporated $\text{Co}_{1-x}\text{Pt}_x$ near the 1:3 composition. In their work, they found that fcc [111] texturing promoted by growing the alloys on Pt buffer layers at growth temperatures of around 200°C was required. Further studies by Weller et al⁽³⁾ on the magnetic and magneto-optical properties of these alloys indicates that the intrinsic Kerr rotation of said alloys at short wavelengths is considerably higher than equivalent multilayers containing the same volume content of Co atoms. This makes this class of materials extremely attractive for high density magneto-optical recording.

To study the origins of the perpendicular anisotropy, we have utilized in this work, MBE growth of $\text{Co}_x\text{Pt}_{1-x}$ ($x \sim 0.25$) alloy films deposited onto substrates of amorphous carbon, amorphous SiN and fused silica at temperatures ranging from 30 to 500°C. The results are compared with those for highly [111] oriented epitaxial alloy films grown onto basal-plane sapphire substrates under identical conditions.

EXPERIMENTAL TECHNIQUES

The films were grown in a MBE system (VG Semicon-Fisons VG 80M) in a background pressure of below 2×10^{-10} Torr. Co-evaporation from electron beam sources for Co and Pt was used and the respective growth rates were $\approx 0.034 \text{ \AA/s}$ for

Co and $\approx 0.11 \text{ \AA/s}$ for Pt. Films of $\sim 200 \text{ \AA}$ thick were deposited onto a variety of amorphous substrates including amorphous carbon films ($\sim 100 \text{ \AA}$ thick) on mica and SiN films on amorphous carbon on mica. Foils for transmission electron microscopy were formed by simply detaching the carbon films from mica. This method worked for a wide range of substrate temperatures from 30 to 500°C permitting the structural examination of alloy films grown within this temperature range. Additionally, films were grown directly onto silica, carbon on silica, SiN on silica, carbon on silicon [111], silicon [111], SiN on basal-plane sapphire, basal-plane sapphire and basal-plane sapphire that was subjected to Ar^+ -ion etching prior to the Co-Pt alloy deposition in order to amorphize the topmost layers of the substrate. The magnetic properties of the films were studied using polar Kerr magnetometry, VSM and torque magnetometry. Transmission electron microscopy was carried out using JEOL 4000EX (400keV) and Akashi (200keV) electron microscopes. Surface morphology and roughness were examined by atomic force microscopy (AFM). X-ray diffraction studies were carried out utilizing both a Siemens diffractometer for θ - 2θ scans and synchrotron radiation. The latter were performed on beamline 7-2 at the Stanford Synchrotron Radiation Laboratory (SSRL). A Huber 4-circle diffractometer was used in symmetric, asymmetric and grazing incidence modes. Photon energies of 9987 eV were used. The in-plane lattice parameter measurements were performed in the grazing incidence mode⁽⁴⁾. Out of plane lattice parameters and rocking curves were measured in the standard symmetric geometry.

EXPERIMENTAL RESULTS

The strong influence of the growth temperature on magnetic properties is shown in Figure 1, which presents polar Kerr loops (measured at 633nm), rotation and coercivities from a series of films of composition $x \approx 0.24$, 200 \AA thick grown at different growth temperatures onto carbon on mica. There is a progressive increase in perpendicular anisotropy and coercivity from 30 to 300°C . Above this temperature the perpendicular anisotropy and coercivity collapse and the anisotropy is in-plane at 500°C . This trend was also found for films grown directly onto basal-plane sapphire substrates. In the latter case the films were highly oriented with [111] as the growth axis.

Following our work on Co/Pt multilayers which established the strong influence of growth orientation on the perpendicular anisotropy⁽⁵⁾, we investigated the influence of growth orientation on $\text{Co}_{25}\text{Pt}_{75}$ alloys grown at 300°C . Growth on basal-plane [0001] sapphire yielded [111] oriented alloys, whereas [110] SrTiO_3 and [001] NaCl substrates were selected to orient the alloys along the [110] and [001] axes. In all cases the alloys exhibited perpendicular anisotropy and the only significant difference was the magnitude of the coercivity and the squareness of the loops. A full report on the magnetic and structural properties of these epitaxial alloys grown along different crystallographic orientations will be published elsewhere⁽⁶⁾. Growth at the same temperature on amorphous substrates such as silica resulted in even higher values of the coercive force and the highest magnitude of the anisotropy.

The temperature dependence of the coercivity for epitaxial and polycrystalline films is shown in Figure 2. It is clearly seen that the coercivity peaks at a growth temperature of $\approx 300^\circ\text{C}$ for both sets of films, however, the maximum value of the epitaxial films is significantly lower. The magnitude of the perpendicular anisotropy in both sets of films displays the same behavior. To further study the effect of texture and orientation on anisotropy, another series of alloys were grown at 300°C

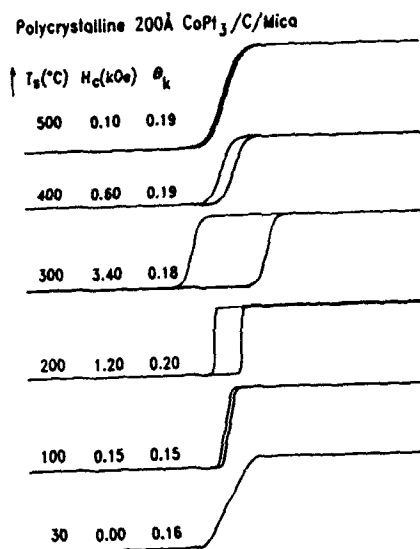


Figure 1. Polar Kerr Hysteresis loops for CoPt₃ deposited on carbon (20 nm)/mica substrates.

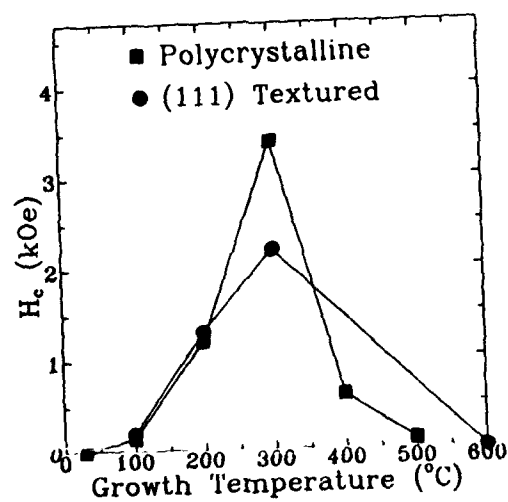


Figure 2. Coercivity vs. substrate temperature for polycrystalline and epitaxial CoPt₃ films.

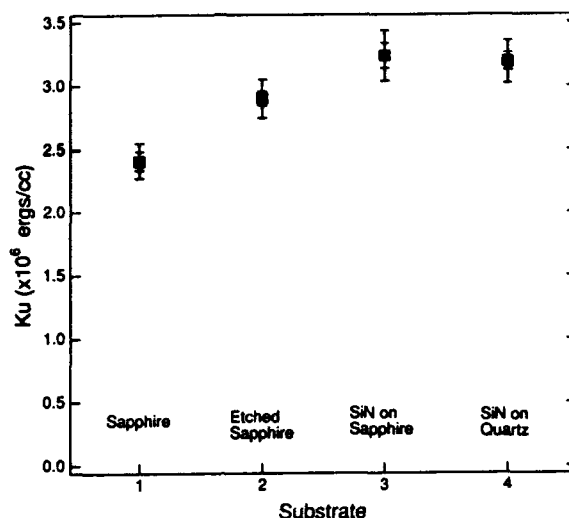


Figure 3. Perpendicular anisotropy of stoichiometrically identical Co-Pt alloys near the 1:3 composition grown on various substrates. Only the growth on sapphire is epitaxial.

simultaneously on the following substrates: basal-plane sapphire, amorphized sapphire (by Ar^+ -ion etching), sapphire with an overlayer of amorphous SiN (40 nm thick), and silica also with an overlayer of SiN. Note that we use "quartz" as a synonym for fused silica elsewhere in this paper.

Figure 3, gives the magnitude of the perpendicular anisotropy for these alloys of identical stoichiometry and growth history. The measurements were performed in fields up to 20 kGauss and the anisotropy values were obtained by extrapolating to infinite field using the 45° method of Miyajima et al⁽⁷⁾. It is evident that the maximum anisotropy is observed for non-epitaxial alloys grown on amorphous SiN underlayers. The data gives the total anisotropy and includes the demagnetizing energy. Background subtraction for both substrate and the holder arrangement has been performed. The error bars correspond to uncertainties in the estimate of the sample volume. Note that the corresponding room temperature coercivities for these samples were measured to be: 1.3 kOe, 4.7 kOe, 5.2 kOe and 5.4 for the structures grown on basal-plane sapphire, etched sapphire, SiN/sapphire and SiN/quartz respectively. In all cases the hysteresis loops showed 100% remanence at room temperature.

In Figure 4, the corresponding rocking curves for these alloys are given. These were taken around the symmetric [111] reflection. The FWHM of these curves are correlated with the anisotropy values. For the sample on sapphire, the FWHM is 0.5° , whereas the etched-sapphire sample exhibits a FWHM of 8.5° . The two samples grown on the SiN underlayers, display no obvious single maxima to which a peak can be fitted but they clearly have even a larger distribution of directions and

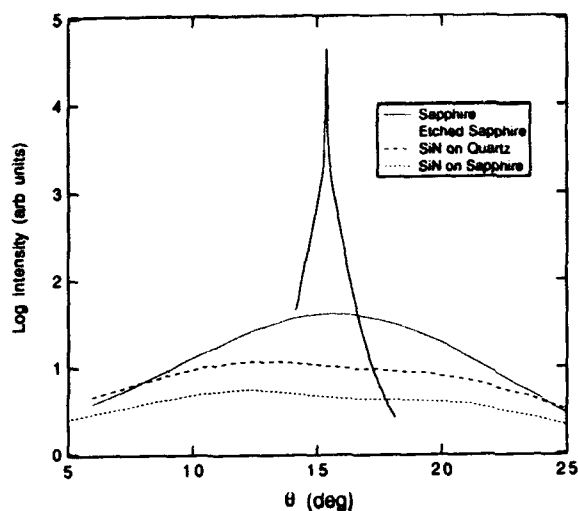


Figure 4. X-ray rocking curves for the symmetric $[111]$ reflection from the alloy peak. The FWHM for the epitaxial alloy is 0.5° . The samples with highest anisotropy show FWHM in excess of 20° .

the FWHM exceeds 20° . Note that the lattice constant of CoPt_3 (3.829\AA) is only 2% smaller than the in-plane spacing of hollow sites in the surface of sapphire. This geometric fit leads to highly oriented $[111]$ growth of CoPt_3 on sapphire. In fact, the film grows with a 180° twinning of Pt about the $[111]$ axis.

The polycrystalline films have a much greater room temperature coercivity than epitaxial ones: 5.4 kOe for growth on SiN/quartz vs. 1.3 kOe for direct growth on sapphire. This behaviour contrasts with that for Co/Pt multilayers⁽⁵⁾ where for films without $[111]$ texture the magnetic anisotropy was in-plane for Co thicknesses $\geq 5\text{\AA}$.

Transmission electron microscopy studies were carried out on alloy films grown onto carbon on mica at 30, 100, 200, 300, 400 and 500°C . In addition, films grown onto SiN on carbon at 300°C were also examined. It was found that the grain size of the films increased smoothly with temperature but that there was a greater spread in grain size for the films grown above 300°C . These results are described in Reference (8) and the most salient result for films grown above 300°C , is the observation of extra diffraction spots in addition to the alloy diffraction rings, which correspond to superstructure diffraction from the chemically ordered L1_2 phase. As discussed in our TEM study⁽⁸⁾, isolated clusters of this phase were observed in films grown at 500°C . At 400°C the clusters are more dispersed whilst at 300°C they are barely detectable by TEM diffraction or imaging. However, recent synchrotron X-ray diffraction studies⁽⁹⁾ has confirmed that chemical ordering is present in both polycrystalline and epitaxial alloy films grown at 300°C . The coherence length for chemical ordering at 300°C is, however, very short ($< 8\text{\AA}$).

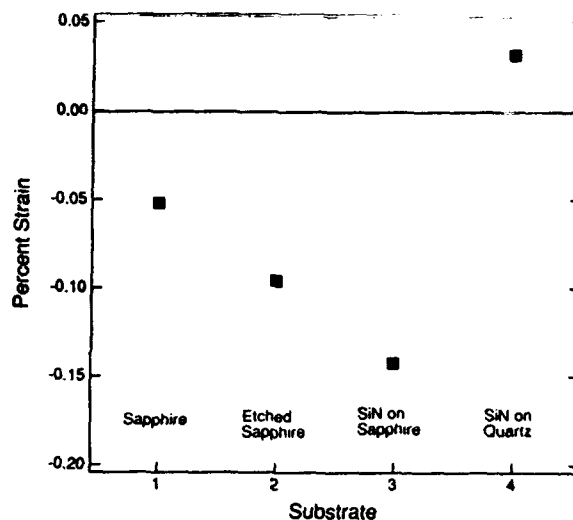


Figure 5. Percentage strain in the alloys of figure 4. The values were obtained from measurements of in-and-out-of-plane lattice parameters.

Surface roughness measurements were made by atomic force microscopy (AFM) measurements of the difference between the highest and lowest points within the studied area (500nm x 500nm) yielded: 4.8 nm, 2.7 nm, 4.3 nm and 5.3 nm for growth on sapphire, etched-sapphire, SiN/sapphire and SiN/quartz respectively. The grain size in all cases is comparable and there appears to be no apparent correlation with the magnitude of the total perpendicular anisotropy here reported.

DISCUSSION

Similarities in grain size and roughness for the alloys with high out-of-plane anisotropy indicates that magnetostatic contributions on account of intergrain exchange interactions is not the driving mechanism for the origin and the strong growth-temperature dependence of the magnetic anisotropy in these alloys. At $\sim 300^\circ\text{C}$, the alloys are essentially disordered fcc structures with grain sizes ranging from 7.5 nm to 20 nm. To check whether lattice strain induced by grain growth could, via magnetostriction, induce the large perpendicular anisotropy, measurements of lattice strain were conducted. Both in-plane and out-of-plane lattice parameters were deduced. The results are presented in Figure 5 and are given as percentage of strain for the alloys of identical stoichiometry and growth history. It is evident from the figure that the degree of strain is small and does not follow the magnetic behavior here reported.

The development of perpendicular anisotropy may be related to the onset of partial chemical ordering⁽¹⁰⁾ in the film at $\sim 300^\circ\text{C}$. At this temperature a dispersion of the ordered phase exists⁽⁹⁾ and the coherence length of this phase may be anisotropic. If the ordered regions are lamellar and parallel to the film plane then more Co-Co pairs will exist along the film normal since the ordered phase contains no Co-Co nearest

neighbors. This could give the uniaxial anisotropy observed. At temperatures below 300°C there is negligible ordering whilst at temperatures above 300°C the ordered regions may become condensed into clusters, via both lateral and vertical diffusion. The anisotropy in coherence length will then be suppressed leading to a peak in perpendicular anisotropy with substrate temperature, as we observe. This idea is tentative and we are conducting further structural studies to determine whether indeed macroscopic structural anisotropy exists in these alloys. EXAFS measurements with the Q-vector in and out of plane of the sample surfaces are planned to establish this mechanism as the origin of the perpendicular anisotropy in these alloys.

CONCLUSIONS

We have investigated the structural origins of the large perpendicular anisotropy in Co-Pt alloys near the 1:3 composition utilizing a variety of structural and magnetic probes. We have established that larger anisotropies and room temperature coercivities are derived when the alloys are grown on amorphous underlayers or substrates. This results in non-oriented polycrystalline films and the largest values of anisotropy and coercivity are measured in films grown at ~300°C. Our experimental results indicate that contributions from magnetostatic and magnetostrictive contributions are small and do not constitute the main source of the anisotropy in these alloys. TEM and synchrotron-diffraction data indicates that the onset of chemical ordering combined to changes in the growth mode of these films at different temperatures, may be the source of this anisotropy.

ACKNOWLEDGEMENTS

This work was partly supported by ONR. One of us (JAB) gratefully acknowledges fellowships from IBM and NSF.

REFERENCES

1. D. Treves, J. T. Jacobs and E. Sawatzky, *J. Appl. Phys.*, **46**, 2760, (1975).
2. C. J. Lin and G. Gorman, *Appl. Phys. Lett.*, **61**, 1600, (1992).
3. D. Weller, H. Brändle, G. Gorman, C.-J. Lin, H. Notarys, *Appl. Phys. Lett.*, **61**, 2726, (1992).
4. P. H. Fuoss and S. Brennan in *Annual Review of Materials Science*, **20**, ed. R. A. Huggins, J. A. Giordmaine and J. B. Wachtman, Jr., 365, (1990).
5. C. H. Lee, R. F. C. Farrow, C. J. Lin, E. E. Marinero, C. J. Chien, *Phys. Rev. B*, **42**, 11384 (1990).
6. R. F. C. Farrow, G. R. Harp, D. Weller, E. E. Marinero, T. A. Rabedeau and M. F. Toney, in preparation.
7. H. Miyajima, K. Sato and T. Mizoguchi, *J. Appl. Phys.*, **47**, 4699, (1976).
8. R. F. C. Farrow, R. H. Geiss, G. Gorman, G. Harp, R. F. Marks and E. E. Marinero, *J. Mag. Soc. Japan*, **17** (Suppl S-1), 140, (1993).
9. T. A. Rabedeau, M. F. Toney, R. F. C. Farrow, G. R. Harp, R. F. Marks and E. E. Marinero to be submitted to *J. Appl. Phys.*
10. The idea of anisotropic coordination in a dispersed, ordered CoPt₃ phase contributing to magnetic anisotropy in Co-Pt films was proposed by C. J. Chien, R. F. C. Farrow, C. H. Lee, C. J. Lin and E. E. Marinero, *J. Mag. Mag. Mat.* **93**, 47, (1991).

HYPERFINE FIELDS IN ULTRATHIN Fe AND FeAu ALLOY FILMS ON Au(111)

M. BROCKMANN, L. PFAU, G. LUGERT AND G. BAYREUTHER
 Universität Regensburg, Institut für Angewandte Physik,
 Universitätsstraße 31, D-8400 Regensburg, Germany

ABSTRACT

Magnetic properties of ultrathin Fe and Fe₄₀Au₄₀ alloy films on Au(111) were studied by SQUID magnetometry and conversion electron Mössbauer spectroscopy. In order to get information on the influence of interdiffusion, iron films with thin alloy zones at the interfaces to Au have been prepared by co-evaporation of iron and gold and compared with iron films with presumably sharp interfaces. It was found that the presence of an 0.5 ML (mass coverage in monolayer) alloy zone reduces the effective magnetic interface anisotropy field and affects the growth mode of a subsequently deposited iron film such that the film is more sensitive to annealing. Groundstate magnetic moments and hyperfine fields are significantly enhanced in Fe/Au(111) ($t_{Fe} \leq 4$ ML) and Fe₄₀Au₄₀ films, compared to bulk Fe.

1. INTRODUCTION

Ultrathin epitaxial Fe films grown on Au(111) show remarkable magnetic properties like enhanced groundstate magnetic moments and a pronounced magnetic interface anisotropy with the easy axis perpendicular to the film plane¹. While for an iron thickness $t_{Fe} > 10$ ML it is well known that iron grows in a bcc lattice with the Fe(110) plane parallel to the Au(111) plane, the lattice structure for films with $t_{Fe} < 10$ ML is controversial. Some authors state that Fe grows in the bcc(110) phase from the first layer on², while others find a pseudomorphic growth of fcc Fe up to 3-4 ML where a transition to the bcc phase sets in³. In any case it is to be expected that the growth mode is affected by the preparation conditions and should manifest itself in the magnetic properties of the sample.

In our Fe/Au(111) films we found a significant dependence of the effective magnetic surface anisotropy field, H_s , on the substrate temperature during film growth, T_s . In epitaxial films grown at $T_s = 310$ K we observe the largest value of $|H_s| = 40 \pm 3$ kOe. This value is large enough to turn the magnetization perpendicular to the film plane if the thickness is smaller than 3 ML. For $T_s = 450$ K we obtain $|H_s| = 13 \pm 5$ kOe. This reduction of the effective magnetic interface anisotropy field can be explained in terms of an interdiffusion of Fe and Au at the interface or by a more three dimensional growth mode at higher substrate temperatures. In order to study the influence of interdiffusion on the magnetic properties we prepared epitaxial ultrathin iron films with thin (0.5 or 2 ML) FeAu alloy zones at the interfaces by co-deposition of Fe and Au. We found $|H_s| = 17 \pm 5$ kOe (for $T_s = 310$ K). In addition, for the identification of an alloy component and its contribution to the magnetic behaviour of the film pure FeAu alloy films have also been investigated. SQUID magnetometry was used to determine integral magnetic properties (average magnetic moment and

magnetic anisotropy) and Mössbauer spectroscopy to get information about local variations of magnetic order via the hyperfine field.

2. EXPERIMENT

Three types of films were prepared by Molecular Beam Epitaxy ($p < 1 \cdot 10^{-7}$ Pa; iron enriched to more than 95% in ^{57}Fe): ultrathin Fe films ($t_{\text{Fe}} \leq 4$ ML), $\text{Fe}_{60}\text{Au}_{40}$ alloy films ($t_{\text{FeAu}} \approx 60$ ML) and Fe films ($t_{\text{Fe}} \leq 4$ ML) with thin $\text{Fe}_{60}\text{Au}_{40}$ alloy zones at the interfaces. All films were deposited on a 400 ML Au(111) substrate film, which in turn was grown on a very smooth fused quartz substrate, and covered by a protective layer of Au ($t \approx 50$ ML). The alloy zones have a nominal thickness of either 0.5 ML or 2 ML at each interface. The preparation of alloy films and alloy zones was done by controlled co-evaporation of Fe and Au. All thickness values are to be understood as mass coverage (determined in situ by quartz crystal monitors and ex situ by X-ray fluorescence) assuming bulk density.

Spontaneous groundstate average magnetic moments $\langle \mu \rangle$ and the effective magnetic interface anisotropy field, H_s , were determined by SQUID magnetometry ($4\text{K} \leq T \leq 400\text{K}$; $-50\text{kOe} \leq H \leq 50\text{kOe}$). The CEMS spectra were measured with a cryogenic proportional counter. By automatic control of He gas flow, pressure, temperature and gas gain, it allows measurements in a temperature range from 77 K to 300 K.

3. RESULTS AND DISCUSSION

Fitting the spectra

A typical $\text{Fe}_{60}\text{Au}_{40}$ alloy spectrum is shown in figure 1. The spectrum is the sum of a broad doublet (dotted line) and an asymmetrically broadened sextet (dashed line). Each of these subspectra itself is a superposition of several subspectra with different values for the hyperfine interactions (isomer shift δ_{loc} , magnetic hyperfine field H_{loc} and quadrupol splitting Δ_{loc}) corresponding to varying local environments. We could fit the spectra with good precision using the simple alloy model of Billard and Chamberod⁴ for the sextet subspectra (alloy-sextet), assuming a purely random alloy. The model takes into account isotropic (δ_i for the isomer shift and h_i for the magnetic hyperfine field) and anisotropic (Δ for the electric field gradient and h_2 for the magnetic field) contributions from nearest neighbour (NN) atoms. For a random alloy

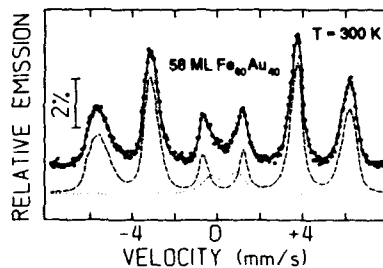


Fig. 1:

Typical alloy spectrum. Subspectra used for the fit: broad doublet (dotted line), asymmetrically broadened sextet (dashed line), generated by a random alloy model

with N nearest neighbour lattice sites the anisotropic contributions lead to an effective line broadening of N subspectra for which the local isomer shift δ_{loc} and the local magnetic hyperfine field H_{loc} depend on the number z_{Fe} ($0 \leq z_{Fe} \leq N$) of iron atoms on the NN lattice sites:

$$\begin{aligned}\delta_{loc} &= \delta_0 + z_{Fe} \cdot \delta_1 \\ H_{loc} &= H_0 + z_{Fe} \cdot h_1\end{aligned}\quad (1)$$

Fits were performed both for bcc ($N = 8$) and fcc ($N=12$) lattices. For the fcc lattice we obtain $\delta_1 = -0.02 \dots -0.05$ mm/s and $h_1 = 0.7 \dots 1.2$ Tesla. For the bcc lattice these numbers have to be multiplied with a factor of 3/2. The signs of δ_1 and h_1 mean that if on a NN lattice site an Fe atom is replaced by a Au atom the isomer shift is increased (by reduction of the s-electron density) and the magnetic hyperfine field is decreased. The values we found for δ_1 are in accordance with Window's Mössbauer study³ of Fe_xAu_{1-x} alloys ($x = 0.02 \dots 0.4$).

For fitting the spectra of the ultrathin iron films (with and without alloy zones at the interfaces) we used the same subspectra (doublet, alloy-sextet) as for the alloy spectra, plus another symmetrical sextet in order to take into account the higher number of iron atoms with mostly iron nearest neighbours.

Annealing

Annealing the films for one hour at 400 K causes an increase of the relative intensity of the doublet in the CEMS-spectra of the alloy films and the Fe films with alloy zones at the interfaces. At the same time no significant changes can be observed in the parameters of the sextet subspectra (except for their relative intensity).

For 58 ML $Fe_{50}Au_{40}$ the doublet intensity is 12% both in spectra measured at 77 K and 300 K prior to annealing. After annealing it is 30% at 77 K and 45% at 300 K. In a 4 ML Fe film with 2×0.5 ML alloy zone at the interfaces we find an increase from 11% before to 20% after annealing. Since the doublet line width decreases with increasing temperature (in case of the alloy film from 1.33 ± 0.04 mm/s at 77 K to 0.74 ± 0.01 mm/s at 300 K) we attribute the doublet to small superparamagnetic particles. Then, annealing must cause a structural change in a way that more superparamagnetic particles are formed. This is consistent with our observation that annealing does not alter the groundstate average magnetic moment of the alloy films.

Influence of the alloy zone on subsequently grown iron

The presence of 0.5 ML alloy zone at the interfaces reduces the magnetic interface anisotropy field $|H_s|$ from 40 ± 3 kOe to 17 ± 5 kOe. Expanding the thickness of the alloy zone from 0.5 ML to 2 ML does not cause a further reduction of $|H_s|$. Similarly, in Mössbauer spectra measured after annealing the films for one hour at 400 K the presence of the

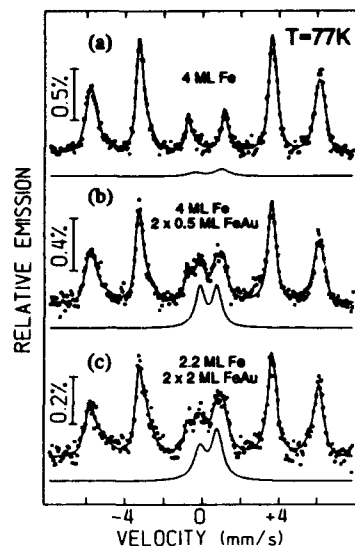


Fig. 2: Spectra of ultrathin Fe films containing approximately 4 ML iron and alloy zones of varying thickness

alloy zone is indicated by a significant increase of the relative intensity, I_D , of the doublet. Figure 2 shows spectra of films with a total iron thickness (iron contained in the iron- and alloy-layers) of about 4 ML and varying alloy zone thickness. For the 4 ML Fe film with sharp interfaces (fig. 2a) we obtain a doublet intensity of $I_D = 4\%$. For a 4 ML film with an alloy zone thickness of 0.5 ML (fig. 2b) it is 19% while only 11% of the total iron in this film is contained in the alloy zone. On the other hand in a 2.2 ML Fe film with 2 ML thick alloy zones (fig. 2c) I_D is still 20%, though in that case almost 50% of the iron is within the alloy zone. This means that I_D is not proportional to the alloy zone thickness. Thus there is no one-to-one correspondence of the doublet intensity and the amount of iron in the alloy zone. Instead, the alloy zone affects the growth mode of the Fe film in a way that the iron layers themselves contribute to the doublet intensity. It is possible that interdiffusion between the substrate and protective Au layers and the iron film is enhanced by a higher concentration of lattice defects due to the alloy zone.

Temperature dependence of the average magnetic hyperfine field

For a 4 ML Fe film, a 58 ML $\text{Fe}_{90}\text{Au}_{10}$ film and a 2.2 ML Fe film with 2 ML alloy zones we determined the average values $\langle H_{\text{eff}} \rangle$ of the effective magnetic hyperfine field H_{eff} at various temperatures between 77 and 300 K. The values are plotted in figure 3. Table I presents the result of fitting relation (2) to the data, with the groundstate average magnetic hyperfine field $H_{\text{eff}}(0)$, the spinwave parameter B and the exponent x as the fit variables.

$$\langle H_{\text{eff}}(T) \rangle = \langle H_{\text{eff}}(0) \rangle \cdot [1 - B \cdot T^x] \quad (2)$$

From table I it can be seen, that H_{eff} clearly shows a $T^{3/2}$ -dependence (within the uncertainty of the fit), and that for all films $H_{\text{eff}}(0)$ and B are considerably increased compared to the values of bulk iron.

The enhancement of the spinwave parameter is caused by a reduction of the aver-

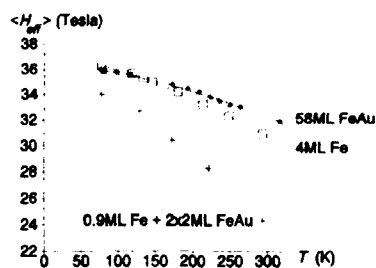


Fig. 3: temperature dependence of the average hyperfine field $\langle H_{\text{eff}} \rangle$ of thin FeAu alloy films and Fe films with and without alloy zones at the Fe/Au interfaces

Table I

Groundstate value $H_{eff}(0)$, spinwave parameter B , and exponent x for the temperature dependence of the effective hyperfine field in thin Fe and FeAu alloy films on Au(111) in comparison with bulk α -iron.

film	$H_{eff}(0)$ in Tesla	B in $10^5 \text{ K}^{3/2}$	x
1 ML Fe + 2x2 ML FeAu	35.5 ± 0.1	5.6 ± 0.1	1.52 ± 0.01
4 ML Fe	37.2 ± 0.2	4.0 ± 0.5	1.46 ± 0.06
58 ML $\text{Fe}_{60}\text{Au}_{40}$	36.4 ± 0.2	1.0 ± 0.1	1.6 ± 0.1
bulk α -iron	33.9	0.5	3/2

age exchange energy per iron atom which is (for a Heisenberg ferromagnet) approximately proportional to the average number, $\langle z_{Fe} \rangle$, of iron atoms on nearest neighbour lattice sites. First, $\langle z_{Fe} \rangle$ is reduced by occupation of NN sites with Au atoms in the alloy and second, it is reduced further due to the Au interfaces as the film thickness is decreased.

Along with the groundstate average hyperfine fields, enhanced average magnetic moments are found. For the 58 ML alloy film we find $\langle \mu \rangle = 2.8 \pm 0.3 \mu_B$. This can be understood considering Felsch's work⁶. He studied $\text{Fe}_x\text{Au}_{1-x}$ alloy films ($x = 0 \dots 1$) by XRD and magnetometry. In films with bcc structure ($x > 0.6$) he found groundstate magnetic moments close to the bulk value, whereas for lower Fe concentrations ($0.45 < x < 0.6$) he found fcc structure and moments of about $2.9 \mu_B$. Thus, the high magnetic moment indicates that the structure of the alloy film is fcc, which is also compatible with the nominal composition of 60at% Fe and 40at% Au. Furthermore the subspectra used in our fit do not include a spectrum which would correspond to bulk iron (zero isomer shift and $H_{eff} = 33.9$ Tesla and 33.0 Tesla at 77 K and 300 K respectively). Indeed each subspectrum (including the doublet) has an isomer shift of more than 0.1 mm/s with respect to α -iron. We conclude that no larger α -iron precipitates are contained in the alloy film and that in this sense the alloy may be considered 'homogenous'.

It should be pointed out that groundstate magnetic moments and hyperfine fields are not enhanced equally. $\langle \mu \rangle$ is increased by 27% compared to the bulk value of $2.2 \mu_B$, while the H_{eff} is enhanced by only 7%. This can be explained by the fact that there are several contributions to the magnetic hyperfine field: $H_{eff} = H_{cp} + H_{ce} + H_{dp}$, where H_{cp} , H_{ce} and H_{dp} are the contributions from core polarization, conduction electrons and magnetic dipole fields, respectively. While H_{cp} is proportional to the local magnetic moment, H_{ce} , H_{dp} and thus H_{eff} will also strongly depend on the configuration of neighbour atoms and, hence, not be proportional to the moment.

For the 1 ML iron film with 2 ML alloy zones $\langle H_{eff}(0) \rangle$ is smaller than in the 58 ML alloy film, while for the magnetic moment we still obtain $2.8 \pm 0.3 \mu_B$. This can be understood in the light of the alloy model (see equ. 1) where, for a given structure, $\langle H_{eff} \rangle$ depends linearly on the average number, $\langle z_{Fe} \rangle$, of iron atoms on nearest neighbour lattice sites if we assume H_0 to be constant. If during annealing an interdiffusion between the Au of substrate and covering layer and the film takes place this will result in a smaller $\langle z_{Fe} \rangle$, thereby reducing $\langle H_{eff} \rangle$.

For the 4 ML Fe film, the value of $\langle H_{\text{eff}}(0) \rangle = 37.2$ Tesla results from large hyperfine fields in both the interface and the center layers (assuming a smooth continuous film). Determining the groundstate values for the hyperfine fields of the two sextets which we attribute to interface ($\delta = 0.24 \pm 0.01$ mm/s) and center layers ($\delta = 0.11 \pm 0.01$ mm/s), we obtain 36.9 ± 0.2 Tesla for the interface and 37.5 ± 0.2 Tesla for the center layers. Isomer shift and hyperfine field of both sextets definitely differ from those of an α -iron sextet what may be evidence for the presence of an fcc Fe phase. This is somewhat unexpected, since it is in contrast to the results for an Fe(110)/Ag(111) film⁷, where the two center layers could be identified as α -iron, and $\langle H_{\text{eff}}(0) \rangle$ is enhanced only for the interface layers. It seems also to be in contrast to the interpretation of our earlier magnetometer measurements¹, where, varying the iron thickness from $t_{\text{Fe}} < 1$ ML (where we might have fcc iron) to $t_{\text{Fe}} > 50$ ML (where we certainly have bcc Fe(110)/Au(111)) no discontinuity in the magnetic moments or the magnetic anisotropy could be found, which would be expected for a switch from a fcc to a bcc phase. In order to clarify to what extent slightly differing preparation condition can result in different film structure, more detailed experiments combining LEED, MEED, CEMS, STM are under way.

4. SUMMARY

Using SQUID magnetometry and CEMS we studied magnetic and structural properties of epitaxial ultrathin Fe films on Au(111), thin Fe₆₀Au₄₀ alloy films and ultrathin Fe films with alloy zones at the Fe/Au interfaces. The alloy zone thicknesses were either 0.5 ML or 2 ML.

FeAu alloy films and iron films with or without alloy zones at the interfaces show ferromagnetic ordering with a $T^{3/2}$ temperature dependence of the effective magnetic hyperfine field. Groundstate magnetic moments, groundstate hyperfine fields and spinwave excitation are significantly enhanced in comparison with bulk iron.

In alloy films and Fe films with alloy zones, annealing at 400 K causes a structural modification which has no influence on the magnetic moment but is indicated by a doublet in the Mössbauer spectra and interpreted by formation of small superparamagnetic particles.

Compared to Fe films with smooth interfaces, Fe films with alloy zones at the interfaces show a reduced magnetic surface anisotropy field $|H_s|$ and a much stronger doublet intensity. Since there is no significant difference in the properties of films with 0.5 ML and 2 ML alloy zones, we conclude that the presence of only 0.5 ML alloy zone critically affects the growth mode of subsequently deposited iron, leading to a structure which is less stable under annealing than in Fe films with sharp interfaces.

1. G. Lugert, W. Robl, L. Pfau, M. Brockmann and G. Bayreuther, J.M.M.M april 1993 (in press).
2. C. Marlière, J. P. Chauvineau and D. Renard, Thin Solid Films **189**, 359 (1990).
3. J. A. Strosio, D. T. Pierce, R. A. Dragose and P. N. First, J.Vac.Sci.Technol. **A10**, 1981 (1992)
4. L. Billard, A. Chamberod, Solid State Comm. **17**, 113 (1975)
5. B. Window, Phys. Rev. B **6**, 2013 (1972)
6. W. Felsch, Z. Angew. Phys. **29**, 217 (1970)
7. G. Lugert, G. Bayreuther, Phys. Rev. B **38**, 11 068 (1988)

THE MICROSTRUCTURE OF Fe_7C_3 FORMED AT 300°C BY PLASMA ENHANCED CHEMICAL VAPOR DEPOSITION (PECVD)

H. Siriwardane,[†] P. Fraundorf,^{*} J.W. Newkirk,[‡] O.A. Pringle,[†] and W.J. James[‡]

Departments of [†]Physics, [‡]Metallurgical Engineering, and [‡]Chemistry and the Graduate Center for Material Research, University of Missouri-Rolla, Rolla, MO 65401 (U.S.A.).

^{}Department of Physics, University of Missouri-St. Louis, St. Louis, MO 63121 (U.S.A.).*

Thin iron carbide films were prepared by introducing iron penta carbonyl (FeCO_5) and hydrogen (H_2) into a glow discharge. The films are of potential interest in corrosion and wear resistant applications. X-ray diffraction data of films ($\approx 7000 \text{ \AA}$ thick) deposited on glass at 300°C evidenced only Fe_7C_3 . Thinner films were required for examination by analytical and high resolution transmission electron microscopy. Therefore, two sets of films ("thin" $< 200 \text{ \AA}$ and "thick" $\approx 800 \text{ \AA}$) were plasma-deposited on carbon or holey carbon films supported on copper grids. The thin TEM specimens exhibited a fine texture and gave rise to ring diffraction patterns, whereas the thick TEM specimens evidenced two types of structure: (i) half-micron sized grains separated from one another by 1-2 microns on the support, although sometimes interconnected by single crystal platelets and (ii) 300 \AA grape-like clumps of 100-200 \AA crystals, each individually surrounded by a 50 \AA non-crystalline coating. The latter structure may result from a post-formation oxidation process which expels carbon from the iron phase into grain boundaries.

1. INTRODUCTION

Plasma enhanced chemical vapor deposition (PECVD) has been widely used in recent years to form thin films¹⁻⁶ and to modify surfaces of materials. Bulk Fe_7C_3 is usually formed under very high temperatures and pressures. We have been successful in preparing Fe_7C_3 films by PECVD, using iron pentacarbonyl and hydrogen as a scavenging gas. Thin films of Fe_7C_3 are produced at temperatures around 300°C and pressures of 50-100 millitorr. This is possible because of the high electron temperatures of the glow discharge plasma, which trigger chemical reactions at moderately low temperatures, and the non-equilibrium nature of the glow discharge.⁷⁻¹² The usefulness of Fe_7C_3 as magnetic recording media has been investigated.¹³ They have a high magnetic saturation,¹³ and show evidenced of magnetic hardness as well as preferred orientation of their magnetic moments normal to the plane of the film.¹⁴ The magnetic applications of these films depend on the microstructure, crystal structure and the magnetic structure. The objective of this study is to investigate the microstructure of iron carbide films deposited at 300°C.

2. EXPERIMENTAL RESULTS

A cylindrical glow discharge reactor, identical to that described by Li et al.^{7,8} was used to prepare the films. Operating parameters for the preparation of Fe_7C_3 films are identical to those described in ref. 10. Pre-cleaned glass slides, carbon coated glass slides, carbon, and holey carbon support films on copper grids were used as substrates for film deposition. For all substrates, argon ion cleaning in an r.f. glow discharge was performed for 30 minutes before film deposition. Iron pentacarbonyl, $\text{Fe}(\text{CO})_5$, was introduced along with H_2 into a glow discharge. H_2 serves as a scavenger gas for oxygen.

An Auger analysis was performed on more than fifty films deposited at 300°C on glass microscope slides, and eight films deposited on carbon support films and prepared under the same experimental conditions. The Auger data of the above samples were collected at argon ion sputtering rates between 18-35 Å/minute. The depth profiling commenced after \approx one minute of argon ion sputtering to remove the physisorbed CO_2 and H_2O . The film compositions at an approximate depth of 600 Å were 60-70 atomic percent iron, 23-35 atomic percent carbon, and 1-4 atomic percent of oxygen, indicating the formation of the Fe_7C_3 phase. If it is assumed that all of the oxygen is bonded to iron in the form of Fe_3O_4 , then there is a slight excess of carbon present in the films. The carbide satellite peaks were clearly seen on every sample subjected to Auger analysis (see Fig. 1).

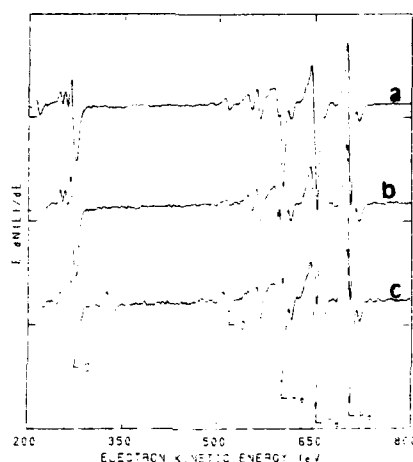


Figure 1. The Auger depth profiling data of films deposited at 300°C, showing carbon satellite peaks which indicate the presence of a carbide phase. The substrates are: (a) glass (b) carbon coated glass (c) carbon support films on grids.

To determine the microstructural details, TEM, x-ray, and electron diffraction techniques were used. The XRD spectra of films of different thicknesses were collected by using a SCINTAG 2000 XRD diffractometer. The step sizes and preset times varied between 0.01-0.03 degrees and 3.0-12.0 seconds, depending on the quality of the data required from the patterns. The XRD spectra of films grown on glass evidenced low-intensity broadened peaks (see Figure. 2). The experimentally determined interplanar spacing agreed with the JCPDS interplanar spacings of the Fe_7C_3 phase. The quality of the XRD patterns improved with increasing film thickness. Films grown on support films (holey carbon or carbon) under identical experimental conditions were too thin to produce XRD patterns. As a consequence, the XRD spectra of grid samples are not known.

For TEM characterization, two sets of films (thin < 200 Å and thick ≈ 800 Å) were deposited on carbon or holey support films on copper grids. These films were grown under identical experimental conditions as the films grown on glass, except that their deposition times were much shorter in order to produce films thin enough to be examined by the TEM. The principle idea behind using the holey support films on copper grids as substrates was to deposit thin films and observe crystals at the edges of holes.

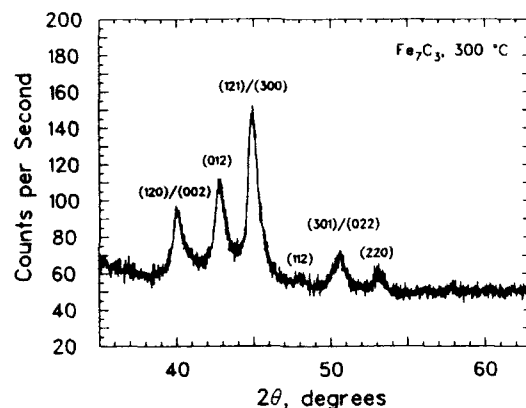


Figure 2. XRD pattern of a PECVD carbide film deposited at 300°C on a glass substrate.

In this TEM study, six thick (≈ 800 Å) films and three thin films (< 200 Å) made under identical experimental conditions were used to collect data. The latter three samples were deposited for approximately three minutes, whereas the thick films were deposited for twenty minutes on six different occasions in order to check the reproducibility. The camera constant used in the analysis of the TEM data was obtained by using aluminum standards. By finding the camera constant for the Phillips 430 EM electron microscope, and measuring the diameters of the rings on the negatives with a ruler, the interplanar spacings were calculated. Four measurements were made on each ring and the average value was taken as the true diameter of each ring. The obtained d-spacings were then compared to the JCPDS card file d-spacings of Fe_3O_4 , Fe_7C_3 , and Fe_3C . A comparison was made with only Fe_3O_4 , Fe_7C_3 , and Fe_3C because the XRD patterns of films deposited on glass at 200°, 300° and 400°C evidenced only the above three phases, respectively.⁹ The possibility of the presence of α -Fe was ruled out by investigating the spacings and the angles of single crystal Fourier spectra obtained from HRTEM images.¹¹

The thin specimens (< 200 Å) deposited at 300°C on carbon or holey films exhibited a fine texture and produced ring diffraction patterns on photographic films (see Figure 3a). The rings that contained spots corresponded to both Fe_3O_4 and Fe_7C_3 .

The electron diffraction patterns obtained from thick (≈ 800 Å) samples gave rise to ring diffraction patterns, single crystal and convergent beam diffraction patterns. The obtained d-spacings from the ring patterns were also compared with Fe_7C_3 , Fe_3C and Fe_3O_4 phases. The d-spacings of these phases were also profiled by azimuthal averaging of the intensities in these patterns (see Fig. 3b).^{12,15} The single crystal and convergent beam diffraction data were also analyzed by using the crystallographic program "SX".¹⁶ At this point in our study we have been unable to correlate the thick film morphologies with individual phases.

The thick specimens (≈ 800 Å thick) evidenced two types of morphologies. Morphology type I consists of half-micron platelets separated from one another by 1-2 microns on the support, although sometimes interconnected by grains of 0.1-0.2 microns (see Figs. 4a, 4b and 5a). These grains are capable of producing single crystal diffraction patterns and converging beam patterns, which could be indexed with either Fe_7C_3 or Fe_3C (see Fig 5b). Morphology type II consists of 300 Å grape-like clumps of 100-200 Å crystals, each individually surrounded by 50 Å non-crystalline coatings (see Fig. 6). The above two morphologies were seen in all thick TEM samples.

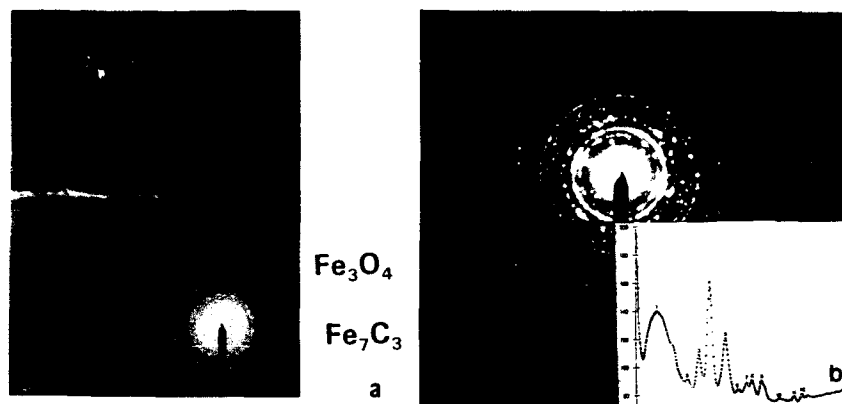


Figure 3. (a) A TEM micrograph and its SAD pattern of a PECVD thin ($< 200 \text{ \AA}$) carbide film deposited at 300°C on a holey carbon grid. (b) A TEM diffraction pattern of a thick ($\approx 800 \text{ \AA}$) PECVD film deposited at 300°C on a carbon support film.

(i) Morphology type I

Figures 4 and 5 show morphology type I, which is seen in continuous-film regions of the 800 \AA films.

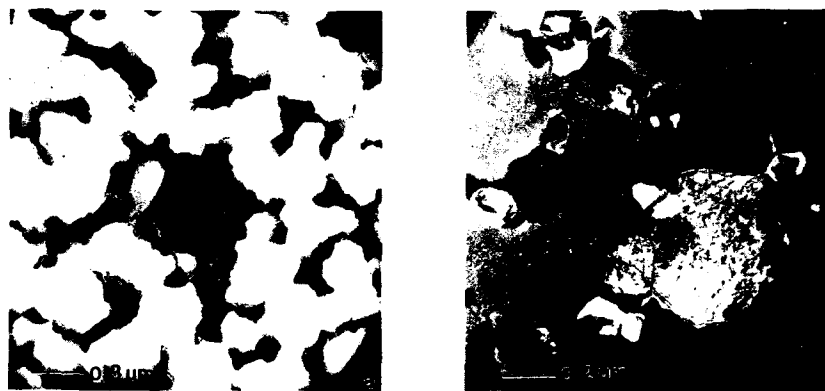


Figure 4. (a) Bright field image of morphology type I grains, showing small $0.1 \mu\text{m}$ grains in clumps separated by $0.3 \mu\text{m}$ distances. The center of the image shows a half-micron platelet connecting a number of clumps together. (b) Dark field image of a platelet, showing its single crystal character. This platelet could be indexed only with Fe_3C .



Figure 5. (a) Bright field image of morphology type I crystals, showing bend extinction contours in two half-micron platelets. (b) A converging beam diffraction pattern obtained from a large platelet which could be indexed only with Fe_7C_3 .

(ii) *Morphology type II*

The second type of morphology observed in these thick films consists of 300 Å grape-like clumps of 100-200 Å crystals, each individually surrounded by a 50 Å non-crystalline coating which appears as curved fringes around the crystals. This morphology is mostly seen at the edges of the carbon support films. The peaks and the interplanar angles obtained from the Fourier spectra of the crystals can be indexed with Fe_7C_3 planes. The coating gives rise to a variable d-spacing, which looks like a birds foot in the Fourier spectra, indicating the non-crystalline nature of the coating. The d-spacings for the coating ranged from 3.2-4.1 Å. This behavior and the obtained range of spacings are typical for poorly crystalline graphite.^{7,18}

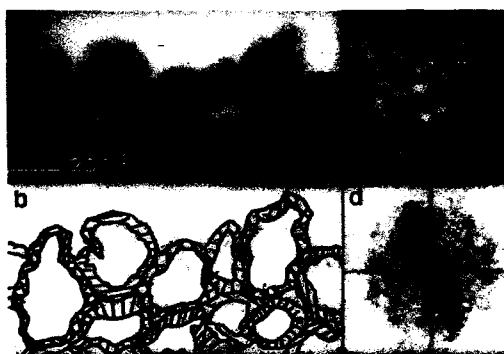


Figure 6. (a,b) Grape-like clumps, showing 50 Å non-crystalline coatings covering 100-200 Å crystals. The outlines of the grain boundaries have been artificially enhanced in (b). (c) An enlarged image of crystal which has a non-crystalline coating. (d) The Fourier spectrum of Fig. 5c.

3. DISCUSSION AND CONCLUSIONS

Iron carbide films were produced by PECVD, at temperatures of 300°C and pressures of 50-100 millitorr. The primary phase deposited is Fe_7C_3 . The electron diffraction data obtained on ≈ 800 Å thick films and thin films (< 200 Å) showed the presence of Fe_3O_4 , Fe_3C and Fe_7C_3 . Fe_3O_4 and Fe_3C were not seen on 7000 Å PECVD films deposited at 300°C on glass and carbon coated glass substrates due to the small quantities of these phases present. The ability to observe Fe_3O_4 and Fe_3C by electron diffraction may be due to the large surface to volume ratio of the specimens thin enough for the TEM study.

The electron diffraction ring patterns of the ≈ 800 Å films had more spots and more intense rings than the diffraction patterns of the < 200 Å films, presumably because of the larger size and number of crystals in the thicker films. The diffuse rings observed in these diffraction patterns correspond to Fe_3O_4 , and the spotty rings correspond to Fe_3C and Fe_7C_3 , indicating that the grains of the carbide phases are larger than the grains of the oxide phase. This is a direct result of the deposition atmosphere, which is highly reducing, and favors the formation of the carbide phases.

The carbide rings in the electron diffraction patterns of the ≈ 800 Å films are composed largely of spots of varying sizes along with some continuous intensity. This indicates that both small and large coherent diffracting grains consisting of Fe_7C_3 and Fe_3C are present in these ≈ 800 Å thick films.

The half-micron sized platelets observed in the morphology type I were always seen in continuous film regions. The columnar microstructure observed in some PECVD iron carbide films^{8,9} may be a result of the preferential growth of the platelets, which are surrounded by 1000-2000 Å size grains.

The unusual 50 Å non-crystalline mantles, which surround the 100-200 Å iron carbide crystals, exhibited curved fringes in the high resolution TEM images, characteristic of poorly crystalline graphite with d-spacings of 3.2-4.1 Å.^{17,18} There are two possible mechanisms that could explain the formation of these coatings: (i) a post formation oxidation process, which expels carbon into the grain boundaries; or (ii) the diffusion of carbon from the support film into the grain boundaries, made possible by a high diffusion gradient between the heated substrate and the depositing plasma species.

4. REFERENCES

1. J. M. Blocher, Jr., *J. Vac. Sci. Technol.* **11**, 680 (1974).
2. J. A. Thornton, *Ann. Rev. Mater. Sci.* **7**, 239 (1977).
3. R. F. Bunshah, *Vacuum* **27**, 353 (1977).
4. H. T. G. Hentzell, C. R. M. Grovenor and D. A. Smith, *J. Vac. Sci. Technol.* **A2**, 218 (1984).
5. H. F. Winters and P. Sigmund, *J. Appl. Phys.* **54**, 4760 (1974).
6. S. Veprek, *Thin Solid Films* **97**, 17 (1982).
7. J. L. Li, W. J. James and T. J. O'Keefe, *Mat. Sci. Eng.* **B7**, 359 (1990); **15** (1990).
8. H. Siriwardane, W. J. James, O. A. Pringle and J. Newkirk, submitted to *Scripta Met.*
9. H. Siriwardane, J. Newkirk, W. J. James and O. A. Pringle, submitted to *Thin Solid Films*.
10. H. Siriwardane, S. A. Howard, O. A. Pringle and W. J. James, Conf. App. X-Ray Anal., Session D-4, (1992).
11. H. Siriwardane, W. J. James, O. A. Pringle, and J. W. Newkirk, submitted to *Mat. Res. Soc. Symp. Proc.*
12. P. Fraundorf and G. Keefe, *Micron* **13**, 49 (1982).
13. Shin Tajima and Shin-ichi Hirano, *Jpn. J. App. Phys.* **29**, 662 (1990).
14. O. A. Pringle, G. J. Long, J. L. Li, W. J. James, F. Grandjean and G. C. Hadjipanayis, *IEEE Trans. Magn.* **28**, 2862 (1992).
15. W. Caray, E. Zinne, P. Fraundorf and R. S. Lewis, *Meteoritics* **22**, 349 (1987).
16. A. Bourret, J. Thibault-Desseaux and D. N. Seidman, *J. Appl. Phys.* **55**, 825 (1984).
17. P. R. Buseck and H. Bo-Jun, *Geochimica et Cosmochimica Acta* **49**, 2003 (1985).
18. F. J. M. Rietmeijer and I. D. R. Mackinnon, *Nature* **315**, 733 (1985).

UHV PREPARATION AND IN-SITU SURFACE ANALYSIS OF MNFE/NIFE EXCHANGE STRUCTURES: INTERFACIAL IMPURITY INCORPORATION

SUSAN L. COHEN*, JOHN M. BAKER*, MICHAEL A. RUSSAK**, GERALD J. SCILLA***, CHERNGYE HWANG**, STEPHEN M. ROSSNAGEL*

*IBM T.J. Watson Research Center, P.O. Box 218, Yorktown Heights, NY 10598

**IBM-ADSTAR, 5600 Cottle Road, San Jose, CA 95193

***IBM Technology Products, 1000 River Road, Essex Junction, VT 05452

ABSTRACT

MnFe/NiFe exchange structures have been prepared in an ultra-high vacuum sputtering/surface analysis system. Controlled introduction of residual gas impurities such as O₂ and H₂O at the MnFe/NiFe interface is studied by in-situ x-ray photoelectron spectroscopy (XPS) and the exchange structures are magnetically characterized. Due to the extreme reactivity of the NiFe surface towards O₂, the exchange coupling is severely degraded by only small exposures of this molecule to the NiFe surface. In contrast, H₂O does not oxidize the NiFe surface and therefore can be tolerated in greater quantities in the sputtering chamber without detrimental loss of exchange. This understanding of the basic surface chemistry of the MnFe and NiFe surfaces can lead to improved sputtering practices in actual manufacturing applications.

INTRODUCTION

The antiferromagnetic/ferromagnetic MnFe/NiFe exchange structure has received considerable attention due to its importance as a means for suppression of domain switching (Barkhausen noise) in NiFe based magnetoresistive sensors.[1-4] The MnFe/NiFe exchange interaction is believed to require growth of the antiferromagnetic fcc γ MnFe phase on the fcc NiFe substrate. Although the fcc γ MnFe phase is the stable phase in bulk form at room temperature, [5-9], thin film samples of MnFe deposited on amorphous substrates crystallize in the α MnFe (Al₂O₃ Mn) structure [10-12]. Thus intimate contact between the MnFe and the fcc NiFe substrate is required in order to make the MnFe film conform to the desired fcc structure. Since this is an interfacial effect, impurity incorporation at the MnFe/NiFe interface can be quite detrimental to the magnetic performance of these structures.[12]

The goal of this study is to systematically understand the factors which lead to interfacial impurity contamination and to determine the effect of these impurities on the magnitude of the exchange coupling across the MnFe/NiFe interface. These experiments were performed in an ultra high vacuum (UHV) sputtering/analysis system which has been previously described [13]; the UHV conditions prevent unintentional contamination of the NiFe surface thus making it possible to independently control the impurity level at the MnFe/NiFe interface. The clean NiFe surface has been intentionally exposed to both H₂O and O₂ prior to MnFe deposition. The correlation between in-situ surface analysis using X-ray Photoelectron Spectroscopy (XPS) and ex-situ magnetic measurements suggests that while O₂ adsorption at the MnFe/NiFe interface is quite detrimental to the exchange coupling, this interface is significantly more tolerant to the presence of H₂O vapor in the vacuum system.

RESULTS AND DISCUSSION

Oxygen Introduction at the MnFe/NiFe Interface

An air exposed NiFe substrate is covered with a thin (10-15Å) oxide composed of NiO and Fe⁺⁺ oxides/hydroxides.[13, 14] Prior to MnFe deposition, this NiFe surface was cleaned

by in-situ ion beam sputtering so as to produce a surface characteristic of only Fe and Ni metal as shown in Figure 1. A series of MnFe/NiFe exchange structures were then prepared by exposing the clean NiFe surface to controlled amounts of O_2 followed by MnFe deposition. XPS spectra of these O_2 dosed NiFe surfaces before MnFe deposition are shown in Figure 1.

In the XPS data in Figure 1, the angle between the surface plane and the axis of the analyzer is 19° ; in this configuration the measurement is sensitive to predominantly the top 6 Å of the NiFe surface. Exposing the NiFe surface to 1 Langmuir (L) of O_2 ($1 \text{ L} = 1 \times 10^{-5} \text{ torr-sec}$), causes the surface oxygen coverage to increase to 0.3 monolayers, although no oxidation of either the Ni or the Fe metal is observed. (Oxygen coverages, θ , are estimated using known values of the photoionization cross section [15], electron escape depth, and analyzer transmission function and are similar to published results on NiFe single crystals. [16]) The surface oxygen coverage increases further after a 6L exposure to $\theta \sim 0.5$ monolayer; the surface is still predominantly metallic, however the shape of the Fe 2p line indicates that a small amount of Fe has been oxidized. Exposure of the NiFe surface to 40L O_2 ($\theta \sim 1.0$ monolayer) leads to complete preferential oxidation of the Fe to Fe^{3+} while the Ni is still mainly metallic. These results are all consistent with the observations of Brundle and coworkers [16] on single crystal Ni₃Fe surfaces. Continued O_2 exposure up to several hundred Langmuir (not shown) leads to saturation of the surface oxidation at $\theta \sim 3$ monolayer, [13, 16] at which point the surface is composed of predominantly Fe_2O_3 and NiO.

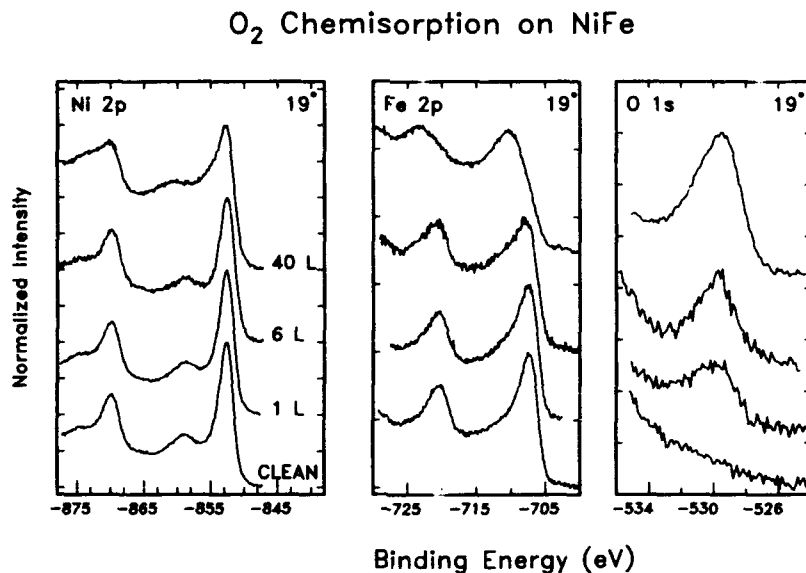


Figure 1. Mg $K\alpha$ XPS of O_2 chemisorption on NiFe surface prior to MnFe deposition. In this experimental geometry the XPS spectra are most sensitive to the top 6 Å of the NiFe surface.

Exchange structures were fabricated by MnFe deposition on these oxygen covered NiFe surfaces and the measured exchange coupling as a function of oxygen coverage is illustrated in Figure 2. The unidirectional exchange anisotropy, H_{ex} , is approximately 30 Oersteads (Oe) for MnFe deposition on a clean 400Å NiFe film. There is clearly, however, a decrease in H_{ex} as the oxygen content at the interface increases. For the NiFe surfaces covered with approximately 0.3 to 0.5 monolayers of chemisorbed oxygen atoms, the magnitude of H_{ex} has dropped by greater than 50 % relative to the structure prepared with a clean NiFe surface. However, in this coverage range, even though the magnitude of H_{ex} has decreased, the coupling between layers is not completely eliminated.

By an oxygen coverage of $\theta = 1.0$ monolayer, the MnFe film is no longer magnetically coupled to the NiFe surface below, ($H_{ex} = 0$ Oe.). The XPS data in Figure 1. indicate that at this coverage, complete oxidation of the surface Fe has occurred. It is interesting to note that in the NiFe single crystal oxidation study [16], a LEED pattern attributed to chemisorbed oxygen on Ni is still maintained for coverages of approximately 1.0 monolayer (and greater), even though significant oxidation of the Fe is observed. Thus, distinct patches of Fe_2O_3 and ordered O/Ni metal coexist on the oxidized single crystal NiFe surface in this coverage regime. Although the NiFe surfaces used for our studies are polycrystalline, the similarity of the XPS spectra suggests that a similar situation may occur on these surfaces. Thus by $\theta = 1.0$ monolayer, although some areas correspond to chemisorbed oxygen on surface Ni atoms, there are also coexisting patches of Fe_2O_3 . Thus, it is not necessary to have complete surface oxidation in order to completely eliminate the exchange coupling across the MnFe/NiFe interface.

Water Introduction at the MnFe/NiFe Interface

Since H_2O is the most common residual gas in most sputtering chambers, it is important to understand the effect of H_2O adsorption at the MnFe/NiFe interface and to compare this to the effects of O_2 as discussed above. Our results indicate that the reactivity of H_2O towards the NiFe surface is significantly less than is observed for equivalent O_2 exposures. This is consistent with results obtained on Ni [17, 18] Fe [19] and MnFe [13] surfaces, where the sticking coefficient for H_2O is significantly less than for molecular oxygen. For H_2O exposures of up to 44,000 L there is no oxidation of either the Ni or the Fe on the NiFe surface, even though XPS analysis shows evidence for the dissociative adsorption of H_2O into OH fragments: an O 1s peak at ~ 529.6 eV is observed with an intensity that corresponds to approximately $\theta = 0.3$ monolayer.

The lower reactivity of H_2O relative to O_2 for the NiFe surface translates into a greater tolerance of the MnFe/NiFe exchange structure to H_2O exposure, as illustrated in Figure 3. A series of MnFe/NiFe exchange structures were prepared in which the NiFe surface was dosed with 1200L - 44,000L H_2O before MnFe deposition. (These exposures are much greater than generally experienced under normal processing conditions. For example in a sputter chamber with a partial pressure of H_2O equal to 1×10^{-7} torr, if the NiFe surface is exposed for 2 minutes this would correspond to a 12L exposure.) After 1200- 44,000L the measured exchange value decreased by approximately 40% relative to a film prepared without H_2O at the interface. This should be contrasted to the effect observed for significantly lower exposures of O_2 . Due to the rapid oxidation of the NiFe surface, a 40L O_2 exposure on NiFe is sufficient to completely destroy the exchange coupling. Thus, for equivalent exposures of O_2 and H_2O at the interface, the exchange coupling will degrade significantly less with exposure to H_2O due to the lower reactivity of water vapor for the NiFe surface.

Implications to MnFe/ NiFe Sputtering Tools

It is important to understand the role of residual gas chemisorption on clean MnFe films since the MnFe coated chamber walls and MnFe target are exposed to the residual gas environment in the chamber. While these exposed surfaces can act as high surface areas to getter contaminants from the sputtering atmosphere, contaminants adsorbed on the MnFe walls can also potentially be driven back onto the NiFe surface causing degradation of exchange coupling.

Both O_2 and H_2O react with the MnFe surface to form a surface oxide layer; [13] the reaction with O_2 quickly leads to formation of a thick (35 Å) oxide composed of predominantly MnO and Fe_2O_3 . [13] The interaction with H_2O is more sluggish, giving approximately 5 Å of a Mn oxide/hydroxide after a 34,000 L H_2O exposure. The high reactivity of O_2 with MnFe surfaces [13] means that immediately after MnFe sputtering, the walls of the chamber will be an excellent getter for this impurity if any is present in the vacuum system. Thus a MnFe presputter step prior to NiFe surface cleaning is worthwhile so as to minimize O_2 exposure to the clean NiFe surface. If a significant amount of H_2O is present in the vacuum system (which is often the case for o-ring sealed vacuum systems), although it will not react with and form an oxide on the NiFe surface, it will react and form a thin oxide film on the MnFe coated chamber walls and MnFe target. Thus, when the MnFe deposition process begins, surface Mn oxides and adsorbed impurities will likely be sputtered or desorbed off the walls and target onto the clean NiFe surface. The plasma environment during deposition likely enhances the reactivity of gas phase H_2O molecules through dissociation and/or ionization thus increasing the possibility of reaction with the NiFe surface.

Thus, if the process chamber has been exposed to significant amounts of residual gases in between the NiFe surface cleaning and MnFe deposition, the final exchange coupling will be much higher if the NiFe surface is protected by a shutter when the MnFe sputtering begins. To test this, a NiFe surface was exposed to 7500 L H_2O and deposition was initiated without shuttering the NiFe surface: no exchange coupling across the MnFe/NiFe interface was measured as indicated by the point in Figure 3. Thus, exposure of the clean NiFe surface to this reactive plasma environment in the presence of impurities can severely degrade the integrity of the MnFe/NiFe interface.

In summary, as long as good standard sputtering practices are followed, preparation of MnFe/NiFe should be possible and quite reproducible in most sputtering systems. However, since O_2 reacts extremely quickly to oxidize the NiFe surface, the presence of a significant air leak or impure sputtering gases can severely limit the exchange coupling. On the other hand, due to the lower reactivity of H_2O for the NiFe surface, high pressures of H_2O vapor can be tolerated in the sputtering system. Presputtering of the MnFe target while the NiFe surface is shuttered, is critical to the successful exchange coupling. This practice serves to remove residual gases adsorbed on the walls of the chamber and react them into the depositing MnFe film and it cleans the MnFe target of any oxide which has formed on the surface. Thus line of sight reactions of these reactive species with the clean NiFe surface is prevented.

Use of a residual gas analyzer for continuous monitoring of these impurity gases during the the pumpdown, chamber conditioning (presputtering), and deposition process can lead to improved magnetic performance and maximum throughput of the sputtering tool. On a related note, while this work shows that interfacial impurities have a detrimental effect on the MnFe/ NiFe exchange interaction, a recent study has shown that controlled impurity incorporation away from the NiFe/MnFe interface is actually beneficial. [20]

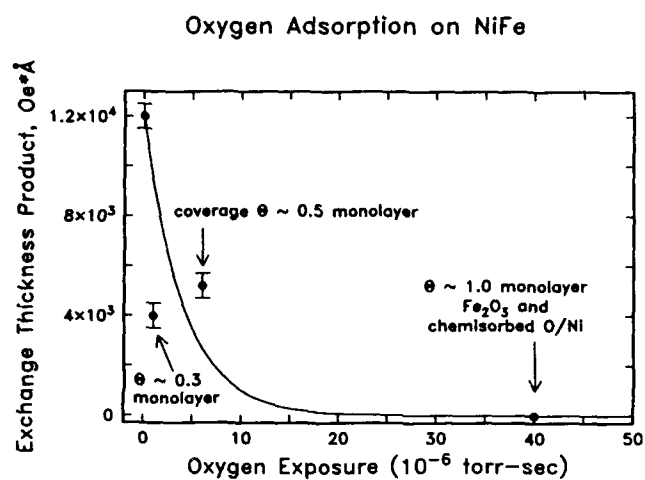


Figure 2. Degradation in exchange coupling due to oxygen adsorption on the NiFe surface. The unit of gas exposure is 1 Langmuir (L) which is equal to 1×10^{-6} torr-sec.

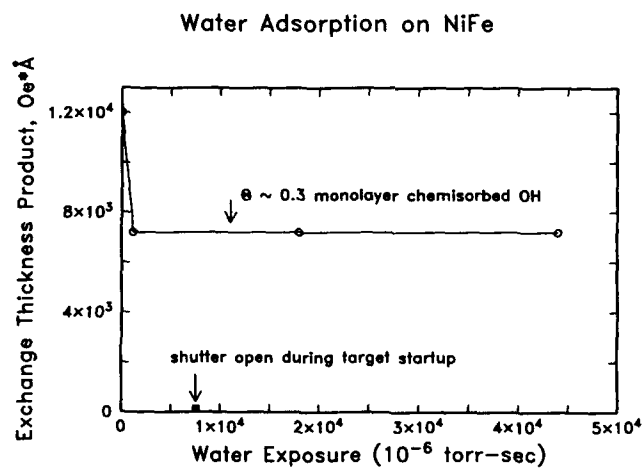


Figure 3. Effect of H_2O adsorption at the NiFe interface on exchange coupling; while water exposure leads to adsorption of ~ 0.3 monolayer of surface OH groups, this does not prevent magnetic coupling across the MnFe/NiFe interface. The unit of gas exposure is 1 Langmuir (L) which is equal to 1×10^{-6} torr-sec.

The authors gratefully acknowledge the technical assistance of Michael Cobb and Christopher Jahnes.

BIBLIOGRAPHY

- ¹ R. D. Hempstead, S. Krongelb and D. A. Thompson, IEEE Trans. Magnet. **MAG-14**, 521-3 (1978).
- ² C. Tsang, N. Heiman and K. Lee, J. Appl. Phys. **52**, 2471-3 (1981).
- ³ C. Tsang and K. Lee, J. Appl. Phys. **53**, 2605-7 (1982).
- ⁴ A. Yelon, Physics of Thin Films **6**, 205-300 (1971).
- ⁵ Y. Ishikawa and Y. Endoh, J. Phys. Soc. Jap. **23**, 205 (1967).
- ⁶ T. Hashimoto and Y. Ishikawa, J. Phys. Soc. Jap. **23**, 213 (1967).
- ⁷ Y. Ishikawa, H. Sekine and K. Yamada, J. Phys. Soc. Jap. **37**, 874 (1974).
- ⁸ C. Kimball, W. D. Gerber and A. Arrott, J. Appl. Phys. **34**, 1046 (1963).
- ⁹ Y. Endoh and Y. Ishikawa, J. Phys. Soc. Jap. **30**, 1614 (1971).
- ¹⁰ K. Sumiyama, N. Ohshima and Y. Nakamura, Phys. Stat. Sol. **98**, 229 (1986).
- ¹¹ C. Hwang, R. Geiss and J. K. Howard, J. Appl. Phys. **64**(10), 6115 (1988).
- ¹² M. A. Russak, S. M. Rossnagel, S. L. Cohen, T. R. McGuire, G. J. Scilla, C. V. Jahnes, J. M. Baker and J. J. Cuomo, J. Electrochem. Soc. **136**(6), 1793 (1989).
- ¹³ S. L. Cohen, M. A. Russak, J. M. Baker, T. R. McGuire, G. J. Scilla and S. M. Rossnagel, J. Vac. Sci. Tech. A **6**(3), 918 (1988).
- ¹⁴ R. A. Pollak and C. H. Bajorek, J. Appl. Phys. **46**, 1382-88 (1975).
- ¹⁵ J. H. Scofield, J. Elec. Spectrosc. Relat. Phenom. **8**, 129-137 (1976).
- ¹⁶ C. R. Brundle, E. Silverman and R. J. Madix, J. Vac. Sci. Tech. **16**, 474 (1979).
- ¹⁷ P. R. Norton, R. L. Tapping and J. W. Goodale, Surf. Sci. **65**, 13-36 (1977).
- ¹⁸ C. Benndorf, C. Nobl, M. Rusenberg and F. Thieme, Surf. Sci. **111**, 87-101 (1981).
- ¹⁹ M. W. Roberts and P. R. Wood, J. Elec. Spectr. Relat. Phenom. **11**, 431-37 (1977).
- ²⁰ O. Allegranza and M. - . Chen, Paper EB02, 36th Conference on Magnetism and Magnetic Materials (Dec 1-4, 1992).

Section B—Interfaces and Characterization

PART IV

Nanostructural Characterization

APPLICATION OF HIGH-RESOLUTION ELECTRON MICROSCOPY TO THE STUDY OF MAGNETIC THIN FILMS AND MULTILAYERS

R. Sinclair, T.P. Nolan, G.A. Bertero and M.R. Visokay
Department of Materials Science and Engineering, Stanford University, Stanford CA, 94305

ABSTRACT

The performance of a wide range of modern magnetic thin-film materials for information storage is found to depend dramatically on grain nucleation and coherence at interfaces. Three such systems, Fe/Pt multilayers, Co/Pt multilayers, and CoCrTa/Cr bilayers are considered here. High-resolution electron microscopy (HREM) shows that ordered CoPt and FePt L_{10} structures can be formed and oriented, using coherence with the substrate, with their magnetically easy c-axes perpendicular to the film plane. This orientation results in the perpendicular magnetization required for magneto-optic recording media. Different sputtering gases used in producing Co/Pt multilayers result in varying degrees of interfacial intermixing, which is shown to strongly affect the perpendicular magnetic anisotropy energy. The required high in-plane coercivity of longitudinal recording media is also correlated with the observed interface coherence and the resulting oriented growth of CoCrTa with the magnetically hard $\langle 110 \rangle$ axis perpendicular to the film plane. Many features of the microstructure can be observed directly at the atomic level by HREM, and so the usefulness of this technique is emphasized in this paper.

INTRODUCTION

The microstructural components which make up contemporary magnetic thin films are rapidly approaching the atomic level. For example magnetic multilayers may be comprised of metal films only a few monolayers thick. The crystal sizes of recording media are often 10-20 nm in lateral dimension. Accordingly the interface structure plays an important role in determining the properties, and higher resolution techniques are required to study the important microstructural features. High-resolution electron microscopy (HREM) can now reveal atomic arrangements even in close-packed metals and so is well-suited to this endeavor. This paper describes some of our recent work using HREM, drawing on examples from multilayer systems (e.g., Co/Pt, Fe/Pt) and from longitudinal recording media (e.g. CoCrTa alloy).

EXPERIMENTAL PROCEDURE

The magnetic thin films were made by sputtering techniques. They are examined in cross-section and through-foil geometries in a Philips EM430 (300 kV) transmission electron microscope which has about 0.19 nm resolution. Additional characterization is performed using standard bright and dark field imaging, selected area and microdiffraction, elongated probe microdiffraction and x-ray energy dispersive microanalysis [1]. Bulk studies are also carried out by x-ray diffraction, vibrating sample magnetometry, magneto-optic Kerr rotation and torque magnetometry.

RESULTS

CoPt and FePt (001) Annealed Films

There has been significant interest lately in magnetic alloys with perpendicular magnetic anisotropy, with possible applications in magneto-optic recording. Promising magnetic and magneto-optic properties have been found in $\text{Co}_{1-x}\text{Pt}_x$ [2] and $\text{Fe}_{1-x}\text{Pt}_x$ [3] disordered alloy films as well as ordered FePt alloy films and multilayers[4]. Our investigation has centered upon producing perpendicular magnetization using crystallographically oriented, ordered alloys, focusing on the tetragonal compounds CoPt and FePt. Both compounds adopt the $L1_0$ structure and have a magnetic easy axis along the unique (c) direction.

Accordingly, c-axis oriented CoPt and FePt thin films would be expected to possess perpendicular anisotropy. The formation of these (001) oriented phases in thin film form has been accomplished by annealing epitaxial multilayers that are stacked along [001] [5,6]. The films are produced by DC magnetron sputtering in argon onto MgO (001) polished single crystal substrates. The as-deposited structure of a (13 Å Co/19 Å Pt)₃₂ multilayer is shown in Figure 1,

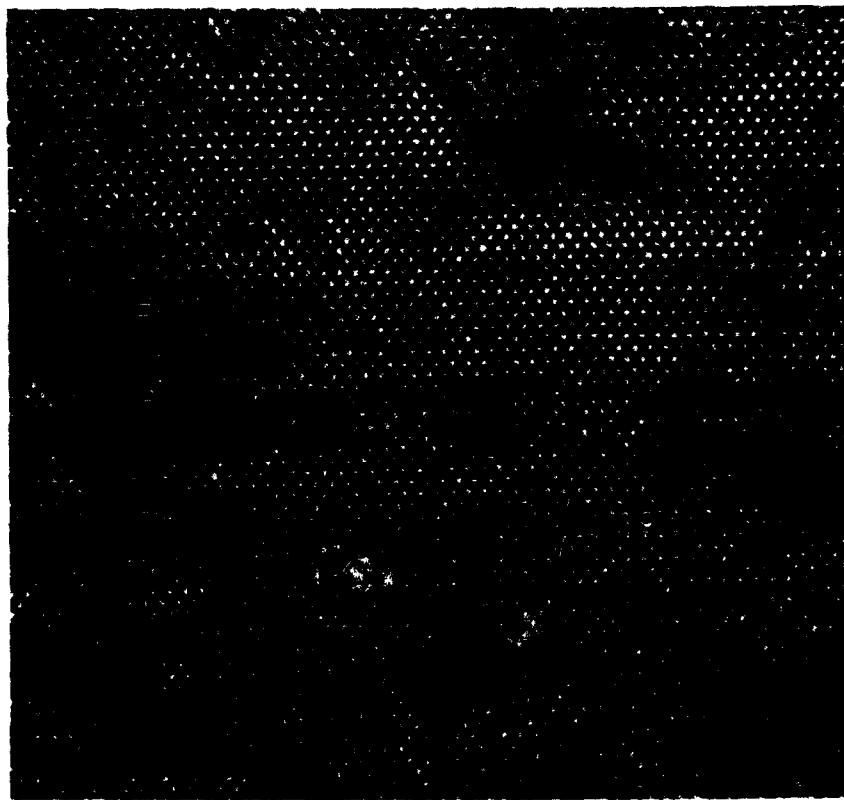


Figure 1. High resolution cross-section image of a (13 Å Co/19 Å Pt)₃₂ multilayer deposited onto (001) oriented single crystal MgO, taken in the MgO [110] orientation with the growth direction vertical in the picture. The lattice fringes are consistent with the [110] projection of an fcc material throughout.



Figure 2. High resolution cross-section image of the film shown in Figure 1 after annealing at 675 °C for 14 hours. The orientation is again MgO [110] and the growth direction is vertical in the picture. The fringes are due to CoPt (001) and (110) planes, with 3.7 Å and 2.7 Å spacings, respectively. These fringes are indicative of the presence of ordered CoPt.

which is a high resolution cross-section image taken in the MgO [110] orientation, with the growth direction vertical. The lattice fringes in both the Co and Pt layers are consistent with a [110] zone axis image of an FCC material, indicating that the film is fcc throughout. This film exhibited an in-plane magnetic easy axis before annealing.

After annealing at 675°C for 14 hours, the magnetic easy axis switched to out-of-plane with a net perpendicular magnetic anisotropy of 1.9×10^7 erg/cm³, and a magneto-optic Kerr rotation of 0.4° at saturation, for a wavelength of 633 nm. This dramatic change in magnetic properties was a direct result of the formation of c-axis oriented CoPt upon annealing. Figure 2 shows a high resolution cross section image of the same film shown in Figure 1, after annealing. The zone axis is again MgO [110] and the growth direction is vertical. In this case the fringes seen in the image are due to the (001) and (110) planes in the ordered structure, with spacings of approximately 3.7 Å and 2.7 Å, respectively. These planes are forbidden for any of the constituent materials in the film and will only appear as a result of ordering, so the image shown in Figure 2, as well as extensive x-ray diffraction measurements, conclusively demonstrate the presence of a significant amount of the ordered phase. Similar results have been obtained for FePt films stacked along [001], which show a dramatic improvement in magnetic properties upon annealing to form c-axis oriented FePt[6,7]. It is worthwhile noting that HREM easily distinguishes the ordered L₁₀ phase from the fcc disordered alloy. Thus we can say that there is no evidence of ordering as the as-deposited Co-Pt interfaces in our images. It will be of interest to determine the extent that ordering can be detected in such images by computer simulation (e.g. [8]) and this work is currently underway.

Perpendicular Anisotropy in Pt/Co Multilayers

Pt/Co multilayers oriented along the [111] out-of-plane direction present the most promising magneto-optic recording properties in the blue-range wavelengths [9]. These multilayers have been shown to display large magnetic coercivities and perpendicular magnetocrystalline anisotropies and have remanent perpendicular magnetization of about 100% [2, 9-11]. In spite of this, there has not been a large scale effort to characterize these structures by TEM and correlate the relevant magneto-optic properties with microstructural features. The most promising combination of properties in the Pt/Co multilayer structures is achieved when the individual Co layer thicknesses corresponds to the stacking of two close-packed planes and the Pt layer thicknesses correspond to five to seven monolayers [2,9-16]. For these cases, the perpendicular anisotropy energy, K_{\perp} , is maximum. Maximizing the anisotropy energy becomes important because it aids in the stabilization of the magnetic domains which is a critical aspect for high density recording. It is well known that cubic symmetry does not allow for a uniaxial magnetic anisotropy and therefore the presence of hcp Co was thought largely responsible for giving origin to a bulk anisotropy contribution term. A Néel type symmetry breaking effect contributing to K_{\perp} through an interface anisotropy term is also believed important [15]. Therefore, sharp interfaces between the Co and the Pt were thought beneficial.

In this work we contrast the magnetic properties and high resolution TEM images from two multilayers with identical period but sputtered with different gas compositions. Figure 3 shows the microstructure resulting from a film sputtered in a 100% Ar atmosphere while Figure 4 shows the high resolution image from the film sputtered in an Ar/Xe mixture. The sample in Fig. 4 was additionally annealed at 340 °C for 3.25 h. It is evident from the figures that the atomic structures are quite different. The Ar/Xe sputtered film shows 100% fcc stacking. The composition

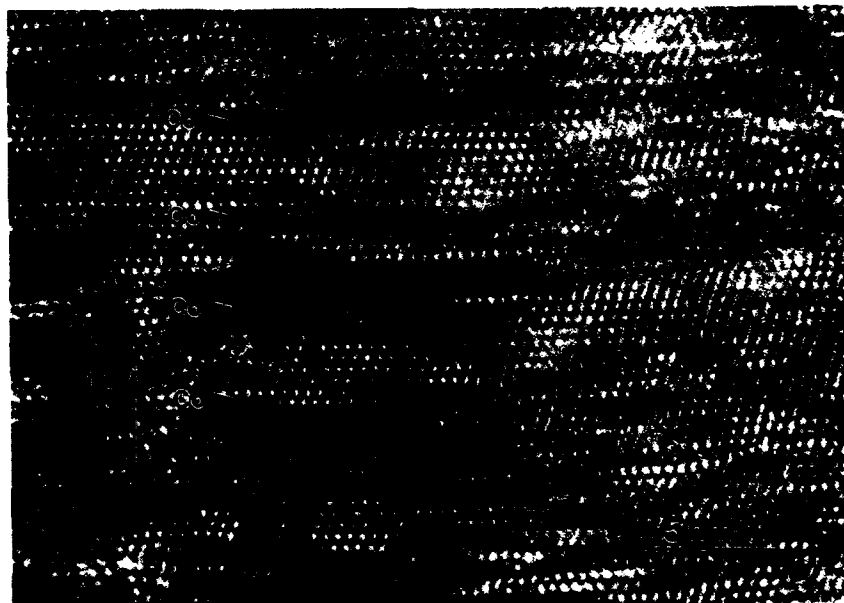


Figure 3. High resolution TEM micrograph from a Pt/Co multilayer structure sputtered in a 100% Ar ambient at 1.5 mTorr. The horizontal fringes are traces of the (111) close packed planes. A large number of stacking faults are present. The stacking is mostly fcc although hcp is also present. The composition modulation is not visible under these imaging conditions.

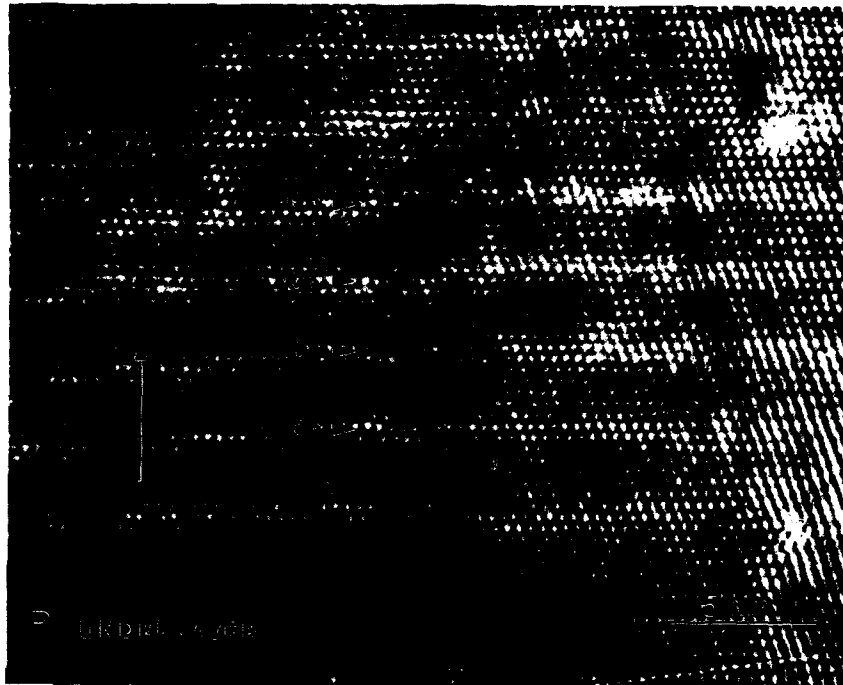


Figure 4: High resolution TEM micrograph from a Pt/Co multilayer structure sputtered in a mixed Ar/Xe ambient at 5 mTorr. The stacking is 100% fcc and free of stacking faults. The composition modulation is visible and indicated by arrows.

modulation can also be clearly distinguished and the interfaces do not appear to be chemically sharp. In this regard, it is very difficult to quantify the degree of intermixing at the interfaces from these type of images. However, Pt and Co are miscible in each other and therefore mixing at the interfaces is expected to take place. On the other hand, the Ar sputtered film shows a heavily faulted structure. A study of this and other micrographs indicates that the Co is in both fcc and hcp form. These stacking faults were attributed to the presence of hcp Co but they are often also seen within the Pt layer themselves [16].

The association of these faults with hcp Co led to the proposition that their presence might be responsible for enhancing the uniaxial anisotropy energy [16]. Following these arguments it would be reasonable to think that the faulted structure would yield a larger value for the perpendicular magnetic anisotropy compared to the unfaulted one. However, torque magnetometry indicates a value of $6 \times 10^6 \text{ erg/cm}^3$ for K_{\perp} for the Xe/Ar sputtered sample and $1.8 \times 10^6 \text{ erg/cm}^3$ for the Ar sputtered film. Our results therefore indicate that the presence of hcp Co is not necessary to produce a highly anisotropic magnetic uniaxial film. Furthermore, the necessity of sharp interfaces also appears to be unfounded. The origin of the large magnetic anisotropy of the Xe/Ar sputtered sample cannot be easily explained at present. The use of TEM techniques to study the atomic structure and correlate it to the magnetic measurements can be instrumental in arriving at more satisfactory models to explain such behavior.

Longitudinal Recording Media

The magnetic performance of cobalt alloy longitudinal magnetic recording media is just as interface dependent as that of magneto-optic multilayer media. Present-day production recording

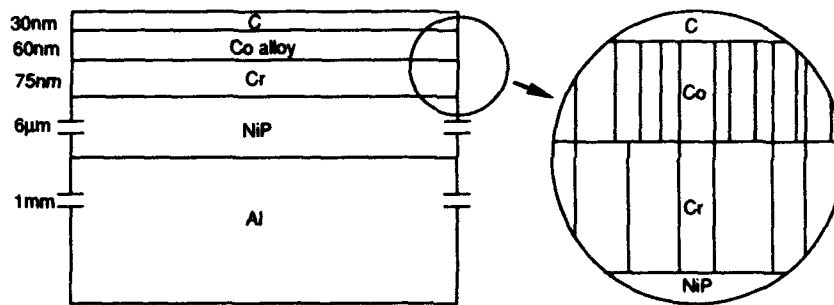


Figure 5. Schematic cross-section of a longitudinal recording medium.

media often consist of NiP plated aluminum substrates on which three sputtered thin films are deposited as shown schematically in Figure 5. The ferromagnetic cobalt (Co) alloy layer is generally preceded by a 500Å-2000Å chromium (Cr) underlayer which forms a columnar, crystalline microstructure on top of the amorphous plated layer as in Figure 6 [17, 18]. The morphology and crystallography at the top surface of the Cr layer can, however, depend dramatically on sputtering parameters such as temperature, morphology and bias of the substrate, chamber argon pressure, and sputtering time and power [19, 20]. The details of the Co alloy microstructure and the resulting magnetic properties of the complete recording media are then a strong function of both the detailed microstructure of the Cr template and of the nucleation, growth and coherence level at the Co alloy/Cr interface, which can be observed in the CoCrTa/Cr sample (Figure 7) [21, 22].



Figure 6. Cross-section HRTEM image of the Cr/NiP interface showing the formation of crystalline Cr on the amorphous substrate.



Figure 7. Cross-section HRTEM image of the CoCrTa/Cr interface showing the semicoherent interface which controls the crystallographic orientation of the Co alloy layer.



Figure 8. Plan-view HRTEM image of the CoCrTa layer showing in-plane c-axis orientation of the hcp grains, stacking faults and intergranular separation as labeled.

For example, the medium in Figures 6 and 7 was deposited at 250°C, and has a high coercivity of 1300 Oe. An identical CoCrTa film deposited without a Cr underlayer is not oriented, and has a much lower coercivity of about 600 Oe. A room temperature deposited CoCrTa/Cr medium, otherwise identical to that shown in Figures 6 and 7, also has a coercivity of about 600 Oe. Under such low mobility conditions the films are incoherent, and again the preferred orientation is lost. High values of coercivity (the magnetic field required to change the sign of the magnetization) are desired for low noise and to avoid accidental overwrite of neighboring bits.

The effect of the interface structure on the resulting Co alloy grain structure can be observed by plan-view HRTEM of the CoCrTa layer (Figure 8) [23]. Observed changes in the intergranular separation, orientation, predominance of the hcp Co alloy phase and the stacking fault density can all affect magnetic performance and are all controlled in large by the initial growth of Cr at the substrate interface and of the cobalt alloy at the Co alloy/Cr interface.

CONCLUSIONS

HREM can play an extremely important illuminating role in characterizing the structure, especially at interfaces in magnetic thin films. Examples of studies on Co/Pt and Fe/Pt multilayers, and Co-alloy based recording media, illustrate the type of information which is readily available. More detailed analysis is possible as the range of applicability becomes increasingly sophisticated.

Financial support from Kobe Steel U.S.A. and Komag Corporation is gratefully acknowledged. We would also like to thank Bruce Lairson, Toyo Konno, Tom Yamashita and Rajiv Ranjan for helpful and stimulating discussions.

REFERENCES

1. T. P. Nolan, R. Sinclair, R. Ranjan, and T. Yamashita, *Ultramicroscopy* **47** 437 (1992).
2. D. Weller, H. Brandle, G. Gorman, C.J. Lin and H. Notarys, *Appl. Phys. Lett.* **61** 2726 (1992).
3. T. Katayama, T. Sugimoto, Y. Suzuki, M. Hashimoto, P.d. Haan and J.C. Lodder, *J. Magn. Magn. Mater.* **104-107** 1002 (1992).
4. M. Watanabe, K. Takanashi and H. Fujimori, *J. Magn. Magn. Mater.* **113** 110 (1992).
5. B.M. Lairson, M.R. Visokay, R. Sinclair and B.M. Clemens, *J. Magn. Magn. Mater.*, in press.
6. B.M. Lairson, M.R. Visokay, R. Sinclair and B.M. Clemens, *Appl. Phys. Lett.* **62** 639 (1993).
7. M.R. Visokay, B.M. Lairson, B.M. Clemens and R. Sinclair, *J. Magn. Magn. Mater.*, in press.
8. R. Sinclair, K. Schneider and G. Thomas, *Acta Metall.* **23** 501 (1975).
9. D. Weller, J. Hurst, H. Notarys, H. Brandle, R.F.C. Farrow, R. Marks and G. Harp, *MORIS 1992 proceedings*.
10. W.B. Zeper, H.W. van Kesteren, B.A.J. Jacobs, J.H.M. Spruits, and P.F. Carcia, *J. Appl. Phys.* **70**, 2264 (1991).
11. W.B. Zeper, H. van Kesteren, and P. Carcia, *Adv. Mater.* **3**, 379 (1991).
12. S. Hashimoto, Y. Ochiai, and K. Aso, *J. Appl. Phys.* **67** 2136 (1990).
13. F.J.A.M. Greidanus and W. B. Zeper, *MRS Bulletin*, April 1990, p. 31.
14. M.H. Kryder, *J. Mag. Magn. Mater.* **83** 1 (1990).
15. F.J.A. den Broeder, W. Hoving and P.J.H. Bloemen, *J. Magn. Magn. Mat.* **93** 562 (1991).
16. C.J. Chien, R.F.C. Farrow, C.H. Lee, C.J. Lin and E.E. Marinero, *J. Magn. Magn. Mat.* **93** 47 (1991).
17. T. Lin, *J. Magn. Magn. Mat.* **86** 159 (1990).
18. T. Yeh, J. M. Sivertsen and J. H. Judy, *IEEE Trans. Magn.* **26** 1590 (1990).
19. T. P. Nolan, R. Sinclair, R. Ranjan and T. Yamashita, *IEEE Trans. Magn.* **29** 292 (1993).
20. J. C. Lin, C. D. Wu and J. M. Sivertsen, *IEEE Trans. Magn.* **26** 39 (1990).
21. R. Ranjan, J. A. Christner and D. R. Ravipati, *IEEE Trans. Magn.* **26** 322 (1990).
22. M. R. Khan, R. D. Fisher and N. Heiman, *IEEE Trans. Magn.* **26** 118 (1990).
23. T. P. Nolan, R. Sinclair, R. Ranjan and T. Yamashita, *J. Appl. Phys.* in press (1993).

INITIAL GROWTH AND MORPHOLOGY OF ULTRATHIN MAGNETIC FILMS STUDIED USING SCANNING TUNNELING MICROSCOPY.

DAVID D. CHAMBLISS, K.E. JOHNSON, K. KALKI, S. CHANG AND R.J. WILSON
IBM Research Division, Almaden Research Center, 650 Harry Road,
San Jose, California 95120-6099

ABSTRACT

The room-temperature growth of Fe on Cu(100) has been studied using the scanning tunneling microscope (STM) to determine low-coverage growth mode and local structures related to the FCC-BCC structural transformation. Results for submonolayer deposition demonstrate an initial interchange of deposited Fe atoms with substrate Cu. This leads to a highly rough Fe-Cu interface and growth characteristics that for different experimental techniques can resemble 3-D island growth or layer-by-layer growth. For a thickness ~ 14 monolayers, the FCC-BCC transition is observed to occur via the formation of fairly large martensitic grains, rather than by a change in atomic aggregation. The implications of the instability of FCC-Fe, as evident in both low- and high-coverage data, are considered.

INTRODUCTION

A great deal of effort is being devoted to understanding the magnetic properties of ultrathin metal films and layered structures, with layers typically less than 10 atoms thick. A serious hindrance to the complete understanding of these properties has been uncertainty about the actual structure of the films. Of obvious importance is the film morphology, since films of a uniform thickness can differ markedly in magnetic properties from films whose thickness varies by only a few atomic diameters over length scales of several nanometers. Equally interesting are local or global variations in atomic structure in the films such as strain and defects. In recent years it has become increasingly clear that the scanning tunneling microscope (STM) is an excellent tool for investigating these questions.

Fe grown epitaxially on Cu(100), which is the subject of this paper, is a magnetically important system that illustrates the richness of structural variation possible in these very thin films. This is ironic, since early hopes were that one could determine the physics of a simple monolayer of face-centered cubic Fe readily. Soon after the growth of face-centered cubic (FCC) Fe on Cu(100) was reported,¹ contradictions began to appear in the literature regarding its room-temperature growth mode. Auger electron spectroscopy (AES) breakpoints were interpreted initially as indicating layer-by-layer² and later as bilayer-by-bilayer growth.³ Anisotropies of AES and x-ray photoemission (XPS) intensities indicated that a significant fraction of Fe atoms in a submonolayer deposit were buried beneath other atoms, which seemed to indicate the growth of bilayer or 3-D islands.^{4, 5} The variations in diffracted intensity observed using reflection high-energy electron diffraction (RHEED)⁶, medium-energy electron diffraction (MEED)⁷, and helium atom scattering (HAS)^{8, 9} have been interpreted as indicating an initial 3-D growth followed by island coalescence. This appears in conflict with STM observations of only monolayer-high islands for low-coverage (< 0.2 monolayer (ML)) Fe deposits.¹⁰ An additional complication, and indeed an essential element for understanding the actual structure and resolving these contradictions, is the intermixing of Cu atoms with the deposited Fe first observed using XPS⁵ and examined in more detail with STM.¹⁰

These disparate conclusions about the structure of Fe on Cu(100) are sometimes dismissed as differences in sample preparation, since the structure could prove anomalously sensitive to variations in substrate quality, vacuum cleanliness, and deposition conditions. We note, however, that different groups using essentially similar techniques (e.g., AES or XPS forward scattering; or various topography-sensitive diffraction methods) have usually found very similar data, these lab-to-lab variations notwithstanding. It seems instead that differences in interpretation have arisen because each technique measures only a few characteristics of the growth, and these are insufficient to characterize behavior that lies outside our conventionally accepted modes. Indeed, the extensive STM results described here (and presented more thoroughly elsewhere^{11, 12}) demonstrate a mode that can be

described as "intermixing-controlled nucleation," the results of which can appear similar to either a layer-by-layer mode or 3-D growth, depending on the measurements made.

(A further source of confusion is the inconsistent use of growth-mode terminology. The onset of second- and higher-layer growth before the first layer is complete can occur because of kinetic limitations, such as an energy barrier that keeps atoms from crossing atomic steps. Depending on the amount of the higher-layer growth, we call this "nearly layer-by-layer" or "simultaneous multilayer" growth. In the STM this is easily distinguished from true 3-D growth, which occurs when there is both a thermodynamic driving force and sufficient step-crossing mobility for deposited atoms to form 3-D clusters that minimize their surface energy. For many experimental techniques, however, these will yield similar results.)

With further deposition (> 4 ML) there is more agreement about the growth mode, which becomes nearly layer-by-layer⁷ and presumably yields a film of good FCC Fe. This continues until the Fe film converts to its bulk-stable body-centered cubic (BCC) structure, at a thickness of ~ 14 ML, a value that can depend on contamination and temperature.¹³ Transmission electron microscopy¹⁴ and more recently low-energy electron diffraction (LEED) and STM¹⁵ have been used to show that the BCC Fe exists in the Pitsch orientational relationship¹⁶ in which $[110]_{\text{BCC}}$ lies parallel to the $[100]_{\text{FCC}}$ surface normal, and the close-packed directions $\langle 111 \rangle_{\text{BCC}}$ and $\langle 011 \rangle_{\text{FCC}}$ are parallel. This yields four different grain orientations, generated by reflections through (011) and (011) mirror planes of the substrate. As one expects, the structural transition changes measurable properties such as magnon dispersions.¹⁷ Little has been known about the processes and forces responsible for the FCC-BCC transformation in these films, however. In the second section of this paper we show that STM can reveal a great deal about this structural transition. The results show a martensitic transformation that occurs locally in the "bulk" of the thin film.

EXPERIMENTAL

The experiments were performed in a multi-chamber ultra-high-vacuum (UHV) system¹⁸ in which samples were prepared, characterized, and examined with the STM in the same UHV environment. Single-crystal Cu(100) substrates were cleaned by repeated Ar-ion bombardment and brief 600°C anneals. A cooling time of > 1 hour after the final annealing step left the sample at nominal room temperature (RT), $295\text{K} < T < 310\text{K}$, during deposition. For some experiments the sample holder for deposition was cooled with liquid nitrogen or heated with an embedded resistive heater. Fe deposition was from a coiled 1mm wire of 99.998% Fe $\sim 50\text{cm}$ from the sample, heated by electron bombardment to yield a typical rate of 1 ML/80s. Evaporator operation caused a rise in background pressure of $\sim 7 \times 10^{-10}$ Torr, and a small carbon peak was usually seen in AES spectra after deposition. Deposition rate was usually monitored using an ion gauge exposed to part of the evaporated Fe flux, which measured 3×10^{-8} Torr at our standard deposition rate. As suggested by Egelhoff,¹⁹ the difference between this ion-gauge reading and the background pressure was integrated to determine the total Fe dose. Total deposited amounts were determined with the STM by measuring the volume of aggregated material (islands plus deposits at steps); care was taken to choose representative areas and to minimize errors due to the broadening of island images by the finite STM tip. For depositions of < 2 ML, these STM measurements agreed with the ion-gauge estimates of Fe dose to within 5%. This not only confirms the accuracy of the ion-gauge method but also verifies a one-to-one correspondence between deposited material and apparent aggregates on the surface. Thicker deposits consumed enough of the total Fe charge to change the spatial distribution of Fe vapor and thus the gauge calibration, so coverages in the second section of the paper are estimates based on Auger electron intensity ratios and on other reports of the FCC-BCC transition in the literature.^{7, 15}

RESULTS AND DISCUSSION: INITIAL GROWTH

STM measurements show that, for depositions up to 0.7 ML, most island area is only 1 atomic layer high (fig. 1(a)). Incident atoms that land atop an island that has already formed are therefore able to contribute to first-layer aggregation, either by stepping over the island edge or by some atomic interchange. While the topography rules out a true bilayer or

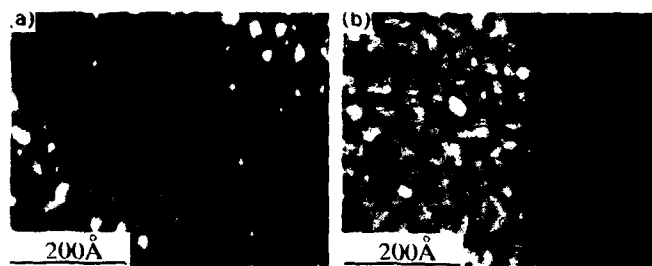


Figure 1. Layer growth in Fe deposited on Cu(100) at 300K. (a) STM image of 0.66ML Fe deposited on Cu(100). This coverage is just below the first-layer percolation threshold, so first-layer islands have coalesced into fairly large but still separate aggregates. A large number of second-layer islands accounts for 10% of the surface area; most of the surface is covered just 1ML deep. (b) STM image of 1.30ML Fe on Cu(100). Second-layer growth now covers 45% of the surface, and 15% of layer 0 remains uncovered.

3-D island growth mode on our samples, it does not indicate ideal layer-by-layer growth. First, it is shown below that a significant fraction of the deposited Fe atoms form inclusions *within* the top layer of the Cu(100) surface ("layer 0"), and a corresponding amount of the first-layer aggregate consists not of Fe but of Cu atoms displaced by Fe atoms. Second, beyond the 0.7ML threshold, the second-layer coverage (i.e., the fraction of the surface covered by aggregates 2 or more layers thick) begins to increase rapidly. A 1ML deposit leaves ~20% of the sample covered with bilayer aggregates and ~20% of layer 0 (the starting substrate surface) exposed. After 1.3ML is deposited (fig. 1(b)), 45% of the second layer is filled, while 15% of layer 0 remains exposed. The rate of second-layer growth beyond the 0.7ML threshold shows that almost every atom that lands atop a first-layer aggregate contributes to second-layer coverage. It is surprising at first to find this fairly abrupt change in atomic behavior, and perhaps more surprising that it coincides with the coalescence of first-layer islands into a percolating network. But downward steps can be highly reflective boundaries for adatoms diffusing on the upper terrace, so those adatoms may reside atop an island for a considerable time before finally stepping down to the first layer. Before coalescence, such adatoms are constrained atop small islands, so repeated reflections do not change the adatoms' ultimate fate, except if enough atoms reside on the same island long enough to nucleate a new second-layer island. After percolation, such an adatom can travel a long distance atop the network until it finds a second-layer island that will absorb it. In this model, the absorption of adatoms by the second-layer islands should suppress the nucleation of new second-layer islands after percolation, and this is observed in the STM data.

The change in growth behavior has an important consequence for the interpretation of diffraction intensity results.⁷ The nearly layer-by-layer aspect of the growth before the transition accounts very well for the sharp decrease in diffracted intensity. (We note that true 3-D islands would cover less surface area and, at least in an antiphase kinematic analysis, produce a much slower dropoff.) A continued layer-by-layer topography would cause an intensity maximum when the first layer is completed, but this is suppressed by the onset of second-layer growth. The 20%-60%-20% distribution of exposed layer heights at 1ML deposition corresponds to a relative kinematic intensity of $(0.6 - (0.2 + 0.2))^2 = 0.04$, roughly consistent with experimental diffraction results. A full analysis incorporating the length scales of the measured topography²⁰ yields good quantitative agreement between predictions from STM data and published MEED results.

Fe inclusions

As is noted above, there is considerable evidence that room-temperature deposition does not lead to simple Fe aggregation atop an undisturbed Cu(100) surface; some sort of intermixing is clearly present. STM images indicate, directly and indirectly, how Cu atoms are redistributed by Fe deposition. Exposure of a 0.92ML Fe deposit to O_2 , for example, reveals the compositional heterogeneity of the first-layer aggregate by leaving Cu regions unchanged but converting monolayer Fe to a hexagonal FeO layer with easily observed atomic corrugation.^{11, 12} The unusual evolution of the island size distribution, discussed below, proves that some modifications of the substrate are involved in island nucleation, though by itself this does not demonstrate intermixing as the cause. The most direct picture of intermixing, however, is found in STM images at coverage < 0.2 ML (figure 2). After room-temperature deposition, two distinct kinds of features are always seen. True topographic features (steps and islands) have apparent heights and shapes that are mostly independent of bias voltage and tip condition. An island number density $n = 3.5/(100\text{\AA})^2$ is typical for low-coverage RT deposition at 1ML/80s. Also observed are smaller (typ. $< 10\text{\AA}$ wide), more numerous ($n = 50/(100\text{\AA})^2$) features that may appear higher or lower than the surrounding terrace, depending on tip condition and bias. Our initial report of these features concentrated on an unusual (and not easily reproduced) imaging mode that apparently involved reversible tip changes.¹⁰ Many later measurements have shown that these patches could be imaged fairly reliably as shallow apparent depressions in the surface. The tip- and bias-sensitivity demonstrates that the patches differ electronically or chemically from the surrounding Cu surface, presumably due to a composition difference. There may also be a systematic height difference between the patches and the surrounding Cu, but that difference must be small compared to the 1.8\AA height of Cu(100) steps.

We have determined that the patches are Fe inclusions embedded in the Cu surface (layer 0). The aggregate area of patches agrees with the total amount of Fe deposited, in particular within 0.01ML for a 0.11ML sample, although area measurements of such small patches has a fairly large relative uncertainty (15%). When no Fe is deposited the patches are not observed, and when deposition is slowed by a factor of 10 to increase the amount of contamination relative to Fe, the patch area is again the amount of deposited Fe. For this slow deposition (fig. 2(a,b)), the spacing between patches is increased somewhat, which also occurs when deposition is onto a sample heated to $\sim 100^\circ\text{C}$ (fig. 2(c)). Fe deposited onto a sample at 120K and subsequently annealed to RT, which in XPS studies did not exhibit intermixing,⁵ also does not exhibit patches in the STM (fig. 2(d)). This proves that the patches do not arise merely from the adsorption of contamination during or after deposition. Heating the sample of fig. 2(d) to $\sim 150^\circ\text{C}$, a temperature sufficient to cause intermixing in XPS studies, does produce Fe inclusions with a similar STM appearance to those in room-temperature samples. While it is conceivable that contamination could in some way facilitate the formation of Fe inclusions or, more likely, their visibility in the STM, it is certain that the inclusions themselves are composed mostly of the deposited Fe atoms.

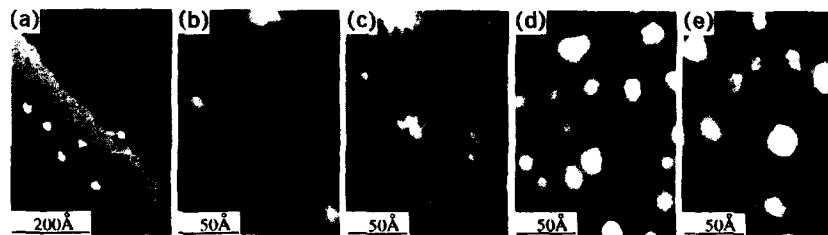


Figure 2. Fe inclusions in Fe deposited on Cu(100) at 300K. (a) Wide scan of ~ 0.05 ML Fe deposited slowly (1ML/800s) shows both Cu islands (light spots) and more numerous Fe inclusions (darker patches on each terrace). (b) Closer view of the same sample shown in (a). (c) Deposition of 0.1ML at 80°C yields somewhat larger patches. Appearance of most islands is altered by patches near edge. (d) 0.2ML Fe deposited at $\sim 120\text{K}$ and annealed to 300K. (e) Sample of (d) after further annealing to 420K.

The contrast mechanism that makes Fe inclusions visible in the STM does not show a distinction between Fe and Cu in all circumstances. In particular, the nearly pure Fe islands produced by deposition at 120K and RT annealing do not show a bias-dependent reduced height; these islands have a normal topographic appearance. In images of RT deposits above about 0.2ML, for which Fe atoms have started contributing to first-layer aggregation, patches with appearance similar to inclusions do appear when the Fe component of the first layer is small. The Fe-Cu boundary is not usually imaged clearly, however, when the first-layer Fe areas are fairly large. It is easy to imagine, but difficult to prove, that the contrast for inclusions may arise from electronic states or preferential contaminant adsorption that depends on the size of the Fe cluster or the detailed atomic arrangement at the Fe-Cu boundary. Supporting this possibility is the observation that the Fe-Cu contrast seen for inclusions is not a simple level shift but also may contain a significant edge component, as can be seen in fig. 2 (b) and (c).

The existence of the Fe inclusions, and their response to temperature, raise interesting questions about the surface thermodynamics of this system. The formation of segregated inclusions rather than a random Fe-Cu alloy implies that clustering of implanted Fe atoms reduces total energy; i.e., Fe-Cu mixing at the surface is endothermic, as in bulk. The conversion of some Fe islands into inclusions upon moderate annealing suggests that inclusions are energetically favorable to monolayer islands. Changing an Fe island into an inclusion requires removing an equal number of Cu atoms from the surface and making an island with them. To the extent that a single layer of atoms can be described with continuum surface/interface energies acting on an enclosing box, the increase in Cu surface and in Cu-Fe interface are both equal to the decrease in Fe surface area, namely the area of the island's outer edge. Then the surface and interface energies must be related by $\gamma_{Fe} > \gamma_{Cu} + \gamma_{Fe-Cu}$, where the Fe terms are not for bulk FCC Fe but for FCC Fe strained to match the Cu lattice. A plausible model for inclusion formation is that Fe adatoms on Cu(100) diffuse only a short distance at RT before undergoing an atomic exchange with a substrate atom, like the exchange process involved in self-diffusion on some FCC(100) metal surfaces.²¹ This is driven by atomistic energetics that correspond to the relation between continuum surface-energies stated above: an Fe adatom on Cu(100) has a higher total energy than a Cu adatom plus an Fe substitutional impurity. The thermodynamic force toward Fe segregation may appear as a larger energy release and a smaller activation barrier for Fe-Cu exchange next to other Fe atoms. After an atom exchange, the Cu adatom that is released behaves as would a deposited Cu atom, which during early deposition stages means it either diffuses to a step or encounters enough other Cu atoms to form an island nucleus.

With deposition beyond 0.2ML it becomes increasingly difficult to find Fe inclusions in the exposed substrate, though compositional heterogeneity in first-layer growth is usually visible, as discussed above. At these coverages the dominant growth is still confined to the first layer, but the island nucleation and growth becomes complicated. In normal island growth an initial nucleation stage is followed by a growth phase in which islands absorb the available adatoms and suppress further island nucleation, so that island number density is nearly constant and the average island size increases steadily. For Fe on Cu(100), however, new small islands continue to form even after the larger islands have begun to coalesce. The new islands are nucleated heterogeneously by the Fe inclusions; one indication of this is that the final spacing of these small islands is very nearly the spacing of inclusions at low coverage. The high surface energy of Fe discussed above makes Fe inclusions favorable sites for Fe or Cu adatom aggregation. With islands closely spaced, deposited Fe atoms more frequently attach to these islands than exchange with Cu atoms, so little more intermixing occurs. This behavior continues until second-layer growth becomes dominant as described above.

The structure that results from this evolution of the aggregation behavior is shown in Fig. 3. The low-coverage figures (b and c) illustrate the early formation of Fe inclusion and the nucleation of islands by these inclusions; the length scales are chosen to match those observed in STM images. At 1ML, the Fe is distributed as roughly 20%/60%/20% in layer 0 (originally Cu)/layer 1/layer 2, respectively. By this point the Fe inclusions have been covered by first-layer growth, so the portions of layer 0 that remain exposed (amounting to 20% of the surface) consist of Cu. The locations of second-layer islands in STM images show that they tend to grow atop first-layer Fe, leaving exposed most of the Cu atoms that have been incorporated into the first layer by the Fe-Cu exchange process; this accounts for

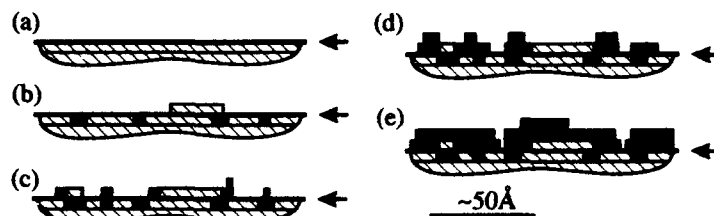


Figure 3. Schematic cross sections of initial Fe growth on Cu(100) (300K). Black and hatched regions denote Fe and Cu, respectively. Arrows and heavy horizontal lines indicate original position of substrate surface. Approximate amounts of deposited Fe are: (a) 0; (b) 0.05ML; (c) 0.3ML; (d) 1.0ML (e) 2.0ML. Cross sections are chosen to illustrate typical sizes and spacings of islands and Fe inclusions. At low coverage these sections intersect more islands and inclusions than would a random section, so the proportion of black regions in (b) and (c) is greater than the amount of Fe deposited on the sample. Length scales are different for horizontal and vertical directions (step heights are 1.8Å).

another 15-20% of the surface. Thus about 35-40% of the exposed atoms at this point are Cu. The tendency for Fe atoms to be covered in the structures described in fig. 3 explains why these structures yield signals suggestive of bilayer island growth in AES and XPS. Both integrated intensities and angular distributions measure the environment of emitting atoms within a lateral scale of only a few atomic spacings, so these methods cannot identify the vertical positions of islands relative to the original Cu surface. In fact, the true structure at 1ML is almost that of small, quasi-3-D islands embedded in the substrate, due largely to the high Fe surface energy that could have been expected to yield 3-D growth. The essential difference is that true 3-D growth will not revert to a smooth film, whereas the topography in this system is still fairly flat (3 exposed layers account for >98% of the surface), which allows a nearly layer-by-layer mode to return with further Fe deposition.

Some structural aspects portrayed in fig. 3 remain uncertain. The figure suggests that Cu atoms in level 1 islands do not get promoted to higher levels by further Fe-Cu exchange. This is plausible, since an Fe adatom atop an island may be absorbed at an island boundary before undergoing exchange, particularly if the outer parts of the island consist of Fe. For comparison, we note that Fe-Cu exchange in layer 0 is effectively suppressed after 0.2ML has been deposited, at which point many inclusions and islands are present to absorb Fe atoms. Islands are typically smaller than the spacing between these features, so island edges are presumably also effective at suppressing exchange. However, we have no direct evidence to support or refute the promotion of a small amount of Cu (a few percent of a ML) from level 1 to level 2.

It is also not known from STM results how much of the Fe in inclusions is covered by second-layer growth after 1ML is deposited, i.e., how much Fe is "doubly buried." For the 20%-60%-20% distribution of Fe atoms, this could be as great as 0.2ML (if Fe inclusions and layer-2 islands are somehow strongly correlated), as low as 0.0ML (if completely anticorrelated), or 0.05ML (if uncorrelated beyond the constraint that all Fe inclusions are covered by first-layer growth). A weak positive correlation, with 0.05-0.10ML of doubly buried Fe, is the most likely result of the island nucleation in layers 1 and 2. These atoms can be identified using AES or XPS by a forward scattering peak along the surface normal, and researchers using these diffraction methods have reported the presence⁵ and the absence⁴ of such a peak for 1ML deposited at 300K. Results for this peak were not expressed quantitatively in these studies, but angular distributions for different nominal 1.0ML deposits (Fig. 3 in Ref. 4) show intensity variations along the surface normal that would be consistent with roughly 0.0-0.1ML of doubly buried Fe. The variability in Ref. 4, and the contradictory finding in Ref. 5, can be explained in our model by small coverage variations, since the amount of doubly-covered Fe rises rapidly with coverage in this range because of the second-layer-growth threshold discussed above.

RESULTS AND DISCUSSION: MARTENSITE TRANSFORMATION

The structural complexity of the initial growth can be understood as resulting from the independent motion on the surface of single atoms, with occasional atom-pair motion required for the Fe-Cu atomic exchange. One might expect the eventual change to BCC growth would also occur via surface processes. The change from layer growth to 3-D growth of Au on Ag(110), for example, can be explained by changes in local sticking coefficients for single Au adatoms diffusing on the surface.^{22, 23} For Fe on Cu(100) we find, however, that the FCC-BCC transition occurs by the collective shear transformation of fairly large grains (typ. 150Å wide and >2000Å long) extending deep into the Fe film. While this kind of transformation is unusual in very thin films, these characteristics are just those of martensitic transitions studied in bulk metals for decades.²⁴

A snapshot of the FCC-BCC transition is seen in STM images of a sample with nominal Fe thickness of 14ML (Figure 4). LEED for this sample showed a coexistence of FCC(100) and BCC(110) patterns, oriented with $[110]_{\text{BCC}} \parallel [100]_{\text{FCC}}$ and $\langle 111 \rangle_{\text{BCC}} \parallel \langle 011 \rangle_{\text{FCC}}$. Long, narrow grains are seen as slightly raised ridges along the close-packed directions of the FCC substrate. The islands atop these ridges have a characteristic orientation in which most island edges make an angle of $\sim 55^\circ$ to the grain axis. This is the angle between the $[11\bar{1}]$ and $[001]$ directions in the (110) plane, identifying these grains as the BCC(110) regions of the film. It is a characteristic of martensitic transformations that grain boundaries between the initial and final phases align approximately with the shared close-packed direction, since this can be either an invariant plane for the shear transformation relating the two structures or a low-energy slip plane. Close examination of island orientation on neighboring grains often shows they are related by a mirror plane containing the grains' common axis. The existence of such twin pairs is a mechanism for strain energy minimization characteristic of bulk martensites²⁴ and is closely related to the long-range ordering of some surface reconstructions.²⁵⁻²⁷

A clearer determination of BCC and FCC regions is found in the different heights of atomic steps (fig. 4(b,c)). Accurate absolute step height measurements are not always possible in the STM, in part because the nominal FCC surface regions have considerable undulations ($\sim 0.3\text{\AA}$) that make definition of an average level difficult. Nonetheless the difference between BCC (2.0Å) and FCC (1.7Å) steps is unambiguous. Thus in fig. 4(b), regions (i) and (ii) are BCC(110) while (iii) is FCC(100). The relationships of island structure between these regions are worth noting. In particular, the steps that bound islands and holes in (iii) continue across the $\sim 1.2\text{\AA}$ height change and sloping regions that define the boundary with (ii). Samples in which the FCC-BCC transition is incomplete show a number of such boundaries, where islands and steps are shifted vertically, or tilted, by a constant amount in a

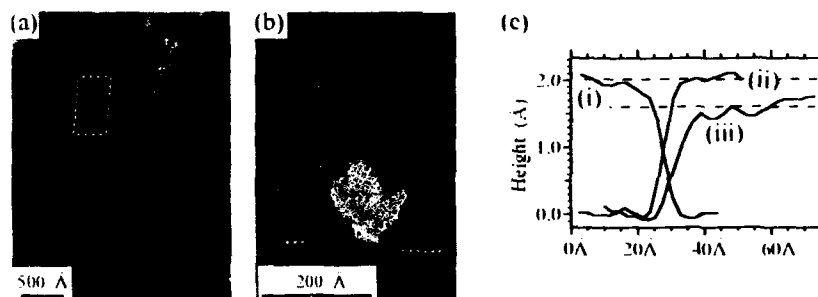


Figure 4. Martensitic BCC Fe grains on Cu(100). (a) Wide scan of $\sim 14\text{ML}$ Fe deposited at 300K. Elongated grains of BCC Fe lie along $\langle 011 \rangle_{\text{FCC}}$ directions, which are rotated $\sim 15^\circ$ clockwise from vertical and horizontal. Dotted parallelogram marks region scanned in (b). Parallelogram shape of image is result of thermal drift compensation after data acquisition is complete. (b) Closer view of (a). Brackets and labels (i) & (ii) indicate two grains that converted to BCC at different times, and (iii) marks a region that retains the FCC structure. Dotted lines indicate locations of line scans graphed in (c). (c) Sections of line scans across island edges shows 2.0Å step characteristic of BCC-Fe(110) (regions (i) and (ii)) and 1.7Å step of FCC-Fe(100) (region (iii)).

fairly large region, and appear otherwise unchanged. Such boundaries are characteristic of a subsurface structural change that either is very rapid compared to deposition or occurs after deposition is complete. In other studies these have been produced after deposition by STM-tip-induced local sample fracture.²⁸ In this case the change is the local FCC-BCC conversion of the film, which produces a height change appropriate to the expected volume change if the full 14ML film is converted. The oriented island growth atop many such grains shows that these conversions occur rapidly during deposition, not afterwards. A bulk martensitic transformation propagates within a grain at roughly the speed of sound in the metal,²⁴ which is effectively instantaneous on the time scale of deposition and aggregation.

The different island structures in (i) and (ii) may be explained by different times of the structural transformation. The oriented islands in (i) are on average almost 1ML thick. They exhibit a uniaxial structure in which steps along $\langle 001 \rangle_{\text{BCC}}$ are preferred (i.e., step normal $\langle 110 \rangle_{\text{BCC}}$), and substantial second-layer growth well before the first-layer islands have coalesced (simultaneous multilayer growth). These are exactly the characteristics recently reported for Fe growth on single-crystal BCC-Fe(110).²⁹ In region (ii) too little aggregation has occurred after conversion to create islands with clear BCC(110) directionality. We point out that in these and other regions, and also for thicker films, there does not appear to be any true 3-D growth. Nonetheless, by most measures the surface is regarded as rough.

The FCC-BCC transition begins before the film thickness of fig. 4 is reached, and continues with further deposition. Its full evolution is beyond the scope of this paper. A variety of different structures occur during the transformation; ultimately most of the surface is covered with grains like those in fig. 4. At the low-thickness end of the transition, very narrow (40Å) in-plane needle-like grains are seen, with sloping surfaces indicative of tilted FCC-BCC boundaries. When much of the surface is covered with the large grains discussed above, there also exist some fairly small tilted grains that apparently accommodate strain between large grains that run either parallel or perpendicular. The orientation of long grains in fig. 4 is apparently determined by the coexistence of FCC and BCC regions, since thicker films exhibit a different grain shapes, though with the same relationship between FCC and BCC lattices.

CONCLUSION

The growth of Fe on Cu(100) has proved much more interesting structurally than was expected. At low coverage the STM results revealed not a simple growth mode of monolayer, bilayer, or multilayer islands, but a complex pattern of growth ultimately caused by the very high surface energy of FCC-Fe(100). The model of fig. 3 explains a great deal of the experimental data presented thus far on the structure of these films. It does not, however, show how one can grow smooth, non-intermixed ultrathin films of Fe on Cu(100). While low-temperature deposition does suppress intermixing, mild annealing is not sufficient to heal the high density of steps at island boundaries that result. It is hard to escape the physical fact that FCC Fe on Cu(100) is in a high-energy configuration.

The conversion of the Fe films to BCC structure at a fairly low threshold thickness is another demonstration of the instability of FCC Fe. A strong tendency toward a BCC local structure must be present to cause the transformation to extend deep into the film, presumably to the Fe-Cu interface. One must suspect that this tendency may cause structural variations or distortions even in films too thin for a large-scale transition to BCC structure. Indeed, the most plausible models proposed for the reconstructions apparent in LEED at fairly low coverage³⁰ involve in-plane shear displacements almost identical to those involved in the martensitic transformation.

The historical confusion about low-coverage Fe on Cu(100) has shown that area-averaging methods can yield misleading results when the full implications of heterogeneity are not taken into account. Now that the structures at either end of the thickness range are better understood, data on the supposedly well-behaved films of Fe on Cu(100) should be examined critically for possible evidence of heterogeneity related to the FCC-BCC instability. A true understanding of the relationship of magnetism to structure in Fe/Cu(100) will require accurate determinations of local structure that go well beyond the many careful studies that have already been performed.

This work was supported in part by the Office of Naval Research (N00014-89-C-0099) and by the A. von Humboldt Foundation.

REFERENCES

- ¹ M. Onellion, M. A. Thompson, J. L. Fu, J. L. Hirskine, and A. J. Freeman, *Phys. Rev. B* **33**, 7322 (1986).
- ² D. Pescia, M. Stampanoni, G. L. Bona, A. Vaterlaus, F. Meier, G. Jennings, and R. F. Willis, *Phys. Rev. Lett.* **60**, 2559 (1988).
- ³ H. Glatzel, T. Fauster, B. M. Scherzer, and V. Dose, *Surf. Sci.* **254**, 58 (1992).
- ⁴ S. A. Chambers, T. J. Wagener, and J. H. Weaver, *Phys. Rev. B* **36**, 8992 (1987).
- ⁵ D. A. Steigerwald, I. Jacob, and W. F. Egelhoff Jr., *Surf. Sci.* **202**, 472 (1988).
- ⁶ D. A. Steigerwald and W. F. Egelhoff Jr., *Surf. Sci.* **192**, 1887 (1987).
- ⁷ J. Thomassen, B. Feldmann, and M. Wuttig, *Surf. Sci.* **264**, 406 (1992).
- ⁸ M. Arnott, E. M. McCash, and W. Allison, *Surf. Sci.* **269/270**, 724 (1992).
- ⁹ P. Dastoor, M. Arnott, E. M. McCash, and W. Allison, *Surf. Sci.* **272**, 154 (1992).
- ¹⁰ D. D. Chambliss, R. J. Wilson, and S. Chiang, *J. Vac. Sci. Technol. B* **10**, 1993 (1992).
- ¹¹ K. E. Johnson, D. D. Chambliss, R. J. Wilson, and S. Chiang, *J. Vac. Sci. Technol. A* **11**, xxxx (1993).
- ¹² K. E. Johnson, D. D. Chambliss, R. J. Wilson, and S. Chiang, (to be published).
- ¹³ J. Thomassen, F. May, B. Feldmann, M. Wuttig, and H. Ibach, *Phys. Rev. Lett.* **69**, 3831 (1992).
- ¹⁴ J. Koike and M. Nastasi, in *Evolution of Thin Film and Surface Microstructure* (Mat. Res. Soc. Proc., Vol. 202, Pittsburgh, PA, 1991), p. 13.
- ¹⁵ M. Wuttig, B. Feldmann, J. Thomassen, F. May, H. Zillgen, A. Brodde, H. Hannemann, and H. Neddermeyer, (to be published).
- ¹⁶ W. Pitsch, *Phil. Mag.* **4**, 477 (1959).
- ¹⁷ P. Xhonneux and E. Courtens, *Phys. Rev. B* **46**, 556 (1992).
- ¹⁸ S. Chiang, R. J. Wilson, C. Gerber, and V. M. Hallmark, *J. Vac. Sci. Technol. A* **6**, 386 (1988).
- ¹⁹ W. E. Egelhoff Jr., *J. Vac. Sci. Technol. A* **3**, 1511 (1985).
- ²⁰ K. E. Johnson and D. D. Chambliss, (to be published).
- ²¹ P. J. Feibelman, *Phys. Rev. Lett.* **65**, 729 (1990).
- ²² S. Rousset, S. Chiang, D. E. Fowler, and D. D. Chambliss, *Phys. Rev. Lett.* **69**, 3200 (1992).
- ²³ S. Chiang, (private communication).

- ²⁴ C. M. Wayman, in *Physical Metallurgy*, edited by R. W. Cahn and P. Haasen (North-Holland, New York, 1983), pp. 1031-1074.
- ²⁵ D. D. Chambliss, R. J. Wilson, and S. Chiang, *Phys. Rev. Lett.* **66**, 1721 (1991).
- ²⁶ O. Alerhand, D. Vanderbilt, R. Meade, and J. Joannopoulos, *Phys. Rev. Lett.* **61**, 1973 (1988).
- ²⁷ S. Narasimhan and D. Vanderbilt, *Phys. Rev. Lett.* **69**, 1564 (1992).
- ²⁸ D. D. Chambliss and R. J. Wilson, *J. Vac. Sci. Technol. B* **9**, 928 (1991).
- ²⁹ M. Albrecht, H. Fritzsche, and U. Gradmann, presented at the 1993 MRS Spring Meeting, San Francisco, CA, 1993 (unpublished).
- ³⁰ W. Daum, C. Stuhlman, and H. Ibach, *Phys. Rev. Lett.* **60**, 2741 (1988).

SCANNING-ION MICROSCOPY WITH POLARIZATION ANALYSIS (SIMPA)

N. J. Zheng and C. Rau

Department of Physics and Rice Quantum Institute, Rice University, Houston, TX 77251.

ABSTRACT

We have developed a novel, high-resolution magnetic imaging technique, scanning-ion microscopy with polarization analysis (SIMPA). In SIMPA, a highly-focused, scanning Ga^+ ion beam is used to excite spin-polarized electrons at surfaces of ferromagnetic materials. By measuring the intensity and the spin polarization of the emitted electrons using a newly developed, compact Mott polarimeter, topographic and magnetic images of magnetic structures are obtained. We report on first SIMPA studies on single-crystalline Fe samples.

INTRODUCTION

Quite recently, secondary electron emission (SEE) has attracted, particularly in combination with analysis of the electron spin polarization (ESP), broad scientific attention. This has been shown by the implementation of secondary electron microscopy with polarization analysis (SEMPA) [1] and of spin-polarized electron emission spectroscopy (SPEES) [2]. Electron- and ion-induced SEE provides a high electron yield which is needed for efficient, high-resolution topographic and spectroscopic imaging of surfaces. Besides this, there are two additional features that show the great scientific and technological potential of the use of SEE for the topographic and magnetic imaging of surfaces. Firstly, the ESP of low-energy electrons ($< 10 \text{ eV}$) emitted from ferromagnetic surfaces materials is enhanced by a factor of two or three as compared to the average magnetization of the material (valence band polarization) [3]. This, when utilized for magnetic imaging, will enhance the image contrast by a factor of four to six. Secondly, the inelastic mean free path of these low-energy electrons in 3d transition metals is, as recently found [4], only of the order of one or two monolayers, which is much shorter than the values published ($3 \text{ nm} - 5 \text{ nm}$) in the past decades. It is especially this characteristic that makes the use of SEE very attractive for high-resolution, topographic and magnetic imaging of bulk and ultra-thin film materials.

With growing interest in magnetism in thin film and multilayer-structured systems, especially with respect to their potential technological applications, a deeper and more fundamental understanding of the influence of the geometrical and chemical micro-structure on surface and interface magnetic properties becomes an area of revived scientific research.

In this paper, we report on a novel, high-resolution magnetic imaging technique, scanning-ion microscopy with polarization analysis (SIMPA). In SIMPA, a micro-focussed ion beam is used to excite electrons at the surface and in deeper-lying layers of a magnetic material. As shown in several recent publications, these ion-induced electrons are spin-polarized [2, 5, 6]. An enhancement of the ESP of the emitted low-energy electrons is found similar to that detected in electron-induced SEE from magnetic materials. In addition, it is found that the surface sensitivity can be varied either by modifying the ion beam energy [5] or the incidence angle of the ions [6,7].

thus offering a promising way to study layer-dependent, microstructural magnetic properties at surfaces of bulk and thin film materials.

Our motivation for the work, presented here, was to develop a new element-specific and spin-sensitive, magnetic and nonmagnetic imaging technique which allows us to vary the probing depth from the topmost surface to deeper layers. In addition, by varying the intensity of the incident ions, SIMPA offers the capability to use the technique not only for imaging but also for depth-profiling and for the etching of 3D patterns. To this, we note that the technique of secondary ion mass spectroscopy (SIMS) is already widely recognized as a reliable technique for chemical depth profiling [8].

By measuring the ESP of emitted Auger electrons, SIMPA offers an additional attractive feature which allows the element-specific imaging of surface magnetic properties. We note that as regards this feature, technical constraints as regards a timely compilation of the data have yet to be overcome. At present, a combination of SIMPA and SIMS seems to be more advantageous than to use solely SIMPA for scanning Auger electron imaging in order to be able to understand the effects of chemical composition on micro-structural magnetic properties.

We note that there is evidence that ion beam sputtering does not alter magnetic properties during depth profiling. Kirschner et. al. [9] recently measured the ESP of secondary electrons emitted from an oxidized Fe crystal as function of oxide film thickness. From the results of their experiments, they conclude that ion beam sputtering does not modify the magnetic properties of the Fe crystal.

EXPERIMENTAL

For our studies on topographical and magnetic surface imaging, we used an ion gun system with a Ga⁺ liquid metal (LM) ion source which is installed in an ultrahigh vacuum system with base pressure of 5×10^{-11} mbar. This system is utilized to provide a micro-focussed (minimum beam spot size: 50 nm) Ga⁺ ion beam for the studies presented here. The beam energy can be varied from 7 to 30 keV. The entire experimental set-up (2 interconnected UHV systems) is suspended by six air springs to isolate floor vibrations during imaging at high resolution. The two interconnected UHV systems are used for sample preparation, thin film growth, sample characterization (RHEED, AES, etc.) and for imaging studies. A 48-inch long mechanically and magnetically coupled linear/rotary feedthrough is used for in situ sample transfer between the two UHV chambers. This manipulator is part of a fast entry-air lock system which enables us to load samples from ambient pressures first into a pressure stage, working at 10^{-7} mbar, and then into the UHV system.

The SIMPA setup, together with a CMA Auger spectrometer and a scanning tunneling microscope is housed in the characterization chamber as shown in Fig. 1. The samples are mounted on a manipulator which is located at the center of the characterization chamber. For the surface imaging, we use Ga⁺ ions incident at an angle of 45° towards the surface to be imaged. The ion-induced electrons emitted from the sample surface are collected using an extracting lens system which is connected to a Mott polarimeter operating at 20 keV. At present, we are analyzing the two in-plane components of the ESP of the collected electrons. For fast adjustment of imaging parameters and precise location of surface areas to be imaged, we use a conventional electron detector and collect secondary electrons which allows for the display of images on a TV monitor at TV rates.

Using a Mott polarimeter, the ESP of electrons is determined by measuring the asymmetry in the 120°-scattering of spin-up and spin-down electrons from a high-Z material which is due to spin-orbit interaction. Without including instrumental asymmetry, the component P of the ESP

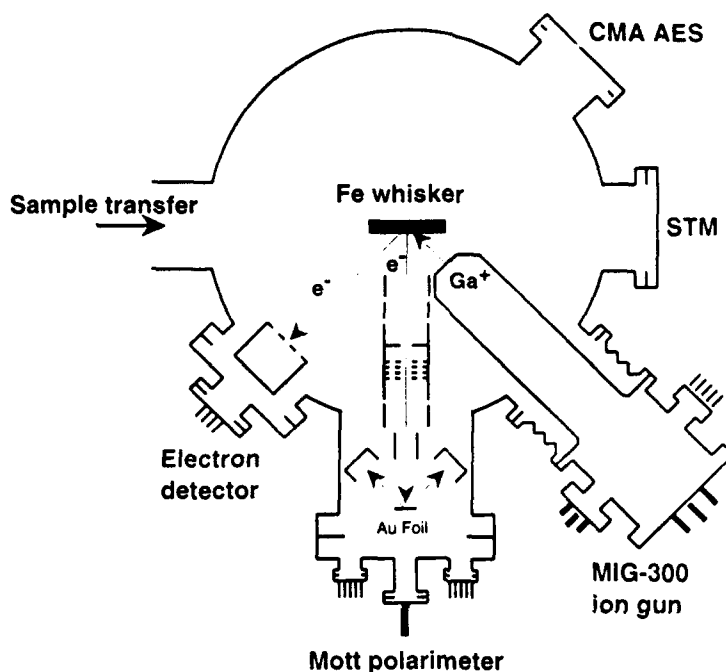


Fig. 1. Schematic of SIMPA set-up.

along the direction normal to the scattering plane is determined by

$$S^*P = (1 - A) / (1 + A), \quad (1)$$

where S is the Sherman function (≈ 0.1) and $A = N_R / N_L$ is the scattering asymmetry with N_R and N_L being the count rates of electrons detected in the channeltrons R and L , respectively.

The relative inefficiency of electron backscattering requires a longer acquisition time for a magnetic image than for a topographic image. Therefore, our electron extracting lens system for the Mott polarimeter is designed to take advantage of the high ESP and high intensity of low-energy electrons in SEE from magnetic materials. Our lens design possesses an acceptance angle of 180° for electrons with energy below 6 eV and of 140° for electrons with energy above 10 eV. These values are determined using a computer (SIMION) program for calculation of trajectories of charged particles. We note that the influence of strong electric fields, applied at the entrance of the extracting lens system, has a negligible effect on the trajectories of the ions used for scanning the surface. For spectroscopic measurements, four retarding grids are incorporated into the lens system. The presence of these grids, however, reduces the transmissivity of the lens system to 64%. Details and performance of the electron polarimeter will be given elsewhere.

An L-shaped, single crystalline Fe whisker is used as sample for our first SIMPA imaging measurements. The sample surface is cleaned in situ by Ar⁺ sputtering, and the surface cleanliness is checked using CMA AES. Residual carbon and oxygen concentrations are less than 2%.

RESULTS AND DISCUSSION

Figure 2 shows an intensity spectrum of electrons emitted from a polycrystalline Fe surface as a function of applied retarding voltage (0-30 V). From the results of this experiment, where we used a 12 keV Ga⁺ ion beam, it is obvious that cascading electrons with energies below 6 eV have a major contribution to the total electron yield being used as signal for magnetic imaging. From this, we estimate collection efficiency of our extracting lens system to be at around 60%.

The inset in Fig. 2 shows the electron yield, γ , as a function of ion energy E_i . γ increases from 0.5 at $E_i = 9$ keV to 1.3 at $E_i = 25$ keV.

For fast ESP measurements, high electron intensities are required because of the low efficiency of the Mott polarimeter. The statistical error in the ESP is determined by

$$\Delta P = (1/FN)^{1/2}, \quad (2)$$

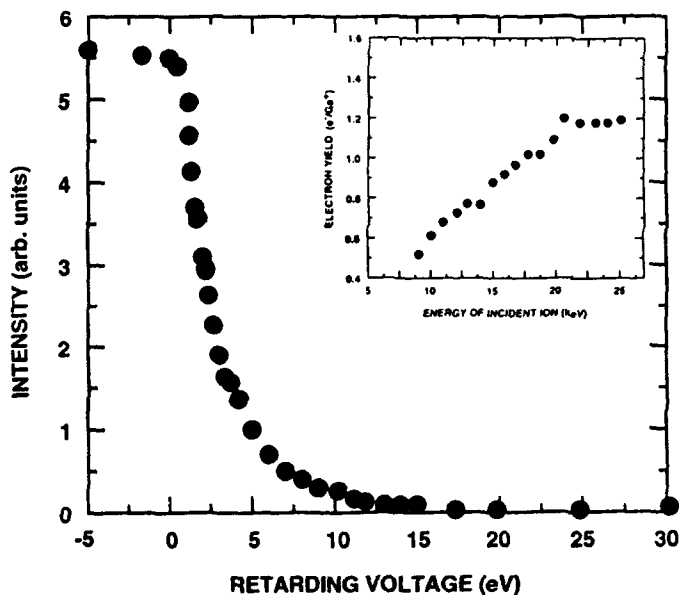


Fig. 2. Ion-induced electron emission spectrum of an Fe surface as a function of retarding voltage with incident beam energy of 12 keV. The inset shows the electron yield as a function of the energy of incident ions.

where F is the figure of merit of the spin polarimeter ($\approx 10^4$) and N is the number of electrons to be analyzed. To achieve a statistical error smaller than 5%, N needs to be $\approx 10^7$. In our present, we use an ion beam current of less than 1 nA for the magnetic imaging and record one image (256×256 pixels) in about 100s.

The upper section of Figure 3 shows a magnetic (a) and a topographic (b) image of a selected area ($500 \mu\text{m} \times 500 \mu\text{m}$) of the surface of the L-shaped Fe whisker. The two images are obtained simultaneously. The incident beam energy and the beam current are 15 keV and 0.5 nA, respectively. The magnetic image clearly shows two large magnetic domains. It appears that two small topographic defects (small black spots) displayed in Fig. 3(b) pins the domain walls recorded in the magnetic image which is shown in Fig. 3(a). The lower sections of Fig. 3(a) and 3(b) display two line profiles of the magnetic signal and of the total electron intensity along the traces marked in the upper section of Fig. 3. From this, it is obvious that the topographic line scan displays a

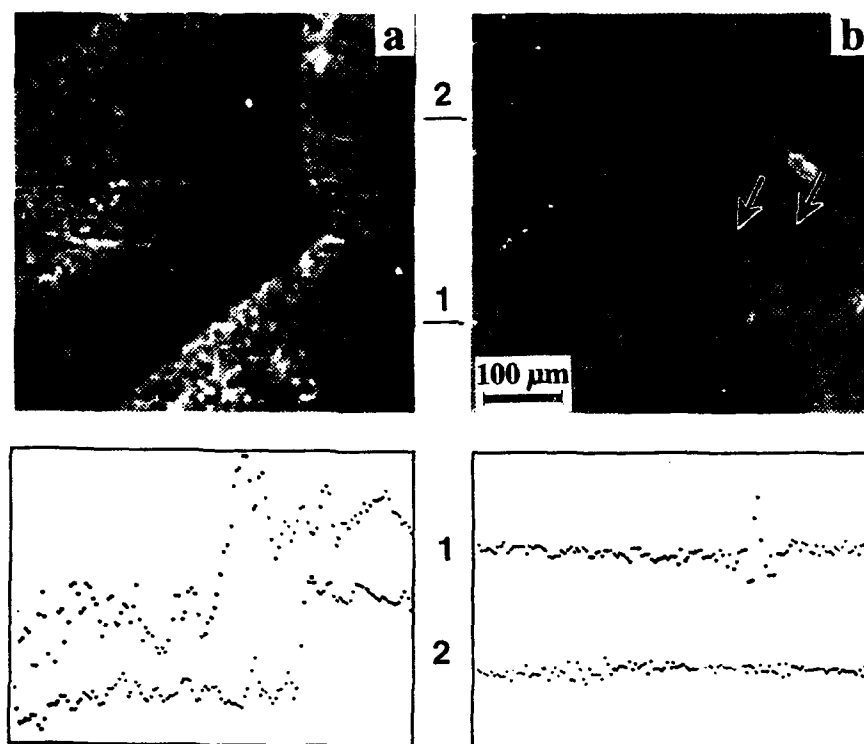


Fig. 3. Simultaneously-acquired SIMPA images of (a) magnetic and (b) topographic structure of an L-shaped single crystal Fe whisker. The image size is $500 \times 500 \mu\text{m}^2$. The bottom section shows the line profiles of magnetic and intensity signals along the traces marked in the upper section, respectively.

smooth surface, and that the magnetic line scan displays ESP values which are abruptly changing from -30% to +30% as expected when the ion beam scans across a magnetic domain wall. This directly show the power and applicability of SIMPA for magnetic domain imaging.

CONCLUSION

We have presented first domain images of the surface of a single crystal Fe whisker using a new technique for domain imaging. SIMPA is a new novel and very promising technique which offers many potential applications such as the use of a variable probing depth, magnetic depth profiling, element-specific chemical and magnetic imaging, and etching of magnetic 3D patterns.

ACKNOWLEDGMENT

We thank H. P. Oepen for many exciting discussions and for providing us an Fe whisker sample.

REFERENCES

1. K. Koike and K. Haykawa, Jpn. J. Appl. Phys. **23**, L187 (1984); J. Unguris, G. G. Hembree, R. J. Celotta and D. T. Pierce, J. Microsc. **139**, SRP1-2 (1985); H. P. Oepen and J. Kirschner, J. Phys. (Paris) Colloq. **49**, C8-1853 (1985).
2. C. Rau, K. Waters and N. Chen, Phys. Rev. Lett. **64**, 1441 (1990).
3. J. Unguris, D. T. Pierce, A. Galejs and R. J. Celotta, Phys. Rev. Lett. **49**, 72 (1982).
4. D. L. Abraham and H. Hopster, Phys. Rev. Lett. **58**, 13 (1987).
5. J. Kirschner, K. Koike and H. P. Oepen, Vacuum **41**, 818 (1990).
6. C. Rau, N. J. Zheng and M. Lu, J. Magn. Magn. Mat. (1993), in print.
7. N. J. Zheng and C. Rau, J. Vac. Sci. Technol. (1993), in print.
8. D. S. McPhail, in *Secondary Ion Mass Spectrometry*, edited by J. C. Vickerman, A. Brown and N. M. Reed (Oxford University Press, New York, 1989), p. 105.
9. J. Kirschner, K. Koike and H. P. Oepen, Phys. Rev. Lett. **59**, 2099 (1987).

Section B—Interfaces and Characterization

PART V

**Magnetism in Multilayers:
Structure and Properties**

STRUCTURE AND MAGNETIC PROPERTIES OF FE/ZR MULTILAYER FILMS

Toyohiko J. Konno*, Takenori Nakayama**, Bruce M. Clemens* and Robert Sinclair*

*Department of Materials Science and Engineering, Stanford University
Stanford, CA 94305, U.S.A.

**Materials Research Laboratory, Kobe Steel, Ltd., Kobe, 651, Japan

ABSTRACT

We investigated structural and magnetic properties of Fe/Zr multilayer films using high-resolution transmission electron microscopy, X-ray diffraction and vibrating sample magnetometry. For films with wavelength (Λ) $\geq 80\text{\AA}$, the interface region between the Fe and Zr layers exhibits a 15-20 \AA thick amorphous structure. The magnetization curves of these films showed a monotonous decrease in the saturation magnetizations with Λ , whose trend is well explained by a simple asymptotic model that assumes the interface amorphous layer to be non-ferromagnetic. Films with $\Lambda \leq 40\text{\AA}$ exhibit a compositionally-modulated amorphous structure. The latter films are paramagnetic except for the one with $\Lambda = 40\text{\AA}$, which showed a superparamagnetic behavior.

INTRODUCTION

Understanding the effect of intermixed amorphous layers between a ferromagnetic and a non-ferromagnetic metal layer on the overall magnetic properties of thin film systems is of technological and scientific importance. Such layers between two elemental metal layers are frequently observed in as-deposited multilayer films in which a solid-state amorphization reaction can occur. One example is an Fe/Zr multilayer, a system for which an amorphous alloy phase is reported to develop if it is annealed 350°C.[1] Several Mössbauer studies done on as-deposited Fe/Zr multilayer films have shown that the multilayer films change from ferromagnetic to paramagnetic below a certain value of the modulation length of the layered film, indicating that intermixed non-ferromagnetic layers become dominant as Λ decreases. Williamson and Clemens, for example, reported that Fe/Zr multilayer films become paramagnetic when each layer is about ten monolayers thick.[2] From this observation, they deduced the thickness of the intermixed layer. Kiauka et al. reported that Fe/Zr multilayer films, deposited at 120K, showed only a weak non-magnetic spectral contribution, which corresponds to one to two intermixed atomic layers at the Fe/Zr interface.[3]

On the other hand, only a few direct observations of the interface layers exist for Fe-based multilayer systems. Bourret and Rouvière used high-resolution transmission electron microscopy (TEM) to probe the interface of a Fe/Ti multilayer film and found that it exhibits an amorphous structure.[4] Krebs et al. made TEM observations on annealed Fe/Zr multilayers in the study of the phase separation process in amorphous Fe-Zr.[5] The purpose of the present study is to provide a direct correlation between the interface structure of the as-deposited Fe/Zr multilayer observed by TEM and its magnetic properties as a function of Λ . Our results show that the decrease in saturation magnetization for films with a small modulation length, Λ , can well be explained by the presence of amorphous interface layers. In addition, the susceptibility of the $\Lambda = 40\text{\AA}$ sample indicates that the intermixed amorphous layer is superparamagnetic for that modulation length.

EXPERIMENTAL PROCEDURE

We prepared a series of Fe/Zr multilayer films by DC magnetron sputtering on Si(100) and glass substrates. We placed the substrates on a rotating table in a chamber, an arrangement which has been described previously [6]. The purity of the target materials was 99.99% for both Fe and Zr. The base pressure of the chamber was less than 3×10^{-7} torr, and the sputtering was done in a Ti-gettered 3mtorr Ar atmosphere. We cleaned the Si wafers using

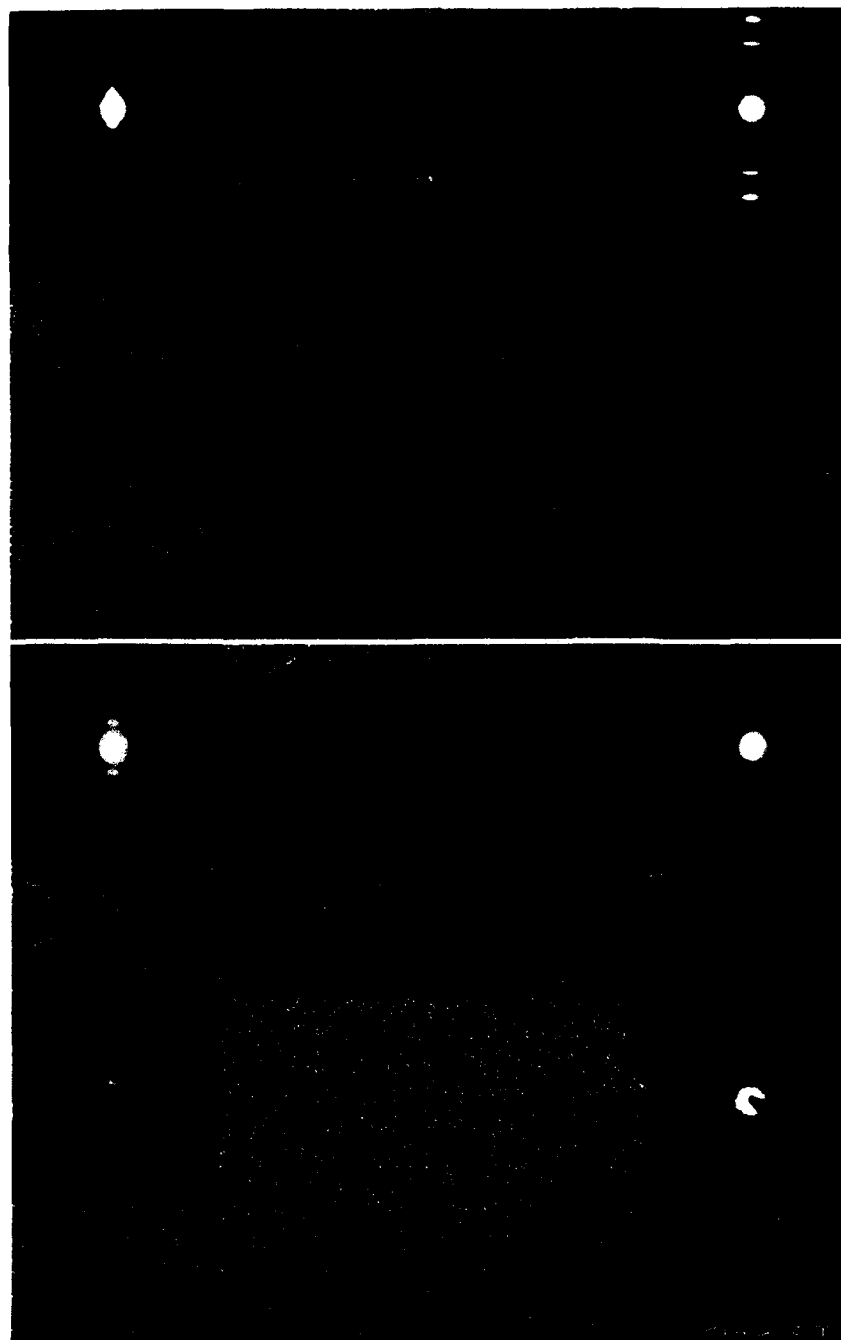




Fig.1 Cross-section TEM micrographs of as-deposited Fe/Zr multilayer films.
(a) $\Lambda = 80 \text{ \AA}$, (b) $\Lambda = 40 \text{ \AA}$, (c) $\Lambda = 16 \text{ \AA}$, and (d) $\Lambda = 4 \text{ \AA}$.

$\text{NH}_4\text{OH} + \text{H}_2\text{O}_2$ and $\text{HCl} + \text{H}_2\text{O}_2$ solutions, but we left a thin Si oxide layer ($\approx 10 \text{ \AA}$) on the Si wafers in order to avoid a possible reaction between the Si substrate and the film. The power of the guns and the table rotation speed were adjusted to obtain the desired modulation length and composition. The thickness ratio of the Fe to the Zr layer, $d_{\text{Fe}}/d_{\text{Zr}}$, was held constant ($d_{\text{Fe}}/d_{\text{Zr}} = 0.7$) so that the composition of Fe and Zr was about equal. The modulation length, Λ ($\Lambda = d_{\text{Fe}} + d_{\text{Zr}}$), was varied from 6 to 800 \AA .

The structural analysis consisted of X-ray diffraction (XRD) and transmission electron microscopy (TEM). We used a Philips diffractometer in the Bragg-Bratano geometry for the XRD study. The modulation length, Λ , was determined from the XRD low-angle diffraction pattern with the method proposed by Miceli et al. [7]. For the TEM study, we used a Philips 430ST microscope operating at 300 kV (resolution 1.9 \AA). The TEM cross-section samples of as-deposited films were made by the standard procedure [8]. We ion-milled the samples at 5 kV \times 0.5 mA using a liquid nitrogen stage in order to avoid any reaction during the sample preparation. The magnetization of the samples was measured with a vibrating sample magnetometer (VSM) in a magnetic field up to 15 kOe. The background of the magnetization was determined with a plain Si wafer. The magnetization curves are shown after background subtraction.

RESULTS AND DISCUSSION

Fig.1 (a) shows the high-resolution cross-section TEM images of the as-deposited Fe/Zr multilayer film with $\Lambda = 80 \text{ \AA}$. The thinner, darker layer is the crystalline Fe (c-Fe) layer while the thicker, brighter layer is the crystalline Zr (c-Zr) layer. Also clearly shown in this picture is the interface amorphous region between the c-Fe and c-Zr layers. The thickness of this region varies but on the average it is 15-20 \AA . The inset normal diffraction pattern (right) shows three partial rings in the substrate-normal direction, indicating a strong texture of the crystalline phases in the film. The spacings of these partial rings are 2.77, 2.56, and 2.04 \AA , respectively. These values can be compared with 2.798 \AA for $(10\cdot0)_{\text{hex-Zr}}$, 2.574 \AA for $(00\cdot2)_{\text{hex-Zr}}$ and 2.552 \AA for $(110)_{\text{bcc-Zr}}$, and 2.027 \AA for $(110)_{\text{bcc-Fe}}$, respectively. Note that parts of the innermost ring are also shown 60° from the substrate-normal direction, supporting the suggestion that this ring is $(10\cdot0)_{\text{hex-Zr}}$. The outermost ring, whose reciprocal spacing corresponds well to that of Fe (110) , shows arcs 60° and 90° from the substrate-normal, as is expected: the angles between pairs of $\{110\}$ type planes are 60° and 90° . An interesting observation is that the second inner ring also shows a non-negligible intensity at 60° and 90° from the substrate normal. This indicates that this ring is composed of $(00\cdot2)_{\text{hex-Zr}}$ and $(110)_{\text{bcc-Zr}}$, suggesting that a relatively large amount of the (110) textured bcc-Zr phase is present.

Fig.1 (b) shows the cross-section image of the film with $\Lambda = 40 \text{ \AA}$. The alternating light and dark layers of this picture indicate that this film is compositionally modulated. The inset low-angle diffraction pattern clearly shows spots arising from the modulated structure. The normal diffraction pattern shows a weak $(100)_{\text{hex-Zr}}$ ring as well as a halo, indicating that this film

consists of disordered small grains and amorphous. Fig.1 (c) shows the cross-section image of the film with $\Lambda=16\text{\AA}$. The alternating light and dark layers are seen in this picture as well, indicating that this film is still compositionally modulated. The inset low-angle diffraction pattern also shows spots arising from the modulated structure, while the normal diffraction pattern shows that the film is completely amorphous. Fig.1 (d) shows the cross-section image of the film with $\Lambda=4\text{\AA}$. This picture shows that the modulation has completely disappeared and that the film is amorphous. Also shown in the picture is the white native oxide layer between the film and the Si (100) substrate.

Fig.2 shows a set of low-angle (on the left) and high-angle (on the right) X-ray diffraction (XRD) patterns. Sharp Fe (110) and Zr (100)_{hex} peaks in the high angle XRD pattern for the samples with $\Lambda \geq 80\text{\AA}$ show that Fe and Zr are crystalline, while peaks in the low-angle XRD show modulated structures. The disappearance of sharp Fe (110) and Zr (002) peaks and the emergence of a broad peak in the high-angle XRD pattern for samples with $\Lambda \leq 16\text{\AA}$ indicates that the films have amorphous structure, while peaks in the low angle XRD show that the films are still compositionally modulated.

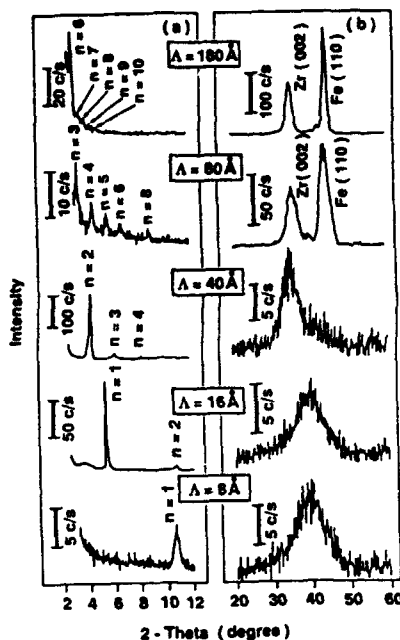


Fig.2 X-ray diffraction of Fe/Zr multilayer films.

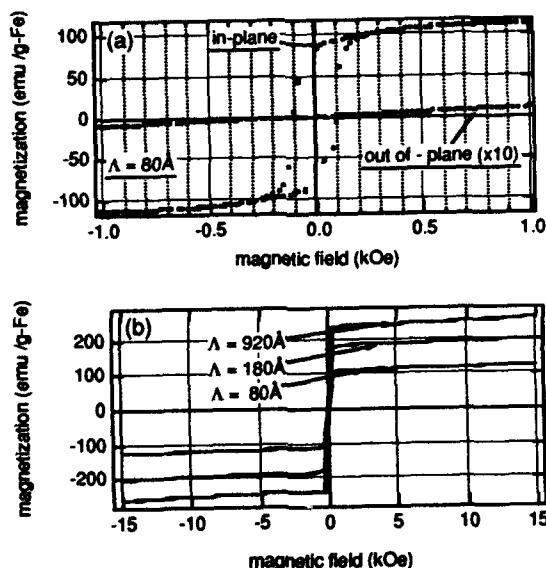


Fig.3 Magnetization of the multilayer films: (a) in-plane and out-of-plane (x10) magnetization for $\Lambda=80\text{\AA}$ sample and (b) comparison of the in-plane magnetization for films with different modulation length.

Fig.3 (a) shows a magnetization curve obtained for the film with $\Lambda=80\text{\AA}$, with the magnetic field parallel and perpendicular to the sample plane at room temperature. These magnetization curves show strong anisotropy, that is, the easy-magnetization axis lies in the plane, as expected from the strong (110) texture of c-Fe grains. We observed similar anisotropy for the films with $\Lambda \geq 80\text{\AA}$. The in-plane magnetization curves of these films are compared in Fig.3 (b).

As shown in the figure, the saturation magnetization (M_s) decreases as Λ decreases. Assuming that the intermixed amorphous layer is non-ferromagnetic, we can express the fraction of ferromagnetic Fe atoms approximately as follows:

$$\begin{aligned} N_{\text{ferro}} &= N_{\text{total}} - N_{\text{dead}} \\ &= N_{\text{total}} \left(1 - \frac{N_{\text{dead}}}{N_{\text{total}}}\right) \\ &= N_{\text{total}} \left(1 - \frac{2 \cdot d_{\text{dead}}}{\Lambda}\right), \end{aligned} \quad (1)$$

where N_{ferro} , N_{total} and N_{dead} are the number of ferromagnetically-active, total, and non-ferromagnetic Fe atoms, respectively, while d_{dead} is the thickness of the intermixed non-magnetic layer. The factor, 2, in the second term in Eq. (1) arises from the fact that each Fe layer is in contact with two intermixed layers, which we assume to be non-ferromagnetic. Eq. (1) is only a rough estimation since we neglected the variation of the Fe concentration in the intermixed layers. Fig.4 shows the saturation magnetization as a function of modulation length for the films with $\Lambda=920$, 180, and 80Å. We fitted these points using Eq. (1). The best fit was obtained by assuming $d_{\text{dead}} = 23.6\text{\AA}$. This value can be compared with 15-20Å, the thickness of the interface amorphous layer observed in high-resolution TEM. Taking into account the crudeness of the derivation, the agreement between these values is reasonably good.

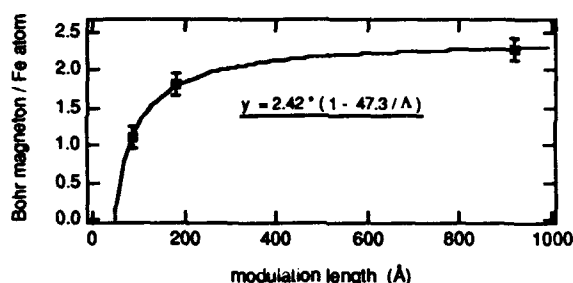


Fig. 4 Saturation magnetization of Fe/Zr multilayers

For the films with $\Lambda \leq 40\text{\AA}$, the magnetization decreases drastically. Fig.5 shows a series of magnetization curves for these films. For the sake of clarity, the scale of the y-axis in the figure is expanded by a factor of twenty. The in-plane and the perpendicular curves for these specimens almost coincide, showing the loss of anisotropy, although a very weak anisotropy is still observed for the film with $\Lambda=40\text{\AA}$. Note the relatively large slope of the curve for the film with $\Lambda=40\text{\AA}$. The atomic susceptibility of this film is about $0.04 \text{ (cm}^3/\text{mol-Fe)}$, which may be compared with 1.5×10^{-3} , the susceptibility of paramagnetic g-Fe. This high value indicates that this film is superparamagnetic.

Bushow and Smit reported that the Curie temperature of amorphous $\text{Fe}_x\text{Zr}_{1-x}$ alloys with $x \leq 0.8$ is below room temperature. They also reported that the magnetic moment of the Fe atom decreases considerably as the Zr content increases and that it disappears at $x=0.6$. [9] A decrease in the Curie temperature was also reported by Hiroyoshi and Fukamichi in a study of ferromagnetic-to-spin glass transition. [10] We speculate that at a certain composition or modulation length, the Fe atoms form a magnetic cluster, resulting in the superparamagnetic character.

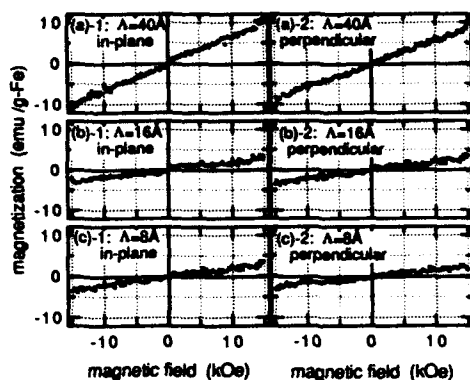


Fig. 5 Magnetization Curves for Fe/Zr multilayer films with $\Lambda \leq 40 \text{ \AA}$

CONCLUSION

We made Fe/Zr multilayer films by sputtering and observed the following. For films with $\Lambda \geq 80 \text{ \AA}$, the interface region between the Fe and Zr layers exhibits a 15-20 Å thick amorphous structure. The magnetization curves of these films show a monotonous decrease in the saturation magnetizations, whose trend is well explained by a simple asymptotic model that assumes the interface amorphous layer to be non-ferromagnetic. Films with $\Lambda \leq 40 \text{ \AA}$ exhibit a compositionally-modulated amorphous structure. The latter films are paramagnetic except for the one with $\Lambda = 40 \text{ \AA}$, which showed a probable superparamagnetic behavior.

ACKNOWLEDGMENT

We thank Drs. B.M. Lairson and N. Rensing for their help during the VSM operation. We are also grateful to Prof. R.L. White for stimulating discussions. T.J.K. and R.S. are supported by the National Science Foundation (grant number DMR-8902232).

REFERENCES

1. B. R. Clemens and M. J. Suchoski, *Appl. Phys. Lett.*, **47**, 943 (1985)
2. D. E. Williamson and B. M. Clemens, *Hyp. Int.*, **42**, 967-970 (1988)
3. W. Kiauka, W. Keune, T. Shinjo and N. Hosoi, *J. Mag. Magn. Mat.*, **93**, 494-498 (1991)
4. A. Bourret and J. L. Rouvière, *Phil. Mag.*, **62**, 415-434 (1990)
5. H. U. Krebs, D. J. Webb and A. F. Marshall, *Phys. Rev. B*, **35**, 5329-5395 (1987)
6. T. W. Barbee Jr. and D. L. Keith, in *Synthesis and Properties of Metastable Phases*, edited by E. S. Mashlin and T. J. Rowland, p.93-113, The Metallurgical Society of AIME, (1980)
7. P. F. Mececi, D. A. Neumann and H. Zabel, *Appl. Phys. Lett.*, **48**, 24-26 (1986)
8. J. C. Bravman and R. Sinclair, *J. Elec. Micro. Tech.*, **1**, 53-61 (1984)
9. K. H. J. Buschow and P. H. Smit, *J. Magn. Mag. Mat.*, **23**, 85-91 (1981)
10. H. Hiroyoshi and K. Fukamishi, *J. Appl. Phys.*, **53**, 2226-2228 (1982)

STRUCTURAL AND MAGNETORESISTANCE PROPERTIES OF Co/Cu MULTILAYERS DOPED WITH Fe

J.M. GEORGE*, A. BARTHELEMY*, O. DURAND**, J. L. DUVAIL*, A. FERT*, P. GALTIER**, O. HECKMANN***, L.G. PEREIRA*, F. PETROFF*, T. VALET**

*Laboratoire de Physique des Solides, Université Paris-Sud, 91405 Orsay, France

**Laboratoire Central de Recherches, Thomson CSF, 91404 Orsay, France

***Laboratoire pour l'Utilisation du Rayonnement Electromagnétique, Université Paris-Sud, 91405 Orsay, France

ABSTRACT

We have studied the influence of ultra-thin interfacial Fe layers on the structural and magnetoresistance properties of Co/Cu multilayers. Our results show that the giant magnetoresistance arises from spin dependent scattering at the Co/Cu interfaces and in the bulk of Co, the interfacial contribution being predominant. We also demonstrate that the close-packed crystallographic structure of Co and Cu is very sensitive to the insertion of interfacial bcc Fe layers : for small thicknesses, Co as well as Cu adopt a metastable bcc structure.

INTRODUCTION

The giant magnetoresistance (MR), first discovered in epitaxial Fe/Cr(001) superlattices [1,2] has now been observed in a large variety of ferromagnetic/non-magnetic multilayered structures and very large MR have been recently reported for sputtered Co/Cu multilayers [3,4]. Planar doping, i.e. introducing thin interfacial layers of additional elements, is a powerful method to experimentally investigate the microscopic mechanisms of spin dependent scattering and the respective roles of interfacial versus bulk scattering. In this paper, we report on the MR of Co/Cu multilayers in which thin Fe layers are introduced at the interfaces. A structural study, based on X-ray diffraction (XRD), Transmission Electron Microscopy (TEM) and X-ray Absorption Spectroscopy (XAS), has also been performed.

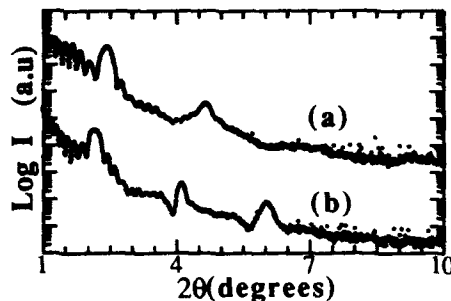
EXPERIMENTAL DETAILS

The multilayers were prepared by rf diode sputtering in a Nordiko NS 2000 high-vacuum automated sputter deposition system with a base pressure in the 10^{-8} Torr range. Chemically etched Si(100) wafers were used as substrates and either Fe or Cr buffer layers (40Å thick) were first grown on the Si substrates. The films were then deposited at room temperature in an Ar pressure of 5 mTorr at typical deposition rates of 0.2-1 Å/s. XRD measurements were performed in the θ -2 θ geometry on a two-axis spectrometer using CuK α radiation monochromated after the sample with the (002) reflection of pyrolytic graphite. TEM observations were made using a Topcon ABT 002B microscope operated at 200 kV. Plane views and cross sections were prepared by polishing and dimpling followed by argon milling. The XAS experiments were performed at the Laboratoire pour l'Utilisation du Rayonnement Electromagnétique (LURE) on the DW21 synchrotron line using a Si(311) double crystal monochromator installed on the DCI storage ring. The variations of the X-ray absorption coefficient of some selected samples were measured above the K edges of Fe (7112 eV), Co (7709 eV) and Cu (8980 eV), in the total yield mode. MR measurements were made using a low frequency ac lock-in technique.

RESULTS AND DISCUSSION: STRUCTURE

Typical low angle XRD spectra observed for Co/Cu multilayers with and without thin interfacial Fe layers are shown in Fig. 1. The Co/Cu spectrum (a) displays two well-defined superlattice Bragg peaks and Kiessig fringes, which ensures that the multilayer stack is regular.

Figure 1 Low angle X-ray spectra for $(\text{Co}15\text{\AA}/\text{Cu}20\text{\AA})_{10}$ (a) and $(\text{Co}12\text{\AA}/\text{Fe}3\text{\AA}/\text{Cu}20\text{\AA}/\text{Fe}3\text{\AA})_{10}$ (b)



It can be seen from spectrum (b) that introducing 3Å thick interfacial Fe layers seems to have little effect on the overall quality of the layering. The appearance of a third order peak is probably due to the higher X-ray contrast between Fe and Cu. High angle spectra (not shown) reveal that the multilayers have a weak (111) out-of-plane texture. This is in contrast with previous work on highly (111) textured Co/Cu multilayers [3,4] prepared by dc magnetron sputtering and emphasizes the role of sputtering parameters on the texture and microstructure [5].

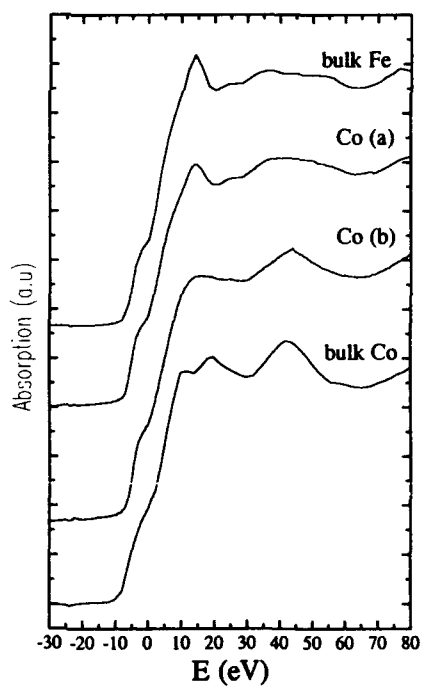
TEM observations were made on Co/Cu multilayers with thin interfacial Fe layers. Plane views show that the samples are polycrystalline with grain sizes of about 500Å. Electron diffractions reveal that the bcc and fcc contributions are predominant. The balance between the bcc and fcc phases appears to be strongly dependent on the thickness of the interfacial Fe layers. This can be evaluated with a comparison between the intensities of the (111)fcc and the (110)bcc contributions. In that we can notice that the intensity of the (111)fcc contribution is dramatically lowered relative to that of (110)bcc when the interfacial Fe layers thicknesses change from 3 to 4.5Å. We will come back to this behaviour later. A bright field image in cross section of a $(\text{Co}15\text{\AA}/\text{Fe}4.5\text{\AA}/\text{Cu}20\text{\AA}/\text{Fe}4.5\text{\AA})_{20}$ is shown in Fig. 2. It has been obtained in strongly defocusing the microscope leading to a *Fresnel fringes image* which overcomes the poor contrast expected from the close values of the atomic number of the elements. In that case the Fresnel fringes do not represent the multilayer stacking in a straightforward manner [6]. Nevertheless, the inspection of such images is sufficient to evaluate the layers regularity and to measure the superlattice period. The existence of the multilayer stacking is clearly visible and confirms the low angle XRD results. The period of the multilayer as measured from the Fresnel images are in agreement with that given by the superlattice peak spacings observed in small angle electron diffraction. The detail of the Fresnel images can be assessed by comparison with simulations [6]. It can be shown that the Fresnel contrast is mainly due to the scattering coefficients of Cu, Co and Fe. Thus, because Co and Fe exhibit very close scattering coefficients, they cannot be distinguished easily and no ready conclusions can be given concerning the continuity and regularity of the interfacial Fe layers. Nevertheless we observe that the Fresnel fringes are continuous, a fact which suggests that the Cu layers are continuous too.

We will now present the results of X-ray absorption near edge spectroscopy (XANES) and Extended X-ray absorption fine structure (EXAFS) which are element specific probes of the local structure. The XANES spectra of Co for two $\text{Co}15\text{\AA}/\text{Cu}20\text{\AA}$ multilayers with interfacial Fe layers of different thicknesses (3Å and 4.5Å) are reported on Fig. 3 together with those of bulk hcp Co and bulk bcc Fe. First we recall that bcc and close-packed (hcp or fcc) transition metals display characteristic XANES profiles as can be seen for Co and Fe in Fig. 3. A comparison of the Co XANES profiles of the samples and the references shows that one (4.5Å Fe) is clearly of the bcc type while the other (3Å Fe) is more typical of the close-packed stacking but less structured. This result underlines a very sharp transition from hcp/fcc Co to a metastable bcc Co and it can explain the variation of the intensities of the bcc(110) and fcc(111) rings seen in electron diffraction. More information is obtained from the EXAFS data on two series of samples, namely $\text{Co}15\text{\AA}/\text{Fe}r_{\text{Fe}}/\text{Cu}20\text{\AA}$ and $\text{Co}15\text{\AA}/\text{Fe}r_{\text{Fe}}/\text{Cu}7\text{\AA}$ with r_{Fe} ranging from 3 to 6 Å. The results show that the stabilization of metastable bcc phases depends strongly on the respective thicknesses of Cu and Fe. For the Cu 7Å series, Co but also Cu are bcc



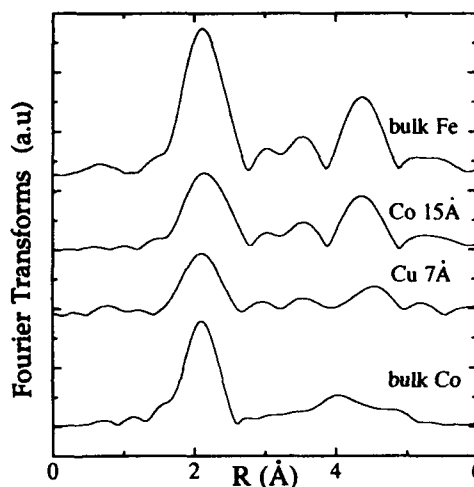
Figure 2. Bright field image of a $(\text{Co}15\text{\AA}/\text{Fe}4.5\text{\AA}/\text{Cu}20\text{\AA}/\text{Fe}4.5\text{\AA})_{20}$ multilayer. The space bar represents 100 Å. Defocus = +2000Å

Figure 3. Co K-edge XANES spectra for two $(\text{Co}15\text{\AA}/\text{Cu}20\text{\AA})_{20}$ with respectively (b) 3Å and (a) 4.5Å Fe layers at the interfaces. The spectra for bulk Co and Fe are shown for comparison. The data were taken with the polarization of the synchrotron beam in the plane of the layers.



whatever the thickness of Fe. The Fourier transforms of the EXAFS data for Co15Å and Cu7Å are shown in Fig.4 together with those of bulk Fe and bulk Co. In particular, the intense peak around 4.45Å, a typical feature of the bcc structure, is observed with however a reduced intensity with respect to bulk Fe. For the Cu 20Å series, Co and Cu are fcc for 3Å thick interfacial Fe layers whereas for 6Å of Fe, Co becomes bcc and Cu stays fcc. Quantitative analysis of the EXAFS data using a standard procedure gives the number and distances of nearest and next nearest neighbours with an estimation of the disorder through a Debye-Waller factor. We found for Co15Å, 8 first neighbours at $2.48\pm 0.01\text{Å}$ and 6 second neighbours at 2.83Å , and for Cu7Å, 8 first neighbours at $2.47\pm 0.01\text{Å}$ and 6 second neighbours at 2.87Å . These values are in good agreement with recent reports on bcc Co in Co/Fe multilayers [7] and bcc Cu in Fe/Cu multilayers [8]. However, the Debye-Waller factors derived from our analysis are large indicating a departure from perfect bcc structures.

Figure 4. Fourier transforms of EXAFS data for Co and Cu in the multilayer (Co15Å/Fe3Å/Cu7Å/Fe3Å)₂₀. The spectra for bulk Co and Fe are also shown. The data were taken with the polarization of the synchrotron beam in the plane of the layers.



RESULTS AND DISCUSSION: MAGNETORESISTANCE

We present now the MR measurements on the Co/Fe/Cu/Fe multilayers. In light of the structural results presented above, we will mainly focus on the results obtained for the Co/Fe 3Å/Cu series where Co and Cu are fcc. First we note that despite the weak texturing, the "pure" Co/Cu multilayers display well defined MR oscillations with first and second peaks around 9 and 20 Å as previously observed for Co/Cu(111) multilayers [3,4]. However the exchange coupling is weaker and the MR smaller by about a factor of 2.5 at the first maxima. The Co/Fe3Å/Cu series displays also MR oscillations with about the same maxima as in Co/Cu but a strongly reduced amplitude. As the MR is much smaller in Fe/Cu than in Co/Cu [9], the interfaces between Fe and Cu are expected to present much smaller spin dependent effects than those between Co and Cu. This is clearly demonstrated on Fig. 5 where the MR of the Co15Å/Fe/Cu20Å series is plotted versus the interfacial Fe thickness. The thickness of Cu was set to 20Å (second MR maxima) to avoid artefacts related to exchange coupling. Fig. 5 shows a steep decrease of the MR as a function of Fe and at 3Å (thickness for which Co is still fcc) most of the contribution from the Co/Cu interface has been suppressed. The very efficient spin dependent scattering of Co/Cu interfaces is evident from these results in agreement with recent reports on Co, NiFe and Cu based multilayers [10].

Once the contribution from the Co/Cu interface has been suppressed the residual MR depends on the proportion of Co and Fe in the magnetic layers. Increasing the Co layers thicknesses, at fixed t_{Fe} , should provide information about a possible contribution of spin

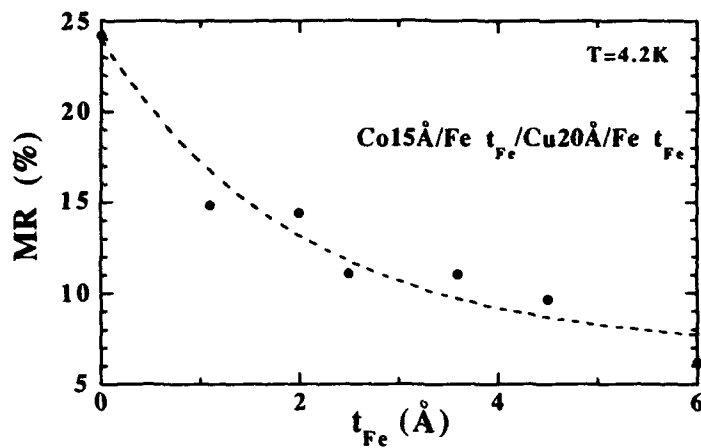


Figure 5. Variation of the MR ratio in $\text{Co}15\text{\AA}/\text{Fe}/\text{Cu}20\text{\AA}/\text{Fe}$ multilayers as a function of the thickness t_{Fe} of the interfacial Fe layers. Data were taken at 4.2 K. The line is a guide for the eye.

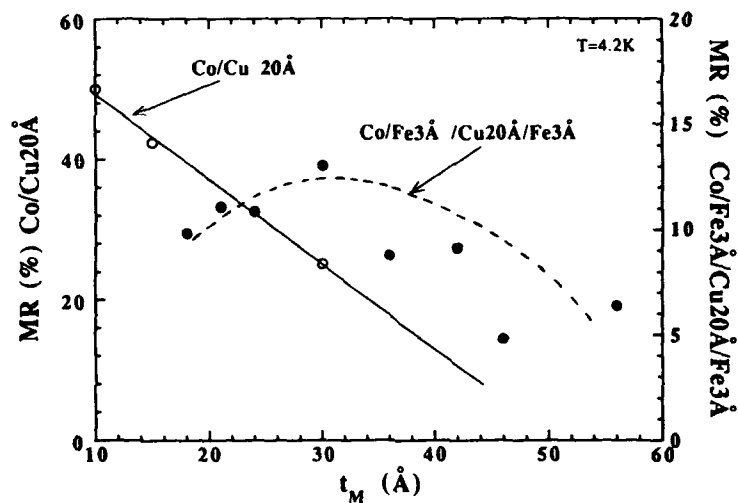


Figure 6. Variations of the MR ratio in $\text{Co}/\text{Fe}3\text{\AA}/\text{Cu}20\text{\AA}$ (black dots) and $\text{Co}/\text{Cu}20\text{\AA}$ (white dots) multilayers as a function of the ferromagnetic layers thicknesses, $t_M=t_{Co}+2t_{Fe}$ and $t_M=t_{Co}$ respectively. Data were taken at 4.2 K. The $\text{Co}/\text{Cu}20\text{\AA}$ data are from ref.[11]. Notice the different vertical scales. The dashed line is a guide for the eye.

dependent scattering in the Co layers. Fig. 6 displays the MR variation with increasing Co thickness for the Co/Fe₃A/Cu 20Å series. The MR increases slightly and goes through a rounded maximum around 30Å for the total thickness of the magnetic layers, before decreasing at higher thickness. This is in contrast with the variation of Co/Cu multilayers without Fe (white dots in Fig. 6), taken from ref. [11], and is the typical behaviour expected for systems with *bulk spin dependent scattering*. If there was no bulk contribution, one would expect a continuous decrease of the MR with increasing magnetic thickness. This infers that, once the strong contribution from the Co/Cu interfaces has been suppressed, one sees the non negligible bulk contribution from the Co layers. We emphasize that we have checked by EXAFS that the fcc structure of Co and Cu remains practically unchanged as a function of Co thickness in Fig. 6, showing that the observed MR variation can not be due to structural changes.

CONCLUSIONS

We have shown by EXAFS and TEM experiments that introducing thin Fe layers at the interfaces of Co/Cu multilayers can change the structure and stabilize the metastable bcc phase of Co and Cu. The Co and Cu layers, if they are not too thin, remain fcc when the thickness of the interfacial Fe layers is of the order of 3Å or less. The MR measurements on samples with 3Å interfacial Fe layers show that the high MR of Co/Cu is due to a predominant contribution from interface spin dependent scattering and to a smaller but non negligible bulk contribution.

ACKNOWLEDGEMENTS

This work was supported in part by the Ministère de la Recherche et de l'Espace and by the Esprit program of the EEC. Thanks to Dr H. Magnan and Dr D. Chandesris for help in the XAS experiments and useful discussions.

REFERENCES

- [1] M.N. Baibich, J.M. Broto, A. Fert, F. Nguyen Van Dau, F. Petroff, P. Etienne, G. Creuzet, A. Friederich, and J. Chazelas, *Phys. Rev. Lett.* **61**, 2472 (1988).
- [2] G. Binasch, P. Grünberg, F. Saurenbach, and W. Zinn, *Phys. Rev. B*, **39**, 4828 (1989).
- [3] D.H. Mosca, F. Petroff, A. Fert, P.A. Schroeder, W.P. Pratt Jr., and R. Loloee, *J. Magn. Magn. Mat.* **94**, 1 (1991).
- [4] S.S.P. Parkin, R. Bhadja, and K.P. Roche, *Phys. Rev. Lett.* **66**, 2152 (1991).
- [5] R.J. Highmore, W.C. Shih, R.E. Somekh, and J.E. Evetts, *J. Magn. Magn. Mat.* **116**, 249 (1992).
- [6] F. Galtier, T. Valet, O. Durand, J.C. Jacquet, and J.P. Chevalier, this conference.
- [7] P. Boher, F. Giron, Ph. Houdy, F. Baudelet, A. Fontaine, J.M. Ladouceur, E. Dartyge, P. Beauvillain, C. Chappert, P. Veillet, and K. Le Dang, *J. Appl. Phys.* **71**, 1798 (1992).
- [8] S. Pizzini, F. Baudelet, D. Chandesris, A. Fontaine, H. Magnan, J. M. George, F. Petroff, A. Barthélémy, A. Fert, R. Loloee, P.A. Schroeder, *Phys. Rev. B*, **46**, 1253 (1992).
- [9] F. Petroff, A. Barthélémy, D. H. Mosca, D. K. Lottis, A. Fert, P. A. Schroeder, W. P. Pratt Jr, and R. Loloee, *Phys. Rev. B*, **44**, 5355 (1991).
- [10] S.S.P. Parkin, *Appl. Phys. Lett.* **61**, 1358 (1992); B. Dieny, V.S. Speriosu, J.P. Nozières, B.A. Gurney, A. Vedyayev, and N. Ryzhanova, *Proceedings of the "NATO Workshop" in Cargèse* (1992).
- [11] D.H. Mosca and F. Petroff (unpublished).

RESISTANCE AND MAGNETORESISTANCE OF GADOLINIUM/TUNGSTEN MULTILAYERS

A. HEYS*, P. E. DONOVAN*, E. G. ASTRAKHARCHIK** AND B. GEORGE***

*Physics Department, Birkbeck College, Malet Street, London WC1E 7HX, UK

** permanent address: Kapitza Institute for Physical Problems, Moscow, Russia

*** Laboratoire de Physique du Solide, University of Nancy, Vandoeuvre-les-Nancy, France

ABSTRACT

The resistance and magnetoresistance of Gd/W multilayers have been measured at temperatures between 300K and 4K and in fields of up to 7 Tesla. The temperature coefficient of resistance is strongly influenced by the thickness of the Gd layers, becoming negative at a Gd layer thickness of 0.8nm. The magnetoresistance is dominated by the Gd below about 100K. Multilayers which show reduced saturation magnetisation at 4K also have an unusual form of magnetoresistance around 100K. We suggest that this may be due to antiferromagnetic alignment of the Gd and W moments at low applied fields.

INTRODUCTION

Gadolinium/tungsten (Gd/W) multilayers have been shown to have very unusual magnetic properties at low temperature (4 Kelvin). As reported previously [1,2], we have observed an enhancement of the saturation magnetisation of the multilayers, i.e. the saturation magnetisation may be greater than that expected for the gadolinium layers alone. The effect is largest at small Gd layer thicknesses and shows an interesting oscillatory dependence on W layer thickness, so that at some W thicknesses the magnetisation is greater, and at other thicknesses less, than the expected value for the Gd layers. In specimens with the thinnest Gd layers the measured saturation moment is too large to be accounted for by the gadolinium, so we conclude that a moment has been induced in the tungsten layers. This effect has never been predicted theoretically or observed experimentally before. To investigate the behaviour further we have measured the low temperature resistance and magnetoresistance of Gd/W multilayers and have found that these also show interesting and unusual features. Here we present our results for a selection of multilayers with a range of Gd and W thicknesses.

EXPERIMENTAL

Gd/W multilayers were prepared by DC magnetron sputtering onto glass substrates in a UHV sputtering system with base pressure below $2 \cdot 10^{-10}$ torr. All specimens were deposited at ambient temperature, in an atmosphere of 99.99% pure argon at a pressure of $4.2 \cdot 10^{-2}$ torr. Each multilayer consisted of 50 bilayers. Films of the pure metals 200nm thick were prepared under the same conditions, and alloy films of Gd and W were also prepared by sputtering from both targets simultaneously. Multilayers have been produced with bilayer thicknesses, Λ , between 2.4nm and 13.5nm and with individual layer thicknesses between 0.6 and 10.9nm. Two series of Gd/W multilayer specimens have been prepared, one in which all the specimens had approximately the same W layer thickness (about 1.7nm) but different Gd layer thicknesses (between 0.8 and 6.4 nm), and another in which the specimens all had approximately the same Gd thickness (about 4.3nm) and different W thicknesses (between 0.6 and 3.0nm).

The multilayers were characterised by low angle X-ray diffraction. Several orders of reflection from the periodic multilayer structure were observed for all the specimens. Λ was determined by measuring the angles of the reflections and correcting for refraction of the X-rays in the material [3]. The average values of the individual layer thicknesses were determined by matching the relative intensities of the reflections to computer-simulated diffraction patterns of model structures. The regularity and distinctness of the multilayer structure were confirmed for a selection of Gd/W specimens by high resolution electron microscopy (HREM) on cross-sections through the multilayers. Details of these observations have been published elsewhere [4]. HREM confirmed the values for the average layer thicknesses determined by X-ray diffraction and provided information on the structure of the materials within the layers. Even the thinnest layers were found to be polycrystalline, rather than amorphous. The W crystals in each layer were randomly oriented but the Gd layers showed an [0001] crystallographic

texture. A very thin ($<0.3\text{nm}$) zone of interfacial mixing was observed between the layers. Electron microscopy also revealed that in most specimens the Gd layers contained up to 5% by volume of the face-centred cubic compound gadolinium hydride (GdH_2). This compound is commonly found in vacuum-deposited thin gadolinium layers [5]. Microanalysis with a windowless X-ray detector also showed the presence of hydrogen and a small concentration of argon in the Gd layers, but no other contaminants were detected. HREM showed that the co-sputtered alloy films of gadolinium and tungsten were non-crystalline.

Resistance measurements were carried out between room temperature and 4.2K using a four-terminal direct current method with a constant current of 1mA. Resistance values were recorded alternately for both forward and reverse currents to eliminate thermal emfs. The temperature of the sample was monitored with a calibrated carbon-glass thermometer. Magnetoresistance measurements were made in a field of up to 7 Tesla, using a specially designed sample holder which allows the specimen to be rotated so that the resistance could be measured for arbitrary angles between the current and the field. In one set of experiments the field was applied parallel and perpendicular to the current but in the plane of the layers; in another set of experiments the field was also applied in directions perpendicular to the plane of the specimen.

RESULTS

1. Resistance in zero field

The resistance of the multilayers, single films of W and Gd and of co-sputtered alloys of the two elements was measured as a function of temperature in zero applied magnetic field. The resistance of W and Gd films shows normal metallic behaviour, falling as the temperature decreases and levelling off at a residual value. The resistance of the Gd/W multilayers depends strikingly on the thickness of the individual Gd layers, as illustrated in Figure 1. Multilayers with fairly thick Gd and W layers show normal metallic behaviour with an abrupt decrease in resistance at 20K (the Neel temperature of antiferromagnetic GdH_2 [6]). The high temperature resistance is relatively independent of temperature as expected for thin, polycrystalline metallic layers. However, specimens with thinner Gd layers ($<1.5\text{nm}$) show a minimum in resistance at fairly low temperature, followed by an increase in resistance on further cooling, with no sign of a drop in resistance at 20K. The temperature at which the resistance minimum occurs is higher the thinner the Gd. Both the alloy films and the multilayer with the thinnest Gd (0.8nm) show "non-metallic" behaviour, with increasing resistance as the temperature decreases.

2. Magnetoresistance

The magnetisation curves of Gd/W multilayers have been described in detail elsewhere [1,2]. Briefly, the multilayers are all extremely difficult to saturate, with saturation fields (in-plane) greater than 7 Tesla. The in-plane coercive fields, however, are moderate (usually between 0.1 and 1 Tesla). 200nm Gd films are easier to saturate, with saturation fields of the order of 5 Tesla, but have similar coercivities. The magnetic response of the 200nm W films was below the detection threshold of the magnetometer.

The pure W film showed the magnetoresistance expected of tungsten, with a very small, parabolic, positive magnetoresistance (resistance increasing in increasing field). The Gd film also showed the expected larger, negative magnetoresistance with hysteresis at low applied fields. The magnetoresistance of Gd/W multilayers appears to be dominated by the gadolinium layers. At 4.2K all the multilayers, even those with the thinnest Gd, show negative magnetoresistance like that of the Gd film. When the field is applied in the specimen plane two hysteretic peaks in resistance are observed, corresponding to the positive and negative coercive field, whereas if the field is applied perpendicular to the sample plane a single, broader peak with no hysteresis is seen, as shown in Figure 2. These observations indicate that at this temperature the atomic moments lie in the plane of the layers.

The effect of temperature on the magnetoresistance of a multilayer with thin (1.0nm) Gd layers is illustrated in Figure 3. Although the magnetoresistance is strongly negative at low temperatures it decreases in magnitude as the temperature increases, becoming positive above 80K. An interesting temperature dependence of magnetoresistance has been observed in some

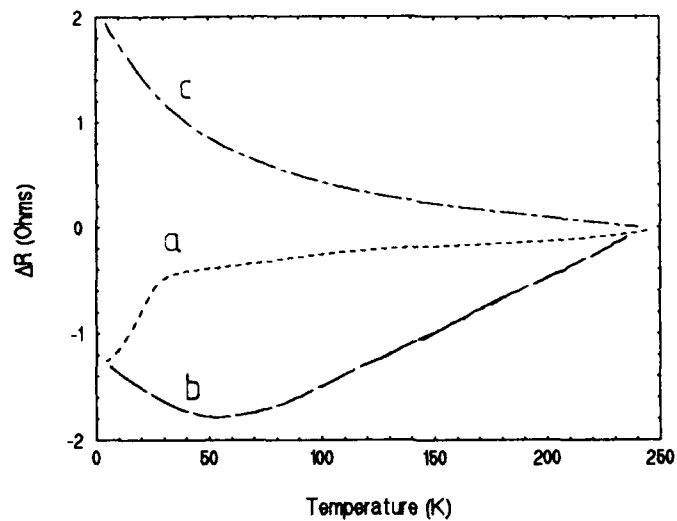


Figure 1: Change in resistance on cooling of three Gd/W multilayers with $t_W = 1.7\text{nm}$; a) $t_{\text{Gd}} = 5.7\text{nm}$, $R(250\text{K}) = 31.3\Omega$, b) $t_{\text{Gd}} = 1.95\text{nm}$, $R(250\text{K}) = 40.5\Omega$, c) $t_{\text{Gd}} = 0.8\text{nm}$, $R(250\text{K}) = 57.1\Omega$.

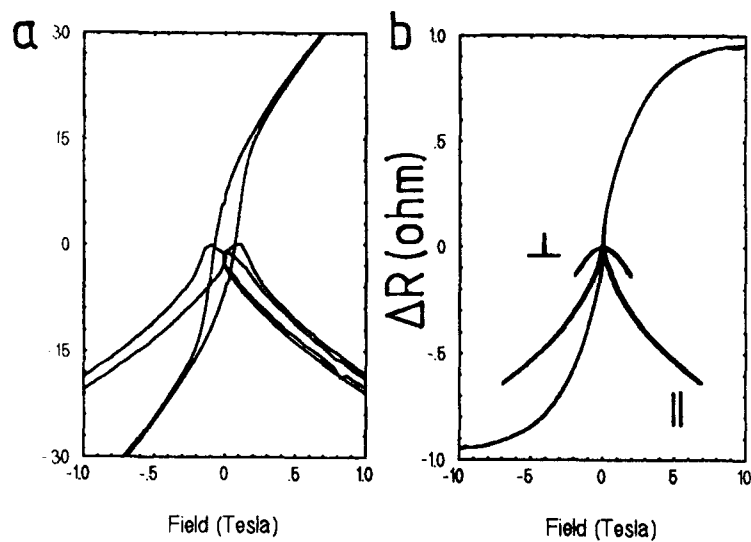


Figure 2: Magnetoresistance of a typical Gd/W multilayer at 4.2K. Resistance in zero field = 14.4Ω . a) Magnetoresistance and magnetisation curve at low in-plane applied fields, showing the resistance peaks at the coercive field; b) Magnetisation and in-plane and perpendicular magnetoresistance up to high applied fields.

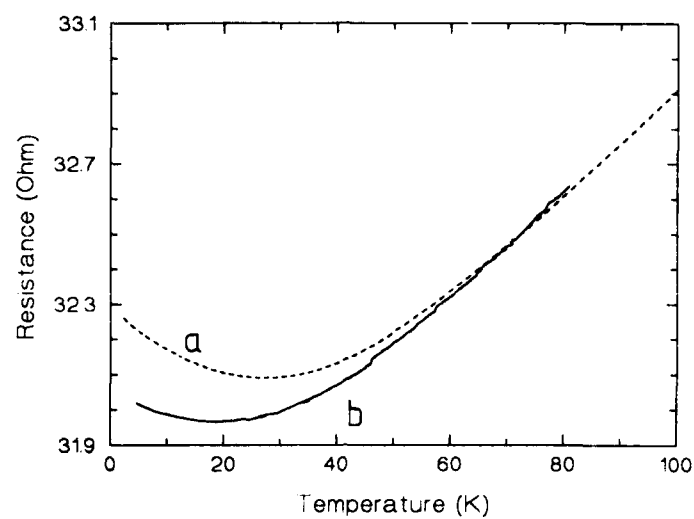


Figure 3: Resistance of a Gd/W multilayer as a function of temperature; a) in zero field; b) in 7 Tesla (in plane). $t_{\text{Gd}} = 0.97\text{nm}$, $t_{\text{W}} = 1.6\text{nm}$.

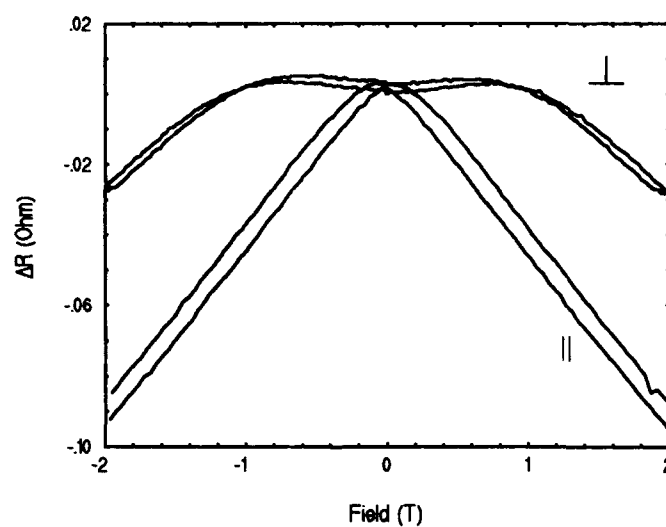


Figure 4: Magnetoresistance of a Gd/W multilayer at 100K. Resistance in zero field = 15.9Ω .

specimens with moderately thick Gd and W layers, as shown in Figure 4. At temperatures between 100K and 150K the resistance of these specimens increases at first and then decreases, without measurable hysteresis, when the field is perpendicular to the specimen plane. At higher temperatures the initial increase disappears. This unusual behaviour is observed only in those multilayers which show reduced magnetisation at 4.2K[2].

DISCUSSION

1. Resistance in zero field

The results we have obtained for the dependence of the zero-field resistance on layer thicknesses are similar to those obtained for other multilayer systems including Nb/Al [7], Cu/Ti [8], Mo/Ni [9] and Nb/Cu [10]. As discussed in [7], a transition from metallic to non-metallic behaviour occurs as the mean free path of the conduction electrons decreases and approaches the interatomic spacing. A negative temperature coefficient of resistance (TCR) is thus characteristic of all disordered metal systems with high resistivities, including bulk alloys and amorphous metals [11,12] as well as thin films. The results in figure 1 show the expected correlation of negative TCR with high resistivity (see figure caption). The fact that we observe a negative TCR in amorphous GdW alloy films is also agrees with this well-established trend.

In multilayers the decreasing mean free path at small layer thicknesses is generally attributed to an increasing contribution from interface scattering [7]. In Gd/W multilayers the interface scattering will include a magnetic contribution, and is therefore expected to be larger than in non-magnetic systems such as Nb/Al and thus may become important at relatively large layer thicknesses. Although the layers are fully crystalline their interfaces are zones of chemical disorder and as such will have a negative TCR. The interplay between bulk and interface scattering is evident in specimens such as that shown in figure 1b, where the TCR of the specimen changes sign with falling temperature. This can be interpreted as due to a cross-over from a high temperature regime, in which temperature-dependent phonon and magnon scattering within the layers is dominant, to a low-temperature regime in which the mean free path within the layers is longer than the layer thickness so that the scattering is dominated by the negative TCR associated with the layer interfaces. As expected, the temperature at which the cross-over occurs is observed to increase as the Gd layer thickness decreases.

To a first approximation, a multilayer can be regarded as two resistances in parallel, although the validity of this simplified model depends on a number of conditions which are not necessarily fulfilled [7]. Nevertheless, this model is useful as a starting point for the interpretation of resistance data. The absolute resistivity of pure bulk W is considerably lower than that of bulk Gd at room temperature [13] and a simple parallel-resistors calculation shows that in our multilayers most of the current should be carried by the W layers. (At low temperatures conduction in the Gd layers should become more significant, at least in specimens with relatively thick Gd, because gadolinium has a larger TCR than tungsten.) However, if the current is flowing mainly through the tungsten this would lead us to expect the three specimens shown in Figure 1 to have the same resistance, since they all contain the same number of 1.7nm W layers, and this is clearly not the case. We conclude that in our multilayers the Gd layers are carrying most of the current. This implies that the 1.7nm tungsten layers have a resistivity considerably higher than that of bulk W whereas the resistivity of Gd layers less than 2nm in thickness is equal to, or only slightly higher than, the bulk value. The origin of the high W resistivity in our specimens is not yet clear. It could be related to the induced magnetic moment we have observed in the tungsten [1,2], but other possibilities, such as cross-contamination of the tungsten with a low concentration of Gd during deposition, have not yet been definitely ruled out. Further work is in progress to clarify this point.

2. Magnetoresistance

Our observations show that the magnetoresistance of the multilayers is dominated by the negative magnetoresistance of gadolinium. This also suggests that the current is mainly flowing through the Gd layers. However, any current being carried by the tungsten layers will be influenced by the magnetic state of the Gd atoms at the interfaces, so that as the Gd moments align in an applied field the spin-disorder contribution to the interface scattering will be

reduced. This effect will be particularly important at low temperatures where interface scattering is dominant, and we believe this is why all the multilayers, both those with positive TCR and those with negative TCR, show the same negative form of magnetoresistance at low temperature. The change in sign of the magnetoresistance at higher temperature, seen, for example, in Figure 3, suggests that in this specimen the W layers are becoming the main conduction channel above about 80K and that their conductivity is dominated by bulk scattering within the layers rather than by the Gd layer interfaces.

The results shown in figure 4 are extremely interesting. This specimen has relatively thick Gd layers (4.25nm) and normal, metallic resistance like that shown in figure 1a, so bulk scattering within the layers should be the main contribution to the resistance at this temperature. The negative magnetoresistance indicates that gadolinium is controlling the magnetoresistance. However, the magnetoresistance curve in perpendicular field is unlike anything we have observed in pure Gd films. It bears a strong resemblance to the magnetoresistance curves of Gd/Fe multilayers [14], in which the two components are antiferromagnetically coupled at low fields, and since we have only observed curves of this form in multilayers with reduced magnetisation at 4.2K [2] we believe it may be associated with antiferromagnetic alignment of the moments in the Gd and W layers. Further experiments to investigate this are in progress.

CONCLUSIONS

The resistance and magnetoresistance of Gd/W multilayers show a number of interesting and unusual features which appear to be correlated with the oscillatory enhancement or reduction in saturation moment reported previously. The temperature dependence of the resistance as a function of Gd layer thickness indicates that interface scattering is dominant at small layer thicknesses, as has been observed in other metallic multilayers. The gadolinium layers dominate the magnetoresistance at low temperatures while the tungsten plays an increasing role as the temperature is increased. However, many details of the magnetoresistance remain to be interpreted, especially in the cross-over region between these two regimes. Further experiments on this and related multilayer systems are in progress.

ACKNOWLEDGEMENTS

This research has been supported by SERC grants GR/E94371 and GR/H27823 and by a grant from the British Council Alliance programme. The X-ray diffraction measurements were made using the powder diffractometer in the Department of Crystallography, Birkbeck College. The authors would like to thank G. Akyetey, R. Cywinski, A. K. Petford-Long and M. Vickers for assistance with the experiments. E. G. Astrakharchik would like to thank the Royal Society for a Kapitza Fellowship.

REFERENCES

1. A. Heys, P E Donovan, A K Petford-Long and R Cywinski, submitted to J.Magn.Magn.Mater.
2. A. Heys and P E Donovan, J.Magn.Magn.Mater. (in press)
3. E. Spiller, Rev. Phys. Appl. 23, (1988) 1687
4. A.K. Petford-Long, P.E. Donovan and A. Heys, Ultramicroscopy 47, (1992) 323
5. M. Gasgnier, Phys. Stat. Sol. A57, (1981) 11
6. J. P. Burger, J. N. Daou and P. Vajda, J.Magn.Magn.Mater. 90-91, (1990) 110
7. M. Gurvitch, Phys. Rev. B34, (1986) 540
8. M. P. Fontana, P. Podini, J. Zujmin and L. Wen, Phys. Rev. B42 (1990) 5859
9. M. R. Khan, C. S. L. Chun, G. P. Flecher, M. Grimsditch, A. Kueny, C. Falco and I. K. Schuller, Phys. Rev. B27, (1983) 7186
10. T. R. Werner, I. Banerjee, Q. S. Yang, C. Falco and I. K. Schuller, Phys. Rev. Lett. 26 (1982) 2224
11. J. H. Mooij, Phys. Stat. Sol. A 17 (1973) 521
12. C. C. Tsuei, Phys. Rev. Lett. 57 (1986) 1943
13. G. Kaye and T. Laby, Tables of Physical and Chemical Constants, 15th edition, Longman, London and New York, (1986) pp 117-118
14. B. George (to be published)

TRANSMISSION ELECTRON MICROSCOPY STUDIES OF NiFe/Cu/Co/Cu ON Si.

P. GALTIER, T. VALET, O. DURAND, J.C. JACQUET, AND J.P. CHEVALIER*

Laboratoire Central de Recherches, Thomson-CSF, 91404 Orsay, France

*Centre d'Etude de Chimie Métallurgique, CNRS, 15 rue G. Urbain, 94407 Vitry Cedex, France

ABSTRACT:

(NiFe/Cu/Co/Cu) multilayers grown on (100)Si by RF sputtering have been studied by transmission electron microscopy. The samples are found to be polycrystalline and are only weakly textured. The period of the multilayers is clearly visible by small angle electron diffraction and Fresnel imaging. The waviness of the layers appears to be related to the columnar structure of the samples. Experimental images with Fresnel contrast are compared with simulations in order to assess the thickness and roughness of each individual layer.

INTRODUCTION:

The growth of ultrathin Metallic Multilayers (MLs) has received increasing attention in recent years due to their novel magnetic properties^{1,2}. Various growth techniques such as Molecular Beam Epitaxy (MBE) and sputtering have been used to produce high quality stacks. The interpretation of the magnetic properties of films with thicknesses of a few nanometers requires a detailed knowledge of the structural features of the structures fabricated. Thus a wide range of in-situ and ex-situ characterization tools are generally necessary. The aim of this work is to present a study using Transmission Electron Microscopy (TEM) of the Ni₈₀Fe₂₀/Cu/Co/Cu system grown on (100)Si by sputtering. Giant magnetoresistance has been reported^{3,4} in these samples previously. We present first a detailed analysis of the microstructural aspects of these MLs. The effect of the thickness of the Co layers notably on the structure and texture of the layers has been investigated. We show that conventional contrast modes, which usually leads the usual information on the structure and microstructure, fail to visualize the details of the multilayer stacking. We then show that the use of Fresnel contrast is a powerful tool to image the details of the multilayers when they are composed of elements with close atomic number. We demonstrate that the complicated features of the Fresnel fringe pattern can be qualitatively described using simple simulations in order to approach the details of the MLs.

EXPERIMENTAL:

Sputtered Ni₈₀Fe₂₀/Cu/Co multilayers were prepared in a high vacuum RF diode sputtering system with a base pressure of 5×10^{-8} Torr on chemically etched (100)Si wafers^{3,4}. The deposition rate was of the order of 0.5 \AA s^{-1} . In order to improve the structural quality, a buffer layer of 50 Å of Fe were deposited on the Si substrate prior to the growth of the MLs.

Plane views and cross sections were prepared by polishing and dimpling followed by argon milling performed using a liquid nitrogen cooled stage equipped with a sector speed control. Great care was taken to lower the Ar beam energy in order to reduce artefacts due to overheating. The observations were performed using a Topcon ABT 002B microscope operated at 200 kV. It was fitted with a Cs 0.4 mm pole piece. Fresnel contrast images were recorded at a magnification of 200K with a beam divergence of about 0.5 mrad and an objective aperture giving a resolution of 2.5 Å.

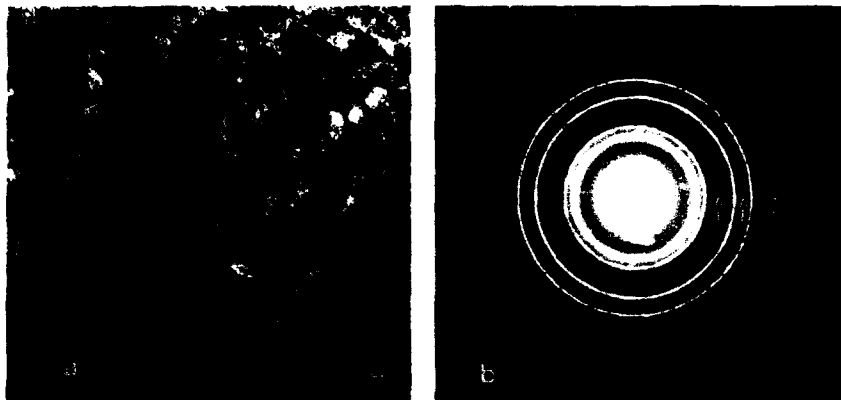


Figure 1: Plane view observation of $[\text{NiFe}(50\text{\AA})/\text{Cu}(50\text{\AA})/\text{Co}(10\text{\AA})/\text{Cu}(50\text{\AA})] \times 8$. a) Bright field image. The bar represents 1000 Å. b) Diffraction pattern. The arrows show the weak contributions due to a hcp phase.

MICROSTRUCTURE:

TEM observations were initially carried out on two samples with different Co layer thicknesses in order to examine the influence of Co on the structure of the MLs. These correspond to the following sequences:

- $[\text{NiFe}(50\text{\AA})/\text{Cu}(50\text{\AA})/\text{Co}(10\text{\AA})/\text{Cu}(50\text{\AA})] \times 12$
- $[\text{NiFe}(50\text{\AA})/\text{Cu}(50\text{\AA})/\text{Co}(50\text{\AA})/\text{Cu}(50\text{\AA})] \times 8$.

Figure 1.a shows a plane view of the MLs. The sample is polycrystalline with grain sizes ranging from 500 to 2000 Å. We have not observed a noticeable modification of the morphology with the thickness of the Co layers. Electron diffractions show that the structure is predominantly fcc despite some residual hcp contribution presumably originating from the Co layer (Figure 1.b). This hcp contribution is very weak but diffraction rings from (100), (102), (110) and (103) planes are clearly observable on the sample with a Co thickness of 10 Å. The amount of hcp phase tends to increase with the Co thickness in agreement with Nuclear Magnetic Resonance (NMR) results^{4,5}.

Figure 2.a is a bright field image of a cross-section. The columnar structure of the sample is clearly visible (see arrows in Figure 2). This structure appears to originate at the substrate surface and develops laterally with increasing the total thickness. This columnar structure is correlated with the appearance of a substantial roughness ($\approx 50\text{\AA}$) at the surface. Electron diffraction on cross-sections show that the MLs are practically not textured. This result contrasts with previous observations⁶ on similar materials fabricated by DC magnetron sputtering where a strong (111) texture parallel to the growth axis is observed. Nevertheless, we observe a slight (111) texture on samples with Co layer thicknesses of 10 Å.

A detailed analysis of the small angle contribution in the electron diffraction pattern obtained on cross-sections reveals some extra reflections on each side of the central peak (see insert of Figure 2.a). These are the signature of a superlattice structure in the material and demonstrate the existence of the multilayer period. This result has been confirmed by small angle X-ray

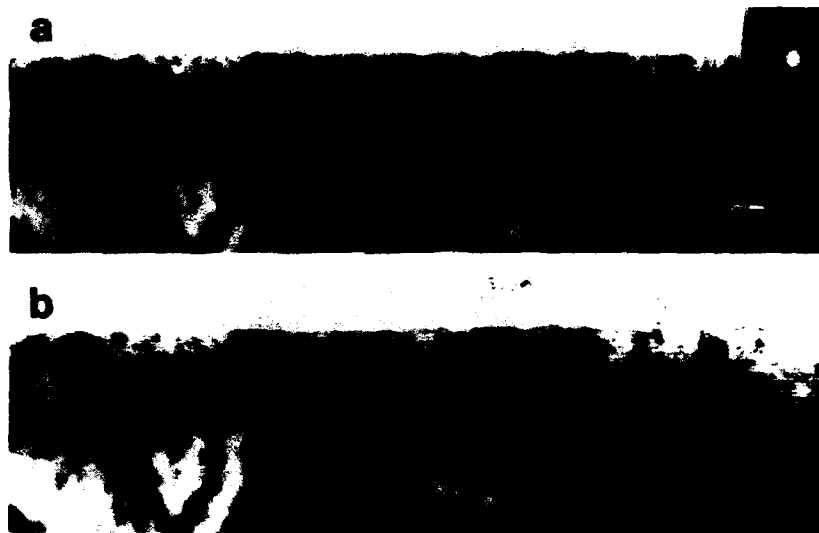


Figure 2: Bright field images of $[\text{NiFe}(50\text{\AA})/\text{Cu}(50\text{\AA})/\text{Co}(50\text{\AA})/\text{Cu}(50\text{\AA})] \times 8$. a): Defocus=0 nm, insert: low angle electron diffraction. b): Defocus=-20 μm . The bar represent 1000 \AA .

diffraction where similar diffraction effects are observed. Thus, although the existence of a multilayer structure is clearly demonstrated by diffraction, this does not appear clearly in the images in diffraction contrast (Figure 2.a). This can be readily understood: if the crystals in the layers are not in strong diffracting condition, absorption is the predominant cause of contrast, and since the constituent elements have extremely close Z , the absorption will be virtually identical for all the layers (hence little or no contrast). However, the contrast can be enhanced by defocusing the objective lens leading to the appearance of Fresnel fringes. An image of the MLs obtained under such condition is shown in Figure 2.b. The aspect of the Fresnel contrast is not straightforward and depends on the focus conditions. An attempt to describe these features is presented in the next section. Nevertheless a rapid inspection of the details in the image is sufficient to obtain informations on the stacking regularity. We notice that near the substrate, the layers are almost flat with a roughness of about 10 \AA . Above approximately 500 \AA of thickness an undulation of the fringes appears which leads to an increase of the roughness to about 50 \AA at the top of the sample. These undulations appear to be related to the columnar structure observed previously. However, the fringes appear continuous, suggesting that the layers are continuous too (the continuity of the thinnest layers, i.e. when the layer thickness is of the same order as the Fresnel fringe thickness, has to be verified). A periodicity is clearly visible in the system of Fresnel fringes (Figure 2.b). Its value is a direct measurement of the period of the superlattice. Here we find a value of 250 \AA in good agreement with that deduced from peaks spacing measured in the small angle electron diffraction (inset of Figure 2.a). Furthermore the MLs period measured on the Fresnel fringe system does not vary significantly in the sample despite the observed waviness. This waviness appears to play an important role in the magnetotransport properties in strongly reducing the Co coercivity. Such an effect can be dramatically reduced if samples with lower total thicknesses are grown⁴.

Dark field imaging reveals clearly the effect of texture. Figure 3.a is a dark field image which highlights grains with a (111) texture along the growth axis. These grains are found to be large enough to extend through the total thickness of the MLs.

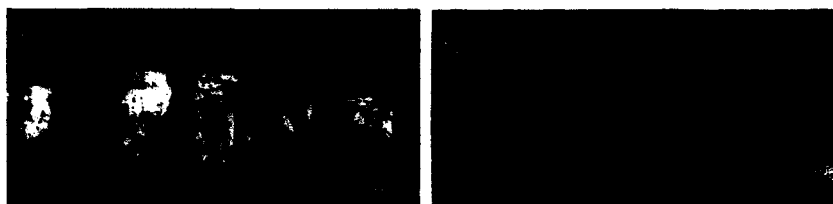


Figure 3: a) Dark Field image with $g=(111)$ parallel to the growth axis obtained on $[\text{NiFe}(50\text{\AA})/\text{Cu}(50\text{\AA})/\text{Co}(10\text{\AA})/\text{Cu}(50\text{\AA})]\times 8$. b) Dark field image formed with the diffuse scattering. The amorphous layer is shown by an arrow. The bars represent 1000 Å.

A close examination of the high resolution images of the interface between the Fe buffer layer and the Si interface reveals an amorphous or microcrystalline layer of about 15 Å thick. This layer is also observable in the dark field image obtained with the diffused scattering (Figure 3.b). This thin layer is not systematically observed on all the samples. Thus it is attributed preferentially to a residual of SiO_2 due to substrate preparation previous to the growth rather than to an eventual reaction of Fe with Si.

FRESNEL CONTRAST:

Fresnel contrast is due to refraction of the electron waves at the interfaces between media with different mean inner potentials. This technique has been widely used for the determination of boundary layer thicknesses⁷⁻¹⁰. An interesting feature of this method is that the contrast of the Fresnel fringes between two materials with close atomic number can be enhanced under strong defocusing conditions. Thus Fresnel imaging is a useful tool to study MLs composed of elements like Fe, Ni, Co, Cu, Cr and their alloys: these materials, often produced by sputtering techniques, are generally not monocrystalline, and hence large angle X-ray diffraction cannot be used to assess the regularity and period of the MLs. In practice through focal series of TEM images are recorded and compared to simulations which assume the nature of the boundary layer (i.e. its mean inner potential V_0), its width and diffusivity.

The detailed shape of the profiles of the Fresnel fringes cannot be directly and uniquely interpreted in order to recognize the layers and determine the interfaces' properties. This is because the recorded images result from the convolution of the transmitted electron wave function by the electron optical transfer function of the instrument. Examples of the influence of the operating conditions are shown in Figures 4. It is obvious that the contrast is totally modified by the focusing conditions. At zero defocus (i.e. image perfectly focused) only a very weak contrast is observed as expected. By increasing the out of focus, Fresnel contrast is generated, but the contrast varies substantially (it can be reversed between underfocus and overfocus) and no ready conclusions can be made excepted concerning the regularity of the layers (comparing the sequence of the Fresnel fringes to that of the MLs). This point becomes critical when the layer thickness and the Fresnel fringe width are similar. Thus the only way to correctly extract information from Fresnel images is to compare them with simulations.

The main features of the Fresnel fringe system can be described with simple assumptions concerning the interaction of the electron beam with the material. For a mean inner potential V_0 and in the kinematical limit, the wave function Ψ at the exit face of the sample can be written as follows^{7,10}:

$$\Psi = \alpha e^{-i\beta} \quad \text{with} \quad \beta = \pi V_0 \epsilon / \lambda E$$

where α is the absorption, ϵ the thickness of the TEM sample and E and λ the energy and

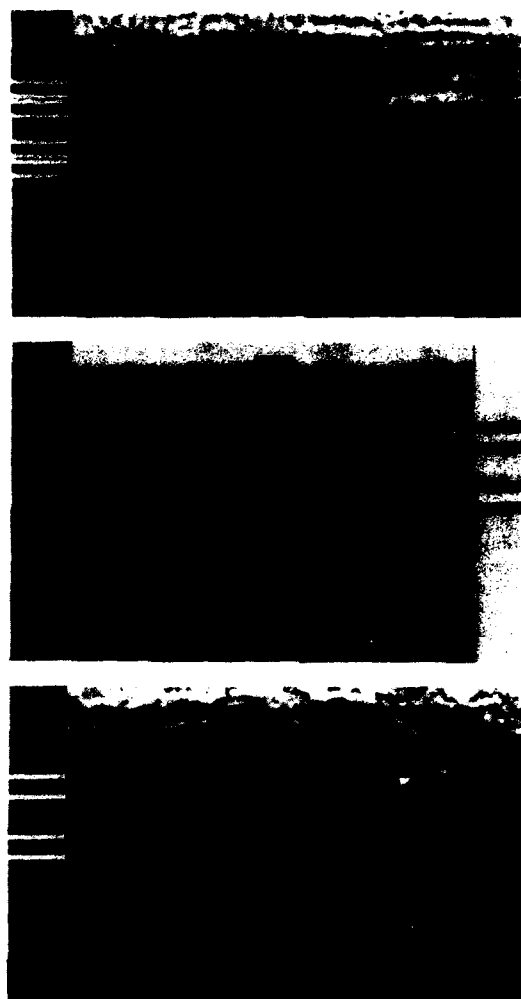


Figure 4: Comparison between experimental (right) and simulated (left) Fresnel images of $[\text{Co}(20\text{\AA})/\text{Cu}(10\text{\AA})/\text{FeNi}(50)/\text{Cu}(10)] \times 3$ at different defoci. The bar represents 50 Å. An interface diffuseness of 8 Å has been included in the simulations. a): Defocus = +400 nm. b): In focus. Right: stacking sequence used for the simulations. c): Defocus = -400 nm.

wavelength of the electron beam. Due to the close values of the atomic numbers of Cu, Co, Fe and Ni we assume the same value for the absorption term α for all the elements. V_0 can be deduced from the atomic scattering factors^{7,9} for zero scattering angle. The values used for V_0 are respectively 22.7, 28.5 and 29.5 eV for Cu, $\text{Ni}_{80}\text{Fe}_{20}$ and Co. The parameters of the transfer function of the microscope include spherical and chromatic aberrations, divergence and objective aperture. The main limitation of this description is the kinematical limit which imposes the study of very thin TEM foils if well oriented monocrystalline materials are studied, in order to avoid strong diffraction effects. Fortunately, in our case the MLs are polycrystalline with only a very slight texture. Thus it is possible to observe the MLs "edge on" provided that the observed zones

are not in Bragg condition (i.e. the grains are not oriented parallel to the electron beam). Our aim was in a first step to describe qualitatively the Fresnel contrast, so no attempt was made to compare absolute intensity between calculated and recorded images. A value of 150 Å for the thickness t of the cross-section sample was assumed. This parameter does not qualitatively affect the results of the calculations except for the values of absolute intensities.

Comparison between experimental and calculated images are shown in Figure 4 for samples with different Cu thicknesses. We have simulated only the sequence NiFe/Cu/Co/Cu/NiFe/Cu/Co/Cu/NiFe shown on the right part of Figure 4.b. It should be noted that the appearance of a reasonable Fresnel contrast in this system is fortuitous: this is due to the low value of V_0 for Cu with respect to Co, Fe and Ni, and for example we have observed little or no contrast at Fe/Co interfaces. If we compare the simulations with the experimental images, the agreement is rather good. We see that the true multilayer sequence cannot be deduced directly from the Fresnel fringes but requires the use of simulations. The calculations presented here were performed assuming layer thicknesses given by the calibration of the sputtering machine.

A qualitative information on the interface diffuseness can be deduced from the evolution of the contrast with the defocus value. For example, for perfectly abrupt interfaces, residual Fresnel fringes should be observed at Zero defocus. Furthermore, the maximum value of contrast of these fringes should be observed at about -50nm defocus. This is not observed experimentally, and to obtain a reasonable qualitative agreement, an interface diffuseness of about 8 Å has to be introduced. This value, although quite imprecise because TEM averages any details along the electron beam axis (the thickness of the cross-section foil), agrees with NMR results obtained on the Co/Cu interface⁴.

Further improvement in the study of metallic MLs by the Fresnel method should include the recording of the absolute intensity of the images for the purpose of direct comparisons with calculations. Refinement in the calculation could include a less phenomenological treatment of inelastic scattering as well as the dynamical effects⁸. In that case, we can expect more accurate information on the interface characteristics. Nevertheless, we think that the most serious limitation of this technique arises from the intensity fluctuations observed in the experimental images. These fluctuations may be related to sample damage created during the argon milling and the main task we have to tackle in the future remains the reduction of the roughness and amorphization at the surface of the cross-section samples.

CONCLUSIONS:

A detailed structural analysis of NiFe/Cu/Co/Cu multilayers grown by RF sputtering has been presented. RF sputtering appears to give rise to samples less textured than DC magnetron sputtering. High quality MLs stacking can be obtained provided that the total thickness of the samples does not exceed 500 Å. We show that the difficulties in imaging the layers, related to the close atomic numbers of the constituents, can be overcome using Fresnel imaging.

Acknowledgments: The authors would like to thank C. Chenu for her expertise in sample preparation for the electron microscopy experiments.

REFERENCES:

1. M.N. Baibich, J.M. Broto, A. Fert, N. Nguyen Van Dau, F. Petroff, P. Etienne, G. Creuzet, A. Friederich and J. Chazelas, *Phys. Rev. Lett.* **61**, 2472 (1988).
2. W.P. Pratt, Jr, S.F. Lee, J.M. Slaughter, R. Loloee, P.A. Schroeder and J. Bass, *Phys. Rev. Lett.* **66**, 3060 (1991).
3. T. Valet, J.C. Jacquet, P. Galtier, J.M. Coutellier, L.G. Pereira, R. Morel, D. Lottis and A. Fert, *Appl. Phys. Lett.* **61**, 3187 (1992).
4. T. Valet, P. Galtier, J.C. Jacquet, C. Meny and P. Panissod, *J. Magn. Magn. Mater.* **121**, (1993).
5. C. Meny, P. Panissod and R. Loloee, *Phys. Rev. B* **45**, 12269 (1992).
6. S.S.P. Parkin, Z.G. Li and D.J. Smith, *Appl. Phys. Lett.* **58**, 2710 (1991).
7. D.R. Clarke, *Ultramicroscopy* **4**, 33 (1979).
8. J.N. Ness, W. Stobbs and T.F. Page, *Phil. Mag. A* **54**, 679 (1986).
9. J.N. Ness, W. Stobbs, *Phil. Mag. A* **63**, 1 (1991).
10. S. Mellul, PhD Thesis, University Paris 6 (1988).

NEUTRON SCATTERING MEASUREMENTS OF THE STAGGERED MAGNETIZATION OF AN ANTIFERROMAGNETIC EPITAXIAL THIN FILM FeF₂

D. P. BELANGER*, M. LUI**, AND R. W. ERWIN***

*Physics Department, University of California, Santa Cruz, CA 95064

**Hughes Research Laboratories, 3011 Malibu Canyon Rd., Malibu, CA 90265

***National Institute of Standards and Technology, Gaithersburg, MD 20877

ABSTRACT

Elastic neutron scattering measurements performed at the NIST reactor have been used to measure the staggered magnetization near the transition temperature in a thin antiferromagnetic epitaxial film of FeF₂ of thickness 0.8 μ m and diameter 1cm grown on a diamagnetic (001) ZnF₂ substrate by MBE. The use of a thin film permits extinction-free Bragg intensities, something which has proven impossible in bulk crystals. The growth techniques yield sufficient crystal quality to observed resolution limited magnetic Bragg scattering peaks and to approach the transition within a reduced temperature of $|t| = 0.003$. The structure quality of this sample has been characterized using X-ray double crystal diffraction with a measured rocking curve linewidth of less than 30 arc sec. The sample thickness, while small enough to eliminate extinction, is sufficiently large to assure three-dimensional Ising model critical behavior. We indeed observe critical behavior consistent with theoretical predictions. The success of the thin film experiments demonstrates the possibilities of extinction-free Bragg scattering measurements in a variety of antiferromagnetic materials, including multilayered systems.

INTRODUCTION

Neutron scattering techniques can be extremely useful in the characterization of phase transitions in antiferromagnetic materials. The fluctuation correlation length, the staggered magnetization, and the staggered susceptibility can, in principle, be measured from the scattering intensity in the vicinity of the antiferromagnetic Bragg position. With the exception of the staggered magnetization, this is routinely done in bulk single crystals in which phase transitions to three-dimensional ($d = 3$) magnetic order take place[1].

In principle, since the order parameter is proportional to the square root of the Bragg scattering intensity, one should observe the asymptotic Bragg scattering intensity

$$I \sim M_s^2 = M_0^2 |t|^{2\beta} \quad (1)$$

where M_s is the staggered magnetization, $t = T/T_N - 1$, and β is the order parameter exponent characteristic of the universality class of the transition. In practice, however, the determination of the critical behavior of the order parameter is often not realized for $d = 3$ antiferromagnetic transitions using high quality crystals. Since the magnetic Bragg scattering occurs at points in reciprocal space, the scattering crosssection can be so large that all of the neutrons that can scatter will do so in the first few microns of sample, a phenomenon known as extinction. As a consequence the staggered magnetization appears to quickly saturate as the temperature is lowered below T_N . Analyzing the data assuming the power law behavior in Eq. 1 results in the wrong value for the critical exponent β . Hence, accurate critical behavior measurements of the $d = 3$ staggered magnetization in bulk samples of high quality FeF₂ have not been made using neutron scattering techniques. Instead Mössbauer techniques[2] have been used to determine the critical exponent $\beta = 0.325 \pm 0.005$, which corresponds exceedingly well to the theoretical[3, 4] value $\beta = 0.325 \pm 0.001$.

The FeF_2 system is one of the most ideal and thoroughly characterized Ising systems. It is ideal since it has only one significant exchange interaction, that between second-nearest-neighbors, and the anisotropy is large[5], making it a particularly simple system with a large asymptotic power law region $|t| < 0.02$. As well as being a model Ising system, FeF_2 can be diluted by growing it in solution with the diamagnet ZnF_2 . Any concentration can be grown and, with care, the concentration can be made quite uniform. The mixed system $Fe_xZn_{1-x}F_2$ still can be described exceedingly well using only the second-nearest-neighbor interaction and an anisotropy that increases slightly upon dilution[6]. $Fe_xZn_{1-x}F_2$ is ideally suited for studying the random-exchange Ising model. Upon application of a magnetic field along the easy axis, the random-field Ising model is realized. It was in this system that the random-field $d = 3$ Ising phase transition was first observed using birefringence techniques[7]. Mössbauer measurements have yielded the exponent $\beta = 0.35 \pm 0.01$ for this random-exchange system[8]. The random-exchange exponent is in excellent agreement with the theoretical value[9, 10] $\beta = 0.349 \pm 0.002$. The random-field behavior of the order parameter, which should be realized with a field applied, has so far proven difficult to interpret in Mössbauer experiments. Neutron scattering experiments have also failed to yield the exponent β , in part because the $d = 3$ bulk samples suffer severely from extinction. This is unfortunate since the exponent is predicted to decrease from the random-exchange value of about $1/3$ to the random-field value of 0.05 or smaller[11, 12] upon application of a magnetic field. The only indication of a decrease in β comes somewhat indirectly from dilation experiments[13]. This large and interesting crossover from random-exchange to random-field critical behavior was one of our motivations to develop a method for using neutron scattering in which we eliminate the problems of extinction. The successful technique involves the epitaxial growth of a magnetic film of the insulating antiferromagnet FeF_2 on a diamagnetic insulating substrate ZnF_2 . The antiferromagnetic film is thin enough to preclude the effects of extinction.

Another equally important motivation for developing the thin film technique is that it opens many new avenues for studying novel materials formed from the epitaxial growth of insulating antiferromagnetic thin films. For example, multilayered samples in which each alternating layer has a different exchange strength could be studied. One specific case[14] would be when one type of layer is diamagnetic ZnF_2 and the other is antiferromagnetic FeF_2 . As the magnetic layer thickness is decreased, one should observe the crossover from three to two dimensional critical behavior. Another example is $(FeF_2)_M(CoF_2)_N$, a multilayer thin film which has been studied as a function of M and N , as reported in another manuscript in these proceedings[15].

In the process of developing the thin film technique, we first fabricated pure FeF_2 films on ZnF_2 substrates. We report here the results of the first successful neutron measurements on such a film. Since the critical behavior of the staggered magnetization has already been determined experimentally[2] in FeF_2 , the purpose of our study was not to accomplish this determination but instead to establish the feasibility and validity of the technique of using epitaxial films to study critical behavior studies of the staggered magnetization of $d = 3$ phase transitions.

EXPERIMENTAL TECHNIQUES

The epitaxial FeF_2 layer was grown by MBE techniques in a modified Varian UHV system equipped with cyropanels to reduce pressure increases during the oxide removal and growth processes. The base pressure of the system is less than 10^{-9} Torr with the pressure rising no higher than 5×10^{-9} Torr during growth. Oxide removal of the ZnF_2 substrate was first carried out at 450 degrees celsius for 10 minutes, after which the temperature was lowered to a growth temperature of 300 degrees celsius. The FeF_2 film was vaporized from an open pyrolyzed graphite crucible at a rate of approximately 1 micron/hr. The film thickness was determined using a quartz crystal oscillator[16].

Unlike semiconductor such as GaAs, ZnF_2 substrates are not available commercially. It was necessary therefore, to develop substrate growth and preparation techniques. The (001) ZnF_2 substrate was grown by the Bridgman method and carefully aligned with the c-axis perpendicular to the substrate surface using an X-ray Laue Camera. The substrate was mechanically polished

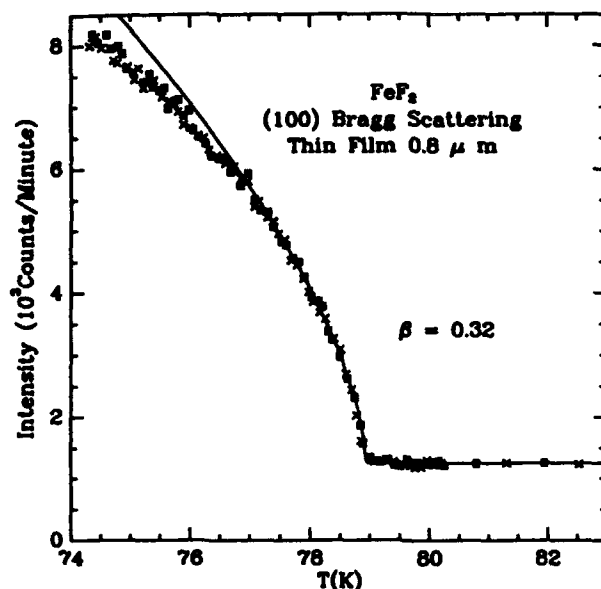


Figure 1: The Bragg scattering intensity, which is proportional to the square of the staggered magnetization, versus temperature for a pure FeF_2 thin epitaxial film on a ZnF_2 substrate. The solid curve is a fit to Eq. 1 with $\beta = 0.32$ and a constant background term. The crosses (squares) are for increasing (decreasing) T .

using diamond paste on a custom polishing system. A combined mechanical/chemical etching technique was used as the last polishing step in order to remove damage left by the mechanical polishing steps. A 20% HCL solution was used in conjunction with a custom etch polishing system. A final free etch in 20% HCL was used before loading the substrate into the high vacuum MBE growth chamber. The necessity for such an elaborate polishing scheme for high quality layers was established during capacitance studies on FeF_2 epitaxial films[17].

The structural quality of the FeF_2 epitaxial film was determined by X-ray double crystal diffraction. The observed rocking curve linewidth may be compared to its intrinsic value as calculated by dynamical diffraction theory. For the 0.8μ FeF_2 film used in this study, a measured linewidth of 30 arc secs was observed compared to an intrinsic value of 22 arc sec. The rocking curve linewidth is almost intrinsically limited indicative of extremely high quality material[18].

In the present study, we have characterized the Bragg intensity of a 0.8μ epitaxial thin film of FeF_2 which has its c -axis, along which the spins order, perpendicular to the film plane. The elastic measurements were performed at the National Institute of Standards and Technology reactor on the BT-9 triple-axis spectrometer at an energy of 14.8meV using a pyrolyzed graphite monochromator and analyzer. The collimations used in the measurements were 45 minutes of arc before the monochromator, 20 minutes between the monochromator and sample, 20 minutes between the sample and analyzer, and 45 minutes between the analyzer and detector. A pyrolyzed graphite filter was employed to reduce contamination from higher energy neutrons.

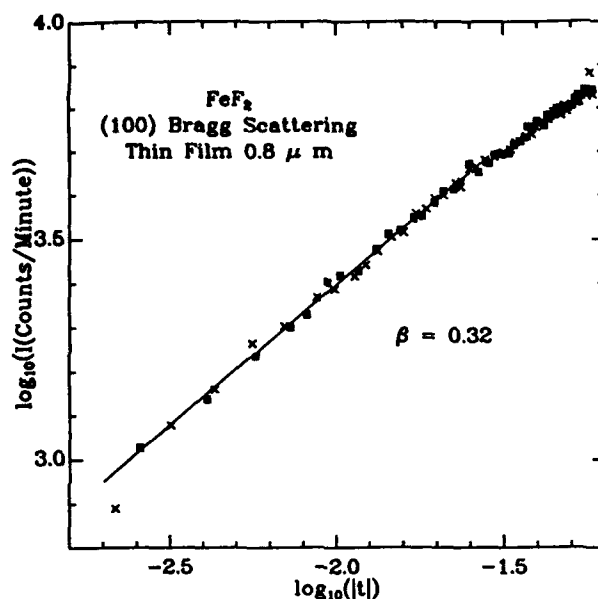


Figure 2: The logarithm of the Bragg scattering intensity versus the logarithm of the reduced temperature for the same data as in Fig. 1, but with the constant background term subtracted. The solid curve is a fit with $\beta = 0.32$.

Because the sample is quite thin, the measurements were taken over a long period, typically one minute per point with a six minute wait after changing the temperature. A relatively large background signal is present in the intensity measurements[19] but is constant far above the transition and is relatively easily determined in the fits to the data. Scattering from fluctuations are in principle measured along with the Bragg intensity at $q = 0$. However, we attempted to measure the scattering from fluctuations away from the Bragg point, $q \neq 0$, and were unsuccessful since the intensity from the thin film is too small. Hence, we believe that the contribution from fluctuations is insignificant in comparison to the Bragg intensity and affect the results very little. The sample was aligned with the film in the scattering plane. Only a minute misalignment of the film plane from the a-b crystalline plane roughly by an angle $\Theta \approx \delta t/d$, where δt is the film thickness and d is the film diameter, is adequate to avoid extinction. Since the crystalline plane of the substrate is aligned with an accuracy of about 0.1 degrees, this situation is easily satisfied. A rocking curve indicates that the Bragg peak from the film is essentially resolution limited with a half width at half maximum (HWHM) of 0.002 reciprocal lattice units.

EXPERIMENTAL RESULTS

The intensity at $q = 0$ versus T is shown in Fig. 1 along with a fit to Eq. 1 plus a constant for the background. Very little rounding of the transition is evident, attesting to the high quality of the film. The data are consistent with the known critical exponent $\beta = 0.325$, as illustrated

in Fig. 2, where the logarithm of the intensity with the background removed is shown versus the logarithm of $|t|$. A fit to Eq. 1 is shown over the range $0.002 < |T| < 0.025$.

CONCLUSIONS

We have established that the limitations of extinction which plague Bragg intensity measurements in bulk antiferromagnetic insulators can be overcome by measurements on thin epitaxial films of suitable quality. The measurements on a $0.8\mu\text{m}$ film are consistent with measured and calculated critical exponent β , indicating the absence of extinction. The way is now open for studies of dilute magnetic systems and in particular the elusive random-field Ising order parameter critical behavior. Efforts are underway on this problem. Studies of multilayer epitaxial thin films systems are also being conducted.

ACKNOWLEDGEMENTS

We would like to thank A. R. King and V. Jaccarino for discussions and support of this work. This work was supported in part by the Department of Energy grant No. DE-FG03-87ER45324.

REFERENCES

1. M. F. Collins, *Magnetic Critical Scattering*, Oxford University Press, 1989.
2. G. K. Wertheim and D. N. E. Buchanan, *Phys. Rev.* **161**, 478 (1967).
3. G. A. Baker, B. G. Nickel, and D. I. Meiron, *Phys. Rev. B* **17**, 1365 (1978).
4. J. C. LeGuillou and J. Zinn-Justin, *Phys. Rev. Lett.* **39**, 95 (1977).
5. M. T. Hutchings, B. D. Rainford and H. J. Guggenheim,
6. C. B. Araújo, *Phys. Rev. B* **22**, 266 (1980).
7. D. P. Belanger, A. R. King, V. Jaccarino and J. L. Cardy, *Phys. Rev. B* **28**, 2522 (1983).
8. P. H. Barret, *Phys. Rev. B* **34**, 3513 (1986).
9. K. E. Newman and E. K. Riedel, *Phys. Rev. B* **25**, 264 (1982).
10. G. Jug, *Phys. Rev. B* **27**, 609 (1983).
11. A. P. Young and M. Nauenberg, *Phys. Rev. Lett.* **54**, 2429 (1985).
12. A. T. Ogielski, *Phys. Rev. Lett.* **57**, 1251 (1986).
13. C. A. Ramos, A. R. King, V. Jaccarino and S. M. Rezende, *J. de Physique C8*, 1241 (1988).
14. D. Lederman, Thesis (unpublished), University of California, Santa Barbara (1992).
15. D. Lederman, D. P. Belanger, J. Wang, S-J. Han, C. Paduani, C. A. Ramos, and R. M. Nicklow, see these proceedings.
16. M. Lui, thesis (unpublished), University of California, Santa Barbara (1989).
17. M. Lui, A. R. King, V. Jaccarino, and S. L. Snider, *Phys. Rev. B* **40**, 4898 (1989).
18. M. Lui, A. R. King, V. Jaccarino, R. F. C. Farrow, and S. S. P. Parkins, *Mat. Res. Soc. Symp. Proc.* Vol. 187, 267 (1990).
19. In subsequent experiments, we found that the use of two pyrolyzed filters reduced the background substantially[15].

POLARIZED NEUTRON REFLECTIVITY MEASUREMENTS OF COLLINEAR AND NON-COLLINEAR MAGNETIC STRUCTURES IN Fe/Cr(100) SUPERLATTICES

J.F. Ankner*, A. Schreyer**, Th. Zeidler**, C.F. Majkrzak*, H. Zabel**, J.A. Wolf†, and P. Grünberg†

*National Institute of Standards and Technology, Gaithersburg, MD 20899

**Ruhr Universität Bochum, D-4630 Bochum, Federal Republic of Germany

†Forschungszentrum Jülich, D-5170 Jülich, Federal Republic of Germany

ABSTRACT

We have used polarized neutron reflectivity to study the magnetic microstructure of two Fe/Cr(100) superlattices grown by molecular beam epitaxy. The first film, of nominal composition [0.9 nm Cr/5.5 nm Fe]_s, and atomically sharp interfaces, exhibits classical collinear antiferromagnetic structure. The other film ([1.2 nm Cr/5.5 nm Fe]_s), grown at a higher temperature, shows the field-dependent non-collinear features attributed to biquadratic coupling. We will describe these measurements and our preliminary structural analysis.

HISTORY AND MOTIVATION

The Fe/Cr system possesses a rich history and has served as the point of discovery for most of the novel aspects of magnetic coupling in transition-metal multilayers, wedges, and films. The observations of the antiferromagnetic coupling of iron across a chromium interlayer [1], the giant magnetoresistive effect [2, 3], and oscillatory interlayer coupling [4, 5] preceded similar discoveries in other systems and have spawned a large industry devoted to the study of transition-metal layers. Recent work has maintained this trend, with the measurement of oscillations with a period of two Cr layers [6-8] and non-collinear ("biquadratic") coupling [9]. We present polarized neutron reflectivity data from samples exhibiting both simple collinear antiferromagnetic order and non-collinear structure. Other workers have studied the Fe/Cr system using neutrons [10-15], but have not drawn a clear distinction between collinear and non-collinear structure.

The samples used in this study were prepared by molecular-beam epitaxy (MBE) on the same GaAs/Fe/Ag substrate-buffer system described in ref. [9]. Instead of wedge structures, two superlattices of nominal composition [*x* nm Cr/5.5 nm Fe]_s, with *x* = 0.9 and 1.2 nm, were grown at *T* = 293 and 523 K, respectively (see refs. [16-18] for details). In the following sections, we will present a qualitative comparison of the two different types of structure by means of magneto-optic Kerr effect and neutron reflectivity measurements.

POLARIZED-NEUTRON REFLECTIVITY

By measuring the specular reflectivity of neutrons, one can determine the layer-averaged, depth-dependent chemical and magnetic structure of planar samples. The theory of polarized-neutron reflectivity has been described by a number of authors [19-23], so we will simply outline it here. Figure 1 shows a beam of neutrons of wavelength λ incident onto and specularly reflected from a flat surface. The reflectivity depends on the specular glancing angle θ and is conventionally described in terms of the wavevector transfer, $\vec{Q} = -(4\pi \sin \theta / \lambda) \hat{z}$, where \hat{z} is normal to the surface. The incident neutrons have been polarized by Fe/Si supermirrors either parallel or antiparallel to a uniform field \vec{H} applied in the plane of the film surface. The reflected neutrons are then analyzed for their polarization state and accumulated in a ³He proportional counter as a function of θ (see ref. [23] for details).

Using the arrangement outlined above, one can measure the intensity of four possible neutron scattering processes relative to \vec{H} : incident parallel, specular parallel (++) ; incident parallel,

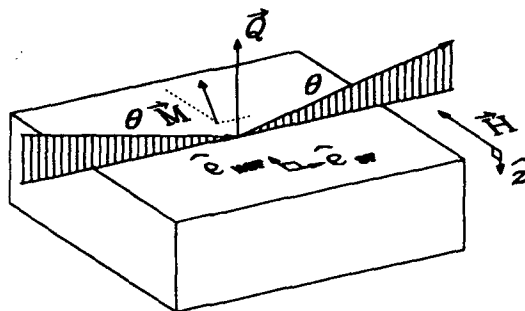


Figure 1: Reflection geometry. A monochromatic (λ) polarized neutron beam is incident at glancing angle θ onto the surface of a flat sample and specularly reflected [$\vec{Q} = -(4\pi \sin \theta / \lambda) \hat{z}$]. The projection of the sample magnetization $\vec{M}(z)$ onto the quantizing field \vec{H} defines the character of the scattering. Magnetization components perpendicular to \vec{H} (\hat{e}_{SF} direction) produce spin-flip (SF) intensity, while the parallel components (\hat{e}_{NSF}) and the nuclei scatter in the non-spin-flip (NSF) channel.

specular anti-parallel (+-); incident anti-parallel, specular parallel (-+); and incident anti-parallel, specular anti-parallel (--). The intensity scattered into these channels depends on the microscopic distribution of nuclear and magnetic scatterers at and below the surface of the sample. For the purposes of this discussion, let us assume that the sample moment $\vec{M}(z)$ is confined to planes parallel to the surface ($\vec{M}(z) \perp \vec{Q}$). The neutron-sample interactions can then be grouped into two different classes, the spin-flip processes (SF) corresponding to the $(\pm\mp)$ cross sections and the non-spin-flip processes (NSF) corresponding to $(\pm\pm)$. As can be shown from elementary quantum mechanics, the only structural features that can flip the neutron spin are components of the magnetization perpendicular to the quantization axis, so the $(\pm\mp)$ intensities depend only on $\vec{M}(z) \cdot \hat{e}_{SF}$, where $\hat{e}_{SF} \perp \vec{H} \perp \vec{Q}$. The NSF channel contains all of the nuclear scattering and the remaining magnetic intensity [$\vec{M}(z) \cdot \hat{e}_{NSF}$], with $\hat{e}_{NSF} \parallel \vec{H} \perp \vec{Q}$. Employing a modeling scheme similar to that used for unpolarized reflectivity [24], one can, by simultaneously fitting the intensity in the four cross sections, extract the nuclear and magnetic density profiles and the depth dependence of the magnetization orientation.

ANTIFERROMAGNETIC STRUCTURE

Antiferromagnetic (AF) structures possess characteristic signatures for both bulk magnetization and neutron diffraction. Fig. 2a shows a magneto-optic Kerr effect (MOKE) loop from a sample of nominal composition $[0.9 \text{ nm Cr}/5.5 \text{ nm Fe}]_5$, grown at 293 K. The absence of remanent magnetization reveals that the sample is essentially completely antiferromagnetic. By means of neutron reflectivity, one can determine the exact nature of this antiferromagnetic order. Before being mounted on the BT-7 reflectometer at NIST, the sample was placed in a 700 Oe field parallel to the eventual NSF axis. This treatment was designed to induce the antiferromagnetically coupled moments to be oriented in the spin-flop state, with the spins lying parallel to the SF axis after removal from the magnet. The sample was then placed on the reflectometer in a 14 Oe

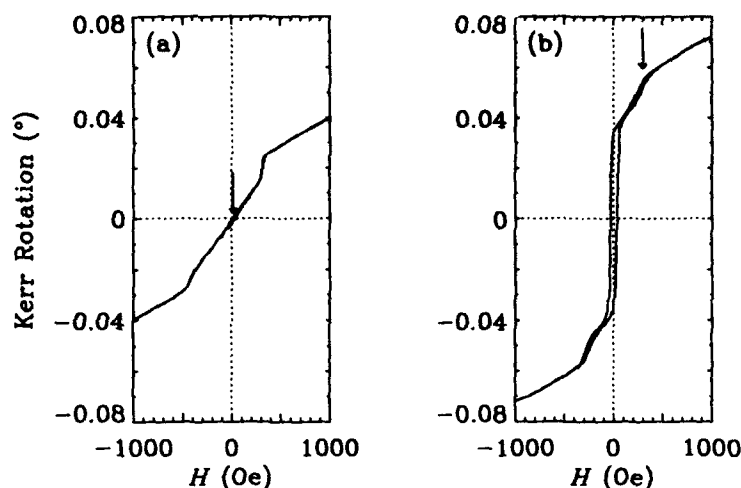


Figure 2: Magneto-optic Kerr effect measurements. (a) MOKE loop from sample of composition $[0.9 \text{ nm Cr}/5.5 \text{ nm Fe}]_s$ that exhibits the zero remanence characteristic of simple antiferromagnetic coupling. (b) MOKE loop from sample of composition $[1.2 \text{ nm Cr}/5.5 \text{ nm Fe}]_s$ showing more complex pattern attributed to biquadratic coupling. The arrows indicate the fields at which the data described below were taken.

quantizing field. Fig. 3 shows the reflectivity of the film in the four cross sections $[(+-)$ and $(-+)$ intensities are identical and have been added to improve counting statistics]. The bilayer spacing of the film should produce a structural superlattice peak at $Q \approx 2\pi/(6.4 \text{ nm}) \approx 1.0 \text{ nm}^{-1}$. Such a peak is visible in the NSF data. Now, adjacent iron layers with parallel moments exhibit the same periodicity as the structural modulation, but produce different intensities in the $(++)$ and $(--)$ cross sections. In addition, a net magnetization over the entire thickness of the film would cause the $(++)$ and $(--)$ cross sections to exhibit different critical wavevectors at $Q \approx 0.2 \text{ nm}^{-1}$. The absence of splitting in the NSF and the absence of intensity in the SF at $Q \approx 1.0 \text{ nm}^{-1}$ therefore imply that there is no significant ferromagnetic order in this sample at $H = 14 \text{ Oe}$. The large peak in the SF at $Q \approx 0.5 \text{ nm}^{-1}$ indicates the presence of antiferromagnetic structure: adjacent iron layers possess oppositely aligned moments, thereby doubling the unit cell size. A similar feature is visible in the NSF data. Preliminary analysis indicates that 85% of the sample resides in the spin-flop state, with the remainder of the intensity (15%) being caused by AF domains aligned parallel to \vec{A} .

NON-COLLINEAR STRUCTURE

Deviations from the pure antiferromagnetic structure discussed above produce clear features in both MOKE and neutron reflectivity. In Fig. 2b is shown the MOKE loop from a sample of composition $[1.2 \text{ nm Cr}/5.5 \text{ nm Fe}]_s$, grown at 523 K. The MOKE curve bears the characteristic signs of biquadratic coupling: remanent magnetization of about half the saturation value followed by a gradual saturation as the spins are pulled into alignment with the field. The coexistence

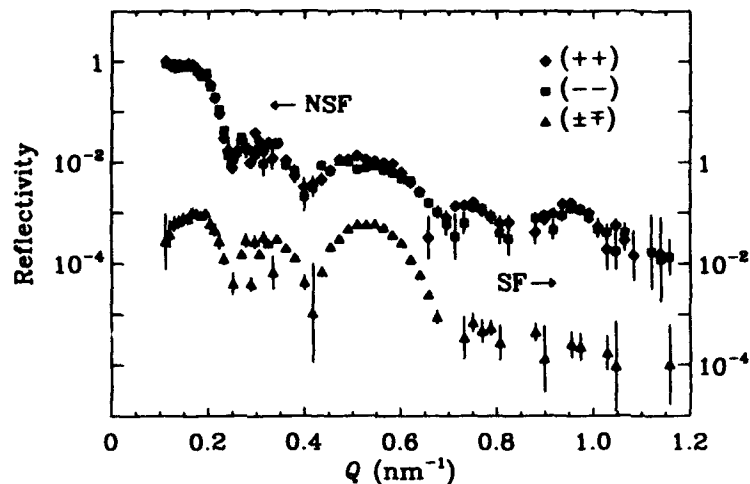


Figure 3: Neutron reflectivity from simple antiferromagnet (composition $[0.9 \text{ nm Cr}/5.5 \text{ nm Fe}]_5$) in 14 Oe applied field. The non-spin-flip (NSF) cross sections, $(++)$ and $(--)$, exhibit the same intensity at the chemical first-order superlattice peak $[Q = 2\pi/(6.4 \text{ nm}) \approx 1.0 \text{ nm}^{-1}]$ and at the total-reflection wavevector ($Q \approx 0.2 \text{ nm}^{-1}$) and therefore show no evidence of ferromagnetic order. The spin-flip (SF) cross sections (\pm) have a large peak at $Q \approx 0.5 \text{ nm}^{-1}$ corresponding to the doubled antiferromagnetic unit cell. The SF data has been offset by 10^{-2} and is plotted against the scale on the right axis.

of ferromagnetic and antiferromagnetic features characteristic of biquadratic coupling is clearly seen in the neutron reflectivity data (Fig. 4). The NSF cross sections show the pronounced splitting at both the total-reflection wavevector and first-order superlattice peak characteristic of ferromagnetic order, while the SF cross sections exhibit strong half-order intensity. This observation of ferromagnetic order parallel to \vec{H} (NSF) and antiferromagnetic order perpendicular to it (SF) qualitatively agrees with a 90° coupling angle. We have eliminated the possibility that the scattering is caused by a coexistence of ferromagnetic and antiferromagnetic domains by observing a qualitative rotational invariance of the reflectivities in a 14 Oe field (less than the 40 Oe coercive field). If ferromagnetic domains were present, upon rotation of the film about its normal (\hat{z}) we would have observed a peak in the SF intensity at $Q \approx 1.0 \text{ nm}^{-1}$. Our initial quantitative analysis of the film reproduces the features but not the intensities of the data. We believe this discrepancy to be related to the larger amount of disorder observed in the biquadratic relative to the bilinear film and are attempting to model this structure.

CONCLUSION

We have shown how the depth-averaged information available in a MOKE measurement can be resolved by the use of polarized neutron diffraction into microscopic structure and have identified characteristic features of such data. The neutron data can be analyzed quantitatively to yield the depth profile of the magnetization and the population of different domains (see [25] for an example). By making use of the sensitivity of polarized neutrons to the orientation and magnitude of in-plane magnetic moments, we have for the first time demonstrated the ability to observe

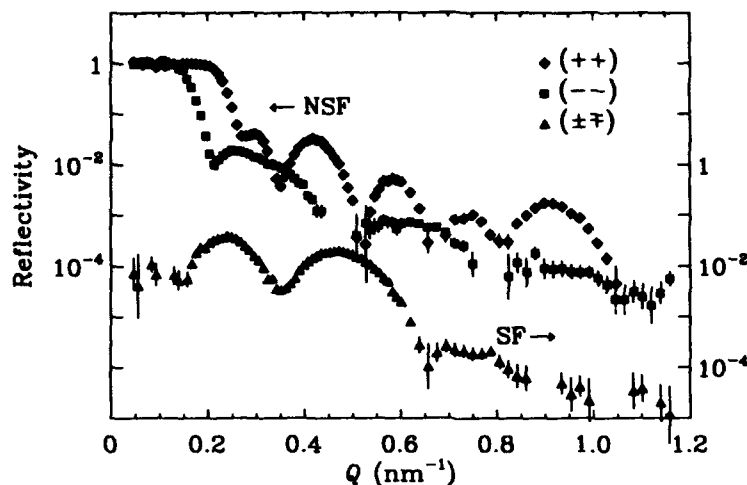


Figure 4: Neutron reflectivity from biquadratically coupled sample (composition [1.2 nm Cr/5.5 nm Fe]_s) in 300 Oe applied field. The non-spin-flip (NSF) cross sections, $(++)$ and $(--)$, 'early differ for all Q , indicating a net moment along the NSF axis. The spin-flip (SF) cross sections $(\pm\pm)$, retain the strong half-order peak at $Q \approx 0.5 \text{ nm}^{-1}$ corresponding to the doubled antiferromagnetic unit cell. The SF data has been offset by 10^{-2} and is plotted against the scale on the right axis.

non-collinear magnetization profiles. A combined neutron, x-ray, and MOKE study of the effect of the structural properties and growth temperature on the coupling behavior as a function of Cr thickness is underway.

ACKNOWLEDGMENTS

We would like to thank M. Schäfer for helpful discussions and R. Schreiber for technical help with the sample preparation. The work in Bochum was supported by the Deutsche Forschungsgemeinschaft through SFB 166 and the Bundesministerium für Forschung und Technologie through grant 03-ZA3BOC. Furthermore, we would like to acknowledge travel support from the North Atlantic Treaty Organization through grant CRG 901064.

REFERENCES

1. P. Grünberg, R. Schreiber, Y. Pang, M.B. Brodsky, and H. Sowers, Phys. Rev. Lett. **57**, 2442 (1986).
2. M.N. Baibich, J.M. Broto, A. Fert, F. Nguyen Van Dau, F. Petroff, P. Etienne, G. Creuzet, A. Friedrich, and J. Chazelas, Phys. Rev. Lett. **61**, 2472 (1988).
3. G. Binasch, P. Grünberg, F. Saurenbach, and W. Zinn, Phys. Rev. B **39**, 4828 (1989).
4. S.S.P. Parkin, N. More, and K.P. Roche, Phys. Rev. Lett. **64**, 2304 (1990).

5. P. Grünberg, S. Demokritov, A. Fuss, M. Vohl, and J.A. Wolf, *J. Appl. Phys.* **69**, 4789 (1991).
6. J. Unguris, R.J. Celotta, and D.T. Pierce, *Phys. Rev. Lett.* **67**, 140 (1991).
7. S.T. Purcell, W. Folkerts, M.T. Johnson, N.W.E. McGee, K. Jager, J. aan de Stegge, W.B. Zeper, W. Hoving, and P. Grünberg, *Phys. Rev. Lett.* **67**, 903 (1991).
8. S. Demokritov, J.A. Wolf, P. Grünberg, and W. Zinn, in *Magnetic Surfaces, Thin Films, and Multilayers*, edited by S.S.P. Parkin, H. Hopster, J.-P. Renard, T. Shinjo, W. Zinn, volume 231 of *Materials Research Society Symposium Proceedings*, page 133, Pittsburgh, 1992, Materials Research Society.
9. M. Rühlig, R. Schäfer, A. Hubert, R. Mosler, J.A. Wolf, S. Demokritov, and P. Grünberg, *Phys. Status Solidi A* **125**, 635 (1991).
10. A. Barthélémy, A. Fert, M.N. Baibich, S. Hadjoudj, F. Petroff, P. Etienne, R. Cabanel, S. Lequien, F. Nguyen Van Dau, and G. Creuzet, *J. Appl. Phys.* **67**, 5908 (1990).
11. N. Hosoi, S. Araki, K. Mibu, and T. Shinjo, *J. Phys. Soc. Jpn.* **59**, 1925 (1990).
12. S.S.P. Parkin, A. Mansour, and G.P. Felcher, *Appl. Phys. Lett.* **58**, 1473 (1991).
13. J.A.C. Bland, A.D. Johnson, H.J. Lauter, R.D. Bateson, S.J. Blundell, C. Shackleton, and J. Penfold, *J. Magn. Magn. Mater.* **93**, 513 (1991).
14. N. Hosoi, K. Mibu, S. Araki, T. Shinjo, S. Itoh, and Y. Endoh, *J. Phys. Soc. Jpn.* **61**, 300 (1992).
15. M. Löwenhaupt, W. Hahn, Y.Y. Huang, G.P. Felcher, and S.S.P. Parkin, to be published in *Int. J. Phys. B*.
16. S. Demokritov, J.A. Wolf, and P. Grünberg, *Europhys. Lett.* **15**, 881 (1991).
17. J.A. Wolf, Q. Leng, R. Schreiber, P. Grünberg, and W. Zinn, to be published in *J. Magn. Magn. Mater.*
18. Q. Leng, J.A. Wolf, P. Grünberg, and W. Zinn, to be published in *Int. J. Phys. B*.
19. P.J. Sivadere, *Acta Crystallogr. Sect. A* **31**, 340 (1975).
20. V.A. Belyakov and R.Ch. Bokun, *Fiz. Tverd. Tela (Leningrad)* **18**, 2399 (1976), [*Sov. Phys. Solid State* **18**, 1399 (1976)].
21. S.K. Mendiratta and M. Blume, *Phys. Rev. B* **14**, 144 (1976).
22. G.P. Felcher, R.O. Hilleke, R.K. Crawford, J. Haumann, R. Kleb, and G. Ostrowski, *Rev. Sci. Instrum.* **58**, 609 (1987).
23. C.F. Majkrzak, *Physica B* **173**, 75 (1991).
24. J.F. Ankner and C.F. Majkrzak, in *Neutron Optical Devices and Applications*, edited by C.F. Majkrzak and J.L. Wood, volume 1738 of *Proc. SPIE*, page 260, Bellingham, Wash. 1992, SPIE.
25. J.F. Ankner, A. Schreyer, C.F. Majkrzak, K. Bröhl, Th. Zeidler, P. Bödeker, and H. Zabel, in this volume.

NEUTRON SCATTERING STUDY OF ANTIFERROMAGNETIC AND FERROMAGNETIC COUPLING IN Ni/Ag MULTILAYERS

B. RODMACQ*, P. BURLET*, Ph. MANGIN** and M. HENNION***

*CEA/Département de Recherche Fondamentale sur la Matière Condensée,
BP 85X, 38041 Grenoble Cédex, France

**Laboratoire de Métallurgie Physique et de Sciences des Matériaux,
Université de Nancy, BP 239, 54506 Vandoeuvre Cédex, France

***CEA/Laboratoire Léon Brillouin, Centre d'Etudes de Saclay, 91191 Gif
sur Yvette Cédex, France.

ABSTRACT

Indirect magnetic coupling in sputtered Ni/Ag multilayers has been recently studied by magnetization and magnetoresistance techniques. These experiments indicate that coupling is antiferromagnetic through 11 and 30 Å of silver, and probably ferromagnetic through 20 Å. We present here direct evidence for such a magnetic coupling for all three thicknesses, as obtained from low angle neutron scattering experiments. Multilayers in which the Ag layer thickness is either 11 or 30 Å both exhibit a supplementary diffraction peak at a q value corresponding to twice the chemical period. Its evolution with both temperature and applied field confirms its purely magnetic origin. In order to study the coupling through 20 Å of silver, we prepared a multilayer in which the Ag layers are alternately 11 and 20 Å thick. In this case, we also observe a doubling of the chemical period. The coupling through 11 Å being antiferromagnetic, this unambiguously shows that the coupling through 20 Å is ferromagnetic.

INTRODUCTION

Antiferromagnetic coupling between ferromagnetic layers through non magnetic ones has first been observed in Fe/Cr multilayers by Grünberg et al. [1]. It was shown later that in fact such a coupling was an oscillatory function of the thickness of the non-magnetic layer [2], and this effect has been now evidenced in a large number of Fe-, Co- and Ni-based multilayers [2-4].

A lot of techniques can indirectly provide information on the magnetic structure of such systems but neutron scattering is the natural tool for the investigation of long range magnetic order in magnetic materials. Information on the magnetic structure in zero field as well as its field and temperature dependences can be easily obtained and in most cases this information can be interpreted quite directly. This technique has been used to detect antiferromagnetic coupling in different multilayered systems [5-10].

We present here neutron scattering results obtained on Ni/Ag multilayers with different thicknesses of the Ag layers. These results confirm our previous magnetization and magnetoresistance studies [4,11] concerning the oscillatory behaviour of the indirect coupling between Ni layers. The coupling through 11 and 30 Å of silver is found to be antiferromagnetic, whereas coupling through 20 Å of silver is found to be ferromagnetic, as deduced from the neutron results obtained on a sample made of silver layers alternately 11 and 20 Å thick.

EXPERIMENTAL SECTION

The samples were prepared by dc sputtering, depositing sequentially Ag and Ni layers onto glass substrates kept at a temperature of 100 K, up to a total thickness of 0.5 μm . The quality of the samples was checked by low angle X ray diffraction using Co wavelength. The neutron experiments were carried out both on G43 instrument at Laboratoire Léon Brillouin in Saclay and on DN3 instrument at Siloé in CEN Grenoble. The magnetization curves were measured using a SQUID magnetometer. In all these experiments the magnetic field was applied parallel to the plane of the layers.

ANTIFERROMAGNETIC COUPLING

Recent studies of Ag/Ni multilayers have shown the existence of antiferromagnetic (AF) coupling between the Ni layers through the Ag ones [4,10]. Related giant magnetoresistance (MR) effects have also been seen, the MR amplitude oscillating as a function of the Ag thickness with maxima in the regions of AF coupling [11].

A description of this system has been proposed from magnetization experiments and non polarized neutron scattering experiments. This system appears to behave as a classical antiferromagnet with small anisotropy. Under small applied field the magnetizations of adjacent nickel layers (ie of the two sublattices) are oriented antiparallel to each other and perpendicular to the field. When the magnetic field increases, the angle 2θ between the magnetizations decreases. The net magnetization is proportional to $\cos \theta$ and increases linearly with the applied field up to the saturation field H_s at which $\cos \theta = 1$. Above H_s the magnetization is nearly constant.

These results have been recently confirmed by polarized neutron scattering experiments [12]. The expected polarized neutron intensities defined with respect to the two polarization states (+ and -) before and after scattering at the sample (I^{++} and I^{--} at a scattering vector $q_1 = 2\pi/\Lambda$, where Λ is the period of the multilayer, and I^{+-} at a scattering vector $q_{1/2} = q_1/2$) have been found to vary with the applied field according to the above model above an anisotropy field of about 400 Oe. The value of the magnetic moment of the nickel atoms obtained from these experiments has been found to be equal to 0.48 μ_B at low temperature, in very good agreement with the value extracted from magnetization measurements on samples with similar Ni layer thicknesses [13].

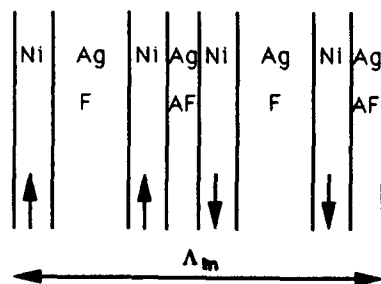


Figure 1: Magnetic structure in the case of alternating ferromagnetic and antiferromagnetic couplings. The magnetic periodicity Λ_m is twice the chemical one.

Non polarized neutron experiments were also performed on a sample with Ag layers 29 Å thick. Antiferromagnetic coupling was confirmed for such a thickness by the observation of a magnetic period twice the chemical one at low temperature. Accordingly, the intensity of the superstructure peak was found to decrease with increasing temperature, leading to a transition temperature slightly above room temperature.

FERROMAGNETIC COUPLING

In the Fe-, Co- or Ni-based multilayers mentioned above, the coupling varies in strength and sign with the thickness of the spacer layer, and thus becomes ferromagnetic for specific thicknesses. Ferromagnetic coupling between NiCo layers through Ru ones has been studied by Parkin and Mauri [14], using spin engineered structures where one of the NiCo layers is strongly antiferromagnetically coupled to a Co one. If the coupling between the NiCo layers is ferromagnetic, the magnetizations of these layers are thus both antiparallel to the field in small applied field, up to a critical field characteristic of the ferromagnetic coupling, at which the free NiCo layer rotates towards the direction of the field.

In neutron scattering, such a coupling is often difficult to evidence since it does not lead to any extra scattering peak because of the identical chemical and magnetic periodicities. It can be checked from the difference between I^{++} and I^{--} intensities but, since it is necessary to apply an external field to align the domains, the possibility of no coupling in zero field (or even weak antiferromagnetic coupling overcome by the field) cannot be eliminated. With the same restrictions, one can also measure the Q_+^* and Q_-^* critical scattering vectors of total reflection. Their relative positions are related to the difference between the average potentials experienced by the + and - neutrons [9]. Another possibility is, provided the magnetic ordering temperature is not too high, to deduce the ferromagnetic contribution from the difference in intensities of the chemical Bragg peak below and above T_c .

A more straightforward possibility is to prepare a sample in which, keeping the thickness of the magnetic layers constant, one alternates the thicknesses of the spacer layer, one leading to antiferromagnetic coupling and the other one to the supposed ferromagnetic coupling [15]. Thus, if the coupling is really ferromagnetic, one has in zero field the spin configuration depicted in Figure 1. As was the case for purely antiferromagnetic structures, the magnetic unit cell is again twice the chemical one and supplementary diffraction peaks will be observed.

Figure 2 presents the unpolarized neutron scattering curve measured at 50 K on a sample made of 100 repeat units of the form (11.4 Å Ag / 9 Å Ni / 22.8 Å Ag / 9 Å Ni). Peaks labelled 1 and 2 at scattering vectors of 0.12 and 0.24 Å⁻¹ correspond to the chemical periodicity of 52.2 Å, in agreement with X ray experiments performed on the same sample at room temperature. The two other diffraction peaks 1/2 and 3/2, which were absent in the X ray diagram, were also observed by neutron scattering at room temperature, but with a much smaller intensity. These extra peaks, of magnetic origin, correspond to a period twice the chemical one. This unambiguously shows that the coupling through 23 Å of silver is ferromagnetic, since antiferromagnetic coupling would lead to a magnetic period equal to the chemical one (with magnetic peaks at the same positions as the nuclear ones). The possibility of zero coupling can also be disregarded since in this case the absence of long range magnetic coherence would also lead to the absence of such extra peaks. Finally, the width of the magnetic peaks is comparable to the width of the nuclear ones, indicating comparable magnetic and structural coherence lengths.

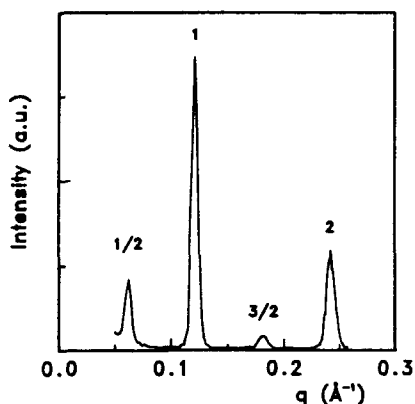


Figure 2: Neutron scattering pattern at 50 K of a (11.4 Å Ag / 9 Å Ni / 22.8 Å Ag / 9 Å Ni) multilayer. The peaks labelled 1 and 2 arise from the chemical periodicity.

Figure 3 gives the temperature variation of the integrated intensity of the first order magnetic peak. This intensity progressively decreases with increasing temperature, and falls to zero at about 320 K. Such a variation well agrees with the thermal evolution of the spontaneous magnetization. Figure 4 compares the field dependences at 100 K of both the intensity of the second magnetic peak and the magnetization. Since the magnetization is linked to the angle θ between magnetic moments and magnetic field through $M = M_s \cos \theta$ and since the intensity of the magnetic peak is related to this same angle through $I = I_0 \sin^2 \theta$, both quantities M/M_s and $(1 - I/I_0)^{1/2}$ must lead to identical field dependences. The results presented in Fig. 4 agree with such a picture. The saturation field is about 800 Oe, that is smaller by a factor of about 2 than the one measured in purely antiferromagnetic samples [4]. This is easily explained by the fact that the two ferromagnetically coupled layers behave as just one layer under field. For a given value of the antiferromagnetic coupling constant, the saturation field will thus be twice as small than in the case of a purely antiferromagnetic system since the equivalent thickness of the magnetic layer is twice as large.

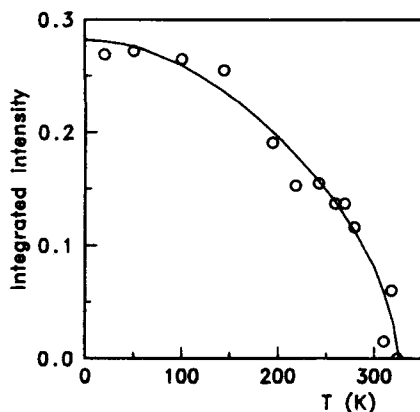


Figure 3: Temperature dependence of the integrated intensity of the first magnetic diffraction peak (normalized to that of the first nuclear peak). The line is a guide to the eye.

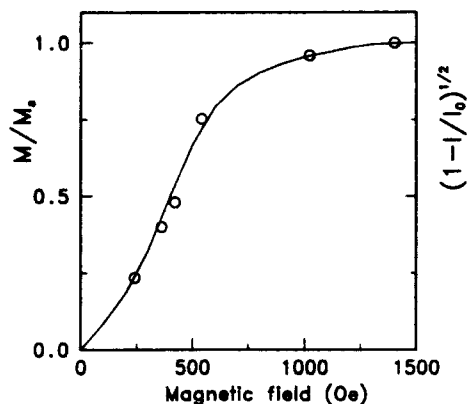


Figure 4: Compared variations at 100 K of M/M_s (full line) and $(1-I/I_0)^{1/2}$ (open circles) with magnetic field. I is the intensity of the second magnetic diffraction peak.

CONCLUSION

We have presented in this paper neutron results on magnetically coupled Ni/Ag multilayers. Antiferromagnetic coupling through 11 and 30 Å of silver manifests itself by the appearance of extra diffraction peaks which indicate that the magnetic period is twice the chemical one, as expected for antiferromagnetic coupling. The coupling through 20 Å of silver is characterized in samples with alternating 11 and 20 Å thick Ag layers. In this case superstructure neutron magnetic peaks are also observed. This unambiguously shows that the coupling through 20 Å of silver is ferromagnetic.

REFERENCES

1. P. Grünberg, R. Schreiber, Y. Pang, M.B. Brodsky and H. Sowers, Phys. Rev. Lett. **57**, 2442 (1986)
2. S.S.P. Parkin, N. More and K.P. Roche, Phys. Rev. Lett. **64**, 2304 (1990)
3. D.H. Mosca, F. Petroff, A. Fert, P.A. Schroeder, W.P. Pratt and R. Loloee, J. Magn. Magn. Mater. **94**, L1 (1991); S.S.P. Parkin, Z.G. Li and D.J. Smith, Appl. Phys. Lett. **58**, 2710 (1991)
4. C.A. dos Santos, B. Rodmacq, M. Vaezzadeh and B. George, Appl. Phys. Lett. **59**, 126 (1991)
5. A. Cebollada, J.L. Martinez, J.M. Gallego, J.J. de Miguel, R. Miranda, S. Ferrer, F. Batallan, G. Fillion and J.P. Rebouillat, Phys. Rev. B **39**, 9726 (1989)
6. A. Bartelemy, A. Fert, M. N. Baibich, S. Hadjoudj, F. Petroff, P. Etienne, R. Cabanel, R. Lequien, F. Nguyen van Dau and G. Creuzet, J. Appl. Phys. **67**, 5908 (1990)

7. S.S.P. Parkin, A. Mansour and G.P. Felcher, Appl. Phys. Lett. **58**, 1473 (1991)
8. N. Hosoi, K. Mibu, S. Araki, T. Shinjo, S. Itoh and Y. Endoh, J. Phys. Soc. Jap. **61**, 300 (1992)
9. Y.Y. Huang, G.P. Felcher and S.S.P. Parkin, J. Magn. Magn. Mater. **99**, L31 (1991)
10. B. Rodmacq, P. Mangin and C. Vettier, Europhys. Lett. **15**, 503 (1991)
11. B. Rodmacq, B. George, M. Vaezzadeh and Ph. Mangin, Phys. Rev. B **46**, 1206 (1992)
12. B. Rodmacq, K. Dumesnil, M. Vergnat, Ph. Mangin and M. Hennin, to be published
13. B. Rodmacq, C.A. Dos Santos, J. Magn. Magn. Mater. **109**, 298 (1992)
14. S.S.P. Parkin and D. Mauri, Phys. Rev. B **44**, 7131 (1991)
15. C.F. Majkrzak, J. Kwo, M. Hong, Y. Yafet, D. Gibbs, C.L. Chien and J. Bohr, Advances in Physics **40**, 99 (1991)

A COMPARATIVE STUDY OF STRUCTURAL, MAGNETIC, AND TRANSPORT PROPERTIES OF Co-Re SUPERLATTICES SPUTTERED ON GLASS AND Si SUBSTRATES

J.L.Leal¹, N.P.Barradas¹, J.C.Souares¹, M.F.da Silva², M.Rots³, and P.P.Freitas^{4,5}

1-CFNUL, Av. Prof. Gama Pinto 2, 1699 Lisbon, Portugal

2-LNETI, EN 10, 2685 Sacavem, Portugal

3-IKS-KUL, Celestijnenlaan 200 D, 3001 Leuven, Belgium

4-INESC, R.Alves Redol 9-3, 1000 Lisbon, Portugal

5-IST, R.Rovisco Pais 1000, Lisbon, Portugal

ABSTRACT

Antiferromagnetically coupled $(\text{Co}_{17.4}\text{Re}_{5.4})_{\times 15}$ superlattices were deposited simultaneously onto glass and Si substrates, with an intervening Re buffer layer. Samples grown on glass show sharper interfaces than those grown on Si. This effect reflects on magnetoresistance, magnetization, Rutherford backscattering, and hyperfine field results. The influence of the Re buffer layer thickness and annealing temperature on these properties is discussed.

1-Introduction

Oscillatory coupling and enhanced magnetoresistance associated with antiferromagnetically coupled Co-Re superlattices have been previously described[1]. In this paper we discuss in detail the effect of substrate preparation, Re buffer thickness, and annealing, on the magnetic, transport, and structural properties of these antiferromagnetically coupled films. The superlattices were prepared in a high-vacuum sputtering system with a base pressure of 5×10^{-8} Torr. Co was deposited by RF magnetron sputtering at 5 mTorr, and a rate of 1.2 Å/s. Re was deposited by DC magnetron sputtering at a rate of 0.8 Å/s and a pressure of 2.5 mTorr. Film thickness was monitored in situ by quartz crystals and absolute calibrations were made by profilometer and Rutherford backscattering analysis. X-ray analysis of our first superlattices revealed an highly textured growth with the c-axis perpendicular to the plane of the film and a superlattice periodicity inferred from satellite positioning within 5% of that expected from nominal thicknesses[2]. The superlattice structure was then directly probed by transmission electron microscopy (TEM) analysis. For Co thicknesses less than 20 Å both X-Ray and TEM indicate a smaller grain size, when compared with structures with thicker Co layers. The layers remain however remarkably continuous over distances of thousands of Angstroms. The value of the Co layer moment, measured with a vibrating sample magnetometer(VSM), and assuming sharp interfaces does not deviate by more than 6% from the bulk hcp Co moment. We used Corning glass 7059 or Si[111] substrates. The bare Si wafers were taken straight from the box with only dry nitrogen blowing to remove particles, or were first oxidized, and then chemically etched with the following process: $\text{H}_2\text{SO}_4/\text{H}_2\text{O}_2 + \text{HF}/\text{H}_2\text{O}$ /drying.

2-Experimental method

Sample preparation was described in the previous chapter. Magnetic characterization was done using a VSM with a resolution of 5×10^{-6} emu. The substrate and sample holder contributions were removed. Transport characterization was done by a DC four-probe technique. Rutherford backscattering analysis (RBS) was done using an incident grazing angle geometry, with a 1.6 MeV He^+ beam. The hyperfine field at implanted $^{111}\text{In}/^{111}\text{Cd}$ probes(80 KeV) were measured by the Perturbed Angular Cor-

relation technique[3](PAC). A conventional four BaF_2 detectors slow-fast set-up with 0.7 ns time resolution was used. Some samples were annealed for 60 min periods under a 5×10^{-6} Torr vacuum at several temperatures.

3-Magnetization measurements

Magnetization data were taken on $(\text{Re}_{54}\text{Co}_{174})_{15}/\text{Re}$ buffer/substrate antiferromagnetically coupled structures with variable Re buffer thicknesses, and on various substrate types (Figs.1a and 1b). Fig.1c shows the remanence dependence on Re buffer thickness. For the M_r/M_s data shown in Figs.1c and 1.d we used the real saturation magnetization obtained in measurements up to 10kOe. First, notice that the absence of buffer leads to non-zero remanence due to the existence of contacts between the Co layers, for all types of substrates. As the Re buffer layer thickness increases,

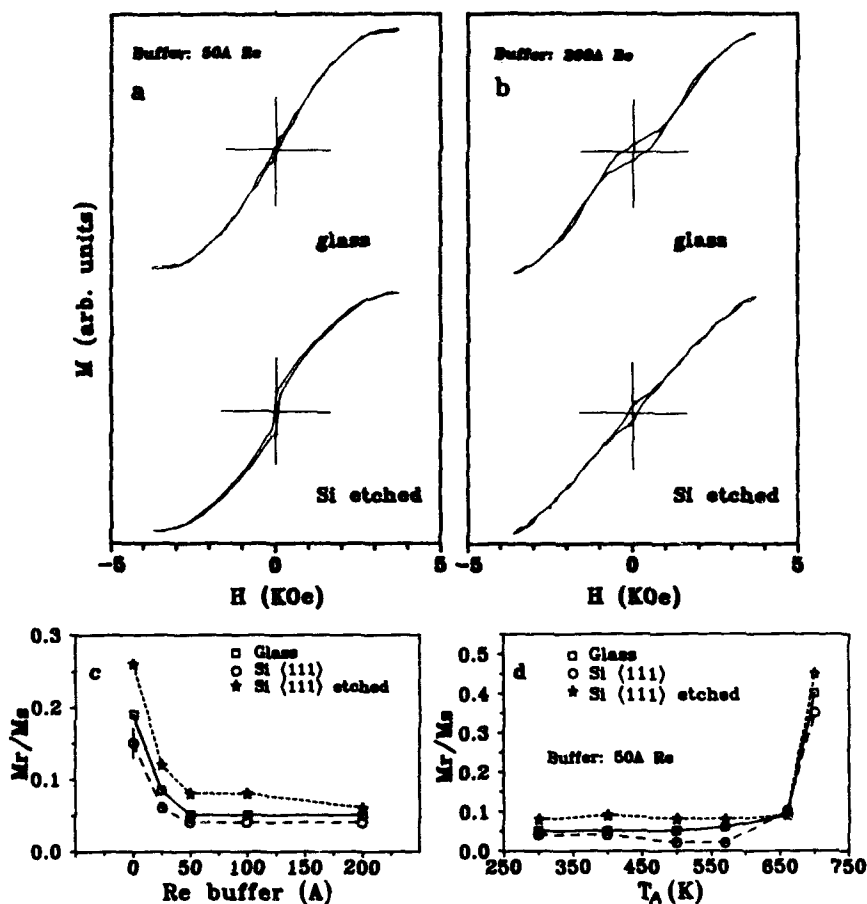


Fig.1-Magnetization hysteresis cycles for $(\text{Re}_{54}\text{Co}_{174})_{15}/\text{Re}$ buffer/substrate antiferromagnetically coupled structures with a Re buffer thickness of 50Å (Fig.1a), and of 200Å (Fig.1b). Fig.1c summarizes the remanence data versus Re buffer thickness for all substrates. Fig.1d shows remanence data versus annealing temperature.

the topography of the buffer surface is smoothed out. A 50 Å Re buffer is sufficient to enable the 5 Å Re intermediate layer to be continuous and effectively separate the two Co layers for a sample on glass. A perfect antiferromagnetic hysteresis cycle results, with very small remanence and a linear field dependence near the origin (see hysteresis cycle for the sample deposited on glass, Fig. 1a). The substrate effect is seen in more detail in Fig. 1a and Fig. 1b where we show results for superlattices deposited on a 50 Å or 200 Å Re buffers respectively. Samples deposited on Si etched in our lab show higher remanence and a broken hysteresis cycle, when compared with those deposited on glass. This can be caused by relevant surface topography (steps with heights comparable with the Re layer thickness) such that the 5 Å Re layer cannot effectively cover the steps without breaking continuity. Contact between Co layers then occurs leading to ferromagnetic coupling regions and increase in remanence. For 200 Å thick buffers (Fig. 1b), the film deposited on etched Si has a hysteresis cycle similar to that deposited on glass with a 50 Å buffer layer. This means that substrate surface corrugation has been planarized with the thick buffer layer. If we start with the flatter glass substrate an interesting development occurs. The observed type of hysteresis cycle can be simulated either with introduction of in-plane anisotropy or biquadratic exchange. VSM measurements rule out in-plane anisotropy but domain observation is needed before biquadratic exchange can be proved. Notice however that biquadratic coupling increases with terrace size, that should be larger in this sample than on the sample deposited on the thinner Re buffer. We also found that we need a top Re cap layer to avoid oxidation of the last Co layer. When the Re cap is absent, non-zero remanence reappears. A CoO layer is formed at the surface which is antiferromagnetic with a Neel temperature close to room temperature. Short-range exchange coupling could then be responsible for the non-zero remanence. An annealing study done on all these samples shows a strong increase in remanence for annealing temperatures

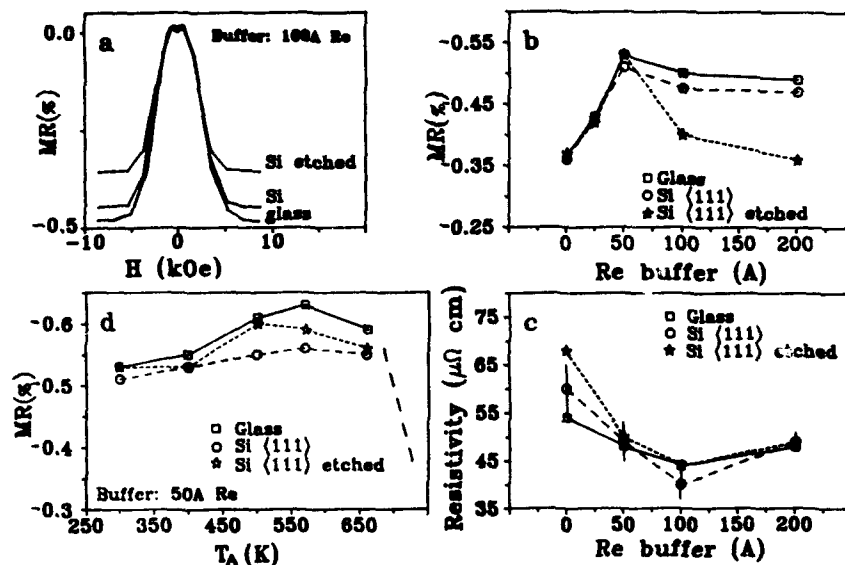


Fig. 2-Magnetoconductance and resistivity data for $(\text{Re}_{0.44}\text{Co}_{0.56})_{15}/\text{Re buffer/substrate}$ antiferromagnetically coupled structures. Fig. 2d shows the effect of 1 hour annealings under vacuum at different temperatures.

above 650K. These data are essentially independent of the type of substrate. This is associated with the start of chemical diffusion which to first order is independent on surface topography.

4-Magnetoresistance measurements

Figs.2a-c show magnetoresistance ($\Delta\rho/\rho$) and resistivity (ρ) data for ($\text{Re}_{5\text{\AA}}\text{Co}_{17\text{\AA}}$)_{x15}/Re buffer/substrate structures. For these samples the anisotropic contribution to the magnetoresistance is an order of magnitude smaller than the spin-valve effect. For relatively thick buffers, the MR is 50-60% higher on samples deposited on glass than on etched Si. Since for thick buffers the resistivities of these samples are independent of substrate type, this means that $\Delta\rho$ itself is dependent on substrate nature. Comparison with magnetization data shows that samples with lower remanence show higher MR, and this is correlated with flatter interfaces (see Fig.3). For buffer thicknesses less than 50Å both the resistivity and $\Delta\rho$ are substrate dependent. The MR is found to increase by 60% when the buffer thickness increases up to 50Å. This corresponds to a decrease in the total film resistivity, and an increase of $\Delta\rho$. The $\Delta\rho$ increase arises due to improved continuity of the 5Å Re spacer, as evidenced by the observed decrease in remanence value. Fig.2d shows the effect of annealing at different temperatures. Two regimes are observed. A slight improvement in the MR value is observed for annealing temperatures between 350K and 550K, while a decrease in MR is observed for higher annealing temperatures. The latter is caused by strong chemical interdiffusion as was already observed for the magnetization data. The former comes from resistivity decrease upon annealing since $\Delta\rho$ and remanence are essentially constant for this range of annealing temperatures. The MR value is found to vary linearly with the remanence. This is evidenced in Fig.3 where we plotted MR versus remanence for all samples used in this study with all substrate types and annealing treatments up to 575K. The arrows indicate annealing steps. For buffers thinner than 50Å the annealing affects both remanence and MR values (oblique arrows). For thick buffers, the remanence remains essentially the same while the MR increases (vertical arrows).

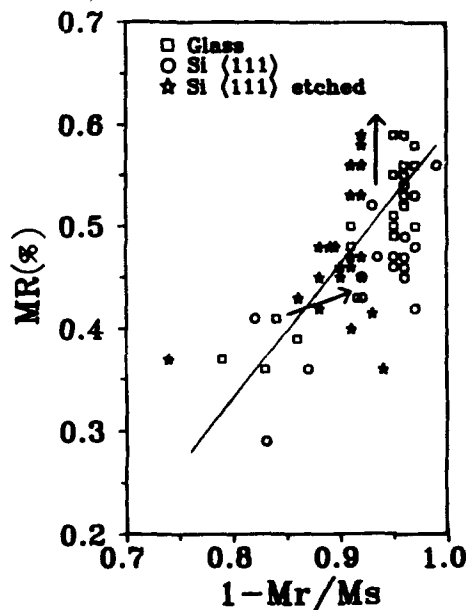


Fig.3- Plot of MR versus remanence for all samples measured, including annealed samples (arrows). The general trend is the increase of MR value with decreasing remanence.

5. Rutherford backscattering results

Since our previous results have shown a strong dependence of the magnetic and transport properties on buffer thickness and type of substrate we decided to study the substrate/Re and Re/Co interfaces by Rutherford backscattering at a 8° grazing angle geometry. Fig. 4a shows RBS data and Fig. 4b the deduced profile for $\text{Co}_{22\text{\AA}}\text{Re}_{37\text{\AA}}$ substrate structures on glass and etched Si substrates. From the theoretical simulations [3] one concludes that the glass/Re interface is chemically sharp (less than 5 Å thick) while a 10-15 Å thick interdiffusion layer is found at the Si/Re interface. For the film deposited on Si, the simulation indicates a Re/Co interface 8-12 Å thick, while for the film deposited on glass, mixing seems to occur at 1-2 monolayer level. However, RBS is not sensitive to the difference between a surface topography constituted of steps with an average height of 10.4 (about 4 monolayers) or to chemical diffusion over this range. Our absolute magnetization data, on the other hand, clearly indicates

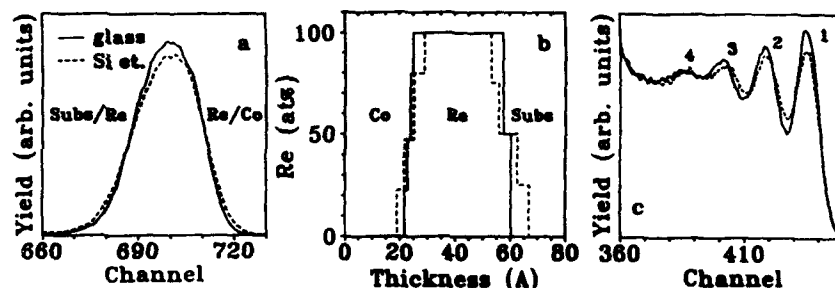


Fig. 4- RBS data (a) and deduced profiles (b) for two $\text{Co}_{22\text{\AA}}\text{Re}_{37\text{\AA}}$ substrate structures on glass and Si. Notice the sharper substrate/Re and Re/Co interfaces for structures deposited on glass when compared with those deposited on Si. Fig. 4c shows RBS data for a $(\text{Re}_{5\text{\AA}}\text{Co}_{17\text{\AA}})_{15}$ /Re buffer/substrate structure on glass and Si substrates.

that such an amount of chemical diffusion is not present. The conclusion is that surface topography exists and is more relevant than eventual chemical diffusion. Fig. 4c shows RBS data for $(\text{Re}_{5\text{\AA}}\text{Co}_{17\text{\AA}})_{15}$ /Re buffer/substrate structures. The grazing angle geometry has enough resolution to see the first 4 Re layers. We observe that the superlattice modulation is better observed in the film deposited on glass than that deposited on Si. From the theoretical simulations one obtains a Re/Co interface 7-12 Å thick for the film deposited on Si, and a sharp interface for that deposited on glass (less than 2 ML).

6. Perturbed angular correlation measurements

The perturbed angular correlation technique was used to measure the local hyperfine fields at the Co layers. Fig. 5a compares the Fourier transform of PAC data for two $\text{Co}_{300\text{\AA}}\text{Re}_{300\text{\AA}}$ substrate structures on glass and Si. The main difference in the results is the stacking fault content, which is two times higher in the film deposited on Si than that deposited on glass. Fig. 5b compares the measured hyperfine fields in a thick hcp Co film (1), a $(\text{Co}_{50\text{\AA}}\text{Re}_{50\text{\AA}})_6$ /Re/glass superlattice (2), and a $(\text{Co}_{17\text{\AA}}\text{Re}_{5\text{\AA}})_{15}$ /Re/glass structure (3). While the first two films have quite well defined hyperfine fields corresponding to the expected values for hcp Co, the 17 Å thick Co layers in our Co-Re superlattices show a rather broad field distribution centered at the expected hcp Co value for such a thin film. This broad distribution reflects that a large percentage of

the In probe atoms do not feel the hcp Co environment, but rather defect and interface contributions. This same distribution also occurs for films deposited on Si, but now centered at a lower field value (see inset, Fig. 5b). The hyperfine fields obtained in these superlattices were then compared to those measured in thin Co films [3] (inset, Fig. 5b).

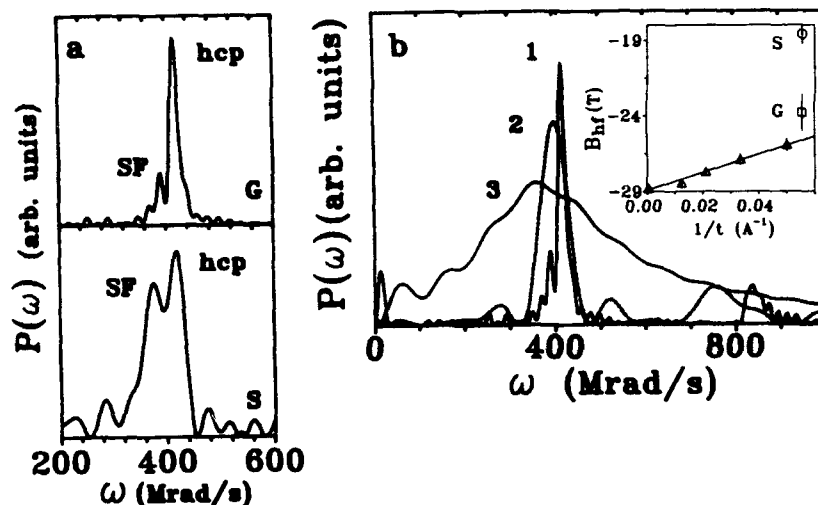


Fig. 5a-PAC results for two $\text{Co}_{300\text{\AA}}\text{Re}_{300\text{\AA}}$ structures on glass (G) and Si (S) substrates-SF denotes stacking fault fraction. In Fig. 5b we compare hyperfine fields for a thick Co film (1), and two Co-Re superlattices with Co layers 50 Å (2) and 17 Å (3) thick, respectively. In the inset we compare the hyperfine fields for the superlattices with 17 Å thick Co layers deposited on Si and glass substrates (S and G), with data for Co films with variable thickness deposited on Si (open triangles).

7-Discussion and conclusions

We correlated magnetic, transport, and structural properties of Co-Re superlattices deposited on glass and Si substrates. It is found that the interface topography rather than chemical interdiffusion is responsible for the observed changes in magnetization and magnetoresistance values. Larger MR values and lower remanences are observed for samples deposited on glass that evidence flatter interfaces.

We thank S. Molina and R. Garcia for preliminary TEM work. J.L.L. and N.P.B. acknowledge JNICT grants under Programa Ciencia. P.P.F. acknowledges JNICT support under grant 514/MPF/90.

8-References

- 1-P.P.Freitas, L.V.Melo, I.G.Trindade, M.From, J.Ferreira, and P.Monteiro, *Phys.Rev.B* 45, 2495(1992)
- 2-L.V.Melo, I.G.Trindade, M.From, P.P.Freitas, N.Teixeira, M.F.da Silva, and J.C.Souares, *J.Appl.Phys.* 70, 7370(1991)
- 3-N.Barradas, J.Leal, H.Wolters, M.F.da Silva, A.A.Melo, J.C.Souares, L.V.Melo, P.P.Freitas, B.Swinnen, and M.Rots, *J.Magn.Magn.Mater.* 121, 80(1993)

INTERFACIAL EXCHANGE COUPLING AND THE MAGNETIZATION OF IRON OXIDE/NICKEL OXIDE SUPERLATTICES

S. D. BERRY*, D. M. LIND*, E. LOCHNER*, K. A. SHAW*, D. HILTON*, R. W. ERWIN**, and J. A. BORCHERS**

*Department of Physics and Center for Materials Research and Technology (MARTECH), Florida State University, Tallahassee, FL 32306

**NIST, Gaithersburg, MD 20899

ABSTRACT

The role of interfacial exchange coupling in the magnetic behavior of metal oxide materials has been investigated through the study of $\text{Fe}_3\text{O}_4/\text{NiO}$ superlattices. We report results on a series of superlattices grown where one bilayer constituent was held to a fixed thickness while varying the other from single unit cell dimensions upward. High crystalline quality was confirmed by XRD, RHEED and neutron diffraction. Magnetization profiles show substantial deviations from bulk-like iron oxide results, with an increase in domain rotation energies observed in the superlattices over that of bulk iron oxide (increasing with NiO layer thickness) indicating the strong nature of $\text{Fe}_3\text{O}_4/\text{NiO}$ interfacial linkage. Neutron scattering at elevated temperatures shows that the NiO remains ordered above the 523 K bulk Néel temperature. This suggests that at least a portion of the NiO within a layer remains ordered well above the Néel temperature, with an increase in effective Néel transition temperature that approaches the Fe_3O_4 Curie temperature in the limit of very thin NiO layers. Although the exchange coupling dominates these effects, strain also plays an important role.

INTRODUCTION

Following the pioneering work of Y. Bando and coworkers[1], there has been recent significant progress in applying advanced crystal growth techniques, such as reactive sputtering and MBE to the growth of thin films and superlattices of metal oxide materials[2][3]. These researchers all report, for various combinations of the oxides Fe_3O_4 , NiO, and CoO in superlattice form, novel magnetic effects which are indicative of the strong interfacial exchange coupling that is expected for these strongly ordered local moment systems.

We report here progress in the investigation of the $\text{Fe}_3\text{O}_4/\text{NiO}$ superlattice system, which has previously shown novel linear magnetization in short period superlattices[4], enhanced NiO high temperature ordering [5], and highly anisotropic electron transport[6]. By combining results from XRD, SQUID magnetometry, and neutron scattering, we can begin to link the magnetic behavior in this system to the particular structural ordering present.

GROWTH AND STRUCTURAL CHARACTERIZATION

All of the superlattices discussed here were grown in an oxygen plasma-assisted molecular beam epitaxy facility at Florida State University. Significant details of our growth procedures have been published elsewhere [3][7], so here we will only briefly review our techniques. The superlattice constituents are both cubic, with the NiO sharing the rocksalt structure of the substrate MgO, with a slightly smaller unit cell (4.177 Å versus 4.212 Å, or a 0.8% lattice mismatch). Fe_3O_4 exists in the spinel structure (unit cell 8.394 Å) with an oxygen sublattice which is about midway between that of NiO and MgO. (Therefore each film constituent must stretch in-plane to match the MgO substrate lattice). The closeness of the lattice parameters allows us to grow single crystal superlattices with each layer maintaining its fundamental structure, except for a tetragonal distortion due to each layer's mismatch with the underlying lattice.

Atomic metal fluxes were evaporated from high purity iron and nickel in e^- -gun sources (alternately shuttered) and combined with oxygen at the sample surface emitted from an electron cyclotron resonance plasma source (which provided a mixture of O and O^+ favoring the latter). Background pressures in the vacuum system were typically $\sim 10^{-8}$ Torr, and during growth oxygen pressure was held to $\sim 6 \times 10^{-5}$ Torr. Substrates of high quality polished MgO(001) were held at a temperature ~ 520 K, and the subsequently grown films ranged in thickness from 1000 Å to 4 microns, with 1 micron typical. The substrates were approximately 0.2-0.3 mm thick to minimize the diamagnetic signal from the substrate. During sample growth the surface of the films were monitored by *in-situ* RHEED, and we observed the expected alternation in lattice rods as the layers changed due to the doubled periodicity of the Fe_3O_4 unit cell.

After growth, we performed characterization of all of our samples by both low and mid angle XRD. A representative series of low angle scans is presented in Figure 1, for a series of films where the iron oxide thickness was held constant at a nominal 68 Å. The very high quality of the films is evidenced by the large number of diffraction peaks present for each film. In addition, the widths of the lines of higher order tend to increase, which is often an indication of step disorder caused by the incomplete termination of an individual layer [8].

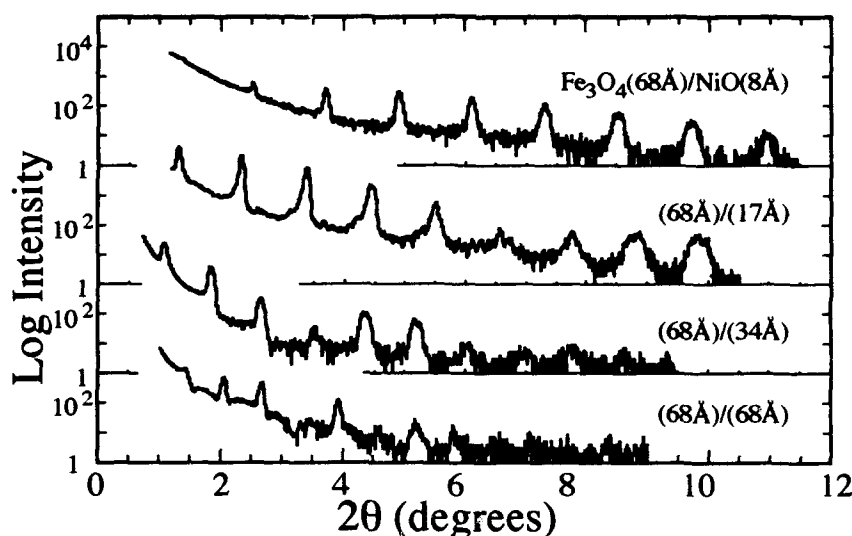


Figure 1: Low angle XRD results for a selection of superlattices with the iron oxide thickness held to a nominal 68 Å, and various nickel oxide thicknesses within a single bilayer.

Measured lattice parameters in the growth (001) direction show a contraction from the bulk values, which is expected from the epitaxial stretching of the film atoms to align with the previous layer. This change, typically 0.5 %, is largest for those superlattices with small bilayer thicknesses, where it can approach 1 %. For a few of our samples, we have directly verified that the iron oxide layers align epitaxially in plane with the substrates by making XRD measurements in a direction different from the growth direction (i.e. typically using the [026] and [066] reflections) [9].

For some of our films, in particular those with short bilayer thicknesses (less than 80 Å), we have often seen cracks appearing in the film in (100) directions only, breaking the film into large ($\sim 100 \mu$) rectangular regions. These cracks are more dense near the film/substrate interface, and the regions between the cracks have no visible structure using SEM characterization at a resolution to 40 Å. We believe that this is a mechanism by which the films relieve strain, and provides extra evidence of the single crystal nature of our films, as well as the high degree of crystalline strain

present due to the tetragonal distortion present with nonmatched epitaxial growth. This is in accord with the general observation that larger strain accompanies shorter bilayer thicknesses.

MAGNETIZATION PROFILE MEASUREMENTS

Previously we have reported on the magnetization of a series of films grown with equal constituent thicknesses within each bilayer, and total bilayer thicknesses ranging from $\sim 17 \text{ \AA}$ to $\sim 250 \text{ \AA}$ [4], and a few superlattices with iron oxide thicknesses held at a nominal 68 \AA [5]. For large bilayer thicknesses, the superlattices show magnetization profiles which do not reach saturation, even at an applied field of 5.5 Tesla, and which show a decreased magnetization value as the bilayer thickness is decreased. If the bilayer thickness is less than $\sim 80 \text{ \AA}$, we find a linear or nearly linear behavior with little or no hysteresis. We also observe little difference in hysteresis profiles as a function of sample orientation, which is primarily due to shape anisotropy effects from our planar samples.

We have argued that this behavior is directly linked to very strong coupling across the $\text{Fe}_3\text{O}_4/\text{NiO}$ interfaces, as well as to the large tetragonal strain present within the films [4]. We know the individual iron oxide and nickel oxide layers remain ferrimagnetically and antiferromagnetically ordered, as is expected in local moment systems, with the cross-boundary coupling in a direction which more closely aligns with the nickel oxide spin axis, due to its much larger bulk anisotropy value ($\sim 7.0 \times 10^{-6} \text{ ergs/cm}^3$ for NiO, and $\sim 2.0 \times 10^{-5} \text{ ergs/cm}^3$ for Fe_3O_4).

Here we extend our results, to briefly report ongoing measurements [10] which investigate the magnetic behavior of the films when one constituent thickness is held fixed and the other allowed to vary. Magnetization measurements of our films were performed using a Quantum Design MPMS SQUID magnetometer. Measured moment and applied external magnetic field were along a (100) direction in the plane of the film. To make an accurate background subtraction the magnetic moment of the substrates were measured in field at multiple temperatures prior to film growth. Magnetization results are normalized to the total iron oxide volumes within our films, as NiO remains locally ordered as an antiferromagnet.

A selection of room temperature results is shown in Figure 2. The films with iron oxide thicknesses exceeding 60 \AA per layer all show the sigmoidal shape that is found for Fe_3O_4 films, with a substantially decreased saturation at the highest applied magnetic fields, as well as decreased remanence. For the thinnest nickel oxide layer thicknesses (at this iron oxide thickness), we observe a substantial change from the iron oxide film profile indicative of an increase in domain rotation anisotropy energy from that of iron oxide to that approaching nickel oxide. With an increase in the nickel oxide thickness, the iron oxide magnetization is further suppressed until the nickel oxide thickness reaches a value of about 50 \AA , after which little variation in the overall hysteresis profile is seen. For iron oxide thicknesses of about 34 \AA (about 4 spinel unit cells thick), we observe either a linear magnetization behavior (nickel oxide thicknesses up to 34 \AA), or a combination of sigmoidal and linear behavior (nickel oxide thickness $\sim 68 \text{ \AA}$).

In all cases where the iron oxide thickness is less than 4 spinel unit cells thick, we observe linear or nearly linear magnetic behavior. For these samples, we find only slight variation in the slope of the magnetization versus field profiles even when the iron oxide layer thickness is $\sim 8 \text{ \AA}$, and the NiO thickness is $\sim 70 \text{ \AA}$. As an example, the measured value for the highest field (55 kOe) for both $\text{Fe}_3\text{O}_4(8.5 \text{ \AA})/\text{NiO}(8.5 \text{ \AA})$ [11] and $\text{Fe}_3\text{O}_4(10 \text{ \AA})/\text{NiO}(70 \text{ \AA})$ superlattices is about 125 Gauss, even though there are drastically differing NiO thicknesses in each bilayer. We believe this profile universality indicates complete pinning of iron oxide moments to the NiO spin directions, throughout the entire iron oxide volumes in these films, with the small variation in slope due to the differing amount of strain present in the individual superlattices. Comparable low temperature measurements have also been taken (typically at $\sim 30 \text{ K}$), which show a somewhat larger hysteresis, and an increased magnetization at highest applied field, consistent with the variation in bulk-like Fe_3O_4 magnetization with temperature.

The near universality of magnetization profiles for Fe_3O_4 thicknesses less than $\sim 34 \text{ \AA}$ suggests that there is a limiting thickness ($\sim 15 \text{ \AA}$) below which the iron oxide magnetic moment directions

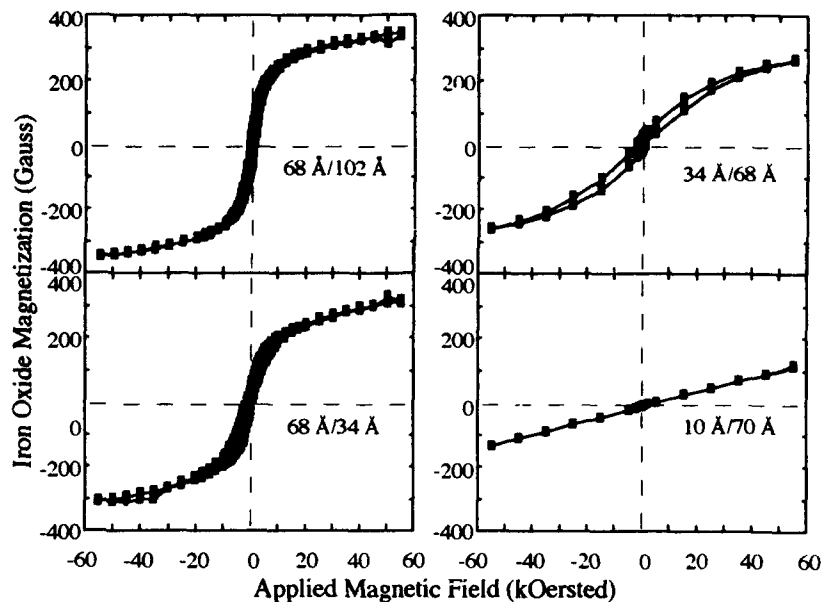


Figure 2: Room temperature SQUID magnetization profiles for selected superlattices. An iron oxide film would reach saturation of 500 Gauss before an applied field of ~ 10 kOe, but clearly there is no saturation evident here. All of the superlattices we have grown with bilayer thicknesses less than ~ 80 Å have shown similar linear magnetization behavior as the $\text{Fe}_3\text{O}_4(10 \text{ Å})/\text{NiO}(70 \text{ Å})$ superlattice shown in the lower right.

are completely determined at the boundaries with the NiO layers. When the iron oxide is thicker than 34 Å, the central region of the iron oxide layer can behave more like bulk Fe_3O_4 , while the outer portions of the layer are still highly constrained by the adjacent NiO layers.

NEUTRON DIFFRACTION MEASUREMENTS

To further confirm our magnetization profile measurements, we have performed neutron diffraction measurements, at zero external applied field, on a selection of constituent layer thicknesses as well as on a Fe_3O_4 film. Through a combination of reflection directions, which represent various combinations of signals from NiO and Fe_3O_4 magnetization and (chemical) structure, we have been able to determine several key points.

We have confirmed measurements of the crystalline and chemical ordering found by XRD, by measurements of neutron (222) reflections, which are predominately structural in character. Scans in the growth (00 ℓ) direction also show a high number of sidebands reflecting the chemical modulation regularity. We have observed up to six sidebands on each side of the central peak[5].

We have measured (220) reflections, which can only arise from scattering from Fe_3O_4 planes, due to symmetry. These results show that for $\text{Fe}_3\text{O}_4(67 \text{ \AA})/\text{NiO}(33 \text{ \AA})$, $\text{Fe}_3\text{O}_4(34 \text{ \AA})/\text{NiO}(68 \text{ \AA})$, and $\text{Fe}_3\text{O}_4(15 \text{ \AA})/\text{NiO}(70 \text{ \AA})$ superlattices, the iron oxide coherence lengths for magnetic ordering is less than a single bilayer thickness, reflecting stacking faults in Fe_3O_4 layer growth, although the $\text{Fe}_3\text{O}_4(70 \text{ \AA})/\text{NiO}(10 \text{ \AA})$ superlattice shows a much longer coherence length (> 3 bilayers) indicating that the thin NiO layers still allow the next Fe_3O_4 layer to grow without stacking faults.

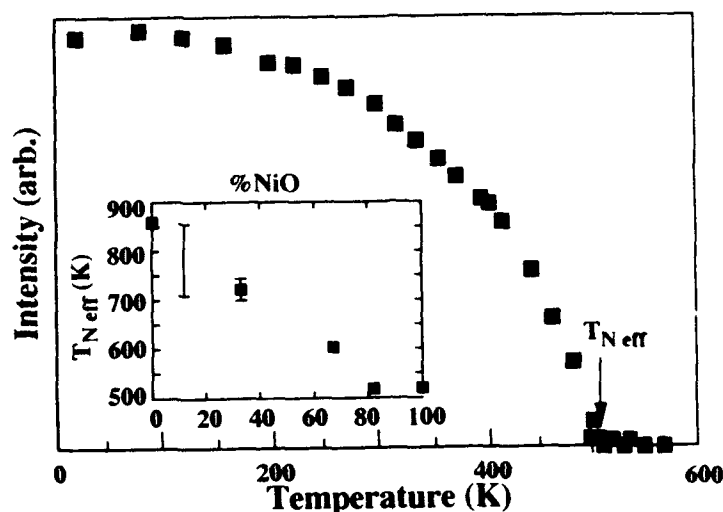


Figure 3: A typical (111) peak intensity plot versus temperature, here for a superlattice with iron oxide thickness of 15 \AA and a nickel oxide thickness of 70 \AA within each bilayer. The inset shows the variation of effective Néel temperature with relative NiO content within a superlattice. The large range shown for the $\text{Fe}_3\text{O}_4(70 \text{ \AA})/\text{NiO}(10 \text{ \AA})$ sample is due to our inability to perform measurements on these superlattices above a temperature of $\sim 700 \text{ K}$. Only above 700 K have we observed [4] irreversible behavior due to interdiffusion.

We have extended the measurements in Lind, *et al.* [5] which demonstrate the extended ordering of at least a portion of NiO within superlattices due to the adjacent presence of ferrimagnetic magnetite, over a complete set of samples where the relative amount of NiO within a bilayer varies from zero to a fraction of 0.823. These measurements follow the (111) scattering peaks as a function of temperature, which is primarily due to NiO magnetic scattering, along with a small amount of scattering due to magnetic and structural components in Fe_3O_4 . The portion of the peak signal due to NiO magnetic scattering, which is a measure of the Ni moment order parameter, disappears at successively higher values as the relative NiO content of a superlattice bilayer is increased, as is shown in Figure 3. The extension of the NiO order parameter to higher temperatures as the NiO relative thickness decreases suggests that at least some boundary layer of the nickel oxide has an increased effective Néel temperature due to coupling to adjacent magnetically ordered iron oxide, which has a Curie temperature of 858 K , and is consistent with mean field magnetic ordering calculations performed recently which show strong enhancement due to just this type of interfacial coupling [2].

CONCLUSIONS

The continuous manner in which the magnetization profiles in $\text{Fe}_3\text{O}_4/\text{NiO}$ superlattices evolves from sigmoidal, bulk-like behavior to linear suggests that the iron oxide layers have a boundary region ($\sim 15 \text{ \AA}$) which is constrained to align with the NiO spin axes. In addition, the neutron measurements also suggest that a least a portion of the NiO layers remains ordered above the bulk NiO Néel temperature, which is consistent with this strong interfacial exchange coupling.

We would like to thank G. Chern and H. Mathias for their fruitful discussions into the work presented here. This work was supported by grant support from the National Science Foundation.

REFERENCES

1. T. Terashima and Y. Bando, *Thin Solid Films* **152**, 455 (1987), and references therein.
2. M. J. Carey, F. E. Spada, A. E. Berkowitz, W. Cao, and G. Thomas, *J. Mater. Res.* **6**, 2680 (1991); M. J. Carey, A. E. Berkowitz, J. A. Borchers, and R. W. Erwin, unpublished; M. J. Carey and A. E. Berkowitz, *J. Appl. Phys.* **73**, (15 May 1993).
3. D. M. Lind, S. D. Berry, G. Chern, H. Mathias, and L. R. Testardi, *Phys. Rev. B* **45**, 1838 (1992).
4. S. D. Berry, D. M. Lind, G. Chern, and H. Mathias, *J. Mag. Mag. Mater.*, in press.
5. D. M. Lind, S.-P. Tay, S. D. Berry, J. A. Borchers, and R. W. Erwin, *J. Appl. Phys.* **73**, (15 May 1993).
6. G. Chern, S. D. Berry, D. M. Lind, H. Mathias, and L. R. Testardi, *Phys. Rev. B* **45**, 3644 (1992); G. Chern, S. D. Berry, D. M. Lind, H. Mathias, and L. R. Testardi, *Appl. Phys. Lett.* **58**, 2512 (1992); G. Chern, S. D. Berry, H. Mathias, and L. R. Testardi, *Phys. Rev. Lett.* **68**, 114 (1992).
7. D. M. Lind, in *Proceedings of the 6th International Conference on Ferrites*, edited by T. Yamaguchi and M. Abe, (Japan Society for Powder and Powder Metallurgy, 1992).
8. E. E. Fullerton, I. K. Schuller, H. Vanderstraeten, and Y. Bruynseraede, *Phys. Rev. B* **45**, 9292 (1992).
9. D. Hilton, H. Mathias, S.-P. Tay, and D. M. Lind, unpublished.
10. J. A. Borchers, R. W. Erwin, S. D. Berry, D. M. Lind, E. Lochner, K. A. Shaw, and D. Hilton, unpublished.
11. Each parenthetical dimension refers to the individual thickness within a single bilayer.

MAGNETIC AND MAGNETO-OPTIC PROPERTIES OF dc MAGNETRON SPUTTERED Co-Cr/Al MULTILAYERS

G.W. Auner, R. Naik*, U.M. Rao*, Y. Zhao, and B. Wang

Department of Electrical and Computer Engineering, Wayne State University, Detroit, MI 48202;

*Department of Physics, Wayne State University, Detroit, MI 48202

ABSTRACT

Single layers of Co₈₂Cr₁₈ with thickness in the range of 100-1500Å and multilayers of Co-Cr/Al with Co-Cr thickness in the range of 100-200Å and Al at 7Å were prepared by dc magnetron sputtering. The films were deposited on to Si(111) and glass substrates at room temperature. A 100Å thick Al buffer layer was deposited to improve the c-axis orientation. X-ray diffraction (XRD) measurements on the multilayers show a predominant Co-Cr (00.2) peak. Polar magneto-optic measurements were performed to determine the Kerr rotation (θ_K) and figure of merit. The results indicated an enhancement in the figure of merit at $\lambda = 632.8$ nm for the multilayered structures compared to single layer samples. All of the films show a $4\pi M_s$ value around 6 kG and ferromagnetic resonance measurements indicate an enhancement in the perpendicular anisotropy field for the 150Å multilayered sample.

INTRODUCTION

Since Iwasaki [1] et al. proposed the use of Co-Cr films as perpendicular recording media, numerous studies on Co-Cr films have been performed on a wide range of topics from fabrication methods to film microstructure [2-10]. The positive anisotropy is considered to be one of the basic favorable properties. The magnetic properties are very sensitive to the microstructure, though a clear relationship between them has not been established. The primary problem associated with microstructure is phase segregation. The magnetic properties have been studied by measurement of magnetization curves, torque measurements and ferromagnetic resonance method [7,8]. There are very few reports about the magneto-optic properties of Co-Cr/Al films [9,10]. Co-Cr films prepared by rf diode and dc magnetron sputtering methods show a θ_K values of 0.036° and 0.066°, respectively. Recent observation of a large magneto-optic Kerr rotation of 0.4-0.5° for Co-Cr/Al prepared by Facing Target Sputtering (FTS) is very encouraging [10]. In this paper we present the results of magnetic and magneto-optic properties of dc magnetron sputtered single layer and multilayer Co₈₂Cr₁₈/Al films.

EXPERIMENTAL

Samples of Glass and Si (111) were cleaned ultrasonically in acetone and methanol. The Si samples were etched with 10% HF for one minute immediately prior to loading into the deposition system in order to facilitate a hydrogen terminated surface. The samples were deposited in a UHV magnetron sputter deposition system with a rotating substrate holder [11]. The deposition system was evacuated to a base pressure of 4×10^{-8} Torr prior to backfilling with 99.999% pure Ar gas. The samples were deposited using approximately 200 watts dc power at a system pressure of 3.5 mTorr. The target to substrate distance was ten inches. This distance was chosen in order to minimize plasma-substrate interactions. Deposition rates were held to approximately 1.2Å/sec. Samples were grown at room temperature on a 100Å Al buffer layer, to promote c-axis orientation, and capped with 7Å of Al following the Co₈₂Cr₁₈ deposition. Film deposition was achieved using separate Al and Co₈₂Cr₁₈ sputtering targets. The Co₈₂Cr₁₈ target was preconditioned to eliminate preferential sputtering effects. Single layer Co₈₂Cr₁₈ were grown on Si(111) and glass

substrates rotating at 50 RPM. Multilayered samples were grown using an alternating shutter system on the individual sputtering sources controlled by a quartz crystal thickness monitor. The multilayers samples were grown with $\text{Co}_{82}\text{Cr}_{18}$ thicknesses of 100Å, 150Å, and 200Å with 7Å of Al between each layer. The amount of CoCr was held constant by varying the number of layers in the multilayer samples, i.e., 22, 15, and 11 for the 100Å, 150Å, and 200Å layer thickness samples, respectively. Standard θ -2 θ x-ray diffraction (XRD) scans were performed with Cu-K α radiation. High angle XRD measurements were carried out on all samples to check the c-axis orientation of the films.

Magnetization measurements were carried out by Faraday technique using a Cahn electro-balance. The multilayered sample volume was estimated from the cumulative thickness of the magnetic layers and the area of the specimen. The ferromagnetic resonance (FMR) data were taken at room temperature using a standard ferromagnetic-resonance spectrometer. The microwave reflection spectrometer operates at a frequency of 12 GHz and employs magnetic-field modulation with phase-sensitive detection so that the detected signal is proportional to the field derivative of the absorbed power. The dc magnetic field, provided by a 12-inch Varian electromagnet, has a range of 0-13 kG and can be rotated in the horizontal plane through a total angle of 360°. Typical FMR samples were 3mm x 3mm. The sample is mounted in a TE₁₀₁ rectangular cavity on a vertical side wall for "out-of-plane" measurements, i.e., to measure FMR as a function of dc magnetic field orientation in a plane perpendicular to the film.

The magneto-optic polar Kerr effect measurements on these samples were made using a simple electro-optic system with a He-Ne laser (633 nm). The sample to be tested is magnetized in either up magnetization or down magnetization. Two output signals (S_1 and S_2) from the photodetectors are fed into IBM/PC through the data acquisition system. A complete measurement process includes two measurements: first in up magnetization and then down magnetization. The angle between the linearly polarized incident beam and the horizontal axis is predetermined and usually equals to 35°. The magneto-optic polar Kerr rotation θ_K , reflectance R and shot-noise-limited figure of merit (FOM), which is defined as $\sqrt{R}\theta_K$ can be calculated accordingly.

RESULTS AND DISCUSSION

Figure 1 shows high angle XRD pattern of a 1500Å thick CoCr film indicating two dominant preferred orientations hcp[00.2] and hcp[10.1] of CoCr. However, measurements on multilayered samples show predominantly [00.2] peak, demonstrating an increase in the c-axis orientation. For example, Figure 2 shows XRD pattern for a $[\text{Co-Cr}(150\text{Å})/\text{Al}(7\text{Å})]_{15}$ multilayer.

Magnetization measurements on the films using Faraday balance yield $4\pi M_s$ values of approximately 6 kG. FMR measurements on all of the single layer samples showed a single absorption peak indicating a homogeneous magnetic component. However, for all of the multilayer samples, in addition to the main resonance peak, we also observed a broad absorption to the left of the main peak when the field is perpendicular to the plane of the sample. In our FMR analysis we have used only the dominant resonance mode. Figure 3 shows the resonance field versus Φ_H for a single layered sample of $[\text{Co-Cr}(1500\text{Å})/\text{Al}(7\text{Å})]$, where Φ_H is the angle made by the dc magnetic field with the film plane. We have fitted the experimental data by writing the free energy density expression as described in reference [12]. The resonance and equilibrium conditions give:

$$\left[\frac{\omega}{\gamma} \right]^2 = \left[H \cos(\Phi_H - \Phi) + 4\pi M_{eff} \cos 2\phi \right] \left[H \cos(\Phi_H - \Phi) - 4\pi M_{eff} \sin^2 \Phi \right] \quad (1)$$

and

$$H \sin(\Phi_H - \Phi) = 4\pi M_{eff} \sin \Phi \cos \Phi \quad (2)$$

where ω is the resonance frequency, $\gamma = ge/2mc$ is the gyromagnetic ratio, Φ is the angle subtended by the equilibrium magnetization M with the film plane and $4\pi M_{\text{eff}} = 4\pi M_s - H_u$ where $H_u = 2K_u/M$, is the uniaxial perpendicular anisotropy field. Equations (1) and (2) were used to fit the angular dependence of the FMR data to obtain $4\pi M_{\text{eff}}$ values. Table I lists the fitted parameter $4\pi M_{\text{eff}}$ for the samples studied along with the values of $H_u = 4\pi M_s - 4\pi M_{\text{eff}}$. The measurements indicate an increase in the uniaxial perpendicular anisotropy field for multilayer with Co-Cr thickness of 150 Å.

Table I- Magnetic and magneto-optic properties of CoCr/Al single and multilayer films.

Sample	θ_K (deg)	FOM	$4\pi M_{\text{eff}}$ (kG) (FMR Data)	H_u (kG) $= 4\pi M_s^* - 4\pi M_{\text{eff}}$
Single Layer				
Glass/Co-Cr(1500Å)/Al(7Å)	0.07	0.04	-	-
Si/Co-Cr(1500Å)/Al(7Å)	0.08	0.05	5.2	0.8
Glass/Co-Cr18(100Å)	0.06	0.05	5.5	0.5
Si/Co-Cr(150Å)/Al(7Å)	0.07	0.06	5.3	0.7
Glass/Co-Cr(200Å)	0.07	0.05	-	-
Si/Co-Cr(200Å)	0.08	0.06	-	-
Multilayers				
Glass/[Co-Cr(100Å)] ₂₂ /Al((7Å)	0.09	0.06	-	-
Si/[Co-Cr(100Å)] ₂₂ /Al((7Å)	0.10	0.07	5.8	0.2
Glass/[Co-Cr(150Å)] ₁₅ /Al((7Å)	0.11	0.08	4.8	1.2
Si/[Co-Cr(150Å)] ₁₅ /Al((7Å)	0.15	0.12	4.2	1.8
Glass/[Co-Cr(200Å)] ₁₁ /Al((7Å)	0.09	0.07	5.9	0.1
Si/[Co-Cr(200Å)] ₁₁ /Al((7Å)	0.11	0.09	5.8	0.2

* An average $4\pi M_s$ value of 6 kG is assumed for all samples.

Magneto-optic Kerr rotation and FOM measured at $\lambda = 632.8$ nm are listed in Table I. These measurements show an enhancement in θ_K for multilayered samples compared to single layer films. We attribute this observation to an improved c-axis orientation in the multilayered samples with Al interlayers.

SUMMARY

Magnetic and magneto-optic properties of dc magnetron sputtered single layers of $\text{Co}_{82}\text{Cr}_{18}$ with thickness in the range of 100-1500Å and multilayers of Co-Cr/Al with Co-Cr thickness in the range of 100-200Å and Al at 7Å were measured. X-ray diffraction measurements indicate that the c-axis orientation is improved by multilayering with ultra-thin interlayers of Al, which is demonstrated by the presence of predominantly (00.2) peak of Co-Cr. All of the samples show a saturation magnetization of approximately 6 kG at room

temperature. Ferromagnetic resonance measurements indicate a positive uniaxial perpendicular anisotropy field of about 1.8 kG for multilayer samples with 150 Å thick Co-Cr layers on Si(111). Magneto-optic measurements at $\lambda = 632.8$ nm show an enhancement of θ_K for multilayered samples compared to single layer film. This is attributed to an improvement of the c-axis orientation in the multilayered samples with Al interlayers.

REFERENCES

1. S. Iwasaki and K. Ouchi, IEEE Trans. Mag. **MAG-14**, 849 (1978)
2. C. W. Chen, J. Mater. Sc., 26, 1705 (1991).
3. R. D. Fisher, V. S. Au Yeung and B. B. Sabo, IEEE Trans. Mag. **MAG-20**, 806 (1984).
4. H. Masuya and H. Awano, IEEE Trans. Mag., **MAG-23**, 2064 (1987).
5. J. E. Snyder, M. H. Kryder and P. Wynblatt, J. Appl. Phys. **67**, 5172 (1990).
6. B. G. Demczyk and J. O. Artman, J. Phys. **D 24**, 1627 (1991).
7. P. V. Mitchell, A. Layadi, N. S. VanderVen and J. O. Artman, J. Appl. Phys. **57**, 3976 (1985).
8. C. L. Ma and C. F. Schwerdtfeger, Solid State Comm. **64**, 651 (1987)
9. K. Tsutsumi, Y. Fujii, M. Komori, T. Numata and Y. Sakurai, IEEE Trans. Mag. **MAG-19**, 1760 (1983).
10. T. Hirata and M. Naoe, IEEE Trans. Mag. **MAG-28**, 2964 (1992).
11. T. Lenane, Development of a pulsed r.f. magnetron sputtering system with activated/dissociated nitrogen bombardment for the growth of III-V nitride heterostructures, Masters Thesis, Wayne State University, Department of Electrical and Computer Engineering, 1993.
12. K. L. Hogue, C. Kota and H. M. Naik, Structure and Properties of Interfaces and Materials/1992, edited by W. A. T. Clark, U. Dahmen, C. L. Briant (Mater. Res. Soc. Proc. 238, Pittsburgh, PA 1992), p341.

INTERFACE AND VOLUME ANISOTROPY OF MBE-GROWN Co/Pt (111), (110) and (001) and SPUTTERED Co/Pt MULTILAYERS

D. Weller, R.F.C. Farrow, R.F. Marks, G.R. Harp, H. Notarys, G. Gorman

IBM Research Division, Almaden Research Center, San Jose CA 95120

* This work was supported in part by ONR.

ABSTRACT

A quantitative determination of interface (K_S) and volume anisotropy (K_V) constants of MBE and sputtered Co/Pt multilayers is reported. Torque and VSM magnetometry were used to determine the total average anisotropy and the room temperature magnetization of four different series of films with varying Co thickness and nearly constant Pt thickness. All films were characterized with X-ray diffraction and X-ray fluorescence, allowing the determination of the "magnetic" volume with good accuracy. Both K_S and K_V are found to be orientation dependent. We find the following results for MBE films grown on Ag buffered GaAs substrates and highly $\langle 111 \rangle$ textured films, grown on etched SiN_x buffers:

(111) $K_S = 0.97 \text{ mJ/m}^2$, $K_V^{\text{eff}} = -0.74 \text{ MJ/m}^3$ MBE

(111) $K_S = 0.92 \text{ mJ/m}^2$, $K_V^{\text{eff}} = -1.11 \text{ MJ/m}^3$ sputtered

(110) $K_S = 0.42 \text{ mJ/m}^2$, $K_V^{\text{eff}} = -1.95 \text{ MJ/m}^3$ MBE

(001) $K_S = 0.59 \text{ mJ/m}^2$, $K_V^{\text{eff}} = -5.98 \text{ MJ/m}^3$ MBE

The [110]-oriented MBE films show in addition a large (intrinsic) in-plane anisotropy constant $K_{\parallel}^0 \approx -3 \text{ MJ/m}^3$, which is found to be independent of the Co thickness. [100] is the easy and [110] the hard in-plane direction.

1. INTRODUCTION

The structural and magnetic properties of Co/Pt multilayers are of continuing interest because of the potential for such multilayers as media for high-density magneto-optical recording in the blue spectral range. In 1990 Lee et al. [1, 2] demonstrated, via seeded epitaxy, the extreme dependence of magnetic anisotropy of Co/Pt multilayers on the orientation of the growth axis. Similar results had first been reported for textured [111] and [001] oriented Co/Pd multilayers [3] and were subsequently obtained for the three orientations of MBE grown Co/Pd superlattices [4] and more recently for Ni/Co/Ni sandwiches [5]. A variety of structural probes were used in the case of Co/Pt superlattices to investigate the degree of interface intermixing [6-8]. Chien et al. [9] suggested that perpendicularly aligned Co-Co pairs at stacking faults in a partially chemically ordered CoPt_3 phase at the interfaces might explain the orientation dependence including the strong uniaxial in-plane anisotropy for [110]-oriented multilayers. However, the density of stacking faults necessary to produce a considerable number of Co-Co pairs could not be confirmed [10, 11]. Nevertheless, short-range chemical ordering was detected in [111]-oriented multilayers [12] using synchrotron X-ray diffraction. The percentage of ordered CoPt_3 phase was found to be large ($\sim 80\%$) at 300°C growth temperature but only about 20% for the 100°C grown films, that are under investigation here. Thus one has to conclude that there is indeed the possibility of interfaces (or structural boundaries) between alloyed and/or chemically ordered compound regions and Co and Pt, which can be expected to (at least) modify the interface contribution K_S to the total magnetic anisotropy. Such contributions should be in the order of 20% for the current growth temperature of 100°C and much larger at higher temperatures.

On the theory side, Victora and Maclaren [13] in an extended Néel model [14] confirmed the results of Engel et al. [4] for Co/Pd superlattices, who reported one

single K_s value for all three orientations. No interfacial mixing was assumed, but the strain values determined from the experiments were incorporated in this model. In contrast, no such orientation independent K_s was found in Ni/Co/Ni sandwiches [5] and it was pointed out that the experimental finding in Co/Pd was perhaps a coincidence related to the particular strain situation in that system. Also, first principles calculations of the magnetic anisotropy of Co/X systems [15] showed, that the different electronic environment encountered in different crystallographic orientations should give rise to different K_s contributions. In agreement with the work of Johnson et al. [5] on Ni/Co/Ni sandwiches, we find this expectation confirmed in our Co/Pt multilayers and report an orientation-dependent interface anisotropy K_s . We compare our values to those obtained by Victora and MacLaren [13] in model calculations and experimental results obtained by McGee et al. [16] in a Pt/Co-wedge/Pt(111) sandwich. Finally we point out, that the anisotropy in the present Co/Pt system may be influenced by graded rather than abrupt Co/Pt interfaces and note that such realistic interfaces could be tested in future theoretical work.

2. EPITAXY AND CHARACTERIZATION

The epitaxial films were grown in a VG 80-M MBE system (VG Semicon Ltd.) using electron-beam sources for Co and Pt. During growth the background pressure was $\sim 1.10^{-10}$ mbar. Co and Pt growth rates were $\sim 0.2\text{\AA}/\text{s}$, and the substrate was held at 100°C during film growth. The seeded epitaxy of the multilayers, on GaAs substrates, has been described elsewhere [1, 2].

Highly-textured (111) oriented multilayers were sputtered on ion-etched SiN buffered Si(111) substrates using techniques described earlier [17, 18]. The ion etching of the SiN buffer films turned out to be essential for promoting (111)-oriented columnar growth with typical grain diameters of $\sim 10\text{nm}$. Rocking curve widths of $\sim 5^\circ$ confirmed the strong preferred (111) orientation.

The Co and Pt thicknesses in the multilayers were determined using a combination of X-ray fluorescence for multilayer composition and X-ray diffraction for the multilayer period. Torque magnetometry (45° method [19]) was used to determine $K_\perp = K^0 - 1/2\mu_0 M_s^2$ and K_\parallel . Here K_\perp^0 refers to the intrinsic perpendicular anisotropy constant. No such distinction between K and K^0 is necessary for the in-plane measurements K_\parallel . The saturation magnetizations were independently measured with VSM in both in-plane and out-of-plane orientation, to reduce the error. All measurements were made at room temperature. No distinction between K_1 and K_2 is made, i.e. K_2 is assumed to be negligible as compared to K_1 . Furthermore, M_s and all anisotropy energies have been normalized to the amount of Co in the present structures.

3. EXPERIMENTAL RESULTS

If the total perpendicular anisotropy energy per Co volume and including the demagnetization term $1/2\mu_0 M_s^2$ for the multilayers is written as

$$K_\perp d_{\text{Co}} = K_\perp^{\text{eff}} d_{\text{Co}} + 2K_s, \quad (1)$$

then plots of $K_\perp d_{\text{Co}}$ versus d_{Co} should give lines of slope K_\perp^{eff} and intercept $2K_s$ in this simple phenomenological approach which is based on Neél's model [14] of an additional interface or surface anisotropy term K_s . Fig. 1 (a) shows the measured total effective magnetic anisotropy energy (per Co volume) K_\perp versus d_{Co} whilst Fig. 1 (b) shows the plots of $K_\perp d_{\text{Co}}$ versus d_{Co} . From the linear sections in Fig. 1 (b) one can deduce an interface contribution which varies in the expected $1/d_{\text{Co}}$ manner. The extracted values of K_s and K_\perp^{eff} are indicated in the figure and also summarized in Table 1. Note that each multilayer orientation has a different slope and intercept. The value of K_s for the [111] multilayers, 0.97 mJ/m^2 , is

larger than that (0.92 mJ/m^2) found in the sputtered multilayers and smaller than that (1.15 mJ/m^2) for the MBE-grown Pt/Co/Pt wedge (single sandwich) of McGee et al. [16].

TABLE 1. Comparison of interface and volume anisotropies of differently oriented MBE superlattices and textured sputtered films (this work) in comparison with results of McGee et al. [16] on a Pt/Co/Pt wedge and model calculations of Victora and McLaren [13].

	this work, see also ref. [20]		Pt/Co-wedge/Pt, ref. [16]		theory, ref. [13]	
Co/Pt Orientation	K_S in mJ/m^2	K_V^{eff} in MJ/m^3	K_S in mJ/m^2	K_V^{eff} in MJ/m^3	K_S in mJ/m^2	K_V^{eff} in MJ/m^3
(111) MBE	0.97	-0.74	1.15	-0.77	0.85	-1.3
(111) sputtered	0.92	-1.11				
(110) MBE	0.42	-1.95			0.7	-4.2
(001) MBE	0.59	-5.98			0.6	-6.4

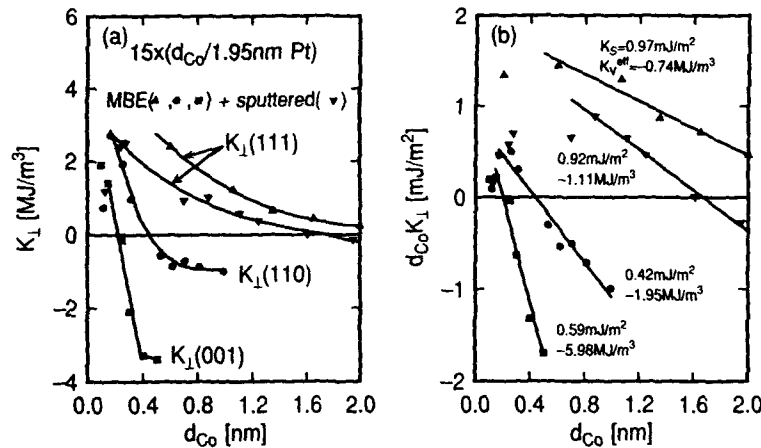


Fig. 1: Plot of (a) K_{\perp} and (b) $d_{\text{Co}} \times K_{\perp}$ as a function of d_{Co} for epitaxial and sputtered Co/Pt multilayers. All data were taken at room temperature.

The (001) multilayers have a very large negative volume anisotropy term which may be induced by the coherency strain for these multilayers [21], as originally pointed out by den Broeder et al. for Co/Pd(100) multilayers [3].

In the case of the [110]-oriented multilayers a dual behavior is observed (see also [20]): both torque magnetometry and VSM measurements confirmed that the [110]-oriented multilayers had an additional uniaxial in-plane anisotropy. The easy directions were [001] and [00 $\bar{1}$], while along the hard directions ([110] and [110]), large ($>20 \text{ KOe}$) fields were needed to saturate the magnetization. This in-plane anisotropy in the case of the (110) orientation was first reported by Lin et al. [22] and by Chien et al. [9] and recently also been confirmed by LeDang et al. [23] in NMR experiments. A detailed discussion of in-plane anisotropies in (110) oriented multilayers in conjunction with an elastic strain theory was recently given by Hillebrands et al. [24, 25]. For these samples the anisotropy energy can be written phenomenologically as

$$E_A = K_0 + K_{\parallel} \sin^2 \theta \cos^2 \phi + K_{\perp} \sin^2 \theta, \quad (2)$$

where ϕ is the angle between the magnetization and the in-plane easy axis [001], θ the angle between the magnetization and the sample normal [110], K_{\perp} and K_{\parallel} are the out-of-plane and in-plane anisotropy constants and K_0 is a constant, independent of θ and ϕ . Torque magnetometry measurements were made in three different in-plane and out-of-plane geometries for $\phi = 90^\circ$ ($\theta = 0-360^\circ$), $\phi = 0^\circ$ ($\theta = 0-360^\circ$) and $\theta = 90^\circ$ ($\phi = 0-360^\circ$). From these three independent measurements the anisotropy constants K_{\perp} , $(K_{\perp} + K_{\parallel})$ and K_{\parallel} were derived. Fig. 2(a) shows the data. In this figure the line through the upper set of data points is the sum of the fits to the K_{\parallel} and K_{\perp} data. There is good agreement between the $K_{\parallel} + K_{\perp}$ data points and the sum curve. Fig. 2(b) shows the plot of $d_{\text{Co}} K_{\perp}$ versus d_{Co} and the straight line fit to the data, resulting in the K_S and K_V^{eff} values as given in Table 1. We have also measured the anisotropy constants for a multilayer containing thick ($\sim 2\text{nm}$) Co films and find that the in-plane anisotropy is about 2MJ/m^3 .

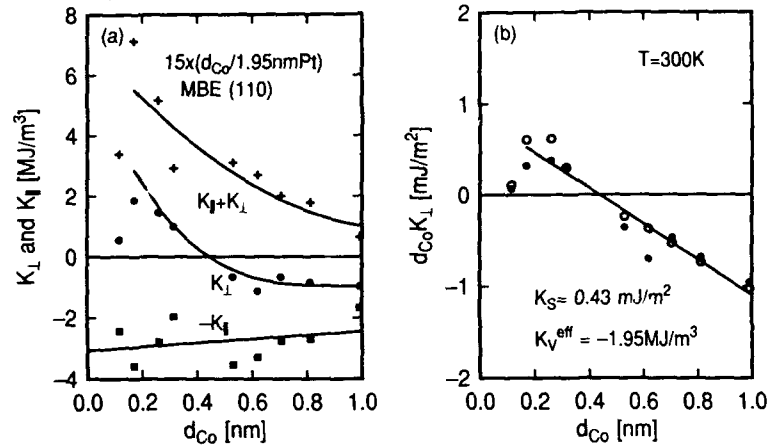


Fig. 2: (a) Anisotropy constants K_{\perp} (\bullet), K_{\parallel} (\blacksquare) and $(K_{\perp} + K_{\parallel})$ ($+$) versus Co thickness in [110] oriented Co/Pt multilayers. (see text for details) and (b) Plot of $d_{\text{Co}} K_{\perp}$ versus d_{Co} for [110] oriented multilayers. K_{\perp} was taken from the direct measurement (\bullet) and in addition determined indirectly (\circ) by subtraction of K_{\parallel} from $(K_{\perp} + K_{\parallel})$, thus improving the quality of the fit.

Magnetization measurements were made for all the multilayers grown on GaAs substrates and Fig. 3 (a) shows the saturation magnetization, measured at room temperature. M_S refers to the magnetization divided by the Co volume in the multilayer and can be compared with the value for bulk (hcp) Co of 1422 kA/m. An enhanced magnetization is evident for the MBE multilayers over the thickness range $\sim 0.3-1.5\text{nm}$. All three MBE orientations basically fall onto the same line, whereas some of the sputtered multilayers obviously do not show the enhancement in that Co thickness regime. The enhancement, first of all, can be attributed to exchange polarization of interfacial Pt atoms by the Co layers. A reason for the discrepancy between some of the sputtered and the MBE multilayers might be that in the case of sputtering, columnar growth with relatively small grain diameters of $\sim 10\text{nm}$ was observed. This can lead to "non-magnetic" intergrain regions (voids, non magnetic Pt etc.) which then accordingly reduce the average magnetization obtained by VSM magnetometry. Another argument may be, that the induced Pt polarization in the case of sputtered films, which were grown at lower temperatures (room temperature as opposed to 100°C in the MBE case) might also be smaller (see below!). At large ($> 1.5\text{nm}$) Co thicknesses the

magnetization approaches that of bulk Co in all films, since the relative number of interfacial atoms is diminished. On the other hand, for Co thicknesses below 0.3 nm the magnetization per Co volume drops off indicating a dilute Co alloy with reduced Curie temperature and/or the formation of a 2D magnetic layer (Co or Co-Pt alloy) which can also lead to a reduction in T_C due to reduced symmetry.

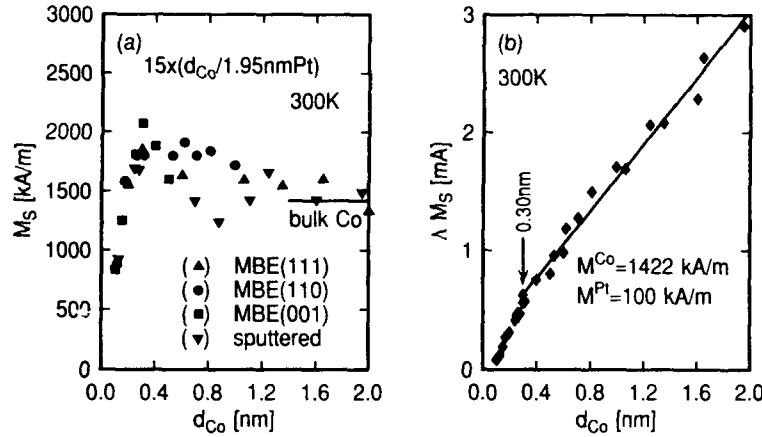


Fig. 3: (a) Room temperature saturation magnetization per Co volume for the present MBE grown Co/Pt multilayers. The different orientations are once again distinguished by the respective symbols explained in the figure. (b) Evaluation of the Pt contribution to the saturation magnetization according to eq.(3) from all the data in (a).

Assuming that the total magnetization can be written in the following manner,

$$\Lambda M_S = M_S^{Co} d_{Co} + M_S^{Pt} d_{Pt} \quad (3)$$

where $\Lambda = d_{Co} + d_{Pt}$ refers to the multilayer period and d_{Co} and d_{Pt} are the individual Co and Pt layer thicknesses, respectively, we can extract a Co magnetization of ~ 1400 kA/m from the slope and an average Pt magnetization of ~ 100 kA/m from the intercept in these structures. Both numbers are reasonable and assuming a Co moment of $1.7\mu_B$ per Co atom, we conclude that the average moment per Pt atom is in the order of $0.12\mu_B$. This is quite high given that we have nominally about 9-10 atomic layers of Pt in between Co layers. Note, that a single atomic layer of Pt adjacent to Co should pick up a moment per Pt atom of only about $0.20\mu_B$ and that the moment in the second Pt layer is expected to drop off rapidly if the interfaces are atomically sharp [26]. An average moment per Pt of only about $0.03-0.05\mu_B$ was predicted and found to be in overall agreement with x-ray dichroism data obtained from (room temperature) evaporated Co/Pt multilayers [26, 27]. If alloying is present, the induced moment per Pt atom is expected to be higher due to the (3D) alloy environment and the moment reduction will be deferred to nominally thicker Pt spacings. E.g. Pt impurity atoms in a Co matrix have been reported to have moments in the order of $0.3-0.4\mu_B$ per Pt atom [28]. An intermixing zone of roughly about ± 1 monolayer at each interface therefore readily explains our experimental finding.

A relatively sharp change in the slope is observed at ~ 0.3 nm Co thickness, indicating a reduction of the total moment due to the combined effects of a suppression of the Curie temperature and alloying. A similar "cut-off" thickness is obvious in Figs. 1+2 and we finally mention, that that range was generally avoided in the evaluation of the slopes and intercepts (K_V^{eff} and $2K_S$).

4. COMPARISON WITH THEORY

Inspection of Table 1 shows that the theory of Victora and Maclaren[13] gives good agreement for both K_S and K_V for the [001]-oriented multilayers but poor agreement for the other orientations. The theory predicts a value of K_S which is too small for all the [111]-oriented multilayers and especially for the Pt/Co/Pt wedge sample of McGee et al. [16]. We find that the sputtered multilayers show a similar value of K_S to the [111]-oriented multilayers. Since all the multilayers contain internal interfaces between materials with different electronic structure the basic assumption of abrupt Co/Pt interfaces is not a realistic starting point for a theoretical model. Coherency strain for the [001] multilayers [21] is experimentally confirmed and appears to control K_V for this orientation. However, it is clear that the model should also incorporate the effects of alloying, chemical ordering and Pt polarization at the internal interfaces. These effects become obviously more important at higher growth temperatures and we note, that we have meanwhile fabricated respective multilayer structures on Pt seed sapphire(0001) substrates, in which we observe a strong enhancement of K_{\perp} if we increase the substrate temperature.

5. CONCLUSIONS

We report a quantitative determination of K_S and K_V for MBE-grown, epitaxial and textured, sputtered Co/Pt multilayers. K_S is dependent on the orientation of the multilayer growth axis. A strong uniaxial in-plane anisotropy is found for the [110]-oriented multilayers for all Co film thicknesses investigated, which was up to 1nm. For the [001]-oriented multilayers the volume anisotropy term is very large, consistent with a strain-driven effect. The theory of Victora and Maclaren[13] is not in agreement with our data and we believe that one reason is perhaps the neglect of interfacial mixing and the formation of alloy interfaces, e.g. between CoPt_3 phases and Co and Pt respectively. Our data confirm that Pt has an induced moment and this leads to an enhanced magnetization per Co volume for MBE grown multilayers in the thickness range 0.35-1.5 nm. No such enhancement was observed for the case of sputtered (111) textured and strongly oriented films, which however showed a very large interface anisotropy contribution.

6. REFERENCES

- [1] C.H. Lee, R.F.C. Farrow, C.J. Lin, E.E. Marinero, C.J. Chien, *Phys. Rev. B*, 42, 1990, 11384.
- [2] C.H. Lee, R.F.C. Farrow, B.D. Hermsmeier, R.F. Marks, and W.R. Bennet, C.J. Lin, E.E. Marinero, P.D. Kirchner, C.J. Chien, *J. Magn. Mater.*, 93, 1991, 592.
- [3] F.J.A. den Broeder, D. Kuiper, H.C. Donkersloot, W. Hoving, Comparison of the magnetic anisotropy of (001) and (111) oriented Co/Pd multilayers, *Appl. Phys. A*, 49, 1989, 507-512.
- [4] B.N. Engel, C.D. England, R.A. vanLeeuwen, M.H. Wiedmann, and C.M. Falco, *Phys. Rev. Lett.*, 67, 1991, 1910.
- [5] M.T. Johnson, J.J. de Vries, N.W.E. McGee, J. aan de Stegge, and F.J.A. den Broeder, Orientational Dependence of the Interface Magnetic Anisotropy in Epitaxial Ni/Co/Ni Sandwiches, *Phys. Rev. Lett.*, 69, 1992, 3575.
- [6] B.D. Hermsmeier, R.F.C. Farrow, C.H. Lee, R.F. Marks, and E.E. Marinero, C.J. Lin, R.F. Marks, C.J. Chien, *J. Appl. Phys.*, 69, 1991, 5646.
- [7] R.F.C. Farrow, B.D. Hermsmeier, C.H. Lee, R.F. Marks and E.E. Marinero, C.J. Lin, C.J. Chien, S.B. Hagstrom, *Mat. Res. Symp. Proc.*, 229, 1991, 115.

- [8] X. Yan, T. Egami, E.E. Marinero, R.F.C. Farrow, C.H. Lee, *J. Mat. Res.*, 7, 1992, 1309.
- [9] C.J. Chien, B.M. Clemens, S.B. Hagstrom, R.F.C. Farrow and C.H. Lee, E.E. Marinero, C.J. Lin, *Mat. Res. Soc. Proc.*, 231, 1991, 465.
- [10] N.-H. Cho, Kannan M. Krishnan, C.A. Lucas, R.F.C. Farrow, Microstructure and magnetic anisotropy of ultrathin Co/Pt multilayers grown on GaAs(111) by molecular-beam epitaxy, *J. Appl. Phys.*, 72, 1992, 5799-5807.
- [11] M. Toney, *unpublished data*, 1992.
- [12] M.F. Toney, R.F.C. Farrow, R.F. Marks, G. Harp, T.A. Rabedeau, *Mat. Res. Soc. Symp. Proc.*, 263, 1992, 237.
- [13] R.H. Victora and J.M. MacLaren, Theory of anisotropy in strained superlattices, *J. Appl. Phys.*, 73, 1993, 6415.
- [14] L. Néel, *J. Phys. Radium*, 15, 1954, 376.
- [15] G.H.O. Daalderop, P.J. Kelly, M.F.H. Schuurmans, First-principles calculations of the magnetic anisotropy energy of (Co), *Phys. Rev. B*, 42, 1990, 7270-7273.
- [16] N. W. E. McGee, M.T. Johnson, J.J. de Vries, J. aan de Stegge, Localised Kerr study of the Magnetic Properties of an Ultrathin Epitaxial Co Wedge grown on Pt(111), *J. Appl. Phys.*, 73, 1993, 3418.
- [17] T. Suzuki, H. Notarys, D. Dobberty, C.-J. Lin, D. Weller and D. Miller and G. Gorman, Microstructure and magnetic properties in Co/Pt multilayer films, *IEEE Trans. Mag.*, 28, 1992, 2754.
- [18] D. Weller, H. Notarys, T. Suzuki, G. Gorman, T. Logan, and I. McFadyen, C.J. Chien, Thickness Dependent Coercivity in Sputtered Co/Pt Multilayers, *IEEE Trans. Mag.*, 28, 1992, 2500-2502.
- [19] H. Miyajima, K. Sato, T. Mizoguchi, Simple analysis of torque measurement of magnetic thin films, *J. Appl. Phys.*, 47, 1976, 4669.
- [20] R.F.C. Farrow, C.H. Lee, R.F. Marks, G. Harp, M. Toney and T.A. Rabedeau, D. Weller, H. Brändle, in *"Magnetism and Structure in Systems of Reduced Dimensions"*, NATO ASI series, eds. R.F.C. Farrow et al., Plenum Publishing Corp., New York, 1993.
- [21] T.A. Rabedeau, G.R. Harp, R.F. Marks, R.F.C. Farrow, M.F. Toney, (unpublished), 1993.
- [22] C.-J. Lin, H.V. Do, Magneto-optical recording on evaporated Co/Pt multilayer films, *IEEE Trans. Magn.*, 26, 1990, 1700-1702.
- [23] K. LeDang, P. Veillet, C. Chappert, R.F.C. Farrow, R.F. Marks and D. Weller, Orthorhombic distortion of Co lattice in a (110) Co/Pt multilayer grown on (001) GaAs substrate, *Phys. Rev. B (submitted)*, 1993.
- [24] B. Hillebrands and J.R. Dutcher, Origin of very large in-plane anisotropies in (110)-oriented Co/Pd and Co/Pt coherent superlattices, *Phys. Rev. B / Brief Reports*, 47, 1993, 6126.
- [25] B. Hillebrands, J.V. Harzer, G. Güntherodt, J.R. Dutcher, Study of Co-based multilayers by Brillouin light scattering. *J. Magn. Soc. Jpn.*, 17 Supp. S1, 1993, 17-22.
- [26] H. Ebert, S. Ruegg, G. Schütz, R. Wienke, W.B. Zeper, Magnetic properties of Co/Pt multilayers, *J. Magn. Magn. Mater.*, 93, 1991, 601-604.
- [27] H. Ebert, G. Schütz, R. Wienke, S. Ruegg, W. Wilhelm and W.B. Zeper, *J. Magn. Magn. Mater.*, 93, 1991, 601.
- [28] T.R. McGuire, J.A. Aboaf, E. Klokholm, Magnetic and transport properties of Co-Pt thin films, *J. Appl. Phys.*, 55, 1984, 1951.

STRUCTURAL CHARACTERIZATION OF Pt/Co MULTILAYERS FOR MAGNETOOPTIC RECORDING USING X-RAY DIFFRACTION

James A. Bain,* Bruce M. Clemens,* Sean Brennar.**

*Dept. of Materials Science and Engineering, Stanford University, Stanford CA, 94305-2205

**Stanford Synchrotron Radiation Lab. Stanford, CA 94309

ABSTRACT

Structural features in magnetic multilayer films such as interfacial sharpness and in-plane stress are regarded as responsible for the perpendicular magnetic anisotropy observed in these films. The multilayers often consist of alternating magnetic and non-magnetic layers, and the degree of interfacial sharpness between the two is a critical component in producing perpendicular anisotropy. Additionally, in-plane stress affects the anisotropy through magnetostriction. In this work, we measure both the composition modulation and the stress in multilayers of Pt/Co with x-ray diffraction. Quantitative information about the composition modulation is extracted by recursively fitting a model of multilayer diffraction to the high angle superlattice lines. The model incorporates a composition modulation of variable amplitude, along with a statistical description of the layer thickness fluctuations.

INTRODUCTION

Two major (potential) contributions to the perpendicular magnetic anisotropy in Pt/Co multilayers are stress and interfacial anisotropy [1, 2]. In this work we examine the intrinsic stresses and interfacial sharpness in epitaxial multilayers of Pt/Co, using x-ray diffraction. Identical multilayer structures were deposited using DC magnetron sputtering at two different Ar pressures. We found that both stress and interfacial sharpness were affected by sputtering pressure, but that only the interfacial sharpness correlated with the changes in the perpendicular magnetic anisotropy.

Magnetic Anisotropy

Magnetic anisotropy is the dependence of the magnetic energy of a material on the direction of magnetization. For Pt/Co multilayers, the major contribution to the anisotropy is the term associated with single axis of easy magnetization parallel to the film normal, such that the magnetic energy, E^{mag} , takes the form:

$$E^{mag} = K_u \sin^2 \phi + C \quad (1)$$

where K_u is the magnitude of this energy dependence, the magnetic anisotropy, ϕ is the angle between the surface normal and the magnetization, and C is a constant.

Stress can contribute to perpendicular magnetic anisotropy through an inverse magnetostrictive effect. For an cubic thin film with a [111] surface normal, K_u^σ is given by:

$$K_u^\sigma = -3/2 \lambda_{111} \sigma \quad (2)$$

where λ_{111} is one of the two magnetostriction coefficients which relate magnetization and strain [3], and σ is the in-plane stress. Specifically, λ_{111} is defined as the change in length of a crystal in the [111] direction when it is magnetized in the [111] direction.

Interfacial anisotropy is another contributor to the anisotropy. It's dependence on the structure is not so clear. A common approach is to assume each interface introduces a fixed anisotropy and to count interfaces [4, 5]. This leads to the "1/t" behavior, where t is the magnetic layer thickness. The (extrinsic) anisotropy energy per unit area of a bilayer is given by:

$$K_u t = K_u^b t + K_u^s \quad (3)$$

where K_u^b is the anisotropy of the bulk of each layer (intrinsic) and K_u^s is the surface anisotropy energy of each interface (intrinsic) [4, 5]. This model assumes that K_u^s is independent of bilayer period, which is unlikely in light of the intermixing at low bilayer periods which is shown below.

X-RAY MEASUREMENTS

The analysis which was used to extract the stress in a given phase from x-ray diffraction measurements also gives the unstrained lattice parameter. In this work, only the Pt-rich phase was visible at all bilayer periods. The details of the formalism are given in [6]. Additionally, the structural refinement technique of Fullerton et al [7] was used to estimate structural parameters of the multilayers. This technique employs a non-linear least-squares fit of a calculated diffraction spectra to the high angle symmetric diffraction pattern from the multilayers. We have constructed a fitting program which incorporates the scattering power (and therefore the composition) of the atomic planes as fittable parameters.

EXPERIMENTAL

The samples for this study were fabricated in a customized UHV sputter deposition system which is housed in the Vapor Phase Deposition Laboratory of the Center for Materials Research, at Stanford University. Substrates were polished single crystal sapphire cut with an (0001) surface normal. A 115 Å thick Pt underlayer grown at 550°C was used to induce (111) growth texture in the multilayers, as well as an in-plane epitaxial orientation, with the Pt (220) parallel to the sapphire (3030). Multilayers were deposited on the underlayers at room temperature for a range of bilayer periods between 8 and 150 Å. At all bilayer periods the global composition was 75 at% Pt. Sample sets were deposited at 3 and 25 mtorr of Ar, at a source to substrate distance of 2.5 inches and growth rates of approximately 0.5 Å/s.

Measurements of magnetic moment and hysteresis were performed with a TOEI Vibrating Sample Magnetometer in fields up to 20 KGauss at room temperature. Holder and substrate background were subtracted from the data. Measurements of perpendicular anisotropy were performed using a TOEI torque magnetometer, also in fields up to 20 KGauss and at room temperature. Background torques associated with the apparatus were subtracted, and the torque was determined by extrapolating the torque at 45° from the easy axis to infinite field [8].

The asymmetric x-ray scattering measurements (for the determination of stress and intermixing) were performed on beamline 7-2 at Stanford Synchrotron Radiation Laboratory (SSRL). A Huber 4-circle diffractometer was used in symmetric, asymmetric and grazing incidence modes. Photon energies of 9987 eV ($\lambda = 1.2414$ Å) were used. The symmetric data (for the determination of composition modulation using structural refinement) were taken using a Phillips powder diffractometer and Cu K_α radiation.

RESULTS

Magnetic Properties

Figures 1a) and 1b) shows the perpendicular magnetic anisotropy and the saturation magnetization, respectively, of the multilayer samples in this study. Two important trends are visible in the anisotropy data. Firstly, sputtering at higher pressures produces a larger perpendicular anisotropy for a given bilayer period. Secondly, K_u increases with decreasing bilayer period for all but the smallest bilayer periods.

The saturation magnetization, M_s , of these samples showed a small sensitivity to bilayer period, but a large sensitivity to sputtering pressure. The exception to this trend is the decrease in the M_s values at low bilayer periods. This decrease is an artifact of the deposition process, owing to a reduction of the amount of Co deposited at low bilayer periods. Consequently, the total moment of the film is reduced. The rest of the trends are a competition between two processes associated with intermixing of the Pt and Co. First, there will be a reduction in the magnetic moment due to a reduction in the Curie temperature as intermixing occurs (since θ_C of the alloy decreases monotonically with increasing Pt content) [9]. Secondly, intermixing may also increase the total magnetic moment due to the position of an increasing number of Pt atoms [9]. The increase in moment at low sputtering pressure is consistent with the latter mechanism in light of the fact that x-ray measurements show below that there is increased intermixing at low sputtering pressures.

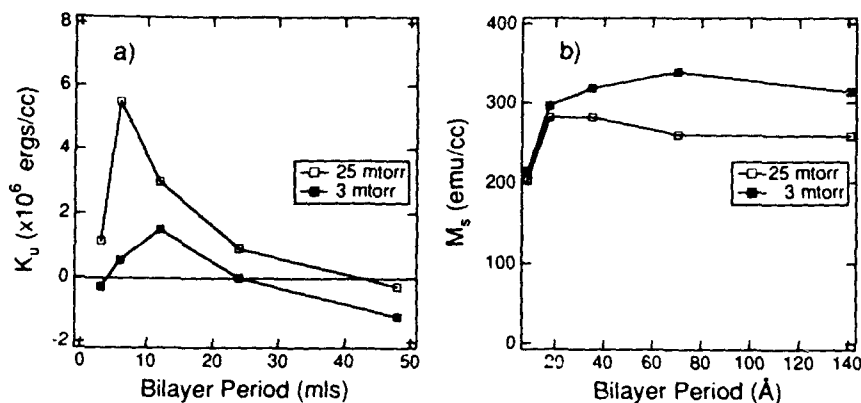


Figure 1: a) Perpendicular magnetic anisotropy for epitaxial samples on sapphire (0001), as measured with torque magnetometry. b) Saturation magnetization of epitaxial samples on sapphire (0001) as measured with vibrating sample magnetometry. The entire film volume was used as the volume of magnetic material in all cases.

Stress and Intermixing

In all samples, it was found that for decreasing bilayer periods, the Pt-rich phase contained increasing amounts of Co. This is consistent with an intermixed region at the interface between Co and Pt. As the bilayer period decreases, this phase dominates the behavior of the material. Figure 2a) shows the unstrained lattice parameter and the stress, respectively, in the Pt rich phase, as extracted using the x-ray diffraction analysis outlined in [6]. In addition to the unstrained lattice parameters, Figure 2b) shows the variation of stress in the Pt-rich regions of the films with bilayer period and with sputtering pressure. The samples deposited at high pressure were in a more tensile state than those deposited at low pressure. This is consistent with an atomic peening mechanism [10, 11, 12]. Furthermore, at both pressures, there is a peak in the compressive stress around a bilayer period of 15-20 Å.

Evidence for intermixing was also seen in the superlattice lines in symmetric x-ray scans of the epitaxial samples. Figure 3 shows the high angle superlattice lines and the recursive fits to these diffraction spectra using the model discussed above. All the fits indicate a composition modulation amplitude which is less than the maximum composition difference. Furthermore, the fits indicate that the intermixing is more pronounced at lower sputtering pressures and at lower bilayer periods. Table I shows the composition of Pt in the Pt and Co layers as extracted from the fit, as well as the number of layers of each in the average bilayer.

DISCUSSION

The level of intermixing correlates well with the anisotropy found in these samples. There is a trade off between increasing numbers of interfaces and decreasing composition modulation with decreasing bilayer period. At the smallest bilayer periods, the lack of composition modulation dominates and the anisotropy is greatly reduced. The intermixing behavior is plausible in terms of a kinetic model of sputter deposition. The arriving atomic species have less kinetic energy upon arriving at the substrate when deposition is performed at a high sputtering pressure (there

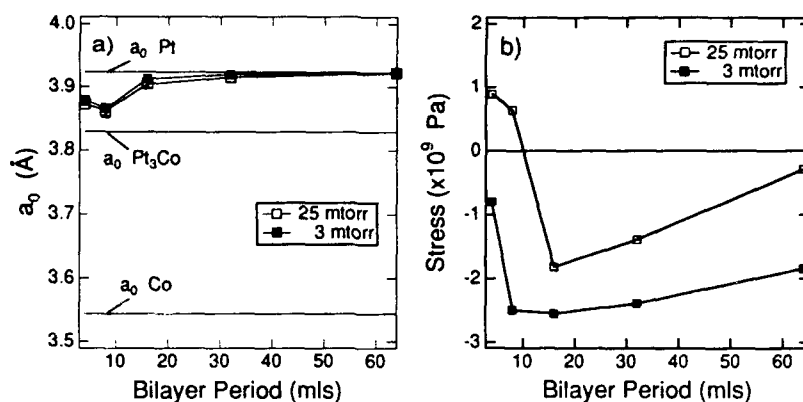


Figure 2: a) The unstrained lattice parameter of the Pt-rich region of the samples, as measured with x-ray diffraction. Increasing amounts of Co are seen in the Pt with decreasing bilayer period. b) The stress in the Pt-rich regions of the epitaxial samples on sapphire (0001) as measured by x-ray diffraction. The elastic constants used in this calculation were those for pure Pt.

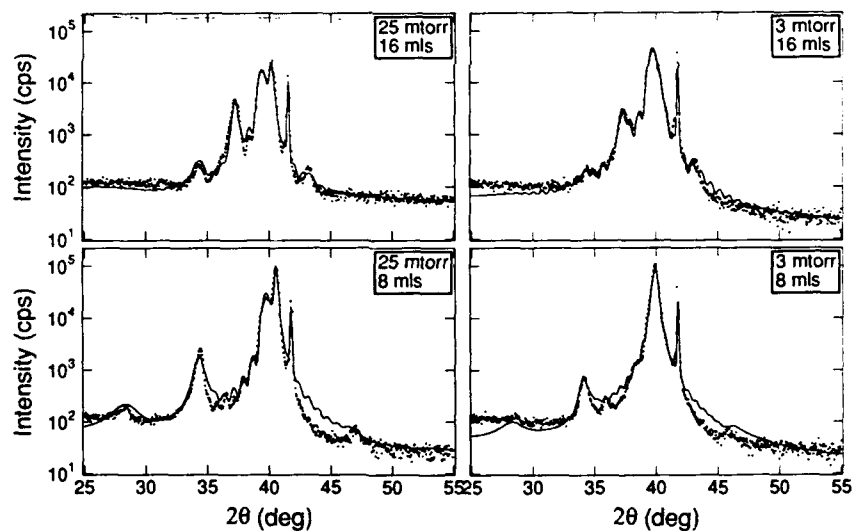


Figure 3: Recursive fits of a diffraction model to the symmetric x-ray diffraction from the epitaxial samples on sapphire (0001). This model is discussed at length in [7].

Table I: The results of the structural refinement calculations, showing the composition and thickness of the Pt and Co layers in the average bilayer.

Sputtering Pressure	Bilayer Period	Pt		Co	
		No. Layers	At% Pt	No. Layers	At% Pt
25 mtorr	34 Å	25.0	0.94	9.0	0.01
3 mtorr	34 Å	24.2	0.83	8.8	0.04
25 mtorr	15 Å	11.0	1.00	4.0	0.45
3 mtorr	15 Å	10.9	0.75	4.1	0.51

are more collisions with gas atoms for a metal atom on its way to the substrate). Therefore, they are kinetically limited in reaching the intermixed (or lowest energy [9]) state at high sputtering pressure.

In contrast, stress appears not to play a role in the anisotropy of these films. According to equation 4, there is a linear proportionality between stress and K_u . Figure 4 shows that there is no correlation between stress and the value of K_u . This figure needs several qualifications.

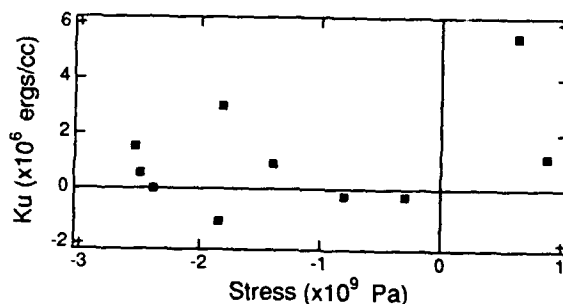


Figure 4: A comparison of K_u and stress in the Pt-rich regions of the multilayers.

Obviously, it is the stress in the Co which matters for magnetostriction. There are two pieces of evidence which suggest that stress in the Pt is representative of the stress in the Co. Firstly, measurements on a similar sample set deposited on Si wafers indicated agreement between the global or average stress in the multilayers and the Pt. This was accomplished by comparing substrate curvature and x-ray diffraction data. Secondly, at low bilayers periods, the intermixing indicates that the Pt-rich region encompasses the entire film, such that there can be no region under an appreciably different stress.

CONCLUSIONS

From this work we can draw several conclusions regarding the relationship among film growth conditions, microstructure and perpendicular magnetic anisotropy. K_u was larger at a given bilayer period for sputter deposition at high pressures. Furthermore, K_u increased with decreasing bilayer period, up until a point after which decreases in bilayer period reduced the anisotropy. The corresponding trends in microstructure showed that both decreases in bilayer period and low sputtering pressure produced increasing amounts of intermixing. The correlation between intermixing and a reduction in K_u strongly suggests an interfacial anisotropy. Stress in the Pt-rich phase, while large, did not correlate with anisotropy.

ACKNOWLEDGEMENTS

Work done (partially) at SSRL which is operated by the Department of Energy, Office of Basic Energy Science, Division of Chemical Sciences. One of us (JAB) gratefully acknowledges fellowships from NSF and IBM Corp. Sample fabrication was performed at Stanford Center for Materials Research, in the Vapor Phase Synthesis Laboratory.

REFERENCES

1. S. Hashimoto, Y. Ochiai and K Aso, J. of Appl. Phys., **66**, 4908 (1989).
2. K. Spörl and D. Weller, J. of Mag. and Mag. Mat., **93**, 379 (1991).
3. S. Chikazumi and S.H. Charap, Physics of Magnetism. (R.E. Krieger Pub. Co., Malabar, Florida, 1986).
4. S. Hashimoto, Y. Ochiai, and K. Aso, J. of Mag. and Mag. Mat., **66**, 4909 (1989).
5. F.J.A. den Broeder, W. Hoving, and P.J.H. Bloemen, J. of Mag. and Mag. Mat., **93**, 562 (1991).
6. B.M. Clemens and J.A. Bain, MRS Bulletin, **17**, 46 (1992).
7. E.E. Fullerton, I.K. Schuller, H. Vanderstraeten, Y. Bruynseraede, Phys. Rev. B, **45**, 9292 (1992).
8. H. Miyajima, K. Sato and T. Mizoguchi, J. of Appl. Phys., **47**, 4669 (1976).
9. J.M. Sanchez, J.L. Morán-López, C. Leroux and M.C. Cadeville, J. Phys: Cond. Matt., **1**, 491 (1989).
10. D.W. Hoffman and J.A. Thornton, J. of Vac. Sci. Technol., **16**, 134 (1979).
11. D.W. Hoffman and J.A. Thornton, J. of Vac. Sci. Technol., **20**, 355 (1982).
12. D.W. Hoffman, Thin Solid Films, **107**, 353 (1983).

MAGNETIC AND MAGNETO-OPTIC PROPERTIES OF PtFe(001) AND PtCo(001) THIN FILMS

Bruce M. Lairson, Mark R. Visokay, Robert Sinclair and Bruce M. Clemens
Department of Materials Science and Engineering
Stanford University, Stanford, CA 94305-2205

ABSTRACT

We report on the magnetic and magneto-optical properties of PtFe and PtCo intermetallic thin films when they have the CuAu(I) tetragonal structure and their crystallographic c axis is oriented out of the film plane. These films possess large perpendicular magnetic anisotropy energies. We observe changes in the magneto-optic Kerr rotations of Pt-Fe and Pt-Co alloys associated with the formation of the uniaxial CuAu(I) crystal structure. In particular, we report the observation of up to 60% enhancement in the magneto-optic Kerr rotation for ordered, epitaxial PtFe intermetallic alloy over that of the random face centered cubic alloy. This enhancement is wavelength dependent, with a peak in the visible light range at 2.0 eV.

INTRODUCTION

Thin films possessing perpendicular magnetic anisotropy are important for a number of applications, including magnetic recording. The Pt/Co and Pt/Fe alloy and multilayer systems have been studied extensively because they are found to possess perpendicular magnetic anisotropy when they are stacked along the [111] crystallographic direction, and because they have acceptable magneto-optic recording figures of merit for recording at short optical wavelengths. Here, we present magnetic and magneto-optic Kerr rotation results for multilayers based on a different kind of stacking, that of the naturally occurring superlattices PtFe and PtCo, consisting of atomic monolayers stacked along the [001] axis. These phases possess large magnetocrystalline anisotropy, approaching 20×10^6 ergs/cm³. They are also of interest in thin film form because of the large magneto-optic Kerr rotations available from PtCo and PtFe alloys and intermetallic compounds[1], their relatively large magnetizations (500-600emu/cm³), and their thermodynamic stability. The formation of these phases with the c axis oriented out of the film plane is accompanied by large perpendicular magnetic anisotropy and perpendicular remanent magnetization, as well as enhanced polar Kerr rotations at some wavelengths. The ordered PtFe and PtCo intermetallic compounds have Curie temperatures from 400 to 500°C, making thermomagnetic writing possible, although the transition temperature is higher than optimal. Alloying, for instance with Ni, produces CuAu(I) structure phases with lower transition temperatures.

SAMPLE PREPARATION

Epitaxial multilayers were grown by sputtering onto epitaxial Pt(001) oriented seed layers. The seed layers were deposited onto polished single crystals of MgO(001) using a

technique described elsewhere[2]. The equiatomic multilayers consisted of multiple bilayers of Pt/Fe and Pt/Co deposited at 100°C. This yielded epitaxial multilayers with the [001] cube axes out of plane for the FCC Pt and FCC Co in the Pt/Co multilayers, and BCC Fe and FCC Pt in the Pt/Fe multilayers. X-ray diffraction detected no other phases present in the as-deposited samples. After magnetic and X-ray measurements, the samples were annealed in a 5×10^{-7} Torr vacuum at temperatures from 475 to 640°C for 14 hours, forming the tetragonal phase with the unique axis oriented out of the film plane. The structural transformation which occurs upon annealing is accompanied by a change in the magnetic properties of the films[3,4].

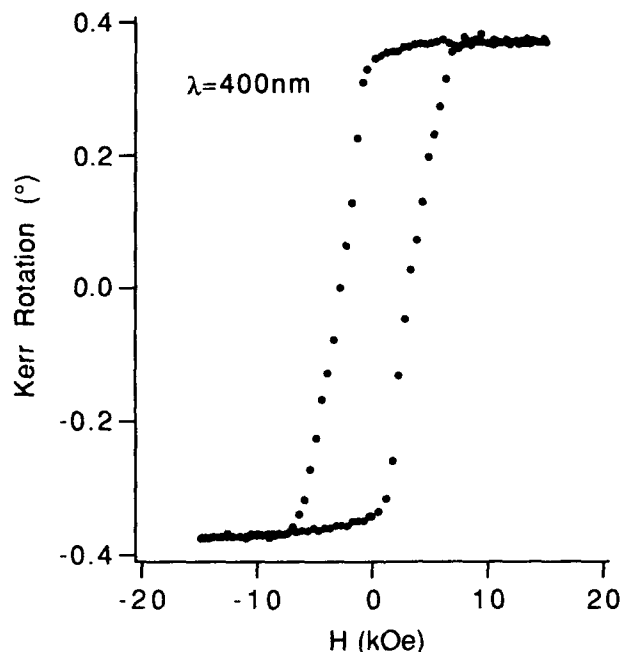


Figure 1: Polar Kerr rotation versus applied field for a 320Å thick PtCo(001) film.

MAGNETO OPTIC KERR HYSTERESIS LOOPS

Figure 1 shows a polar Kerr hysteresis loop for a PtCo film prepared in this fashion. Before annealing, the film consisted of 8 bilayers of 14Å Co(001) and 20Å Pt(001) deposited onto a 50Å Pt seed layer. The 320Å PtCo (001) film for which data are shown in the figure has a coercive field out of the film plane of 2.9kOe, a saturation field of 7kOe, and a perpendicular remanence ratio of 0.93. The remanent rotation is 0.35° at 400nm. Thermomagnetic writing was found to be possible on this film, although high write power (~200mW) was required. A 1000Å thick PtCo film prepared under similar conditions was found to have a saturation moment of 550emu/cm³, and a perpendicular magnetic anisotropy of 19×10^6 ergs/cm³.

Figure 2 shows the magneto-optic Kerr rotation from a PtFe(001) film. Before annealing, the sample consisted of 8 bilayers of 23Å Fe(001) and 29Å Pt(001), while after annealing, it exists as the oriented superlattice CuAu(1) phase with the c axis aligned out of

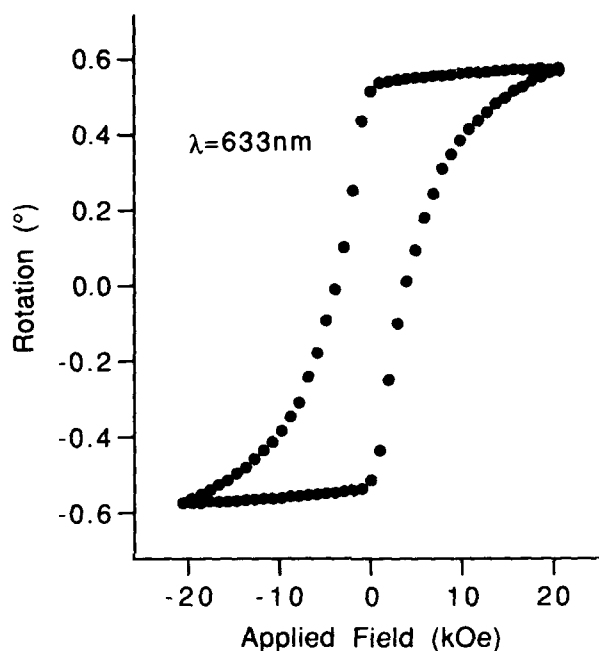


Figure 2: Polar Kerr rotation versus applied field for an approximately 300Å thick PtFe(001) film.

the plane. The seed layer has become a polycrystalline layer[4,5]. This film shows a coercive field of 3.5 kOe, but unlike the PtCo films, the film could not be saturated up to an applied field of 22kOe. This film, in addition to displaying symmetric X-ray peaks from the PtFe c-axis oriented phase, also shows peaks corresponding to a-axis oriented PtFe. The inhomogeneous microstructure which this implies may make domain wall motion difficult, causing some regions of the film to be difficult to magnetize. We have not yet determined the saturation magnetization of this thin film phase. It should be noted that the value of saturation rotation observed for the ordered PtFe phase at 633nm is quite large, 0.6°. Insight into the large value of Kerr rotation for the ordered uniaxial PtFe(001) can be gained by considering the wavelength dependence of the Kerr rotation.

KERR ROTATION SPECTRA

In addition to requiring perpendicular magnetic anisotropy, application of thin films to magneto-optic recording requires large magneto-optic Kerr rotations. It is therefore interesting to investigate whether enhancement of the Kerr rotation occurs as a result of forming

the ordered PtFe and PtCo phases. Recently, increases of the Kerr rotation have been reported in polycrystalline Fe/Cu[6], and for ultra thin epitaxial Fe/Au[7]. In some cases, enhancements of up to two times the rotation of pure Fe have been reported. Several sources for these enhancements have been proposed. In the case of epitaxial Fe/Au, the appearance of a wavelength-dependent peak in the MOKE spectrum was attributed to the development of a d-surface band, whose characteristics were reflected in the MOKE spectrum. Such increases in the MOKE rotation are of obvious scientific interest, and are also of technological interest for magneto-optical recording if such enhanced rotations are accompanied by perpendicular magnetic anisotropy.

Changes in the MOKE spectrum are expected due to site ordering of an alloy. For intra-band transitions, increased rotation can occur because of Fermi surface changes and because of the greater electronic relaxation times associated with the greater regularity of the ordered lattice relative to that of the randomly occupied lattice. Inter-band electronic effects are also expected upon ordering of a random alloy, particularly in the case where a strong net structural anisotropy appears, since this anisotropy correlates with the existence of uniaxial electronic states which do not exist in the disordered (cubic) alloy. Such states can appear in multilayers, for instance, as surface states. Site ordering is often accompanied by a change in the average number of nearest neighbors of a given species, which is also expected to affect inter-band optical transitions.

The ordering of PtFe and PtCo compounds are of interest in this regard. Both can exist as either a randomly site occupied FCC alloy (random alloy) or as a naturally occurring tetragonal superlattice structure. The tetragonal phase, denoted as CuAu(I), consists of alternate planes of Pt and Fe or Co stacked along the [001] direction. Physical properties will be affected by the electronic structure differences existing between the ordered compound and the random alloy. One such effect is the appearance of very strong uniaxial magnetic anisotropy in these compounds, in which the easy axis of magnetization lies along the [001] direction. Another possible result of the ordering is a change in the large magneto-optic Kerr rotations observed in the random alloys of these and similar systems[1].

Room temperature magneto-optic measurements were made between 1.2 and 3.5eV on a commercial Nihonkagaku Engineering BH-M800, with a Soma S010 monochromator and a halogen lamp. The angle of incidence was 15° from the surface normal. The magnetic field was varied between ± 20 kOe and was applied perpendicular to the sample surface. Saturation rotations were taken to be half of the total difference in rotation associated with reversing the direction of the 20 kOe field.

Figure 3 shows a comparison between the behavior of an ordered, oriented, CuAu(I) phase formed by annealing as described above, and an epitaxial FCC random PtFe alloy, with a MOKE spectrum which agrees with rotations measured for random alloys of PtFe bulk specimens[1]. It is clear from comparison of the behavior of multilayer samples (not shown here) that the wavelength dependence of the Kerr rotation varies with the bilayer period. However the most striking comparison is between the behavior of the random alloy and ordered compound. A dramatic change in the spectral dependence of the magneto-optic Kerr rotation is observed as a result of the formation of the ordered intermetallic phase. The rotation at 2.0 eV is approximately 60% higher than that of the compositionally modulated Pt/Fe multilayers. This feature is due to a change in the electronic structure of the alloy as a result of the anneal. The sample reflectivity we measure at the peak in the spectrum is 59%. Essentially the same MOKE spectrum is obtained for a variety of film thicknesses, confirming that the spectra we observe are not due to thin film

interference effects. Recent *ab initio* calculations have predicted the existence of such a peak in the MOKE spectrum for ordered PtFe[8].

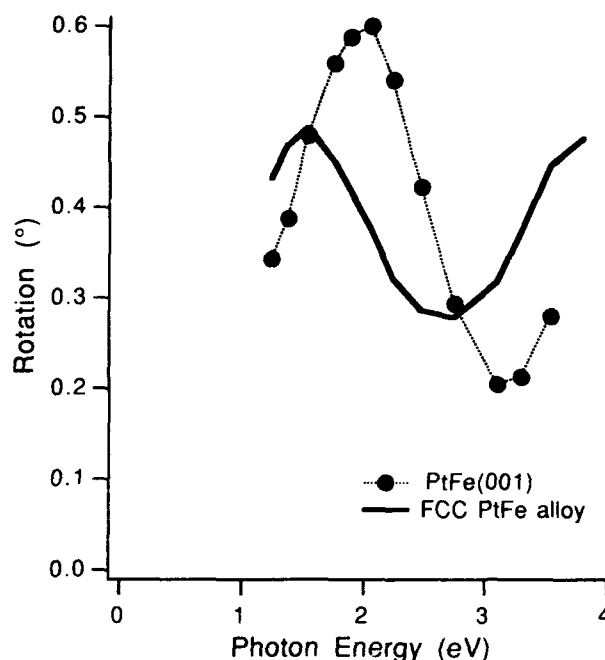


Figure 3. Saturation magneto-optic Kerr rotation vs. photon energy for the tetragonally ordered PtFe thin film and for a randomly site occupied equiatomic PtFe sample.

We have also observed small changes in the MOKE spectra when the ordered PtCo phase is produced, although the changes are much less pronounced than for the PtFe. The artificial multilayer spectra are similar to spectra which have been published for random FCC PtCo[1]. Changes in the spectral shape occur upon ordering for this system as well, although they are less pronounced than those which we observe for PtFe. Recent work on uniaxial PtCo films shows a small peak in the same wavelength range as we are here reporting for PtFe[9].

Several notable changes occur upon site ordering from a random FCC lattice to the CuAu(I) structure. The average number of 6 Fe nearest neighbors in the FCC phase changes to 4 for the Fe atoms and 8 for the Pt atoms, while the atomic site symmetry changes from cubic to tetragonal. We tentatively ascribe the new spectral feature in the MOKE spectrum to hybridization of the Fe 3d orbitals in the presence of the uniaxial crystal field, resulting in different energies and oscillator strengths than have been previously postulated for random FCC alloys. This notion is supported in the MOKE spectra of the ordered alloy compared that of the disordered alloy and of pure Fe[1] by the apparent absence of the customarily observed peak at approximately 1.2 eV. It is possible, however, that such a peak is present but obscured by the larger peak at 2.0 eV. Further

insight into the magneto-optic behavior of materials can also be gained from consideration of band structures. A more certain assignment of the 2.0 eV spectral feature will require magneto-optic rotation and ellipticity measurements over a wider energy range and a detailed comparison to band structure calculations for the tetragonal cell, as well as the production of other 3d transition metal-Pt and Pd compounds with the CuAu(I) structure.

We also note the possibility for observing anisotropy in the spectral shape depending on the direction of the wave vector relative to the unit cell, e.g. by measurement of longitudinal Kerr rotations for these films. Such anisotropy in Kerr spectra have been noted for the case of Gd[10]. Finally, we point out that many magnetic intermetallic phases exist, some of which may exhibit enhanced Kerr rotations upon ordering. Several of these phases have the CuAu(I) structure and possess uniaxial magnetic anisotropy, hence they may be candidates for magneto-optical recording applications.

CONCLUSIONS

In conclusion, we have shown that a strong enhancement of the MOKE spectrum occurs upon ordering of epitaxial precursor multilayers to form the PtFe(001) natural superlattice. Less dramatic changes in the MOKE spectra are also evident for the ordered alloys PtCo. These anisotropic thin films are promising for magnetic recording applications if they can be prepared easily with suitable coercivity and remanent perpendicular magnetization. Similar changes in MOKE spectra may be expected for other intermetallic compounds, particularly with the CuAu(I) structure.

The authors would like to thank E. Marinero, D. Weller, W. Harrison, T. Hufnagel, M. Kautzky, F. J. A. den Broeder and T. Miyamoto for helpful discussions and assistance. Financial support from Kobe Steel USA Inc. is much appreciated.

1. K. H. J. Buschow in *Ferromagnetic Materials*, Vol. 4, E. P. Wohlfarth and K. H. J. Buschow, ed., Elsevier Science Publishers B.V. (1988).
2. B. M. Lairson, M. R. Visokay, R. Sinclair, and B. M. Clemens, *Appl. Phys. Lett.*, **61**, 1390 (1992).
3. B. M. Lairson, M. R. Visokay, R. Sinclair, and B. M. Clemens, *J. Appl. Phys.* in press (1993).
4. B. M. Lairson, M. R. Visokay, R. Sinclair, and B. M. Clemens, *Appl. Phys. Lett.*, **62**, 639 (1993).
5. M. R. Visokay, B. M. Lairson, R. Sinclair, and B. M. Clemens, *Proceedings of Session 0, Spring 1993 MRS Meeting*.
6. T. Katayama, Y. Suzuki, H. Awano, Y. Nishihara, and N. Koshizuka, *Phys. Rev. Lett.*, **60**, 1426 (1988).
7. Y. Suzuki, T. Katayama, S. Yoshida, K. Tanaka and K. Sato, *Phys. Rev. Lett.*, **68**, 3355, (1992).
8. J. Sticht et al., unpublished.
9. D. Weller et al., these proceedings.
10. J. L. Erskine and E. A. Stern, *Phys. Rev. B* **8**, 1239 (1973).

**Valence Instability and Magnetic Polarization of Ce Atoms
near the Interface of Ce/Fe Multilayers Studied by Magnetic Circular
X-Ray Dichroism.**

F. KLOSE*, S. PIZZINI**, C. GIORGETTI**, O. SCHULTE**, F. BAUDELET**,
E. DARTYGE**, G. KRILL**, W. FELSCH* and A. FONTAINE**

*I. Physikalisches Institut, Universität Göttingen,
Bunsenstr. 9, 3400 Göttingen, Germany

**LURE, Bâtiment 209D, Université Paris-Sud, 91405 Orsay, France

ABSTRACT

An experimental study of conventional x-ray absorption and of magnetic circular x-ray dichroism has been performed on Ce/Fe multilayers at the Ce $L_{2,3}$ and the Fe-K edge, to characterize the impact of the interaction of Ce and Fe on the local electronic and magnetic structure of the interface. The spectra reveal that the interaction has two effects. First, on a depth scale of up to 15 Å near the interface, the Ce atoms adopt the electronic structure of the α -phase, with itinerant 4f states. Second, a large portion (≈ 10 Å) of these α -like Ce atoms is magnetically polarized and carries an ordered magnetic 5d moment. The Fe-3d and Ce-5d moments are antiferromagnetically coupled. Interface mixing on a length scale of the magnetic polarization can be excluded.

INTRODUCTION

During the last years, the synthesis and study of thin layer and multilayer structures composed of different metals have attracted considerable interest. This is because the properties of such artificial materials can be significantly different from those of any of the components. The present paper deals with multilayers prepared of cerium and iron. The stacking of a rare earth and a transition metal is particularly attractive in view of the resulting magnetic properties, as more localized 4f and itinerant d electronic states are combined. Consequences originating from the interaction of such states are immediately evident in intermetallic compounds. In CeFe_2 for example, a compound well known for its peculiar properties, which is of particular interest in the present context, delocalization of the Ce-4f states and quenching of their orbital moment due to a strong hybridization with the Fe-3d states results in ferromagnetic order with an unusually low Curie temperature (≈ 230 K), a small magnetic moment of the Fe ions ($\approx 1.4 \mu_B$) and a magnetic moment of the Ce ions ($\approx 0.5 \mu_B$) coupled antiferromagnetically to the Fe moment[1]. It has been shown recently that the saturation magnetization of Ce/Fe multilayers at room temperature is considerably reduced as compared to bulk Fe[2]. This addresses the problem of the interaction of Ce and Fe at the interface of these multilayers. It is the aim of this work to provide a microscopic characterization of the electronic and magnetic structure at the Ce-Fe interface. This information is derived by absorption spectroscopy at the $L_{2,3}$ edges of Ce and the K edge of Fe with circularly polarized hard x-rays, taking benefit from the atomic selectivity of the method and the appearance of magnetic dichroism near the absorption edges involved.

MAGNETIC CIRCULAR X-RAY DICHOISM

Conventional x-ray absorption spectroscopy at the $L_{2,3}$ edges of rare earths have been widely used to study their electronic states in intermetallic compounds. The method is of particular importance for Ce systems with their unusual properties which are connected to an anomalous electronic 4f configuration[3]. The interpretation of the spectra has been a matter of controversy, but it has been shown that they yield a reliable image of the rare-earth ground state configuration, in spite of final state effects if the interactions between the photoelectron and the remaining electronic system is properly taken into account [4]. Then the degree of delocalization of the Ce-4f states which varies with the local environment is sensitively reflected in the $L_{2,3}$ absorption-edge profiles.

With circularly polarized x-rays, electrons excited from a core level are spin polarized[5]. The transitions of such electrons into exchange-split unoccupied states at the same site then allows the study of local magnetic properties of the absorbing atomic species in a ferromagnetic or ferrimagnetic material, because the absorption process depends on the polarization direction of the incident light with respect to the direction of the magnetization. This magnetic circular x-ray dichroism (MCXD) is governed by spin-selective electric dipole transitions in the presence of spin-orbit interaction in the initial and final states[6]. MCXD studies performed on multilayers of Nd/Fe[7], Co/Pt[8], Co/Pd[9] and Co/Cu[10] or on ultrathin Fe layers[11] have underlined its importance as a tool for getting access to interfacial magnetism or magnetic anisotropy.

In spite of large efforts the present level of understanding of the MCXD process is rather limited. In the one-electron approach[12], at the $L_{2,3}$ edges of a rare earth and the K edge of a 3d transition metal only the dipole-permitted 2p to 5d and the 1s to 4p transitions contribute to the absorption process. In the case of the rare-earth $L_{2,3}$ and the 3d-transition-metal K edges the dichroic signal essentially results from the spin polarization of the unoccupied 5d and 4p band states, respectively. The 4f and 3d electron states, mainly responsible for the magnetic properties of the material, are only probed indirectly via their exchange coupling with the states reached in the absorption process. Let us point out that the relation between the MCXD signal and the total magnetic moment of the absorbing atom is a matter of a current debate[9-13]. In general the integrated dichroism signals at the individual edges are not proportional to this moment.

EXPERIMENTAL RESULTS

The Ce/Fe multilayers for the present investigation were grown by ion-beam sputtering using Ar gas in an UHV chamber (base pressure $\leq 5 \cdot 10^{-10}$ mbar) on Kapton foils coated with a 10 Å thick Cr buffer layer. Partial pressures of residual gases (e.g. O₂, N₂, H₂O) were below 10^{-10} mbar during deposition. The substrate holder was cooled to liquid nitrogen temperature to minimize diffusion. The samples were protected from oxidation by a 60 Å thick Cr top layer. The deposition process was controlled by a quartz rate monitor and a computer. Deposition rates were typically 0.5 Å/s, the total thickness of the multilayers was near 4000 Å.

The multilayers had been well characterized previously[2, 14]. The structure of the individual Fe and Ce layers depends on their thickness t_{Fe} and t_{Ce} . For the spectroscopic measurements these were chosen such that Fe is crystalline with bcc structure ($t_{Fe} > 24$ Å) and Ce is amorphous ($t_{Ce} < 70$ Å). The Fe layers are strongly textured, with their densest plane (110) in the film plane. The lateral extension of the crystallites is between 80 and 100 Å. Special efforts were devoted to the structural characterization of the interfaces. ⁵⁷Fe Mössbauer spectroscopy reveals that a 5 to 7 Å thick part of the individual Fe layers shows a very small hyperfine field splitting[15], which must be attributed to the influence of the interfaces. This signifies that nominally less than 2 atomic layers of Fe take part in the formation of a Ce/Fe interface. The considerable sharpness of the interfaces was confirmed by small-angle x-ray scattering and subsequent Monte-Carlo simulations of the diagrams[14]. It was found that diffusion is negligible, and fluctuations in the number of atomic layers of the individual Ce and Fe layers, representing "roughness" at the interfaces, are limited to less than ± 1 atomic layer. It can be concluded then that the periodic array of the components in the multilayers is very regular and that the interfaces are sharp. All samples were checked by measurements of the bulk magnetization. The Curie temperatures are far above room temperature, indicating that the individual Fe layers dominate the magnetic properties.

The x-ray absorption spectra were measured in transmission mode at room temperature mainly on the energy-dispersive spectrometer of the DCI storage ring at LURE, using a position-sensitive detector. The MCXD spectra were recorded at 0.3 mrad below the positron orbit plane where the light is right circularly polarized to 80% for two opposite directions of the external magnetic field B_+ and B_- . The field is applied at grazing incidence to the multilayer planes and amounts to 0.5 T, which is strong enough to saturate the magnetization (the samples show in-plane anisotropy). Details of data collection and the experimental setup are described elsewhere[7,16].

Special attention was paid to possible oxygen contaminations of Ce. Separate measurements on a Ce film (γ -Phase) prepared in the way as the other samples testify that the near-edge structures of CeO₂ in the $L_{2,3}$ spectra were absent. The MCXD spectra are presented by the

difference $\mu^-(B_+) - \mu^-(B_-)$ where $\mu^-(B_+)$ and $\mu^-(B_-)$ are the absorption coefficients for right-circularly polarized x-rays (helicity $-h$) and the two field directions B_+ , parallel and B_- , antiparallel to the wave vector of the light. The absorption coefficients μ^- are normalized to one far beyond the edge. This procedure makes the spectra independent of the amount of Ce probed in a measurement.

Fig. 1 shows the Ce L₂ x-ray absorption spectra of three Ce/Fe multilayers with constant thickness of the individual Fe layers ($t_{Fe} = 29 \text{ \AA}$). The results obtained for Ce metal and the compound CeFe₂ are shown for comparison. Differences in the absorption profiles of these Ce systems, which are immediately apparent, reflect differences in the 4f configuration.

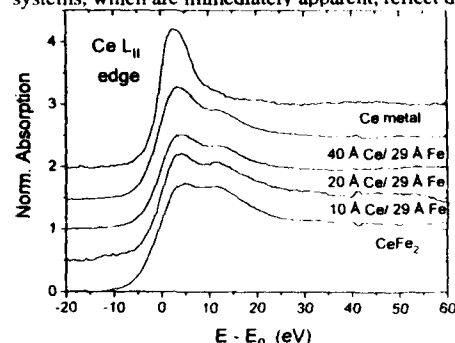


Fig. 1 Normalized Ce-L₂ x-ray absorption spectra of Ce/Fe multilayers (Fe thickness 29 Å, total thickness ≈ 4000 Å), γ Ce metal and the intermetallic compound CeFe₂.

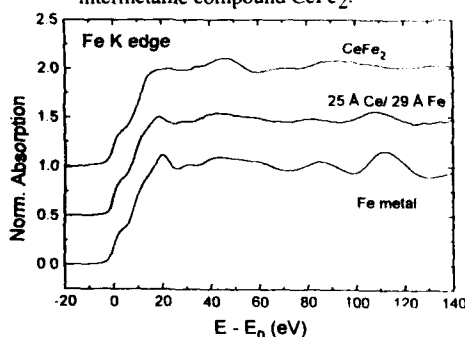


Fig. 2: Normalized Fe-K x-ray absorption spectra of a Ce/Fe multilayer (thickness ≈ 4000 Å), bcc Fe metal and CeFe₂.

In contradistinction to the L₂ spectrum of Ce metal which shows the "white-line" profile of the γ phase with its well-localized 4f electron, those of the multilayers exhibit a second peak located at ≈ 10 eV above the first one and approach, with decreasing thickness of the Ce layers, the spectrum of CeFe₂. This compound is a well-known α-Ce-like system, with delocalized 4f states owing to a strong hybridization of the 4f and conduction band states[1]. The double-peak structure of the Ce-L₂ edge profiles then is a signature of final states effects and reflects the two possible screening mechanisms of the 2p core hole, via a 4f or a 5d electron. The changes in relative intensities of the two peaks in the L₂ spectra of the Ce/Fe multilayers as the Ce-layer thickness decreases indicates the presence of Ce with α-like 4f configuration in addition to γ-like Ce with 4f¹ configuration. The most obvious interpretation is to assume that the α-like Ce atoms are located in the interface region and the γ-like ones in the core of the Ce layers.

In Fig. 2, the conventional x-ray absorption spectra at the Fe K edge of a representative Ce/Fe multilayer, Fe metal and CeFe₂ are compared. Obviously, all features of the bcc-Fe are reproduced for the multilayer and we notice the difference with the case of CeFe₂.

MCXD signals were observed at both the L_{2,3} edges of Ce (Fig. 3, L₂ edge) and the K edge of Fe (Fig. 4) of the multilayers. As for the total absorption spectrum, the magnetic absorption signal at the Fe K edge of the multilayers is a close image of the corresponding signal of Fe metal. It is remarkable that at least a large portion of the Ce atoms in these multilayers carry an ordered 5d magnetic moment at room temperature. As the total absorption signal at the Ce-L_{2,3} edges, the MCXD signal consists of two contributions split by roughly the same energy in both cases. But contrary to the total spectrum, the amplitude ratio of the two lines does not vary with the Ce-layer thickness t_{Ce} in the dichroic spectrum, in spite of a considerable increase of the amplitudes themselves with decreasing t_{Ce} (compare Figs. 3 and 1). Amplitude ratio, splitting,

relative line widths and sign (negative for L₂ positive for L₃) i.e. the overall structure are almost equal to the MCXD spectrum of the α -Ce-like compound CeFe₂ well below its Curie temperature ($T_C \approx 230$ K) [13,16]. It can be concluded then that only α -like Ce atoms carry the ordered magnetic moment reflected in the MCXD signal.

To obtain an estimate of the amount of α -like Ce, we apply a phenomenological analysis, superposing the measured spectra of Ce metal and CeFe₂. The result, expressed in partial thickness of α -like Ce in the individual Ce layers, is shown in Fig. 5a. The data approach

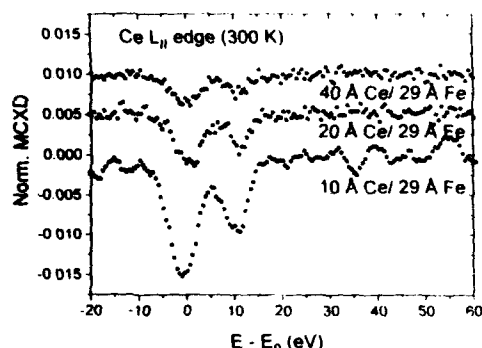


Fig. 3: Normalized MCXD spectra at the Ce-L₂ edge of Ce/Fe multilayers (Fe-layer thickness 29 Å, thickness ≈ 4000 Å) in an external magnetic field at room temperature.

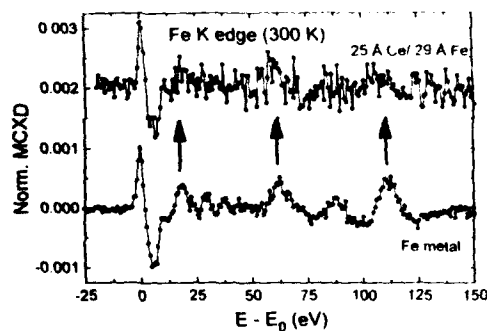


Fig. 4: Normalized MCXD spectra of the Fe-K edge of a Ce/Fe multilayer (thickness ≈ 4000 Å) and bcc Fe metal in an external magnetic field of 0.5 T at room temperature.

It is essential to point out that the MCXD signal does not originate from a possible Ce-Fe compound or alloy at the interface, in spite of the similarities to CeFe₂ just mentioned, since the intensity varies with the amount of α -like Ce in the multilayers, for a fixed thickness of the Fe layers. Furthermore, the magnetic ordering temperatures of all Ce-Fe compounds and alloys known are far below room temperature [18], while the dichroism at the Ce-L_{2,3} edges is observed at room temperature. The overall intensity of the signal decreases with the thickness of the Ce layers. This reveals clearly that it is induced by the Fe layers. Indeed, measurements performed down to 4.2 K demonstrate that the integrated MCXD intensity follows rather closely the temperature variation of the average bulk magnetization of the multilayers. Fig. 5b shows the

saturation value for the α -like Ce part of somewhat below 30 Å for large Ce-layer thicknesses. According to the results of the structural investigations reported above which exclude diffusion [14], this value is much too large to be attributed to a chemical effect which might result from the close proximity of Ce and Fe at the interface. Moreover this is ruled out by the results we get at the Fe K edge. We suggest that Ce near the interface adopts, on a considerable length scale, the α -like electronic configuration and hence a smaller atomic volume [17] to reduce the misfit and strain at the interfaces.

Indeed, the thicknesses of the individual Ce layers in the multilayers under study determined from small-angle x-ray diffraction are significantly smaller than the nominal ones calculated from the mass coverage of the quartz crystal of the thickness monitor and the density of crystalline γ -Ce [14]. This is surprising in view of the amorphous structure of the Ce layers. Apparently, the decrease in thickness due to the adoption of the α -like state outweighs the increase which should result from the lower density of the amorphous structure. An important effect is the driving of mechanism for the magnetic order in the Ce layers near the interface.

integrated intensity of the MCXD spectrum referred to the α -like part of the individual Ce layers as a function of their thickness t_{Ce} , for $t_{\text{Fe}} = 29 \text{ \AA}$. A constant value is adopted for t_{Ce} somewhat above 20 \AA .

The most obvious way to understand this result is to interpret the Ce-layer thickness of $\approx 20 \text{ \AA}$, where the normalized MCXD data merge into a constant value, as the effective thickness of the magnetically polarized Ce atoms in these multilayers. This value for the "magnetic extension" of the interface ($\approx 10 \text{ \AA}$) by far surpasses the above mentioned structural irregularities due to roughness, which were determined by small-angle x-ray diffraction [14]. (We recall that there is no diffusion).

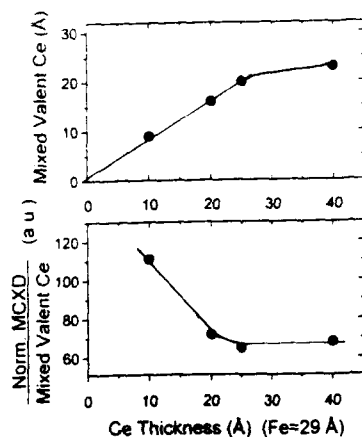


Fig. 5 a) Partial thickness of α -like (mixed-valent) Ce near the interfaces versus the total thickness of the Ce layers. (upper curve)
b) Integrated normalized MCXD intensity referred to the contribution of α -like (mixed valent) Ce as a function of the total Ce-layer thickness. (lower curve)

The results imply that the Fe layers induce, via a 3d-5d exchange interaction near the interface, a magnetic polarization of the 5d states of the α -like Ce atoms, which extends 3 to 4 atomic layers into the Ce layers on each side of the interface. The pronounced up turn of the normalized MCXD intensity for the multilayer Ce10Å/Fe29Å displayed in Fig. 5b finds a natural explanation in that for this sample the thickness of the Ce layers equals the effective magnetic thickness and hence both Fe layers neighbouring a Ce layer contribute to its magnetic polarization.

From the signs of the MCXD signals, which are identical to those found in CeFe₂, we can conclude that there is an antiferromagnetic coupling between the 3d moments of Fe and the 5d moments of α -like Ce near the interfaces in the multilayers. This explains the considerable reduction of the bulk magnetization in the multilayers (only $\approx 70\%$ of the value of the bulk bcc Fe, almost independent of the thickness of the Ce layers [2]).

There is evidence that, quite generally, the MCXD intensity at the L_{2,3} edges of a rare earth and the magnitude of the 5d magnetic moment of the probed atom are linearly related in a rare-earth intermetallic compound, if the 4f orbital moment is quenched [13]. The ratio of the integrated dichroic L₂ and L₃ intensities equals -2 in these systems, which is commonly used as their fingerprint. The L₂/L₃ branching ratio found for the Ce/Fe multilayers is close to this value.

A similar magnetic polarization of a paramagnetic rare-earth metal near the interface with bcc Fe in a layered structure has been observed before, on a comparable length scale, for Nd/Fe multilayers by MCXD at the Nd L₂ [7] edge and for thin Sm overlayers on Fe(100) by spin-resolved 4f photoemission [19]. The Ce/Fe system discussed here is unique in the sense that Ce atoms with localized as well as itinerant 4f states are present in the layered structure and that only the latter ones have their 5d states magnetically polarized.

In conclusion, we have demonstrated that x-ray absorption spectroscopy can be used to obtain information on the interaction between Ce and Fe at the interface of Ce/Fe multilayers. Ce adopts, on a considerable length scale near the interface, the electronic structure of the x-phase which is characterized by delocalized 4f states. It can be derived from the spin-resolved absorption spectra that, on a large portion of these atoms, Fe induces an ordered magnetic moment of 5d origin, which is antiferromagnetically coupled to the Fe moment. The spectra are similar to the ones for CeFe₂, but it has been shown previously that Ce and Fe are well separated near the interfaces of the multilayers. Hence the compound and the artificially layered structure

are quite different systems.

ACKNOWLEDGEMENTS

We thank Dr. Ph. Bauer, Université de Nancy I, for performing Mossbauer experiments. The authors from Gottingen acknowledge the kind hospitality of the Orsay group. The work was supported by SFB 345 of the Deutsche Forschungsgemeinschaft.

REFERENCES

- [1] O. Eriksson, L. Nordstrom, M.S.S. Brooks, and B. Johansson, Phys. Rev. Lett. **60**, 2523 (1988).
- [2] J. Thiele, F. Klose, A. Schurian, O. Schulte, W. Felsch, and O. Bremert, J. Magn. Mater. **119**, 141 (1993)
- [3] see: Handbook on the Physics and Chemistry of Rare Earths, edited by K. A. Gschneidner, L. Eyring, and S. Hufner, Vol. **10**, (North Holland, Amsterdam, 1987)
- [4] D. Malterre, Phys. Rev. B **43**, 1391 (1991)
- [5] U. Fano, Phys. Rev. **178**, 131 (1969); **184**, 250 (1969)
- [6] G. van der Laan, Phys. Rev. Lett. **66**, 2527 (1991); J. Phys. Condens. Matter **3**, 1015 (1991)
- B. T. Thole and G. van der Laan, Phys. Rev. Lett **67**, 3306 (1991)
- [7] F. Baudelet, E. Dartyge, A. Fontaine, C. Brouder, G. Krill, J. P. Kappler, and M. Piecuch, Phys. Rev. B **43**, 5857 (1991)
- [8] S. Rüegg, G. Schütz, P. Fischer, and R. Wienke, J. Appl. Phys. **69**, 5655 (1991)
- [9] Y. Wu, J. Stohr, B. D. Hermsmeier, M. G. Samant, and D. Weller, Phys. Rev. Lett. **69**, 2307 (1992)
- [10] S. Pizzini et al., MRS Spring Meeting, San Francisco 1993
(This conference Symposium Q1)
- [11] J. G. Tobin, G. D. Waddill, and D. P. Pappas, Phys. Rev. Lett. **68**, 3642 (1992)
- [12] C. Brouder and M. Hikam, Phys. Rev. B **43**, 3809 (1991)
- [13] C. Giorgetti, S. Pizzini, E. Dartyge, A. Fontaine, F. Baudelet, C. Brouder, G. Krill, and J. P. Kappler, submitted to Phys. Rev. B
- [14] F. Klose, M. Steins, T. Kacsich, and W. Felsch, J. Appl. Phys., in press.
- [15] P. Bauer (private communication)
- [16] F. Baudelet, C. Brouder, E. Dartyge, A. Fontaine, J. P. Kappler, and G. Krill, Europhys. Lett. **13**, 751 (1990)
- [17] The γ -to- α phase transition in Ce metal is connected with a 17 % decrease of the atomic volume (K. A. Gschneidner, Jr., Bulletin of Alloy Phase Diagrams **11**, 216 (1990))
- [18] The only compounds are CeFe_2 and $\text{Ce}_2\text{Fe}_{17}$; in addition, amorphous alloys exist.
- [19] E. Vescovo, R. Rochow, T. Kachel, and C. Carbone, Phys. Rev. B **46**, 4788 (1992)

MAGNETIC PROPERTIES AND CRYSTALLOGRAPHY OF SELECTED Co/Pt MULTILAYERS WITH RARE-EARTH ADDITIONS

G.A. BERTERO, R.L. WHITE, AND R. SINCLAIR
Department of Materials Science and Engineering
Stanford University, Stanford CA 94305

ABSTRACT

We have sputter-deposited a series of Pt/Co multilayers with differing amounts of rare-earth (RE) in an effort to improve the uniaxial perpendicular anisotropy in these structures. The present work investigates the influence on the magnetic properties of Tb and Ho incorporated both at the interfaces of Pt/Co multilayers and into the Co layers. The uniaxial anisotropy improved significantly only for those multilayers that showed poor perpendicular anisotropy in the undoped state, in particular, those with large (~ 30 Å) bilayer periods. High resolution transmission electron microscopy was used to study these multilayers in cross-section. The multilayer structures present strong [111] texture with grain sizes ranging from 200 to 600 Å. It is found that the RE does not produce a significant change in the growth texture of the multilayers until a critical amount is introduced beyond which the multilayer structure amorphizes resulting in a compositionally modulated amorphous film.

INTRODUCTION

Pt/Co multilayer thin films (with the [111] out-of-plane crystallographic orientation) present maximum Kerr rotations at blue range wavelengths of the order of 0.5° or better depending on the overall composition [1], they have also been shown to display large magnetic coercivities and remanent perpendicular magnetization of about 100% [1-6]. In addition, Pt and Co have a natural tendency to deposit onto amorphous substrates with a [111] texture under most deposition conditions. Thus, these structures are good candidates for use as high density magneto-optic recording media. The most promising combination of properties in the Pt/Co multilayer structures is achieved when the individual Co layer thickness is about 2 monolayers (~ 4 Å for closed-packed planes) and the Pt layer thicknesses corresponding to 5 to 7 monolayers (~ 12 to 16 Å) [1-4]. Increasing the thickness of the Co layers, and maintaining the same Pt/Co ratio, results in a gradual decrease of the perpendicular magnetic anisotropy energy, K_\perp , ($K_\perp = K_u - 2\pi M^2$) [2] where K_u is the uniaxial crystal anisotropy and M is the magnetization in the film. For high density recording, the perpendicular anisotropy energy, K_\perp , becomes increasingly important because it plays a crucial role in the stability of the magnetic domains.

Rare earth-transition metal (RE-TM) alloys and multilayers are known to display large magnetic anisotropy [6-8]. A giant magnetostriction effect has also been reported in these systems [8] and therefore a contribution to K_\perp can be expected from this effect if present. In addition, Tb and Ho have been alloyed with Co and an anti-parallel alignment of magnetic moments was reported [7]. In a previous publication [9] we had shown that the introduction of one third of a monolayer of Tb or Ho at the interfaces of Pt/Co multilayers produced an increase in the perpendicular anisotropy only when the corresponding undoped multilayers displayed poor perpendicular anisotropy. It was argued then that no conclusive evidence of anti-parallel

alignment had been found in these systems between the moments of the Co and those of the RE and that therefore the mechanism by which this improvement in anisotropy was taking place was not an antiferromagnetic coupling as had been expected. In this present work, we deposited a series of multilayers with a larger amount of RE and with thicker Co layers in an effort to induce coupling between the Co and the Tb.

EXPERIMENTAL

Co/Pt multilayer thin films were produced by DC magnetron sputtering in argon onto thermally oxidized silicon substrates. A 100 Å thick Pt underlayer was first deposited to act as a seed layer for the subsequent film. The underlayer films were deposited at approximately 500 °C to optimize the $[111]_P$ out-of-plane texture with the multilayers grown at room temperature. The resulting structures were strongly textured $([111])$ multilayer thin-films. The base pressure in the deposition chamber was 2×10^{-9} Torr employing Ar sputtering pressures of 1.5 and 3 mTorr. Deposition rates were on the order of 0.5 Å/s and the samples were rotated during the deposition.

Magnetic characterization was done with a vibrating sample magnetometer (VSM), a torque magnetometer, and a magneto-optic Kerr rotation analyzer operated at 400 nm. Structural characterization was performed with x-ray diffraction and transmission electron microscopy (TEM) techniques. High resolution cross-section transmission electron microscopy (HRTEM) was performed in a Philips 430 TEM operating at 300 kV with a point resolution of approximately 1.9 Å. The cross section TEM samples were thinned by ion milling from both sides with 12° incidence angle in a LN₂ cooled stage. After perforation, a low angle ($\sim 5^\circ$), low voltage (2 kV) milling step of a few minutes on either side was performed.

RESULTS AND DISCUSSION

Figure 1 shows magnetization hysteresis (MH) curves for two multilayers with periods $(12.2 \text{ Å Co}, 18.1 \text{ Å Pt})_{12}$ and $(6.1 \text{ Å Co}, 2.9 \text{ Å Tb}, 6.1 \text{ Å Co}, 18.1 \text{ Å Pt})_{12}$. The incorporation of a monolayer of Tb (2.9 Å) within the Co layers is seen to produce an improvement in the shape of the loop. Specifically, the saturation magnetization is maintained to lower magnitudes of the applied field and an increase in the slope dM/dH at H_c is noticed. Torque magnetometry indicates a value of $0.4 \times 10^6 \text{ erg/cc}$ for the anisotropy energy for the sample in (a). This rather low value of K_\perp is in agreement with those reported in the literature which show a transition from in-plane to out-of-plane magnetic easy axis, i.e., a change from negative to positive values of K_\perp , for Co thicknesses of about 12 Å [10]. The perpendicular magnetic anisotropy energy for the sample in Fig. 1b is $1.8 \times 10^6 \text{ erg/cc}$. Thus, a four-fold increase in K_\perp is seen to occur with the Tb addition. Under the same deposition conditions, multilayers with periods $(8.1 \text{ Å Co}, 18.1 \text{ Å Pt})_{14}$ and $(4.1 \text{ Å Co}, 2.9 \text{ Å Tb}, 4.1 \text{ Å Co}, 18.1 \text{ Å Pt})_{14}$ showed no significant difference in their magnetic anisotropy energies. For these two films, the perpendicular anisotropy energies, K_\perp , were approximately 2.7 and $2.4 \times 10^6 \text{ erg/cc}$ respectively. These results are consistent with those discussed in Ref. 9 where it was observed that a change from in-plane to out-of-plane magnetic easy axis took place with the addition of one third of a monolayer of Ho or Tb at the Pt/Co interfaces but, that the perpendicular anisotropy for samples that showed good out-of-plane anisotropy (e.i., those with thinner Co layers) in the undoped

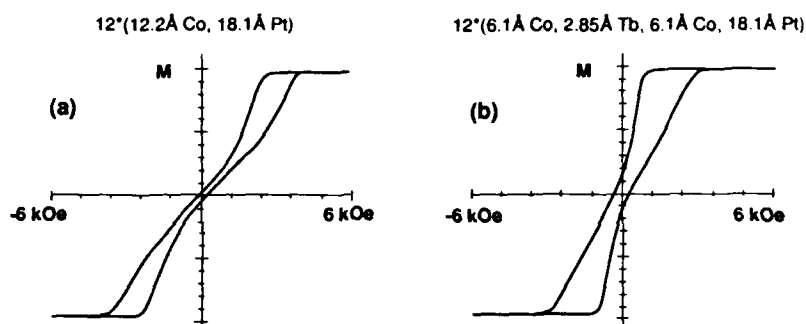


Figure 1: Magnetization hysteresis loops from a Pt/Co and a Pt/Co/Tb/Co multilayer. The film in b has one monolayer of Tb incorporated within the Co layers.

state, showed no improvement with the RE addition. Evidence for antiferromagnetic coupling of Co and Tb moments is absent in these multilayers as well. A slight decrease in the magnitude of the saturation magnetization (M_s) is indeed observed with the RE addition. However, this decrease in M_s can be explained simply by the fact that the period of the multilayer has been increased by an amount corresponding to the thickness of the RE introduced, thus causing a dilution effect similar to that of the Pt in the Pt/Co multilayers; in other words, by assuming that the moments of the RE are not polarized. On the other hand, magnetostriction alone cannot explain the magnitude of the increase in K_{\perp} . A plausible explanation for the increase in the anisotropy might be the formation of new interfaces when the Tb is deposited within the thick Co layers, or an interface modification effect, when the RE is deposited at the Pt/Co interfaces, giving rise to extra anisotropy through the symmetry breaking effect of the type described by Néel [11].

The absence of magnetic coupling in these systems is in contrast to the findings by T. Shinjo et al. in Fe-Dy multilayers [12,13], and Shan et al. [14] in Co/Dy multilayers where they report strong evidence for antiparallel coupling of the TM and RE at room temperature at the TM/RE interfaces. Similarly, FeCoTb amorphous alloys also show strong antiferromagnetic coupling. The Co-Tb and Co-Ho systems are very similar to Fe-Dy from both a chemical and a physical point of view. Therefore, it seems reasonable to assume that magnetic coupling can be induced at the interfaces in these multilayers as well. Thus, unless magnetic coupling between the Co and the RE is induced somehow, this approach seems non-feasible for increasing the value of K_{\perp} for the most technologically attractive multilayers, i.e., those with extremely thin Co layers.

Cross-section electron microscopy reveals very strong [111] textured films. It also shows that the grains are comparable in size for all the multilayers studied and basically determined by the grain structure of the Pt underlayer. Fig. 2 shows a high resolution TEM (HRTEM) micrograph of a Pt/Co multilayer with Tb doped interfaces. The horizontal fringes correspond to the traces of the closed packed planes lying in the plane of the film. A significant number of stacking faults can also be seen. These faults can be expected in order to explain the presence of Co in its usual hcp form. However, they not always coincide with the location of the Co-rich layers and are frequently seen within the Pt layers. Careful examination of this and other HRTEM micrographs suggest that most of the Co is in the fcc form. The introduction of RE into the Pt/Co multilayer structure does not seem to affect the growth texture of the multilayers. Fig. 3a shows a Pt/Co multilayer with one full monolayer deposited at one of the Pt/Co interfaces per period. The RE material in these multilayers cannot be resolved in the TEM even



Figure 2: High resolution TEM micrograph from a $(4.1 \text{ \AA} \text{ Co}, 1 \text{ \AA} \text{ Tb}, 15.9 \text{ \AA} \text{ Pt}, 1 \text{ \AA} \text{ Tb})_{30}$ multilayer showing a strongly diffracting grain in the $[011]$ -type zone axis.

when a full monolayer is deposited. This is probably a consequence of significant intermixing taking place since in these RE-TM systems the TM is known to be a fast diffuser. When an attempt was made to introduce a full monolayer of Tb at each Pt/Co interface in a $(4.1 \text{ \AA} \text{ Co}, 15.9 \text{ \AA} \text{ Pt})$ multilayer, the whole structure underwent a solid state amorphization reaction. The microstructure from this multilayer is shown in Fig. 3b where a compositionally modulated amorphous film has resulted. Solid state reactions are to be expected in these TM-RE systems when the RE is incorporated beyond a certain critical amount [15]. The magnetic coercivity of this film was approximately 90 Oe.

SUMMARY AND CONCLUSIONS

An effort was made to improve the perpendicular magnetic anisotropy in Pt/Co multilayers by the incorporation of RE elements into the layered structure. A series of Pt/Co multilayers were deposited with differing amounts of RE at the interfaces or alternatively within the Co layers. No evidence of antiferromagnetic coupling between the RE and the Co has been found in these structures at room temperature. However, an improvement in K_{\perp} was observed with the RE addition for some multilayer structures. This improvement was only seen for those multilayers with thicker Co layers for which the anisotropy energy is expected to be low in the undoped state. K_{\perp} was not significantly altered for the multilayers that displayed large magnetic anisotropies in the undoped state, namely those with thinner Co layers. TEM observations reveals strong $[111]$ textured films with 100% crystalline samples. However, deposition of two full monolayers of Tb in a 20 Å period Pt/Co multilayer resulted in amorphization of the whole structure including the thicker Pt layers.

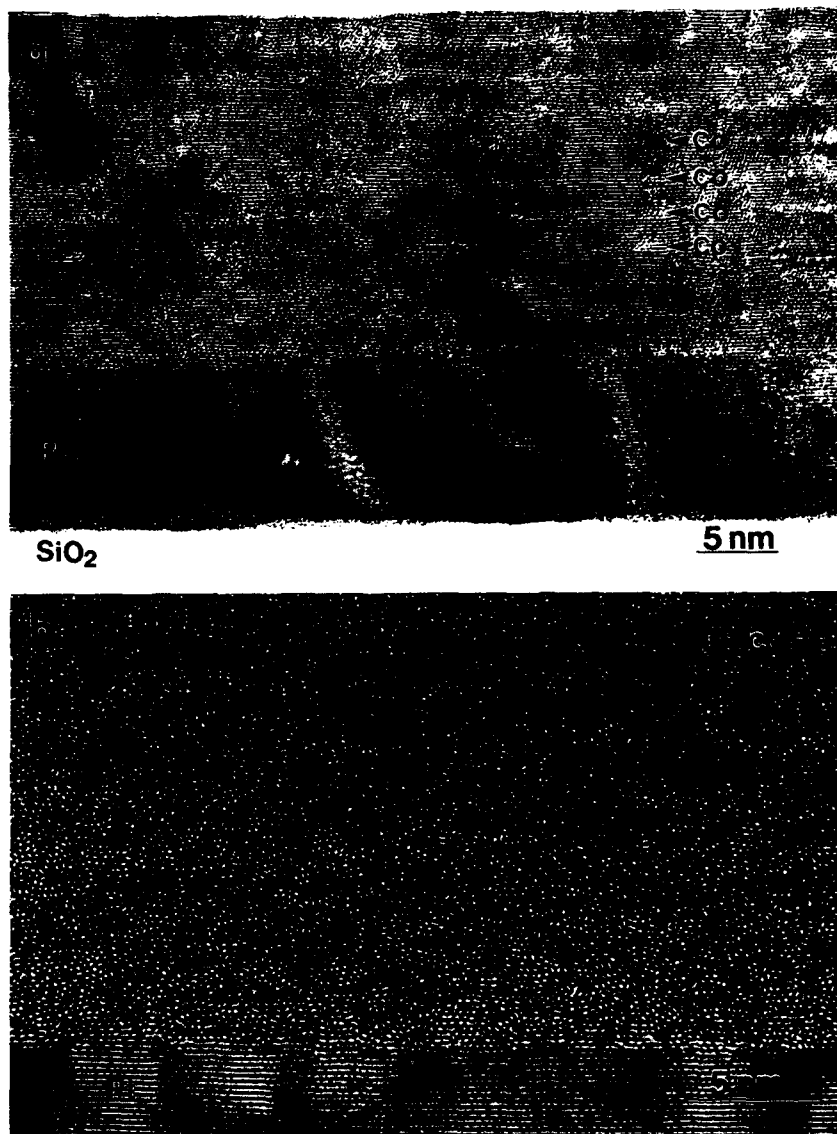


Figure 3: HRTEM micrographs from the two Pt/Tb/Co multilayers. a) Micrograph from a (4.1ÅCo, 2.9ÅTb, 15.9ÅPt) multilayer showing 100% crystalline structure. The horizontal fringes are traces of the (111) planes indicating the presence of strong texture in the film. b) Microstructure from a (4.1ÅCo, 2.9ÅTb, 15.9ÅPt, 2.9ÅTb) multilayer showing a compositionally modulated amorphous structure.

Acknowledgment

Financial support from Kobe Steel Inc. is greatly appreciated.

REFERENCES

- [1] D. Weller, H. Brandle, G. Gorman, C.-J. Lin, and H. Notarys, *Appl. Phys. Lett.*, **61**, 22, 1992, 2726
- [2] W.B. Zeper, H.W. van Kesteren, B.A.J. Jacobs, J.H.M. Spruits, and P.F. Carcia, *J. Appl. Phys.*, **70** (4), 15 August 1991, 2264
- [3] W.B. Zeper, H. van Kesteren, and P. Carcia, *Adv. Mater.*, **3** (1991), No. 7/8, 379
- [4] S. Hashimoto, Y. Ochiai, and K. Aso, *J. Appl. Phys.*, **67** (4), 15 February, 1990, 2136
- [5] F.J.A.M. Greidanus and W. B. Zeper, *MRS Bulletin*, April 1990, 31
- [6] M.H. Kryder, *J. Mag. Mag. Mater.*, **83** (1990), 1
- [7] S. Chikazumi, in: *Physics of Magnetism* (Wiley, New York, 1964), Chap. 20, p. 455
- [8] N.C. Koon, C.M. Williams and B.N. Das, *J. Magn. Mag. Mat*, **100**, 1991, 173
- [9] G. A. Bertero, R.L. White, and R. Sinclair, *J. Magn. Mag. Mat.*, in press (1993).
- [10] W.B. Zeper, F.J.A.M. Greidanus, H.W. van Kesteren, B.A.J. Jacobs, J.H.M. Spruit, and P.F. Carcia, *SPIE*, Vol **1274**, 1990, 282
- [11] L. Néel, *J. Phys. Radium*, **15**, 1954, 376
- [12] T. Shinjo, , K. Yoden, N. Hosoi, J.P. Sanchez, and J.M. Friedt, *J. Phys. Soc. Jap.*, **58**, No.11, Nov. 1989, 4255
- [13] N. Hosoi, K. Yoden, K. Mibu, T. Shinjo, and Y. Endoh, *J. Phys. Soc. Jap.*, **58**, No.5, May 1989, 1775
- [14] Z.S. Shan, D. J. Sellmyer, S.S. Yaswall, Y. J. Wang and J.X. Shen, *Phys. Rev. Lett.*, **63**, 1989, 449
- [15] T.C. Hufnagel, S. Brennan, A.P. Payne, and B.M. Clemens, *J. Mater. Res.* **7**, 1992, 1976

Author Index

- aan de Stegge, J., 93
 Alexander, Jr., C., 339, 345
 Altounian, Z., 405
 Anderson, S.G.H., 205
 Andrieu, Stéphane, 135, 473
 Ankner, J.F., 213, 761
 Arrott, A.S., 485
 Astrakharchik, E.G., 743
 Atwater, H.A., 363
 Auffret, S., 399
 Auner, G.W., 785

 Bain, James A., 677, 799
 Baker, John M., 697
 Ballentine, C.A., 309
 Barbara, B., 399
 Barbier, A., 519
 Bardou, N., 251
 Barlett, Darryl, 35
 Barmak, K., 205
 Barnard, J.A., 73, 191, 339, 345, 419
 Barradas, N.P., 773
 Bartenlian, B., 251
 Barthelemy, A., 737
 Bass, J., 47
 Baudelet, F., 811
 Baur, Ernst, 219
 Baumgarten, L., 643
 Bayreuther, G., 685
 Beaurepaire, E., 637
 Beauvillain, P., 251
 Belanger, D.P., 333, 755
 Bennemann, K.H., 445, 601
 Bennett, L.H., 237
 Berk, N.F., 431
 Berry, S.D., 779
 Bertero, G.A., 705, 817
 Beyers, R., 79
 Bian, X., 405
 Biswas, S.N., 375
 Bloemen, P.J.H., 93, 129
 Bobo, J.F., 467, 625
 Bochi, C., 309
 Bödeker, P., 213
 Boeglin, C., 519, 637
 Bogomolov, S.S., 309
 Borchers, J.A., 779
 Brändle, H., 501
 Brennan, Sean, 799
 Brockmann, M., 685
 Brühl, K., 213
 Brookes, N.B., 609
 Burlet, P., 767
 Butler, W.H., 59

 Camley, R.E., 303, 479
 Carrière, B., 519, 637
 Carter, Jr., Ernest L., 65
 Cates, J.C., 339, 345

 Cebollada, A., 41, 411
 Celinski, Z., 119, 485
 Chamberod, A., 399
 Chambliss, David D., 713
 Chandesris, D., 245
 Chang, Y., 609
 Chappert, C., 179, 251, 457
 Cheeks, T.L., 507
 Cheng, Yuanda, 393
 Chevalier, J.P., 749
 Chiang, S., 713
 Chouairi, A., 595, 601
 Clarke, Roy, 35
 Clemens, Bruce M., 197, 677, 731, 799, 805
 Cochran, J.F., 119
 Cochrane, R.W., 405
 Coehoorn, R., 93, 283
 Coffey, K.R., 85, 205
 Cohen, Susan L., 697
 Colmenares, C.A., 619
 Corno, J., 251

 Dartyge, E., 625, 811
 da Silva, M.F., 773
 De Boeck, J., 507
 de Jonge, W.J.M., 129, 283
 Deline, V.R., 79
 Demangeat, C., 321, 595
 Deville, J.P., 519
 de Vries, J.J., 93
 Dieny, B., 399
 Donovan, P.E., 743
 Dowben, P.A., 451
 Dreyse, H., 297, 595, 601
 Duif, A.M., 129
 Durand, O., 737, 749
 Duvail, J.L., 737

 Edwards, D.M., 171
 Egelhoff, Jr., W.F., 237
 Elmers, Hans-Joachim, 107
 Engel, Brad N., 531
 Erwin, R.W., 755, 779

 Falco, Charles M., 531
 Falicov, L.M., 23
 Farrow, R.F.C., 41, 411, 493, 501, 677, 791
 Felsch, W., 811
 Feng, Y.C., 357
 Ferrer, R., 399
 Fert, A., 737
 Fischer, H., 467, 473
 Florescu, V., 327
 Florez, L.T., 507
 Fontaine, A., 625, 811
 Fraundorf, P., 691
 Freeland, J., 651
 Freeman, A.J., 541
 Freitas, P.P., 773

- Fritzsche, Helmut, 671
 From, M., 119

 Galtier, P., 737, 749
 Garrison, K., 451, 609
 Geiss, R.H., 677
 Genin, J.B., 399
 George, B., 743
 George, J.M., 737
 Gerard, Ph., 185, 399
 Ghatak, Kamakhya P., 375
 Giesbers, J.B., 11
 Gijs, M.A.M., 11
 Giorgetti, C., 625, 811
 Glesener, J.W., 369
 Gorman, G., 79, 791
 Goto, S., 271
 Gouder, T.H., 619
 Gradmann, Ulrich, 107, 671
 Greig, D., 3
 Grünberg, P., 761
 Grunze, M., 631
 Güntherodt, G., 387
 Gurney, B.A., 289

 Haftek, E., 339, 345
 Hall, M.J., 3
 Han, S.-J., 333
 Hanna, C.B., 165
 Harbison, J.P., 507
 Haroun, A., 601
 Harp, G.R., 41, 411, 493, 501, 677, 791
 Harris, V.G., 369
 Harzer, J.V., 387
 Hashim, I., 363
 Heckmann, O., 245, 737
 Heinrich, B., 119, 485
 Hennen, L., 473
 Hennion, Martine, 135, 767
 Herman, F., 179
 Herrmann, M., 387
 Heys, A., 743
 Hickey, B.J., 3
 Hillebrands, B., 387
 Hilton, D., 779
 Himpel, F.J., 143
 Ho, P.S., 205
 Holl-Pellerin, John G., 205
 Holldack, K., 631
 Holody, P., 47
 Honma, Shigeru, 513
 Hood, Randolph Q., 23
 Hopster, H., 381, 451, 457, 565
 Hossain, S., 73, 419
 Howard, J.K., 85, 205
 Howson, M.A., 3
 Hricovini, K., 637
 Hu, Xiao, 513
 Huai, Y., 405
 Hubert, A., 485
 Hübner, W., 445
 Hubsch, J., 473
 Humbert, P., 289

 Hwang, Cherngye, 697
 Hylton, T.L., 85

 Idzerda, Y.U., 369, 659
 Inglefield, H.E., 309

 Jacquet, J.C., 749
 James, W.J., 425, 691
 Jankowski, A.F., 227
 Jay, J.P., 289
 Jensen, P.J., 601
 Jimbo, M., 271
 Johnson, K.E., 713
 Johnson, M.T., 93
 Johnson, P.D., 451, 609
 Jones, B.A., 165
 Jungblut, R., 93

 Kaendl, G., 643
 Kalki, K., 713
 Kanda, T., 271
 Katayama, Toshikazu, 153
 Kawazoe, Yoshiyuki, 513
 Keavney, D., 651
 Kellock, A., 79
 Keramidas, V.G., 507
 Kief, M.T., 237
 Kim, W.S., 315
 Kirschner, J., 631
 Klebanoff, L.E., 589
 Kleinfeld, T., 315
 Klose, F., 811
 Kohlhepp, Juergen, 107
 Konno, H., 485
 Konno, Toyohiko J., 731
 Krebs, J.J., 369
 Krill, G., 625, 637, 811
 Krishnan, Kannan M., 411
 Kusumoto, Y., 525

 Lacy, Fred, 65
 Lairson, Bruce M., 805
 Lam, Q.H., 41
 Lambeth, D.N., 357
 Laughlin, D.E., 357
 Lauhon, Lincoln, 35
 Le Fevre, P., 245
 Leal, J.L., 773
 Lecuyer, B., 251
 Lederman, D., 333
 Lee, S.-F., 47
 Lee, W.Y., 79
 Lefakis, H., 289
 Lenczowski, S.K.J., 11, 129
 Levy, Peter M., 53
 Li, Dongqi, 451
 Liao, L.X., 119
 Lind, D.M., 779
 Lochner, E., 779
 Loloe, R., 47
 Lugert, G., 685
 Lui, M., 755

- Mackenzie, John D., 351
 MacLaren, James M., 59
 Magnan, H., 245
 Majkrzak, C.F., 213, 431, 761
 Mallon, A., 185
 Mander, J.M., 171
 Mandrekar, Tushar, 35
 Mangin, Ph., 767
 Mankey, G.J., 143
 Marinero, E.E., 677
 Marks, R.F., 41, 411, 493, 501, 791
 Mathon, J., 171
 McGee, N.W.E., 93
 Megy, R., 251
 Meinel, K., 631
 Meny, C., 289
 Mibu, Ko, 531
 Miller, D., 79
 Modak, A.R., 437
 Mokrani, A., 321
 Morrish, A.A., 369
 Muniz, R.B., 171
 Myrtle, K., 119

 Naik, R., 785
 Nait-Laziz, H., 321, 595
 Nakayama, Takenori, 731
 Navas, E., 643
 Neiman, D., 79
 Newkirk, J.W., 425, 691
 Nicklow, R.M., 333
 Nolan, T.P., 705
 Nörtemann, F.C., 479
 Notarys, H., 791
 Nozieres, J.P., 289
 Nunez, V., 431

 O'Handley, R.C., 309
 Oepen, H.P., 631
 Ortega, J.E., 143
 Ouannasser, S., 601
 Ould-Mahfoud, S., 251

 Paduani, C., 333
 Panissod, P., 289
 Pappas, D.P., 369, 451, 457, 619
 Parker, M.R., 73, 191, 419
 Parker, Michael A., 85
 Parkin, S.S.P., 41, 179, 411, 437
 Pereira, L.G., 737
 Petroff, F., 737
 Pfau, L., 685
 Philips, B.A., 507
 Pick, S., 297
 Piecuch, Michel, 135, 467, 473, 625
 Pierre, J., 399
 Pinkvos, Heiko, 219
 Pizzini, S., 625, 811
 Pogosova, I.S., 387
 Poppa, Helmut, 219
 Pouliot, R.J., 589
 Pratt, Jr., W.P., 47
 Pringle, O.A., 425, 691

 Prinz, G.A., 369
 Pustogowa, U., 445

 Qiu, G., 339, 345

 Rabedeau, T.A., 41, 411, 493
 Ramaker, D.E., 659
 Ramos, C.A., 333
 Rao, U.M., 785
 Rau, C., 327, 577, 723
 Redon, O., 399
 Reinders, A., 93
 Rensing, Noa More, 197
 Richardson, Steven L., 65
 Rijks, Th.G.S.M., 283
 Rodmacq, B., 185, 399, 767
 Rossnagel, Stephen M., 697
 Rots, M., 773
 Rührig, M., 485
 Russak, Michael A., 697

 Sakuma, Akimasa, 257
 Sands, T.D., 507
 Savoy, R.J., 41, 79
 Schneider, C.M., 119, 631
 Schreyer, A., 213, 761
 Schroeder, P.A., 47
 Schulte, O., 811
 Scilla, Gerald J., 697
 Scott, J.C., 451, 457
 Sczigel, G., 251
 Seale, D., 73, 191, 419
 Shaw, K.A., 779
 Shinjo, Teruya, 531
 Sinclair, Robert, 705, 731, 805, 817
 Siriwardane, H., 425, 691
 Smith, David J., 431
 Soares, J.C., 773
 Speriosu, V.S., 289
 Stamps, R.L., 303, 479
 Starke, Kai, 643
 Stearns, Mary Beth, 393, 553
 Sticht, J., 501
 Storm, D., 651
 Ström-Olsen, J.O., 405
 Sugita, Yutaka, 257
 Sumi, S., 525
 Suzuki, Yoshishige, 153
 Swagten, H.J.M., 129
 Swartzendruber, L.J., 237

 Tan, M., 73, 191, 419
 Tanaka, M., 507
 Tang, H., 451, 457
 Teixeira, S.R., 399
 Teragaki, Y., 525
 Thangaraj, N., 411
 Thompson, C.V., 309
 Tobin, J.G., 227, 619
 Toney, M.F., 41, 411
 Torazawa, K., 525
 Tsuchiya, T., 351
 Tsui, Frank, 35

- Tsunashima, S., 271, 525
 Uchiyama, S., 271, 525
 Uher, Ctirad, 35
 Valentin, J., 315
 Valet, T., 737, 749
 Van Campen, D.G., 589
 Van Kempen, R.J.T., 129
 Van Leeuwen, Robert A., 531
 Vazquez, J., 79
 Veillet, P., 251
 Villeret, M.A., 171
 Visokay, Mark R., 705, 805
 Waddill, G.D., 227, 619
 Waknis, A., 73, 419
 Walker, J. Calvin, 651
 Walker, M.J., 3
 Walker, T.G., 381, 451
 Walters, G.K., 577
 Wang, B., 785
 Wang, Dingsheng, 541
 Wang, J., 333
 Weller, D., 251, 315, 387, 451, 457, 493, 501, 791
 White, R.L., 817
 Wiedmann, Michael H., 531
 Willekens, M.M.H., 129
 Willis, R.F., 143
 Wilson, R.J., 713
 Wolf, J.A., 761
 Wong, Eva M., 351
 Wu, Ruqian, 541
 Wurm, Karsten, 219
 Xu, J., 3
 Yang, Q., 47
 Zabel, H., 213, 761
 Zaluska, A., 405
 Zeidler, Th., 213, 761
 Zhang, Jiandi, 451
 Zhang, Shufeng, 53
 Zhang, X.-G., 59
 Zhao, Y., 785
 Zheng, Haixing, 351
 Zheng, N.J., 327, 723

Subject Index

- Ag_1Co_x , 79
 alloys, 493
 analytic approach, 513
 anisotropy, 107, 129, 251, 297, 309, 315, 327, 485, 493, 531
 magnetic, 493
 perpendicular, 129, 315, 531
 magnetic surface, 107
 annealing, 185, 197, 289, 339, 345, 773
 antiferromagnetic, 41, 197, 297, 303, 333, 381, 479
 alignment, 743
 coupled multilayers, 197, 303, 479
 insulating films, 333
 atomic
 force microscopy, 425
 interchange, 713
 model, 643
 Auger electron(s), 631
 diffraction, 659

 band
 filling, 179
 structure calculations, 501
 Barnas model, 283
 bet phase, 473
 bilayers, 297
 biquadratic, 135
 coupling, 761
 bound states, 165
 Brillouin light scattering, 119, 387

 Camley model, 283
 Ce/Fe multilayers, 811
 characterization, 651
 chemical ordering, 493
 circularly-polarized
 soft x-rays, 631
 x-rays, 619
 clusters, 601
 Co, 107
 Co-Ag, 419
 Co/Ag, 191
 $\text{Co}_x\text{Ag}_{1-x}$, 393
 cobalt ferrite, 351
 Co/Cr, 205
 CoCrTa/Cr, 357
 bilayers, 705
 Co/Cu, 41, 179, 205, 213, 437
 multilayers, 625
 $\text{Co}_x\text{Cu}_{1-x}$, 399
 coercive fields, 485
 coherent potential approximation, 59
 composition modulation, 799
 computer simulation, 513
 conversion electron Mössbauer spectroscopy, 685
 Co/Pt, 315, 493, 519
 alloys, 677
 multilayers, 705, 791
 CoPt₃, 501
 CoPt-alloy, 315, 387
 core-level photoemission, 619
 Co-Re superlattices, 773
 coupling, 3, 41, 107, 119, 129, 135, 143, 165, 171, 179, 213, 467, 479, 513
 bilinear, 119
 biquadratic, 119, 467
 exchange, 3, 41, 129, 171
 interlayer, 135, 179
 magnetic, 143, 513
 multilayered structures, 479
 oscillatory, 41, 107, 143, 171, 393
 RKKY, 165
 CPP-MR, 47
 Cr and Mn on Fe(100), 565
 critical behavior, 577, 755
 crystallographic texture, 357
 Cu, 93, 107, 219, 237
 Fermi surface, 93
 Cu/Co, 47
 Cu/(Ni/Fe), 47
 Cu/Si(001), 363

 2D-magnetism, 445
 density of states, 321
 dichroism, 227
 diffraction, 135
 diffusion, 205
 dislocation, 309
 domain, 315, 327, 387
 nucleation, 315
 size, 553
 structure, 327

 electron microscopy, 393, 437
 electronic
 states, 143
 structure, 445
 energy-resolved photoemission microscopy, 631
 enhanced magnetoresistance, 773
 enhancement of external field, 513
 etching, 525
 EXAFS, 245
 exchange, 3, 93, 119, 387
 coupling, 3, 93
 interaction, 119, 387

 4f levels, 451
 fcc-Fe, 237
 Fe
 films, 589
 on
 Au(111), 685
 Cu(001), 601, 619, 713
 samples, 723
 Fe/Au(100), 153

- Fe/Au/Fe sandwich films, 153
- Fe₉₀Au₁₀ films, 685
- FeCo/Pt, 227
- Fe/Cr, 11, 197, 761
- Fe/Cu multilayers, 625
- Fe/Ni(001), 485
- Fe₃O₄/NiO superlattices, 779
- Fe/Pt multilayers, 705
- Fermi surface, 93, 179
 - Cu, 93
- ferrimagnetic, 351
- ferromagnetic, 303, 467, 507
 - materials, 723
 - pinhole, 467
 - resonance, 785
- FeTaN films, 339, 345
- film growth, 219
- final-state character, 677
- Frank-van-der-Merwe, 457
- Fresnel contrast, 749
- GaAs substrates, 507
- Gd(0001), 451, 457, 565
- Gd/W multilayers, 743
- giant magnetoresistance (MR), 737
- glow discharge, 691
- grain
 - boundary diffusion, 205
 - size, 387
- granular, 393, 399, 405, 419
 - GMR, 73
 - structures, 405, 553
 - system, 399
- ground state, 303, 479
 - spin configuration, 303
- growth
 - mode, 713
 - on bcc-Fe(110), 713
- high(-)
 - moment, 339
 - resolution
 - electron microscopy (HREM), 705
 - transmission electron microscopy, 691
- highly polarized itinerant d electrons, 553
- hole concentration, 179
- hyperfine fields, 685
- hysteresis, 351
- improved sputtering practices, 697
- indirect magnetic coupling, 767
- initial growth mode, 601
- in-plane stress, 799
- interdiffusion, 685
- interface(s), 23, 197, 541, 705, 773
 - anisotropy, 791
- interfacial
 - effect, 697
 - exchange coupling, 779
 - sharpness, 799
- interlayer, 135
- intermetallic alloys, 493
- intermixing, 713
- iron
 - carbide films, 425, 691
 - whisker, 119
- island, 321
 - nucleation, 713
- Kerr
 - effect, 213, 237, 315, 327, 363, 445, 457, 493, 501, 531
 - in situ measurements, 531
 - microscopy, 315
 - optical loops, 457
 - signal, 237
 - rotation, 153, 501, 785
- Korringa-Kohn-Rostoker, 59
- L₁₀ structures, 705
- Larmor clock, 425
- LEED, 519
- low-
 - dimensional magnetic systems, 541
 - field magnetoresistance, 553
- magnetic, 143, 165, 171, 219, 227, 237, 271, 289, 297, 315, 339, 387, 393, 405, 425, 519, 531, 785
 - anisotropy, 297, 791
 - boundaries, 393, 553
 - circular
 - dichroism, 227, 541, 619
 - in photoemission, 631
 - x-ray dichroism, 625, 811
 - coercivity, 531
 - coupling, 565
 - domain(s), 315, 387
 - structure, 631
 - films, 425
 - imaging, 723
 - layered, 553
 - materials, 659
 - moment, 601
 - multilayers, 143, 165, 171, 519
 - performance, 697
 - precipitates, 405
 - properties, 237, 289
 - of Fe/Zr multilayer, 731
 - recording media, 691
 - soft, 339
 - storage, 143
 - surface
 - anisotropy, 671
 - studies, 219
 - thin films, 651
- magnetism, 251, 321, 445, 457
 - 2-dimensional, 445
 - surface, 457
- magnetization, 129, 309, 507, 773
 - perpendicular, 309, 507
- magneto-crystalline anisotropy, 541
- magnetometry, 363, 791
- magneto-optic, 153, 213, 351, 445, 785

- magnetoresistance, 3, 11, 23, 41, 47, 53, 59, 73, 79, 85, 129, 143, 185, 191, 197, 271, 283, 289, 393, 399, 419, 437, 743, 773
 - anisotropic, 283
 - field dependence, 73
 - giant, 3, 23, 41, 79, 85, 143, 271, 399, 419, 437
 - granular, 83
 - low field, 393
 - perpendicular, 11, 47
- magnetoresistive sensors, 697
- magnetostriction, 345
- magnetotransport, 53
- magnetron, 227, 339
 - dc sputtering, 339
 - sputter deposition, 227
- martensitic transformation, 713
- MBE, 3, 41, 93, 213, 473, 507
- MCDAD, 631
- melt-spinning, 399
- metallic multilayers, 749
- metastable bcc structure, 737
- microstructural, 11, 85, 425
- misfit
 - dislocation, 309
 - strain, 309
- Mn, 381
- MnFe/NiFe
 - exchange structures, 697
 - interface, 697
- MnGa, 507
- (MnNi)Ga, 507
- monolayer, 107, 297
 - Co, 107
- morphology, 405, 457
- Mössbauer spectroscopy, 651
- MR slope, 185
- multilayer, 3, 23, 47, 59, 129, 185, 191, 271, 333, 381, 513, 525
 - films, 799
- nanosstructure, 289
- ($\text{NCo}_{70}\text{Fe}_{30}$)_xAg_{1-x}, 399
- neutron, 135, 333, 393
 - diffraction, 135
 - polarized, 213
 - reflectivity, 213
 - scattering, 767
- Ni/Ag multilayers, 767
- Ni/Cu (001), 309
- NiFe, 363
- NiFe/Ag, 185
- ($\text{Ni}_{80}\text{Fe}_{20}$)_xAg_{1-x}, 399
- NiFeCo, 271
- NiFe/Cu/Co/Cu multilayers, 749
- NiFe/Cu/NiFe, 283
- Ni/Ni₈₀Cu₂₀/Cu/Si, 309
- nitrogen flow rates, 345
- NMR, 289
- noble metals on ferromagnetic substrates, 609
- nonlinear optics, 445
- nucleation, 315
- optical Kerr loops, 457
- ordered compounds, 501
 - (111) orientation, 525
- origin of interface polarization, 595
- oscillation period, 179
- oscillatory, 143, 165, 171, 213
 - coupling, 773
- oxide films, 351
- particle-surface scattering, 577
- Pd(111), 219
- Pd(111)/Co/X, 531
- permalloy, 59
- perpendicular
 - magnetic anisotropy, 677, 799
 - magnetization, 671
- phase separating, 419
- photoelectron spectroscopy (XPS), 205
- pinhole, 467
- planar doping, 737
- plasma-deposited, 425
- polarized, 213, 393, 425
 - d conduction electrons, 393
 - neutron(s), 425
 - reflectivity, 213, 761
- polycrystalline Fe film, 637
- potential, 53
 - well, 165
- Pt/Co, 525
 - multilayers, 799, 817
- pure ferromagnetics, 553
- quantum well, 53, 143, 153, 165
 - states, 53, 143, 153
- Re buffer, 773
- recording, 219
 - materials, 501
- relative permeability, 73
- residual gas impurities, 697
- rf-input power, 525
- RF
 - sputter, 357
 - sputtering, 749
- RHEED, 119, 363
- RKKY, 165, 179
- roughness, 525
- Rutherford backscattering spectroscopy, 393
- saturation
 - field, 3, 185
 - magnetization, 743
- scanning-ion microscopy with polarization analysis (SIMPA), 723
- scattering, 11, 425
 - dynamical, 425
 - electron-magnon, 11
- self-consistent mean-field parameterized tight-binding model, 595
- semiclassical, 283
- sensor for circular polarization of soft x-rays, 643
- single phase, 339

- SMOKE, 309
- sol-gel, 351
- spectra, 153
- spectroscopy, 393
- specular reflectivity, 761
- SPEELS, 381
- spin(-), 47, 53, 197, 283, 289, 303, 451, 479
 - channel model, 47
 - dependent scattering, 197, 737
 - ground state configuration, 303, 479
 - polarization, 595
 - of electrons, 723
 - polarized
 - electron spectroscopies, 451, 565
 - photoemission, 609
 - spectroscopies, 577
 - resolved photoemission, 589
 - scattering, 53
 - valves, 283, 289
 - waves, 303, 479
- SPLLEEM, 219
- sputtered, 185, 327, 339, 399
 - magnetron, 339
- strain, 309
- Stranski-Krastanov, 457
- stress, 345
- strong magnetic circular dichroism (MCD), 643
- structural origins, 677
- substrates, 773
- superlattices, 23, 41, 53, 135, 143, 153, 191, 213, 333, 437
 - Co/Cu (111), 41
 - potential, 53
 - wedged, 41
- surface(s)(-), 219, 245, 451, 519, 541
 - and
 - interface magnetism, 637
 - thin film magnetism, 643
- EXAFS, 245
- Gd(0001), 451
- magnetic studies, 219
- physics, 519
- states, 451
- vacuum interface, 577
- TbFe, 327
- TEM, 85
- temperature dependence, 11
- tetragonal structure, 245
- thin-films, 541
- three-dimensional Ising model, 755
- transition-metal multilayers, wedges, and films, 761
- transmission electron microscopy (TEM), 731, 737, 749
- tunneling time, 425
- UFe₂, 619
- ultrathin, 519
 - Fe(110) films on Cr(110), 671
 - layers, 595
 - magnetic films, 619
- underlayers, 525
- uniaxial perpendicular anisotropy, 817
- valence instability, 811
- valves, 289
- vanadium, 321
- volume anisotropy, 791
- W(110), 219
- whisker, 119
- XPS, 589
- x-ray, 191, 197, 205, 227, 333, 393
 - absorption, 619
 - spectroscopy (XAS), 227, 737
 - diffraction, 197, 731, 799
 - diffractometry, 191
 - photoelectron
 - diffraction, 659
 - spectroscopy (XPS), 205, 697
 - photoemission spectroscopy, 637
 - scattering, 333
- XTEM, 363